

**Best  
Available  
Copy**

AD/A-004 586

MATERIALS RESEARCH IN SUPPORT OF  
SUPERCONDUCTING MACHINERY - II

Alan F. Clark, et al

National Bureau of Standards

Prepared for:

Advanced Research Projects Agency

October 1974

DISTRIBUTED BY:

**NTIS**

National Technical Information Service  
U. S. DEPARTMENT OF COMMERCE



SEMI-ANNUAL TECHNICAL REPORTS ON MATERIALS  
RESEARCH IN SUPPORT OF SUPERCONDUCTING MACHINERY - II

for

1 March 1974 to 1 September 1974

Edited by

Alan F. Clark and Richard P. Reed  
National Bureau of Standards

and

Edward C. van Reuth  
Advanced Research Projects Agency

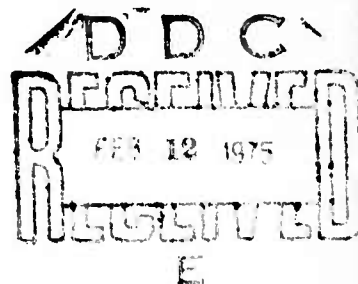
Sponsored by

Advanced Research Projects Agency  
1400 Wilson Boulevard, Arlington, VA 22209  
ARPA Order No. 2569 - Program Code 4 D 10

Contracted for 10 August 1973

by

✓ Cryogenics Division, Institute for Basic Standards  
✓ National Bureau of Standards, Boulder, CO 80302

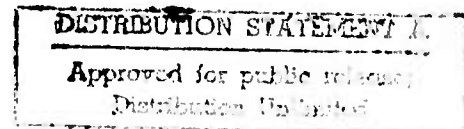


Subcontracts to:

Argonne National Laboratory  
Battelle, Columbus Laboratories  
General Electric Research and Development Center  
Martin Marietta Aerospace, Denver Division  
National Bureau of Standards Cryogenics Division  
Westinghouse Electric Research and Development  
Center

DISCLAIMER

The views and conclusions contained in this document are those of the authors and should not be interpreted as necessarily representing the official policies, either expressed or implied, of the Advanced Research Projects Agency or the U.S. Government.



SUBJECT TO CHANGE

Reproduced by  
NATIONAL TECHNICAL  
INFORMATION SERVICE  
U.S. Department of Commerce  
Springfield VA 2215

187

## SUMMARY

The second semi-annual technical reports are collected from six subcontractors on an ARPA sponsored program on the very low temperature properties of structural materials in support of superconducting machinery. The program is outlined and research progress is reported. Low temperature data are presented for the elastic, tensile, fatigue, and fracture properties, thermal expansion, specific heat, thermal and magnetothermal conductivity, electrical and magnetic properties of structural alloys. Effects of processing, and fabrication are also reported for many of the properties; weld and braze joint properties are included. Low temperature properties for composites are reviewed and limited tensile and flexure data at 4K presented.

## TABLE OF CONTENTS

	Page
SUMMARY.....	iii
INTRODUCTION.....	1
PROGRAM DESCRIPTION .....	1
FIRST YEAR'S PROGRAM .....	3
ORGANIZATIONAL CONTACTS .....	5
RESULTS HIGHLIGHTS.....	6
MATERIALS DATA TABLE .....	8
HANDBOOK.....	10
TECHNICAL REPORTS BY CONTRACTOR .....	ff.
ARGONNE NATIONAL LABORATORY	
Effects of Cyclic Loading on Electrical Conductivity of Superconducting Composites	
Fisher, E. S.	
Linz, R. J.	
Darby, J. G.	
BATTELLE - COLUMBUS LABORATORIES	
Low Temperature Thermal Expansion and Specific Heat Properties of Structural Materials	
Jelinek, F. J.	
Collings, E. W.	
GENERAL ELECTRIC COMPANY	
Composite Structural Materials Investigation at Cryogenic Temperatures	
McLoughlin, J. R.	
Hillig, W. B.	

MARTIN MARIETTA AEROSPACE, DENVER DIVISION

Study of Fracture Behavior of Metals for Superconducting  
Applications

Schwartzberg, F. R.

NATIONAL BUREAU OF STANDARDS

Thermal Conductivity

Hust, J. G.

Giarratano, P. J.

Magnetothermal Conductivity

Sparks, L. L.

Fickett, F. R.

Fatigue and Fracture Toughness Testing at Cryogenic  
Temperatures

Tobler, R. L.

Mikesell, R. P.

Durcholz, R. L.

Reed, R. P.

Advanced Composites

Kasen, M. B.

Schramm, R. E.

Elastic Properties of Engineering Alloys at Cryogenic  
Temperatures

Ledbetter, H. M.

Naimon, E. R.

Weston, W. F.

WESTINGHOUSE RESEARCH LABORATORIES

Structural Materials for Cryogenic Applications

Lessmann, G. G.

Kossowsky, R.

Logsdon, W. A.

Mathur, M. P.

Wells, J. M.

## INTRODUCTION

Bound together in this report are the initial results of a widespread program designed to fulfill the need for materials properties data to assist the design and development of superconducting machinery. The program was conceived and developed jointly by the staffs of the Materials Sciences - Advanced Research Projects Agency and the Cryogenics Division - National Bureau of Standards. This ARPA - sponsored program on "Low Temperature Properties of Structural Materials in Support of Superconducting Machinery" is managed by NBS, with subcontracts to five other laboratories.

## PROGRAM DESCRIPTION

The program's objectives are: 1) to evaluate candidate structural materials for use in superconducting electrical machinery by determining their mechanical and physical properties between 4 and 300 K and the effects on these properties of processing and joining, 2) to explore new materials, such as composites, for potential innovative design applications by performing screening tests on their low temperature properties, and 3) to assist the information transfer of the available low temperature properties data into design use by compiling and publishing what literature data are available and assessing what properties need further study.

The first year's program plan to meet these objectives is shown in Table 1. It outlines the efforts at the six research laboratories with a brief

description of each program. The organizational contacts for each research laboratory are shown in Table 2. It can be easily seen from the first year's program plan that the major thrust has been to initiate fatigue and fracture measurements at low temperatures where virtually no data have previously existed. Exploration of high potential new materials has also begun.

Table 1

## ARPA - Low Temperature Properties of Structural Materials

## First Year Program (FY 74)

<u>Program Area</u>	<u>Organization</u>	<u>Program Description</u>
Mechanical Properties		
1. Fracture and Fatigue		
a. Materials Group a)	NBS-Cryogenics	Fracture toughness, fatigue crack growth rate, fatigue, sustained load crack growth rate tests from 4-300 K on structural alloys.
b. Materials Group b)	Westinghouse	Mechanical, magnetic, electrical loss characterization of alloys currently in use by Westinghouse in DOD sponsored programs. Mechanical tests include tensile, fracture toughness, fatigue.
c. High Load-Large Specimens	Martin-Denver	Fracture toughness, fatigue crack growth rate data on very selected tough alloys requiring loads in excess of 30,000 lbs. to fracture.
2. Effects		
a. Processing	Westinghouse	Identification of effects of fabrication and processing techniques on mechanical properties of selected alloys. Variables include industrial melting practices, powder metallurgy techniques, and cold working.
b. Joining	Westinghouse	Mechanical properties of fabricated metal joints, including welding (GTAW, EB, GMAW) brazing, and soldering from 4-300 K. Properties include tensile, notched tensile, fracture toughness, and fatigue crack growth rate.
3. Elastic Moduli, Tensile	NBS-Cryogenics	Tensile and dynamic elastic (Young's, shear, bulk moduli) measurements on structural alloys from 4-300 K.

Table 1 (continued)

<u>Program Area</u>	<u>Organization</u>	<u>Program Description</u>
Thermal Properties		
4. Thermal Expansion, Specific Heat	Battelle	Thermal expansion and specific heat measurements on selected insulations and structural alloys.
5. Thermal-Magnetothermal Conductivity	NBS-Cryogenics	Thermal conductivity and thermal conductivity in magnetic fields up to 50 kilogauss from 4-300 K of structural alloys.
Composites		
6. Evaluation of Advanced Composites	NBS-Cryogenics	Screening tests (tensile, fatigue at 4 K) on selected candidate metal and non-metal base composites, including B-epoxy, C-epoxy and polyimide, PRD 49-epoxy, borsic-Al, Steel-Al.
7. Screening for Shield Materials	General Electric	Screening study of composites for torque tube and electromagnetic shield applications.
Data Compilation and Evaluation		
8. Handbook	Battelle	Publication of Handbook containing recommended best value data and complete set of references for 39 selected materials (structural alloys, superconductors). Data presented in graphical and tabular formats; mechanical, thermal, magnetic properties from 0-300 K.
Specialized Structures		
9. Effects on Magnet Materials	Argonne	Characterization of change of electrical and mechanical properties of magnet materials as a function of fatigue and temperature.



Table 2

## ARPA - Low Temperature Properties of Structural Materials

## Organizational Contacts

Advanced Research Projects Agency, 1400 Wilson Blvd., Arlington, Virginia 22209

Program Director Edward C. van Reuth 202-694-4750

National Bureau of Standards, Cryogenics Division, Boulder, Colorado 80302

Program Manager	Richard P. Reed	303-499-1000	Ext. 3870
Contract Monitor	Alan F. Clark	303-499-1000	Ext. 3253
Fracture	Ralph L. Tobler	303-499-1000	Ext. 4447
Elastic Moduli	Hassell M. Ledbetter	303-499-1000	Ext. 3232
Thermal Conductivity	Jerome G. Hust	303-499-1000	Ext. 3733
Magnetothermal Conductivity	Frederick R. Fickett	303-499-1000	Ext. 3785
Composites	Maurice B. Kasen	303-499-1000	Ext. 3558

Argonne National Laboratory, 9700 South Cass Avenue, Argonne, Illinois 60439

Program Coordinator	Joseph B. Darby	312-739-2225
Principal Investigators	Edward S. Fisher	312-739-3415
	Ronald Linz	

Battelle, Columbus Laboratories, 505 King Avenue, Columbus, Ohio 43201

Program Manager	James E. Campbell	614-295-8045	Ext. 2829
Mechanical Properties Data	James E. Campbell	614-295-8045	Ext. 2829
Thermal Properties Data	Edward A. Eldridge	614-295-8045	Ext. 2572
Magnetic Properties Data	J. Ken Thompson	614-295-8045	Ext. 2612
Physical Properties Meas't.	Frank Jelinek	614-295-8045	Ext. 1735

General Electric Company, Research and Development Center, P.O. Box 8,  
Schenectady, N.Y. 11506

Program Manager	William B. Hillig	518-346-8771	Ext. 6139
Principal Investigator	J. Bob McLoughlin	518-346-8771	Ext. 6398

Martin Marietta Aerospace, Denver Division, P.O. Box 179, Denver, Colorado 80201

Program Manager	Fred Schwartzberg	303-794-5211	Ext. 2516
Principal Investigator	Emory Beck	303-794-5211	Ext. 3438

Westinghouse Electric Corporation, Research & Development Center, Beulah Road,  
Pittsburgh, Pennsylvania 15235

Program Manager	G. G. Lessmann	412-256-7000	Ext. 3412
Joining & Processing	Joseph M. Wells	412-256-7000	Ext. 3633
Fracture Mechanics	William A. Logsdon	412-256-7000	Ext. 3652
Magnetic Measurements	M. P. Mathur	412-256-7000	Ext. 3289
Metallurgy-Fractography	R. Kossowsky	412-256-7000	Ext. 3684

## RESULTS HIGHLIGHTS

The report for this six months contains a sizable amount of data. A general overview is best obtained by reading the technical summary of each contractor report. A summary of materials included in all programs is presented in Table 3, listed by property and laboratory. We feel it is useful, also, to briefly highlight the major technical accomplishments.

After one year's research the general fracture characteristics at low temperatures have been well described. The rapid emergence of the J-integral test procedure, significantly supported by this program, has permitted the identification of the fracture toughness of many tough, cryogenic alloys with the use of relatively thin plate specimens. Although much work remains, we now know, for the first time, the general fracture characteristics below room temperature of titanium, austenitic stainless steels, and age-hardened stainless steels.

Thermal property measurements have filled in a number of gaps of data for structural alloys. Importantly, we have learned that thermal conductivity in a magnetic field is reduced considerably, even for alloys.

Magnetic measurements have established that the age-hardened stainless steels are slightly ferromagnetic at temperatures below that of liquid nitrogen.

Flexure tensile screening tests at 4 K, coupled with a comprehensive review, have provided a basis for the potential use of composites at 4 K.

Electrical resistivity measurements, concurrent with fatigue at 4 K, have established a tentative relation between resistivity increase and plastic

deformation during fatigue for copper. While these measurements will be terminated for our structural alloy program, there is need for good magnet-related support research, such as this program represents.

Another workshop meeting is scheduled for November 11 and 12 in Vail, Colorado. This workshop will consist of presentation of the first year's research results (much of which is reported here) and discussions of current superconducting machine designs from a materials viewpoint. Significant conclusions from this workshop will be reported in the next set of reports; however, a tentative agenda is included in Table 4.

Table 3

## Project Summary of Materials Properties Measurements for Second Half Year

	Argonne	Battelle	G. E.	Martin	NBS	Westinghouse
Thermal Expansion	-	Inc 750, Kro 58, Inc LEA OFHC, Cu-Sn AISI 310 S Ti-Nb, Ti-Al-Sn	S-glass PRD-49 Modmor II with epoxy resins	-	-	-
Thermal Conductivity	-	-	-	-	OFHC Cu, Inc 750, Inc LEA, Kro 58, AISI 310	-
Magneto-thermal Conductivity	-	-	-	-	Inc 718 OFHC Cu	-
Specific Heat	-	Inc 750, Cu Kro 58, Cu-Sn AISI 310 S Inc LEA	-	-	-	-
Electrical -Magnetic	5-9's Cu OFHC Cu	-	-	-	OFHC Cu, Inc 750 Inc LEA	Inc 750, OFHC AISI 310 S Kro 58
Fracture Toughness	-	-	-	AISI 304L A 286 Inc X 750	AISI 304, 310, 316 Ti-5Al-2.5 Sn Ti-6Al-4V, A 286, Inc 750	Inc 750 AISI 310 S Kro 58 OFHC Cu
Fatigue Crack Growth	-	-	-	AISI 304L A 286 Inc X 750	AISI 304, 310, 316; Ti-5Al-2.5 Sn, Ti-6Al-4V, A 286, Inc 750	Inc 750 AISI 310 S Kro 58 OFHC Cu
Tensile	-	-	-	AISI 304L A 286 Inc X 750	AISI 304, 310, 316 Ti-5Al-2.5 Sn, Ti-6Al-4V, A 286 Inc 750, Boron Epoxy	Inc 750 AISI 310 S Kro 58, OFHC
Elastic Moduli	-	-	-	-	Ti-6Al-4V, Ti-5Al-2.5Sn, Inc 600 and 750 A 286, AISI 304, 310, 316, Al 1100, 5083, 7005 7075 Invar	-
Flexure	-	-	S-glass, PRD-49, Modmor II with epoxy resins	-	-	-
Welds, Brazes, and Processing effects	-	-	-	-	-	Inc 750, AISI 310 S Kro 58

## AGENDA

NBS-ARPA WORKSHOP ON MATERIALS RESEARCH  
IN SUPPORT OF SUPERCONDUCTING MACHINERY

11-12 November 1974

Vail, Colorado

## MONDAY

Introduction

8:45 a.m.	Welcome and picture taking	Clark (NBS)
9:00	ARPA Objectives	van Reuth (ARPA)
9:10	Program overview	Reed (NBS)

Mechanical Properties

9:30	Composites at 4 K	Hillig (G. E.)
9:45	Composites review	Kasen (NBS)
10:00	Coffee break	
10:15	Fatigue and Fracture, Processing, Fabrication Effects	Wells and Logsdon (Westinghouse)
11:15	Elastic properties	Ledbetter (NBS)
11:30	Fracture behavior	Schwartzberg (Martin)
11:45	Fatigue and Fracture	Tobler (NBS)

12:30 Lunch

Machine Design from a Materials Viewpoint

2:00 p.m.	Navy Superconducting Machinery Program Specific Machine Designs	Harrison and Doyle (NSRDC) Jenkins (G. E.) Calderone (AiResearch)
3:15	Coffee break	
3:30	Air Force Program Generator Design	Oberly (APL) McCabria (Westinghouse)
4:00	General Electric's Program	Rios (G. E.)
4:15	U.S.S.R. Low Temperature Materials Research - Review	Reed and Kasen (NBS)
5:00-6:30	Cocktails	

## TUESDAY

Handbook

9:00 a.m.	Handbook and Data Compilation	Campbell (Battelle)
-----------	-------------------------------	---------------------

Thermal and Electrical Properties

10:00	Cyclic Loading Effects in Conductivity	Linz (Argonne)
10:15	Electric and Magnetic Properties	Mathur (Westinghouse)
10:30	Coffee break	
10:45	Thermal Expansion of Alloys	Jelinek (Battelle)
11:00	Specific Heat of Alloys	Collings (Battelle)
11:15	Thermal Conductivity	Hust (NBS)
11:30	Magnetothermal Conductivity	Sparks (NBS)
12:00	Lunch	
1:30 p.m.	Open discussion and evaluation	

## HANDBOOK

One of the most important outputs of this program is, of course, the handbook. It collects in one volume all the data that are available, including the new data generated by this program, on the low temperature properties of structural materials for use in superconducting machinery. This work is being handled by Battelle, Columbus Laboratories under the direction of James E. Campbell. The handbook presents in loose leaf format, so that it can be added to in the succeeding years, mechanical, thermal, electrical, and magnet properties of materials for superconducting machinery. Both tabular and graphical presentations are made for best-value data along with original data and test conditions. The reference sources have been the Materials and Ceramics Information Center (MCIC), the Defense Documentation Center (DDC), and the Cryogenic Information Center (CIC).

The first volume of the handbook is now available. It contains data on more than 40 metals and alloys in various conditions, and is 511 pages long, including 740 references. The handbook is available from the National Technical Information Service (NTIS), Operations Division, Springfield, Virginia 22151, under the following information:

Handbook on Materials for Superconducting  
Machinery -- November 1974  
MCIC - HB- 04.

October 1974

SEMI-ANNUAL TECHNICAL REPORT

EFFECTS OF CYCLIC LOADING ON ELECTRICAL CONDUCTIVITY  
OF SUPERCONDUCTING COMPOSITES

by

ARGONNE NATIONAL LABORATORY  
9700 South Cass Avenue  
Argonne, Illinois 60439

Principal Investigators: E. S. Fisher 312/739-3415

R. J. Linz 312/739-3418

Program Manager: J. B. Darby, Jr. 312/739-2255

Contract Monitor: Cryogenics Division  
National Bureau of Standards  
Boulder, Colorado 80302

Program Code Number: 4D10

Purchase Order Number: 40821-4

Effective Date of Contract: 9/1/73 - 8/31/74

Contract Expiration Date: 10/14/74

Amount of Contract: \$40,000

Sponsored by

Advanced Research Project Agency

ARPA Order No. 2569

The views and conclusions contained in this document are those of the authors and should not be interpreted as necessarily representing the official policies, either expressed or implied, of the Advanced Research Projects Agency or the U.S. Government.

## SUMMARY

The objective of the project is to obtain reliable data on the influence of cyclic-stress loading on the low-temperature electrical and thermal conductivities of metals. The information provided will be used in the design of superconducting devices that will be subjected to cyclic magnetic fields and mechanically and/or thermally induced cyclic-stress loading.

Fatigue damage introduces point defects into the crystal lattice of a metal. Point defects are extremely effective scatterers of electrons and can significantly reduce the low-temperature thermal and electrical conductivities in high-conductivity metals. Point defects accumulate during successive stress cycles because they do not anneal out at temperatures below  $\approx 30$  K. Fatigue damage can thus lead to severe degradation of the transport properties of a metal at a small fraction of the ultimate mechanical fatigue life.

The optimum design of low-temperature machinery depends on the capability to predict the minimum values of electrical and thermal conductivities of a metal that are likely to be encountered. Since data with which to make these predictions accurately are not available, the effort of the project will be to provide such data.

The accomplishments during the last six months include the acquisition of data that indicate the rate and extent of the changes in the electrical resistivity of pure copper test specimens cyclically deformed at predetermined plastic strains up to 0.3%. Each specimen was subjected to a different cycling program, and the resultant increase in electrical resistivity was obtained as a function of the number of cycles and the degree of strain per cycle.



Specimen fatigue is accomplished with an Instron machine capable of operating in a true cyclic compression-tension mode. The specimen is mechanically coupled directly to the Instron machine and is contained in a liquid-helium cryostat mounted on the movable beam of the Instron. A strain-gauge resistance bridge, mounted on extensometer clamps, measures the strain amplitude and the degree of buckling of the specimen. Brass knife edges, attached to the tips of the extensometer clamps, serve as voltage probes for the resistivity measurements. Changes in the electrical resistivity of the specimen are monitored at various increments of cycles by means of standard, four-terminal dc current-voltage techniques. Plastic strain amplitudes during cycling were obtained directly from stress-strain data displayed on an x-y recorder.

Measurements have been performed on 99.999+% pure copper and oxygen-free high conductivity (OFHC) copper + 0.3 wt % sulfur.

From the small quantity of data obtained to date, it appears that the magnitude of the increase in electrical resistivity at a given number of cycles depends solely on the net amount of plastic strain sustained by the specimen during cycling. The change in electrical resistivity,  $\Delta\rho_o$ , for a given percentage change in plastic strain in tension  $\Delta\epsilon_{pt}$ , is estimated to be

$$\Delta\rho_o/\Delta\epsilon_{pt} \sim 0.8 \times 10^{-9} \text{ } \Omega \text{ cm/\% plastic strain}$$

and is independent of the yield stress or degree of work hardening of pure copper. Work is in progress to determine if the same or a similar constant relationship is valid for compressive plastic strains. If so, then it may be possible to predict the change in electrical resistivity at any given number of cycles, N, from purely mechanical stress-strain data, according

to a simplified model

$$\Delta \rho_o(N) = \sum_{j=0}^N \left\{ \left[ \frac{\Delta \rho_o}{\Delta \epsilon_{pt}} \right] \Delta \epsilon(j)_{pt} + \left[ \frac{\Delta \rho_o}{\Delta \epsilon_{pc}} \right] \Delta \epsilon(j)_{pc} \right\}$$

where the  $\Delta \epsilon(j)_p$ 's are the changes in plastic strain sustained during the  $j$ th cycle and  $\Delta \epsilon_{pc}$  is the percentage change in plastic strain in compression.

A slight decrease in  $\rho_o$  was observed during the first few elastic strain cycles in two specimens of OFHC + 0.3 wt % sulfur. The decrease is attributed to a possible rearrangement of residual dislocations in these materials. Work is in progress to determine whether a decrease, which has been reported in the literature for work-hardened gold, also occurs in pure copper. Annealing conditions, of the severity typically encountered during fabrication of superconductors, were not sufficient to substantially remove the dislocations in the OFHC material. This fact as well as a relatively low resistivity ratio,  $\rho_{300}/\rho_{4.2} \sim 65$ , indicate that OFHC + 0.3 wt % sulfur is not a candidate material for a superconductor stabilizer.

Since work-hardening rates are dependent on chemical purity, additional research similar to that described in the present report should be carried out on the resistivities induced in OFHC copper to determine the significance of the purity on design data. Similar studies should be carried out on aluminum, which is also being considered for use as a stabilizing conductor in superconducting magnets.

## I. INTRODUCTION

Low-temperature machinery may be subjected to cyclic mechanical or magnetic stresses during normal operation. Some components of the machinery may be plastically deformed during cycling, i.e., will be subjected to low-cycle fatigue conditions. The plastic deformations encountered during low-cycle fatigue introduce point defects in metallic components. The point defects generated during plastic cycling at temperatures below  $\sim 30$  K can accumulate to a relatively high concentration because thermal energies are too low to enable the point defects to anneal out spontaneously. Point defects are extremely effective scatterers of electrons and, in sufficient quantity, can substantially reduce the low-temperature electrical and thermal conductivities of relatively pure metals. No reliable data are available that indicate the rate or the magnitude of the degradation of these transport properties as a function of fatigue parameters. Without adequate and reliable data, the safety factor criteria in the design of low-temperature machinery may be excessive, which would result in increased cost, size, and weight.

The purpose of the present investigation is to provide reliable design data for typical materials used in low-temperature machinery. These data will indicate the rate and extent of degradation of the thermal and electrical conductivities due to low-cycle fatigue.

## II. EXPERIMENTAL PROGRESS

The accomplishments during the past six months include the acquisition of data that indicate the rate and extent of the changes in the electrical resistivity of pure copper specimens which have been cyclically deformed at

predetermined plastic strains. Each specimen was subjected to a different fatigue mode, and the resultant increase in electrical resistivity was obtained as a function of the number of cycles.

#### A. Specimen Preparation

Fatigue specimens were prepared from American Smelting and Refining Company 99.999% pure copper and OFHC copper containing 0.3 wt% sulfur. The pure copper specimens were annealed at 400°C for 6-8 hr, and the OFHC specimens were annealed at 350°C for 6-8 hr; all specimens were annealed in a helium atmosphere. The specimens have an overall length of 2-1/2 in., and the diameter of the gauge section is 1/4 in.

#### B. Experimental Apparatus

The fatigue apparatus, shown schematically in Fig. 1, consists of an Instron machine, Model TT-CM-L, with crosshead speeds from 0.03 to 5.0 cm/min and a load capability to 10,000 kg. The Instron machine operates in the push-pull mode to produce uniaxial fatigue conditions. A cryostat has been attached directly to the movable crosshead beam of the Instron. Specimen fatigue occurs at liquid-helium temperatures ( $\sim 4.2$  K). The strain gauges that monitor strain amplitude and the voltage probes that measure the changes in electrical resistivity due to fatigue are attached to two "U"-shape extensometer clamps spring mounted directly on the sample. Brass knife edges that serve as voltage probes are attached to, but electrically isolated from, the extensometer clamps. Only one set of probes is electrically active. The distance between the probes is 2 cm. Two strain-gauge resistors are glued to the closed end of each "U"-clamp, with one resistor on each face of both clamps. A resistance bridge constructed from the four strain-gauge resistors determines the strain amplitude. The electrical instrumentation used to measure the stress versus strain characteristics and the resistance

changes of the specimen during fatigue is shown in Fig. 2.

A more detailed description of the experimental apparatus has been given in our Semi-annual Technical Report, March 1974.

### C. Experimental Methodology

Electrical-resistivity data for all specimens was obtained by means of the standard four-probe dc technique with the instrumentation shown in Fig. 2. A known current,  $I$ , is passed through the specimen of cross-sectional area,  $A$ , and produces a potential difference,  $V$ , between potential probes separated by a distance,  $L$ . The electrical resistivity,  $\rho$ , is given by

$$\rho = \frac{V}{I} \frac{A}{L} . \quad (1)$$

To a good approximation,  $\rho$  is analytically described by

$$\rho = \rho_0 + \rho_1(T) \quad (2)$$

where  $\rho_0$  is (usually) a temperature-independent "residual" resistivity due to electron scattering from defects, and  $\rho_1(T)$  is a temperature-dependent resistivity due to electron scattering by the thermal vibrations of the crystal lattice. Changes in defect concentration significantly affect only the magnitude of  $\rho_0$  and so  $\rho_1(T)$  will be ignored in subsequent discussions.

The stress versus strain data were obtained by displaying the output of the strain-gauge bridge on different axes of the x-y recorder on the Instron. The idealized stress versus strain curve shown in Fig. 3 is useful in describing the methodology of the measurements and in defining terminology.

Figure 3 describes the strain or elongation of a hypothetical specimen subjected to an applied stress or load. The strain remains directly proportional to the stress as long as the stress remains within the "elastic" limits of the specimen. When the stress is removed, the specimen returns to its original shape and position at zero strain. On an atomic scale, elastic strains do not generate substantial quantities of defects and thus do not increase the electrical resistivity of the specimen.

Once the applied stress exceeds the elastic limits of the specimen, the specimen deforms plastically. The total strain  $\epsilon_t$  is now composed of an elastic component,  $\epsilon_E$ , and a "plastic" component,  $\epsilon_p$ . If the stress is removed, the specimen returns to zero stress at some permanent elongation. The most significant result of plastic deformation, relevant to this work, is an increase in electrical resistivity due to the generation of large quantities of defects within the specimen.

When cyclic stresses in excess of the elastic limits are applied to a specimen, the stress-strain curve forms a "hysteresis" loop with a width directly related to the amount of plastic strain in the cycle. As cycling progresses, the defects generated during the plastic strains serve to harden the material and allow more and more of the total strain to be accommodated in an elastic manner, i.e., the loop continually narrows during cycling. The specimen will eventually approach a completely elastic behavior if the cycling continues for extended periods.

The shape of an actual hysteresis loop depends on the stress and/or strain limits imposed on the specimen and is usually not symmetric about the origin as indicated in Fig. 3.

The basic experimental procedure followed in this work was to measure the changes in electrical resistivity that result when a specimen is subjected to well-defined cyclic plastic strains. The specimen was mounted in the fatigue apparatus and cooled to liquid helium temperatures,  $\sim 4.2$  K. The specimen was not coupled to the Instron load cell during cool-down to minimize any plastic strains that could result from the differential thermal contraction of the specimen and the fatigue apparatus. The initial resistivity,  $\rho_{01}$ , was determined. The specimen was coupled to the load cell, and the desired stress-strain curve was established. Cycling commenced and was interrupted intermittently to record  $\rho_0$ ,  $\epsilon_p$ , and the number of cycles,  $N$ .

Ideally, the total strain  $\epsilon_t$  could be separated into an elastic component  $\epsilon_E$  and a plastic component  $\epsilon_p$  by noting the point at which the stress-strain curve deviated from linearity. In practice, this separation was difficult to achieve, in most cases, the amount of plastic strain was taken to be one-half the maximum width of the stress-strain loop.

### III. RESULTS

Table I lists the cycling constraints and the original residual resistivity ratios,  $RRR = \rho_{300}/\rho_{01}$ , for six pure copper specimens and two OFHC specimens.

TABLE I. Cycling Constraints and Residual Resistivity Ratios for Each Specimen

Specimen	RRR	Cycling Conditions
A-2	3450	Constant peak load amplitude
A-3	920	Constant peak load amplitude
A-4	920	Constant peak load amplitude
A-7	1000	Constant peak load amplitude
A-8	3050	Constant peak strain amplitude
A-5	2200	Constant peak strain amplitude
OFHC-3	75	Elastic
OFHC-4	75	Elastic

The electrical resistivity versus the number of cycles is given in Figs. 4-10. The right-hand ordinate in most of the figures also gives  $\rho_o/\rho_{oi}$  to indicate the factor by which the resistivity increased. All but one of the figures include either an insert or a supplemental figure to illustrate the details of the cycling conditions. Cycling conditions for specimen A-4 (Fig. 7) are similar to those of specimen A-7 (Fig. 6). The ordinate in each of the supplemental graphs is the load applied to the specimen, in kilograms. Since all specimens are 1/4-in. diam., the loads may be converted to standard stress units of  $\text{kg/mm}^2$  or psi by multiplying by  $3.14 \times 10^{-2}$  or 43.8, respectively.

#### A. Pure Copper Data

##### 1. Electrical Resistivity Changes during Constant Peak Load Cycling

a. Effects of Work Hardening. The primary characteristic of the change in electrical resistivity,  $\Delta\rho = \rho_{oi} - \rho_o$ , during cyclic straining at constant peak loads is the apparent saturation of  $\Delta\rho$  after relatively few cycles. The factors that control  $\Delta\rho$  are the initial plastic strain amplitude,  $\epsilon_{pi}$ , and the plastic strain generated per cycle, which is described by the half-width of the stress-strain loop,  $\epsilon_p/2$ . Figure 4 represents a specimen initially strained by nearly 0.2% and then cycled between constant load limits of +150 and -50 kg. The width of the loop generated is small compared with the total initial plastic strain. Thus, the resistivity of the specimen shows a relatively rapid increase during the first 1/4 cycle and a much smaller increase during subsequent cycling as the loop gradually narrows.  $\rho_o$  increases by < 20% over the first 200 cycles with almost all of the increase occurring in the first 1/4 cycle.



Figure 5 also represents a specimen initially strained by nearly 0.2% and, in this case, cycled between constant load limits of  $\pm 125$  kg. The width of the loop generated is nearly as large as the initial plastic strain induced in the first 1/4 cycle. The specimen work hardens rapidly during the first 10-30 cycles, and by 200 cycles the loop width becomes relatively narrow, indicative of a nearly elastic cycling mode. The rate of decrease in  $\Delta\rho$  appears to parallel the rate of decrease in plastic strain,  $\Delta\epsilon_p$ .  $\rho_0$  increases quite rapidly during the first 10-30 cycles and then gradually levels off as the stress-strain curve becomes nearly elastic.

b. Annealing Effects. Figure 6 shows (1) the change in  $\rho_0$  when the specimen is cycled in a stress-strain loop symmetric with respect to the origin, and (2) the effect of annealing and subsequent cycling on  $\rho_0$ . A symmetric loop of width  $\epsilon_p/2 \approx 0.2\%$  was obtained by starting with a tensile strain of  $\approx 0.01\%$  and then manually increasing the tensile and compressive strains by  $\approx 0.01\%$  on successive cycles. This procedure work hardened the specimen and resulted in a slower rate of decrease in plastic strain amplitude than for the specimen described in Fig. 5. Thus, in contrast to the specimen described in Fig. 5, the saturation or leveling off of  $\rho_0$  with  $N$  is delayed to higher  $N$  values. After  $\sim 800$  cycles, the cycling was stopped and the specimen was warmed to  $\approx 185$  K. The specimen was then re-cooled to 4.2 K.  $\rho_0$  had decreased by  $\approx 30\%$  during the anneal, as indicated by the dashed vertical line in Fig. 6(a). During cycling just prior to the anneal, the fatigue loop still had an appreciable but slowly decreasing width, and the rate of change of  $\rho_0$  was still decreasing at a slow rate.

An unexpected phenomenon was observed when cyclic loading was resumed after the anneal. The anneal at 185 K was expected to soften the specimen, since fewer point defects would be present to impede dislocation motion. When cycling was continued after the anneal under the same cycling conditions, the stress-strain loop was expected to be wider and the rate of increase of  $\rho_0$  was expected to be more rapid. Contrary to these expectations, the specimen evidently hardened during anneal, as indicated by (1) a closing of the loop, and (2) an absence of any detectable increase in  $\rho_0$  during subsequent cycling from 800 to 1000 cycles. Similar hardening effects due to annealing after low-temperature fatigue have been reported in the literature.<sup>1</sup>

The abrupt change in  $d\rho_0/dN$  near  $N = 1000$  is the result of a deliberate increase in load to establish a loop of width  $\epsilon_p/2 \approx 0.33\%$ . The rate of increase,  $d\rho_0/dN$ , is more rapid near  $N = 1000$  than near  $N = 0$ , where  $\epsilon_p/2 \approx 0.2\%$ . The specimen buckled ("x") as a result of a machine malfunction before  $\rho_0$  could level off.

c. Effect of Progressive Increase in Plastic Strain Amplitude or Loop Width. The data in Fig. 7 show the effect of increasing the plastic strain amplitude or loop width. Each abrupt increase in  $\rho_0$  indicates the reestablishment of a stress-strain loop due to an increase in the load. The number placed near each abrupt increase in  $\rho_0$  indicates the new loop width,  $\epsilon_p/2$ . The rate and magnitude of the increase in  $\rho_0$  intensify as the plastic strain amplitude increases. As in Fig. 6, each vertical dashed line indicates an anneal. The anneal near 1800 cycles was at room temperature for  $\sim 2$  days; the remaining anneals were the result of warming to  $\sim 185$  K. The dashed diagonal line near 1500 cycles represents an uncertainty in the cycling count.

Additional evidence that work hardening occurs during annealing is observed in the resistivity data of Fig. 7 prior to and after the room-temperature anneal near 1850 cycles. The load was the same before and after anneal. A rapid increase in  $\rho_0$  is indicated just prior to the anneal, but no increase in  $\rho_0$  is detectable after the anneal, i.e., after the anneal, the specimen no longer sustains any appreciable plastic strain during cycling at the pre-anneal load.

## 2. Electrical Resistivity Changes during Constant Peak Strain Cycling

The experiments at constant peak load, described in Section III.A.1, showed that  $\Delta\rho$  per cycle is closely associated with the amount of plastic strain sustained per cycle. The  $\Delta\rho$  diminished rapidly during constant load cycling because the process of work hardening enabled the specimen to accommodate most of the applied load in a nearly elastic manner at rapidly decreasing peak strain amplitudes. In contrast, the  $\Delta\rho$  should diminish less rapidly during constant peak strain cycling because the peak load increases during cycling and slows the rate at which the specimen approaches a nearly elastic behavior. The two experiments described in Figs. 8 and 9 are consistent with this prediction. Figure 8a shows the change in  $\rho_0$  observed when a pure copper specimen is cycled between constant strain limits (Fig. 8b) of +0.2% in tension and  $\sim$  -0.005% in compression. These data indicate that  $\rho_0$  has increased by greater than a factor of four over the first 250 cycles and is still rising at an appreciable rate. For comparison, the data of Fig. 5, which were also initiated at the same strain limits during the first cycle but subsequently cycled under constant peak load conditions, indicate  $\rho_0$  increased by only a factor of 2.5 over 1500 cycles. The greater rate of increase in  $\rho_0$  seen in Fig. 8a is attributable to a

lower net rate of decrease in plastic strain in the strain-limited cycling mode. The specimen work hardens during each cycle and so the load or stress must be increased to achieve the same peak strain. The increase in load introduces more plastic strain, which maintains a relatively high rate of increase in  $\rho_0$ .

The dashed vertical line on Fig. 8a near 260 cycles indicates a room-temperature anneal for 2 days. After the anneal, cycling continued under the same conditions as before. These data indicate an immediate increase in  $\rho_0$ , and the magnitude of  $\rho_0$  prior to anneal is reestablished after an additional 150 cycles. The increase in  $\rho_0$  observed after anneal in Fig. 8a can be contrasted with the lack of any change in  $\rho_0$  observed for specimens cycled in a constant load-limited mode after anneal (Figs. 6 and 7).

In contrast to Fig. 8, the data of Fig. 9 show the effect of load-unload cycling, a cycling mode encountered during the operation of large superconducting magnets. These data were obtained by introducing a total strain of 0.3% and then cycling between strain limits of +0.3 and +0.1%; the lower strain limit occurred at zero load. The cycling conditions of the first 1-1/4 cycles are similar to the loop shown in the insert. Most of the increase in  $\rho_0$  occurs in the first 1/4 cycle when most of the strain is plastic, but  $\rho_0$  continues to increase at a rather rapid rate at 20 cycles.

#### B. OFHC Data

The OFHC specimens discussed here are not the "certified" grade material commonly used in low-temperature applications, but rather a "free-machining" grade that is more properly described as OFHC +0.3 wt % sulfur. Although specimens were annealed at 350°C for 6 hr, they did not appear to deform

uniformly during plastic deformation. The data presented here are for elastically strained specimens.

Figure 10 shows that the resistivity decreased during the first few elastic cycles. This result was first observed in specimen OFHC-3 and later reproduced in OFHC-4. As the load increased, the decrease in  $\rho_0$  became less pronounced. The initial residual resistivity of these specimens was  $\approx 25 \times 10^{-9} \Omega \text{ cm}$ , so the decrease in  $\rho_0$  due to elastic cycling is  $\sim 10\%$ .

The decrease in resistivity during elastic cycling may be a characteristic of many cold-worked materials. A similar decrease in  $\rho_0$  has been reported in the literature for gold specimens that had been prestrained 1-5% at room temperature prior to cycling at 4.2 K with much smaller strains. It was suggested that the decrease in resistivity is due to a rearrangement of dislocations into dipoles which have a lower electron-scattering efficiency than individual randomly arranged dislocations. The nonuniformity of plastic deformation observed in our OFHC specimens indicates a substantial dislocation density remained after the anneal. Thus, a dislocation rearrangement effect could also explain the decrease we observed in our OFHC specimens during elastic cycling.

#### IV. DISCUSSION

Knowledge of the extent of changes in the electrical resistivity in copper, due to cyclic plastic strains, will find immediate application in the design of large, cryogenic stabilized superconducting devices such as fusion reactor magnets, energy storage magnets, and transmission lines. Such knowledge may be useful in many other low-temperature applications, but those listed above are perhaps the most important from the materials point

of view in that those applications involve the highest magnetic and mechanical stress levels during operation. The stress levels encountered will be sufficiently high so that it will usually be necessary to reinforce the superconductor with a stainless steel or other high-strength structural member to allow the superconductor to carry the applied loads safely. The superconductor stabilizer, probably pure copper or aluminum, will be bonded to the structural member and will thus be strain-limited rather than load-limited during cycling.

The change in resistivity,  $\Delta\rho$  versus the number of cycles after an abrupt change in load is shown in Fig. 11 for most of the pure copper specimens. Note that the right-hand ordinate refers only to the open-circle data of specimen A-7. Most of the specimens appear to obey a behavior such that  $\Delta\rho \propto \ln N$ . Data for specimens cycled under constant load conditions appear to indicate that  $\Delta\rho$  at higher numbers of cycles could be obtained by linear extrapolation. Johnson and Johnson<sup>2</sup> suggest that, within large uncertainty limits,  $\Delta\rho \sim N^{1/4}$ . Their specimens had been prestrained by  $\sim 25\%$  prior to cycling at 4.2 K and at stress limits near 40,000 psi. Since they did not include the parameter we find most important, the plastic strain amplitude, it is difficult to compare their data with ours.

Data for specimen A-5 in Fig. 11, cycled under constant peak strain limits, cannot be fit to the simple  $\Delta\rho \propto \ln N$  dependence and, instead, increase at a much faster rate than data obtained for specimens cycled under constant load conditions. A larger body of data are needed to predict  $\Delta\rho$  at large  $N$  values with confidence. However, for many applications in which the cycling

is strain limited, N values of 30 to 300 cycles would encompass nearly the entire lifetime of the superconducting device. For example, a fusion reactor magnet may encounter only 20-100 such cycles in a 20-year lifetime. Therefore, the data presented here, showing changes in  $\Delta\rho$  by a factor of four over  $\sim 250$  cycles, are relevant to many applications.

The ultimate objective of the work described here is to provide data from which the  $\Delta\rho$  versus N characteristics may be predicted for stabilizing materials subjected to any cyclic strain mode. Our data for pure copper indicate that only the plastic strain amplitudes sustained during cycling are of any importance in changing  $\rho_0$ . In addition, the data of Table II appear to indicate that, at least in tension,  $\Delta\rho$  depends solely on  $\epsilon_p$  and not on other material properties such as yield strength. In particular, the changes in electrical resistivity due to different tensile strains and at various stages of cold work were measured for specimen A-8. Additional data were provided from resistivity measurements after the first 1/4 cycle during fatigue. In Table II, the residual resistivity ratio, RRR, is taken as a rough indicator of both the degree of work hardening and the yield stress of the specimens, since the dislocation density governs these parameters. The yield stress of specimen A-8 increased from  $\sim 3000$  psi to 30,000 psi over the course of these measurements. Data in Table II indicate that

$$\Delta\rho/\Delta\epsilon_{pt} \sim 0.8 \pm 0.4 \times 10^{-9} \text{ } \Omega \text{ cm/\% plastic strain,}$$

independent of yield strength.  $\Delta\epsilon_{pt}$  is the tensile plastic strain.

TABLE II. Correlation between  $\Delta\rho$  and  $\Delta\epsilon_p$

Specimen	$\Delta\epsilon_p$ (%)	$\Delta\rho (10^{-9} \Omega \text{ cm})$	RRR
A-5 <sup>a</sup>	0.16	0.06	2200
A-2 <sup>a</sup>	0.20	0.13	3450
A-8	0.11	0.12	3050
A-8	0.22	0.19	780
A-8	0.10	0.09	700
A-8	0.15	0.13	685
A-8	0.15	0.11	680
A-3 <sup>a</sup>	0.21	0.18	920

<sup>a</sup> $\Delta\epsilon_p$  and  $\Delta\rho$  were obtained at 1/4 cycle.

Work is presently in progress to determine whether the above or a similar constant relationship is valid for compressive plastic strains,  $\epsilon_{pc}$ . If this is the case, it should be possible to predict  $\Delta\rho$  for any cycling mode according to a simplified model

$$\Delta\rho_o(N) = \sum_{j=0}^N \left\{ \left[ \frac{\Delta\rho_o}{\Delta\epsilon_{pt}} \right] \Delta\epsilon(j)_{pt} + \left[ \frac{\Delta\rho_o}{\Delta\epsilon_{pt}} \right] \Delta\epsilon(j)_{pc} \right\} .$$



The change in plastic strain in the  $j^{\text{th}}$  cycle,  $\Delta\epsilon_p(j)$ , hopefully could be obtained from the mechanical properties of the material. Assuming the parameters  $\Delta\rho/\Delta\epsilon_{pt}$  and  $\Delta\rho/\Delta\epsilon_{pc}$  are reasonably constant over a large number of cycles, the above model would be useful in predicting  $\Delta\rho(N)$  over the lifetime of a component subjected to cyclic loading.

## V. CONCLUSIONS

The changes in electrical resistivity of pure copper due to cyclic plastic strains have been measured to 1500 cycles in several cycling modes. The changes in resistivity depend on the initial plastic strain and the total plastic strain per cycle. When cycled at a constant peak strain of 0.2%, the electrical resistivity of annealed pure copper increases by a factor of four over 250 cycles.

The electrical resistivity of partially annealed specimens of OFHC +0.3 wt % sulfur decreased by as much as 10% during elastic cycling. Experiments are planned to determine whether a similar decrease occurs in certified-grade OFHC copper.

A simple working model has been proposed for computing resistivity increases due to uniaxial plastic strain cycling. The principal parameters of the model are the change in resistivity per unit plastic strain,  $\Delta\rho/\Delta\epsilon_p$ , and the total plastic strain per cycle. To establish the validity of this model, more data are needed to determine if  $\Delta\rho/\Delta\epsilon_p$  remains constant in both compression and tension under variable work-hardening conditions. The model can be used to predict operating conditions for large superconductors in magnets where strain per cycle and number of cycles are essential parameters that influence magnet behavior.

Future experiments are planned to determine if the resistivity changes in certified-grade OFHC copper, due to cyclic plastic strains, are similar in magnitude to the changes observed in the pure copper. Some dissimilarities are expected because of the more rapid rate of work hardening in the OFHC copper, which has a greater concentration of impurities. These data will be directly applicable to the design of composite superconductors, where the ratio of copper to superconductor depends on the electrical and thermal resistivities of the stabilizing matrix (usually certified-grade OFHC copper). Resistivity changes during constant peak strain cycling will be emphasized, since this cycling mode is of primary interest in the design of large, mechanically reinforced superconductors.

High-purity aluminum is also a candidate material for use as an electrical conductor at cryogenic temperatures. Therefore, the resistivity changes due to cyclic plastic strains will be measured in several grades of aluminum.

REFERENCES

1. E. W. Johnson and H. H. Johnson, Trans. AIME, 233, 1333 (1965).
2. R. G. Baggerly and H. I. Dawson, Scripta Metal. 5, 319 (1971).

FIGURE CAPTIONS

- Fig. 1. Experimental apparatus used for fatigue and electrical resistivity measurements at 4.2 K.
- Fig. 2. Electrical instrumentation used to obtain stress vs strain and electrical resistivity data.
- Fig. 3. Hysteresis loop formed as a result of cyclic plastic strains in a hypothetical specimen.
- Fig. 4. Electrical resistivity vs number of cycles for a pure copper specimen subjected to the constant peak load cycling indicated in the insert.
- Fig. 5. Electrical resistivity vs number of cycles for a pure copper specimen subjected to the constant peak load cycling indicated in the insert. The insert also illustrates the narrowing of the stress-strain loop due to work hardening of the specimen.
- Fig. 6. (a) Electrical resistivity vs number of cycles for a pure copper specimen. The vertical dashed line indicates a reduction in  $\rho_0$  due to annealing. (b) Typical symmetric cycling conditions encountered from  $N = 0$  to 850.
- Fig. 7. Electrical resistivity vs number of cycles for a pure copper specimen subjected to cycling conditions similar to Fig. 6b. The data indicate the effect on  $\rho_0$  caused by an abrupt increase in the applied load. The numbers near each abrupt increase in  $\rho_0$  indicate the initial loop width,  $\epsilon_p/2$ , established by the load increase.

Fig. 8. (a) Electrical resistivity vs number of cycles for a pure copper specimen cycled under the constant peak strain limits indicated in (b). The dashed vertical line in (a) near  $N = 260$  indicates an anneal.

Fig. 9. Electrical resistivity vs number of cycles for a pure copper specimen cycled under the constant strain limits indicated in the insert. Only the first  $1\frac{1}{4}$  cycles are shown in the insert.

Fig. 10. The change in electrical resistivity vs number of cycles for two OFHC + 0.3 wt % sulfur specimens subjected to cyclic elastic strains.

Fig. 11. The change in electrical resistivity for pure copper specimens vs number of cycles after an abrupt change in load. Solid lines connect data points obtained during constant peak load cycling; dashed lines connect data points obtained during constant peak strain cycling.

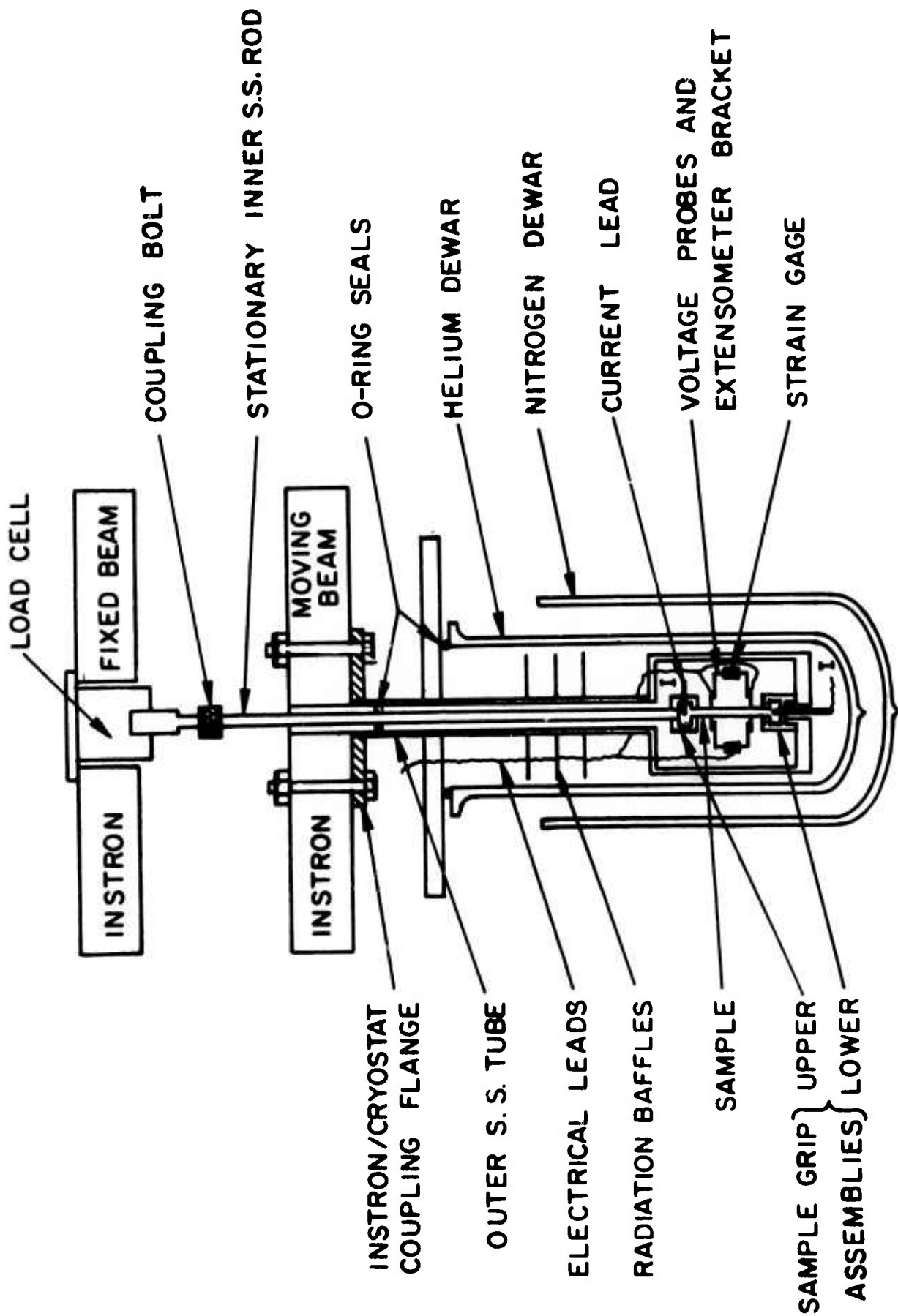


Fig. 1

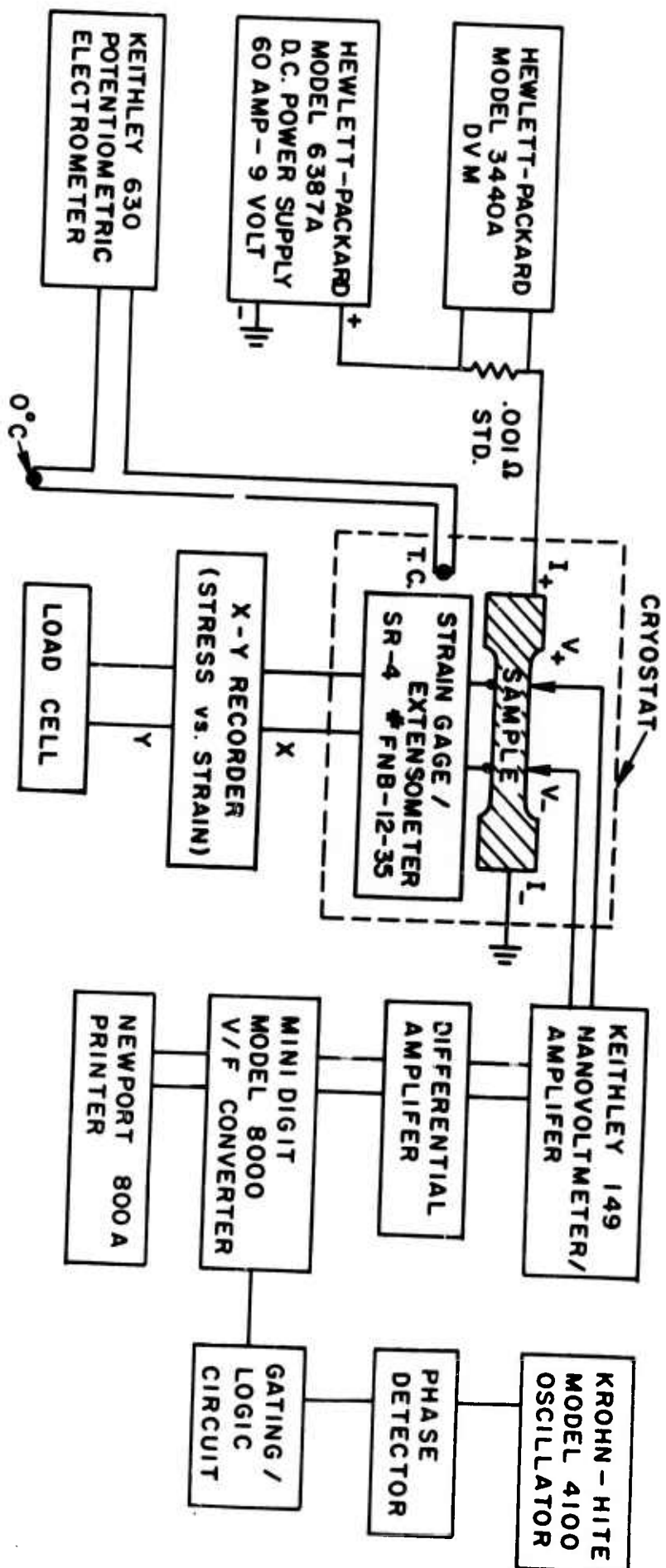


Fig. 2

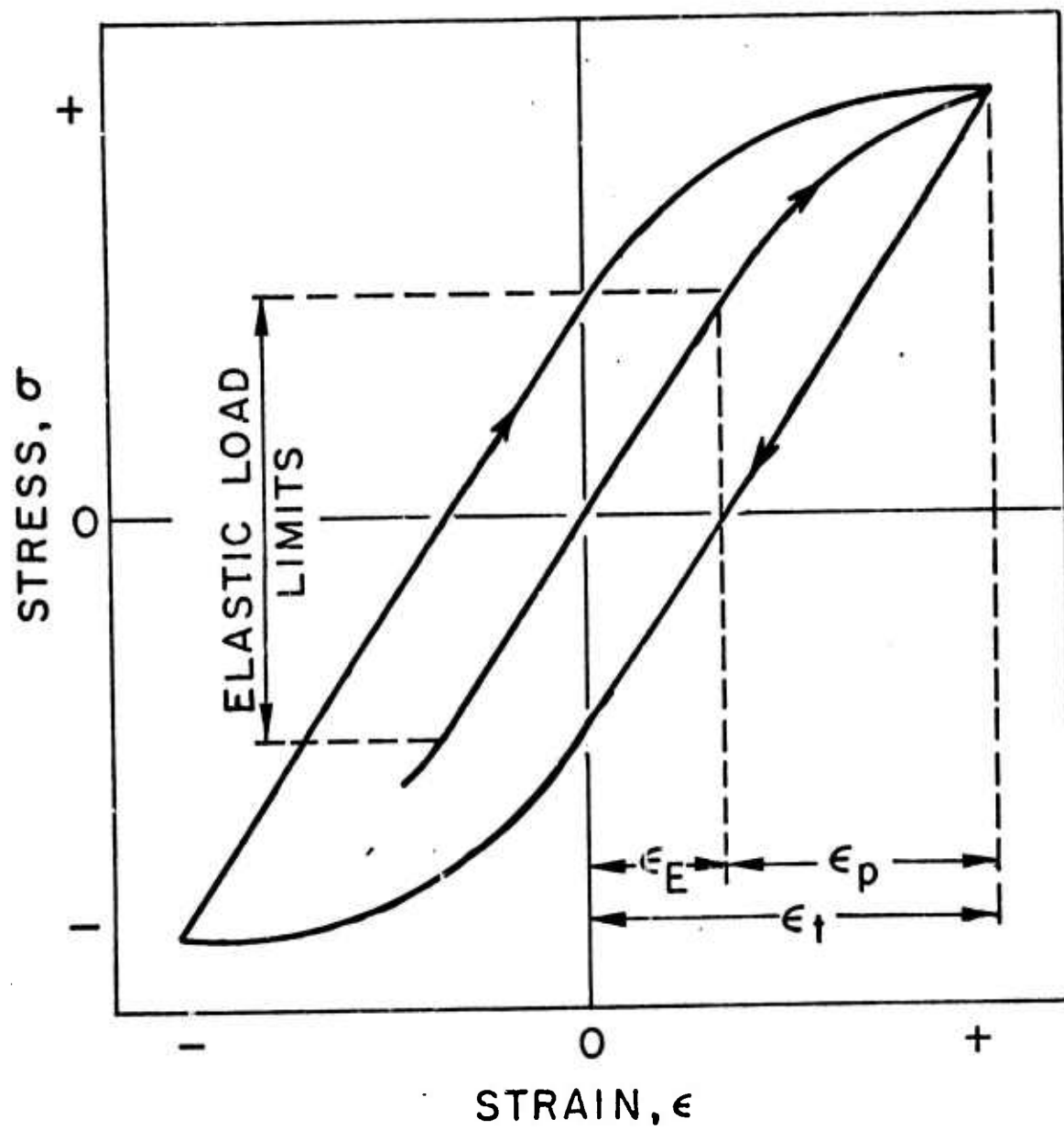


Fig. 3



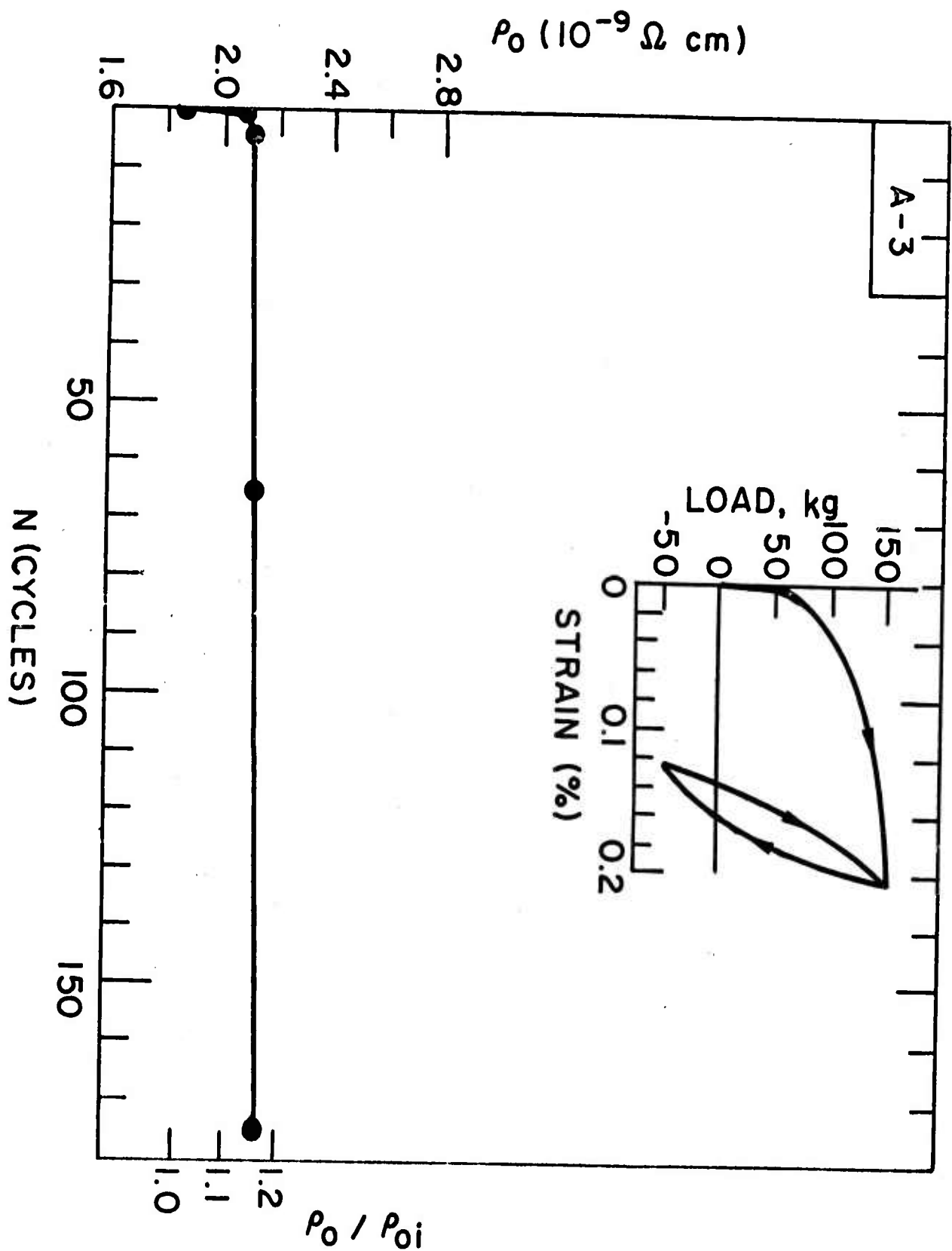


Fig. 4

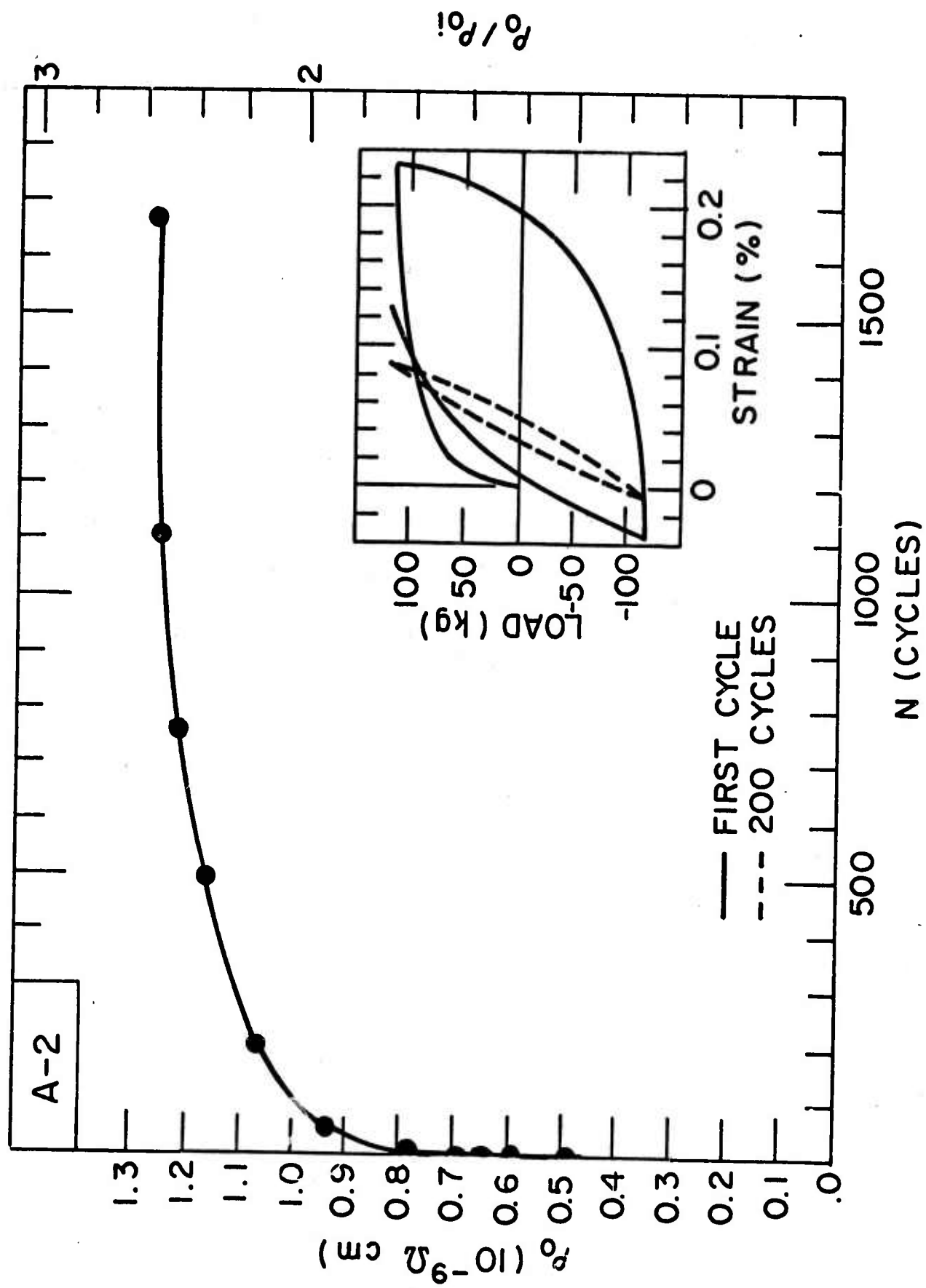


Fig. 5

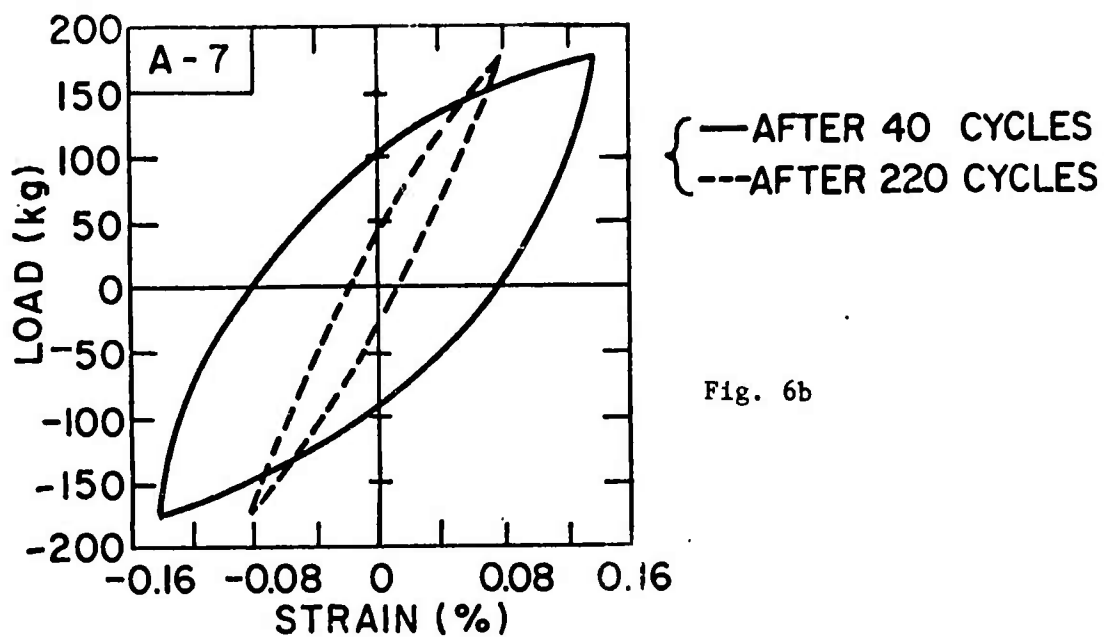


Fig. 6b

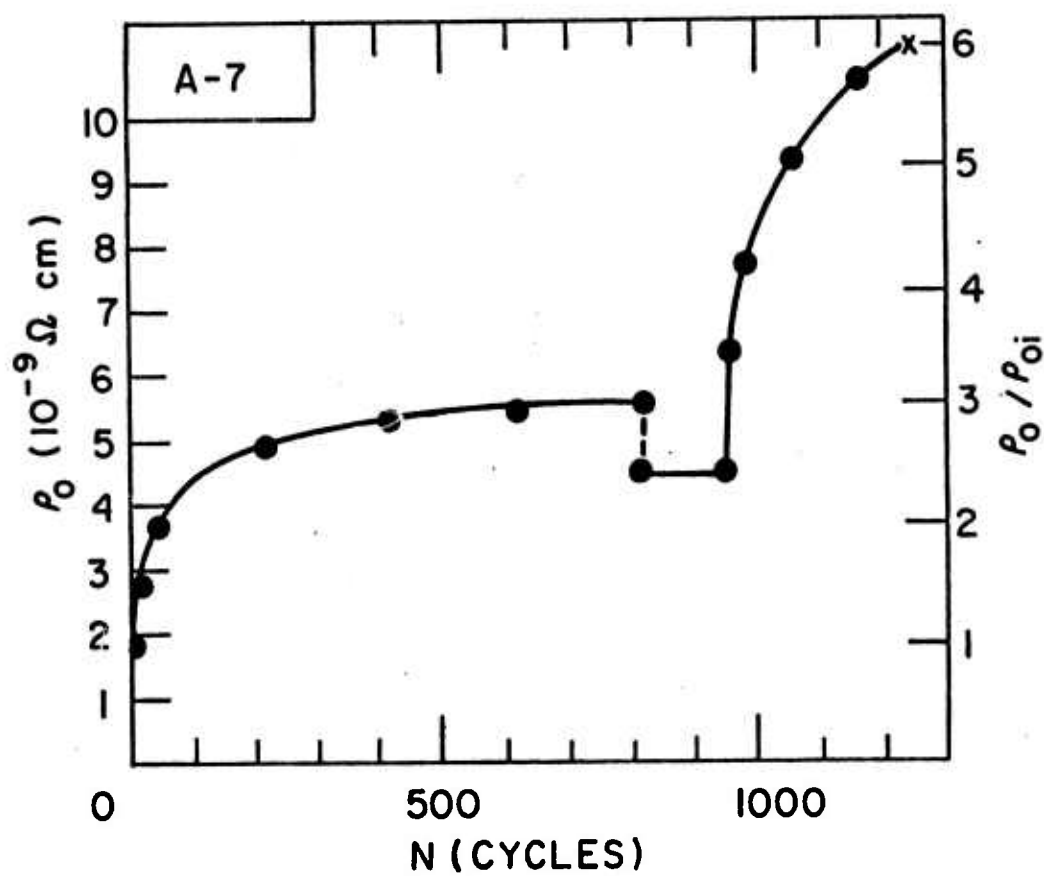


Fig. 6a

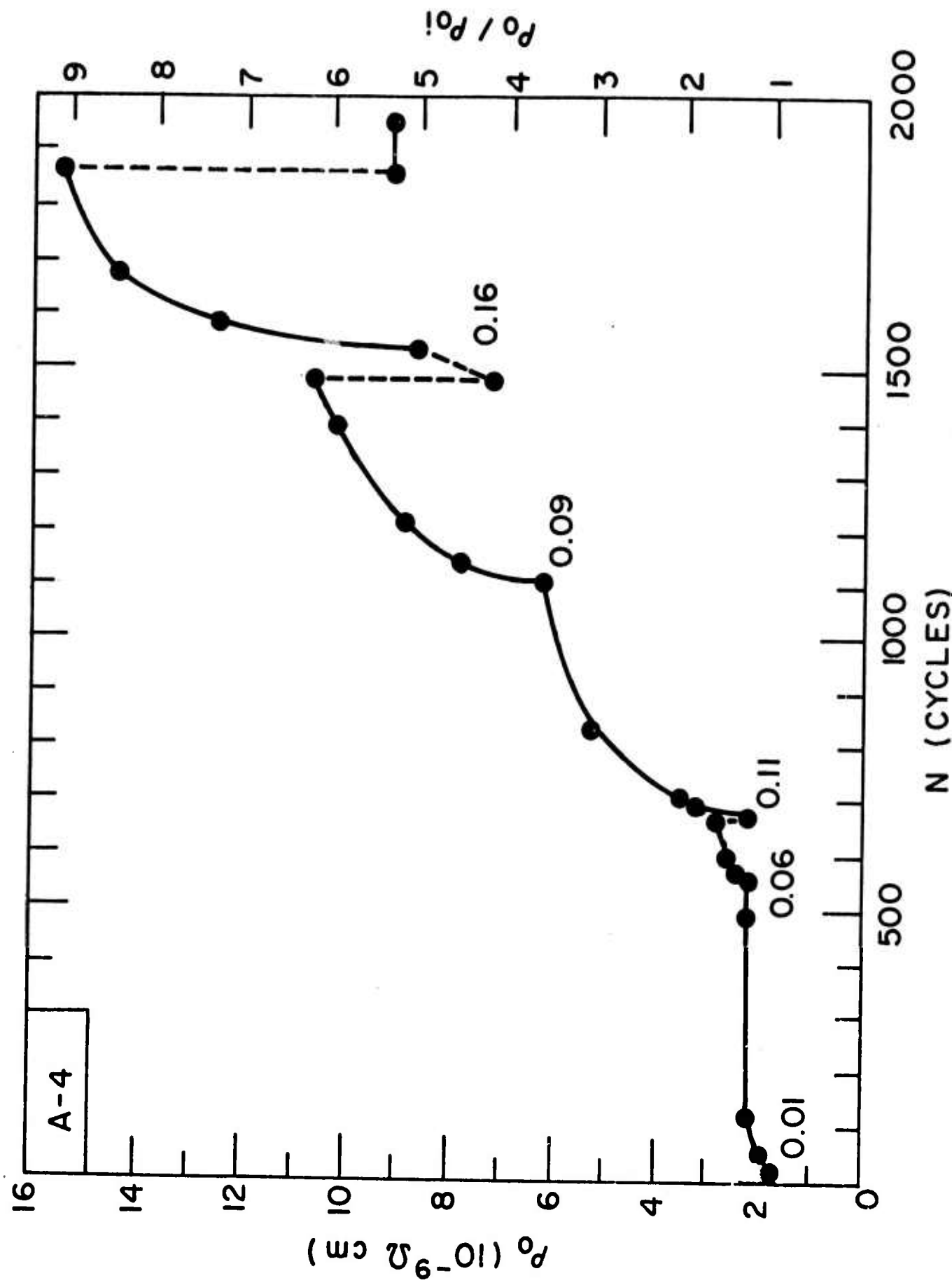


Fig. 7 29<

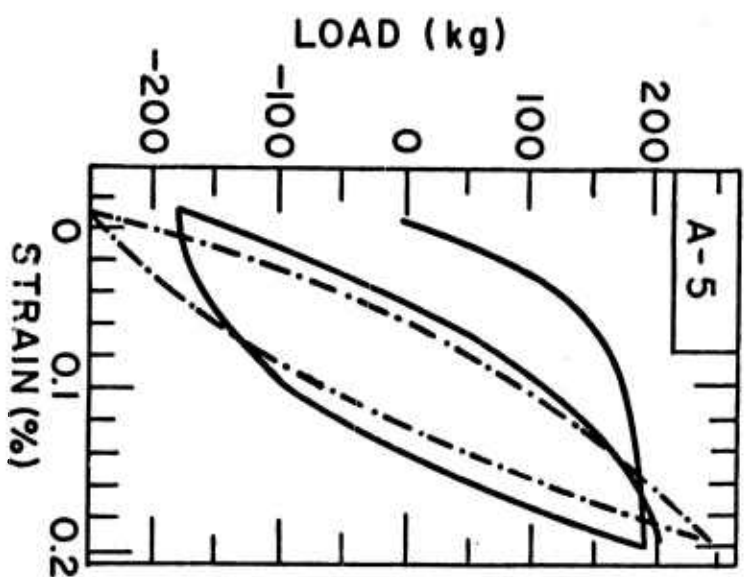


Fig. 8b

— FIRST CYCLE  
 - - - AFTER 20 CYCLES

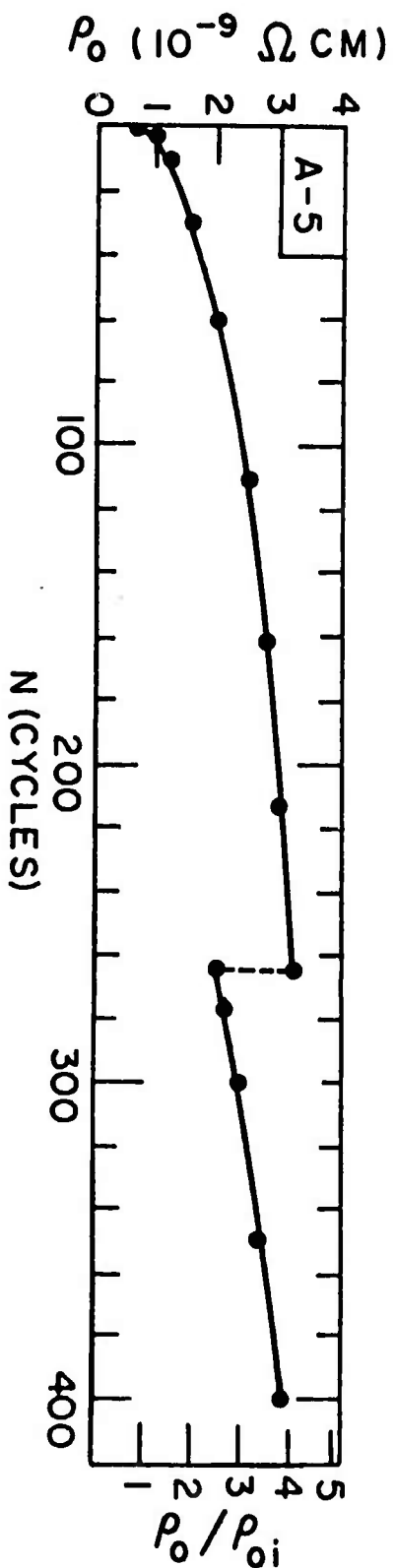


Fig. 8a

30<

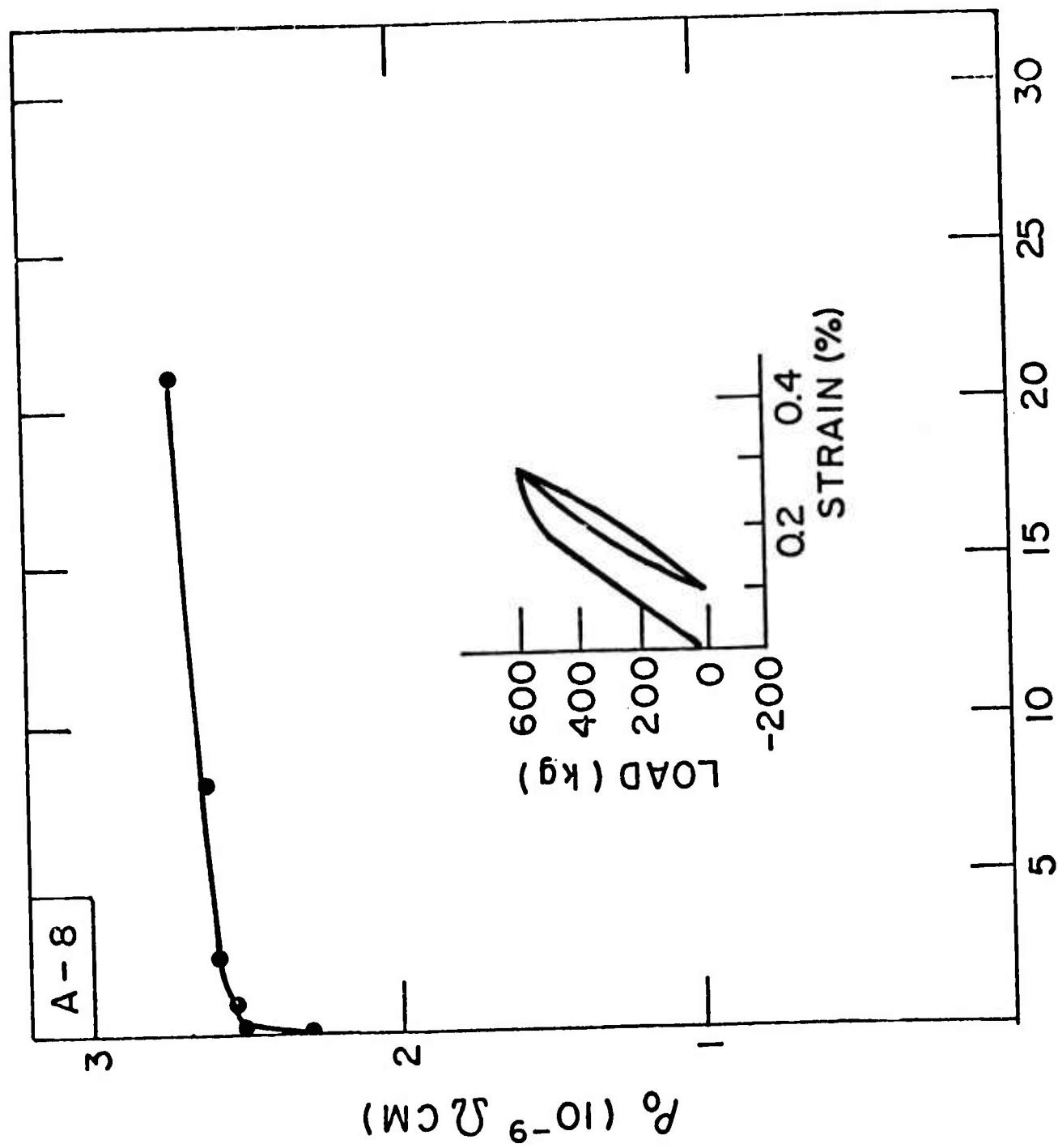


Fig. 9

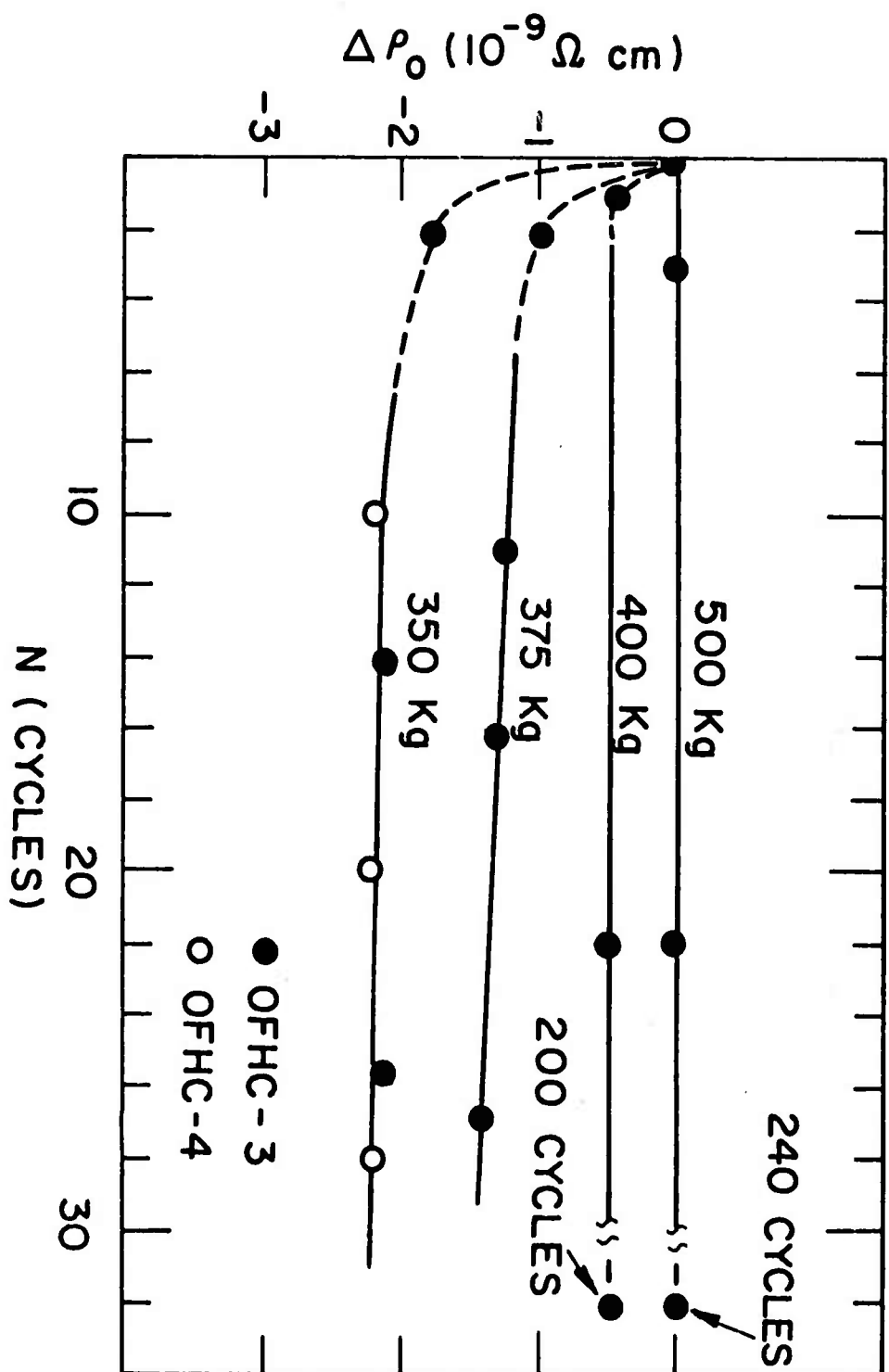


Fig. 10

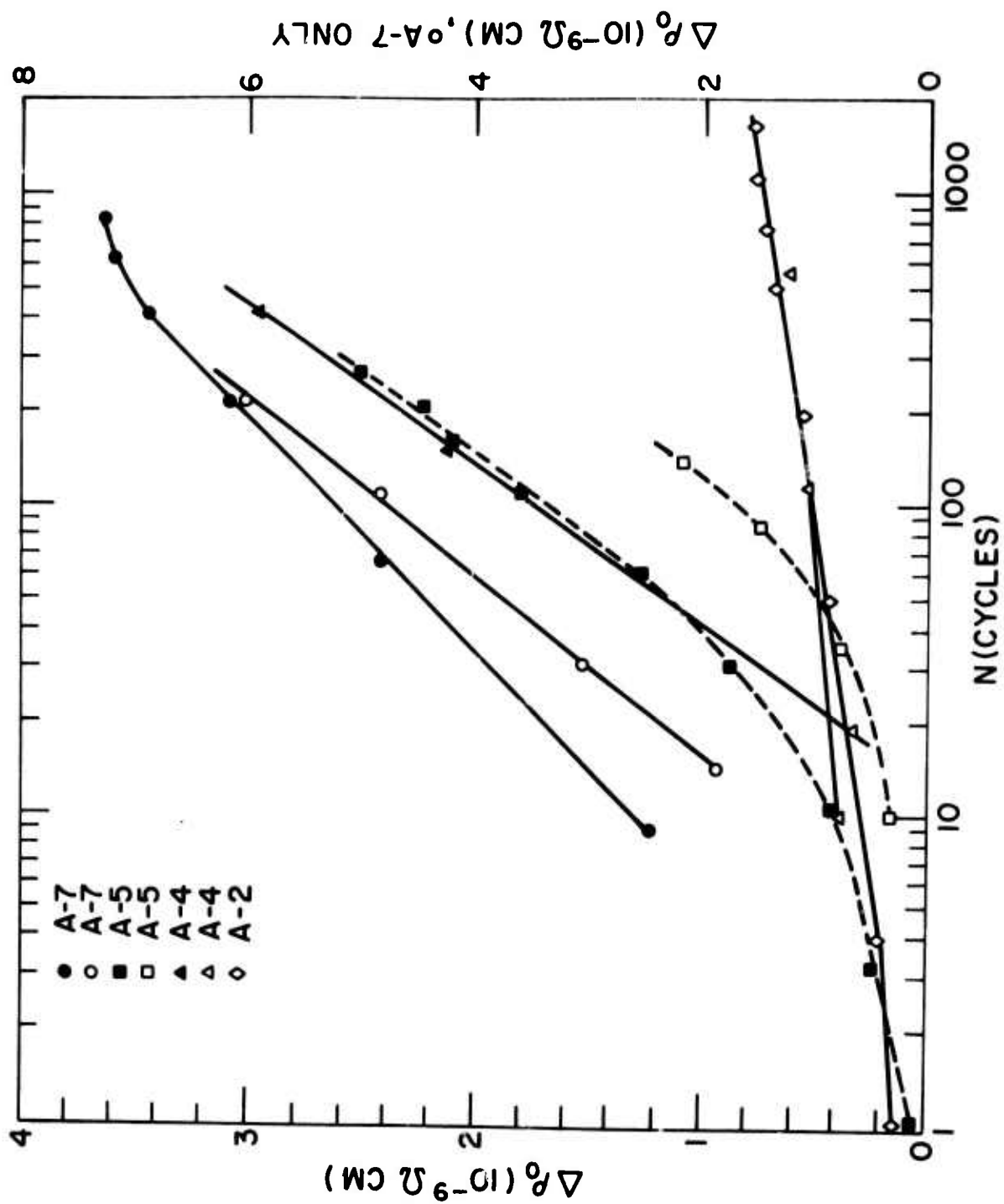


Fig. 11



SECOND SEMIANNUAL TECHNICAL REPORT

on

LOW TEMPERATURE THERMAL EXPANSION  
AND SPECIFIC HEAT PROPERTIES OF  
STRUCTURAL MATERIALS

Sponsored by

ADVANCED RESEARCH PROJECTS AGENCY

ARPA Order No. 2569

Program Code 4D10

Contract No. CST-8303

Contract Monitor

CRYOGENICS DIVISION  
NATIONAL BUREAU OF STANDARDS  
Boulder, Colorado 80302

October 14, 1974

BATTELLE  
Columbus Laboratories  
505 King Avenue  
Columbus, Ohio 43201

#### FOREWORD

This research was supported by the advanced Research Projects Agency of the Department of Defense and was monitored by the Cryogenics Division, National Bureau of Standards under Contract No. CST-8303. Dr. Richard P. Reed was Program Manager, and Dr. Alan F. Clark was Contract Monitor.

The research was carried out under ARPA Order No. 2569 and Program Code 4D10 by the Materials Technology and Metal Science Sections of BCL with F. J. Jelinek (614-299-3151, Extension 1735) and E. W. Collings (614-299-3151, Extension 1664) as Principal Investigators. Contract CST-8303, under the overall management of J. E. Campbell, covers both the handbook program and the property measurement program reported here. Only the property measurement program is presented here. Overall contract funding was \$100,000 with \$50,000 for the laboratory study. Effective date of the contract was September 10, 1973, and the contract expiration date was September 10, 1974.

#### DISCLAIMER

The views and conclusions contained in this document are those of the authors and should not be interpreted as necessarily representing the official policies, either expressed or implied, of the Advanced Research Projects Agency or the U.S. Government.

### TECHNICAL REPORT SUMMARY

The development of superconducting electrical machinery requires the suitable engineering property characterization of all candidate materials at cryogenic temperatures. This program involves the determination of thermal expansion and specific heat for several structural materials in the cryogenic temperature region (4.2 to 300 K).

Several of the materials selected for this study were supplied, for the most part, through the cooperation of Westinghouse R&D. These materials have been utilized for superconducting generator development work at Westinghouse.

Thermal expansion measurements were performed utilizing a fused silica dilatometer with a linear differential transducer as the dilatometer head. The accuracy of the measurement is 1 percent. Specific heat at low temperatures is measured to 1 percent by adiabatic calorimetry from a method developed by Nernst. In this method, small increments of heat are supplied to a thermally insulated sample, and the accompanying temperature increase is measured.

In this reporting period, thermal expansion characteristics of 19 alloy specimens were determined in the temperature range 5 to 300 K. In addition, 13 specific heat specimens were evaluated in the temperature range 4.2 to 20 K. These results are shown in the accompanying text of this report.

## LOW TEMPERATURE HEAT CAPACITY

### 1. Equipment

The equipment used in the low-temperature specific heat investigations has been described in detail in our semi-annual report (March 1, 1974).

### 2. Analysis of the Data

The low-temperature heat capacities (C) of non-superconducting non-magnetic metals are generally found to obey a relationship of the form:

$$C = \gamma T + \beta T^3,$$

where  $\gamma T$  is the conduction-electron heat capacity at temperature T, and  $\beta T^3$  is that of the lattice. Since:

$$\frac{C}{T} = \gamma + \beta T^2,$$

a plot of  $C/T$  versus  $T^2$  is linear with slope  $\beta$  and intercept  $\gamma$ . If the units of specific heat are joules/kg-deg a Debye temperature (low temperature) can be obtained from  $\beta$  using the relation

$$\theta_D = \left( \frac{1.94 \times 10^6}{\beta M} \right)^{1/3},$$

where M is the molar weight of the specimen material. Table I is a list of specimens whose specific heats have been measured, over the temperature range 4 - 20K, during the present contractual year. The first six members

of this Table form a group of materials (henceforth Group A) whose specific heats follow the above-mentioned linear relation when plotted in the format  $C/T$  versus  $T^2$ . The remaining seven members of the Table form a group (Group B) whose specific heat curves in the format  $C/T$  versus  $T^2$  possess a minimum in the low-temperature region. These data seem to follow a  $C/T = A/T + \gamma + \beta T^2$  relationship and are computer best-fitted to a function of that form.

For both Group A and Group B materials the coefficients  $A$ ,  $\gamma$  and  $\beta$  can be obtained from best-fits to the experimental data. These coefficients have the following uses:

- (i) Specific heat values can be computed for a series of "standard" temperatures such as 4.0, 5.0, 10.0, 15.0K, etc., within the  $T^3$  regime, for subsequent tabulation.
- (ii) A Debye temperature ( $\theta_D$ ) can be extracted, as described above, and used in estimating specific heat over the entire temperature range. For the Group A alloys this is done in the following way:

$$C_{\text{electron}} + C_{\text{lattice}}$$

where

$$C_{\text{electron}} = \gamma T, \text{ as before;}$$

and  $C_{\text{lattice}}$  can be computed with the aid of the Debye Function, a universal function of  $\theta/T$ , namely:

$$C_{\text{lattice}} = \frac{3R}{\chi^3} \int_0^\chi \frac{\chi^4 e^\chi d\chi}{(e^\chi - 1)^2}, \quad \chi = \theta/T.$$

For the Group B alloys we must write

$$C = A + C_{\text{electron}} + C_{\text{lattice}}.$$

However, since in practice  $A$  is never greater than 0.4 in the present alloys, the  $A$  contribution is ignored here in estimating the intermediate-temperature specific heat.

### 3. Data Presentation and Tabulations

#### 3.1 Group A Alloys

Figures 1 through 6 present the experimental data for the "A" group of alloys, plotted in the format  $C/T$  versus  $T^2$ . Through these data a straight line  $C/T = \gamma + \beta T^2$  is computer fitted and computer plotted. These Figures are accompanied by Tables 2 through 7 which list the measured specific heat values along with the fitted values at corresponding temperatures. To summarize this activity we present in Tables 8 through 13 a set of "fitted" specific heat data corresponding to the temperatures 4.0, 5.0, 10.0, 15.0 and 20.0K.

#### 3.2 Group B Alloys

Figure 7 through 13 present the experimental data for the "B" group of alloys, plotted in the format  $C/T$  versus  $T^2$ . Through these data a line  $C/T = A/T + \gamma + \beta T^2$  is least-squares computer fitted and computer plotted. These Figures are accompanied by Tables 14 through 20, which list the experimental specific heat values at the actual temperatures of measurement, together with the corresponding computer-fitted data. Finally Tables 21 through 27 give listings of specific heat values corresponding to the "standard temperatures" 4.0K to 20.0K referred to above.

#### 3.3 Debye Temperatures and Estimated Intermediate-Temperature (50 to 300 K) Specific Heats

For alloys whose chemical compositions were known, effective molar weights ( $M$ ) were calculated, enabling Debye temperatures to be derived from the best-fitted  $\beta$ -values using

$$\theta_D = \left( \frac{1.94 \times 10^6}{\bar{M}} \right)^{1/3}$$

Table 28 lists the Debye temperatures so calculated. It is then possible, using the Debye function referred to above, to compute a total specific heat ( $C = C_{\text{electron}} + C_{\text{lattice}}$ ) over the entire temperature range. This has been done, and Figures 14 through 23 are the computer-plotted 50K - 300K total specific heats. Finally for quick reference, calculated total specific heats for temperatures 50.0K, 77.0K and 300.0K are listed in Table 28.

## LOW-TEMPERATURE THERMAL EXPANSION

### 1. Equipment

The equipment used in the low-temperature thermal expansion investigations has been described in detail in our semi-annual report (March 1, 1974).

### 2. Analysis of the Data

The results reported in this work are shown as percent contraction versus temperature (K) with all data normalized at the ice point (273 K).

### 3. Data Presentation and Tabulations

Table 29 lists the materials on which thermal expansion measurements were made. Subsequent Tables 30-37 report expansion behavior for each alloy studied in the temperature range 5-300 K.



FUTURE WORK

The continuation of this program into the second year will include specific heat and thermal expansion measurements on other alloys and polymeric materials used in superconducting rotating machinery. In addition, the total intermediate-temperature specific heats of the present specimens will be measured to verify the results of the above computations.

TABLE 1. LIST OF SPECIFIC HEAT  
SPECIMENS MEASURED

Specimen Name	Processing and Treatment
Copper	OFHC - SR
Copper	OFHC - AR
Bronze - 8 SN	AS - extruded
Bronze - 11 SN	AS - cast
Westinghouse Kromarc 58	STQ
Westinghouse Kromarc 58	CR (~30%)
Inconel X750 (MP1)	ST
Inconel X750 (MP1)	STDA VIM-VAR
Inconel X750 (MP2)	STDA AAM-VAR
Inconel X750 (MP3)	STDA VIM
Stainless Steel AISI 310 S	STQ
Stainless Steel AISI 310 S	STFC
Inco Low-Expansion (LE) Alloy	ST-A

ST Solution treated  
 ST-A Solution treated and aged  
 STDA Solution treated double aged  
 VIM Vacuum induction melted  
 VAR Vacuum arc re-melted  
 STQ Solution treated and quenched  
 STFC Solution treated and furnace cooled  
 CR Cold rolled

## GROUP A

Alloys whose specific-heat data are  
best-fitted to the relationship--

$$C = \gamma T + \beta T^3.$$

Copper OFHC - SR

Copper OFHC - AR

Bronze - 8 SN

Bronze - 11 SN

Westinghouse Kromarc 58 STQ

Westinghouse Kromarc 58 CR (~30%)

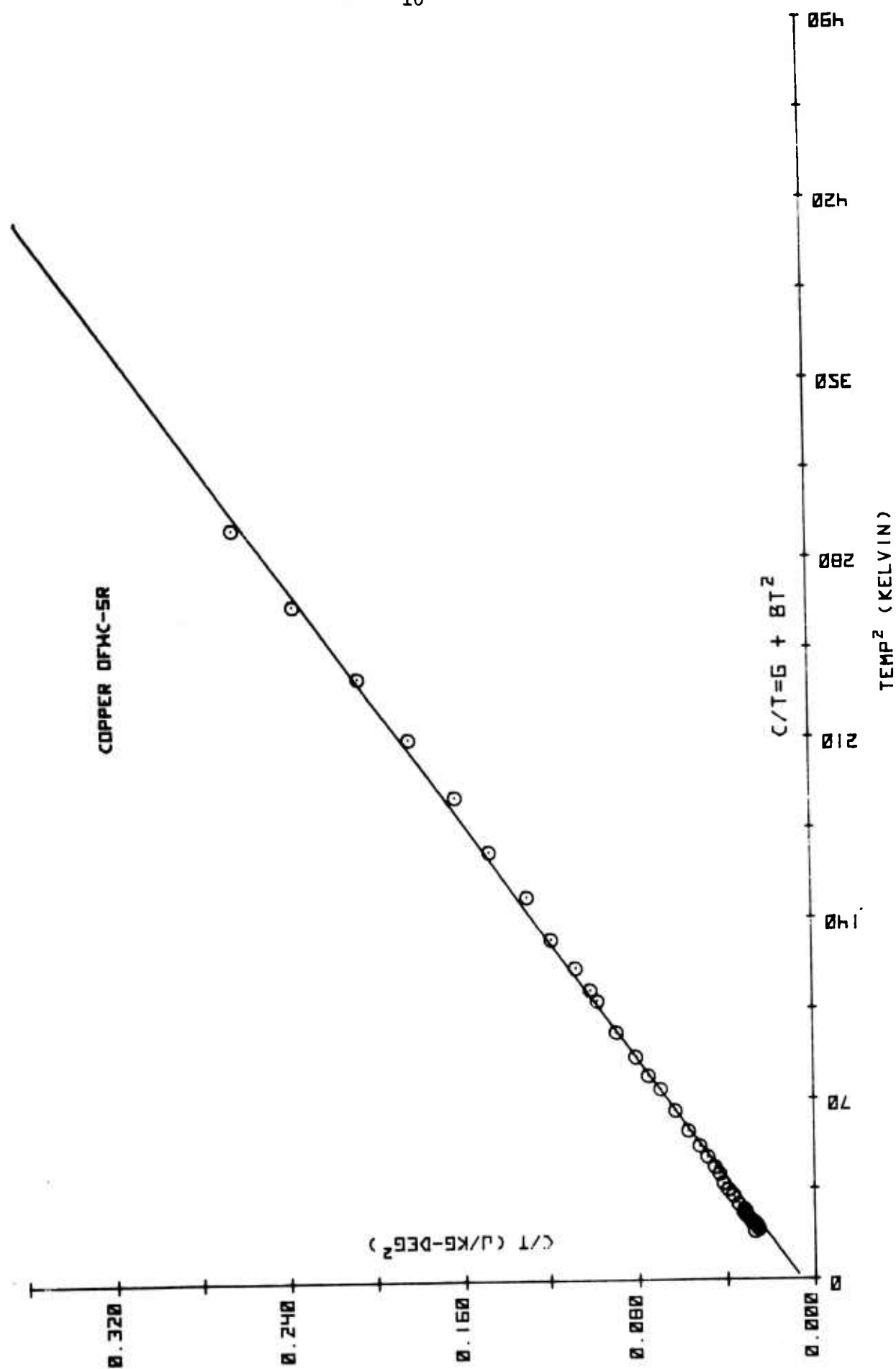


FIGURE 1. SPECIFIC HEAT DATA FOR COPPER OFHC-SR LEAST-SQUARES  
FITTED TO THE FORMULA  $C/T = \gamma + \beta T^2$

TABLE 2. LOW-TEMPERATURE SPECIFIC HEAT OF  
COPPER OFHC - SR FITTED TO

$$C = \gamma T + \beta T^3$$

Temperature, K	Measured Value (J/kg-deg.)	Fitted Value (J/kg-deg.)
4.3	0.119	0.095
4.4	0.114	0.101
4.5	0.119	0.107
4.6	0.124	0.113
4.7	0.132	0.119
4.7	0.137	0.119
4.8	0.142	0.125
4.9	0.151	0.132
5.0	0.158	0.139
5.1	0.166	0.146
5.2	0.166	0.154
5.4	0.188	0.169
5.7	0.212	0.195
5.9	0.233	0.214
6.1	0.253	0.233
6.4	0.277	0.265
6.6	0.299	0.289
6.9	0.335	0.326
7.2	0.375	0.366
7.6	0.435	0.425
8.1	0.511	0.508
8.6	0.600	0.601
8.9	0.670	0.662
9.3	0.752	0.750
9.8	0.878	0.870
10.4	1.019	1.032
10.6	1.070	1.090
11.0	1.182	1.213
11.5	1.361	1.379
12.2	1.578	1.637
12.9	1.895	1.925
13.7	2.226	2.295
14.5	2.654	2.710
15.3	3.146	3.173
16.2	3.812	3.754
17.1	4.485	4.403

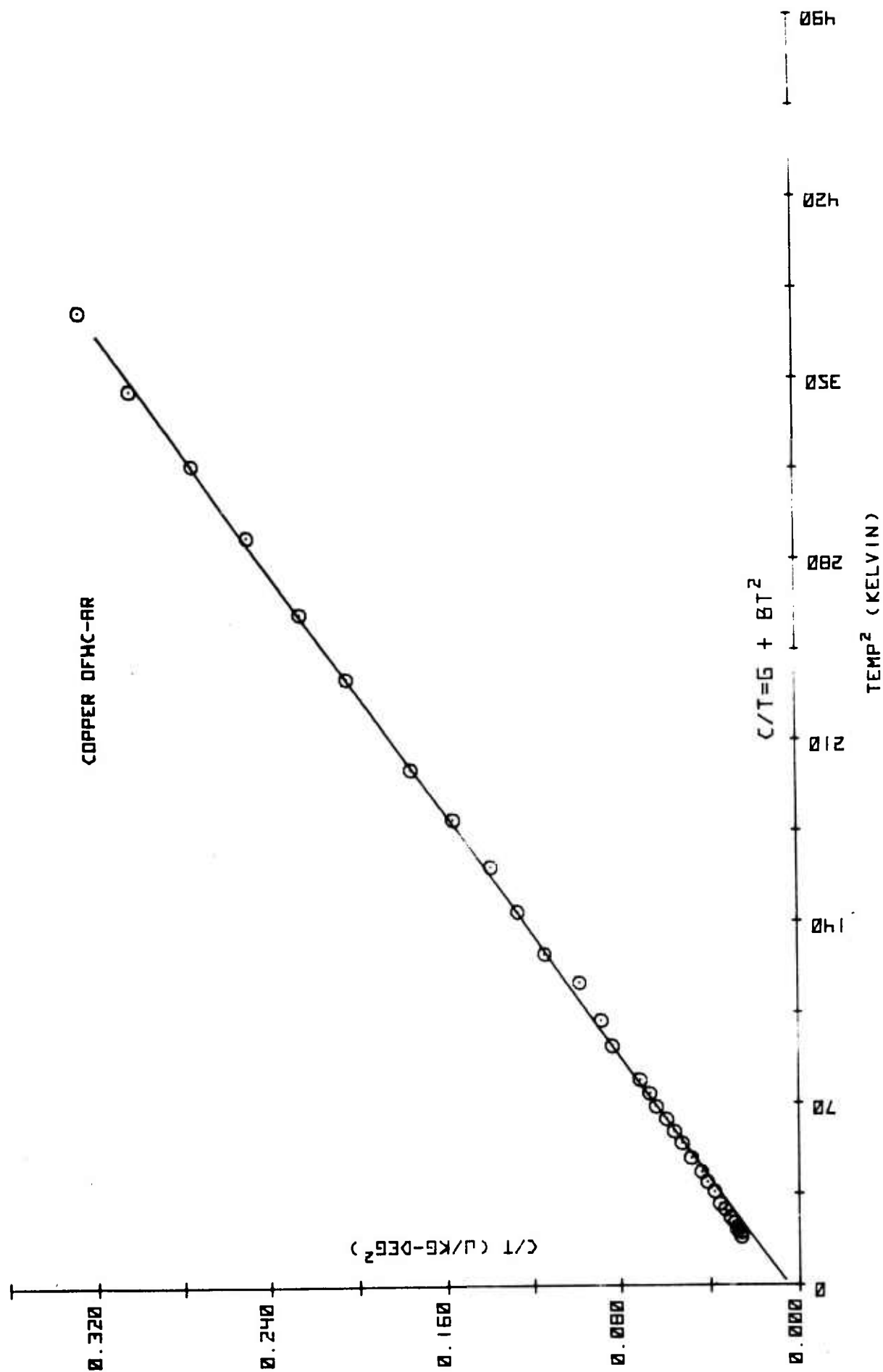


FIGURE 2. SPECIFIC HEAT DATA FOR COPPER OFHC-AR LEAST-SQUARES  
FITTED TO THE FORMULA  $C/T = \gamma + \beta T^2$

TABLE 3. LOW-TEMPERATURE SPECIFIC HEAT  
OF COPPER OFHC - AR FITTED TO

$$C = \gamma T + \beta^3$$

Temperature, K	Measured Value (J/kg-deg.)	Fitted Value (J/kg-deg.)
4.3	0.112	0.089
4.5	0.118	0.100
4.5	0.118	0.100
4.6	0.128	0.106
4.7	0.131	0.112
4.9	0.141	0.125
5.1	0.157	0.138
5.4	0.180	0.161
5.6	0.200	0.177
6.0	0.229	0.214
6.3	0.261	0.244
6.6	0.291	0.278
7.0	0.341	0.327
7.4	0.391	0.382
7.7	0.433	0.427
8.0	0.477	0.475
8.3	0.532	0.528
8.6	0.575	0.584
8.9	0.633	0.644
9.6	0.802	0.800
10.1	0.893	0.926
10.8	1.060	1.125
11.3	1.295	1.283
12.0	1.526	1.529
12.7	1.770	1.805
13.4	2.092	2.112
14.1	2.463	2.453
15.3	3.118	3.121
16.1	3.614	3.627
17.0	4.218	4.261
17.8	4.874	4.882
18.6	5.630	5.562
19.4	6.308	6.302

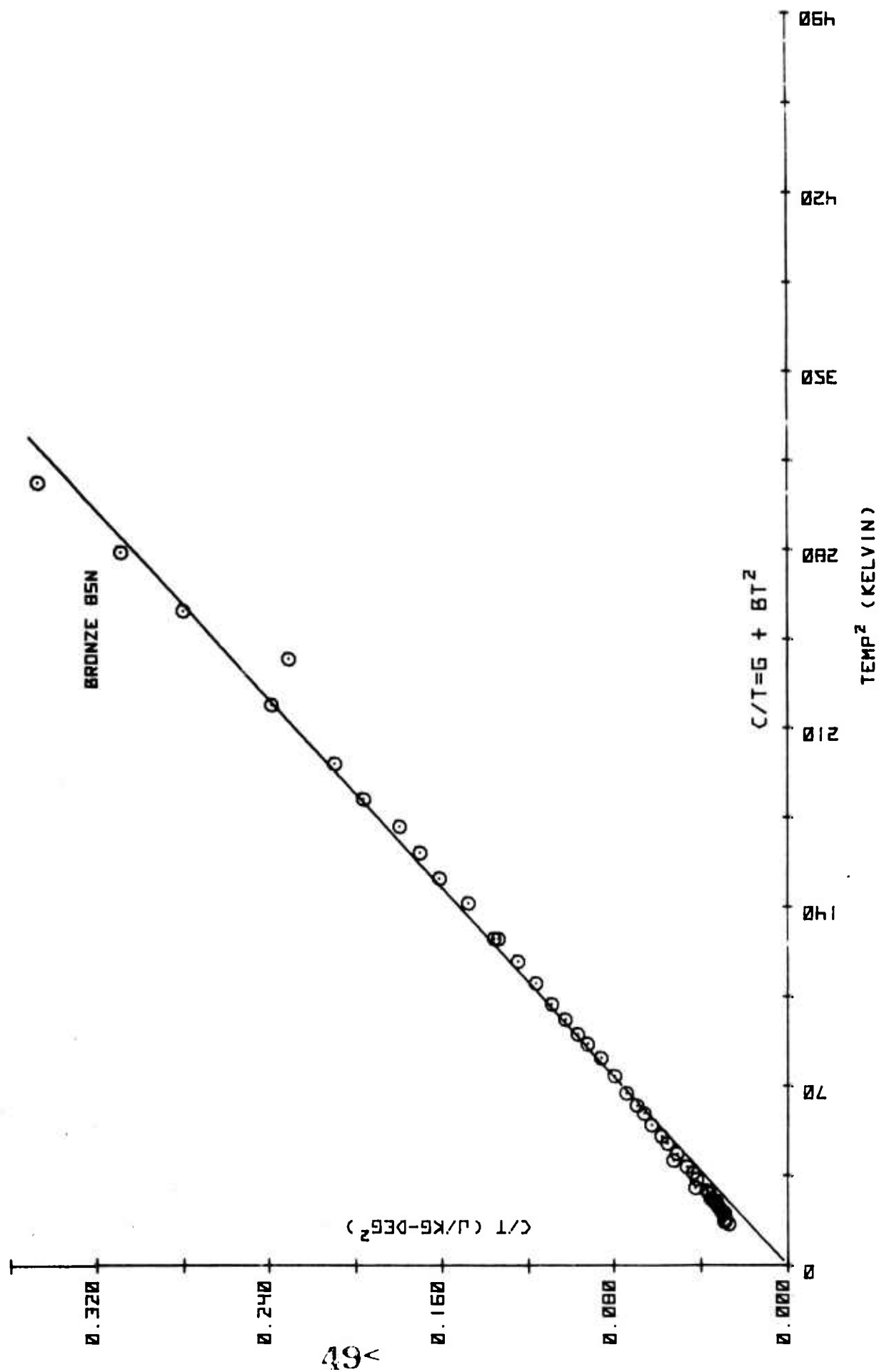


FIGURE 3. SPECIFIC HEAT DATA FOR BRONZE 8SN LEAST-SQUARES  
FITTED TO THE FORMULA  $C/T = \gamma + \beta T^2$



TABLE 4. LOW-TEMPERATURE SPECIFIC HEAT  
OF BRONZE 8 SN FITTED TO

$$C = \gamma T + \beta T^3$$

Temperature, K	Measured Value (J/kg-deg.)	Fitted Value (J/kg-deg.)
4.0	0.109	0.070
4.1	0.120	0.075
4.2	0.121	0.081
4.5	0.131	0.099
4.5	0.136	0.099
4.6	0.140	0.106
4.7	0.148	0.113
4.7	0.148	0.113
4.9	0.161	0.128
4.9	0.162	0.128
5.0	0.166	0.136
5.0	0.170	0.136
5.1	0.181	0.144
5.3	0.193	0.162
5.4	0.202	0.171
5.5	0.235	0.181
5.8	0.244	0.212
6.0	0.262	0.235
6.2	0.289	0.259
6.4	0.338	0.285
6.9	0.384	0.357
7.1	0.414	0.389
7.4	0.466	0.440
6.6	0.338	0.312
7.7	0.511	0.495
7.9	0.550	0.535
8.2	0.610	0.598
8.6	0.686	0.690
9.0	0.774	0.791
9.3	0.859	0.872
9.5	0.921	0.930
9.8	1.008	1.020
10.1	1.103	1.117
10.5	1.225	1.255
10.9	1.363	1.404
11.3	1.516	1.564
11.3	1.539	1.564
11.9	1.761	1.826
12.3	1.983	2.016
12.7	2.161	2.219
13.1	2.353	2.436
13.5	2.651	2.665
14.0	2.933	2.973
14.8	3.529	3.512
15.4	3.546	3.956
16.0	4.484	4.436
16.7	5.156	5.044
17.5	6.073	5.804

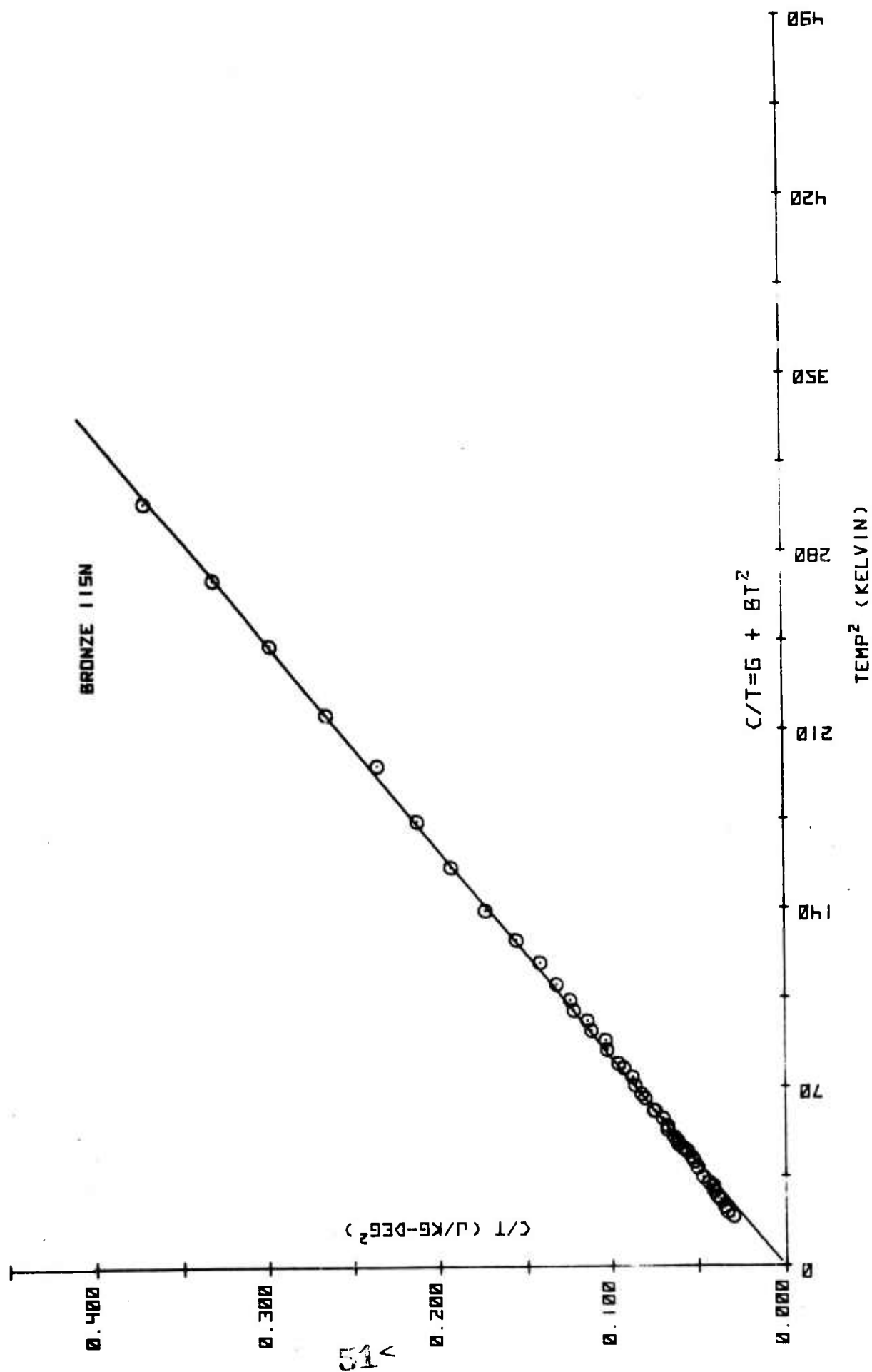


FIGURE 4. SPECIFIC HEAT DATA FOR BRONZE 115N LEAST-SQUARES  
FITTED TO THE FORMULA  $C/T = \gamma + \beta T^2$

TABLE 5. LOW-TEMPERATURE SPECIFIC HEAT  
OF BRONZE 11 SN FITTED TO

$$C = \gamma T + \beta T^3$$

Temperature, K	Measured Value (J/kg-deg.)	Fitted Value (J/kg-deg.)
4.4	0.133	0.107
4.4	0.133	0.107
4.6	0.155	0.122
4.8	0.168	0.139
5.1	0.191	0.166
5.2	0.203	0.176
5.2	0.203	0.176
5.4	0.222	0.196
5.6	0.233	0.219
5.7	0.251	0.230
5.9	0.279	0.255
6.2	0.312	0.296
6.4	0.336	0.325
6.5	0.348	0.340
6.7	0.379	0.372
6.7	0.377	0.372
6.8	0.401	0.389
6.9	0.424	0.406
7.0	0.433	0.424
7.1	0.453	0.442
7.3	0.494	0.480
7.4	0.500	0.500
7.6	0.534	0.542
7.8	0.585	0.585
7.8	0.591	0.585
8.1	0.654	0.655
8.2	0.679	0.679
8.4	0.726	0.730
8.6	0.757	0.783
8.8	0.818	0.838
8.9	0.856	0.867
9.2	0.947	0.957
9.4	0.976	1.021
9.6	1.078	1.087
9.8	1.123	1.156
10.0	1.227	1.228
10.2	1.274	1.303
10.5	1.395	1.421
10.9	1.553	1.589
11.3	1.761	1.770
11.8	2.044	2.015
12.5	2.407	2.394
13.2	2.799	2.817
14.0	3.289	3.360
14.7	3.888	3.889
15.6	4.634	4.646
16.4	5.419	5.397
17.3	6.389	6.333

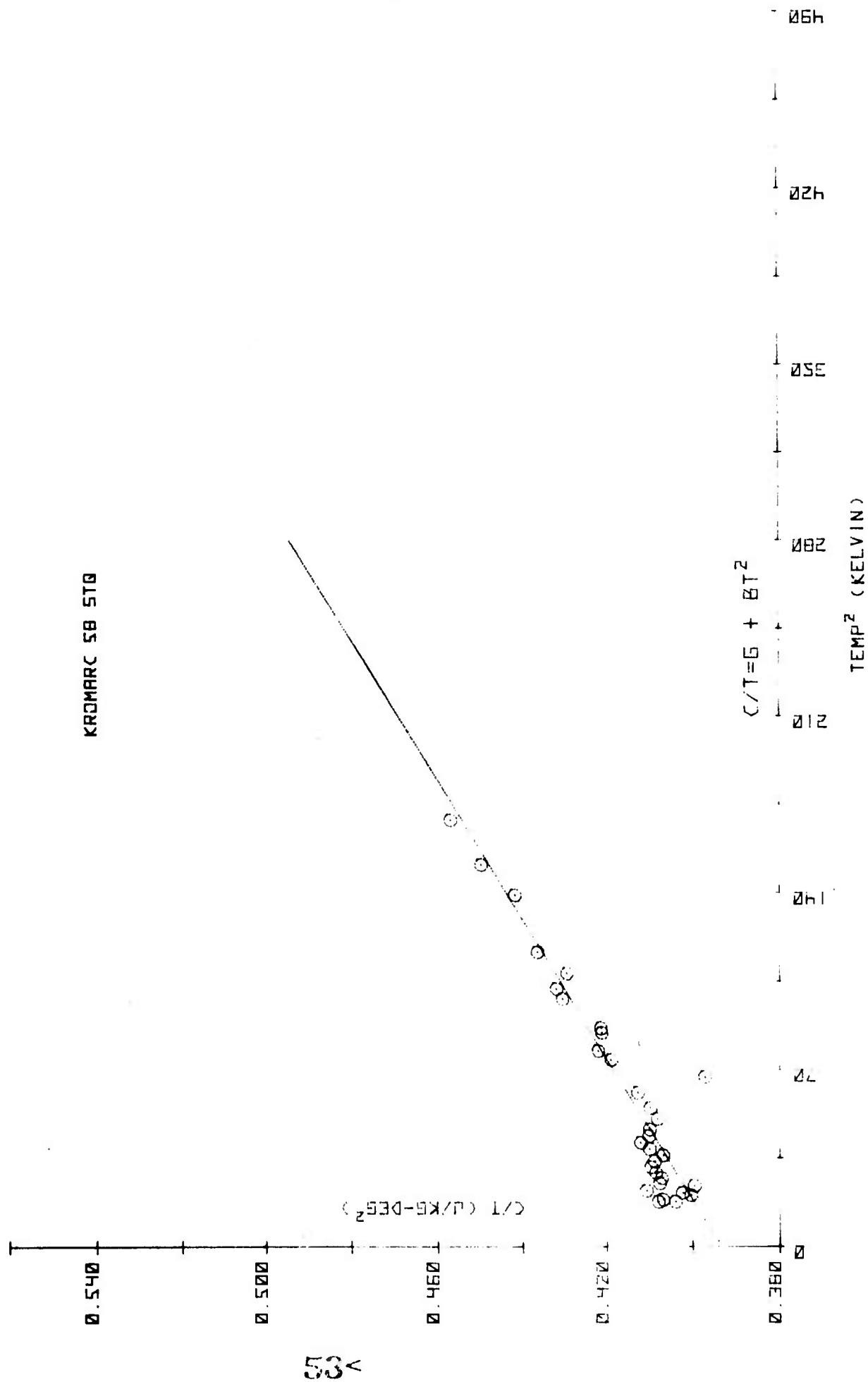


FIGURE 5. SPECIFIC HEAT DATA FOR KROMARC 58 STQ LEAST-SQUARES  
 FITTED TO THE FORMULA  $C/T = \gamma + \beta T^2$

TABLE 6. LOW-TEMPERATURE SPECIFIC HEAT  
OF KROMARC 58 CR FITTED TO

$$C = \gamma T + \beta T^3$$

Temperature, K	Measured Value (J/kg-deg.)	Fitted Value (J/kg-deg.)
4.1	1.691	1.645
4.3	1.738	1.727
4.4	1.783	1.768
4.5	1.814	1.810
4.6	1.863	1.851
4.7	1.924	1.893
4.8	1.985	1.935
5.0	2.066	2.018
5.2	2.155	2.102
5.4	2.244	2.187
5.6	2.305	2.272
5.7	2.362	2.314
5.9	2.458	2.400
6.1	2.561	2.485
6.5	2.792	2.659
6.8	2.795	2.790
7.2	2.951	2.966
7.5	3.087	3.100
7.9	3.240	3.281
8.3	3.434	3.463
8.7	3.621	3.649
9.1	3.813	3.837
9.6	3.978	4.075
10.3	4.320	4.417
10.8	4.565	4.667
11.6	4.852	5.077
13.7	6.346	6.222
14.9	7.022	6.926

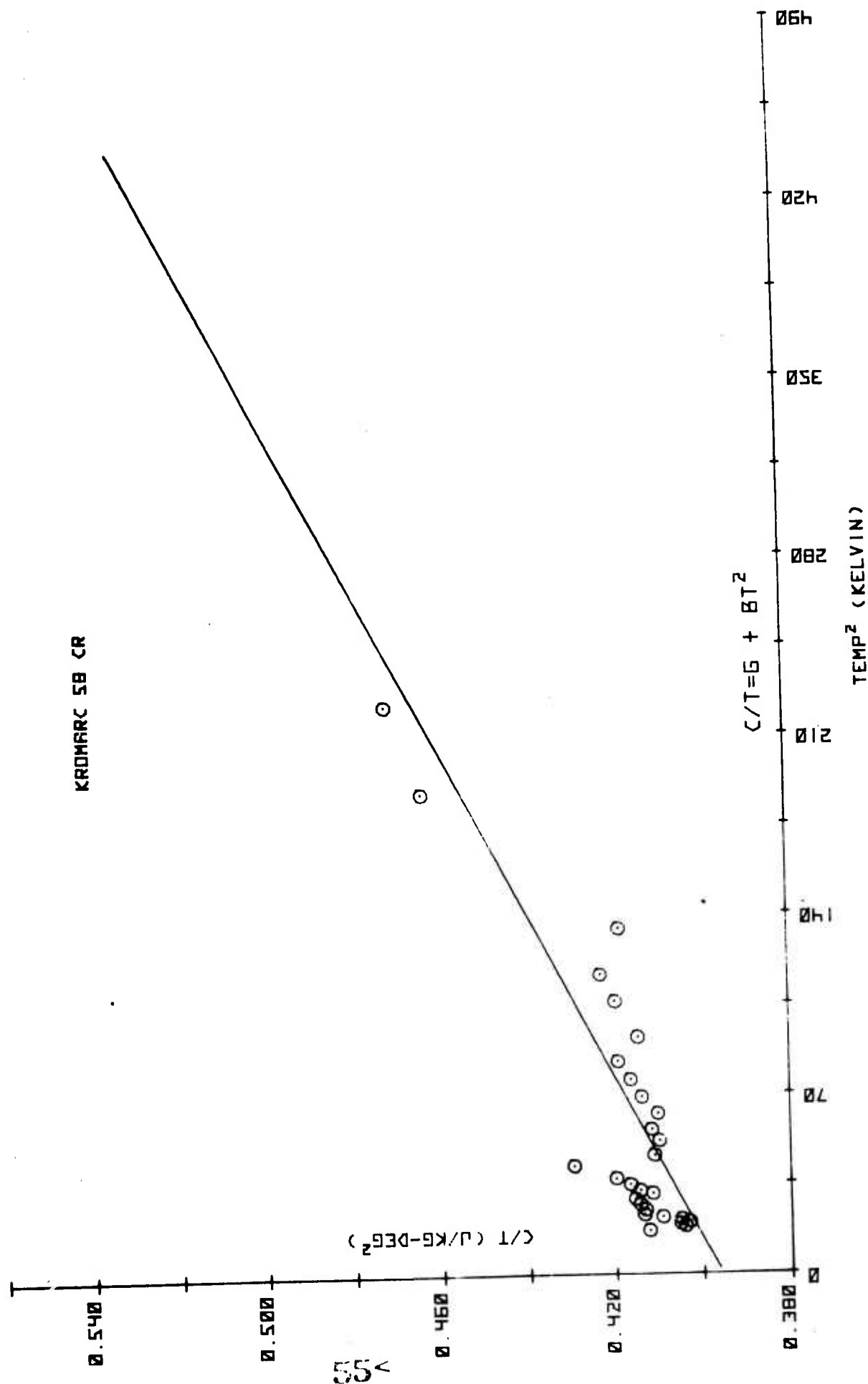


FIGURE 6. SPECIFIC HEAT DATA FOR KROMARC 58 CR LEAST-SQUARES  
FITTED TO THE FORMULA  $C/T = \gamma + \beta T^2$

TABLE 7. LOW-TEMPERATURE SPECIFIC HEAT  
OF KROMARC 58 STQ FITTED TO  
 $C = \gamma T + \beta T^3$

Temperature, K	Measured Value (J/kg-deg.)	Fitted Value (J/kg-deg.)
4.2	1.697	1.679
4.2	1.714	1.679
4.3	1.750	1.720
4.5	1.802	1.803
4.6	1.851	1.845
4.7	1.931	1.886
4.9	1.958	1.970
5.0	2.039	2.012
5.2	2.118	2.096
5.4	2.207	2.181
5.6	2.295	2.266
5.8	2.372	2.352
6.0	2.442	2.438
6.2	2.543	2.525
6.4	2.638	2.612
6.6	2.708	2.700
6.8	2.789	2.788
7.1	2.899	2.922
7.4	3.034	3.057
7.8	3.220	3.239
8.2	3.256	3.424
8.6	3.603	3.612
8.8	3.714	3.707
9.2	3.875	3.899
9.3	3.919	3.947
9.9	4.263	4.243
10.1	4.364	4.343
10.4	4.467	4.495
10.8	4.714	4.701
11.8	5.212	5.232
12.3	5.530	5.506
13.0	5.938	5.902

## SUMMARY OF GROUP A DATA

COMPUTED FROM

$$C = \gamma T + \delta T^3$$



TABLE 8. SPECIFIC HEAT OF COPPER OFHC-SR

$$\gamma = 6.2982 \times 10^{-3}$$

$$\beta = 8.5902 \times 10^{-4}$$

Temperature, K	Specific Heat (J/kg-deg.)
4.0	0.08
5.0	0.14
10.0	0.92
15.0	2.99
20.0	7.00

TABLE 9. SPECIFIC HEAT OF COPPER OFHC-AR

$$\gamma = 5.0363 \times 10^{-3}$$

$$\beta = 8.4977 \times 10^{-4}$$

Temperature, K	Specific Heat (J/kg-deg.)
4.0	0.07
5.0	0.13
10.0	0.90
15.0	2.94
20.0	6.90

TABLE 10. SPECIFIC HEAT OF BRONZE 8 SN

$$\gamma = 1.6491 \times 10^{-4}$$

$$\beta = 1.0824 \times 10^{-3}$$

Temperature, K	Specific Heat (J/kg-deg.)
4.0	0.07
5.0	0.14
10.0	1.08
15.0	3.66
20.0	8.66

TABLE 11. SPECIFIC HEAT OF BRONZE 11 SN

$$\gamma = 7.5596 \times 10^{-4}$$

$$\beta = 1.2207 \times 10^{-3}$$

Temperature, K	Specific Heat (J/kg-deg.)
4.0	0.08
5.0	0.16
10.0	1.23
15.0	4.13
20.0	9.78

TABLE 12. SPECIFIC HEAT OF KROMARC 58 CR

$$\gamma = 3.9590 \times 10^{-1}$$

$$\beta = 3.1049 \times 10^{-4}$$

Temperature, K	Specific Heat (J/kg-deg.)
4.0	1.60
5.0	2.02
10.0	4.27
15.0	6.99
20.0	10.40

TABLE 13. SPECIFIC HEAT OF KROMARC 58 STQ

$$\gamma = 3.9343 \times 10^{-1}$$

$$\beta = 3.5859 \times 10^{-4}$$

Temperature, K	Specific Heat (J/kg-deg.)
4.0	1.60
5.0	2.01
10.0	4.29
15.0	7.11
20.0	10.74

## GROUP B

Alloys whose specific-heat data are  
best-fitted to the relationship--

$$C = A + \gamma T + \beta T^3.$$

Inconel X750 (MP1)	ST
Inconel X750 (MP1)	STDA VIM-VAR
Inconel X750 (MP2)	STDA AAM-VAR
Inconel X750 (MP3)	STDA VIM
Stainless Steel AISI 310 S	STQ
Stainless Steel AISI 310 S	STFC
Inco Low-Expansion (LE) Alloy	ST-A

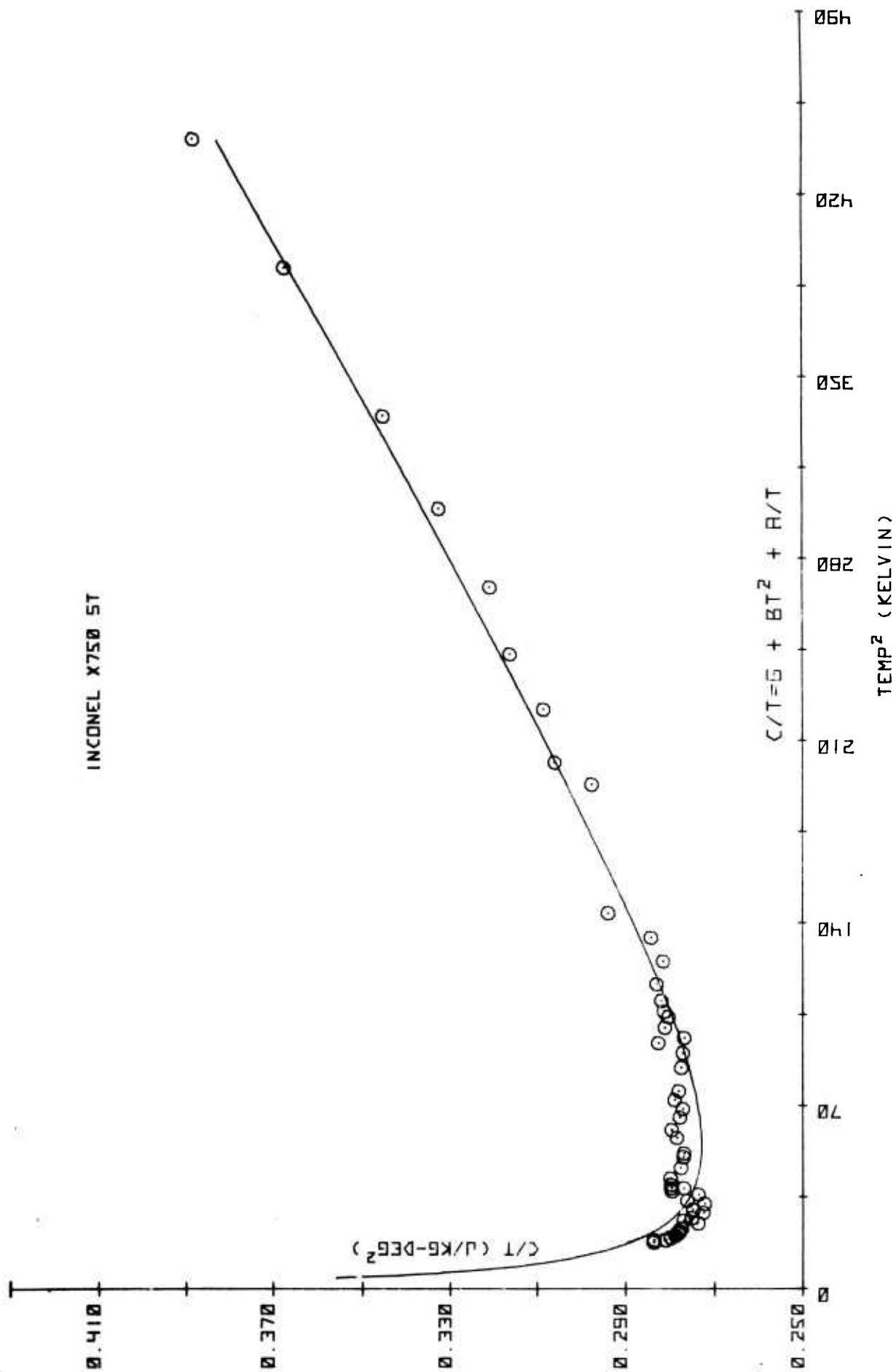


FIGURE 7. SPECIFIC HEAT DATA FOR INCONEL X750 ST LEAST-SQUARES  
FITTED TO THE FORMULA  $C/T = A/T + \gamma + \beta T^2$

TABLE 14. LOW-TEMPERATURE SPECIFIC HEAT OF  
INCONEL X750 ST FITTED TO

$$C = A + \gamma T + \delta T^3$$

Temperature, K	Measured Value (J/kg-deg.)	Fitted Value (J/kg-deg.)
4.2	1.192	1.215
4.3	1.220	1.239
4.3	1.209	1.239
4.4	1.232	1.262
4.5	1.255	1.286
4.6	1.280	1.310
4.7	1.307	1.333
4.8	1.332	1.357
5.0	1.369	1.405
5.1	1.413	1.430
5.2	1.431	1.454
5.4	1.472	1.503
5.5	1.512	1.527
5.7	1.552	1.577
5.8	1.602	1.602
6.0	1.642	1.652
6.1	1.706	1.678
6.2	1.735	1.703
6.3	1.763	1.729
6.5	1.820	1.781
6.2	1.717	1.703
6.8	1.888	1.859
7.1	1.967	1.939
7.2	1.994	1.966
7.6	2.117	2.075
7.8	2.182	2.130
8.1	2.251	2.215
8.3	2.301	2.272
8.5	2.372	2.330
8.7	2.420	2.388
9.2	2.554	2.538
9.5	2.634	2.630
9.7	2.743	2.692
9.8	2.714	2.724
10.0	2.813	2.787
10.2	2.861	2.851
10.3	2.899	2.884
10.5	2.962	2.950
10.8	3.058	3.050
11.2	3.155	3.187
11.6	3.299	3.327
12.0	3.527	3.471
13.9	4.136	4.214
14.2	4.345	4.341
14.9	4.598	4.647
15.6	4.934	4.968
16.4	5.261	5.354
17.3	5.752	5.815
18.3	6.317	6.362
19.8	7.272	7.254
21.0	8.151	8.035

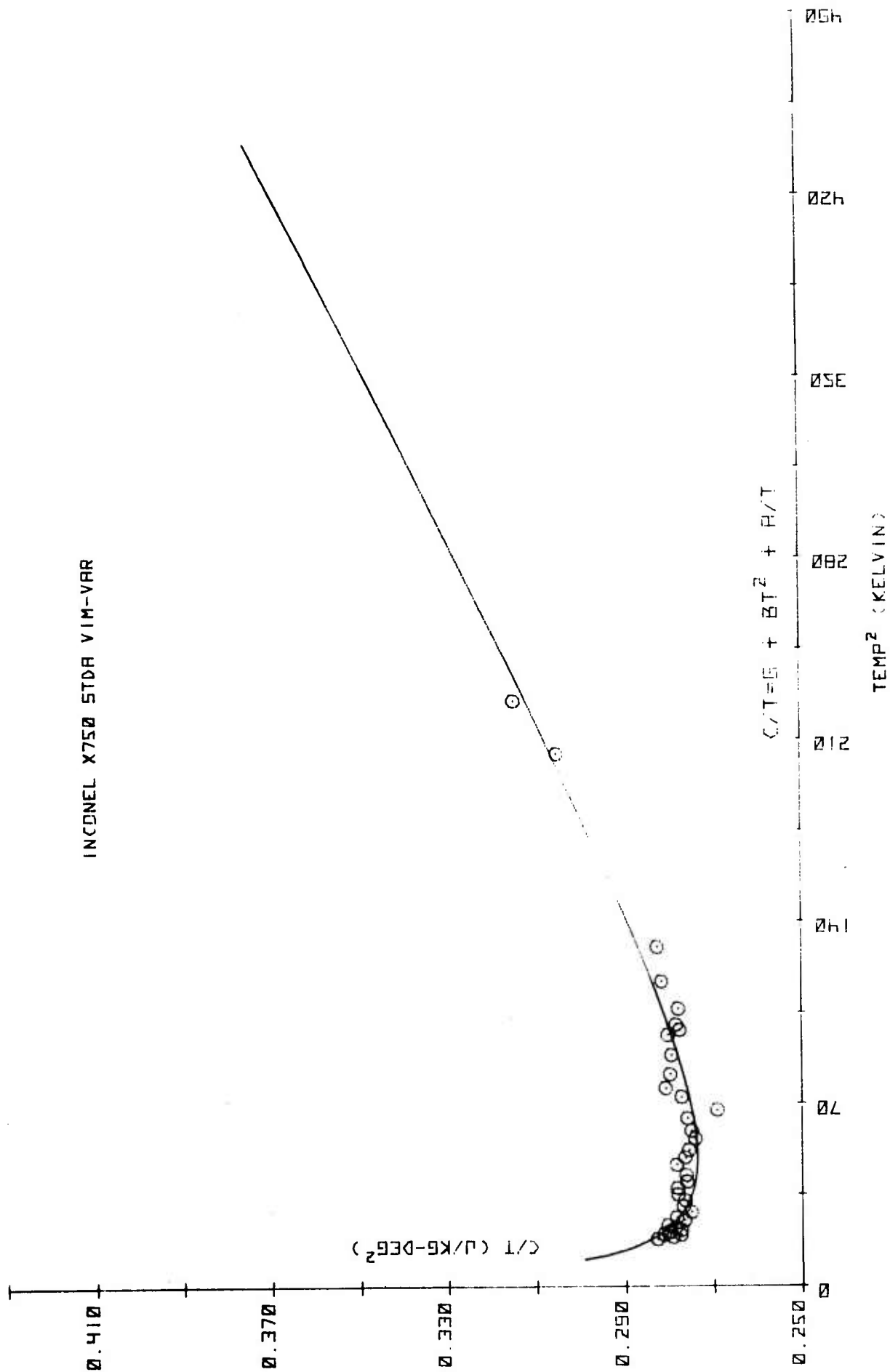


FIGURE 8. SPECIFIC HEAT DATA FOR INCONEL X750 STD VIM-VAR LEAST-SQUARES  
 FITTED TO THE FORMULA  $C/T = A/T + \gamma + \beta T^2$

TABLE 15. LOW-TEMPERATURE SPECIFIC HEAT OF  
INCONEL X750 STDA VIM-VAR FITTED TO

$$C = A + \gamma T + \beta T^3$$

Temperature, K	Measured Value (J/kg-deg.)	Fitted Value (J/kg-deg.)
4.2	1.188	1.195
4.3	1.201	1.219
4.4	1.221	1.244
4.4	1.238	1.244
4.5	1.261	1.268
4.6	1.276	1.293
4.7	1.310	1.318
4.8	1.346	1.343
5.0	1.383	1.393
5.1	1.420	1.418
5.3	1.458	1.468
5.5	1.523	1.519
5.7	1.576	1.571
5.9	1.641	1.622
6.1	1.697	1.675
6.3	1.739	1.727
6.5	1.795	1.780
6.8	1.893	1.861
7.0	1.935	1.915
7.2	1.984	1.970
7.5	2.056	2.054
7.7	2.117	2.110
8.0	2.207	2.195
8.2	2.207	2.253
8.5	2.356	2.341
8.7	2.443	2.400
9.0	2.518	2.491
9.4	2.627	2.613
9.8	2.747	2.739
9.9	2.748	2.770
10.0	2.784	2.802
10.3	2.862	2.899
10.8	3.042	3.065



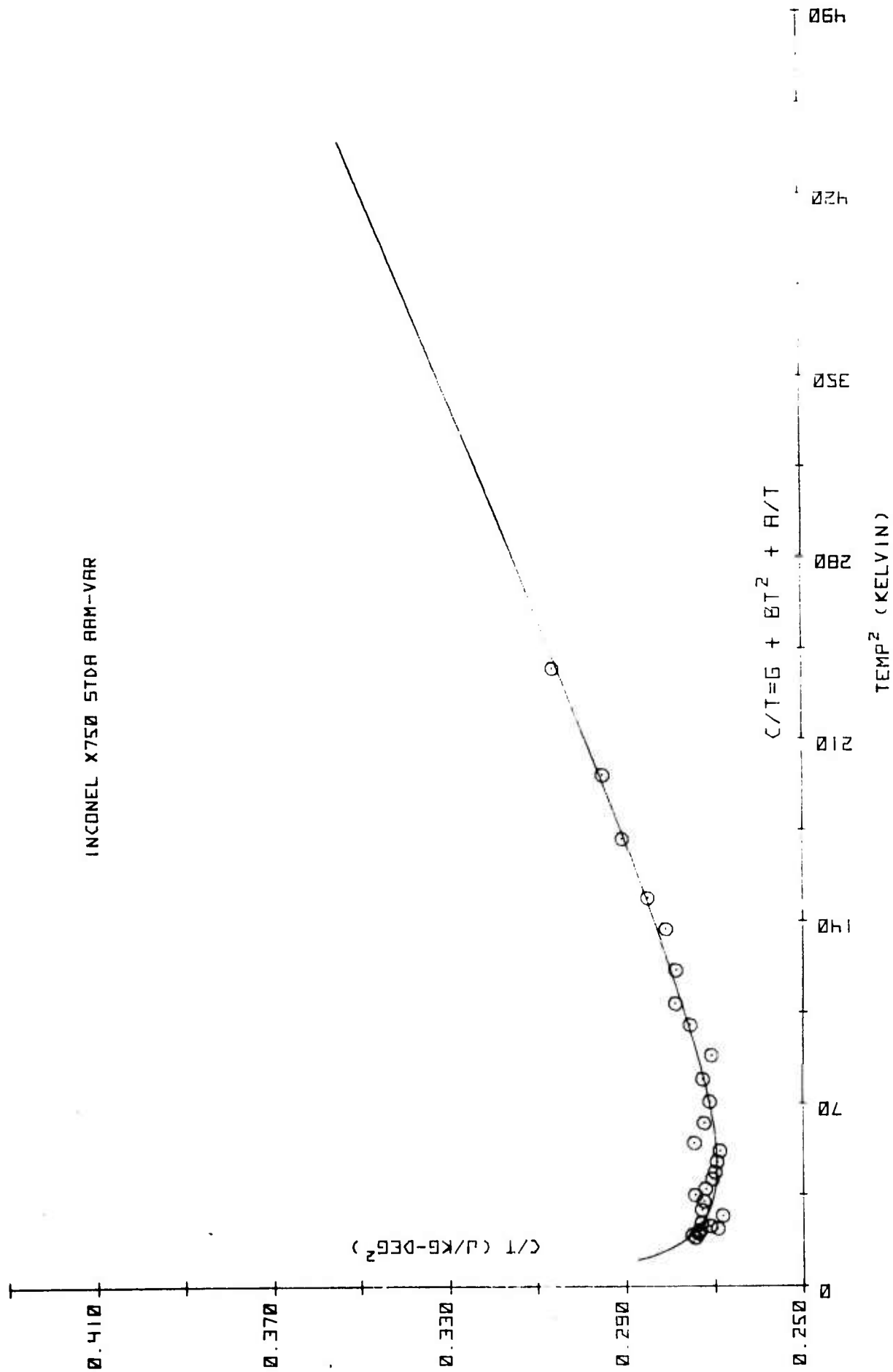


FIGURE 9. SPECIFIC HEAT DATA FOR INCONEL X750 STDA AAM-VAR LEAST-SQUARES  
 FITTED TO THE FORMULA  $C/T = A/T + \gamma + \beta T^2$

TABLE 16. LOW-TEMPERATURE SPECIFIC HEAT OF  
INCONEL X750 STDA AAM-VAR FITTED TO

$$C = A + \gamma T + \beta T^3$$

Temperature, K	Measured Value (J/kg-deg.)	Fitted Value (J/kg-deg.)
4.3	1.180	1.187
4.4	1.210	1.212
4.5	1.232	1.237
4.6	1.258	1.262
4.7	1.266	1.287
4.8	1.301	1.312
4.9	1.338	1.337
5.2	1.395	1.414
5.4	1.474	1.465
5.7	1.553	1.542
5.9	1.619	1.594
6.1	1.660	1.647
6.4	1.732	1.726
6.6	1.782	1.779
6.9	1.860	1.860
7.2	1.936	1.942
7.4	2.032	1.997
7.9	2.152	2.136
8.4	2.278	2.279
8.9	2.427	2.425
9.4	2.545	2.574
10.0	2.754	2.758
10.4	2.898	2.883
11.0	3.064	3.076
11.7	3.286	3.309
12.2	3.477	3.481
13.1	3.808	3.802
14.0	4.130	4.140
15.4	4.715	4.699

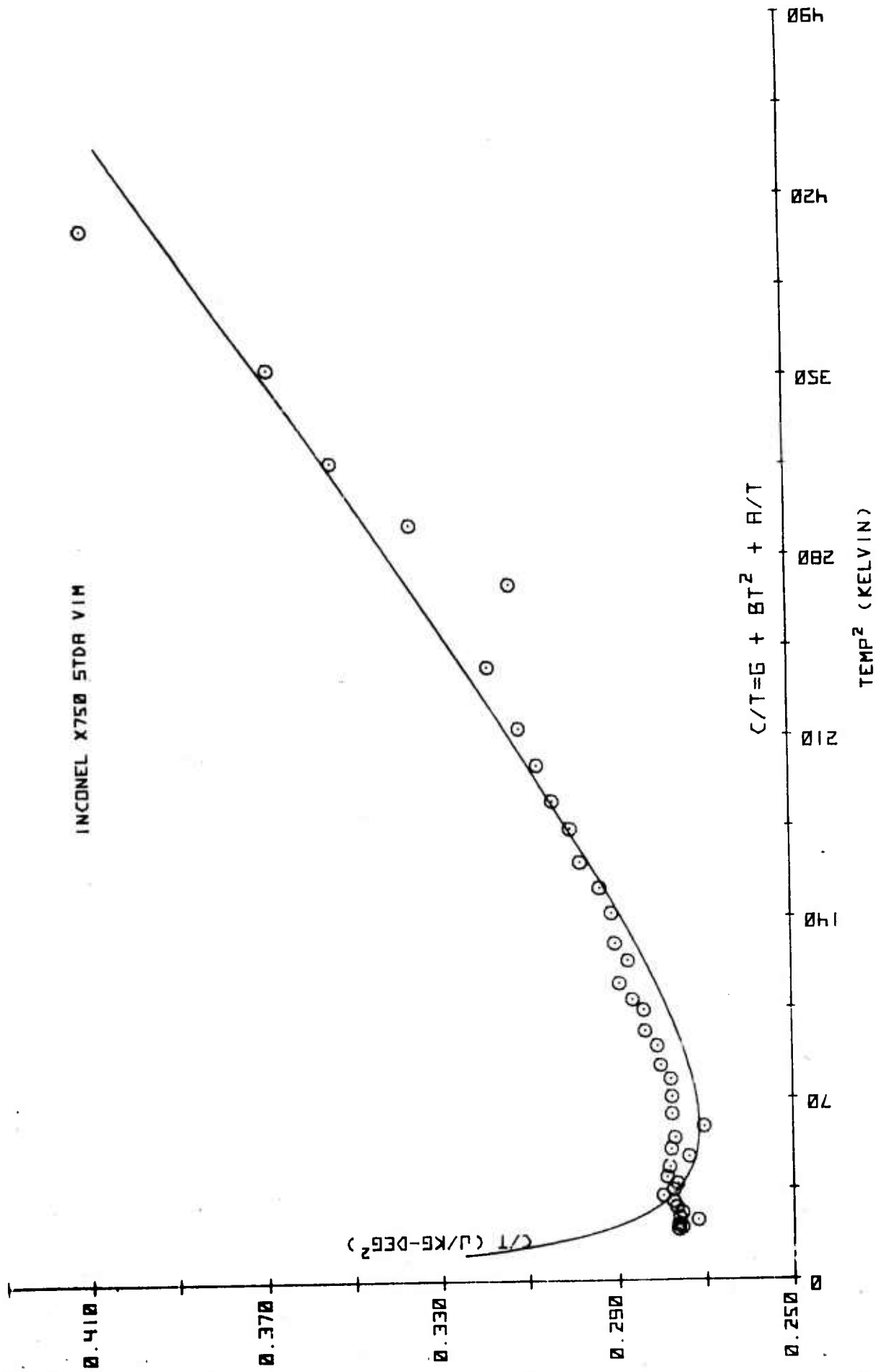


FIGURE 10. SPECIFIC HEAT DATA FOR INCONEL X750 STD R VIM LEAST-SQUARES  
FITTED TO THE FORMULA  $C/T = A/T + \gamma + BT^2$

TABLE 17. LOW-TEMPERATURE SPECIFIC HEAT OF  
INCONEL X750 STDA VIM FITTED TO

$$C = A + \gamma T + \beta T^3$$

Temperature, K	Measured Value (J/kg-deg.)	Fitted Value (J/kg-deg.)
4.4	1.216	1.290
4.5	1.240	1.312
4.6	1.271	1.334
4.8	1.305	1.378
4.9	1.353	1.401
5.1	1.405	1.446
5.3	1.467	1.491
5.5	1.526	1.538
5.7	1.595	1.585
5.9	1.637	1.632
6.1	1.687	1.680
6.3	1.757	1.729
6.6	1.837	1.803
6.9	1.889	1.879
7.1	1.973	1.931
7.4	2.050	2.009
7.7	2.081	2.090
8.0	2.221	2.172
8.4	2.332	2.285
8.8	2.445	2.401
9.1	2.549	2.490
9.5	2.668	2.613
9.8	2.779	2.708
10.2	2.895	2.838
10.4	2.978	2.905
10.7	3.095	3.007
11.1	3.189	3.147
11.4	3.308	3.255
11.9	3.461	3.441
12.3	3.609	3.595
12.7	3.779	3.755
13.2	3.955	3.967
13.6	4.127	4.135
14.1	4.327	4.358
14.6	4.541	4.590
15.4	4.899	4.983
16.4	5.132	5.510
17.1	5.734	5.905
17.8	6.293	6.322
18.8	6.911	6.958
20.2	8.275	7.932

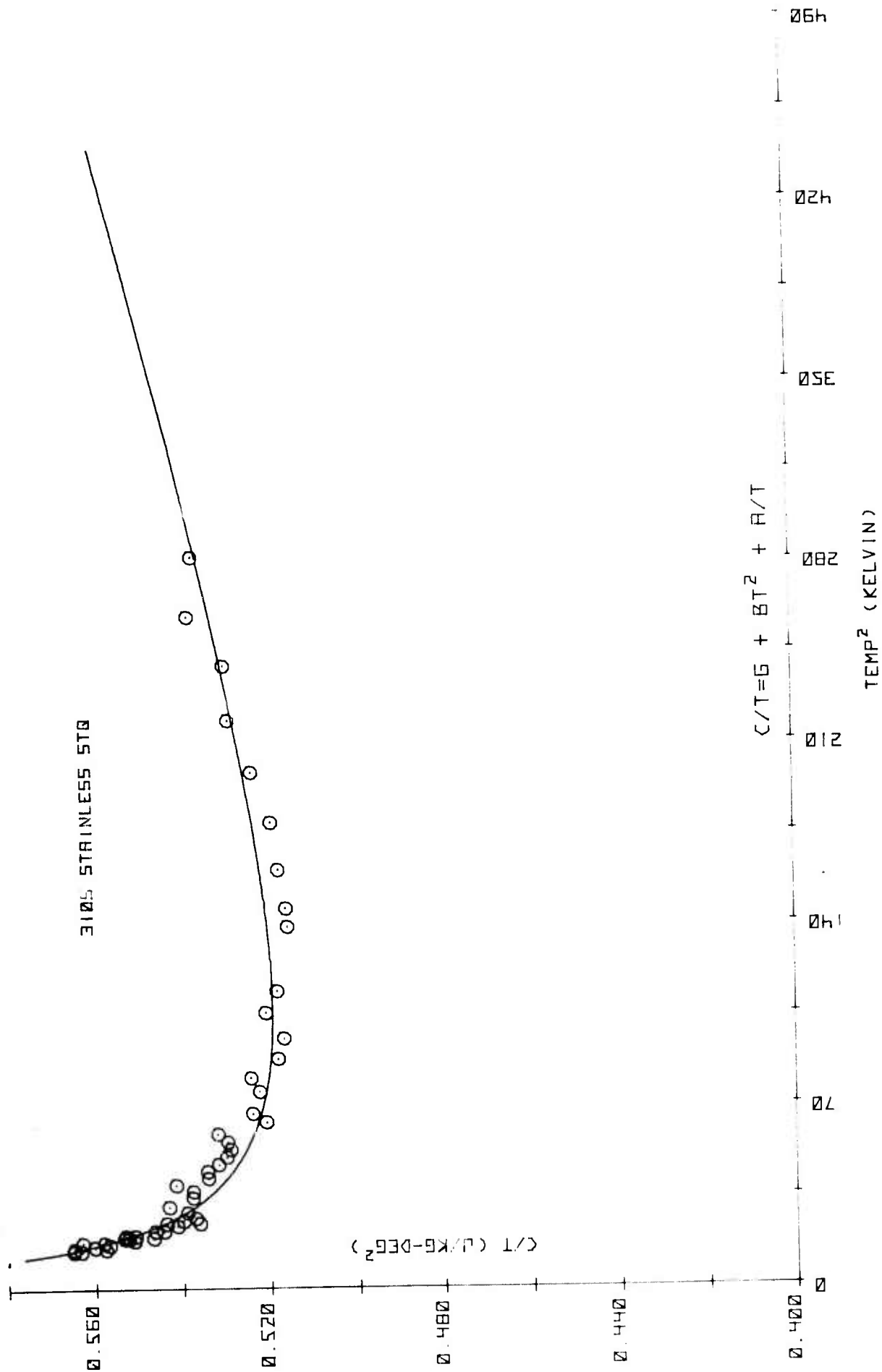


FIGURE 11. SPECIFIC HEAT DATA FOR 3105 STAINLESS STQ LEAST-SQUARES  
FITTED TO THE FORMULA  $C/T = A/T + \gamma + \delta T^2$

TABLE 18. LOW-TEMPERATURE SPECIFIC HEAT OF  
310S STAINLESS STEEL STQ FITTED TO

$$C = A + \gamma T + \beta T^3$$

Temperature, K	Measured Value (J/kg-deg.)	Fitted Value (J/kg-deg.)
3.8	2.141	2.155
3.8	2.148	2.155
3.9	2.175	2.202
3.9	2.204	2.202
4.0	2.241	2.249
4.1	2.283	2.296
4.2	2.344	2.344
4.2	2.365	2.344
4.3	2.370	2.391
4.4	2.406	2.438
4.4	2.435	2.438
4.4	2.431	2.438
4.5	2.479	2.485
4.5	2.489	2.485
4.7	2.568	2.580
4.7	2.559	2.580
4.9	2.653	2.675
5.0	2.681	2.723
5.0	2.719	2.723
5.1	2.754	2.771
5.2	2.793	2.818
5.4	2.911	2.914
5.6	3.042	3.010
5.9	3.173	3.154
6.1	3.280	3.250
6.3	3.412	3.347
6.5	3.472	3.444
6.7	3.580	3.541
6.9	3.669	3.639
7.1	3.762	3.736
7.3	3.861	3.835
7.5	3.972	3.933
7.7	4.095	4.032
8.0	4.166	4.180
8.2	4.295	4.280
8.7	4.543	4.530
9.0	4.717	4.681
9.4	4.869	4.834
9.8	5.063	5.089
10.3	5.362	5.347
10.7	5.543	5.555
11.8	6.083	6.137
12.1	6.242	6.299
12.7	6.572	6.625
13.4	6.954	7.011
14.1	7.376	7.405
14.8	7.818	7.805
15.5	8.202	8.213
16.1	8.651	8.569
16.8	9.008	8.992

**Best Available  
Copy  
for page 37**

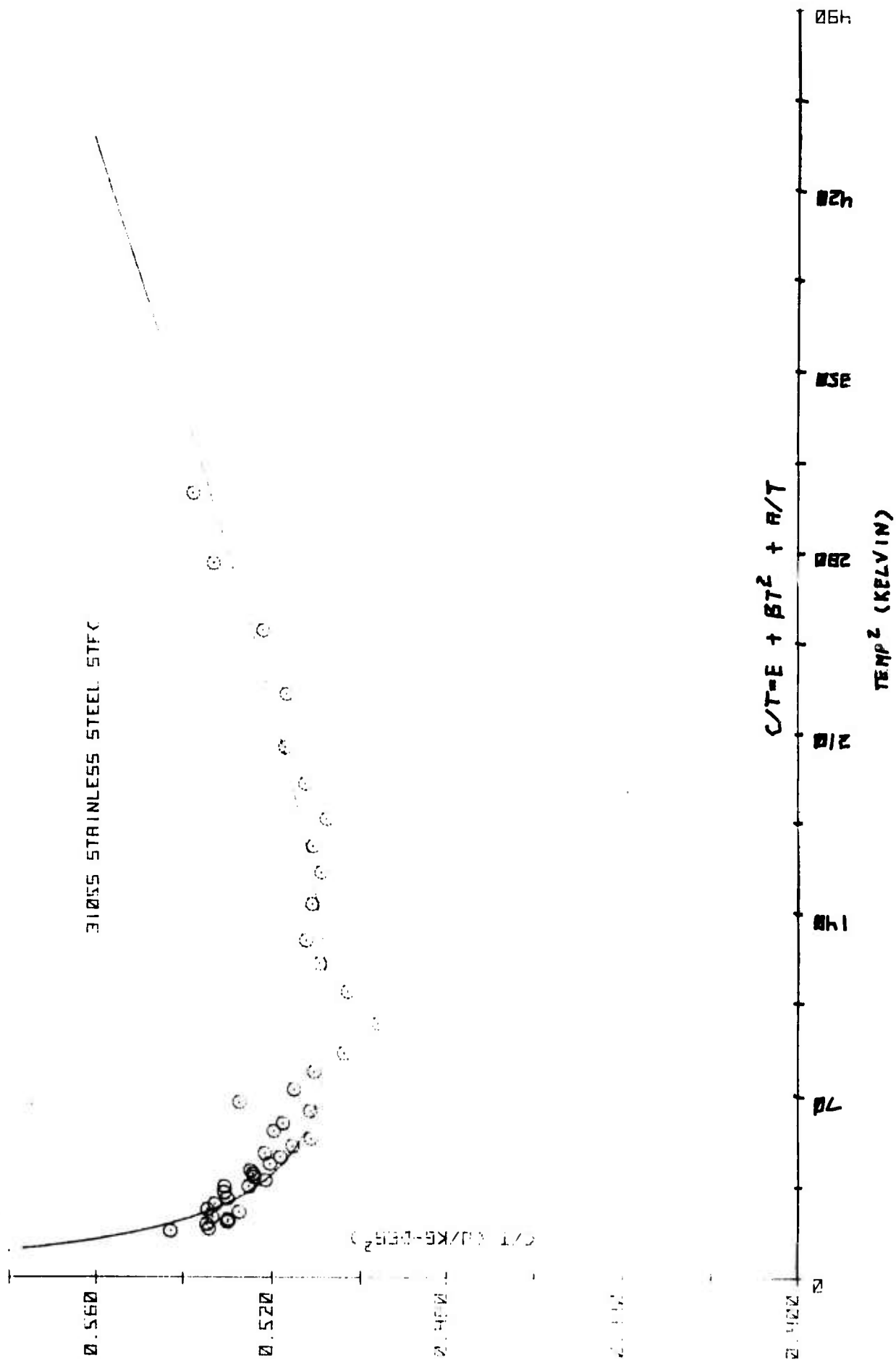


FIGURE 12. SPECIFIC HEAT DATA FOR 31055 STAINLESS STEEL STFC LEAST-SQUARES  
FITTED TO THE FORMULA  $C/T = A/T + \gamma + \beta T^2$



TABLE 19. LOW-TEMPERATURE SPECIFIC HEAT OF  
310S STAINLESS STEEL STFC FITTED TO

$$C = A + \gamma T + \beta T^3$$

Temperature, K	Measured Value (J/kg-deg.)	Fitted Value (J/kg-deg.)
4.2	2.280	2.311
4.3	2.297	2.356
4.5	2.406	2.447
4.6	2.438	2.493
4.7	2.490	2.538
4.8	2.560	2.584
5.0	2.637	2.675
5.1	2.726	2.721
5.3	2.824	2.813
5.5	2.915	2.905
5.7	3.025	2.997
5.9	3.099	3.090
5.9	3.131	3.090
6.1	3.131	3.183
6.2	3.249	3.229
6.3	3.303	3.276
6.4	3.359	3.323
6.6	3.435	3.417
6.8	3.523	3.511
6.9	3.599	3.558
7.1	3.659	3.653
7.3	3.732	3.748
7.5	3.897	3.844
7.7	3.985	3.939
8.0	4.091	4.084
8.2	4.325	4.181
8.5	4.378	4.327
8.9	4.544	4.524
9.3	4.686	4.723
9.9	4.911	5.025
10.5	5.282	5.331
11.0	5.603	5.590
11.4	5.843	5.801
12.0	6.134	6.121
12.5	6.364	6.392
12.9	6.591	6.611
13.3	6.755	6.834
13.8	7.075	7.116
14.3	7.396	7.403
15.0	7.755	7.813
15.8	8.253	8.294
16.6	8.856	8.788
17.4	9.365	9.297

73&lt;

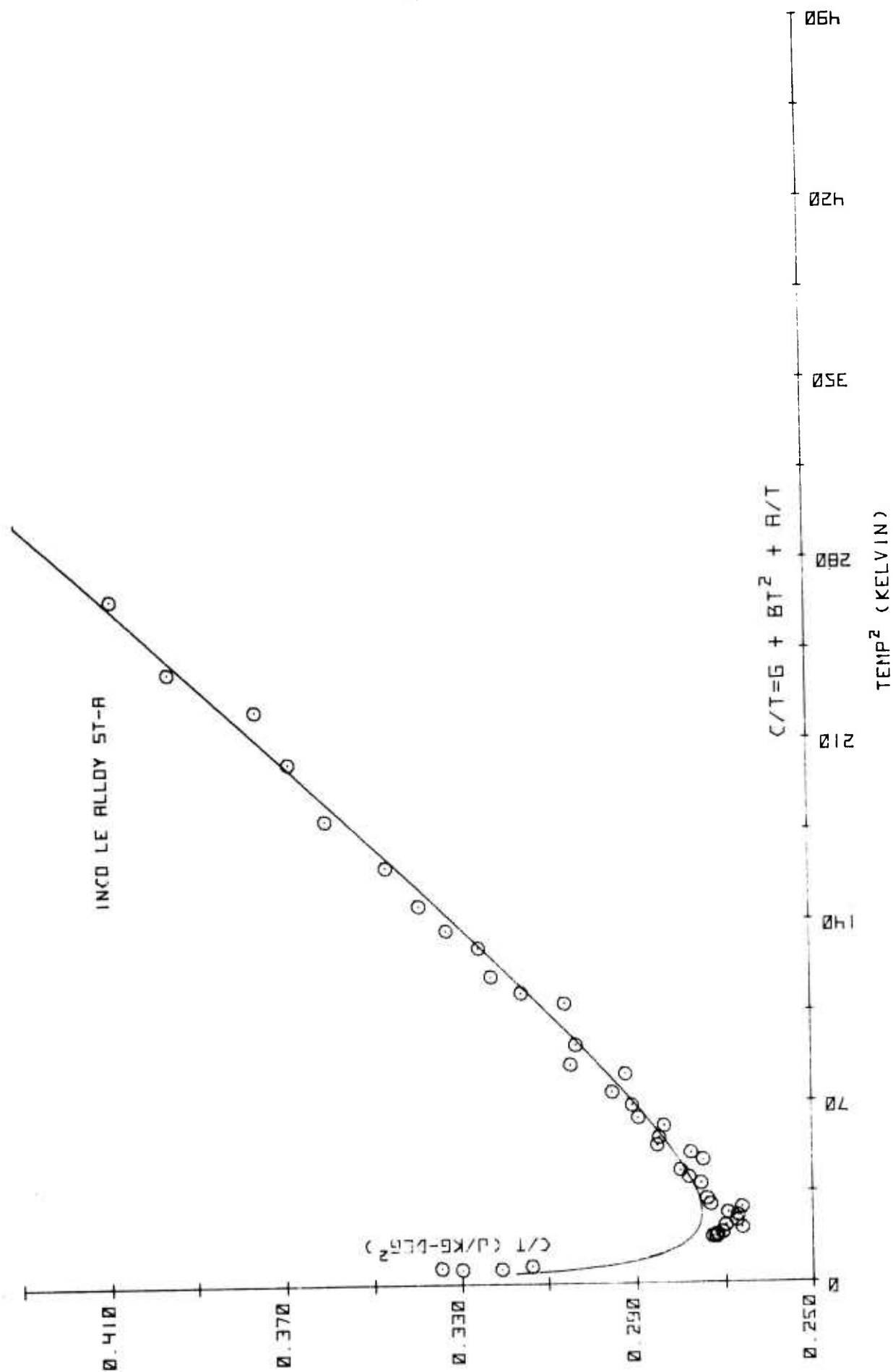


FIGURE 13. SPECIFIC HEAT DATA FOR INCO LE ALLOY ST-A LEAST-SQUARES  
FITTED TO THE FORMULA  $C/T = A/T + \gamma + \beta T^2$

TABLE 20. LOW-TEMPERATURE SPECIFIC HEAT OF  
INCO LE ALLOY ST-A FITTED TO

$$C = A + \sqrt{T} + \beta T^3$$

Temperature, K	Measured Value (J/kg-deg.)	Fitted Value (J/kg-deg.)
2.4	0.792	0.727
2.4	0.770	0.727
2.5	0.837	0.751
2.6	0.816	0.774
4.2	1.143	1.166
4.2	1.146	1.166
4.3	1.169	1.191
4.4	1.191	1.217
4.6	1.225	1.270
4.7	1.269	1.296
4.9	1.311	1.350
5.1	1.363	1.404
5.2	1.401	1.431
5.4	1.438	1.487
5.5	1.503	1.515
5.7	1.562	1.572
6.2	1.707	1.718
6.4	1.779	1.778
6.6	1.847	1.839
6.9	1.896	1.933
7.1	1.970	1.997
7.3	2.081	2.062
7.5	2.135	2.128
7.8	2.211	2.230
8.0	2.315	2.299
8.3	2.413	2.406
8.6	2.539	2.515
9.0	2.630	2.666
9.2	2.803	2.743
9.6	2.915	2.903
10.4	3.181	3.241
10.6	3.346	3.329
10.9	3.515	3.465
11.4	3.708	3.701
11.7	3.893	3.848
12.1	4.101	4.050
12.7	4.398	4.368
13.4	4.822	4.763
14.2	5.227	5.247
14.9	5.595	5.700
15.4	6.089	6.041
16.3	6.657	6.695

## SUMMARY OF GROUP B DATA

COMPUTED FROM

$$C = A + \gamma T + \beta T^3$$

TABLE 21. SPECIFIC HEAT OF INCONEL X750 ST

$$A = 2.8503 \times 10^{-1}$$

$$\gamma = 2.1535 \times 10^{-1}$$

$$\beta = 3.4851 \times 10^{-4}$$

Temperature, K	Specific Heat (J/kg-deg.)
4.0	1.17
5.0	1.41
10.0	2.79
15.0	4.69
20.0	7.38

TABLE 22. SPECIFIC HEAT OF INCONEL X750 STDA VIM-VAR

$$A = 2.1602 \times 10^{-1}$$

$$\gamma = 2.2752 \times 10^{-1}$$

$$\beta = 3.1117 \times 10^{-4}$$

Temperature, K	Specific Heat (J/kg-deg.)
4.0	1.15
5.0	1.39
10.0	2.80
15.0	4.68
20.0	7.26

TABLE 23. SPECIFIC HEAT OF INCONEL X750 STDA AAM-VAR

$$A = 1.5886 \times 10^{-1}$$

$$\gamma = 2.3441 \times 10^{-1}$$

$$\beta = 2.5469 \times 10^{-4}$$

Temperature, K	Specific Heat (J/kg-deg.)
4.0	1.11
5.0	1.36
10.0	2.76
15.0	4.53
20.0	6.88

TABLE 24. SPECIFIC HEAT OF INCONEL X750 STDA VIM

$$A = 4.0437 \times 10^{-1}$$

$$\gamma = 1.9272 \times 10^{-1}$$

$$\beta = 4.4096 \times 10^{-4}$$

Temperature, K	Specific Heat (J/kg-deg.)
4.0	1.20
5.0	1.42
10.0	2.77
15.0	4.78
20.0	7.79

TABLE 25. SPECIFIC HEAT OF STAINLESS STEEL 310S STQ

$$A = 3.8473 \times 10^{-1}$$

$$\gamma = 4.6331 \times 10^{-1}$$

$$\beta = 1.7378 \times 10^{-4}$$

Temperature, K	Specific Heat (J/kg-deg.)
4.0	2.25
5.0	2.72
10.0	5.19
15.0	7.92
20.0	11.04

TABLE 26. SPECIFIC HEAT OF STAINLESS STEEL 310S STFC

$$A = 4.4378 \times 10^{-1}$$

$$\gamma = 4.4063 \times 10^{-1}$$

$$\beta = 2.2522 \times 10^{-4}$$

Temperature, K	Specific Heat (J/kg-deg.)
4.0	2.22
5.0	2.68
10.0	5.08
15.0	7.81
20.0	11.06

TABLE 27. SPECIFIC HEAT OF INCO LE ALLOY ST-A

$$A = 1.8773 \times 10^{-1}$$

$$\gamma = 2.2099 \times 10^{-1}$$

$$\beta = 6.7084 \times 10^{-4}$$

Temperature, K	Specific Heat (J/kg-deg.)
4.0	1.11
5.0	1.38
10.0	3.07
15.0	5.77
20.0	9.97



TABLE 28. COMPUTED VALUES OF A, Y AND B AND ESTIMATED INTERMEDIATE-TEMPERATURE SPECIFIC HEATS AT 50K, 77K and 300K

Group	Specimen Name	A (J/kg-deg)	Y (J/kg-deg <sup>2</sup> )	B (J/kg-deg)	Molar Weight, M	Debye Temperature $\theta_D$ , Kelvins $^\circ$	Estimated Intermediate- Temperature Specific Heat (J/kg-deg)		
							50K	77K	300K
A	Copper OFHC-SR	--	$6.2982 \times 10^{-3}$	$8.5902 \times 10^{-4}$	63.54	329	86	183	372
A	Copper OFHC-AR	--	$5.0363 \times 10^{-3}$	$8.4977 \times 10^{-4}$	63.54	330	86	181	371
A	Bronze - 85Sn	--	$1.6491 \times 10^{-4}$	$10.8240 \times 10^{-4}$	65.97	301	100	195	362
A	Bronze - 115Sn	--	$7.5596 \times 10^{-4}$	$12.2070 \times 10^{-4}$	66.99	287	108	203	356
A	Kromarc 58 STQ	--	$3.9590 \times 10^{-1}$	$3.1049 \times 10^{-4}$	--	--	--	--	--
A	Kromarc 58 CR	--	$3.9343 \times 10^{-1}$	$3.5859 \times 10^{-4}$	--	--	--	--	--
B	Inconel X750 (MD1)ST	$2.8503 \times 10^{-1}$	$2.1535 \times 10^{-1}$	$3.4851 \times 10^{-4}$	57.10	460	53	116	454
B	Inconel X750 (MD1)STDA VIN-VAR	$2.1602 \times 10^{-1}$	$2.2752 \times 10^{-1}$	$3.1117 \times 10^{-4}$	57.10	478	49	126	454
B	Inconel X750 (MD2)STDA AAN-VAR	$1.5886 \times 10^{-1}$	$2.3441 \times 10^{-1}$	$2.5469 \times 10^{-4}$	56.74	512	43	117	452
B	Inconel X750 (MD3)STDA VIM	$4.0437 \times 10^{-1}$	$1.9272 \times 10^{-1}$	$4.4096 \times 10^{-4}$	56.64	427	61	150	456
B	Stainless Steel AISI 310S STA	$3.8473 \times 10^{-1}$	$4.6331 \times 10^{-1}$	$1.7378 \times 10^{-4}$	55.21	587	45	106	515
B	Stainless Steel AISI 310S STFC	$4.4378 \times 10^{-1}$	$4.4063 \times 10^{-1}$	$2.2522 \times 10^{-4}$	55.21	538	50	120	519
B	Inco LE Alloy ST-A	$1.8773 \times 10^{-1}$	$2.2099 \times 10^{-1}$	$6.7084 \times 10^{-4}$	--	--	--	--	--

$$\theta_D = \left( \frac{1.94 \times 10^6}{M} \right)^{1/3}$$

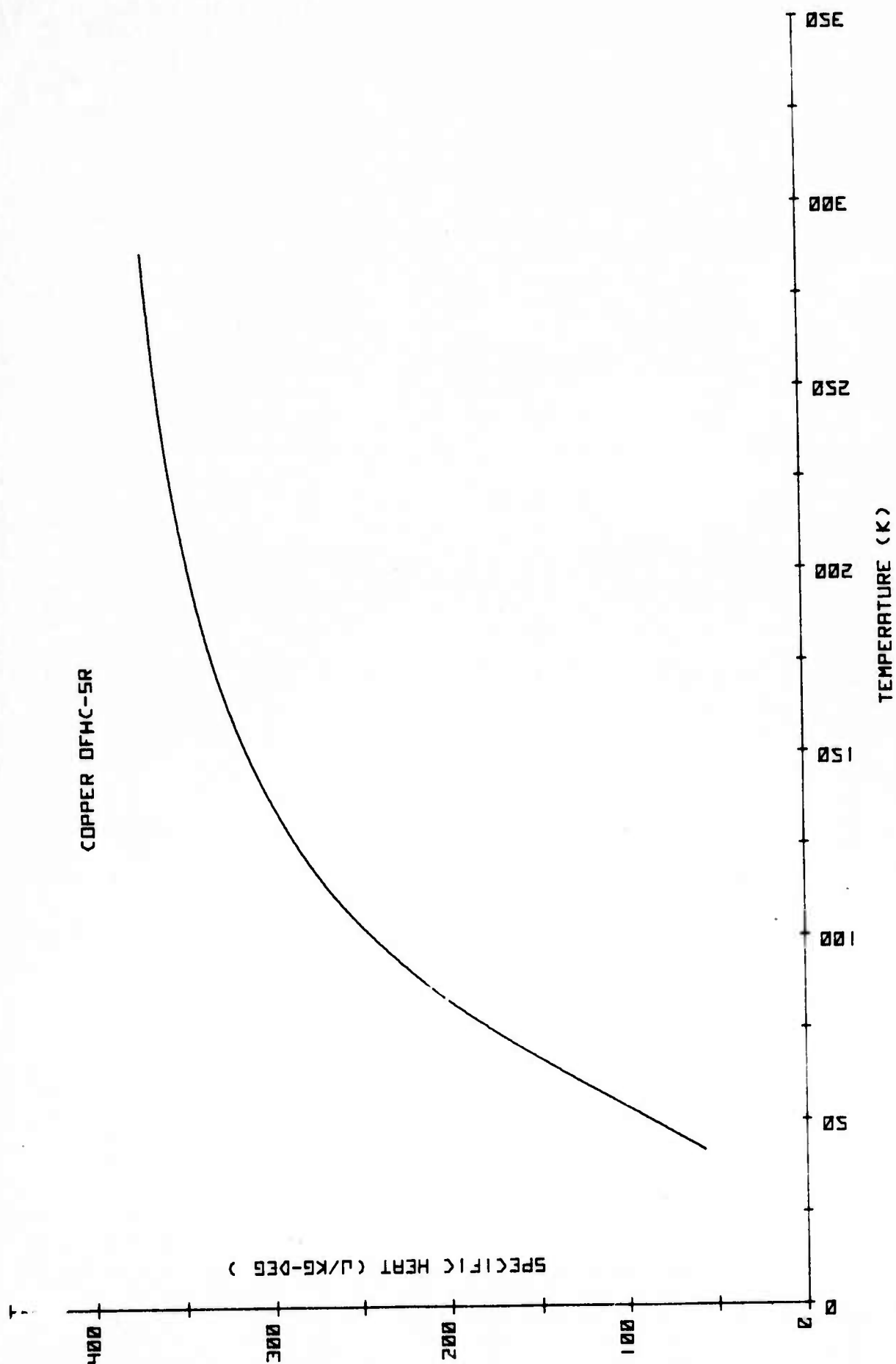


FIGURE 14. ESTIMATED INTERMEDIATE-TEMPERATURE SPECIFIC HEAT OF COPPER OFHC-SR

822

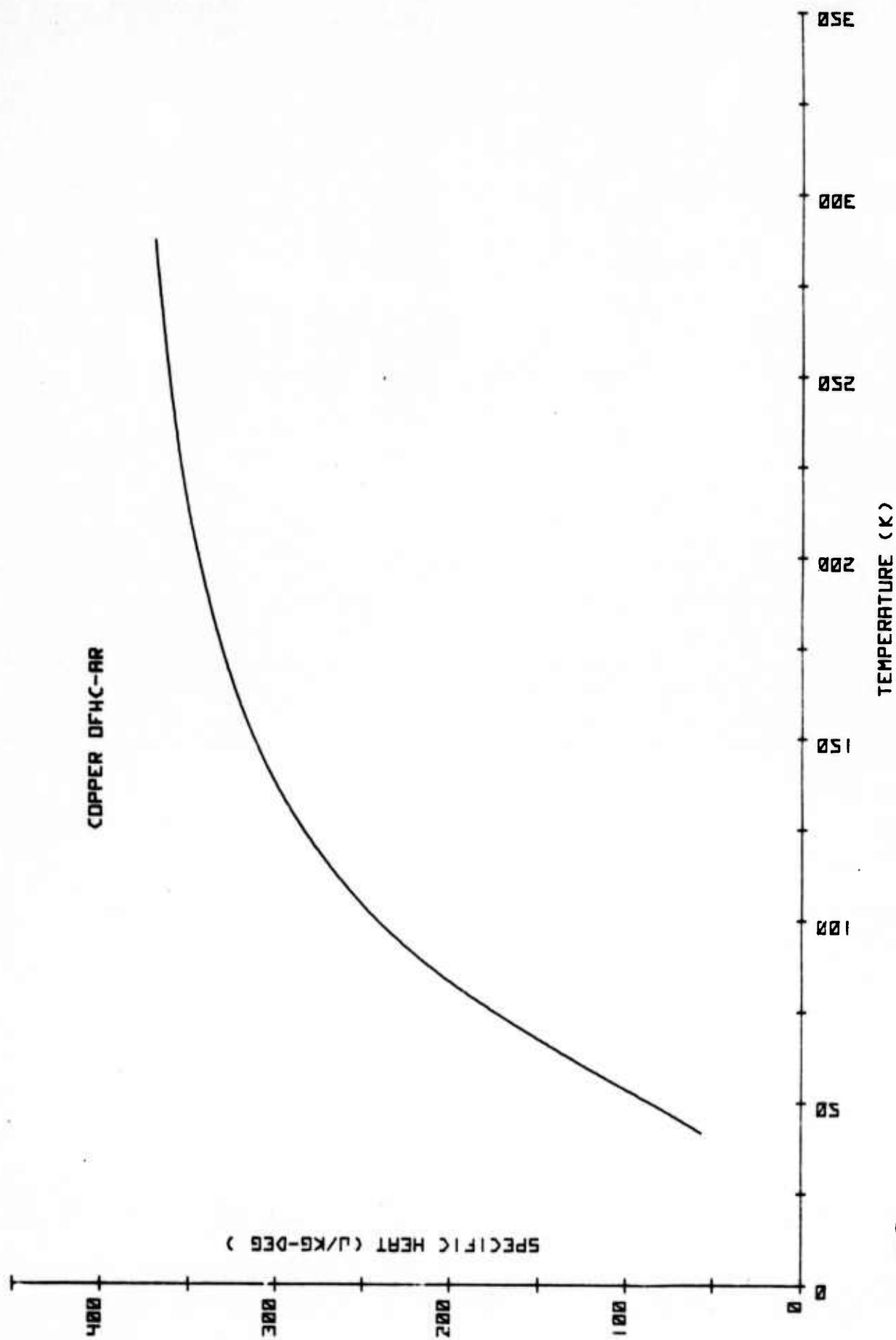


FIGURE 15. ESTIMATED INTERMEDIATE-TEMPERATURE SPECIFIC  
HEAT OF COPPER OFHC-AR

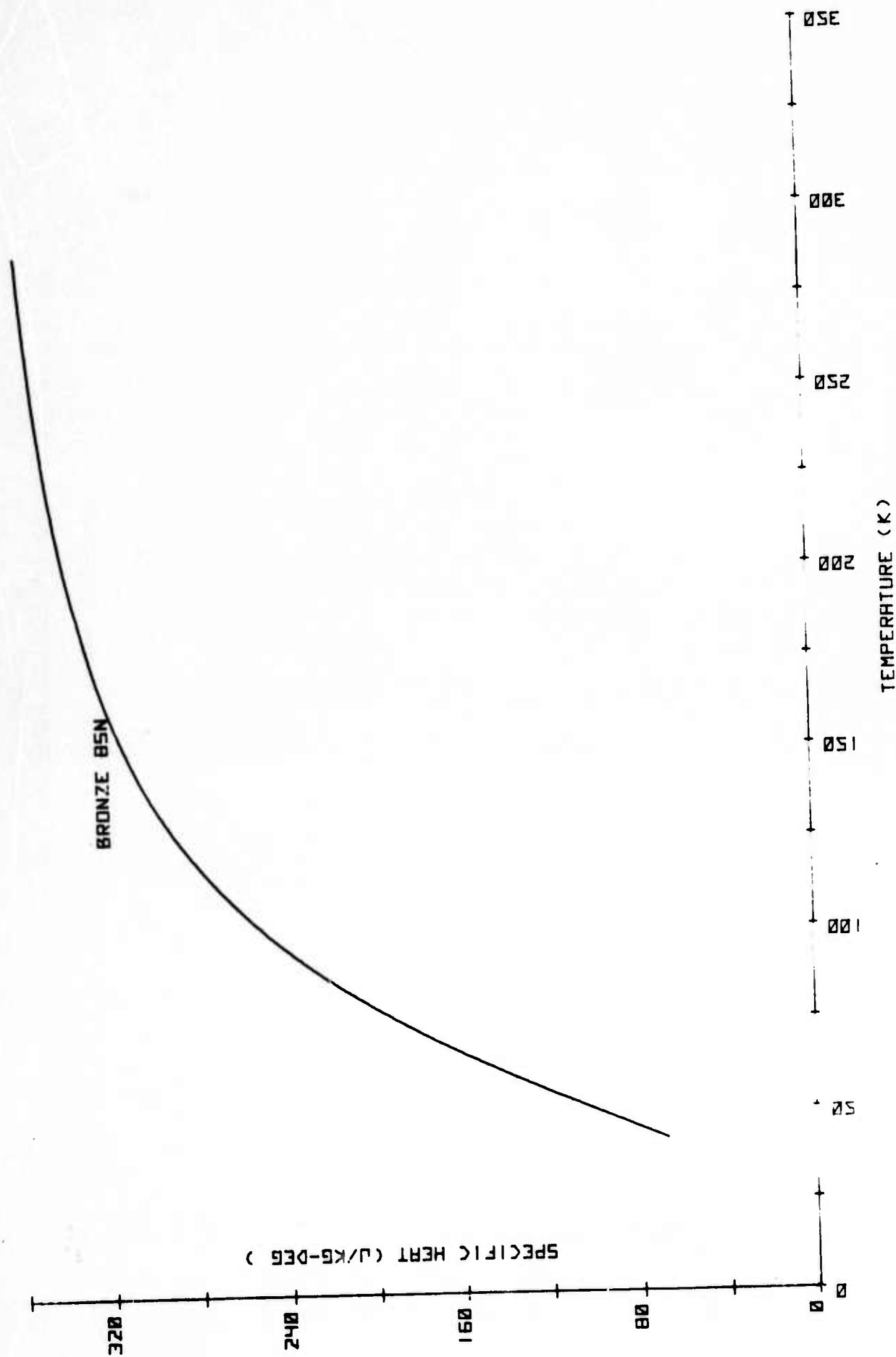


FIGURE 16. ESTIMATED INTERMEDIATE-TEMPERATURE SPECIFIC HEAT OF BRONZE 85N

84

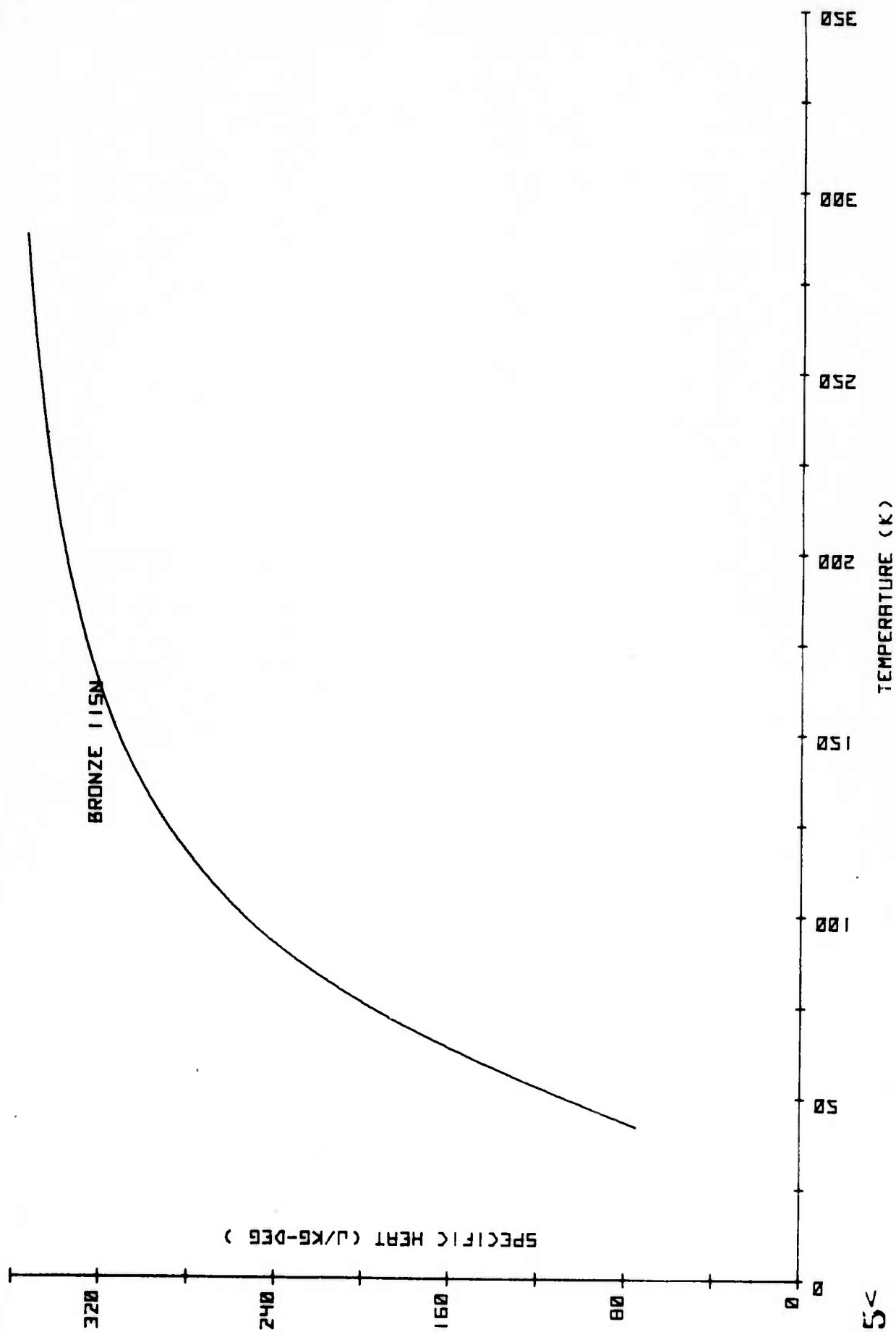


FIGURE 17. ESTIMATED INTERMEDIATE-TEMPERATURE SPECIFIC HEAT OF BRONZE 115N

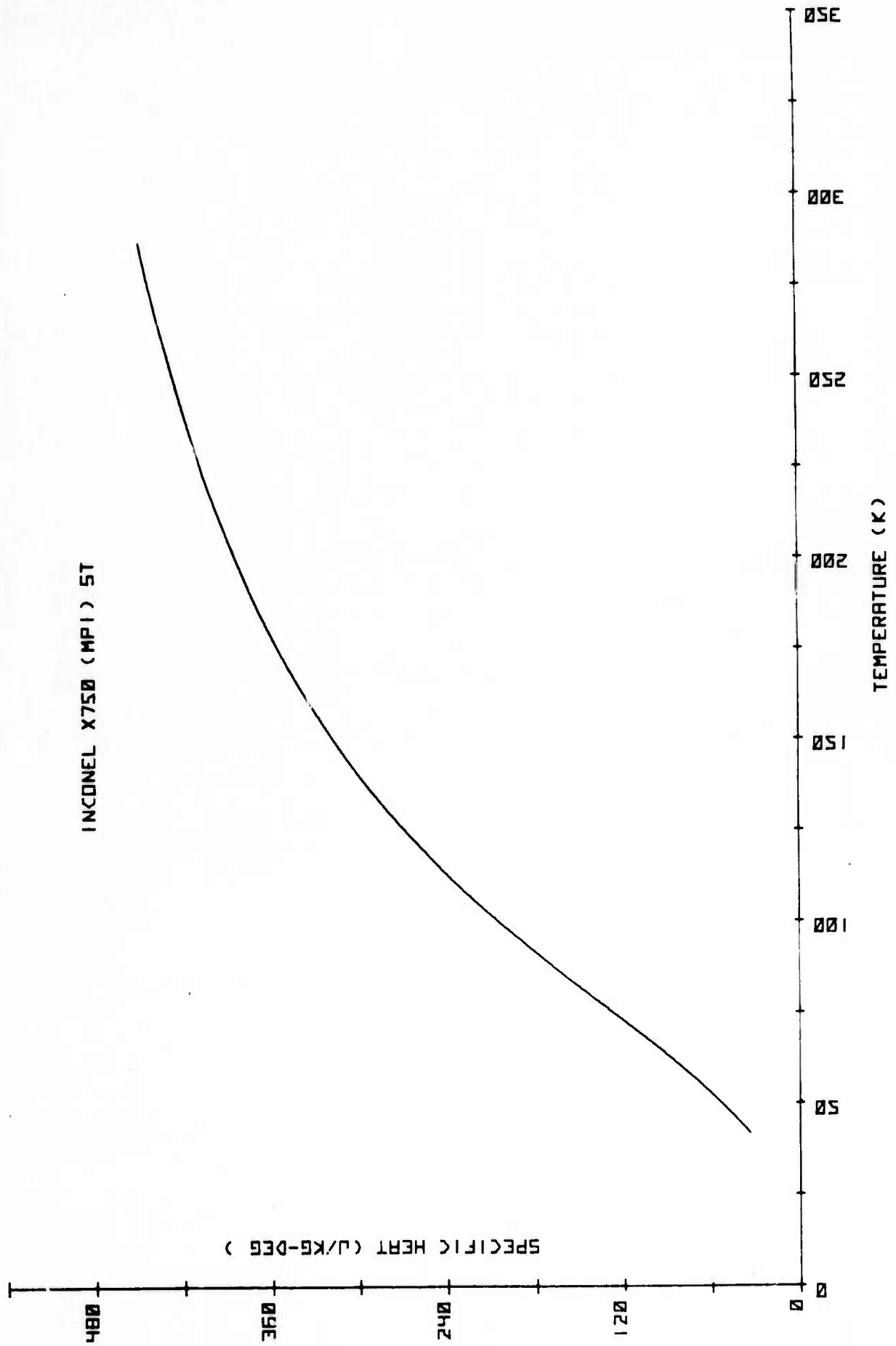


FIGURE 18. ESTIMATED INTERMEDIATE-TEMPERATURE SPECIFIC HEAT OF INCONEL X750 (MPI) ST

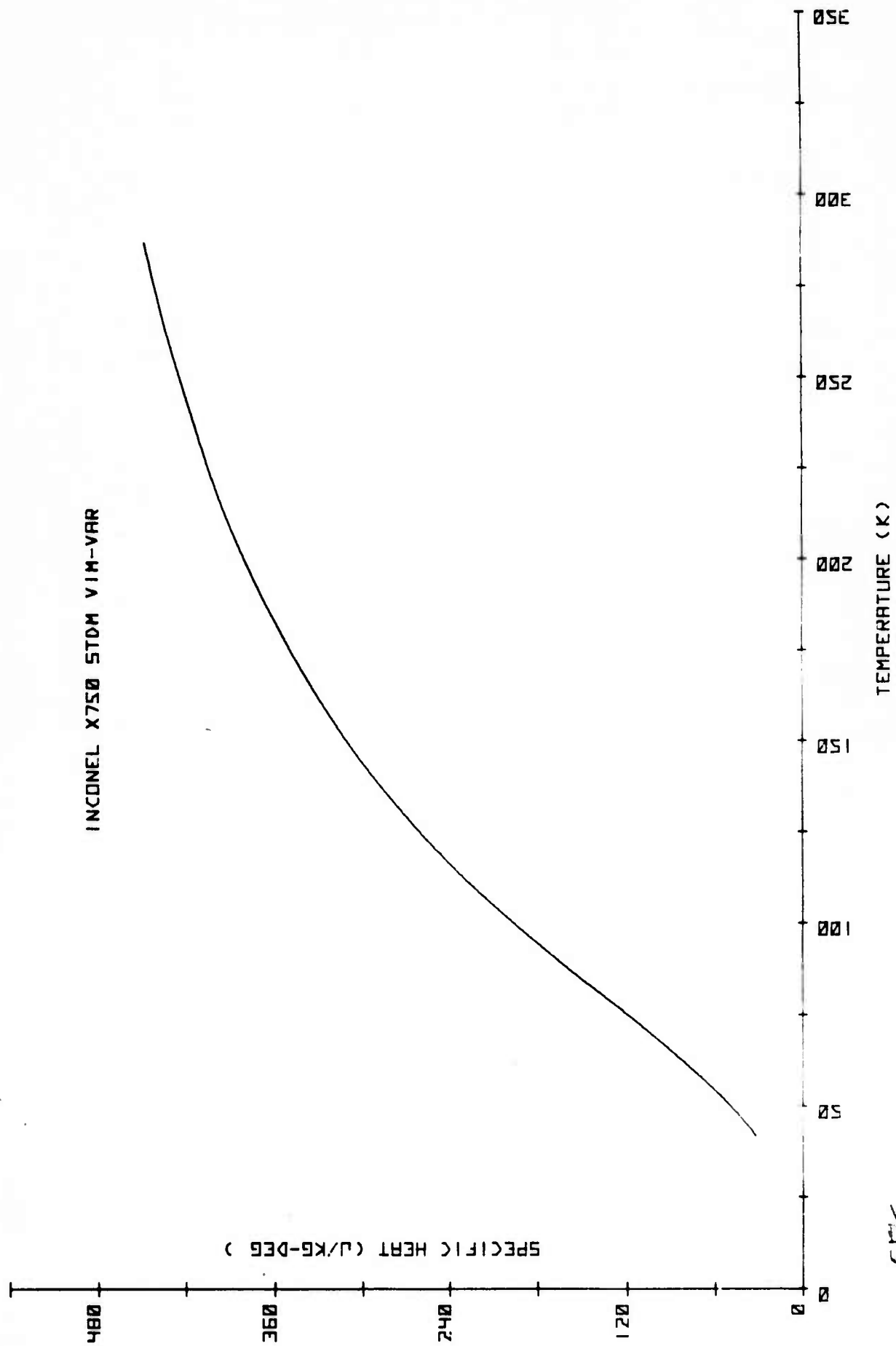


FIGURE 19. ESTIMATED INTERMEDIATE-TEMPERATURE SPECIFIC  
HEAT OF INCONEL X750 STD M VIM-VAR

37

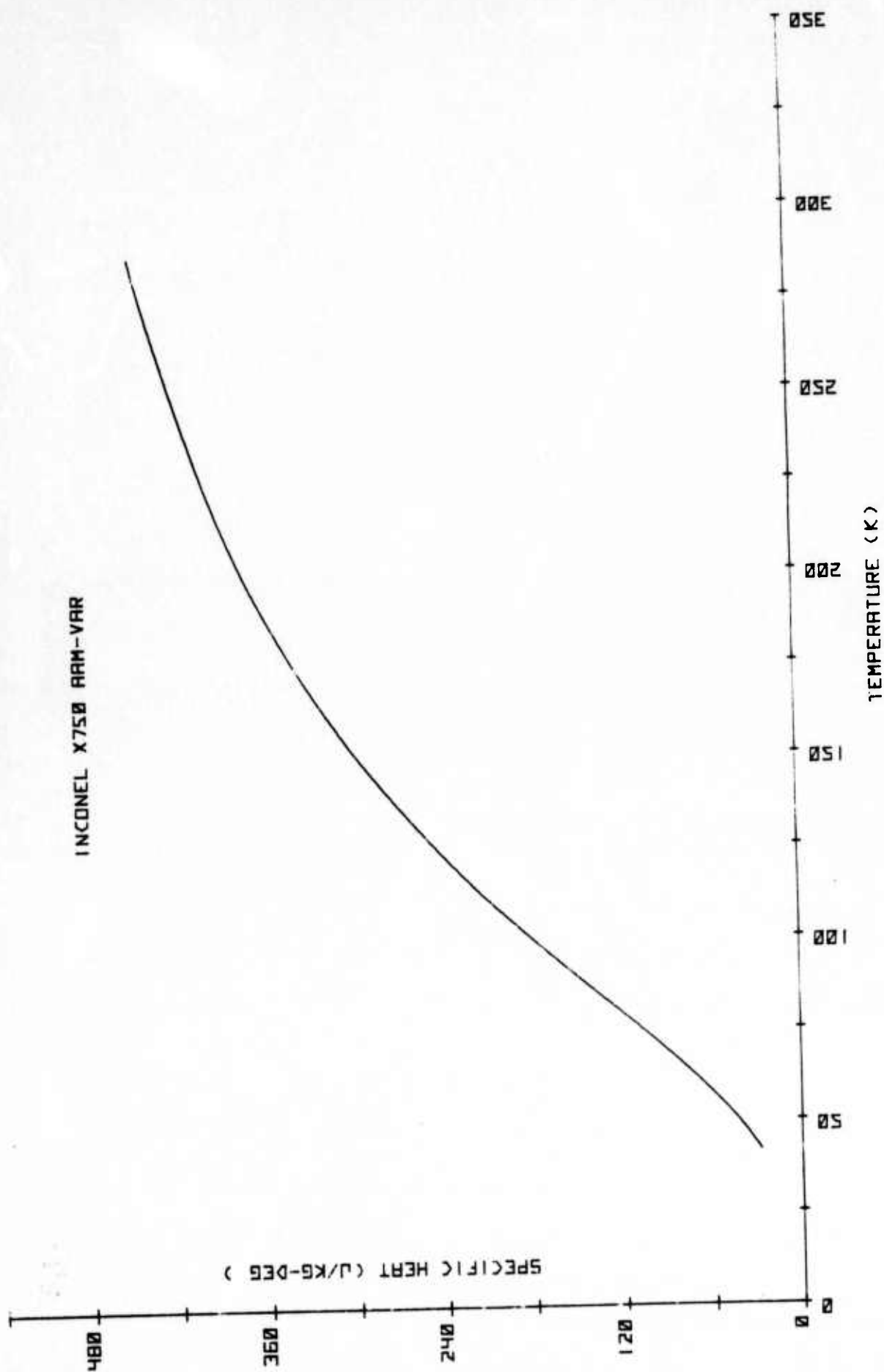


FIGURE 20. ESTIMATED INTERMEDIATE-TEMPERATURE SPECIFIC  
HEAT OF INCONEL X750 AAM-VAR



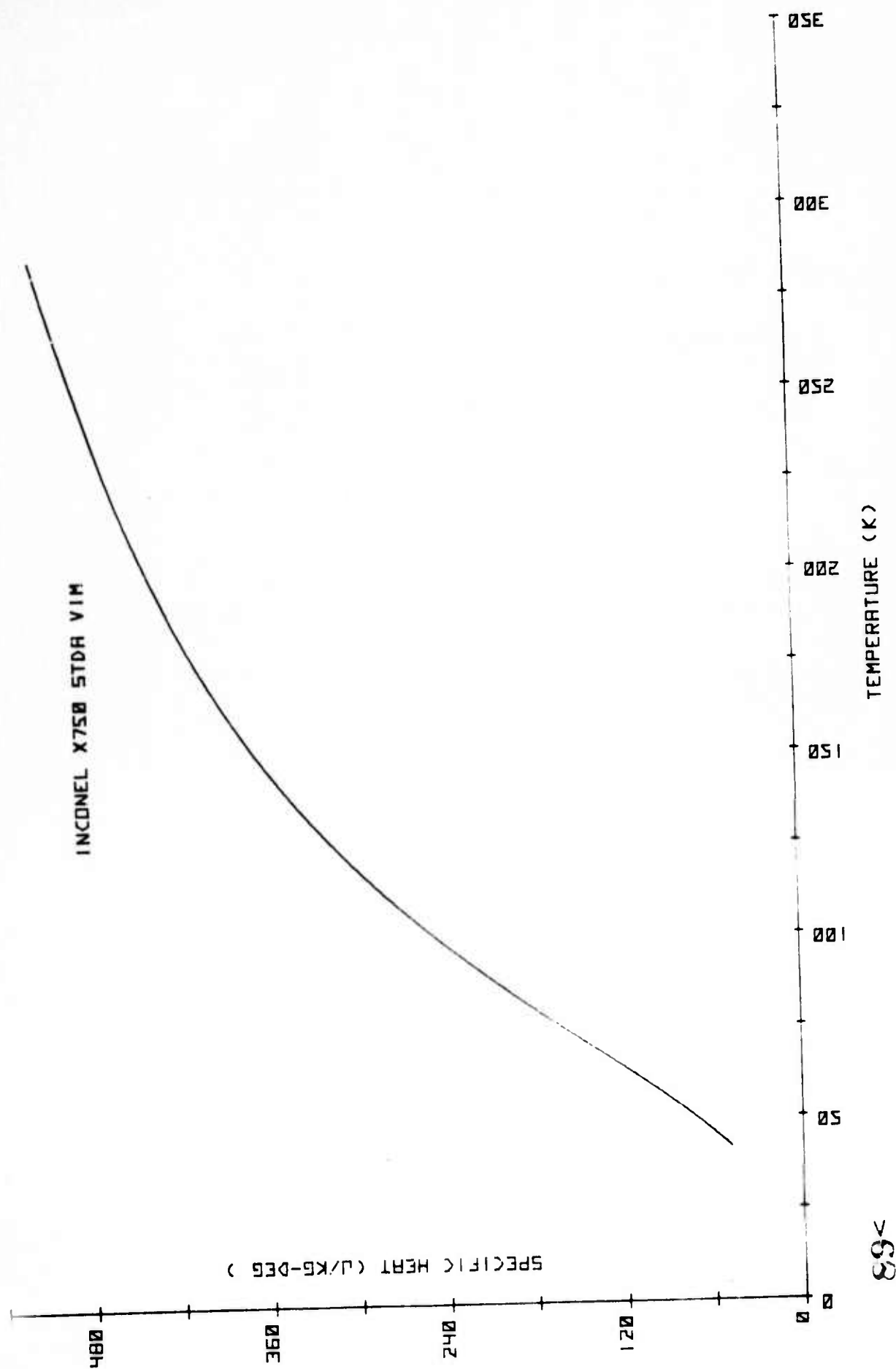


FIGURE 21. ESTIMATED INTERMEDIATE-TEMPERATURE SPECIFIC  
HEAT OF INCONEL X750 STDA VIM

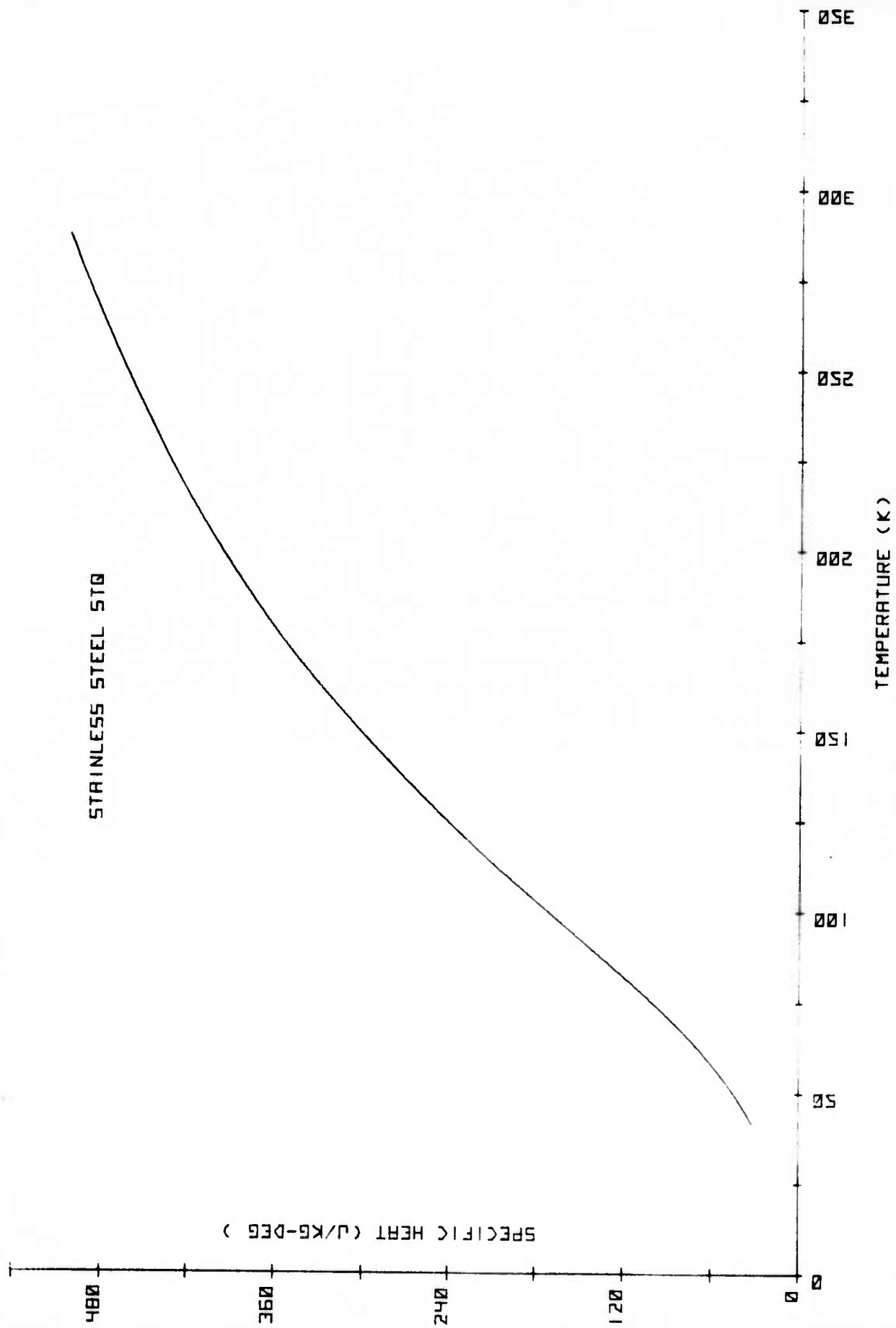


FIGURE 22. ESTIMATED INTERMEDIATE-TEMPERATURE SPECIFIC  
HEAT OF STAINLESS STEEL 510

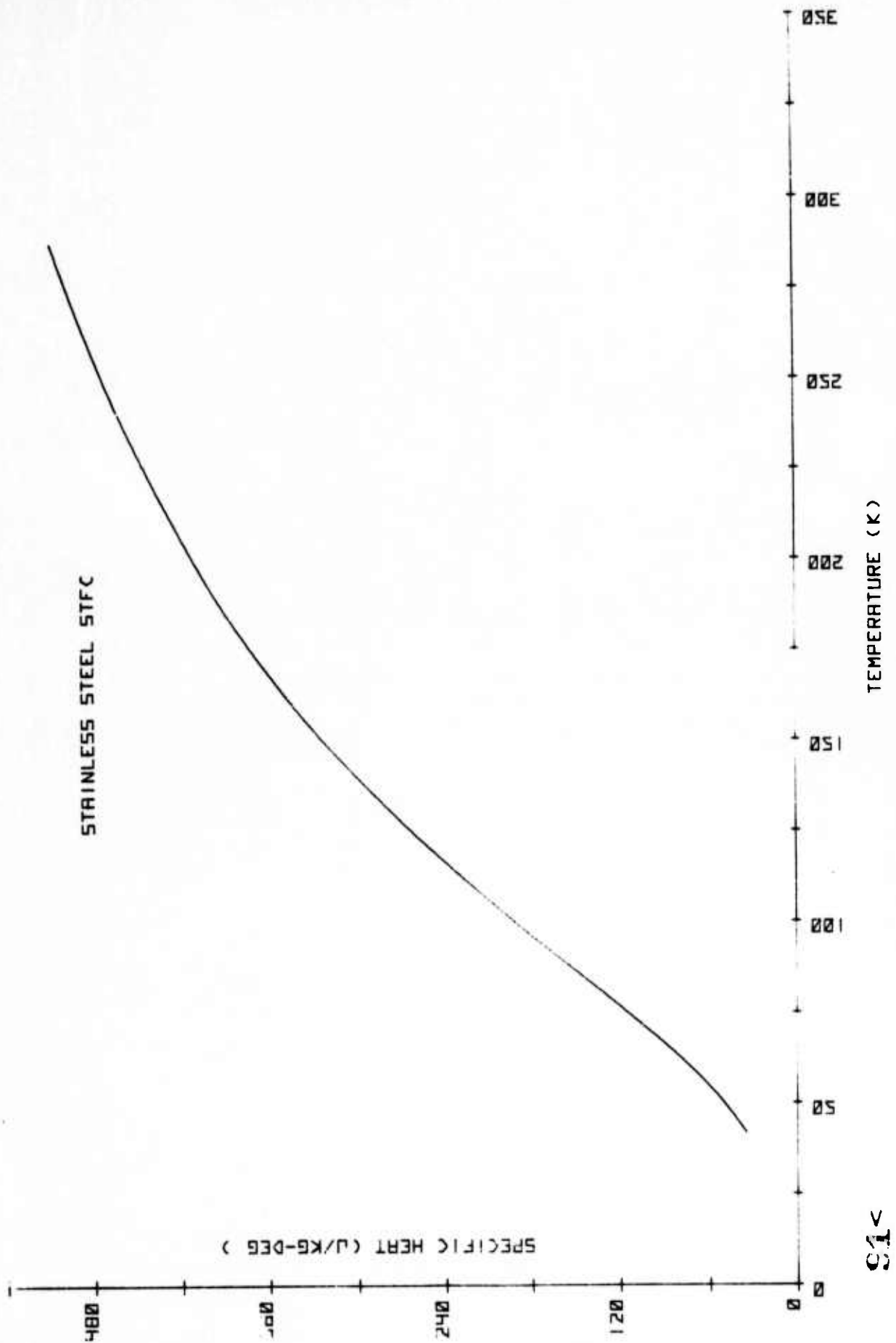


FIGURE 23. ESTIMATED INTERMEDIATE-TEMPERATURE SPECIFIC  
HEAT OF STAINLESS STEEL STFC

TABLE 29. LIST OF THERMAL EXPANSION SPECIMENS  
MEASURED

Specimen Name	Processing and Treatment
Inconel X750 (MP1)	ST
Inconel X750 (MP1)	STDA VIM-VAR
Inconel X750 (MP2)	STDA AAM-VAR
Inconel X750 (MP3)	STDA VIM
Kromarc 58	STQ
Kromarc 58	CR (~ 30%)
Copper	OFHC-AR
Copper	OFHC-SR
Stainless Steel AISI 310S	STQ
Stainless Steel AISI 310S	STFC
Inco Low Expansion (LE) Alloy	STA
Ti-Nb	5 a/o Nb
Ti-Nb	10 a/o Nb
Ti-Nb	15 a/o Nb
Ti-Nb	20 a/o Nb
Bronze-11Sn	As Cast
Ti-5Al-2.5Sn	Annealed
Ti-3.5Al-3.5Sn	Annealed
Ti-2.5Al-2.5Sn	Annealed

TABLE 30. THERMAL EXPANSION BEHAVIOR OF INCONEL X750

T (K)	ST $-\Delta L/L_o$ (%)	STDA VIM-VAR $-\Delta L/L_o$ (%)	MP2 STDA AAM-VAR $-\Delta L/L_o$ (%)	MP3 STDA VIM $-\Delta L/L_o$ (%)
300	-0.039	-0.039	-0.037	-0.042
290	-0.026	-0.025	-0.025	--
280	-0.013	-0.013	-0.013	-0.013
270	0	0	0	0
260	0.013	0.011	0.012	0.013
250	0.025	0.023	0.024	0.024
240	0.037	0.036	0.036	0.035
230	0.050	0.048	0.047	0.048
220	0.062	0.061	0.052	0.060
210	0.074	0.073	0.070	0.073
200	0.086	0.084	0.081	0.083
190	0.098	0.096	0.092	0.094
180	0.108	0.108	0.105	0.107
170	0.120	0.120	0.115	0.116
160	0.131	0.129	0.125	0.127
150	0.141	0.140	0.135	0.137
140	--	0.149	0.144	0.147
130	0.160	0.159	0.155	0.156
120	0.169	0.167	0.163	0.164
110	0.178	0.176	0.172	0.171
100	0.186	0.184	0.180	0.178

TABLE 30. (Continued)

T (K)	ST	STDA VIM-VAR	MP2	MP3
	$-\Delta L/L_o$ (%)	$-\Delta L/L_o$ (%)	STDA AAM-VAR $-\Delta L/L_o$ (%)	STDA VIM $-\Delta L/L_o$ (%)
90	0.193	0.191	0.189	0.184
80	0.200	0.197	0.193	0.190
78	0.201	0.199	0.193	0.191
77	--	--	0.194	0.192
60	0.214	0.208	0.205	0.201
50	0.216	0.212	0.209	0.206
40	0.220	0.216	0.213	0.210
30	0.222	0.219	0.216	0.212
20	0.223	0.220	0.217	0.213
10	0.224	0.222	0.217	0.214
5	0.225	0.223	0.218	0.215

TABLE 31. THERMAL EXPANSION BEHAVIOR OF KROMARC 58

T (K)	STQ $-\Delta L/L_o$ (%)	CW (30%) $-\Delta L/L_o$ (%)
300	-0.044	-0.044
290	-0.029	-0.028
280	-0.011	-0.010
273	0	0
260	0.021	0.020
250	0.036	0.036
240	0.052	0.051
230	0.068	0.066
220	0.084	0.081
210	0.100	0.094
200	0.115	0.107
190	0.129	0.122
180	0.144	0.135
170	0.158	0.149
160	0.171	0.161
150	0.183	0.173
140	0.195	0.185
130	0.207	0.196
120	0.218	0.208
110	0.228	0.219
100	0.238	0.229

TABLE 31. (Continued)

T (K)	STQ $-\Delta L/L_o$ (%)	CW (30%) $-\Delta L/L_o$ (%)
90	0.247	0.237
80	0.255	0.245
78	0.257	0.247
60	0.266	0.255
50	0.270	0.260
40	0.272	0.263
30	0.273	0.263
20	0.274	0.264
10	0.274	0.264
5	0.275	0.264



TABLE 32. THERMAL EXPANSION BEHAVIOR OF OFHC COPPER

T (K)	AR	SR
	$-\Delta L/L_0$ (%)	$-\Delta L/L_0$ (%)
300	-0.052	-0.045
290	-0.034	-0.029
280	-0.017	-0.014
270	0	0
260	0.017	0.014
250	0.033	0.029
240	0.051	0.043
230	0.067	0.060
220	0.083	0.076
210	0.099	0.091
200	0.114	0.107
190	0.130	0.122
180	0.145	0.137
170	0.161	0.152
160	--	0.168
150	0.191	0.183
140	0.205	0.197
130	0.219	0.210
120	0.233	0.223
110	0.246	0.237
100	0.258	0.249

TABLE 32. (Continued)

T (K)	AR $-\Delta L/L_o$ (%)	SR $-\Delta L/L_o$ (%)
90	0.269	0.260
80	0.279	0.270
78	0.280	0.272
60	0.287	0.279
50	0.290	0.282
40	0.292	0.283
30	0.293	0.285
20	0.294	0.286
10	0.295	0.287
5	0.295	0.287

TABLE 33. THERMAL EXPANSION BEHAVIOR OF  
310 STAINLESS STEEL

T (K)	STQ $-\Delta L/L_0$ (%)	STFC $-\Delta L/L_0$ (%)
300	-0.045	-0.035
290	-0.026	-0.026
280	-0.011	-0.009
273	0	0
260	0.020	0.022
250	0.034	0.037
240	0.051	0.052
230	0.066	0.065
220	0.080	0.079
210	0.095	0.093
200	0.112	0.107
190	0.126	0.123
180	0.139	0.138
170	0.153	0.151
160	--	0.162
150	0.177	0.174
140	0.189	0.186
130	0.201	0.196
120	0.213	0.205
110	0.223	0.214
100	0.234	0.221

TABLE 33. (Continued)

T (K)	STQ $-\Delta L/L_o$ (%)	STFC $-\Delta L/L_o$ (%)
90	0.244	0.228
80	0.253	0.234
78	0.254	0.234
60	0.265	0.246
50	0.270	0.251
40	0.274	0.256
30	0.278	0.260
20	0.282	0.262
10	0.283	0.262
5	0.284	0.263

TABLE 34. THERMAL EXPANSION  
BEHAVIOR OF INCO  
LE (UNNAMED)

T (K)	ST-A $-\Delta L/L_o$ (%)
300	-0.010
290	-0.006
280	-0.002
273	0
260	0.003
250	0.006
240	0.012
230	0.015
220	0.018
210	0.022
200	0.027
190	0.031
180	0.036
170	0.041
160	--
150	0.051
140	0.055
130	0.059
120	0.063
110	0.066

TABLE 34. (Continued)

T (K)	ST-A - $\Delta L/L_o$ (%)
1.00	--
90	0.072
80	0.076
78	0.077
60	0.080
50	0.081
40	0.082
30	0.082
20	0.083
10	0.083
5	0.083

TABLE 35. THERMAL EXPANSION BEHAVIOR OF Ti-Nb

Data above 200 K are a linear extrapolation.

T (K)	No. 1 Ti-5 a/o Nb $-\Delta L/L_0$ (%)	No. 2 Ti-10 a/o Nb $-\Delta L/L_0$ (%)	No. 3 Ti-15 a/o Nb $-\Delta L/L_0$ (%)	No. 4 Ti-20 a/o Nb $-\Delta L/L_0$ (%)
300	-0.019	-0.018	-0.017	-0.014
290	-0.012	-0.011	-0.011	-0.009
280	-0.005	-0.005	-0.005	-0.004
273	0	0	0	0
260	0.009	0.009	0.008	0.007
250	0.016	0.015	0.014	0.013
240	0.023	0.021	0.020	0.018
230	0.030	0.028	0.026	0.023
220	0.036	0.034	0.032	0.028
210	0.043	0.041	0.038	0.034
200	0.050	0.047	0.044	0.039
190	0.057	0.054	0.050	0.044
180	0.066	0.062	0.057	0.050
170	0.072	0.069	0.061	0.056
160	0.080	0.076	0.068	0.062
150	0.087	0.083	0.074	0.067
140	0.095	0.090	0.080	0.073
130	0.102	0.096	0.086	0.078
120	0.109	0.101	0.093	0.084
110	0.116	0.107	0.099	0.088
100	0.122	0.113	0.105	0.093
90	0.129	0.120	0.113	0.098
80	0.133	0.121	0.116	0.102
78	0.133	--	0.116	--
77	--	0.123	--	0.103
60	0.142	0.131	0.124	0.110
50	0.146	0.134	0.128	0.113
40	0.149	0.137	0.131	0.115
30	0.152	0.140	0.133	0.117
20	0.154	0.141	0.134	0.118
10	0.155	0.142	0.134	0.119
5	0.155	0.142	0.135	0.120

TABLE 36. THERMAL EXPANSION  
BEHAVIOR OF  
BEARING BRONZE  
(Cu - 11% Sn)

T (K)	As Cast, $-\Delta L/L_0$ (%)
300	-0.052
290	-0.033
280	-0.017
273	0
260	0.015
250	0.033
240	0.048
230	0.066
220	0.082
210	0.097
200	0.113
190	0.128
180	0.146
170	0.161
160	0.178
150	0.193
140	0.209
130	0.222
120	0.236
110	0.249
100	0.263
90	0.276
80	0.287
77	0.291
60	0.306
50	0.314
40	0.320
30	0.325
20	0.330
10	0.332
5	0.333



TABLE 37. THERMAL EXPANSION BEHAVIOR  
OF Ti-Al-Sn ALLOYS

T(K)	Annealed Ti-5Al-2.5Sn $-\Delta L/L_0$ (%)	Annealed Ti-3.5Al-3.5Sn $-\Delta L/L_0$ (%)	Annealed Ti-2.5Al-2.5Sn $-\Delta L/L_0$ (%)
300	-0.018	-0.026	-0.025
290	-0.011	-0.016	-0.015
280	-0.003	-0.007	-0.007
273	0	0	0
260	0.010	0.009	0.010
250	0.019	0.019	0.019
240	0.027	0.028	0.028
230	0.035	0.036	0.037
220	0.042	0.044	0.045
210	0.053	0.050	0.053
200	0.058	0.059	0.062
190	0.066	0.068	0.071
180	0.075	0.076	0.077
170	0.082	0.084	0.088
160	0.089	0.093	0.097
150	0.096	0.100	0.106
140	0.102	0.107	0.115
130	0.110	0.116	0.122
120	0.116	0.123	0.130
110	0.123	0.130	0.136
100	0.128	0.136	0.142
90	0.134	0.140	0.147
80	0.138	0.146	0.151
77	0.139	0.147	0.152
60	0.144	0.152	0.158
50	0.147	0.154	0.160
40	0.149	0.155	0.163
30	0.151	0.156	0.165
20	0.152	0.157	0.167
10	0.152	0.158	0.168
5	0.153	0.158	0.168

**COMPOSITE STRUCTURAL MATERIALS INVESTIGATION  
AT CRYOGENIC TEMPERATURES**

**Semi-Annual Technical Report  
3/1/74 through 8/31/74**

**J. R. McLoughlin  
Principal Investigator**

**Sponsored by  
Advanced Research Projects Agency  
ARPA Order No. 2569  
Program Code 4D10**

**This research was supported by the  
Advanced Research Projects Agency  
of the Department of Defense and was  
monitored by the Cryogenics Division,  
National Bureau of Standards, Boulder,  
Colorado 80302, under Contract No.  
CST-8300, 9/1/73 through 8/31/75,  
\$120,000.**

**The views and conclusions contained in this document are those  
of the author and should not be interpreted as necessarily  
representing the official policies, either expressed or implied,  
of the Advanced Research Projects Agency or the U.S. Government.**

**W. B. Hillig  
Program Manager**

**General Electric Company  
Corporate Research and Development  
P. O. Box 8  
Schenectady, New York 12301**

**Phone: (518) 346-8771**

**SRD-74-104**

### SUMMARY

Tests at 4°K on S-glass fiber, Modmor II carbon fiber, and PRD-49 fiber reinforced epoxy resins show that these composites still retain great strength at this low temperature. S-glass is the strongest reinforcement with better than 600,000 PSI flexural strength and 25,000 interlaminar shear; this material is stronger at 4°K than at room temperature. Carbon fiber and PRD-49 fibers make stiffer composites but not as strong as the S-glass composites. The carbon fiber composite was a little weaker in flexure than at room temperature while PRD-49 was much stronger in flexure than at room temperature, possibly because its compressive strength is better at low temperature.

The coefficients of expansion of these materials are also reported between 298°K and 77°K and 298°K and 4°K.

## COMPOSITE STRUCTURAL MATERIALS INVESTIGATION AT CRYOGENIC TEMPERATURES

During the second half of the contract period covered in this report, further mechanical tests were carried out on miniature composite bars made as described in the previous (semi-annual) report. In addition, considerable effort was put into making some larger samples of one resin formulation using S-glass and PRD-49 fibers separately as the reinforcement. These larger samples were tested in flexure at 4°K with encouraging results. In the case of S-glass epoxy, samples with crossplied layers were also made up and tested in flexure; coefficient of expansion was measured at three orientations on these crossplied samples and at two orientations on unidirectional samples.

### PREPARATION OF RESIN PREIMPREGNATED FIBER SHEETS

In order to determine what the coefficient of expansion was from room temperature to 4°K on glass reinforced epoxy at various fiber orientations, it was found necessary to re-commission a prepregging set-up which we had used in the past for this purpose. This consisted of a dip tank, a drying tower, and a filament winder which accurately layed up the resin impregnated fibers on a 2' diameter drum to form a layer of glass strands lying side by side, up to 6" in width and the circumference of the drum in length. The strands were impregnated with a solvent solution of the resin. The solvent was evaporated in the drying tower, and the resin cure possibly slightly advanced to such a degree that the resin impregnated

glass strands were tack-free after emerging from the drying tower and cooling. In order to increase tack enough to cause the strands to stick together as a continuous sheet of prepreg when wound on the drum, it was found useful to direct a heat gun on the glass strands just before winding on the drum.

The resin used to impregnate the S-glass roving for the preparation of this prepreg was the 828-1031-MNA combination described before:

<u>Component</u>	<u>Parts by Weight</u>
Epon 828	100
Epon 1031	127
Methyl nadic anhydride	300
Benzyl dimethyl amine	3

Enough methyl ethyl ketone was added so that the pickup of resin on the roving was about equal to the weight of the roving. It worked best when the solids concentration was in the range of 75-85%.

The drying tower was mounted vertically immediately above the resin dip tank; it consisted of a glass tube 3 1/2" in diameter and 55" long on which were wrapped four separate heaters surrounded with 1" of insulation. The two lower heaters were operated in series while the upper heaters were also in series and controlled separately. The heater resistance readings from bottom to top were 36, 15, 15, and 15. By adjusting the voltages, up to 240 watts could be supplied to the lower half of the tower, and 400 watts to the upper half. The voltage on each set of heaters was adjusted to give a satisfactory temperature profile. The temperature was monitored

about 2/3 of the way up with a chromel-alumel thermocouple passing through the wall of the tower into the inner space. The power was adjusted so this thermocouple read 250° to 320°C. Combining this temperature with the glass roving speed controlled the dryness of the resin on the roving as it came out of the tower.

The exit orifice at the top of the tower was closed with a baffle containing a hole about 1/2" in diameter through which the roving passed. Immediately above this exit orifice and to one side an exhaust duct leading to the laboratory hood system collected any fumes produced in the tower and kept them out of the room air. Because of the proximity of this exhaust duct (a 4" diameter flexible tube), cold air tended to be sucked up through the tower; hence the exact size of the hole in the baffle at the tower top and the exact position of the exhaust duct influenced the temperature obtained in the tower. Therefore, we were careful not to touch these after achieving the proper conditions. Generally, final control over the tackiness of the roving as it emerged from the tower was achieved by varying the winding speed on the collecting drum and hence the residence time of the roving in the tower. The drum rotation used was 1-2 revolutions per minute (6-12 linear ft/min). Since the feed was at the rate of 34 revolutions per inch, it generally took on the order of an hour to produce a strip of prepreg 4-6" wide and 6' long.

A picture of the prepregging equipment is shown in Fig. 1. The roving was pulled from a storage roll 5 ft above the dip tank, around a pulley under the surface of the resin in the dip tank, up through the drying tower, around two pulleys to

the drum winder, where it passed over a final pulley connected to the traversing mechanism; the traversing mechanism was simply the tool rest of a lathe with the drive for the drum being connected through gear reduction to the lathe drive. This meant that, for a given feed ratio used, the number of revolutions/inch was the same no matter what drum speed was used. The drum speed was controlled by means of a speed controller on the lathe itself.

The procedure used in starting a run was to pass the roving through the bath up through the tower and wind it in one place on the drum until speed was adjusted properly to give the right tackiness. The tool rest holding the feed mechanism was then moved 1/2" or so to leave a gap on the drum and engaged with the feed screw. After winding the desired width of prepreg another gap was produced, and the resin bath was removed allowing dry roving to pass up into the tower before stopping the drum.

The drum surface had been covered with a layer of 10 mil Teflon film before starting. At the end of the run, the film and prepreg were cut at one spot and the 6' x 4" to 6" prepreg sheet on the Teflon support was removed. This prepreg sheet was then cut up into 3 1/4" x 4 1/4" panels for molding purposes.

Molding was carried out by stacking 11 pieces of prepreg in the cold 3 1/4" x 4 1/4" mold, dropping in the upper force, and placing this lay-up in a 12 ton laboratory press whose platens had already been heated to 100°C. Several hundred pounds/square inch pressure was applied when the mold temperature reached 80°C. Excess resin squeezed out of the mold at this point and when the sample thickness had reached a predetermined value, platen temperature was raised to 170°C and molding was carried out at this temperature at 500 to



1000 PSI pressure on the molding. The molded panels were removed from the mold hot and were post-baked overnight at 175°C.

Because the prepreg was made in a precise manner, it was possible to calculate for each molded panel the exact weight of glass roving used (from a knowledge of strands/inch and weight of roving/unit length). Knowing the weight of the finished panel and weight of glass in it, one could calculate the weight of resin and the volume in the panel occupied by glass and by resin. Measurement of density of the panels then made it possible to calculate the volume of voids in each panel. When these calculations were performed on the most successful panels (which were later used for coefficient of expansion measurements and flexural tests), the following results were obtained.

Table 1. S-Glass 828/1031 Panels

<u>Panel</u>	<u>Type of Layup</u>	<u>Fiber Vol.</u> <u>%</u>	<u>Void</u> <u>Vol.</u> <u>%</u>	<u>Density</u> <u>g/ml</u>
6-21-N-1	Unidirectional, axial	48.44	0.83	1.845
6-27-N-1	Crossply (6 plies transverse 5 plies axial)	50.54	1.66	1.861
6-28-N-1	Unidirectional, transverse	57.54	1.78	1.947



### COEFFICIENT OF EXPANSION MEASUREMENTS

The coefficient of expansion measurements were made on an existing piece of equipment, the sensitivity of which was approximately  $\pm 0.2$  mils. Since the samples used were  $4 \frac{1}{4}$ " to  $4 \frac{1}{2}$ " in length, the sensitivity limit for the coefficient  $\Delta L/L^\circ$  was about  $4.4 \times 10^{-5}$ . A more sensitive measurement might have been desirable, but we did not feel the cost of setting such measurements up was within the scope of the present work. The present equipment was good enough to clearly show the relationship between coefficients of expansion for the various composites and between coefficients at several orientations for the S-glass reinforced composites.

The measurement was made in a quartz dilatometer which consisted of a quartz tube 22" long and  $\frac{1}{4}$ " inside diameter, open at the top and provided with a bottom flat on the inside. This tube was supported at the top end in a vertical position with the sample positioned inside it at the bottom. The bottom 10"-12" of the tube were immersed in liquid nitrogen or liquid helium for the low temperature part of the measurement; several holes in the walls of the tube allowed the liquid helium or nitrogen to flow in and out of the tube. A quartz rod,  $\frac{1}{8}$ " in diameter and provided with a flat foot at each end and several enlargements to position it in the tube, was used to feel the length changes in the sample. The top of the rod pressed against the foot of a dilatometer consisting of a linear differential transformer. The core of this transformer (connected to the measuring foot) was spring loaded and restrained to move along a set axis so that no inaccuracies due to random positioning on the top of the quartz rod could exist. The measurement transformer was coupled to a second transformer geared to the chart drive so that the chart was

moved 1" for approximately every .003" of deflection. Exact calibration was obtained by inserting a shim of known thickness between the dilatometer foot and the top of the quartz rod.

Measurements were made by noting the change in length of the sample between room temperature and immersion in liquid nitrogen. The liquid nitrogen dewar was then removed and a double dewar of liquid helium surrounded by liquid nitrogen was immediately put in place. Thermal equilibrium between the samples and liquid nitrogen and liquid helium occurred very quickly (less than 1 minute), but it was necessary to warm the tube with a heat gun and wait for about 1/2 hour to get it back to room temperature for another measurement. Results are listed in Table 2.

#### FLEXURAL MEASUREMENTS ON LARGE BARS

The flexural measurements reported in the previous (semi-annual) report were all made on miniature bars (1.5" x .05" x .08" to .1"). Also, all these measurements were on unidirectional axially reinforced bars made under very carefully controlled conditions to minimize void formation. It was felt that tests on larger bars made from prepreg and with crossplying would give a more practical evaluation of the usefulness of fiber reinforced plastics at low temperature.

For the flexural tests at low temperature on these bars (3 1/2" in length), a new test jig was designed and built as shown in Fig. 2. This jig was designed to bolt on the bottom of a standard Instron crosshead so that there was enough clearance to put in place a double dewar of liquid helium surrounded by liquid nitrogen and remove it at the end of each run. The double dewar system utilized two glass dewars

held apart by plastic foam spacers and clamped together by an outer framework to prevent the inner dewar from floating. The inner dewar measured 3 3/4" in inside diameter, while the outer one was 6" in inside diameter. Space between them was 1/2". Total height was 16".

The procedure used in testing was to fill the outer dewar with liquid nitrogen and the inner with liquid helium (after precooling with liquid nitrogen); then precool the jig by immersing it in another liquid nitrogen dewar. When bubbling had stopped in the liquid nitrogen, that dewar was removed and the double dewar slowly brought up around the jig. A transfer tube with a flexible section in it was then introduced into the liquid helium dewar and left there for the remainder of the test. Liquid helium was transferred into the dewar until a resistance thermometer about 3" above the sample position indicated the helium level had reached that point. The sample was held in liquid helium for ten minutes before testing; liquid helium was added if its level dropped below the resistance thermometer level at any time during the test.

This procedure was fairly economical of liquid helium since the dewar was usually about 1/4 full of liquid helium left from the previous test when the next one started, and this was used in cooling the jig initially.

All tests were run at a crosshead speed of 0.1"/minute although this speed is unlikely to be critical since the samples at liquid helium temperature exhibited almost zero plastic flow. The stress-strain curves were linear right up to the first break.

#### DISCUSSION OF RESULTS

Table 3 summarizes the results of the flexural tests made on the 3 1/2" long bars. The first three samples of

unidirectionally S-glass reinforced 828/1031 were made from prepreg made in our drying tower and vacuum molded. However, vacuum molding in the case of prepreg, with most of the solvent already driven off, may not be as effective in removing trapped gases as for the 1.5" samples which were vacuum molded wet. In the latter case, it is felt that the boiling off of solvent in the mold in vacuum helps to drive off the trapped gas. Two of the samples made from prepreg had fairly large void volumes and yet still showed very good flexural strength at 4°K. This is encouraging, if the effect is true, because it would indicate that the presence of voids may not be as serious a problem at low temperature as we know it to be at room temperature. Certainly, more work would have to be done before being sure that this is so.

The results bracketed and asterisked were carried out at a lower span-to-thickness ratio, and in these tests all four samples failed by interlaminar shear at the values noted in the chart. Because of these failures, it was felt unnecessary to do any special interlaminar shear tests on the large S-glass 828/1031 samples.

The tests made on the samples with fibers running transversely showed the expected low strength. The crossplied samples were also fairly weak even when tested with one layer of fibers lying along the axis of the flexural beam. This may have been because the outermost layer of fibers ran transverse to the sample axis. No samples were tested where the outer layer of fibers in a crossply laminate ran parallel to the axis. This should probably be done. The samples tested at 45° to the fiber directions in the crossply laminate were also fairly weak.

The PRD-49 reinforced bars exhibited flexural strengths far greater than would be expected for this material at room temperature; however, the values were considerably lower than

for the S-glass samples. The higher modulus of this material might make it attractive when coupled with low thermal conductivity. Its low coefficient of expansion might also prove useful.

The carbon reinforced bars were a little weaker than the PRD-49 bars but did exhibit greater stiffness as well as a low coefficient of expansion. Tables 4, 5, 6, and 7 summarize the results of all the tests made on 4 1/2" bars of S-glass reinforced 828/1031 and of Modmor II reinforced 828/1031.

All these results were subjected to statistical analysis to determine how fiber volume content, voids, and density of the samples affected flexural strength, flexural stiffness, percent elongation (outer fiber) at break, and interlaminar shear strength. Table 4 covers the first three dependent variables for S-glass reinforced samples.

For the twenty tests run, the average flexural strength was 586,000 PSI. The main correlation was with density, accounting for 59% of the observed variation. The expression  $F = -403 + 510D$  gives the best line through the points where  $F$  is flexural strength in thousands of PSI, and  $D$  is density in g/ml. At a density of 2.0 (60 volume % fiber) flexural strength from this expression is 617,000. For stiffness the mean value was  $7.86 \times 10^6$  PSI; the best correlation was with fiber volume %. Seventy-seven percent of the variation was explained by the correlation. The best expression was  $M = -2.53 + .176 \times V_f$  where  $M$  = modulus of elasticity in millions of PSI, and  $V_f$  is volume % fiber. At 60% fiber this gives a modulus of 8.03 million PSI. At 70% fiber it would be 9.79 million PSI.

For outer fiber elongation at break, the mean was 6.97%; the best correlation was with voids. The expression

$$E = 7.47 - .15 V$$

where E = elongation in % and V = void volume in %, explains 54% of the variation. At 0% voids, the elongation is 7.47%.

For interlaminar shear only, eight tests were run on S-glass/828-1031. They are shown in Table 5. The mean was 26840 PSI; the best correlation was with voids, explaining 60% of the observed variation. The expression

$$S = 30900 - 2927 V$$

is the best line through the results where S = interlaminar shear in PSI and V = void volume percentage.

For the Modmor II reinforced 828/1031, the flexural test results are shown in Table 6. The mean value for flexural strength was 202,000 PSI; the best correlation was with fiber volume % but only 34% of the variation was explained. A better correlation was obtained by the double regression versus fiber volume % and void volume %, which accounted for 52% of the observed variation.

$$F = 900 - 9.42 V_f - 35.6 V_v$$

where F = flexural strength in thousands of PSI;  $V_f$  = volume % fiber; and  $V_v$  = volume % voids. At 64 volume % fiber and 1% voids, flexural strength from this expression is 261,000 PSI. Obviously, this expression cannot hold over a very large range of fiber volume % since strength is bound to begin to decrease with decreasing fiber volume at some point.



For stiffness, the mean was  $22.8 \times 10^6$  PSI; the best correlation was with density, explaining 66% of the observed variation.

$M = -139.4 + 101.4 D$  is the best line through the points where  $M$  = modulus of elasticity in millions of PSI and  $D$  = density in g/ml. At a density of 1.60 g/ml (approx. 64% fiber), the modulus of elasticity would be 22.8 million PSI.

For outer fiber elongation at break, the mean was 1.25%; the best correlation was with fiber volume %, accounting for 58% of the observed variation.

$E = 7.06 - .0875 V_f$  is the best line through the data where  $E$  is elongation in % and  $V_f$  is fiber volume %. At 64% fiber volume this gives  $E = 1.46\%$ .

For interlaminar shear, the mean of eleven tests was 20350. Best correlation was with fiber volume % and void volume. Only 48% of the variation was explained. With fiber volume alone, the correlation was only 40% of the variation explained. The expression

$$S = 24600 + 677 V_f + 950 V_v$$

is the best line through the results. The fact that shear is higher for higher void volumes is surprising and probably indicates that the correlation is not very meaningful. For 64% fiber volume and 1% voids, shear calculates to be 19700 PSI.

It is surprising that interlaminar shears are so high for both S-glass reinforced bars and for Modmor II reinforced bars at 4°K. This may be caused by the differential coefficient of expansion between reinforcing fiber and resin; the low shrinkage of the fiber on cooling to 4°K would tend

to force the greater resin shrinkage to occur in a transverse direction rather than along the fibers. Thus, the resin may be effectively put into a state of compression transversely which would tend to increase shear strength along planes parallel to the fibers.

The high strength of S-glass epoxy composites at low temperature is undoubtedly due to the higher strength of glass itself at low temperature. The improvement in glass strength is manifested largely as a gross decrease in the rate of decay of strength after application of load. Whereas, at room temperature, as much as 50% of strength can be lost only a few seconds after applying load, the strength is maintained much, much longer at low temperature. This does suggest that experiments on creep rupture of composites at low temperature should be carried out to determine just how fast the material loses strength after application of load, as this would be a critical point in design.

The crossplied specimens seem to be weaker than one would expect. This was particularly true for the samples tested at 45° to the fiber orientation. These samples failed by splitting along the fibers showing that the failure was in adhesion between glass and resin. Probably the crossplied specimens exhibit considerable extra stress concentration in the resin matrix compared with the unidirectionally oriented fiber specimens. This points up the necessity for designing so that the major stresses are carried by the fibers in tension and so that shear stresses between fibers and between layers are minimized. Part of the weakness in crossplied specimens is undoubtedly due to contraction stresses set up between layers with the fibers running in different directions. Here is where carbon fiber and PRD-49 with their smaller coefficient of expansion could prove useful.



The fact that the glass reinforced specimens were so tough (did not shatter in brittle failure) is probably a manifestation of the high elongation these fibers will endure before failure. Carbon and boron, on the other hand, will endure only small elongations so that it is harder to distribute the stress among the fibers more uniformly around a flaw.

In general, these test results on composites at low temperature are encouraging for their future use in low temperature structural applications. However, there are still serious unanswered questions about the feasibility of designing structures for use at such temperatures due to problems of differential coefficient of expansion and adhesion to surrounding components. These should be answered in further work.

### CONCLUSIONS

When unidirectional epoxy matrix composites are stressed parallel to the fibers, the strengths at 4°K are good for all fiber reinforcements studied and are strikingly good in the case of S-glass. The interlaminar (short beam) shear strengths were very good, perhaps attributable to the shrinkage of the resin around the fibers upon cooling as already discussed. The transverse strength was measured in the case of the S-glass composites and gave values comparable to the interlaminar shear strength. Both situations are due to matrix cohesive failure, or fiber-matrix adhesive failure, and do not involve fiber breakage. However, the strain-to-fail in the transverse direction was only 1/10 of that in the parallel direction.

This may account for the relatively low strength observed for the 0°/90° crossplied composite with the same reinforcement

when tested in the 0° direction. Because of the excellent matrix-fiber bonding, transverse cracks in the matrix resin would not be blunted by the well known fiber-matrix delamination mechanism. Instead the cracks in the matrix would act as stress raisers. The same crossplied material, when tested in the 45° direction was weaker yet. If this explanation is correct, then a fiber-matrix resin system with a lesser interlaminar shear strength should lead to an improvement in strength of the crossplied structures.

In any case, these results indicate that the composites intrinsically have good tensile strength, but that design of complex structures will require careful attention to a proper balance of properties.

Table 2. Coefficient of Expansion of S-Glass, PRD-49, and Modmor II Epoxy Composites Between 25°C and 4°K

All Samples were 4 1/4" in Length

Sample Identification	Type	Vol. % Fiber	Vol. % Voids	Density g/ml	$\frac{L_{298}-L_{77}}{L_4}$	$\frac{L_{298}-L_4}{L_4}$
4-22-74-1	S-glass fibers parallel to measurement direction	58.4	6.1	1.938	$.685 \times 10^{-3}$	$.815 \times 10^{-3}$
					.698	.822
					.705	.828
					.657	.787
					.650	.794
				Ave.	.679	.809
4-12-74-1	Modmor II fibers parallel to measurement direction	60.6	0.95	1.573	$.014 \times 10^{-3}$	$.103 \times 10^{-3}$
					.007	.096
					.011	.100
3-28-74-2	PRD-49 fibers parallel to measurement direction	60.6	3.8	1.324	$-.616 \times 10^{-3}$	$-.767 \times 10^{-3}$
					-.650	
					-.633	-.767
6-28-74-N-1-1	S-glass fibers perpendicular to measurement direction	57.5	1.8	1.947	$3.313 \times 10^{-3}$	$3.971 \times 10^{-3}$
					3.424	4.060
					3.567	4.005
					$3.435 \times 10^{-3}$	$4.012 \times 10^{-3}$
6-27-74-N-1-1	S-glass crossply measurement at 0°	50.5	1.7	1.861	$1.506 \times 10^{-3}$	$1.671 \times 10^{-3}$
					1.540	1.725
					1.513	1.808
					1.486	1.691
					1.511	1.724
6-27-74-N-1-2	S-glass crossply measurement at 45°	50.5	1.7	1.861	$1.876 \times 10^{-3}$	$2.054 \times 10^{-3}$
					1.938	2.280
					1.917	2.157
					1.910	2.164

Table 3. Summary of 3 1/2" Bar Flexural Tests

S-Glass, Epon 828/1031, MNA; Tested at 4°K

Identification	Type	Vol. % Fiber	Vol. % Voids	Density g/ml	Flexural Strength Thousands of PSI	Flexural Modulus Millions of PSI	Elongation %	Span/ Thickness	Remarks
4-19-B-1	Unidirectional	56.3	1.6	1.984	630	7.53	8.5	15.2	Vacuum molded
4-22-B-1	"	58.4	6.1	1.938	605	8.3	6.9	15.2	" "
4-24-B-1	"	57.6	7.5	1.903	716	9.2	7.3	15.2	" "
6-21-N-1-1	"	48.4	0.83	1.845	(282)*	5.97	4.7*	9.8	No vacuum; delaminated; 14,300 PSI shear
6-21-N-1-2	"	48.4	0.83	1.845	(349)*	5.3	6.6*	10.2	No vacuum; delaminated; 16,500 PSI shear
6-21-N-1-3	"	48.4	0.83	1.845	(310)*	5.57	6.1*	8.8	Delaminated; 17,400 PSI shear
6-21-N-1-4	"	48.4	0.83	1.845	(343)*	5.96	6.3*	8.8	Delaminated; 19,400 PSI shear
6-28-N-1-2	Unidirectional Transverse	57.5	1.8	1.947	22	3.62	0.63	12.3	
6-28-N-1-4	"	57.5	1.8	1.947	31	3.87	0.62	12.2	
6-28-N-1-3	"	57.5	1.8	1.947	29	4.72	0.61	18.0	
6-28-N-1-5	"	57.5	1.8	1.947	19	3.19	0.60	18.0	
6-27-N-1-3	90° Crossply, Tested 0°	50.5	1.7	1.861	136	3.81	3.5	11.1	
6-27-N-1-7	"	50.5	1.7	1.861	127	3.98	3.5	10.1	
6-27-N-1-4	90° Crossply, Tested 45°	50.5	1.7	1.861	53	3.0	2.8	10.5	
6-27-N-1-5	"	50.5	1.7	1.861	44	3.3	1.4	10.6	

\*Broke in shear; so the flexural strength values are not representative.

Table 3. Cont'd.

PRD-49, Epon 828/1031, MNA; Tested at 4°K

Identification	Type	Vol. % Fiber	Vol. % Voids	Density g/ml	Flexural Strength Thousands of PSI	Flexural Modulus Millions of PSI	Elongation %	Span/ Thickness	Remarks
3-28-B-2	Unidirectional	60.6	3.8	1.324	181	12.0	2.35	15.3	
3-28-B-1	"	"	"	"	"	"	"	"	
4-1-B-1	"	63.0	4.39	1.321	175	12.5	2.20	15.2	
4-1-B-2	"	68.8	1.05	1.374	183	12.3	2.17	15.3	
4-2-B-1	"	---	---	1.312	138	13.3	1.19	15.5	
4-2-B-1	"	62.6	8.2	1.273	143	11.3	2.07	15.3	

Treated Modmor II, Epon 828/1031, MNA; Tested at 4°K

4-11-B-1	Unidirectional	60.1	6.4	1.503	163	14.3	1.16	15.3	
4-12-B-1	"	"	"	"	"	"	"	"	
4-12-B-2	"	60.6	0.95	1.573	164	17.4	0.95	15.2	
4-15-B-1	"	61.3	1.4	1.572	167	17.0	0.98	15.3	
4-15-B-1	"	61.2	1.26	1.573	169	20.1	0.94	15.4	

Table 4. Summary of Flexural Tests at 4°K on 1.5" Long Bars  
of Uniaxially Reinforced S-Glass 828/1031  
All with 16:1 Span-to-Thickness Ratio

Test No.	Sample No.	Vol. % Fiber	Vol. % Voids	Density g/ml	Flexural Strength Thousands of PSI	Flexural Modulus Millions of PSI	Outer Fiber Elongation %
10	10-18-73-2	65.3	0.37	2.055	689	9.11	8.1
11	10-19-73-1	54.9	5.27	1.865	632	7.5	8.4
21	10-22-73-1	52.8	1.88	1.88	529	7.39	6.8
22	10-22-73-2	61.3	0.2	2.007	615	8.94	7.0
23	11-30-73-1	59.9	0.48	1.987	583	6.59	6.5
65	1-18-74-2	52.9	0.41	1.90	576	7.27	7.2
66	1-22-74-2	52.1	14.9	1.71	347	6.71	5.4
67	1-18-74-3	54.7	1.23	1.91	525	7.54	7.0
68	1-18-74-1	55.8	1.9	1.92	553	7.52	7.7
69	1-21-74-1	53.9	1.8	1.9	581	5.77	8.1
70	1-21-74-2	53.3	1.75	1.89	543	6.23	7.4
71	1-21-74-3	52.6	0.98	1.89	604	7.1	7.7
72	1-22-74-1	58.0	12.7	1.81	507	6.61	4.3
73	1-22-74-3	53.4	14.9	1.73	535	6.36	5.6
74	1-17-74-2	55.8	1.93	1.92	686	8.17	6.7
98	1-8-74-1	68.6	1.00	2.088	654	9.55	7.1
99	1-8-74-2	67.3	0.49	2.078	650	9.51	7.7
100	1-16-74-1	69.0	2.65	2.073	617	9.93	6.9
101	1-16-74-2	70.5	0.70	2.116	676	9.29	7.2
102	1-17-74-1	70.3	1.56	2.102	625	10.17	6.6

Table 5. Summary of Interlaminar Shear Tests at 4°K on  
S-Glass Uniaxially Reinforced 828/1031  
All Tests at 6:1 Span-to-Thickness Ratio

Test No.	Sample No.	Vol. % Fiber	Vol. % Voids	Density g/ml	Interlaminar Shear, PSI
112	1-8-74-1-1	68.6	1.00	2.088	28000
114	1-8-74-2-1	67.3	0.49	2.078	28600
115	1-8-74-2-2	67.3	0.49	2.078	28500
116	1-16-74-1-1	69.0	2.65	2.073	20500
117	1-16-74-1-2	69.0	2.65	2.073	24200
118	1-16-74-2-1	70.5	0.70	2.116	29100
119	1-17-74-1-1	70.3	1.56	2.102	30800
120	1-17-74-1-2	70.3	1.56	2.102	25000

Table 6. Summary of Flexural Tests at 4°K on 1.5" Long Bars  
of Uniaxially Reinforced Carbon (Modmor II) 828/1031  
All Tests at 16:1 Span-to-Thickness Ratio

Test No.	Sample No.	Vol. % Fiber	Vol. % Voids	Density g/ml	Flexural Strength Thousands of PSI	Flexural Modulus Millions of PSI	Outer Fiber Elongation %
12	11-13-73-2	70.3	1.38	1.6333	196	28.6	1.21
13	11-2-73-1	67.6	1.95	1.611	172	28.1	1.15
14	11-9-73-1	68.8	1.55	1.623	204	23.3	1.39
51	11-12-73-1	69.8	2.65	1.615	98	22.2	0.69
52	11-12-73-2	70.5	1.94	1.628	195	27.7	0.78
53	11-13-73-1	70.5	1.73	1.63	143	25.0	0.60
54	11-12-73-3	70.4	1.61	1.631	205	22.3	0.97
55	11-13-73-3	70.2	2.38	1.62	152	25.8	0.64
103	3-18-74-1	64.0	2.27	1.575	246	19.9	1.47
104	3-22-74-1	62.7	2.41	1.568	250	22.7	1.64
105	3-21-74-2	62.0	1.41	1.576	239	19.8	1.60
106	3-19-74-2	64.2	1.70	1.584	254	22.4	1.51
107	3-22-74-2	63.7	1.60	1.602	240	21.1	1.51
108	3-26-74-1	62.4	2.22	1.568	170	20.3	1.07
109	3-19-74-1	65.3	2.32	1.582	259	20.9	1.97
110	3-21-74-1	59.8	3.74	1.534	209	14.2	1.80
111	3-25-74-1	64.2	1.75	1.584	177	17.8	1.20



Table 7. Summary of Interlaminar Shear Tests at 4°K on  
 Modmor II Uniaxially Reinforced 828/1031  
 All Tests at 6:1 Span-to-Thickness Ratio

<u>Test No.</u>	<u>Sample No.</u>	<u>Vol. % Fiber</u>	<u>Vol. % Voids</u>	<u>Density g/ml</u>	<u>Interlaminar Shear, PSI</u>
122	3-18-74-1-2	64.0	2.27	1.575	19500
123	3-22-74-1-1	62.7	2.41	1.568	20100
124	3-22-74-1-2	62.7	2.41	1.568	20000
126	3-21-74-2	62.0	1.41	1.576	17100
127	3-19-74-2-1	64.2	1.70	1.584	20900
128	3-19-74-2-2	64.2	1.70	1.584	20200
129	3-22-74-2-1	63.7	1.60	1.602	20500
130	3-22-74-2-2	63.7	1.60	1.602	21200
131	3-26-74-1-1	62.4	2.22	1.568	21200
132	3-19-74-1-1	65.3	2.32	1.582	21800
133	3-19-74-1-2	65.3	2.32	1.582	21400

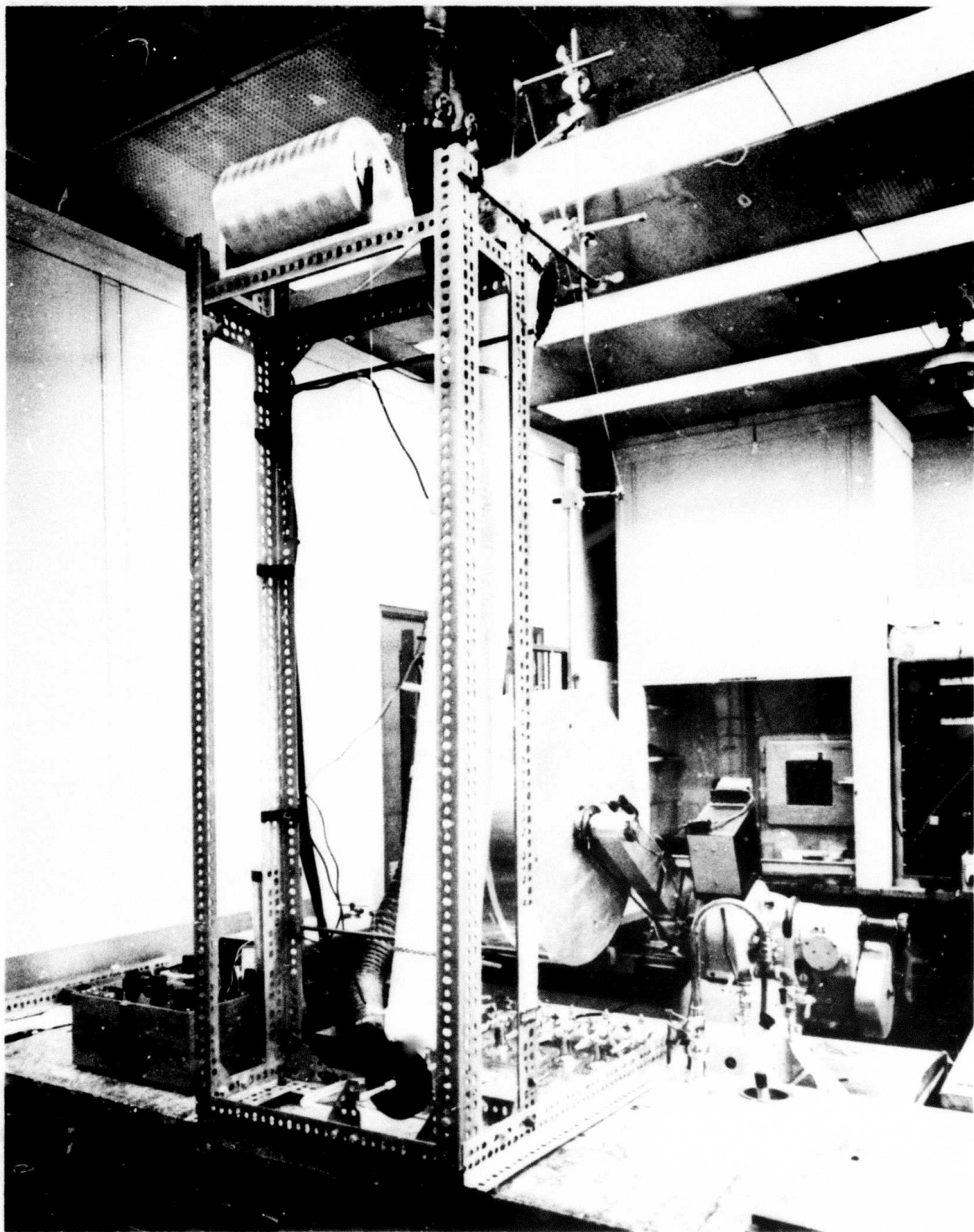


Fig. 1 Prepping equipment.

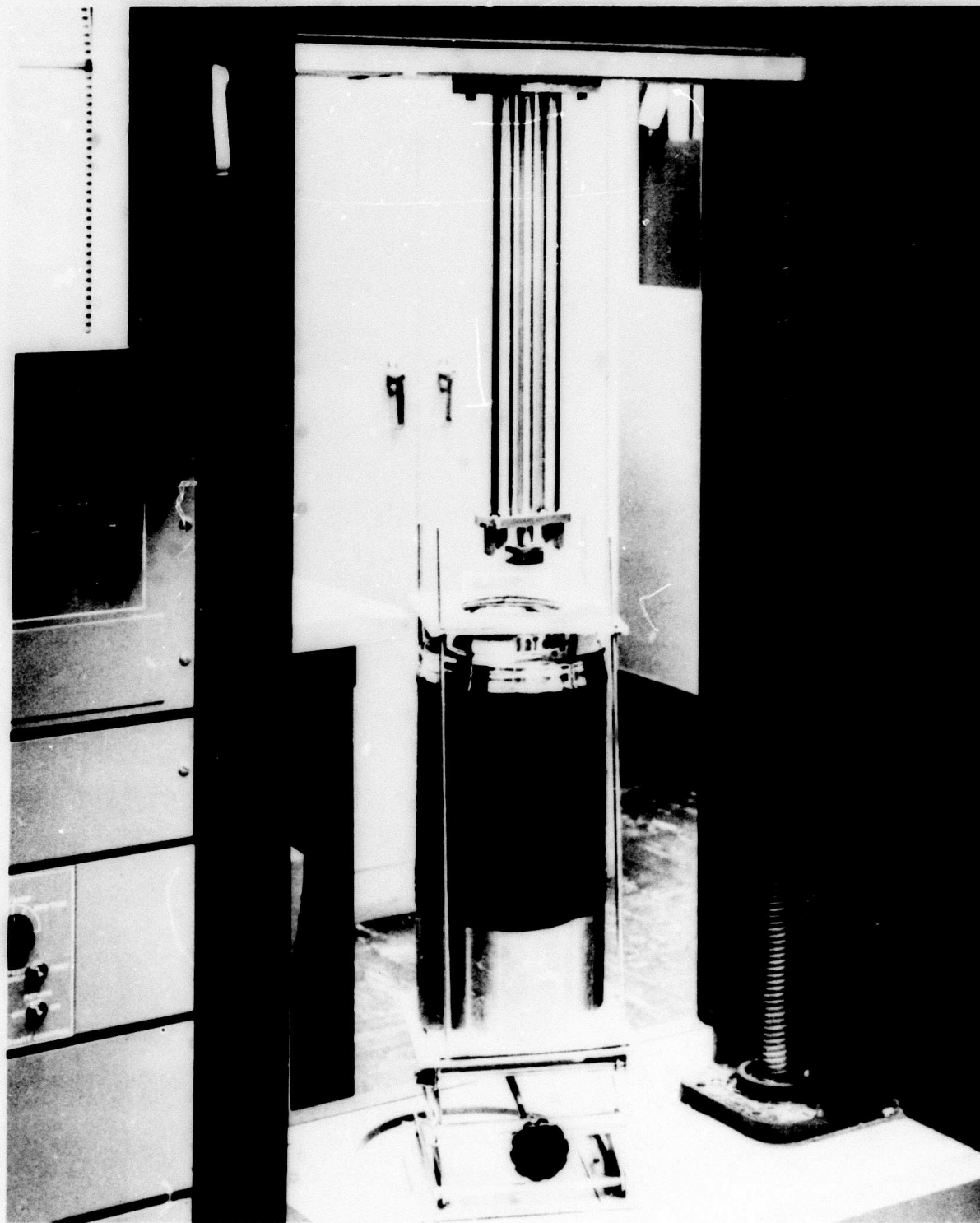


Fig. 2 Equipment used in low temperature flexural tests.

MCR-74-89 (Issue 2)

Annual  
Technical  
Report

October 1974

---

**STUDY OF FRACTURE  
BEHAVIOR OF METALS  
FOR SUPERCONDUCTING  
APPLICATIONS**

Sponsored by Advanced Research Projects  
Agency

ARPA Order No 2569, Program Code 4D10  
Contract Monitor: Cryogenics Division  
National Bureau of Standards, Boulder, Colo.  
80302

NBS Contract No. CST 8301

Period of Performance: 9/1/73 to 10/21/74

Contract Value: \$50,000

Fred R. Schwartzberg  
Program Manager  
303-794-5211, Ext 3438

**MARTIN MARIETTA CORPORATION**  
P.O. Box 179  
Denver, Colorado 80201

FOREWORD

---

This report describes technical activities conducted by the Denver Division of Martin Marietta during the period 1 September 1973 through 1 October 1974 under National Bureau of Standards (NBS) Contract CST-8301.

The views and conclusions contained in this document are those of the authors and should not be interpreted as necessarily representing the official policies, either expressed or implied, of the Advanced Research Projects Agency or the U.S. Government.

## CONTENTS

	<u>Page</u>
I. INTRODUCTION . . . . .	I-1 thru I-3
II. MATERIALS . . . . .	II-1 thru II-5
III. TESTING TECHNIQUES AND APPARATUS . . . . .	III-1 thru III-10
IV. EXPERIMENTAL RESULTS . . . . .	IV-1
A. Static Fracture Toughness . . . . .	IV-1
B. Cyclic Crack Growth Rate Data . . . . .	IV-16 thru IV-23
V. DISCUSSION OF RESULTS . . . . .	V-1 thru V-5

## Figure

II-1	Microstructure of 304L Stainless Steel . . . . .	II-3
II-2	Microstructure of A-286 Stainless Steel . . . . .	II-4
II-3	Microstructure of X-750 Nickel Alloy . . . . .	II-5
III-1	Biaxial Brittle Fracture Specimen as Developed by Manjoine . . . . .	III-2
III-2	K Calibration for T-Type WOL Specimen . . . . .	III-4
III-3	Compact Tension Specimen . . . . .	III-5
III-4	K Calibration for Compact Tension (CT) Specimen . . . . .	III-5
III-5	Close-Up View of Load Train for Liquid Helium Testing System . . . . .	III-7
III-6	Overall View of Liquid Helium Testing System . . . . .	III-8
IV-1	Load vs Load Point Displacement Curves for 2-in.-thick 304L Stainless Steel at 4K . . . . .	IV-8
IV-2	Load versus Load Point Displacement Curves for 2-in.- thick 304L Stainless Steel at 77K . . . . .	IV-9
IV-3	Load versus Load Point Displacement Curves for 1-in.- thick 304L Stainless Steel at 77K . . . . .	IV-10
IV-4	Load versus Load Point Displacement Curves for 2-in.- thick 304L Stainless Steel at 20K . . . . .	IV-11

IV-5	Load versus Load Point Displacement Curves for 1-in.-thick 304L Stainless Steel at 20K . . . . .	IV-12
IV-6	Cyclic Crack Growth Rate Properties of 304L Stainless Steel at 77K . . . . .	IV-18
IV-7	Cyclic Crack Growth Rate Properties of 304L Stainless Steel at 4K . . . . .	IV-19
IV-8	Cyclic Crack Growth Rate Properties of A-286 Stainless Steel at 77K . . . . .	IV-20
IV-9	Cyclic Crack Growth Rate Properties of A-286 Stainless Steel at 4K . . . . .	IV-21
IV-10	Cyclic Crack Growth Rate Properties of X-750 Alloy at 77K . . . . .	IV-22
IV-11	Cyclic Crack Growth Rate Properties of X-750 Alloy at 4K . . . . .	IV-23
V-1	Comparison of J-Integral Data for 304 Stainless Steel . . . . .	V-2
V-2	Comparison of $K_Q$ Data for A-286 Stainless Steel . . . . .	V-4
V-3	Comparison of Cyclic Crack Growth Rates . . . . .	V-5

Table

---

II-1	Certified Test Report Data . . . . .	II-1
II-2	Tensile and Hardness Data for Three Alloys at 298K . . . . .	II-2
IV-1	Static Fracture Toughness Data for 304L Stainless Steel . . . . .	IV-2
IV-2	Static Fracture Toughness Data for A-286 Stainless Steel . . . . .	IV-2
IV-3	Static Fracture Toughness Data for X-750 Nickel Alloy . . . . .	IV-3
IV-4	J-Integral Fracture Toughness for 304L Stainless Steel at 4K . . . . .	IV-14
IV-5	J-Integral Fracture Toughness for 304L Stainless Steel at 20K . . . . .	IV-14
IV-6	J-Integral Fracture Toughness for 304L Stainless Steel at 77K . . . . .	IV-15



I. INTRODUCTION

---

In designing and fabricating hardware, the goal is to produce tough hardware. To claim that a structure is "tough," it is essential to know how tough it is. In other words, how big is the margin and what confidence level exists. The transition temperature approach, as characterized by nondestructive testing (NDT), utilizes  $\Delta T$  as the safety margin. Although the transition temperature approach to design has been widely used in the past, it is rapidly being replaced by the more complex fracture mechanics design approach. The safety margin using fracture mechanics is the crack size.

Although more complex and subject to more limitations, the fracture mechanics approach provides a quantitative relationship between fracture strength, crack size, and a material property called "fracture toughness." This a highly useful relationship because the fracture strength of a cracked component can be estimated from a laboratory test of a crack coupon containing a crack of different size and shape.

The term  $K_{Ic}$  is the most commonly used fracture mechanics term. It is defined as the critical value of the elastic crack tip stress intensity factor under plane strain for the opening mode condition.



The plane-strain term means the minimum toughness value that occurs under conditions of full restraint. To achieve full restraint, there must be sufficient material along and ahead of the advancing crack to keep contractions at their irreducible minimums.

Another common term is  $K_{Ic}$ , which is the critical stress intensity factor estimated from a nominal fracture stress that is not truly elastic. This situation occurs for conditions of less than full restraint.

A concept for predicting postyielding fracture is based on the J-integral approach. J is a proposed material property (units = in.-lb/in.<sup>2</sup>). The objective is to predict the behavior of a flawed structure from measurements of test specimens in essentially the same manner in which K measurements are used. The J-integral basically considers deformation energy over an area surrounding the flaw but does not model crack tip behavior.

The purpose of this portion of the program is to establish preliminary characterization of the fracture and crack growth behavior in thick gages of three alloy candidates being considered for use in superconducting equipment. The three alloys evaluated are:

- 1) 304L stainless steel;
- 2) A-286 stainless steel;
- 3) X-750 nickel alloy.

During the first year, all alloys were evaluated using parent metal stock to provide static fracture toughness and cyclic flaw growth behavior at temperatures in the range of 77 to 4°K.

All fracture and cycling tests were performed using compact tension specimens. The maximum thickness was selected in an attempt to approach valid plane strain conditions, while recognizing that attainment of validity in accordance with ASTM specifications was unlikely.

## II. MATERIALS

---

Stock of each alloy was obtained in both 1-in. and 2-in. thicknesses. The 304L stainless steel was obtained in the form of plate material. No certifications or analyses were available for this material. The 1-in. thick A-286 stainless steel was obtained as 1 in. x 3 in. flat rolled stock. Two-in. A-286 and both gages of X-750 nickel alloy were purchased as forgings (1 in. x 3 in. and 2 in. x 5 in.).

Certified test report data for the A-286 and X-750 materials are given in Table II-1.

*Table II-1 Certified Test Report Data*

Material	Thickness, in.	Heat No.	Condition	Chemical Analysis	Mechanical Properties			
					Tensile Strength, ksi	Yield Strength, ksi	Elongation, %	R.A., %
A-286	1	L2397-K11	STA	24.97 Ni, 14.30 Cr, 2.25 Ti, 1.12 Mo, 1.31 Mn, 0.54 Si, 0.25 V, 0.05 C	147 (L) 144 (T)	103 (L) 112 (T)	24	45
A-286	2	6870-6	STA	26.66 Ni, 15.30 Cr, 2.16 Ti, 1.36 Mo, 0.74 Mn, 0.45 Si, 0.31 V, 0.05 C	156	118	24	49
X-750	1 and 2	31C6X8	ST	73.84 Ni, 15.27 Cr, 6.22 Fe, 2.69 Ti, 0.89 Cb + Ta, 0.05 C	184	140	23	37

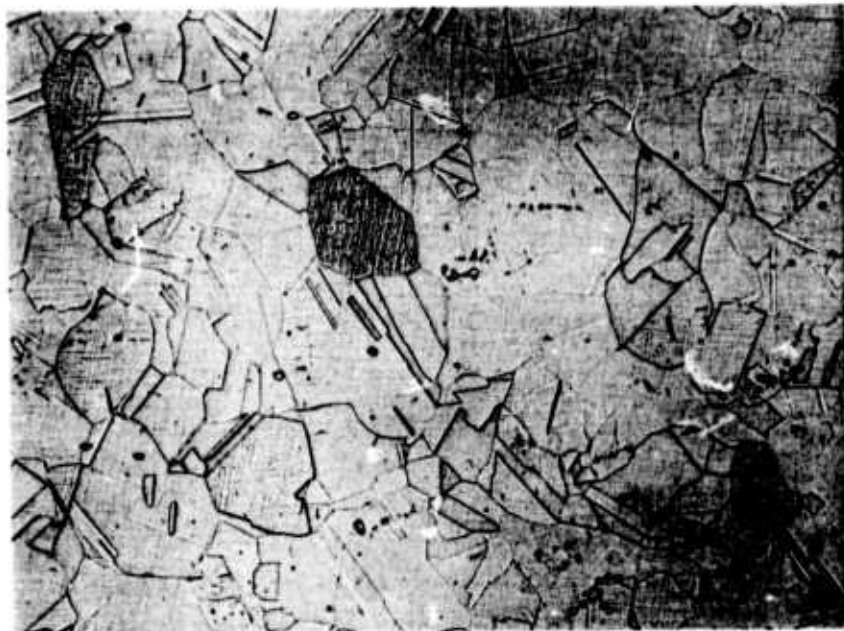
The X-750 alloy was procured in the solution-treated condition. Aging was performed by Martin Marietta for 20 hours at 1300°F, followed by air cooling.

Metallographic examination was performed on sections removed from both gages of each alloy. Normal microstructures were displayed for all conditions except the 2-in. gage of A-286 and X-750. These materials exhibited very coarse grain size. Micrographs for each material condition are given in Figures II-1 thru II-3.

Tensile test specimens were machined from the 2-in. stock and tested at room temperature. Tensile properties as well as hardness properties for both gages are given in Table II-2.

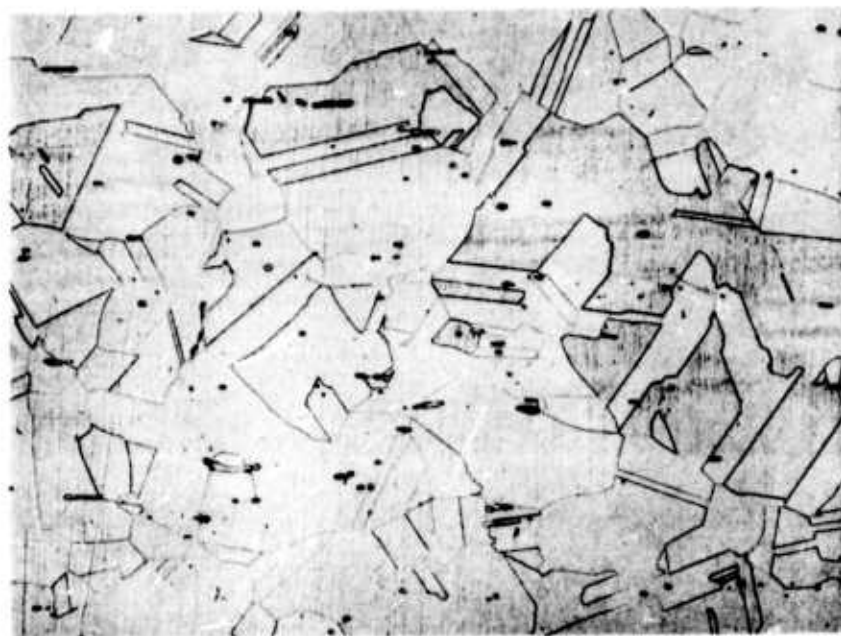
*Table II-2 Tensile\* and hardness Data for the Three Alloys at 298K*

Alloy	Ultimate Strength, ksi	Yield Strength, ksi	Elongation, %	Reduction in Area, %	Hardness (Rockwell)
304L	89.7	43.6	74	75	B85 (2-in.) B86 (1-in.)
A-286	154.3	105.2	27	47	C30 (2-in.) C34 (1-in.)
X-750	159.4	113.8	15	13	C35 (2-in.) C35 (1-in.)
*From 2-in. stock.					



1-in. thick

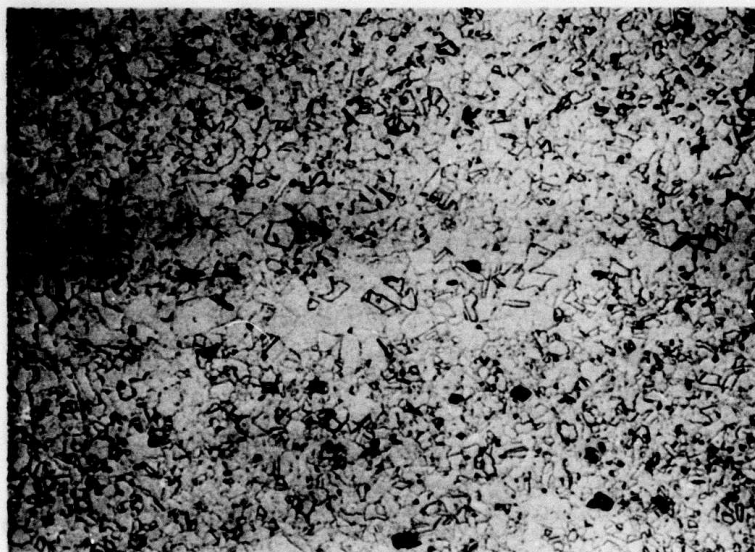
100X



2-in. thick

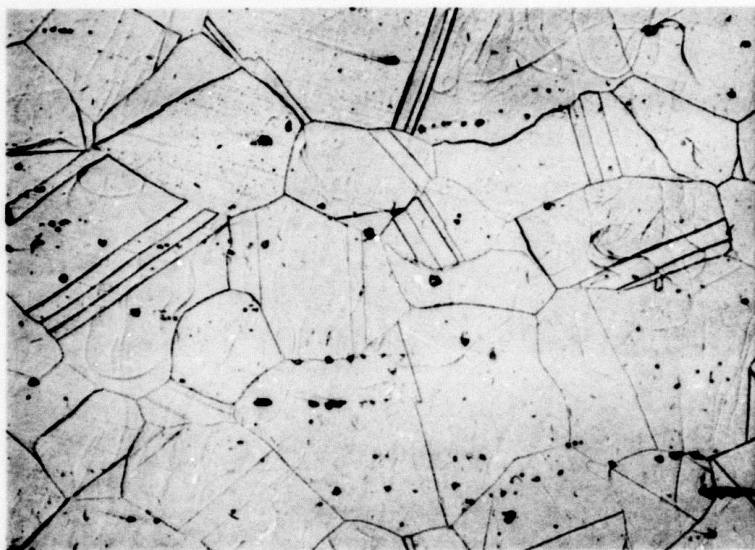
100X

*Figure II-1 Microstructure of 304L Stainless Steel*



1-in. thick

100X



2-in. thick

100X

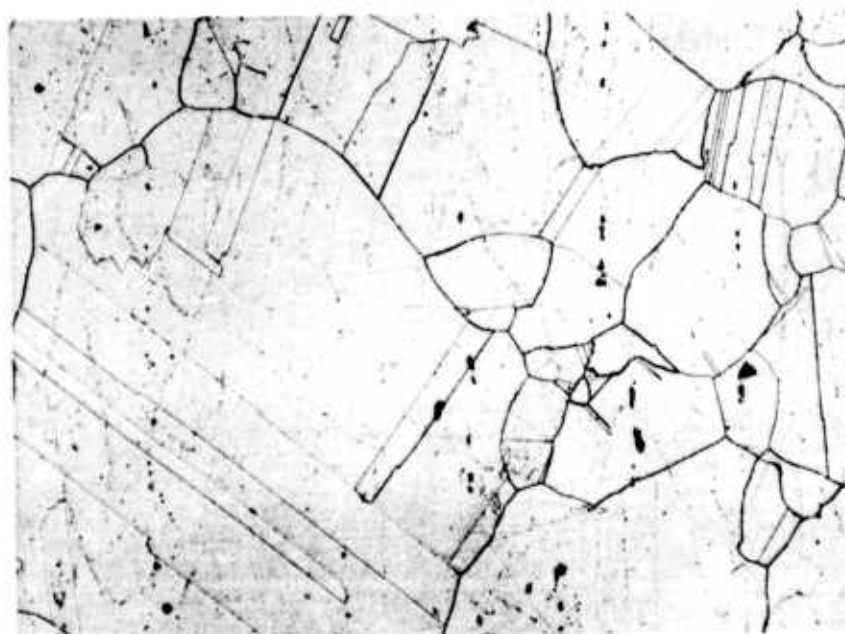
*Figure II-2 Microstructure of A-286 Stainless Steel*





1-in. thick

100X



2-in. thick

100X

*Figure II-3 Microstructure of X-750 Nickel Alloy*

### III. TESTING TECHNIQUES AND APPARATUS

---

This chapter describes the specimen geometries selected, testing apparatus, and techniques used to generate the data contained in this report.

The principal specimen used for this program was the compact tension (CT) type, formerly known as the wedge-opening loading (WOL) type. The following paragraphs describe the development of the specimen type in some detail.

The WOL specimens have been used to determine the  $K_{Ic}$  of a variety of materials.\* In addition to the high-strength relatively brittle materials initially investigated, considerable data have been developed for low- and intermediate-strength steels. For most of these materials,  $K_{Ic}$  has been determined over a wide range of temperatures.

The initial work, reported by Manjoine,<sup>†</sup> was directed toward developing a small test specimen for irradiation damage studies. Figure III-1 shows the general dimensions of the specimen. In utilizing this specimen for fracture mechanics, the basic difficulties with the original specimen were the lack of a precise

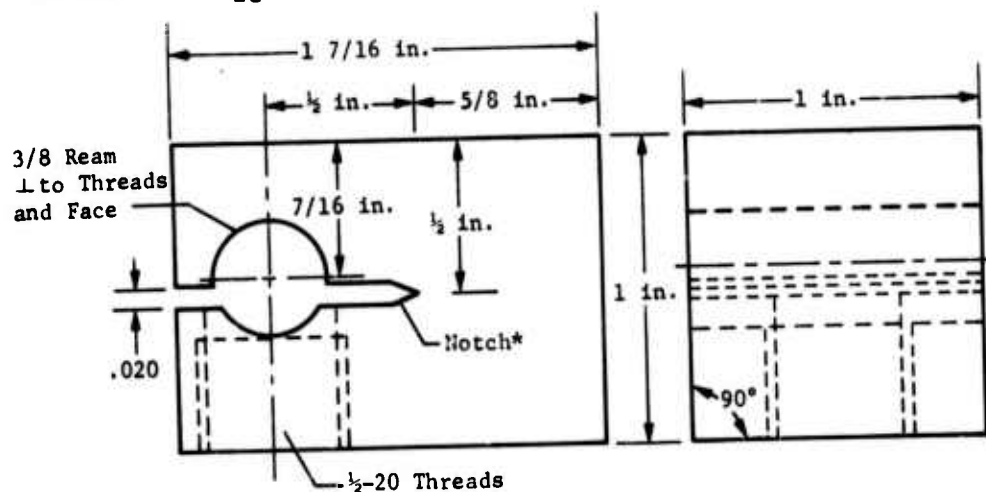
---

\*W. F. Brown, Jr. and J. E. Srawley: "Plane-Strain Crack Toughness Testing of High-Strength Metallic Materials." *ASTM Spec. Tech. Publ.* No. 410, 167.

<sup>†</sup>M. J. Manjoine: "Biaxial Brittle Fracture Tests." *Basic Engng, Trans, ASME*, 1965, pp 293-298.



stress analysis for an exact expression for  $G$  or  $K$ , and the use of a precompression technique to introduce a crack at the root of the machined notch. The latter resulted in residual stresses and plastic deformation that affected the fracture load; hence, the apparent  $K_{Ic}$  values.



\*Crack introduced at root of notch by compressing slot.

Figure III-1  
Biaxial Brittle Fracture Specimen as Developed by Manjoine

Recognizing the merit in the basic concept of the specimen and its potential as a possible small convenient specimen for universal  $G_{Ic}$  or  $K_{Ic}$  fracture toughness testing and subcritical crack growth studies, further efforts were made to refine the specimen and to obtain a precise stress analysis to gain an exact expression for  $K_I$  or  $G_I$ . This work included analytical stress analysis,\* a compliance calibration of a large steel specimen,<sup>†</sup> a

\*A. M. Wahl, M. M. Leven, and W. K. Wilson. "Energy Release Rate for Biaxial Brittle Fracture Test Specimen." AEC Res. Devel. Rep. No. WERL-8844-1, 1963.

<sup>†</sup>A. J. Bush and W. K. Wilson: "Experimental Determination of the Energy Rate Release for Biaxial Brittle Fracture Specimen." AEC Res. Devel. Rep. No. WERL-8844-2, 1964.

three-dimensional photoelastic stress analysis, and more recent analyses employing sophisticated techniques.\*

The nominal plane-strain stress intensity factors are readily determined using the appropriate calibration curves for

$$K_I = Y \cdot \frac{P\sqrt{\alpha}}{BW} = \text{nominal value of plane-strain stress intensity}$$

factor for opening mode of crack extension,

where

Y = numerical constant (dimensionless stress intensity parameter)

obtained from Figure III-2 using appropriate  $\alpha/W$ ,

P = load (lb) from test record at onset of crack instability,

$\alpha$  = crack length (in.) at the time of onset of crack instability,

B = specimen thickness (in.),

W = specimen width (centerline of loading to back edge).

The corresponding calibration curve as determined by the collocation technique is given in Figure III-2.

Further optimization studies<sup>†,§</sup> of the WOL-type of specimen have been conducted. The effort was directed at the possibility

---

\*W. K. Wilson: "Analytic Determination of Stress Intensity Factors for the WOL Brittle Fracture Test Specimen." *AEC Res. Devel. Rep. No. WERL-0029-3*, 1965.

<sup>†</sup>J. E. Srawley: "Notes on Design of Compact Rectangular Crackline-Loaded  $K_{Ic}$  Specimens." *Minutes Mtg Subcommittee I on High-Strength Metallic Materials of Committee E24 on Fracture Testing of Metals*, 1966.

<sup>§</sup>J. E. Srawley: "Compact Crackline-Loaded Specimen Tests on A27075-T651 - Comparison with Bend Test Results." *Notes to Subcommittee I of ASTM Committee E-24*, 1967.

of modifying the present WOL T design to accommodate a two-pin loading arrangement. The configuration of the compact tension specimen is shown in Figure III-3.

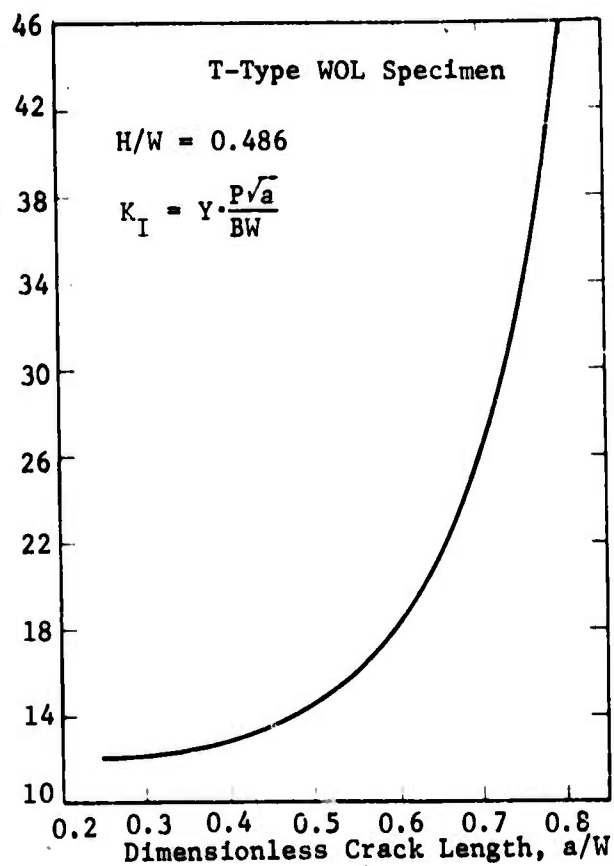


Figure III-2  
K Calibration for T-Type WOL Specimen

The K calibration and expression for this geometry are given in Figure III-4.

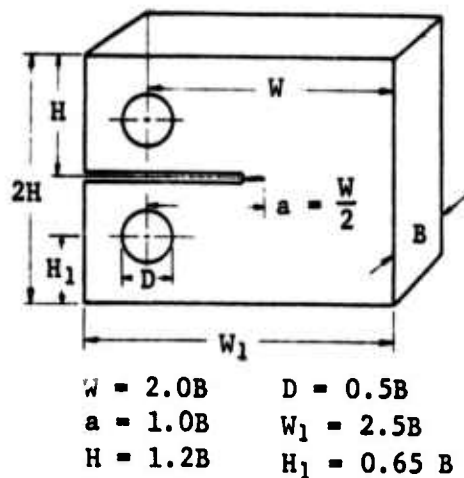


Figure III-3 Compact Tension Specimen

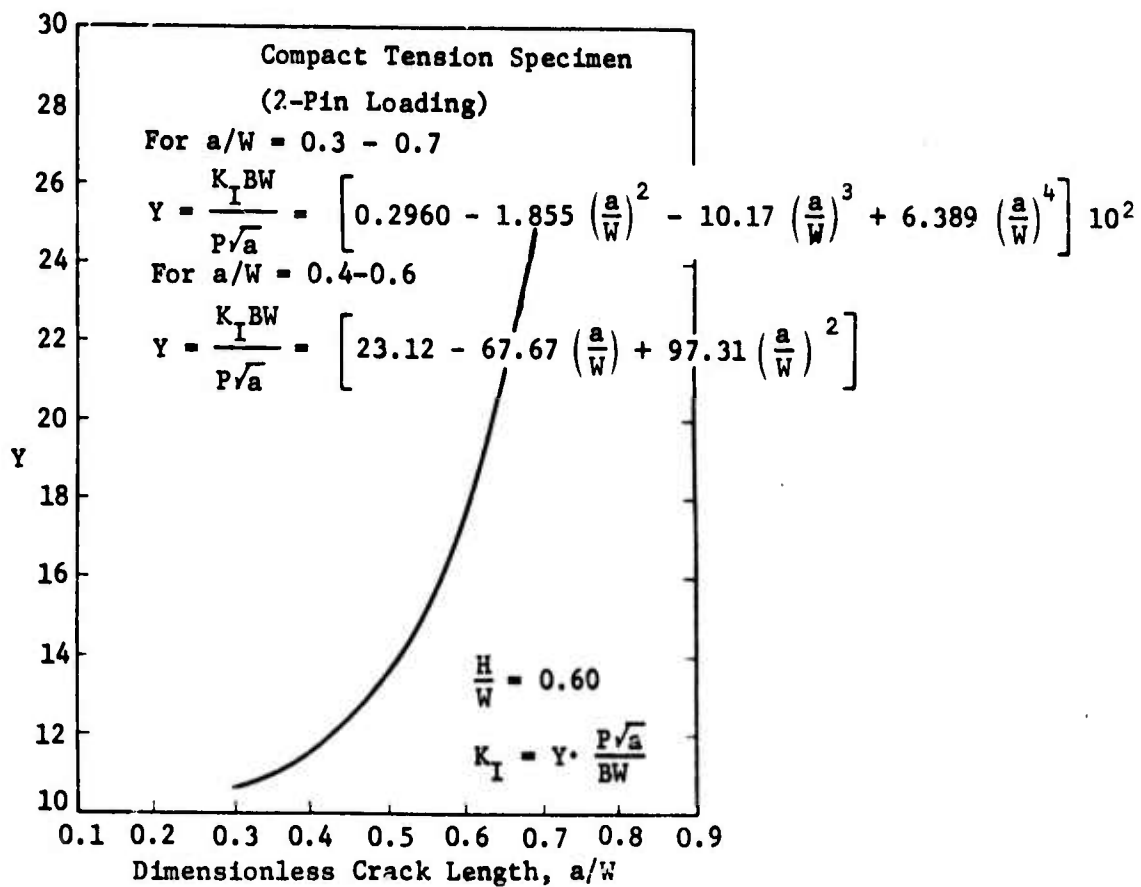


Figure III-4 K Calibration for Compact Tension (CT) Specimen

A liquid helium testing cryostat was designed and fabricated specially for this program. The system consists of an internal load frame fabricated from filament-wound glass-epoxy rods, a titanium base plate, and a liquid nitrogen jacketed helium dewar. The system is designed to accommodate 2-in.-thick standard compact tension specimens and to sustain forces up to 50,000 lb. Figure III-5 shows a close-up view of the load train with a specimen installed. An overall view of the sealed cryostat installed in the 100,000-lb MTS machine is given in Figure III-6. The cryostat is equipped with level sensors so that economical use of liquid helium can be assured. The system is precooled with liquid nitrogen; following cooling, the liquid nitrogen is removed from the system by pressurizing the cryostat. Care is taken to insure that all liquid nitrogen is removed from the system, because of the deleterious effect on helium utilization resulting from residual liquid nitrogen. Typical liquid helium consumption for the system is approximately 40 liters per fill and test of moderate duration. Following test, liquid helium is back transferred to the supply dewar.

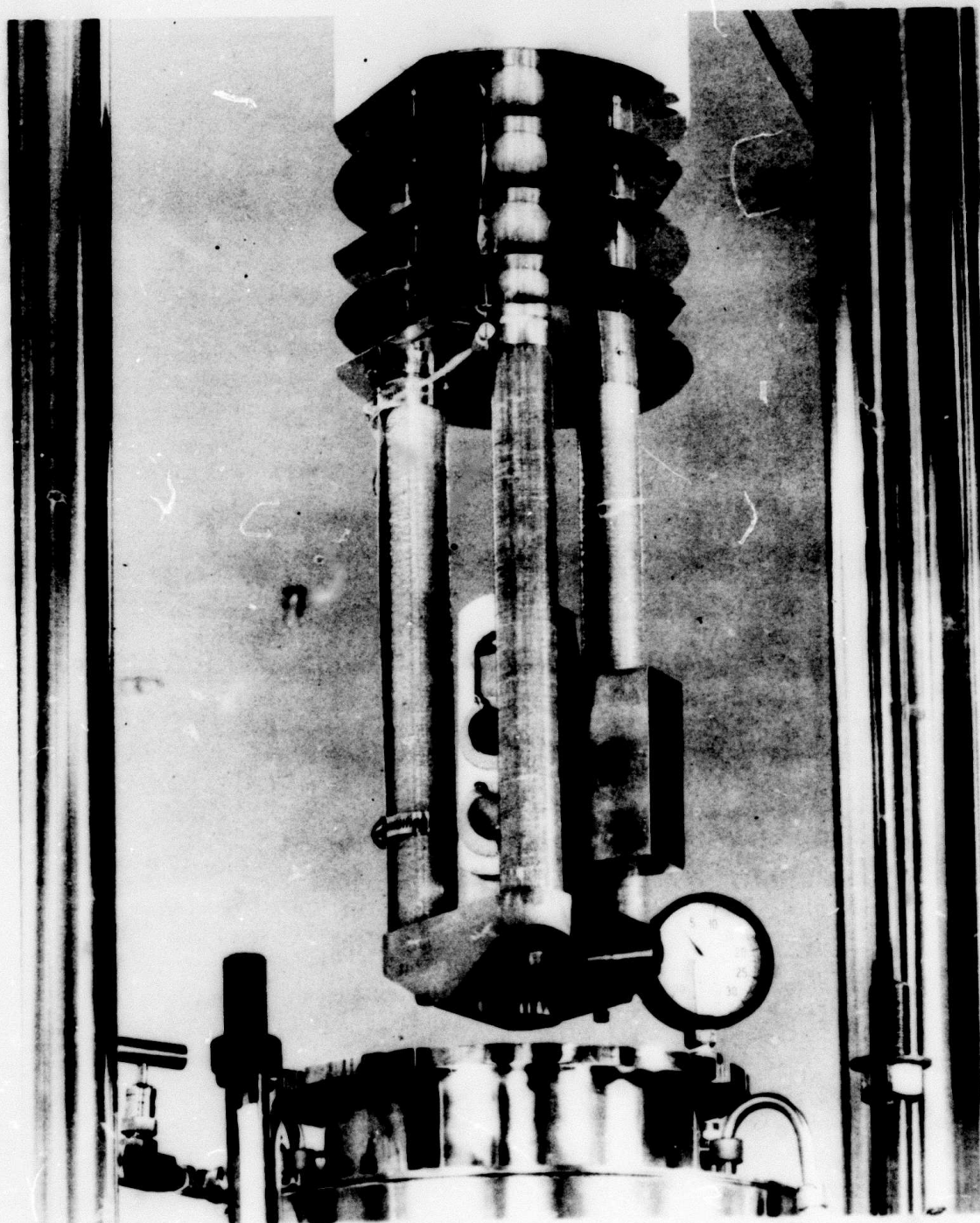
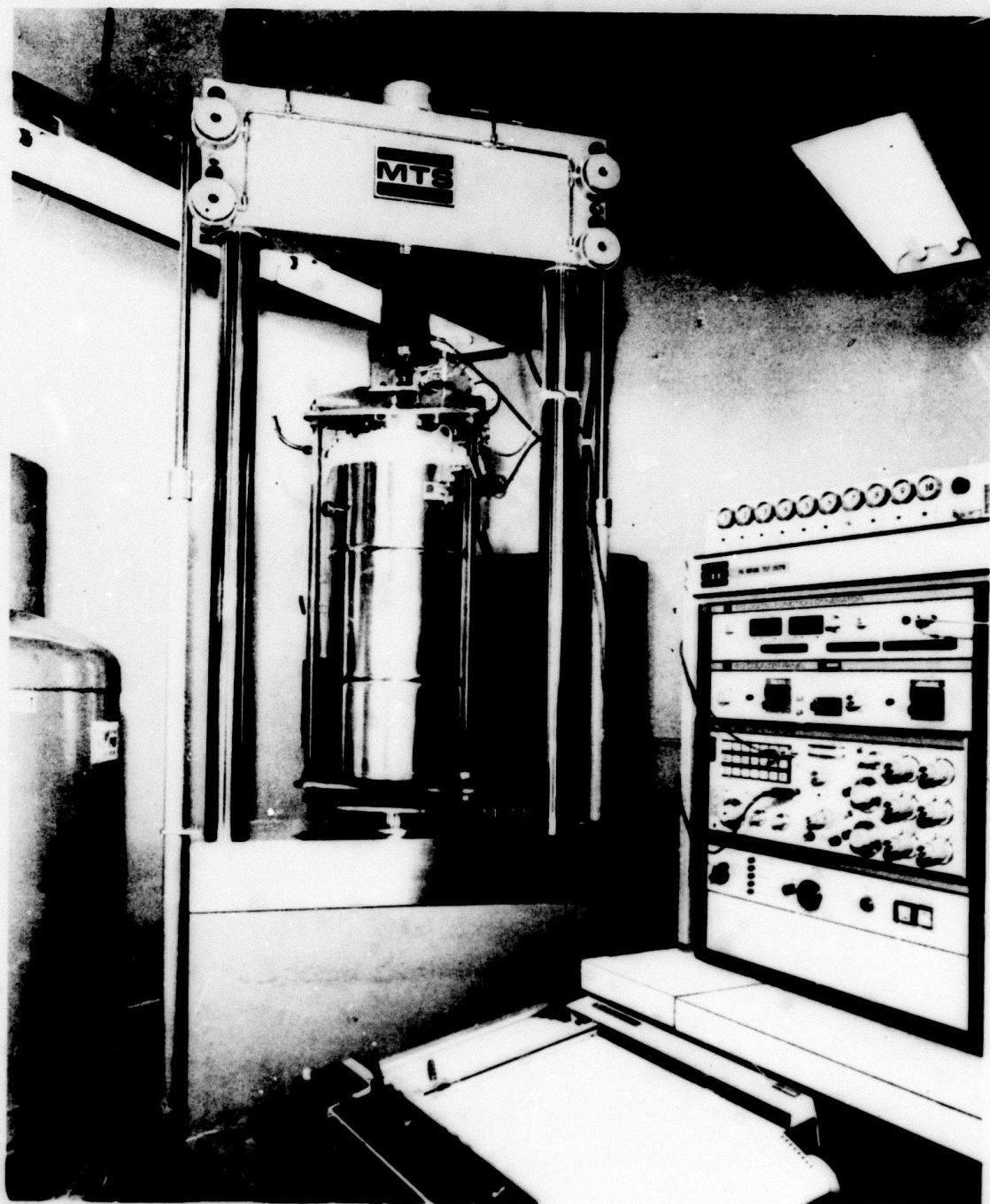


Figure III-5 Close-Up View of Load Train for Liquid Helium Testing System





*Figure III-6 Overall View of Liquid Helium Testing System*

Crack opening displacement measurements were made using a clip gage attached to the specimen by removable knife edges. The clip gage used is a recently developed MTS cryogenic gage (Model 632.02B-21). Performance of the gage was excellent at 4°K; however, it is necessary to operate at low excitation levels to preclude localized boiling of the cryogens.

Compliance curves were determined experimentally for each temperature and alloy. Data points were obtained by cycling to obtain small growth bands at progressively increasing loads for marking purposes. After opening the specimen, actual average crack lengths were measured and plotted versus compliance measurements. In this way, the crack front curvature characteristic of the material is truly incorporated into the compliance measurement. Experiment curves were in fair agreement with calculated curves. It is probable that failure to have good modulus data contributed to the discrepancy. Curves generated at 77 and 4°K (for each alloy) were almost identical.

The compact tension specimens were precracked at room temperature. Force levels were determined on a trial and error basis at the lowest level consistent with obtaining crack sharpening in less than 100,000 cycles. Precracking force are noted for each specimen. Specimens used for obtaining  $da/dN$  at low stress intensity levels were often recracked at low force levels to assure that crack growth rate data were obtained at force levels above that used for precracking.



Two sizes of specimens (1-in. and 2-in. thick) were prepared.  
Geometries were in accordance with those described in E399.

#### IV. EXPERIMENTAL RESULTS

---

##### A. STATIC FRACTURE TOUGHNESS

##### 1. Linear Elastic Tests

Testing to develop critical stress intensity data ( $K_{Ic}$ ) for each alloy was performed. It was recognized that the high toughness of the alloys lowered the probability of obtaining data that satisfied the ASTM E399 validity criteria. However, it was believed that the two heat treatable alloys might produce data that came close to achieving validity.

Experimental data are given in Tables IV-1 thru IV-3. Included in these tables are the validity checks for load ( $P_Q$ ) and geometry (thickness and crack length). Although very few tests satisfied the criteria of  $P_{max} P_Q \leq 1.10$ , calculation of  $K_Q$  and the thickness and crack length criteria

$$a, B \geq 2.5 \left( \frac{K_Q}{\sigma_{ys}} \right)^2$$

were nevertheless performed to provide some insight into the nature of the fracture behavior.

The data show that no valid  $K_{Ic}$  results were obtained.

Table IV-1 Static Fracture Toughness Data for 304L Stainless Steel

Temper- ature, K	Thick- ness, in.	Crack Length		Load, $P_Q$	kips $P_{max}$	$\frac{P_{max}}{P_Q}$	Y	$K_Q$ , ksi $\sqrt{in.}$	$2.5\left(\frac{K_Q}{\sigma_{ys}}\right)^2$	$K_{Ic}$ , ksi $\sqrt{in.}$
		a, in.	a/W							
77	1	1.04	0.520	7.0	17.8	2.54	10.2	50	2.5	No Valid Data
	1	1.24	0.620	4.0	11.5	2.88	14.7	42	1.8	
	1	1.61	0.805	1.3	3.2	2.46	--	--		
20	1	1.05	0.525	9.5	17.5	1.81	10.4	70	2.5	
	1	1.05	0.525	8.0	16.8	2.10	10.4	59	1.8	
77	2	2.26	0.565	29.0	58.8	2.03	11.9	86	7.4	
	2	2.23	0.558	28.0	60.9	2.17	11.6	81	6.6	
	2	2.31	0.578	27.0	56.4	2.09	12.4	84	7.1	
20	2	2.16	0.540	36.0	62.4	1.73	10.9	98	4.9	
	2	2.12	0.530	35.0	66.0	1.89	10.5	92	4.3	
4	2	2.53	0.632	44.9	46.4	1.03	15.5	174	21	
	2	2.73	0.682	21.9	31.2	1.42	19.6	107	8	
	2	2.75	0.687	25.6	31.3	1.22	20.1	129	12	

$\sigma_{ys}$  (77K)  $\approx$  50 ksi  
 $\sigma_{ys}$  (20K)  $\approx$  70 ksi  
 $\sigma_{ys}$  (4K)  $\approx$  60 ksi

Table IV-2 Static Fracture Toughness Data for A-286 Stainless Steel

Temperature, K	Thick- ness, in.	Crack Length		Load, $P_Q$	kips $P_{max}$	$\frac{P_{max}}{P_Q}$	$Y$	$K_Q$ , ksi $\sqrt{in.}$	$2.5\left(\frac{K_Q}{\sigma_{ys}}\right)^2$	$K_{Ic}$ , ksi $\sqrt{in.}$
		a, in.	a/W							
77	1	1.06	0.530	16.0	18.5	1.15	10.5	118.8	1.8	No Valid Data
	1	1.02	0.510	18.5	19.5	1.05	9.9	129.5	2.1	
20	1	1.03	0.520	16.5	18.4	1.12	10.0	116.7	1.5	
	1	1.01	0.505	17.5	18.4	1.05	69.7	120.5	1.6	
77	2	2.47	0.618	50.1	59.6	1.19	14.6	182.8	4.2	
	2	2.32	0.580	54.0	73.2	1.36	12.5	168.8	3.7	
20	2	2.33	0.582	56.2	80.4	1.43	12.6	177.0	3.5	
	2	2.45	0.613	41.5	63.1	1.52	14.3	148.1	2.5	
4	2	2.53	0.632	49.5	52.5	1.06	15.5	191.8	3.6	
	2	2.51	0.628	50.0	57.0	1.14	15.2	190.0	3.5	
	2	2.75	0.688	41.0	44.5	1.09	20.2	207.0	3.4	
$\sigma_{ys}$ (77K) $\approx$ 140 ksi (20K) $\approx$ 150 ksi (4K) $\approx$ 160 ksi										

Table IV-3 Static Fracture Toughness Data for X-750 Nickel Alloy

Temperature, K	Thick- ness, in.	Crack Length		Load, P <sub>Q</sub>	kips P <sub>max</sub>	$\frac{P_{max}}{P_Q}$	Y	K <sub>Q</sub> , ksi/in.	$2.5 \left( \frac{K_Q}{\sigma_{ys}} \right)^2$	K <sub>Ic</sub> , ksi/in.
		a, in.	a/W							
77	1	1.06	0.530	17.5	25.2	1.44	10.5	130	2.5	No Valid Data
	1	1.11	0.555	15.8	20.2	1.28	11.5	129	2.4	
20	1	1.05	0.525	22.0	26.8	1.22	10.4	104	1.4	
	1	1.03	0.515	19.0	27.3	1.44	10.0	134	2.3	
77	2	2.19	0.548	59.7	64.9	1.08	11.1	166	3.5	
	2	2.10	0.525	75.0	83.0	1.11	10.4	195	4.8	
20	2	2.34	0.585	52.5	67.4	1.08	12.8	168	3.6	
	2	2.08	0.520	56.9	64.5	1.15	10.2	145	2.7	
4	2	2.75	0.687	32.4	36.0	1.11	20.2	163	3.2	
	2	2.70	0.675	36.1	40.0	1.11	18.9	171	3.5	
$\sigma_{ys}$ (77K) $\approx$ 130 ksi $\sigma_{ys}$ (20K) $\approx$ 140 ksi $\sigma_{ys}$ (4K) $\approx$ 145 ksi										

As expected, the 304L failed to satisfy the load criteria by a significant degree. However, some of the A-286 and X-750 results came close to satisfying both validity criteria. It is interesting to note that if we consider the K<sub>Q</sub> results and compare data for the two thicknesses, it is found that apparent toughness increases significantly with specimen size. This observation is consistent with data from other sources and handicaps the compact tension specimen as a type that can be expected to provide data useful to service behavior predictions.

## 2. J-Integral Analysis

In its current state, linear elastic fracture mechanics is limited to cases where small crack-tip plasticity is involved, i.e., for low-toughness materials at nominal stresses well below the yield strength. However, there are many important design situations where it is desirable to have a failure criterion that can predict defect-controlled failure for cases of large-scale plasticity. For example, medium strength steels of high fracture toughness used in superconducting machinery generally exhibit considerable crack-tip plasticity that limits the applicability of linear elastic fracture mechanics

The J-integral concept proposed by Rice\* as an analytical tool for elastic-plastic crack tip field analysis has been advanced by Begley and Landes<sup>†,§</sup> as an elastic-plastic fracture criterion. The engineering performance parameter is the rate of change in deformation energy with respect to crack area, called J. J was first measured experimentally from load versus load

---

\*J. R. Rice: "A Path Independent Integral and the Approximate Analysis of Strain Concentration by Notches and Cracks." *Trans. ASME, Journal of Applied Mechanics*. Vol 90, p 379-386, 1968.

<sup>†</sup>J. A. Begley and J. D. Landes: "The J-Integral as a Fracture Criterion: Fracture Toughness." *Proceedings of the 1971 National Symposium on Fracture Mechanics*, Part II, ASTM STP 514, p 1-20, 1972.

<sup>§</sup>J. D. Landes and J. A. Begley: "The Effect of Specimen Geometry on  $J_{Ic}$ : Fracture Toughness." *Proceedings of the 1971 National Symposium on Fracture Mechanics*. Part II, ASTM STP 514, p 24-39, 1972.

point displacement curves using a compliance technique where several specimens of different crack lengths were needed as shown by Begley and Landes. The area under the curves, deformation energy (E) is plotted as a function of crack length (a) for fixed values of displacement ( $\delta$ ). The slope of the curves ( $dE/B_{da}$ ) for given crack lengths, plotted as a function of displacement, is equal to J. The critical J at fracture ( $J_{Ic}$ ) is found from values of a and  $\delta$  at the onset of crack instability. Methods were inter-developed for measuring J from single specimen tests<sup>\*,†</sup>. The method developed Rice<sup>†</sup> for deeply notched bend specimens offers the simplest single specimen technique for measuring J. A bend bar or compact tension specimen ( $a/W \geq 0.6$ ) is loaded to a fixed displacement and J is determined as a function of displacement from the expression,  $J = 2A/Bb$ , where A is the area under the load-load point displacement taken at the displacement of interest, B is the thickness, and b is the uncracked ligament length. The critical J at fracture ( $J_{Ic}$ ) is taken at the value of  $\delta$  where crack extension is first encountered.

---

\*R. J. Bucci, et al.: "J Integral Estimation Procedures: Fracture Toughness." *Proceedings of the 1971 National Symposium on Fracture Mechanics, Part II*, ASTM STP 514, p 40-69, 1972.

†J. R. Rice, P. C. Paris, and J. G. Merkle: "Some Further Results on J Integral and Estimates: Progress in Flaw Growth and Fracture Toughness Testing." ASTM STP 536, 1973.

Initial tests on a Ni-Cr-Mo-V steel in the plastic range by Landes and Begley showed that  $J_{Ic}$  may be essentially independent of crack length and geometry, hence a material constant. In the elastic range  $J_{Ic}$  is identical to the critical strain energy release rate ( $G_{Ic}$ ) from linear elastic fracture mechanics, where fracture toughness ( $K_{Ic}$ ) is related to  $G_{Ic}$  by  $K_{Ic} = \sqrt{E G_{Ic}}$ . Tests on ASTM A216C steel by Landes and Begley\* indicate that it may be possible to characterize elastic fracture toughness ( $K_{Ic}$ ) over any desired temperature range using relatively small elastic-plastic  $J_c$  tests from the approximation,  $K_{Ic} \approx \sqrt{E J_{Ic}}$ .  $K_{Ic}$  values computed from valid  $J_{Ic}$  results from 1-in.-thick compact tension specimens compared favorably with valid  $K_{Ic}$  results from specimens up to 12-in. thick.

Defining crack initiation and determining its onset is the most difficult part of measuring  $J_{Ic}$ . Early work by Begley and Landes on A533B steel and a Ni-Cr-Mo-V steel showed crack initiation to be generally coincident with the maximum load point from the load versus load point displacement curve. One problem with using this criterion for a  $J_{Ic}$  measurement point is that it may not be generally true for a wide range of materials, temperatures, and geometries. A less ambiguous approach\* is to measure the

---

\*J. D. Landes and J. A. Begley: "Test Results from J Integral Studies - An Attempt to Establish a  $J_{Ic}$  Testing Procedure."

Scientific Paper 73-1E7-FMPWR-P3. Westinghouse Research Laboratories, 1973.



the onset of crack initiation directly from the fracture surface (R curve technique). A series of bend specimens with identical crack lengths are loaded to different values of displacement. Each specimen is then marked by heat tinting, dye penetrant, or fatigue, whichever is appropriate. Next each specimen is fractured and the crack extension ( $\Delta a$ ) measured.  $J$  is calculated for each of these specimens at the point of unloading, and then plotted as a function of  $\Delta a$ .  $J_{Ic}$  is defined as that point where crack extension ( $\Delta a$ ) is characterized only by "crack opening stretch" (COS) and not by actual material separation associated with crack growth. For A216 steel this stretch zone ( $\Delta a_o$ ) appeared to have a value equal to  $J/2\sigma_{flow}$  where  $\sigma_{flow} = (\sigma_y + \sigma_u)/2$ .

As a result of the extensive plasticity encountered in testing the 304L stainless steel, a J-integral analysis was performed using the available data.

Surface COD data were empirically adjusted to reflect load line displacements. In the range  $0.6 \leq W \leq 0.7$ , the ratio of  $\delta/COD$  is approximately 0.7, according to Bucci, et al. The resultant load versus load point displacement curves are shown in Figure IV-1 thru IV-5.  $J_Q$  was calculated from the expression

$$[1] \quad J_Q = \frac{2A_c}{Bb}$$



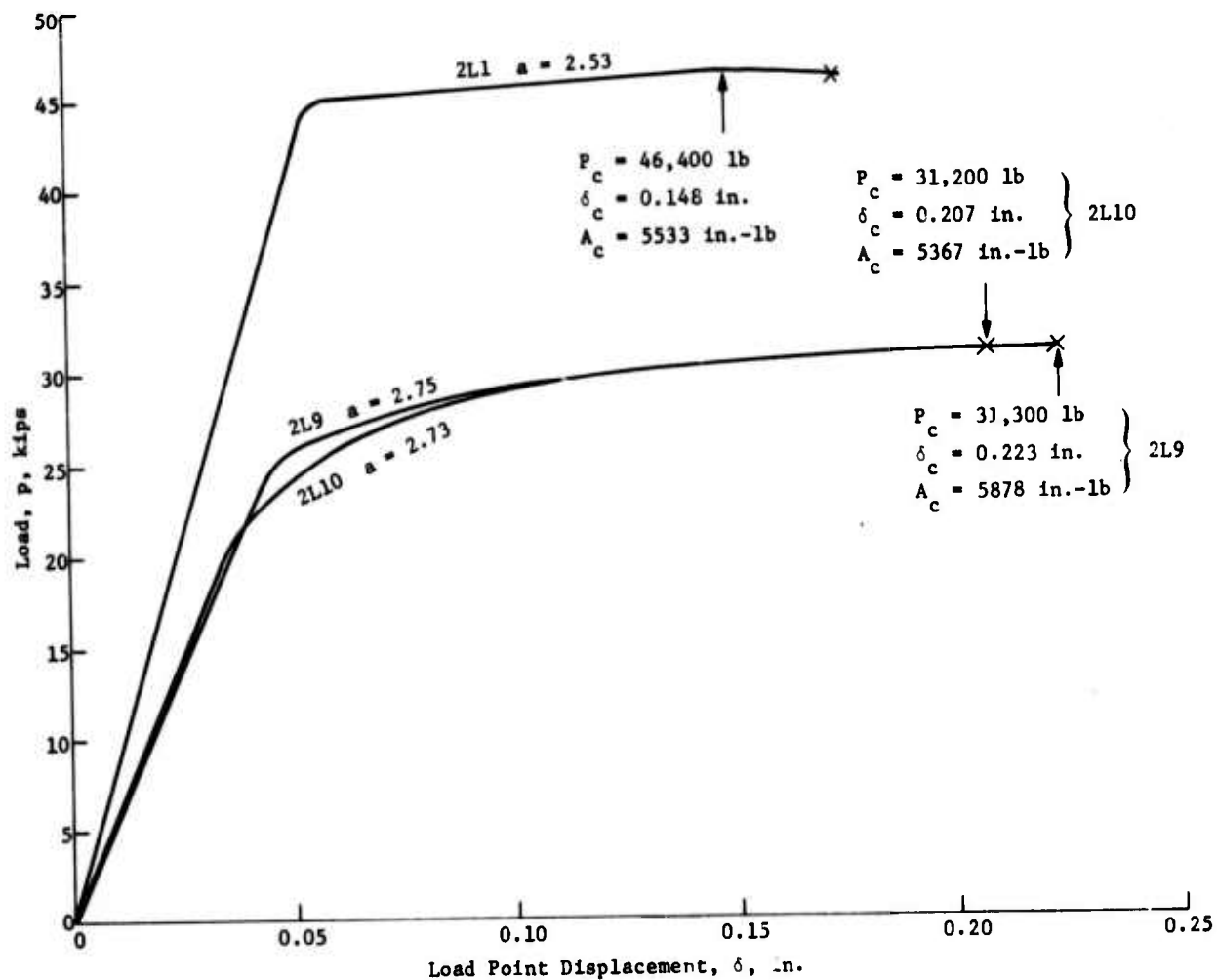


Figure IV-1  
Load versus Load Point Displacement Curves for 2-in.-thick 304L Stainless Steel at 4K

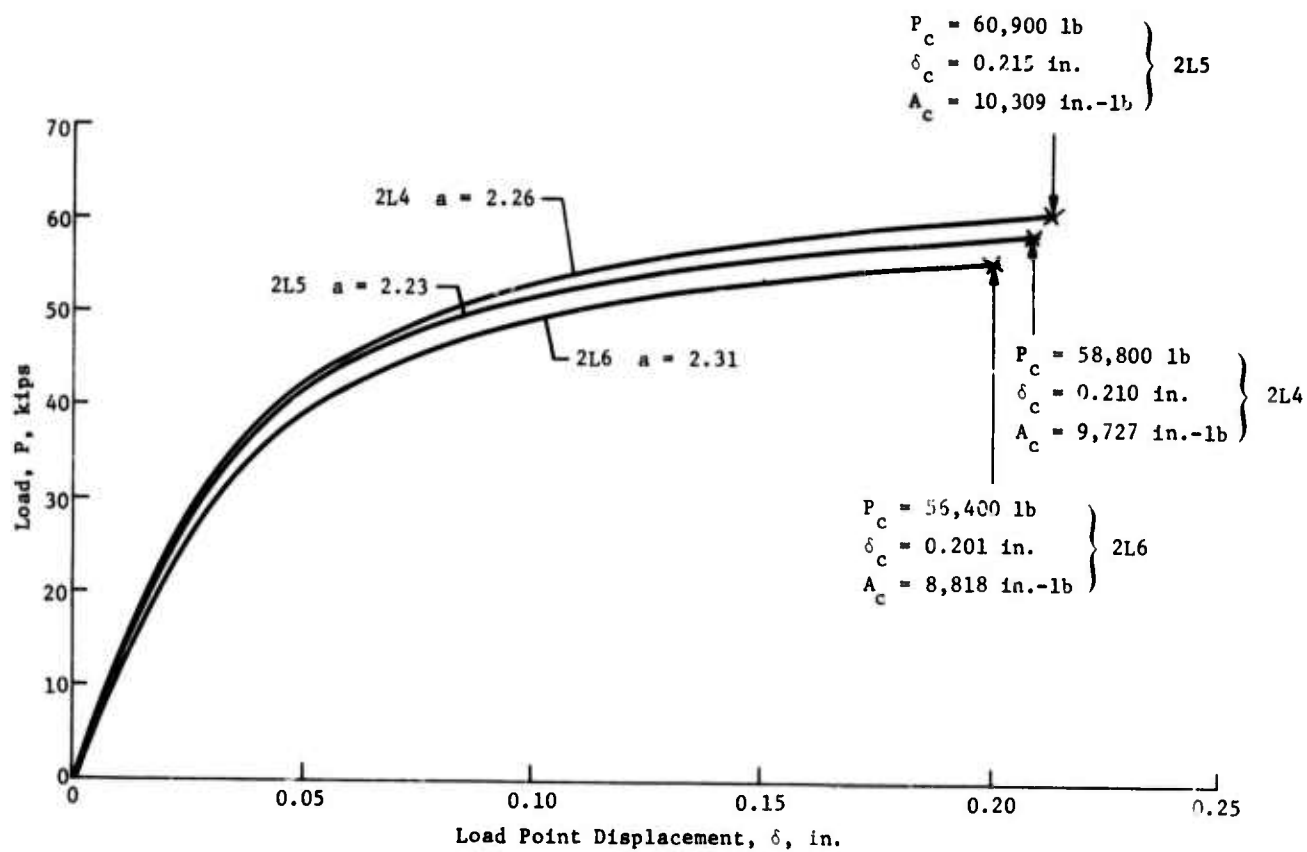


Figure IV-2  
Load versus Load Point Displacement Curves for 2-in.-thick 304L Stainless Steel at 77K

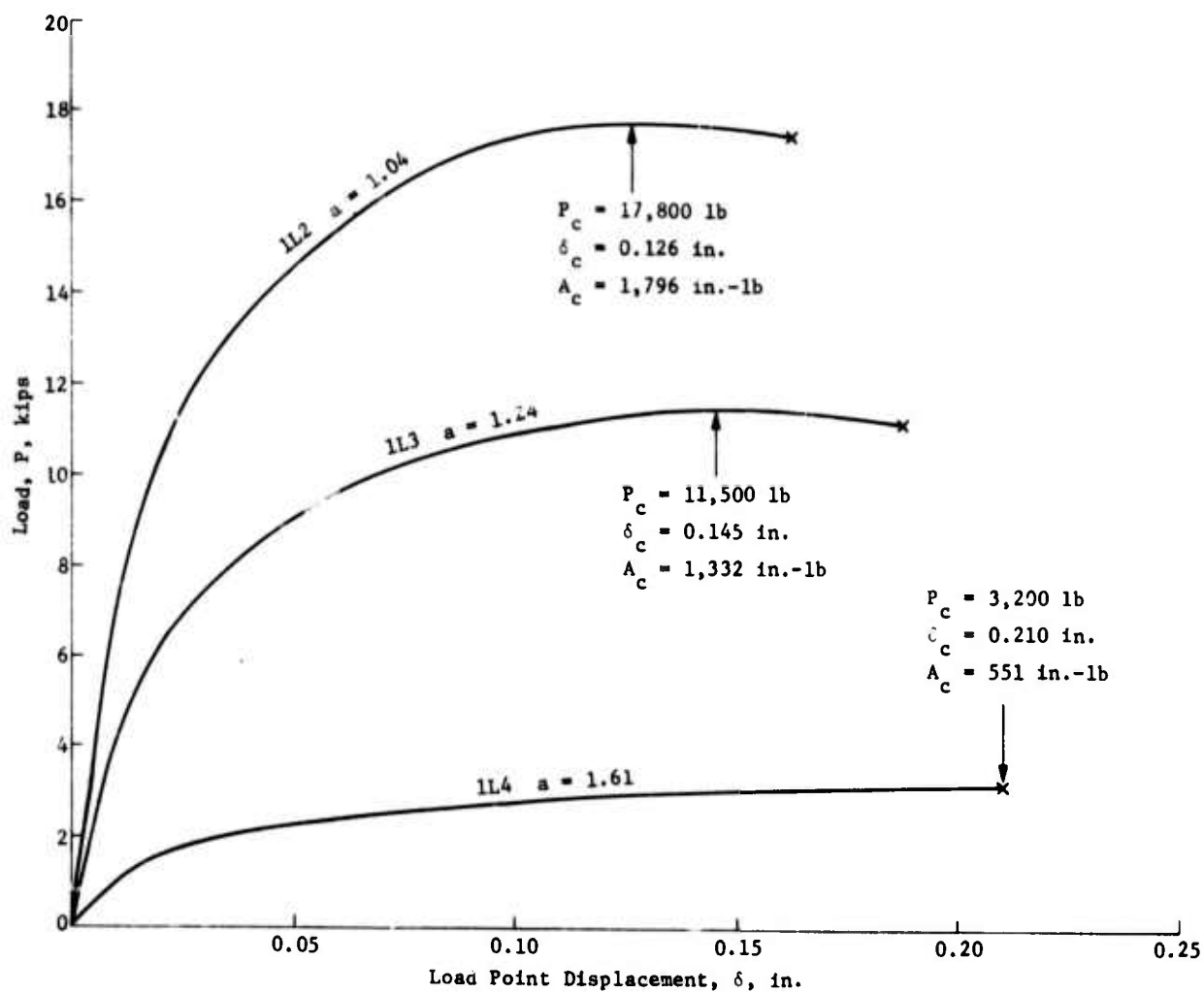


Figure IV-3  
 Load versus Load Point Displacement Curves for 1-in.-thick 304L Stainless Steel at 77K

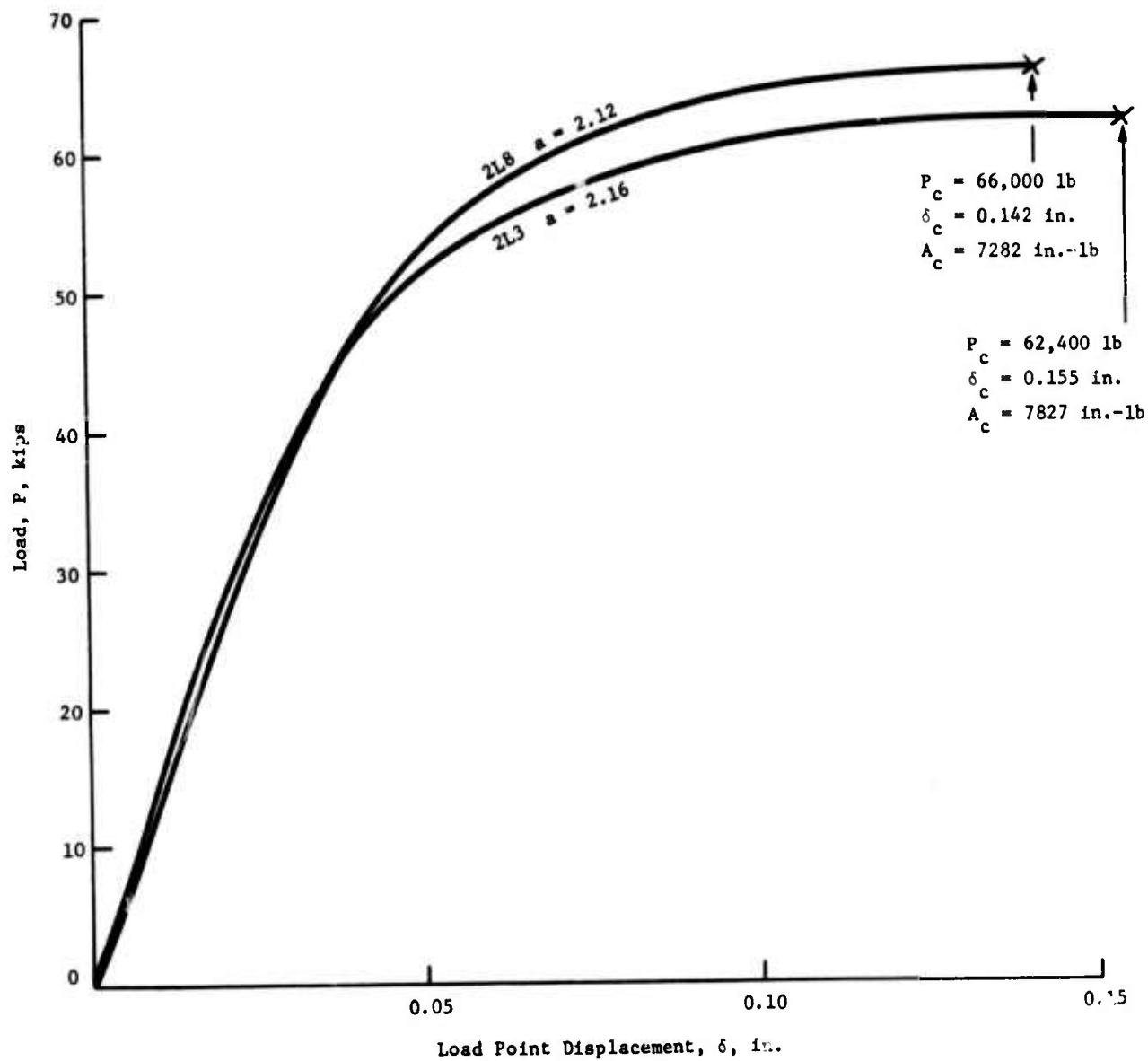


Figure IV-4  
Load versus Load Point Displacement Curves for 2-in.-thick 304L Stainless Steel at 20K

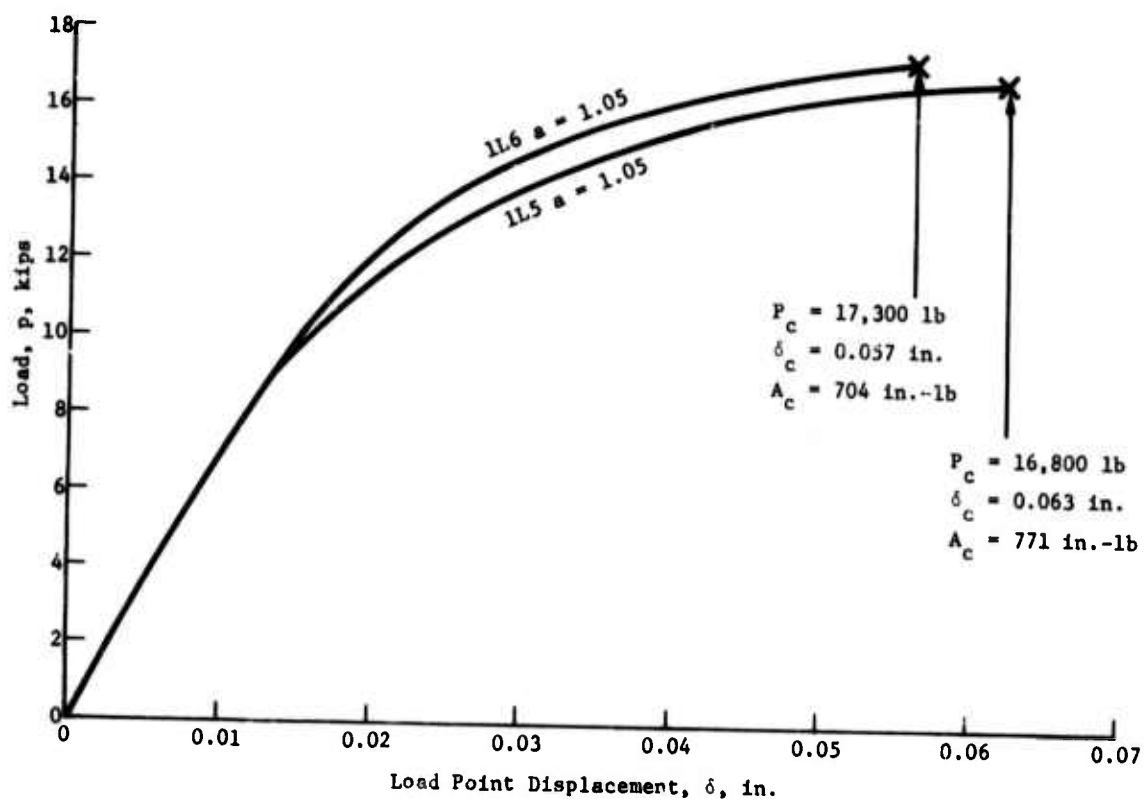


Figure IV-5  
 Load versus Load-Point Displacement Curves for 1-in.-thick 304L Stainless Steel at 20K

where  $A_c$  is the total energy under the curve up to the maximum load point. This implies that the onset of crack growth is coincident with the maximum load point. Tentative ASTM guidelines\* indicate that this is accurate if the applied bending moment at maximum load,  $M_c = [P_c(wta)/2]$ , is greater than  $0.3 Bb^2 \sigma_y$  (i.e., the specimen is close to being fully plastic).  $J_Q$  is a valid  $J_{Ic}$  value if  $a$ ,  $B$ , and  $b$  are approximately greater than  $(25-50) J_Q/\sigma_{flow}$ , where  $\sigma_{flow} = (\sigma_y + \sigma_u)/2$ .  $J_Q$  results are given in Tables IV-4 thru IV-6. Note that the criteria for valid  $J_{Ic}$  are generally satisfied. Average  $K_Q$  values calculated from the expression

$$K_Q = \sqrt{E J_Q}$$

are approximately:

Temperature, K	Thickness, in.	$K_Q$ , ksi $\sqrt{in.}$
4	2.0	350
20	1.0	211
20	2.0	343
77	1.0	312
77	2.0	401

---

\*"Tentative Guidelines for  $J_{Ic}$  Tests." Prepared by ASTM Task Group F24.01.09, 1974.

Table IV-4

Table IV-4 J-Integral Fracture Toughness for 304L Stainless Steel at 4K

Specimen Number	Thickness B, in.	Width W, in.	Crack Length a, in.	Ligament Length b, in.	Critical Load P <sub>c</sub> , lb	Critical Displacement δ <sub>c</sub> , in.	Deformation Energy A <sub>c</sub> , in.-lb	J-Integral J <sub>Q</sub> <sup>+</sup> , in.-lb/in. <sup>2</sup> x 10 <sup>3</sup>	Validity Criteria				Fracture Toughness K <sub>Q</sub> <sup>+</sup> , ksi/in.
									M <sup>++</sup> C Bb <sup>2</sup> σ <sub>y</sub>	a <sup>+</sup> J <sub>Q</sub> /σ <sub>y</sub> flow	B <sup>+</sup> J <sub>Q</sub> /σ <sub>y</sub> flow	b <sup>+</sup> J <sub>Q</sub> /σ <sub>y</sub> flow	
2L1	2.00	4.00	2.53	1.47	46,400	0.148	5,533	3.76	0.5	101	80	59	330
2L10	2.00	4.00	2.73	1.27	31,200	0.207	5,367	4.23	0.5	97	71	45	350
2L9	2.00	4.00	2.75	1.25	31,300	0.223	5,878	4.70	0.5	88	64	40	369

$\sigma_y \approx 70,000$  psi     $*J_Q = 2A_c/Bb$   
 $\sigma_u \approx 230,000$  psi     $**M_C = P_C (w+a)/2$   
 $\sigma_{flow} \approx 150,000$  psi     $M_C/Bb^2\sigma_y \geq 0.3$   
 $E \approx 29 \times 10^6$  psi     $^{++}K_Q = \sqrt{EJ_Q}$

Table IV-5

Table IV-5 J-Integral Fracture Toughness for 304L Stainless Steel at 20K

Specimen Number	Thickness B, in.	Width W, in.	Crack Length a, in.	Ligament Length b, in.	Critical Load P <sub>c</sub> , lb	Critical Displacement δ <sub>c</sub> , in.	Deformation Energy A <sub>c</sub> , in.-lb	J-Integral J <sub>Q</sub> <sup>+</sup> , in.-lb/in. <sup>2</sup> x 10 <sup>3</sup>	Validity Criteria				Fracture Toughness K <sub>Q</sub> <sup>+</sup> , ksi/in.
									M <sup>++</sup> C Bb <sup>2</sup> σ <sub>y</sub>	a <sup>+</sup> J <sub>Q</sub> /σ <sub>y</sub> flow	B <sup>+</sup> J <sub>Q</sub> /σ <sub>y</sub> flow	b <sup>+</sup> J <sub>Q</sub> /σ <sub>y</sub> flow	
2L3	2.00	4.00	2.16	1.84	62,400	0.155	7,827	4.25	0.5	71	66	61	351
2L8	2.00	4.00	2.12	1.88	66,000	0.142	7,282	3.87	0.5	77	72	68	335
1L6	1.00	2.00	1.05	0.95	17,300	0.057	704	1.48	0.5	99	95	90	207
1L	1.00	2.00	1.05	0.95	16,800	0.063	771	1.62	0.5	91	86	82	215

$\sigma_y \approx 60,000$  psi     $*J_Q = 2A_c/Bb$   
 $\sigma_u \approx 220,000$  psi     $**M_C = P_C (w+a)/2$   
 $\sigma_{flow} \approx 140,000$  psi     $M_C/Bb^2\sigma_y \geq 0.3$   
 $E \approx 29 \times 10^6$  psi     $^{++}K_Q = \sqrt{EJ_Q}$

Table IV-6

Table IV-6 J-Integral Fracture Toughness for 304L Stainless Steel at 77K

Specimen Number	Thickness B, in.	Width W, in.	Crack Length a, in.	Ligament Length b, in.	Critical Load P <sub>c</sub> , lb	Critical Displacement δ <sub>c</sub> , in.	Deformation Energy A <sub>c</sub> , in.-lb	J-Integral J <sub>Q</sub> <sup>+</sup> in.-lb/in. <sup>2</sup> x 10 <sup>3</sup>	Validity Criteria				Fracture Toughness K <sub>Q</sub> <sup>††</sup> ksi/in.
									M <sup>**</sup> Bb <sup>2</sup> σ <sub>y</sub>	a <sup>+</sup> J <sub>Q</sub> /σ <sub>flow</sub>	B <sup>+</sup> J <sub>Q</sub> /σ <sub>flow</sub>	b <sup>+</sup> J <sub>Q</sub> /σ <sub>flow</sub>	
2L4	2.00	4.00	2.26	1.74	58,800	0.210	9,727	5.59	0.6	51	45	39	403
2L5	2.00	4.00	2.23	1.77	60,900	0.215	10,309	5.82	0.6	48	43	38	411
2L6	2.00	4.00	2.31	1.69	56,400	0.201	8,818	5.22	0.5	55	48	40	389
1L2	1.00	2.00	1.04	0.96	17,800	0.126	1,796	3.74	0.6	35	33	32	329
1L3	1.00	2.00	1.24	0.76	11,500	0.145	1,332	3.51	0.6	44	36	27	319
1L4	1.00	2.00	1.61	0.39	3,200	0.210	551	2.83	0.8	71	44	17	287

$$\sigma_y \approx 50,000 \text{ psi} \quad *J_Q = 2A_c/Bb \quad \dagger \frac{a_c B_c b_c}{J_Q \sigma_{flow}} \geq (25-50)$$

$$\sigma_u \approx 200,000 \text{ psi} \quad **M_c = P_c (w+a)/2$$

$$\sigma_{flow} \approx 125,000 \text{ psi} \quad M_c/Bb^2\sigma_y \geq 0.3 \quad \dagger\dagger K_Q = \sqrt{EJ_Q}$$

$$E \approx 29 \times 10^6 \text{ psi}$$



## B. CYCLIC CRACK GROWTH RATE DATA

Crack growth rate data tests were performed on 2-in.-thick CT specimens of each alloy at both 77 and 4K.

Data, consisting of both visually observed growth bands (observed on fractured faces) and crack opening displacement measurements, were analyzed to provide crack growth rate ( $da/dN$ ) versus stress intensity range ( $\Delta K$ ) data. A minimum of four specimens was used to obtain each curve.

The value of  $\Delta K$  is defined as  $K_{\max} - K_{\min}$ . For this work,  $K_{\min}$  was sufficiently low (200-400 lb) that it was treated as zero. Therefore:

$$\Delta K = K_{\max}$$

Analysis was performed using a least squares fit of the log of the familiar fatigue growth rate law developed by Paris.\*

$$\frac{da}{dN} = C(\Delta K)^n$$

The computer analysis uses data input in pounds and inches.

---

\*P. C. Paris. The Fracture Mechanics Approach to Fatigue." *Proc., 10th Sagamore Conference*, August 1963, Syracuse U. Press, 1964.

Data are summarized graphically in Figures IV-6 thru IV-11.

A tabular summary of the data is given below:

Alloy	77K		4K	
	C	n	C	n
304L	$2.37 \times 10^{-24}$	4.0	$1.08 \times 10^{-26}$	4.6
A-286	$1.86 \times 10^{-28}$	4.8	$6.05 \times 10^{-30}$	5.1
X-750	$2.87 \times 10^{-28}$	4.8	$2.18 \times 10^{-30}$	5.2

It is readily apparent from the data that the crack growth behavior for the two higher strength alloys (A-286 and X-750) is virtually identical. The tougher 304L exhibited higher growth rates than the higher strength alloys. The change in the constants C and n as a function of temperature were remarkably uniform. The 304L is observed to be slightly more sensitive to temperature change than the A-286 and X-750.

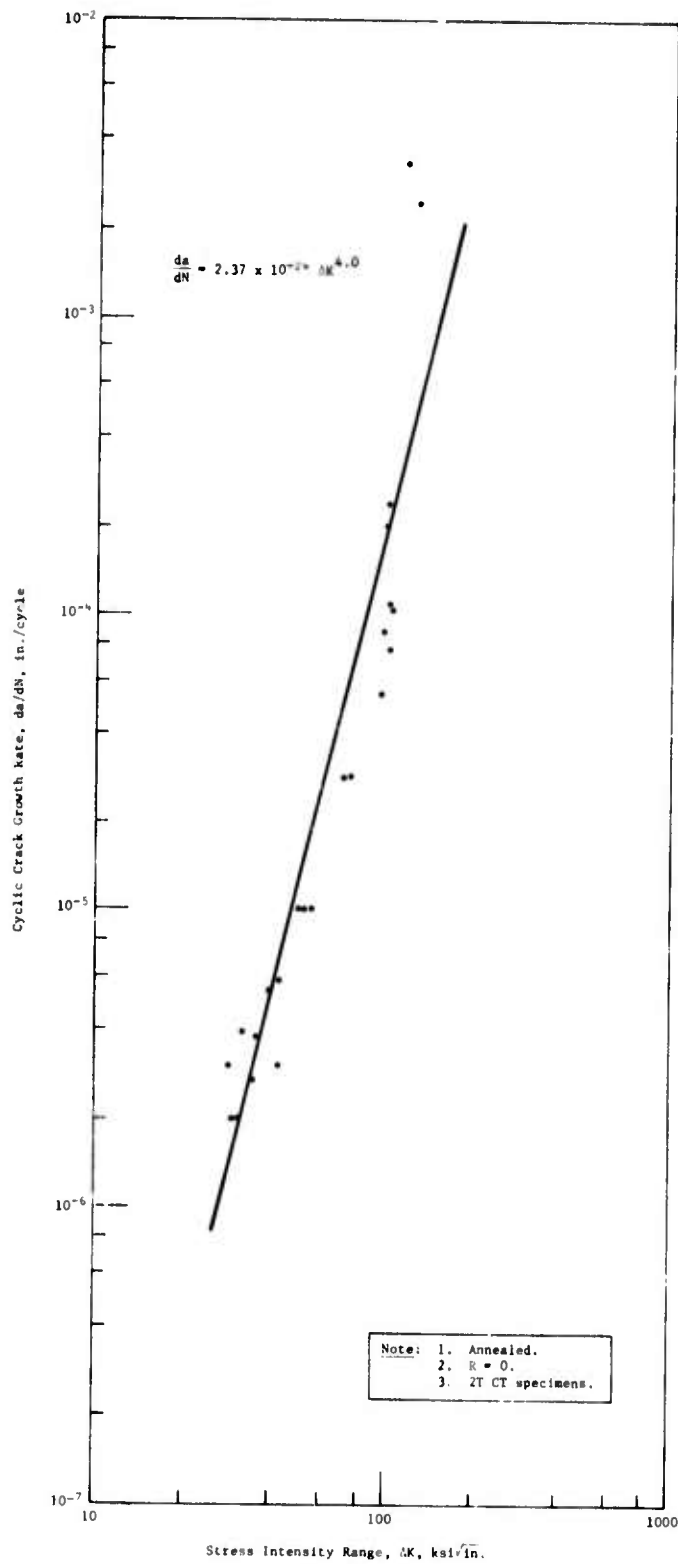


Figure IV-6  
Cyclic Crack Growth Rate Properties of 304L  
Stainless Steel at 77K

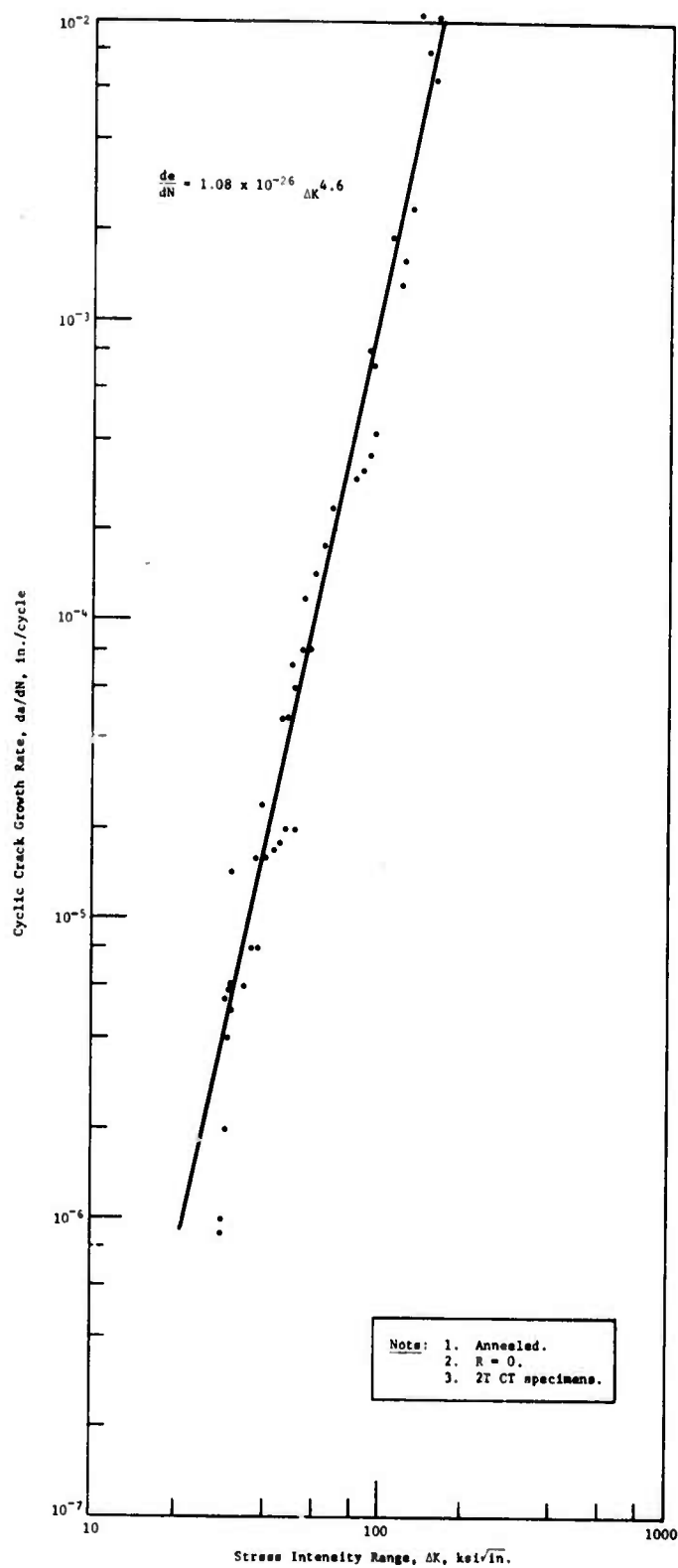


Figure IV-7  
 Cyclic Crack Growth Rate Properties of 304L  
 Stainless Steel at 4K

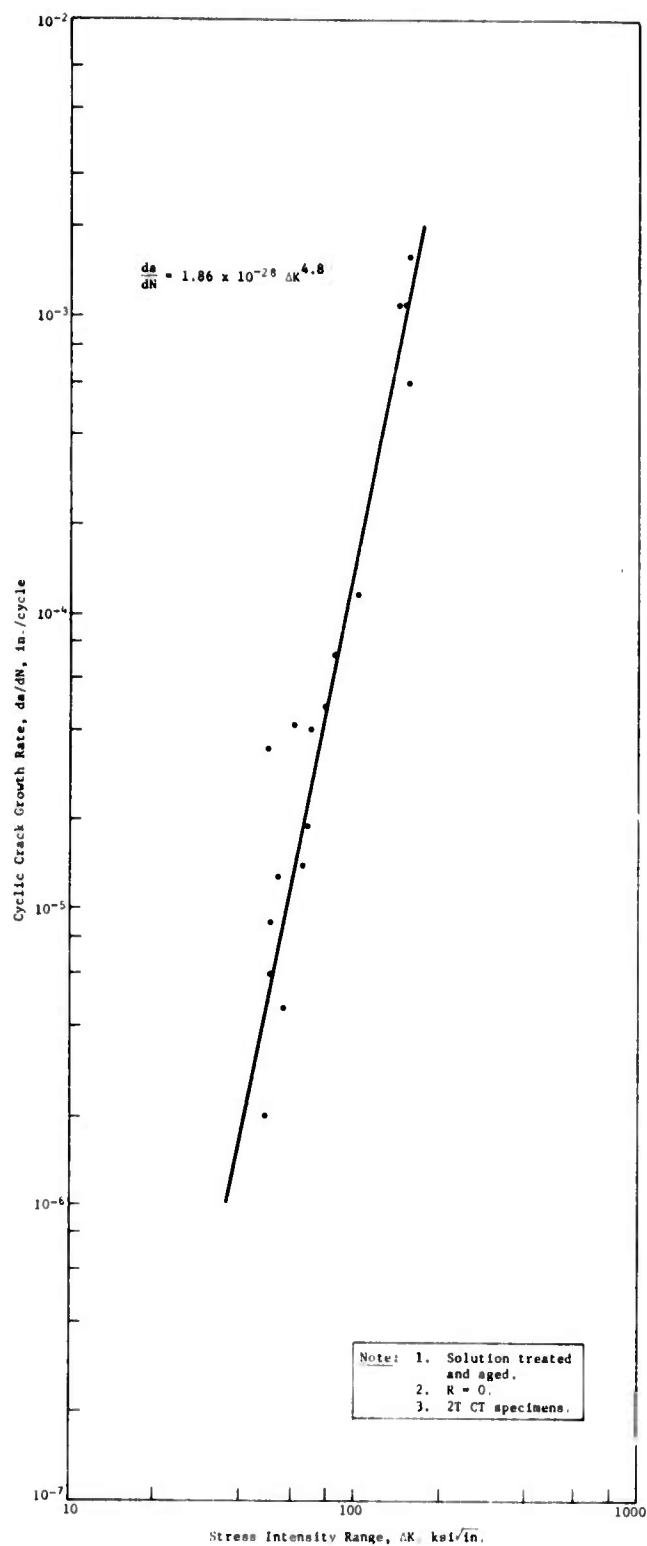


Figure IV-8  
 Cyclic Crack Growth Rate Properties of  
 A-286 Stainless Steel at 77K

IV-20

173<

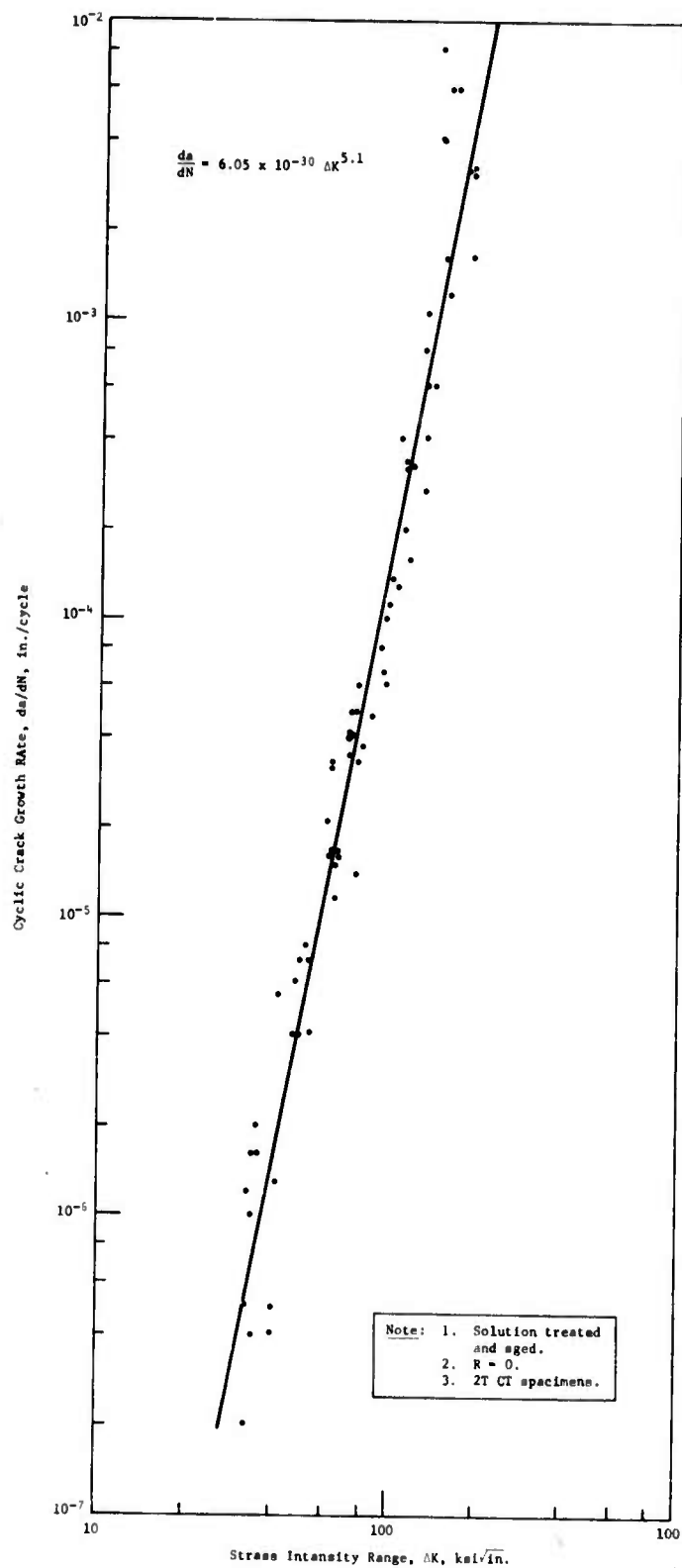


Figure IV-9  
Cyclic Crack Growth Rate Properties of A-286  
Stainless Steel at 4K

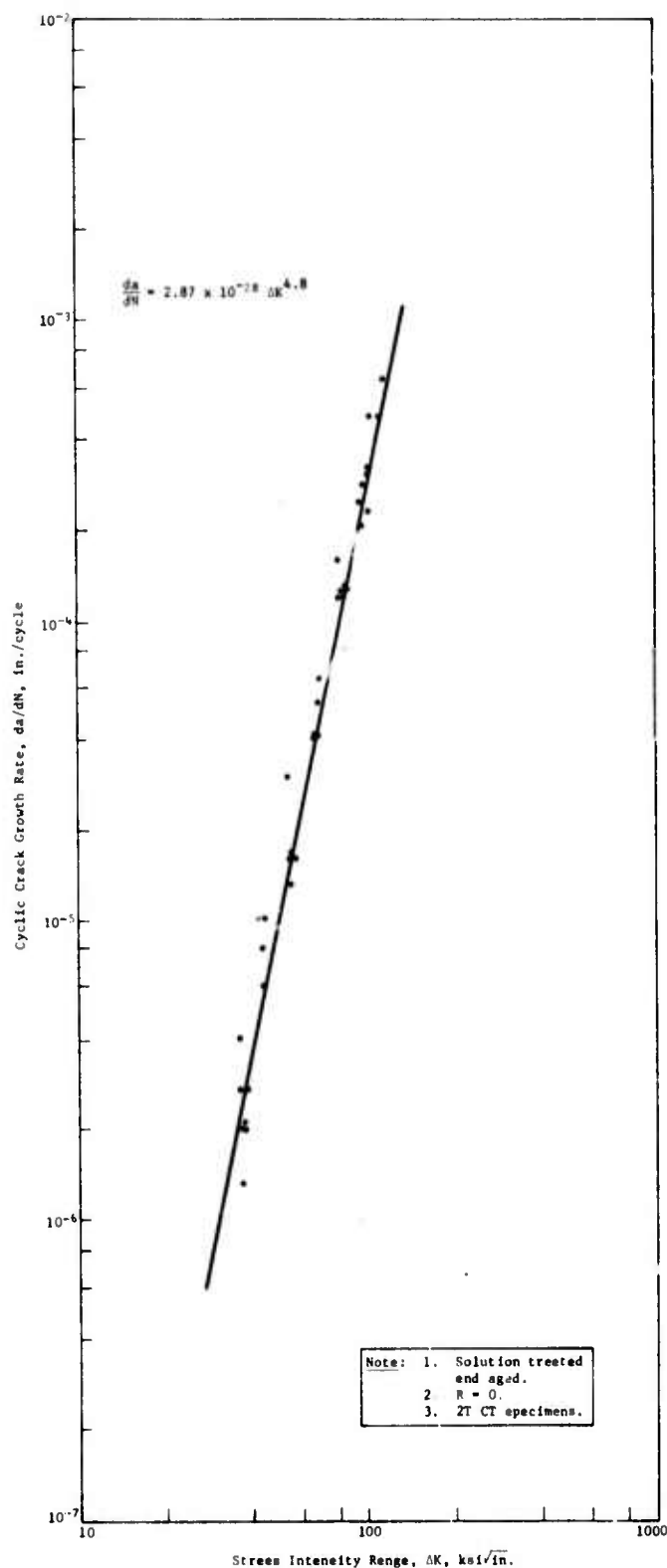


Figure IV-10  
Cyclic Crack Growth Rate Properties of  
X-750 Alloy at 77K

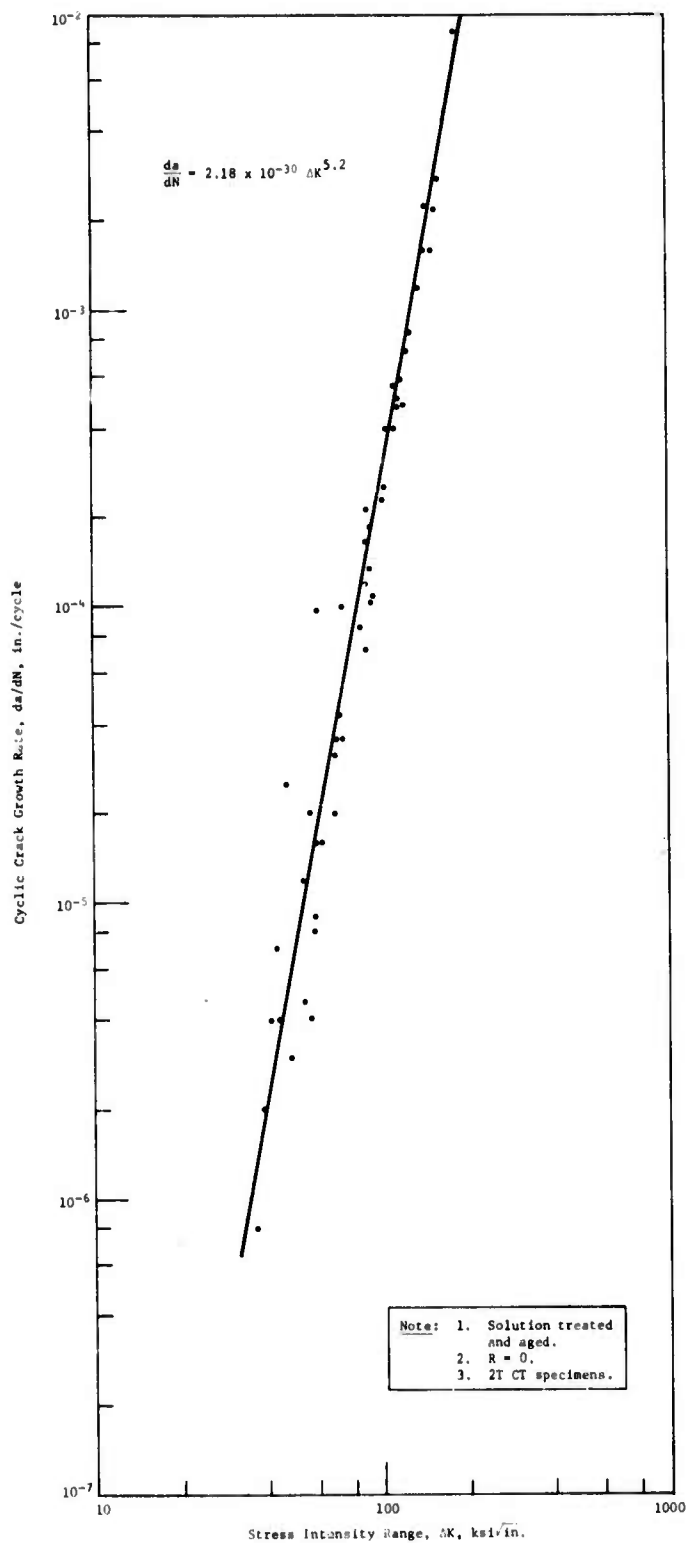


Figure IV-11  
Cyclic Crack Growth Rate Properties of X-750  
Alloy at 4K



## V. DISCUSSION OF RESULTS

---

The static fracture toughness data did not give valid properties in accordance with ASTM E399. However, for some of the cases, the data are probably sufficiently close to the validity criteria to permit consideration of the properties as typical values. The data for the 2-in.-thick specimens of A-286 and X-750 at all temperatures can probably be considered typical. The 1-in.-thick specimen of these alloys give results indicative of insufficient thickness. In all cases the 304 data exhibit such gross plasticity that linear elastic analysis is completely out of the question.

J-integral analysis for the 304L gives values that apparently satisfy the validity criteria for both thickness. However, testing was not performed specifically to obtain J values. That is, the point of crack instability was not determined, but merely assumed to be at maximum load. As a result, the validity of the data should be subject to question. It would be desirable to perform additional testing on remaining specimens to establish the point of crack instability.

The J-integral data show a decrease in toughness with decrease in temperature. The linear analysis data show an increase. J-analysis data for 304 developed by NBS exhibit higher  $J_Q$ -values and an increase in toughness with reduction in temperature. Figure V-1 compares the data generated with the NBS data.

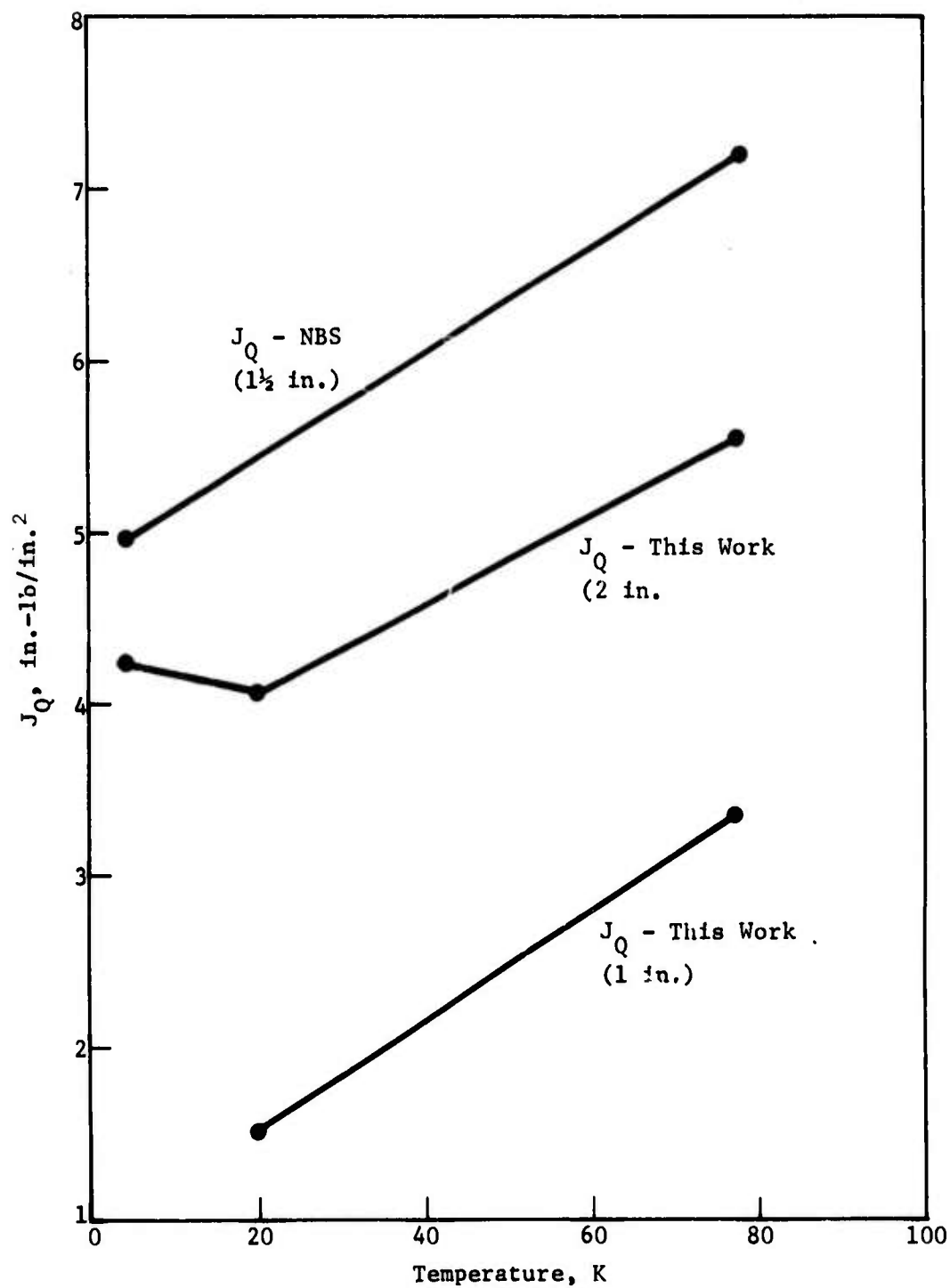


Figure V-1 Comparison of J-Integral Data for 304 Stainless Steel

Data for A-286 showed a slight increase in toughness with decrease in temperature for the 2-in.-thick specimens. Results from the 1-in. tests and the NBS tests (converted from  $J_Q$ ) for 1½-in. material showed little temperature dependence of toughness. Figure V-2 compares the data.

Data for alloy X-750 exhibited virtually no temperature dependence of toughness. A comparison with previous Westinghouse data showed that the results from ½-in. and 1-in.-thick specimens were significantly lower than the results obtained in this work.

A comparison of cyclic crack growth rate data is given in Figure V-3. The relationship of behavior to performance is extremely difficult to assess from the type of data developed in this program. A comparison of behavior has to be quite arbitrary. The simplest comparison that can be made is  $da/dN$  at selected stress intensity levels. At 77K, the crack growth rates for the three alloys are quite similar. However, at 4K, 304L exhibits significantly higher crack growth rates than X-750 and A-286.

The data generated during the first year's work suggest the need for additional testing. It is suggested that an evaluation of the effect of thickness on the J-integral values for 304L be performed. Thicknesses from 1 to 4-in. should be evaluated to determine when validity is achieved. Testing should be performed to obtain the point of crack instability. The behavior of welded A-286 and X-750 should also be evaluated using 2-in.-thick material.

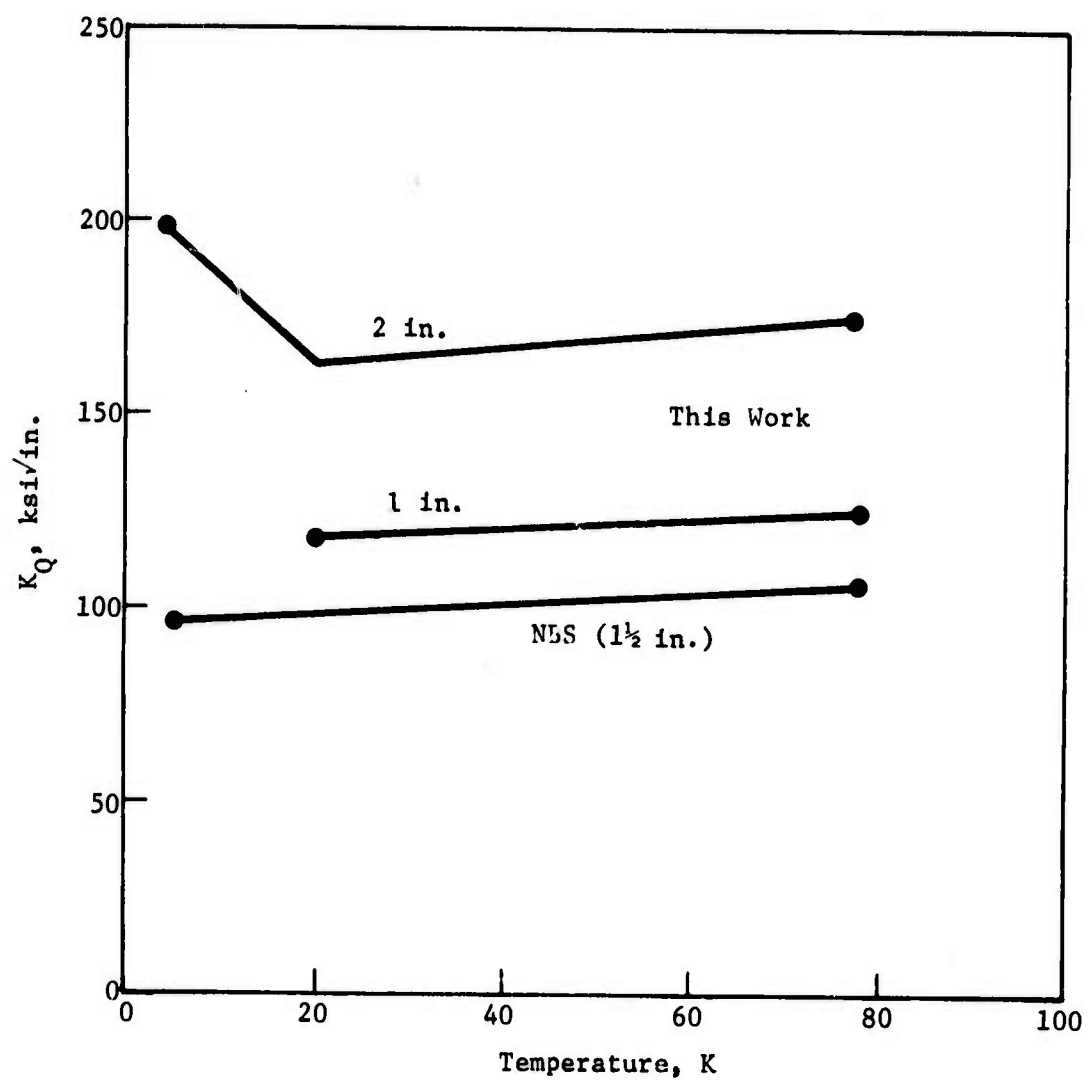


Figure V-2 Comparison of  $K_Q$  Data for A-286 Stainless Steel

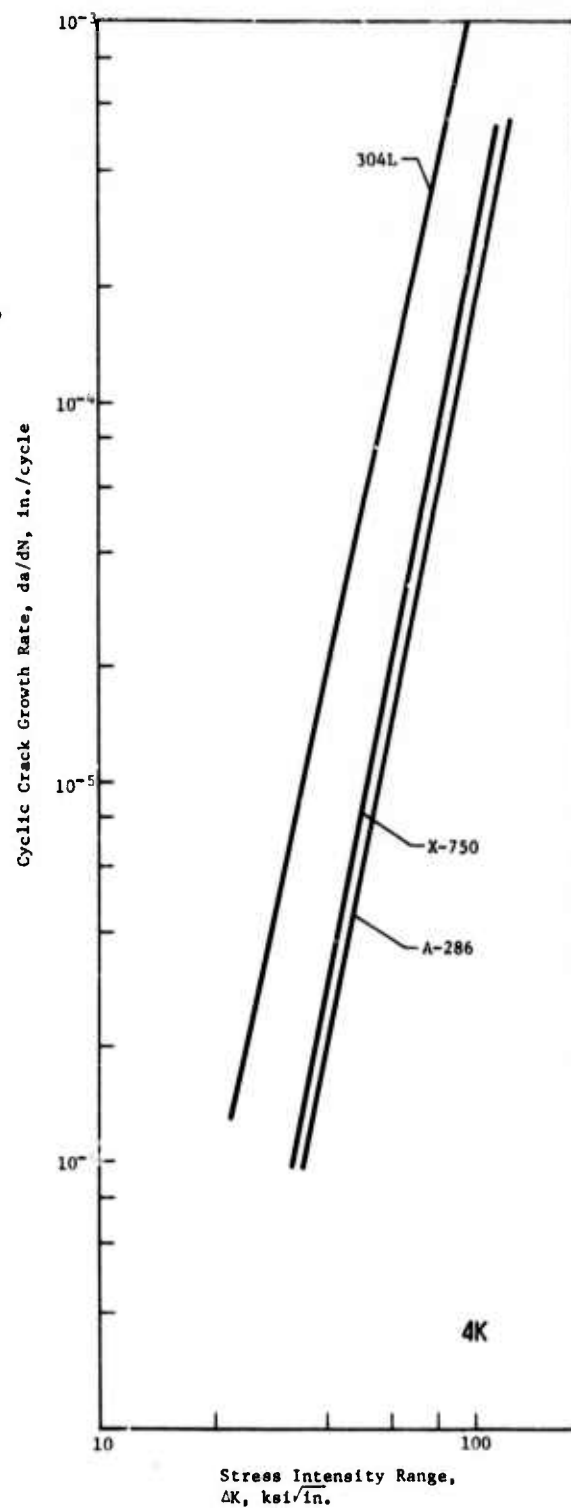
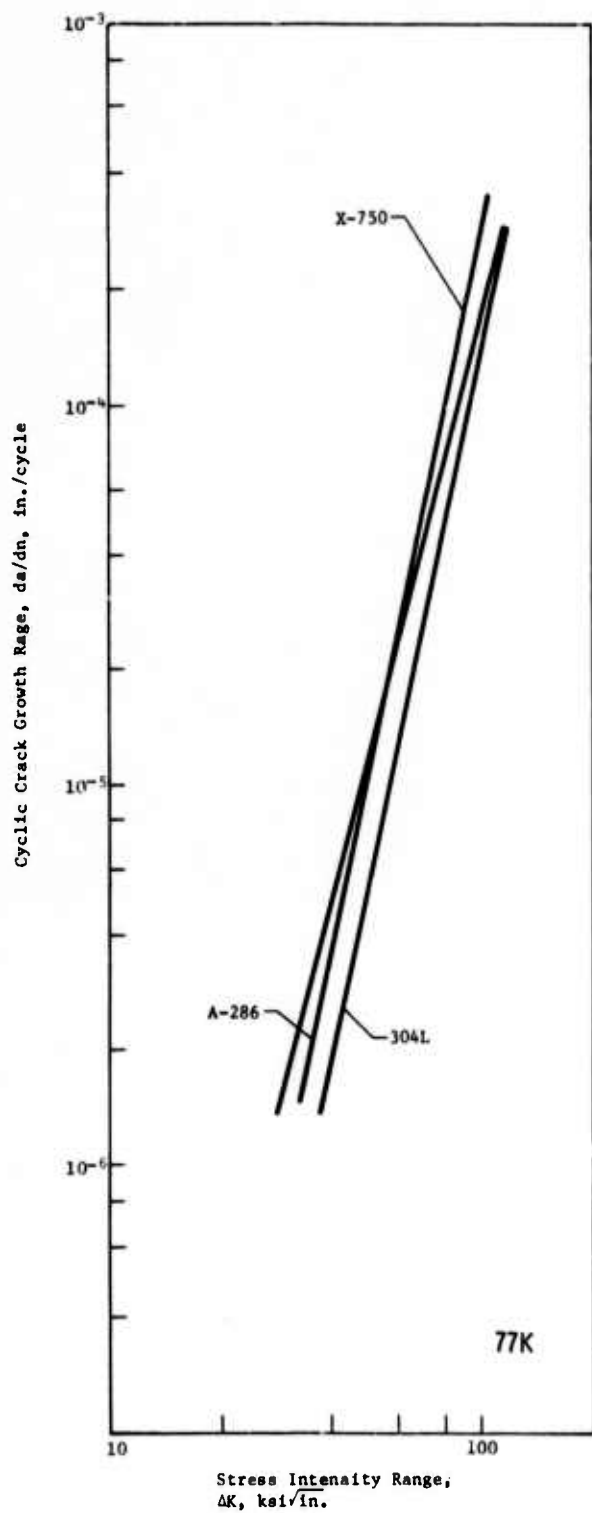


Figure V-3 Comparison of Cyclic Crack Growth Rates

**NBSIR 74-393**

**SEMI-ANNUAL REPORT ON MATERIALS RESEARCH  
IN SUPPORT OF SUPERCONDUCTING MACHINERY**

---

R. P. Reed, R. L. Durcholz, F. R. Fickett, P. J. Giarratano,  
J. G. Hust, M. B. Kasen, H. M. Ledbetter, R. P. Mikesell,  
E. R. Naimon, R. E. Schramm, L. L. Sparks, R. L. Tobler,  
and W. F. Weston

Cryogenics Division  
Institute for Basic Standards  
National Bureau of Standards  
Boulder, Colorado 80302

October 1974

Prepared for  
Advanced Research Projects Agency  
1400 Wilson Boulevard  
Arlington, Virginia 22209



---

U.S. DEPARTMENT OF COMMERCE, Frederick B. Dent, Secretary

NATIONAL BUREAU OF STANDARDS Richard W. Roberts, Director

SEMI-ANNUAL REPORT ON MATERIALS RESEARCH  
IN SUPPORT OF SUPERCONDUCTING MACHINERY

---

Sponsored by  
Advanced Research Projects Agency  
ARPA Order No. 2569  
Program Code 4D10  
August 10, 1973 - August 9, 1974

Program Director  
Dr. E. C. van Reuth  
Materials Sciences  
Advanced Research Projects Agency  
1400 Wilson Boulevard  
Arlington, Virginia 22209

Program Manager  
Dr. R. P. Reed  
Cryogenics Division  
Institute for Basic Standards  
National Bureau of Standards  
Boulder, Colorado 80302

The views and conclusions contained in this document are those of the authors and should not be interpreted as necessarily representing the official policies, either expressed or implied, of the Advanced Research Projects Agency or of the U.S. Government.

### Abstract

Results of six months of study on Materials Research in Support of Superconducting Machinery (April through September, 1974) are reported to the sponsor, the Advanced Research Projects Agency of the U.S. Department of Defense. The report is divided into five sections: thermal conductivity, magnetothermal conductivity, fatigue and fracture-toughness properties, properties of advanced composites, and elastic properties. The temperature range 4 to 300 K is covered by the study. Materials studied are either being used or are candidates for use in superconducting machinery and include: aluminum alloys, composites, inconels, OFHC copper, stainless steels, and titanium alloys.

Special results of the study include: fracture-toughness and fatigue-crack growth-rate data for AISI 310, Ti-5 Al-2.5 Sn, A286 stainless steel, and Inconel 750 at 4, 76, and 300 K; initial reports of tensile testing of composites at 4 K; a second review paper on advanced-composite low-temperature behavior; magnetothermal conductivity measurements on OFHC copper and Inconel 718 indicate that, in a magnetic field, the thermal conductivity may change by 100 percent; anomalous low-temperature elastic behavior of AISI 300 series stainless-steel alloys; and thermal conductivity data for OFHC copper, Inconel 750, and Inco Low-Expansion-Alloy. These data provide considerable insight into material characteristics at extremely low temperatures, assisting in material selection and efficient design.



## Report Contents

	Page
Thermal Conductivity J. G. Hust and P. J. Giarratano . . . . .	1
Magnetothermal Conductivity L. L. Sparks and F. R. Fickett . . . . .	37
Fatigue and Fracture-Toughness Testing at Cryogenic Temperatures R. L. Tobler, R. P. Mikesell, R. L. Durcholz, and R. P. Reed. . . . .	57
Advanced Composites M. B. Kasen and R. E. Schramm . . . . .	123
Elastic Properties of Engineering Materials at Cryogenic Temperatures H. M. Ledbetter, E. R. Naimon, and W. F. Weston . . . . .	217
Appendix A: Publication - E. R. Naimon, W. F. Weston, and H. M. Ledbetter, Elastic properties of two titanium alloys at low temperatures, Cryogenics <u>14</u> (1974) 246-9. . . . .	273

### Disclaimer

Tradenames of equipment and materials are used in this report for clarity and to conform with standard usage in the scientific and engineering literature. Selection of materials for discussion and examination with regard to application in superconducting machinery is based on properties reported in the literature, and must be regarded as preliminary and tentative. In no case does such selection imply recommendation or endorsement by the National Bureau of Standards, nor does it imply that the material or equipment is necessarily the best available for the purpose.

NBSIR

SEMI-ANNUAL REPORT ON MATERIALS RESEARCH IN SUPPORT OF  
SUPERCONDUCTING MACHINERY

THERMAL CONDUCTIVITY

J. G. Hust and P. J. Giarratano

Cryogenics Division  
Institute for Basic Standards  
National Bureau of Standards  
Boulder, Colorado 80302

October 1974

### Summary: Thermal Conductivity

Thermal conductivity, electrical resistivity, thermopower, and Lorenz ratio data have been obtained for OFHC copper, Inconel X-750, and INCO LEA (Low Expansion Alloy). Values of these properties are presented in graphical and tabular form and equations are provided for convenient computer calculations for data at temperatures from 4 to 300 K. The thermal conductivity data are accurate to 2%, which is well within material variability limits expected for production heats. Prediction techniques have been shown to yield thermal conductivity values within 15 percent of experimental values for pure metals, such as OFHC copper.

In addition, thermal conductivity values have been obtained, using the fixed-point apparatus, for Kromarc-58 and AISI-310 stainless steels at 6, 79, 196, and 277 K. These values, accurate to 10%, are presented in graphical and tabular form.

### Contents: Thermal Conductivity

	Page
1. <u>Introduction</u> . . . . .	3
2. <u>Apparatus</u> . . . . .	4
3. <u>Specimen Characterization</u> . . . . .	5
4. <u>Results</u> . . . . .	6
5. <u>Discussion</u> . . . . .	7
6. <u>Acknowledgements</u> . . . . .	9
7. <u>References</u> . . . . .	10
<u>List of Figures</u> . . . . .	11
<u>List of Tables</u> . . . . .	30

## THERMAL CONDUCTIVITY

J. G. Hust and P. J. Giarratano

### 1. Introduction

Optimum design of superconducting machinery requires a knowledge of thermal properties of technically important materials at low temperatures. But, often, components extend from ambient temperatures to low temperatures, and, therefore, data are needed from 4 K to 300 K. Thermal conductivity of metals is a function of the host metal and its constituent elements and temperature; but it also depends on the microstructure of the material, strain, fatigue, and heat treatment; and in some cases environmental effects are important (e.g., in the case of superconducting machinery, magnetic field intensities may produce significant changes). Specific thermal conductivity data for particular components are required to limit heat losses and thermal stresses in machines. With such a myriad of parameters it is difficult (at best) to determine accurately, by experiment, the thermal conductivity of each machine component. Instead, we often rely on a limited number of measurements on specific types of materials, characterized according to the above parameters. Due to material variability effects these values are generally considered accurate to only about 10%.

It should be noted that accurate thermal conductivity measurements are much more expensive and time consuming relative to many other property measurements. The ease with which high accuracy can be obtained is primarily a function of temperature and the conductivity itself. The extremes of conductivity (both very high, such as in pure metals, and very low, such as in insulating materials) promote inaccuracies in measurement. Generally, low temperature data (below about 100 K) are more readily obtained with accuracy because radiation errors can be minimized.

For the above reasons, various methods of obtaining thermal conductivity data are used. The method used depends primarily on the accuracy dictated by the application. Usually accuracies of 10% are sufficient; in other cases values accurate to 50% suffice. The present state-of-the-art in thermal conductivity measurements is about

1% accuracy, but seldom is this required except in theoretical or standardization work.

In this laboratory three methods of data determination are used:

- (a) A variable-temperature apparatus, capable of measuring at any temperature from 4 to 300 K, with an accuracy of about 2%. This apparatus also simultaneously measures electrical resistivity and thermopower for additional specimen characterization and subsequent predictions of similar materials. This apparatus will be used to measure materials that have not been sufficiently measured and characterized previously and for accurate temperature dependence determinations.
- (b) A fixed point apparatus, capable of measuring only near the fixed temperatures of various boiling fluids (such as liquid helium and liquid nitrogen) and melting or subliming solids (such as ice and  $\text{CO}_2$ ). The accuracy of this apparatus is about 10%, depending mainly on the conductivity of the specimen.
- (c) Predictive methods such as those described by Hust and Clark [1] and Hust and Sparks [2]. The latter paper also contains data for many metals and alloys, necessary to carry out such predictions.

## 2. Apparatus

The variable-temperature apparatus was used for the measurements reported for Inconel X-750, OFHC copper, and INCO LEA (Low Expansion Alloy). This is a multi-property apparatus used to simultaneously measure thermal conductivity, electrical resistivity, and thermopower at temperatures between 4 and 300 K. This apparatus is based on the longitudinal heat flow method. The specimen is a rod 23 cm long with a diameter up to 3 cm depending on its conductivity. The top of the specimen is thermally connected to a temperature-controlled floating sink and the gradient heater is connected at the bottom of the specimen. The specimen is surrounded with insulation and a temperature-controlled concentric shield. The longitudinal temperature distribution of the shield is adjusted to match that of the specimen. Eight equally spaced thermocouples are attached to the specimen to determine its longitudinal temperature distribution. These thermocouples are calibrated in-place using accurately calibrated platinum and germanium resistance thermometers. Further details of this apparatus



are documented in an unpublished report available from Hust. A schematic diagram of this cryostat is shown in the previous semi-annual report to ARPA [3].

The fixed-point apparatus was used to measure Kromarc-58 and AISI-310 stainless steels. This longitudinal-heat-flow apparatus is designed to perform measurements of 10% accuracy with greater speed and smaller specimen size than the multiproperty apparatus. The specimen is a 5 cm long rod with a diameter up to 3 cm depending on its conductivity. Further details of this apparatus are available in an unpublished report from Hust. A schematic diagram of this cryostat is shown in the previous semi-annual report to ARPA [3].

### 3. Specimen Characterization

The materials investigated have been selected from a long list of materials that have applications in superconducting machinery. The materials considered here are OFHC copper, Inconel X-750, INCO LEA (Low Expansion Alloy), Kromarc-58 stainless steel, and AISI-310 stainless steel. OFHC copper was chosen as the first specimen to be measured, not only because of its importance in superconducting machines, but also because a good conductor was needed to perform initial checks and thermocouple calibrations of the apparatus.

The OFHC copper specimen was fabricated from production copper as follows: A 6.4 mm copper rod was degreased with freon and etched with a solution of 50% water and 50% nitric acid. The rod was swaged to 3.26 mm with cleaning between each swaging step and vacuum anneals whenever flaking became evident. The final anneal before measurement was 650°C for one hour. Prior to each anneal the specimen was acid etched.

The Inconel X-750, INCO LEA, Kromarc-58 stainless steel, and AISI-310 stainless steel stock material was obtained from Westinghouse Electric Corporation, Research and Development Center and is the same material being tested by them in this program. The Inconel X-750 was in the solution treated (ST) condition (1800°F - one hr - air cooled). The INCO LEA was in the solution treated aged (STA) condition (1800°F - one hr - air cooled - 1225°F - 8 hrs - air cooled). Both of these materials were machined to cylindrical rods 23 cm long and 11.3 mm diameter with no subsequent heat treatment.

The Kromarc-58 stainless steel was annealed at 1800°F for one hour, water quenched, and then cold worked 30% in the transverse direction. The AISI-310 stainless steel was heated to 2000°F for one hour and water quenched. Both of these materials were machined to cylindrical rods 5 cm long and 11.3 mm diameter with no subsequent heat treatment.

#### 4. Results

Measurements were performed on specimens of OFHC copper, Inconel X-750, and INCO LEA (Low Expansion Alloy) over the temperature range 4 to 300 K. Fifty-eight runs were conducted on OFHC copper, 29 on Inconel X-750, and 28 on INCO LEA. OFHC copper was studied more extensively than the other two materials to establish system characteristics and to perform an extensive thermocouple calibration data set. The following equations were least-squares fitted to these data using orthonormal fitting techniques:

$$\ell n \lambda = \sum_{i=1}^n a_i [\ell n T]^{i-1} \quad (1)$$

$$\rho = \sum_{i=1}^m b_i [\ell n T]^{i-1} \quad (2)$$

$$S = \sum_{i=1}^l c_i [\ell n T']^{i-1} / T'; \quad T' = \frac{T}{10} + 1 \quad (3)$$

where  $\lambda$  = thermal conductivity,  $\rho$  = electrical resistivity,  $S$  = thermopower, and  $T$  = temperature. Temperatures are based on the IPTS-68 scale above 20 K and the NBS P2-20 (1965) scale below 20 K. The parameters,  $a_i$ ,  $b_i$ , and  $c_i$  determined by least squares, are presented in table 1. Further details of this procedure are described by Hust, et al. [4]. The deviations of the experimental data from these equations are given in figures 1 through 9. The horizontal bars in figures 2, 3, 5, 6, 8 and 9 indicate the temperature span across the specimen for each run. The "observed" thermal conductivities are computed from the mean temperature gradients indicated by adjacent thermocouples. Calculated values of  $\lambda$ ,  $\rho$ ,  $S$ , and  $L = \rho \lambda / T$  (Lorenz ratio) are presented in tables 2, 3, and 4 and figures 10 through 21.



A detailed error analysis for this system has been performed and is available as an unpublished report from Hust. Based on this analysis of systematic and random errors, typical uncertainty estimates (with 95% confidence) are as follows:

thermal conductivity:	2% from 4 to 20 K, 1% from 20 K to 200 K, and 2% from 200 K to 300 K
electrical resistivity:	0.2%
thermopower:	0.1 $\mu\text{V/K}$ up to 20 K and 0.01 $\mu\text{V/K}$ above 20 K

The actual uncertainties depend on the conductance of the specimen. For Inconel X-750 and INCO LEA the typical values are applicable. Since the conductance of the copper specimen was significantly larger, especially at liquid-helium temperature, the uncertainty for copper is larger at low temperatures. The uncertainties in thermal conductivity and electrical resistivity near 4 K are 4% and 1%, respectively, decreasing to the typical values above 20 K.

The thermopower values given here are absolute values although our measurements were carried out with respect to normal silver wire. The absolute thermopowers of normal silver reported by Borelius, et al. [5] were used to convert the experimental data to the absolute scale.

Thermal conductivity measurements were performed on Kromarc-58 and AISI-310 stainless steels at 6, 79, 196, and 277 K. The results of these measurements are listed in Table 5 and illustrated in figure 22. The smooth curves shown in figure 22 are based on the temperature dependence of similar alloys. The measured values of thermal conductivity have been compared to the fcc steel data tabulated by Childs et al. [6] and are in good agreement with the band of values compiled.

### 5. Discussion

OFHC copper is a relatively pure commercial copper and, therefore, its low-temperature thermal conductivity and electrical resistivity are highly variable from specimen-to-specimen. This variability is due to the fact that the low-temperature conductivity is nearly totally determined by the imperfections (impurities and physical defects) in the

metal. Small absolute variations in impurities represent large relative variations in pure metals. Fortunately, it is relatively simple to characterize the degree of imperfections in a pure metal by electrical resistivity data, which is much easier to obtain than thermal conductivity data. Often the residual resistivity or the residual resistivity ratio is used to indicate the effective electrical purity of the specimen. For all but the most pure research materials the resistivity at 4 K is the residual resistivity. The residual resistivity ratio is the ratio of resistivity at near ambient conditions to the residual resistivity. The resistivity at ambient temperature is a characteristic of the host metal and the residual resistivity is characteristic of its imperfections, both chemical and physical. We normally use the resistivity at the ice-point for defining this ratio,  $RRR = \rho_{273.15K} / \rho_{4K}$ . Other OFHC copper specimens that we have characterized at this laboratory have RRR values ranging from about 50 to 200. The particular specimen reported on here has an RRR of 250, somewhat more electrically pure than normal. This may be due to lower chemical impurity level or to impurity oxidation during the annealing process.

As indicated in the previous semi-annual report on this project [3], thermal conductivity of a pure metal can be predicted reasonably accurately from a knowledge of the Lorenz ratio, residual resistivity, and Matthiessen's rule [1,2]. Based on this information values of thermal conductivity for OFHC copper were presented in the last report. The current measurements show that those predictions were accurate to 10% above 15 K. At 10 K the difference between measurement and prediction is 15%. This exercise serves to illustrate the power of predictive methods for pure metals whose low-temperature conductivities may range over several orders of magnitude. At the lowest temperatures where this method was least accurate, other methods can be applied to yield more accurate predictions, but these are not discussed here.

The thermal conductivity of highly alloyed structural metals is not readily predicted. This is primarily because in such alloys the thermal transport is by quantized lattice vibrations (phonons) as well as by the electrons. The phonon conductivity is often much larger than the

electronic conduction and, thus, the electrical resistivity is no longer directly linked with thermal conductivity through the Lorenz ratio. Inconel X-750 and INCO LEA are part of a class of materials that have very high phonon-to-electronic conductivity at lower temperatures and therefore, their conductivities cannot be predicted from the Lorenz ratio. Lorenz ratios above the classical Sommerfeld value ( $2.443 \times 10^{-8} \text{ V}^2/\text{K}^2$ ) indicate the presence of significant phonon conduction. The low-temperature Lorenz ratio of Inconel X-750 indicates a very high relative phonon component (about ten times greater than the electronic component) while for INCO LEA the phonon component is about twice as large as the electronic component.

#### 6. Acknowledgements

We wish to express our appreciation to Joe Wells of Westinghouse Research Laboratories, Pittsburgh, Pa. for the material which he so generously provided for these measurements.

## 7. References

1. Hust, J. G. and Clark, A. F., The Lorenz ratio as a tool for predicting the thermal conductivity of metals and alloys, *Materials Research and Standards* 11, (No. 8), 22-4 (Aug. 1971).
2. Hust, J. G. and Sparks, L. L., Lorenz ratios of technically important metals and alloys, *Nat. Bur. Stand. (U.S.) Tech. Note* 634, (Feb. 1973) 133 pp.
3. Sparks, L. L., Fickett, F. R., Hust, J. G., et al., Semi-annual report on materials research in support of superconducting machinery, NBSIR 74-359 (1974) 308 pp; available from NTIS, AD 780-596/3WM.
4. Hust, J. G., Weitzel, D. H., and Powell, R. L., Thermal conductivity standard reference materials from 4 to 300 K, I. Armco iron: Including apparatus description and error analysis, *J. Res. NBS* 74A, 673-90 (1970).
5. Borelius, G., Keesom, W. H., Johansson, C. H., and Linde, J. O., Establishment of an absolute scale for the thermoelectric force, *Proc. Kon. Akad. Amsterdam* 35, 10 (1932).
6. Childs, G. E., Ericks, L. J., and Powell, R. L., Thermal conductivity of solids at room temperature and below: A review and compilation of the literature, *Nat. Bur. Stand. (U.S.) Monograph* 131 (Sept. 1973) 608 pp.

### List of Figures

	Page
1. Thermal conductivity deviations for OFHC copper. . . . .	12
2. Electrical resistivity deviations for OFHC copper. . . . .	12
3. Thermovoltage deviations for OFHC copper . . . . .	13
4. Thermal conductivity deviations for Inconel X-750. . . . .	13
5. Electrical resistivity deviations for Inconel X-750. . . . .	14
6. Thermovoltage deviations for Inconel X-750 . . . . .	14
7. Thermal conductivity deviations for INCO LEA . . . . .	15
8. Electrical resistivity deviations for INCO LEA . . . . .	15
9. Thermovoltage deviations for INCO LEA. . . . .	16
10. Thermal conductivity of OFHC copper . . . . .	17
11. Electrical resistivity of OFHC copper. . . . .	18
12. Thermopower of OFHC copper . . . . .	19
13. Lorenz ratio of OFHC copper. . . . .	20
14. Thermal conductivity of Inconel X-750. . . . .	21
15. Electrical resistivity of Inconel X-750. . . . .	22
16. Thermopower of Inconel X-750 . . . . .	23
17. Lorenz ratio of Inconel X-750. . . . .	24
18. Thermal conductivity of INCO LEA . . . . .	25
19. Electrical resistivity of INCO LEA . . . . .	26
20. Thermopower of INCO LEA. . . . .	27
21. Lorenz ratio of INCO LEA . . . . .	28
22. Thermal conductivity of Kromarc-58 and AISI-310 stainless steels . .	29

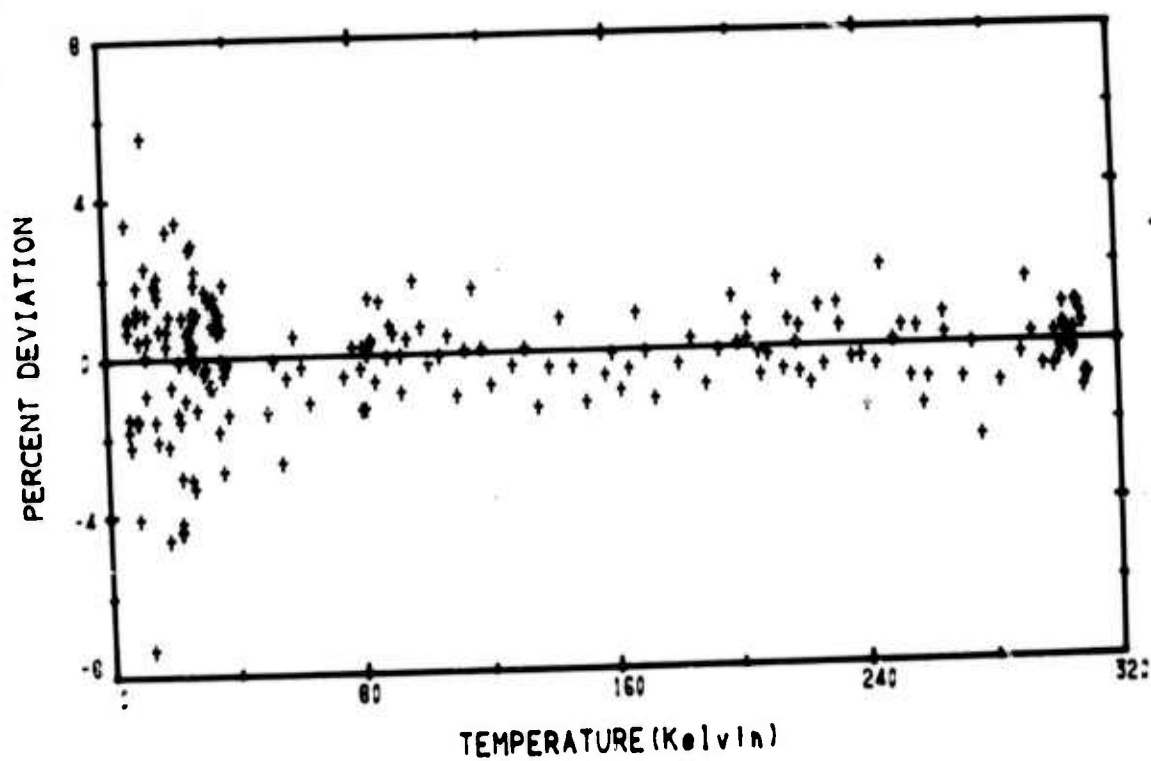


Figure 1. Thermal conductivity deviations for OFHC copper.

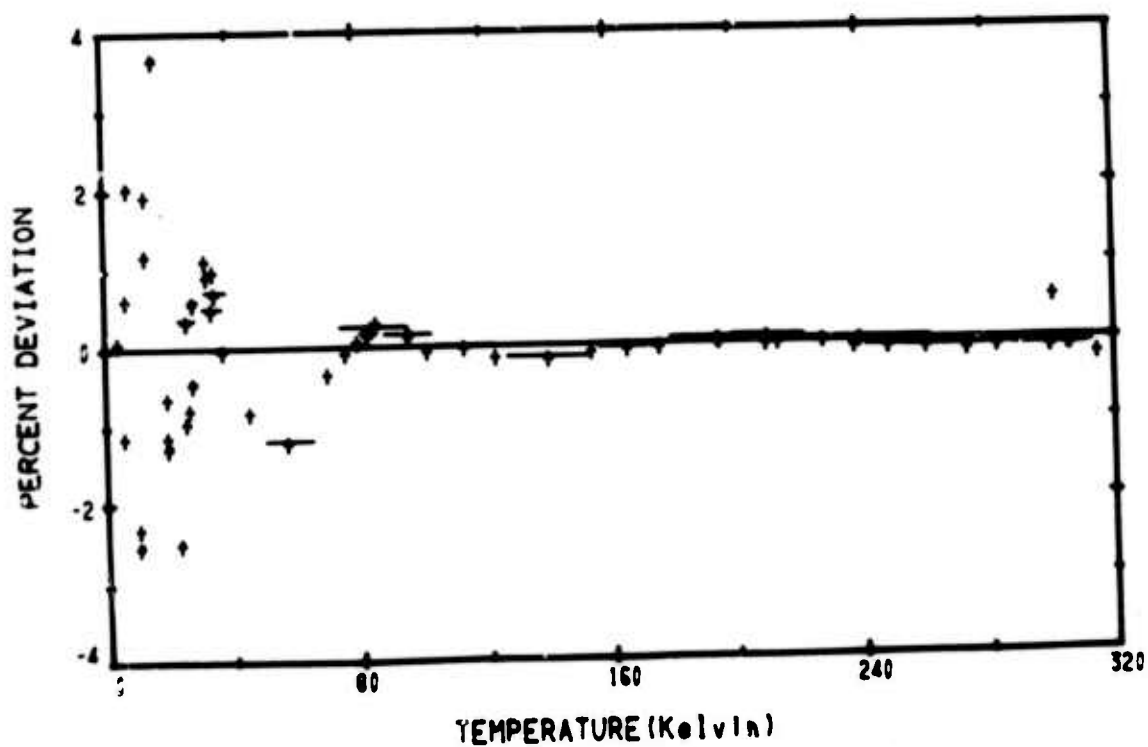


Figure 2. Electrical resistivity deviations for OFHC copper.

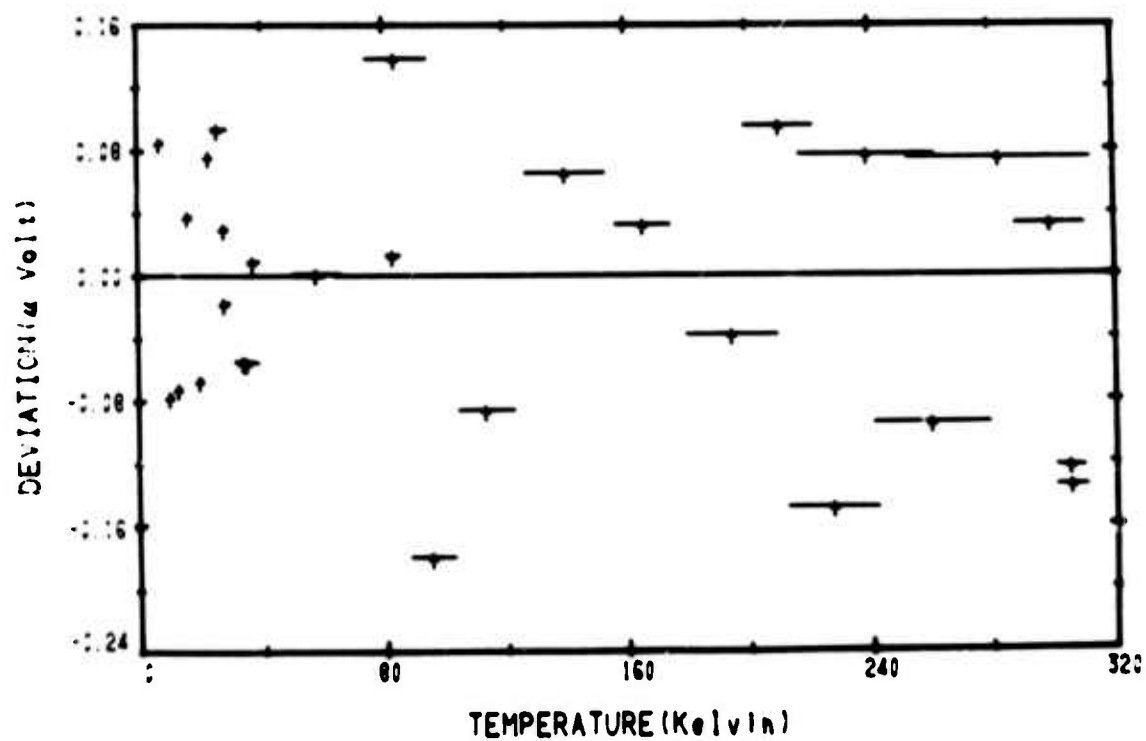


Figure 3. Thermovoltage deviations for OFHC copper.

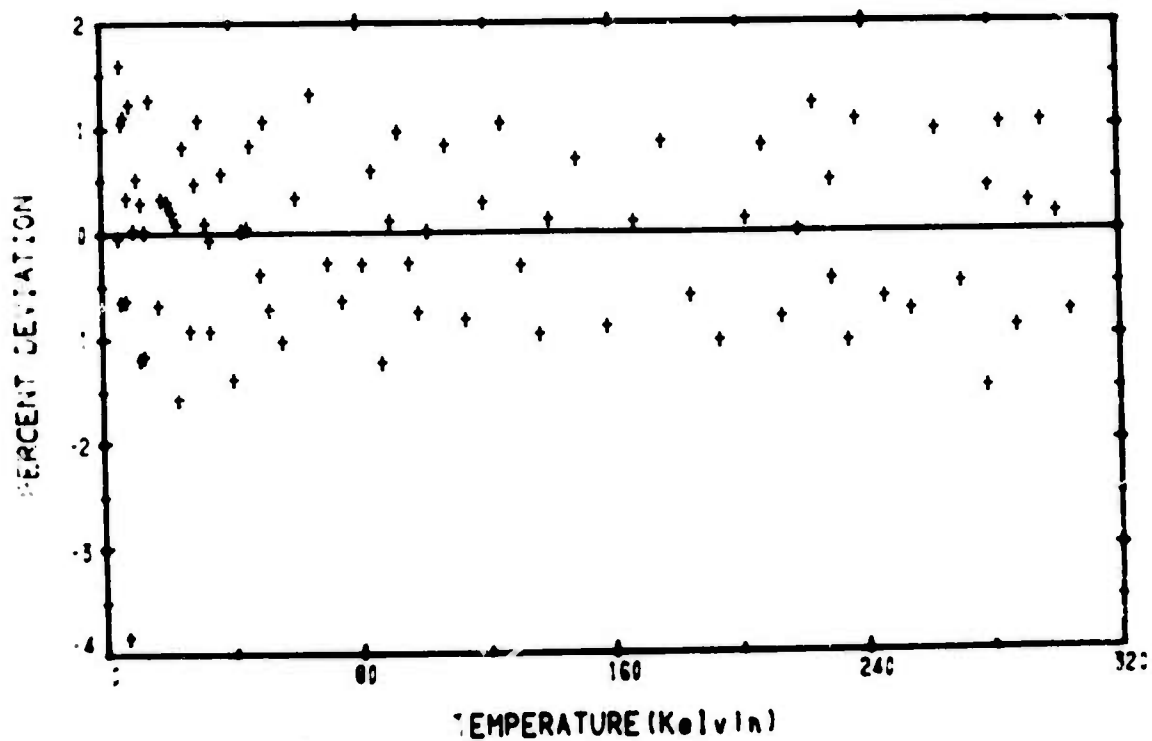


Figure 4. Thermal conductivity deviations for Inconel X-75G.

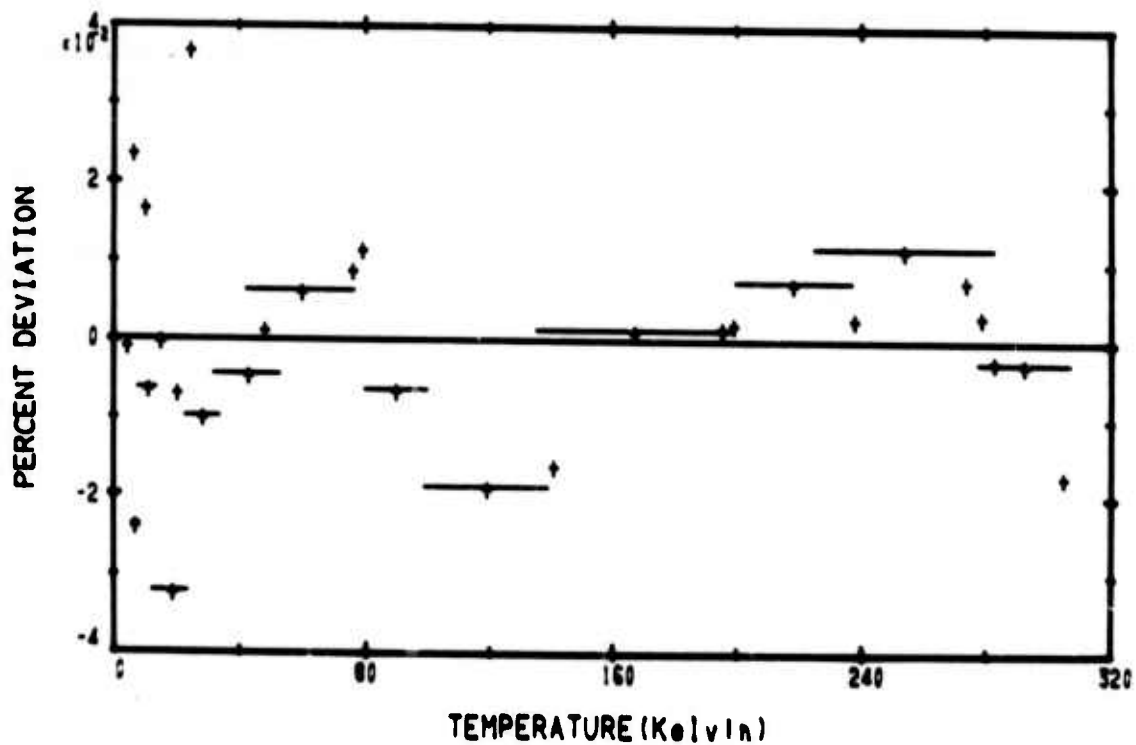


Figure 5. Electrical resistivity deviations for Inconel X-750.

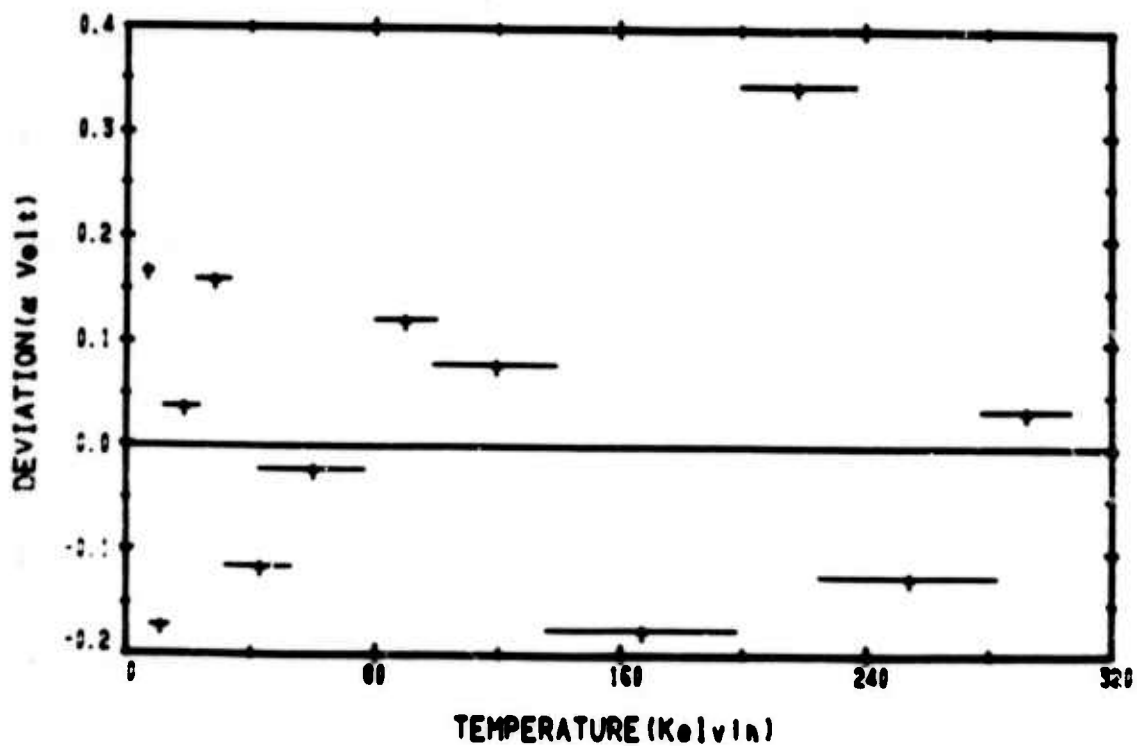


Figure 6. Thermovoltage deviations for Inconel X-750.



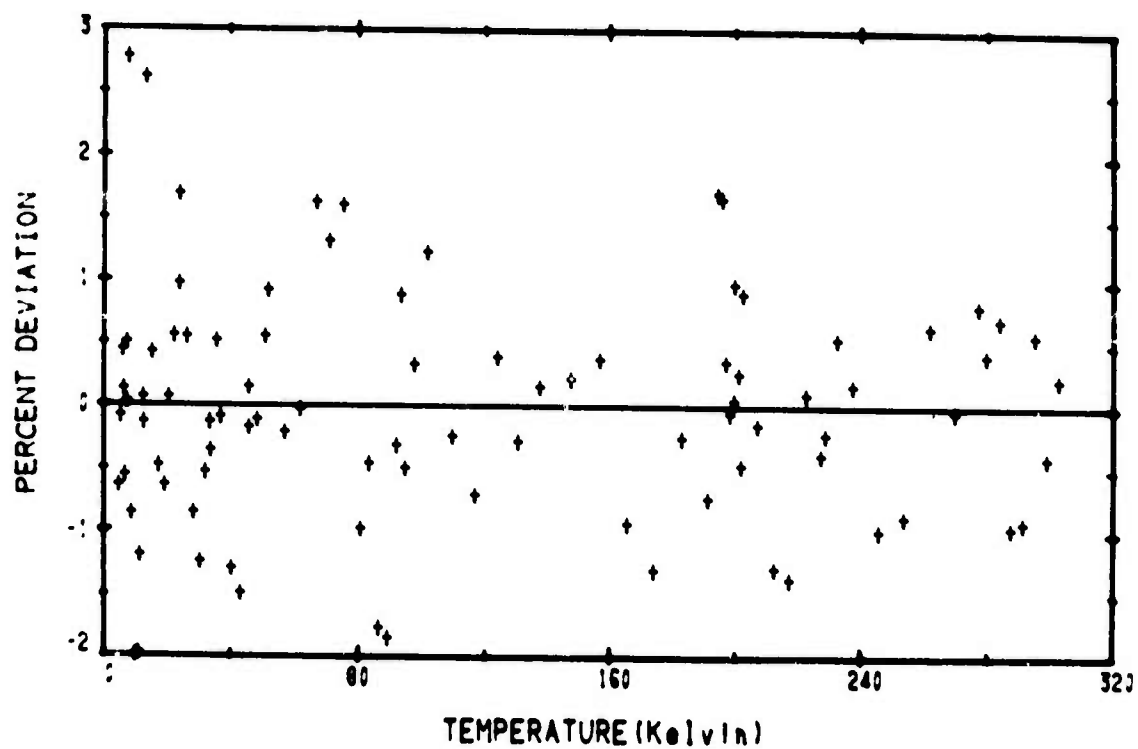


Figure 7. Thermal conductivity deviations for INCO LEA.

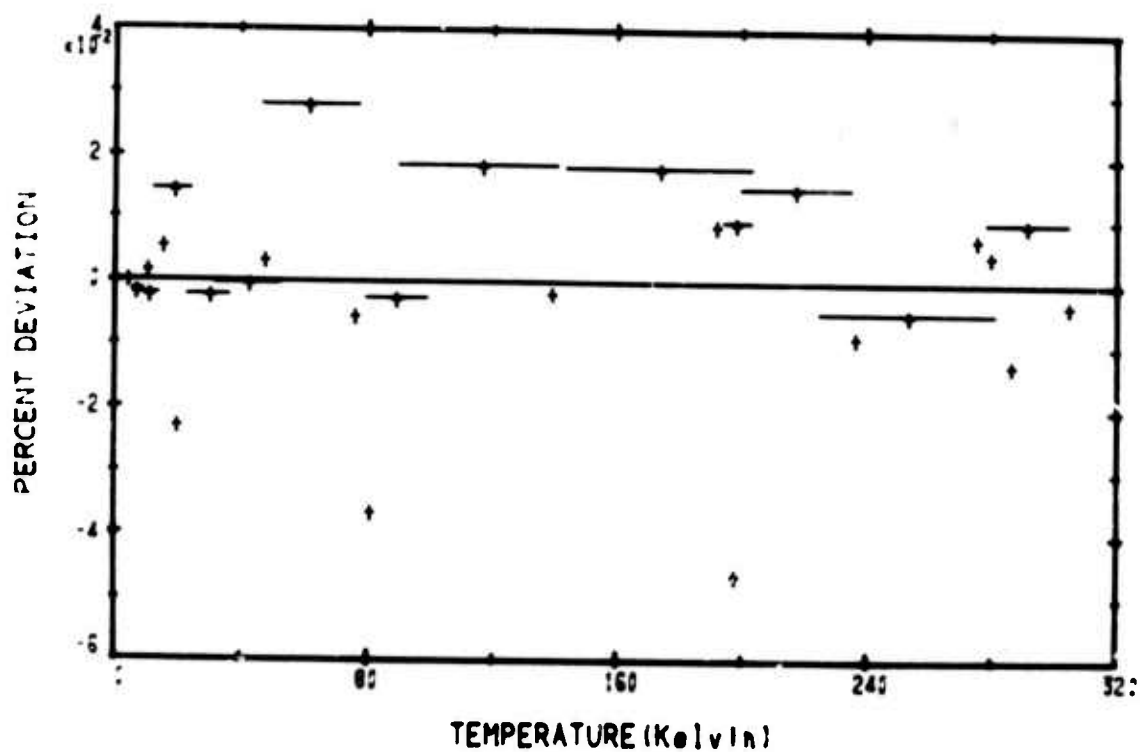


Figure 8. Electrical resistivity deviations for INCO LEA.

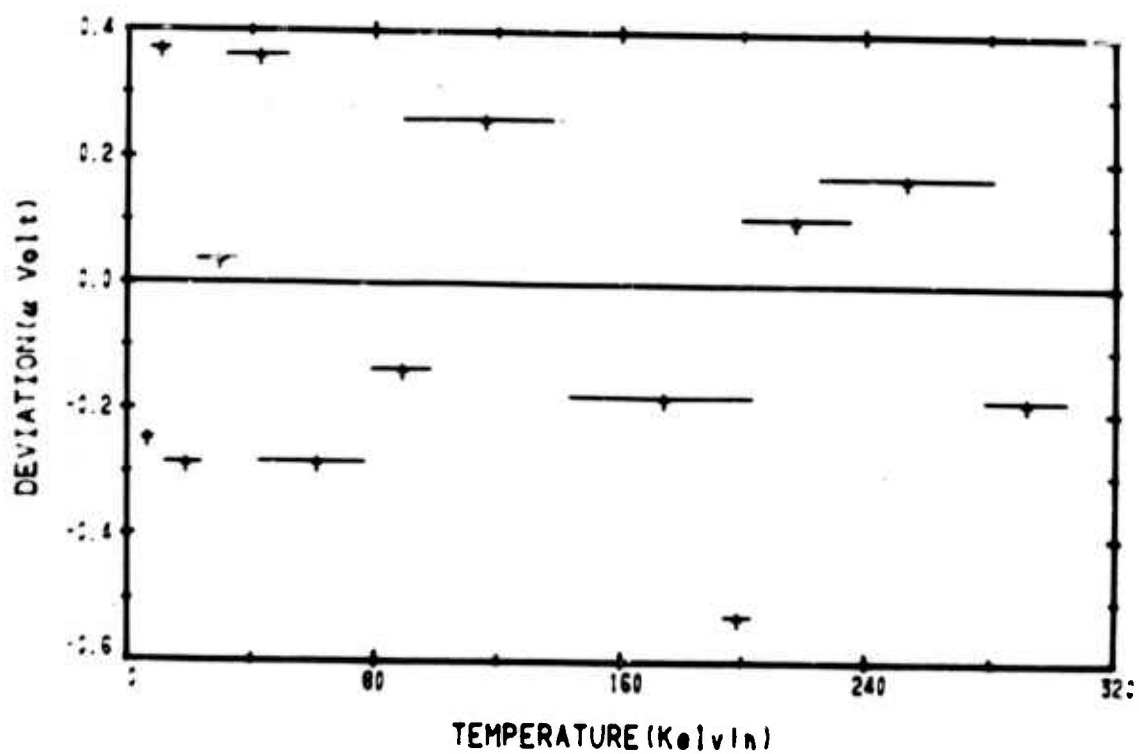


Figure 9. Thermovoltage deviations for INCO LEA.

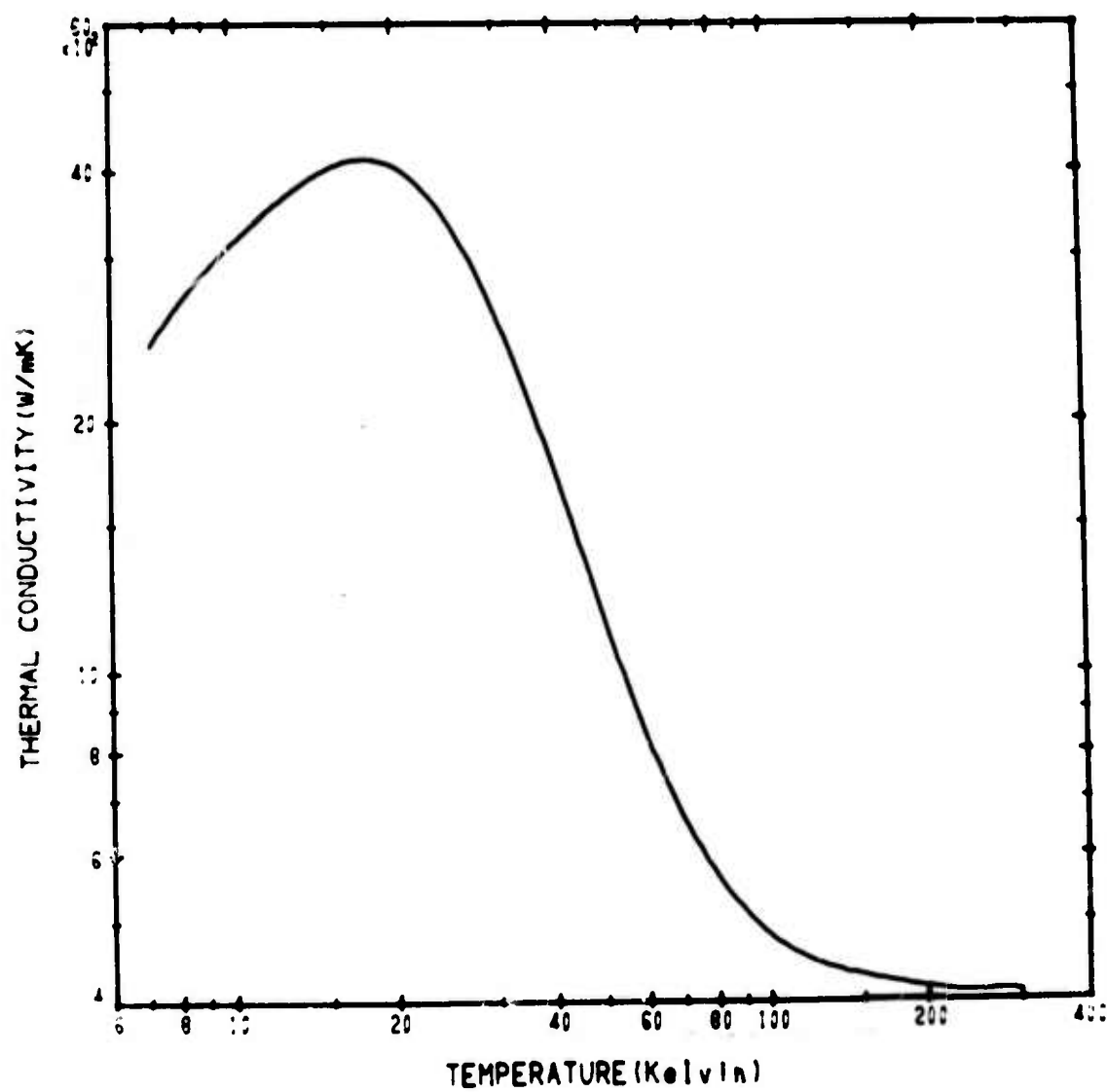


Figure 10. Thermal conductivity of OFHC copper.

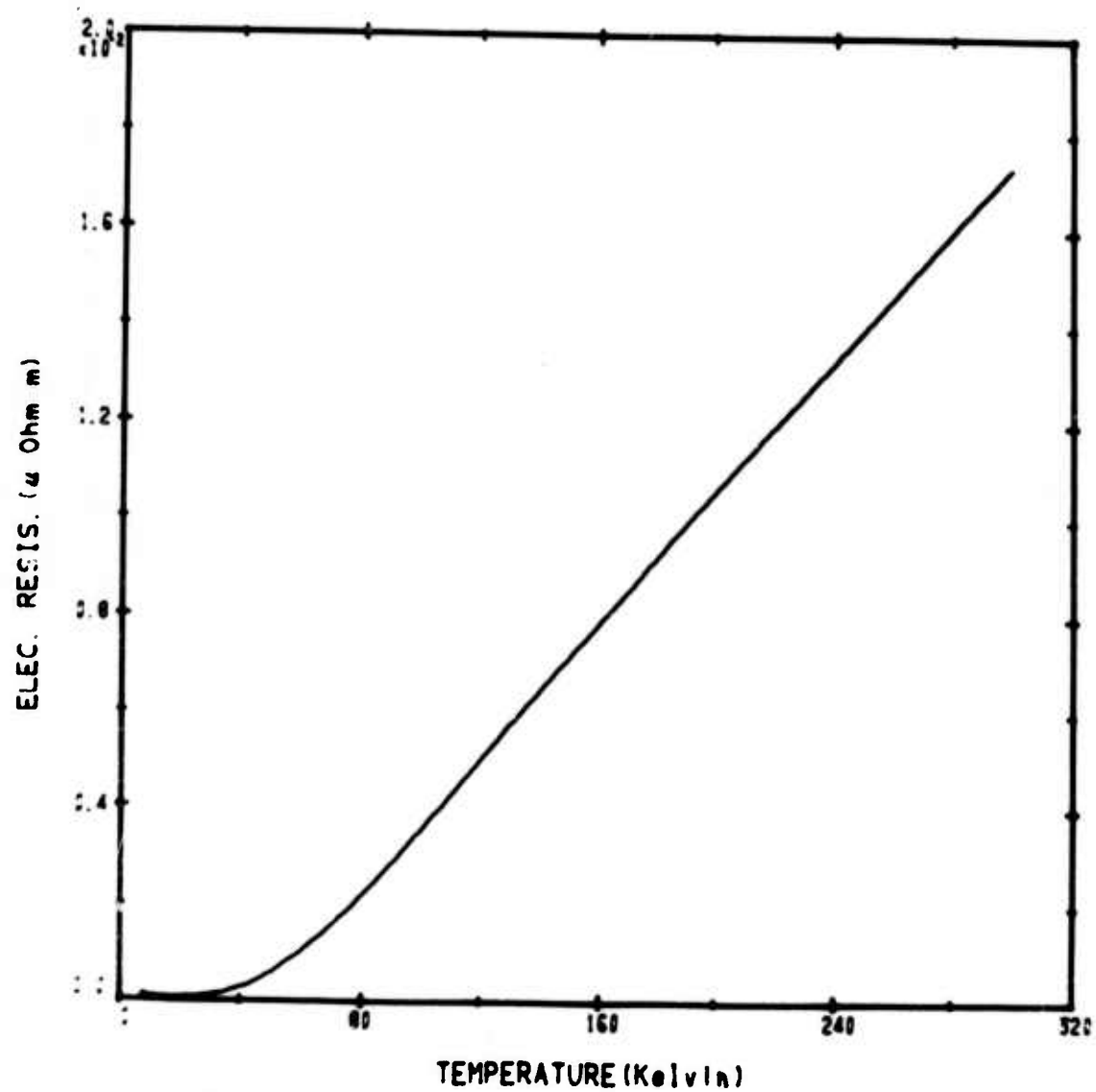


Figure 11. Electrical resistivity of OFHC copper.

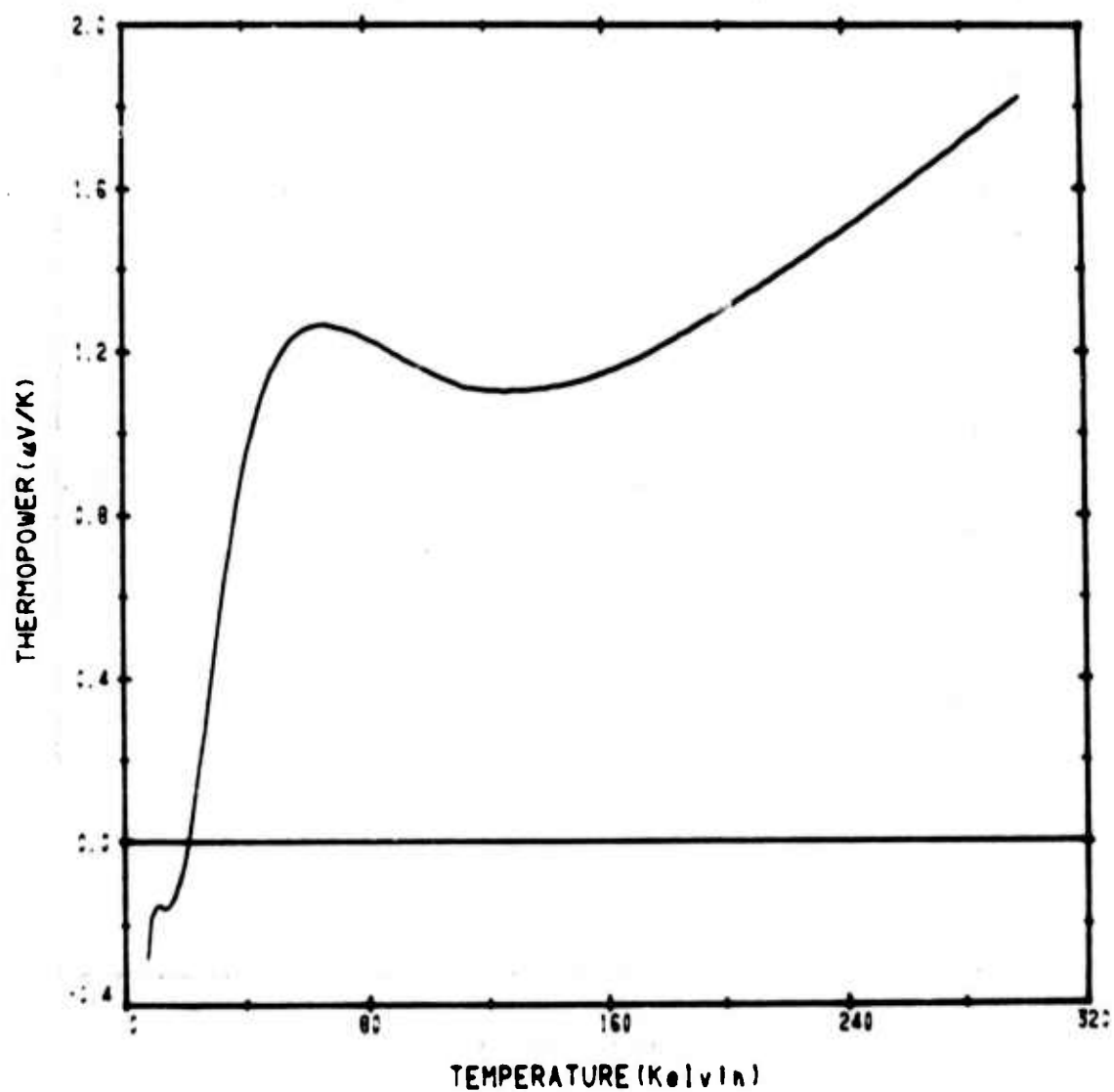


Figure 12. Thermopower of OFHC copper.

Reproduced from  
best available copy.



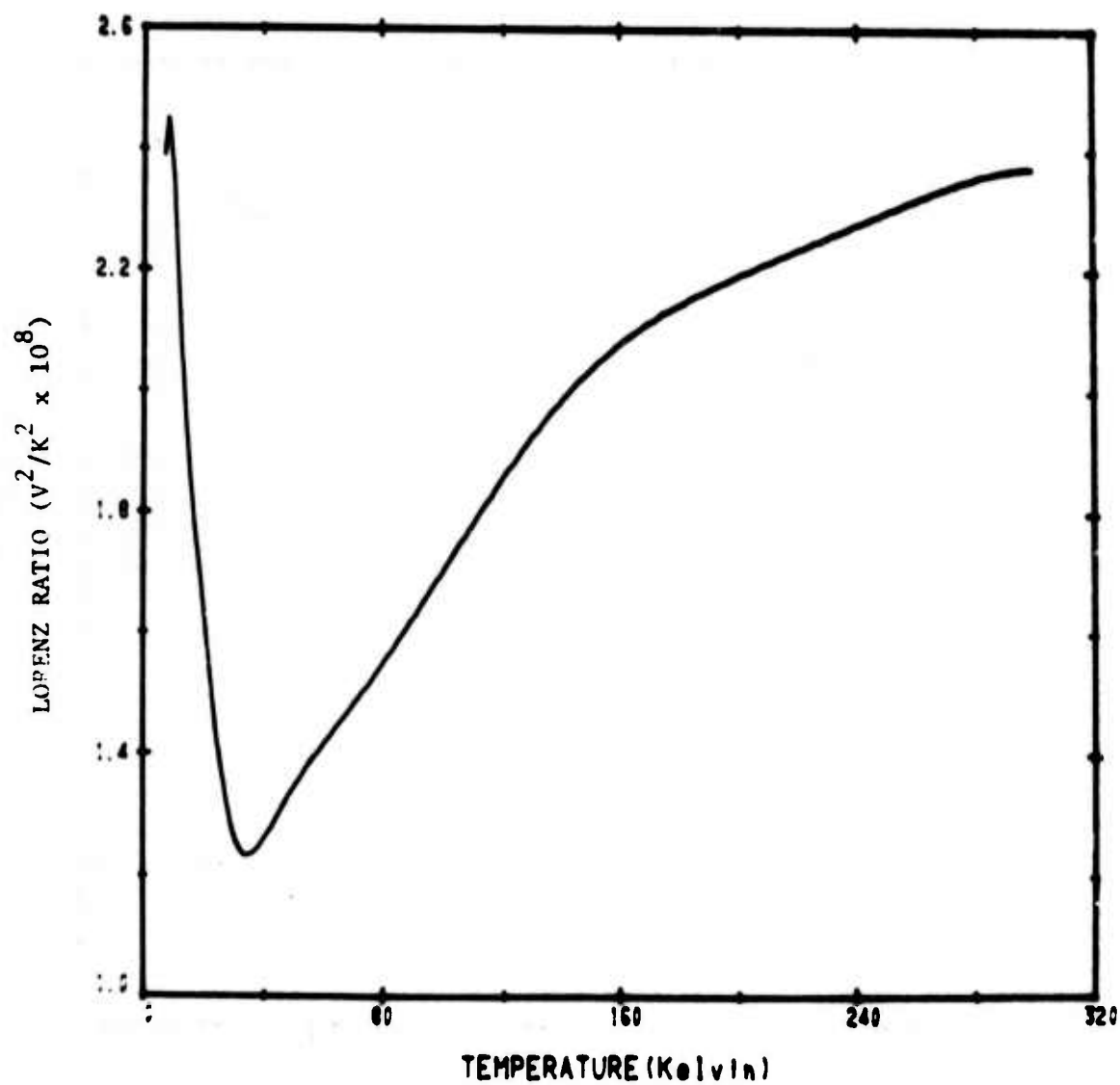


Figure 13. Lorenz ratio of OFHC copper.

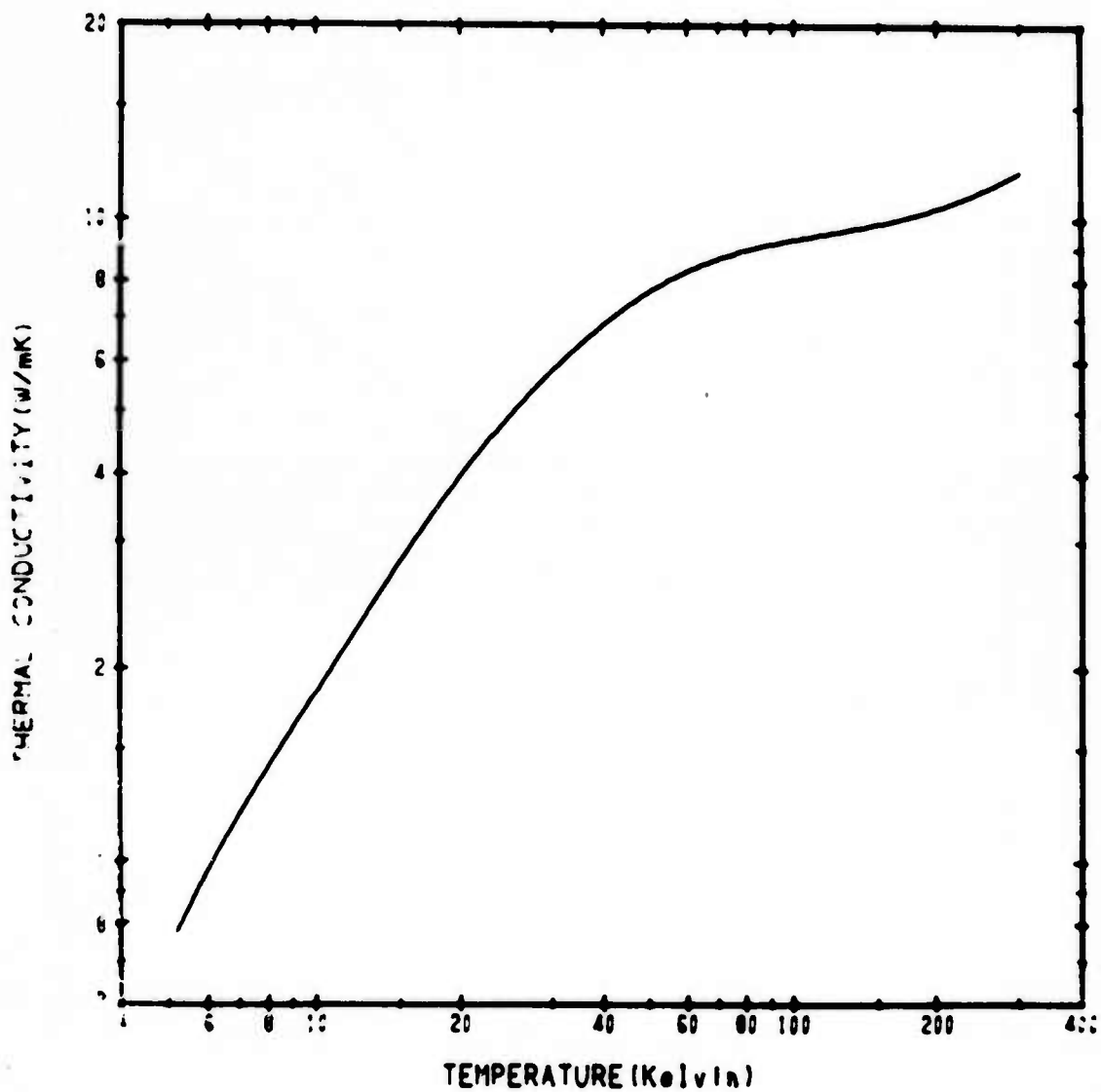


Figure 14. Thermal conductivity of Inconel X-750.

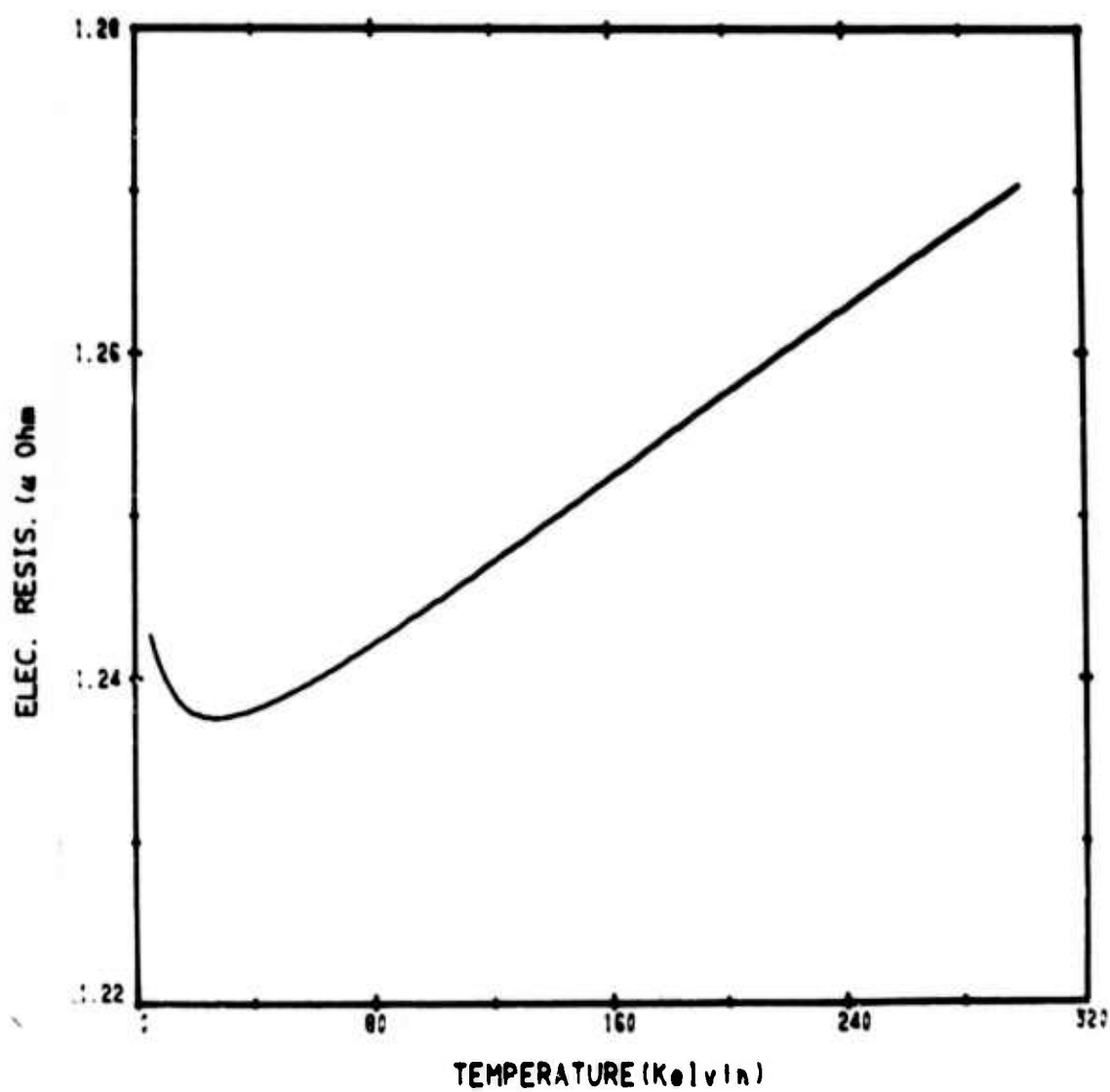


Figure 15. Electrical resistivity of Inconel X-750.



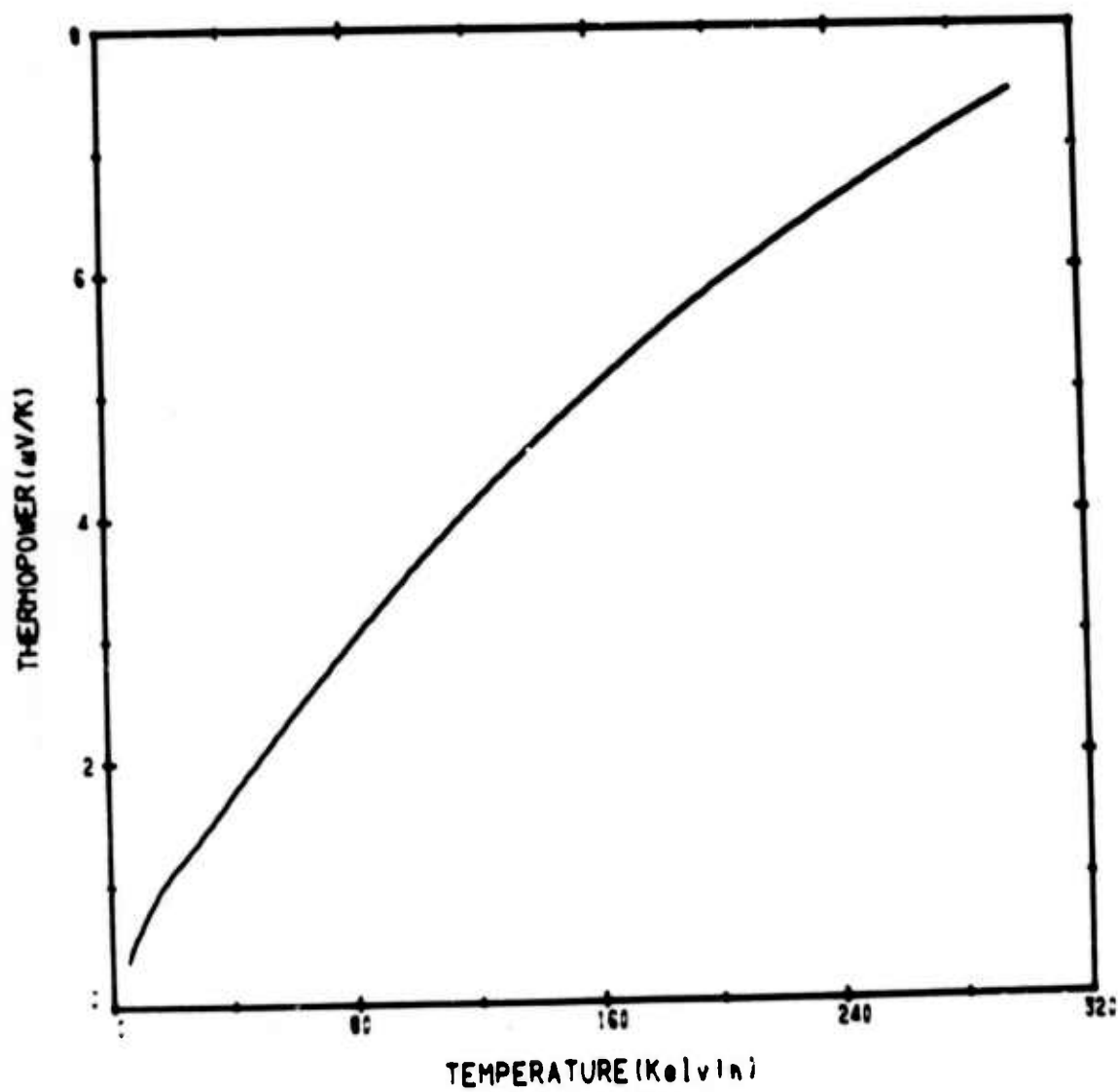


Figure 16. Thermopower of Inconel X-750.

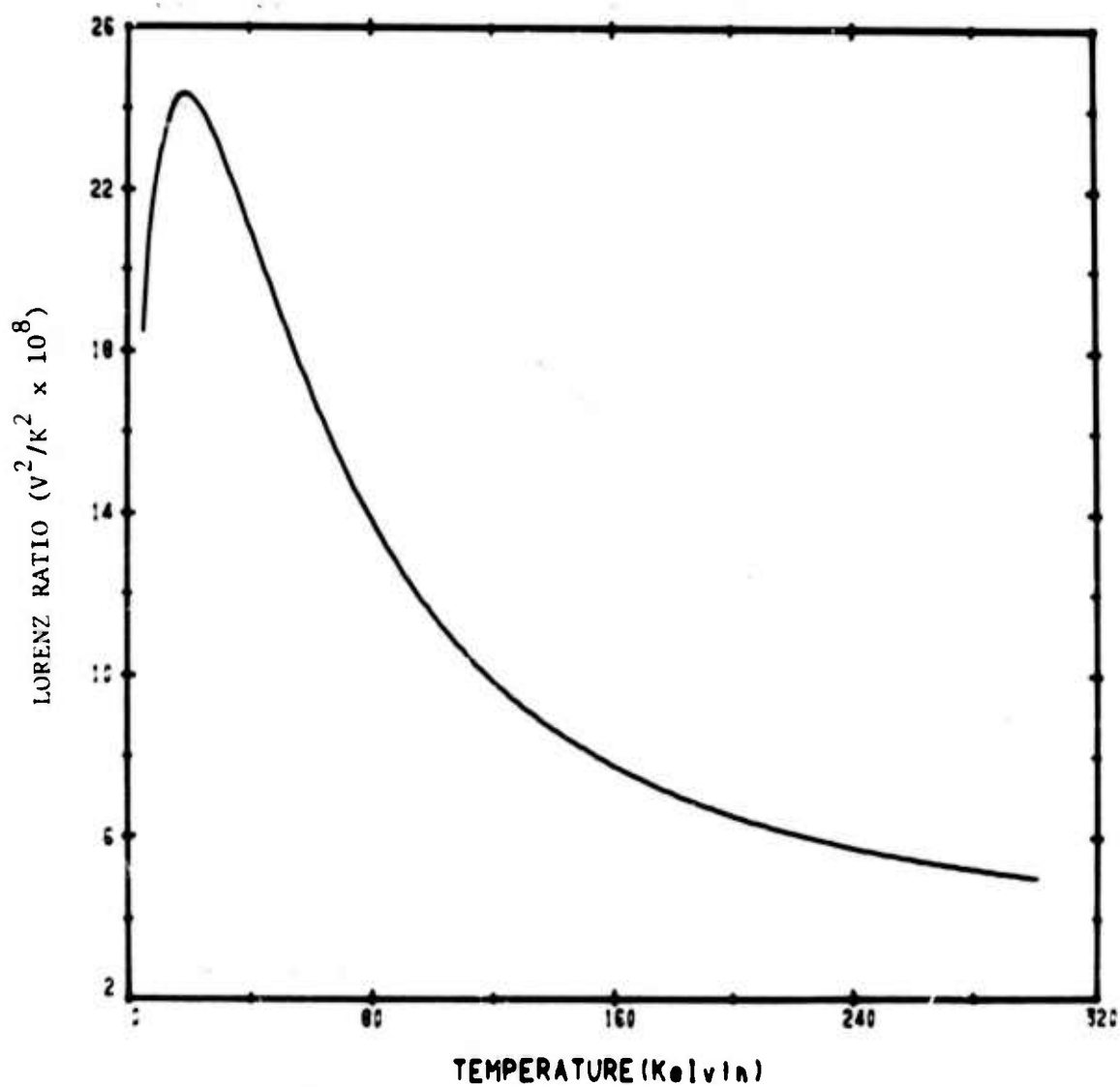


Figure 17. Lorenz ratio of Inconel X-750.

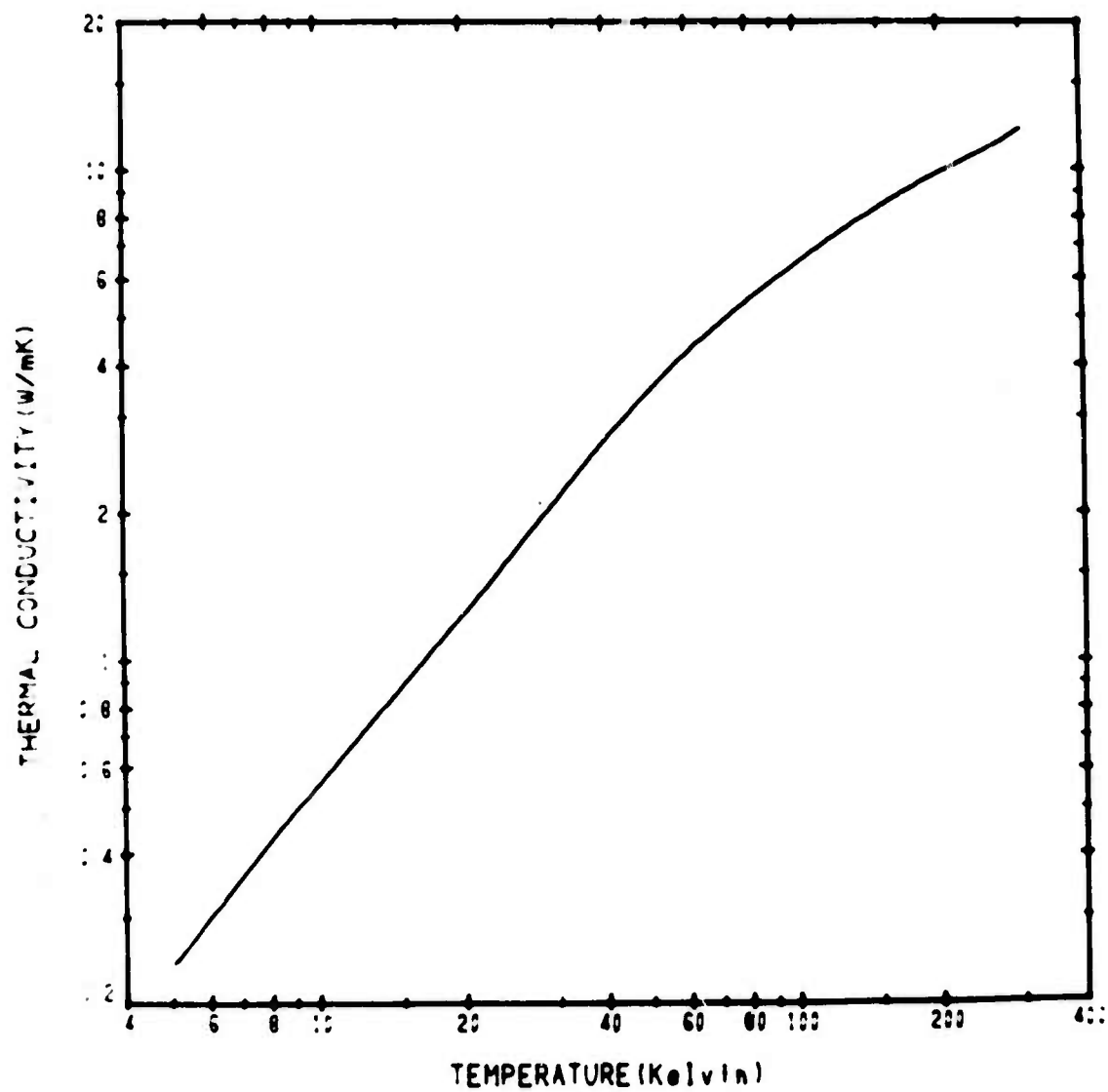


Figure 18. Thermal conductivity of INCO LEA.

Reproduced from  
best available copy.



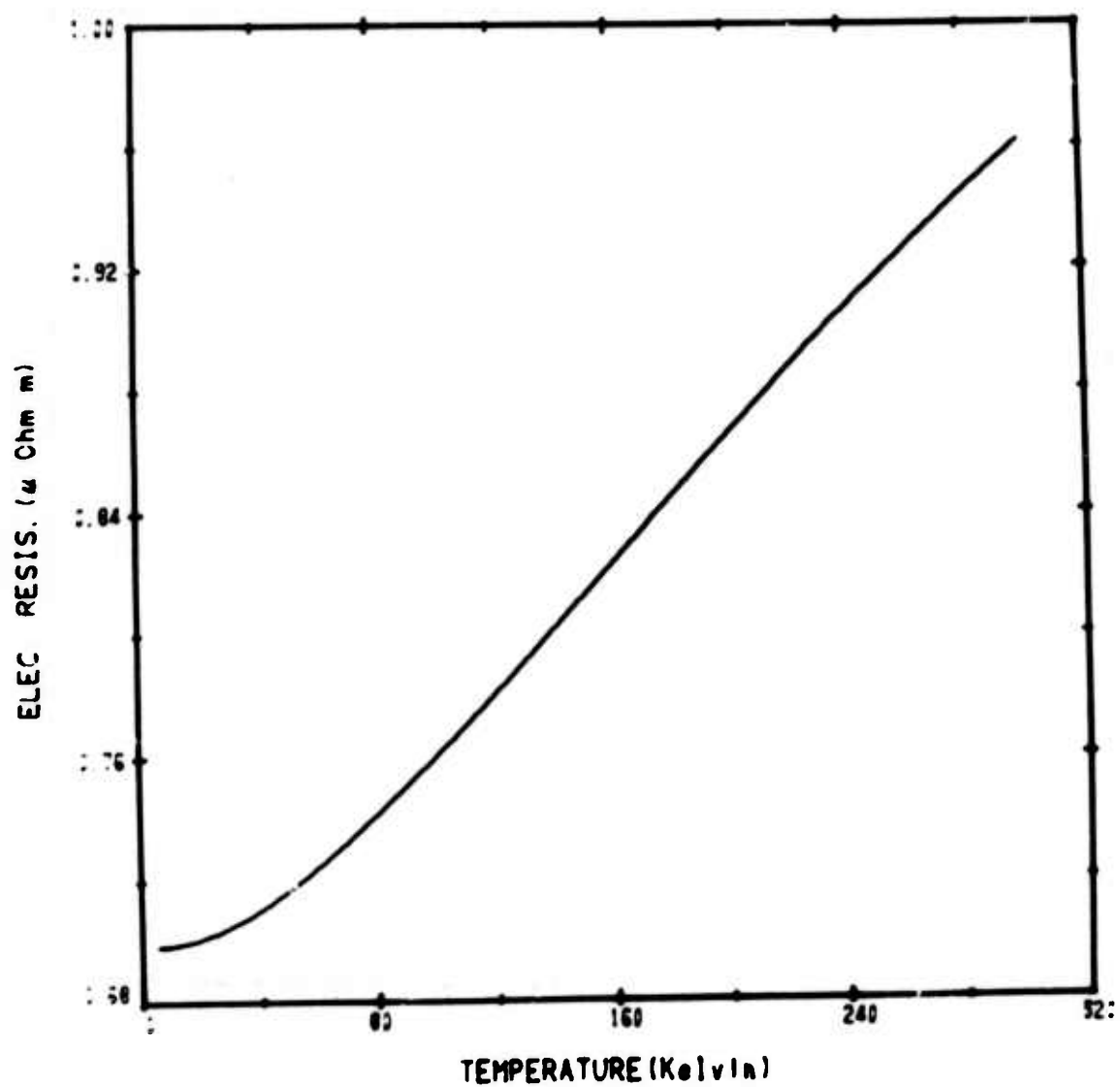


Figure 19. Electrical resistivity of INCO LEA.

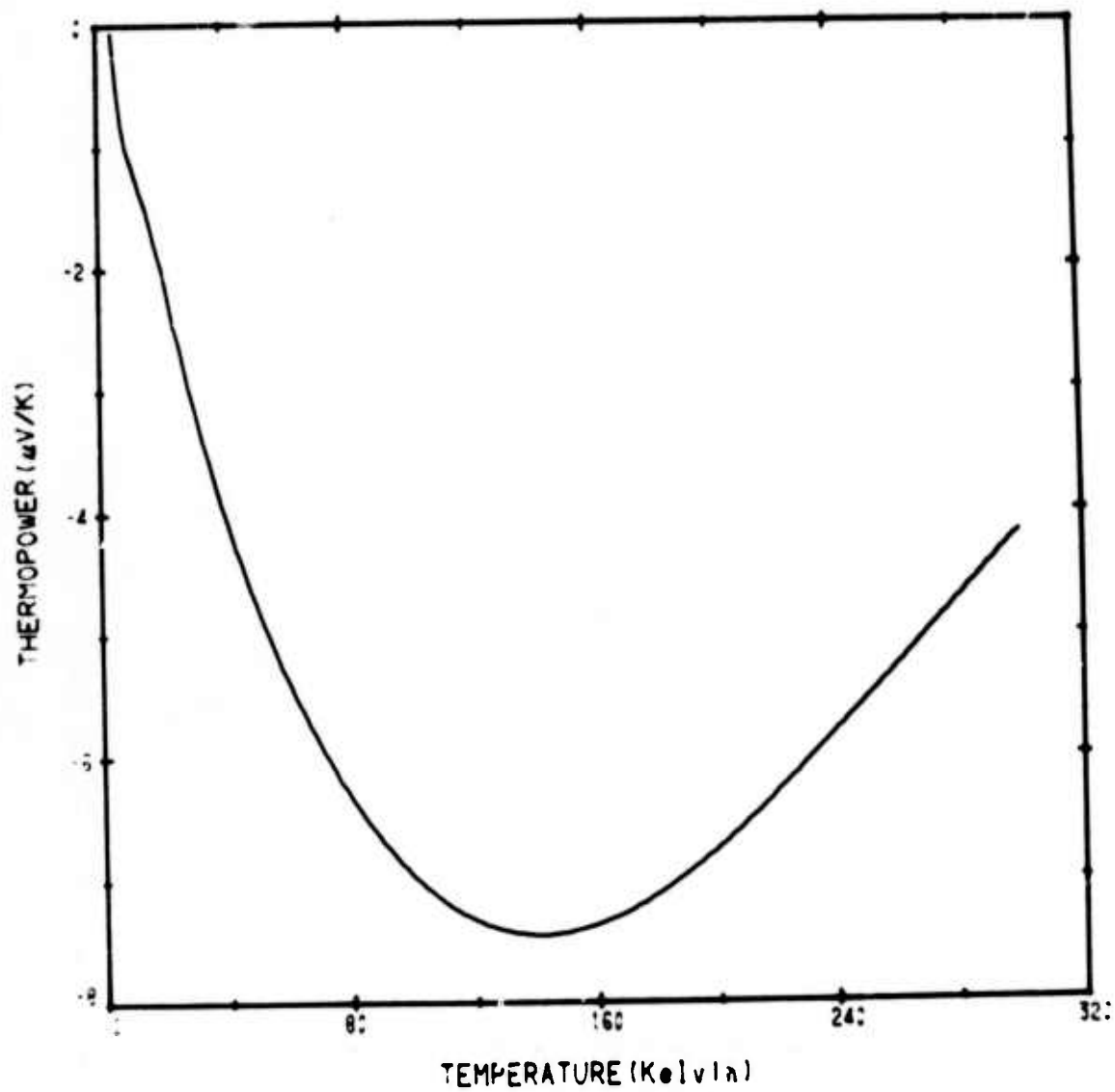


Figure 20. Thermopower of INCO LEA.

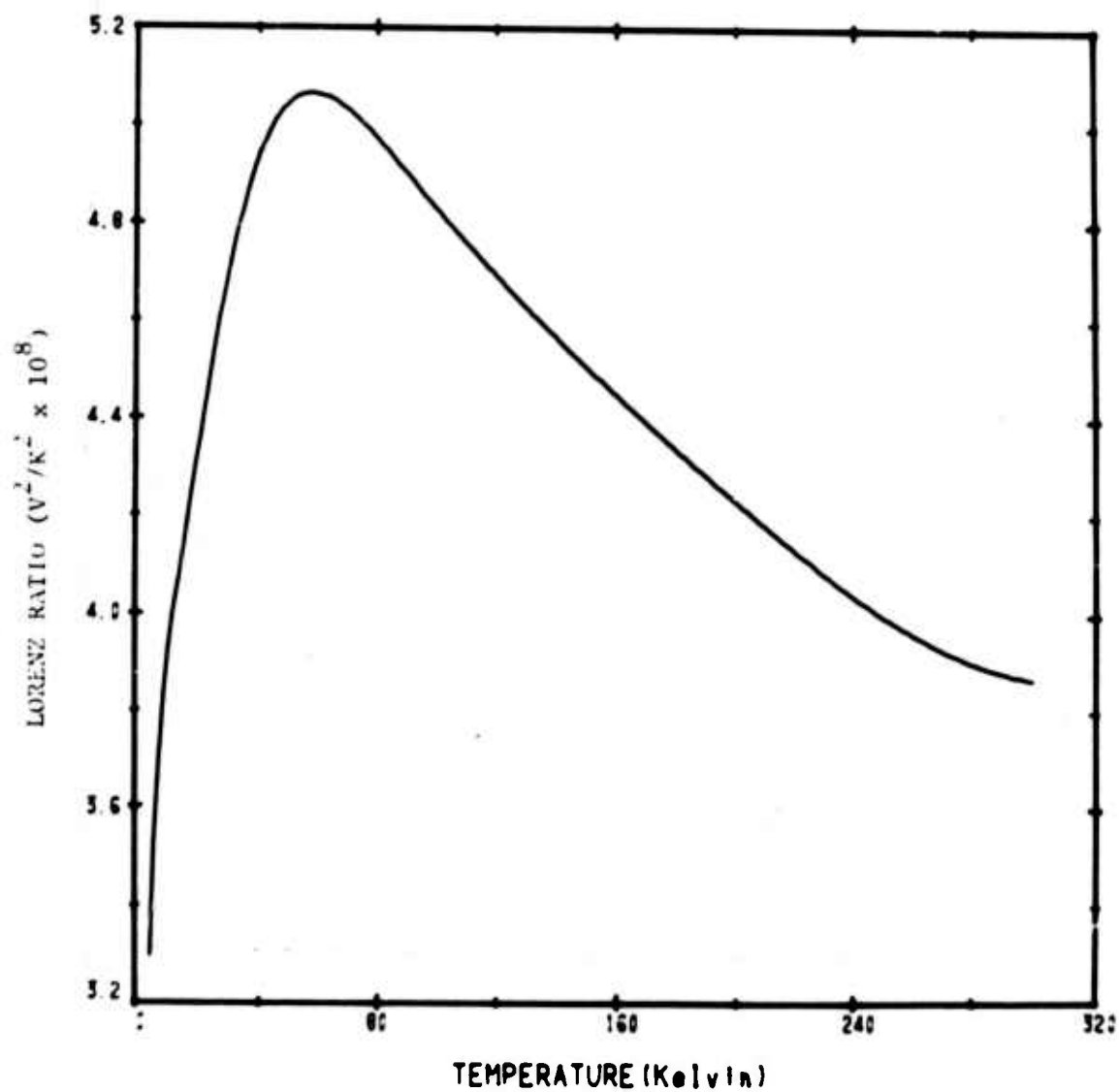


Figure 21. Lorenz ratio of INCO LEA.

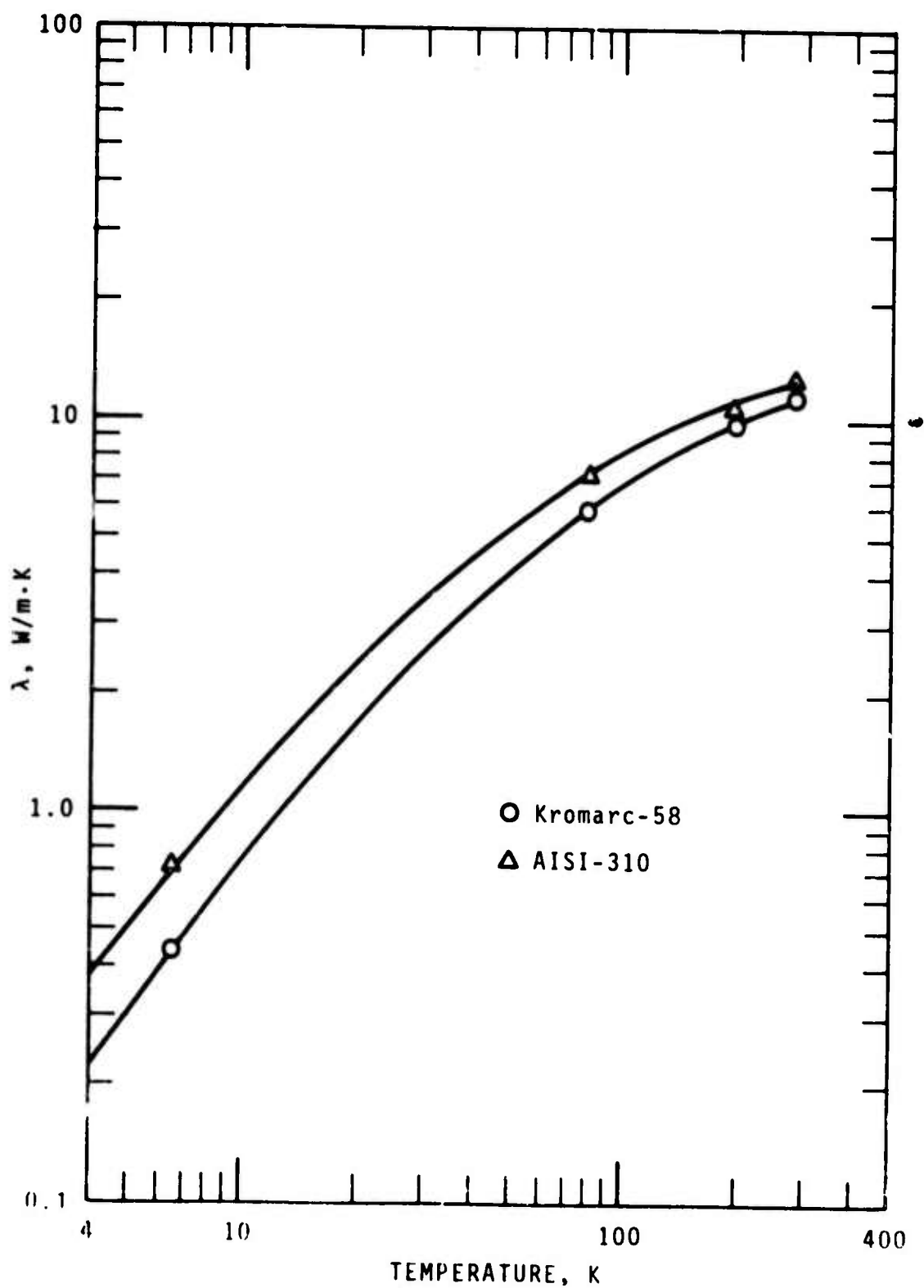


Figure 22. Thermal conductivity data for Kromarc-58 and AISI-310 stainless steels.

List of Tables

	Page
1. Parameters in equations 1, 2, and 3 . . . . .	31
2. Thermal and Electrical Properties of OFHC copper. . . . .	32
3. Thermal and Electrical Properties of Inconel X-750. . . . .	33
4. Thermal and Electrical Properties of INCO LEA . . . . .	34
5. Thermal Conductivity Data for Kromarc-58 and AISI-310 Stainless Steels . . . . .	35



Table 1. Parameters in equations 1, 2, and 3.

OFHC COPPER (1)

	THERMAL CONDUCTIVITY	ELECTRICAL RESISTIVITY	THERMOPOWER
1	-1.36268502+001	-3.03423717-007	-3.00784822+002
2	5.56605061+001	1.08781360-006	1.04739120+003
3	-6.77669751+001	-1.71261727-006	-3.53837071+003
4	4.20585825+001	1.55906711-006	3.39074429+003
5	-1.53173073+001	-9.08503179-007	-1.76743497+003
6	3.41087994+000	3.53969657-007	5.10924193+002
7	-4.57550282-001	-9.33564610-008	-7.71518643+001
8	3.40031769-002	1.64546588-008	4.76151607+000
9	-1.07658075-003	-1.05507554-009	
10	5.03011996-003	1.20856094-010	
11	-1.27146569-004	-3.45814932-012	

INCONEL X-750 STMP (1)

	THERMAL CONDUCTIVITY	ELECTRICAL RESISTIVITY	THERMOPOWER
1	-6.45163672+001	1.21912799-006	-2.25324036+001
2	1.02907693+002	4.51454338-008	1.43026970+002
3	-2.32001559+002	-3.00860094-008	-1.05603514+002
4	1.72630363+002	8.64270587-009	1.07305620+002
5	-8.31769298+001	-1.19334919-009	-2.49926242+001
6	2.70836612+001	7.15256039-011	2.93902707+000
7	-6.03196698+000		
8	9.07810755-001		
9	-8.03870489-002		
10	5.03011996-003		
11	-1.27146569-004		

INCO LEA 57A

	THERMAL CONDUCTIVITY	ELECTRICAL RESISTIVITY	THERMOPOWER
1	-1.781212+001	9.97525213-007	3.33951242+002
2	9.93895753+001	-7.51111281-007	-1.05240704+003
3	-4.561598+001	7.01142521-007	3.95134962+003
4	5.73813284+001	-4.39615174-007	-4.43311928+003
5	-4.547938+001	1.45214569-007	2.74953751+003
6	2.1514384+001	-2.01979268-008	-9.61485142+002
7	-6.4732371-001	2.98151317-009	1.75484331+002
8	5.61891387-002	-1.31724755-010	-1.28795595+001
9	-1.07658075-003	-1.05507554-009	
10	5.03011996-003	1.20856094-010	
11	-1.27146569-004	-3.45814932-012	

Reproduced from  
best available copy.

Table 2. Thermal and Electrical Properties of GFHC copper.

TEMP (K)	THERMAL CONDUCTIVITY (W/M K)	ELECTRICAL RESISTIVITY (NANO OHM M)	LORENZ NUMBER ( $\mu\text{V/K}$ ) $2 \times 10^{-11}$	THERMOPOWER (MICROVOLTS/K)
8	2730	0.07156	2.45	-0.21
9	3000	0.07302	2.44	-0.17
10	3230	0.07305	2.36	-0.16
12	3610	0.07132	2.15	-0.16
14	3900	0.07070	1.97	-0.16
16	4070	0.07243	1.84	-0.14
18	4120	0.07605	1.74	-0.13
20	4050	0.08098	1.64	-0.03
25	3550	0.09911	1.41	0.19
30	2870	0.1324	1.27	0.46
35	2250	0.1915	1.23	0.71
40	1770	0.2845	1.26	0.81
45	1410	0.4146	1.30	0.86
50	1150	0.5819	1.34	0.85
60	834	1.017	1.41	0.25
70	664	1.561	1.48	0.26
80	568	2.180	1.55	0.23
90	513	2.849	1.62	0.19
100	480	3.545	1.70	0.15
120	448	4.972	1.86	0.11
140	434	6.397	1.98	0.11
160	426	7.801	2.08	0.15
180	420	9.185	2.14	0.21
200	415	10.56	2.19	0.31
220	412	11.92	2.23	0.39
240	411	13.28	2.28	0.51
260	412	14.64	2.32	0.61
280	412	15.99	2.35	0.71
300	411	17.32	2.37	0.82

Table 3. Thermal and Electrical Properties of Inconel X-750.

TEMP (K)	THERMAL CONDUCTIVITY (W/M K)	ELECTRICAL RESISTIVITY (NANO OHM M)	LORENZ NUMBER ( $\mu\text{V/K}^2 \times 10^{-8}$ )	THERMOPOWER (MICROVOLTS/K)
6	0.962	1242	19.92	0.41
7	1.18	1242	20.92	0.49
8	1.39	1241	21.55	0.55
9	1.60	1241	22.05	0.60
10	1.81	1240	22.51	0.65
12	2.26	1239	23.29	0.76
14	2.70	1239	23.87	0.85
16	3.13	1238	24.21	0.94
18	3.54	1238	24.35	1.02
20	3.93	1238	24.34	1.10
25	4.82	1238	23.84	1.23
30	5.58	1238	23.01	1.38
35	6.23	1238	22.04	1.54
40	6.79	1238	21.03	1.70
45	7.27	1238	20.00	1.87
50	7.66	1239	18.99	2.03
60	8.26	1240	17.07	2.35
70	8.66	1241	15.35	2.67
80	8.93	1242	13.87	2.98
90	9.12	1243	12.60	3.27
100	9.27	1244	11.54	3.55
120	9.50	1247	9.88	4.09
140	9.71	1250	8.67	4.58
160	9.92	1252	7.77	5.03
180	10.1	1255	7.07	5.45
200	10.4	1257	6.53	5.84
220	10.6	1260	6.09	6.20
240	10.9	1263	5.75	6.54
260	11.2	1265	5.46	6.86
280	11.5	1268	5.22	7.16
300	11.8	1270	5.00	7.45

Table 4. Thermal and Electrical Properties of INCO LEA.

TEMP (K)	THERMAL CONDUCTIVITY (W/M K)	ELECTRICAL RESISTIVITY (MHO CM)	LORENZ NUMBER ( $\mu\text{V/K}^2 \times 10^{-11}$ )	THERMOPOWER (MICROVOLTS/K)
6	1.297	697.4	3.46	-1.37
7	1.361	697.0	3.62	-1.62
8	1.426	698.1	3.72	-1.82
9	1.490	698.4	3.82	-1.95
10	1.554	698.6	3.87	-2.06
12	1.683	699.1	3.98	-2.22
14	1.814	699.5	4.07	-2.37
16	1.948	700.0	4.15	-2.55
18	2.09	700.6	4.23	-2.75
20	2.23	701.2	4.32	-2.97
25	2.61	703.1	4.52	-3.56
30	2.99	705.2	4.69	-4.11
35	2.39	707.1	4.83	-4.61
40	2.78	708.4	4.94	-4.83
45	3.16	713.5	5.00	-4.84
50	3.52	716.0	5.05	-4.76
60	4.21	724.1	5.16	-5.36
70	4.81	732.1	5.23	-5.87
80	5.37	741.9	4.97	-6.31
90	5.88	751.2	4.91	-6.66
100	6.36	759.9	4.83	-6.95
120	7.22	781.3	4.69	-7.32
140	7.97	801.4	4.57	-7.45
160	8.65	822.6	4.45	-7.37
180	9.24	844.3	4.34	-7.13
200	9.77	865.5	4.23	-6.76
220	10.2	886.1	4.13	-6.31
240	10.6	906.1	4.04	-5.81
260	11.0	925.4	3.96	-5.26
280	11.4	943.9	3.91	-4.72
300	11.8	961.4	3.87	-4.17

Reproduced from  
best available copy.



Table 5. Thermal conductivity data for Kromarc-58 and  
AISI-310 stainless steels

Material	Temperature (K)	$\lambda$ (W/mK)
Kromarc-58	6.50	0.440
	79.1	5.90
	196	9.70
	277	11.5
AISI-310	6.46	0.720
	79.4	7.15
	196	10.8
	277	12.5

NBSIR

SEMI-ANNUAL REPORT ON MATERIALS RESEARCH IN SUPPORT OF  
SUPERCONDUCTING MACHINERY

MAGNETOTHERMAL CONDUCTIVITY

L. L. Sparks and F. R. Fickett

Cryogenics Division  
Institute for Basic Standards  
National Bureau of Standards  
Boulder, Colorado 80302

October 1974

### Summary: Magnetothermal Conductivity

The magnetothermal conductivities of Inconel 718 and oxygen-free copper have been determined. The data are presented as thermal conductivity as a function of temperature,  $\lambda(T)$ , thermal conductivity as a function of magnetic field,  $\lambda(H)$ , and as the relative change in thermal resistivity as a function of magnetic field,  $\Delta W/W_0(H)$ . When possible the data are compared to existing data. In these limited instances, agreement is within the accuracy of our measurements. The effect of a magnetic field is always to reduce the thermal conductivity. The reduction, at 8 Tesla, for Inconel 718 is approximately 15% at 5.5 K and 50% at 19.5 K; for copper (RRR = 107), the reduction is about 100% at 5.5 K and 60% at 19.5 K. The magnetic-field effect increases with increasing temperature for Inconel and decreases with increasing temperature for copper. The temperature dependence of  $\Delta W/W_0$  exhibited by Inconel is associated with the negative temperature derivative of the zero field resistivity,  $dp_0/dT$ , shown by Inconel 718 below 20 K.

### Contents: Magnetothermal Conductivity

	Page
1. <u>Introduction</u> . . . . .	39
2. <u>Procedures</u> . . . . .	39
2.1 <u>Apparatus</u> . . . . .	39
2.2 <u>Methods</u> . . . . .	40
2.3 <u>Materials</u> . . . . .	41
3. <u>Results</u> . . . . .	41
4. <u>Discussion</u> . . . . .	42
5. <u>References</u> . . . . .	45
<u>List of Figures</u> . . . . .	46

# MAGNETOTHERMAL CONDUCTIVITY

L. L. Sparks and F. R. Fickett

## 1. Introduction

The objective is to determine the effect of magnetic fields on the thermal conductivity of technically important metals. The need for this information arises from the development of rotating machinery operating at cryogenic temperatures. The existing world's literature on magnetothermal conductivity,  $\lambda(H)$ , is concerned almost exclusively with scientific materials, e.g., very pure materials and single crystals. A complete bibliography of the subject was given by Sparks, et al. [1] in the previous report.

The materials studied in this program are being used in superconducting motors and generators. Optimum design of these machines, which must operate at temperatures between 4 K and 20 K while in magnetic fields up to 10 Tesla, requires a detailed knowledge of how the thermal properties of the constituent materials are affected by a magnetic field. The broad material categories of interest include superconductor stabilizing materials such as copper and aluminum, and structural materials such as Inconels, stainless steels, and metallic composites.

The experimental determination of  $\lambda(H)$  of metals in high fields is complicated by the requirement that the specimen be contained in a region of homogeneous field. For magnets of reasonable size, this restriction necessitates small specimen lengths and resultant small temperature gradients along the specimens. Our  $\lambda(H)$  probe is designed to be used in a superconducting solenoid with a 3.8 cm bore and a 2.5 cm homogeneous (1%) field sphere. Our specimen length is therefore limited to approximately 2.5 cm.

## 2. Procedures

### 2.1 Apparatus

A brief review of the cryostat, instrumentation, and experimental procedures is given below. For further details refer to [1].

Figure 1 shows the principal components of the probe with a specimen mounted in the longitudinal position (magnetic field parallel to the heat flow). A shorter specimen may be mounted horizontally so that the heat flow is perpendicular to the magnetic field for transverse measurements.



The cooling required to attain specimen temperatures in the range between 4 and 20 K is provided by immersing the probe chamber in liquid helium. Radiative heat transfer is minimal in this temperature range, and gas conduction is eliminated by evacuating the specimen chamber to  $5 \times 10^{-6}$  torr. Our operating pressure is reduced to less than this by a gas adsorption agent in the sealed probe space.

The basic operation of the system involves balancing electrical power supplied to three heaters with the heat leak to the liquid helium bath via the THERMAL LINKS (capitalized parts refer to figure 1). The electrical heaters are wound one each on the TEMPERATURE CONTROLLED HEAT SINK (TCHS), the SPECIMEN, and the TEMPERING POST. The power supplied to the TCHS determines the approximate temperature of the specimen; the SPECIMEN HEATER is used to establish a temperature gradient along the specimen; and, the TEMPERING POST HEATER is used to eliminate any temperature difference between the specimen and the tempering post. The TEMPERING POST and TCHS heaters are automatically controlled during all tests while a constant current is supplied to the SPECIMEN HEATER.

The thermometers used in the probe are three 1/8 watt, 100 ohm Allen Bradley carbon resistors (CRT's) and a single calibrated germanium resistor (GRT). The CRT's are located, one each, in the TCHS, and the two THERMOMETER BLOCKS, which are clamped to the specimen. The GRT is located in the TCHS and is used for zero-magnetic-field calibration of the GRT resistors. The effect of the magnetic field on the resistance of the CRT's is taken to be that published by Neuringer and Shapira [2]. All resistance measurements on the two specimen CRT's are made using a lock-in amplifier as both detector and power supply for an AC bridge. Both absolute and difference resistance measurements are possible using this system.

## 2.2 Methods

Determination of  $\lambda(H)$  and the electrical magnetoresistivity,  $\rho(H)$ , requires two types of tests, which are referred to as isothermal tests and gradient tests. For an isothermal test the CRT resistances are read with the specimen heater off. A series of these measurements at different temperatures determines the resistance-versus-temperature characteristics for

each CRT at zero field. Data from Neuringer and Shapira [2], on values of  $(R_H - R_0)/R_0$  then allows the CRT's to be calibrated for  $H \neq 0$ . Gradient tests are made with the SPECIMEN HEATER on. This power establishes a thermal gradient along the specimen. Measurement of the heater power and the resulting CRT resistances allows the specimen thermal conductivity to be determined. Electrical resistance is determined by passing a current through the specimen and measuring the resultant voltage drop. The resistivity is calculated at the average temperature of the specimen.

### 2.3 Materials

Two materials have been tested - Inconel 718 and oxygen-free copper. The Inconel specimen was in the age-hardened condition. The Rockwell hardness was C39 (not B39 as reported in [1]). The copper specimen was cold swaged from 0.476 cm diameter rod to 0.25 cm diameter rod. The rod was etched and annealed several times during the swaging process. The final anneal was at 850°C for one hour in a vacuum of  $10^{-6}$  torr. The resistivity of the resulting specimen at 5 K is 0.146 n $\Omega$ m (RRR = 107).

### 3. Results

The first material to be tested in the magnetothermal conductivity system was Inconel 718. A specimen from the same heat was tested by Hust, et al. [3]; zero field values of  $\lambda$  and  $\rho$  were determined. Their experiment, done in the NBS precision thermal-conductivity apparatus, has an estimated error of not more than 2%. Their results for  $\lambda(T)$  are labeled HUST on figure 2. The figure also shows our data on thermal conductivity as a function of temperature at several magnetic fields. Comparison of electrical resistivities between the two specimens at zero field indicates a difference of about 0.5%.

Figures 3 and 4 present thermal conductivity and relative change in thermal resistance,  $\Delta W/W_0$ , as functions of magnetic field with temperature as a parameter. The ordinate in figure 4 is equivalent to  $(\lambda_0 - \lambda_H)/\lambda_H$  using the general relationship  $W(\text{thermal resistivity}) = 1/\lambda$ . Figure 5 gives thermal conductivity as a function of temperature with magnetic field as a parameter for our copper specimen. Figures 6 and 7 present thermal conductivity and relative change in thermal resistance as functions of magnetic field with temperature as a parameter.

At present the best estimate of the system errors indicates probable uncertainty of 10 - 15% in the thermal conductivity. Comparison of our zero-field data to that of Hust, et al. [3] for Inconel 718 indicates  $\Delta\lambda/\lambda(\text{average}) = 8.6\%$  at 7 K, 5.7% at 12 K, and 4.6% at 19 K. These figures include possible real differences between the two specimens. One possible source of error that will be eliminated in the future is the value of the magnetic field in our solenoid. At the present time the magnetic-field -- magnet-current relationship is uncertain by approximately 2 - 6%. We recently acquired a precision rotating-coil gaussmeter that will allow calibration of the current-field relationship to approximately 0.1%. If, in fact, our present field calibration is significantly changed, both the Inconel 718 and the copper data will be appropriately adjusted.

#### 4. Discussion

Thermal conductivity is a complex phenomenon because many separate mechanisms are operating simultaneously to transmit energy through the material. Thermal conductivity is defined by the heat transfer equation

$$\dot{Q} = \lambda A \frac{dT}{dx} \quad (1)$$

where  $\dot{Q}$  is the heat current in watts (W),  $A$  is the cross sectional area in  $\text{m}^2$ ,  $T$  is in Kelvin (K), and thus  $\lambda$  has the units of W/mK.

Powell [4] gave an overview of transport properties in metals and a useful list of references. Briefly, the thermal energy in most materials is transported both by the lattice vibrations (phonons) and by the conduction electrons. It is conventional to designate the lattice component  $\lambda_g$ , and the electronic component  $\lambda_e$ . These conductivities make up the total thermal conductivity,

$$\lambda = \lambda_e + \lambda_g \quad (2)$$

Thermal resistance to each of these modes of heat flow arises from several interactions. For electrons the principal interactions retarding heat flow are electron-phonon, electron-impurity, and electron-defect; for phonons, the interactions are phonon-electron, phonon--point-defect, and phonon-dislocation. The lattice contribution,  $\lambda_g$ , at low temperatures is generally less

than 20% of the total thermal conductivity in pure metals but may predominate for some alloys [5].

One of the classical methods used to separate  $\lambda_e$  and  $\lambda_g$  is to apply a magnetic field. This has the effect of decreasing  $\lambda_e$  while presumably not affecting  $\lambda_g$  [6]. One would expect that  $\lambda$  (total) of a pure metal would be affected more than  $\lambda$  (total) for an alloy. This is borne out by our data as discussed below, and by the results of Fevrier and Morize [7]; this work will be discussed in more detail below.

The effect of an 80 kOe magnetic field is to decrease  $\lambda(H)$  for Inconel 718 by 14% and for copper by 104% at 5.5 K. At 19.5 K the reduction is 49% for Inconel and 58% for copper. The temperature dependence of  $\Delta W/W_0$  for Inconel, figure 4, is opposite that for copper, figure 7. The slope of  $\Delta W/W_0(T)$  is positive for Inconel and negative for copper. This "anomaly" appears to be a natural consequence of the thermal equivalent of Kohler's rule rather than a manifestation of the ferromagnetism seen in Inconel at these temperatures. Kohler's rule is the classical equation of electrical magnetoresistance and can be written

$$\frac{(\rho_H - \rho_0)}{\rho_0} = \frac{\Delta\rho}{\rho_0} = f\left(\frac{H}{\rho_0}\right), \quad (3)$$

i.e., the temperature dependence of  $\Delta\rho/\rho_0$  arises only through  $\rho_0$ . The ferromagnetic behavior of Inconel 718 below 77 K is a factor in the temperature dependence of  $\Delta W/W_0$ , but only to the extent that it affects  $W_0$ .

Figure 8c indicates the different temperature dependences discussed above. Non-magnetic metals with no magnetic impurities show a low temperature-resistivity versus temperature curve like that shown for copper in figure 8a; magnetic materials, on the other hand, frequently show a negative  $d\rho_0/dT$  below some critical temperature, as is the case with Inconel [3] (figure 8a). Since  $\Delta\rho$  ( $\equiv \rho_H - \rho_0$ ) is not a strong function of temperature,  $\Delta\rho/\rho_0(T)$  increases when  $\rho_0$  becomes smaller (Inconel), and decreases when  $\rho_0$  becomes larger (copper) as shown in figure 8b. There is no reason to expect vast differences between the electrical and thermal resistivities, although they are not identical functions of temperature. The thermal data illustrated in figure 8c seems quite reasonable for both metals.

The relationship between the electronic contribution to the thermal conductivity and the electrical conductivity is expressed by the Wiedemann-Franz-Lorenz law

$$L = \frac{\rho\lambda}{T} . \quad (4)$$

Procedures for predicting  $\lambda$  at  $H = 0$  from  $L$  and  $\rho$  data are reasonably successful and are discussed by Hust, et al. [5]. It is hoped that progress can be made in predictive schemes based on the electrical and thermal conductivities in non-zero fields, i.e.,

$$L(H) = \frac{\rho(H)\lambda(H)}{T} . \quad (5)$$

Magnetothermal data on many alloy groups will be necessary before any such schemes can be evaluated. For the present, let it suffice to observe, in figure 9, that the effect of increasing  $H$  is to reduce  $L$ .

In the case of copper, meaningful comparison to other data is difficult even at zero magnetic field. The electrical and thermal conductivity of pure copper is very sensitive to strain, thermal history, and trace impurities. Fickett [8] discussed the large effect annealing in a partial pressure of oxygen has on the RRR of copper. Fevrier and Morize [7] have reported relative magnetothermal conductivity data for two copper specimens, RRR = 62 and RRR = 162. Figure 10 shows the ratio of  $\lambda(H)/\lambda(0)$  as a function of magnetic field for their two specimens and our specimen (RRR = 107). The temperature of the Fevrier and Morize data is not given in reference [7] but is assumed to be 4 K; the temperature of our measurement is 5.5 K. The general behavior of two sets of data are similar. Resistivity, and therefore Lorenz-ratio data, are not available for our copper specimen due to the low-level voltages involved.

## 5. References

1. Materials research in support of superconducting machinery, National Bureau of Standards, Boulder, Colorado, Cryogenics Division, March 1974, NBSIR-74-359, AD-780 596/3WM.
2. Neuringer, L. J. and Shapira, Y., Low temperature thermometry in high magnetic fields, I. Carbon resistors RSI 40, (No. 10), 1914 (October, 1969).
3. Hust, J. G., Weitzel, D. H. and Powell, R. L., Thermal conductivity, electrical resistivity, and thermopower of aerospace alloys from 4 to 300 K, J. Res. NBS (U.S.) (Phys. and Chem.) 75A (No. 4), 269-277 (July - August, 1971).
4. Powell, R. L., Thermophysical Properties of Metals at Cryogenic Temperatures, ASTM Special Publication No. 387, 134 pp (ASTM, New York, 1966).
5. Hust, J. G. and Sparks, L. L., Lorenz ratios of technically important metals and alloys, Nat. Bur. Stand. (U.S.) Tech. Note 634 (February, 1973) 127 pp.
6. van Witzenburg, W. and Laubitz, M. J., Magnetoresistances and the phonon, Can. J. Phys. 46, 1887 (1968).
7. Fevrier, A. and Morize, D., The effect of magnetic field on the thermal conductivity and electrical resistivity of different materials, Cryogenics 13, 603 (1973).
8. Fickett, F. R., Oxygen aling of copper: a review, Mater. Sci. Eng. 14, 199 (1974).

# List of Figures

	Page
1. Magnetothermal conductivity probe and magnet . . . . .	47
2. Thermal conductivity of Inconel 718 as a function of temperature at several magnetic fields . . . . .	48
3. Thermal conductivity of Inconel 718 as a function of magnetic field at several temperatures . . . . .	49
4. Relative change in thermal resistance of Inconel 718 as a function of magnetic field at several temperatures . . . . .	50
5. Thermal conductivity of copper as a function of temperature at several magnetic fields . . . . .	51
6. Thermal conductivity of copper as a function of magnetic field at several temperatures . . . . .	52
7. Relative change in thermal resistance of copper as a function of magnetic field at several temperatures . . . . .	53
8. Characteristic curves of $\rho_0$ (zero field electrical resistivity), $\Delta\rho/\rho_0$ (relative electrical resistivity change in a magnetic field), and $\Delta W/W_0$ (relative thermal resistivity change in a magnetic field) for Inconel and copper below 20 K . . . . .	54
9. Lorenz ratios of Inconel 718 as a function of temperature at several magnet fields. . . . .	55
10. Comparison of the present magnetothermal conductivity data to that of Fevrier and Morize . . . . .	56

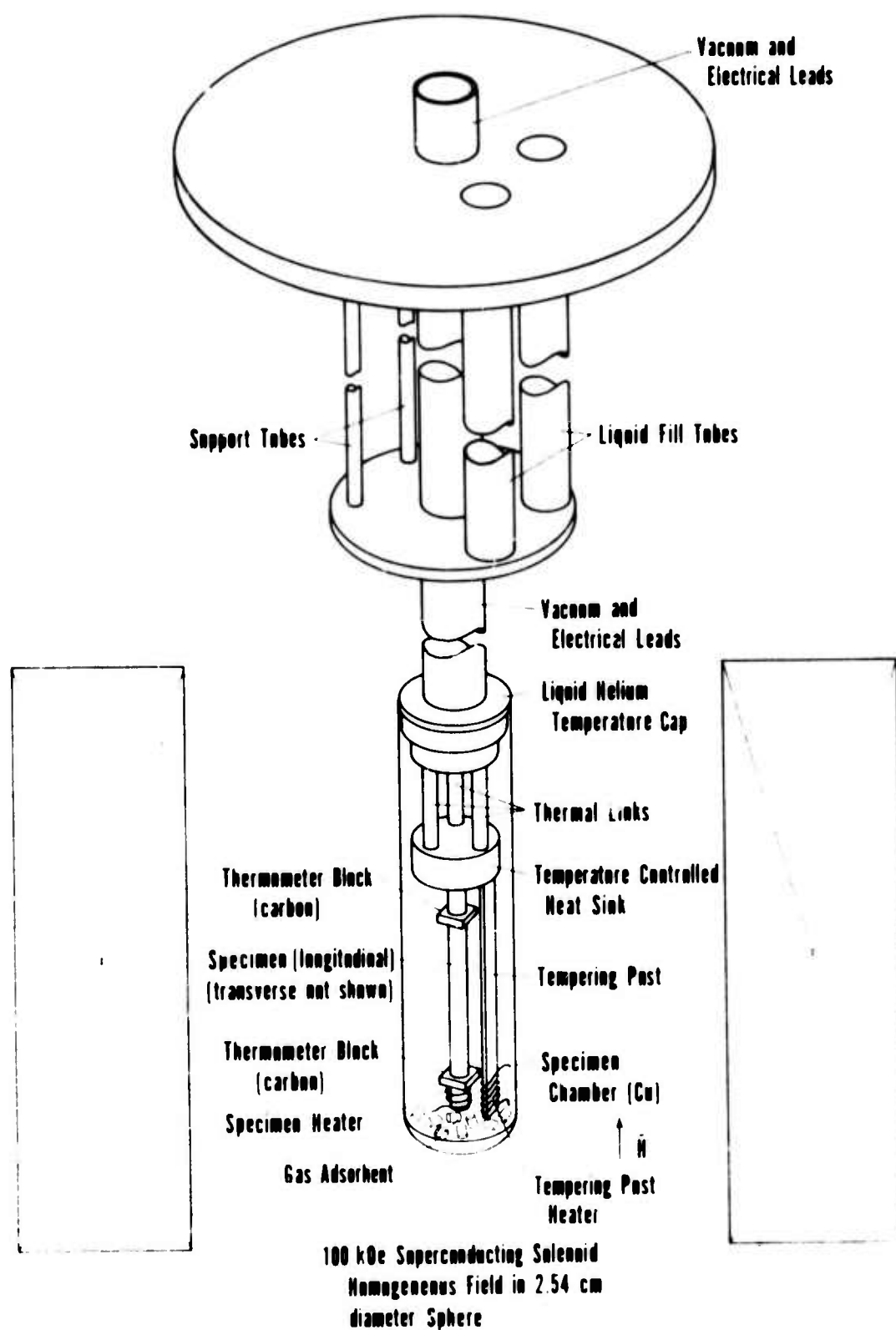


Figure 1. Magnetothermal conductivity probe and magnet.



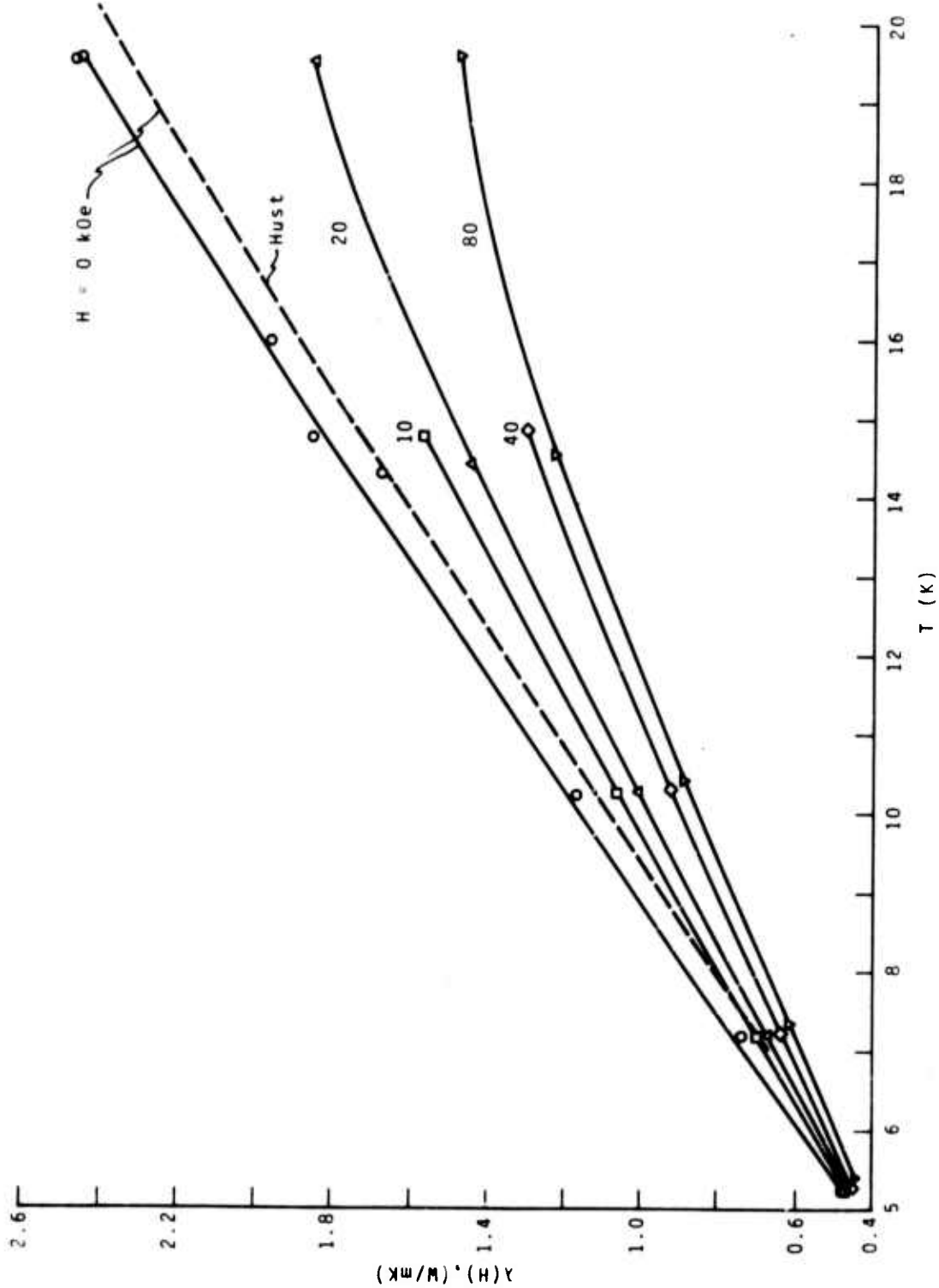


Figure 2. Thermal conductivity of Inconel 718 as a function of temperature at several magnetic fields.

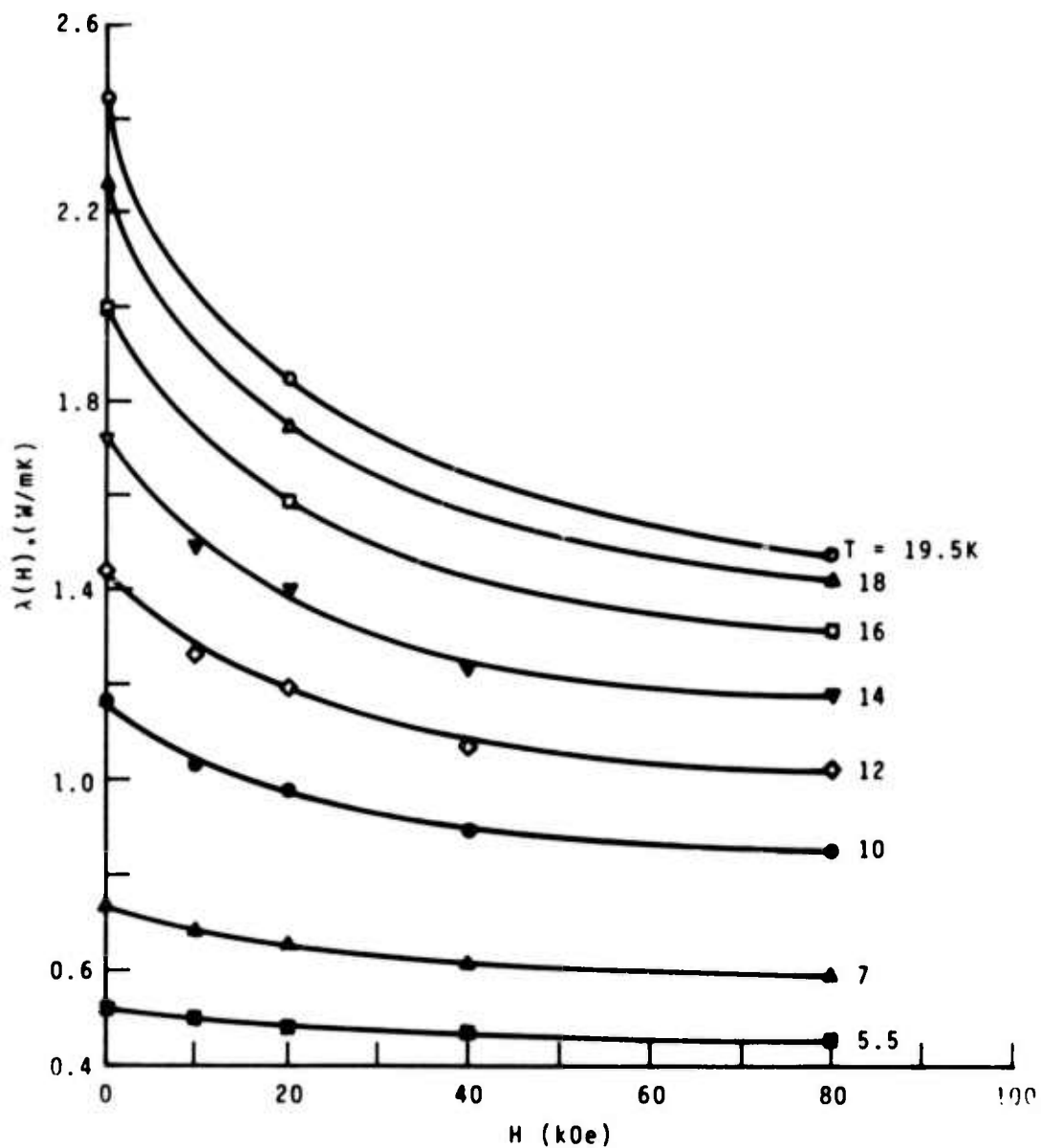


Figure 3. Thermal conductivity of Inconel 718 as a function of magnetic field at several temperatures.

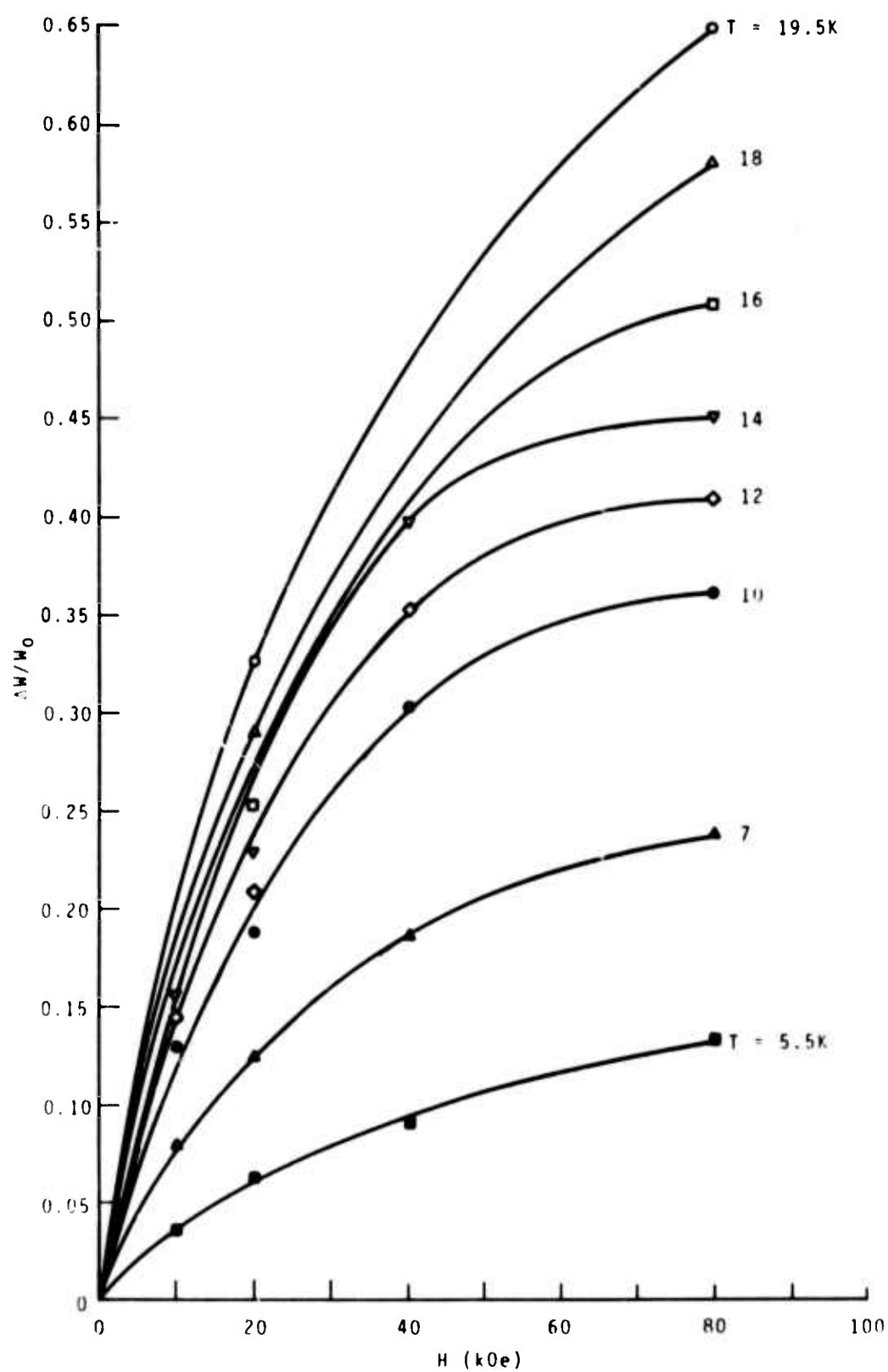


Figure 4. Relative change in thermal resistance of Inconel 718 as a function of magnetic field at several temperatures.

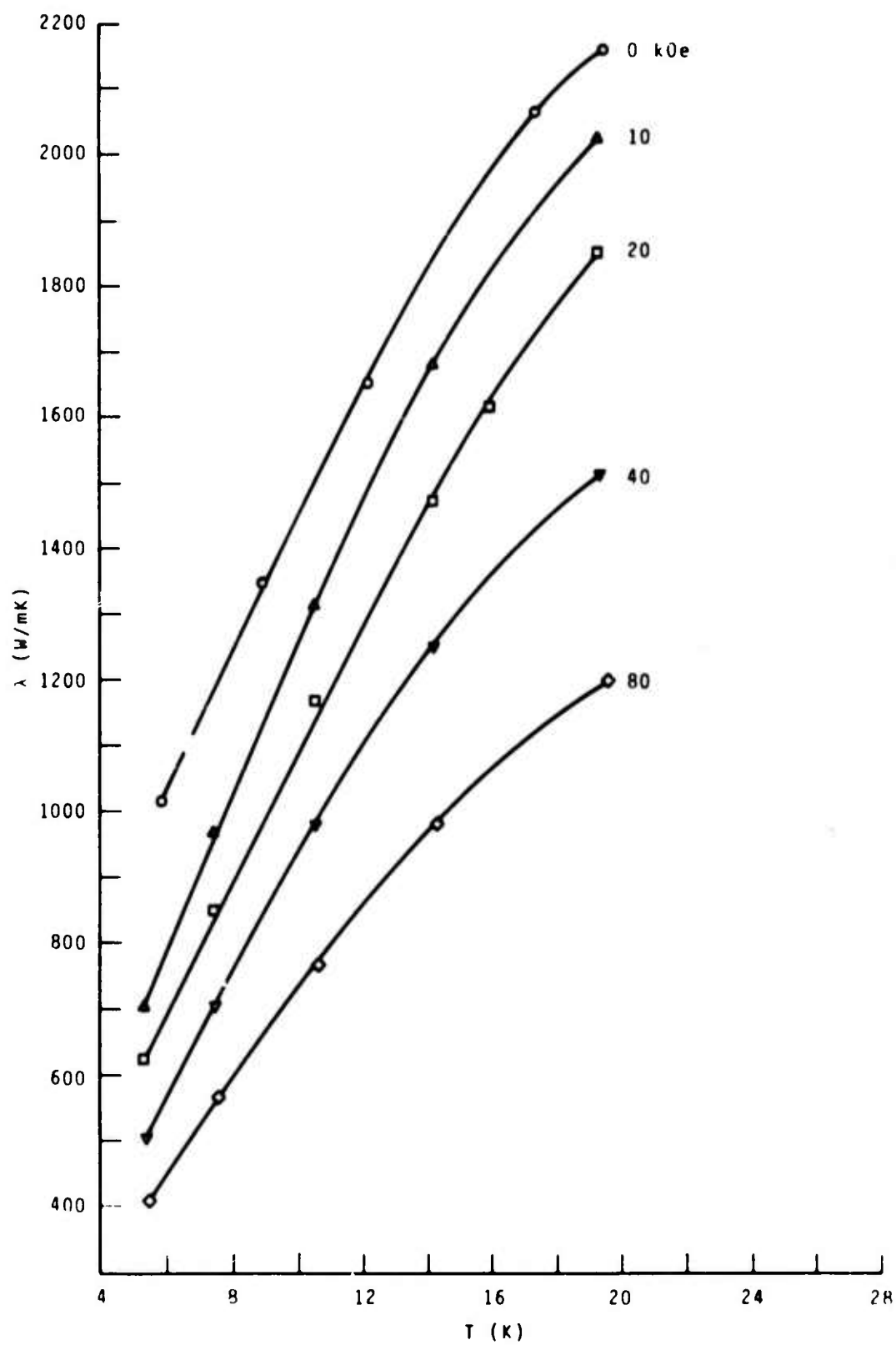


Figure 5. Thermal conductivity of copper as a function of temperature at several magnetic fields.

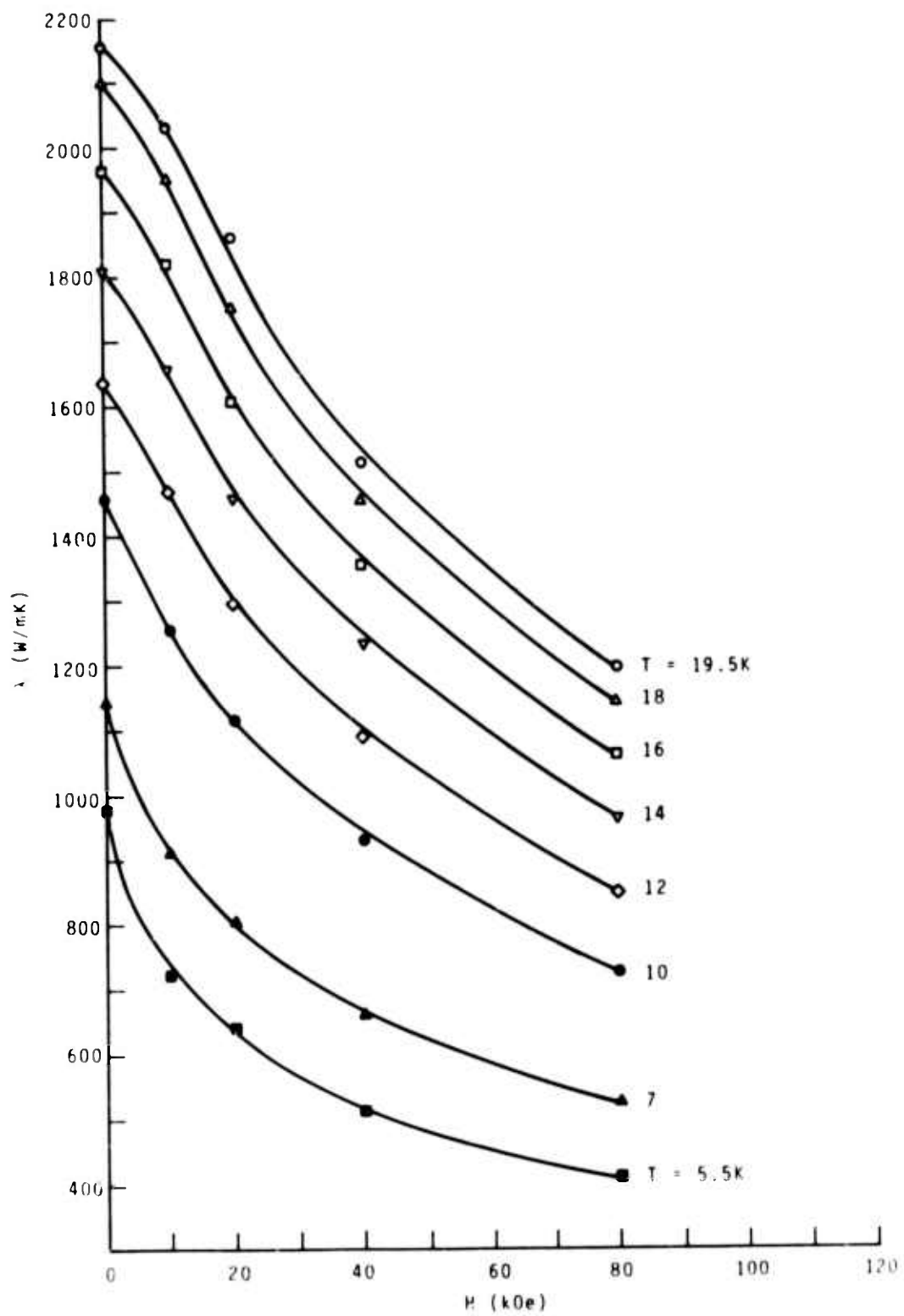


Figure 6. Thermal conductivity of copper as a function of magnetic field at several temperatures.

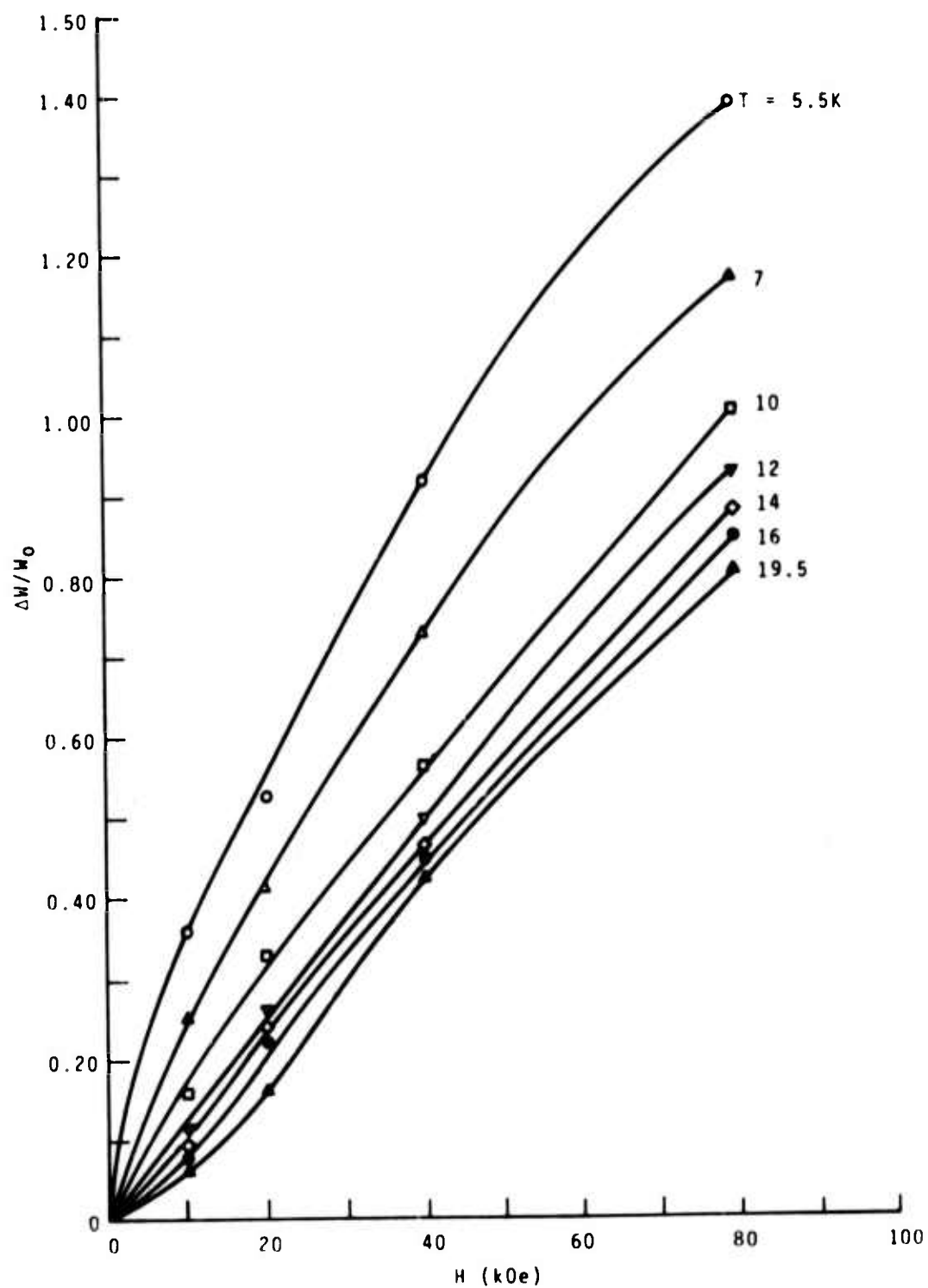


Figure 7. Relative change in thermal resistance of copper as a function of magnetic field at several temperatures.

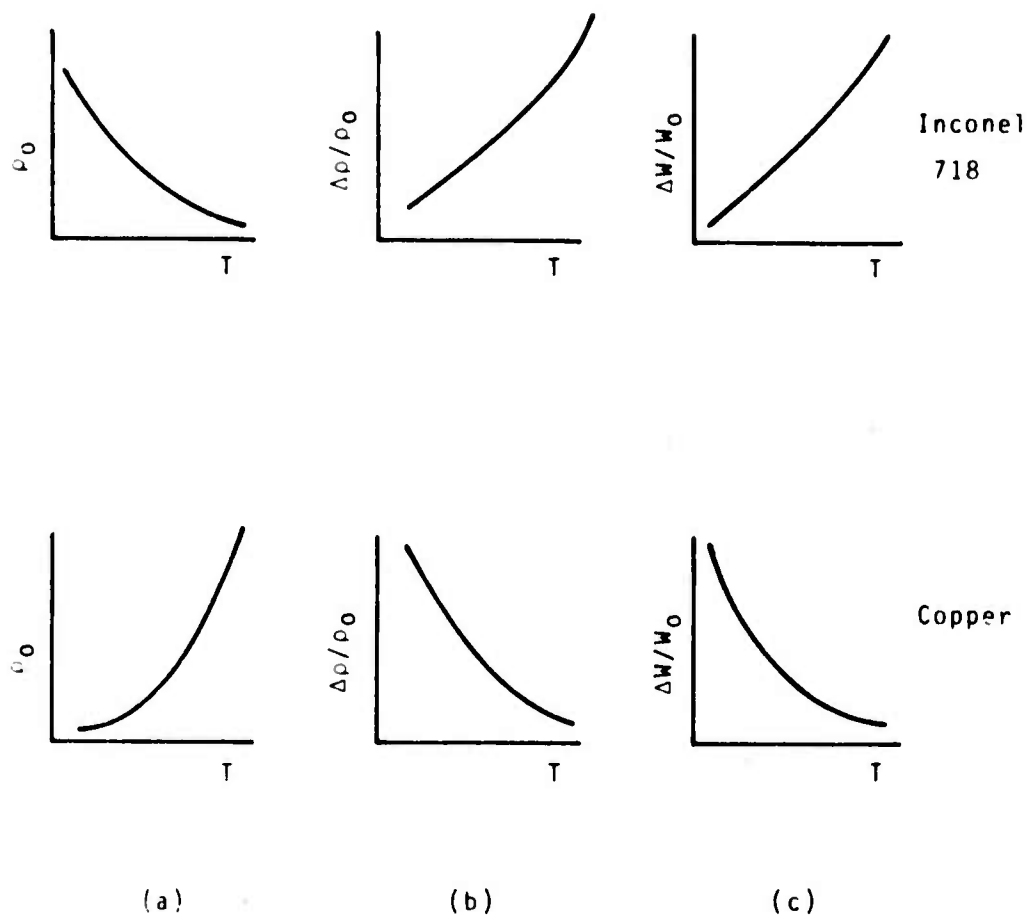


Figure 8. Characteristic curves of  $\rho_0$  (zero field electrical resistivity),  $\Delta\rho/\rho_0$  (relative electrical resistivity change in a magnetic field), and  $\Delta W/W_0$  (relative thermal resistivity change in a magnetic field) for Inconel and copper below 20 K.

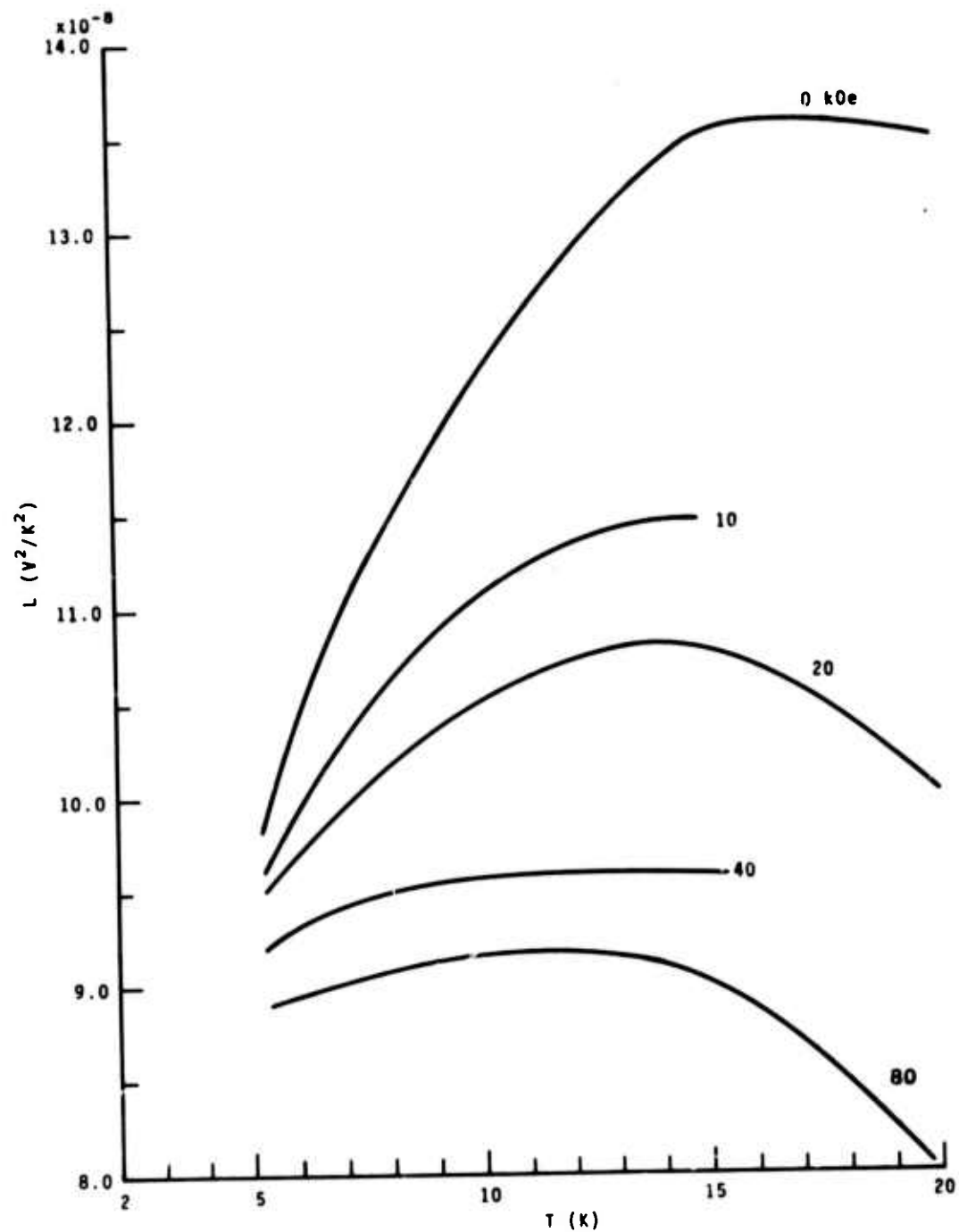


Figure 9. Lorenz ratios of Inconel 718 as a function of temperature at several magnet fields.



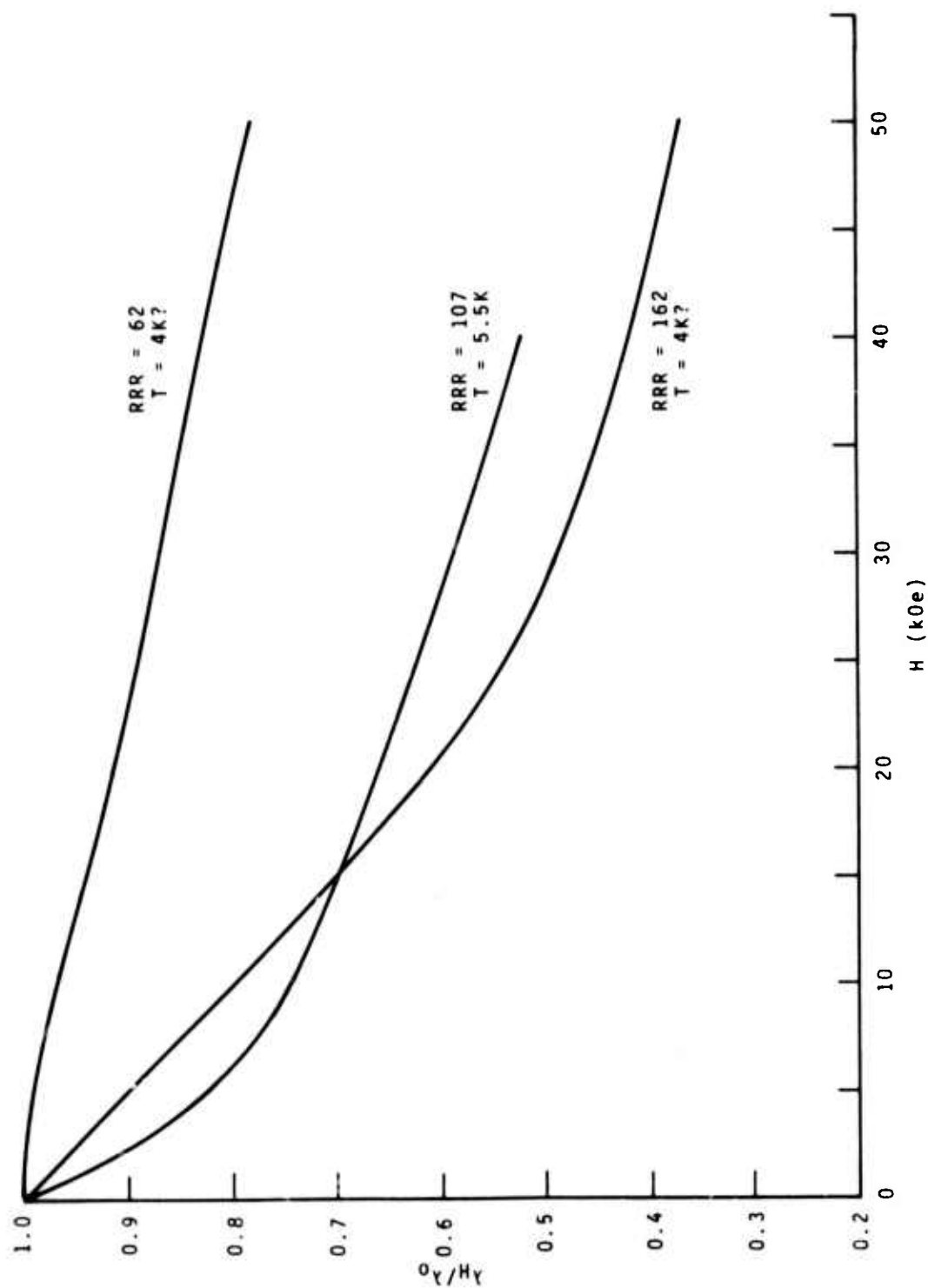


Figure 10. Comparison of the present magnetothermal conductivity data to that of Fevrier and Morize.

NBSIR

SEMI-ANNUAL REPORT ON MATERIALS RESEARCH  
IN SUPPORT OF SUPERCONDUCTING MACHINERY

FATIGUE AND FRACTURE TOUGHNESS  
TESTING AT CRYOGENIC TEMPERATURES

R. L. Tobler, R. P. Mikesell, R. L. Durcholz, and R. P. Reed

Cryogenics Division  
Institute for Basic Standards  
National Bureau of Standards  
Boulder, Colorado 80302

October 1974

#### Summary: Fatigue and Fracture Toughness Testing at Cryogenic Temperatures

Fatigue crack growth rate ( $da/dN$ ), fracture toughness ( $K_{IC}$ ,  $K_{IC}(J)$ ) and tensile properties have been determined at 298, 76, and 4 K for the following structural alloys: Ti-5Al-2.5Sn; Ti-6Al-4V; AISI 304, 310, 316; Inconel 750, and A-286. The titanium alloys Ti-5Al-2.5Sn and Ti-6Al-4V exhibited similar properties: the fatigue crack growth rates were temperature independent over the interval 298 - 4 K. Their fracture toughness at 4 K are equal to within  $3 - 4 \text{ ksi} \cdot \text{in}^{1/2}$ . The stable austenitic alloys AISI 310, A-286, and Inconel 750 exhibit lower crack growth rates at 76 K and 4 K than at 298 K. The fracture toughness of solution treated and aged A-286 alloy decreases by only  $\sim 10\%$  as temperature decreases from 298 - 4 K; the fracture toughness at 4 K is  $109 \text{ ksi} \cdot \text{in}^{1/2}$ . The fracture toughness of solution treated and double aged Inconel 750 appears to decrease by about 10% over the temperature interval 298 - 76 K. The fracture toughness at 76 K is  $\sim 173 \text{ ksi} \cdot \text{in}^{1/2}$ . AISI 310 stainless steel has superior resistance to fatigue crack growth at 4 K, compared with types 304 and 316 stainless steels. Conversely, AISI 304 and 316 stainless steels exhibit higher fracture toughness. These differences appear to be related to the relative stability of the austenitic structure.

## Contents: Fatigue and Fracture Toughness

	Page
<u>1. Introduction</u> . . . . .	60
<u>1.1 Linear Elastic Fracture Mechanics</u> . . . . .	60
<u>1.2 J-Integral Analysis</u> . . . . .	61
<u>2. Experimental</u> . . . . .	62
<u>2.1 Materials</u> . . . . .	62
<u>2.2 Methods</u> . . . . .	63
<u>2.2.1 Tensile Tests</u> . . . . .	63
<u>2.2.2 Low-Temperature Fatigue</u> . . . . .	63
<u>2.2.3 Fracture Toughness</u> . . . . .	66
<u>3. Results</u> . . . . .	67
<u>3.1 Tensile Properties</u> . . . . .	67
<u>3.2 Fatigue Crack Growth Rates</u> . . . . .	68
<u>3.2.1 Ti-5Al-2.5Sn</u> . . . . .	68
<u>3.2.2 A-286</u> . . . . .	69
<u>3.2.3 Inconel 750</u> . . . . .	69
<u>3.2.4 AISI 310</u> . . . . .	69
<u>3.3 Fracture Toughness</u> . . . . .	69
<u>3.3.1 Ti-5Al-2.5Sn</u> . . . . .	69
<u>3.3.2 A-286</u> . . . . .	70
<u>3.3.3 Inconel 750</u> . . . . .	72
<u>3.3.4 AISI 310</u> . . . . .	72
<u>4. Discussion</u> . . . . .	73
<u>5. References</u> . . . . .	77
<u>List of Tables</u> . . . . .	82
<u>List of Figures</u> . . . . .	83

## FATIGUE AND FRACTURE TOUGHNESS TESTING AT CRYOGENIC TEMPERATURES

R. L. Tobler, R. P. Mikesell, R. L. Durcholz and R. P. Reed

### 1. Introduction

Recent interest in superconducting machinery has prompted research on both the physical and mechanical properties of materials at 4 K. Since most structural components of superconducting machinery are cooled with liquid helium to 4 K, there is a need for mechanical property data in this environment.

Conventional tensile and impact tests do not provide design data for predicting the load carrying capability of structures containing fatigue cracks or other common flaws. The safe operating lifetime of a structure and the possibility of brittle failure can be predicted only by fracture mechanics analysis. The essential design parameters are the fracture toughness ( $K_{IC}$  or  $J_{IC}$ ) of a material and the fatigue crack growth rate ( $da/dN$ ).

Some highly stressed components of superconducting motors and generators are expected to sustain billions of fatigue cycles in their lifetime. Prototype machinery were constructed using some very tough austenitic alloys (300-series stainless steels, Inconel 750) and elaborate fabrication techniques employed to lower the probability of failures. Fracture mechanics data at 4 K, previously non-existent, are needed to enable judicious selection of structural materials and accurate lifetime predictions for critical machinery components.

This report presents fatigue crack growth rate and fracture toughness data at 298, 76 and 4 K for the alloys Ti-5Al-2.5Sn, A-286, Inconel 750, and AISI 310 stainless steel. These data are compared to the results obtained in the first six months on AISI 304, AISI 316, and Ti-6Al-4V.

#### 1.1 Linear Elastic Fracture Mechanics

When a negligible amount of plastic deformation occurs prior to fracture, the ASTM Standard Method of Test for Plane Strain Fracture Toughness of Metallic Materials (ASTM E-399-74) [1] can be applied. This method is based on the theory of linear elastic fracture mechanics as discussed in references [2-4]. The approach utilizes the stress intensity factor,  $K$ , to describe fracture behavior.

For test specimens of standard geometry, K is calculated from the relation:

$$K = \frac{P}{BW^{1/2}} \left[ f\left(\frac{a}{W}\right) \right] \quad (1)$$

where P is applied load, B is specimen thickness, W is specimen width, a is crack length, and  $f(a/W)$  is a factor dependent on relative crack length.

A normally ductile material may fail in a relatively brittle manner in the presence of a fatigue crack and under conditions of plane strain. Linear elastic plane strain conditions prevail for thick specimens where the plastic zone at the crack tip is constrained by the surrounding bulk of elastically loaded material. Under these conditions, materials loaded in tension exhibit a critical stress intensity,  $K_{IC}$ , at which failure occurs catastrophically without significant plastic deformation.

The parameter  $K_{IC}$  is a material property and a useful design criterion. Provided that specimen size requirements are met,  $K_{IC}$  may be calculated from eq (1) using the load determined from the fracture test record according to the ASTM E-399-74 method. The size criterion for assuring linear elastic behavior and valid  $K_{IC}$  data is that:

$$B \geq 2.5 \left( \frac{K_{IC}}{\sigma_y} \right)^2 \quad (2)$$

where  $\sigma_y$  is the 0.2% offset yield stress of the material. Subsize specimens result in invalid fracture toughness measurements; these data are referred to as  $K_Q$ .

### 1.2 J-Integral Analysis

Specimens that do not satisfy eq (2) exhibit nonlinear elastic fracture behavior. Plastic deformation at the crack tip becomes appreciable for thin specimens and the concept of stress intensity loses its significance. In such a case, the J-integral fracture criterion may be applied.

The J-integral approach is based on the premise that fracture behavior is governed locally by crack tip conditions, even if plastic deformation precedes fracture. J is an energy term derived from the area under the load versus deflection curve of a precracked specimen loaded in tension or bending. The

critical value,  $J_{IC}$ , is the value of  $J$  just prior to crack extension--the value required to initiate fracture.

The theory of the J-integral was originated by Rice [5]. Subsequent experiments [6-10] verified that  $J_{IC}$  is a useful fracture criterion that may be applied in cases where the specimen exhibits linear elastic, elastic-plastic, or fully plastic load-deflection behavior.

Although the J-integral criterion has been successfully applied to cases of large-scale plasticity, a size criterion is necessary to insure that J-integral test results will be independent of specimen geometry and dimensions. A tentative size criterion for the J-integral test is that [10]:

$$B, b, a, \geq 50 (J/\sigma_{flow}) \quad (3)$$

where  $b$  is the ligament of uncracked specimen and  $\sigma_{flow}$  is the average of the 0.2% offset yield stress and the ultimate flow stress. A very practical consideration is that  $B$  is typically an order of magnitude smaller than the value required for linear elastic tests as calculated from eq (2).

$J_{IC}$  values can be converted to  $K_{IC}$  values using the relation [6, 7, 10]:

$$K_{IC} = \left( \frac{E}{1-\nu^2} \cdot J_{IC} \right)^{1/2} \quad (4)$$

where  $E$  is Young's modulus and  $\nu$  is Poisson's ratio. Thus it is possible to derive  $K_{IC}$  values from J-integral tests on smaller specimens than would normally be required for linear elastic  $K_{IC}$  tests. In this paper, the symbol  $K_{IC}(J)$  is used to distinguish values obtained using eq (4) from  $K_{IC}$  data determined according to ASTM E-399-74.

## 2. Experimental

### 2.1 Materials

The materials tested in this study were the alloys Ti-5Al-2.5Sn, A-286, Inconel 750, and AISI 310 stainless steel. These materials were obtained in the various forms listed in table 1. The Ti-5Al-2.5Sn and AISI 310 alloys were tested in the as-received condition. Specimens of alloys A-286 and Inconel 750 were machined from stock and subsequently heat treated prior to testing.

A-286 was solution treated (1172 K (1650 F), 2 hrs, oil quench) and aged (1005 K (1350 F), 16 hrs, air cool). Inconel 750 was solution treated (1255 K (1800 F), 1 hr, air cool, and double aged (1144 K (1600 F), 24 hr, air cool, followed by 977 K (1300 F), 20 hr, air cool).

The chemical analyses of all materials are given in table 2. Note that the Ti-5Al-2.5Sn alloy contained normal levels of the interstitial elements C, N, O, and H; it was not an extra-low-interstitial grade.

## 2.2 Methods

### 2.2.1 Tensile Tests

Smooth-bar uniaxial tensile tests were conducted to determine the 0.2% offset yield stress and ultimate tensile strength for each material. The tests were conducted according to the ASTM Standard Methods of Tension Testing of Metallic Materials (ASTM designation E8-69) [11].

Testing was performed with a 10,000 lb (44.5 kN) capacity machine that was equipped with a titanium-stainless steel cryostat. The cryostat was described by Reed [12]. The tests were performed using a crosshead rate of  $3.3 \times 10^{-4}$  in-sec<sup>-1</sup> ( $8.4 \times 10^{-3}$  mm-sec<sup>-1</sup>).

Testing in liquid nitrogen (76 K) was accomplished by immersing the specimen and cryostat in a single metal dewar containing the cryogen. Testing in liquid helium (4 K) was accomplished with a double glass dewar arrangement; the outer dewar contained liquid nitrogen.

Tensile specimens had the geometry illustrated in figure 1. All materials were tested in the transverse orientation; the tensile axis was perpendicular to the rolling direction or principal forging axis. Thus, the fracture plane orientation of tensile specimens was equivalent to that of fracture toughness specimens.

Load was monitored with a 10,000 lb (44.5 kN) commercial load cell. Specimen extension was measured with a commercial clip-on extensometer that was calibrated with a dial micrometer at each temperature. The sensitivity of the extensometer at 4 K corresponded to a strain increment of  $3.65 \times 10^{-4}$  per millimeter of chart paper.

### 2.2.2 Low Temperature Fatigue

Fatigue tests were conducted with a 22,500 lb (100 kN) capacity servo-hydraulic mechanical testing machine. This was a cryogenic model; the fatigue



actuator was positioned above the specimen level to accommodate the cryostat and to permit access from below for assembling dewars. The testing machine and associated equipment are shown in figure 2.

Tests were conducted using a 22,500 (100 kN) capacity cryostat. The cryostat and dewar arrangement for tests in liquid helium are illustrated in figure 3. A more detailed description of the design of this cryostat and associated apparatus was given previously [13].

Compact tensile specimens having the geometries shown in figures 4 and 5 were employed in all fatigue and fracture tests. All specimens were 1.50 inch (3.81 cm) thick and were proportioned in accordance with ASTM standard E-399-74.

AISI 310 alloy specimens were machined with the crack starter notch parallel to the rolling direction of the original stock -- a TL orientation [1]. For all other materials the plane of the notch was parallel to the principal forging axis -- a TS orientation [1].

Fatigue tests were performed using load control. Dynamic fatigue loads were measured and controlled to within 1 percent by means of a digital peak recording device. The load cycle was sinusoidal at a constant frequency of 20 Hz and a constant stress ratio (minimum load/maximum load) of 0.1.

Most crack growth data were obtained during precracking of specimens for fracture tests. For these specimens the final crack length was limited to a ratio  $a/W$  between 0.45 and 0.60. Fatigue loads and stress intensities were limited to low or intermediate values as shown in table 3. A few specimens were tested solely for crack growth data at high stress intensities; for these specimens the cracks were extended to  $a/W = 0.70$  using loads up to 10,500 lbs (47 kN).

ASTM type clip gages were used at all testing temperatures. Commercially available foil resistance strain gage films were bonded to the clip gage beams using an adhesive recommended for low temperature applications. The clip gages were calibrated at temperatures from 298 K to 4 K, but sensitivity was not significantly temperature dependent. Clip gage linearity met ASTM standards for  $K_{IC}$  testing [1].

For linear elastic  $K_{IC}$  tests of Ti-5Al-2.5Sn, deflections were measured between attachable knife edges located at the specimen edge as shown in figure 4. For all other test specimens a modification in notch configuration was introduced to measure load-line deflections as shown in figure 5. Roberts' [14] K calibration was used in each case.

Crack growth was monitored by compliance measurements. Direct measurement of crack lengths at the specimen surface was not possible during cryogenic tests. The compliance technique is based on the fact that for a given load, the specimen compliance (reciprocal of stiffness) increases with increasing crack length. Compliance methods are discussed in detail elsewhere [4, 15].

Experimental crack-length -- compliance correlations were obtained for each material and temperature. An X-Y recorder was used to measure the compliance for a number of specimens of varying crack lengths. Fatigue striations were generated by load changes during precracking and crack growth rate tests so that several crack-length -- compliance measurements were obtained from each specimen. The data were plotted as a function of crack length, which was measured as an average of three readings at the center and quarter points of specimen thickness.

Theoretical crack-length -- compliance curves were calculated from the generalized solution given by Roberts [14], but these were not in complete agreement with the experimental correlations. Comparison showed that the calculated curves consistently underestimated the true crack lengths. The difference between the calculated and experimental curves usually amounted to about 5%.

The procedure for determining crack growth rates involved plotting the static compliance at intervals during the tests. Using the experimental crack-length -- compliance correlation, crack length could then be obtained, within  $\pm 2$  percent. The crack length,  $a$ , was plotted versus the total number,  $N$ , of fatigue cycles, and the crack growth rate ( $da/dN$ ) was determined by graphical differentiation of the  $a$ -versus- $N$  curve.

It is well known that the rate of crack growth can be retarded by changing from a higher to a lower stress intensity range. Crack growth rates can also be influenced by abrupt temperature changes. Whenever these kinds of changes were made the crack growth rate was allowed to stabilize before data were accepted as valid. Crack growth data under the new conditions were ignored until the crack had advanced an increment equal to or greater than the plastic zone size as calculated according to Irwin's formula [16].

### 2.2.3 Fracture Toughness

Fracture tests of Ti-5Al-2.5Sn were performed with the 22,500 lb. (100 kN) servo-hydraulic test machine. The tests were performed using stroke control at a rate of  $3.9 \times 10^{-3} \text{ in} \cdot \text{sec}^{-1}$  ( $100 \text{ mm} \cdot \text{sec}^{-1}$ ).

J-integral fracture tests of A-286, Inconel 750, and AISI 310 alloys were performed using a 60,000 lb (267 kN) capacity hydraulic test machine.  $K_Q$  was measured using the same J-integral test specimens. The tests were conducted at a crosshead rate of  $3.3 \times 10^{-4} \text{ in} \cdot \text{sec}^{-1}$  ( $8.4 \times 10^{-3} \text{ mm} \cdot \text{sec}^{-1}$ ). The 60,000 lb (267 kN) capacity cryostat and associated fracture testing apparatus were described previously [13].

The majority of fracture tests were conducted at temperatures of 298, 76, and 4 K. A single test of Ti-5Al-2.5Sn was performed at 173 K in an atmosphere of nitrogen vapor. The specimens were allowed twenty to sixty minutes to reach thermal equilibrium before testing.

A temperature-control system with a chromel-constantan thermocouple was used to maintain a temperature of  $173 \text{ K} \pm 4 \text{ K}$ . The control thermocouple was located on the specimen at the level of the fatigue crack. Vapor from a pressurized liquid nitrogen dewar was introduced to the cryostat through a solenoid valve. The valve admitted cold vapor to the cryostat as required by opening and closing automatically in response to the electrical signal from a commercial temperature recorder.

The specimens were precracked at the temperature of subsequent fracture testing unless otherwise noted in the text. Ti-5Al-2.5Sn specimens were precracked according to ASTM E-399-74 criteria. The precracking conditions for other alloys are listed in table 3.

For the compact tensile specimens described in this report, J was calculated from the equation [17]:

$$J = \frac{2A}{Bb} \quad (5)$$

where A is the area under the load-deflection curve to a particular value of displacement. The critical value,  $J_{IC}$ , was taken as the value of J just prior to material separation. For elastic-plastic or fully plastic fracture tests,

the  $J_{IC}$  value was obtained by extrapolation of the  $J$  versus  $\Delta a$  curve.

The extrapolation technique was based on a method outlined by Landes and Begley [10]. Following their procedure, 3 to 5 nearly identical specimens with average crack lengths agreeing to approximately 3 percent were tested at each temperature. A series of load-deflection curves were obtained by loading each specimen to a level sufficient to cause decreasing amounts of crack extension. The specimens were then unloaded and heat tinted<sup>1</sup> to oxidize the surfaces where crack extension had occurred. The specimens were subsequently pulled apart at either 298 K or 76 K. The average values of  $\Delta a$  were measured and plotted versus the corresponding values of  $J$ .

In some tests a measurable deformation at the crack tip preceded material separation. Apparent crack extension therefore included a contribution due to deformation in addition to actual material separation.

To account for apparent crack extension due to deformation, the  $J/2\sigma_{flow}$  line was plotted as described by Landes and Begley [10]. The intersection of the  $J$  versus  $\Delta a$  curve and the  $J/2\sigma_{flow}$  line represents the initial point of material separation;  $J_{IC}$  was taken as the value of  $J$  at the point of intersection.

For AISI 310 specimens the length of the stretch zone was also measured directly from the fracture surfaces with a traveling microscope. An average value from several specimens was plotted as a vertical line on the  $J$ - $\Delta a$  curves.

When the  $J$ - $\Delta a$  graphs appeared to be nonlinear beyond the stretch zone region, a concave upward curve was used to extrapolate the data. The concave curve results from increasing overestimation in  $J$  with increasing crack extension [10]. In some cases a well defined curve in the  $J$ - $\Delta a$  plots was not exhibited due to data scatter. Uncertainty in the value of  $J_{IC}$  was accounted for by examining a number of reasonable extrapolations.

$K_{IC}(J)$  values were calculated from  $J_{IC}$  values using eq (4). Data for  $E$  and  $\nu$  at the temperatures of interest were taken from the work of Ledbetter, Naimon, and Weston [18].

### 3. Results

#### 3.1 Tensile Properties

Tables 4-7 list the yield and tensile strengths for all alloys. The results are shown as a function of temperature in figures 6-8. The stress-

---

1 Specimens were heat tinted for 15-30 minutes at 1300 - 1400 F.

strain curves are given in figures 9-12.

The yield strength and tensile strength of the Ti-5Al-2.5Sn alloy nearly doubled with a decrease in temperature from 298 K to 4 K. At a value of  $\sim 225$  ksi ( $155 \times 10^7 \text{ Nm}^{-2}$ ) the yield strength in liquid helium exceeds that of the other alloys tested. However, ductility is low at 4 K, as indicated by the stress-strain curves of figure 9.

The tensile behavior of AISI 310 was similar to that reported previously [13] for AISI 304 and 316 stainless steels. Typically, these alloys exhibit high ductility, work hardening capability at temperatures as low as 4 K, and discontinuous yielding behavior at 4 K. As shown in figures 10-12 the AISI 310, A-286, and Inconel 750 alloys plastically deformed via the discontinuous yielding process at 4 K. This was observed for AISI 304 and 316 alloys also [13].

Figure 8 shows that the yield strength of AISI 310 increases considerably with decreasing temperature over the interval 298 - 4 K. However, the yield strength at 4 K was lower in comparison to the values obtained for A-286, Inconel 750, and Ti-5Al-2.5Sn.

### 3.2 Fatigue Crack Growth Rates

#### 3.2.1 Ti-5Al-2.5Sn

The preliminary room temperature crack growth rate data previously reported [13] for the Ti-5Al-2.5Sn alloy were inaccurate and have been corrected. The preliminary data were calculated using Roberts' [14] theoretical compliance correlation. The data have been corrected using a better compliance correlation, experimentally determined.

Fatigue crack growth rate data for Ti-5Al-2.5Sn are shown in figure 13. The data represent tests of at least three specimens per temperature. At 298, 76, and 4 K, the rates are nearly equivalent. Any effect of temperature is indistinguishable compared to the degree of scatter among specimens. All crack growth rate data fit within a scatter band having a width of about  $5 \text{ ksi} \cdot \text{in}^{1/2}$  ( $5.5 \text{ MNm}^{-2} \cdot \text{m}^{1/2}$ ). The scatter in data is somewhat greater at 4 K than at 298 or 76 K.

Also shown in figure 13 is a straight line approximation of the data previously reported [13] for Ti-6Al-4V. The crack growth resistance of the Ti-5Al-2.5Sn alloy is superior over the range of stress intensities examined.

### 3.2.2 A-286

Fatigue crack growth rate data for the A-286 alloy are shown in figure 14. Most of this data was reported earlier [13].

Results at 298, 76, and 4 K demonstrate that cracks propagate at lower rates at cryogenic temperatures than at room temperature. At  $\Delta K = 40 \text{ ksi} \cdot \text{in}^{1/2}$  ( $43.9 \text{ MNm}^{-2} \cdot \text{m}^{1/2}$ ), the crack growth rate at 76 K or 4 K is lowered by a factor of two from the room temperature value. There is no measurable difference in crack growth rates at 76 and 4 K.

### 3.2.3 Inconel 750

Fatigue crack growth rate data for Inconel 750 are shown in figure 15. The scatter in data at each temperature was particularly low.

The crack growth rate decreased with decreasing temperature. The rate of decrease between room temperature and 76 K was large and similar to that observed for A-286. Similarly, there was only a small reduction in growth rate between 76 K and 4 K.

### 3.2.4 AISI 310

The results for AISI 310 stainless steel are shown in figure 16. Similar to A-286 and Inconel 750, the crack growth rate is lower at cryogenic temperatures than at room temperature. A relatively large reduction in crack growth rate occurs between 298 K and 76 K, but there appears to be no measurable difference between 76 K and 4 K.

In Figure 17 the results at 4 K for 310 stainless steel are compared to results previously obtained [13] for types 304 and 316. Wide bands of scatter were observed in the results for types 304 and 316. Over the range of crack growth rate from about  $da/dN = 10^{-6} - 10^{-4} \text{ in} \cdot \text{cycle}^{-1}$  ( $2.54 \times 10^{-6} - 2.54 \times 10^{-4} \text{ cm} \cdot \text{cycle}^{-1}$ ), figure 17 indicates that cracks propagate more rapidly for AISI 304 and 316 stainless steels than for 310. The crack growth rate for 310 stainless steel is lower by a factor of about two.

## 3.3 Fracture Toughness

### 3.3.1 Ti-5Al-2.5Sn

Fracture test records for Ti-5Al-2.5Sn specimens are illustrated in figure 18. At cryogenic temperatures the load-deflection curves were ideally linear elastic; failure occurred instantaneously at the critical stress intensity. A minor deviation from linearity was observed only in tests at room temperature, where pop-in (unstable crack extension) occurred. Each pop-in was marked by a discontinuity in the terminal portion of the test record just prior to failure.

Table 8 lists the values of  $K_Q$  and  $K_{IC}$  for ten specimens. The specimen size criterion was amply satisfied, as demonstrated in table 9.

Several results were invalid according to a strict application of ASTM E-399-74. The data for three specimens were designated  $K_Q$  because of minor deviations from fatigue crack uniformity. The invalidating criteria are cited in table 9. However, these irregularities appear to have had no influence; scatter in the data is quite low, and  $K_Q$  values are in good agreement with  $K_{IC}$  values at each temperature.

Figure 19 illustrates the temperature dependence of fracture toughness for the Ti-5Al-2.5Sn alloy. Other results [22-23] for extra-low-interstitial (ELI) Ti-5Al-2.5Sn alloys are presented, as well as data previously reported for a mill annealed Ti-6Al-4V alloy [13]. The room temperature fracture toughness of Ti-5Al-2.5Sn is considerably higher than that of the Ti-6Al-4V alloy, but there is only a small difference in  $K_{IC}$  values at 4 K. A marked temperature dependence reduces the fracture toughness of the Ti-5Al-2.5Sn alloy from  $70.3 \text{ ksi} \cdot \text{in}^{1/2}$  ( $77.2 \text{ MNm}^{-2} \cdot \text{m}^{1/2}$ ) at 298 K to  $38.3 \text{ ksi} \cdot \text{in}^{1/2}$  ( $43 \text{ MNm}^{-2} \cdot \text{m}^{1/2}$ ) at 76 K or 4 K, a decrease of 46%.

The fracture surface appearances of specimens tested at room temperature and in liquid helium were predominantly flat. The width of the shear portion at the specimen edge is less than 3% of total thickness. The shear portion is practically non-existent at 76 or 4 K.

In load-deflection behavior, in  $K_{IC}$  values, and in fracture surface appearance, the results at 76 K and 4 K were indistinguishable.

### 3.3.2 A-286

Fracture test records for A-286 specimens are shown in figure 20. Deviations from linearity were noticeable in the load-deflection curves at each temperature. The degree of linearity increased at lower temperatures but the ASTM E-399-74 specimen thickness criterion for linear-elastic behavior was never satisfied. Discontinuities in load-deflection behavior and audible pop-in phenomena occurred at all temperatures. Heat-tinting experiments revealed that small increments of stable crack extension always preceded pop-in. The amount of stable crack extension that could occur prior to pop-in was estimated to decrease from about 0.07 inch (.178 cm) at 298 K to about 0.01 inch (0.025 cm) at 4 K.



J-integral test results are given in figure 21 and in table 10. As illustrated in figure 21, the  $J/2\sigma_{flow}$  lines at 298, 76, and 4 K are rather steep and coincide. The points of intersection of the  $J-\Delta a$  curves with the  $J/2\sigma_{flow}$  lines occurs for each temperature at  $\Delta a \cdot 10^{-3}$  inch ( $2.54 \times 10^{-3}$  cm). Thus, the deformation at the crack tip prior to material separation is quite small; a stretch zone was not visible on the fractured surfaces of test specimens.

At 76 and 4 K the  $J_{IC}$  values are well defined. In one test at 76 K, an average crack extension of only 0.004 inch (0.01 cm) was observed. The heat-tinted fracture surface of this specimen revealed that crack extension initiated discontinuously at several locations along the crack front. The value of  $J$  for this test was very nearly the critical value,  $J_{IC}$ .

The scatter in the data at 298 K and the lack of data at very low values of  $\Delta a$  contributed to uncertainty in the room temperature results. A number of extrapolations indicate that  $J_{IC}$  lies in the region from 420 - 490 in  $\cdot$  lb  $\cdot$  in $^{-2}$  (0.073 - 0.086 MJ  $\cdot$  m $^{-2}$ ).

The  $K_Q$  values shown in table 11 are not valid  $K_{IC}$  data because the linear-elastic specimen thickness requirement was not satisfied. The data of table 12 indicate that a 1.75 inch (4.44 cm) thick specimen is required to assure valid  $K_{IC}$  results at 4 K. The required thickness is significantly greater at higher temperatures.

Shown in table 11 are calculations of the specimen strength ratio<sup>1</sup>,  $R_{SC}$  [1]) at 298, 76, and 4 K. The  $K_Q$  and  $K_{IC}(J)$  parameters are shown as a function of temperature in figure 22. Of these parameters, only the  $K_{IC}(J)$  values represent a meaningful measure of fracture toughness. The  $R_{SC}$  values illustrate qualitatively the effect of temperature on fracture toughness.

The J-integral results demonstrate that the A-286 alloy undergoes only a small reduction in fracture toughness over the temperature interval 298 - 4 K;  $K_{IC}(J)$  decreases from  $\sim 119$  ksi  $\cdot$  in $^{1/2}$  ( $130.6$  MNm $^{-2} \cdot$  m $^{1/2}$ ) at 298 K to  $\sim 109$  ksi  $\cdot$  in $^{1/2}$  ( $119.7$  MNm $^{-2} \cdot$  m $^{1/2}$ ) at 4 K, a decline of about 10%.

---

1 The specimen strength ratio,  $R_{SC} = \frac{2P_m(2W+a)}{B(W-a)^2\sigma_y}$ , is the ratio of the maximum nominal net-section stress to the tensile yield strength.



### 3.3.3 Inconel 750

Fracture data for Inconel 750 at 4 K have not been completely evaluated. The results obtained at 298 K and 76 K are reported here.

Fracture test records for Inconel 750 are shown in figure 23. At 298 K and 76 K fracture occurred by stable, ductile tearing. The load-deflection curves deviated substantially from linearity. Valid  $K_{IC}$  data could not be obtained according to the ASTM E-399-74 method due to inadequate specimen thickness as indicated in table 13. The  $K_Q$  values obtained by this method are listed in table 14. The J-integral tests results are shown in table 15 and in figure 24. The size criterion for J-integral tests is amply satisfied as shown in table 13.

At 298 K the J- $\Delta a$  curve is concave upward. At 76 K the trend of the J- $\Delta a$  curve is obscured by scatter, but the  $J_{IC}$  value is rather well defined because two data points are very near the  $J/2\sigma_{flow}$  line.

Figure 25 indicates that the fracture toughness of Inconel 750 decreases from a  $K_{IC}(J)$  value of  $\sim 189 \text{ ksi} \cdot \text{in}^{1/2}$  ( $207.5 \text{ Nm}^{-2} \cdot \text{m}^{1/2}$ ) at 298 K to a value of  $\sim 173 \text{ ksi} \cdot \text{in}^{1/2}$  ( $190 \text{ Nm}^{-2} \cdot \text{m}^{1/2}$ ) at 76 K, a decrease of 10%.

### 3.3.4 AISI 310

Fracture tests of AISI 310 at 4 K are now in progress. Results at 298 K and 76 K are presented here.

An outstanding characteristic of room temperature tests was the large amount of plastic deformation that occurred at the crack tip prior to material separation. Loading caused a noticeable blunting of the crack tip and an apparent crack extension of about 0.08 inch (0.2 cm). The deformation was visible on the surfaces of fractured specimens as a zone of stretch between the fatigue cracked region and the torn ligament. This deformed zone curved upward, out of the plane of the fatigue crack.

The fracture test records for AISI 310 are shown in figure 26. The load-deflection curves indicate fully plastic behavior. At 298 K and 76 K the mode of fracture was stable, ductile tearing. Discontinuities occur in the 4 K curves probably due to adiabatic, localized specimen heating.

J-integral test results are shown in table 18 and in figure 27. At room temperature the  $J/2\sigma_{flow}$  line has a slope nearly equal to the slope of the extrapolated J- $\Delta a$  curve. The vertical stretch zone line, the  $J/2\sigma_{flow}$  line,

and the  $J-\Delta a$  curve appear to meet at a point of triple intersection. The  $J/2\sigma_{\text{flow}}$  line appears to be in agreement with the datum point for a specimen tested to a  $\Delta a$  value in the stretch zone.

At 76 K the  $J/2\sigma_{\text{flow}}$  line predicts a larger stretch zone than was actually measured. The value of  $J_{\text{IC}}$  for this temperature was determined by extrapolating the  $J-\Delta a$  curve, to the measured value for the stretch zone. The first three data points were weighted more heavily; this yields a more conservative estimate of  $J_{\text{IC}}$  than if the fourth datum point were equally weighted. The value given for  $J_{\text{IC}}$  at 76 K is preliminary; additional data are needed at  $\Delta a \leq 0.015$  inch (0.38 cm).

The  $K_Q$  values listed in table 16 do not represent valid fracture toughness measurements. The ratio of fracture toughness to yield stress is very high at each temperature; hence, linear elastic plane strain behavior could never be observed in practical test specimen sizes. Table 17 indicates that at 76 K linear elastic behavior would be observed in 18 inch (46 cm) thick specimens. On the other hand, specimens  $\sim 0.6$  inch (1.5 cm) are sufficient for J-integral tests.

The  $K_{\text{IC}}(J)$  values converted from the  $J_{\text{IC}}$  data are shown in figure 28. The  $K_{\text{IC}}(J)$  value at 76 K is substantially higher than the value at 298 K--a clear indication that the fracture toughness of AISI 310 increases at cryogenic temperatures.

The fracture surfaces of AISI 310 specimens were not ferromagnetic, in contrast to the findings reported for AISI 304 and AISI 316 stainless steels [13]. This indicates that there was no austenite-to-martensite transformation for the AISI 310 alloy, even when deformed and fractured in liquid helium. This is in agreement with other observations that the austenitic 310 alloy remains stable during deformation at low temperatures whereas 304 and 316 stainless steels do not [25, 26].

#### 4. Discussion

The tensile results for the alloys Ti-5Al-2.5Sn, Inconel 750, and AISI 310 were in close agreement with data from the literature [12, 21-23, 27-38] but the yield strengths determined for the precipitation hardened A-286 alloy were  $\sim 15\%$  lower than might be expected. Data in the literature [37-45] indicate that room temperature yield strengths of about 105 ksi ( $72.4 \times 10^7 \text{ Nm}^{-2}$ ) and higher can be achieved. Probably due to the complex

metallurgical structure of alloy A-286, it has been found [46] that the optimum tensile properties are not always achieved with the standard heat treatment.

Fracture toughness data for Ti-5Al-2.5Sn at cryogenic temperatures are available in the literature [22, 23, 47-51] but the existing data are incomplete. Some data [47, 50, 51] obtained for thin sheet materials ( $B \leq .5$  inch) were not sufficient to provide valid  $K_{IC}$  data over the entire cryogenic to ambient temperature range. No data at 4 K had been reported.

Although it is generally accepted that ELI grades of Ti-5Al-2.5Sn exhibit superior low temperature toughness compared to normal interstitial grades, there has been a lack of quantitative data relating  $K_{IC}$  values to interstitial content. The present results should provide a useful basis for comparison.

In figure 19 the data of Pyle et al. [22] and Carman et al. [23] were presented. These authors performed tests on ELI grades of Ti-5Al-2.5Sn having a total Fe + C + O + N content of 0.28 - 0.46%. At 20 K, the average  $K_{IC}$  values are  $\sim 9 \text{ ksi} \cdot \text{in}^{1/2}$  higher than the normal interstitial (Fe + C + O + N = .52%) Ti-5Al-2.5Sn alloy reported here. It may be significant to note that the ELI grades exhibited considerable variability. Scatter in the results of Pyle et al. and Carman et al. amounted to  $\pm 14\%$ .

The  $K_{IC}(J)$  values for Inconel 750 at 76 K were in the range 161-185  $\text{ksi} \cdot \text{in}^{1/2}$ . Scatter in the data between specimens may have been due partly to the fact that the specimens were obtained from individual forgings. Data reported by Lessman, Logsdon, Kossowsky, Mathur, and Wells [21] showed  $K_{IC}(J)$  values of about 70  $\text{ksi} \cdot \text{in}^{1/2}$  for Inconel 750 at 76 K. The material tested by Lessman, et al. was solution treated and double aged using different heat treatment conditions than those applied in the present investigation. Thus, processing and heat treatment apparently influence the fracture toughness of Inconel 750 significantly.

Depending primarily on alloy composition, the AISI 300 series austenitic stainless steels are metastable. At low temperatures the austenitic phase ( $\gamma$ ) may transform to bcc ( $\alpha'$ ) or to hcp ( $\epsilon$ ) martensitic structures. Literature

is available describing the effect of transformation on low temperature strength and ductility [25, 52-55] but little has been published concerning the effect of such transformations on fatigue crack growth rates and plane strain fracture toughness.

In the present studies, magnetic measurements revealed that cyclic loading of AISI 304 and 316 stainless steels during crack growth experiments at 4 K caused considerable formation of martensite. There was no evidence of transformation for AISI 310, agreeing with tensile data [25, 26]. As much as 95% martensite may result from strain induced transformations in AISI 304 and 316 alloys [25, 26].

When crack growth rate data for AISI 310 were compared with previous results [13] for AISI 304 and 316 alloys, the crack growth rates at room temperature were nearly equivalent. At room temperature, the three alloys are essentially stable and the data represent the rate of crack propagation through austenite.

During tests of AISI 304 and 316 alloys at 76 and 4 K, it can be assumed that the martensitic transformation occurred locally in the plastic zone ahead of the crack tip; transformation preceded material separation. The parameter measured in these tests was the rate of crack propagation through partially martensitic material. But, the data for AISI 310 represent the rate of propagation through stable austenite. The comparison in figure 17 for 4 K data indicated that over the range of stress intensity examined, the crack growth rate in the metastable alloys (AISI 304, 316) is higher. But, at room temperature all alloys (304, 310, 316) exhibit equivalent crack growth rates. It is suggested that the crack growth rate behavior of AISI 300 series stainless steels is influenced by the martensitic transformation; apparently, transformation preceding crack growth results in higher crack growth rates.

The AISI 310 alloy exhibits excellent fracture toughness at cryogenic temperatures, but the fracture toughness of 304 and 316 stainless steels are greater. The austenite to martensite transformation provides a plausible explanation for the difference since the transformation is an energy absorbing process. For materials that transform during fracturing, not all the energy absorbed during the test goes into crack extension [56]. Martensitic phase transformations account for the high fracture toughness observed in TRIP (transformation induced plasticity) steels [57].

The mechanical properties of the materials that we have investigated at 4 K are compared in table 19. The alloys are classified in three groups that represent a wide range of mechanical behavior. The fracture toughness data for these materials, based on the  $K_{IC}$  and  $K_{IC(J)}$  parameters, varies by over an order of magnitude from  $35 \text{ ksi} \cdot \text{in}^{1/2}$  for the Ti-6Al-4V alloy to  $\sim 475 \text{ ksi} \cdot \text{in}^{1/2}$  for AISI 304. The same materials vary in yield strength by a factor of three. The precipitation-hardened austenitic alloys occupy an intermediate position, combining a balance of fracture toughness and yield stress with high resistance to fatigue crack growth at cryogenic temperatures.

The choice of materials for specific applications must be made on the basis of several interrelated design criteria. The alloys in table 19 are ranked in descending order according to fracture toughness but on the basis of yield strength the ranking would be exactly reversed. The fact that fracture toughness and yield stress are inversely related is a typical example of the trade-offs that are involved in materials selection.

## 5. References

1. Standard method of tests for plane strain fracture toughness of metallic materials, E-399-74, Annual Book of ASTM Standards, part 10, pp 432-451 (Amer. Soc. Test. Mater., Easton, Md., 1974).
2. Fracture Toughness Testing and its Applications, ASTM STP 381, pp 1-409, (Amer. Soc. Test. Mater., Baltimore, Md., 1965).
3. Brown, W. F., Jr., and Srawley, J. E., Plane Strain Crack Toughness Testing of High Strength Metallic Materials, ASTM STP 410, pp 1-129 (Amer. Soc. for Test. and Mater., Baltimore, 1966).
4. Review of Developments in Plane Strain Fracture Toughness Testing, ASTM STP 463, Ed. W. F. Brown, Jr., pp 1-170, (Amer. Soc. Test. Mater. and NASA, Lutherville-Timonium, Md, 1970).
5. Rice, J. R., A path independent integral and the approximate analysis of strain concentration by notches and cracks, J. Appl. Mech., Trans. ASME 35, 379-386 (1968).
6. Begley, J. A. and Landes, J. D., The J-integral as a fracture criterion, in Fracture Toughness, Proc. of the 1971 National Symposium on Fracture Mechanics, Part II, ASTM STP 514, pp. 1-20 (Amer. Soc. Test. Mater., Philadelphia, Pa., 1972).
7. Landes, J. D., and Begley, J. A., The effect of specimen geometry on  $J_{IC}$ , in Fracture Toughness, Proc. of the 1971 National Symposium on Fracture Mechanics, Part II, ASTM STP 514, pp. 24-39 (Amer. Soc. Test. Mater., Philadelphia, Pa., 1972).
8. Yoder, G. R. and Griffis, C. A., J-integral and the initiation of crack extension in a titanium alloy, NRL report 7662, Naval Res. Lab., (1973), 20 pp.
9. Kobayashi, A. S., Chiu, S. T., and Beeuwkes, R., A numerical and experimental investigation on the use of the J-integral, Eng. Fract. Mech. 5, 298-305 (1973).
10. Landes, J. D., and Begley, J. A., Test results from J-integral studies: an attempt to establish a  $J_{IC}$  testing procedure, in Fracture Analysis, ASTM STP 560 (Amer. Soc. Test. Mater., Easton, Md., 1974).
11. Standard methods of tension testing of metallic materials, E8-69, Annual Book of ASTM Standards, part 10, pp. 90-110 (Amer. Soc. Test. Mater., Easton, Md., 1974).
12. Reed, R. P., A cryostat for tensile tests in the temperature range 300° to 4°K, paper K-3, in Advances in Cryogenic Engineering, 7, Ed. K. D. Timmerhaus, pp. 448-454 (Plenum, New York, 1962).

13. Tobler, R. L., Mikesell, R. P., Durcholz, R. L., Fowlkes, C. W., and Reed, R. P., Fatigue and fracture toughness testing at cryogenic temperatures, in Semi-Annual Report on Materials Research in Support of Superconducting Machinery, NBSIR 74-359, Nat. Bur. Stands. (1974) 308 pp; available from NTIS, AD 780-596/3WM.
14. Roberts, E., Jr., Elastic crack-edge displacements for the compact tension specimen, Mater. Res. Stand. 9, 27 (1969).
15. Bubsey, R. T., Fisher, D. M., Jones, M. H., and Strawley, J. E., Compliance measurements, Chap. 4, in Experimental Techniques in Fracture Mechanics, Ed. A. S. Kobayashi, First Edition, pp. 76-95, (Soc. Exper. Stress Anal. and Iowa State Univ., Westport, Conn., 1973).
16. Irwin, G. R., Fracture, Handbuch der Physik, 6, pp. 551-590 (Springer Verlag, Berlin, 1958).
17. Rice, J. R., Paris, P. C., and Merkle, J. G., Some further results on J-integral and estimates, in Progress in Flaw Growth and Fracture Toughness Testing, ASTM STP 536, pp. 231-244, (Amer. Soc. Test. Mater., Baltimore, Md., 1973).
18. Ledbetter, H. M., Naimon, E. R., and Weston, W. F., Elastic properties of engineering alloys at cryogenic temperatures, in Semi-Annual Report on Materials Research in Support of Superconducting Machinery, NBSIR 74-359, Nat. Bur. Stand (1974), 308 pp; available from NTIS, AD 780-596/3WM.
19. Warren, K. A., and Reed, R. P., Tensile and Impact Properties of Selected Materials from 20 to 300°K, Nat. Bur. Stand. Monograph 63, pp. 1-51 (Washington, D.C., 1963).
20. Basinski, Z. S., The instability of plastic flow of metals at very low temperatures, Proc. Roy. Soc. Lond. A240, 229-242 (1957).
21. Lessman, G. G., Logsdon, W. A., Kossowski, R., Mathur, M. P., and Wells, J. M., Structural materials for cryogenic applications, 74-9D4-CRYMT-RI, (Westinghouse Research Labs., Pittsburgh, Pa., 1974) 59 pp.
22. Pyle, R., Schillinger, D. E., and Carman, C. M., Plane strain fracture toughness and mechanical properties of 2219-T87 aluminum and 5Al-2.5Sn ELI titanium alloy weldments and one inch thick 5Al-2.5Sn ELI titanium plate, NASA CR-72154, Frankford Arsenal, (1968) 86 pp.
23. Carman, C. M., Forney, J. W., and Katlin, J. M., Plane strain fracture toughness and mechanical properties of 5Al-2.5Sn ELI titanium at room and cryogenic temperatures, NASA CR-54296, Frankford Arsenal (1966), 59 pp.



24. Freed, C. N., and Kraft, J. M., Effect of side grooving on measurements of plane strain fracture toughness, *J. Mater.*, 1, No. 4, 770-789 (1966).
25. Gunter, C. J., and Reed, R. P., The effect of experimental variables including the martensite transformation on the low temperature mechanical properties of austenitic stainless steels, *Trans. Quart.*, 55, No. 3, 399-419 (1962).
26. Larbalestier, D. C., and King, H. W., Austenitic stainless steels at cryogenic temperatures: 1 - structural stability and magnetic properties, *Cryogenics* 13, No. 3, 160-168 (1973).
27. Espey, G. B., Jones, M. H., and Brown, W. F., Jr., Sharp-edge-notch tensile characteristics of several high strength titanium-sheet alloys at room and cryogenic temperatures, in *Low Temperature Properties of High Strength Aircraft and Missile Materials*, ASTM STP 287, pp. 74-96, (Amer. Soc. Test Mater., Baltimore, Md., 1960).
28. Hoke, J. H., Mabus, P. G., and Collier, G. N., Mechanical properties of the stainless steels at subzero temperatures, *Met. Prog.*, 55, 643 (1949).
29. Kropschot, R. H., and Graham, W. F., Mechanical properties of the austenitic stainless steels at low temperatures, NBS 5009, Nat. Bur. Stand. (1956) 6 pp.
30. Desisto, T. S., and Carr, F. L., Low Temperature Mechanical Properties of 300 series stainless steel and titanium, Watertown Arsenal Laboratories, (1960) 15 pp AD 609909.
31. Schwartzberg, F. R., Osgood, S. H., Keys, R. D., and Kiefer, T. F., Cryogenic materials data handbook, AFML-TDR-64-280, Martin Marietta Corp. (1964).
32. Belton, J. H., Godby, L. L., Taft, B. L., Materials for use at liquid hydrogen temperature, in *Low Temperature Properties of High Strength Aircraft and Missile Materials*, ASTM STP 287, pp. 108-121, (Amer. Soc. Test. Mater., Baltimore, Md., 1960).
33. Shogan, R. P., Tensile properties of irradiated Inconel 718 and Inconel X-750 at cryogenic temperatures, WANL-TME-1922, Westinghouse Electric, (1969) 38 pp.
34. Watson, J. F., and Christian, J. L., Low temperature properties of K-Monel, Inconel-X, Rene 41, Haynes 25 and Hastelloy B Sheet Alloys. *J. Basic Eng.*, 84, 265-277 (1962).
35. Welleff, W., McQueen, H. S., and Emmons, W. F., Cryogenic tensile properties of selected aerospace materials, paper A-2, in *Advances in Cryogenic Engineering*, 10, Ed. K. D. Timmerhaus, p. 14-25 (Plenum, New York, 1965).



36. Lovoy, C. V., Low-temp mechanical properties of Inconel-X and its weldments, IN-P and VE-M-62-5, Marshall Space Flight Center (1962), 34 pp.
37. Low temperature mechanical properties of various alloys, a compilation, NASA-SP-5921(01), NASA, (1970), 24 pp.
38. Martin, H. L., Miller, P. C., Imgram, A. G., Campbell, J. E., Effects of low temperatures on the mechanical properties of structural metals, NASA-SP-5012(01), NASA, (1968) 35 pp.
39. Roberts, D. A., Roach, D. B., Hall, A. M., Physical and mechanical properties of nine commercial precipitation hardenable stainless steels, Defense Metals Information Center Report 112 (1959).
40. Montano, J. W., Mechanical properties of high strength A-286 bolts at cryogenic temperatures, IN-P and VE-M-64-1, Marshall Space Flight Center (1964).
41. Slunder, C. J., Hoenie, A. F., and Hall, A. M., Thermal and mechanical treatments for precipitation hardenable stainless steels and their effect on mechanical properties, NASA TM-X-53578, Marshall Space Flight Center (1967).
42. Schwanbeck, C. A., Effects of interim warming on tensile properties of A-286 stainless steel, LAC ER-10008, Lockheed-Georgia Co. (1968) 20 pp.
43. Masteller, R. D., et al., Properties of cryogenically worked materials, NASA CR-72638 (N70-27114), Martin Marietta Corp., (1970).
44. Montano, J. W., An evaluation of the mechanical and stress corrosion properties of cold worked A-286 alloy, NASA-TM-X-64569, NASA, (1971).
45. Anonymous, Armco A-286, Product data bulletin SA-1, Armco Steel Corp. (1966) 8 pp.
46. Amer. soc. met. committee on heat resisting alloys, Heat treating of heat resisting alloys, in Metals Handbook, 2, Heat Treating, Cleaning and Finishing, 8th Edition, pp. 257-268 (1964).
47. Witzell, W. E., Fracture mechanics - plane strain characteristics of several materials, GDC-ERR-AN-1228, General Dynamics/Convair (1967) 35 pp. AD 854611L.
48. Witzell, W. E., Fracture data for materials at cryogenic temperatures, AFML-TR-67-257, Air Force Materials Laboratory (1967) 73 pp.
49. McClaren, S. W., and Foreman, C. R., Cryogenic design data for materials subjected to uniaxial and multiaxial stress field, AFML-TR-65-140, ITV Aerospace Corp. (1965) 144 pp.

50. Tiffany, C. F., Lorenz, P. M., and Hall, L. R., Investigation of plane-strain flaw growth in thick walled tanks, NASA CR-54837, The Boeing Company (1966) 63 pp.
51. Sullivan, T. L., Uniaxial and biaxial fracture toughness of extra-low-interstitial 5Al-2.5Sn titanium alloy sheet at 20°K, NASA-TN-D-4016, Lewis Research Center (1967) 20 pp.
52. Reed, R. P., The spontaneous martensitic transformation in 18% Cr, 8% Ni steels, *Acta Met.*, 10, p. 865-877 (1962).
53. Watson, J. F., Christian, J. L., Low temperature properties of cold-rolled AISI types 301, 302, 304 ELC, and 310 stainless steel sheet, in *Low Temperature Properties of High Strength Aircraft and Missile Materials*, ASTM STP 287, pp. 170-194 (American Soc. Test Mater., Baltimore, Md., 1960).
54. Watson, J. F., and Christian, J. L., A study of austenite decomposition at cryogenic temperatures, *Trans. AIME*, 224, 998-1005 (1962).
55. Bhandarkar, D., Zackay, V. F., and Parker, E. R., Stability and mechanical properties of some metastable austenitic steels, *Met. Trans.*, 3, 2619-2631 (1972).
56. Antolovich, S. D., Fracture toughness and strain-induced phase transformations, *Trans. AIME*, 242, 2371-2373 (1968).
57. Gerberich, W. W., Hemmings, P. L., Zackay, V. F., Parker, E. R., Interactions between crack growth and strain-induced transformation, paper 24, in *Fracture 1969*, Ed. P. L. Pratt (Chapman and Hall Ltd., London, 1969) pp. 288-296.

### List of Tables

	Page
1. Material condition and form as received . . . . .	84
2. Chemical analyses (wt %) . . . . .	84
3. Fatigue cracking conditions . . . . .	85
4. Yield and ultimate tensile strength for Ti-5Al-2.5Sn . . . . .	86
5. Yield and ultimate tensile strength for A-286 . . . . .	86
6. Yield and ultimate tensile strength for Inconel 750 . . . . .	87
7. Yield and ultimate tensile strength for AISI 310 . . . . .	87
8. Fracture toughness of Ti-5Al-2.5Sn . . . . .	88
9. Thickness required for valid $K_{IC}$ tests of Ti-5Al-2.5Sn . . . . .	88
10. J-integral test results for alloy A-286 . . . . .	89
11. $K_Q$ and $R_{SC}$ parameters for A-286 . . . . .	89
12. Specimen thickness required for valid fracture tests of A-286 . . . . .	90
13. Specimen thickness required for valid fracture tests of Inconel 750 . . . . .	90
14. $K_Q$ parameters for Inconel 750 . . . . .	90
15. J-integral results for Inconel 750 . . . . .	91
16. $K_Q$ parameters for AISI 310 . . . . .	92
17. Specimen thickness required for valid fracture tests of AISI 310 . . . . .	92
18. J-integral results for AISI 310 . . . . .	93
19. Summary of mechanical properties at 4 K . . . . .	93

# List of Figures

	Page
1. Tensile specimen (1 in = 2.54 cm) . . . . .	94
2. Cryogenic fatigue testing apparatus . . . . .	95
3. Liquid helium fatigue cryostat . . . . .	96
4. Compact tensile specimen used for fracture tests of Ti-5Al-2.5Sn; B = 1.50 in, W = 3.00 in (1 in = 2.54 cm) . . . . .	97
5. Compact tensile specimen used for J-integral tests of A-286 Inconel 750 and AISI 310 alloys (1 in = 2.54 cm) . . . . .	98
6. Yield and tensile strengths of Ti-5Al-2.5Sn as a function of temperature . . . . .	99
7. Yield and tensile strengths of Inconel 750 as a function of temperature . . . . .	100
8. Yield and tensile strengths of AISI 310 as a function of temperature . . . . .	101
9. Stress-strain curves for Ti-5Al-2.5Sn . . . . .	102
10. Stress-strain curves for A-286 . . . . .	103
11. Stress-strain curves for Inconel 750 . . . . .	104
12. Stress-strain curves for AISI 310 . . . . .	105
13. Crack growth data for Ti-5Al-2.5Sn . . . . .	106
14. Crack growth data for A-286 . . . . .	107
15. Crack growth data for Inconel 750 . . . . .	108
16. Crack growth data for AISI 310 . . . . .	109
17. Crack growth data for AISI 310, 304 and 316 stainless steels at 4 K . . . . .	110
18. Fracture test records for Ti-5Al-2.5Sn (1 lb = 454 gm) . . . . .	111
19. Temperature dependence of fracture toughness of titanium alloys . . . . .	112
20. Fracture test records for A-286 . . . . .	113
21. J-integral versus crack extension for A-286 . . . . .	114
22. Temperature dependence of fracture toughness of A-286 . . . . .	115
23. Fracture test records for Inconel 750 (1 in = 2.54 cm, 1 lb = 4.47 N) . . . . .	116
24. J-integral versus crack extension for Inconel 750 . . . . .	117
25. Temperature dependence of fracture toughness for Inconel 750 . . . . .	118
26. Fracture test records for AISI 310 (1 in = 2.54 cm, 1 lb = 4.47 N) . . . . .	119
27. J-integral versus crack extension for AISI 310 . . . . .	120
28. Fracture toughness of AISI 310 at 298 K and 76 K . . . . .	121

Table 1. Material condition and form as received.

Material	Form	Condition as Received
Ti-5Al-2.5Sn	4 3/4" square bar	Commercial annealed
A-286	4 1/2" square bar	Forged and annealed
Inconel 750	4 1/4 x 4 1/4 x 1 3/4" Forgings	Forged, hot-finished
AISI 310	1.5" Plate	Commercial annealed

NOTE: 1 inch = 2.54 cm.

Table 2. Chemical analyses (wt%).

Ti-5Al-2.5Sn	5.28Al, 0.327Fe, 2.46Sn, 0.01C, 0.01N, 0.174O, 40 ppm H
AISI 310	Bal Fe, 0.038C, 1.41Mn, 0.023P, 0.016S, 0.72Si, 24.65Cr, 20.4Ni, 0.13Mo, 0.14Cu
A-286	Bal Fe, 0.05C, 1.52Mn, 0.016P, 0.007S, 0.54Si, 13.96Cr, 24.97Ni, 1.30Mo, 2.23Ti, 0.004 B, 0.30 V, 0.19 Al
Inconel 750	6.58Fe, 0.04C, 0.20Mn, 0.007S, 0.25Si, 15.16Cr, 73.52Ni, 0.04 Cu, 2.51 Ti, 0.78 Al, 0.89 Cb + Ta

Table 3. Fatigue cracking conditions.

Alloy	Temperatures	a/W	$(P_f/P_m)^a$	$(K_f)^b$
Ti-5Al-2.5Sn	298, 76, 4 K	.45 - .55	~ 0.5	$K_f \leq .6K_Q$ ; $K_f \leq .002 E$
A-286	298, 76, 4 K	~ 0.55	0.4	$K_f \leq .55K_Q$ ; $K_f \leq .002 E$
Inconel 750	298, 76, 4 K	~ 0.60	0.3	$K_f \leq .5K_Q$ ; $K_f \leq .0014 E$
AISI 310	298 K	~ 0.63	0.7	$K_f \leq .8K_Q$ ; $K_f \leq .002 E$
	76, 4 K	~ 0.63	0.4	$K_f \leq .65K_Q$ ; $K_f \leq .002 E$

<sup>a</sup> $P_f/P_m$  is the ratio of maximum fatigue load/maximum load to fracture.

<sup>b</sup> $K_f$  is the maximum stress intensity during fatigue, E is Young's modulus.

Table 4. Yield and ultimate tensile strengths for Ti-5Al-2.5Sn

Temperature (K)	0.2% Yield Strength (ksi)	Ultimate Tensile Strength (ksi)
298	127.8 126.0 Avg= 127	135.2 133.0 Avg= 134
4	225.4 N/A Avg=225	226.4 224.7 Avg= 226

NOTE: 1 ksi =  $0.689 \times 10^7 \text{ Nm}^{-2}$

Table 5. Yield and ultimate tensile strengths for A-286

Source	Temperature (K)	Orientation	0.2% Yield Strength (ksi)	Ultimate Tensile Strength (ksi)
This Report	298	Trans.	93.3 83.0 Avg = 88	150 <sup>a</sup>
	76	Trans.	110.5 106.5 Avg = 108	198 <sup>a</sup>
	4	Trans.	129.1 128.7 Avg = 129	215 <sup>a</sup>
Warren and Reed	298	Long.	111	160
	195	Long.	120	176
	76	Long.	135	209
	20	Long.	150	235

NOTE: 1 ksi =  $.689 \times 10^7 \text{ Nm}^{-2}$

<sup>a</sup> An estimation based on the data of Warren and Reed [19].

Table 6. Yield and ultimate tensile strength for Inconel 750.

Temperature (K)	0.2% Yield Strength (ksi)	Ultimate Tensile Strength (ksi)
298	106.0	174.9
	<u>100.7</u>	<u>166.7</u>
	Avg=103	Avg=171
76	119.6	205.9
	<u>115.7</u>	<u>203.9</u>
	Avg=118	Avg=205
4	128.1	226.6
	<u>124.7</u>	<u>224.2</u>
	Avg=126	Avg=225

NOTE: 1 ksi =  $0.689 \times 10^7 \text{ Nm}^{-2}$

Table 7. Yield and tensile strength for AISI 310.

Temperature (K)	0.2% Yield Stress (ksi)	Ultimate Tensile Strength (ksi)
298	35.3	78.9
	<u>34.2</u>	<u>78.7</u>
	Avg=35	Avg=79
76	79.2	151.7
	<u>77.7</u>	<u>153.6</u>
	Avg=78	Avg=153
4	111.0 <sup>a</sup>	171

NOTE: 1 ksi =  $0.689 \times 10^7 \text{ Nm}^{-2}$

<sup>a</sup> Measured according to crosshead travel.



Table 8. Fracture toughness of Ti-5Al-2.5Sn.

Temperature (K)	Specimen	a/W	$K_{IC}$ (ksi·in <sup>1/2</sup> )	$K_Q$ (ksi·in <sup>1/2</sup> )
298	1	.552	68.9	-
	3	.562	71.7	-
	4	.561	-	71.6 <sup>a</sup>
173	10	.629	-	53.2 <sup>b</sup>
76	8	.462	-	39.9 <sup>a</sup>
	9	.460	38.3	-
	12	.495	-	39.5 <sup>c</sup>
4	6	.473	39.4	-
	13	.552	37.1	-
	14	.504	-	36.6 <sup>d</sup>

<sup>a</sup>Fatigue crack plane deviated ~13° from notch plane; ≤10° is acceptable.

<sup>b</sup>Fatigue stress intensity exceeded 0.60  $K_Q$ .

<sup>c</sup>Side grooved specimen;  $K_Q$  calculated according to Freed et al. [24].

<sup>d</sup>Edge crack = 89.5% of average crack length; ≥90% is acceptable.

NOTE: 1 ksi·in<sup>1/2</sup> = 1.098 × 10<sup>6</sup> Nm<sup>-2</sup>·m<sup>1/2</sup>

Table 9. Specimen thickness required for valid  $K_{IC}$  for Ti-5Al-2.5Sn.

Temperature (K)	a (in)	B (in)	$\sigma_y$ (ksi)	$K_{IC}$ (ksi·in <sup>1/2</sup> )	$2.5 (K_{IC}/\sigma_y)^2$ (in)
298	1.35 - 1.65	1.5	122	70.3	0.835
76	1.35 - 1.65	1.5	200	39.2	0.096
4	1.35 - 1.65	1.5	225	38.3	0.072

NOTES: 1 in = 2.54 cm.

$$1 \text{ ksi} = .689 \times 10^7 \text{ Nm}^{-2}$$

$$1 \text{ ksi} \cdot \text{in}^{1/2} = 1.098 \times 10^6 \text{ Nm}^{-2} \cdot \text{m}^{1/2}$$

Table 10. J-integral test results for alloy A-286.

Temperature (K)	Specimen	a/W	J (in·lb·in <sup>-2</sup> )	Δa (in)	J <sub>IC</sub> (in·lb·in <sup>-2</sup> )	E/(1-ν <sup>2</sup> ) (10 <sup>6</sup> psi)	K <sub>IC</sub> (J) (ksi·in <sup>1/2</sup> )
298	2	.548	725	.076	455 ± 9%	31.22	119 ± 4.5%
	4	.554	806	.101			
	5	.543	507	.015			
	15	.546	527	.038			
76	6	.542	396	.005	385 ± 6%	33.17	113 ± 3%
	8	.556	658	.056			
	13	.545	462	.012			
4	0	.550	402	.035	360 ± 4%	33.22	109 ± 2%
	7	.555	543	.148			
	10	.548	373	.022			

NOTES: 1 in = 2.54 cm  
 $1 \text{ ksi} \cdot \text{in}^{1/2} = 1.098 \times 10^6 \text{ Nm}^{-2} \cdot \text{m}^{1/2}$   
 $1 \text{ in} \cdot \text{lb} \cdot \text{in}^{-2} = 1.75 \times 10^{-4} \text{ MJm}^{-2}$

Table 11. K<sub>Q</sub> and R<sub>SC</sub> parameters for A-286

Temperature (K)	Specimen	a/W	K <sub>Q</sub> (ksi·in <sup>1/2</sup> )	R <sub>SC</sub>
298	2	.548	95	1.72
	4	.554	111	
	5	.543	105	
	15	.546	101	
			Avg=103	
76	6	.542	117	1.49
	8	.556	135	
	13	.545	122	
	9	.565	122	
4	0	.550	120	1.20
	7	.555	114	
	10	.548	116	
			Avg=117	

NOTE:  $1 \text{ ksi} \cdot \text{in}^{1/2} = 1.098 \cdot 10^6 \text{ Nm}^{-2} \cdot \text{m}^{1/2}$ .

Table 12. Specimen thickness required for valid fracture tests of A-286

Temperature (K)	$2.5 (K_Q/\sigma_y)^2$ (in)	$2.5 [K_{IC}(J)/\sigma_y]^2$ (in)	$50 J_{IC}/\sigma_{flow}$ (in)
298	3.1	4.5	0.20
76	3.3	2.7	0.13
4	2.1	1.8	0.10

NOTE: 1 inch = 2.54 cm

Table 13. Specimen thickness required for valid fracture tests of Inconel 750.

Temperature (K)	$2.5 [K_{IC}(J)/\sigma_y]^2$ (in)	$50 (J_{IC}/\sigma_{flow})$ (in)
298	8.6	.41
76	5.7	.29

NOTE: 1 inch = 2.54 cm

Table 14.  $K_Q$  parameters for Inconel 750

Temperature (K)	Specimen (No.)	a/W	$K_Q$ (ksi·in <sup>1/2</sup> )
298	2	.601	104
	7	.603	118
	10	.602	106
	5	.604	123
			Avg = 113
76	8	.605	118
	11	.602	139
	4	.599	160
			Avg = 139

NOTE: 1 ksi =  $1.098 \times 10^6 \text{ Nm}^{-2}$  · m<sup>1/2</sup>

Table 15. J-integral results for Inconel 750.

Temperature (K)	Specimen (No.)	b (inch)	J (in·lb·in <sup>-2</sup> )	Δa (inch)	J <sub>IC</sub> (in·lb·in <sup>-2</sup> )	E/(1-ν <sup>2</sup> ) (10 <sup>6</sup> psi)	K <sub>IC</sub> (J) <sub>(ksi·in<sup>3/2</sup>)</sub>
298	2	1.20	1200	.009	1100 ± 7%	32.6	189 ± 3.5%
	7	1.19	2970	.048			
	10	1.20	1930	.034			
	5	1.19	1630	.028			
76	8	1.19	1030	.004	880 ± 14%	34.2	173 ± 7%
	11	1.19	1420	.069			
	4	1.20	2280	.061			
	1	1.20	798	.004			

NOTES: 1 in = 2.54 cm

1 in·lb·in<sup>-2</sup> = 1.75 x 10<sup>-4</sup> MJm<sup>-2</sup>

1 psi = .689 x 10<sup>7</sup> Nm<sup>-2</sup>

1 ksi·in<sup>1/2</sup> = 1.098 x 10<sup>6</sup> Nm<sup>-2</sup>·m<sup>1/2</sup>

Table 16.  $K_Q$  Parameters for AISI 310

Temperature (K)	Specimen (No.)	a/W	$K_Q$ (ksi·in <sup>1/2</sup> )
298	4	.628	40.6
	2	.630	45.1
	9	.635	44.1
	5	.640	48.0
			Avg= 44.5
76	12	.643	97.2
	1	.618	80.8
	13	.618	77.8
	8	.609	83.2
			Avg= 84.8

NOTE: 1 ksi·in<sup>1/2</sup> = 1.098 x 10<sup>6</sup> Nm<sup>-2</sup>·m<sup>1/2</sup>

Table 17. Specimen thickness required for valid fracture tests of AISI 310

Temperature (K)	$2.5 [K_{IC}(J)/\sigma_y]^2$ (inch)	$50 (J_{IC}/\sigma_{flow})$ (inch)
298	54	1.23
76	17.6	0.60

NOTE: 1 in = 2.54 cm.

Table 18. J-Integral results for AISI 310

Temperature (K)	Specimen (No.)	b (in)	J (in·lb·in <sup>-2</sup> )	Aa (in)	J <sub>IC</sub> (in·lb·in <sup>-2</sup> )	E/(1-ν <sup>2</sup> ) (10 <sup>6</sup> psi)	K <sub>IC</sub> (J) (ksi·in <sup>1/2</sup> )
298	4	1.13	1140	.014			
	2	1.22	701	.007			
	9	1.10	1560	.015	900 ± 11%	29.4	162.6 ± 5.5%
	5	1.08	3490	.038			
76	12	1.07	1920	.016			
	1	1.16	2670	.022			
	13	1.16	3560	.040	14.25 ± 11%	31.4	211.5 ± 5.5%
	8	1.19	2310	.018			

NOTES: 1 inch = 2.54 cm      1 in·lb·in<sup>-2</sup> = 1.75 x 10<sup>4</sup> MJm<sup>-2</sup>      1 psi = 0.689 x 10<sup>4</sup> Nm<sup>-2</sup>  
 1 ksi·in<sup>1/2</sup> = 1.098 x 10<sup>6</sup> Nm<sup>-1/2</sup>·m<sup>1/2</sup>

Table 19. Summary of mechanical properties at 4 K

Class of Material	Alloy	Fracture Toughness K <sub>IC</sub> or K <sub>IC</sub> (J) (ksi·in <sup>1/2</sup> )	Yield Stress (ksi)	Rank in Terms of Resistance to Fatigue Crack Propagation
Annealed 300 series stainless steels	304	476	65	average
	316	430	79	average
	310	~220 <sup>a</sup>	111	good
Precipitation hardened austenitic alloys	Inconel 750	~173 <sup>a</sup>	127	good
	A-286	102	129	good
Titanium alloys	Ti-5Al-2.5Sn	38	225	poor
	Ti-6Al-4V	35	264	poor

<sup>a</sup> Estimate based on preliminary data.

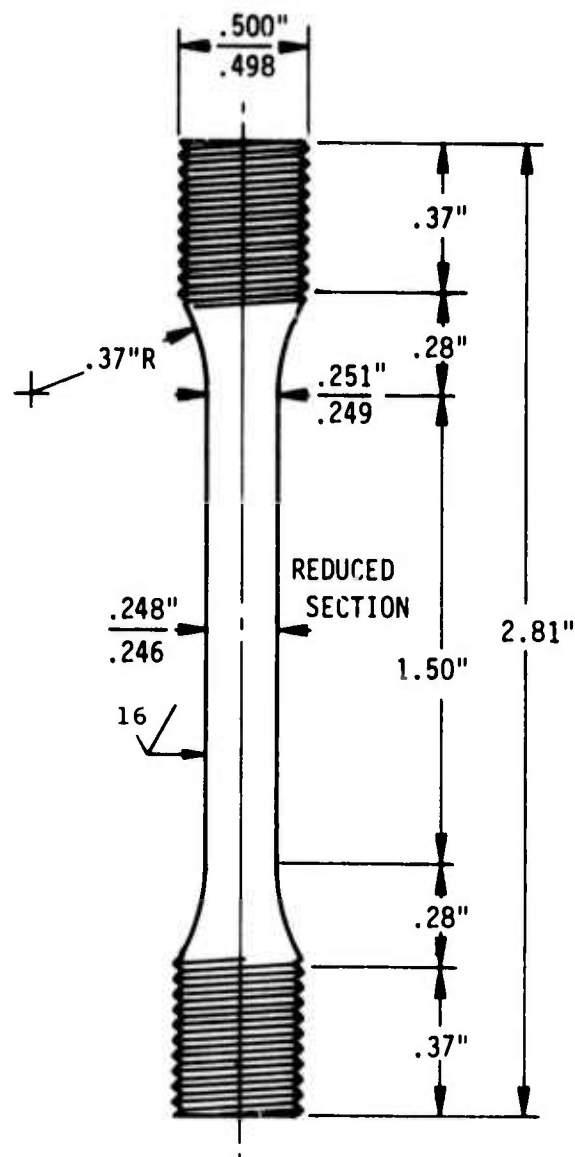


FIGURE 1 - Tensile Specimen (1 in. = 2.54 cm)

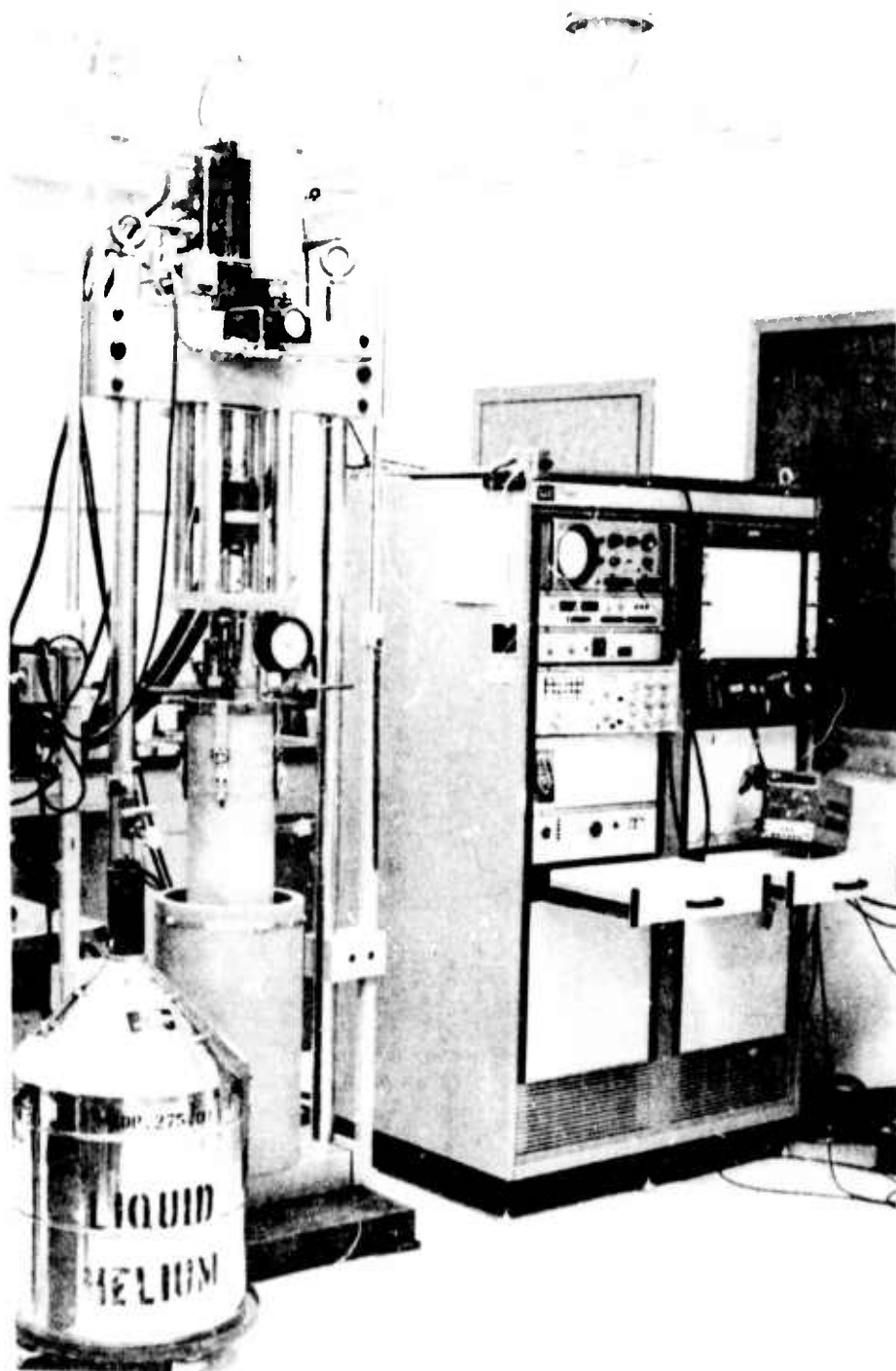


Figure 2 Cryogenic Fatigue Testing Apparatus



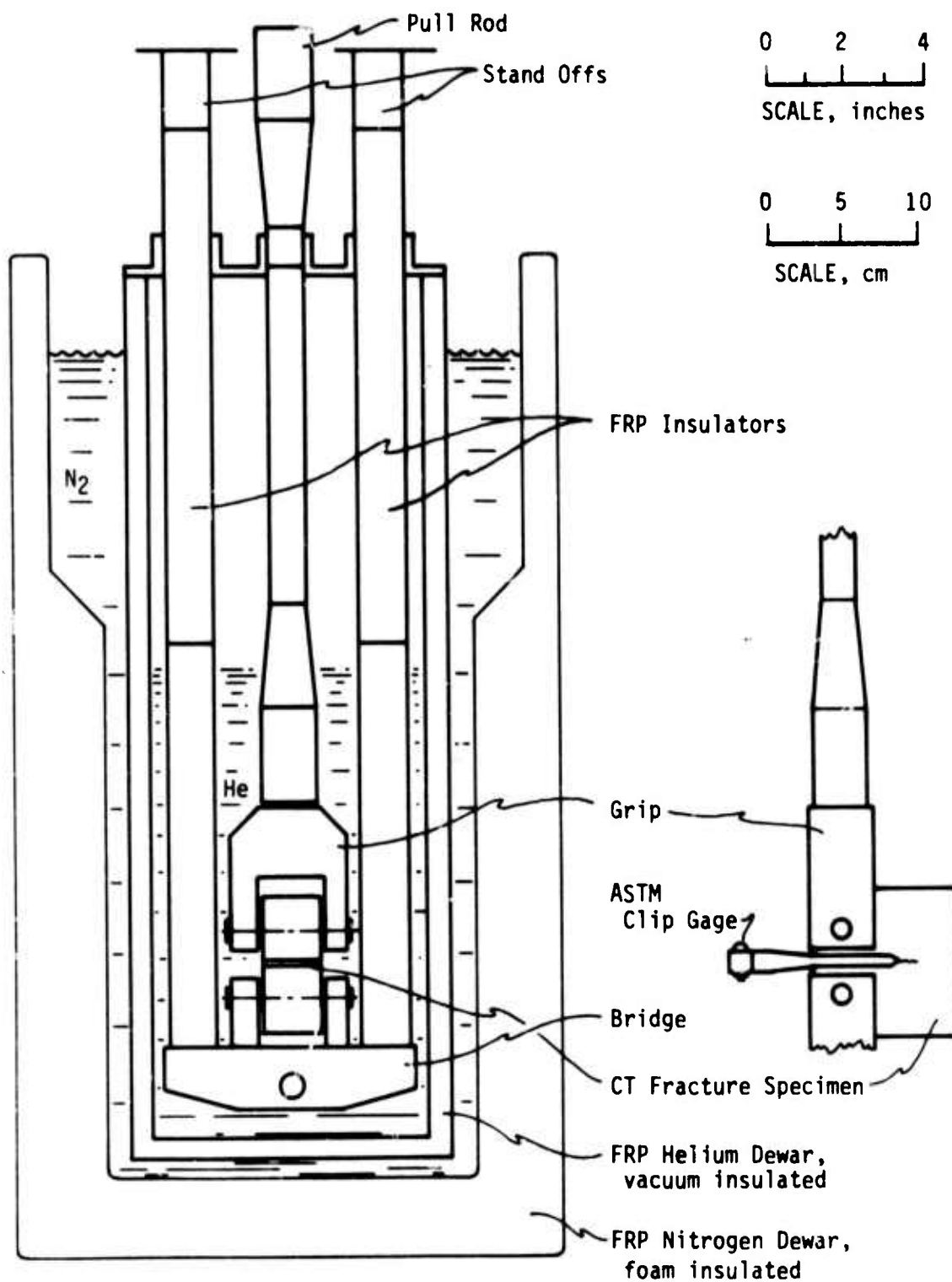
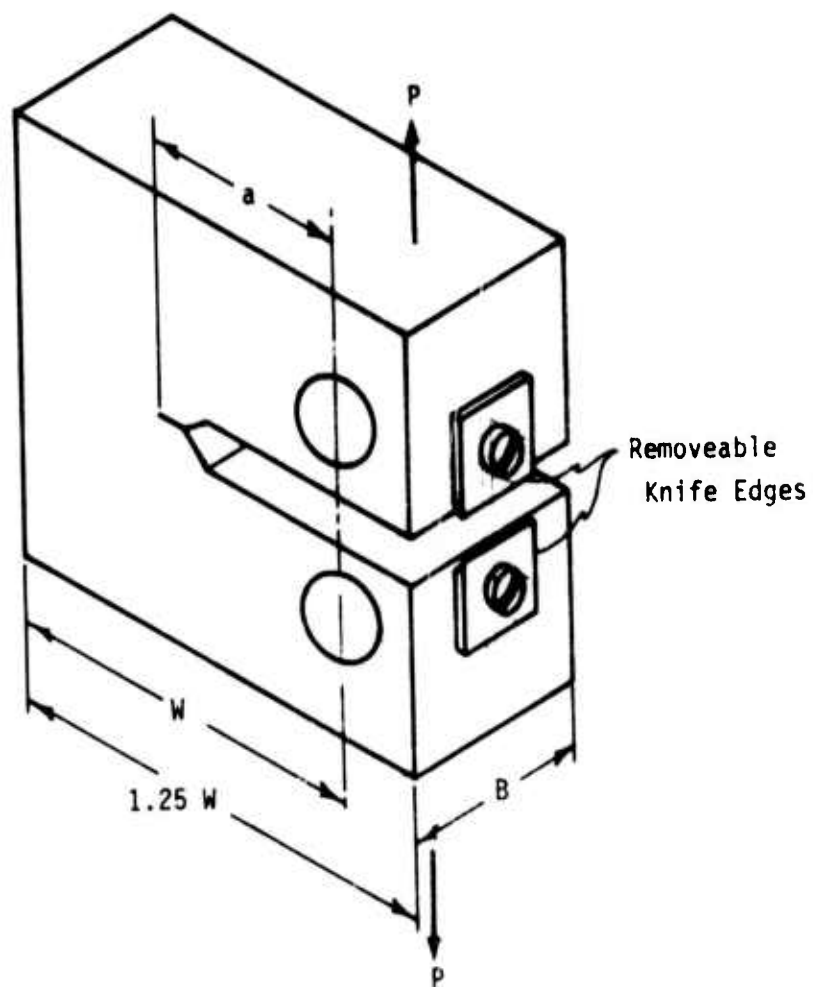


FIGURE 3 - Liquid helium fatigue cryostat.



$B = 1.50 \text{ in}$   
 $W = 3.00 \text{ in}$   
 $(1 \text{ in} = 2.54 \text{ cm})$

FIGURE 4 - Compact tensile specimen used for fracture tests of Ti-5Al-2.5Sn

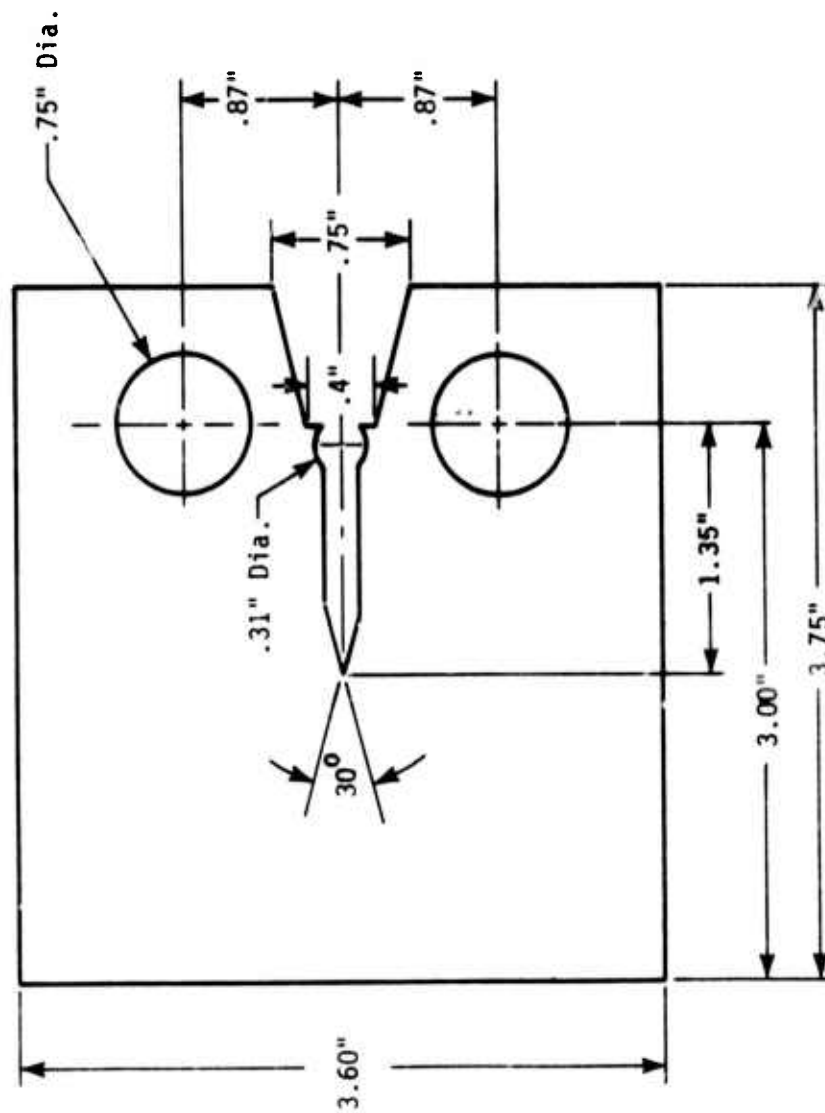


FIGURE 5 - Compact tensile specimen used for J-integral tests  
of A-286, Inconel 750 and AISI 310 alloys.  
(1 in = 2.54 cm)

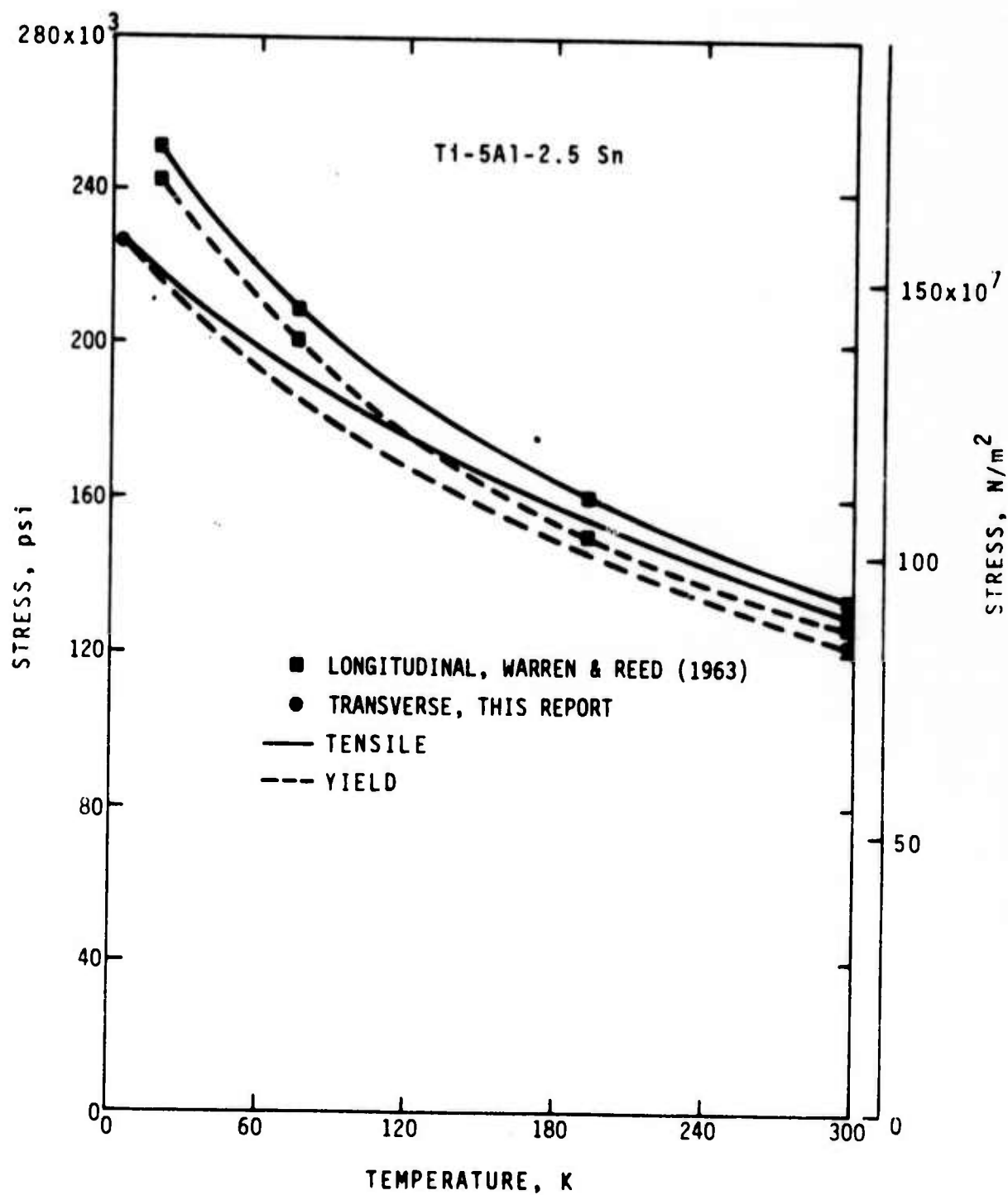


FIGURE 6 - Yield and tensile strength of Ti-5Al-2.5Sn as a function of temperature.

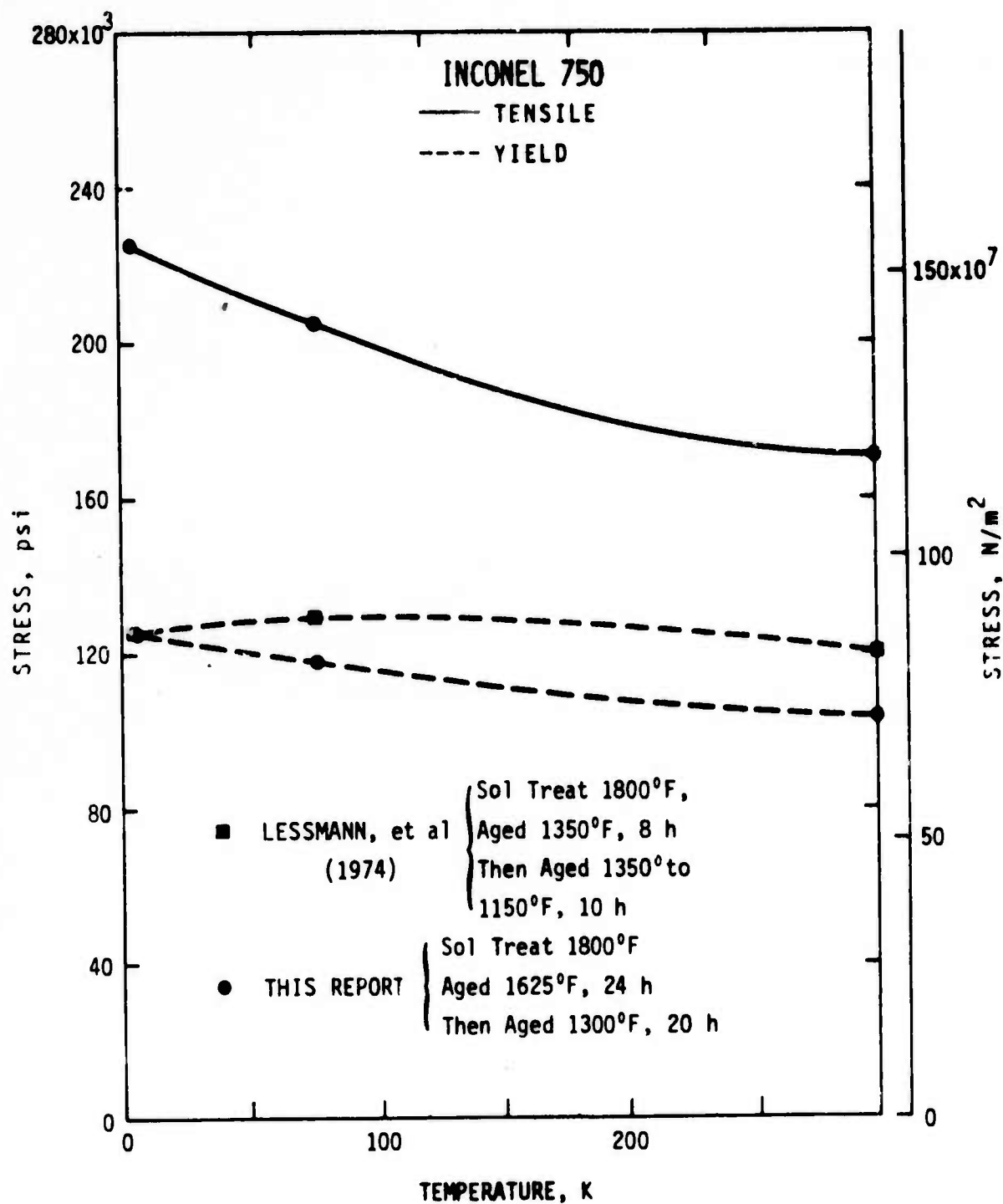


FIGURE 7 - Yield and tensile strength of Inconel 750 as a function of temperature.

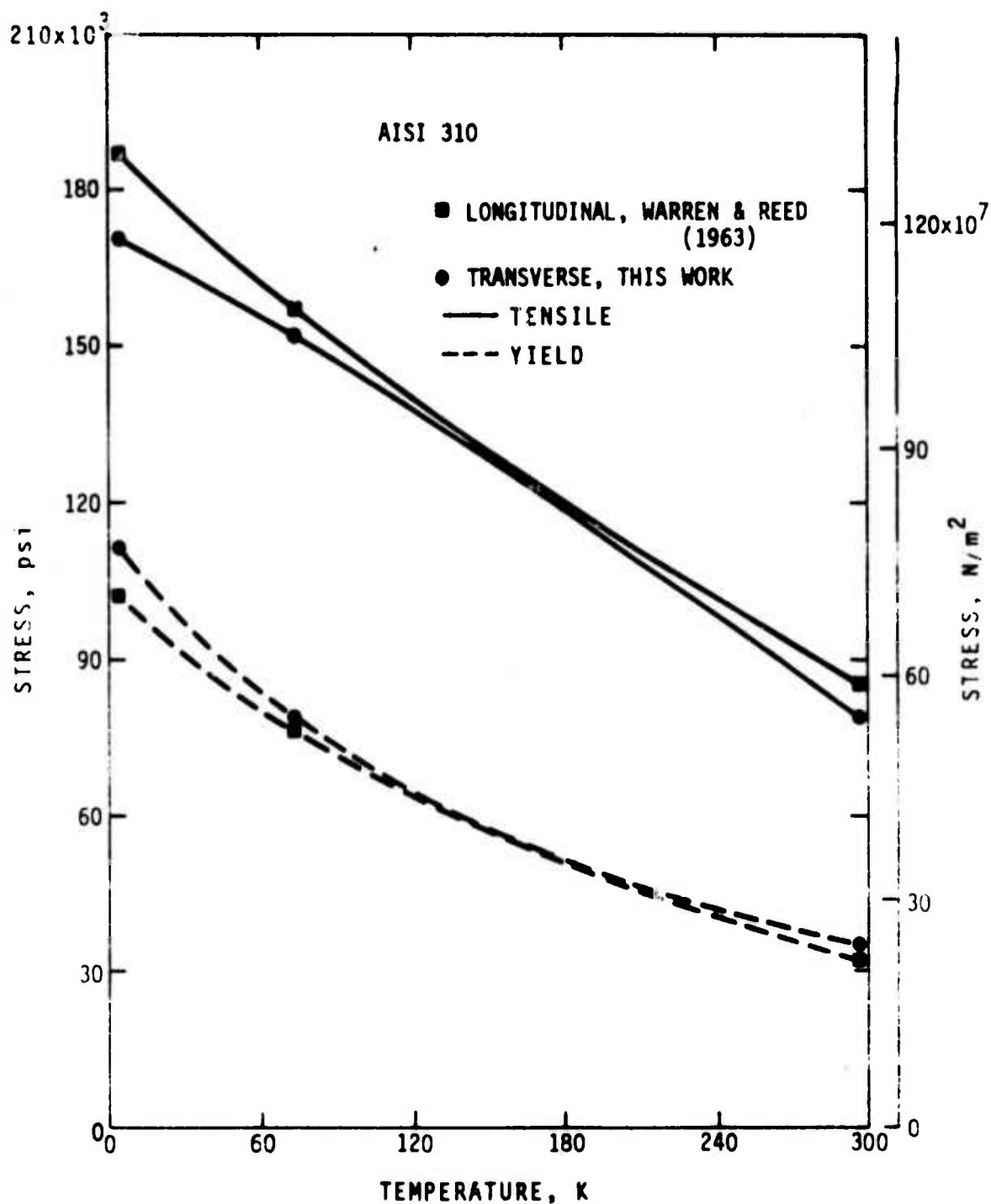


FIGURE 8 - Yield and tensile strengths of AISI 310 as a function of temperature.

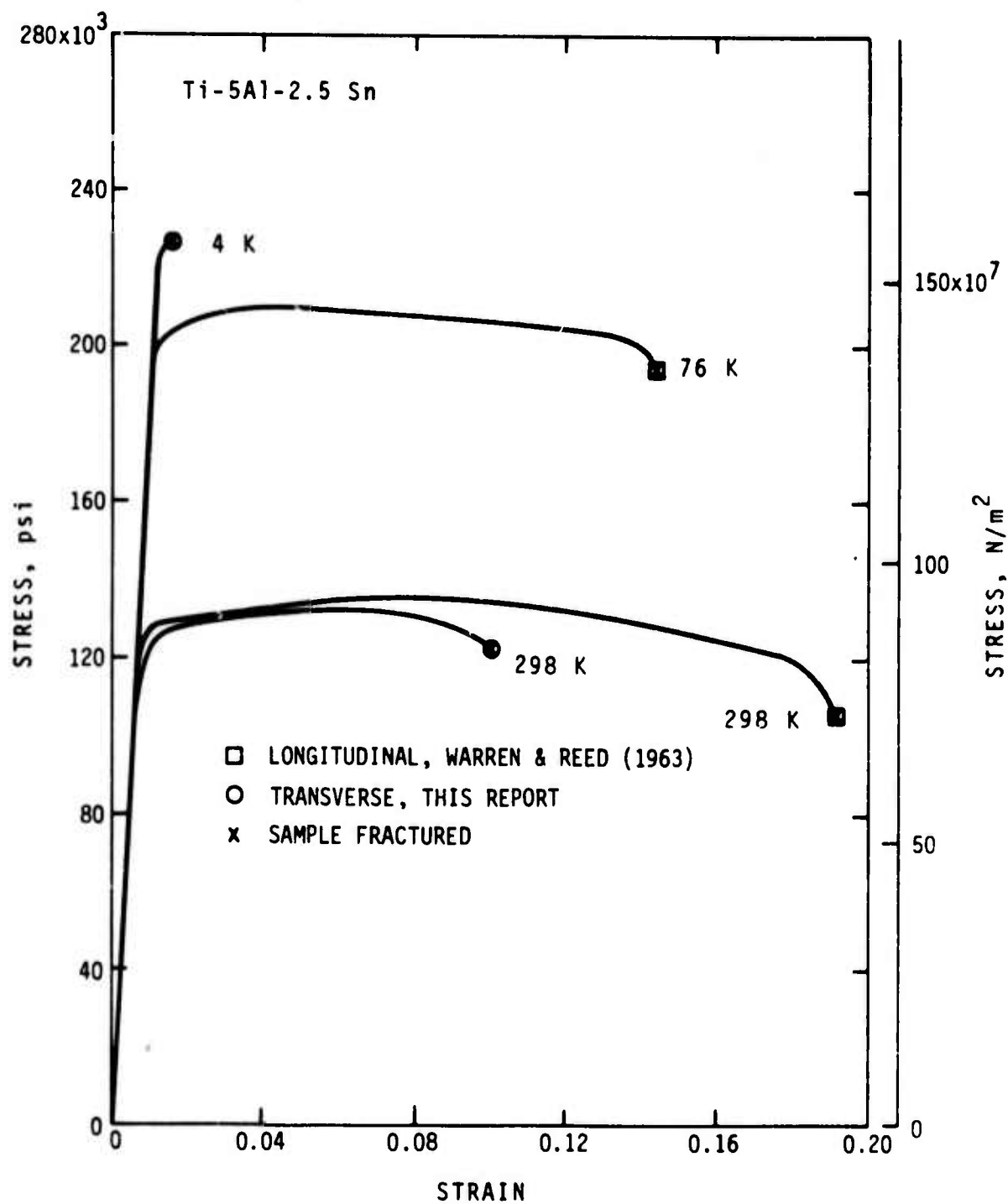


FIGURE 9 - Stress-strain curves for Ti-5Al-2.5Sn.

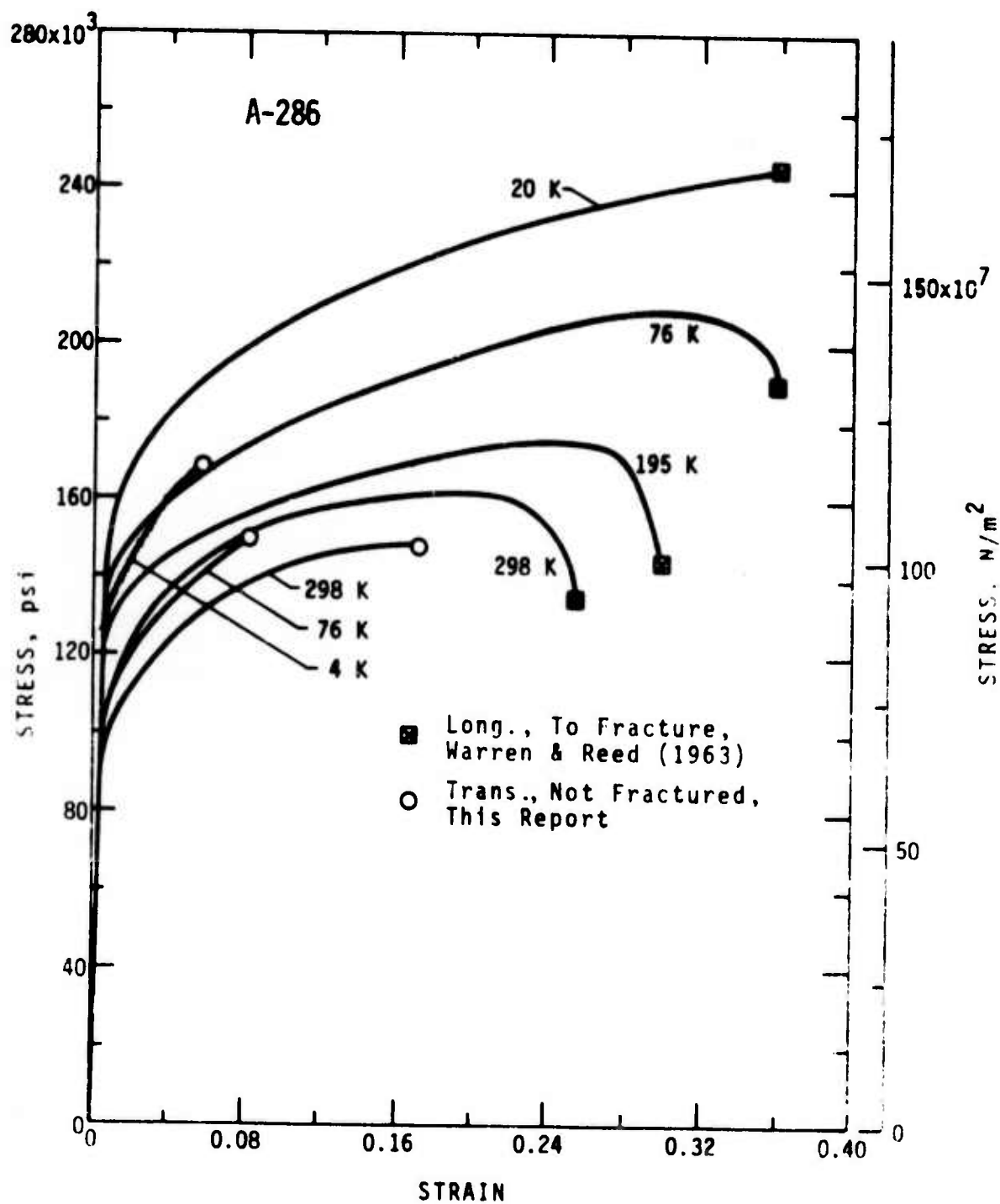


FIGURE 10 - Stress-strain curves for A-286



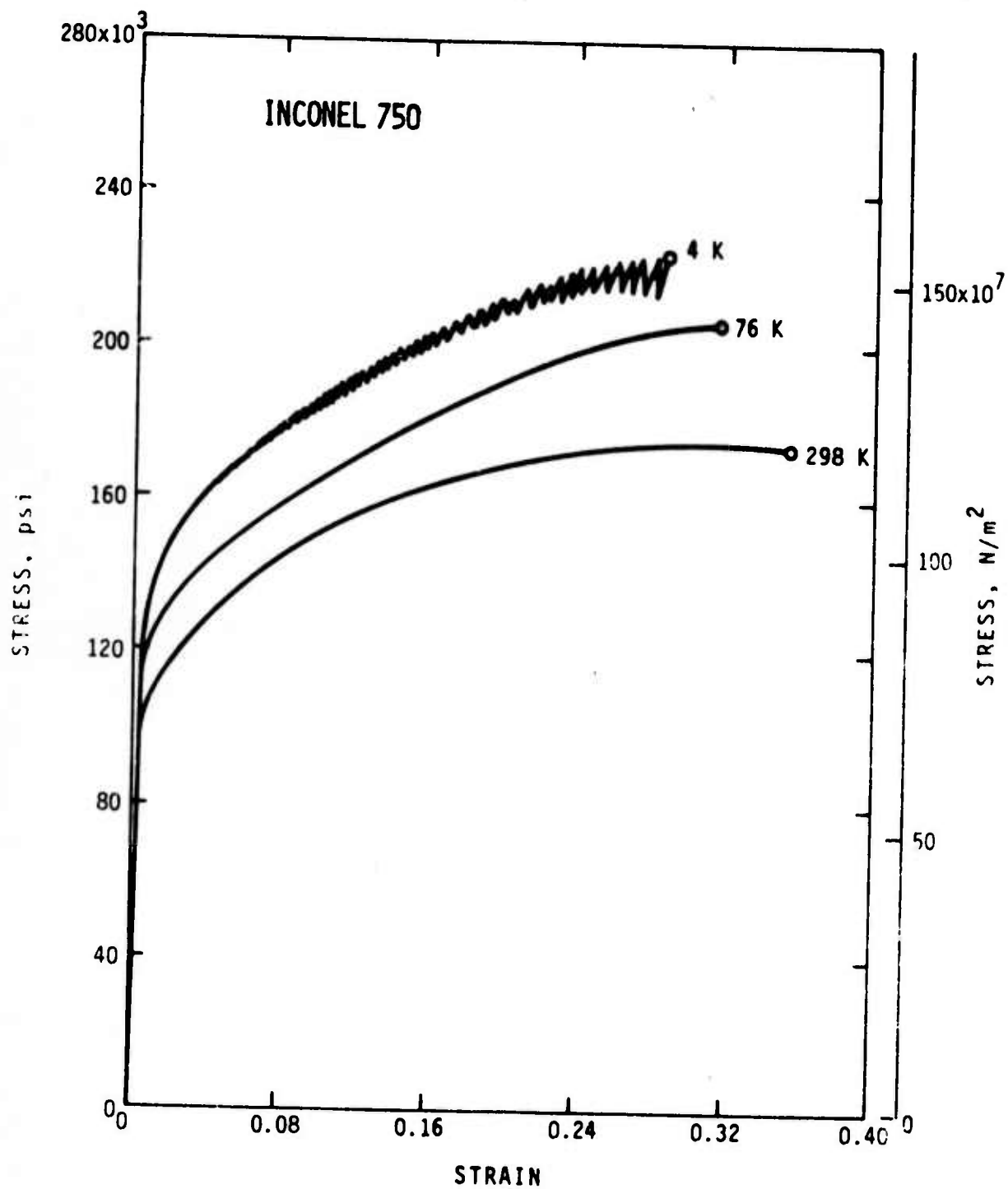


FIGURE 11 - Stress-strain curves for Inconel 750.

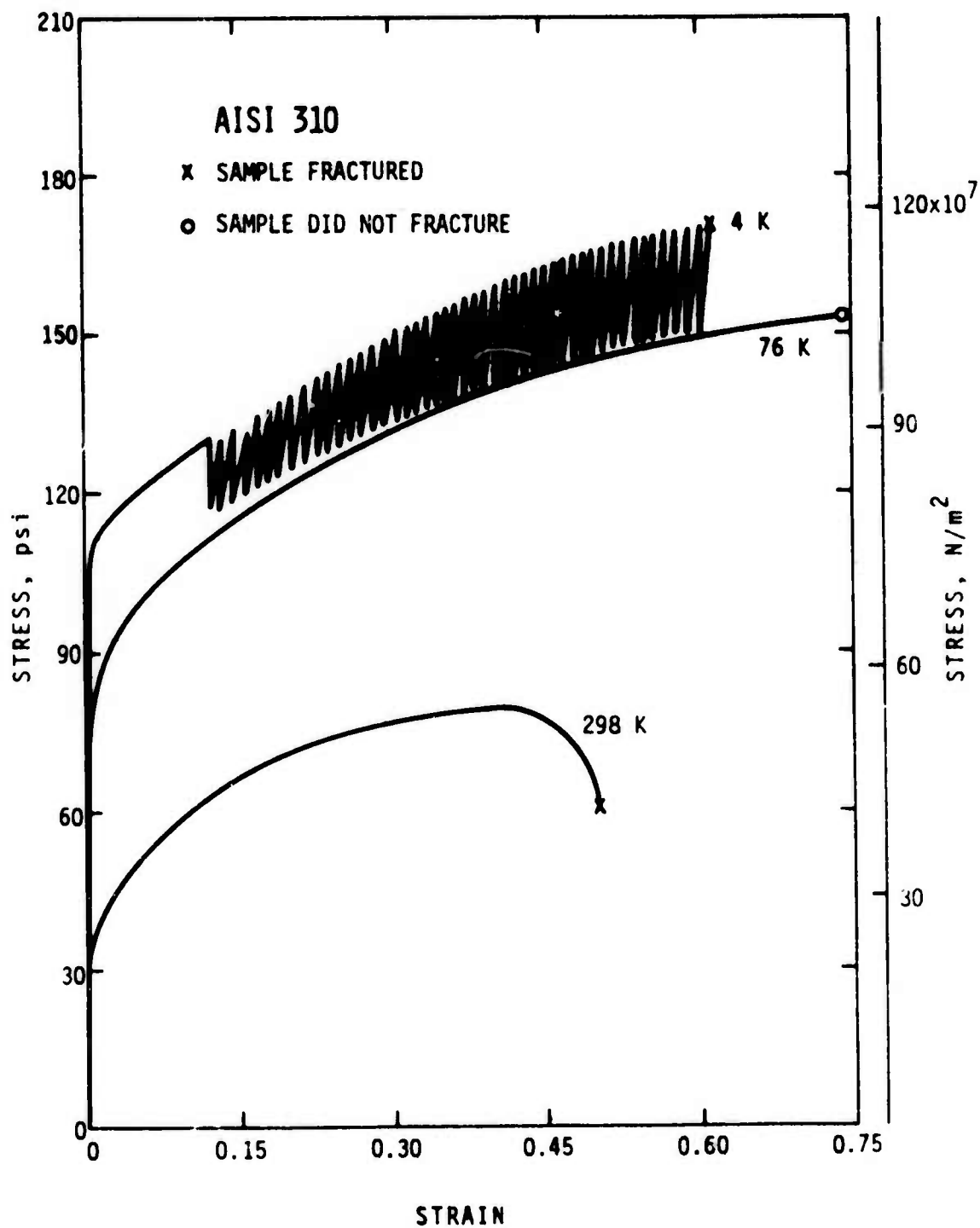


FIGURE 12 - Stress-strain curves for AISI 310.

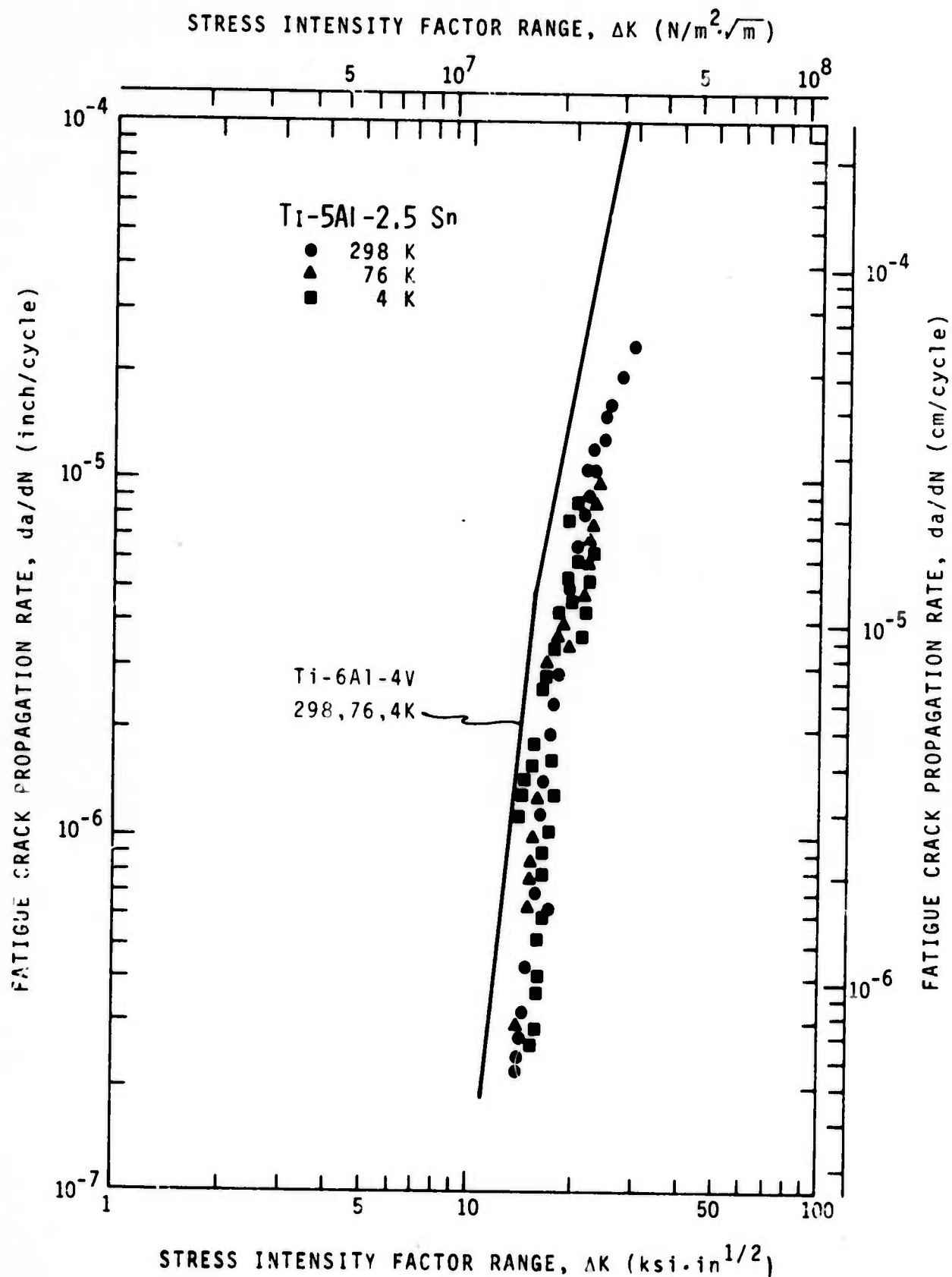


FIGURE 13 - Crack growth data for Ti-5Al-2.5Sn.

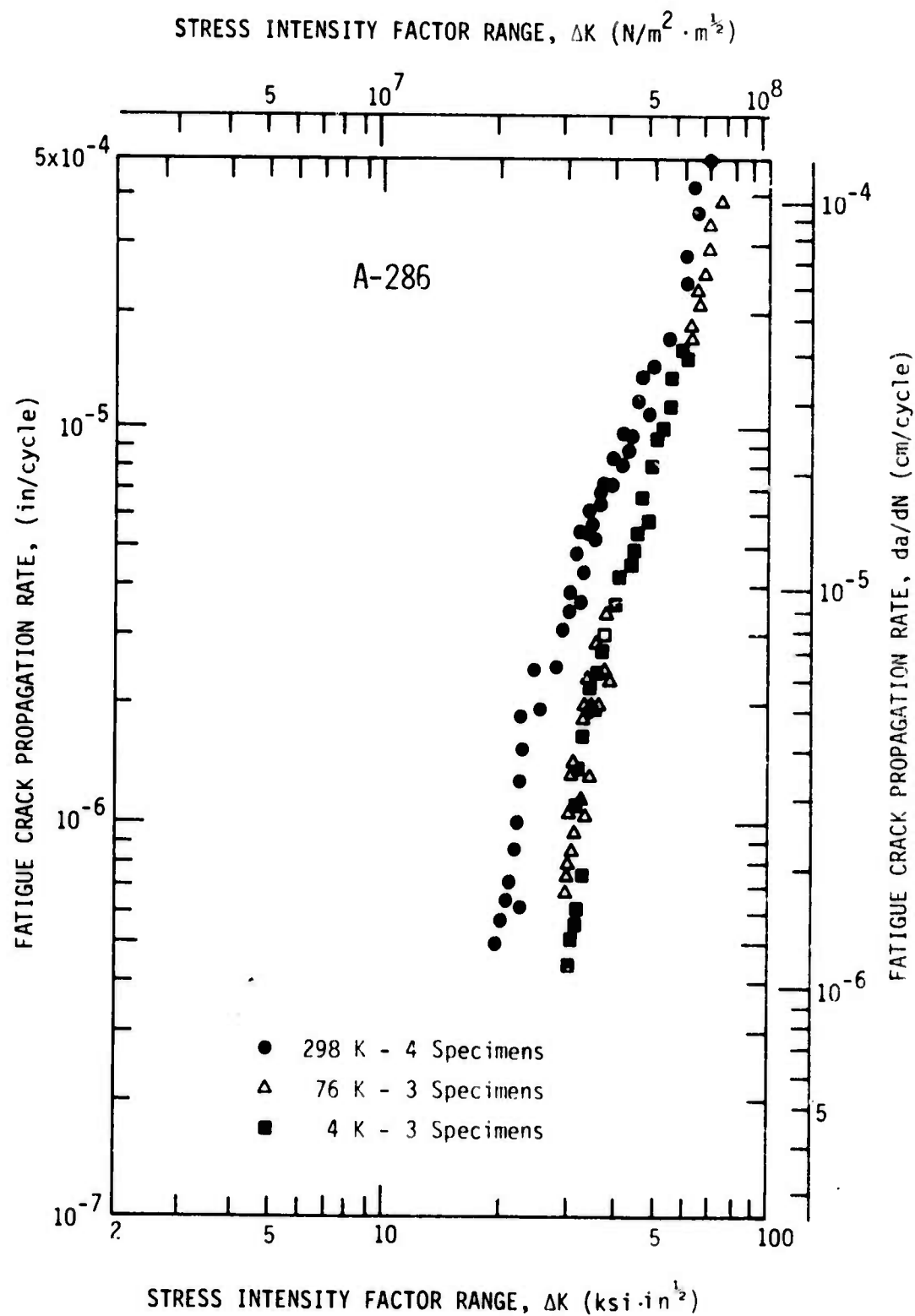


FIGURE 14 - Crack growth data for A-286.

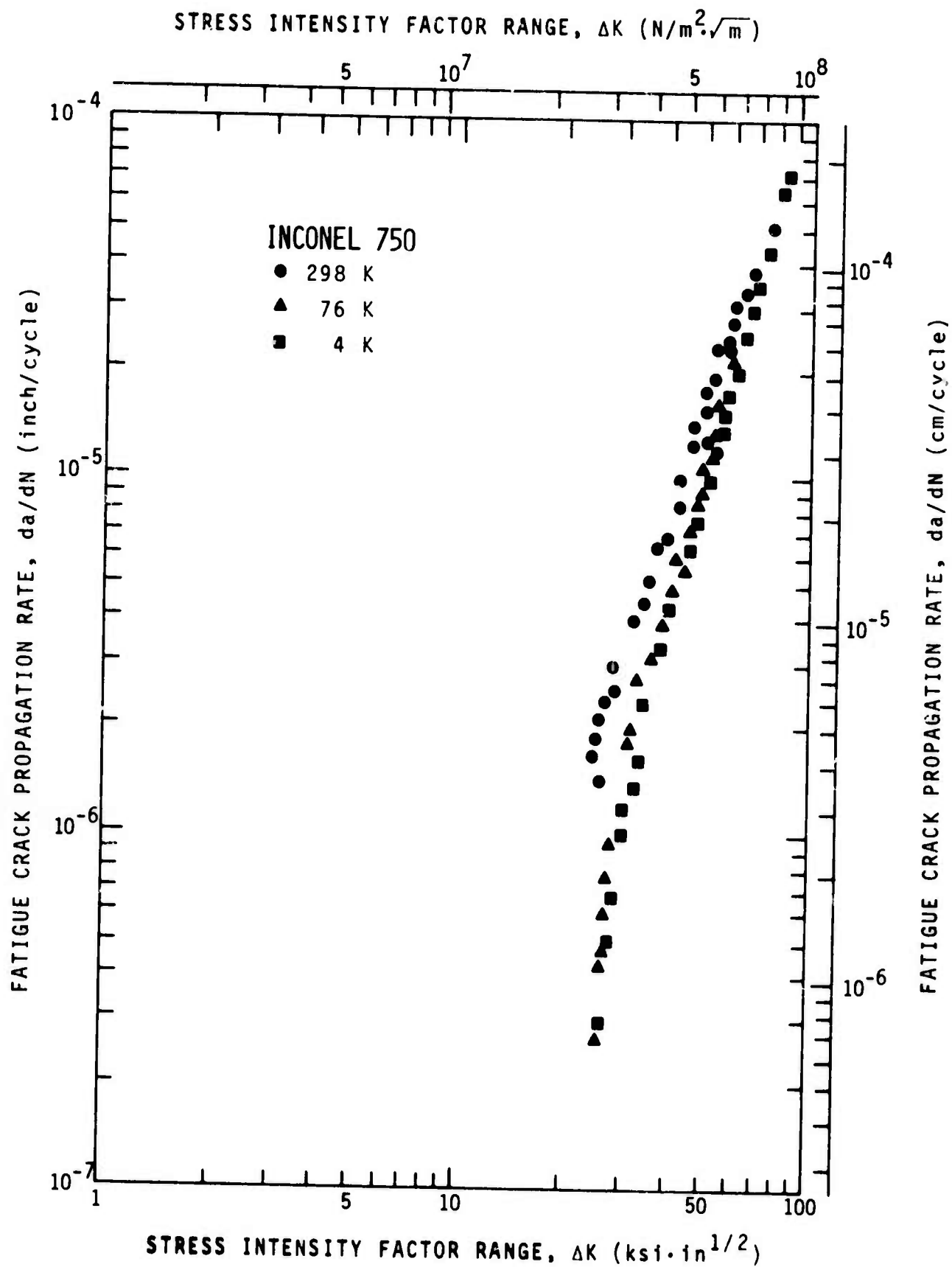


FIGURE 15 - Crack growth data for Inconel 750.

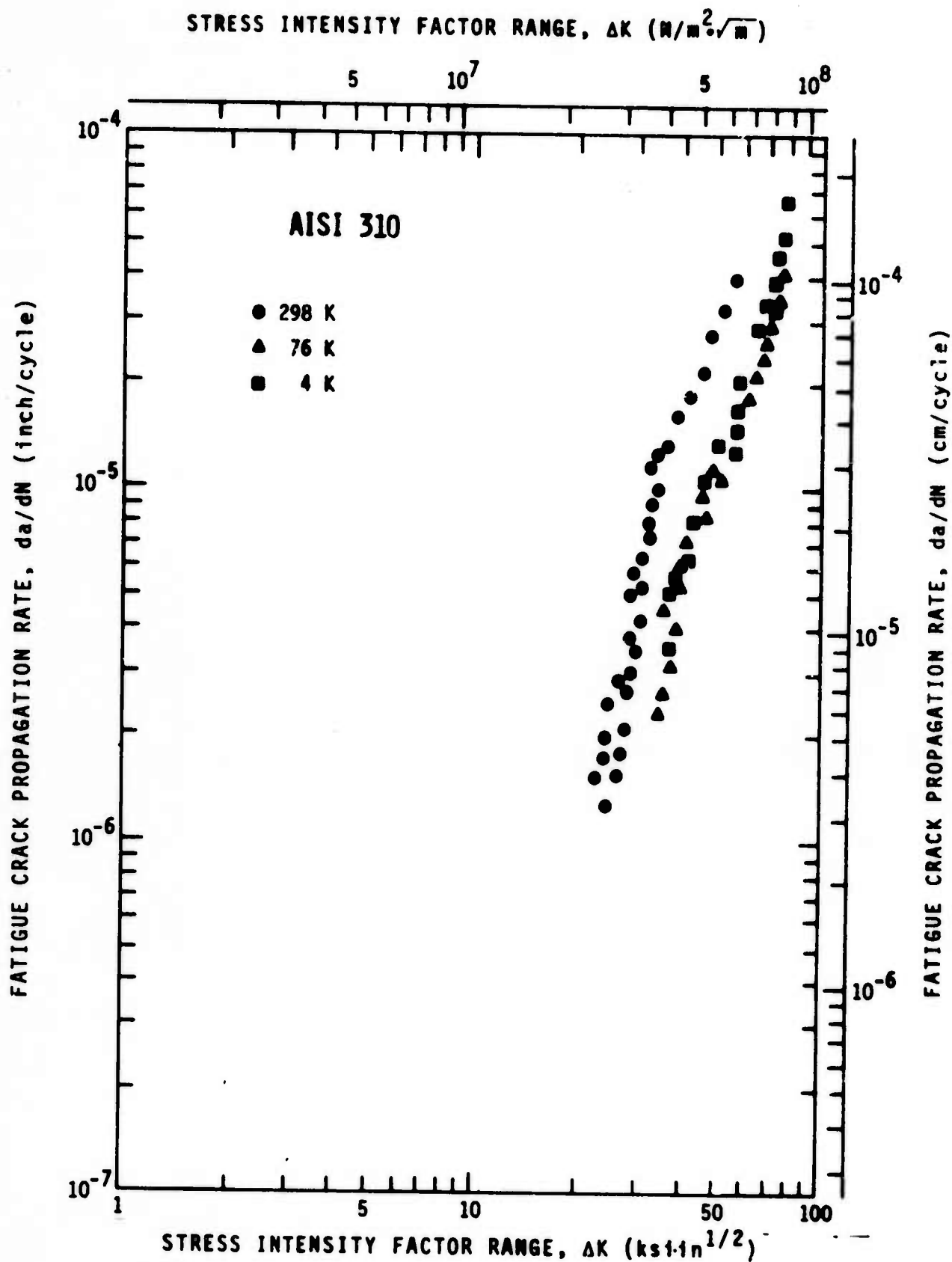


FIGURE 16 - Crack growth data for AISI 310.

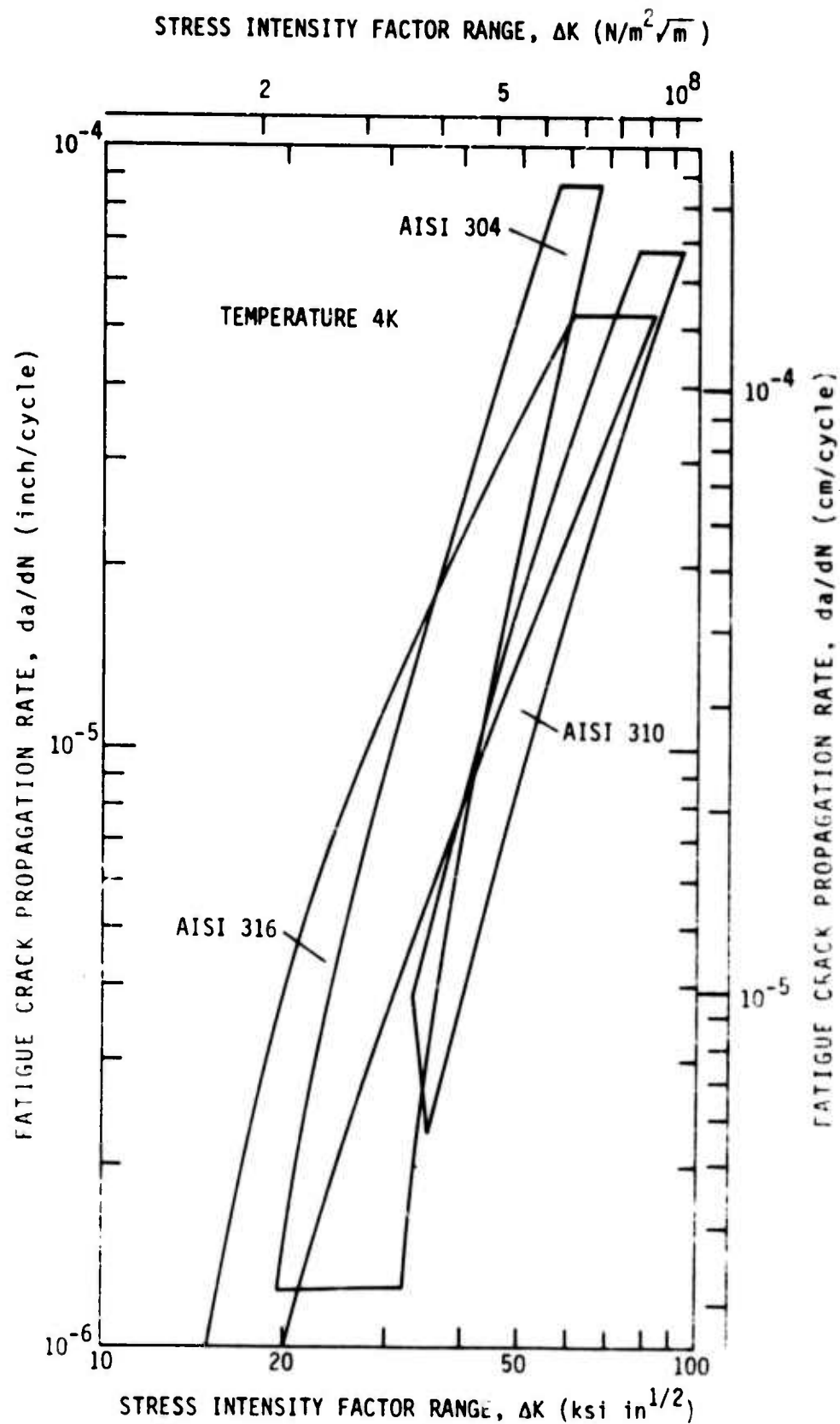


FIGURE 17 - Crack growth data for AISI 304, 310, and 316 stainless steels at 4K.

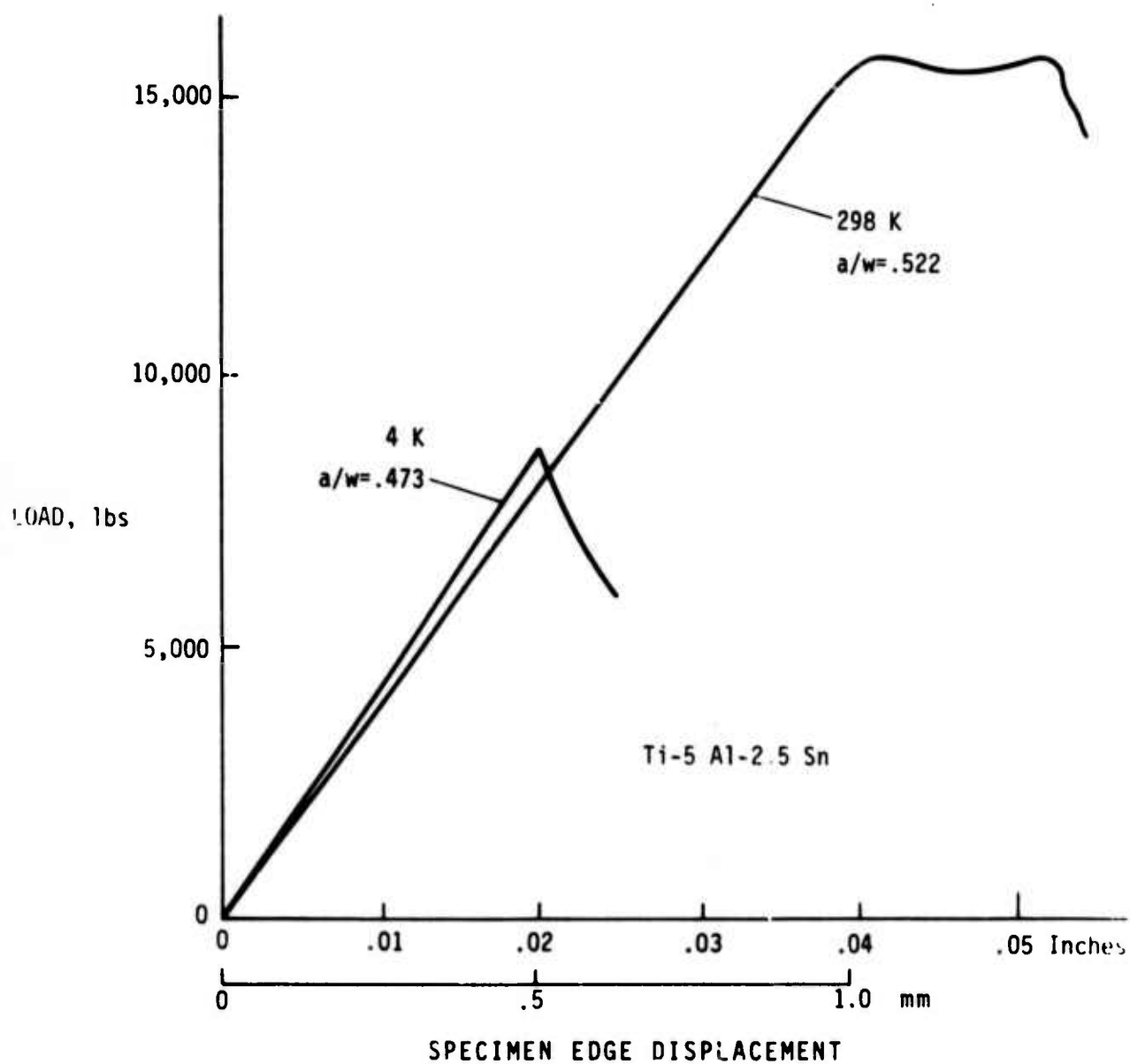


FIGURE 18 - Fracture test records for Ti-5Al-2.5Sn.



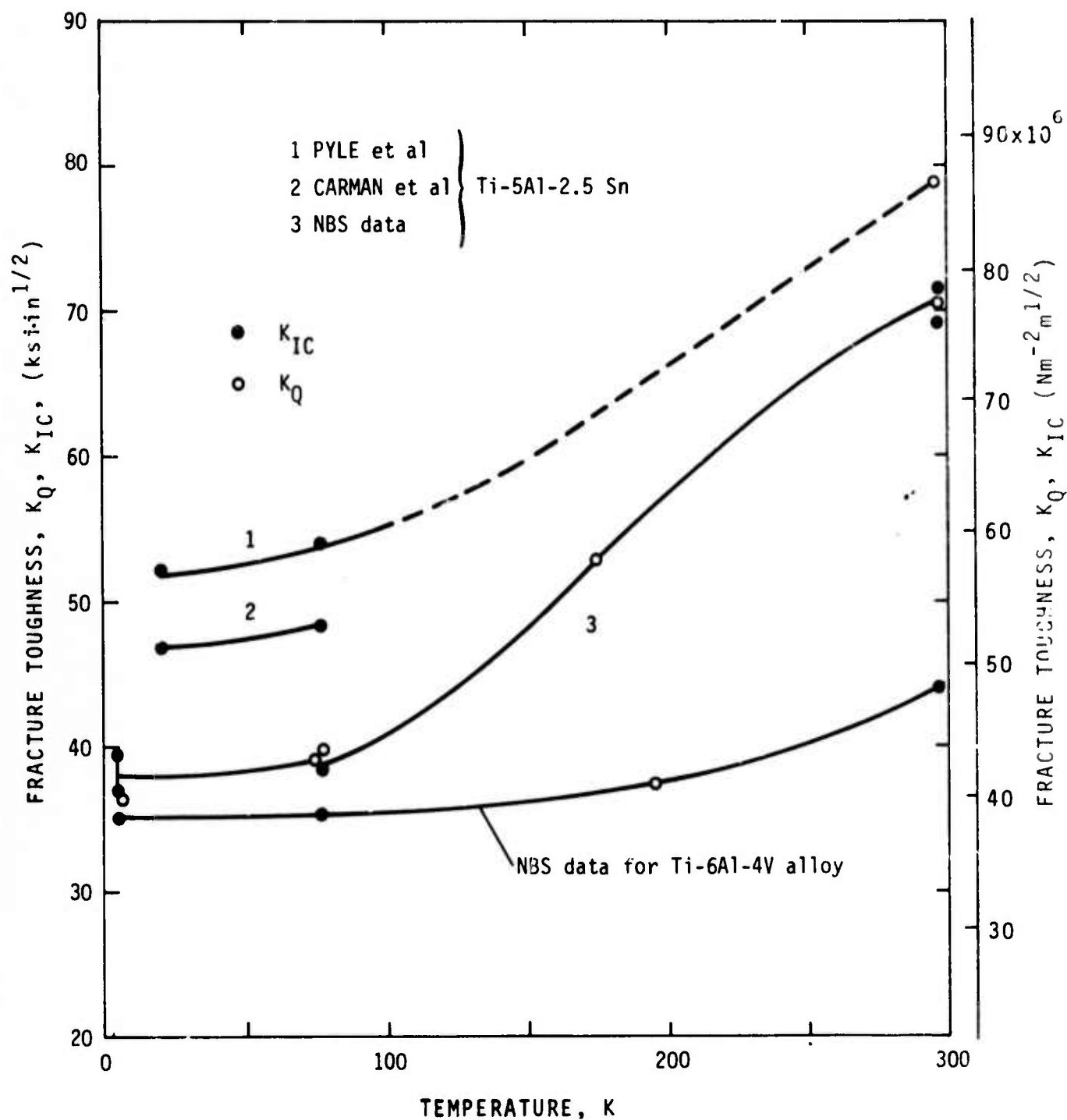


FIGURE 19 - Temperature dependence of fracture toughness of titanium alloys.

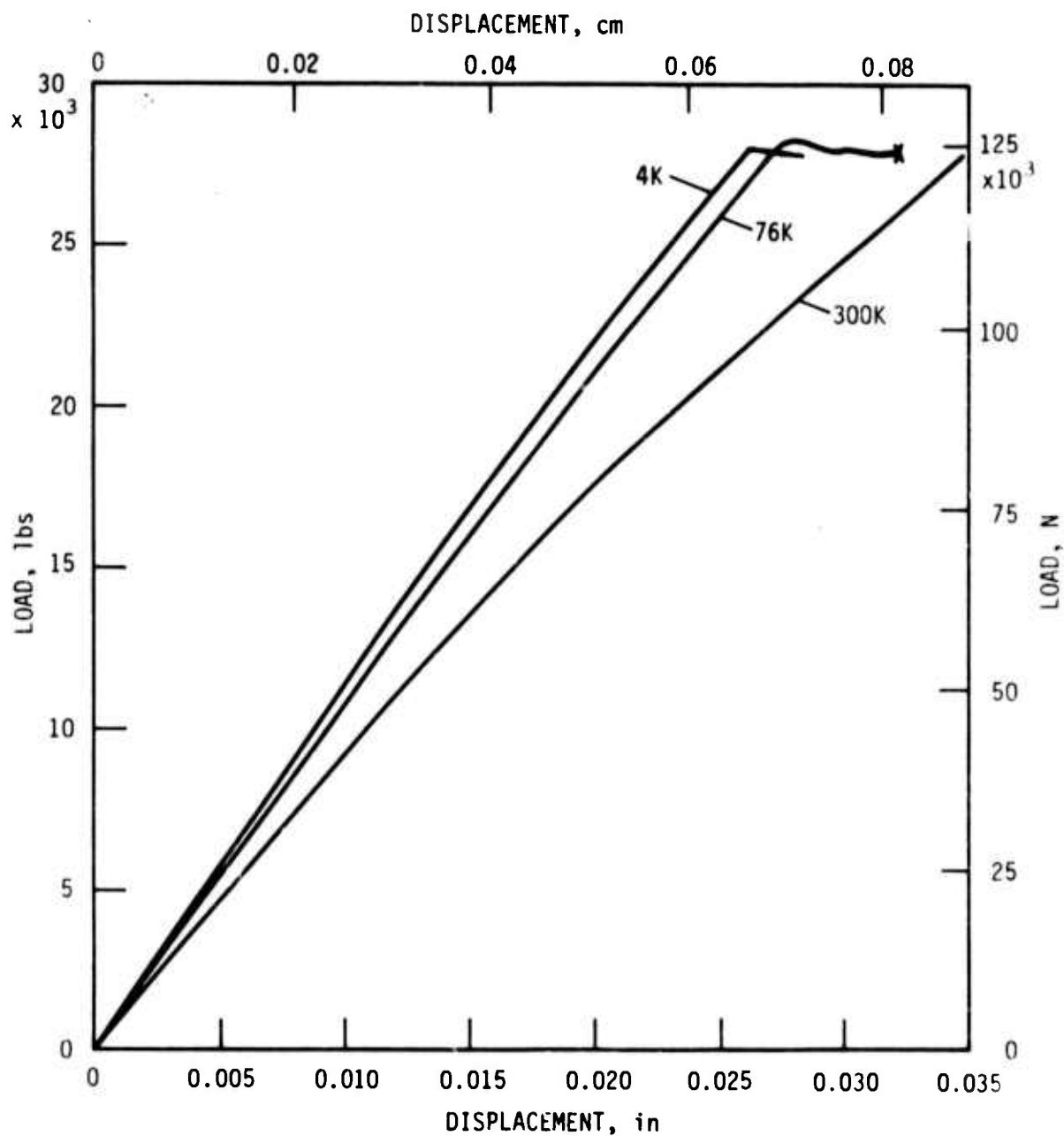


FIGURE 20 - Fracture test records for A-286.

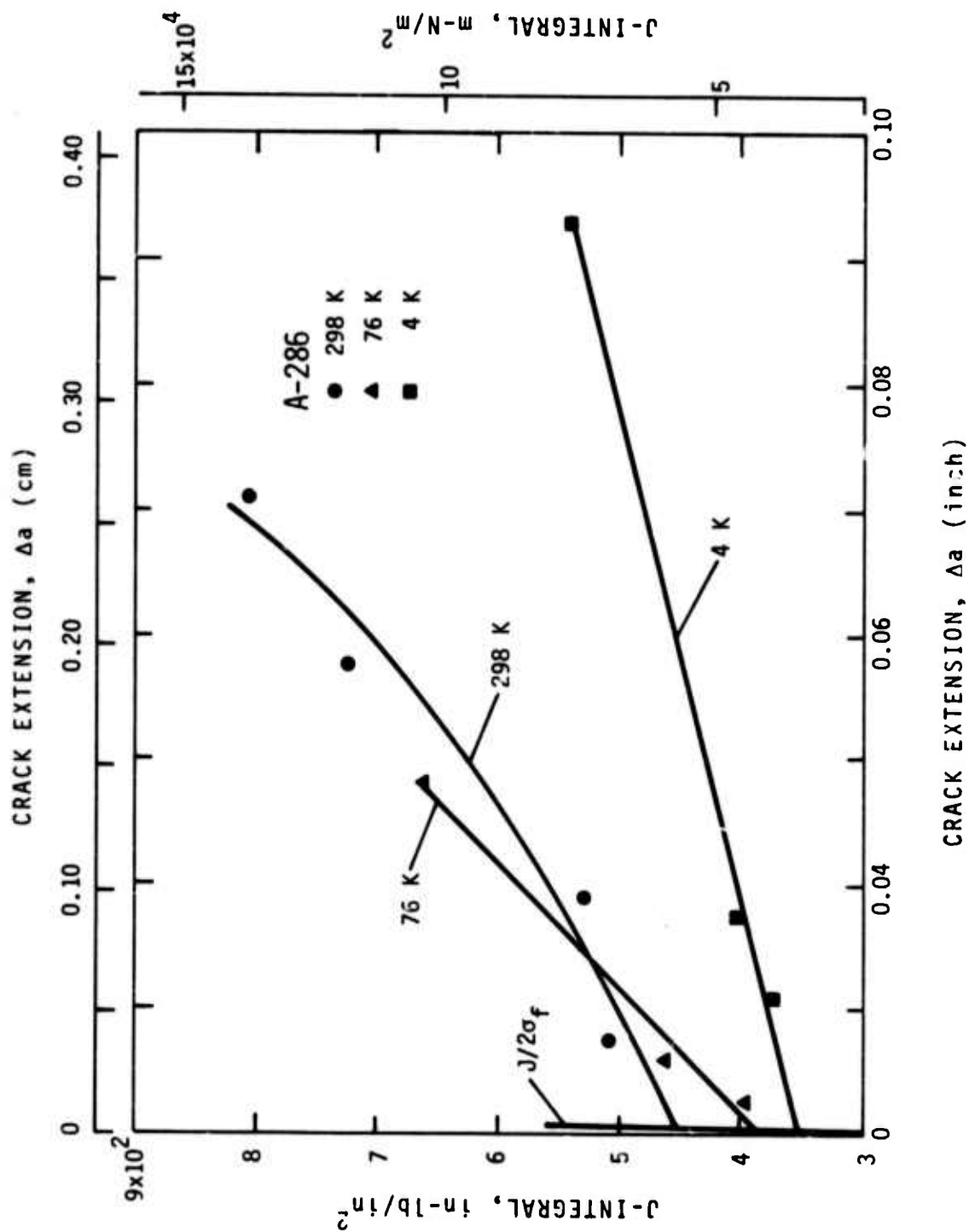


FIGURE 21 - J-integral versus crack extension for A-286.

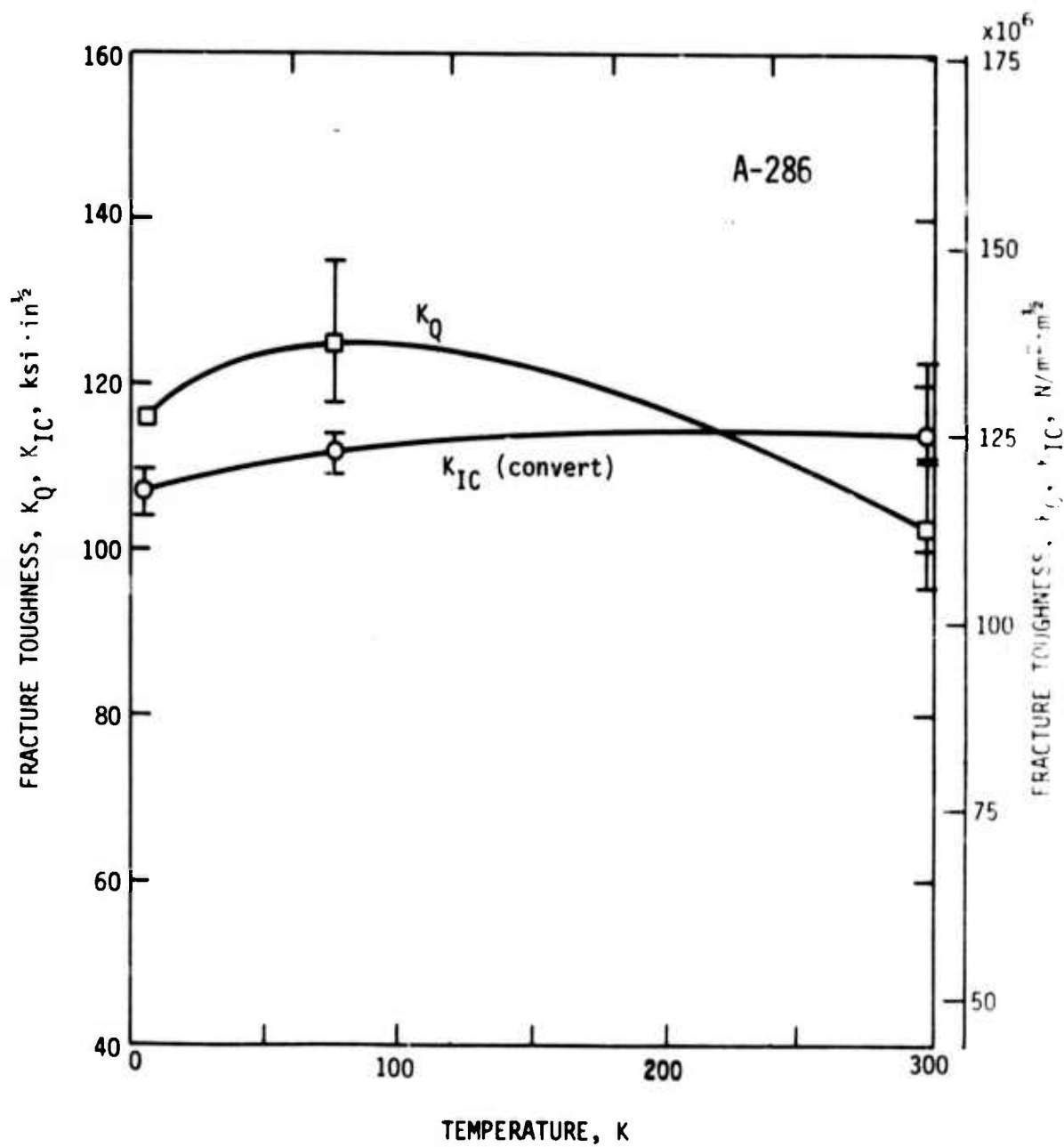


FIGURE 22 - Temperature dependence of fracture toughness for A-286.

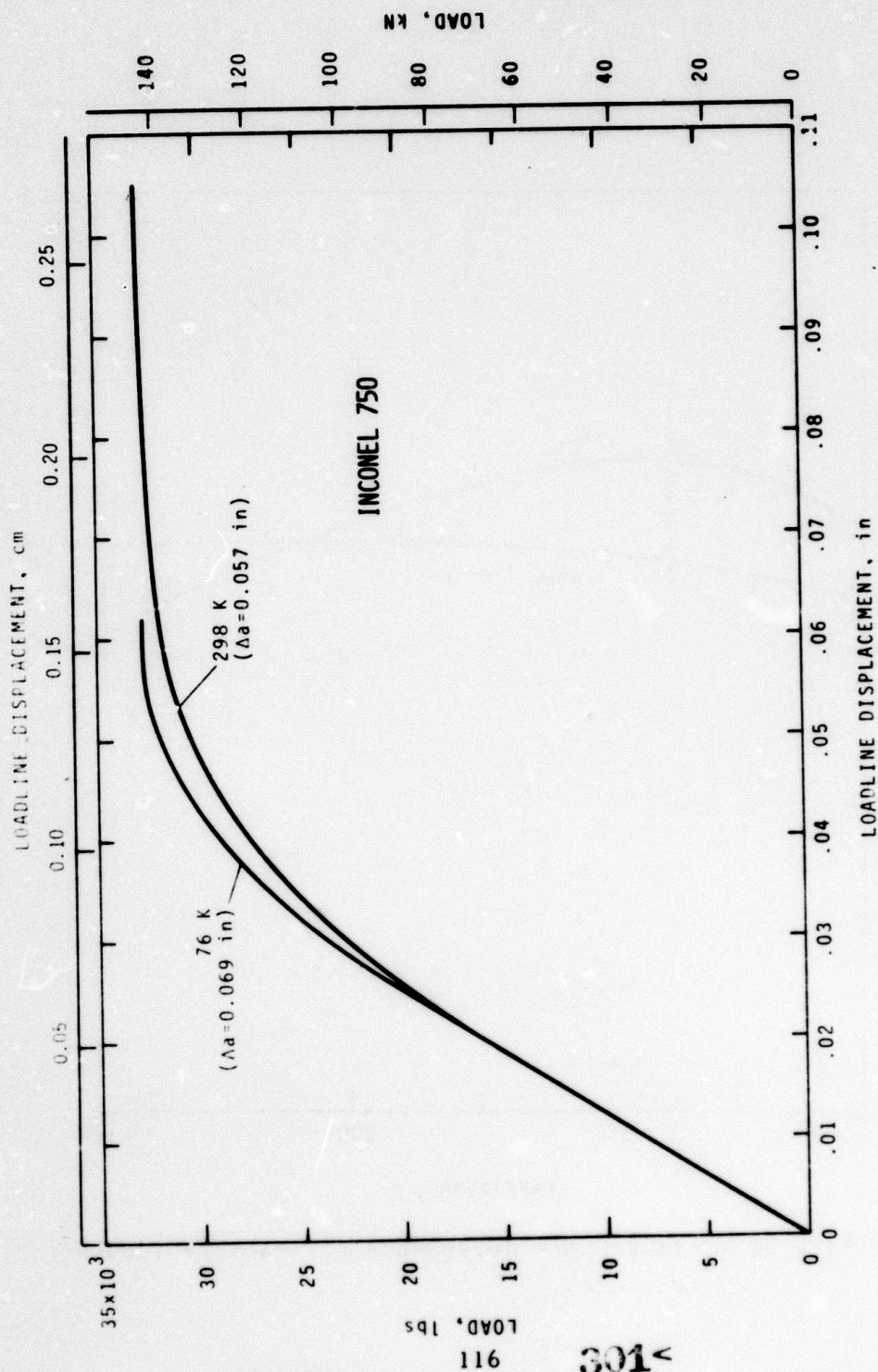


FIGURE 23 - Fracture test records for Inconel 750.

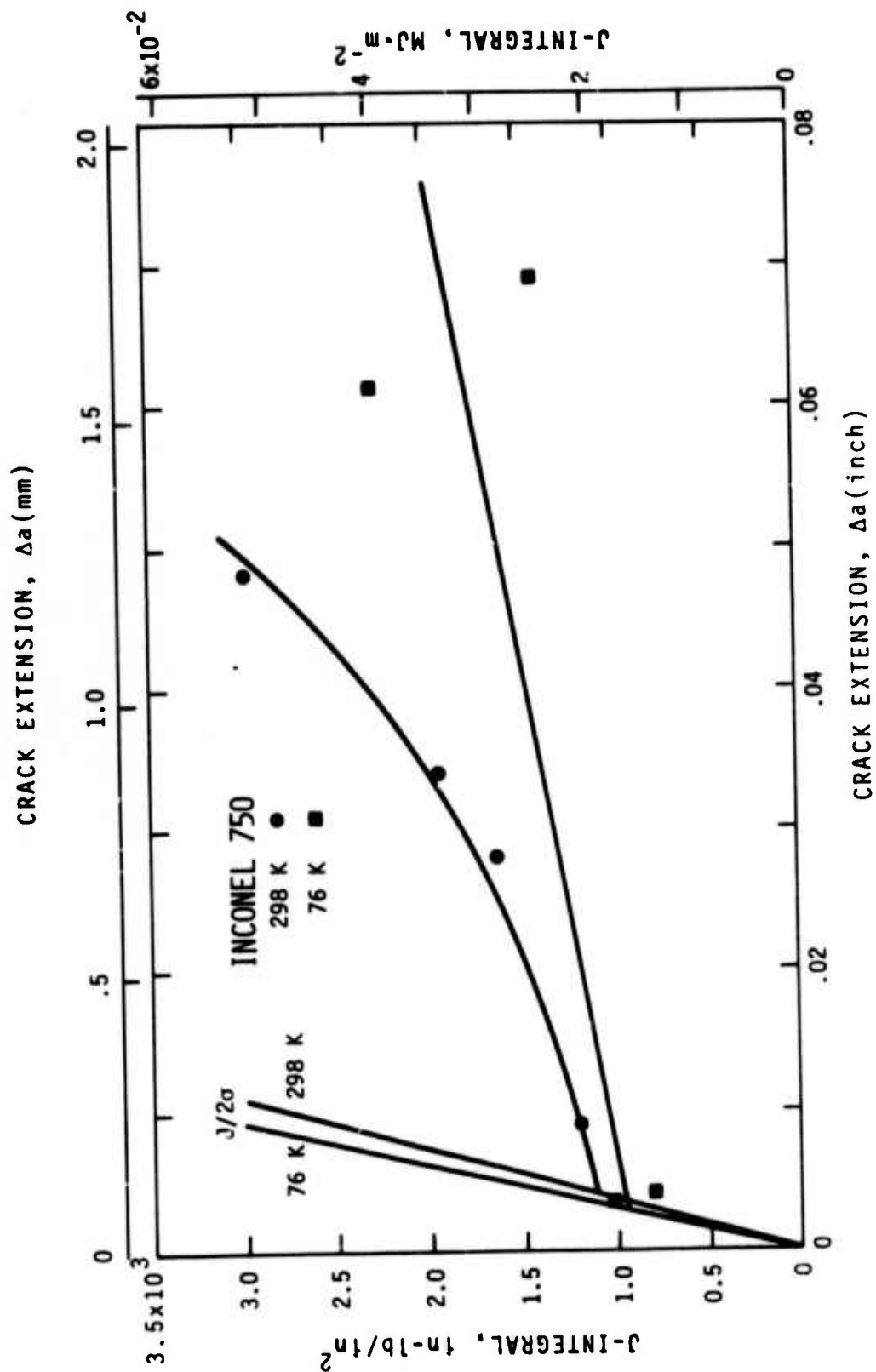


FIGURE 24 - J-integral versus crack extension for Inconel 750.

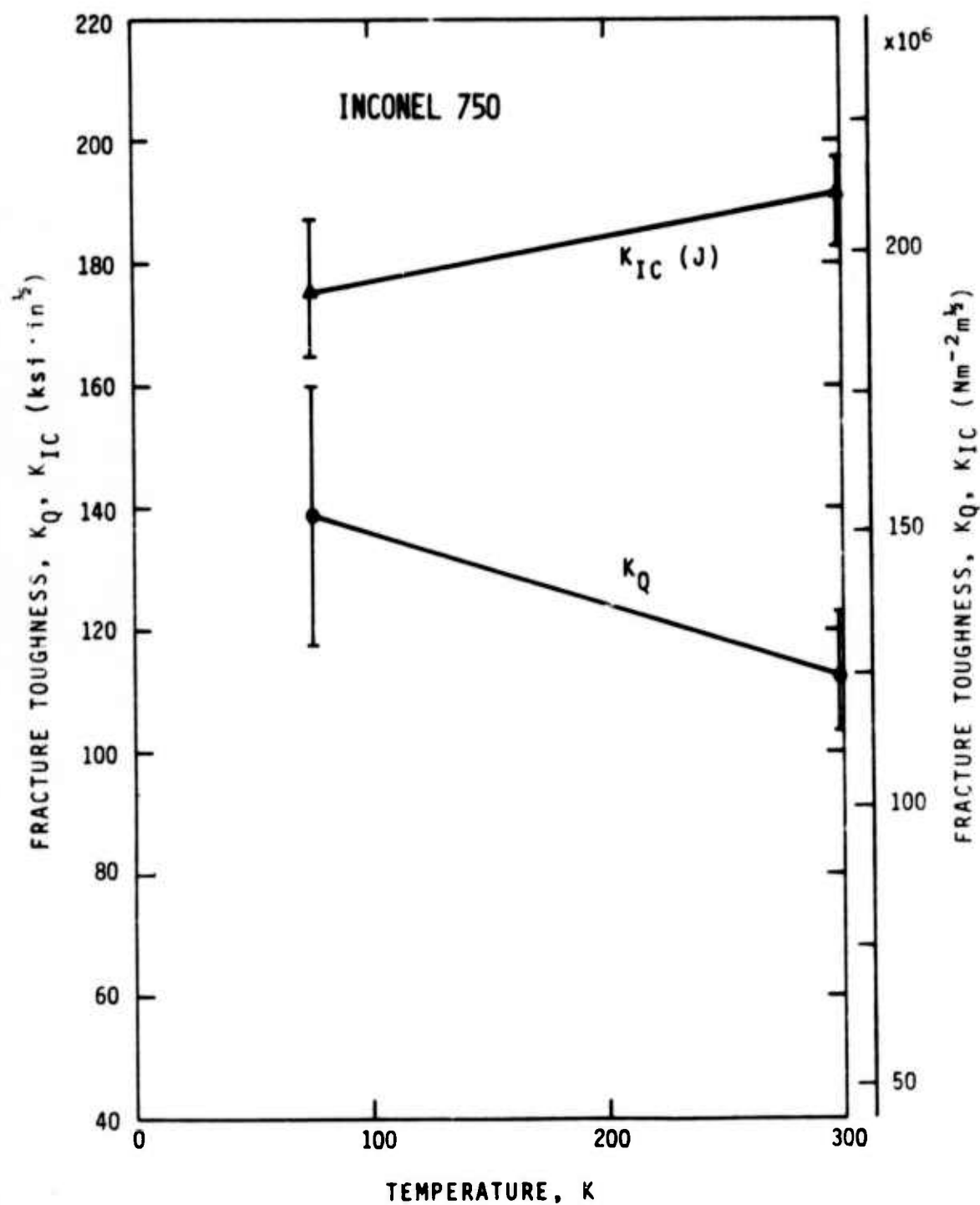


FIGURE 25 - Temperature dependence of fracture toughness for Inconel 750.



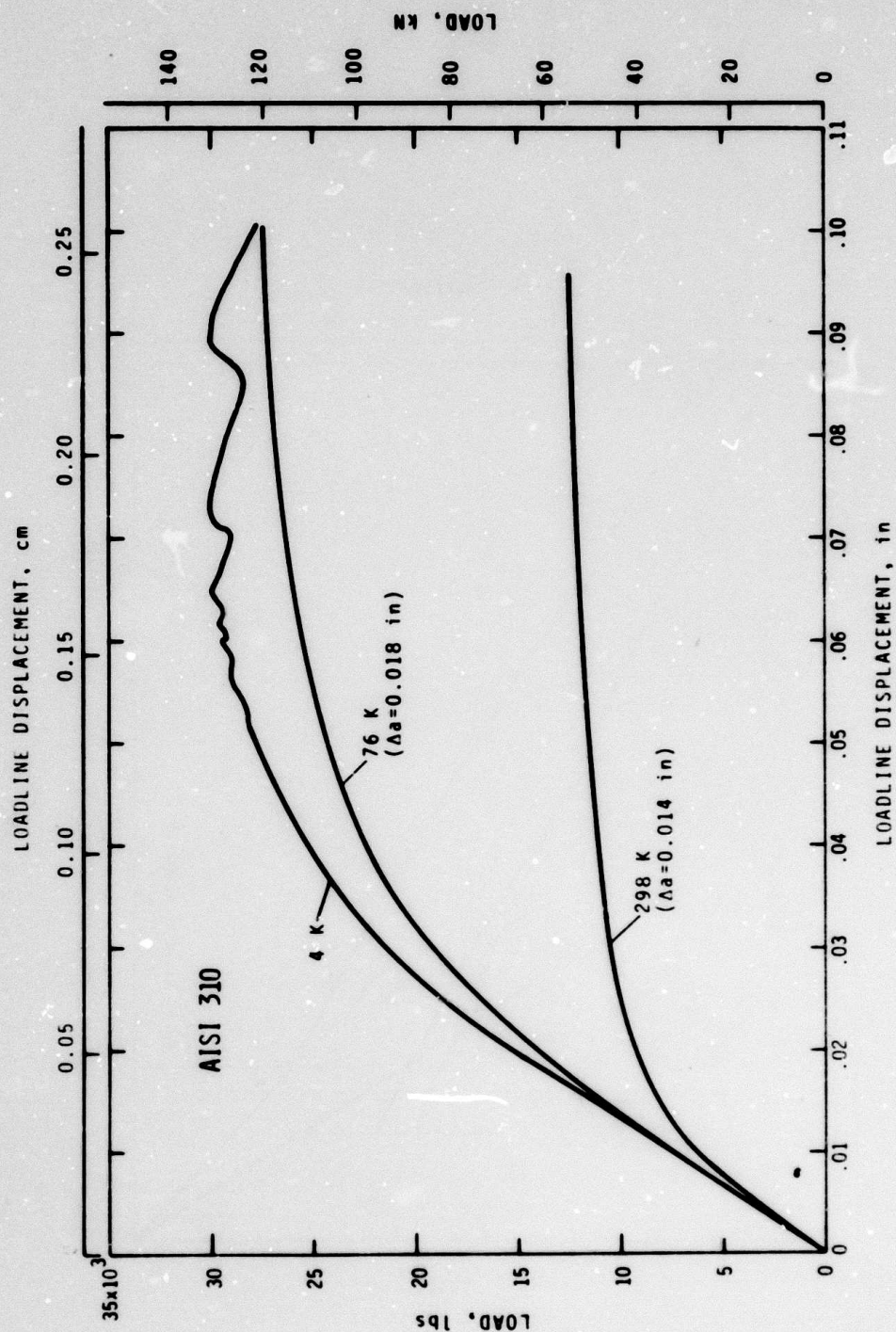


FIGURE 26 - Fracture test records for AISI 310.



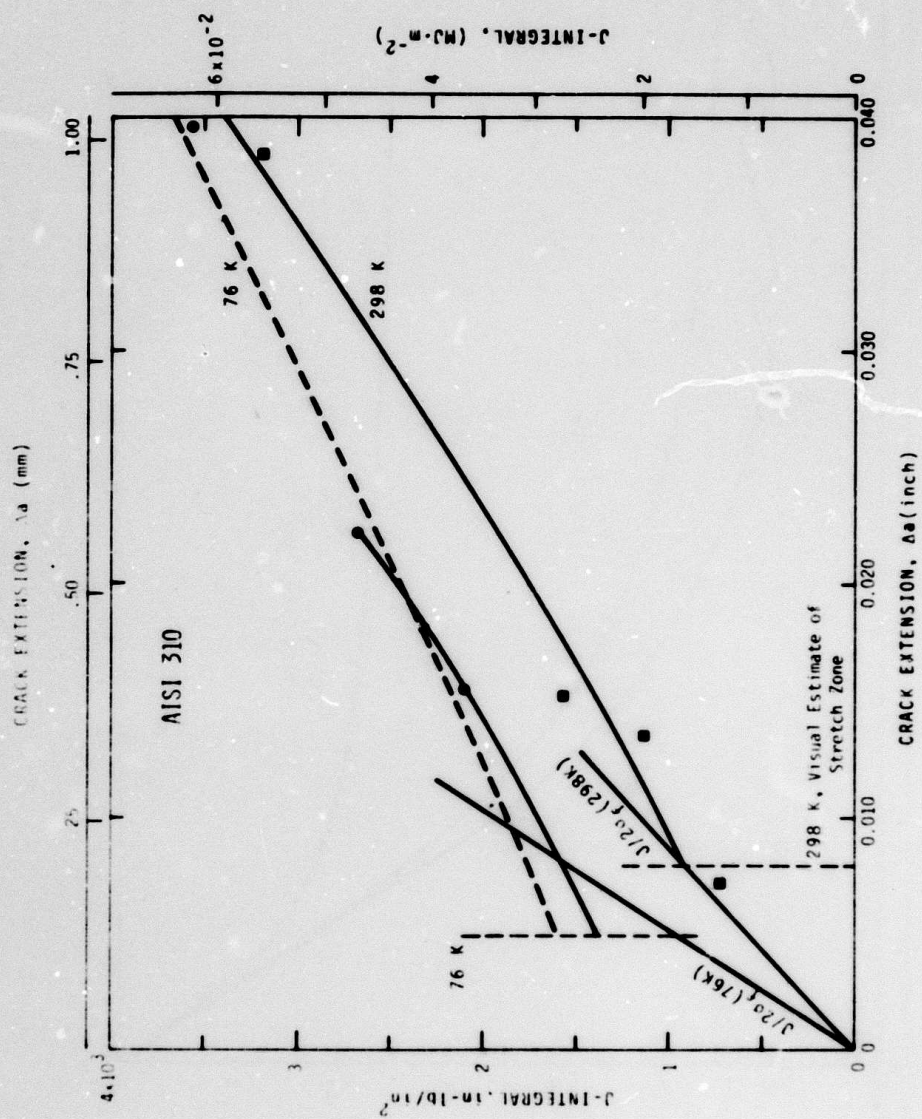


FIGURE 27 - J-integral versus crack extension for AISI 310.

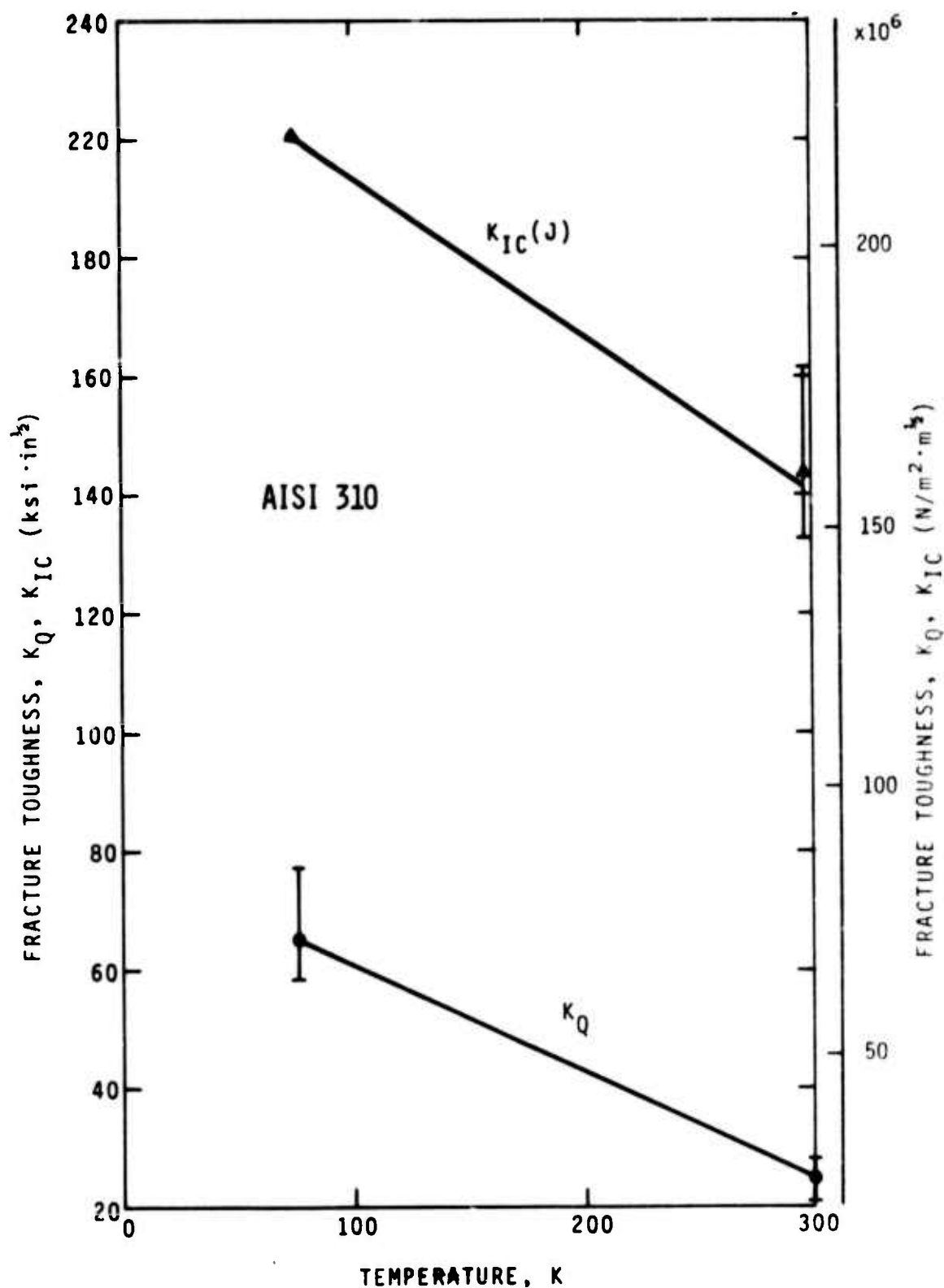


FIGURE 28 - Fracture toughness for AISI 310 at 298K and 76K.

NBSIR

SEMI-ANNUAL REPORT ON MATERIALS RESEARCH  
IN SUPPORT OF SUPERCONDUCTING MACHINERY

ADVANCED COMPOSITES

M. B. Kasen, and R. E. Schramm

Cryogenics Division  
Institute for Basic Standards  
National Bureau of Standards  
Boulder, Colorado 80302

October 1974

### Summary: Advanced Composites

The experimental work in this program will be conducted in two phases. Phase I, already underway, will have the objectives a) to thoroughly check out and refine experimental methodology, instrumentation and equipment and, b) to obtain base data on commercial boron/epoxy and graphite/epoxy against which to compare the results obtained in Phase II. Phase I work will be confined to evaluation of uniaxial longitudinal and uniaxial transverse tensile strength and moduli at 295 K, 77 K and 4 K.

Phase II will provide an in-depth characterization of the static mechanical properties of uniaxial lamellae of boron/epoxy, boron/aluminum, graphite/epoxy, Kevlar 49/epoxy and glass/epoxy down to 4 K, emphasizing the latter temperature as it is of most interest to superconducting technology. The program is designed to yield data which may be used by designers faced with the problem of calculating the properties of complex fiber layups in real engineering structures. Phase II materials will consist of commercial boron/epoxy and boron/aluminum, while the glass, Kevlar 49 and graphite fibers will utilize an epoxy matrix optimized for cryogenic use.

Sufficient Phase II material has been ordered to permit thermal expansion (contraction), thermal conductivity, dynamic elastic modulus characterization of the materials.

A comprehensive review of the literature on the mechanical and thermal properties of advanced-fiber reinforced structural composites at cryogenic temperatures has been completed and is included in this report. This is Part II of a two-part series, Part I reviewed the literature on glass-reinforced composites and was included in the ARPA Semi-Annual Technical Report May 1974.

The Part II review includes tensile, flexural and compressive strength and moduli, interlaminar shear, ultimate tensile strain, bearing strength, dynamic fatigue and impact, thermal expansion (contraction), thermal conductivity and specific heat. Only uniaxial longitudinal and uniaxial transverse data are considered. Composite classes include boron/epoxy, boron/aluminum, graphite/epoxy and Kevlar 49/epoxy. Data are presented for several hybrids (combinations of reinforcing materials) for comparative purposes. The amount of data available varied greatly among the composite types. In a few cases, a very large amount of data were available for a specific property of a specific composite type (e.g., flexural data on HT-S/X-904 graphite/epoxy); however, in most cases, available data reflected the results of only a few tests.

The literature indicates that the advanced-fiber composites have potential application in cryogenic structures where a high modulus is required along with excellent strength and (except for aluminum-matrix composites) low thermal conductivity. The commercial boron/epoxy and boron/aluminum composites appear to perform exceptionally well without optimization for cryogenic service. Results with graphite-reinforcement are less clear. Available data suggest some erratic behavior at cryogenic temperatures for these latter materials; however, some successful practical applications of graphite/epoxy composites at cryogenic temperatures suggests the possibility that the erratic experimental data may reflect problems of test method rather than inherent material deficiency. Additional study is needed in this area.

The relatively new Kevlar 49 fiber in epoxy matrices appears promising for cryogenic work, although available data are minimal. The advantage of this fiber is relatively low cost combined with a substantially higher modulus than is obtained with glass reinforcement.

For most properties and most materials, available data do not extend below 77 K. No direct data (as distinct from that generated in pressure vessel evaluation tests) exists for fatigue performance of advanced composites at cryogenic temperatures. Although there is no a priori reason to believe that the generally excellent fatigue properties of such materials at room temperature will be degraded by cooling, this parameter warrants further investigation.

Available data on polymeric-matrix composites are almost entirely confined to epoxy matrices, although a small amount of data were available for a polyimide matrix. The epoxies were for the most part conventional formulations not optimized for cryogenic use. While this does not appear to be a factor in the boron/epoxy types, data suggest that the graphite and Kevlar 49 fiber composites may benefit from matrix optimization.

Contents: Advanced Composites

	Page
A. COMPOSITE TESTING PROGRAM . . . . .	
1. <u>Introduction</u> . . . . .	127
2. <u>Phase I: Preliminary Work</u> . . . . .	128
2.1 <u>Procedural Checkout</u> . . . . .	128
2.2 <u>Acquisition of Initial Data</u> . . . . .	131
3. <u>Phase II: Planned Testing Program</u> . . . . .	135
3.1 <u>Materials Selection</u> . . . . .	135
3.2 <u>Mechanical Test Matrix</u> . . . . .	138
3.3 <u>Provisions for Additional Characterization</u> . . . . .	140
4. <u>Future Work Requirements</u> . . . . .	140
B. MECHANICAL AND THERMAL PROPERTIES OF FILAMENTARY-REINFORCED STRUCTURAL COMPOSITES AT CRYOGENIC TEMPERATURES-II: Advanced Composites . . . . .	143



## COMPOSITE TESTING PROGRAM

### 1. Introduction

The composite testing program was finalized following completion of the literature review, Part II of which precedes this Section. This review led to the following conclusions relative to the test program:

1) Much of the literature data are of questionable value due to the lack of standard test procedures, inadequate numbers of specimen replications or to poor experimental technique. For the most part, cryogenic data were incidental to the main testing program with little attempt to optimize test procedures for low temperature conditions.

2) Much of the literature data are of less value than desired due to failure to report the full characterization of the material under test, i.e., void fraction, fiber density, processing details, location and type of fracture, etc.

3) Existing data, while useful in illustrating trends, are of relatively little use to designers, as the data are insufficiently complete to permit prediction of crossply properties.

4) Existing data extend only to 20 K for glass, while most of the advanced composite data terminate at 77 K.

5) The commercial boron/epoxies and boron/aluminum (6061) composites appear to perform sufficiently well at cryogenic temperatures as to preclude the need for optimization. However, the glass, graphite and Kevlar 49 composites appear to benefit from the use of an epoxy matrix optimized for cryogenic use.

Based on these considerations, a two-phase testing program has been initiated.

## 2. Phase I: Preliminary Work

This phase has been designed in particular response to item (1) above. Its immediate objectives are to firmly establish the validity of the method for tensile testing down to 4 K. At the same time, this phase will produce mechanical property data on commercial boron/epoxy and commercial graphite/epoxy which will be useful as a base line for comparison with results obtained in the subsequent, more comprehensive program.

The composite materials used in this preliminary study have been donated by two producers of commercial prepreg materials, all material being unidirectional:

Material	Supplier	Plies	Orientation
5.6 mil Boron/Epoxy	A	4	longitudinal
5.6 mil Boron/Epoxy	A	11	transverse
5.6 mil Boron/Epoxy	B	6	longitudinal
Graphite/Epoxy	A	6	longitudinal
Graphite/Epoxy	A	16	transverse

### 2.1 Procedural Checkout

The procedure for tensile testing was based on ASTM D 3039-71T, Tentative Method of Test for Tensile Properties of Oriented Fiber Composites, with the gripping system modified for cryogenic testing. All specimens are 28 cm (11 in) long with a 15.2 cm (6 in) gage length. Longitudinal specimens are 1.27 cm (1/2 in) wide, while transverse specimens are 2.54 cm (1 in) wide.

The prior experience of our laboratory and the available literature concur in selecting strain gages over extensometers for precise strain measurement; furthermore, determination of the overall Poisson's ratios requires transverse strain data for which purpose strain gages must be used.



One of the major problems in mechanical testing of composites is obtaining valid tensile fractures in the uniaxial longitudinal test mode, i.e., obtaining fractures within the gage length rather than within the grips. The problem is basically one of transferring the tensile load from the grips into the filaments of the composite. Our approach to solving this problem differs from ASTM D 3039 in that we do not plan to use reinforcing tabs. Rather, we have chosen to use the grip system illustrated in Figure 1. In this arrangement, a piece of 100 mesh stainless steel screen of 0.01 cm (0.0045 in) wire is wrapped around each end of the specimen for a distance of about 6.4 cm (2.5 in). The specimen ends are then sandwiched between two sheets of 0.16 cm (1/16 in) Ti-6Al-4V titanium alloy which has been cross-serrated with 10 teeth per inch on the sides contacting the specimen. Finally, two plates of 0.48 cm (3/16 in) thick stainless steel pressure plates are bolted onto the assembly. In this arrangement, the tensile load is transferred only through the titanium part of the grip.

The pressure is applied by a row of six 8-32 machine screws on each side of the grip. The torque on the screws is decreased systematically going from the grip ends toward the gage section so as to introduce the load into the specimen in a systematic manner. For example, with boron/epoxy material, a satisfactory arrangement has been found to be 0.25 N · m (35 in-oz) of torque applied to the four screws closest to the specimen end, 0.23 N · m (33 in-oz) for the screws fifth from the end and 0.22 N · m (31 in-oz) for the screws closest to the gage length. The grips and specimens are mated in an alignment fixture prior to insertion into the tensile cryostat.

As an initial step in the procedural checkout, the alignment of the specimen as mounted in the cryostat was determined by the multiple-gage technique

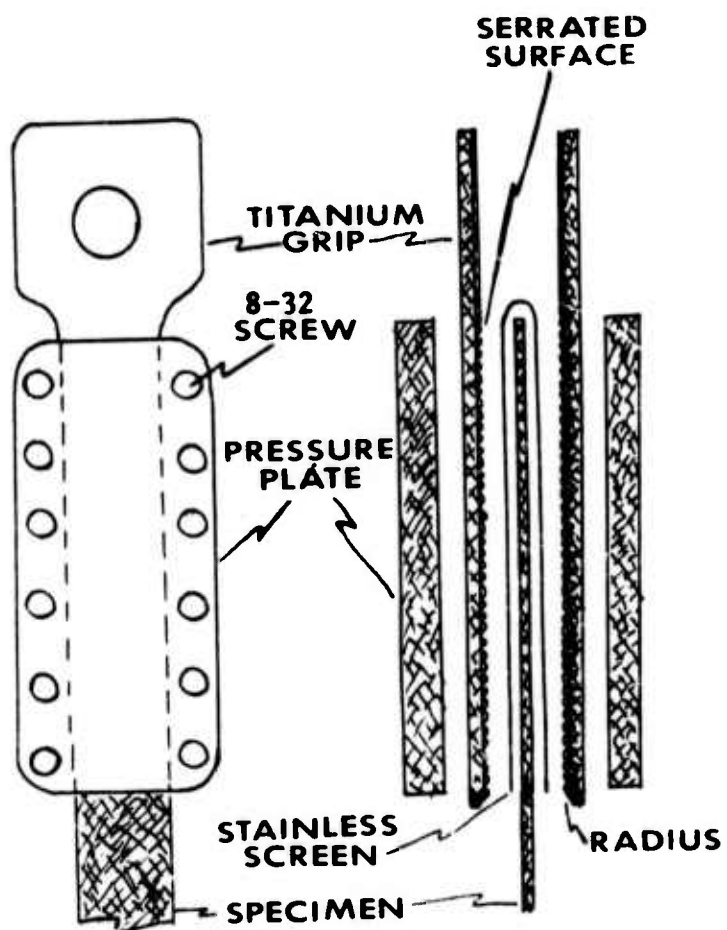


Figure A-1 Grip Assembly for Tensile Testing of Uniaxial Composites at Cryogenic Temperatures

specified in ASTM D 3039-71T and was found to be in compliance with the stated criteria. At the same time, the two separate strain gage balance, amplification and recording systems as required for Poisson's ratio determination were checked out and proven satisfactory.

## 2.2 Acquisition of Initial Data

The initial run was made using a 4-ply 5.6 mil boron/epoxy longitudinal specimen from supplier A. This specimen was cycled through a portion of its elastic region three times at room temperature (295 K) and the longitudinal and transverse modulus was determined. The procedure was then repeated at liquid nitrogen temperature (77 K) and in liquid helium (4 K). The specimen was stressed to failure on the fourth cycle at 4 K. The failure was a valid fracture, occurring near the center of the gage length. The fracture is illustrated in Figure 2.

The data obtained from these tests are illustrated schematically on Figure 3 and is summarized on Table 1. The latter table also contains initial ultimate tensile data obtained at 77 K on another specimen. This work confirmed adequate sensitivity of the measurement system. As is usual for composite specimens, the initial cycle at room temperature produced a distinct hysteresis loop which did not reappear during subsequent cycling. This initial hysteresis is conventionally attributed to isolated failure of some of the filaments, perhaps at filament kinks.

The small  $3\sigma$  values associated with the repeated determinations on Table 3 confirm excellent repeatability of the test system. Unfortunately, a lead to the transverse gage became disconnected during cooldown to 4 K, preventing calculation of the Poisson's ratio for this temperature.



Figure A-2 Typical Tensile Fracture in 4-Ply Uniaxial  
Longitudinal 4.6 mil Boron/Epoxy at 4 K.  $M = 3$

specified in ASTM D 3039-71T and was found to be in compliance with the stated criteria. At the same time, the two separate strain gage balance, amplification and recording systems as required for Poisson's ratio determination were checked out and proven satisfactory.

## 2.2 Acquisition of Initial Data

The initial run was made using a 4-ply 5.6 mil boron/epoxy longitudinal specimen from supplier A. This specimen was cycled through a portion of its elastic region three times at room temperature (295 K) and the longitudinal and transverse modulus was determined. The procedure was then repeated at liquid nitrogen temperature (77 K) and in liquid helium (4 K). The specimen was stressed to failure on the fourth cycle at 4 K. The failure was a valid fracture, occurring near the center of the gage length. The fracture is illustrated in Figure 2.

The data obtained from these tests are illustrated schematically on Figure 3 and is summarized on Table 1. The latter table also contains initial ultimate tensile data obtained at 77 K on another specimen. This work confirmed adequate sensitivity of the measurement system. As is usual for composite specimens, the initial cycle at room temperature produced a distinct hysteresis loop which did not reappear during subsequent cycling. This initial hysteresis is conventionally attributed to isolated failure of some of the filaments, perhaps at filament kinks.

The small  $3\sigma$  values associated with the repeated determinations on Table 3 confirm excellent repeatability of the test system. Unfortunately, a lead to the transverse gage became disconnected during cooldown to 4 K, preventing calculation of the Poisson's ratio for this temperature.



Figure A-2 Typical Tensile Fracture in 4-Ply Uniaxial  
Longitudinal 4.6 mil Boron/Epoxy at 4 K.  $M = 3$

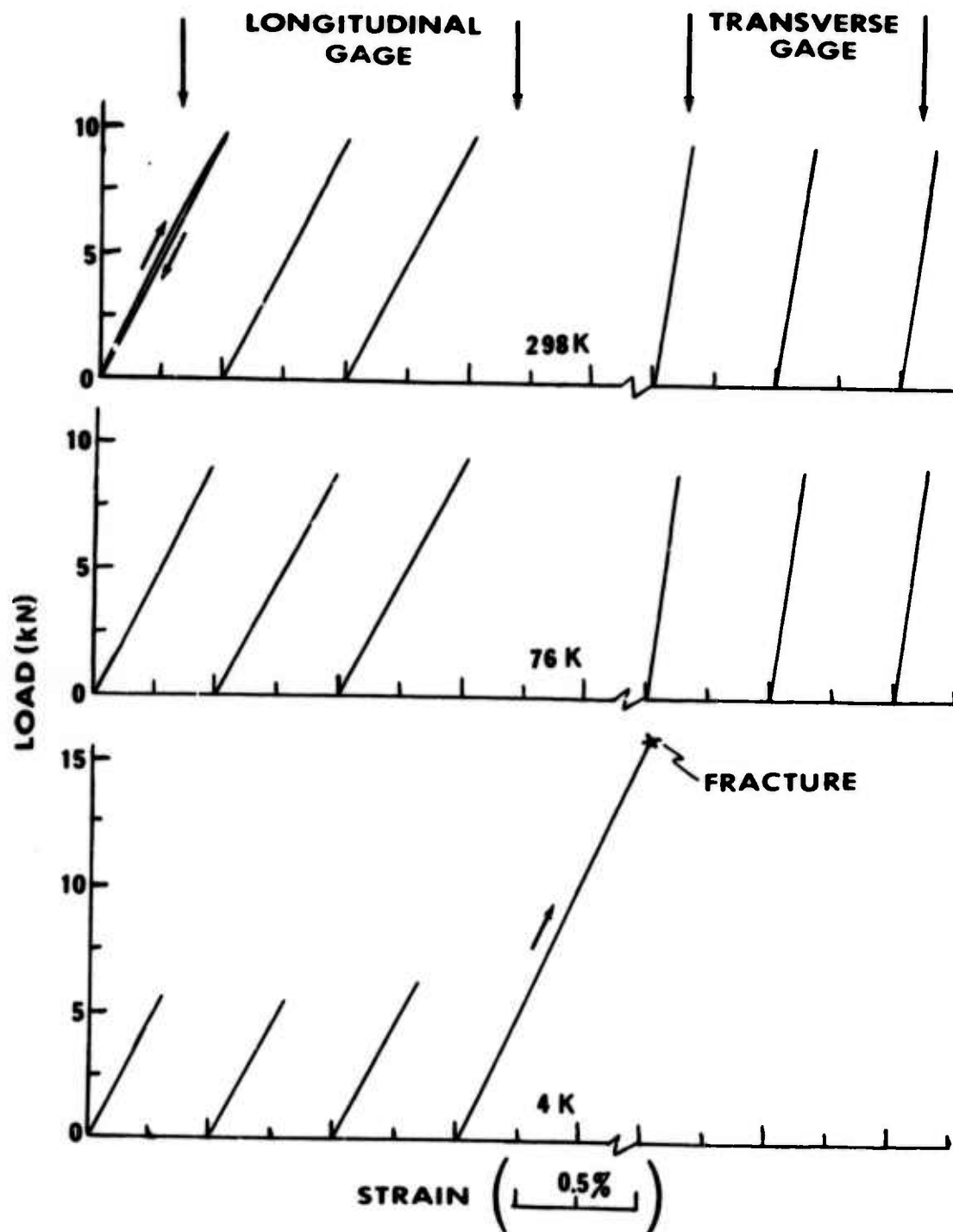


Figure A-3 Longitudinal and Transverse Stress-Strain Data Obtained From a 4-Ply 5.6 mil Boron/Epoxy Specimen Tested in the Uniaxial Longitudinal Mode at 298 K, 76 K and 4 K

The 273 KSI ultimate tensile strength measured at 4 K and the 256 KSI at 77 K in the present work is somewhat higher than the average literature values presented in the review section of this report. However, the present experimental results are reasonably in line with the highest literature values since, as noted in the review text, a 77 K value of 226 KSI was reported for the ultimate tensile strength of 4.0 mil boron/epoxy by Hertz, et al.<sup>(13)</sup>. A similar comparison of the temperature dependence of the longitudinal modulus values of Table 1 with the literature averages presented in the review show the present experimental data to be consistently about  $2 \times 10^{10} \text{ N} \cdot \text{m}^{-2}$  ( $3 \times 10^6 \text{ psi}$ ) higher than previously reported.

The helium consumption of about 15 liters was rather high during this initial test. It is expected that system improvements and operating experience will significantly reduce the quantity required per test.

TABLE 1  
INITIAL CRYOGENIC MECHANICAL PROPERTY DATA  
ON 4-PLY 5.6 MIL UNIAXIAL LONGITUDINAL BORON/EPOXY

Property		<u>Temperature</u>		
		295 K	77 K	4 K
$E_1^{\text{tu}}$	$10^9 \text{ N} \cdot \text{m}^{-2}$	238(1)*	249(1)	253(2)
	$10^6 \text{ psi}$	34.5(0.2)	36.2(0.2)	36.6(0.3)
$\gamma$	--	0.236(0.003)	0.256(0.030)	--
$\sigma^{\text{tu}}$	$10^8 \text{ N} \cdot \text{m}^{-2}$	--	17.7	18.8
	$10^3 \text{ psi}$	--	256	273
$\epsilon^{\text{tu}}$	$10^{-3}$	--	7.8	7.4

\*() = 30 values for successive modulus determinations on same specimen.



### 3. Phase II: Planned Testing Program

This Section describes the rationale for selecting the materials and describes the specific composites to be included in the program. The rationale for the specific testing program is described and the testing matrix is illustrated. Finally, additional desired follow-up work is described.

#### 3.1 Materials Selection

Composites having potential use in superconducting machinery are boron-reinforced aluminum and boron-, graphite- glass- and Kevlar 49-reinforced epoxies. The characteristics of each of these composite classes are summarized on Table 2.

The literature review indicated that composites fabricated directly from commercial boron/aluminum 6061 alloy "green" tape and from boron/epoxy "prepreg" tape will have excellent strength and will show little temperature sensitivity on cooling to cryogenic temperatures. These materials have therefore been ordered as state-of-the-art commercial composites.

As fabrication of boron/aluminum composites requires specialized equipment, this material has been ordered fabricated directly to the desired shape from a primary supplier. The remaining composites have been ordered from a commercial job shop specializing in supplying polymeric-matrix structural composite components to industry. The latter materials will therefore be representative of commercial production. The boron/epoxy composites will be fabricated from commercial 3-inch wide prepreg tape. However, the glass, graphite and Kevlar 49 composites will be produced with a NASA Resin 2 matrix, as the latter resin has been specially developed to provide increased flexibility at cryogenic temperatures.

The selected composite test materials are listed in Table 3. S-glass has been selected as it is the most common type used in high strength glass

TABLE 2

## CHARACTERISTICS OF SELECTED COMPOSITE CLASSES

<u>Composite Class</u>	<u>Characteristics</u>
Boron/Aluminum	High strength, high modulus, limited formability of finished sheet, high thermal conductivity, high thermal contraction, low electrical resistivity, high cost
Boron/Epoxy	High strength, high modulus, low thermal conductivity, low thermal contraction, high electrical resistivity, high cost
Graphite/Epoxy	Moderate strength, medium modulus, medium thermal conductivity, very low thermal expansion, moderate electrical conductivity, moderate cost
Kevlar 49/Epoxy	Moderate strength, medium modulus, low thermal conductivity, high thermal expansion, high electrical resistivity, low cost
Glass/Epoxy	Very high strength, very low modulus, low thermal conductivity, low thermal contraction, high electrical resistivity, low cost

TABLE 3

## SELECTED COMPOSITE TEST MATERIALS

Composite Type	Number of Panels	Size (in.)	Thickness	Filament Orientation	Use
S-901 glass/Resin 2	1	11 x 11	6 ply	Uniaxial	(1)
Kevlar 49/Resin 2	2	11 x 11	15 ply	Uniaxial	(2)
Type A Graphite/Resin 2	2	11 x 11	10 ply	$\pm 45^\circ$ , symmetrical	(3)
5.6 mil Boron/Epoxy	1	4 x 4	0.150 in.	Uniaxial	(4)
	1	1 x 1 x 2	----	Uniaxial to 2"	(5)
	1	1 x 1 x 2	----	Transverse to 2"	(6)
5.6 mil Boron/6061 Aluminum	1	11 x 6	6 ply	Uniaxial to 6"	(1)
	2	11 x 6	15 ply	Uniaxial to 11"	(2)
	2	11 x 6	10 ply	$\pm 45^\circ$ , symmetrical	(3)
	1	4 x 4	0.150 in.	Uniaxial	(4)
	1	1/2 x 1/2 x 2	----	Uniaxial to 2"	(5)
	1	1/2 x 1/2 x 2	----	Transverse to 2"	(6)

## Use:

- (1) Uniaxial longitudinal tensile
- (2) Uniaxial transverse tensile and transverse compression
- (3) In-Plane (intralaminar) shear
- (4) Longitudinal compression, longitudinal and transverse dynamic modulus (resonance method)
- (5) Longitudinal thermal conductivity and longitudinal dynamic modulus (pulse-echo method)
- (6) Transverse thermal conductivity and transverse dynamic modulus (pulse-echo method)

composites. Type A (or AS) graphite fiber will be used as these are relatively low cost fibers of intermediate strength and modulus and are well characterized. Boron 5.6 mil diameter has been selected as this diameter fiber is currently replacing the previously used 4 mil size.

### 3.2 Mechanical Test Matrix

The principle underlying the mechanical testing program is to provide a basic static mechanical property characterization of a uniaxial lamella of each composite type at 4 K. Characterization will also be undertaken at 77 K and 295 K where such data are not already available. Highest priority will be placed on the 4 K characterization.

From the stress-strain curves in longitudinal tension, transverse tension, longitudinal compression, transverse compression and in-plane shear, the elastic constants  $E_{11}$ ,  $E_{22}$ ,  $\gamma_{12}$  and  $G_{12}$  will be determined along with the proportional limits and ultimate strengths. These data may then be used by designers to make a limiting static strength analysis of off-axis laminates made from the composite of each basic lamella. This approach is based upon modern composite strength theory and is currently extensively used in the aircraft and other industries.

The test matrix of Table 4 summarizes the test series required to obtain this objective. A minimum of five valid test results must be averaged for each parameter variation in order to establish the required confidence levels. Priority will be given to obtaining longitudinal and transverse tensile and in-plane shear data at 4 K, as these data by themselves suffice for design approximations if it is assumed that the compressive strengths are equal to those in tension. As the compressive strengths are in fact superior to those in tension, this assumption leads to a very conservative limiting static

TABLE 4  
MECHANICAL CHARACTERIZATION TEST MATRIX

Legend:

BFRP - boron fiber reinforced plastic	TT - transverse tension
BFRM - boron fiber reinforced metal	LT - longitudinal tension
GFRP - glass fiber reinforced plastic	TC - transverse compression
CFRP - carbon fiber reinforced plastic	LC - longitudinal compression
K49RP - Kevlar 49 reinforced plastic	S - in-plane (intralaminar) shear

Composite Type	Test Type	Temperature and Number of Specimens		
		295 K	77 K	4 K
BFRP <sup>(1)</sup>	LT	5	5	5
"	TT	5	5	5
"	LC	5	5	5
"	TC	5	5	5
"	S	5	5	5
BFRM <sup>(2)</sup>	LT	5	5	5
"	TT	5	5	5
"	LC	5	5	5
"	TC	5	5	5
"	S	5	5	5
CFRP <sup>(3)</sup>	LT	5	5	5
"	TT	5	5	5
"	LC	5	5	5
"	TC	5	5	5
"	S	5	5	5
K49RP	LT	5	5	5
"	TT	5	5	5
"	LC	5	5	5
"	TC	5	5	5
"	S	5	5	5
GFRP <sup>(5)</sup>	LT	5	5	5
"	TT	5	5	5
"	LC	5	5	5
"	TC	5	5	5
"	S	5	5	5

- (1) 5.6 mil commercial boron/epoxy  
 (2) 5.6 mil commercial boron/6061 aluminum  
 (3) Type A (or AS) graphite/NASA Resin 2  
 (4) Kevlar 49/NASA Resin 2  
 (5) S-901 glass/NASA Resin 2

strength prediction and probable overdesign of components. Consequently, the next priority will be given to obtaining valid compressive strength data at 4 K. Following this work, the static property data at 77 K and 295 K will be obtained, the latter data being useful in designing components exposed to a range of temperature.

In addition to the defined 4 K characterization studies, a few ad hoc tests will be performed to obtain preliminary data on the extent to which the strength and modulus of these composites may become degraded by repeated thermal cycling (thermal fatigue) over the 295 K-4 K temperature range.

### 3.3 Provisions for Additional Characterization

Sufficient material is being obtained in each composite type to permit thermal characterization of the materials as needed to verify existing data and to extend existing data to 4 K. Such characterization includes dimensional changes on cooling and the temperature dependence of thermal conductivity.

Additionally, sufficient materials are being obtained to facilitate a study of the feasibility of using dynamic methods of determining the significant engineering elastic constants in lieu of the conventional mechanical method. Direct comparison of values obtained by each method on the same composite will be possible. The dynamic modulus will be investigated by both the pulse-echo and the resonance methods.

## 4. Future Work Requirements

Aside from the ad hoc thermal fatigue tests mentioned above, the present program is confined to characterizing static mechanical properties. Performance of composites under dynamic loading conditions at cryogenic temperatures also must be determined before such materials can be used with confidence in rotating components of superconducting machinery. Unfortunately, dynamic fatigue testing

at cryogenic temperatures is exceedingly expensive. Equipment must be tied up for a long time, the cryogen consumption is high and the anisotropic nature of composites requires analysis of several fiber orientations. Cryogenic fatigue testing must therefore be confined to those composites appearing most applicable for specific superconducting machinery components and such tests must be carefully planned to produce the maximum amount of useful data.

MECHANICAL AND THERMAL PROPERTIES OF FILAMENTARY-  
REINFORCED STRUCTURAL COMPOSITES AT CRYOGENIC  
TEMPERATURES-II: Advanced Composites

Maurice B. Kasen

Cryogenics Division, NBS-Institute  
for Basic Standards  
Boulder, Colorado 80302

ABSTRACT

This article is an extensive review of the literature on the mechanical and thermal properties of advanced-fiber reinforced structural composites at cryogenic temperatures. The objective is to provide an understanding of the general magnitude of the property values obtainable within the cryogenic temperature range, to provide a feel for the general ranking of various specific composite types with regard to specific properties, and to impart an understanding of the temperature dependence of the property of interest. A comprehensive Bibliography and Bibliography-Property Cross-Reference is included.

This is Part II of a two-part series. Part I considered glass-reinforced composites.

This research was supported by the Advanced Research  
Projects Agency of the Department of Defense under  
ARPA Order No. 2569.



# SYMBOL NOMENCLATURE

The following symbol nomenclature is used in this report:

$\sigma^{tu}$	-	tensile ultimate strength
$\sigma^{ty}$	-	tensile yield strength
$E_1^t$	-	initial tensile modulus
$E_2^t$	-	secondary tensile modulus
$\epsilon^{tu}$	-	tensile ultimate strain
$n^{tu}$	-	tensile fatigue failure stress
$\sigma^{fu}$	-	flexural ultimate strength
$E_1^f$	-	initial flexural modulus
$E_2^f$	-	secondary flexural modulus
$\sigma^{cu}$	-	compressive ultimate strength
$E^c$	-	compressive modulus
$\sigma^{si}$	-	interlaminar shear strength
$\sigma^{by}$	-	bearing yield strength
$\sigma^{bu}$	-	bearing ultimate strength
$\sigma^l$	-	impact strength
$\lambda$	-	thermal conductivity
$\Delta L/L$	-	thermal contraction
$C_p$	-	specific heat
$\rho$	-	density
psi	-	pounds per square inch
KSI	-	psi x $10^3$
$N \cdot m^2$	-	Newtons per meter squared (Pascal)
$J \cdot K_g^{-1} K^{-1}$	-	Joules per kilogram - Kelvin
$W \cdot m^{-1} K^{-1}$	-	Watts per meter-Kelvin

## INTRODUCTION

The objectives of this review are fourfold: a) to provide the designer with a feel for the general magnitude of property values that may reasonably be expected from a given category and class\* of composites within the cryogenic range, b) to provide him with a feel for the ranking of specific composite classes with regard to a specific property, c) to impart a feel for whether the property of interest is likely to increase, remain unaffected, or decrease with lowering of temperature, and d) to define those areas in which additional data are needed and to define the direction that future work should take in this area. Readers with more specific interests are referred to the Bibliography and Bibliography-Property Cross-Reference for retrieval of specific documents. The Bibliography in this report is similar to that in Part I and includes references to both the glass- and advanced-fiber reinforced composite literature. The scope of the literature survey has already been described in Part I.

Several differences will be noted between the presentation of the data in this work and in Part I. First, because of the wide variation in properties among the advanced fibers (and, therefore, among the composites in which they are used), separate data are presented on each specific reinforcement type. Secondly, as no data were available on woven-cloth advanced-fiber composites at cryogenic temperatures, present data are restricted to uniaxial-transverse layups. Finally, the overwhelming majority of the data for advanced composite polymeric systems are reported for epoxy matrices, in contrast to the variety of matrix types reported for glass-reinforced systems.

---

\* We define a composite category by the general reinforcement type, e.g., glass-fiber or advanced fiber (graphite, boron, etc.). We subdivide the category into composite classes by the general matrix type, e.g., glass/polyester or graphite/epoxy. We further subdivide the class by referring to a composite type when a specific reinforcement/matrix combination is specified, e.g., HT-S/X-904 epoxy.

In other respects, the data presentation follows that used in Part I, i.e., literature property values are presented in graphical form as a function of temperatures at 295 K, 200 K, 77 K, 20 K and 4 K. The absence of a data point for a given temperature indicates failure to find significant data. References are given for each plotted curve.

The reader is cautioned that curves presenting data averaged from several sources may have a considerable scatter band associated with them. We discuss the range of values associated with such curves and emphasize those specific types for which the best values were reported.

The author has attempted to make this review as comprehensive as possible. Nevertheless, the complexity of the subject makes it unavoidable that some data worthy of inclusion have been inadvertently overlooked. The author would appreciate having such omissions brought to his attention. The author also wishes to emphasize that the data presented in the review reflect the published results of the cited authors. These data have not been experimentally verified by NBS, and the conclusions and evaluations presented herein do not imply approval, endorsement, or recommendation of any commercial product by NBS.

In considering the mechanical property data, the reader should be aware that there exists no universally accepted method of determining most of these properties. It is often difficult to obtain valid uniaxial longitudinal tensile fractures because of the difficulty of transferring the load from flat specimen grips into the fibers of the specimen. Failure within or adjacent to the grips is not uncommon. This problem is particularly acute when testing CFRP materials due to the small fiber diameter. Problems also arise in uniaxial longitudinal compression testing where an unsupported specimen may fail by "brooming" of its ends or by column buckling. However, such premature failures result in property values lower than the true values and tend to bias the data accordingly.

The reader should also be aware that the discussion of properties of the composites included in this review does not take into consideration the effect of variations in fiber/resin content of specific types of composites and test specimens, as this characteristic was not reported for all referenced works. Composite properties may be strongly influenced by this ratio. The property data discussed in this paper reflect actual values and trends reported for specific composites. Controlled variations in many of the properties are obtainable in practice by specific variation of the fiber content of the composites.

Finally, the reader should be aware that composite technology is developing so rapidly that some of the data presented in this review may not reflect the current state of the art. New reinforcing fibers, improved composite fabrication techniques and refined test methods will very likely result in overall improvement in both the level and the consistency of composite mechanical properties.

For the reader unfamiliar with the development of advanced composite technology, it will be useful to establish a perspective on the field. The two primary reinforcement systems are boron filaments produced by vapor deposition of boron on a very fine tungsten wire substrate and graphite fiber produced by graphitization (pyrolysis) of an organic precursor fiber. Additionally, a proprietary organic fiber called Kevlar 49\* is currently receiving attention. The boron filaments are normally produced to 4 mil diameter, although 5.6 mil diameter filaments are also coming into use. Boron fiber coated with a thin layer of silicon carbide is produced under the trade name of Borsic\* and is reported to have improved interfacial bonding to certain matrix types. The graphite fiber field is much more complex, as it is not only possible to produce

---

\* The use in this paper of trade names of specific products is essential to the proper understanding of the work presented. Their use in no way implies approval, endorsement or recommendation by NBS.

such fibers from different precursor materials,\* but it is also possible to vary the production process to produce fibers differing greatly in modulus and strength. As the properties obtainable with graphite reinforcement may approach those with boron reinforcement at a somewhat lower cost, development of graphite fibers has proceeded at a very rapid rate until today the user is confronted with an abundance of fiber choices, many of which are not well characterized and many of which will disappear to be replaced by newer types. At the present time, the potential user of these materials would be wise to restrict his interest to those types whose behavior is reasonably well known, barring compelling reasons for doing otherwise.

Graphite fibers may be produced with elastic moduli varying from 25-75 x 10<sup>6</sup> psi (17-50 x 10<sup>10</sup> Pa), with strengths varying inversely to moduli. In the present report, these fibers are classified according to low, medium or high modulus, the differentiation being <40, 40-60 and > 60 x 10<sup>6</sup> psi, respectively.

As composites are frequently used where weight is critical or where high specific strengths are required, typical composite densities have been summarized in Table 1.

#### STATIC MECHANICAL PROPERTIES

For most mechanical properties, the data for the CFRP composites has been separated from those of the other advanced composites. This reflects the larger amount of available data on CFRP materials and the large variety of graphite fibers for which data have been published.

##### Composite Tensile Strength

Figure 1 summarizes the available data on the temperature dependence of the ultimate tensile strength of graphite-reinforced epoxy composites from

---

\* The two most common are rayon and polyacrylonitrile (PAN).

room temperature into the cryogenic temperature range for the uniaxial longitudinal and uniaxial transverse orientations. A surprisingly large amount of data were found in the literature for CFRP materials--58 separate reports of test data, each report being the average of several tests on a given composite. Undoubtedly, this large effort reflects the desire to exploit the relatively low cost of graphite fibers. Unfortunately, the available data summarized on Figure 1 indicate that CFRP composites suffer significant strength losses upon cooling to 77 K and, as was observed with the glass-reinforced materials in Part I, the strength behavior below 77 K appears to become erratic.

Figure 1(a) indicates that the uniaxial tensile strength obtainable in CFRP composites is about 30% of that obtainable with glass-fiber reinforcement in the cryogenic range. The ultimate tensile strength of composites tested in the uniaxial longitudinal mode should be fiber controlled; hence, it would be expected that the tensile strengths would inversely follow the modulus of the fiber. This trend is not reflected in the data of Figure 1(a)--indeed, the averaged data indicate the converse, higher strengths are associated with higher modulus fibers and lower strengths with lower modulus fibers. However, a more detailed examination of the data averaged into these curves shows that the expected correlation does exist if one considers only the highest values reported for each modulus range. Thus, the highest overall ultimate strength at 77 K was 147 KSI reported for the low-modulus HT-S fiber in X-904 resin,<sup>13</sup> the next highest was 130 KSI reported for HMG-50 in an ERLB polyblend,<sup>10</sup> for Modmor I and for Samco 360 in modified ERL 2256,<sup>8</sup> all medium modulus fibers, while 126 KSI was the maximum reported for the high-modulus Thornel 75 fiber in ERLB 4617.<sup>51</sup> This suggests that the higher strengths associated with the lower modulus fibers may have been lost in the averaging process due

to variations in composite quality or perhaps due to difficulties in obtaining valid tensile fractures. The latter is a prime possibility, as it is particularly difficult to obtain valid tensile fractures in uniaxial CFRP specimens loaded in the fiber direction. Additional evidence that the test method is affecting the results is found in the work of Simon and Larsen<sup>10</sup> who report almost diametrically opposite temperature dependence of the ultimate tensile strength in HT-S reinforced NASA Resin 2\* and in an HT-S reinforced 4617 polyblend when each was tested first as flat tensile coupons and subsequently as NOL (Naval Ordnance Laboratory) ring specimens.

The uniaxial longitudinal tensile strength data for other types of advanced composites are presented in Figure 2(a). The data for PRD 49/epoxy, boron/epoxy, boron (Borsic)/aluminum,\*\* stainless steel/aluminum and the hybrid Borsic-steel/aluminum and Borsic-titanium/aluminum composites all have higher absolute values of tensile strength and retain their strength to lower temperatures than do the CFRP composites. The hybrid Borsic-steel/aluminum composite contained 4.2 mil Borsic fibers in the tensile direction of 6061 aluminum and stainless wires in the transverse direction.<sup>13</sup> The hybrid Borsic-titanium/aluminum composite contained 4.2 mil Borsic fibers in the tensile direction with  $\beta$ -3Ti foil interleaved between the boron lamellae.<sup>13</sup> The latter composites are therefore not strictly uniaxial; however, they have been included to illustrate the interesting possibilities of hybrids. Of the two remaining uniaxial composites, the HT-S/polyimide (Skybond 703) material displayed a comparatively low strength and showed a significant decrease of strength upon cooling. Conversely, a very

\* An epoxy resin formulation optimized for cryogenic service by Soffer and Molho<sup>5</sup> and consisting of Epon 828/DSA/EMPOL 1040/BDMA in proportions 100/115.9/20/1 pbw.

\*\* Data for Borsic and boron fiber composites have been combined except where differences in reported values justified separating the data.



sharp rise in strength on cooling was reported for, the HT-S/epoxy-phenolic (HT-424 Primer), but its overall strength was not high.

The stainless steel reinforced composite contained NS-355 stainless wires in a 2024 aluminum alloy matrix. This type of composite is available commercially on special order; however, it has not received wide acceptance in view of the wider availability of boron reinforced aluminum which has similar strength properties.

Boron/aluminum composites are available commercially with either 4 mil or 5.6 mil boron or Borsic reinforcement. The literature values on the uniaxial tensile strength at 77 K ranged from 163-202 KSI, with highest values reported for 5.6 mil Borsic/6061.<sup>13</sup> Data were not available for any other aluminum alloy matrix. Boron/epoxy composites have been developed to an even higher degree and are commercially available in the form of prepreg tape, i.e., with the plastic matrix partially cured to facilitate component fabrication and to improve composite quality. The literature values for boron/epoxy composites tested in the longitudinal direction at 77 K varied from 167-226 KSI, the highest value being reported for the commercial SP-272 product.<sup>13</sup>

PRD 49 (Kevlar 49) is a relatively new type of organic fiber. Present data indicate that this fiber in an epoxy matrix is capable of developing tensile strengths comparable to that developed with graphite fibers at cryogenic temperatures. Hoggatt<sup>59</sup> reports NOL ring ultimate strengths of 146 KSI for PRD 49-1 in a NASA Resin 2 matrix and 183 KSI in an ERLB 4617 matrix at 20 K. There is some evidence of a slight decrease in strength on cooling to 77 K; however, available data indicate that the ultimate tensile strength of this material is relatively independent of temperature within the cryogenic range.

The hybrids Borsic-steel/aluminum and Borsic-titanium/aluminum complete the group of advanced composites that have reasonably high strength in uniaxial



tension. The lower strength of these hybrids compared to the conventional boron/aluminum composite reflects the reduced density of boron fibers in the direction of loading.

In uniaxial transverse tension, Figure 2(b) shows the hybrid Borsic-titanium/aluminum composite to have higher strength than the conventional boron/aluminum type, which is precisely the reason for creation of the hybrid. In this case, the benefit of the interleaved titanium foil increases the transverse tensile strength at 295 K and 200 K; however, the effect appears to diminish rapidly as the material is cooled to 77 K. While the transverse strength of the boron/epoxy composite is much lower than that of the metal-matrix materials; values are still in excess of those developed with the graphite fiber reinforcement.

The literature reported a transverse ultimate strength of 14.2 KSI for 4.2 mil Borsic/6061 aluminum<sup>13</sup> and a somewhat higher value of 24.9 KSI for 5.6 mil boron reinforcement,<sup>13</sup> all at 77 K. It is probable that this strength difference is real; however, available data also indicate that the observed difference may be due to residual stresses inherent in the small diameter fiber rather than to the presence or absence of a silicon carbide coating. The reader is referred to the section on ultimate tensile strain for further discussion of this subject.

#### Composite Tensile Modulus

The primary reason for development of advanced composites is the high modulus obtainable with the newer types of fiber reinforcement. In contrast to a maximum of about one million for glass-reinforced composites in the fiber direction, Figures 3(a) and 4(a) show that moduli ranging from  $30-40 \times 10^6$  psi are obtainable with several of the advanced fiber composites. Thus, while glass-reinforced composites may at their best equal the modulus of aluminum,

the modulus of composites using advanced fibers may equal and often exceed that of steel.

Looking first at the graphite/epoxy composites, Figure 3(a) shows that the modulus of the composite does, on the average, reflect the modulus of the fiber when tested in the uniaxial longitudinal mode. The available data indicate that the modulus of the Thorne 75 composite (the only representative of the high-modulus fibers) declines to about that of the medium modulus fibers at 77 K. With this exception, the averaged data indicate that the moduli in the fiber direction slightly increases on cooling to 77 K. No correlation is observed between fiber modulus and transverse composite moduli in Figure 3(b); indeed, none is expected, as the latter is controlled by the properties of the matrix and by the fiber-matrix interfacial bond strength.

A comparison of Figures 3(b) and 4(b) shows that the uniaxial transverse tensile moduli of graphite/epoxy composites is much lower than that developed by the other advanced composites over the entire cryogenic temperature range.

A closer look at the literature data from which Figure 3(a) was prepared revealed that among the medium modulus fibers, the modulus at 77 K was a respectable  $39-43 \times 10^6$  psi for Samco 360, the highest value being reported with a modified ERL 2256 resin.<sup>8</sup> (Note that these same fibers developed excellent uniaxial tensile strengths.) A distinctly lower range of  $26-33 \times 10^6$  psi was reported for Thorne 50, highest values being reported for a modified ERL 2256 composite.<sup>8</sup> Among the low-modulus fibers, HT-S (the most tested fiber) produced  $15-10 \times 10^6$  psi, highest value being reported with X-904 resin,<sup>13</sup> while  $17-22 \times 10^6$  psi was the reported range for HMG-25, the highest values being obtained in a NASA Resin 2 matrix.<sup>8</sup>

As the transverse modulus properties are matrix dominated, Figure 3(b) shows significant differences for HT-S fiber in different epoxies. The data illustrated are for the same composites as appear in Figure 1(b). Here, the lower moduli of the HT-S/NASA Resin 2 and the HT-S/4617 polyblend are due to the additions of flexibilizers and elastomers to the epoxy resin while the highest modulus was developed with the conventional X-904 matrix. In general, the transverse modulus increases with decreasing temperature. A lower modulus value was reported for the high-modulus Thornel 75 fiber in ERLB 4617 than for HT-S/X-904.

Leaving the graphite-reinforced composites and turning to those reinforced with other advanced fibers, we observe on Figure 4(a) that the uniaxial longitudinal moduli reported for the boron/epoxy, the boron/aluminum and the hybrid Borsic-titanium/aluminum and Borsic-steel/aluminum composites all cluster around  $30\text{--}35 \times 10^6$  psi, with little temperature dependence. The PRD 49/epoxy modulus is reported to be significantly lower, at  $16\text{--}18 \times 10^6$  psi, but undergoing a significant rise between 77 K and 20 K. In general, these uniaxial-longitudinal moduli values compare favorable with those of the graphite-epoxies. The uniaxial transverse moduli are another matter. As seen in Figure 4(b), the transverse moduli of the aluminum-matrix materials are far higher than those of the graphite/epoxies and are, in fact, almost twice as high as that of unreinforced 6061 aluminum. The transverse moduli of the boron/epoxy is much lower than that for the same fiber in an aluminum matrix but is still almost twice that of the graphite/epoxy materials. These data reflect the contribution made by fiber-matrix interface to the transverse modulus.

Looking in more detail at the uniaxial longitudinal data, we find that the boron(Borsic)/aluminum data ranged from  $30.4\text{--}36.2 \times 10^6$  psi with little temperature dependence. These data combine values obtained from fibers of 4 mil

and 5.6 mil in the two production variants, as no significant difference was reported for these materials. The boron/epoxy represents average data reported by Nadler, et al.<sup>81</sup> on SP-272 and Narmco 5505 (data range not available). The hybrids, Borsic-titanium/aluminum and Borsic-steel/aluminum were the same composites discussed in reference to the tensile data of Figure 2(a). The slightly lower uniaxial tensile modulus of the hybrids compared to that of the conventional boron/aluminum reflects the lower density of fibers in the stress direction.

The PRD 49 data reflect input from both an ERLB 4617 and a NASA Resin 2 matrix.<sup>59,60</sup> The ERLB 4617 composite produced a slightly increased tensile modulus at all temperatures, its value being  $18.5 \times 10^6$  psi at 77 K compared to  $17.5 \times 10^6$  psi for the NASA Resin 2. The large rise in modulus between 77 K and 20 K was reported for both matrices.

Considering the transverse data of Figure 4(b) in more detail, we observe that the three aluminum matrix composites have similar moduli, about  $20 \times 10^6$  psi. The boron/aluminum data was again the average of data obtained from 4.2 mil Borsic and 5.6 mil boron, similar values being reported for each variant. The boron/epoxy data of Figure 4(b) again reflect the average values obtained from the commercial SP-272 and Narmco 5505 materials.<sup>81</sup>

#### Composite Flexural Strength and Modulus

Less data were available on the temperature dependence of the flexural strength and elastic modulus than for tensile properties--furthermore, most of that available was reported for graphite/epoxy composites. Figure 5 summarizes the flexural strength data for the latter, while Figure 6 summarizes the available data for other types of reinforcements or matrices. The minimal available data on flexural modulus properties appear in Figure 7.

Comparison of Figure 5 with Figure 1 shows that the graphite/epoxy flexural strength data spans a much greater range of values than does the tensile strength in both the longitudinal and transverse directions. The expected higher strength of the lower modulus fibers is more in evidence for the flexural test than it was for the tensile test mode.

By far the largest amount of data were available for HT-S/epoxy composites; furthermore, such composites had the highest reported longitudinal flexural strength of all the CFRP materials for which data were available. Strengths were reported over a 113-234 KSI range at 77 K. This is significantly lower than the 325-470 KSI range reported for uniaxial glass-epoxies in Part I. These data included test series designed to investigate cure cycles, aging effects and environmental effects.<sup>12,13,58</sup> Most of the work was done with E-350, X-915 or X-904 matrices for which the average flexural strengths at 77 K were reported to be very similar, varying only from 167 to 178 KSI.<sup>13</sup>

It is beyond the scope of the present paper to discuss in detail the effect of composite processing procedures on the resultant mechanical properties. Nevertheless, the available data on the HT-S fiber composites remind us that processing variables are important; in particular, those variables that affect the void content. Detailed examination of the data shows that in 84 of the 89 reported test series, the flexural strength of composites made with HT-S fiber declined markedly on cooling to 77 K. The five series for which strength increases were noted were reported by Maximovich, et al.<sup>12</sup> to have occurred concomitant with a change to a vacuum bagging method of fabrication. This suggests that at least a part of the observed drop in flexural strength on cooling may be due to the presence of voids in the composites.

Continuing on with the other fibers, we observe on Figure 5(a) that the order of decreasing strength is Modmor II, GY-70, and Fibrallloy 300, arriving finally at a group comprising the lowest strengths and consisting of Courtaulds HM, HMG-25 and Thornel 50 fibers. The flexure strength of this latter group is only about 1/3 that of the HT-S fiber composites. Among these other fibers, most data were available for the high-modulus GY-70, for which the spread of values at 77 K was 85-133 KSI, the highest being reported in X-904 epoxy resin.<sup>13</sup>

The clear separation between the transverse flexural strengths of the low-modulus HT-S composites and the high-modulus GY-70 composites in Figure 5(b) suggests that there are differences in the fiber-matrix bond strength between these two fiber types, the high-modulus fiber having the poorer bonding. Note that X-904 and 1004 epoxies were used with both fiber types.

Before leaving the data of Figure 5, it is of interest to consider whether or not the literature data supports the contention that the relatively inexpensive flexure test may be used to obtain comparative ranking of composite strength in lieu of the more expensive tensile test. A visual comparison of the data on Figure 5(a) with that of Figure 1(a) is hardly convincing; however, such a comparison is nebulous because these graphs present data from different composite types. To clarify this question, the literature data were examined more closely and a comparison of ranking of strength in longitudinal tension versus longitudinal flexure was made at 77 K for eight specific composite types (same fiber and matrix) for which data were available. The result is summarized in Table 2, and suggests that the flexure test results are indeed not a very good measure of the relative tensile strengths of graphite/epoxy composites at 77 K. Insufficient data existed for comparisons with other

mechanical properties; however, the good performance of the HT-S fiber composites in interlaminar shear (Figure 11) suggests that the flexural test may correlate more closely with this parameter.

Flexure data on other types of advanced composites were somewhat meager. Figure 6 does indicate that the uniaxial longitudinal flexural strength of boron/epoxy in the form of the commercial SP-272 product is much higher than that of the graphite/epoxies, still lower than that developed with glass reinforcement. A quite rapidly declining strength is observed on cooling to 77 K. The latter effect was not observed in the comparable tensile data (cf. Figure 2(a)). Data were available for two polyimide composites, one with the high-modulus GY-70 fiber and one with the low-modulus HT-S fiber. Of these, the HT-S developed the higher strength. A small decrease in flexure strength is evidenced in these composites 77 K, but the magnitude is less than that reported for the uniaxial tensile strength. Finally, the HT-S/epoxy-phenolic (HT-424 Primer) appears to possess reasonable flexure strength with little temperature dependence in contrast to the comparatively low strength and significant temperature dependence reported for the same composite in longitudinal tension (cf. Figure 2(a)).

Very little data were available on the flexural modulus. Data for the longitudinal mode appearing on Figure 7 reflect the modulus of the reinforcing fibers and appear to agree reasonably well with the moduli of the same composites in tension. The Thornel 50 data is an average of data from two matrix types, a modified ERL 2256 epoxy and for NASA Resin 2.<sup>8</sup> A slightly higher modulus was reported for the latter at both 295 K and 77 K.

#### Composite Compressive Strength and Modulus

Data on the compressive properties of advanced composites at cryogenic temperatures were also relatively sparse. Those which were available appear in



Figures 8 and 9, combining the graphite/epoxy data with those of the other composite types.

These data show that the advanced composites have excellent compressive strength properties. In contrast to the tensile and flexural strength, the compressive strengths and moduli of the advanced composites are significantly higher than those of the glass-reinforced composites. Comparison of Figure 8 with Figures 1 and 2 also shows that the compressive strengths are 100-200% higher than the tensile strengths for the same composites.

The highest uniaxial longitudinal compressive strength was reported for the commercial boron/epoxy types SP-272 and Narmco 5505.<sup>81</sup> The very large strength increase on cooling to 77 K is most impressive for this composite type. The boron/aluminum has a lower, but still respectable, uniaxial compressive strength. The latter data reflect input from both 4.2 mil Borsic and 5.6 mil boron fiber composites.<sup>13</sup> A slightly higher strength was reported for the 5.6 mil composite, but not sufficiently to justify a separate plot. Again, the Borsic-titanium/aluminum and Borsic-steel/aluminum hybrids developed strengths somewhat below that of the conventional boron/aluminum, reflecting the decreased density of boron fibers in the stress direction. Lowest uniaxial longitudinal compressive strengths were reported for the HT-S/X-904 graphite/epoxy composite; however, even this composite developed a compressive strength about twice that developed in tension. Furthermore, the compressive strength of the graphite/epoxy composite was reported to increase with cooling, in contrast to the tensile behavior.

The available data on the transverse compressive strengths of boron/epoxy, boron/aluminum and graphite/epoxy composites are compared on Figure 8(b), showing these composites to be in the same relative order of strength as in the longitudinal test mode. Again, the commercial SP-272 and Narmco 5505



boron/epoxy products indicate a substantial increase in compressive strength on cooling. Lesser increases are observed in the boron/aluminum and in the HT-S/X-904 CFRP.

All else being equal, the compressive modulus of a composite should be the same as the tensile modulus of the same composite. This is found to be generally true for the HT-S/X-904 CFRP material, for the boron/epoxy for the Borsic/aluminum composites and for the Borsic/steel/aluminum hybrid, as may be seen by comparing the compressive moduli values of Figures 9(a) with the tensile moduli values of the same composites on Figures 3 and 4. The Borsic-titanium/aluminum data are at variance with this principle, with some  $10^6$  psi higher modulus being reported in compression than in tension. The boron/aluminum and the boron/aluminum hybrids again show the highest longitudinal moduli with the boron/epoxy only slightly lower. The modulus of the HT-S/X-904 CFRP composite is again much lower than that of the boron-reinforced materials. There does not appear to be a significant temperature sensitivity of this parameter. Also, as in the tensile case, the boron/aluminum demonstrates a clearly higher transverse compressive modulus as compared to the boron/epoxy or to the HT-S/X-904 CFRP composite.

#### Composite Interlaminar Shear Strength

Interlaminar shear strength is the resistance to failure of a composite subjected to pure shear in the plane of the fibers, i.e., the shear strength between two lamellae in a laminate along the plane of their interface.\* Interlaminar shear is measured either by the guillotine method in which shear is forced by the imposition of opposing but offset cuts in the sides of a flat tensile specimen or by the short-beam method in which the specimen resembles

\* Not to be confused with intralaminar shear which refers to shear within a single lamina without reference to adjacent lamellae (sometimes referred to as in-plane shear).

a flat flexural specimen but is designed to fail by shear on the central layers of the composite. The guillotine method is the most simple and is reputed to produce less scatter; however, the values obtained are usually higher than those obtained with the short-beam method. The latter is considered to be the more reliable method and is the most widely used. A modification of the short-beam test is used with filament-wound NOL ring specimens; here, a short section of the ring (concave downward) is substituted for the flat specimen. Unfortunately, the results of the NOL segment and the flat short-beam tests are not comparable.

The interlaminar shear properties are believed to strongly affect structural integrity of a composite, particularly in compression loading and in flexure. Like the flexural test, interlaminar shear tests simultaneously evaluate several parameters of the composite including resin strength, resin-fiber bond strength, filament distribution and matrix void content. Such tests are therefore often used to evaluate overall composite quality.

Because this test is a measure of composite quality, a wide range of interlaminar shear strength values may be obtained with a single composite type. An example of this is given in Figure 10(a) where a frequency histogram depicts the range of longitudinal interlaminar shear strength reported in the literature for the CFRP composite HT-S/X-904 at 77 K. A relatively substantial amount of data are available for this composite, due in large part to a comprehensive study of the effect of processing variables by Maximovich et al.<sup>12</sup> Such studies are of great value in perfecting fabrication methods; however, it is evident from the strength distribution on Figure 10(a) that discussion of average literature values of interlaminar shear strength (as has been done with other properties discussed in this paper) would be relatively meaningless. More useful would be knowledge of the maximum value obtainable in a "perfect"

composite of a specific type and the extent to which various defects degrade the property. While available data within the cryogenic temperature range do not permit such a detailed analysis, it is of interest to look at the higher values reported for each reinforcement type in order to get a feel for what the limiting interlaminar shear strength might be.

Before pursuing this objective, it is worthwhile to analyze the extensive HT-S/X-904 data a bit further to determine what this relatively large body of data can tell statistically about the temperature dependence of interlaminar shear strength. From the frequency histogram of Figure 10(b) we observe that the reported change in this parameter upon cooling from 295 K to 77 K approximates a normal distribution around zero change, suggesting that interlaminar shear strength is relatively independent of temperature for this composite over this temperature range.

Figures 11 and 12 reflect the upper bounds of uniaxial longitudinal interlaminar shear strength obtainable with various types of advanced composites based on available literature. In preparing these Figures, the highest five reported values were averaged for the HT-S/X-904 data, while the data for the other fibers reflect the average of all available data when the data spread was minimal or, in a few cases, the selection of the higher of two groups of data when such a grouping was obvious. Curves based on only one set of data are identified by an asterisk.

Among the CFRP composites, the data suggest that the highest interlaminar shear strengths will be obtained with the low-modulus HT-S fiber. These data include three evaluations with X-904 resin by Hertz,<sup>13</sup> one evaluation with Ciba 8183, also by Hertz<sup>58</sup> and one evaluation of NASA Resin 2 by Larsen, et al.<sup>10</sup> The 77 K values ranged from about 17,500 psi for the X-904 composites to 21,000 psi for NASA Resin 2, indicating that such high values

are not unreasonable for good quality composites made with this fiber. The room temperature data for the X-904 and Ciba 8183 specimens ranged from 13,000 to 16,000 psi; however, the NASA Resin 2 specimens developed only 7500 psi at this temperature, underlining that this latter resin sacrifices elevated temperature properties for desired performance in the cryogenic range. Figure 11 also indicates a further increase in strength of HT-S composites upon cooling to 20 K. The latter data lacks literature corroboration, reflecting only the data published by Larsen, et al.<sup>10</sup> with a NASA Resin 2 matrix.

Figure 11 indicates an appreciable increase in interlaminar shear strength with lowering of temperature for the selected HT-S composites in contradiction to the negligible dependence inferred statistically by Figure 10(b) for the same type of composite. As there is no reason to question the validity of either of these data, it would appear that processing variables may be affecting the temperature dependence, high-quality composites increasing their interlaminar shear strength at lower temperatures, while lower quality composites show no change.

The available data indicate that the other graphite-epoxy composites have somewhat lower interlaminar shear strengths, ranging from about 10,000 psi down to about 3000 psi with no systematic temperature dependence being evident. At 77 K, there appears to be a somewhat higher strength group composed of Modmor I and II, HMC-25, HMC-50 and HM-S developing strengths on the order of 7500-10,500 psi, while Samco 360, Thornel 50, Fibrallloy 300, GY-70 and Thornel 75 form a somewhat lower group at about 3000-5500 psi. Aside from the very high strength of the low-modulus HT-S fiber composites, there is no evidence of a dependence of interlaminar shear strength on fiber modulus.

Available data on the temperature dependence of interlaminar shear strengths of boron/epoxy, boron/aluminum and PRD 49/epoxy appear on Figure 12. Data reported for experimental Borsic-titanium/aluminum and Borsic-steel/aluminum hybrids<sup>13</sup> and for experimental CFRP composites of HT-S fiber in polyimide and in epoxy-phenolic matrices<sup>58</sup> are included for comparative purposes.

The interlaminar shear strength was reported to increase upon cooling for all of these composites except for the PRD 49/epoxy, which appears to be insensitive to temperature down to 20 K. The highest strength was reported for the Borsic-titanium/aluminum hybrid; however, values reported for the conventional boron/aluminum and SP-272 boron/epoxy composites were almost as high, both ranging from about 15,500 psi to 19,000 psi at 77 K.<sup>13,58</sup> The boron/aluminum curve reflects data obtained with both 4.2 mil Borsic and 5.6 mil boron fibers, the highest values at 77 K being reported for the latter. The HT-S/epoxy-phenolic, the Borsic-steel/aluminum hybrid and the HT-S/polyimide composites appear to develop somewhat lower interlaminar shear strengths, ranging from about 10-14,000 psi at 77 K. The HT-S/epoxy-phenolic material displayed a particularly large increase in shear strength with decreasing temperature. A comparatively low value of interlaminar shear strength was reported for PRD 49/epoxy. The curve for this material reflects results obtained with both ERLB 4617 and NASA Resin 2 matrices, the latter producing shear values 40-70% higher than the former.<sup>59,60</sup>

In summary, these data indicate that the best of the HT-S/epoxy CFRP composites and the conventional boron/epoxies and boron/6061 aluminum composites are capable of providing equivalent high levels of interlaminar shear strengths at cryogenic temperatures, the values varying from about

14,000 psi at 295 K to about 19,000 psi at 77 K. These values are slightly higher than those reported in Part I for uniaxial glass-reinforced composites tested by the short beam method.

#### Composite Failure Strain

Available data on the temperature dependence of ultimate tensile strain for advanced composites are minimal; all of that which has been published reflects the work of Hertz, et al.<sup>13</sup> Nevertheless, these data suffice to illustrate that: (a) the strain at tensile fracture is very low for the advanced composites, being on the order of  $1-9 \times 10^{-3}$  in the longitudinal uniaxial direction and, (b) the strain at tensile fracture is relatively independent of temperature within the cryogenic range. These data are summarized on Figure 13. These strains are about an order of magnitude lower than those for glass-reinforced composites, reflecting the negligible fracture strain of the advanced fibers.

Figure 13 includes data on one CFRP composite (HT-S/X-904), on two conventional boron/aluminum composites (4.2 mil Borsic and 5.6 mil boron, both in 6061) and on the two Borsic/aluminum hybrids discussed previously with reference to the other properties. Both longitudinal and transverse ultimate fracture strains are graphed on Figure 13 for each material.

The data on Figure 13 shows the transverse fracture strain of the HT-S/X-904 CFRP composite to be very low at about  $2 \times 10^{-3}$ , only about 25% of that reported for the longitudinal strain. By comparison, the transverse fracture strain for the commercial HT-S/3002 composite is reported at  $7.8 \times 10^{-3}$ , only slightly less than its longitudinal fracture strain of  $8.6 \times 10^{-3}$ , both room temperature data.<sup>125</sup> Hertz, et al. do not comment on this low transverse strain in HT-S/X-904 and, as their data reflect the average of six specimens taken from panels carefully prepared for design allowable studies, it must be assumed that these data are valid for the HT-S/X-904 composite.

Figure 13 shows that a 5.6 mil boron/6061 aluminum composite is expected to fail at about the same strain in both the longitudinal and transverse directions, while the 4.2 mil Borsic/6061 composite is expected to fail at a much lower strain when tested in the transverse direction. Hertz, et al.<sup>13</sup> found that the 4.2 mil Borsic fiber was failing by longitudinal fiber splitting during transverse testing, while such splitting did not occur in the larger diameter fiber. The authors concluded that the problem was related to the use of plasma-sprayed tape, as higher transverse strains were observed in the same type of composite when diffusion-bonded tape was used to make the test specimens. They concluded that diffusion-bonded boron/aluminum tape was superior for oriented-ply applications. Kreider<sup>126</sup> has proposed an alternative explanation for longitudinal splitting of the small diameter boron fibers, citing results of diametral-compression tests of individual fibers, which indicate that such splitting reflects strength anisotropy in the small fibers due to residual stresses retained from the original fiber manufacturing process and due to residual stresses retained from the original fiber manufacturing process and from pre-existing flaws in the fibers. Such anisotropy was not observed in the larger fibers. Fiber splitting was not directly related to the presence or absence of a silicon carbide coating on the fibers.\*

The Borsic-titanium/aluminum hybrid developed higher strain values in both directions than did the conventional 4.2 mil Borsic/aluminum, but lower values than that of the composite reinforced with 5.6 mil boron. The Borsic-steel/aluminum hybrid shows clearly the increase in transverse strain capability due to the presence of stainless wires oriented in this direction. The longitudinal strain of this hybrid did not appear to be significantly affected by the transverse reinforcement.

---

\* Manufacturers of boron-aluminum tape report that current fabrication technology has overcome the problem of fiber splitting.



The only data available on the temperature dependence of compressive strain within the cryogenic temperature range was for the HT-S/X-904 CFRP composite, again reflecting the work of Hertz, et al.<sup>13</sup> These data indicate an increasing compressive strain capability for this composite type as the temperature is lowered, with a substantially higher strain capability in the transverse direction. Again, these strain values are substantially lower than those reported for a conventional HT-S/3002 CFRP composite.<sup>125</sup>

#### Composite Bearing Strength

The only data found in the literature on the temperature dependence of bearing properties of advanced composites in the cryogenic range were published by Hertz, et al.<sup>13</sup> for boron- and Borsic-reinforced 5061 aluminum, including the steel and titanium reinforced hybrids. These data, appearing on Figure 15, are for bearing strength in the uniaxial longitudinal direction, i.e., the stress required for bearing pull-out, rather than the more conventional bearing yield strength. The data of Figure 15 refer to material hole-to-free surface dimensions two and four times the diameter of a No. 10 steel pin (~ 0.19 in.). An increase in bearing strength with lowering temperature is observed for both conventional boron and Borsic-reinforced materials, the effect being more pronounced in the 4D tests. The Borsic-steel/aluminum hybrid performed much like the conventional materials, while the Borsic-titanium/aluminum hybrid performed somewhat erratically, although the highest strengths were developed with this composite.

### DYNAMIC MECHANICAL PROPERTIES

#### Composite Fatigue

The only available data on the temperature dependence of the fatigue properties of advanced composites were generated during cyclic pressure testing



of filament-wound pressure vessels. As the composites in these vessels were crossplied and were subjected to biaxial stressing, the data are of value only in a comparative sense.

Hanson<sup>45</sup> has studied the cyclic fatigue performance of pressure vessels overwrapped with Thornel 50 graphite fiber using an ERL 2256/ZZL 0820 commercial filament-winding resin. The fatigue life at 77 K was found to be similar to that at 295 K with 90% of the relevant single-cycle strength being retained after 10,000 cycles. This compares to a retention of only about 45% of the single-cycle strength for glass-fiber reinforced vessels. Hanson concluded that on the basis of specific strength, CFRP vessels would have fatigue performance superior to that of GFRP vessels after only 80 cycles.

Alfring, et al.<sup>20</sup> have reported cryogenic cyclic fatigue data on pressure vessels filament-wound with 4 mil boron in a Polaris resin matrix.\* The results were again reported to be independent of temperature (down to 20 K); however, the fatigue life of the boron-reinforced vessels was found to be relatively low, with residual strengths falling to 40-50% of single-cycle values after 10,000 cycles. This is about the same as for glass reinforcement.

These data suggest that graphite may be superior to boron as a reinforcement fiber for composite structures subject to fatigue at cryogenic temperatures; however, these data must be considered to be very tentative in view of the aforementioned tendency for the 4 mil boron fiber to split longitudinally when subjected to transverse stresses such as are present in biaxially-loaded pressure vessels. If splitting is adversely affecting the fatigue strength, the performance of BFRP composites reinforced with 5.6 mil fiber should be substantially better.

---

\* Polaris resin consists of Epon 828/Epon 1031/NMA/BDMA in proportions 50/50/90/0.55 pbw. Commercial designations are E-787 and 58-68R.

### Composite Impact Strength

Few data were available on the impact strength of advanced composites at cryogenic temperatures. The Advanced Composites Design Guide<sup>117</sup> includes some unpublished data on the Charpy V-notch impact values of commercial 5505-4 boron/epoxy material in the uniaxial longitudinal direction. These data indicate a slight increase in impact strength from 22.8 ft lb in<sup>-1</sup> at 295 K to 27.0 ft lb in<sup>-1</sup> at 20 K. Concomitantly, a slight decrease from 46.3 to 39.5 ft lb in<sup>-1</sup> was reported for unnotched specimens over this temperature range. The notched/unnotched ratios of about 0.49 at 295 K and about 0.68 at 20 K, indicate some notch sensitivity. Sumner et al.<sup>7</sup> have reported a 12 ft lb in<sup>-1</sup> Charpy V-notch strength at 295 K for 25 v/o stainless steel wire reinforced 2024 aluminum, this value increasing to 18 ft. lb. in<sup>-1</sup> at 77 K. Cryogenic impact strength data were not available for the other types of advanced composites; however, room temperature data indicate that the CFRP type composites have substantially lower impact strengths than BFRP type and there is no a priori reason to expect this relationship to change at cryogenic temperatures. Such impact strengths are substantially lower than those discussed in Part I for glass-reinforcement where notched values for uniaxial longitudinal composites were seen to range from 67-162 ft lb in<sup>-1</sup> at 77 K.<sup>4</sup> The critical factor has been identified as the stress-strain behavior of the fiber reinforcement, higher impact values being associated with higher failure strains of the fiber whenever tests are made in the longitudinal (cross-fiber fracture) mode.<sup>127,128</sup>

Impact strengths of uniaxial composites tested in the transverse direction are essentially matrix controlled. Since composite structures are usually of crossply construction and subjected to complex stresses, an improvement in the impact strength of the matrix offers the possibility of an overall improvement

of composite toughness. Larsen<sup>9</sup> has reported efforts to improve the impact properties of crossplied HT-S/epoxy materials at cryogenic temperatures by addition of elastomeric components to the matrix. Results of this work were reported in terms of energy density, i.e., the area under the force-deflection curve using a cleavage-type specimen. This work showed that some improvement was indeed possible with CBTN modified ERLB 4617 epoxy; however, the benefit gained was negated by a significant lowering of the room temperature impact properties and by unpredictable performance at cryogenic temperatures. Larsen concluded that better overall cryogenic properties would be obtained by use of the NASA Resin 2 epoxy formulation with CFKP composites.

It appears at this time that substantial improvement of impact strength of the advanced composites will require development of hybrids, possibly combining glass with the advanced fibers.

#### THERMAL PROPERTIES

##### Composite Thermal Expansion and Contraction

Unlike the glass-reinforced composites, some advanced-fiber composites expand in the fiber direction when cooled to cryogenic temperatures. Available data for the temperature dependence of dimensional changes in the uniaxial longitudinal direction are summarized in Figure 16, while comparable data for the uniaxial transverse direction appear in Figure 17.

The CFRP composites display a very small longitudinal expansion on cooling, slightly larger expansions being reported for the high modulus Thornel 75 and GY-70 fiber composites than for the medium-modulus Fibrallloy 300 and the low-modulus HT-S fiber composites. The slight reversal in expansion indicated by a dashed line below 77 K for the HT-S composite is apparently a real effect documented by Larsen and Simon<sup>10</sup> in both HT-S/NASA Resin 2 and HT-S/4617 Polyblend composites. The PRD 49

(Kevlar 49) composites undergo a comparatively large longitudinal expansion on cooling, reportedly reaching a maximum of about  $8-10 \times 10^{-4}$  at about 77 K. Slightly larger expansion was reported with a NASA Resin 2 matrix than with ERLA 4617. The other advanced composites contracted on cooling. Least longitudinal contraction was reported for the commercial SP-272 boron/epoxy product, while the boron/aluminums undergo the largest contractions. The matrix contraction properties appear to be dominating, in the latter as relatively little difference is seen among the four variants, including the hybrids. The 5.6 mil composite displays a slightly lower contraction than does the 4 mil product. The longitudinal thermal contractions of these boron/aluminum composites are about 25% of that for unreinforced 6061 aluminum alloy.

Dimensional changes in the transverse direction are strongly influenced by the matrix, all advanced composites showing contraction in this direction on cooling. These contractions are large compared to changes observed in the fiber direction, as witnessed by the necessity to change the ordinate scale for Figure 17. The data indicate that boron/epoxy composites have the least transverse contraction of the group, yet even this relatively low value is three times larger than its longitudinal change. The CFRP composites appear to undergo about twice the transverse thermal contraction of the BFRP composites, reflecting the lesser constraint provided in this direction by the small graphite fibers. A slightly higher transverse contraction is reported for the high-modulus GY-70/X-904 composite than for the low-modulus HT-S/X-904 material; however, such a small difference could easily be accounted for by variations in fiber volume fraction. The conventional boron/6061 aluminum composites have the next largest transverse contraction. By comparison with the contraction of unreinforced 6061 alloy (dashed curve), it is seen that the transverse contraction of boron/aluminum is almost completely matrix

dominated. No significant differences were reported for 4.2 mil Borsic and 5.6 mil boron fiber composites.

The PRD 49/epoxy composites have by far the largest transverse thermal contraction. Comparing the temperature dependence of PRD49-I/NASA Resin 2 (curve 8) with that reported by Soffer and Molho<sup>5</sup> for NASA Resin 2 alone (dashed curve), indicates that the matrix is also dominating the transverse dimensional changes in this composite. The PRD 49 fibers do not offer appreciable restraint to transverse contraction of the matrix because, as seen in Figure 16, this fiber expands significantly in the longitudinal direction during cooling which, of necessity, is accompanied by significant transverse fiber contraction. Thus, cooling to cryogenic temperatures would be expected to produce sizeable interfacial shear forces between the fiber and matrix, with lesser forces normal to the fibers.

#### Composite Thermal Conductivity

Few data were available on the temperature dependence of uniaxial longitudinal and uniaxial transverse thermal conductivity of advanced composites. Those which were available are plotted in Figure 18. In considering these data, the reader should be aware of the difficulties and potential sources of error in determining such conductivities in the cryogenic range. The comments made in Part I of this paper on this subject apply equally well here. Furthermore, the volume fraction of fiber will influence the conductivities, particularly in graphite-reinforced composites. For these reasons, the data on Figure 18 should be considered as only indicating trends.

The CFRP composites have relatively high thermal conductivities in the fiber direction, reflecting relatively high conductivity of the graphite fibers compared to epoxy. Longitudinal conductivity in these materials is highly temperature de-

pendent. The BFRP composites have much lower conductivities than do the CFRP composites in the fiber direction and show a comparatively small temperature dependence of thermal conductivity. Data were not available for boron-reinforced aluminum; however, the thermal conductivity of such materials will certainly be much higher than that of a polymeric matrix composite. The conductivity should be approximately half that of unreinforced aluminum in a typical 50 volume percent boron/aluminum composite. Transverse thermal conductivities are matrix dominated and very low for both the CFRP and BFRP materials.

These data suffice to show that the thermal conductivities of the epoxy-matrix advanced composites, particularly boron-reinforced, are low enough to make them attractive for cryogenic structural components.

#### Composite Specific Heat

Figure 19 shows the specific heat of the advanced composites to be similar to those of the glass-reinforced composites discussed in Part I of this paper. Again, an almost linear temperature dependence of  $C_p$  is observed from 295 K to 77 K. As a group, the values are slightly lower than aluminum for much of the region between 295 K and 77 K, but substantially higher than that for copper and most other metals down to 77 K. The temperature dependence of  $C_p$  for aluminum, copper and titanium are included on Figure 19 for comparative purposes.

The highest specific heat at cryogenic temperatures was reported for boron/aluminum, the aluminum matrix undoubtedly contributing significantly to this relatively high value. The depicted curve is the average of data reported by Hertz et al.<sup>13</sup> for 4.2 mil Borsic/6061 and 5.6 mil boron/6061. Slightly higher values were reported at 295 K and 200 K for the larger filament size, falling to slightly lower at 77 K. The data indicate that the Borsic/aluminum hybrids had slightly lower specific heats, probably reflecting the contributions from

the steel and titanium reinforcements. The specific heat of the boron/epoxy composite lies between that of the boron/aluminum and the graphite/epoxy. The specific heat of the latter has undoubtedly been lowered by the graphite which, as shown by the dashed curve on Figure 19, has itself a relatively low specific heat.

The data indicate that boron/epoxy has a comparatively high specific heat at room temperature. This is not unreasonable, as boron has a room temperature specific heat of about  $12.9 \times 10^2 \text{ J Kg}^{-1} \text{ K}^{-1}$ . No cryogenic specific heat data were available for boron or epoxy; however, the composite data suggest a rapidly decreasing value of  $C_p$  for boron as temperature decreases, while indicating that the specific heat of epoxy probably lies between the curves for boron/epoxy and graphite/epoxy.

#### COMMENTS ON ADVANCED COMPOSITES

The purpose of this review is to give the reader an understanding of the present state of knowledge as to the magnitude and temperature dependence of the properties of advanced fiber composites at cryogenic temperatures. It is apparent that present knowledge is incomplete in many respects; nevertheless, the available data justify considerable optimism as to the future applicability for these materials for structural components operating at cryogenic temperatures.

The cryogenic performance of the commercial state-of-the-art boron-reinforced epoxies and aluminum are particularly impressive as they consistently display excellent tensile and compressive strengths and elastic moduli which remain constant or improve as the temperature is lowered. Equally impressive is the relatively small scatter in the data which is indicative of a high degree of reliability for components made from boron-reinforced composites. The data suggest that the commercial products may be used effectively at cryogenic temperatures without optimization of the composite matrix.



Available data on the cryogenic performance of the graphite-reinforced epoxy class of composites are less convincing. Ultimate tensile strengths are lower than for boron reinforcement and show a disturbing tendency to decrease with cooling. Test results are sometimes very unpredictable and contradictory. Larsen and Simon<sup>10</sup> report diametrically opposed temperature dependence of the tensile strength for both HT-S/NASA Resin 2 and HT-S/ERLB 4617 polyblend composites when each was tested first as flat uniaxial specimens and subsequently by the NOL-ring method. Results of this type suggest that much of the apparent erratic and inconsistent behavior in CFRP composites may be due to the difficulty of obtaining valid measurements of strength at cryogenic temperatures with this class of composite. Certainly, the overall performance of graphite-fiber overwrapped pressure vessels also reported by Larsen and Simon was much better than could have been predicted from their basic test data. In contrast to the boron-reinforced materials, data suggest that the CFRP composites may benefit from matrix optimization. Larsen and Simon recommend NASA Resin 2 for both uniaxial and crossply CFRP composites on the basis of their research. This would appear to be a reasonable choice, as this resin system was developed by Soffer and Molho<sup>5</sup> to provide improved performance at low temperatures. The potential user is cautioned, however, that this resin has relatively poor properties at room temperature and above. Particular caution must be taken to properly support components made with this resin whenever elevated temperature vacuum degassing is required prior to cryogenic service.

Kevlar 49 (PRD 49) is currently attracting a good deal of attention for cryogenic applications. This fiber is often considered as a replacement for glass as it is relatively inexpensive and imparts to a composite a significantly higher modulus. Based on current knowledge, the NASA Resin 2 epoxy formulation



is perhaps the most acceptable matrix material for this fiber; however, the aforementioned warning on the low room temperature properties must be heeded.

In part I of this paper, the author mentioned the possibility that the cryogen in which mechanical property measurements are made might be affecting the results obtained with glass-reinforced polymers. This cautionary note was based on the recent discovery that the onset of crazing in certain polymers could be caused by the activity of the liquefied gas (particularly nitrogen) relative to the polymer surface.<sup>129</sup> The possibility exists that a similar phenomenon is affecting the mechanical properties of the graphite- and PRD 49-reinforced composites. In the few cases where mechanical property measurements on such composites were carried to below 77 K, the data tended to become erratic in the same manner as was observed for glass. The ultimate tensile strength data for the HT-S fiber in Figures 1(a) and 1(b) may be cited as examples, as may the modulus of PRD 49 in Figure 4(a). It is difficult to accept such precipitous changes in temperature dependence as inherent characteristics of the materials.

Much work remains before the behavior of advanced composites under cryogenic conditions can be said to be thoroughly understood. The follow-on work suggested in Part I for the glass-reinforced composites applies equally well to the advanced composites. Following the suggested method of approach, a program of research is being started at NBS to characterize selected GFRP, CFRP, BFRP, BFRM (aluminum) and Kevlar 49 composites from 295 K to 4 K both mechanically and thermally. Hopefully, data derived during the course of this program will provide firm bases for the understanding of composite performance at cryogenic temperatures.

#### ACKNOWLEDGMENTS

The author thanks Dr. R. P. Reed for consultation and review of the completed manuscript. Many thanks are also due the NBS-NOAA library staff of the Boulder Laboratories for their assistance in retrieving the documents on which this work depended. This research was supported by the Advanced Research Projects Agency.

## APPENDIX

The following materials are referred to in this report:

### Fibers

#### Graphite

HT-S, HM-S  
HMG-25, HMG-50  
Modmor I, II  
Thornel 25, 50  
Samco 320  
Fibralloy 300  
GY-70

Courtaulds Ltd.  
Hitco Corp.  
Morganite Ltd.  
Union Carbide Corp.  
Samco Corp.  
Monsanto Corp.  
Celanese Corp.

#### Boron

Borsic

Hamilton Standard Corp.

#### Others

PRD 49 (Kevlar 49)

E. I. DuPont de Nemours, Inc.

### Resins

#### Epoxies

X-904, X-915  
ERL 2256, ERLB 4617  
Epon 828, 1031, 58-68R  
E-350, E-787  
Ciba 8183/137  
3002

Fiberite Corp.  
Union Carbide Plastics Co.  
Shell Chemical Corp., Plastics & Resin Div.  
U.S. Polymeric Corp.

Hercules Corp.

#### Others

Skybond 703 (polyimide)  
HT-424 (epoxy-phenolic)

Monsanto Corp.  
American Cyanamid.

### Flexibilizers, Coupling Agents, Hardners

ZZL 0820  
Empol 1040

Union Carbide Plastics Co.  
Emery Industries, Inc.

### Boron Composite Products

SP-272  
5505

Minnesota Mining & Manufacturing Co.  
Avco Corporation

### Miscellaneous Materials

DSA - dodecenyl succinic anhydride  
BDMA - benzyldimethylamine  
NMA - nadic methyl anhydride

## BIBLIOGRAPHY

### CONTRACT BIBLIOGRAPHY

#### I - MECHANICAL PROPERTIES

##### Contract AF-33(616)-8289

Contractor: Directorate of Materials and Processes, Aeronautical Systems Division, Air Force Systems Command, Wright-Patterson Air Force Base, Ohio.

Research Facility: Narmco Research and Development, San Diego, California.

1. Brink, N. O., "Determination of the Performance of Plastic Laminates Under Cryogenic Temperatures", ASD-TDR-62-794, August 1962 (AD 288 944).
  - 1.1 Ibid., "Mechanical Behavior of Reinforced Plastics at Cryogenic Temperatures", Technical Papers, 20th Annual Technical Conference, Society of Plastics Engineers, Vol. 10, Section XV-2, 1964, pp. 1-19.
  - 1.2 Ibid., "Mechanical Behavior of Reinforced Plastics at Cryogenic Temperatures", Society of Plastics Engineers Journal, Vol. 20, 1964, pp. 1123-1131.
  - 1.3 Ibid., "Mechanical Behavior of Reinforced Plastics at Cryogenic Temperatures", Narmco Research and Development Report, Code No. 105-4, 1964.
2. Chamberlain, D. W., Lloyd, B. R. and Tennant, R. L., "Determination of the Performance of Plastic Laminates at Cryogenic Temperatures", ASD-TDR-62-794, Part II, March 1964 (N64-24212).
  - 2.1 Chamberlain, D. W., "Tensile Fatigue Testing at Temperatures Down to 20 K", Advances in Cryogenic Engineering, Vol. 9, 1964, pp. 131-138.
  - 2.2 Ibid., "Mechanical Properties Testing of Plastic Laminate Materials Down to 20 K", Advances in Cryogenic Engineering, Vol. 10, 1965, pp. 117-125.

##### Contract NAS 8-11070

Contractor: National Aeronautics and Space Administration, George C. Marshall Space Flight Center, Huntsville, Alabama.

Research Facility: Goodyear Aerospace Corporation, Akron, Ohio.

3. Toth, L. W., Boller, T. J., Butcher, I. R., Kariotis, A. H. and Yoder, F. D., "Program for the Evaluation of Structural Reinforced Plastic Materials at Cryogenic Temperatures", NASA CR-80061 (Final), August 1966 (N67-12051).

- 3.1 Toth, L. W., "Properties Testing of Reinforced Plastic Laminates Through the 20 degree K Range", Technical Papers, 20th Annual Technical Conference, Society of the Plastics Industry, Section 7-C, 1965, pp. 1-10.
- 3.2 Toth, L. W. and Kariotis, A. H., "An Assessment of Test Specimens and Test Techniques Useful to the Evaluation of Structural Reinforced Plastic Materials at Cryogenic Temperatures", Advances in Cryogenic Engineering, Vol. 10, 1965, pp. 126-133.
- 3.3 Toth, L. W., "Properties of Glass-Reinforced Epoxy Through the 20 K Range", Modern Plastics, Vol. 42, August 1965, pp. 123-130.
- 3.4 Toth, L. W. and Burkley, R. A., "Mechanical Response at Cryogenic Temperatures of Selected Reinforced Plastic Composite Systems", Goodyear Aerospace Report GER-13169, Paper No. 16, Seventieth Annual Meeting of the American Society for Testing and Materials, June 1967.
- 3.5 Toth, L. W., Boller, T. J., Kariotis, A. H. and Yoder, F. D., "Program for the Evaluation of Structural Reinforced Plastic Materials at Cryogenic Temperatures", NASA CR-64005, June 1963 through June 1964 (N65-29724).

Contract NAS 3-6297

Contractor: National Aeronautics and Space Administration, Lewis Research Center, Cleveland, Ohio.

Research Facility: Aerojet General Corporation, Azuza, California.

4. Lewis, A. and Bush, G. E., "Improved Cryogenic Resin-Glass Filament Wound Composites", NASA CR-72163 (Final), March 1967 (N67-31856).
- 4.1 Lewis, A., Bush, G. E. and Creedon, J., "Improved Cryogenic Resin/Glass Filament-Wound Composites", NASA Interim Report CR-54867, May 1966 (N66-28040).

Contract NAS 6-6287

Contractor: National Aeronautics and Space Administration, Lewis Research Center, Cleveland, Ohio.

Research Facility: Aerojet General Corporation, Azuza, California.

5. Soffer, L. M. and Molho, R., "Cryogenic Resins for Glass Filament-Wound Composites", NASA CR-72114 (Final), January 1967 (N67-25076).
- 5.1 Ibid., "Mechanical Properties of Epoxy Resins and Glass/Epoxy Composites at Cryogenic Temperatures", Cryogenic Properties of Polymers, J. L. Koenig, Ed., Marcel Dekker, New York, 1968, pp. 87-117. (Identical to NASA CR-84451, 1967, (N67-27217).

Contract F04701-69-C-0059

Contractor: Space and Missiles Systems Organization, Air Force  
Systems Command, Los Angeles Air Force Station,  
Los Angeles, California.

Research Facility: The Aerospace Corporation, El Segundo, California.

6. Pepper, R. T., Rossi, R. E., Upp, U. W. and Riley, W. E., "Development of an Aluminum-Graphite Composite", SAMSO-TR-70-301, August 1970 (AD 718 409).

6.1 Pepper, R. T., Upp, J. W., Rossi, R. C. and Kendall, E. G., "Aluminum-Graphite Composites", SAMSO-TR-70-174, April 1970 (AD 706 883). (Identical to Metallurgical Transactions, Vol. 2, January 1971, pp. 117-120.)

6.2 Rossi, R. C., Pepper, R. T., Upp, J. W. and Riley, W. C., "Development of Aluminum-Graphite Composites", Ceramic Bulletin, Vol. 50, May 1971, pp. 484-487.

Contract NAS 8-11508

Contractor: National Aeronautics and Space Administration, George  
C. Marshall Space Flight Center, Huntsville, Alabama.

Research Facility: Harvey Engineering Laboratories, Torrance,  
California.

7. Sumner, E. V. and Davis, L. W., "Development of Ultrahigh Strength, Low Density Aluminum Sheet and Plate Composites", NASA CR-85863 (Final), July 1966 (N67-31181).

7.1 Davis, L. W., "Composites at Low Temperature", Paper No. 15, Seventieth Annual Meeting of the American Society for Testing Materials, June 1967.

Contract NASA DPR C 10360-B

Contractor: National Aeronautics and Space Administration, Lewis Research Center, Cleveland, Ohio.

Research Facility: Naval Ordnance Laboratory, Silver Springs,  
Maryland.

8. Simon, R. A. and Alfring, R., "Properties of Graphite Fiber Composites at Cryogenic Temperatures", NASA CR-72652 (NOLTR 69-183), May 1970, Tasks I and II (AD 746 885).

9. Larsen, J. V., "Properties of Graphite Fiber Composites at Cryogenic Temperatures -- Effect of Elastomeric Additions to Resin Systems", NASA CR-72804 (NOLTR 70-195), March 1971, Task III (AD 882 972).

10. Larsen, J. V. and Simon, R. A., "Carbon Fiber Composites for Cryogenic Filament-Wound Vessels", NASA CR-120899, (NOLTR 71-201), May 1972, Tasks IV, V and VI, (N73-11553).

- 10.1 Simon, R. A., "Graphite Fiber Composites at Cryogenic Temperatures", Technical Papers, 26th Annual Technical Conference, Society of the Plastics Industry, Section 10-D, 1971, pp. 1-4.

- 10.2 Larsen, J. W., "Fracture Energy of CBTN/Epoxy-Carbon Fiber Composites", Technical Papers, 26th Annual Technical Conference, Society of the Plastics Industry, Section 10-D, 1971, pp. 1-4.

Contract NAS 8-26198

Contractor: George C. Marshall Space Flight Center, Huntsville, Alabama.

Research Facility: General Dynamics/Convair, San Diego, California.

11. Scheck, W. G., "Development of Design Data for Graphite Reinforced Epoxy and polyimide Composites", NASA TN-D2970, Report No. GDC-DBG-70-005, Final National Aeronautics and Space Administration, Marshall Space Flight Center, Alabama, May 1974.
12. Scheck, W. G., "Development of Design Data for Graphite Reinforced Epoxy and Polyimide Composites", Report No. GDC-DBG70-005, General Dynamics Quarterly Report No. 1, 1970. (See also Maximovich, M. and Scheck, W. G. Quarterly Report No. 2, 1970).
- 12.1 Stuckey, J. M. and Scheck, W. G., "Development of Graphite/Polyimide Composites", National-Technical Conference, Society of Aerospace Material and Process Engineers, Vol. 3, 1971, pp. 717-723.

Contract F33615-70-1442

Contractor: Air Force Materials Laboratory, Wright-Patterson Air Force Base, Ohio.

Research Facility: General Dynamics/Convair, San Diego, California.

13. Hertz, J., Christian, J. L. and Varlas, M., "Advanced Composite Applications for Spacecraft and Missiles, Phase I Final Report, Volume II: Material Development", AFML-TR 71-186, Vol. 2, March 1972 (AD 893 715L).
- 13.1 Forest, J. D., Fujimoto, A. F. and Foelsch, G. F., "Advanced Composite Applications for Spacecraft and Missiles, Phase I Final Report, Volume I: Structural Development", AFML-TR-71-186, Vol. 1, March 1972.
  - 13.2 Forest, J. D. and Varlas, M., "Advanced Composite Applications for Spacecraft and Missiles, Final Report", AFML-TR-72-278, March 1973.

- 13.3 Christian, J. L. and Campbell, M. D., "Mechanical and Physical Properties of Several Advanced Metal-Matrix Composite Materials", Advances in Cryogenic Engineering, Vol. 18, 1973, pp. 175-183.

## II THERMOPHYSICAL PROPERTIES

### Contract AF-33(657)-9160

Contractor: Air Force Materials Laboratory, Wright-Patterson Air Force Base, Ohio.

Research Facility: General Dynamics/Astronautics, San Diego, California

The following reports are in a series entitled "Thermophysical Properties of Plastic Materials and Composites to Liquid Hydrogen Temperature (-423°F)".

14. Haskins, J. F., Campbell, M. C., Hertz, J. and Percy, J. L., ML-TDR-64-33, Part I, June 1964 (AD 601 337).
15. Campbell, M. D., Hertz, J., O'Barr, H. L. and Haskins, J. F., ML-TDR-64-33, Part II, March 1965 (X65-18921).
16. Campbell, M. D., O'Barr, G. L., Haskins, J. F. and Hertz, J., ML-TDR-64-33, Part III, August 1965 (AD 468 155).
- 16.1 Hertz, J. and Haskins, J. F., "Thermal Conductivity of Reinforced Plastics at Cryogenic Temperatures", Advances in Cryogenic Engineering, Vol. 10, 1965, pp. 163-169.
- 16.2 Campbell, M. D., "Thermal Expansion Characteristics of Some Plastic Materials and Composites from Room Temperature to -253°C", Advances in Cryogenic Engineering, Vol. 10, 1965, pp. 154-162.
- 16.3 Campbell, M. D., Haskins, J. F., O'Barr, G. L. and Hertz, J., "Thermophysical Properties of Reinforced Plastics at Cryogenic Temperatures", Journal of Spacecraft, Vol. 3, April 1966, pp. 596-599.

(See also Ref. 13.)

### Contract F33615-73-C1388 (Work currently in progress)

Contractor: Air Force Materials Laboratory, Wright-Patterson Air Force Base, Ohio.

Research Facility: General Dynamics/Convair, San Diego, California.



17. Forest, J. D. and Schaeffer, W. H., "Advanced Composite Missile and Space Design Data", General Dynamics Report GDCA-CHB72-001-1, Progress Report No. 1, October 1972.
18. Forest, J. D., "Advanced Composite Missile and Space Design Data", General Dynamics Report GDCA-CHB72-001-2, Progress Report No. 2, January, 1973.

### III - GENERAL BIBLIOGRAPHY

19. Aleck, B., "Fiberglass-Overwrapped 2219-T87 Aluminum Alloy Low-Pressure Cryogenic Tankage", Society of Aerospace Material and Process Engineers National Technical Conference, Space Shuttle Materials, Vol. 3, 1971, pp. 131-134.
20. Alfring, R. J., Morris, E. E. and Landes, R. E., "Cycle-Testing of Boron Filament-Wound Tanks", NASA CR-72899, National Aeronautics and Space Administration, Lewis Research Center, August 1971 (N71-38023).
21. Barber, J. R., "Design and Fabrication of Shadow Shield Systems for Thermal Protection of Cryogenic Propellants", NASA CR-72595, National Aeronautics and Space Administration, Lewis Research Center, Cleveland, Ohio, November 1969 (N70-25098).
22. Baucom, R. M., "Tensile Behavior of Boron Filament-Reinforced Epoxy Rings and Belts", NASA TN D-5053, Langley Research Center, Hampton, Virginia, March 1969 (N69-19918).
23. Benton, W., Carr, R., Cohen, A., Gustafson, G., Lankton, C. and Zeldin, B., "Propellant Storability in Space", RPL-TDR-64-75 (Final), Air Force Systems Command, Edwards Air Force Base, California, June 1964 (AD 603 215).
24. Brechna, H., "Superconducting Magnets for High Energy Physics Applications", Proceedings 1st International Cryogenic Conference, Tokyo and Kyoto, Japan, April 1967, Heywood Temple Industrial Publishers, Ltd., London, 1968, pp. 119-129 (CFSCI N67-36009).
25. Bullard, B. R., "Cryogenic Tank Support Evaluation", NASA CR-72546, NASA Lewis Research Center, Cleveland, Ohio, December 1969 (N70-13085).
26. Campbell, M. D., "Development of Thermal Expansion Capabilities and the Investigation of Expansion Characteristics of Space Vehicle Materials", General Dynamics/Astronautics Report ERR-AN-251, 14 December 1962.

27. Campbell, M. D., "Development of the Thermal Expansion Capabilities and the Investigation of the Thermal Expansion Characteristics of Space Vehicle Materials (II)", General Dynamics/Astronautics Report ERR-AN-450, 26 December 1963.
28. Caren, R. P., Coston, R. M., Holmes, A. M. C. and Dubus, F., "Low-Temperature Tensile, Thermal Contraction, and Gaseous Hydrogen Permeability Data on Hydrogen-Vapor Barrier Materials", Advances in Cryogenic Engineering, Vol. 10, 1965, pp. 171-180.
29. Chiao, T. T. and Moore, R. L., "Tensile Properties of PRD-49 Fiber in Epoxy Matrix", Journal of Composite Materials, Vol. 6, October 1972, pp. 547-551.
30. Cooper, G. A. and Sillwood, J. M., "Multiple Fracture in a Steel Reinforced Epoxy Resin Composite", Journal of Materials Science, Vol. 7, 1972, pp. 325-333.
31. Darwish, F. and Tetelman, A. S., "Mechanical Behavior of SiO<sub>2</sub>-Epoxy Composite", Conference Proceedings No. 63, Advisory Group for Aerospace Research and Development, Symposium on Composite Materials, Paper No. 9, Paris, April 1970 (Hartford House, London).
32. Davis, J. G. and Zender, G. W., "Mechanical Behavior of Carbon Fiber Reinforced-Epoxy Composites", 12th National Symposium, Society of Aerospace Material and Process Engineers, Vol. 12, 1967, Section AC-10.
33. Dervy, A. J., "Reinforced Plastics of High Strength/Weight Ratio for Space Applications", Technical Papers, 17th Annual Technical Conference, Society of the Plastics Industry, Section 7-D, 1962, pp. 1-10.
34. Fontana, M. G., Bishop, S. M. and Spretnak, J. W., "Investigation of Mechanical Properties and Physical Metallurgy of Aircraft Alloys at Very Low Temperatures, Part 5 - Mechanical Properties of Metals and a Plastic Laminate at Low Temperatures", AF Technical Report 5662, Part 5, Materials Laboratory, Wright-Patterson Air Force Base, Ohio, December 1953 (AD 27726).
35. Freeman, S. M., "Properties of Vapor Barriers, Adhesives and Foams at Cryogenic and Elevated Temperatures", Lockheed Aircraft Corporation Report ER-5687, April 1962.
36. Freeman, W. T. and Campbell, M. D., "Thermal Expansion Characteristics of Graphite Reinforced Composite Materials", Composite Materials: Testing and Design (Second Conference), ASTM STP 497, American Society for Testing and Materials, 1972, pp. 121-142.

37. Funk, C. W. and Dixon, C. E., "Cryogenic Radiation Damage in Structural Polymers", Transactions of the American Nuclear Society, Vol. 9, 1966, pp. 406.
38. Gille, J. P., "Development of Advanced Materials for Integrated Tank Insulation System for the Long Term Storage of Cryogenics in Space", NASA CR-102570 (Final), National Aeronautics and Space Administration, Huntsville, Alabama, September 1969 (N70-23348).
39. Gleich, D., "Development of a Filament-Overwrapped Cryoformed Metal Pressure Vessel", NASA CR-72753, National Aeronautics and Space Administration, Lewis Research Center, Cleveland, Ohio, January 1971 (N71-22401).
40. Gray, P. D., Cornelius, G. K., O'Donnell, J. D., and Howard, W. W., "Rockets in Space Environment, Volume 1: The Experimental Program", RTD-TDR-63-1050, Aerojet General Corporation, February 1963 (N63-20999).
41. Greer, F., "Flexural Properties of Conolon 506 at Room Temperature, -320°F and -423°F", Convair/Astronautics Report 55E 522, June 1961 (AD 677 565).
42. Hale, D. V., "Study of Thermal Conductivity Requirements: MSFC 20-Inch and 105-Inch Cryogenic Tank Analyses", NASA CR-61288, National Aeronautics and Space Administration, Marshall Space Flight Center, Alabama, June 1969 (N69-35811).
43. Hall, J., "Cryogenic Tensile Tests - Epoxy Fiberglass", Douglas Aircraft Company Report MP 1348, September 1961.
44. Hanson, M. P., "Effects of Temperature and Creep Characteristics of PRD-49 Fiber/Epoxy Composites", NASA TN D-7120, National Aeronautics and Space Administration, Lewis Research Center, Cleveland, Ohio, November 1972 (N73-12607).
45. Hanson, M. P., "Tensile and Cyclic Fatigue Properties of Graphite Filament-Wound Pressure Vessels at Ambient and Cryogenic Temperatures", NASA TN D-5354, National Aeronautics and Space Administration, Lewis Research Center, Cleveland, Ohio, July 1969 (N69-31300). (Identical to SAMPE Vol. 15, pp. 249-256).
46. Hanson, M. P., Richards, H. T. and Hickel, R. O., "Preliminary Investigation of Filament-Wound Glass-Reinforced Plastics and Liners for Cryogenic Pressure Vessels", NASA TN D-2741, National Aeronautics and Space Administration, Lewis Research Center, Cleveland, Ohio, March 1965.

47. Hanson, M. P., "Glass-, Boron-, and Graphite-Filament-wound Resin Composites and Liners for Cryogenic Pressure Vessels", NASA TN D-4412, National Aeronautics and Space Administration, Lewis Research Center, Cleveland, Ohio, February 1968. (Identical to NASA TM X-52350, 1967.)
48. Hanson, M. P., "Static and Dynamic Fatigue Behavior of Glass Filament-Wound pressure Vessels at Ambient and Cryogenic Temperatures", NASA TN D-5807, National Aeronautics and Space Administration, Lewis Research Center, Cleveland, Ohio, May 1970 (CFSTI-CSCL-20 K).
49. Haskins, J. F. and Hertz, J., "Thermal Conductivity Testing of Coast F-224-6 Phenolic-Fiberglass Laminate", General Dynamics/Convair Report No. AR-592-1-482, July 1963.
50. Haskins, J. F. and Hurlich, A., "Measured Values for the Coefficients of Linear Expansion of Plycel 420 and Conolon 506 at Low Temperatures", Convair/Astronautics Report MRG-154, May 1960.
51. Haylett, J. W., Rottmayer, E. and Butcher, I., "Advanced Composite Material Study for Millimeter Wavelength Antennas", Technical Report AFML-TR-71-205, Vol. 1, Air Force Materials Laboratory, Wright-Patterson Air Force Base, Ohio, October 1971 (AD 893 368).
52. Haylett, C. E., "Advanced Composite Material Study for Millimeter Wavelength Antennas, Volume II, Environmental Tests", AFML-TR-71-205-Vol. 2, Air Force Materials Laboratory, Wright-Patterson Air Force Base, Ohio, October 1971 (AD 893 358 L).
53. Herring, H. W., Baucom, R. M. and Pride, R. A., "Research on Boron Filaments and Boron Reinforced Composites", 10th National Symposium, Society of Aerospace Material and Process Engineers, Vol. 10, 1966, pp. B-21 to B-34.
54. Hertz, J., "Tensile Testing of Conolon 506 at Room and Sub-Zero Temperatures", Convair/Astronautics Report MRG-120, December 1959.
55. Hertz, J., "Tensile Testing of Adlock 851, Adlock PG-LA and Adlock EG-11A-81A from -423°F to 78°F", Convair/Astronautics Report MRG 237, June 1961.
56. Hertz, J., "Investigation of Potential Low Temperature Insulations", General Dynamics/Astronautics Report GS/A-ERR-AN-668, December 1964.
57. Hertz, J., "The Effect of Cryogenic Temperatures on the Mechanical Properties of Reinforced Plastic Laminates", General Dynamics Report AR-592-1-415, March 1963 (AD 405 170).

58. Hertz, J., "Investigation into the High-Temperature Strength Degradation of Fiber-Reinforced Resin Composite During Ambient Aging", General Dynamics/Convair Report No. GDCA-DBG73-005 (Final Contract NAS 8-27435), June 1973.
59. Hoggatt, J. T., "Development of Cryogenic PRD-49-1 Filament-Wound Tanks", NASA CR-120835, National Aeronautics and Space Administration, Lewis Research Center, Cleveland, Ohio, December 1971 (N72-24941).
60. Hoggatt, J. T., "High Performance Filament Wound Composites for Pressure Vessel Applications", Society of Aerospace Material and Process Engineers National Technical Conference, Space Shuttle Materials, Vol. 3, 1971, pp. 157-167.
61. Hust, J. G., "Thermal Conductivity of an Epoxy-Fiberglass Laminate", National Bureau of Standards Cryogenic Division Unpublished Laboratory Note 73-1, January 1973.
62. Johnston, H. L. and Brooks, H. E., "Impact Strength of Various Metals at Temperatures down to 20° Absolute", Ohio State University Cryogenic Laboratory Report TR 264-17, May 1952.
63. Keller, C. W., "Fiberglass Supports for Cryogenic Tanks", NASA CR-120937 (Final), National Aeronautics and Space Administration, Lewis Research Center, Cleveland, Ohio, October 1972 (N72-33564).
64. Kerlin, E. E. and Smith, E. T., "Measured Effects of the Various Combinations of Nuclear Radiation, Vacuum and Cryotemperatures on Engineering Materials: Biennial Report", NASA CR-77772, National Aeronautics and Space Administration, George C. Marshall Space Flight Center, Huntsville, Alabama, July 1966 (N66-35963).
65. Kerlin, E. E. and Smith, E. T., "Measured Effects of the Various Combinations of Nuclear Radiation, Vacuum and Cryotemperatures on Engineering Materials: Annual Report", NASA CR-58830, National Aeronautics and Space Administration, George C. Marshall Space Flight Center, Huntsville, Alabama, May 1964 (N64-33043).
66. Keys, R. D., Kiefer, T. F. and Schwartzberg, F. R., "Cryogenic Properties of High-Strength Glass-Reinforced Plastics", Advances in Cryogenic Engineering, Vol. 11, 1966, pp. 470-477.
67. Krause, D. R., "Development of Lightweight Material Composites to Insulate Cryogenic Tanks for 30-Day Storage in Outer Space", NASA CR-123797, National Aeronautics and Space Administration, George C. Marshall Space Flight Center, Huntsville, Alabama, June 1972 (N72-30495).



68. Krause, D. R., Fredrickson, G. O. and Klevatt, P. L., "Effects of Cyclical Environments on High-Performance Multi-Layer Insulation Materials", Society of Aerospace Material and Process Engineers National Technical Conference, Space Shuttle Materials, Vol. 3, 1971, pp. 639-643.
69. Lantz, R. B., "Materials for Filament Wound Cryogenic Pressure Vessels", 6th National Symposium, Society of Aerospace Materials and Process Engineers, Vol. 2, Engineering Paper No. 1750.
70. Lavengood, R. E. and Anderson, R. M., "Matrix Properties Controlling Torsional Fatigue Life of Fiber Reinforced Composites", Technical Papers, 24th Annual Technical Conference, Society of the Plastics Industry, Section 11-E, 1969, pp. 1-7.
71. Levin, V. A., Naumenkov, P. G. and Shchitov, M. V., "Some Properties of Plastics at Low Temperatures", Plasticheska Massy, Vol. 11, 1966, pp. 64-65.
72. Luikov, A. V., Vasiliev, L. L. and Shashkov, A. G., "A Method for the Simultaneous Determination of all Thermal Properties of Poor Heat Conductors Over the Temperature Range 80 to 500 K", Proceedings, Third American Society of Mechanical Engineers Symposium, Purdue University, March 1965, pp. 314-319.
73. Lyon, D. N. and Parrish, W. R., "Low Temperature Thermal Conductivities of Two High Compressive Strength Materials", Cryogenics, Vol. 7, No. 1, 1967.
74. Maher, L. E., "Some Problems Arising from the Use of Hydrogen-Fuelled Propulsion Systems", Journal of the Royal Aeronautical Society, Vol. 68, November 1964, pp. 765-771.
75. McKannon, E. C. and Gause, R. L., "Effects of Nuclear Radiation and Cryogenic Temperatures on Non-Metallic Engineering Materials", Journal of Spacecraft, Vol. 2, August 1965, pp. 558-564.
76. Morris, E. E., "Glass-Fiber-Reinforced Metallic Tanks for Cryogenic Service", 12th National Symposium, Society of Aerospace Materials and Process Engineers, Vol. 12, October 1967, Section AS-4. (Also NASA CR-72224.)
77. Morris, E. E., "The Performance of Glass-Filament-Wound Pressure Vessels with Metal Liners at Cryogenic Temperatures", Journal of Materials, Vol. 4, December 1969, pp. 970-1004.

78. Morris, E. E. and Alfring, R. J., "Cryogenic Boron-Filament-Wound Pressure Vessels", Composite Materials: Testing and Design, ASTM STP 460, American Society for Testing and Materials, 1969, pp. 430-443.
79. Morris, E. E. and Landes, R. E., "Cryogenic Glass-Filament-Wound Tank Evaluation", NASA CR-72948 (Final), National Aeronautics and Space Administration, NASA Lewis Research Center, Cleveland, Ohio, July 1971 (N72-14696).
80. Mowers, R. E., Leib, J. H. and Sherman, S., "Program of Testing Nonmetallic Materials at Cryogenic Temperatures", Rocketdyne Corporation Report R-3498, Rocket Propulsion Laboratories, Edwards, California, December 1962 (AD 294 772).
81. Nadler, M. A., Yoshino, S. Y. and Darms, F. J., "Boron/Epoxy Support Strut for Non-Integral Cryogenic Tankage", North American Rockwell Space Division Report SD 68-99501, February 25, 1969. (See also 15th National Symposium SAMPE April 1969 and North American Rockwell Report SD 995 2, 1968.)
82. Nelson, L. F., "Compressive Strength of Conolon 506 at +75°F and -320°F", Convair/Astronautics Report No. 27E 1336, January 1962.
83. Nelson, L. R., "Mechanical Properties of Adlock 851 at Room Temperature, 1000°, -320° and -423°F", Convair/Astronautics Report No. 55E 812, July 1961.
84. Nelson, P. T. and Archer, J. S., "Graphite Reinforced Plastic EHF Antenna", TRW Systems Group, Redondo Beach, California Report No. 99900-7128-RO-11, December 1969.
85. Patten, P. M., "Internal Insulation Liner Alteration", Douglas Aircraft Company Report No. SM 45975, August 1964.
86. Perkins-Elmer Optical Group, Norwalk, Connecticut, Work-In-Progress on Contract No. F33615-72-C-2033, Air Force Systems Command, Wright-Patterson Air Force Base, Ohio.
87. Pink, E. and Campbell, J. D., "The Effect of Strain Rate and Temperature on the Deformation Behavior of Reinforced and Unreinforced Epoxy Resin", Oxford University Department of Engineering Report No. 1040/72, Oxford, England, July 1972 (N73-10568).
88. Pirgon, O., Wostenholm, G. H. and Yates, B., "Thermal Expansion at Elevated Temperatures, IV. Carbon-Fibre Composites", Journal of Physics D: Applied Physics, Vol. 6, 1973, pp. 309-321.

89. Pride, R. A., Stein, B. A. and Schmidt, F. W., "Mechanical Properties of Polyimide-Resin/Glass-Fiber Laminates for Various Time, Temperature and Pressure Exposures", Technical Papers, 23rd Annual Reinforced Plastics Technical and Management Conference, Washington, DC, 1968, Section 17-c, pp. 1-8.
90. Ratcliffe, E. H., "Thermal Conductivities of Plastics with Glass, Asbestos and Cellulosic Fiber Reinforcements", Applied Material Research, Vol. 5, 1966, pp. 200-201.
91. Roseland, L. M., "Materials for Cryogenic Usage", Technical Papers, 21st Annual Technical Conference, Society of the Plastics Industry, 1966, Section 4-C, pp. 1-6.
92. Roseland, L. M., "Investigation of Structural Properties at Cryogenic Temperatures of Filament-Wound Pressure Vessels Containing Both Organic and Glass Filaments", Douglas Aircraft Corporation Report No. SM-48409, January 1966.
93. Ross, J. E., "Fiberglass Laminate- Ultimate Tensile and Flexural Strength Tests at Room Temperature, -100°F and 320°F", Convair Astronautics Report No. 7E 1687, June 1959 (AD 830 230).
94. Sanders, R. H. and Weleff, W., "Final Report on GTR-17 Effects of Radiation on Organic Materials Irradiated in Liquid Hydrogen", Aerojet-General Corporation Report No. RN-S-0327, March 1967.
95. Sanger, M. J., Molho, R. and Howard, W. W., "Exploratory Evaluation of Filament-Wound Composites for Tankage of Rocket Oxidizers and Fuels", AFML-TR-65-381, Air Force Materials Laboratory, Wright-Patterson Air Force Base, Ohio, January 1966 (AD 477 455).
96. Sanger, M. J. and Reinhart, T. J., "Development of Filament-Wound Tankage for Rocket Oxidizers and Fuels", Technical Papers, 12th National Symposium, Society of Aerospace Material and Process Engineers, 1967, Section AS-7.
97. Sewell, J. J. and Kuno, J. K., "Aerospace Use of Plastic Hardware and Thermal Insulation", Technical Papers, 17th Annual Technical Conference, Society of the Plastics Industry, 1962, Section 7-A, pp. 1-14.
98. Shriver, C. B., "Design and Fabrication of an Internally Insulated Filament Wound Liquid Hydrogen Propellant Tank", NASA CR-127, National Aeronautics and Space Administration, Washington, DC, November 1964 (N65-10775).



99. Soltysiak, D. J. and Toth, J. M., "Static Fatigue of Fiber Glass Pressure Vessels from Ambient to Cryogenic Temperatures", Technical Papers, 22nd Annual Technical Conference, Society of the Plastics Industry, 1967, Section 14-E, pp. 1-14.
100. Speare, J. C., "Preliminary Sizing of Filament-Wound RNS Tanks", Report No. TOR-0066 (5759-07)-13, Space and Missile Systems Organization, Air Force Systems Command, Los Angeles Air Force Station, Los Angeles, California, June 1970 (AD 872 626).
101. Steinhauer, R. A., "Linear Thermal Expansion of 828CL 181 Cloth Laminate", Douglas Aircraft Company Report No. MP 11,979, August 1961.
102. Stinnett, W. D., "Cryogenic Tensile Properties of Selected Materials", NASA CR-71751, AEC-NASA Space Nuclear Propulsion Office, Report No. 2712, January 1964 (N66-22816).
103. Suezawa, Y., Hojo, H. and Nakamura, K., "Impact Characteristics of Fiberglass Reinforced Plastics at Low Temperatures", Kagaku Kogaku (Chemical Engineering, Japan), Vol. 33, 1969, pp. 1051-1059.
104. Toth, J. M., "Barrier Films for Filament-Wound Fiberglass Cryogenic Vessels", Advances in Cryogenic Engineering, Vol. 1, 1964, pp. 537-544.
105. Toth, J. M. and Soltysiak, D. J., "Investigation of Smooth-Bonded Metal Liners for Glass Fiber Filament-Wound Pressure Vessels", NASA CR-72165 (Final), National Aeronautics and Space Administration, Lewis Research Center, Cleveland, Ohio, May 1967 (N67-25070).
106. Toth, J. M., Sherman, W. C. and Soltysiak, D. J., "Investigation of Smooth-Bonded Metal Liners for Glass Fiber Filament-Wound Pressure Vessels", Douglas Missile and Space Systems Division Report No. SM-49384, Quarterly Report No. 3, Contract No. NAS 3 6293, NASA Lewis Research Center, Cleveland, Ohio, April 1966.
107. Toth, J. M., Sherman, W. C. and Soltysiak, D. J., "Investigation of Structural Properties of Fiber-Glass Filament-Wound Pressure Vessels at Cryogenic Temperatures", NASA CR-54393, National Aeronautics and Space Administration, Lewis Research Center, Cleveland, Ohio, 1965 (N65-35392).
108. Toth, J. M. and Barber, J. R., "Structural Properties of Glass-Fiber Filament-Wound Cryogenic Pressure Vessels", Advances in Cryogenic Engineering, Vol. 10, 1965, pp. 134-144.

109. Voloshenko-Klimovitskii, Yu. Ya., Belyaev, Yu. A., L'vov, B. S. and Schpakovskaya, E. I., "Strength of Cold-Hardening GRPs Based on PN-1 Resin Under Impact Tension at Normal (20°C) and Low (-196°C) Temperatures", Plasticheski Massy, Vol. 6, 1964, pp. 39-40.
110. Voloshenko-Klimovitskii, Yu. Ya., Belyaev, Yu. A. and Korenkov, Yu. A., "Impact Tensile Tests on Glass-Fibre Reinforced Plastics at Normal and Low Temperatures", Plasticheski Massy, No. 5, 1963, pp. 51-54.
111. Watson, J. F., Christian, J. L. and Hertz, J., "Selection of Materials for Cryogenic Applications in Missiles and Aerospace Vehicles", Convair/Astronautics Report No. MRG 132-1, February, 1960.
112. Welleff, W., "Effect of Nuclear Radiation and Liquid Hydrogen on Mechanical Properties of Three Phenolic Materials", Advances in Cryogenic Engineering, Vol. 11, 1966, pp. 486-491.
113. Welleff, W., "Final Report, GTR-16 Radiation Effects Test on Structural Materials at -423°F", Aerojet-General Corporation Report No. RN-S-0290, November 1966.

#### IV - HANDBOOKS AND REVIEWS

114. Coston, R. M., "Handbook of Thermal Design Data for Multilayer Insulation Systems", LMSC-A847882, Vol. II (Final), George C. Marshall Space Flight Center, Huntsville, Alabama, June 1967 (N67-34910).
115. Hertz, J., "The Effect of Cryogenic Temperatures on the Mechanical Properties of Reinforced Plastic Laminates", Society of Plastics Engineers Journal, Vol. 21, February 1965, pp. 181-189.
116. Hertz, J. and Knowles, D., "Survey of Thermal Properties of Selected Materials", General Dynamics/Convair Report AAL-65-008 (AR-504-1-553), February 1965 (N65-31775).
117. Jurevic, W. G. and Rittenhouse, J. B., "Structural Applications Handbook", AFML TR-67-332, Air Force Materials Laboratory, Wright-Patterson Air Force Base, Ohio, August 1968 (AD 804 585).
118. Lackman, L. M., Arvin, G. H., et al., "Advanced Composite Design Guide, Third Edition, Volume IV: Materials", Air Force Materials Laboratory, Wright-Patterson Air Force Base, Ohio, January 1973.

119. Landrock, A. H., "Properties of Plastics and Related Materials at Cryogenic Temperatures", Plastec Report No. 20, Plastics Technical Evaluation Center, Picatinny Arsenal, Dover, New Jersey, July 1965 (AD 469 126).
120. Maximovich, M. and Scheck, W. G., "Data Summary and Reference File for Graphite and Boron Reinforced Composite Materials", General Dynamics/Convair Report No. GDCA-DBG71-006, 1971 (Contract NAS 8-26198, George C. Marshall Space Flight Center, Huntsville, Alabama).
121. Nored, D. L., Hennings, G., Sinclair, D. H., Smith, G. T., Smolak, G. R. and Stofan, A. J., "Storage and Handling of Cryogenic Fluids", NASA Special Publication SP-5053, Proceedings of Conference on Selected Technology for the Petroleum Industry, Lewis Research Center, Cleveland, Ohio, December 1965 (N66-33674).
122. "Plastics for Aerospace Vehicles, Part 1. Reinforced Plastics", MIL-HDBK-17A, Department of Defense, Washington, DC, January 1971.
123. Rittenhouse, J. B. and Singletary, J. B., "Space Materials Handbook", Third Edition, NASA Special Publication SP-3051, National Aeronautics and Space Administration, Washington, DC, 1969 (Limited publication as AFML-TR-68-205).
124. Schwartzberg, F. R., Hertzog, R. G., Osgood, S. H., et al., "Cryogenic Materials Data Handbook (Revised), Volume II", AFML-TDR-64-280-Vol. II (Revised), Air Force Materials Laboratory, Wright-Patterson Air Force Base, Ohio, July 1970 (AD 713 620).

#### V - MISCELLANEOUS REFERENCES

125. "Advanced Composites Design Guide", Third Edition, Volume IV, Materials, Air Force Materials Laboratory, Wright-Patterson Air Force Base, Ohio, January 1973.
126. Kreider, K. G. and Prew, K. M., "The Transverse Strength of Boron Fibers", Composite Materials, Testing and Design, ASTM STP 497, 1972, pp. 539-550.
127. Arp, V., Wilson, J. H., Windich, L. and Sikora, P., "Thermal Expansion of Some Engineering Materials from 20 to 293 K", Cryogenics, June 1962, p. 230.
128. Novak, R. C. and DeCrescente, M. D., "Impact Behavior of Unidirectional Resin Matrix Composites Tested in the Fiber Direction", Composite Materials, Testing-and-Design, ASTM STP 497, 1972, pp. 311-323.
129. Kastelic, J. R., Hiltner, A. and Baer, E., "Crazing, Yielding and Fracture in Polycarbonate and Polyethylene Terephthalate at Low Temperatures", Journal of Macro Molecular Science-Physics, B7(4), 1973, pp. 679-703.

Property	Glass Epoxy	Glass Polyester	Glass Phenolic	Glass Teflon	Glass Silicone	Glass Polyurethane	Glass Phenyl Siloxane	Glass Polysiloxane
o <sub>tu</sub>	1-1.3, 2-2.2, 3-3.5, 4, 5, 5.1, 22, 24, 28, 33, 35, 40, 43, 46, 47, 52, 54, 55, 57, 66, 71, 87	1-1.3, 2-2.2, 3-3.5, 4, 5, 5.1, 22, 24, 28, 33, 35, 40, 43, 46, 47, 52, 54, 55, 57, 66, 71, 87	1-1.3, 2-2.2, 3-3.5, 4, 5, 5.1, 22, 24, 28, 33, 35, 40, 43, 46, 47, 52, 54, 55, 57, 66, 71, 87	2-2.2, 37, 67, 68, 80, 94, 102, 113	1-1.3, 2-2.2, 24, 40, 57, 64, 66, 68, 97	2-2.2, 85	2-2.2, 57, 66	2-2.2
o <sub>1</sub>	1-1.3, 2-2.2, 3-3.5, 4, 5, 5.1, 22, 24, 28, 33, 35, 40, 43, 46, 47, 52, 54, 55, 57, 66, 71, 87	1-1.3, 2-2.2, 3-3.5, 4, 5, 5.1, 22, 24, 28, 33, 35, 40, 43, 46, 47, 52, 54, 55, 57, 66, 71, 87	1-1.3, 2-2.2, 3-3.5, 4, 5, 5.1, 22, 24, 28, 33, 35, 40, 43, 46, 47, 52, 54, 55, 57, 66, 71, 87	2-2.2, 80	1-1.3, 2-2.2, 24, 57	2-2.2	2-2.2, 57, 66	2-2.2, 24
o <sub>2</sub>	1-1.3, 2-2.2, 3-3.5, 4, 5, 5.1, 22, 24, 28, 33, 35, 40, 43, 46, 47, 52, 54, 55, 57, 66, 71, 87	1-1.3, 2-2.2, 3-3.5, 4, 5, 5.1, 22, 24, 28, 33, 35, 40, 43, 46, 47, 52, 54, 55, 57, 66, 71, 87	1-1.3, 2-2.2, 3-3.5, 4, 5, 5.1, 22, 24, 28, 33, 35, 40, 43, 46, 47, 52, 54, 55, 57, 66, 71, 87	2-2.2, 80	1-1.3, 2, 57	2	2, 57	2
o <sub>3</sub>	1-1.3, 2-2.2, 3-3.5, 4, 5, 5.1, 22, 24, 28, 33, 35, 40, 43, 46, 47, 52, 54, 55, 57, 66, 71, 87	1-1.3, 2-2.2, 3-3.5, 4, 5, 5.1, 22, 24, 28, 33, 35, 40, 43, 46, 47, 52, 54, 55, 57, 66, 71, 87	1-1.3, 2-2.2, 3-3.5, 4, 5, 5.1, 22, 24, 28, 33, 35, 40, 43, 46, 47, 52, 54, 55, 57, 66, 71, 87	30, 89, 102	64	85		
o <sub>4</sub>	1-1.3, 2-2.2, 3-3.5, 4, 5, 5.1, 22, 24, 28, 33, 35, 40, 43, 46, 47, 52, 54, 55, 57, 66, 71, 87	1-1.3, 2-2.2, 3-3.5, 4, 5, 5.1, 22, 24, 28, 33, 35, 40, 43, 46, 47, 52, 54, 55, 57, 66, 71, 87	1-1.3, 2-2.2, 3-3.5, 4, 5, 5.1, 22, 24, 28, 33, 35, 40, 43, 46, 47, 52, 54, 55, 57, 66, 71, 87	2-2.2, 80	1-1.3, 2-2.2, 40, 57, 97	2-2.2	2-2.2	2-2.2
o <sub>5</sub>	1-1.3, 2-2.2, 3-3.5, 4, 5, 5.1, 22, 24, 28, 33, 35, 40, 43, 46, 47, 52, 54, 55, 57, 66, 71, 87	1-1.3, 2-2.2, 3-3.5, 4, 5, 5.1, 22, 24, 28, 33, 35, 40, 43, 46, 47, 52, 54, 55, 57, 66, 71, 87	1-1.3, 2-2.2, 3-3.5, 4, 5, 5.1, 22, 24, 28, 33, 35, 40, 43, 46, 47, 52, 54, 55, 57, 66, 71, 87	2-2.2, 80	1-1.3, 2-2.2, 57	2-2.2	2-2.2	2-2.2
o <sub>6</sub>	1-1.3, 2-2.2, 3-3.5, 4, 5, 5.1, 22, 24, 28, 33, 35, 40, 43, 46, 47, 52, 54, 55, 57, 66, 71, 87	1-1.3, 2-2.2, 3-3.5, 4, 5, 5.1, 22, 24, 28, 33, 35, 40, 43, 46, 47, 52, 54, 55, 57, 66, 71, 87	1-1.3, 2-2.2, 3-3.5, 4, 5, 5.1, 22, 24, 28, 33, 35, 40, 43, 46, 47, 52, 54, 55, 57, 66, 71, 87	2-2.2, 80	1-1.3, 2	2	2	2-2.2, 24
o <sub>7</sub>	1-1.3, 2-2.2, 3-3.5, 4, 5, 5.1, 22, 24, 28, 33, 35, 40, 43, 46, 47, 52, 54, 55, 57, 66, 71, 87	1-1.3, 2-2.2, 3-3.5, 4, 5, 5.1, 22, 24, 28, 33, 35, 40, 43, 46, 47, 52, 54, 55, 57, 66, 71, 87	1-1.3, 2-2.2, 3-3.5, 4, 5, 5.1, 22, 24, 28, 33, 35, 40, 43, 46, 47, 52, 54, 55, 57, 66, 71, 87	2-2.2, 80	1-1.3, 2-2.2, 24, 57	2-2.2	2-2.2, 57	2-2.2, 24
o <sub>8</sub>	1-1.3, 2-2.2, 3-3.5, 4, 5, 5.1, 22, 24, 28, 33, 35, 40, 43, 46, 47, 52, 54, 55, 57, 66, 71, 87	1-1.3, 2-2.2, 3-3.5, 4, 5, 5.1, 22, 24, 28, 33, 35, 40, 43, 46, 47, 52, 54, 55, 57, 66, 71, 87	1-1.3, 2-2.2, 3-3.5, 4, 5, 5.1, 22, 24, 28, 33, 35, 40, 43, 46, 47, 52, 54, 55, 57, 66, 71, 87	2-2.2, 80	1-1.3, 2-2.2, 57	2-2.2	2-2.2	2-2.2
o <sub>9</sub>	1-1.3, 2-2.2, 3-3.5, 4, 5, 5.1, 22, 24, 28, 33, 35, 40, 43, 46, 47, 52, 54, 55, 57, 66, 71, 87	1-1.3, 2-2.2, 3-3.5, 4, 5, 5.1, 22, 24, 28, 33, 35, 40, 43, 46, 47, 52, 54, 55, 57, 66, 71, 87	1-1.3, 2-2.2, 3-3.5, 4, 5, 5.1, 22, 24, 28, 33, 35, 40, 43, 46, 47, 52, 54, 55, 57, 66, 71, 87	2-2.2, 80	1-1.3, 2	2	2	2-2.2
o <sub>10</sub>	1-1.3, 2-2.2, 3-3.5, 4, 5, 5.1, 22, 24, 28, 33, 35, 40, 43, 46, 47, 52, 54, 55, 57, 66, 71, 87	1-1.3, 2-2.2, 3-3.5, 4, 5, 5.1, 22, 24, 28, 33, 35						

- Includes Fractur. Vouchers

polybenzimidazole

**Reproduced from  
best available copy.**



BIBLIOGRAPHY-PROPERTY CROSS REFERENCE (Cont'd)

Property	Graphite-Epoxy	Boron-Epoxy	Boron-Aluminum	PRD-49 Epoxy
$\sigma_{tu}$	d, 9, 10, 10.2, 13, 20, 22, 13, 13.2, 3, 47, 53, 58, 47, 51, 58	13, 20, 22, 47, 53, 58, 81	13, 13.3	29, 44, 59, 60
$E^t$	8, 9, 10, 10.1, 13, 51	13, 81	13, 13.3	44, 59, 60
$E^c$	13	20	13	
$\sigma_{tu}$	d, 10, 10.1, 11, 12, 13, 13.2, 58	58		
$E^t$	d, 10.1			
$E^c$	13	13, 81	13, 13.3	
$E^c$	13		13, 13.3	
$\sigma_{si}$	8, 9, 10, 10.1, 10.2, 12, 13, 13.2, 47, 58	13, 22, 47, 58, 81	13, 13.3	59, 60
$\eta^t$	45	20		
$\sigma_{py}$			13, 13.3	
$\sigma_{I^0}$	9, 10.2	81		
$\lambda$	13, 17, 18, 38	13, 38, 63, 81		
L/L	10, 13, 13.2, 17, 18, 38, 51, 52, 84, 88	13	13, 13.3	59, 60
$C_p$	13	13	13, 13.3	

<sup>a</sup>Includes fracture toughness

MISCELLANEOUS PROPERTIES

Notch Tensile Strength Glass-Epoxy (3-3.2, 3.4, 3.5, 43, 46)  
 Vapor Permeability Glass-Epoxy (28)  
 Modulus of Rigidity Glass-Epoxy (53), Glass-Teflon (50), Boron-Epoxy (53)  
 Poisons Ratio Glass-Epoxy (53), Boron-Epoxy (53)  
 Proportional Limit in Tension Glass-Epoxy (55, 56), Glass-Polyester (1-1.3, 55, 56)  
 Static Fatigue Glass-Epoxy (66, 99), PRD 49-Epoxy (44)  
 Environmental Effects Glass-Epoxy (4-4.1), Graphite-Epoxy (13, 13.2, 17, 58)  
 Boron-Epoxy (13, 58), Boron-Aluminum (13, 36), PRD 49-Epoxy (44)  
 Electrical Resistivity Graphite-Epoxy (13), Boron-Epoxy (13)  
 Thermo-Optical Effects Graphite-Epoxy (13, 36), Boron-Epoxy (13)  
 Density Glass-Epoxy, Polyester, Phenolic, Silicone, Phenyl Silane (14, 57),  
 Glass-Teflon (14), Glass-Polybenzimidazole (16), Graphite-Epoxy (9, 13),  
 Graphite-Phenolic (14), Graphite-polyimide (14.1)  
 Radiation Effects (14.2, 33, 37, 44, 53, 64, 65, 75, 76, 77, 110, 113)  
 Thermal Conductivity (57)

MISCELLANEOUS COMPOSITES

Glass-Polyimide  $\sigma_{tu}$ (24, 67, 68),  $\sigma_{tu}$ (89),  $\sigma_{si}$ (12.1, 89)  
 AL/L(67)  
 Glass-Melamine  $\sigma_{tu}$ (65),  $E^t$ (65),  $\lambda$ (90)  
 Glass-Viton  $\sigma_{tu}$ (68)  
 Glass-Phenyl Formaldehyde  $\sigma_{I^0}$ (110),  $\lambda$ (72),  $C_p$ (72)  
 SiO<sub>2</sub>-Epoxy  $\sigma_{tu}$ (31), AL/L(28)  
 Graphite-Aluminum  $\sigma_{tu}$ (thermal cycling effects 6-6.2)  
 Graphite-Polyimide  $\sigma_{tu}$ (13),  $\sigma_{tu}$ (11, 12.1, 13),  $\sigma_{si}$ (13),  
 AL/L(36)  
 Graphite-Phenolic  $\lambda$ (14, 16-16.3), AL/L(14, 16-16.3)  
 Steel-Aluminum  $\sigma_{tu}$ (7, 7.1),  $E^t$ (7.1),  $\sigma_{I^0}$ (7, 7.1)  
 Steel-Epoxy  $\sigma_{tu}$ (2, 30),  $E^t$ (2, 30),  $\sigma_{tu}$ (2),  $E^t$ (2),  $\sigma_{tu}$ (2),  
 $E^c$ (2),  $\sigma_{tu}$ (2)  
 Boron/Steel-Aluminum  $\sigma_{tu}$ ,  $E^t$ ,  $\sigma_{tu}$ ,  $E^c$ ,  $\sigma_{tu}$ , AL/L,  $C_p$ ,  
 Boron/Titanium-Aluminum {13, 13.3},  $\sigma_{si}$ ,  $E^t$ ,  $\sigma_{tu}$ (13)  
 Potassium Titanoate-Epoxy  $\lambda$ (16),  $C_p$ (16)

PRESSURE VESSEL APPLICATIONS

Glass-Filament  
 (19, 20, 39, 42, 46-48, 53, 67, 69, 76, 77,  
 91, 92, 95, 96, 98-100, 104-108, 113)  
 Graphite-Filament  
 (5, 10, 10.1, 45, 47, 100)  
 Boron-Filament  
 (20, 47, 53, 76)  
 PRD 49-Filament  
 (59, 60)

TABLE 1  
TYPICAL COMPOSITE DENSITIES

<u>Composite System</u>	<u>Fiber/Resin Ratio</u>	<u>Density, lb in<sup>-3</sup> (kg m<sup>-3</sup> x 10<sup>-4</sup>)</u>
s-glass/epoxy	60-67	0.068-0.074 (1.87-2.04)
Kevlar 49/epoxy	60-65	0.047-0.050 (1.3-1.38)
boron/epoxy	55	0.070-0.074 (1.93-2.04)
graphite/epoxy	55-60	0.050-0.055 (1.38-1.52)
boron/aluminum (4 mil)	50	0.10 (2.62)

TABLE 2  
COMPARISON OF RANKING OF SPECIFIC UNIAXIAL GRAPHITE/EPOXY COMPOSITES  
BY LONGITUDINAL FLEXURE STRENGTH AND BY  
LONGITUDINAL TENSILE STRENGTH (77 K)

<u>Composite Type</u>	<u><math>\sigma^{fu}</math>, KSI</u>	<u>Rank</u>	<u><math>\sigma^{tu}</math>, KSI</u>	<u>Rank</u>
HT-S/X-904	178	1	147	1
HT-S/E-350	172	2	87	6
HT-S/X-915	167	3	103	2
HT-S/Ciba 8183	146	4	45	8
GY-70/X-904	117	5	92	4
Thornel 50/Resin 2	58	6	91	5
HMG-25/Resin 2	55	7	71	7
Thornel 50/ERL 2256	54	8	93	3

# LIST OF FIGURES

	Page
Figure 1 Ultimate Tensile Strength, $\sigma^{tu}$ , of Graphite/Epoxy Composites . .	199
Figure 2 Ultimate Tensile Strength, $\sigma^{tu}$ , of Miscellaneous Advanced Composites . . . . .	200
Figure 3 Initial Tensile Modulus, $E_1^t$ , of Graphite/Epoxy Composites . . .	201
Figure 4 Initial Tensile Modulus, $E_1^t$ , of Miscellaneous Advanced Composites . . . . .	202
Figure 5 Ultimate Flexural Strength, $\sigma^{fu}$ , of Graphite/Epoxy Composites. .	203
Figure 6 Ultimate Flexural Strength, $\sigma^{tu}$ , of Miscellaneous Advanced Composites . . . . .	204
Figure 7 Flexural Modulus, $E_f$ , of Advanced Composites . . . . .	204
Figure 8 Ultimate Compressive Strength, $\sigma^{cu}$ , of Advanced Composites . . .	205
Figure 9 Compressive Modulus, $E_c$ , of Advanced Composites . . . . .	206
Figure 10 Histograms Illustrating the Reported Range; of Longitudinal Interlaminar Shear Strength, $\sigma^{sl}$ , as reported for HT-S/X-904 Graphite/Epoxy at 77 K (a) and the Reported Changes in Interlaminar Shear Strength in the Same Composite Upon Cooling From 295 K to 77 K . . . . .	207
Figure 11 Interlaminar Shear Strength, $\sigma^{sl}$ , of Graphite/Epoxy Composites Data Reflect Highest Values Reported (See Text for Details). Flat Short-beam Test Data except as noted . . . . .	208
Figure 12 Interlaminar Shear Strength, $\sigma^{sl}$ , of Miscellaneous Advanced Composites. Flat Short-beam Test Data Except Where Noted . . . .	209
Figure 13 Ultimate Tensile Strain, $\epsilon^{tu}$ , of Advanced Composites . . . . .	210
Figure 14 Ultimate Compressive Strain, $\epsilon^{cu}$ , of Graphite/Epoxy Composites. .	211
Figure 15 Ultimate Bearing Strength, $\sigma^{bu}$ , of Boron/Aluminum Composites, Uniaxial Longitudinal Direction . . . . .	212
Figure 16 Longitudinal Thermal Expansion, $\Delta L/L$ , of Uniaxial Advanced Composites . . . . .	213
Figure 17 Transverse Thermal Expansion, $\Delta L/L$ , of Uniaxial Advanced Composites . . . . .	214
Figure 18 Thermal Conductivities, $\lambda$ , of Advanced Composites . . . . .	215
Figure 19 Specific Heat, $C_p$ , of Advanced Composites . . . . .	216

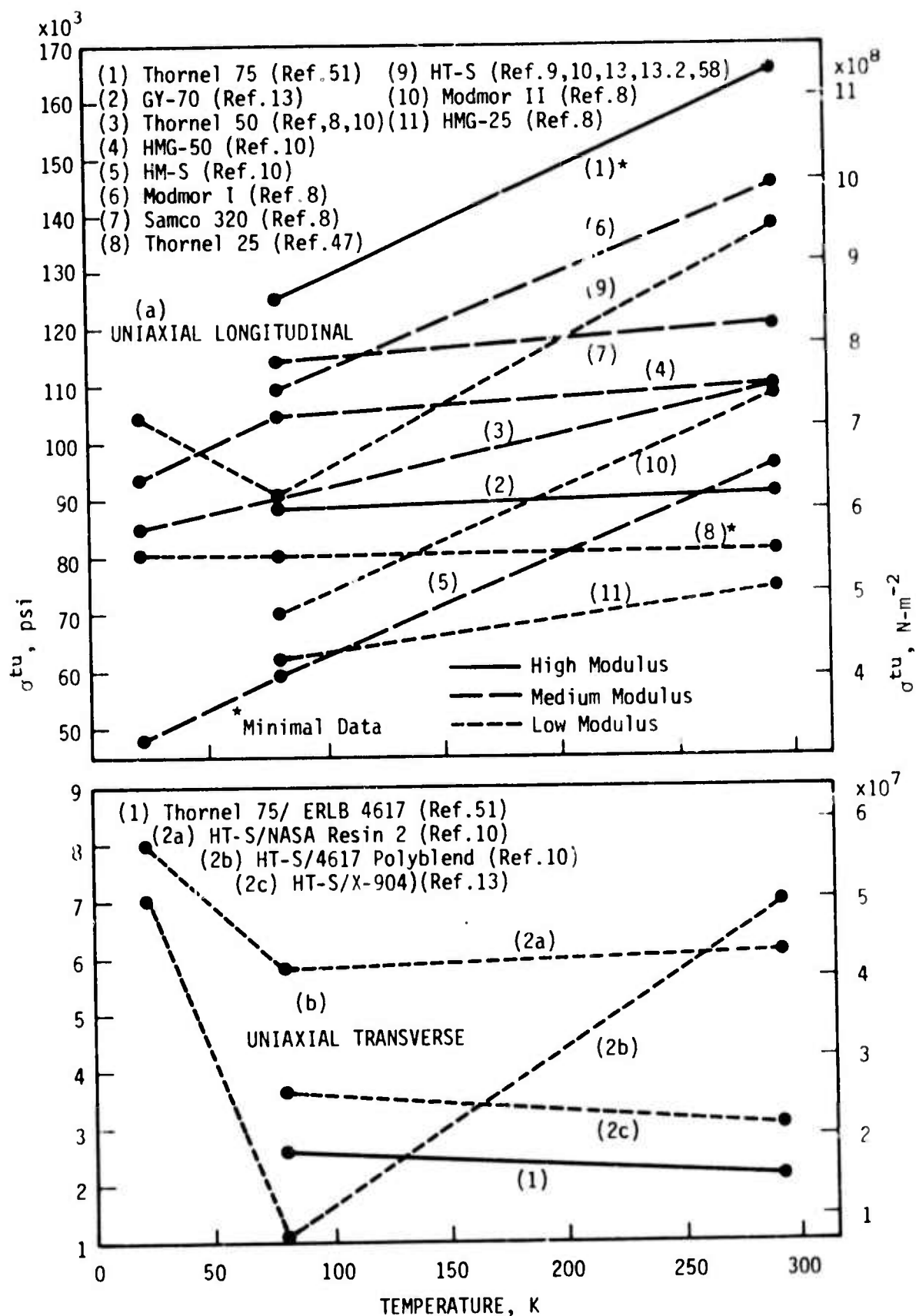


FIGURE 1 - Ultimate Tensile Strength,  $\sigma^{tu}$ , of Graphite-Epoxy Composites.



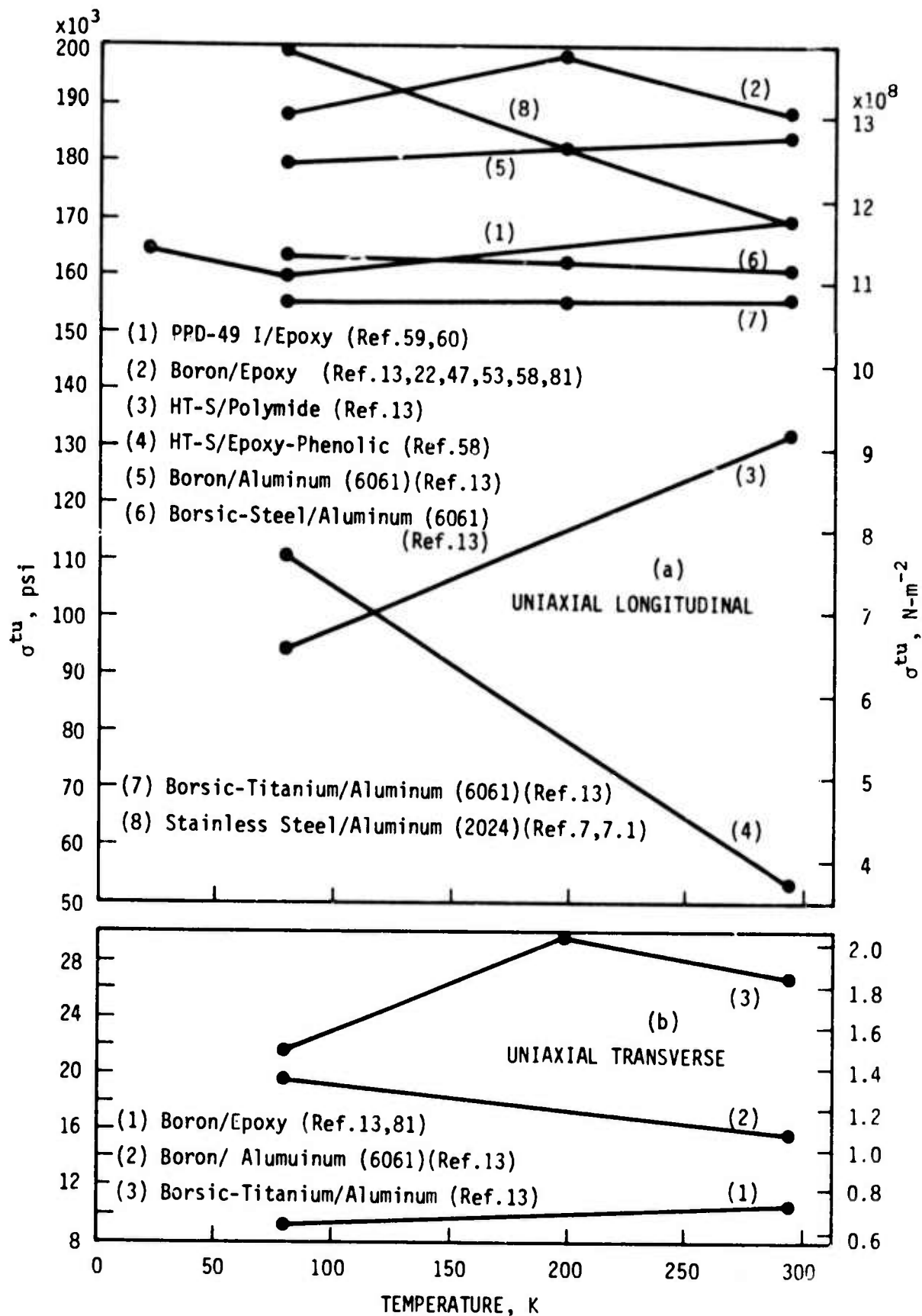


FIGURE 2 - Ultimate Tensile Strength,  $\sigma^{tu}$ , of Miscellaneous Advanced Composites.

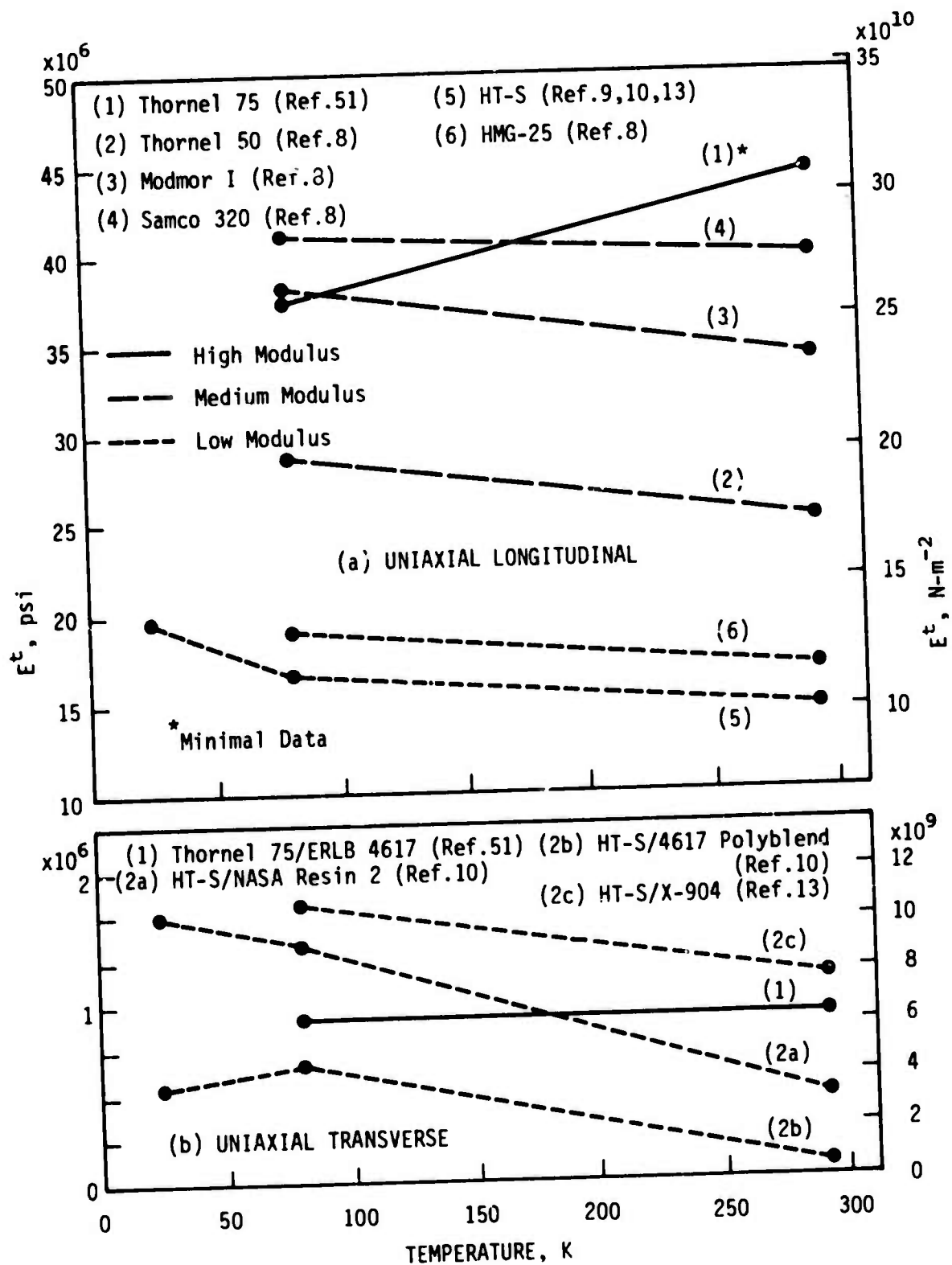


FIGURE 3 - Initial Tensile Modulus,  $E_1^t$ , of Graphite-Epoxy Composites.

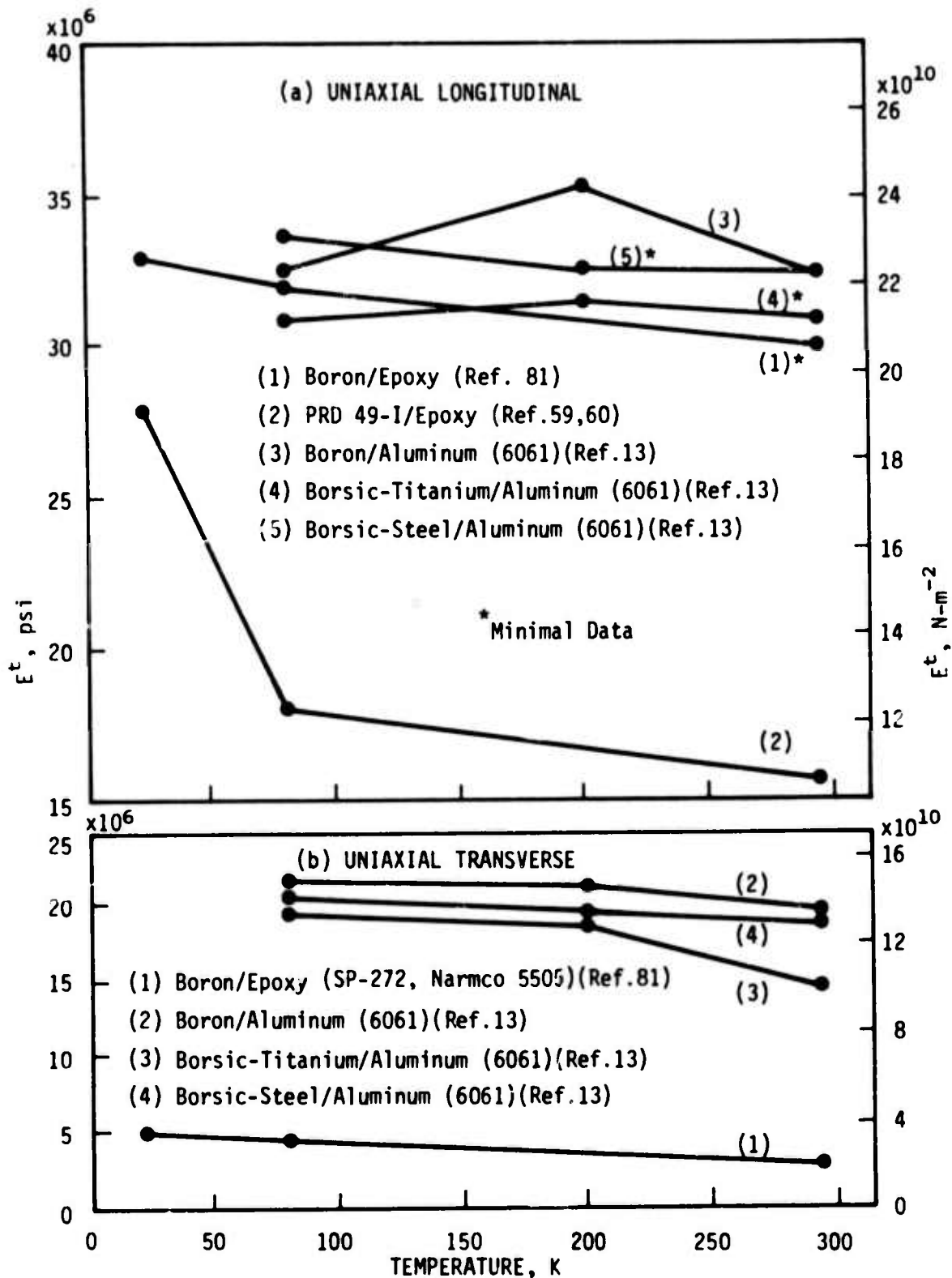


FIGURE 4 - Initial Tensile Modulus,  $E_1^t$ , of Miscellaneous Advanced Composites.

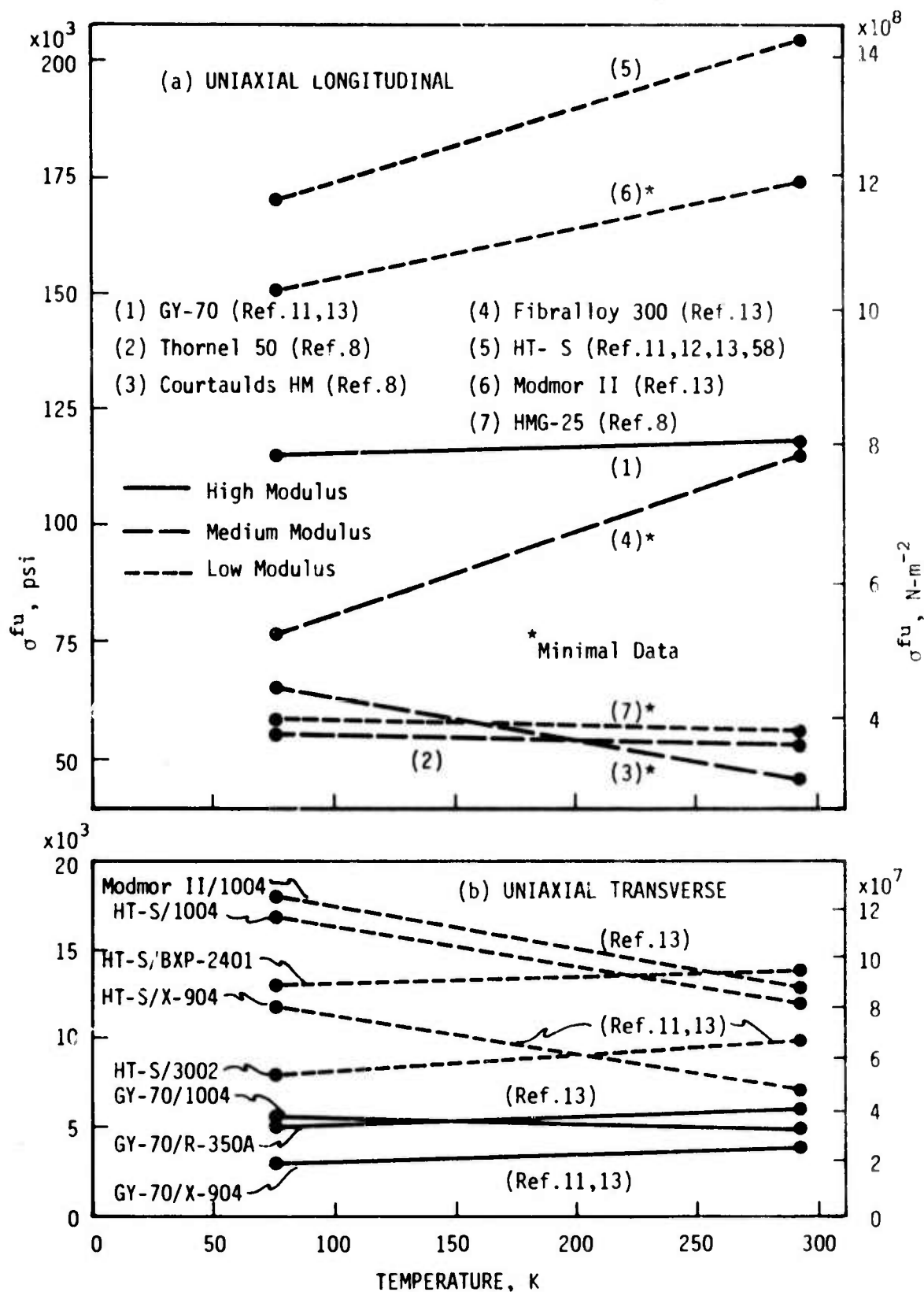


FIGURE 5 - Ultimate Flexural Strength,  $\sigma^{fu}$ , of Graphite/Epoxy Composites.

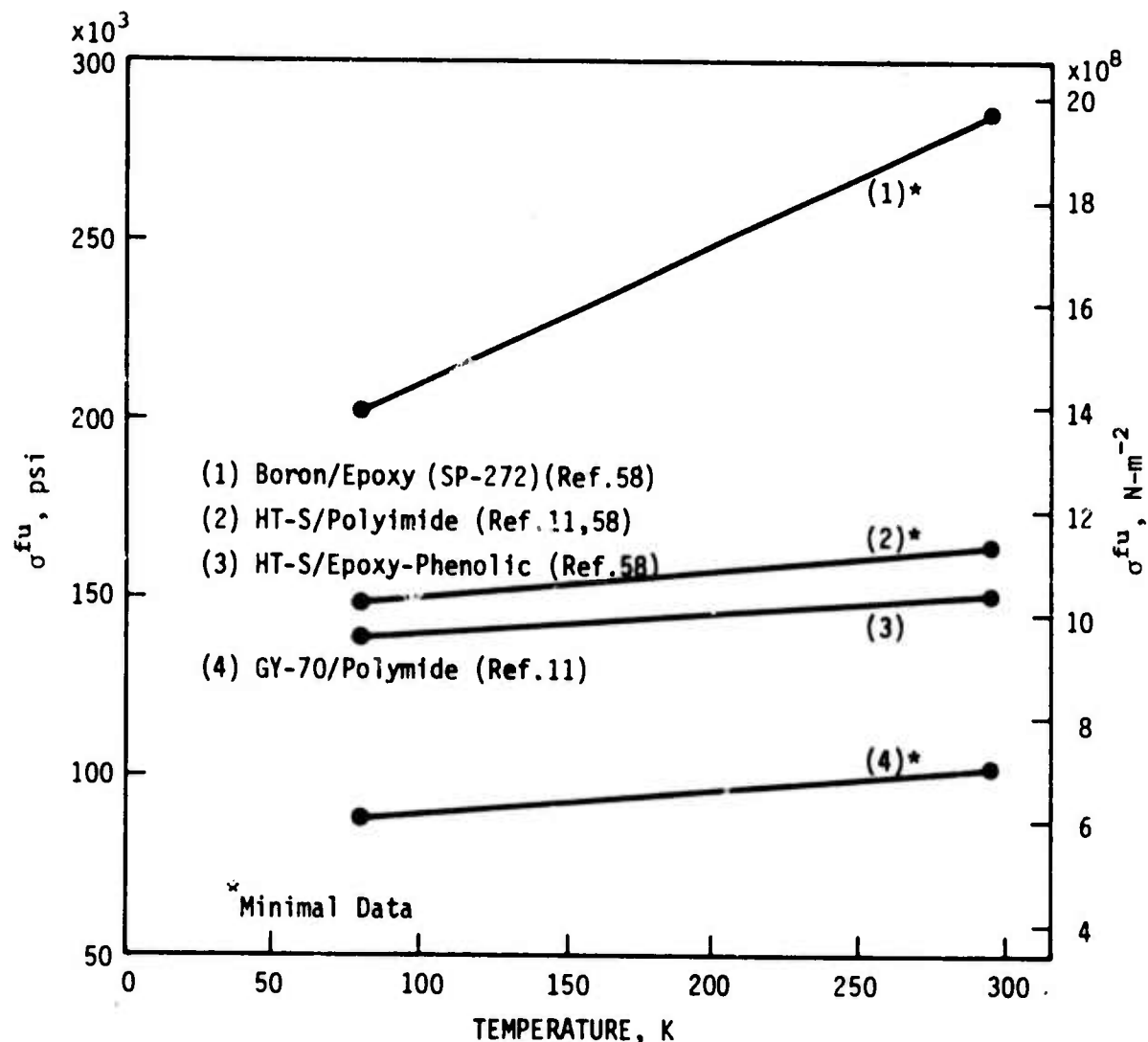


FIGURE 6 - Ultimate Flexural Strength,  $\sigma^{fu}$ , of Miscellaneous Advanced Composites.

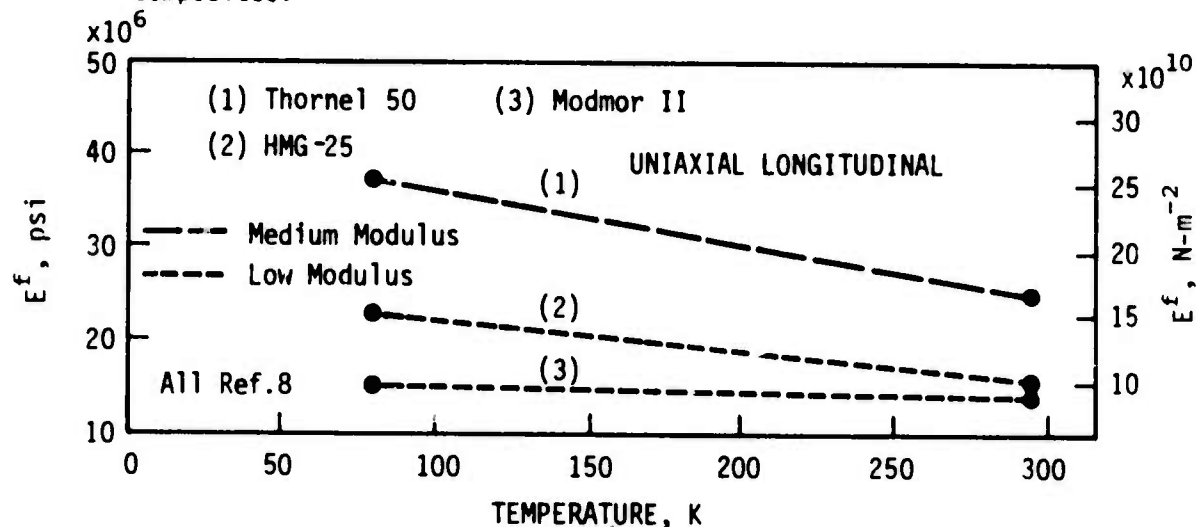


FIGURE 7 - Flexural Modulus,  $E^f$ , of Advanced Composites.

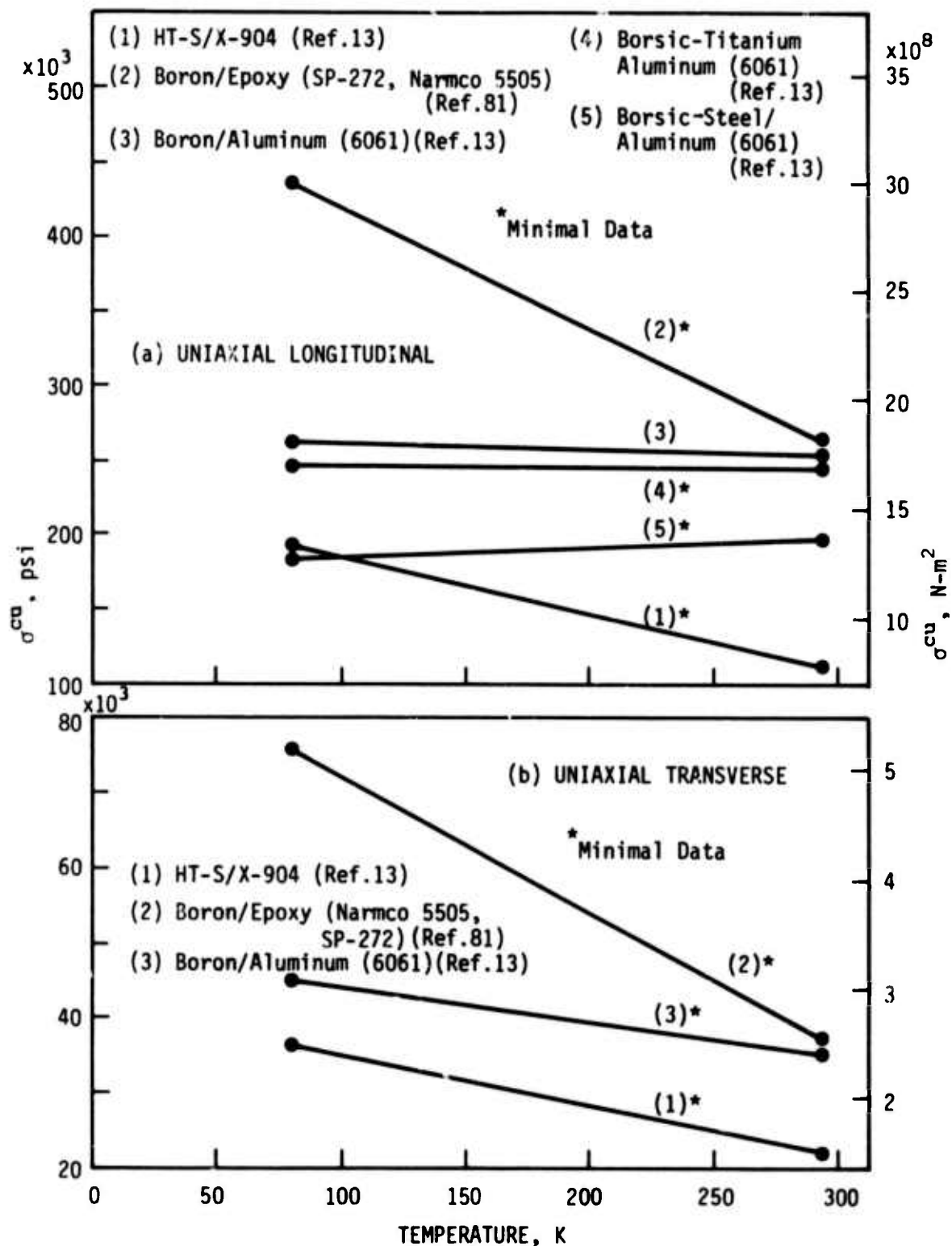


FIGURE 8 - Ultimate Compressive Strength,  $\sigma^{cu}$ , of Advanced Composites.

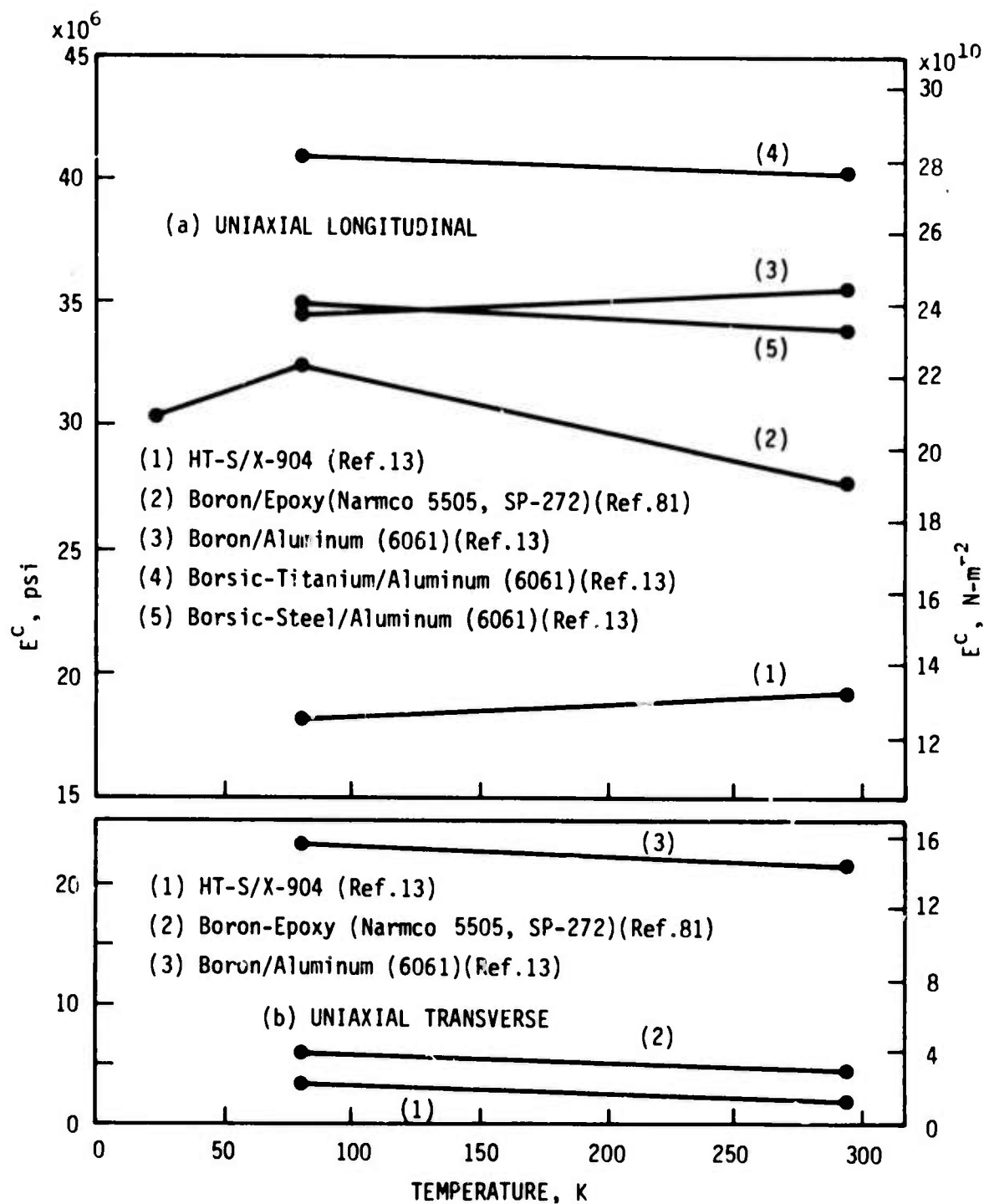


FIGURE 9 - Compressive Modulus,  $E^C$ , of Advanced Composites.

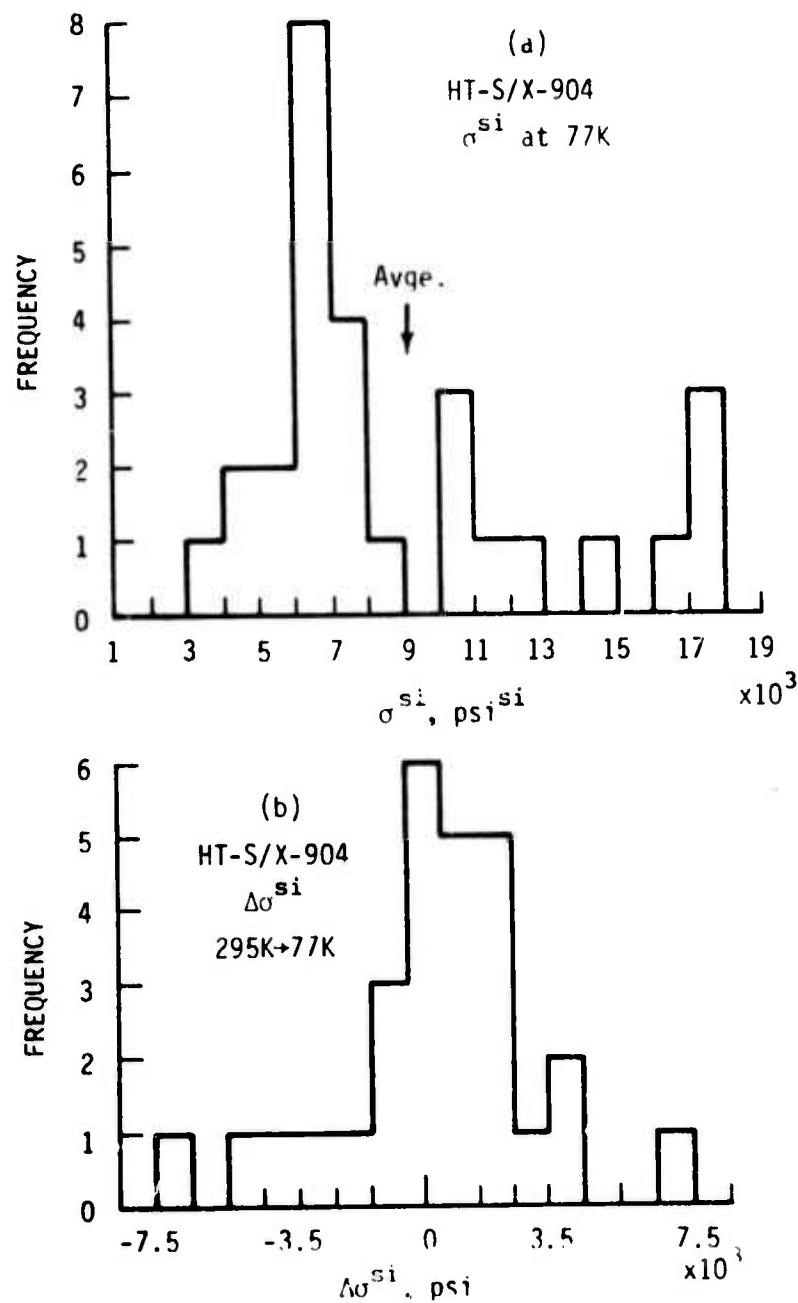


FIGURE 10 - Histograms illustrating the range of longitudinal interlaminar shear strength,  $\sigma^{si}$ , as reported for HT-S/X-904 Graphite-Epoxy at 77K (a) and the reported changes in interlaminar shear strength in the same composite upon cooling from 295K to 77K (b).



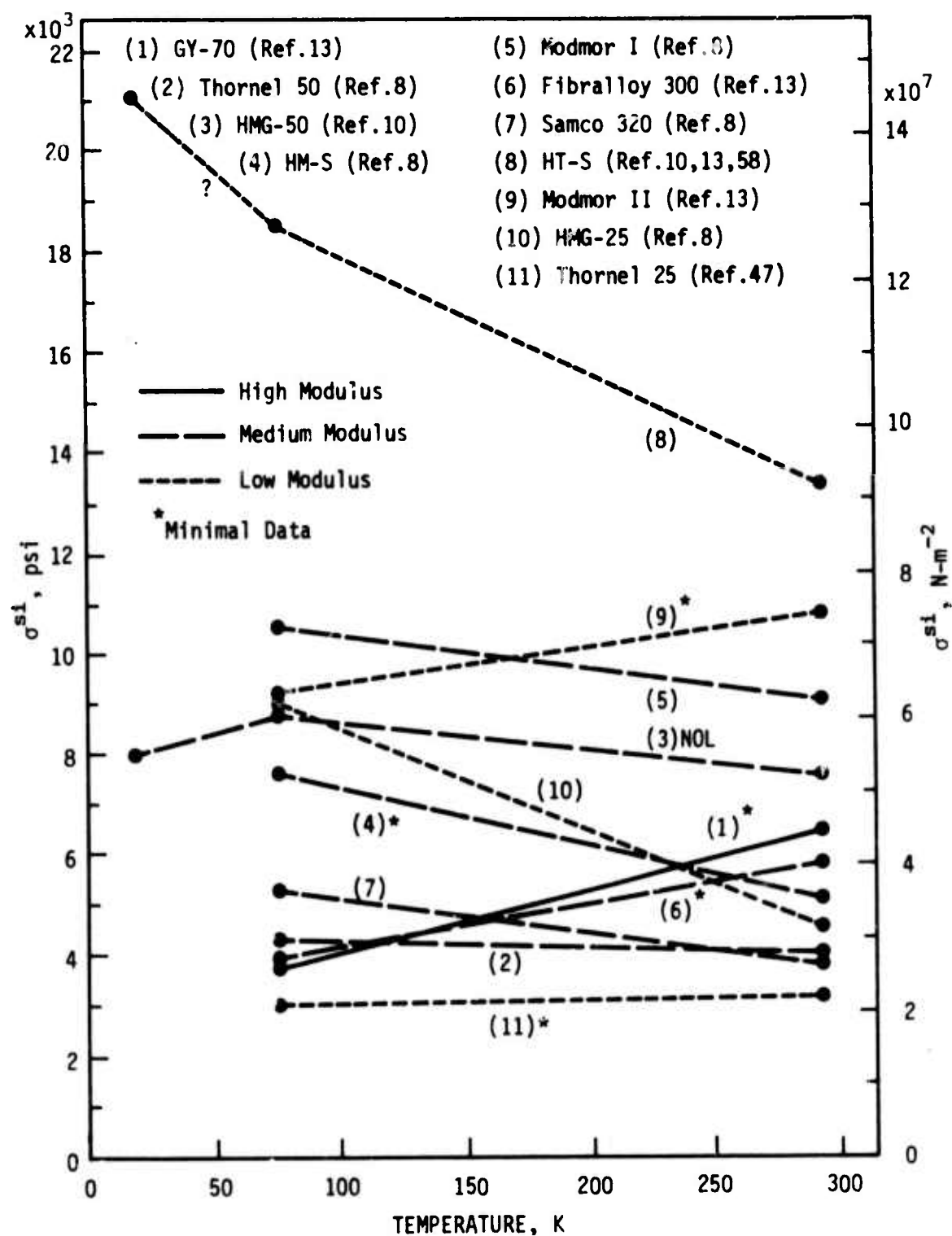


FIGURE 11 - Interlaminar Shear Strength,  $\sigma^{sl}$ , Graphite-Epoxy Composites. Data Reflects Highest Values Reported (See text for details). Flat Short-beam Test Data except as noted.

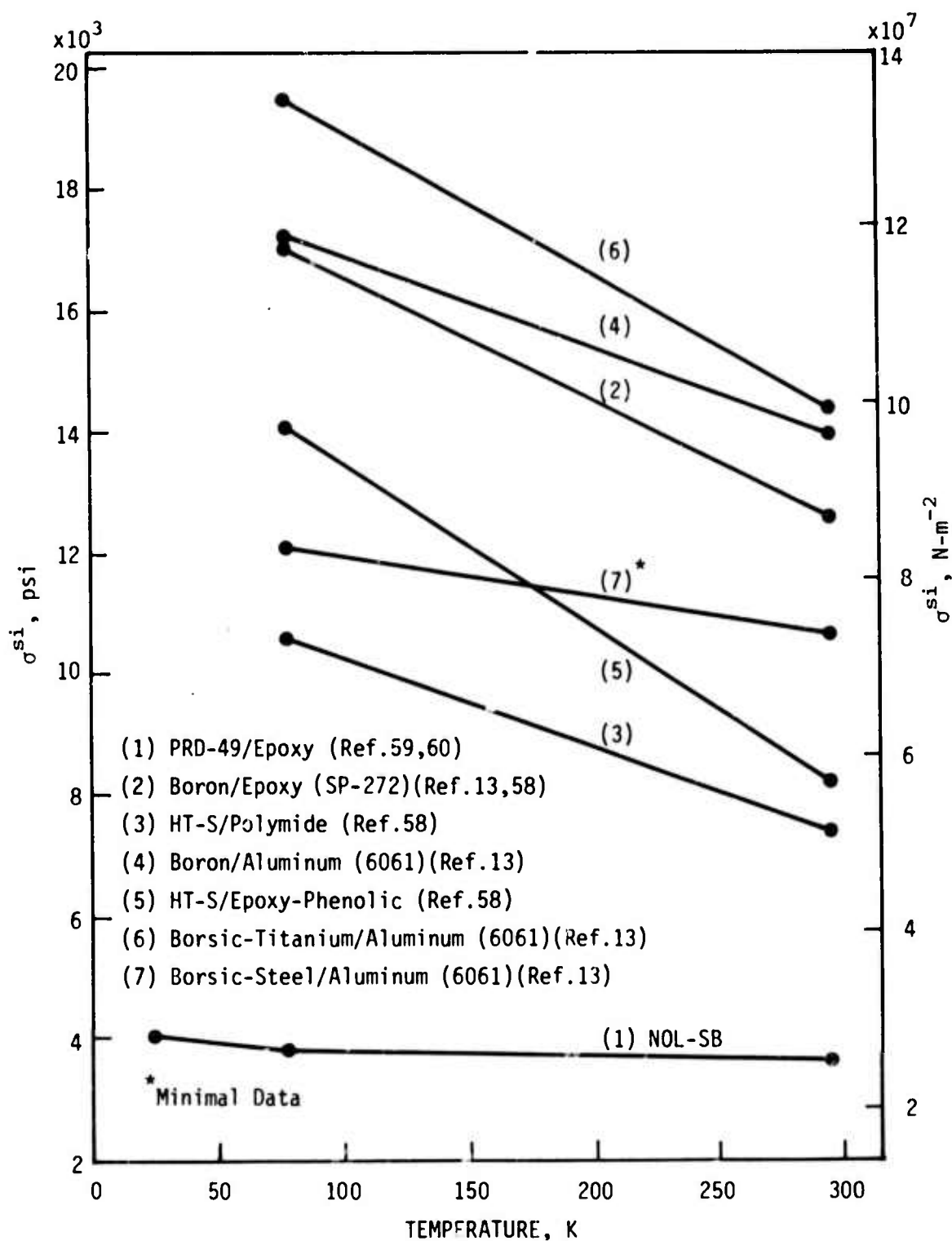


FIGURE 12 - Interlaminar Shear Strength,  $\sigma^{si}$ , of Miscellaneous Advanced Composites. Flat Short-beam Test Data except where noted.

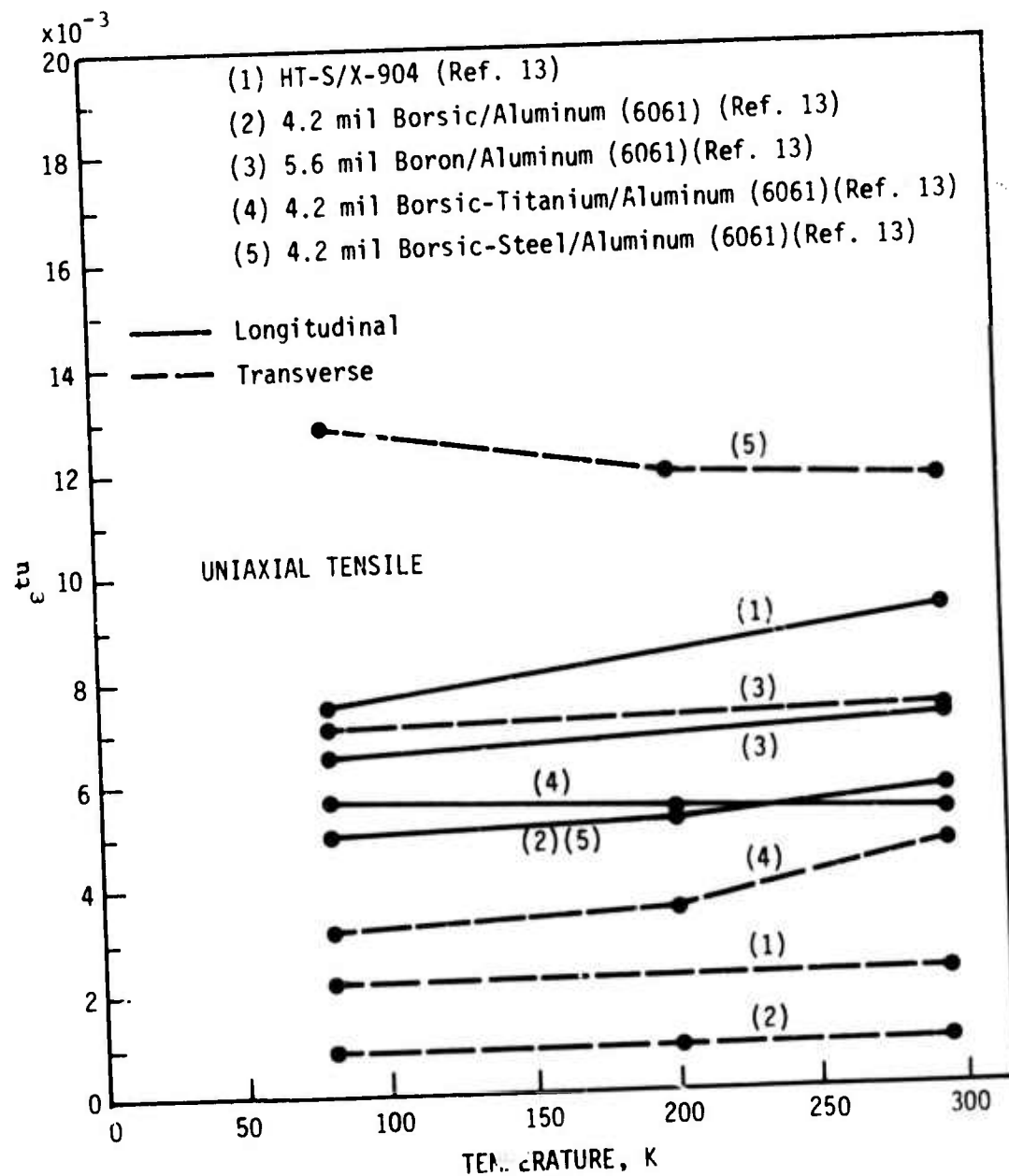


FIGURE 13 - Ultimate Tensile Strain,  $\epsilon^{tu}$ , of Advanced Composites

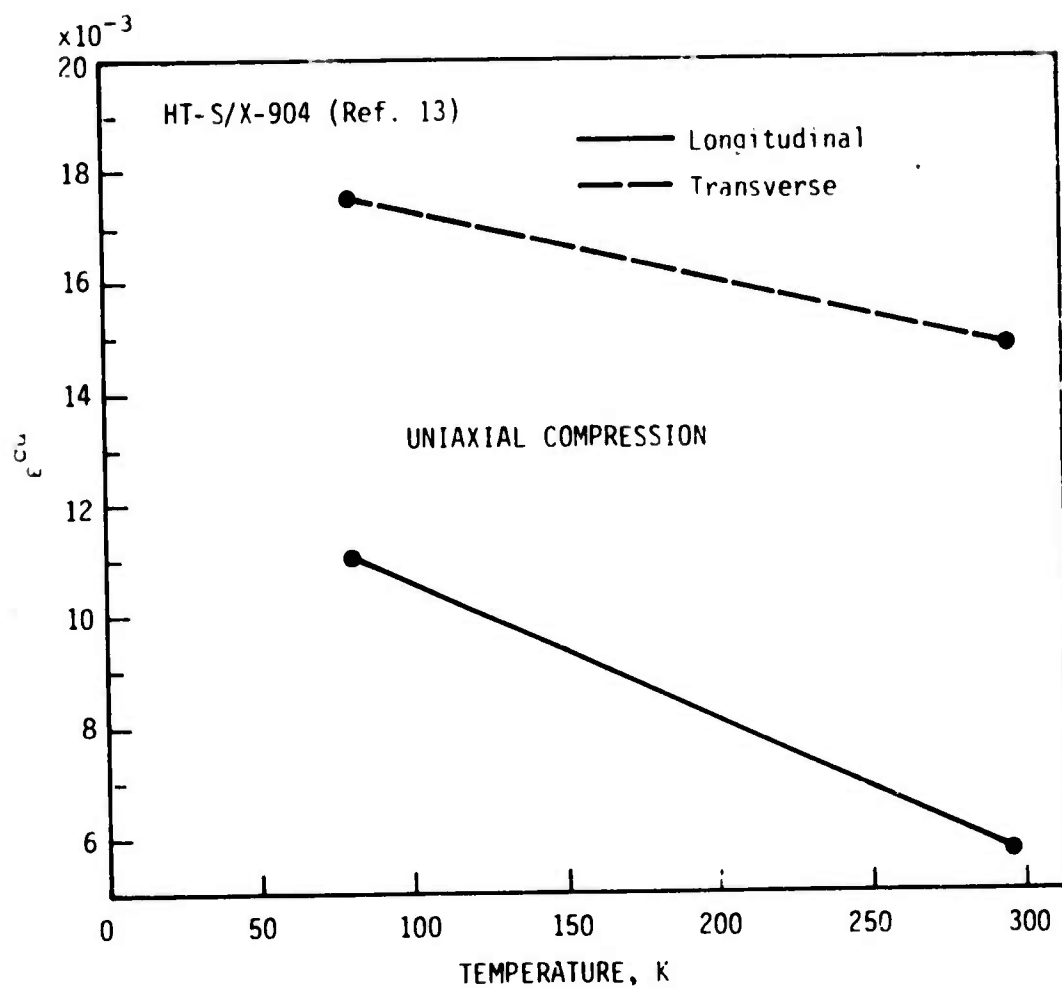


FIGURE 14 - Ultimate Compressive Strain,  $\epsilon^{cu}$ , Graphite/Epoxy Composites.

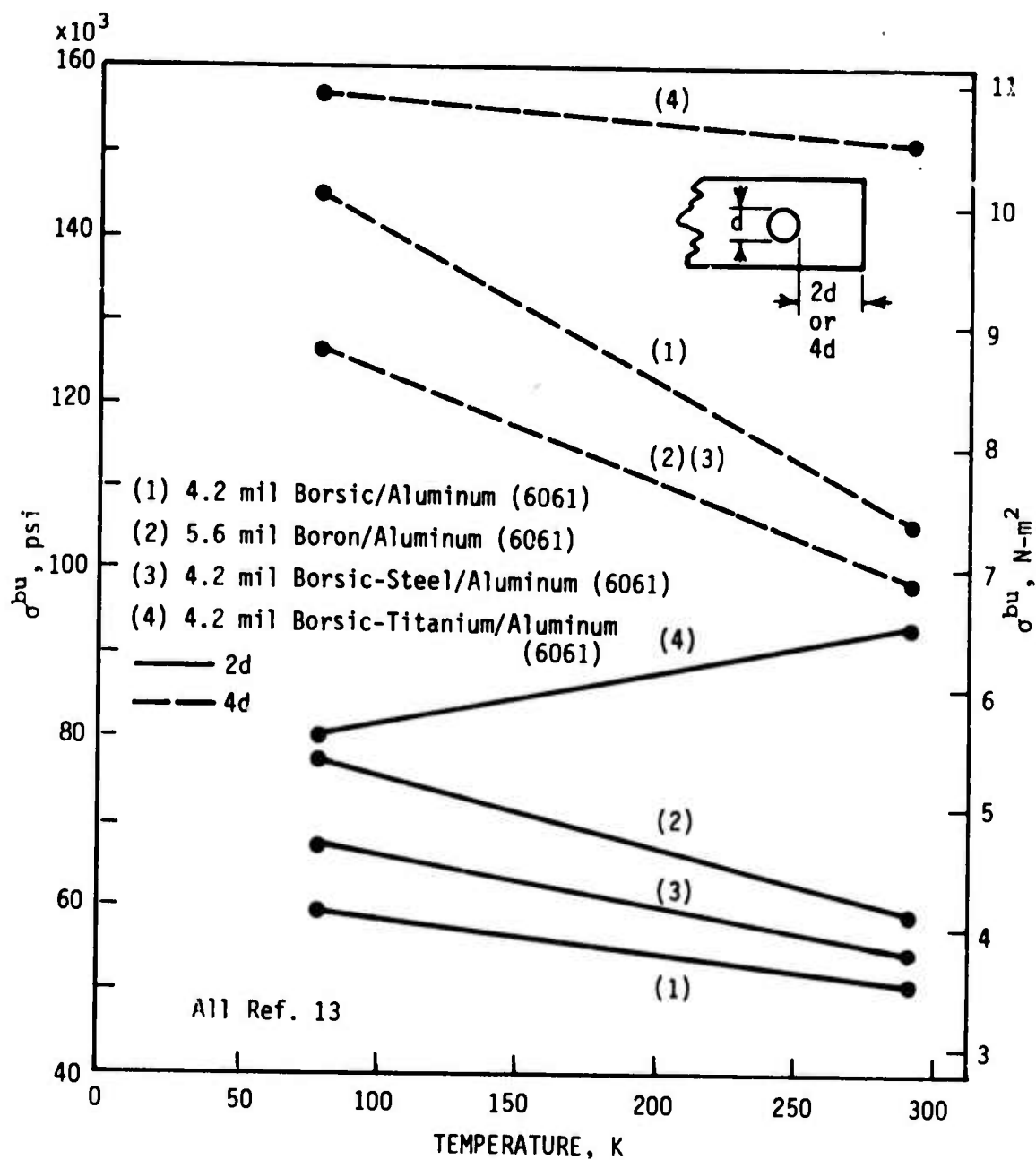


FIGURE 15 - Ultimate Bearing Strength,  $\sigma^{bu}$ , of Boron/Aluminum Composites, Uniaxial Longitudinal Direction.

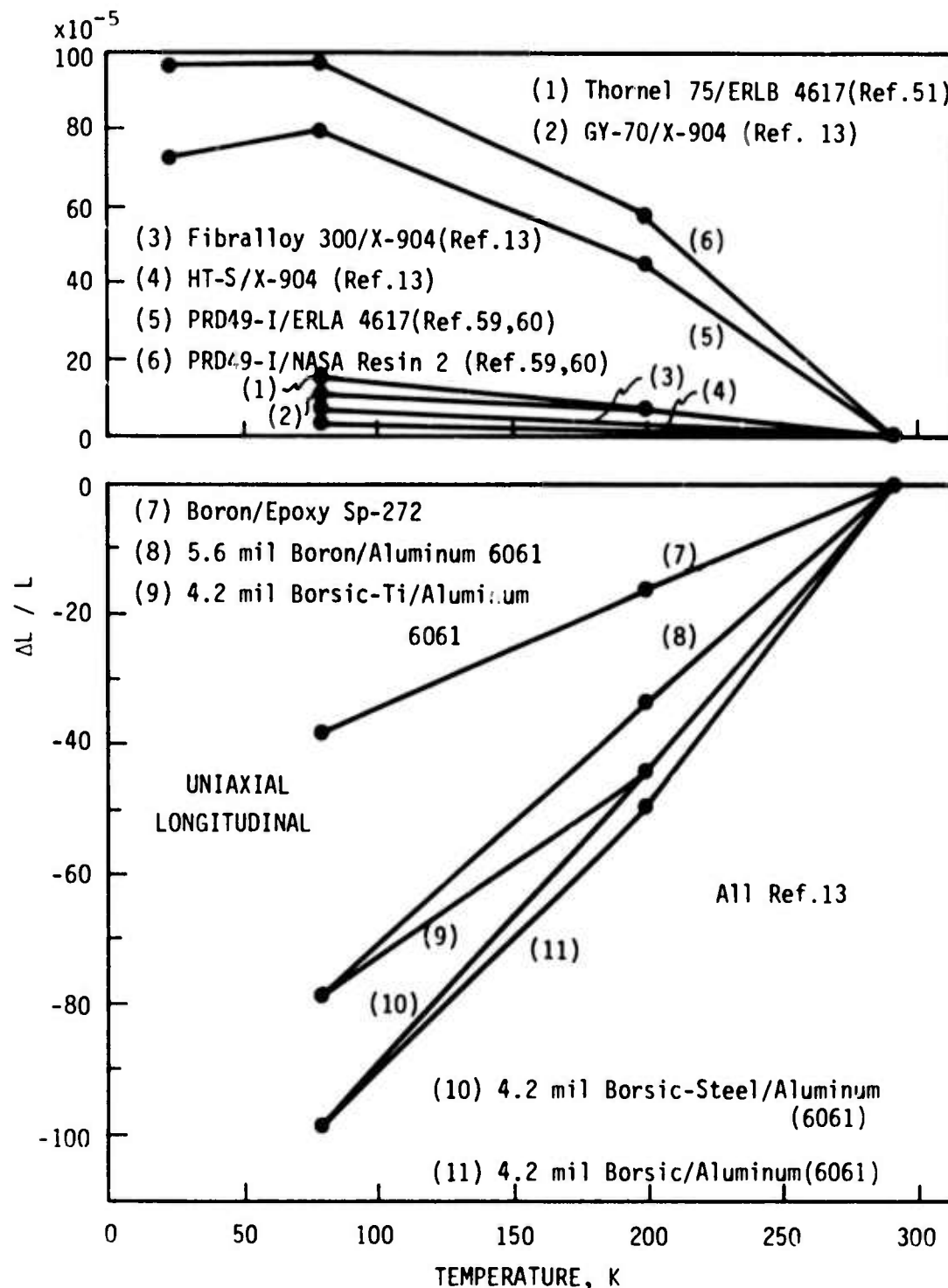


FIGURE 16 - Longitudinal Thermal Expansion,  $\Delta L/L$ , of Uniaxial Advanced Composites.

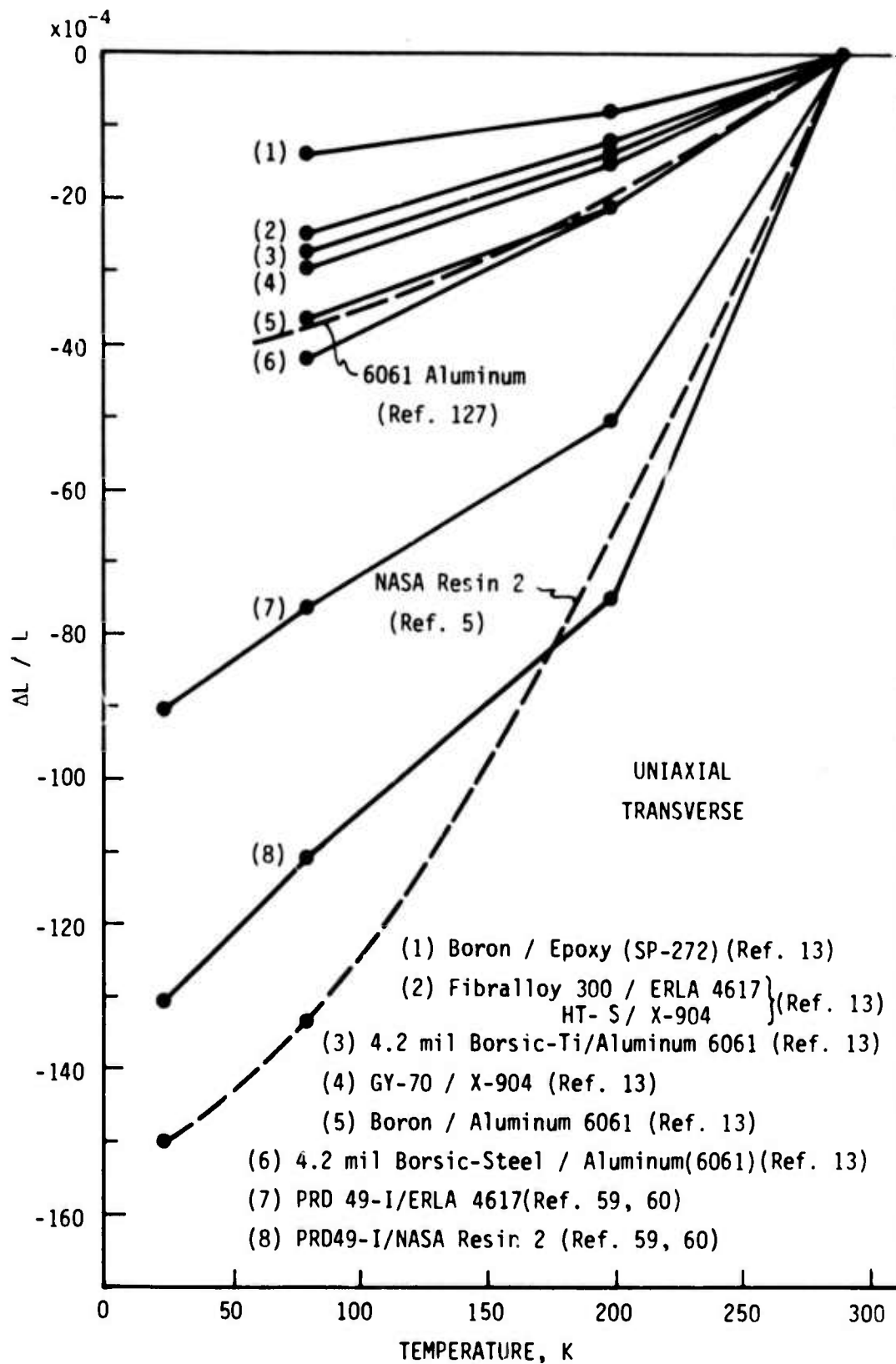


FIGURE 17 - Transverse Thermal Expansion,  $\Delta L/L$ , of Uniaxial Advanced Composites.

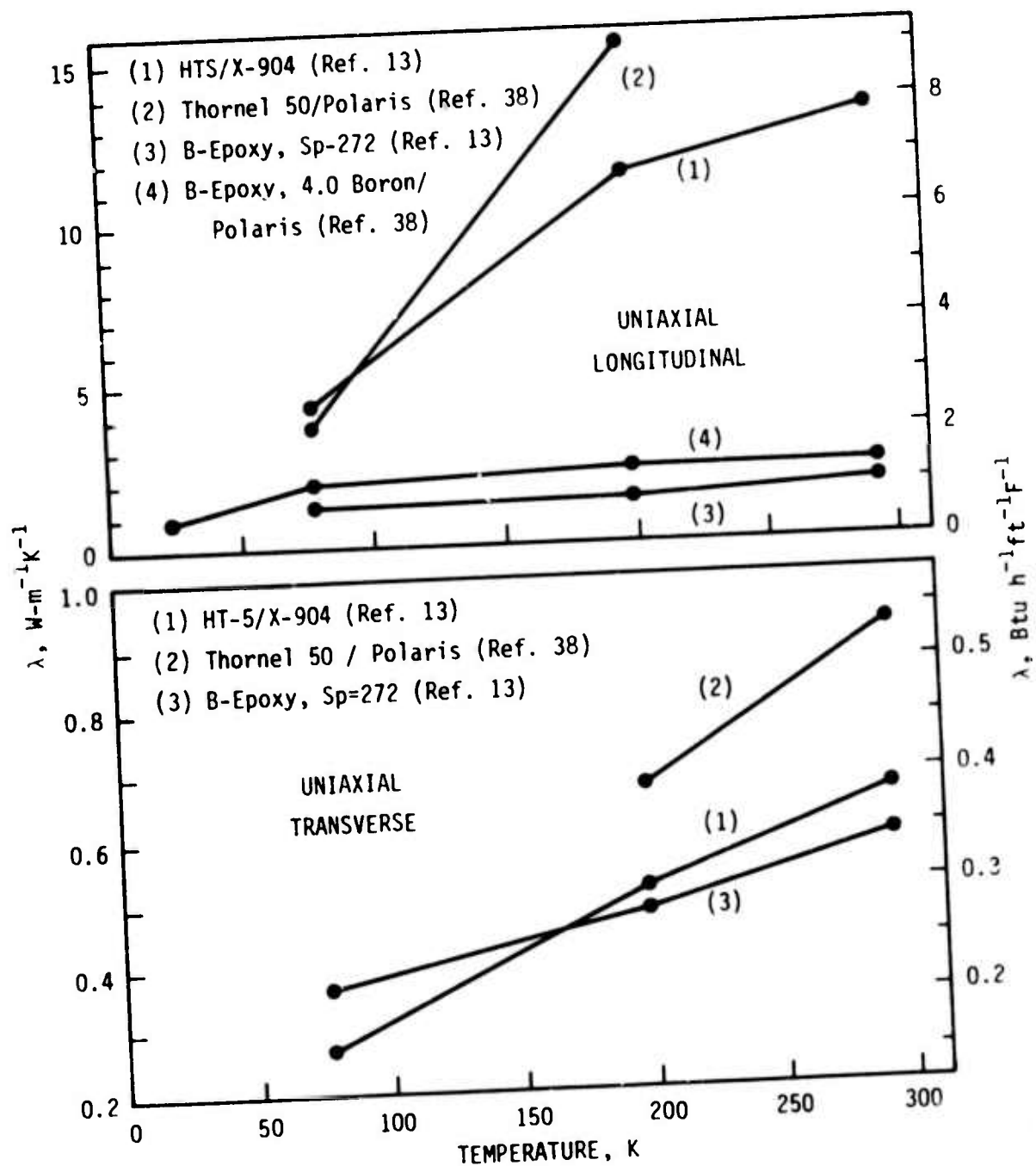


FIGURE 18 - Thermal Conductivities,  $\lambda$ , of Advanced Composites.



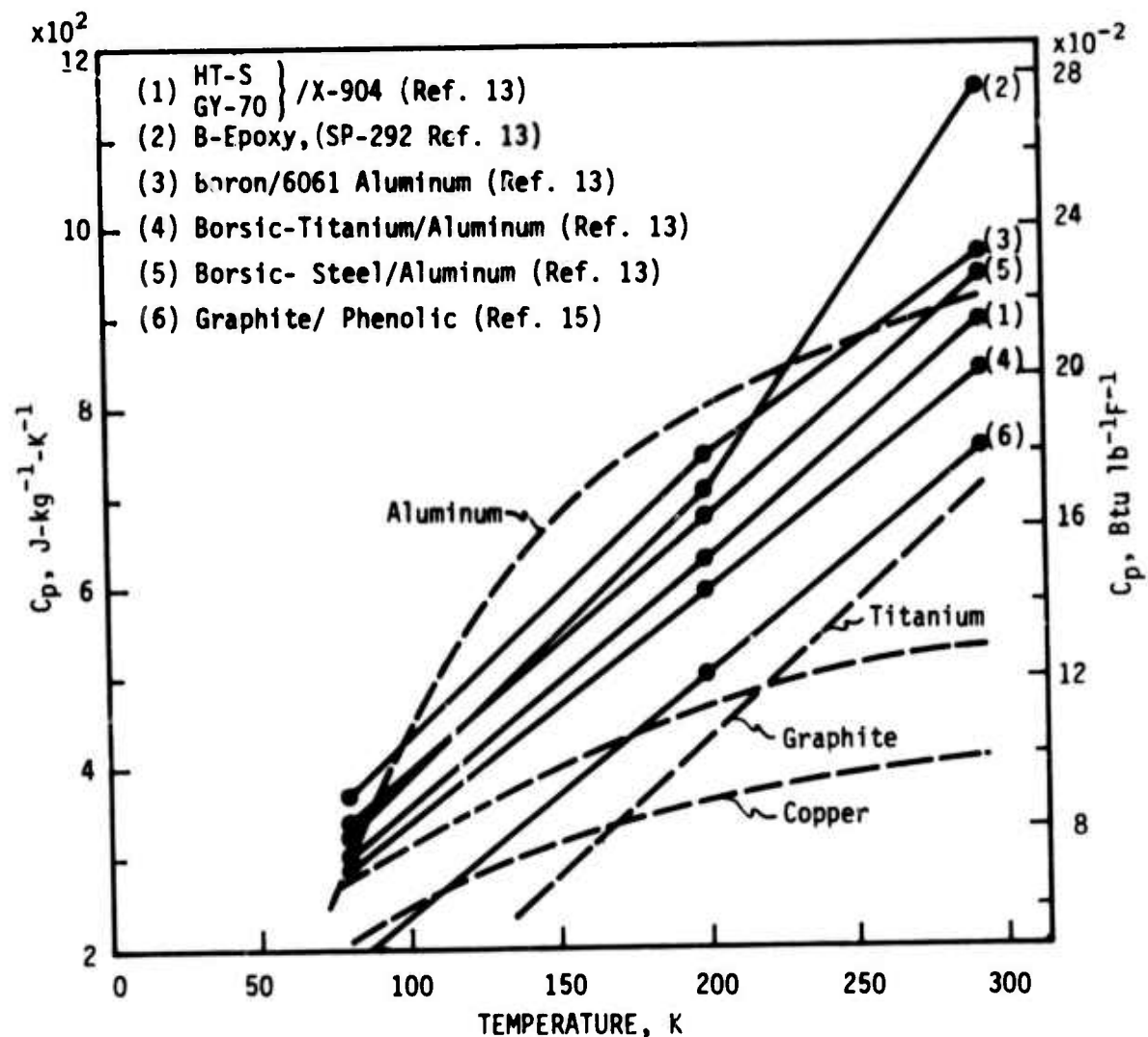


FIGURE 19 - Specific Heat,  $C_p$ , of Advanced Composites.

NBSIR

SEMI-ANNUAL REPORT ON MATERIALS RESEARCH  
IN SUPPORT OF SUPERCONDUCTING MACHINERY

ELASTIC PROPERTIES OF ENGINEERING MATERIALS  
AT CRYOGENIC TEMPERATURES

H. M. Ledbetter, E. R. Naimon, and W. F. Weston

Cryogenics Division  
Institute for Basic Standards  
National Bureau of Standards  
Boulder, Colorado 80302

October 1974

#### Summary: Elastic Properties

During the past year, the elastic properties of thirteen alloys have been studied at cryogenic temperatures. All of the alloys are commercially available engineering materials that are candidates for low-temperature applications, including superconducting machinery. They were studied between room temperature and liquid-helium temperature (300-4 K). Previously, very little low-temperature elastic data existed for most of these materials. Ultrasonic (10 MHz) pulse-echo and pulse-echo-superposition methods were used to determine the longitudinal and transverse sound-wave velocities, which are related simply via the mass density to the elastic constants. These constants include: Young's modulus, shear modulus, bulk modulus (reciprocal compressibility), longitudinal modulus, Poisson's ratio, and elastic Debye temperature. Measurements were made semi-continuously on cooling and also on heating.

In the previous semi-annual report, data and discussions were given for four materials: Ti-6Al-4V, Ti-5Al-2.5Sn (see Appendix A), Inconel 600, and Inconel X-750. In this report, data and discussions (in the form of manuscripts intended for publication) are given for eight additional materials: aluminum alloys 1100, 5083, 7005, and 7075; and austenitic stainless steels AISI 304, AISI 310, AISI 316, and A286. Also in this report, data are given for invar (iron ~ 36 nickel). All the stainless steels and invar have low-temperature magnetic transitions that cause anomalies in the low-temperature elastic properties of these materials. Invar is a particularly complicated material magnetically and elastically, and it will be discussed in the next report. The dynamic magneto-elastic behavior of the stainless steels is much simpler and is interpreted in terms of the Döring effect.

Contents: Elastic Properties

	Page
Manuscript: Low-temperature elastic properties of four wrought aluminum alloys . . . . .	220
Manuscript: Low-temperature elastic properties of four austenitic stainless steels . . . . .	243
Elastic properties of invar (data only) . . . . .	267
Appendix A: Reprint: Elastic properties of two titanium alloys at low temperatures . . . . .	273

LOW-TEMPERATURE ELASTIC PROPERTIES OF FOUR WROUGHT  
ALUMINUM ALLOYS

E. R. Naimon\*†, H. M. Ledbetter, and W. F. Weston\*

Cryogenics Division  
Institute for Basic Standards  
National Bureau of Standards  
Boulder, Colorado 80302

Abstract

The elastic properties of four annealed polycrystalline commercial aluminum alloys were studied between 4 and 300 K using a pulse-superposition method. Results are given for: longitudinal sound velocity, transverse sound velocity, Young's modulus, shear modulus, bulk modulus (reciprocal compressibility), Poisson's ratio, and elastic Debye temperature. The elastic stiffnesses of the alloys increase four to thirteen percent on cooling from room temperature to liquid-helium temperature. The elastic-constant-temperature curves exhibit regular behavior.

Key words: Aluminum; aluminum alloys; bulk modulus; compressibility; Debye temperature; elastic constants; elasticity; Poisson ratio; pulse-echo method; sound velocity; Young's modulus.

---

Contribution of NBS, not subject to copyright.

\* NRC-NBS Postdoctoral Research Associate, 1973-4.

† Present address: Dow Chemical USA, Rocky Flats Division, Golden, Colorado 80401.

LOW-TEMPERATURE ELASTIC PROPERTIES  
OF FOUR WROUGHT ALUMINUM ALLOYS

E. R. Naimon, H. M. Ledbetter, and W. F. Weston

Cryogenics Division  
Institute for Basic Standards  
National Bureau of Standards  
Boulder, Colorado 80302

1. INTRODUCTION

Aluminum alloys are used extensively at cryogenic temperatures because of their favorable mechanical properties. These properties include: increased strength without loss of ductility at lower temperatures; absence of a ductile-brittle fracture transition; and, for some alloys, high strength-to-weight ratios.

Knowledge of a material's elastic constants is essential to understanding its mechanical behavior. Most mechanical behavior is best described by a dislocation model, and the elastic constants (usually the shear modulus and Poisson's ratio) occur in most equations describing the stress-strain state of a dislocated solid.

In this paper, the elastic properties of four wrought aluminum alloys — commonly designated 1100, 5083, 7005, and 7075 — are reported over the temperature range 300 to 4 K. These properties include: the longitudinal modulus, Young's modulus, the shear modulus, the bulk modulus (reciprocal compressibility), and Poisson's ratio. While the changes of the elastic constants in this temperature range are only moderate, four to thirteen percent, exact values of the elastic constants are very useful design parameters, permitting accurate calculations of deflections for any combination of stress and temperature. Low-temperature elastic constants are also quite valuable theoretically; they permit the calculation of the Debye characteristic temperature, which is related in turn to a wide variety of solid-state phenomena that depends on the vibrational properties of solids.

An ultrasonic (10 MHz) pulse-superposition method was used for determining the velocity  $v$  of a sound pulse propagated through the specimen. The elastic modulus  $C$  is then given by  $C = \rho v^2$ , where  $\rho$  is the mass density. Different elastic constants were determined from different modes of ultrasonic excitation. This method has many advantages: small specimens are sufficient; thus, ancillary equipment such as probes and dewars can also be small, and refrigeration costs are low; specimens can have a simple geometry and can be easily prepared; measurements can be made as nearly continuously as desired; relative precision is high, about one part in  $10^5$  for the velocities; laboratory-to-laboratory variations of the elastic constants are typically a few percent or less; and tests are completely non-destructive.

Low-temperature elastic data for aluminum alloys have two-fold interest. First, the elastic constants provide basic information about interatomic forces. Second, the same numbers are essential design parameters for stress-bearing members. Data given here permit the load-deflection behavior of the alloys to be accurately predicted between room temperature and liquid-helium temperature. Accurate elastic data become especially important in applications involving high stresses, large structural parts, or precision parts.

## 2. MATERIALS

Aluminum alloy 1100 is commercial-quality aluminum. It has good corrosion resistance, high electrical and thermal conductivities, high ductility, but low strength properties. Strength can be improved somewhat by strain hardening without significantly decreasing other properties. The main impurities in this alloy are usually iron and silicon.

Aluminum alloy 5083 is characterized by good welding properties and by good corrosion resistance in marine environment. Magnesium is the major alloying element and, along with manganese, produces a moderately strong, yet ductile, alloy, which does not respond to heat treatment. The strength properties of 5083 improve with lower temperatures. The main advantage of 5083 seems to be its weldability; welds as strong as the base metal can be obtained. Currently this alloy is being used in a number of applications involving the manufacture, transfer, and storage of liquefied natural gas; these applications require many millions of kilograms of materials.



Aluminum alloy 7005 is a heat-treatable alloy containing zinc and magnesium, which are balanced to obtain a natural-aging alloy. Chromium is added to reduce corrosion of the heat-affected weld zones, and zirconium is added to reduce weld cracking and to improve mechanical properties.

Aluminum alloy 7075 contains zinc as the major alloying element. Together with a small percentage of magnesium, this alloy can be precipitation hardened to produce high strength.

Details of compositions, heat treatments, mass densities, and hardnesses of the alloys are given in Tables I and II.

### 3. EXPERIMENTAL

Alloys were obtained from commercial sources; 1100 and 7075 in the form of 3/4-in. (1.9-cm) rods, 5083 and 7005 in the form of 3/4-in. (1.9-cm) thick plate. Cylindrical specimens 5/8-in. (1.6-cm) in diameter and 5/8-in. (1.6-cm) long were prepared by grinding. Opposite faces were flat and parallel within  $10^{-4}$  in. (2.5  $\mu$ m). Specimens were annealed at a pressure of  $5 \times 10^{-6}$  torr, or less, and cooled in the furnace. Hardnesses were determined by standard metallurgical methods, and mass densities were determined by Archimedes's method using distilled water as a standard.

Quartz transducers (10 MHz) were bonded to the specimens with phenyl salicylate for room-temperature measurements and with a stopcock grease for lower temperatures. In a few cases, failure of these bonds at very low temperatures required using a silicone fluid (viscosity = 200,000 cP at 25°C) for bonding. The low-temperature apparatus was described previously [1].

A pulse-superposition method was used to determine the sound-wave velocities over the temperature range 300-4 K. Details concerning this method were given elsewhere [2].

#### 4. RESULTS

Quantities that were measured directly are the longitudinal and the transverse sound-wave velocities  $v_l$  and  $v_t$ . From these, the longitudinal modulus  $C_l$  and the transverse modulus  $C_t$  were calculated according to

$$C_l = \rho v_l^2 \quad (1)$$

and

$$C_t = \rho v_t^2. \quad (2)$$

These moduli are shown in Figs. 1 and 2 for the temperature range studied. Errors in the absolute velocities are believed to be about one-half percent or less. All of the other elastic constants that are used to describe polycrystalline aggregates are simply related to these two moduli. The moduli considered here -- the shear modulus  $G$ , Young's modulus  $E$ , the bulk modulus  $B$ , and Poisson's ratio  $\nu$  are given by:

$$G = C_t, \quad (3)$$

$$E = 3C(C_l - \frac{4}{3} C_t)/(C_l - C_t), \quad (4)$$

$$B = C_l - \frac{4}{3} C_t, \quad (5)$$

and

$$\nu = \frac{1}{2} (C_l - 2C_t)/(C_l - C_t). \quad (6)$$

The elastic constants obtained from these relationships are shown as functions of temperature in Figs. 3-5. Values of the elastic constants at selected temperatures are given in Table III.

The temperature variations of the elastic constants can be described mathematically in various ways. In this case, the temperature dependences of both  $C_l$  and  $C_t$  were fitted to a theoretical relationship suggested by Varshni [3]:

$$C = C^0 - \frac{g}{e^{t/T} - 1}, \quad (7)$$

where  $C$  is any elastic constant ( $C_l$  and  $C_t$  in this case),  $C^\circ$ ,  $s$ , and  $t$  are adjustable parameters and  $T$  is temperature. The value of  $C$  at  $T = 0$  K is  $C^\circ$ , and  $-s/t$  is the high-temperature limit of the temperature derivative  $dC/dT$ . By invoking an Einstein oscillator model of solids, it can be shown (in the absence of electronic effects) that  $t$  is the Einstein characteristic temperature. Parameters  $C^\circ$ ,  $s$ , and  $t$  are given in Table IV. Room-temperature values of the temperature coefficients of the elastic moduli are given in Table V; these values occur in the linear high-temperature region. Average differences between measured and curve values are 0.03% and 0.06% for the longitudinal and transverse moduli, respectively.

The elastic Debye temperature  $\theta$  can be calculated from the elastic wave velocities by [5]:

$$\theta = K \langle v \rangle, \quad (8)$$

where

$$K = \frac{h}{k} \left( \frac{3N\rho}{4\pi A} \right)^{1/3}. \quad (9)$$

Here  $h$  is Planck's constant,  $k$  is Boltzmann's constant,  $N$  is Avogadro's constant,  $\rho$  is the mass density, and  $A$  is the effective atomic weight. The average velocity is given by

$$\langle v \rangle = \frac{v_l^{-3} + 2v_t^{-3}}{3}. \quad (10)$$

The elastic Debye temperatures for the four alloys at  $T = 0$  K, and also for unalloyed aluminum are given in Table VI.

## 5. DISCUSSION

As shown by the data in Table VI, changes in the elastic constants of aluminum and its alloys between 300 and 4 K are about four percent for B, twelve percent for E, twelve percent for G, and four percent for  $\nu$ . These changes are somewhat larger than those observed in alloys based on copper or iron, for example. Most of the changes occur above about 100 K. Below this temperature the elastic constants change only slightly with temperature. Thus, any changes in the mechanical behavior of these alloys in this temperature region probably cannot be ascribed to an elastic origin.

The temperature behavior of the elastic constants of the aluminum alloys reported on here is quite regular. The regular decrease of the moduli with increasing temperature and the relative flatness of the modulus-temperature curves at lower temperatures has already been mentioned. Also, in accord with the third law of thermodynamics, the slopes  $dC/dT$  approach zero at zero temperature. And a linear temperature dependence is exhibited at higher temperatures, those higher than about 150 K, which is roughly one-third of the Debye temperature. Besides indicating the absence of magnetic or structural transitions, this ideal temperature behavior suggests that the anharmonic properties of these alloys can probably be explained by a relatively simple model.

These alloys were not examined for texture. However, texture would have little effect on their elastic properties. Aluminum single crystals are only slightly anisotropic; the Zener anisotropy ratio for aluminum is 1.2; it is 1.0 for the isotropic case. Aluminum's isotropy is purely accidental since aluminum, because of its three valence electrons, has a large band-structure contribution to the elastic constants [10]. This contribution is usually anisotropic; the anisotropy is canceled in the case of aluminum by other energy terms. Thus, since aluminum single crystals are only slightly anisotropic, even a strongly textured polycrystalline aggregate of aluminum would have nearly isotropic elastic behavior.

It should be emphasized that the data reported here are dynamic (adiabatic) rather than static (isothermal); they apply strictly to rapid rather than slow loading. However, the differences between

adiabatic and isothermal elastic constants are small. They become smaller at lower temperatures because of the diminishing thermal-expansion coefficient, and they vanish at zero temperature. Using formulas given by Landau and Lifshitz [6] it can be shown for aluminum at room temperature:

$$\begin{aligned} \frac{E_S - E_T}{E_T} &= 0.005, & \frac{B_S - B_T}{B_T} &= 0.045 & (11) \\ \frac{\nu_S - \nu_T}{\nu_T} &= 0.020, & \text{and } \frac{G_S - G_T}{G_S} &= 0, \end{aligned}$$

where subscripts S and T denote the adiabatic and the isothermal cases, respectively. For E, B,  $\nu$ , and G, these corrections are typically in the ratio 1:9:4:0 if  $\nu$  has a value near 1/3.

Effects of alloying on the elastic properties of aluminum cannot be accurately determined from the present study because of the large number of alloying elements and their interactions. Such effects have been considered elsewhere [11]. However, some general observations can be made concerning alloying. Disregarding alloy 1100, with respect to 'pure' aluminum, the shear modulus and Young's modulus increased in all cases while the bulk modulus decreased, and by a larger percentage. Poisson's ratio decreased in all four alloys. The 1100 alloy, which contains only one percent of impurities, presents an interesting case. The data indicate that while the shear modulus of this alloy is identical to that of unalloyed aluminum, the bulk modulus is higher by about five percent. Since the bulk modulus is not measured directly, but is calculated from the difference of two velocities according to Equation 5, a compounding of errors may account for this discrepancy. If the effect is real, then it has important consequences for the problem of averaging single-crystal elastic coefficients to obtain the bulk modulus of a polycrystalline aggregate.

Finally, approximate relationships among the elastic constants are indicated. For all of the alloys, and for all temperatures, as a first approximation:

$$\nu \approx 1/3 \quad (12)$$

and

$$B \approx E \approx 8/3 G. \quad (13)$$

These should be useful for many engineering purposes where only rough numbers are needed and only one of the elastic constants is known.

#### CONCLUSIONS

From the results of this study the following conclusions are drawn:

1. All the elastic properties of aluminum alloys 1100, 5083, 7005, and 7075 behave regularly with respect to temperature.
2. For all alloys studied, the temperature behavior of both  $C_Q$  and  $C_t$  can be described accurately by a theoretical relationship suggested by Varshni.
3. In this series of alloys, alloy 5083 has the highest Young's modulus, the highest shear (rigidity) modulus, and the lowest Poisson's ratio. Alloy 7005 has the highest bulk modulus.

#### ACKNOWLEDGMENT

This work was supported in part by the Advanced Research Projects Agency of the U.S. Department of Defense.

#### REFERENCES

1. E. R. Naimon, W. F. Weston, and H. M. Ledbetter, *Cryogenics* 14 (1974) 246.
2. H. J. McSkimin, *J. Acoust. Soc. Amer.* 33 (1961) 12.
3. Y. P. Varshni, *Phys. Rev.* B2 (1970) 3952.
4. G. N. Kamm and G. A. Alers, *J. Appl. Phys.* 35 (1964) 327.
5. P. Debye, *Ann. Phys. (Leipz.)* 39 (1912) 789.
6. L. D. Landau and E. M. Lifshitz, *Theory of Elasticity* (Pergamon, London, 1959) p. 17.
7. T. Lyman (Ed.), *Metals Handbook* (Am. Soc. for Metals, Metals Park, Ohio, 1961).
8. R. Develay, A. Faure, S. Lehongre, D. Mugnier, and D. Schroeter, in *Advances in Cryogenic Engineering*, Vol. 12, K. Timmerhaus (Ed.) (Plenum, New York, 1967) p. 484.
9. J. L. Christian and J. F. Watson, in *Advances in Cryogenic Engineering*, Vol. 6, K. Timmerhaus (Ed.) (Plenum, New York, 1961) p. 604.
10. T. Suzuki, *Phys. Rev.* B3 (1971) 4007.
11. W. Köster, *Z. Metallk.* 32 (1940) 282.

### List of Tables

I.	Compositions of the alloys, mill analyses, wt. pct. . . . .	232
II.	Properties of the alloys . . . . .	233
III.	Values of the elastic constants of aluminum alloys at selected temperatures in units of $10^{11}$ N/m <sup>2</sup> except $\nu$ , which is dimensionless . . . . .	234
IV.	Parameters in equation 7 . . . . .	235
V.	Temperature coefficients of the elastic constants at room temperature ( $10^{-4}$ K <sup>-1</sup> ) . . . . .	236
VI.	Elastic Debye temperatures at $T = 0$ K . . . . .	237

### List of Figures

1.	Temperature variation of the longitudinal modulus . . . . .	238
2.	Temperature variation of the shear modulus . . . . .	239
3.	Temperature variation of Young's modulus . . . . .	240
4.	Temperature variation of the bulk modulus (reciprocal compressibility) . . . . .	241
5.	Temperature variation of Poisson's ratio . . . . .	242



Table I. Compositions of the alloys, mill analyses, wt. pct.

Alloy	Al	Cr	Cu	Fe	Mg	Mn	Ni	Si	Ti	V	Zn	Zr
1100	Bal		.2	.6				.1				
5083	Bal	.13	.04	.19	4.75	.63	.003	.08	.01	.007	.04	
7005	Bal	.25	<.1	<.4	1.2	<.2		<.3	<.1		4.6	.3
7075	Bal	.3	1.6	.7	2.5	.3		.5	.2		5.6	

Table II. Properties of the alloys

Alloy	Hardness (DPH No., 1 kg load)	Mass density <sub>3</sub> at 294 K, g/cm <sup>3</sup>	Condition
1100	28	2.818	Annealed 345°C; furnace cooled
5083	78	2.666	Annealed 413°C, 1/2 h; furnace cooled
7005	77	2.779	Annealed 400°C, 3 h; furnace cooled
7075	67	2.721	Annealed 413°C, 3 h; furnace cooled

Table III. Values of the elastic constants of aluminum alloys at selected temperatures in units of  $10^{11}$  N/m<sup>2</sup> except  $\nu$ , which is dimensionless

Alloy	Temperature (K)	Present Results					Previous Results†				
		B	E	G	$\nu$	Reference	Temperature (K)	B	E	G	$\nu$
1100	300	.724	.694	.259	.340	[7]	300	(.697)	.689	.258	0.33
	200	.738	.728	.273	.336						
	100	.749	.758	.285	.331						
	0	.751	.769	.289	.329						
5083	300	.716	.715	.268	.333	[1]	300	(.762)	.710	.264	0.33
	200	.729	.758	.286	.327						
	100	.739	.796	.301	.321						
	0	.742	.809	.307	.318						
7005	300	.749	.705	.262	.343	[8]	300	(.635)	.711	.271	(.313)
	200	.765	.743	.278	.338		77	(.735)	.779	.294	(.323)
	100	.777	.777	.291	.333		20	(.671)	.792	.304	(.303)
	0	.780	.789	.296	.331						
7075	300	.707	.707	.265	.333	[9]	298		.731		
	200	.718	.742	.279	.328		200		.786		
	100	.728	.773	.292	.323		20		.786		
	0	.731	.783	.296	.321						
Aluminum*	300	.761	.701	.260	.347						
	200	.777	.738	.275	.342						
	100	.790	.771	.288	.337						
	0	.794	.784	.293	.336						

\* Calculated from single-crystal data in reference [4].

† Entries in parentheses were derived using standard formulas.

Table IV. Parameters in equation 7

Alloy	Mode	$C^o$	$s$	$t$
		$10^{11} \text{ N/m}^2$	$10^{11} \text{ N/m}^2$	K
1100	l	1.136	0.0903	255.9
	t	0.2892	0.0301	206.9
5083	l	1.151	0.0926	235.3
	t	0.3067	0.0381	206.7
7005	l	1.175	0.0928	240.0
	t	0.2963	0.0327	203.4
7075	l	1.126	0.0707	219.6
	t	0.2961	0.0344	223.3

Table V. Temperature coefficients of the elastic constants  
at room temperature ( $10^{-4} \text{ K}^{-1}$ )

Alloy	$\frac{1}{B} \frac{dB}{dT}$	$\frac{1}{E} \frac{dE}{dT}$	$\frac{1}{G} \frac{dG}{dT}$	$\frac{1}{v} \frac{dv}{dT}$
1100	-2.01	-5.01	-5.37	1.41
5083	-1.92	-6.06	-6.58	2.08
7005	-2.13	-5.48	-5.88	1.54
7075	-1.58	-5.08	-5.52	1.75
Aluminum*	-1.97	-5.53	-5.77	1.80

\* Derived from single-crystal data in reference [4].

Table VI. Elastic Debye temperatures at  $T = 0$  K

Alloy	$\Theta(K)$
1100	426.2
5083	440.4
7005	425.9
7075	422.2
Aluminum	430.6*

\* Calculated from single-crystal data in reference [4].

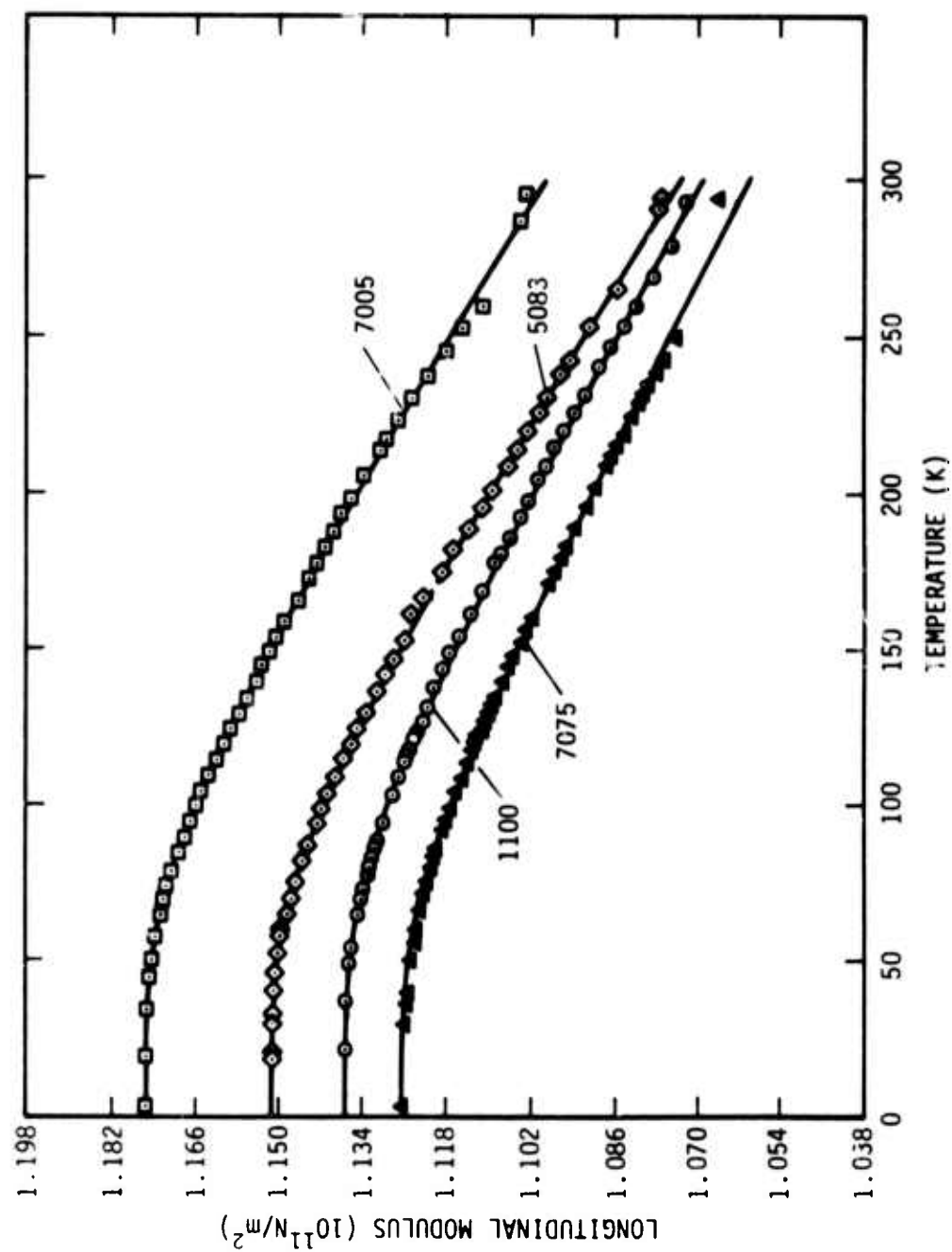


Figure 1. Temperature variation of the longitudinal modulus.

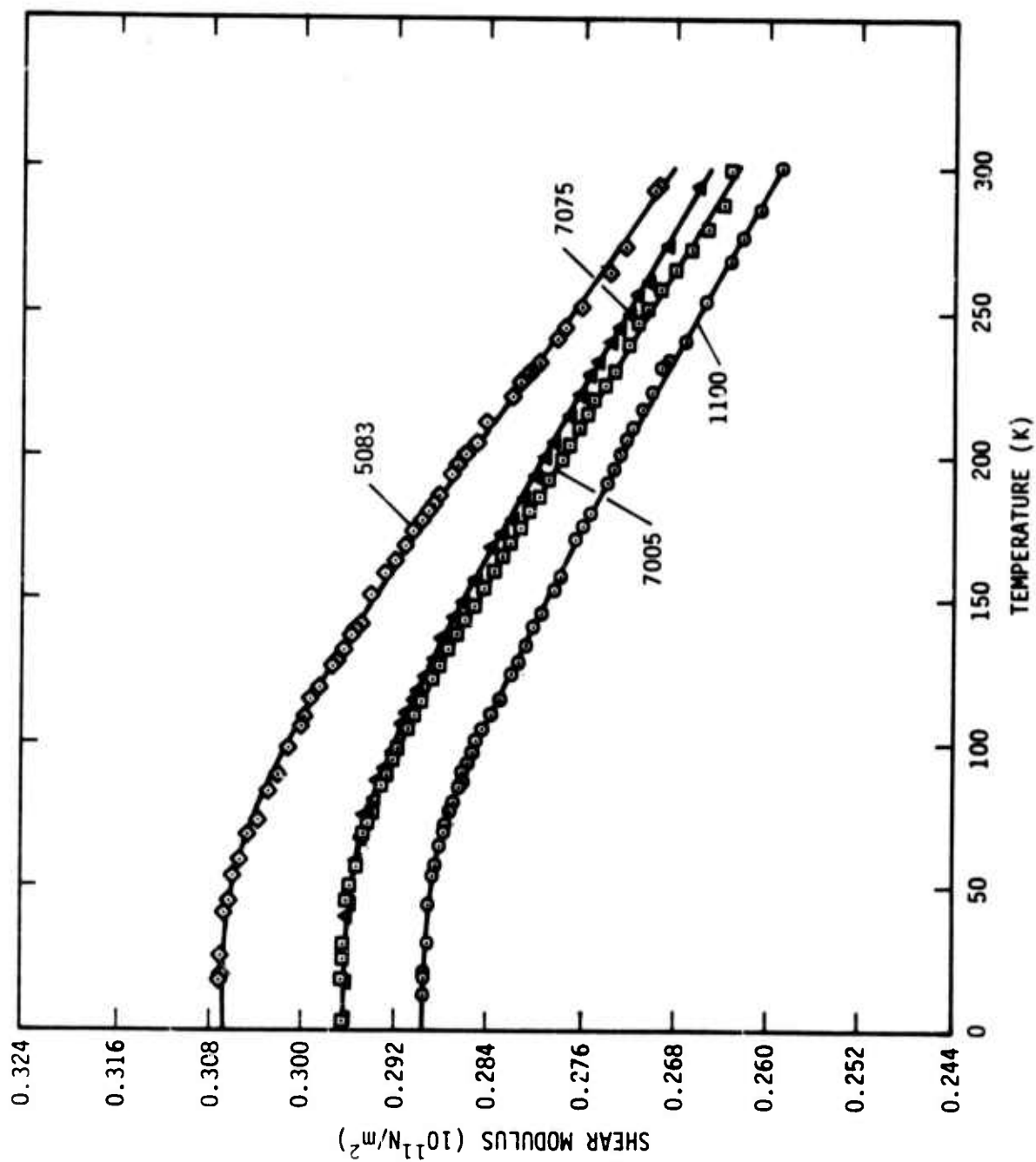


Figure 2. Temperature variation of the shear modulus.



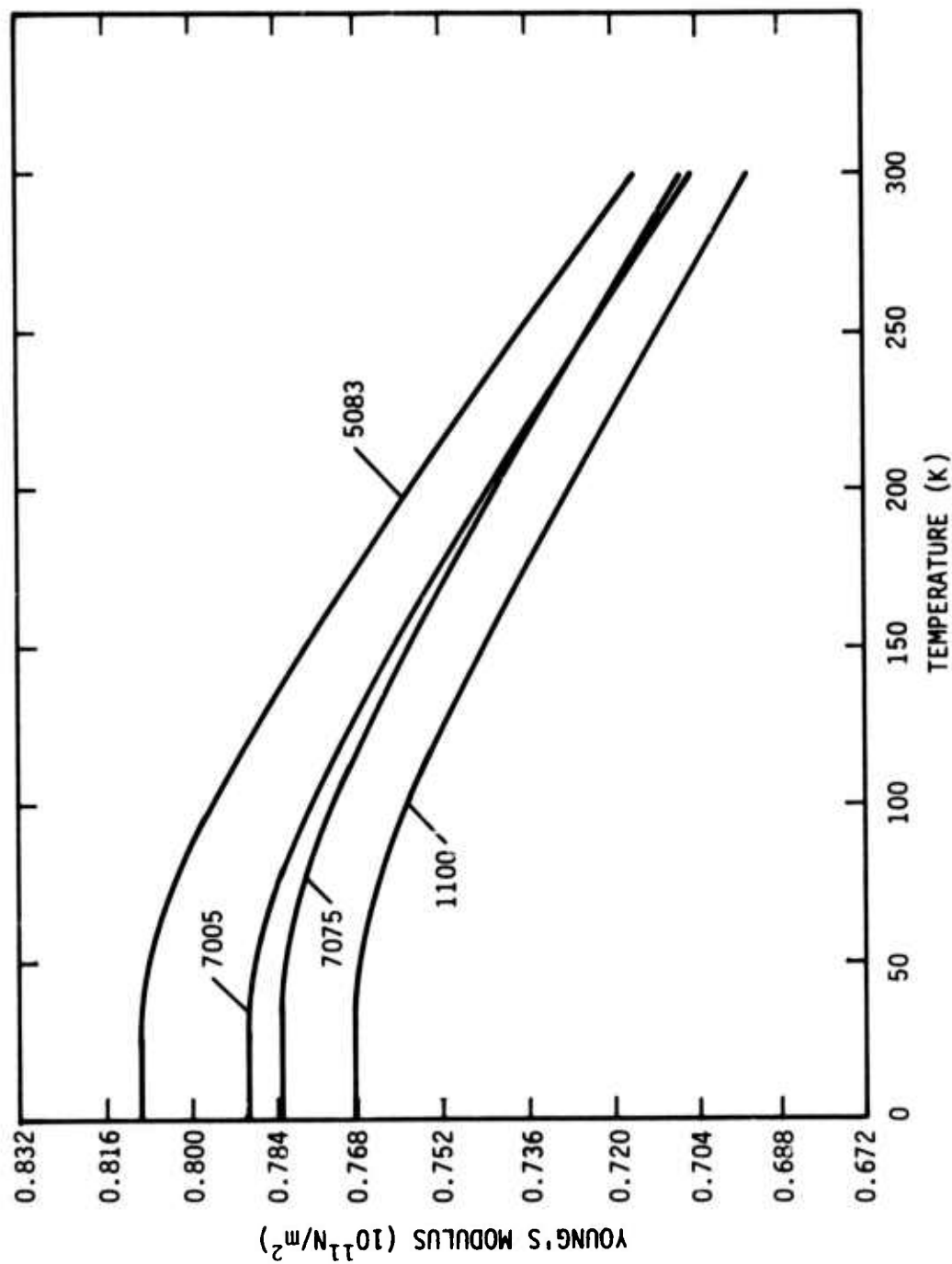


Figure 3. Temperature variation of Young's modulus.

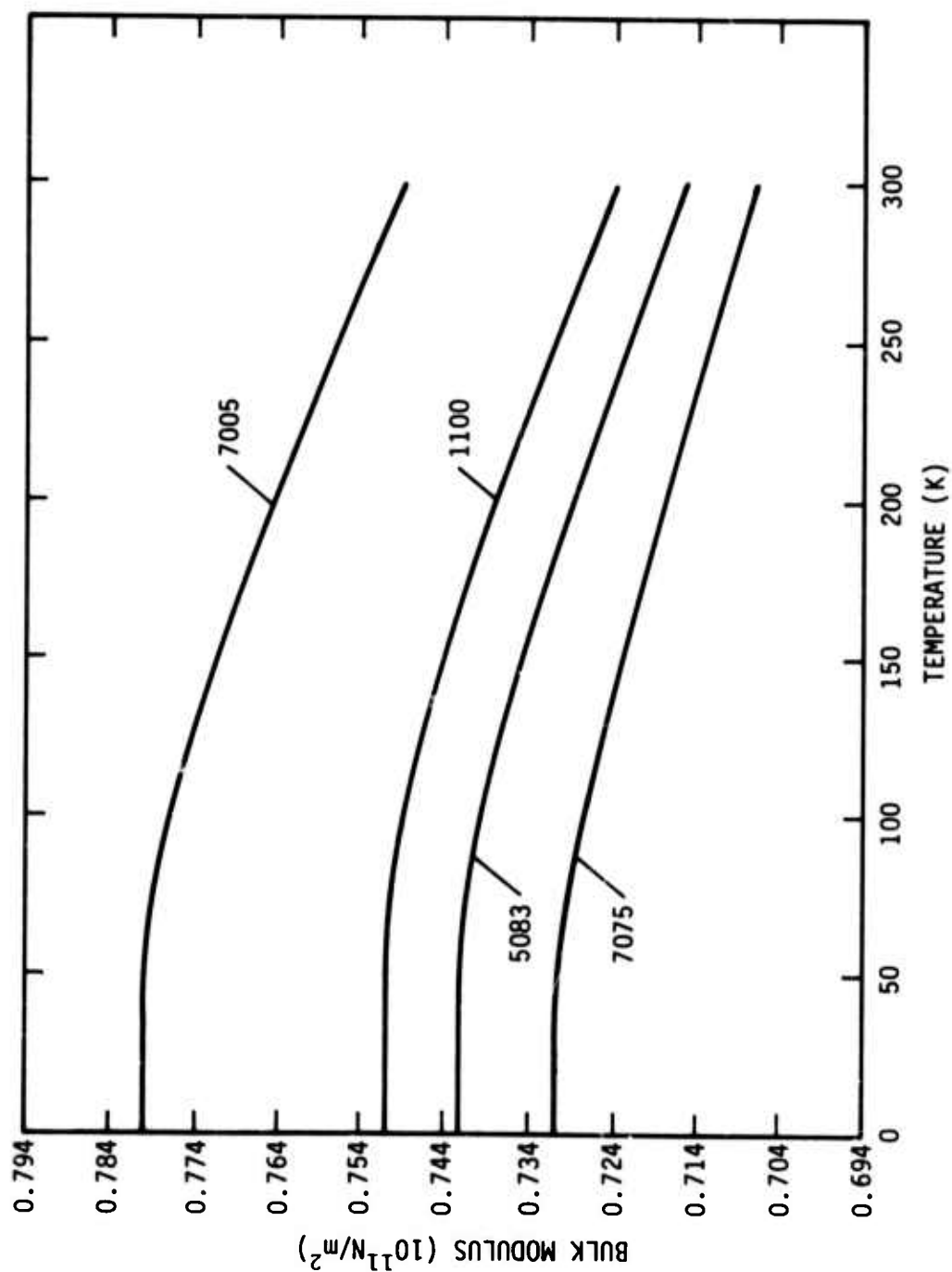


Figure 4. Temperature variation of the bulk modulus (reciprocal compressibility).

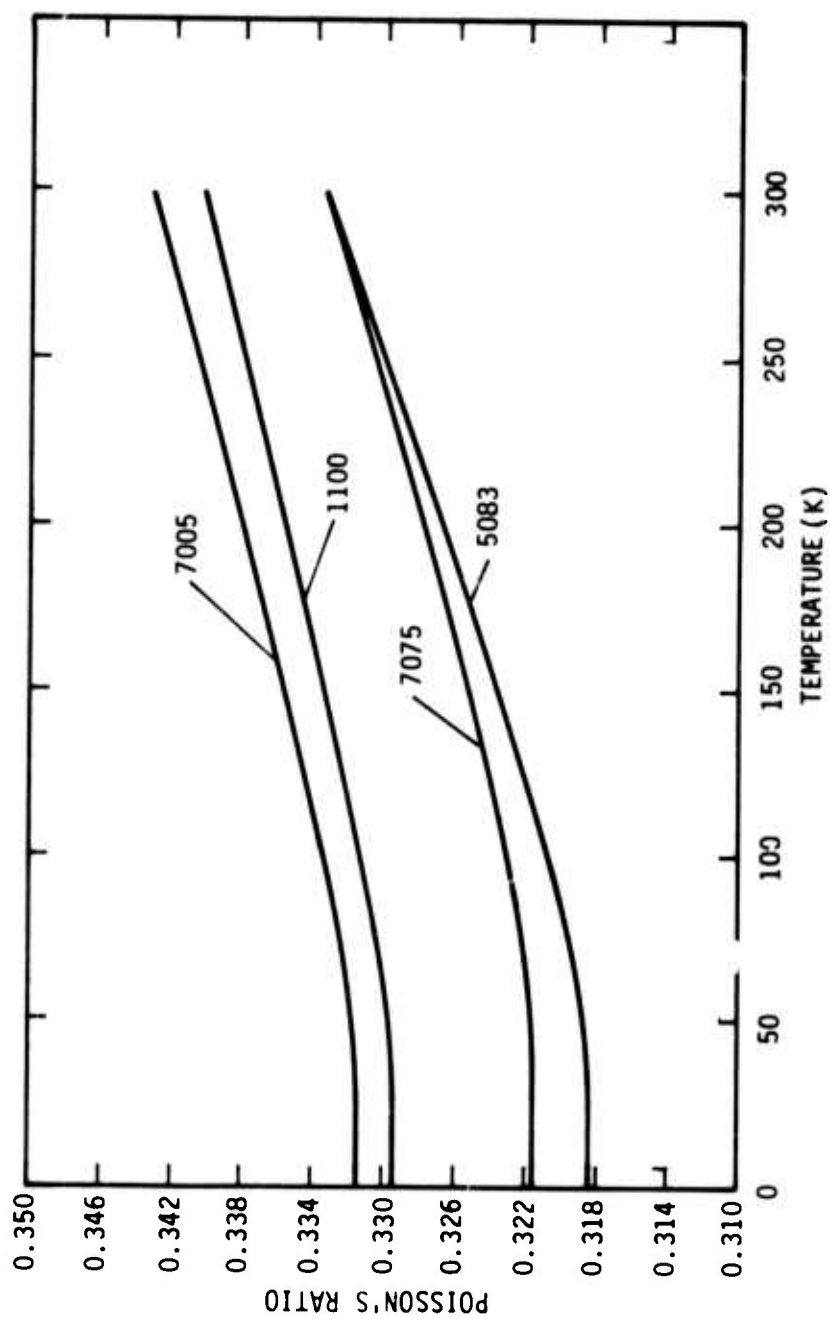


Figure 5. Temperature variation of Poisson's ratio.

## LOW-TEMPERATURE ELASTIC PROPERTIES OF FOUR AUSTENITIC STAINLESS STEELS†

H. M. Ledbetter, W. F. Weston\*, and E. R. Naimon\*†

Cryogenics Division, Institute for Basic Standards,  
National Bureau of Standards, Boulder, Colorado 80302

### Abstract

The elastic properties of four austenitic stainless steels -- AISI 304, AISI 310, AISI 316, and A286 -- are reported over the temperature range 300 to 4 K. These properties include: longitudinal modulus, shear modulus, Young's modulus, bulk modulus (reciprocal compressibility), Poisson's ratio, and elastic Debye temperature. Elastic constants were determined from measurements of longitudinal and transverse sound-wave velocities using an ultrasonic (10 MHz) pulse-superposition method. Measurements were made in the absence of a magnetic field; these alloys undergo paramagnetic-to-antiferromagnetic transitions at low temperatures. For all four alloys, the shear modulus behaves regularly with respect to temperature. The other elastic constants, all of which have a dilatational component, decrease anomalously at temperatures below 80 K. The largest anomaly, about 3%, is in the bulk modulus of the 304 alloy; this modulus is lower at 0 K than at 300 K. Results are interpreted on the basis of the Döring effect, which results from a large volume magnetostriction in the magnetic phase. This may be the first report of a Döring effect in antiferromagnetic materials.

Key words: Bulk modulus; chromium alloys; compressibility; Debye temperature; Döring effect; elastic constants; iron alloys; magnetic transition; nickel alloys; Poisson's ratio; pulse-echo method; sound velocity; Young's modulus.

---

† Contribution of NBS, not subject to copyright.

\* NRC-NBS Postdoctoral Research Associate, 1973-4.

† Present address: Dow Chemical USA, Rocky Flats Div., Golden, CO 80401.

## LOW-TEMPERATURE ELASTIC PROPERTIES OF FOUR AUSTENITIC STAINLESS STEELS

H. M. Ledbetter, W. F. Weston, and E. R. Naimon

Cryogenics Division, Institute for Basic Standards, National Bureau of Standards, Boulder, Colorado 80302

### I. INTRODUCTION

Austenitic stainless steels are attractive materials for mechanical applications at low temperatures. Primarily, this is due to their having, at room temperature, a face-centered cubic (fcc) crystal structure. Metals having this crystal structure usually do not become brittle at lower temperatures. In general, steels that remain austenitic at cryogenic temperatures show increased tensile strength, a smaller increase in yield strength, and little change in ductility. However, it is not axiomatic that fcc materials will always perform well at low temperatures. For example, lower temperatures may promote a change of the crystal structure from fcc to body-centered cubic (bcc) or to close-packed hexagonal (cph), thus probably embrittling the material. Other changes such as atomic ordering or magnetic ordering may also occur at low temperatures; these also affect mechanical behavior. Thus, the nature and the magnitude of a material's low-temperature properties cannot be predicted a priori from room-temperature observations, and there is no substitute for careful low-temperature experimental determinations of the important properties of each material of interest.

Gilman<sup>1</sup> concluded that "the most important mechanical characteristic of a crystal is its elastic modulus." While its significance may often be obscured by impurities, microstructure, grain boundaries, residual stresses and strains, and temperature, it nevertheless remains fundamental to a material's mechanical behavior. Trends in elastic constants can be correlated with phase instabilities; changes in crystal structure are generally accompanied by discontinuities in the elastic constants. Higher-order phase transitions such as order-disorder and nonmagnetic-magnetic also exhibit elastic anomalies. From elastic constant data, information on interatomic potentials can be deduced; similarly, the validity of proposed interatomic potentials can be accurately tested by calculating elastic constants from them and comparing results with observation. By invoking a model,

interatomic force constants can be derived from the elastic constants; the force constants are fundamental in that they describe directly the strength of interatomic "bonds." Debye characteristic temperatures can be calculated simply from elastic constant data; the Debye temperature relates in turn to a wide variety of solid-state phenomena including atomic diffusion, lattice thermal conductivity, sound velocities, vibrational entropies, zero-point energies, electrical conductivity, Bragg-reflection intensities, atomic vibrational amplitudes, and melting. Also, Grüneisen parameters can be calculated from higher-order elastic constants; these relate in turn to a variety of anharmonic solid-state properties, such as thermal expansion and attenuation of acoustic waves in solids. Besides the examples cited above, other metallurgical problem areas where elastic constants play a key role include: theories of solid-solution strengthening, alloy development, models of maximum ultimate strength, and dislocation models of plastic behavior. a dislocation description often involves the shear modulus and Poisson's ratio.

The same elastic constants that are related to fundamental interatomic forces in solids are also used in engineering design. For example, Poisson's ratio is an essential design parameter in problems of plate buckling or of pressure-vessel design. Young's modulus and Poisson's ratio are required if plane-stress data and plane-strain data are to be interconverted, a technique used often in the elastic stress-strain analysis of solids.

In this paper, the dynamic zero-magnetic-field elastic properties of four austenitic stainless steels -- commonly designated AISI 304, AISI 310, AISI 316, and A286\* -- are reported between 300 and 4 K. These properties include: longitudinal modulus, shear modulus, Young's modulus, bulk modulus (reciprocal compressibility), and Poisson's ratio. These elastic constants were determined dynamically, by measuring the velocity of longitudinally polarized and transversely polarized ultrasonic (10 MHz) pulses propagating through polycrystalline specimens of commercial as-received alloys. At low temperatures, elastic anomalies were observed in all four materials. These are believed to be associated with transitions to antiferromagnetic states. A magneto-elastic interpretation of the anomalies is given.

---

\* This tradename is used to describe the material; its use does not imply an endorsement by NBS of a particular product.

## II. EXPERIMENTAL

### A. Specimens

Materials were obtained from commercial sources in the form of 3/4 - in (1.9 - cm) diameter rods. Their chemical compositions are given in Table I. Hardness and mass-density data on the alloys are given in Table II. Hardnesses were measured by standard metallurgical methods, and mass densities were measured by Archimedes's method using distilled water as a standard. Materials were tested in their as-received conditions. Samples were prepared by grinding cylinders 1/2 - in (1.2 - cm) thick with faces flat and parallel within  $10^{-4}$  in ( $2.5 \mu\text{m}$ ).

### B. Procedures

A pulse-superposition<sup>2,3</sup> method was used to measure the longitudinal and transverse sound-wave velocities between room temperature and liquid-helium temperature. The specimen holder, which was described previously<sup>4</sup>, was placed in the ullage of a helium dewar and lowered (raised) stepwise to achieve cooling (heating). Measurements were made semi-continuously on cooling, and a few points were checked on heating to verify reversibility. Temperatures were measured by a chromel-constantan thermocouple contacting the specimen. Quartz transducers (10 MHz) were bonded to the specimens with phenyl salicylate for room-temperature measurements and with stopcock grease for lower temperatures. No bond corrections were made since these are insignificant for present purposes. No thermal-contraction corrections were made; for the alloys of interest this introduces a maximum error of 0.3% over the 300 K temperature range. Maximum uncertainties in the absolute velocity measurements are estimated to be about one percent. The imprecision in the relative velocities is a few parts in  $10^5$ .

## III. RESULTS

Longitudinal and transverse moduli are shown in Figs. 1 and 2 as a function of temperature. The longitudinal modulus  $C_L$  is given by

$$C_L = \rho v_L^2, \quad (1)$$

where  $\rho$  is the mass density and  $v_L$  is the longitudinal wave velocity. The transverse modulus  $C_t$  is identically equal to the shear modulus  $G$  and is given by

$$C_t \equiv G = \rho v_t^2, \quad (2)$$

where  $v_t$  is the transverse wave velocity. Young's modulus  $E$  is given by

$$E = 3C_t(C_l - \frac{4}{3}C_t)/(C_l - C_t) \quad (3)$$

and is shown in Fig. 3. The bulk modulus  $B$ , or reciprocal compressibility, is given by

$$B = C_l - \frac{4}{3}C_t \quad (4)$$

and is shown in Fig. 4. Poisson's ratio  $\nu$  is given by

$$\nu = \frac{1}{2} (C_l - 2C_t)/(C_l - C_t) \quad (5)$$

and is shown in Fig. 5.

Temperature dependences of both  $C_l$  and  $C_t$  were fitted to a semi-theoretical relationship suggested by Varshni<sup>5</sup>:

$$C = C^0 - \frac{s}{e^{t/T} - 1} \quad (6)$$

where  $C^0$ ,  $s$ , and  $t$  are adjustable parameters and  $T$  is temperature. The value of  $C$  at  $T = 0$  K is  $C^0$ , and  $-s/t$  is the high-temperature limit of the temperature derivative  $dC/dT$ . By invoking an Einstein oscillator model of solids, it can be shown (in the absence of electronic effects) that  $t$  is the Einstein characteristic temperature. Parameters  $C^0$ ,  $s$ , and  $t$  are given in Table III. Of course, the low-temperature elastic anomalies are not described by Eq. (6), which describes the extrapolated higher-temperature behavior shown as dashed lines in the figures. Temperature coefficients of the elastic constants at room-temperature are given in Table IV.

Elastic Debye temperatures were calculated for both the antiferromagnetic and the extrapolated paramagnetic states, and these are given in Table V. The elastic Debye temperature  $\theta$  is related to the average sound-wave velocity according to

$$\theta = K \langle v \rangle \quad (7)$$



where

$$K = \frac{h}{k} \left( \frac{3N\rho}{4\pi A} \right)^{1/3} \quad (8)$$

Here  $h$  is Planck's constant,  $k$  is Boltzmann's constant,  $N$  is Avogadro's number,  $\rho$  is the mass density, and  $A$  is the effective atomic weight. The average velocity is given by

$$\langle v \rangle = \left( \frac{v_l^{-3} + 2v_t^{-3}}{3} \right)^{-1/3} \quad (9)$$

For comparison, the elastic Debye temperatures at  $T = 0$  K of iron, chromium, and nickel are also included in Table V.

#### IV. DISCUSSION

The elastic constants of all four materials exhibit regular behavior from room temperature to about 80 K or lower. Below about 80 K, anomalous changes in the elastic constants occur for all four materials. These anomalies occur only in the elastic constants that have a dilatational component -- the longitudinal modulus, the bulk modulus, Young's modulus, and Poisson's ratio. No anomalies occur for the shear modulus.

The elastic properties of some of these alloys have been studied previously at low temperatures. For example stress-strain tests for  $E$  and  $G$  at 295, 77, and 4 K indicated anomalies somewhere below 77 K for both AISI 302 and AISI 303, but not for AISI 310.<sup>6</sup> Resonance tests on AISI 303 for  $E$  and  $G$  simultaneously at temperatures between 320 and 4 K showed anomalies below 80 K.<sup>7</sup> All these anomalous results can be interpreted in terms of the usual  $\Delta E = \Delta E_\lambda$  effect (discussed below) and are not directly related to the low-temperature elastic anomalies reported in the present work.

The most likely causes of the anomalies are magnetic transitions. Stainless-steel-type alloys have been shown to be antiferromagnetic at lower temperatures; Néel temperatures near 40 K have been reported<sup>6,8</sup> for 304-type alloys. However, no Néel transition was detected for a 310-type alloy cooled to liquid-helium temperature.<sup>6</sup> This suggests that effects due to local, rather than long-range, magnetic ordering may be occurring in these alloys. This would also account for the difference in the 304 alloy between the Néel temperature (40 K) and the

temperature below which anomalous elastic behavior is observed (80 K). Short-range magnetic-order effects have been discussed by Schlosser<sup>9</sup> for face-centered cubic iron-nickel alloys. Changes of crystal structure are probably not the cause of the anomalies since the changes were observed to be reversible within experimental error; changes of elastic constants due to crystal-structure changes are generally irreversible, showing a particularly large hysteresis in iron-base alloys. The elastic constants reported here showed a reversible behavior and indicate that the magnetic transition occurs smoothly over a range of temperatures rather than at a unique transition temperature. Thus, the transition seems to be of the second-order type.<sup>10</sup>

The usual so-called  $\Delta E$  effect, better designated  $\Delta E_\lambda$ , due to linear magnetostriction strains induced by an applied stress, and usually interpreted by invoking a Weiss domain model (with domain rotations and domain-wall motions) can also be excluded as a possible source of the anomalous elastic behavior. Linear magnetostriction affects Young's modulus, the shear modulus, and Poisson's ratio, but it does not affect the bulk modulus because no magnetomechanical process will respond to the application of a hydrostatic stress.<sup>11</sup> Also, effects due to  $\Delta E_\lambda$  are not observed at high frequencies<sup>12</sup> because the domain-wall displacements cannot follow the applied stress, and therefore cannot contribute an additional strain that lowers the observed elastic stiffness. Thus, for present purposes, a high-frequency applied stress is essentially equivalent to applying a saturating magnetic field; both nullify domain-wall contributions to the strain.

In the presence of a saturating magnetic field (or its effective equivalent), the only magnetic effect that alters  $E$ ,  $B$ , and  $\nu$  without affecting  $G$  is the effect due to spontaneous volume magnetostriction. This effect is designated  $\Delta E_\omega$ , where  $\omega = (V - V_p)/V_p$  is the spontaneous volume magnetostriction,  $V$  is the total volume, and  $V_p$  is the volume in the paramagnetic state. The effect was first reported by Engler<sup>13</sup> for an Fe-42 Ni alloy. It was explained first by Döring<sup>14</sup> using a thermodynamic analysis. Herein, this phenomenon will be called the Döring effect. Döring reasoned that in the paramagnetic region the elastic constant is measured at constant magnetization  $M$ , while in the ferromagnetic or antiferromagnetic region the elastic constant is measured at constant magnetic field  $H$ . Döring showed that the magnitude of the anomaly in the Young's modulus is given by:

$$\Delta E_{\omega}/E^2 = (1/E)_M - (1/E)_H = - \frac{1}{9} (\partial\omega/\partial H)_{\sigma,T}^2 / (\partial M/\partial H)_{\sigma,T}, \quad (10)$$

where  $\partial\omega/\partial H$  is the forced volume magnetostriction due to the magnetization,  $\partial M/\partial H$  is the high-field susceptibility  $\chi$ ,  $E^2$  is  $E_M E_H$ , and  $\sigma$  is the tensile stress. An alternative derivation of Eq. (10) was given by Hausch.<sup>15</sup> The factor of 1/9 in Eq. (10) is really  $(1 - 2\nu)^2$  where  $\nu$  is Poisson's ratio<sup>16</sup>; thus, 1/9 applies strictly only when  $\nu = 1/3$ . From the data in Fig. 5,  $\nu$  ranges from 0.27 to 0.31 for the materials and temperatures of interest here; thus 1/9 should be replaced by 0.17 as an average value for present purposes. It should be noted that the Döring effect always lowers the moduli ( $E_M > E_H$ ), whether the volume magnetostriction is positive or negative. This is related to the fact that a relaxation mechanism is involved in going to an antiferromagnetic state, and such mechanisms always soften the elastic stiffnesses. The Döring effect in iron-nickel alloys was discussed by Köster,<sup>17</sup> who denoted it as  $\Delta E_{\lambda}$  rather than as  $\Delta E_{\omega}$ . The effect has been invoked by several authors to explain elastic anomalies in magnetic materials, usually of the invar type. Hausch<sup>15</sup> criticized the relevance of the Döring effect in most of these cases. Schlosser<sup>18</sup> discussed the magneto-volume contribution to the compressibility of invar, but Hausch<sup>15</sup> showed that an exchange-energy contribution is also required in this case. The present data for iron-chromium-nickel (stainless steel) alloys seem to constitute a clear case of the Döring effect.

If the Döring effect is responsible for the elastic anomalies observed in stainless-steel-type alloys, then  $\Delta E_{\omega}$  calculated from Eq. (10) should agree roughly with the magnitude of the observed anomalies. Apparently, the volume magnetostriction of these alloys has not yet been determined. Using data for invar,<sup>15</sup> an iron alloy containing about 35 pct. Ni and having the same crystal structure as the alloys considered here, it is calculated from Eq. (10) that  $\Delta E_{\omega}/E^2 = - 1.4 \times 10^{-14} \text{ cm}^2/\text{dyn}$ . For the 304 stainless steel alloy, the present results give for the bulk modulus  $\Delta E/E^2 = - 0.2 \times 10^{-14} \text{ cm}^2/\text{dyn}$ . Thus, the observed anomalies show a reasonable correspondence to the magnitude of the predicted Döring effect. A more exact correspondence could be established if the volume magnetostrictions of these alloys were known. If the Döring effect is the correct interpretation of the data, then the volume magnetostriction of these alloys must be quite large since it is large in invar-type alloys. Besides invar and other iron-nickel alloys, large magneto-volume effects

have also been observed in iron-manganese, iron-palladium, iron-platinum, and iron-cobalt alloys.<sup>19</sup> A quantitative correspondence is also precluded because the alloys reported on here were studied in mechanically deformed states. Köster<sup>17</sup> showed that the  $\Delta E$  effect depends sensitively on metallurgical variables. The usual  $\Delta E = \Delta E_\lambda$  effect is usually suppressed by mechanical deformation. No studies seem to have been made on the effect of mechanical deformation on  $\Delta E_\omega$ . It would be expected that the  $\Delta E_\omega$  effect will be enhanced in annealed materials since the residual stresses due to mechanical deformation would not interfere with domain-wall motions.

The best parameter for evaluating the Döring effect is the bulk modulus, which characterizes purely dilatational elastic distortions. Shear distortions are isovolumic and should not change the magnitude of the magnetization. Young's modulus and Poisson's ratio are less satisfactory parameters in this case because they depend more on shear distortions than on dilatational distortions. Using the familiar relationship

$$E = 9GB/(G + 3B), \quad (11)$$

it follows from Eq. (10) that the defect in the bulk modulus due to the Döring effect is

$$\Delta B_\omega/B^2 = (1/B)_M - (1/B)_H = -9(1 - 2\nu)^2 (\partial\omega/\partial H)_{\sigma,T}^2 / (\partial M/\partial H)_{\sigma,T}, \quad (12)$$

where  $B^2 = B_H B_M$  and  $P$  is pressure. And from the relationship

$$\nu = [E/(2G)] - 1, \quad (13)$$

it follows that

$$\Delta\nu_\omega/\nu^2 = -\frac{1 + \nu}{\nu^2} \frac{(1 - 2\nu)^2}{E} (\partial\omega/\partial H)_{\sigma,T}^2 / (\partial M/\partial H)_{\sigma,T}, \quad (14)$$

and, of course,  $\Delta G_\omega = 0$ .

Alers, Neighbors, and Sato<sup>20</sup> have discussed the Döring effect as arising from the change in spontaneous magnetization due to volume changes resulting from the measurement process itself. Thus, this effect is not an intrinsic part

of the magnetization change, and it is not related fundamentally to the interatomic magnetic interaction. This is also clear from the work of Hausch,<sup>15</sup> who considered the Döring effect to be due to a stress-induced change in the magnetization intensity. (The usual fundamental magnetic energy terms are the exchange, anisotropy, magnetoelastic, and magnetostatic<sup>21</sup>; the latter vanishes for zero external field.) Since the elastic constants only have a practical meaning when they are being "measured," either in the laboratory or in a stress-bearing structure, the viewpoint of Alers et al. does not mean that the dashed curves in the figures are a more appropriate measure of the elastic constants. The thrust of the considerations of Alers et al. is that there is no fundamental interatomic interaction that would, if accounted for, predict the Döring effect. Recall that any energy term, magnetic or not, contributes to the elastic constants through its second spatial derivative. For the Döring effect there is an "extra" or "extrinsic" negative elastic constant that is not related to a fundamental energy term of the material. The more familiar  $\Delta E = \Delta E_\lambda$  effect is also not a fundamental magnetic effect in the sense discussed here.

It is interesting to note that if S and T are substituted for M and H in Eq. (12), then

$$\Delta B/B^2 = (1/B)_S - (1/B)_T = -\alpha^2/C_p, \quad (15)$$

which is a standard thermodynamic result,<sup>22</sup> where  $\alpha = (1/V)(\partial V/\partial T)_p$  and  $C_p = T(\partial S/\partial T)_p$ . This emphasizes the value of the thermodynamic approach to phenomena such as the Döring effect and suggests other thermodynamic correlations. For example, from the well-known relationship

$$B_S/B_T = C_p/C_v, \quad (16)$$

where  $C_v = T(\partial S/\partial T)_v$ , the corresponding relationship in magnetic variables is

$$B_M/B_H = \chi_p/\chi_v. \quad (17)$$

Thus, a model connecting  $\chi_p$  and  $\chi_v$ , the constant-pressure and constant-volume susceptibilities, would permit an estimate of the magnitude of  $\Delta B_\omega$ .

It was suggested by Hayes and Miodownik<sup>23</sup> that both  $\Delta E_\omega$  and  $\Delta B_\omega$  are proportional to  $B_M$ . The present data do not support this suggestion, but the effect could be masked by random errors arising from inhomogeneities, mechanical deformation, absence of a technically saturating magnetic field, etc.

Of the four alloys, the smallest elastic anomalies were observed in the 310 alloy and in the A286 alloy. These materials have a much higher nickel content. Thus, it is suggested that in stainless-steel-type alloys the effect of nickel is to reduce the volume magnetostriction but not to suppress the occurrence of the antiferromagnetic phase.

The desirability of further studies on these alloys, especially with respect to the Döring effect, is indicated. Ideally, carefully prepared alloy single crystals would be tested in magnetic fields.

Since changes in elastic constants are usually accompanied by significant changes in internal friction, it would also be interesting to study the low-temperature anelastic properties of these alloys. The magnitude of the mechanical damping determines the magnitude of stresses established in vibrating parts. And all of these alloys are candidate materials for low-temperature uses where vibrations may occur. Magnetomechanical hysteresis has already been established as an important damping mechanism in ferromagnetic materials.<sup>24</sup>

## V. CONCLUSIONS

From the results of the present study the following conclusions are drawn:

1. Stainless-steel alloys AISI 304, AISI 310, AISI 316, and A286 have qualitatively similar elastic-property variations with temperature.
2. The shear modulus behaves regularly over the entire temperature range studied.
3. The elastic constants with dilatational components -- Young's modulus, the longitudinal modulus, the bulk modulus, and Poisson's ratio -- behave regularly above about 80 K, but anomalously at lower temperatures. The anomalies are largest for the bulk modulus and smallest for Young's modulus.
4. The anomalies are largest in the AISI 304 and AISI 316 alloys and smallest in the AISI 310 and A286 alloys. A relationship between the magnitude of the anomaly and nickel content is suggested.
5. As suggested first by Döring, the anomalies can be interpreted thermodynamically as the difference between constant-magnetization and constant-field bulk moduli.



#### ACKNOWLEDGMENT

This work was supported in part by the Advanced Research Projects Agency of the Department of Defense.

#### REFERENCES

1. J. J. Gilman, Austral. J. Phys. 13, 327 (1960).
2. H. J. McSkimin, J. Acoust. Soc. Amer. 33, 12 (1961).
3. H. J. McSkimin and P. Andreatch, J. Acoust. Soc. Amer. 34, 609 (1962).
4. E. R. Naimon, W. F. Weston, and H. M. Ledbetter, Cryogenics 14, 246 (1974).
5. Y. P. Varshni, Phys. Rev. B2, 3952 (1970).
6. R. P. Mikesell and R. P. Reed, J. Res. Nat. Bur. Stds. (U.S.) 70C, 207 (1966).
7. P. E. Armstrong and D. T. Eash, in Advances in Cryogenic Engineering, Vol. 14 (K. D. Timmerhaus, ed., Plenum, New York, 1959), p. 64.
8. E. I. Kondorsky and V. L. Sedov, Sov. Phys. JETP 35, 1104 (1959).
9. W. F. Schlosser, J. Phys. Chem. Solids 32, 939 (1971).
10. J. W. Christian, The Theory of Transformations in Metals and Alloys (Pergamon, Oxford, 1965), p. 214.
11. W. F. Brown, Jr., Phys. Rev. 50, 1165 (1936).
12. R. M. Bozorth, W. P. Mason, and H. J. McSkimin, Bell Syst. Tech. Jour. 30, 970 (1951).
13. O. Engler, Ann. Phys. Leipz. 31, 145 (1938).
14. W. Döring, Ann. Phys. Leipz. 32, 465 (1938).
15. G. Hausch, Phys. Status solidi (a) 15, 501 (1973).
16. E. P. Wohlfarth, Phys. Status Solidi (a) 10, K39 (1972).
17. W. Köster, Z. Metallkde. 35, 194 (1943).
18. W. F. Schlosser, Phys. Status Solidi (a) 18, 235 (1973).
19. W. F. Schlosser, Intern. J. Magnetism 2, 167 (1972).

20. G. A. Alers, J. R. Neighbours, and H. Sato, J. Phys. Chem. Solids 13, 40 (1960).
21. C. Kittel, Rev. Mod. Phys. 21, 541 (1949).
22. L. D. Landau and E. M. Lifshitz, Theory of Elasticity (Pergamon, London, 1959), p. 17.
23. E. J. Hayes and A. P. Miodownik, Phys. Status Solidi (a) 10, K43 (1972).
24. A. Cochardt, Trans. Amer. Soc. Mech. Engrs. 75, A196 (1953).



## LIST OF TABLES

I.	Chemical analyses of the alloys, wt. pct., obtained from mill analyses . . . . .	257
II.	Densities and hardnesses of the alloys . . . . .	258
III.	Parameters in the temperature-dependence equation (6) . . . . .	259
IV.	Temperature coefficients of the elastic constants at room temperature ( $10^{-4} \text{ K}^{-1}$ ) . . . . .	260
V.	Elastic Debye temperatures at $T = 0 \text{ K}$ . . . . .	261

## LIST OF FIGURES

1.	Temperature dependence of the longitudinal moduli of four stainless-steel alloys . . . . .	262
2.	Temperature dependence of the transverse (shear) moduli of four stainless-steel alloys . . . . .	263
3.	Temperature dependence of the Young's moduli of four stainless-steel alloys . . . . .	264
4.	Temperature dependence of the bulk moduli (reciprocal compressibilities) of four stainless-steel alloys . . . . .	265
5.	Temperature dependence of Poisson's ratios of four stainless-steel alloys . . . . .	266

Table I. Chemical analyses of the alloys, wt. pct., obtained from mill analyses

Alloy	Al	C	Cr	Cu	Mo	Mn	Ni	P	S	Si	Ti	V	Fe
304		.02	18.4			1.4	9.7	.02	.01	.6			Bal
310		.08	24.8	.1	.1	1.7	20.8	.02	.02	.7			Bal
316		.05	16.8	.2	2.1	1.9	11.7	.03	.02	.4			Bal
A286	.2	.04	14.8		1.2	1.4	25.4	.01	.01	.6	2.1	.3	Bal

Table II. Densities and hardnesses of the alloys

Alloy	Mass density (g/cm <sup>3</sup> )	Hardness (DPHN, 1 kg load)
304	7.86	225
310	7.85	220
316	7.97	210
A286	7.95	275

Table III. Parameters in the temperature-dependence equation (6)

Alloy	Mode	$C^0$ ( $10^{11} \text{ N/m}^2$ )	$s$ ( $10^{11} \text{ N/m}^2$ )	$t$ (K)
304	$\ell$	2.608	0.297	371.8
	$t$	0.803	0.089	251.8
310	$\ell$	2.647	0.175	271.8
	$t$	0.767	0.051	173.7
316	$\ell$	3.028	0.332	369.7
	$t$	0.914	0.099	243.5
A286	$\ell$	2.636	0.334	454.4
	$t$	0.809	0.080	243.1

Table IV. Temperature coefficients of the elastic constants at room temperature ( $10^{-4} \text{ K}^{-1}$ )

Alloy	$\frac{1}{B} \frac{dB}{dT}$	$\frac{1}{E} \frac{dE}{dT}$	$\frac{1}{G} \frac{dG}{dT}$	$\frac{1}{\nu} \frac{d\nu}{dT}$
304	-1.69	-4.15	-4.54	1.78
310	-1.39	-3.71	-4.05	1.45
316	-1.41	-4.17	-4.61	1.89
A286	-1.22	-3.77	-4.18	1.81

Table V. Elastic Debye temperatures at  $T = 0$  K

Alloy	$\theta$ (K) magnetic	$\theta$ (K) extrapolated paramagnetic
304	467.8	468.1
310	459.0	459.0
316	496.7	496.8
A286	467.6	467.7
Iron (bcc) <sup>a</sup>	472.4	
Chromium <sup>b</sup>	453.0	
Nickel <sup>a</sup>	476.0	

<sup>a</sup> R. Wanner, Can. J. Phys. 48, 1270 (1970).

<sup>b</sup> F. H. Herbstein, Adv. Phys. 10, 313 (1961).

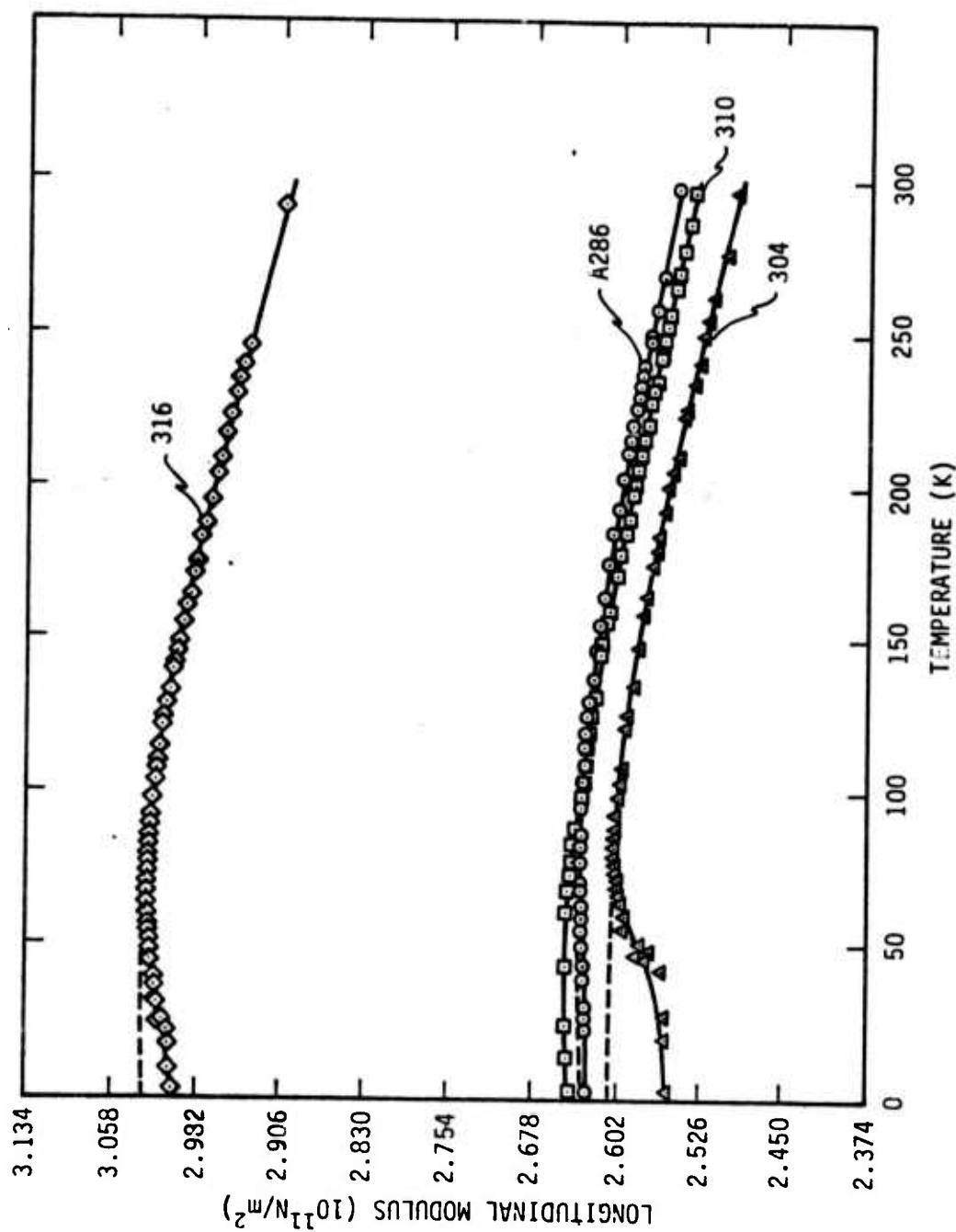


Figure 1. Temperature dependence of the longitudinal modulus of four stainless-steel alloys.

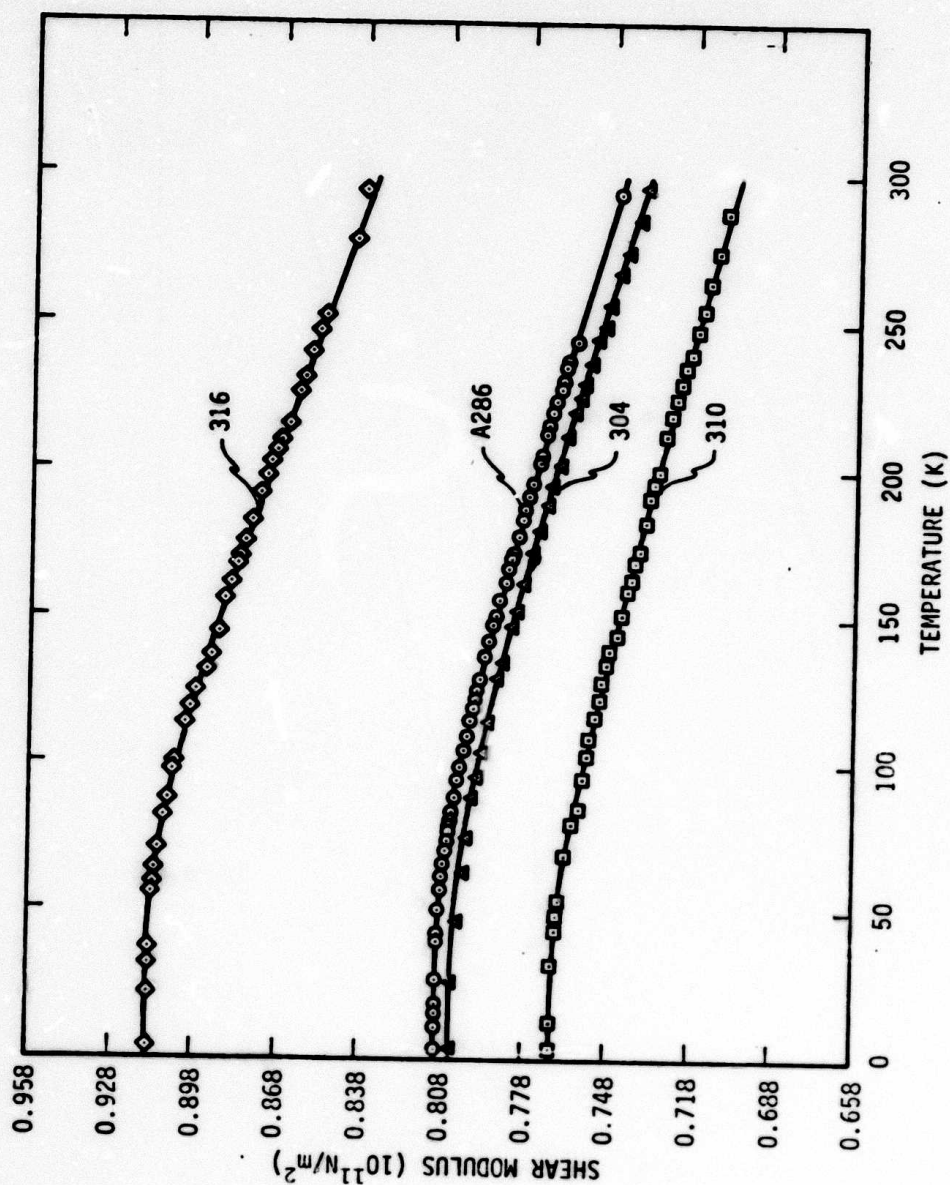


Figure 2. Temperature dependence of the transverse (shear) moduli of four stainless-steel alloys.



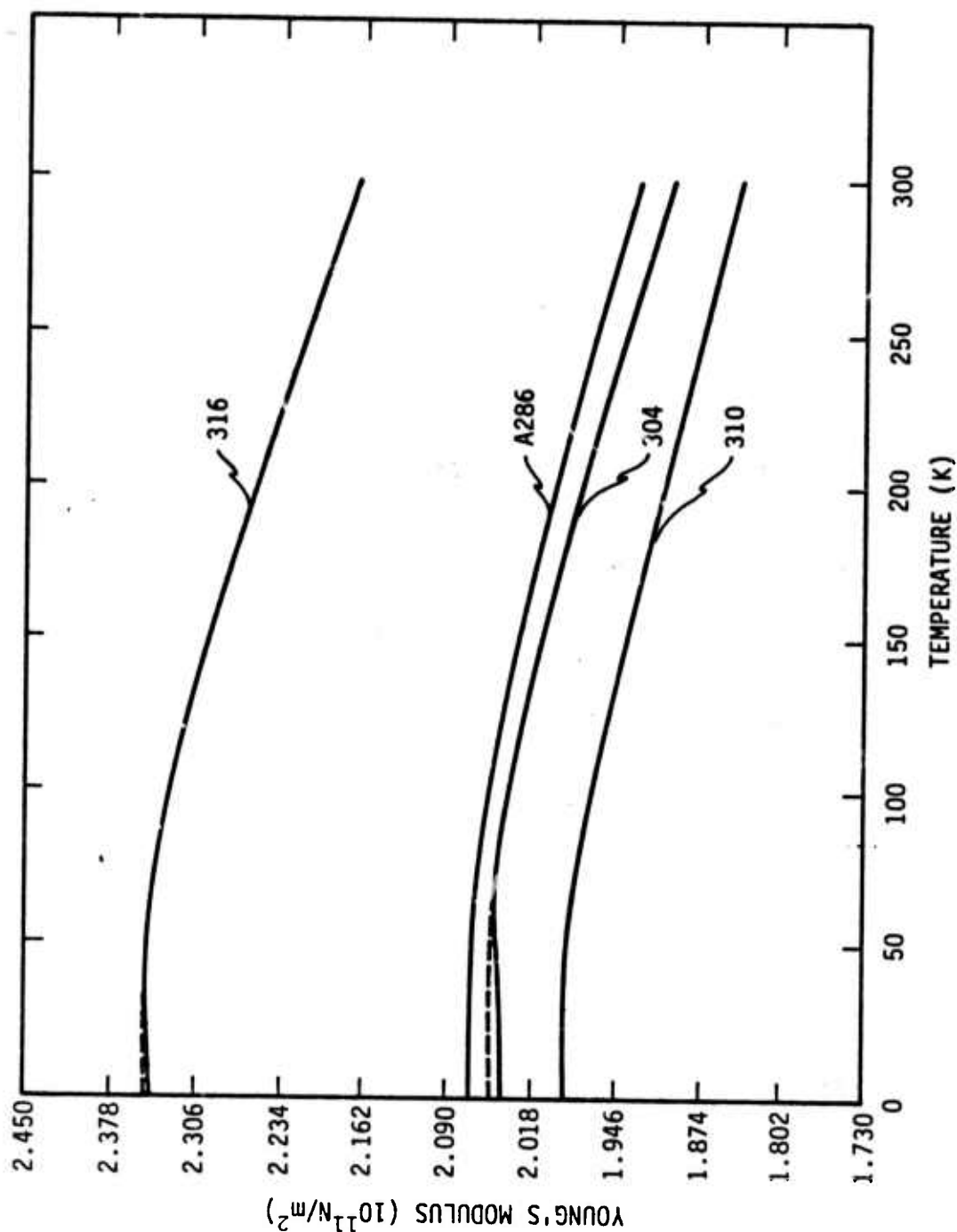


Figure 3. Temperature dependence of the Young's moduli of four stainless-steel alloys.

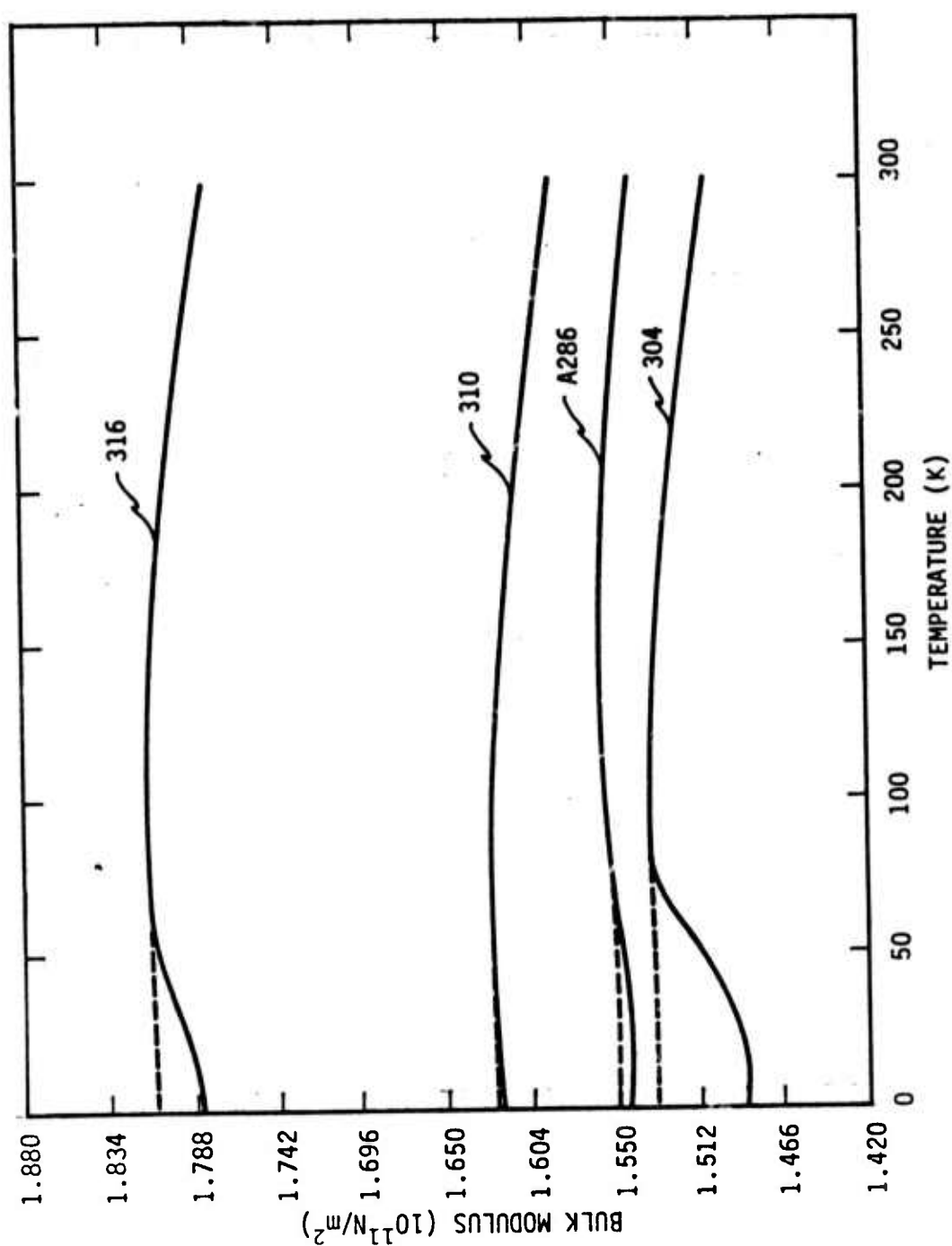


Figure 4. Temperature dependence of the bulk moduli (reciprocal compressibilities) of four stainless-steel alloys.

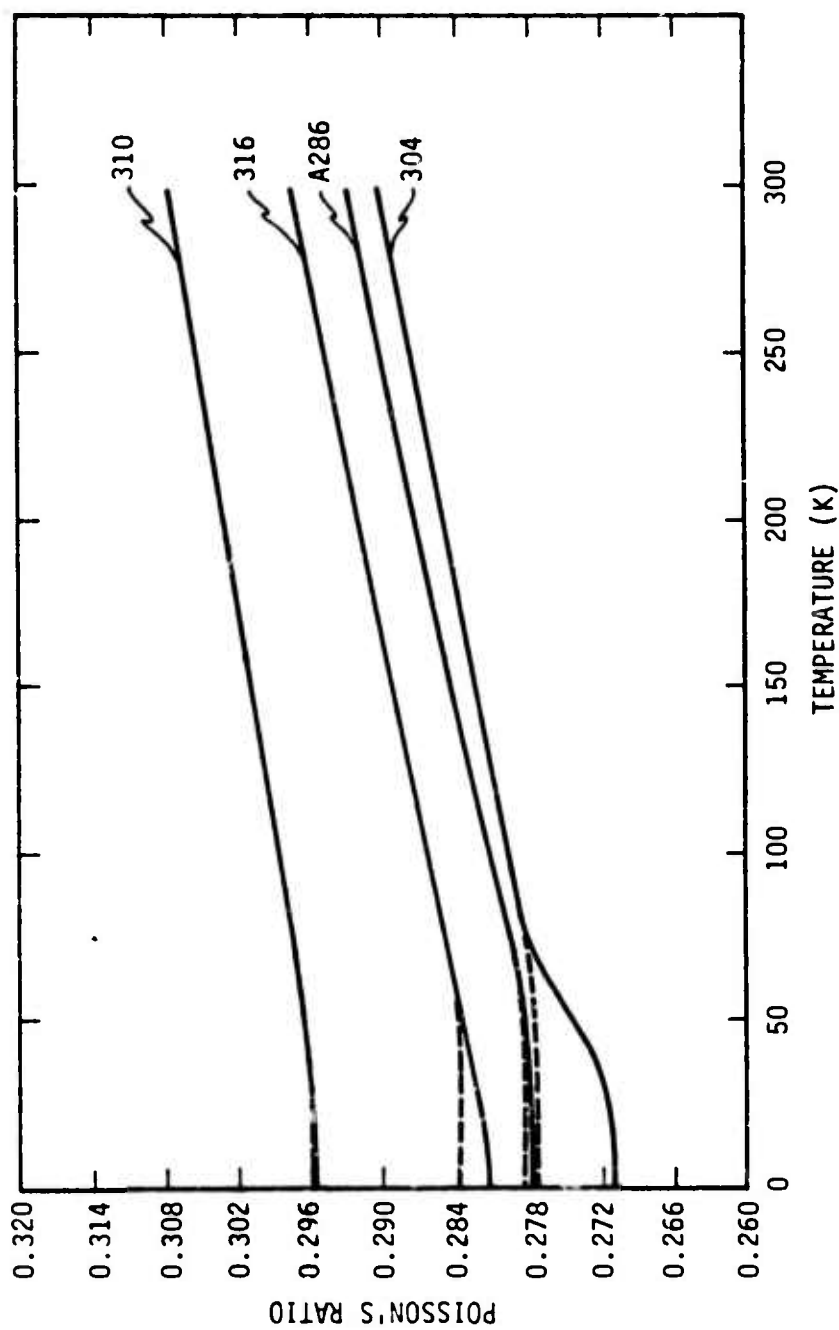


Figure 5. Temperature dependence of Poisson's ratio of four stainless-steel alloys.

## ELASTIC PROPERTIES OF INVARI

### List of Figures -- Invar

	Page
1. Temperature dependence of the longitudinal modulus of invar (Fe-35Ni) . . . . .	268
2. Temperature dependence of the shear modulus of invar (Fe-35Ni) . . . .	269
3. Temperature dependence of Young's modulus of invar (Fe-35Ni) . . . .	270
4. Temperature dependence of the bulk modulus of invar (Fe-35Ni) . . . .	271
5. Temperature dependence of Poisson's ratio of invar (Fe-35Ni) . . . .	272

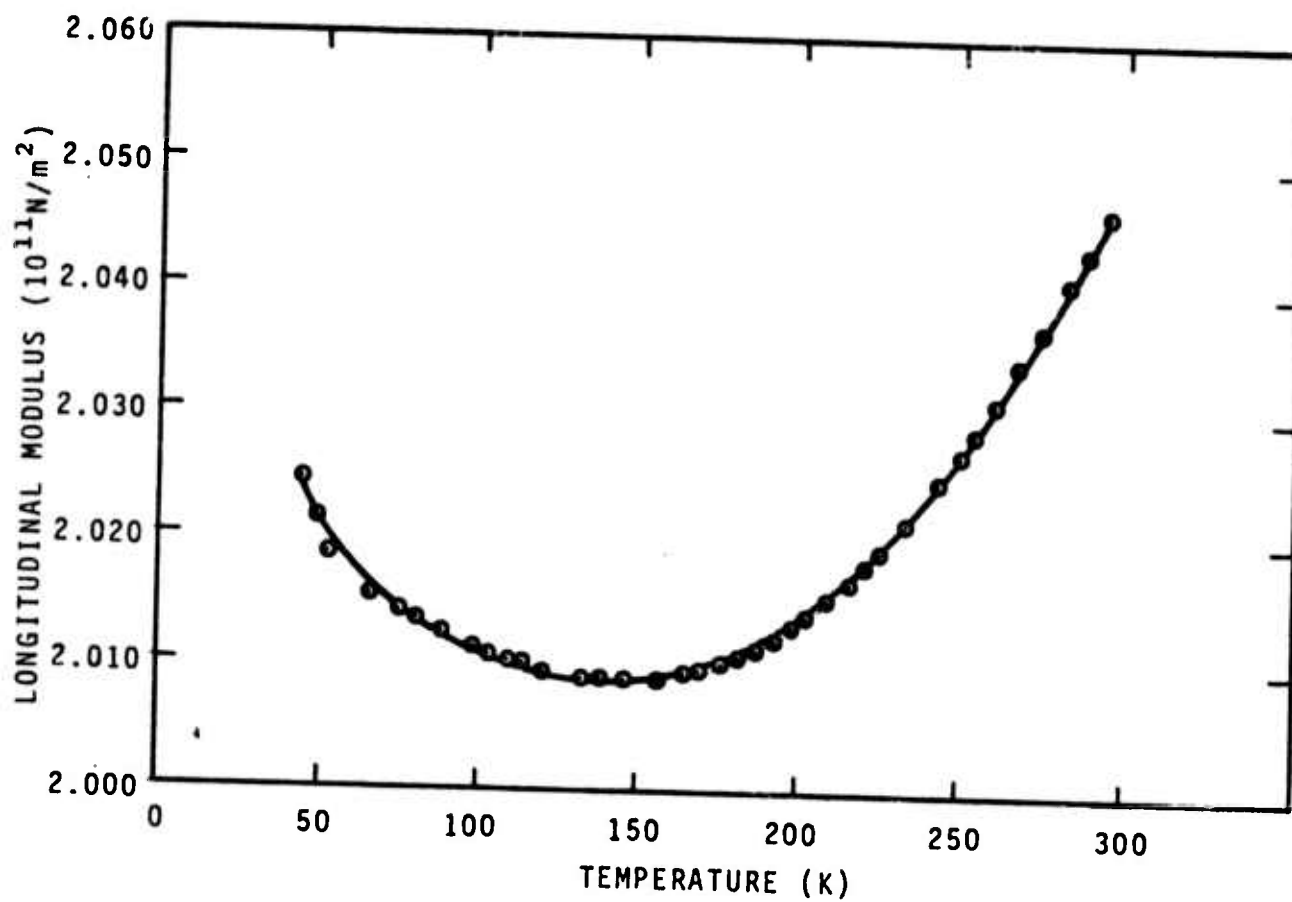


Figure 1. Temperature dependence of the longitudinal modulus of Invar (Fe-35Ni)

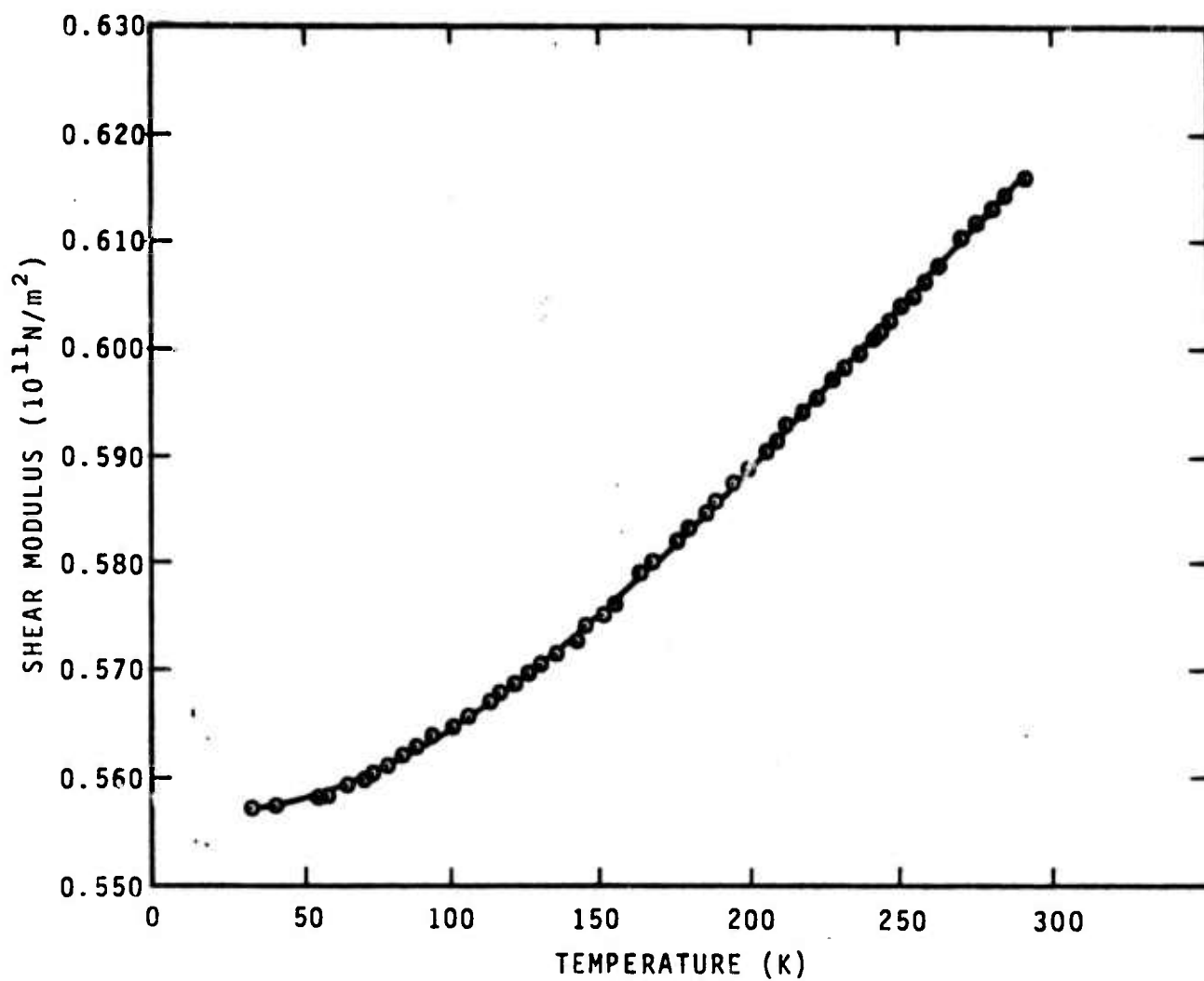


Figure 2. Temperature dependence of the shear modulus of invar (Fe-35Ni)

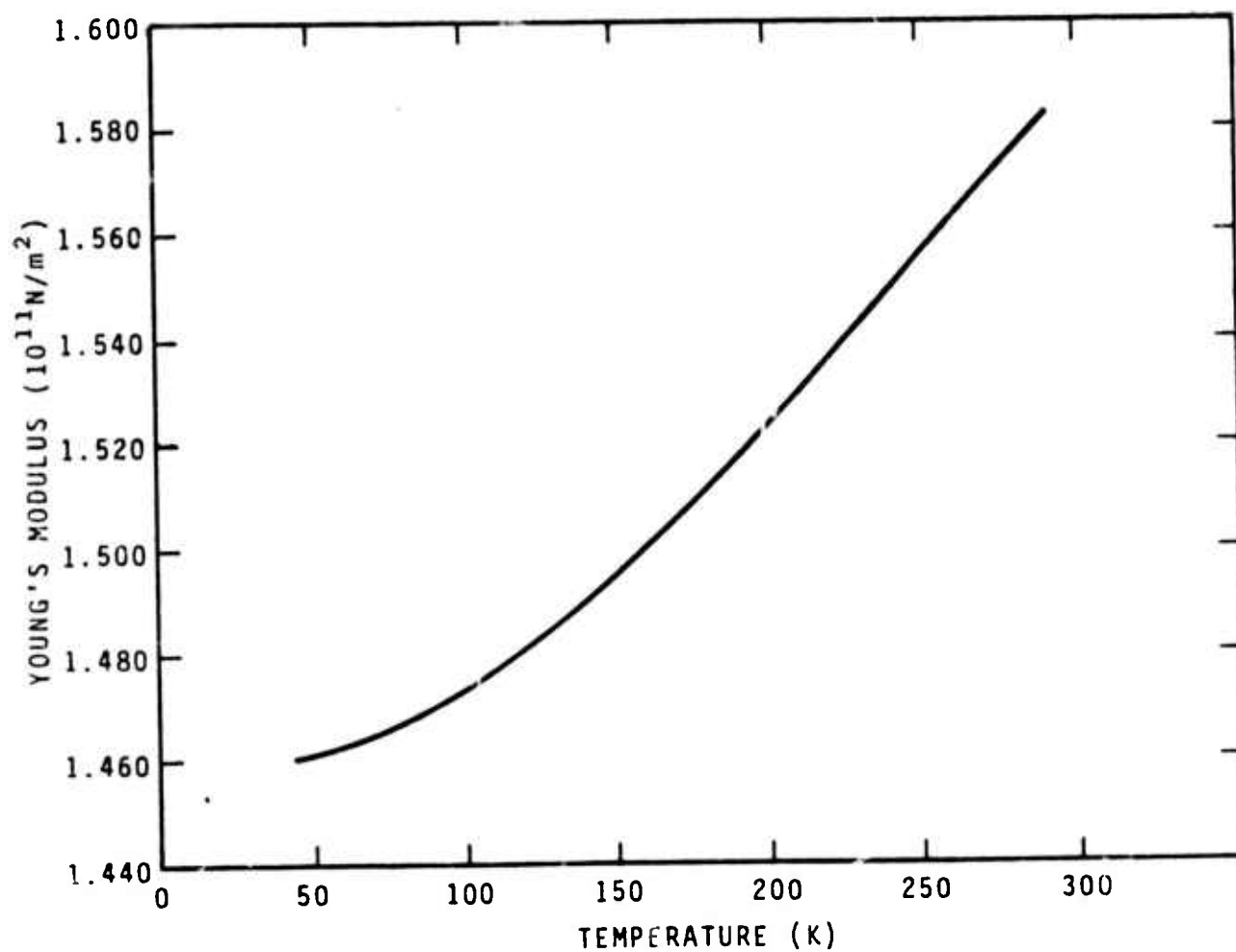


Figure 3. Temperature dependence of Young's modulus of invar (Fe-35Ni)

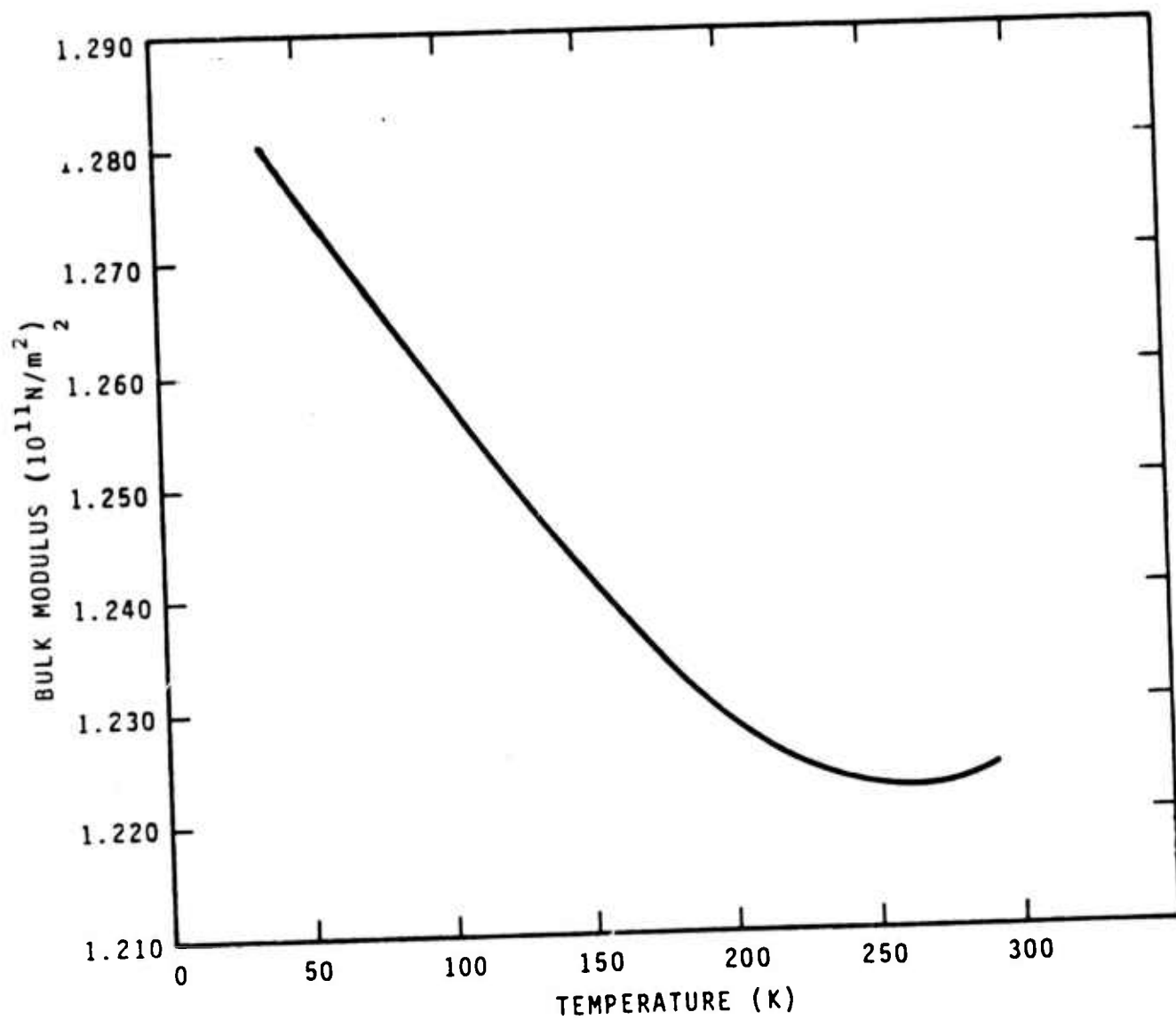


Figure 4. Temperature dependence of the bulk modulus of invar (Fe-35Ni)



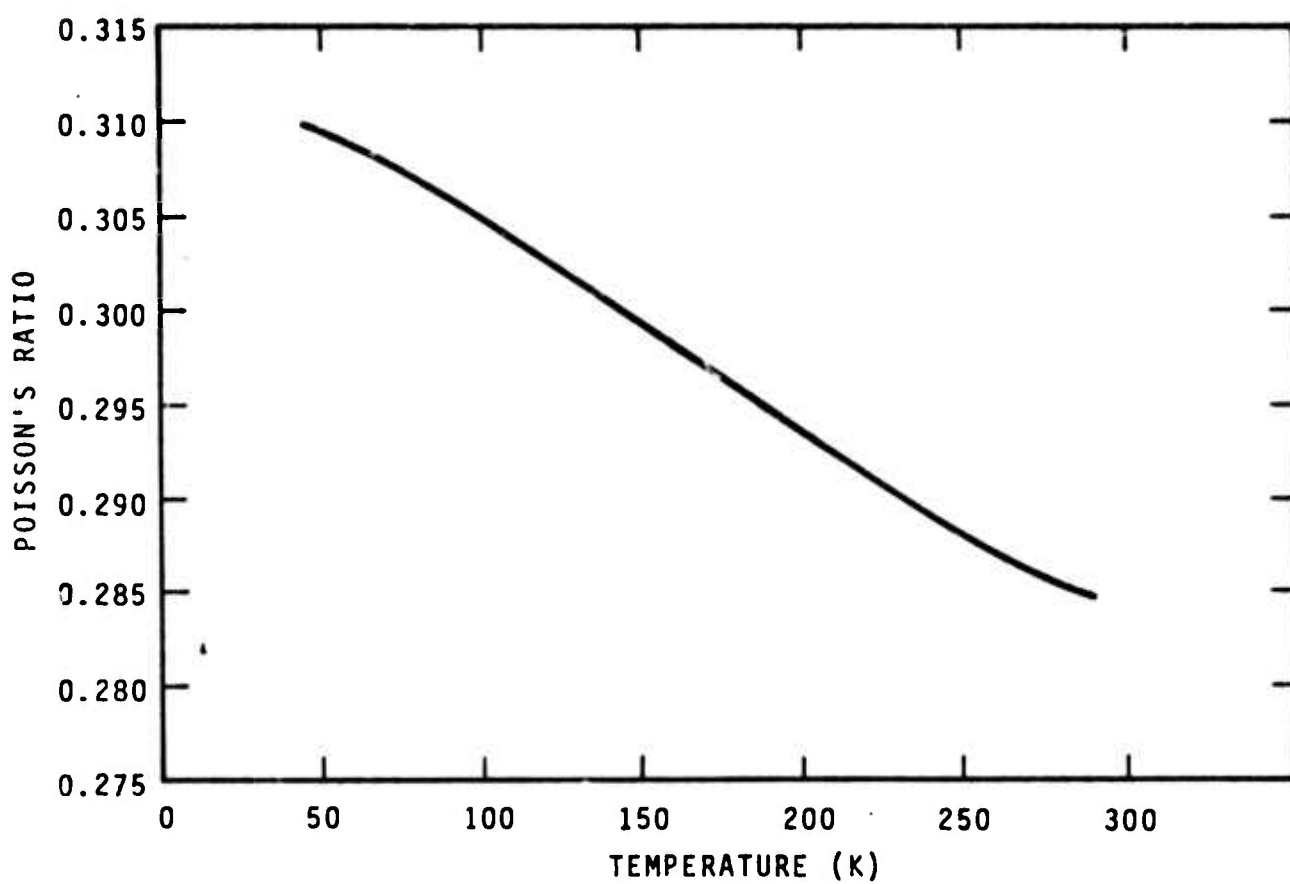


Figure 5. Temperature dependence of Poisson's ratio of invar (Fe-35Ni)

Appendix A

Sound velocities and elastic constants were determined semi-continuously for two annealed polycrystalline titanium alloys between 4 and 300 K. Results are given for: longitudinal sound velocity, transverse sound velocity, Young's modulus, shear modulus, bulk modulus, Poisson's ratio, and elastic Debye temperature. A pulse-superposition technique was used.

## Elastic properties of two titanium alloys at low temperatures

E. R. Naimon, W. F. Weston, and H. M. Ledbetter

Despite the fact that titanium alloys Ti-6Al-4V and Ti-5Al-2.5Sn are intended mainly for high strength, high temperature applications, they also have cryogenic uses. Their important properties include: ease of fabrication, corrosion resistance, high strength-to-density ratios (especially at cryogenic temperatures), and high strength-to-thermal-conductivity ratios.

The low temperature elastic properties of these alloys are reported here. A pulse-superposition method was used to determine the ultrasonic wave velocities in annealed specimens. From longitudinal and transverse wave velocities, together with the mass density, the elastic constants were calculated. Young's modulus, shear modulus, bulk modulus (reciprocal compressibility), Poisson's ratio, and the elastic Debye temperature. These constants are useful in a wide variety of applications, from engineering design to equations of state for solids.

### Experimental procedures

Alloys were obtained from commercial sources in the form of  $\frac{1}{8}$  in (1.9 cm) diameter rods. Cylindrical specimens  $\frac{5}{16}$  in (1.6 cm) in diameter and  $\frac{5}{8}$  in (1.6 cm) long were prepared by grinding. Opposite faces were flat and parallel within  $100 \times 10^{-6}$  in (2.5  $\mu$ m). Specimens were annealed at a pressure of  $5 \times 10^{-6}$  torr, or less, and cooled in the furnace. Annealing times and temperatures are given in Table I, together with chemical compositions (obtained from mill analyses), hardness numbers, microstructures, grain sizes, and mass densities. Hardness, microstructure, and grain size were determined by standard metallurgical methods. Mass density was determined by Archimedes' method using distilled water as a standard.

The specimen holder is shown in Fig. 1. The holder was placed in the ullage of a helium dewar and lowered stepwise to achieve cooling. Temperatures were monitored with a chromel-constantan thermocouple contacting the specimen.

Quartz transducers (10 MHz) were bonded to the specimens with phenyl salicylate for room-temperature measurements and with a stopcock grease for lower temperatures. In a few cases, failure of these bonds at very low temperatures required using a silicone fluid (viscosity = 200 000 cP at 25°C) for bonding.

The authors are with the Cryogenics Division, Institute for Basic Standards, National Bureau of Standards, Boulder, Colorado 80302, USA. ERN and WFW are NRC-NBS Postdoctoral Research Associates for 1973-74. Received 28 December 1973.

A pulse-superposition method<sup>1,2</sup> was used to determine the sound-wave velocities over the temperature range 4–300 K. No thermal contraction corrections were made; for titanium alloys this introduces a maximum error (over a 300 K range) of about 0.2%. No bond corrections were made; this error is insignificant for the purposes of the present study. Maximum uncertainties in the velocity measurements are estimated to be about 1%.

### Results

Longitudinal and transverse sound-wave velocity data are shown in Figs 2 and 3, where the longitudinal modulus is given by

$$C_l = \rho v_l^2 = B + \frac{4}{3} G \quad (1)$$

and the transverse modulus is given by

$$C_t = \rho v_t^2 = G \quad (2)$$

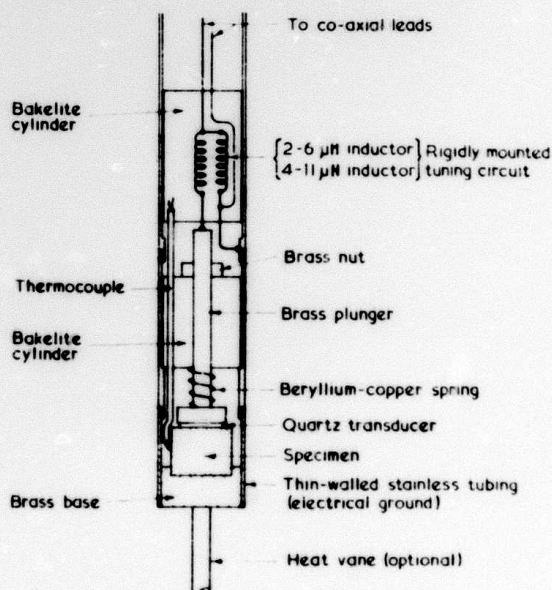
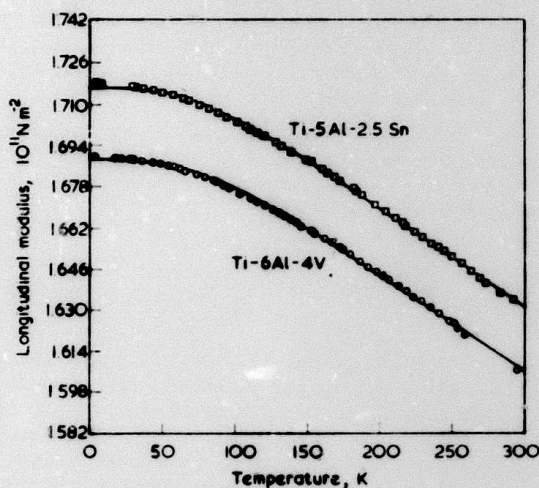


Fig. 1 Specimen holder

**Table 1** Compositions and properties of alloys

Alloy	Chemical composition, mill analyses, wt %								Hardness (DPH No 1000 g load)	Grain size, average dia, mm	Mass density at 294 K, g cm <sup>-3</sup>	Conditions	Microstructure
	Ti	Al	V	Sn	Fe	C	N	H					
Ti-6Al-4V	Balance	6.2	4.0	—	0.1	0.01	0.01	0.01	320	0.005	4.42	Annealed (800 °C, 2 h)	Equiaxed alpha grains with inter- granular beta
Ti-5Al-2.5Sn	Balance	5.5	—	2.5	0.2	0.07	—	0.02	330	0.02	4.47	Annealed (816 °C, 1/2 h)	Equiaxed alpha grains in a mottled dark etching (Kroll's re- agent) matrix phase, pro- bably acicular alpha



**Fig. 2** Longitudinal modulus  $C_1 = \rho v_l^2$  of two titanium alloys

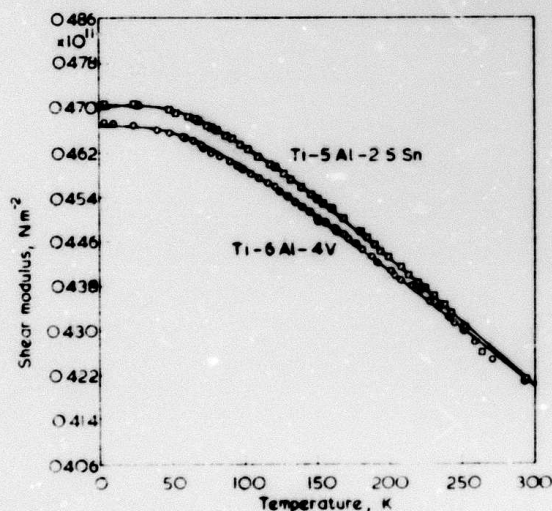


**Fig. 3** Transverse or shear modulus  $C_2 = G = \rho v_t^2$  of two titanium alloys

**Table 2** Parameters in equation 3

Alloy	$C^0$ , Mode $10^{11}$ N m <sup>-2</sup>	$s$ , $10^{11}$ N m <sup>-2</sup>	$t$ , K
Ti-6Al-4V	$\rho v_l^2$ 1.688	0.085	213.7
	$\rho v_t^2$ 0.467	0.039	183.6
Ti-5Al-2.5Sn	$\rho v_l^2$ 1.716	0.085	208.8
	$\rho v_t^2$ 0.470	0.051	210.4

**Table 3** Temperature derivatives of elastic constants at room temperature ( $10^{-4}$  K<sup>-1</sup>)

Alloy	$\frac{1}{B} \frac{dB}{dT}$	$\frac{1}{E} \frac{dE}{dT}$	$\frac{1}{G} \frac{dG}{dT}$	$\frac{1}{\nu} \frac{d\nu}{dT}$
Ti-6Al-4V	-1.01	-4.44	-4.90	1.89
Ti-5Al-2.5Sn	-0.75	-4.99	-5.55	2.26
Pure Ti*	-0.93	-6.63	-7.15	2.80

\*Calculated from data in reference 5 using a Voigt-Reuss-Hill average.

Here  $v_l$  and  $v_t$  are the longitudinal and transverse sound-wave velocities,  $\rho$  is the mass density,  $B$  is the bulk modulus, and  $G$  is the shear modulus.

Temperature dependences of both  $C_1$  and  $C_2$  were fitted to a semi-theoretical relationship suggested by Varshni<sup>3</sup>

$$C = C^0 \frac{s}{e^{t/T} - 1} \quad (3)$$

where  $C^0$ ,  $s$ , and  $t$  are adjustable parameters and  $T$  is temperature. The value of  $C$  at  $T = 0$  K is  $C^0$ , and  $s/t$  is the high temperature limit of the temperature derivative  $dC/dT$ . By invoking an Einstein oscillator model of solids it can be shown (in the absence of electronic effects) that  $t$  is the Einstein characteristic temperature. Parameters  $C^0$ ,  $s$ , and  $t$  are given in Table 2. Room temperature values of the temperature coefficients of the elastic moduli are given in Table 3.



Curves in Figs 2 and 3 are plots of (3) determined by an unweighted least-squares fit of the data. Average percentage differences between measured and curve values are 0.03% and 0.07% for the longitudinal and transverse moduli, respectively.

While polycrystalline aggregates (quasi-isotropic solids) have only two independent elastic constants, several constants are commonly used for various applications. The four most common are the bulk modulus  $B$ , Young's modulus  $E$ , the shear modulus  $G$ , and Poisson's ratio  $\nu$ . The relationships among these are

$$\frac{1}{E} = \frac{1}{3G} + \frac{1}{9B} \quad (4)$$

and

$$\nu = \frac{E}{2G} - 1 \quad (5)$$

These elastic constants were calculated from the moduli shown in Figs 2 and 3 by the relationships

$$E = \frac{3C_l \left( C_l - \frac{4}{3} C_t \right)}{C_l - C_t} \quad (6)$$

$$B = C_l - \frac{4}{3} C_t \quad (7)$$

and

$$\nu = \frac{1}{2} \left( \frac{C_l - 2C_t}{C_l - C_t} \right) \quad (8)$$

The constants  $E$ ,  $B$ , and  $\nu$  are shown in Figs 4–6.

The elastic Debye temperature  $\theta$  is of fundamental importance in the lattice properties of solids and is related to the elastic wave velocities by <sup>4</sup>

$$\theta = K \langle v \rangle \quad (9)$$

where

$$K = \frac{h}{k} \left( \frac{3N\rho}{4\pi A} \right)^{1/3} \quad (10)$$

Here  $h$  is Planck's constant,  $k$  is Boltzmann's constant,  $N$  is Avogadro's constant,  $\rho$  is the mass density, and  $A$  is the atomic weight. The average velocity is given by

$$\langle v \rangle = \left( \frac{v_l^{-3} + 2v_t^{-3}}{3} \right)^{-1/3} \quad (11)$$

The Debye temperatures for the two alloys at  $T = 0$  K, and also for pure titanium, are given in Table 4.

## Discussion

The elastic properties of both Ti-6Al-4V and Ti-5Al-2.5Sn behave regularly with respect to temperature. All of the elastic moduli ( $C_l$ ,  $C_t$ ,  $G$ ,  $B$ ,  $E$ ) decrease with increasing

**Table 4** Elastic Debye temperatures at  $T = 0$  K

Alloy	$\theta$ , K
Ti-6Al-4V	418.1
Ti-5Al-2.5Sn	416.9
Pure Ti	425.7*

\*Reference 5

temperature, show a relative flatness at low temperatures, achieve zero slope at  $T = 0$ , and approach linear behaviour at high temperatures. Poisson's ratio also behaves regularly, having a positive temperature coefficient.

Assuming that the specimens studied are representative of the two alloys, then conclusions concerning their relative elastic behaviour can be drawn. Not surprisingly, as shown in Figs 2–6 and Tables 2 and 3, for most practical purposes the two alloys are elastically identical. Thus, whether the second alloying element is vanadium or tin, the elastic properties are essentially the same.

As is well known, titanium undergoes a cph to bcc ( $\alpha$  to  $\beta$ ) crystal-structure transition when heated to 1155 K. Fisher and Renken <sup>5</sup> found a large temperature dependence of the  $c_{66}$  shear modulus in titanium

$$\frac{1}{c_{66}} \frac{dc_{66}}{dT} = -11.93 \times 10^{-4} \text{ K}^{-1}$$

A small value of  $c_{66}$  is expected from the shear mechanism of a cph to bcc transition proposed by Burgers.<sup>6</sup> For hexagonal symmetry, the shear modulus  $G$  is an approximate average of the two single-crystal shear constants  $c_{66}$  and  $c_{44}$ . Thus, from the smaller values of  $(1/G)(dG/dT)$  in Table 3 one can infer that both alloys have higher cph to bcc transition temperatures than pure titanium. That is, the  $\alpha$ -titanium phase is stabilized in the alloys. As shown in Hansen and Anderko,<sup>7</sup> aluminium is a strong stabilizer of  $\alpha$  titanium, while both vanadium and tin are moderate stabilizers of  $\beta$  titanium.

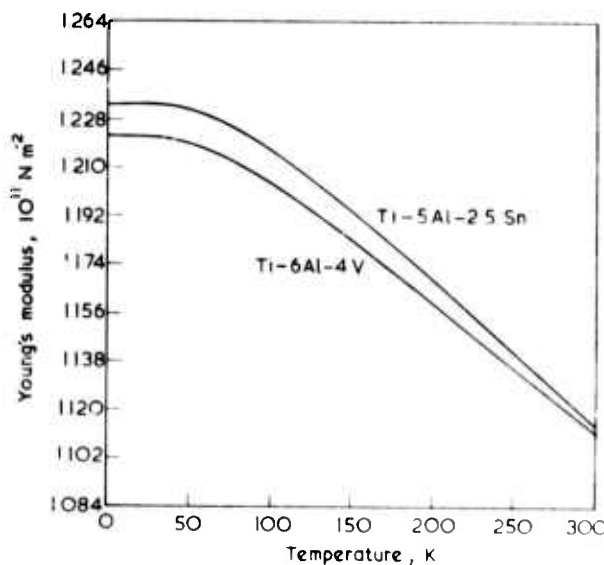


**Fig. 4** Young's modulus of two titanium alloys

**Table 5** Comparison of present and previously reported results; room temperature values; units of  $10^{11}$  N m<sup>-2</sup> except  $\nu$  (dimensionless)

Source	Ti-5Al-2.5Sn				Ti-6Al-4V			
	<i>E</i>	<i>G</i>	<i>B</i>	$\nu$	<i>E</i>	<i>G</i>	<i>B</i>	$\nu$
Reference 12	—	—	—	—	1.11	0.421	1.06	0.325
Reference 8	1.14	—	—	—	—	—	—	—
Reference 9	0.96–1.17	—	—	—	1.07–1.21	0.421	—	—
Reference 10	1.07	—	1.07	—	1.10	—	1.13	—
Reference 11	1.10	—	—	—	1.03	—	—	—
Present	1.11	0.420	1.07	0.327	1.11	0.420	1.05	0.323

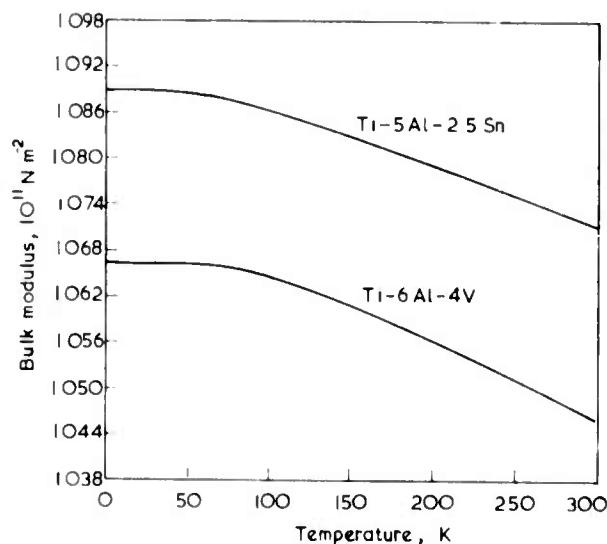


**Fig.5** Bulk modulus (reciprocal compressibility) of two titanium alloys

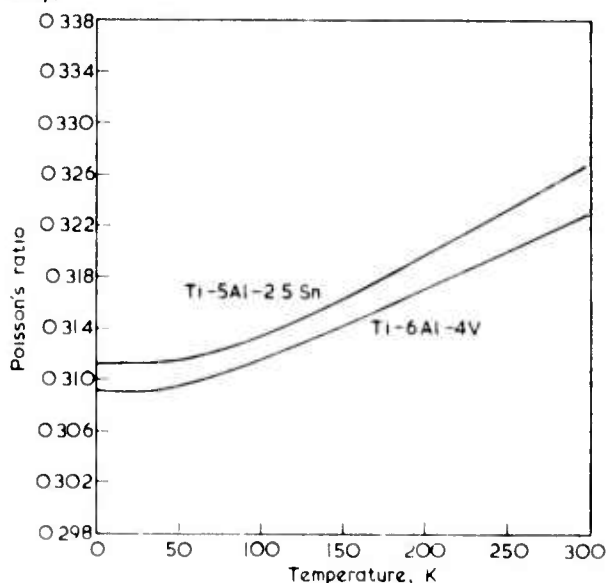


**Fig.6** Poisson's ratio of two titanium alloys

Despite the extensive use of these alloys, very little elastic data exist for them. Most information has appeared in engineering reports and is summarized in references 8–12. For comparison, the room temperature values of *E*, *G*, *B*, and  $\nu$  are given in Table 5. Generally good agreement is observed between previous and present results.

The elastic moduli of both alloys are several percent higher than those reported for commercial-grade titanium.<sup>12</sup> But they are lower by several percent than the quasi-isotropic

moduli obtained from a Voigt–Reuss–Hill average of the data obtained from zone-refined single crystals.<sup>5</sup> The elastic Debye temperatures of the alloys are also about 2% lower than that calculated from the single-crystal elastic data of titanium. The relatively low elastic anisotropy of titanium does not allow for a large error in the Voigt–Reuss–Hill averages. Thus, existing data suggest a strong impurity effect on the elastic constants of titanium, perhaps due to interstitial impurities.

Finally, it is emphasized that the data reported here are dynamic (adiabatic) rather than static (isothermal) and apply to rapid, rather than slow, loading. In most cases the differences between adiabatic and isothermal elastic constants are small. Conversion formulas are given in Landau and Lifshitz,<sup>13</sup> for example. For titanium at room temperature

$$\frac{E_S - E_T}{E_S} = 0.001 \quad \frac{B_S - B_T}{B_S} = 0.009$$

$$\frac{\nu_S - \nu_T}{\nu_S} = 0.005 \quad \text{and} \quad \frac{G_S - G_T}{G_S} \approx 0$$

where subscripts S and T denote adiabatic and isothermal, respectively.

This work was supported in part by the Advanced Research Projects Agency of the Department of Defense and was monitored by the Cryogenics Division, NBS, Boulder under contract No 2569.

## References

- McSkimin, H. J. *J Acoust Soc Amer* 33 (1961) 12
- McSkimin, H. J., Andreatch, P. *J Acoust Soc Amer* 34 (1962) 609
- Varshni, Y. P. *Phys Rev B2* (1970) 3952
- Debye, P. *Ann Phys (Leipzig)* 39 (1912) 789
- Fisher, E. S., Renken, C. J. *Phys Rev* 135 (1964) A482
- Burgers, W. G. *Physica* 1 (1934) 561
- Hansen, M., Anderko, K. *Constitution of Binary Alloys* (McGraw Hill, New York, 1958)
- Metals Handbook, 8th edn, Vol 1: Properties and Selection of Metals (Amer Soc Metals, Metals Park, Ohio, 1961)
- Cryogenic Materials Data Handbook, AFML Rep No ML-1DR-64-280 (PB 171809, revised, 1964)
- NERVA Program Materials Properties Data Book, Vol 1: Introduction and Light Metal Alloys (Aerojet Nuclear Systems, Sacramento, Calif, 1970)
- Hanlein, S. L., Hincley, W. M., Stecher, E. P. *NO TR Report* 70-141 (1970)
- Fahey, N. H. *WAL Tech Rep No TR 118.1/1* (1960)
- Landau, L. D., Lifshitz, E. M. *Theory of Elasticity* (Pergamon, London 1959) 17

U.S. DEPT. OF COMM. <b>BIBLIOGRAPHIC DATA SHEET</b>		1. PUBLICATION OR REPORT NO. <b>NBSIR74- 393</b>	2. Gov't Accession No.	3. Recipient's Accession No.
4. TITLE AND SUBTITLE <b>Semi-Annual Report on Materials Research in Support of Superconducting Machinery</b> <b>by Reed, Durcholz, Fickett, Giarratano, Hust, Kasen</b>			5. Publication Date <b>October 1974</b>	
			6. Performing Organization Code <b>275.03</b>	
7. AUTHOR(S) <b>Ledbetter, Mikesell, Naimon, Schramm, Sparks Tobler, and Weston</b>			8. Performing Organ. Report No.	
9. PERFORMING ORGANIZATION NAME AND ADDRESS  <b>NATIONAL BUREAU OF STANDARDS, Boulder Labs. DEPARTMENT OF COMMERCE WASHINGTON, D.C. 20234</b>			10. Project/Task/Work Unit No. <b>2756530</b>	
			11. Contract/Grant No. <b>ARPA Order No. 2569</b>	
12. Sponsoring Organization Name and Complete Address (Street, City, State, ZIP) <b>Advanced Research Projects Agency Department of Defense Washington, D. C.</b>			13. Type of Report & Period Covered	
			14. Sponsoring Agency Code <b>ARPA</b>	
15. SUPPLEMENTARY NOTES				
16. ABSTRACT (A 200-word or less factual summary of most significant information. If document includes a significant bibliography or literature survey, mention it here.) <b>Results of six months of study on Materials Research in Support of Superconducting Machinery (April through September, 1974) are reported to the sponsor, the Advanced Research Projects Agency of the U.S. Department of Defense. The report is divided into five sections: thermal conductivity, magnetothermal conductivity, fatigue and fracture-toughness properties, properties of advanced composites, and elastic properties. The temperature range 4 to 300 K is covered by the study. Materials studied are either being used or are candidates for use in superconducting machinery and include: aluminum alloys, composites, inconels, OFHC copper, stainless steels, and titanium alloys.</b>  <b>Special results of the study include: fracture-toughness and fatigue-crack growth-rate data for AISI 310, Ti-5 Al-2.5 Sn, A286 stainless steel, and Inconel 750 at 4, 76, and 300 K; initial reports of tensile testing of composites at 4 K; a second review paper on advanced-composite low-temperature behavior; magnetothermal conductivity measurements on OFHC copper and Inconel 718 indicate that, in a magnetic field, the thermal conductivity may change by 100 percent; anomalous low-temperature elastic behavior of AISI 300 series stainless-steel alloys; and thermal conductivity data for OFHC copper, Inconel 750, and Inco Low-Expansion-Alloy. These data provide considerable insight into material characteristics at extremely low temperatures, assisting</b>				
17. KEY WORDS in material selection and efficient design. <i>(name; separated by semicolons)</i> <b>elastic properties; Composites; fracture; liquid helium; mechanical properties; structural materials; superconducting machinery; thermal conductivity.</b>				
18. AVAILABILITY <input type="checkbox"/> Unlimited		19. SECURITY CLASS (THIS REPORT)  <b>UNCLASSIFIED</b>		21. NO. OF PAGES
<input type="checkbox"/> <del>Order From Sup. of Doc., U.S. Government Printing Office Washington, D.C. 20402, SD Cat. No. C13</del> <input type="checkbox"/> Order From National Technical Information Service (NTIS) Springfield, Virginia 22151		20. SECURITY CLASS (THIS PAGE)  <b>UNCLASSIFIED</b>		22. Price

Research Report 74-9D4-CRYMT-R2  
Westinghouse Program 9D43-CRYMT  
NBS Contract No. CST-8304

STRUCTURAL MATERIALS FOR CRYOGENIC APPLICATIONS  
(Second Semi-Annual Technical Report)

G. G. Lessmann, R. Kossowsky, W. A. Logsdon,  
M. P. Mathur and J. M. Wells

Westinghouse Electric Corporation  
Research and Development Center  
Pittsburgh, Pennsylvania 15235

September 9, 1974

The views and conclusions contained in this document are those of the authors and should not be interpreted as necessarily representing official policies, expressed or implied, of the Advanced Research Projects Agency or the U.S. Government.



This research was supported by the  
Advanced Research Projects Agency of  
the Department of Defense and was moni-  
tored by the Cryogenics Div., NBS,  
Boulder, CO under Contract No. CST-8304  
Contract Amount \$157K

Sponsored by Advanced Research  
Projects Agency ARPA Order No.  
2569, Program Code No. 4D10

TITLE: Structural Materials for Cryogenic Applications  
(Second Semi-Annual Technical Report - September 9, 1974)

CONTRACTOR: Westinghouse Electric Corporation  
Research and Development Center  
Pittsburgh, Pennsylvania 15235

Westinghouse Program Manager: G. G. Lessmann (412) 256-3412

Westinghouse Principal Investigators:

Mr. W. A. Logsdon	(412) 256-3652
Dr. R. Kossowsky	(412) 256-3684
Dr. M. P. Mathur	(412) 256-3289
Dr. J. M. Wells	(412) 256-3633

FY 74 Contract Start Date: September 10, 1973

FY 74 Contract Expiration Date: September 9, 1974

FY 75 Contract Start Date: September 10, 1974

FY 75 Contract Expiration Date: September 9, 1975

## TABLE OF CONTENTS

	<u>Page</u>
LIST OF FIGURES . . . . .	iv
LIST OF TABLES . . . . .	xvii
1.0 ABSTRACT . . . . .	1
2.0 INTRODUCTION . . . . .	3
3.0 INTERPRETIVE SUMMARY . . . . .	7
3.1 Test Status . . . . .	7
3.2 Alloy Selection and Use . . . . .	7
3.3 Mechanical Properties . . . . .	8
3.4 Processing . . . . .	10
3.5 Fabrication . . . . .	12
3.6 Physical Properties . . . . .	14
4.0 WESTINGHOUSE PROJECT DESCRIPTION . . . . .	17
4.1 First Year (FY 74) Westinghouse Project . . . . .	17
4.2 Second Year (FY 75) Westinghouse Project. . . . .	18
5.0 GENERAL CRYOGENIC STRUCTURAL MATERIALS/PROCESSING/ FABRICATION CONSIDERATIONS . . . . .	21
5.1 Materials Selection . . . . .	23
5.1.1 Establishment of Materials Selection and Utilization Criteria . . . . .	23
5.1.2 Candidate Materials for Structural Cryogenic Applications . . . . .	24
5.1.3 Candidate Materials For Westinghouse FY 75 Project Extension . . . . .	24
5.2 Materials Processing Considerations . . . . .	25
5.2.1 Melting Practice in Inconel X750 . . . . .	25
5.2.2 Hot Isostatic Pressed Inconel X750 . . . . .	28
5.2.3 Cold Working of Kromarc 58 Stainless Steel . .	31
5.2.4 Kromarc 58 Filler Wire . . . . .	34

## TABLE OF CONTENTS (CONT'D)

	<u>Page</u>
5.3 Materials Fabrication Considerations . . . . .	35
5.3.1 Welding . . . . .	35
5.3.1.1 Weldments in Oxygen-Free Copper . . .	35
5.3.1.2 Weldments in AISI 310S Stainless Steel . . . . .	36
5.3.1.3 Weldments in Inconel X750 Super- alloy . . . . .	37
5.3.1.4 Weldments in Kromarc 58 Stain- less Steel . . . . .	39
5.3.2 Brazing . . . . .	41
5.3.2.1 Copper Brazement in Inconel X750 . .	42
5.3.2.2 Silver Brazement in OFHC Copper . . .	43
5.3.3 Soldering . . . . .	44
5.3.3.1 Solder Joints In OFHC Copper . . . .	44
6.0 FRACTURE MECHANICS . . . . .	51
Introduction . . . . .	51
Status . . . . .	51
6.1 Tensile Results . . . . .	52
6.2 Notched Tensile Results . . . . .	56
6.3 Fracture Toughness Results . . . . .	57
6.4 Crack Growth Rate Results . . . . .	62
6.5 Design Example - Estimating Cyclic Life of a Superconducting Generator Rotor . . . . .	64
References - Section 6 . . . . .	71
7.0 MICROSTRUCTURAL ANALYSIS . . . . .	73
7.1 Inconel X750 Welds . . . . .	73
7.1.1 Tensile Specimens . . . . .	73
7.1.2 Fatigue Crack Growth Rate Specimens . . . . .	77
7.1.3 Comments . . . . .	78

# TABLE OF CONTENTS (CONT'D)

	<u>Page</u>
7.2 Processing Practices, Inconel X750 . . . . .	79
7.2.1 Tensile Specimens . . . . .	79
7.2.2 Microprobe Analysis . . . . .	82
7.2.3 Comments . . . . .	83
7.3 Kromarc-58 . . . . .	84
7.4 Correlation of Structure and Properties . . . . .	85
7.4.1 Inconel X-750 . . . . .	85
8.0 PHYSICAL PROPERTIES . . . . .	89
8.1 Magnetic Study . . . . .	89
8.1.1 Review of Different Types of Magnetic Behavior . . . . .	91
8.1.2 AISI 310S Stainless Steel . . . . .	93
8.1.3 Kromarc 53 Stainless Steel . . . . .	95
8.1.4 Inconel 718 and X750 . . . . .	97
8.2 Electrical Resistivity . . . . .	99
8.2.1 Experimental . . . . .	99
8.2.2 Results and Discussion . . . . .	100
ACKNOWLEDGMENT . . . . .	105
APPENDIX I - ADDITIONAL KROMARC 58 DATA . . . . .	107

## LIST OF FIGURES

- FIGURE 3-1 Summary Comparison of Mechanical Strength and Ductility at RT, 77°K and 4.2°K of Oxygen Free Copper and AISI 310S Stainless Steel for Various Processing and Welding Conditions
- FIGURE 3-2 Summary Comparison of Mechanical Strength and Ductility at RT, 77°K and 4.2°K of Inconel X-750 for Various Processing Conditions.
- FIGURE 3-3 Summary Comparison of Mechanical Strength and Ductility at RT, 77°K and 4.2°K for Inconel X-750 (VIM-VAR) Base Metal, HVEB and GTA Composite Weldments
- FIGURE 3-4 Summary Comparison of Mechanical Strength and Ductility at RT, 77°K and 4.2°K of Kromarc 58 Stainless Steel for Various Processing and GTA Welding Conditions
- FIGURE 3-5 Summary Comparison of Fracture Toughness at 4.2°K
- FIGURE 4-1 ☺ Program Outline - Structural Materials for Cryogenic Applications
- FIGURE 4-2 Westinghouse Project Organization
- FIGURE 4-3 Task I (FY 74) - Characterization of Current Cryogenic Structural Materials
- FIGURE 4-4 Task II (FY 74) - Processing Effects on Properties of Structural Cryogenic Materials
- FIGURE 4-5 Task III (FY 74) - Evaluation of Joints in Structural Cryogenic Materials
- FIGURE 4-6 Task I (Westinghouse FY 75 Project) - Characterization of Structural Base Materials For Advanced Cryogenic Applications
- FIGURE 4-7 Task II (Westinghouse FY 75 Project) - Processing Effects on Cryogenic Structural Materials Properties
- FIGURE 4-8 Task III (Westinghouse FY 75 Project) - Fabricated Joints in Cryogenic Structural Materials
- FIGURE 5-1 Prototype Superconducting Generator Rotor Assembly Indicating Structural Materials Utilization and Design/Fabrication Complexity
- FIGURE 5-2 Photomicrographs of Inconel X750 Material As-Received, MP-1 (VIM/VAR), MP-2 (AAM/VAR), and MP-3 (VIM), (X200)

### LIST OF FIGURES (CONT'D)

- FIGURE 5-3      Photograph of Hot Isostatic Press (HIP) Facility at Westinghouse Research Laboratories, Metals Processing Section
- FIGURE 5-4      Scanning Electron Micrographs of HIP Inconel X-750, Sample HX-1, 1/2" Dia., Transverse Section
- FIGURE 5-5      Scanning Electron Micrographs of HIP Inconel X-750, Sample HX-2, 1/2" Dia., Transverse Section
- FIGURE 5-6      Photographs Showing Hot Isostatic Press (HIP) Samples of Inconel X-750. (A) Initial Test Sample, HX-2, as 1/2" Dia. As-HIPed, and (B) Initial Flat Plate Test Sample 3/4" Thick, HX-3, on Bottom Showing Biaxial Warpage from HIPing in Unmodified Container (on Top)
- FIGURE 5-7      Photograph of Hot Isostatic Pressed (HIP) Plate Samples of Inconel X-750 Shown as HIPed Before Removal of AISI 304 Stainless Containment Shells
- FIGURE 5-8      Microhardness Traverse Across Transverse Section of Kromarc 58 Weldment (Plate K-1, GTAW and Cold Worked ~37%) For Samples (A) As Cold Worked, and (B - F) Heat Treated for 1 hour in Argon at Temperatures Indicated
- FIGURE 5-9      Microhardness Changes and Accompanying Microstructural Changes of Base Metal, (BM), and Fusion Zone, (FZ), in Kromarc 58 Stainless Steel GTA Welded and Worked Followed by Heat Treatment at the Indicated Temperature (X200)
- FIGURE 5-10     Photographs Showing Defects Experienced in Initial Attempt at Fabricating Kromarc 58 Stainless Filler Wire (X200)
- FIGURE 5-11     Photographs of Final Kromarc 58 Filler Wire of .090" Dia. Produced In-House for GTA Welding
- FIGURE 5-12     Photographs of GMA Weld Radiographs, RD74168, GMA Weld Plate Cu-3 (Code 12XX), RD74169, GMA Weld Plate Cu-4 (Code 12XX), RD74170, GMA Weld Plate Cu-5, (Code 12XX), Material OFHC Copper Plate 1/2" Thick
- FIGURE 5-13     Photomacrograph (A) and Photomicrographs of GMA Weldment in OFHC Copper, (Code 12XX), (B) Weld Fusion Zone, (C) Weld FZ-HAZ Transition and (D) Base Metal

LIST OF FIGURES (CONT'D)

- FIGURE 5-14 Photomicrographs of AISI 310S Stainless Steel (A&B) Solution Treated at 2000°F - 1 hr and Water Quenched, (STQ - Code 20XX), (C&D) Solution Treated at 2000°F - 1 hr and Furnace Cooled, (STFC - Code 21XX) X200
- FIGURE 5-15 Photographs of SMA Weld Radiographs, RD73716, SMA Weld Plate No. 310-2 First Half (Code 22XX); RD73717, SMA Weld Plate No. 310-2, Second Half (Code 22XX), Material AISI-310S Stainless Steel - Plate 5/8" Thick
- FIGURE 5-16 Photographs of SMA Weld Radiographs, RD73789, SMA Weld Plate No. 310-3, First Half, (Code 22XX) RD73790, SMA Weld Plate No. 310-3, Second Half, Code (22XX), Material- AISI 310S Stainless Steel - Plate 5/8" Thick
- FIGURE 5-17 Macro (A) and Microstructure (B,C, &D) of 310S Stainless Steel Base Metal and Typical SMA Weldment (5/8" Thick) Using E 310-16 Covered Electrode (Code 22XX)
- FIGURE 5-18 Photographs of Vacuum Electron Beam Weld Radiographs, RD73643- EB Plate No. 1 ST/EBW (Code 32XX), RD73642 - EB Plate No. 2 STDA/EBW (Code 33XX), RD73641-EB Plate No. 3 EBW/STDA (Code 34XX), Material Inconel X-750 (VIM-VAR) - Plate 5/8" Thick
- FIGURE 5-19 Photographs of Vacuum Electron Beam Weld Radiographs, RD74645, EB Pieces 1&2, 3&4, EBW/STDA (Code 34XX), RD74646, EB Pieces 5&6, 7&8, ST/EBW (Code 32XX), RD74647, EB Pieces 9&10, 11&12, STDA/EBW (Code 33XX), Material Inconel X-750 (VIM-VAR) - Plate 5/8" Thick
- FIGURE 5-20 Photographs Showing Macro and Microstructure of HVEB Weld Defects in IN X-750, EB Plate Sample No. 2 (Code 33XX). Both Defects are in EB Weld Fusion Zone Centerline and are Visible on RD73642 Radiograph
- FIGURE 5-21 Photographs of GTA Weld Radiographs, RD73841 - GTA Weld Plate No. 4A ST/GTAW (Code 35XX), RD73841 - GTA Weld Plate No. 4B STDA/GTAW (Code 36XX), Material Inconel X-750 (VIM-VAR) - Plate 5/8" Thick
- FIGURE 5-22 Photographs of GTA Weld Radiographs, RD73836 - GTA Weld Plate No. 5A, 5B and 5C ST/GTAW (Code 35XX) Material Inconel X-750 (VIM-VAR) - Plate 5/8" Thick

LIST OF FIGURES (CONT'D)

- FIGURE 5-23 Photographs of GTA Weld Radiographs, RD73842 - GTA Weld Plate No. 6A, 6B & 6C STDA/GTAW (Code 36XX) Material Inconel X-750 (VIM-VAR) - Plate 5/8" Thick
- FIGURE 5-24 Photographs of GTA Weld Radiographs, RD73835 - GTA Weld Plate No. 7A, 7B & 7C GTAW/STDA (Code 37XX) Material Inconel X-750 (VIM-VAR) - Plate 5/8" Thick
- FIGURE 5-25 Photographs of GTA Weld Radiographs, RD74366 - GTA Weld Plate K58-7, First Half STQ/GTAW (Code 82XX), RD74367, GTA Weld Plate K58-7, Second Half, STQ/GTAW (Code 82XX), Material Kromarc 58 Stainless Steel - Plate Thickness 5/8 Inch
- FIGURE 5-26 Photographs of GTA Weld Radiographs, RD74368 GTA Weld Plate K58-8 First Half STQ/GTAW (Code 82XX), RD74372 - GTA Weld Plate K58-8. Second Half STQ/GTAW (Code 82XX), Material Kromarc 58 Stainless Steel - Plate Thickness 5/8 Inch
- FIGURE 5-27 Photographs of GTA Weld Radiographs, RD74370 - GTA Weld Plate K58-9 First Half, CW/GTAW (Code 83XX), RD74371 - GTA Weld Plate No. K58-9. Second Half, CW/GTAW (Code 83XX), Material Kromarc 58 Stainless Steel - Plate Thickness 5/8 Inch
- FIGURE 5-28 Photographs of GTA Weld Radiographs, RD74338 - GTA Weld Plate No. K58-1 GTAW/CW/AN (Code 85XX) and RD74343 - GTA Weld Plate No. K58-4 GTAW/CW (Code 84XX), Material Kromarc 58 Stainless Steel - Plate Thickness 1" As-Welded.
- FIGURE 5-29 Photograph of Kromarc 58 Stainless Steel GTA Weld Plates Shown As-Welded (A) Plate K-7, (B) Plate K-8, (C) Plate K-9, (D) Plate K-4, and (E) Plate K-1
- FIGURE 5-30 Macro Photographs of Kromarc 58 Stainless Weldments in Transverse Section (A) As GTA Welded (Code 82XX), (B) GTAW/Cold Worked 37% (Code 84XX), (C) Partially Recrystallized GTAW/CW 1500°F (Code 85XX), and (D) Fully Recrystallized GTAW/CW/1600°F (Code 86XX)
- FIGURE 5-31 Macro (A) and Microstructure (B,C,&D) of Kromarc 58 Stainless Steel Base Metal and Typical GTA Weldment (1" Thick As-Welded) Using Kromarc 58 Filler Wire (Code 84XX)



### LIST OF FIGURES (CONT'D)

- FIGURE 5-32 Microhardness Survey (A&B), Macrostructure (C) (X4), and Microstructure of GTA Welded Kromarc 58 Stainless Steel (Plate K-1) As Welded (D) Through (H) (X200)
- FIGURE 5-33 Photographs of Copper Plated Inconel X750 Braze Specimen Before (A&B) and After (C&D) Unsuccessful Initial Brazing Test
- FIGURE 5-34 Photographs of Initial Copper Solder and Brazed Test Samples
- FIGURE 6-1 Tensile Properties of Inconel X-750 (AAM-VAR)
- FIGURE 6-2 Tensile Properties of Inconel X-750 (VIM)
- FIGURE 6-3 Tensile Properties of Hot Isostatic Pressed Inconel X-750
- FIGURE 6-4 Tensile Properties of Solution Treated and Double Aged Hot Isostatic Pressed Inconel X-750
- FIGURE 6-5 0.2% Yield Strengths of Inconel X-750, Various Manufacturing Processes
- FIGURE 6-6 Tensile Properties of OFHC Copper Gas Metal Arc Welds
- FIGURE 6-7 Tensile Properties of Kromarc 58 Stainless Steel STQ
- FIGURE 6-8 Tensile Properties of Kromarc 58 Stainless Steel CW
- FIGURE 6-9 Tensile Properties of Kromarc 58 Stainless Steel Gas Tungsten Arc Welds
- FIGURE 6-10 Tensile Properties of Kromarc 58 Stainless Steel (Cold Worked/Gas Tungsten Arc Welded)
- FIGURE 6-11 Tensile Properties of Kromarc 58 Stainless Steel (Gas Tungsten Arc Welded/Cold Worked)
- FIGURE 6-12 Yield Strength and Notched Tensile Fracture Strength of Inconel X-750 (AAM-VAR)
- FIGURE 6-13 Yield Strength and Notched Tensile Fracture Strength of Inconel X-750 (VIM)
- FIGURE 6-14 Yield Strength and Notched Tensile Fracture Strength of Hot Isostatic Pressed Inconel X-750

LIST OF FIGURES (CONT'D)

- FIGURE 6-15 Yield Strength and Notched Tensile Fracture Strength of Solution Treated and Double Aged Hot Isostatic Pressed Inconel X-750
- FIGURE 6-16 Yield Strength and Notched Tensile Fracture Strength of Solution Treated and Water Quenched Kromarc 58 Stainless Steel
- FIGURE 6-17 Yield Strength and Notched Tensile Fracture Strength of 30 percent Cold Worked Kromarc 58 Stainless Steel
- FIGURE 6-18 Procedure for  $J_{IC}$  Measurement
- FIGURE 6-19 J Resistance Curve for Solution Treated Inconel X-750 at a Temperature of  $-452^{\circ}\text{F}$
- FIGURE 6-20 J Resistance Curve for Solution Treated Inconel X-750 at a Temperature of  $75^{\circ}\text{F}$
- FIGURE 6-21 J Resistance Curve for Solution Treated and Double Aged Inconel X-750 at a Temperature of  $-452^{\circ}\text{F}$
- FIGURE 6-22 J Resistance Curve for Inconel X-750 Electron Beam Welds (ST/W/STDA) at a Temperature of  $-452^{\circ}\text{F}$
- FIGURE 6-23 J Resistance Curve for Inconel X-750 Gas Tungsten Arc Welds (ST/W) at a Temperature of  $-452^{\circ}\text{F}$
- FIGURE 6-24 J Resistance Curve for Inconel X-750 Gas Tungsten Arc Welds (STDA/W) at a Temperature of  $-452^{\circ}\text{F}$
- FIGURE 6-25 J Resistance Curve for Inconel X-750 Gas Tungsten Arc Welds (ST/W/STDA) at a Temperature of  $-452^{\circ}\text{F}$
- FIGURE 6-26 J Resistance Curve for Inconel X-750 (AAM-VAR) at a Temperature of  $-452^{\circ}\text{F}$
- FIGURE 6-27 J Resistance Curve for Inconel X-750 (VIM) at a Temperature of  $-452^{\circ}\text{F}$
- FIGURE 6-28 J Resistance Curve for Hot Isostatic Pressed Inconel X-750 at a Temperature of  $-452^{\circ}\text{F}$
- FIGURE 6-29 J Resistance Curve for Solution Treated and Double Aged Hot Isostatic Pressed Inconel X-750 at a Temperature of  $-452^{\circ}\text{F}$

LIST OF FIGURES (CONT'D)

- FIGURE 6-30 J Resistance Curve for Solution Treated and Water Quenched 310S Stainless Steel at a Temperature of  $-452^{\circ}\text{F}$
- FIGURE 6-31 J Resistance Curve for 310S Stainless Steel Shielded Metal Arc Welds at a Temperature of  $-452^{\circ}\text{F}$
- FIGURE 6-32 J Resistance Curve for Solution Treated and Water Quenched Kromarc 58 Stainless Steel at a Temperature of  $-452^{\circ}\text{F}$
- FIGURE 6-33 J Resistance Curve for 30 Percent Cold Worked Kromarc 58 Stainless Steel at a Temperature of  $-452^{\circ}\text{F}$
- FIGURE 6-34 Fatigue Crack Growth Rate Properties of Inconel X-750 Electron Beam Welds in Cryogenic Environments
- FIGURE 6-35 Fatigue Crack Growth Rate Properties of Inconel X-750 Gas Tungsten Arc Welds in Cryogenic Environments (ST/GTW)
- FIGURE 6-36 Fatigue Crack Growth Rate Properties of Inconel X-750 Gas Tungsten Arc Welds in Cryogenic Environments (STDA/W)
- FIGURE 6-37 Fatigue Crack Growth Rate Properties of Inconel X-750 Gas Tungsten Arc Welds in Cryogenic Environments (ST/W/STDA)
- FIGURE 6-38 Flaw Shape Parameter Curves for Surface and Internal Cracks
- FIGURE 6-39 Cyclic Life Curves for Inconel X750 Superconducting Generator Rotor
- FIGURE 6-40 Cyclic Life Curves for Inconel X750 Superconducting Generator Rotor
- FIGURE 7-1 Light Micrographs Showing Longitudinal Sections Near Fracture. Inco X-750, Solution Treated and Welded Specimen (Code-3511) Tested at Room Temperature. (a) 50X (b) Detail 200X
- FIGURE 7-2 Light Micrographs (50X) Showing Longitudinal Sections Near Fracture (a) and About 2 cm Away from the Fracture (b). Welded Specimen (Code 3513) Tested at  $4.2^{\circ}\text{K}$
- FIGURE 7-3 SEM Micrograph Identifying the Origin of Fracture (Arrow) in Specimen 3511-T1 (Fig. 7-1). The Bright Impurity Particles are Rich in Al and Si (Energy Dispersive X-Ray Analysis). The Variations in Shading are Caused by Charging Effects from the Non-Conductive Particles
- FIGURE 7-4 SEM Micrographs of Fracture Surface of Specimen 3511 (Fig. 7-1). Intergranular Cracking is Evident in Both Photos. Fissioning is Marked by Long Arrows. The Particles Marked (P) in (a) and Covering the Surface in (b) are (Ti; Nb) C (MC Carbides)

LIST OF FIGURES (CONT'D)

- FIGURE 7-5 Light Micrographs (50X) of Longitudinal Sections Near the Fracture Surface (a) and 25 mm Away from the Fracture at the Weld Interface (b) Welded Specimens (Code 3711-T11) Heat Treated After Welding, Tested at Room Temperature
- FIGURE 7-6 Light Micrographs (50X) of Longitudinal Sections Near the Fracture Surface (a) and 22 mm Away from the Fracture at the Weld Interface (b) Welded Specimen, Heat Treated After Welding, Tested at 4.2°K (Code 3713).
- FIGURE 7-7 SEM Micrographs of the Fracture Surface in a Specimen Heat Treated After Welding (Code 3712-12) Tested at 77°K. Ductile Deformation Within the Grain and Final Failure by Intergranular Cracking
- FIGURE 7-8 Light Micrographs (50X) of Longitudinal Sections Near the Fracture Surface (a) and 25 mm Away from the Fracture (b) Near the Thread of the Specimen. Welded Specimen (Code 3613-T8) Heat Treated Prior to Welding. No Post Weld Treatment, Tested at 4.2°K
- FIGURE 7-9 Light Micrographs of Longitudinal Section Near Fracture (a) and 30 mm Away from Fracture (b). SEM of Fracture Surface (c) Electron Beam Weld Specimen, Not Treated After Welding (Code 3211), Tested at Room Temperature.
- FIGURE 7-10 Light Micrographs Showing Longitudinal Sections Near the Fracture (a) and About 23 mm Away from the Fracture (b) Welded Specimen (Code 3213) Tested at 4.2°K
- FIGURE 7-11 SEM Micrographs of Fracture Surfaces of Specimen Welded by Electron Beam. (a) Specimen Tested at Room Temperature With No Post Weld Treatment (Code 3311). Note High Incidence of MC Carbides on Fracture Surface (Arrows) (b) Specimen Tested at 77°K, Heat Treated After Weld (Code 3412)
- FIGURE 7-12 SEM Micrographs of Fracture Surface of Specimen 3312-T7. Origin of Failure is Associated With Al-Si Rich Molten Defects
- FIGURE 7-12c Energy-Dispersive X-Ray Data from Particles Shown in Fig. 7-12b
- FIGURE 7-13 SEM Micrographs of Fracture Surfaces, Crack Growth in Tungsten Arc Weld. (Code 3552-3). (a) RT pre-crack. (b) Fatigue Striations Due to Crack Propagation at 77°K

LIST OF FIGURES (CONT'D)

- FIGURE 7-14 SEM Detail of Fig. 7-14-b, 6700X. Pockets of MC Carbides Indicated. Weld was Not Subjected to Heat-Treatment
- FIGURE 7-14a Energy-Dispersive X-Ray Data from Pockets of MC Carbides Shown in Fig. 7-14
- FIGURE 7-15 Fatigue Striations and  $\text{Cr}_{23}\text{C}_6$  Carbides in Weld Specimen Post Weld Treated, (Code 3753-3) Tested at 4.2°K. (3000X)
- FIGURE 7-16 Crack Growth Fracture Surfaces, Tungsten-Arc Welds. Crack Front Direction Shown by Large Arrows. Note Massive Secondary Cracking Normal to Crack Front Specimens Tested at 4.2°K. (a) Specimen Code 3753-2, No Post Weld Treatment
- FIGURE 7-17 Fatigue Crack Growth in Electron-Beam Weld, No Post Weld Treatment, Tested at 4.2°K (Code 3253-1). Note Crystallographic Orientation of Crack Front and Secondary Cracking at "Grain" Boundaries in (b) SEM, (2700X)
- FIGURE 7-18 Crack Front Propagation in Electron Beam Weld Subjected to Post-Weld Heat Treatment, Tested at 77°K. Arrow Indicate Direction of Crack Front Motion (2800X)
- FIGURE 7-19 Light Micrographs Showing General Grain Structure of X-750 Material From Three Melting Practices (a) MP1 (Code 31XX) (b) MP2 (Code 40XX) (c) MP3 (Code 50XX). Note Smaller Grain Size in MP2 and Binodal Distribution in MP3 Caused by Bands of Larger Grains
- FIGURE 7-20 Light Micrographs Showing Longitudinal Sections at the Fracture Surface (a) and 30 mm Away from the Fracture, MP2 Tensile Specimen (Code 4013-T3) Tested at 4.2°K (200X)
- FIGURE 7-21 Light Micrographs Showing Longitudinal Sections at the Fracture Surface (a) and 28 mm Away from the Fracture (b), MP3 Tensile Specimen (Code 5013-T3) tested at 4.2°K (200X)
- FIGURE 7-22 SEM Micrographs of Fracture Surfaces, MP3 and MP2, X-750 Materials. (a) MP3 Material (Code 5013-T3) Tested at 4.2°K (b) Detail in Small Grain Area (c) Details in Large Grain Band
- FIGURE 7-22 (cont) MP2 Material (Code 4013) Tested at 4.2°K (d) 200X (e) Detail at Higher Magnification. Intergranular (Nb, Ti) C Carbides Marked by Arrows

LIST OF FIGURES (CONT'D)

- FIGURE 7-23 Light Micrograph Showing Typical Microstructural Fractures of HIP X-750 Material. Note Sub-Boundaries in Large Particles. 200X (Code 6113-T4)
- FIGURE 7-24 Light Micrograph of Longitudinal Section. HIP Specimen Tested at 4.2°K (Code 6113-T4). 500X
- FIGURE 7-25 SEM Micrographs of Fracture Surfaces Inconel X-750 Material, 400X. (a) HIP Specimen (Code 6113) (b) MP1 Specimen (Code 3113). Both Specimen Solution Treated and Aged and Tested at 4.2°K. Note Mostly Cross Granular Failure in (a), Intergranular Failure in (b)
- FIGURE 7-26 Micrographs Showing Microprobe Traces in X-750 Specimens. Details of Traces for the Various Elements are Shown in the Corresponding Figures, al-cl. (a) MP-2 Material 500X (b) MP-3 Material 500X (c) HIP Material 200X
- FIGURE 7-26-al Microprobe Traces of Ti, Ni, Al, Nb, Fe and Cr Along the Line Shown in Fig. 7-26-a. MP-1 Material. Note (Nb, Ti) C and Al Peaks Around the Carbides
- FIGURE 7-26-bl Microprobe Traces of Nb, Ti, Ni, Al, Cr and Fe in MP-3 Material Shown in Fig. 7-26-b. Note Uniform Distribution of Fe, Cr and Ni and (Nb, Ti) C Carbides in High Angle Boundaries
- FIGURE 7-26-cl Microprobe Traces of Nb, Ti, Fe, Ni and Cr Along Line Shown in Fig. a. HIP Material. Note (Nb, Ti) C Type Carbides in High Angle Boundaries
- FIGURE 7-27 Tensile Specimens, K-58 (Code 8011) Solution Treated and Quenched, Tested at R.T. (a) Longitudinal Section, (b) Cross Section. 200X
- FIGURE 7-28 Tensile specimens K-58 (Code 8111) CW 30% Tested at R.T. (a) Longitudinal Section (b) Cross Section, 200X
- FIGURE 7-29 SEM Micrographs, Fracture Surface, K-58, (Specimen Code 8022) Tested at 4.2°K. (a) Ductile Fracture (b) Low Melting Particles Containing Al, Si, Mo, K and Ca (Slag?) 100X
- FIGURE 7-30 SEM Micrograph, K-58, 30% C.W. (Specimen Code 8113-T10) Tested at 4.2°K. Ductile Fracture and a Deep Fissure
- FIGURE 7-31 Microprobe Trace, K-58 Material, Specimen 8022-NT2. Fissures Appear to be Holes. 500X

LIST OF FIGURES (CONT'D)

- FIGURE 7-31-a Microprobe Traces of Fe, Cr, and Ni Along a Line Shown in Fig. 7-30. The Dark Fissures Seen Also in Figs. 7-28-b and 7-30 Appear to be Holes
- FIGURE 8-1 Total Magnetic Moment as a Function of the External Field for AISI-310S/STQ/(20XX)
- FIGURE 8-2 Magnetization Data at Low Temperature for AISI 310S/STQ (20XX)
- FIGURE 8-3 Total Magnetic Moment as a Function of the External Field for AISI 310S/STFC/(21XX)
- FIGURE 8-4 Magnetization Data at Low Temperature for AISI 310S/STFC/(21XX)
- FIGURE 8-5 Extrapolated Magnetic Moment at Zero Field as a Function of Temperature for AISI 310S/STQ and STFC Samples
- FIGURE 8-6 Total Magnetic Moment as a Function of External Field for Kromarc 58/STQ/(80XX) at 4.8°K
- FIGURE 8-7 Total Magnetic Moment as a Function of the External Field for Kromarc 58/STQ/(80XX) at 11.4°K
- FIGURE 8-8 Total Magnetic Moment as a Function of the External Field for Kromarc 58/STQ/(80XX) at 125°K
- FIGURE 8-9 Magnetic Moment at 13 kOe as a Function of the Temperature for Kromarc 58/STQ/(80XX)
- FIGURE 8-10 Magnetic Moment as a Function of the External Field for Kromarc 58/CW/(81XX)
- FIGURE 8-11 Magnetic Moment as a Function of the External Field for Kromarc 58/CW/(81XX)
- FIGURE 8-12 Magnetic Moment as a Function of the External Field for Kromarc 58/CW/(81XX)
- FIGURE 8-13 Magnetic Moment at 13 kOe as a Function of the Temperature for Kromarc 58/CW/(81XX)
- FIGURE 8-14 Magnetic Moment as a Function of the External Field for Kromarc 58/GTAW/(82XX)
- FIGURE 8-15 Magnetic Moment as a Function of the External Field at 55.7°K for Kromarc 58/GTAW/(82XX)

LIST OF FIGURES (CONT'D)

- FIGURE 8-16      Magnetic Moment as a Function of the External Field for Kromarc 58/GTAW/(82XX) at Various Temperatures
- FIGURE 8-17      Magnetic Moment as a Function of the External Field for Kromarc 58/CW/GTAW/(83XX)
- FIGURE 8-18      Magnetic Moment as a Function of the External Field for Kromarc 58/CW/GTAW/(83XX) at 4.2°K
- FIGURE 8-19      Magnetic Moment as a Function of the External Field for Kromarc 58/CW/GTAW/(83XX) at Various Temperatures
- FIGURE 8-20      Magnetic Moment as a Function of the External Field for Kromarc 58/CW/GTAW/(83XX) at Various Temperatures
- FIGURE 8-21      Magnetic Moment as a Function of the External Field for Kromarc 58/GTAW/CW/(84XX) at 4.0°K
- FIGURE 8-22      Magnetic Moment as a Function of the External Fields for Kromarc 58/GTAW/CW/(84XX) at Various Temperatures
- FIGURE 8-23      Magnetic Moment as a Function of the External Fields for IN-X750/ST/(30XX) at Low Temperatures
- FIGURE 8-24      Magnetic Moment as a Function of the External Fields for IN-X750/ST/(30XX) at Higher Temperatures
- FIGURE 8-25      Magnetic Moment as a Function of the External Field for Tensile Specimen IN-X750/STDA/(31XX) at Low Temperatures
- FIGURE 8-26      Magnetic Moment as a Function of the External Field for Tensile Specimen IN-X750/STDA/(31XX)
- FIGURE 8-27      Magnetic Moment as a Function of the External Field for Unstrained Specimen IN-X750/STDA\*/(31XX)
- FIGURE 8-28      Magnetic Moment as a Function of the External Field for Unstrained Specimen IN-X750/STDA\*/(31XX)
- FIGURE 8-29      Magnetic Moment (Extrapolated to Zero Field) as a Function of the Temperature for All IN-X750 and IN718 Samples
- FIGURE 8-30      Magnetic Moment as a Function of the External Field for IN718/STDA at Low Temperature
- FIGURE 8-31      Magnetic Moment as a Function of the External Field for IN718/STDA at High Temperatures



LIST OF FIGURES (CONT'D)

- FIGURE 8-32 Resistivity as a Function of Temperature for Kromarc 58/  
(80XX) and Kromarc 58/(81XX)
- FIGURE 8-33 Resistivity as a Function of Temperature for Various  
Kromarc 58/ Samples
- FIGURE 8-34 Resistivity as a function of Temperature for Various  
IN-X750 and IN-718 Samples
- FIGURE 8-35 Resistivity as a Function of Temperature for Various AISI  
310S Stainless Steels

### LIST OF TABLES

TABLE 3-1	SUMMARY PROJECT TEST MATRIX FOR STRUCTURAL MATERIALS FOR CRYOGENIC APPLICATIONS (W FY 74)
TABLE 5-1	CANDIDATE MATERIALS FOR STRUCTURAL CRYOGENIC APPLICATIONS
TABLE 5-2	(W) FY 74 PROJECT TEST SPECIMEN IDENTIFICATION SYSTEM
TABLE 5-3	CHEMICAL COMPOSITION OF (W) FY 74 PROJECT MATERIALS
TABLE 5-4	MATERIAL DOCUMENTATION DATA
TABLE 5-5	PROCESSING AND HEAT TREATMENT SCHEDULES
TABLE 5-6	MATERIAL HARDNESS AND GRAIN SIZE MEASUREMENTS
TABLE 5-7	CHARACTERIZATION DATA FOR INCONEL X-750 POWDER
TABLE 5-8	PROCESSING SCHEDULE FOR KROMARC 58 STAINLESS FILLER WIRE
TABLE 5-9	SUMMARY TABLE OF WELDING PROCESSES AND PARAMETERS
TABLE 6-1	TENSILE AND NOTCHED TENSILE PROPERTIES OF INCONEL X-750 AT 75°F (297°K)
TABLE 6-2	TENSILE AND NOTCHED TENSILE PROPERTIES OF INCONEL X-750 AT -320°F (77°K)
TABLE 6-3	TENSILE AND NOTCHED TENSILE PROPERTIES OF INCONEL X-750 AT -452°F (4.2°K)
TABLE 6-4	TENSILE AND NOTCHED TENSILE PROPERTIES OF OFHC COPPER PLUS 310S AND KROMARC 58 STAINLESS STEELS AT 75°F (297°K)
TABLE 6-5	TENSILE AND NOTCHED TENSILE PROPERTIES OF OFHC COPPER PLUS 310S AND KROMARC 58 STAINLESS STEELS AT -320°F (77°K)
TABLE 6-6	TENSILE AND NOTCHED TENSILE PROPERTIES OF OFHC COPPER, 310S AND KROMARC 58 STAINLESS STEELS AT -452°F (4.2°K)
TABLE 6-7	FRACTURE TOUGHNESS AND FATIGUE CRACK GROWTH RATE PROPERTIES OF INCONEL X750 AND 310S PLUS KROMARC 58 STAINLESS STEELS.

LIST OF TABLES (CONT'D)

TABLE 7-1	GRAIN SIZE OF WELDED INCONEL X-750 SPECIMENS
TABLE 7-2	GRAIN SIZE DISTRIBUTION IN MP-2 AND MP-3, INCONEL X-750 MATERIALS
TABLE 7-3	MICROPROBE X-RAY COUNTS IN THE GRAIN INTERIOR OF MP-1, MP-2, MP-3, HIP AND K-58 MATERIALS
TABLE 8-1	SUMMARY OF MAGNETIC BEHAVIOR
TABLE 8-2	SUMMARY OF RESISTIVITY BEHAVIOR

## 1.0 ABSTRACT

Progress in the second semi-annual period (March - September, 1974) on ARPA - NBS Contract CST 8304 is reported. General considerations of cryogenic structural materials characterization is further discussed including aspects of materials selection, processing and fabrication. Results and analyses include mechanical and fracture mechanics test data from R.T. to 4.2°K for four present generation candidate cryogenic structural materials. A variety of common metallurgical conditions of these materials is included in this evaluation to assure that mechanical performance will be predictable and that structural reliability analyses can be extrapolated to advanced fabricated structures.

The materials evaluated include OFHC Copper, AISI 310S Stainless Steel, Kromarc 58 Stainless Steel and Inconel X750 Nickel Base Superalloy. Metallurgical-structural variables include the wrought and heat treated forms resulting from cold working, stress relief, solution annealing, quenching, aging and sensitization to which these respective metal alloys are exposed in routine processing for fabricated hardware.

Ingot consolidation and secondary refining practice is also being evaluated to provide additional but necessary flexibility in process selection and property control. Three melting practices in Inconel X750 are considered, namely: (1) Vacuum Induction Melting - Vacuum Arc Remelt; (2) Air Arc Melting - Vacuum Arc Remelt, and (3) Vacuum Induction Melting. Conversion from powder to wrought structure by hot isostatic pressing (HIP) is also evaluated as an additional processing alternative.

Structural fabrication requirements are screened by evaluation of basic metals joining techniques including: gas tungsten arc welding (GTAW), high vacuum electron beam welding (HVEBW), gas metal arc welding (GMAW), shielded metal arc welding (SMAW), brazing and soldering.

The primary screening and alloy assessment technique is by mechanical testing. Current state-of-the-art fracture mechanics technology coupled with special low temperature test techniques and advanced analytic capabilities are employed to provide the basis for optimized structural reliability in designing and fabricating cryogenic structures. This systematic evaluation includes testing at RT, 77°K and 4.2°K for tensile, notched tensile, fracture toughness  $K_{IC}$  (via  $J_{IC}$ ), and fatigue crack growth rate behavior. This information is then used to demonstrate the principles and techniques for reliability analyses and to assist in predicting future data base requirements for successful cryogenic structural design. A complete structural characterization of test materials is included for pre and post test evaluation. Hence, an assessment of structural effects on mechanical properties is being provided. A physical property screening study (magnetization and electrical resistivity) is integrated into this effort to assure that these austenitic alloys maintain their desirable magnetic and structural stability at low temperatures.

## 2.0 INTRODUCTION

Work described in this report represents the Westinghouse Electric Corporation contribution to the Advanced Research Project Agency program for Low Temperature Properties of Structural Materials. Program management is the responsibility of the Cryogenics Division of the National Bureau of Standards. Dr. Edward C. van Reuth is the ARPA sponsor while Dr. Richard P. Reed, NBS-Boulder, is overall program manager and Dr. Alan F. Clark, NBS-Boulder, is contract monitor.

The total program is divided into the general categories of mechanical properties, thermal properties, composites, data compilation and evaluation, and specialized structures. The program will continue for three years with annual reevaluation regarding program scope and participation. Table 2-1 indicates the first year's program, the research organizations doing the work and a brief description of each effort.

From a glance at the table it is obvious that the initial major effort is to provide low temperature fatigue and fracture data which are needed for current design. The effects of size, processing, and fabrication are also being pursued. Thermal properties are being measured early in the program for design data. The properties and potential applications of composite materials are being investigated as well as the effects of the dynamic loading of magnet materials. The accumulation and compilation of all this data are an essential part of the effort.

The output of the program is expected to take four forms:

- (1) Semiannual technical reports will be distributed to all the contractors as well as to ARPA and the various "user" groups in the agencies,
- (2) it is hoped that most data will be published in the open literature,
- (3) data

will be incorporated into the Handbook in the year subsequent to its generation, and (4) possibly a reference book, complementary to the Handbook, will be composed by contributions from each laboratory and edited by NBS.

The Westinghouse Electric Corporation responsibilities in the current year's effort are divided into three tasks:

- |          |  |
|----------|--|
| Task I   | Characterization of Current Cryogenic Structural Materials         |
| Task II  | Processing Effects on Properties of Structural Cryogenic Materials |
| Task III | Evaluation of Joints in Structural Cryogenic Materials             |

This second report presents continuing results of these three tasks based on the functional areas of investigation: materials, fracture mechanics, microstructural analysis, and magnetic properties. In addition to semi-annual technical reports, a tentative list of technical publications which are planned for release all or in part under this contract include the following:

- Materials Considerations for Structural Cryogenic Applications
- Low Temperature Mechanical Properties of Austenitic Alloys
- Low Temperature Mechanical Behavior of Joints in Austenitic Alloys
- Fracture Mechanics Reliability Analysis Relative to the 5 mVA - 12,000 rpm Generator, Reference Contract USAF, F33615-71-C-1591

TABLE 2-1

ARPA - Low Temperature Properties of Structural Materials  
First Year Program (FY 74)

<u>Program Area</u>	<u>Program Description</u>
Mechanical Properties	
1. Fracture and Fatigue	
a. Materials Group (NBS-Cryogenics)	Fracture toughness, fatigue crack growth rate, fatigue, sustained load crack growth rate tests from 4-300 K on structural alloys.
b. Materials Group (Westinghouse)	Mechanical, magnetic, electrical loss characterization of alloys currently in use by Westinghouse in DOD sponsored programs. Mechanical tests include tensile, fracture toughness, fatigue.
c. High Load-Large Specimens (Martin-Denver)	Fracture toughness, fatigue crack growth rate data on very selected tough alloys requiring loads in excess of 30,000 lbs to fracture.
2. Effects	
a. Processing (Westinghouse)	Identification of effects of fabrication and processing techniques on mechanical properties of selected alloys. Variables include industrial melting practices, powder metallurgy techniques, and cold working.
b. Joining (Westinghouse)	Mechanical properties of fabricated metal joints, including welding (GTAW, EB, GMAW) brazing, and soldering from 4-300 K. Properties include tensile, notched tensile, fracture toughness, and fatigue crack growth rate.
3. Elastic Moduli, Tensile (NBS-Cryogenics)	Tensile and dynamic elastic (Young's, shear, bulk moduli) measurements on structural alloys from 4-300 K.
Thermal Properties	
4. Thermal Expansion, Specific Heat (Battelle)	Thermal expansion and specific heat measurements on selected insulations and structural alloys.
5. Thermal-Magnetothermal Conductivity (NBS-Cryogenics)	Thermal conductivity and thermal conductivity in magnetic fields up to 50 kilogauss from 4-300 K of structural alloys.
Composites	
6. Evaluation of Advanced Composites (NBS-Cryogenics)	Screening tests (tensile, fatigue at 4 K) on selected candidate metal and non-metal base composites, including B-epoxy, C-epoxy and polyimide, PRD 49-epoxy, borsic-Al, Steel-Al.



TABLE 2-1 (Continued)

<u>Program Area</u>	<u>Program Description</u>
7. Screening for Shield Materials (General Electric)	Screening study of composites for torque tube and electromagnetic shield applications.
Data Compilation and Evaluation	
8. Handbook (Battelle)	Publication of Handbook containing recommended best value data and complete set of references for 39 selected materials (structural alloys, superconductors). Data presented in graphical and tabular formats; mechanical, thermal, magnetic properties from 0-300 K.
Specialized Structures	
9. Effects on Magnet Materials (Argonne)	Characterization of change of electrical and mechanical properties of magnet materials as a function of fatigue and temperature.

### 3.0 SUMMARY

#### 3.1 Test Status

A test status summary for this entire program is shown in Table 3-1. All basic work is completed through mechanical testing. Extensive additional use of  $J_{IC}$  techniques over the planned effort has assured development of meaningful fracture toughness design data. Also, additional magnetic and resistivity measurements were provided in areas of greatest interest.

Several longer lead time items associated with welding and brazing requiring special welding wires or procedures are still in progress. Hence, results on brazed joints in copper and X750 are delayed along with welds in Kromarc-58 where filler wire had to be drawn in-house. A portion of the fractography remains in progress as this effort was logically delayed until completion of an analysis of the impact of processing effects on low temperature properties.

#### 3.2 Alloy Selection and Use

This FY 74 testing has provided essential low temperature properties for materials which have already seen cryogenic structural service. Hence, selection of these materials was dictated by the immediate need to support short range "best" judgement decisions made for actual prototype machines. In subsequent work on this project additional candidate structural materials are being selected based on general cryogenic hardware requirements. These requirements were discussed in detail in Section 5.0 of the First Semi-Annual Report for this program.

The important first generation machine materials included were AISI 310S stainless steel, Inconel X750, Kromarc-58 and OFHC copper.

The first three are structural candidates whereas copper is not always self supporting but functionally required for other than structural reasons.

One additional aspect in material selection which is becoming increasingly important is conservation of scarce materials. In this regard, Kromarc-58 is both stronger and less alloyed than 310S stainless, Cr + Ni at about 45% for 310S vs. 38% for K-58. The further additional strength advantages in X750 are realized in part by switching from the iron-base system giving a Cr + Ni content of about 88%.

The 310S stainless steel and Inconel X750 alloys proved adequate in testing for main structural applications in respective low and high speed first generation prototype S.C. machinery. Kromarc-58 previously used for static applications in bubble chambers, would also be adequate for structural rotating hardware based on this test program. Basic property data on OFHC copper was developed to provide additional design flexibility in its application to rotating machinery even in those situations where it is not self supporting. Copper was shown to retain excellent toughness to the lowest test temperature, 4.2°K.

### 3.3 Mechanical Properties

On a first-cut basis the three structural alloys in wrought form and standard heat treatment compare in yield strength at 4.2°K approximately as follows:

AISI 310S	Solution treated and quenched	120,000 psi
Kromarc 58	Solution treated and quenched	160,000 psi
Inconel X750	Solution treated and Double Aged	125,000 psi to 170,000 psi

The spread in Inconel X-750 values reflects the emphasis in this program on developing a realistic perspective on the effect of processing history. X750 was used for this purpose with the evaluation of a number of heats with different initial melting practices and thermo-mechanical treatments.

Reasonably good fracture toughness can be achieved along with the high yield strength for these materials at 4.2°K. Using the  $K_{IC}$ /oys

ratio as the "most tough" indicator and  $(K_{IC}/\sigma_{ys})^2$  as the defect size tolerance indicator gives the following for these alloys\*:

	<u>Condition</u>	$\frac{K_{IC}}{\sigma_{ys}}$	$\frac{K_{IC}^2}{(\sigma_{ys})^2}$
AISI 310S Stainless	STQ	1.99	3.98
Kromarc-58	STQ	1.23	1.52
Inconel X750	STDA	.55	.30
	to	1.53	2.34

\* An expanded summary is shown in Figure 3-5

Again, X750 was tested over a greater variety of material histories. The highest fracture toughness value shown was obtained for an intermediate strength of 140,000 psi yield. If X750 processing is tuned for strength, say 170,000 psi yield, then some drop in toughness occurs. Likewise, if processing cannot be optimized a penalty is also paid. This latter situation occurs in practice when a component size exceeds normal industrial wrought product size limiting flexibility in breaking down the cast billet structure.

In addition to the basic fracture toughness which gives a defect tolerance for component failure, crack growth rate data is being generated which permits calculation of maximum allowable defect size at "start of life". Most of the results of this effort are on Inconel X750 which would typically be the higher stressed alloy and was evaluated most extensively in terms of processing and fabrication effects. This data is treated in Section 6 of this report as a function of flaw configuration, stress in % of yield, and permissible calculated initial "start of life" flaw size. Results show that structural integrity of new machinery can be quantitatively specified for design and fabrication.

The basic tensile properties including notched strength generated in this program are summarized in Figs. 3-1 through 3-4. These figures show the wide variety of processing conditions factored into this evaluation. Several major aspects in the use of these materials are

evident in these figures:

- Most noticeable and expected is the low strength of copper. Interestingly, yield strength from room temperature to 4.2°K has essentially no temperature dependence; Fig. 3-1. Hence, OFHC copper is not considered a high strength structural alloy as are the other materials and will require independent support in high load applications. As a result of its excellent notch tensile toughness (Ratio Notched Tensile Strength to Unnotched Yield Strength) no additional fracture mechanics tests were required. Toughness and ductility in combination should give excellent design flexibility particularly if thermal strains require that plasticity be considered in machine designs. Tensile elongation of copper actually increased with decreasing temperature by as much as 60%.
- An advantage of X750 compared to 310S stainless and K-58 is the lower temperature dependence of yield strength. Whereas the yield strength advantage of X750 is modest at 4.2°K, its advantage increases as temperature increases toward ambient.
- All three structural materials responded favorably to notch tensile testing and are notch tough (i.e.  $NTS/UYS \geq 1$ ) throughout the temperature range for all processing and fabrication variables. Also, the overall stability anticipated in the use of fully austenitic materials for first generation machines is verified in a general way by these tests.

### 3.4 Processing

Several important facets of processing and fabrication considerations can be related to the mechanical properties results summarized in Figs. 3-1 through 3-5.

- The significant impact of different melting and working histories on properties of X750 is shown in Fig. 3-2 and Fig. 3-5. Although this processing data was generated specifically with Inconel X750, one can generally expect that an important trade-off for increased strength among other alloy systems will be an increased sensitivity of

mechanical properties to processing. Typically, use of more promising alloys entails greater effort in processing to assure that adequate metallurgical structures are obtained.

- The major processing constraint demonstrated for X750 is inferred as the requirement for adequate secondary working in breaking down cast ingot structures into wrought structures. This shows up as improved ductility in Fig. 3-2 for MP-2 and MP-3 vs. MP-1. Also, higher fracture toughness in Fig. 3-5, MP-2 vs. MP-1. Again, this shows up as higher strength in MP-3 but with some loss in fracture toughness compared with MP-2. These trade-offs are not unexpected. In this case, the more heavily worked structures were both stronger and tougher. MP-1 was the largest as received billet and MP-3 the smallest. Strength levels were inverse to size. To a point, all properties improve with increased ingot breakdown, MP-2. With even higher strength, MP-3, toughness is again compromised. Obviously, these differences must be accommodated in processing materials for specific design requirements.
- Structural observations confirm the generalized processing history responses in that strength appears to be an inverse function of grain size as expected from the Hall-Petch relation  $\sigma = \sigma_0 + Kd^{-1/2}$ . In addition, the finer grained structures of MP-2 and MP-3 demonstrate a transition from intergranular to cross-granular failure at low temperature. Hence, from a general fracture standpoint the finer grain size implies improved fracture behavior at low temperatures.
- Confirmation of grain size effects (more independently of thermo-mechanical treatments) is obtained in the powder processed (HIP) X750. This is consolidated directly to a finished form using powder made from MP-1 stock. Conversion from powder to plate stock was accomplished in one step without subsequent working by hot isostatic pressing (HIP) with a significant resultant grain refinement relative to MP-1. A modest strength increase and improved ductility and toughness were realized.

- The hot isostatically pressed X750 properties show also that this process can be considered as an alternative conversion process for components in cryogenic applications.
- The effect of using cold work to enhance strength was demonstrated using Kromarc-58 with 30% cold reduction. A resulting trade-off in fracture toughness of about 45% accompanied about a 30% increase in yield strength.
- Sensitization of stainless steel was considered as the major conventional processing problem. In tensile testing properties have proven to be essentially comparable but properties are compromised in fracture toughness results. A deformation mode change to intergranular fracture at low temperatures indicates a continued concern which may be clarified by crack growth rate tests still in progress.

### 3.5 Fabrication

The major aspect of fabrication considered in this project are the properties of welded and brazed joints. Much of the welding work is completed providing a measure of the weldability of these materials obtained during fabrication and inspection of the weldments. Gas tungsten arc welds had satisfactory quality as used for Kromarc-58 and Inconel X750. Shielded metal arc welds in 310S stainless were also good, of general commercial quality. Porosity was experienced in gas metal arc welds in copper. This did not seem to impair properties and was most likely caused by poor shielding. Electron beam welds in X750 had cracks in the weld center and also the heat affected zone. Hence, electron beam welds in X750 require careful inspection. The cracks were avoided in test specimen lay out and hence seemed to have no effect on tensile properties. Transverse weld specimens always failed in the base metal well removed from any source of weld defects in X750 electron beam welds for material without a post weld heat treatment.

Mechanical property results for weldments has been encouraging from the standpoint of equivalence to base metal test results.

- In the case of X750, all weldments had generally good fracture toughness, Fig. 3-5. Only one base metal condition was significantly better. All unnotched transverse tensile tests failed outside the weld. However, the weldment base metal proved to be the weakest of the three melting practices obtained for this project (MP-1)
- Notched tensile properties of X750 weldments are basically good. Additional considerations must be factored into this conclusion. First, the yield strength of a transverse weld specimen isn't necessarily a true weld value since elongation may not be uniform along the gage length. This would have an unknown affect on true yield strength. Secondly, while notched specimens fail at the weld (in the notch), plain specimens always fail outside the weld. Hence, some consideration should be given to estimating the lowest possible notched tensile strength to unnotched yield strength ratio for weldments. The best approach available is to compare the weld notched tensile strength to the highest strength X750 base metal evaluated, MP-3 as solution treated and double aged. All values are greater than 1.0 indicating good notch-tough weldments even though somewhat more conservative than shown on Fig. 3-3.

Weld Metal Notched Strength/Unnotched Y.S. of MP-3, STDA

	<u>R.T.</u>	<u>77°K</u>	<u>4.2°K</u>
ST/EBW	1.1	1.1	1.1
STDA/EBW	1.1	1.2	1.2
ST/GTAW	1.2	1.2	1.2
ST/GTAW	1.3	1.2	1.2

- A similar consideration for notched strength in 310S weldments shows that these are reasonably accurately shown on Fig. 3-1. 310S weldments likewise failed in the base metal when not pre-notched. In the case of Kromarc-58 tensile failures did occur in the weld or heat affected zone. Again, a most conservative treatment for K-58



indicates that the notched strength ratios shown on Fig. 3-4 are reasonable.

- Weldment evaluation from a ductility standpoint shows comparable results to the base metal for all three alloys. Since transverse weldments do not necessarily yield uniformly, the best "weld to base metal" ductility comparison is reduction in area. This is decidedly a compromise compared with testing all weld metal samples except in cases like K-58 where failures occurred in the weld.

### 3.6 Physical Properties

Two important materials responses at cryogenic temperature were measured for the basic alloys in several forms including both cold worked and welded. Samples of Inconel 718 were also included. The basic characteristics studied were:

- Magnetization to a field strength of 70 kOe from room temperature to 4.2°K.
- Resistivity from room temperature to 4.2°K

Both characteristics are important to design of cryogenic electrical machinery. Transformation of non-magnetic structural materials to magnetic states is undesirable because of the resultant interaction with strong magnetic environments in superconducting machines, and also because of the potential dimensional instability which accompanies structural transformation. Electrical resistivity measurements provide an estimate of thermal conductivity, an important design parameter for cryogenic machines. Thermal losses represent a significant leverage on machine losses at low temperatures, i.e., a one watt loss at 4.2°K can represent a cooling system input requirement as high as 1000 watts.

Magnetic behavior is summarized in Table 8.1. All materials appear satisfactory for design from both a magnetic and structural stability standpoint. Very slight ferromagnetization is displayed by

AISI 310S, X750 and Inconel 718 at 4.2°K at values 2% to 3% of iron. Kromarc-58 is particularly stable even as-welded.

Resistivity measurements are summarized in Table 8.2. Again, all program materials were tested over a broad range of finished conditions including as-welded and cold worked. Again, Inconel 718 tests were also run. Generally, equivalent properties were measured for different forms of the same structural alloys. On the other hand, much higher resistivities were noted for weldments in copper vs. base metal, particularly at lower temperatures. This most likely reflects both alloying element effects in the filler wire and oxygen contamination during welding which was also implied by high porosity found in copper welds.

TABLE 3-1 STRUCTURAL MATERIALS FOR CRYOGENIC APPLICATIONS

Overall Program Status As Of September 9, 1974

Material Code	Condition	Chem. Analy.	Metallography		Physical Prop.		Processing	Joining	Tensile			Notched Tensile			K1C			J1C <sup>(3)</sup>		FCGR			Fractography <sup>(4)</sup>		
			(1)	(2)	Mag.	Res.			R	N	H	R	N	H	R	N	H	R	H	R	N	H	R	N	H
OFHC-Cu																									
10XX ◇	AR	/1	1/1	1		1			1/1	1/1	1/1	1/1	1/1	1/1	1/2	1/2				1/2	1/3	1/1	3/3	3/3	
11XX ◇	SR		1/1	1			1/1		1/1	1/1	1/1	1/1	1/1	1/1	1/2	1/2				1/2	1/3		3/3		
12XX ◇	GMAW		2/2			1		3/2	2/2	2/2	2/2	2/1	2/2	2/2	1/2	1/2				1/2		1/1	1/1	1/3	
13XX ◇	B		1/2					1/2	1/2	1/2	1/2	1/1	1/2	1/2	1/2	1/2						1/1	1/1	1/2	
14XX ◇	S		1/2					1/2	1/2	1/2	1/2	1/1	1/2	1/2	1/2	1/2						1/1	1/1	1/2	
AISI 310S																									
20XX	STQ	□/1	2/2	1	2/1	2/1	1/1		1/1	3/2	4/2	1/1	1/2	1/2	1/1	2/2	2/3	4	□/1	1/2	2/3	1/2	1/3	1/3	
21XX ◇	STFC		1/1	1		1	1/1		1/1	1/2	2/2	1/1	1/2	1/2	1/1	2/2	2/3	□/1	1/2	1/3	1/2	1/3	1/3		
22XX ◇	SMW	□	2/2		1/1	1/1	2/2	2/2	2/2	2/2	2/2	2/1	2/2	2/2	1/2	1/3		6		1/2	1/2	1/1	1/3	1/3	
Inconel X750																									
30XX ◇	ST	2/1	2/2	2	2/2	2/2	2/2		1/1	2/2	2/2	1/1	2/2	2/2	1/1	4/2	2/3	5	4	2/2	1/2	2/3	2/2	2/3	2/4
31XX ◇	STDA		2/2	2	2/1	2/1	2/2		1/1	2/2	2/2	1/1	2/2	2/2	1/1	4/2	2/3	5	2/2	1/2	4/3	2/2	2/3	2/3	
32XX	ST/EBW		2/3	1			3/3	3/3	1/1	1/2	1/2	1/1	1/2	1/2	1/2	1/2		2	1/1	2/1	1/1	1/2	2/2		
33XX	STDA/EBW		2/3	1			3/3	3/3	1/1	1/2	1/2	1/1	1/2	1/2	1/2	1/2		2	1/1	1/1			2/2		
34XX	EBW/STDA		2/3				3/3	3/3	1/1	1/2	1/2	1/1	1/2	1/2	1/2	1/2		3	1/2	2/2			2/2		
35XX	ST/GTW		3/3	1			3/3	4/3	1/1	1/2	1/2	1/1	1/2	1/2	1/2	1/2		6	1/1	2/2			2/2		
36XX	STDA/GTW		3/3	1			3/3	4/3	1/1	1/2	1/2	1/1	1/2	1/2	1/2	1/2		5	1/1	2/2			2/2		
37XX	GTW/STDA		3/3				3/3	3/3	1/1	1/2	1/2	1/1	1/2	1/2	1/2	1/2		5	1/1	2/2			2/2		
38XX ◇	B		1/2					1/2	1/2	1/2	1/2	1/1	1/2	1/2	1/2	1/2						1/2	1/2		
40XX	MP 2/STDA	□/1	2/2				2/2		1/1	2/2	2/2	1/1	2/2	2/2	1/2	1/2		6					2/2		
50XX	MP 3/STDA	□/1	2/2				2/2		1/1	2/2	2/2	1/1	2/2	2/2	1/2	1/2		7					2/2		
60XX ◇	HIP	2/2	2/2				5/2		2/1	2/2	2/2	2/1	2/2	2/2	1/2	1/2		7		1/2	1/2	1/1	2/2	2/2	
61XX ◇	HIP/STDA	1	2/2		1	1	3/2		2/1	2/2	2/2	2/1	2/2	2/2	1/2	1/2		6		1/2	1/2		1/2		
Kromarc 58																									
80XX ◇	STQ	1/1	1/2		1/1	1/1	2/2		1/1	2/2	2/2	1/1	2/2	2/2	1/2	1/3		5	□/2	1/2	1/3	1/2	1/3	2/3	
81XX ◇	CW		2/2		1/1	1/1	2/2		1/1	2/2	2/2	1/1	2/2	2/2	1/2	1/3		5	□/2	1/2	1/3	1/2	1/3	2/3	
82XX ◇	GTW	1/1	4/2		1	1	2/2	2/2	1/1	2/2	2/2	1/1	1/2	1/2	1/2	1/3				1/2	1/2	1/1	1/3	1/3	
83XX ◇	CW/GTW		1/2		1	1	1/1	1/1	2/1	2/2	2/2	1/1	1/2	1/2	1/2	1/3							1/2		
84XX ◇	GTW/CW		1/2		1	1	1/1	1/1	2/1	2/2	2/2	1/1	1/2	1/2	1/2	1/2							1/2		
85XX ◇	GTW/C W/A N		1/2				3/1	1/1	1/1	1/2	1/2	1/1	1/2	1/2	1/2	1/2							1/2		

Notes: 1 Optical Microscopy

2 Replicate and Transmission Electron Microscopy. X-Ray Dispersive and Microprobe Analysis to be Incorporated as Required

3 Elastic-Plastic (J<sub>IC</sub>) Testing and Analysis Techniques to be Incorporated Where Linear-Elastic (K<sub>IC</sub>) Data is Non-Valid

4 Macro- and Microfractographic (SEM) Examination Schedule to be Adjusted in Response to Exhibition of Unusual Material Behavior

\* Available Specimen Size Invalid for Meaningful K<sub>IC</sub> Interpretation - Test Eliminated

□ Certified Chemical Analysis from Supplier - Additional

■ Ditto-Additional Interstitial Analysis Completed at ...

→ J<sub>IC</sub> Tests Substituted for K<sub>IC</sub>

● Test Eliminated

◇ Testing Still in Progress Where Fraction Numerator Open

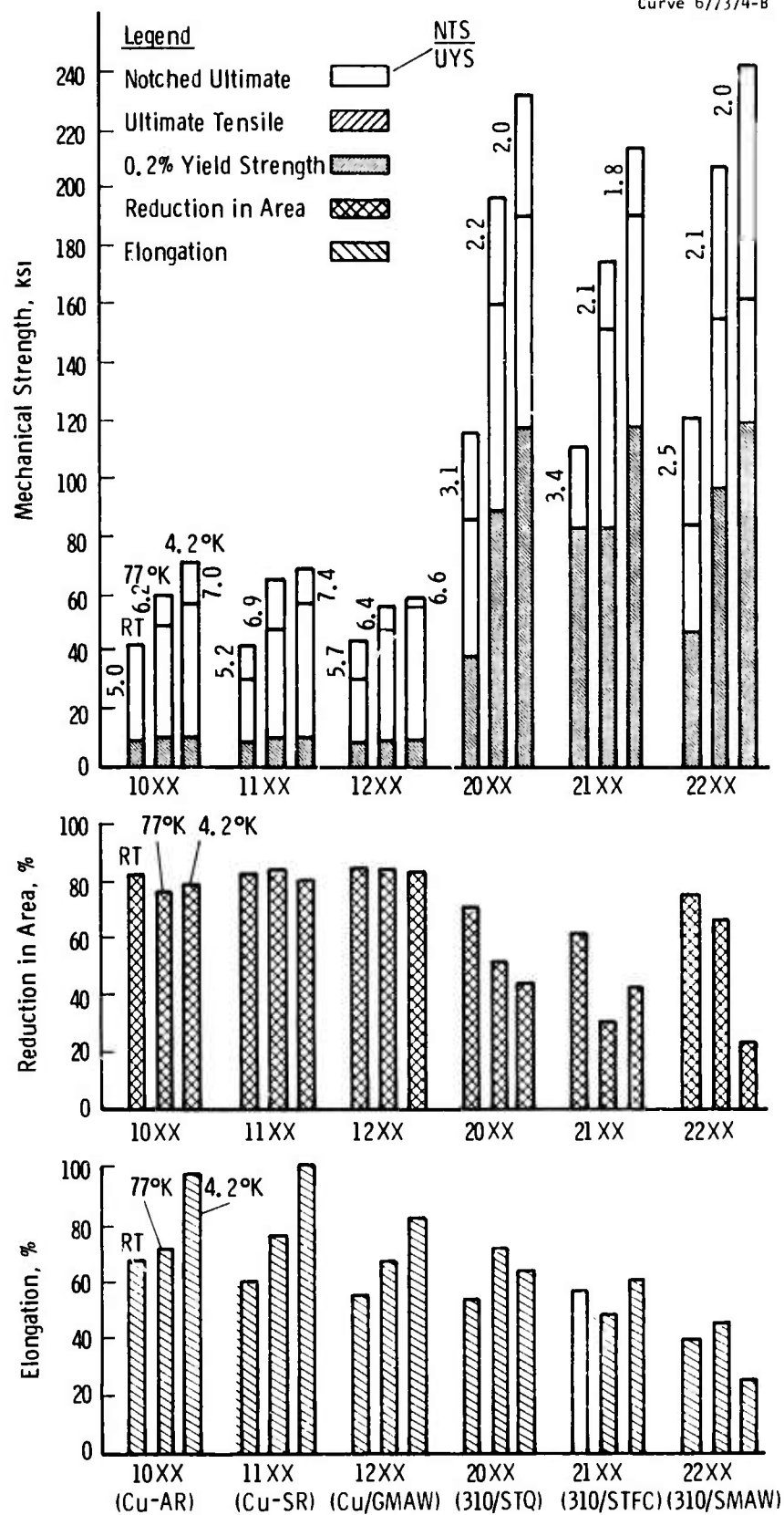


Fig. 3-1- Summary comparison of mechanical strength and ductility at RT, 77°K & 4.2°K of oxygen free copper and AISI 310S stainless steel for various processing and welding conditions, Cu-AR (code 10XX); Cu-SR (code 11XX); Cu-GMAW (code 12XX); 310S/STQ (code 20XX); 310S/STFC (code 21XX); 310S/SMAW (code 22XX)

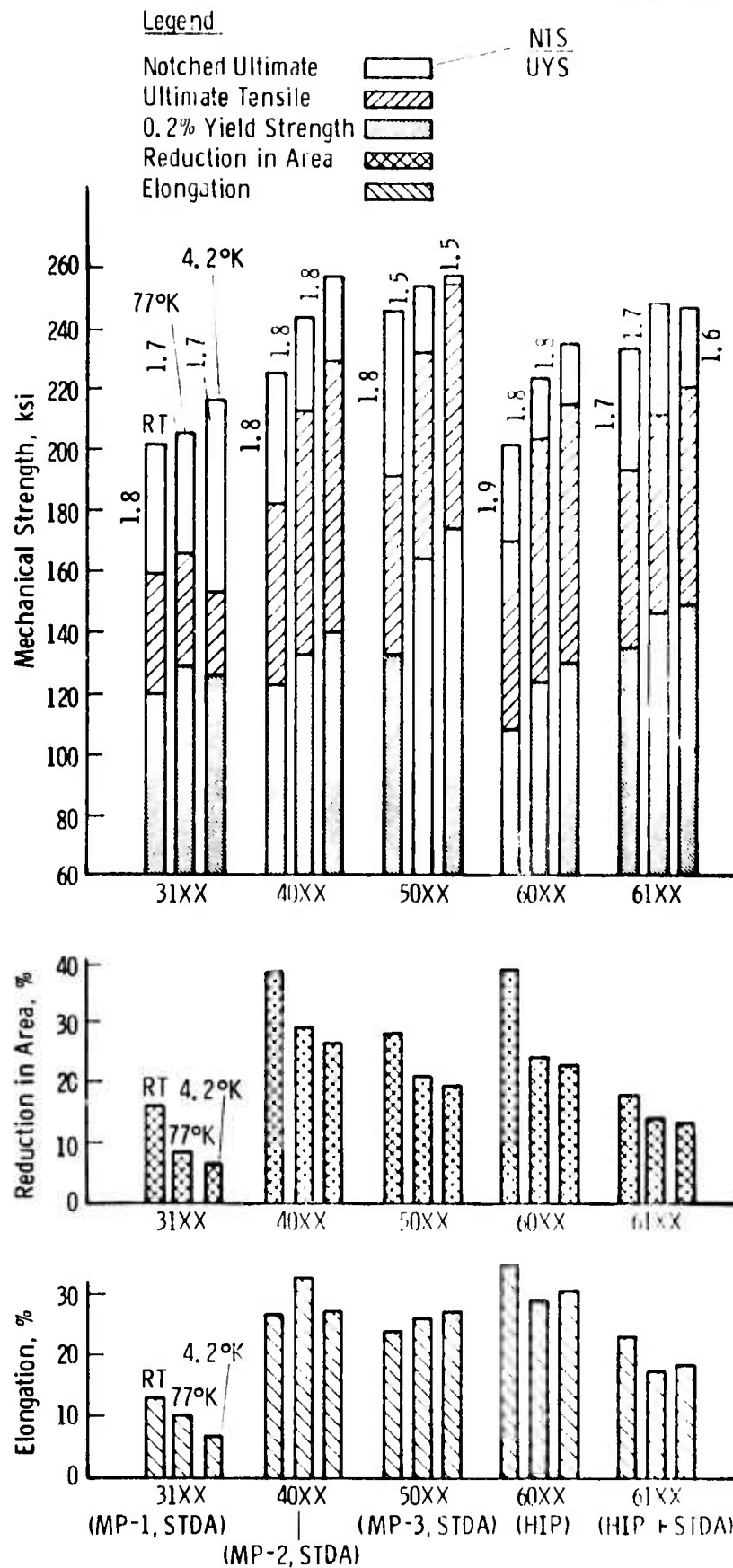


Fig. 3-2— Summary comparison of mechanical strength and ductility at RT, 77°K & 4.2°K of Inconel X750 for various processing conditions, VIM-VAR, STDA (code 31XX); AAM-VAR, STDA (code 40XX); VIM, STDA (code 50XX); VIM-VAR, HIP (code 60XX); VIM-VAR, HIP + STDA (code 61XX)

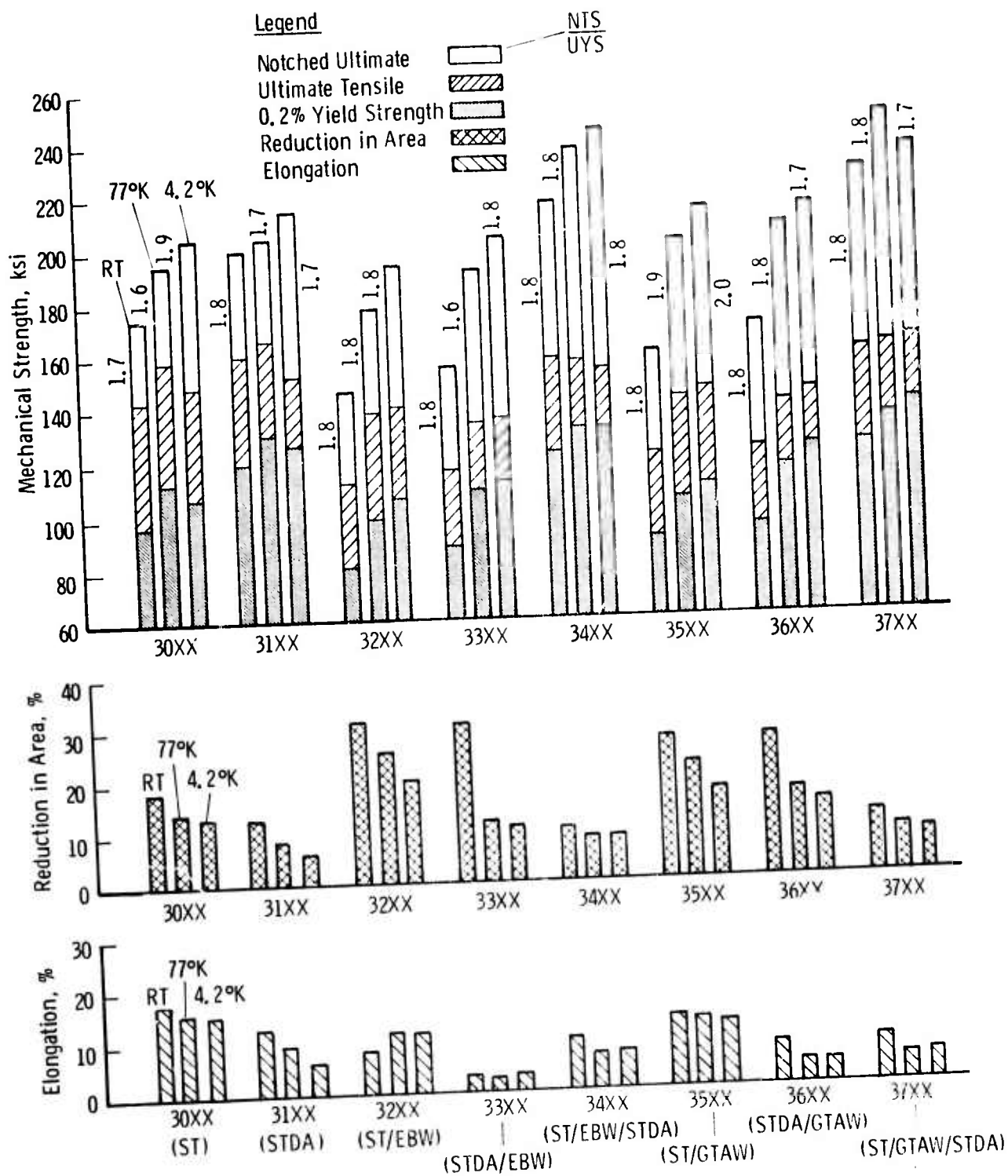


Fig. 3-3— Summary comparison of mechanical strength and ductility at RT, 77°K & 4.2°K for Inconel X750 (VIM-VAR) base metal, HVEB and GTA composite weldments



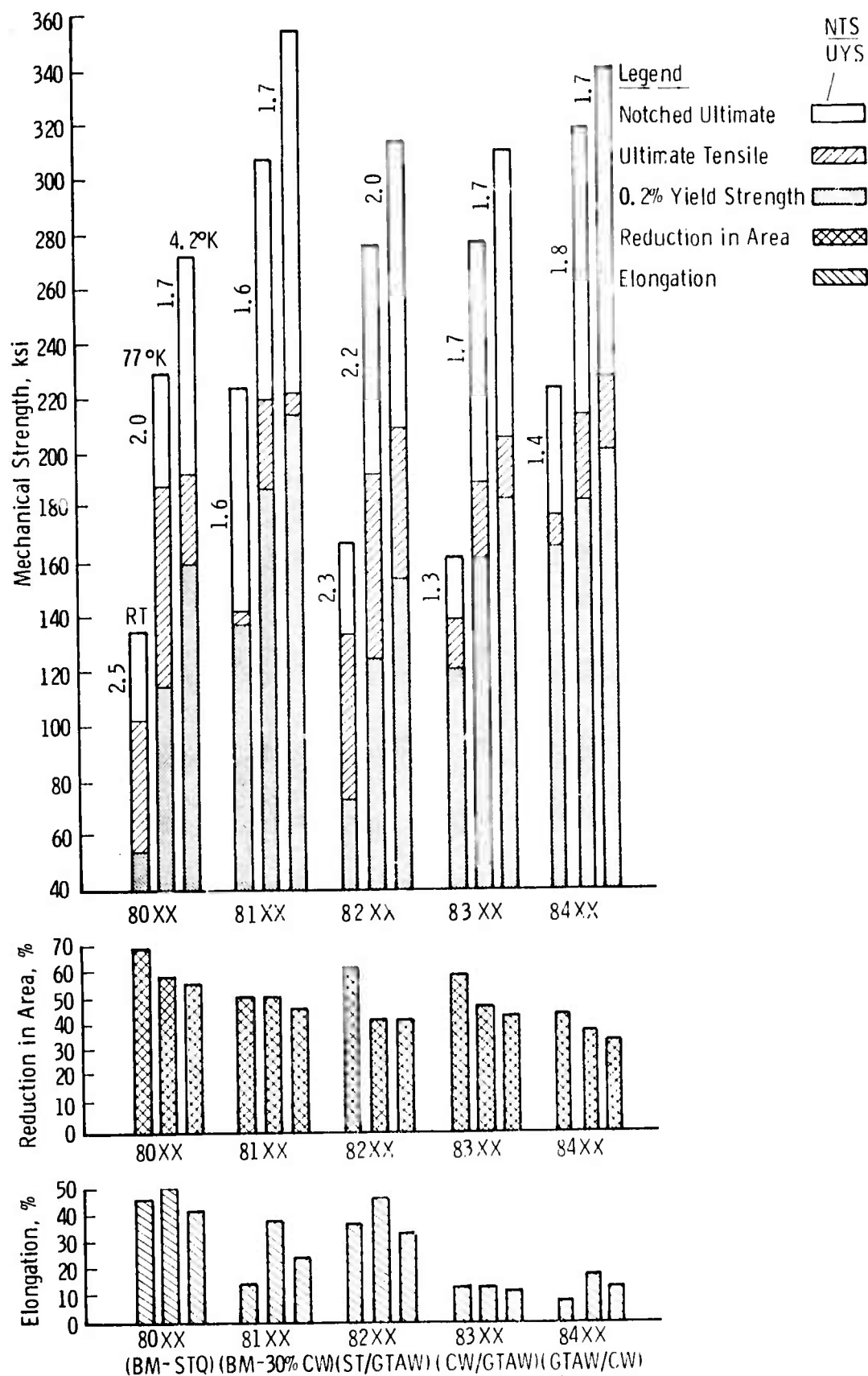


Fig. 3-4—Summary comparison of mechanical strength and ductility at RT, 77°K & 4.2°K of Kromarc 58 stainless steel for various processing and GTA welding conditions, STQ, (code 80XX); 30% cold work (code 81XX); STQ/GTAW (code 82XX); STQ/GTAW (code 83XX); GTAW/CW (code 84XX)

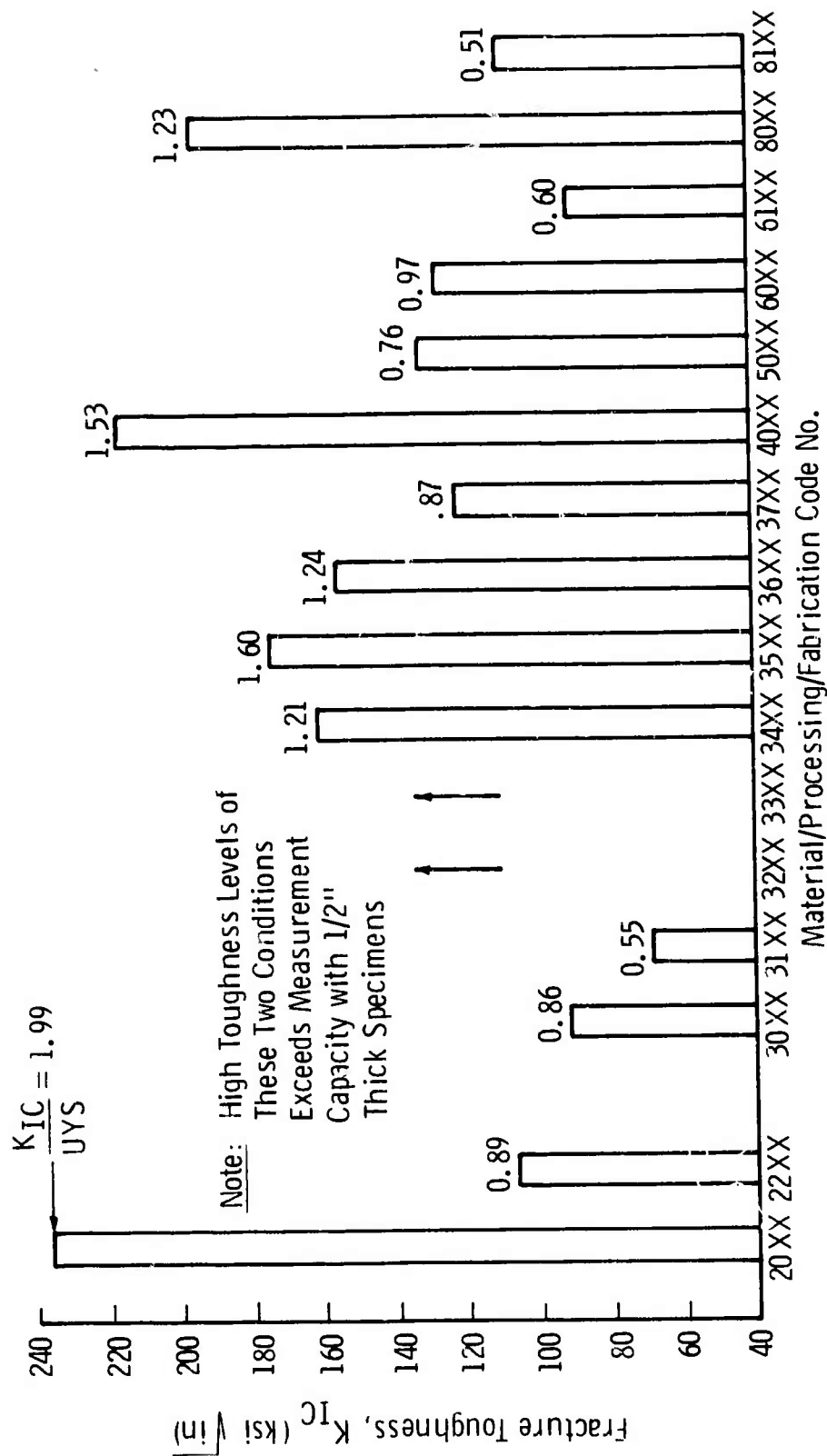


Fig. 3-5-- Summary comparison of fracture toughness at 4.2°K

Code 20XX - 310S, STQ	Code 32XX - X750, ST/EBW	Code 40XX - X750, MP-2/STDA
Code 22XX - 310S, SMAW	Code 33XX - X750, STDA/EBW	Code 50XX - X750, MP-3/STDA
Code 30XX - X750, MP-1/ST	Code 34XX - X750, EBW/STDA	Code 60XX - X750, HIP
Code 31XX - X750, MP-1/STDA	Code 35XX - X750, ST/GTAW	Code 61XX - X750, HIP/STDA
	Code 36XX - X750, STDA/GTAW	Code 80XX - K5B, STQ
	Code 37XX - X750, GTAW/STDA	Code 81XX - K5B, 30% CW



#### 4.0 WESTINGHOUSE PROJECT DESCRIPTION

This project represents the active participation of the Research Laboratories of the Westinghouse Electric Corporation under Contract CST-8304 in a comprehensive overall program for cryogenic structural materials monitored by the Cryogenics Division of the National Bureau of Standards. The overall program is sponsored by the Advanced Research Projects Agency (ARPA) of the Department of Defense.

Several advanced cryogenic application areas are identified in which the subject matter of this program will be mutually beneficial. One such advanced application area for cryogenic structural materials requiring immediate attention is that of superconducting electrical machinery<sup>(1)</sup> as typified by two recent 5 MVA S.C. generator prototypes developed by Westinghouse<sup>(2-3)</sup>. Other important cryogenic application areas include electrical transmission lines, superconducting magnet support structures for Controlled Thermonuclear Reactor (CTR) devices, and structural materials for second generation rotating superconducting machinery designs.

##### 4.1 FY 74 Project

The first year's programs (Sept. 73 - Sept. 74) key off typical structural materials requirements for S.C. machinery prototypes. The overall outline for this FY 74 Westinghouse portion of the ARPA-NBS program is shown schematically in Fig. 4-1. The principal personnel involved are listed in Fig. 4-2 according to their respective functional project responsibility areas. This project is subdivided into three tasks as follows:

### Task I

Characterization of four materials currently being considered for superconducting machinery applications. These materials include OFHC Copper (CDA No. 102), AISI 310S Stainless Steel, Inconel X750 Superalloy and Kromarc-58 Stainless Steel. An operational flow chart of Task I is shown in Fig. 4-3.

### Task II

Evaluation of selected processing effects on the structure and properties of two representative structural materials being considered for cryogenic applications. These processing considerations include three different commercial melting practices of Inconel X750, hot isostatically pressed (HIP) consolidation of Inconel X750 powder, and the combined effects of cold working and welding in Kromarc-58 stainless steel alloy. An operational flow chart of Task II is shown as Fig. 4-4.

### Task III

Evaluation of selective joint fabrication methods in four materials for cryogenic applications. Joining techniques include shielded metal arc (SMA), gas metal arc (GMA), gas tungsten arc (GTA), vacuum electron beam (EB) welding, brazing and soldering. An operational flow chart of Task III is shown as Fig. 4-5.

## 4.2 FY 75 Project

The FY 1975 continuation of the Westinghouse portion of this ARPA-NBS program is also divided into three similar task areas which are outlined schematically in Figs. 4-6 to 4-8.

The approach to this continuation effort will be similar to the present FY 74 effort reported herein. All material will be procured and identified with respect to heat number, melting practice employed, chemical composition and microstructural analysis in the as-received condition. One judiciously selected thermal treatment will be identified and performed on each of the three selected base materials. Then, the previously employed functional test areas will be used in characterizing these materials.

In addition to the characterization of weld fusion zones on composite weldment specimens of these additional materials, testing will also be conducted on the heat-affected-zone (HAZ) areas of selected weldments in HIP Inconel X750 and Inconel 718. For this effort, specially prepared weldments using "J" or "K" shaped joint designs with their essentially planar (on one side) HAZ will be employed.

The results of the FY 75 respective study elements will be presented, analyzed and summarized in a quantitative as well as a qualitative manner. In addition, a relative interpretation of these results will be conducted with respect to the similar previously attained information on FY 74 materials and with respect to the relative overall applicability of these selected materials for general and specific cryogenic structural applications.

#### References

1. J. Bishop, Jr., "Study of the Markets for Large Rotating Electrical Machinery 1970-2000", A. D. Little, Inc. Report to U.S. Dept. of Commerce, NBS, Contract CST-8221, February 1973.
2. C. J. Mole, T. J. Faban, H. E. Haller, III, D. C. Litz and A. Patterson, "Five MVA Superconducting Generator Development", Westinghouse Research Laboratories Paper 72-1J2-CRYAL-P3 (Unrestricted), Sept. 22, 1972.
3. R. D. Blougher, T. J. Fagan, J. H. Parker, Jr., J. M. Wells and J. L. McCabria, "A High Speed Superconducting Generator", Inter. Cryogenic Eng. Conf. held in Kyoto, Japan, May 1974 (Proceedings to be published).

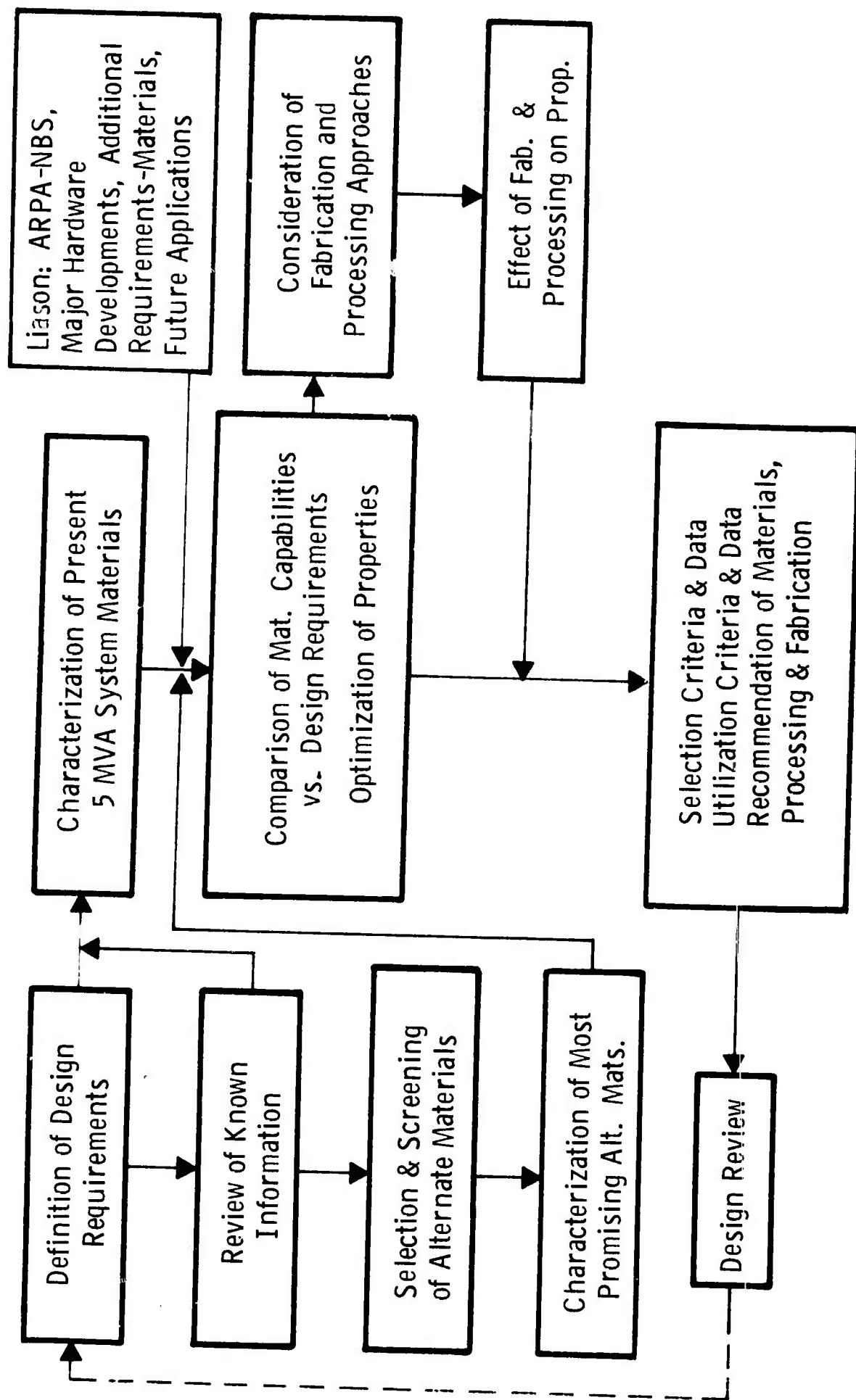


Fig. 4-1 Program Outline - Structural Materials for Cryogenic Applications

# EVALUATION OF CRYOGENIC STRUCTURAL MATERIALS, NBS CONTRACT 8304

Functions	Task I	Task II	Task III
	Basic Characterization	Processing Effects	Joint Behavior
Metallurgy, Processing, Joining	•	•	•
Fracture Mechanics	•	•	•
Fractographic & Micro-Structural Analysis	•	•	•
Magnetic Properties	•		

## Westinghouse Project Organization

### Management

Project Manager - G. G. Lessmann  
Fracture Mechanics - E. T. Wessel

### Principal Investigators

Materials, Fabrication, Processing - J. M. Wells  
Fracture Mechanics - W. A. Logsdon  
Microstructural Analysis - R. Kossowsky  
Magnetic Properties - M. P. Mathur

Fig. 4-2 Westinghouse Project Organization

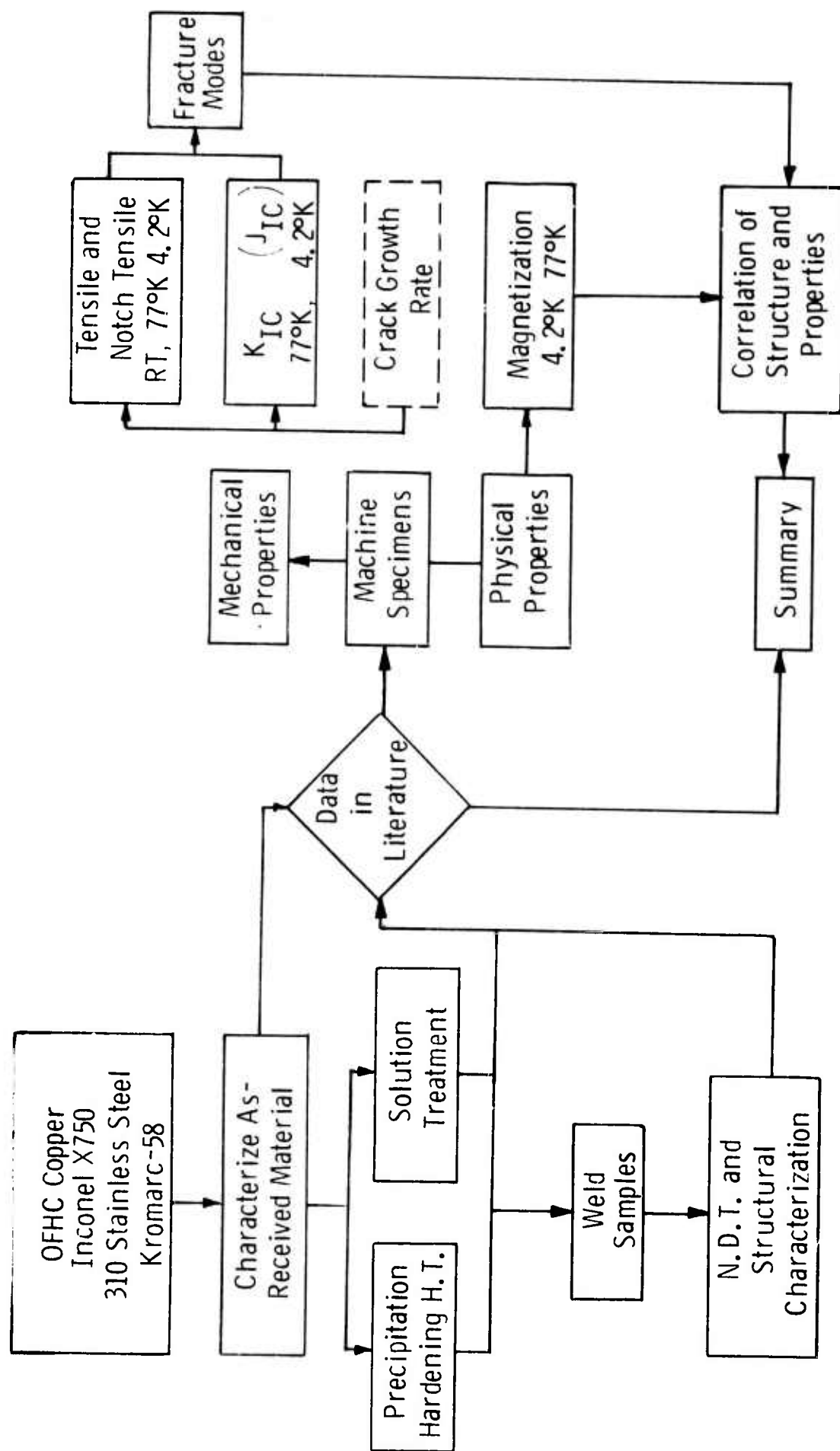


FIG. 4-3 TASK I—CHARACTERIZATION OF CURRENT CRYOGENIC STRUCTURAL MATERIALS.

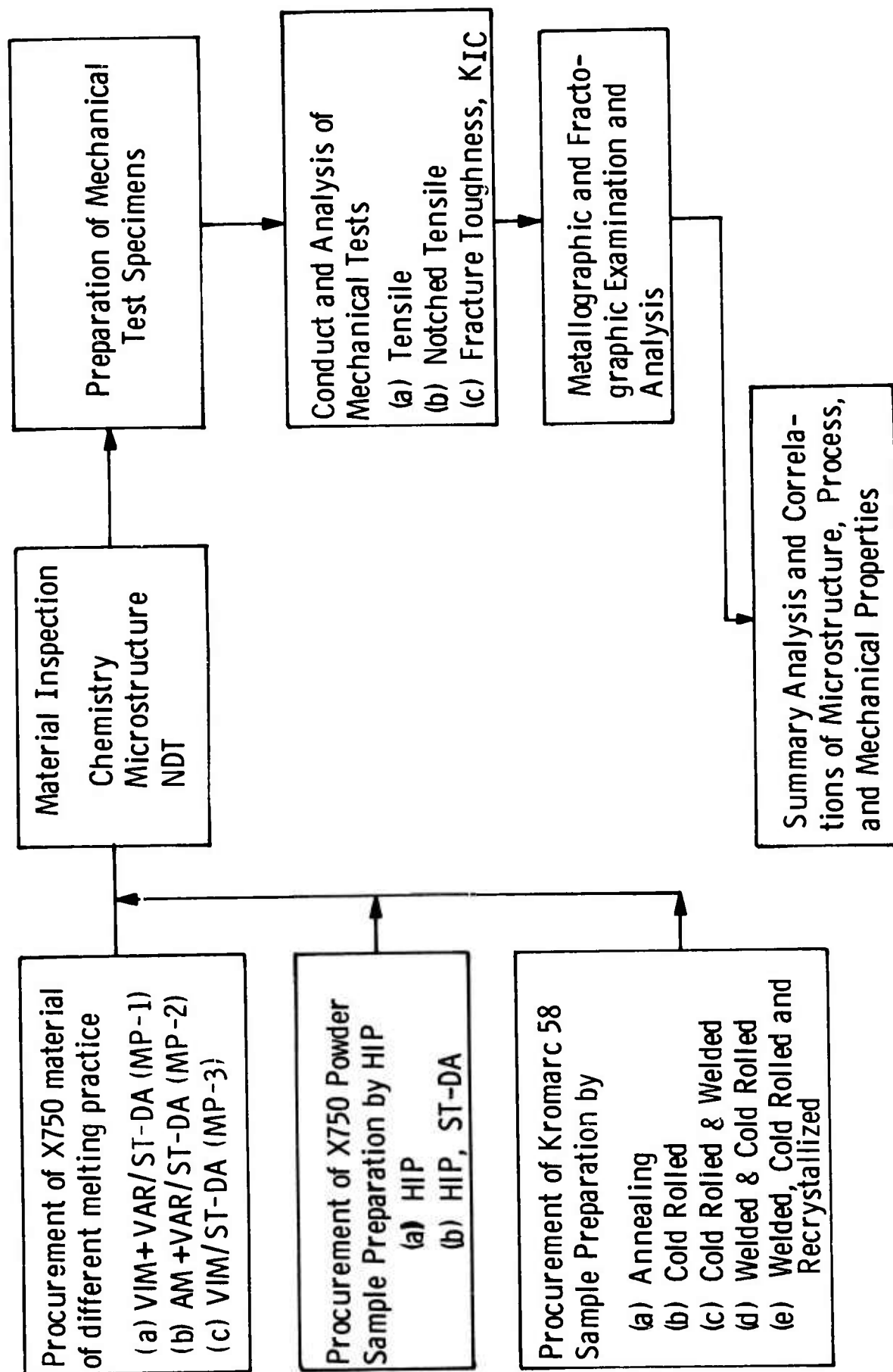


FIG. 4-4 TASK II-PROCESSING EFFECTS ON PROPERTIES OF STRUCTURAL CRYOGENIC MATERIALS.

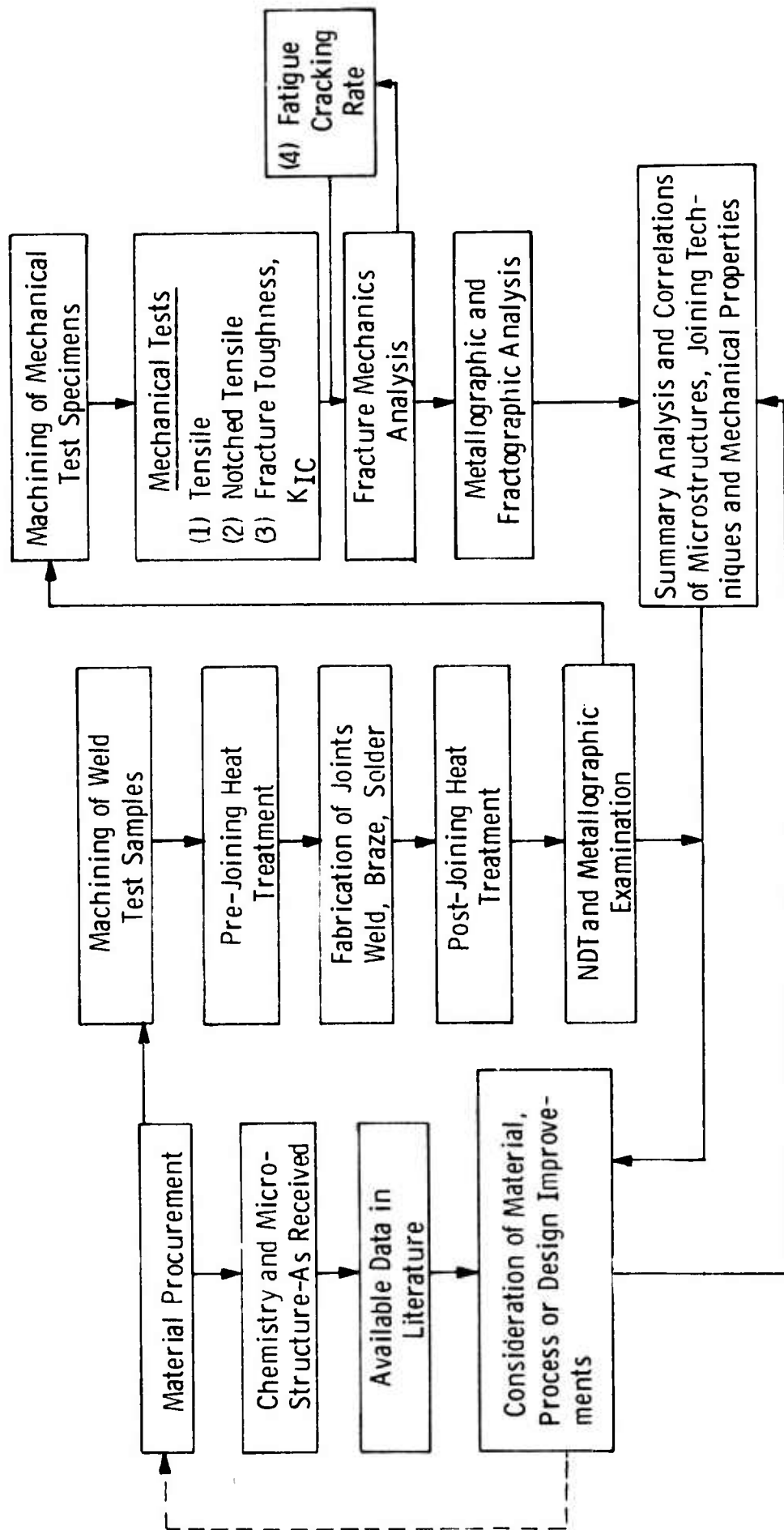


FIG. 4-5 TASK III--EVALUATION OF JOINTS IN STRUCTURAL CRYOGENIC MATERIALS



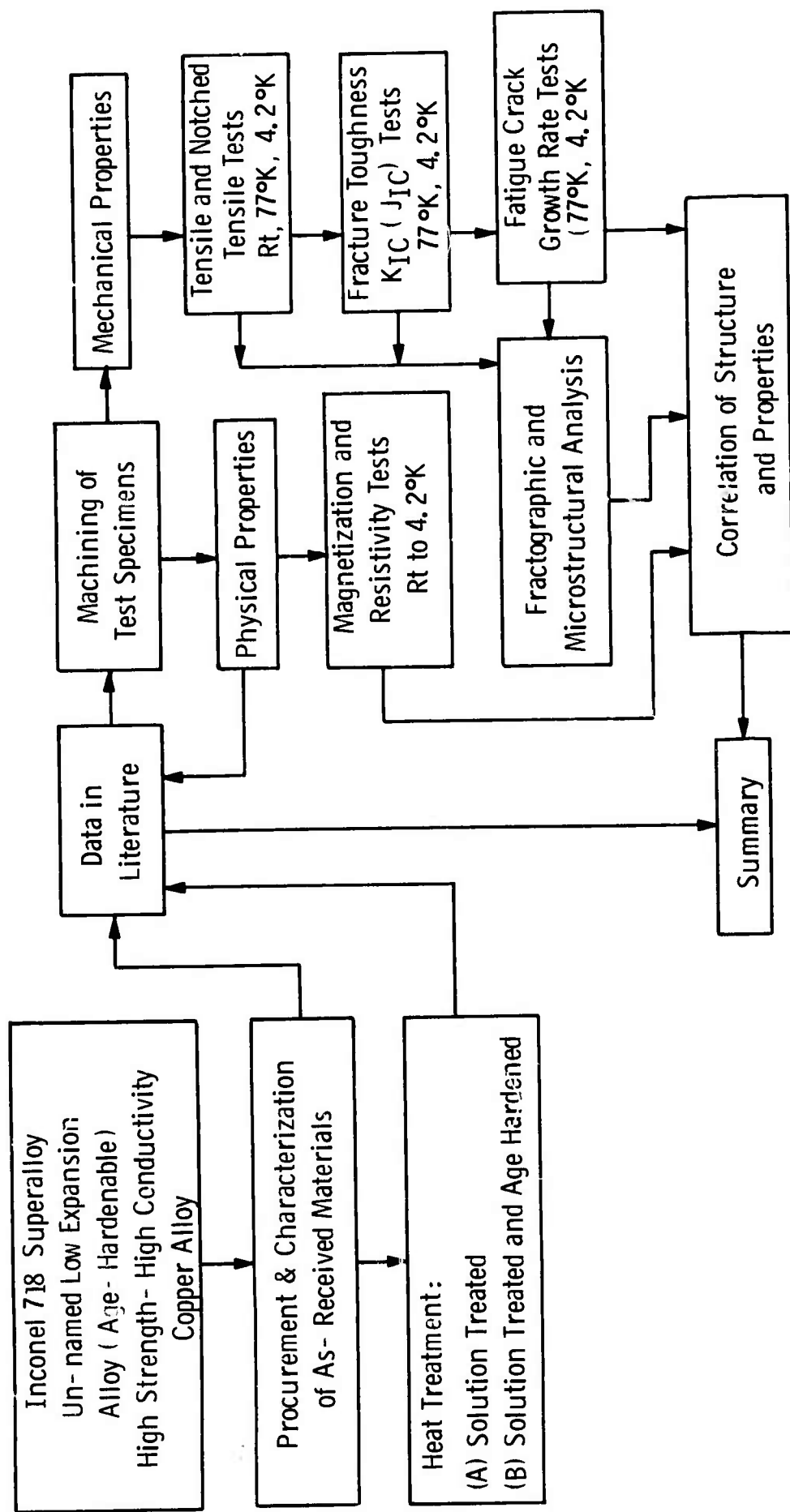


Fig. 4-6 — Task I (FY 75 Project) Characterization of structural base- materials for advanced cryogenic applications

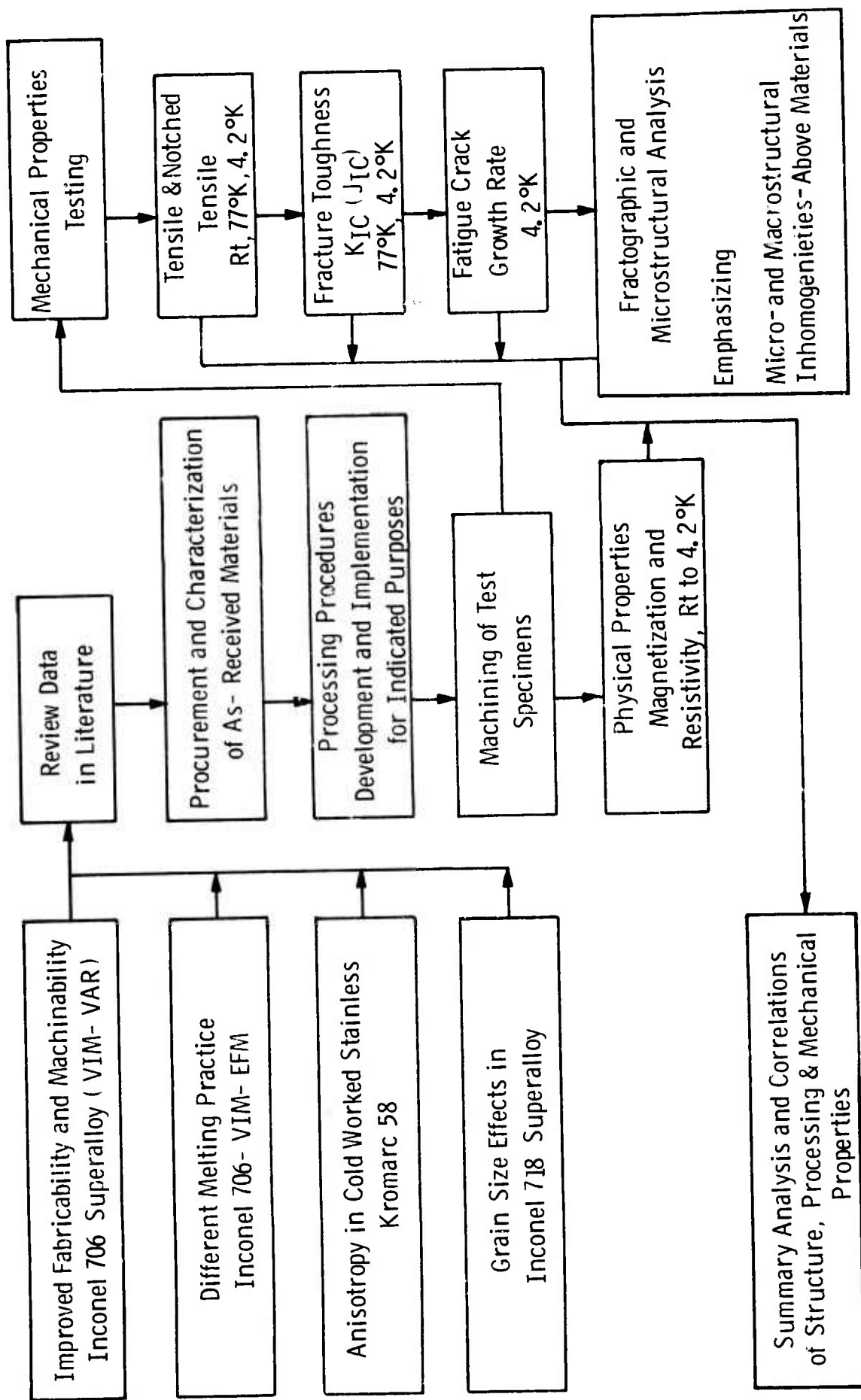


Fig. 4-7 - Task II ( FY75 Project) - Processing effects on cryogenic structural materials properties

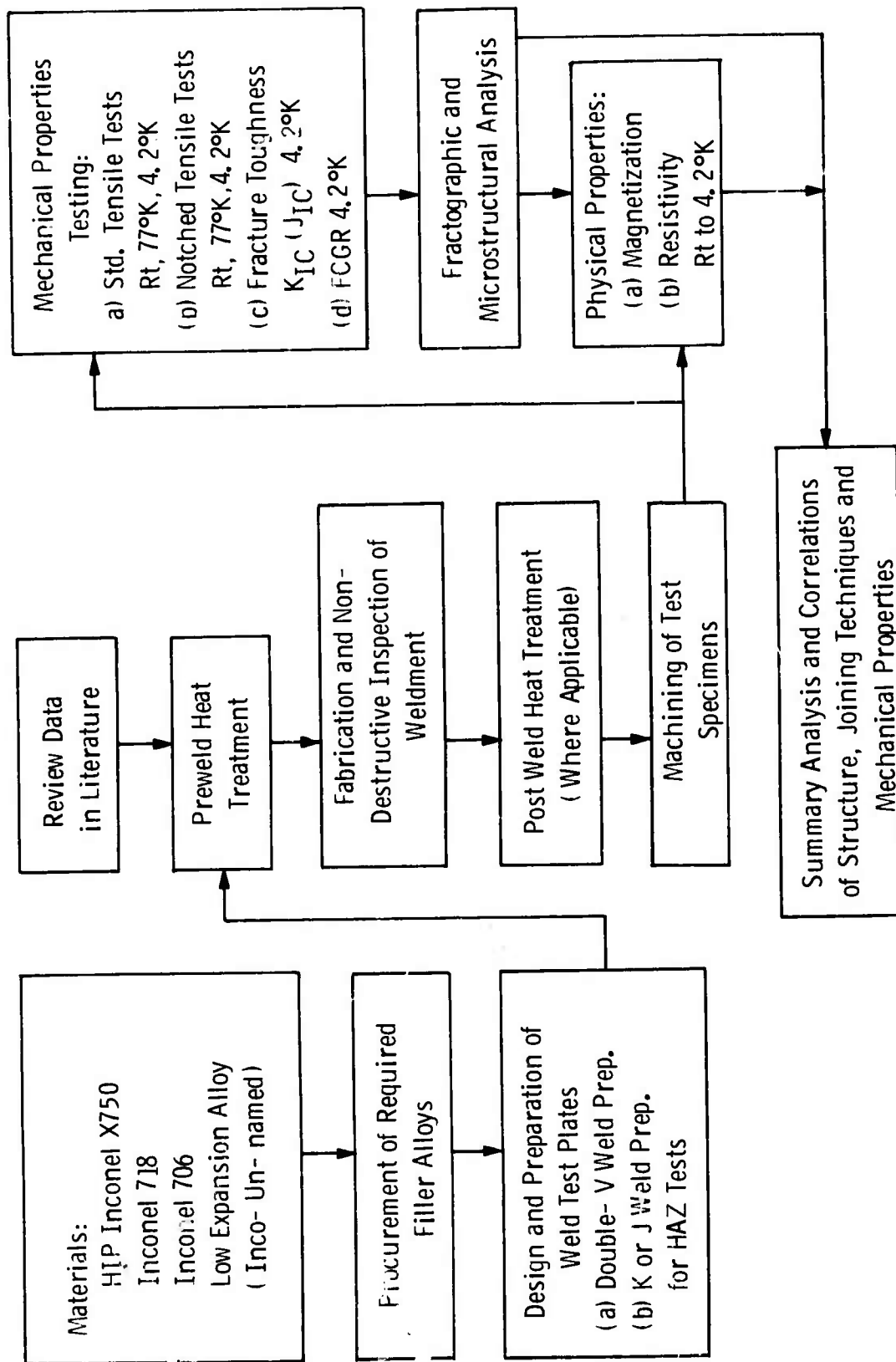


Fig. 4-8 — Task III (FY75 Project) - Fabricated joints in cryogenic structural materials

## 5.0 GENERAL CRYOGENIC STRUCTURAL MATERIALS/ PROCESSING/FABRICATION CONSIDERATIONS

A brief consideration of the two primary categories of cryogenic structural materials applications, the materials data required, and the limitations and scarcity of such explicit materials data available for failure safe design reliability, was discussed in Section 5.0 of the previous report<sup>(1)</sup> and, consequently, will not be repeated here. The general approach of this project conforms to the recommendations of the Committee on Characterization of Materials of the Materials Advisory Board<sup>(2)</sup>. The MAB report provides the "working definition" of characterization:

"Characterization describes those features of the composition and structure (including defects) of a material that are significant for a particular preparation, study of properties, or use, and suffice for the reproduction of the material."

Coupling MAB recommendations, other references (Refs. 3 - 8) and actual experience in the fabrication of superconducting generator prototypes (see Fig. 5-1) results in the following basis for the materials/processing/fabrication data being generated in this program:

- The present data base for materials selection and utilization required for advanced cryogenic structural applications is inadequate.
- The most productive (and most useful) improvement in the existing data base can and should be made at this time by improved characterization of existing materials, rather than by a "basic" alloy development program.

- A realistic assessment requires an interdisciplinary team approach typically involving the contributions of the designer, materials scientist, fracture mechanics engineer, welding engineer, physical scientist, nondestructive testing and inspection engineer, and manufacturing engineer.
- Characterization requires judicious selection and employment of basic "predictive tests" which are defined by the NMAB<sup>(3)</sup> as tests "whose purpose is to ensure confidence in the achievement of the design objective and/or performance capabilities of the component or structure for the specified purpose." Hence, the fracture mechanics tests and analysis in this program will assist in providing this capability.
- Many potential materials/processing/fabrication combinations and permutations are easily identified. An essential key to achieving the quantitative data and useful interpretations with a reasonable effort is to employ a closed decision making loop approach as outlined in Fig. 4-1.
- Materials data presented in various compilations and made available to the design engineer should be identifiable in all critical aspects. Users of such data should be made aware of the significant variation in properties which can arise from the same alloy or material but in various forms (i.e., sheet, plate, rod, tubing, forgings, casting, etc.), processed conditions (i.e., heat treatments, cold worked, melting practice, grain size, inclusion contents, etc.), and fabricated condition (i.e., forged, welded, brazed, soldered, coated, machined, etc.).
- Materials data used in design calculations must be closely representative of material properties actually attained in finished fabricated components of real structures.
- Manufacturing, inspection and quality assurance personnel must similarly be aware of materials, processing and fabrication deviations or defects levels which can, if not detected and corrected, seriously degrade the operational performance of the intended components or assemblies.

## 5.1 Materials Selection

### 5.1.1 Establishment of Materials Selection and Utilization Criteria

The rationale for establishment of materials selection and utilization criteria were discussed in Section 5.1.1 of the previous report. Two additional papers<sup>(8-9)</sup> have recently been published and reviewed which further elaborate specifically on the fracture mechanics aspects in establishing materials selection and design criteria.

As pointed out by Harrigan<sup>(7)</sup>, many government agencies are now incorporating contractual requirements for the use of fracture mechanics in aerospace, defense and power generation systems. Such system specifications generally require (1) fracture mechanics principles be employed in the design of fracture-critical parts, and (2) those parts be constructed from materials which are guaranteed to exhibit the level of fracture mechanics properties required by design. Thus fracture mechanics should be considered as an additional tool to use in designing good parts and structures. All of the other design criteria must also be applied to fracture critical parts and be satisfied. Furthermore, little is presently known about controlling the fracture mechanics properties of most materials which were not developed for the purpose of optimizing such properties.

Clark<sup>(8)</sup> has discussed the fatigue crack initiation and growth rate behavior of various structural alloys as two distinct mechanisms, and the role of each mechanism in materials selection and design utilization. Basically, Clark concludes that the inert-environment fatigue crack growth rate properties of a wide range of alloys within a given metals system are remarkably similar, but initiation properties depend primarily on the materials' static strength (in high cycle fatigue), or on the cyclic stress-strain behavior (in low cycle fatigue). Hence, the fatigue crack initiation properties cannot be related to those of fatigue crack growth rate. Thus, it is presently necessary to carefully evaluate the loading conditions associated with the intended application (design criteria input) to determine the important variables, and to conduct materials evaluation

tests under conditions representative of those likely to be encountered in service.

#### 5.1.2 Candidate Materials for Structural Cryogenic Applications

A review of various metal alloy classes and an initial list (Table 5-1) of candidate materials for structural cryogenic applications was included in Section 5.1.2 of the preceeding report<sup>(1)</sup>. Four of these candidate alloys were selected for the Westinghouse FY 1974 project reported herein. These FY 74 candidate materials are as follows:

- (a) OFHC Copper (CDA No. 102)
- (b) AISI 310S Stainless Steel
- (c) Inconel X750 Nickel Base Superalloy
- (d) Kromarc 58 Stainless Steel

The chemical compositions of these materials used is given in Table 5-3. Additional material documentation data is given in Table 5-4. Various processing and heat treatment schedules employed are listed in Table 5-5. Grain size and hardness measurements pertaining to these materials are included in Table 5-6. Characterization data for the Inconel X750 material as starting powder for the hot isostatic pressed (HIP) material is given in Table 5-7. The processing schedule for the Kromarc 58 stainless steel filler wire used in GTA welding is summarized in Table 5-8. The summarized welding processes and parameters are listed in Table 5-9.

#### 5.1.3 Candidate Materials for Westinghouse FY 75 Project Extension

The Westinghouse Electric Corporation has been awarded an extension of the present project covering the period from September 10, 1974 to September 9, 1975. This extension is referred herein as the ② FY 75 project. The summarized outline of the FY 75 effort is discussed in Section 4.2 of this report. The candidate materials to be evaluated in this FY 75 effort include the following:

- (a) Inconel 718 (VIM-VAR) Nickel Base Superalloy

This material is somewhat similar to Inconel X750 but has a greater strength level and slower age-hardening characteristics.

- (b) Inconel 706 (VIM-VAR and VIM-EFM) Nickel Base Superalloy  
This material is similar to Inconel 718, but possesses improved fabricability and machinability.
- (c) An Age-Hardenable, Low Expansion Iron-Nickel Alloy  
This unnamed alloy was developed by Inco, and appears potentially quite useful for high strength and low thermal expansion cryogenic applications.
- (d) High Strength, High Conductivity Copper Base Alloy  
This alloy would be one of the three such alloys listed in Table 5-1. Final selection of the specific alloy will be made following a more detailed review of the available technical literature as well as consideration of the physical availability of a suitable form and quantity of the selected alloy.
- (e) HIP Inconel X750 - Weldments in the consolidated powder of Inconel X750 (HIP) will be evaluated during the FY 75 project and the data compared with the base metal HIP material reported in the FY 75 project effort.
- (f) Kromarc 58 - The effect of preferred orientation in cold worked K58 material will also be evaluated and compared with present data on this alloy reported herein.

## 5.2 Materials Processing Considerations

### 5.2.1 Melting Practice in Inconel X750

Several techniques are employed in the commercial melting and refining of high temperature alloys and superalloys<sup>(9-14)</sup>. Many of these techniques were developed for reasons of greater economy and productivity, and also for added capability in terms of larger ingot capacity. Hence, an additional concern for the user is the performance variation in the same basic alloy produced by different melting practices and secondary refining techniques. The significance of variations in "as received" material depends upon both the design requirements and the sensitivity to subsequent processing/fabrication operations. Where a component failure



would result in an unacceptable risk, or where the costs of repair and downtime are unacceptable, performance variations in primary metal stock should be adequately assessed in the overall product reliability evaluation. An additional consideration is that the material produced with a less expensive melting and refining practice might well be totally adequate and available, whereas the same material produced by a more expensive melting and refining practice may not.

Consequently, the objective of this effort was to evaluate the mechanical and fracture mechanics behavior to 4.2°K of one candidate cryogenic structural alloy (Inconel X750) procured in several different commercial melting practices.

The materials available and obtained for this purpose were as follows:

MP-1 - Vacuum induction melted followed by vacuum arc remelt (VIM/VAR).

MP-2 - Air arc melted followed by vacuum arc remelt (AAM/VAR).

MP-3 - Vacuum induction melted (VIM).

The chemical compositions and other supporting documentation data for these three materials are listed in Tables 5-3 to 5-6. The MP-1 material was purchased as a 10-inch diameter, hot finished forging quality (HFFQ) round (HT56C1XY). The MP-2 material was obtained\* as a four-inch diameter, HFFQ round (HT1250XV). The MP-3 materials was obtained as a two-inch diameter hot finished (HF) round (HT57F8XS). It was originally intended to procure all material in the same form and size. Large diameter round stock was desired since such MP-1 material was already on hand and had been used successfully in the fabrication of a 5 MVA S.C. generator rotor prototype. Unfortunately, MP-2 and MP-3 materials were only available to us in sizes given above.

---

\* MP-2 and MP-3 materials were supplied without charge by the Huntington Alloys Division of the International Nickel Company, Inc.

All materials were melted as ingots and refined by hotworking by the same manufacturer. Consequently, the trademarked designation of "Inconel" was retained throughout this project for the X750 material, although this material is available from other manufacturers as well. An AISI designation of No. 688 is listed for this alloy in Ref. 15 without specification as to a particular melting practice.

The chemical compositions listed for these respective materials in Table 5-3 all fall within the following limiting chemical composition of Ref. 16 :

Nickel (plus cobalt)	70.00 min.
Chromium	14.00/17.00
Iron	5.00/9.00
Titanium	2.25/2.75
Aluminum	0.40/1.00
Columbium (plus Tantalum)	0.70/1.20
Manganese	1.00 max.
Silicon	0.50 max.
Sulphur	0.010 max.
Copper	0.50 max.
Carbon	0.08 max.
Cobalt	1.00 max.

The microstructure of these "as received" X750 materials are shown in Fig. 5-2 where the large grain size differences are readily apparent. The largest grain size is associated with MP-1 and the smallest with MP-3, while significant grain size differences between adjacent grains within a particular microstructure are readily apparent in both MP-1 and MP-2 materials. Further microstructural discussion of MP-2 and MP-3 materials and additional details concerning the subsequent hot reduction of the original ingot stock melted by these various melting practices is presented in Section 7.2.

### 5.2.2 Hot Isostatic Pressed Inconel X750

The hot isostatic pressing (HIP) of Inconel X750 nickel base superalloy was included in the materials evaluation for cryogenic applications for the following reasons:

The HIP process provides a method of attaining a small grain size in an austenitic type material where no allotropic transformation is available to permit a grain size reduction through conventional heat-treatment without mechanical deformation.

The HIP process permits a somewhat more uniform grain size and chemical homogeneity throughout the cross section of large volume components.

The HIP process involves low material scrap generation and reduced additional processing costs such as extensive rough machining by initially achieving a close-to-final-sized component as HIPed.

Although consolidation processing of many superalloy powder materials has been well reported<sup>(17-22)</sup> this is believed to be the first such attempt to HIP this particular wrought alloy. Most of the HIP work reported in the literature pertaining to superalloy materials applies to those superalloys which are only available in low ductility wrought or cast forms. In addition, this is likewise believed to be the first attempt at evaluating a HIP superalloy for extreme cryogenic applications.

The starting material was Inconel X750 VIM-VAR billet stock which was reduced to powder through the inert gas atomizing process by Federal-Mogul. Characterization data and scanning electron micrographs of the as-received powder were included as Table 5-7 and Fig. 5-2, respectively, of the proceeding report<sup>(1)</sup>. Two candidate HIP processing conditions were initially selected as:

- (1) HX-1, HIP at 1120°C (2050°F) and 10,000 psi (Argon)
- (2) HX-2, HIP at 1200°C (2190°F) and 10,000 psi (Argon)

One initial sample was made at each of these HIP conditions by containing the X750 powder in a 6-inch long by 1/2-inch diameter AISI 304 stainless steel tube, heating to approximately 370°C (700°F) for about 4 hours while evacuating to a vacuum of approximately  $3 \times 10^{-5}$  torr and sealed by hot forge welding. The samples were HIPed in the apparatus shown in Fig. 5-3. The diametrical shrinkage of these specimens was measured as 8.5 percent while the longitudinal reduction was measured at 4.7 percent over a four-inch gage length. A section from both HIPed samples was given the solution treatment at 1800°F for 1 hour and followed by a double aging heat treatment at 1350°F for 8 hours and furnace cooled to 1150°F, and held for 8 hours and air cooled. Microstructures of these samples both as-HIPed and HIP+STDA were presented as Fig. 5-3 of the previous report.

Further examination of these samples was conducted with scanning electron microscopy with the resulting microstructures shown in Figs. 5-4 and 5-5 of this report. Although a few infrequent small pores were observed at interparticle boundaries, full consolidation was considered achieved with both initial HIP conditions. A light constituent observed outlining the interparticle boundaries, is identified in Section 7.2.2 as being a MC Type carbide, (Nb, Ti) C.

Hardness measurements on these samples were as follows:

Inconel X750	- As HIP	Rc 35
	- HIP + STDA	Rc 41

These hardness readings are significantly higher than those of the corresponding X750 base metal hardness of ~ Rc 30 solution treated and ~ Rc 36, solution treated and double-aged.

Measurements of impurity gas content in the starting base metal (MP-1) and the various HIP stages are compared below:

	<u>O</u>	<u>N</u>	<u>H</u>	<u>Ar</u>
IN X750 As received billet	.0016	.004	.00012	---
As received powder	.0105	.0038	.0005	.0007
As HIPed	.0099	.0056	.000004	.0001
HIP + STDA	.013	.0060	.000022	.0001

There is an appreciably higher oxygen and hydrogen content in the as-received X750 powder over the starting billet materials apparently due to some contamination during the production of the powder during the inert gas atomization process. While the oxygen level of the HIP and HIP + STDA material remains high, the hydrogen content in the HIP and HIP + STDA conditions is considerably reduced even below that of the starting billet material. No apparent pick up of argon (the pressure medium in the HIP Press) was observed in the HIP or HIP + STDA material\*.

The first flat plate type sample, HX-3, was HIPed in a rectangular 304 stainless steel with GTA welded seams along both end caps and only one face. This assembly distorted significantly during the HIP processing as shown in Fig. 5-6b. The stainless container was subsequently redesigned to contain symmetrical welded seams on both faces and a heavier gage (.050") material. Four subsequent plate-type specimens were HIPed at 1200°C and 10,000 psi in the modified stainless containers with considerably less distortion as shown in Fig. 5-7. These HIP plate samples identified as HX-4, HX-5, HX-6 and HX-7 were leak tested both before and after HIPing by pressurizing in a separate leak test pressure vessel for about 30 minutes in argon at 800 psi and R.T. and immediately immersing under water. No indications of leaks were observed in any samples, indicating proper hermetic containment of the powder sample. Original dimensions of these sealed containers before HIPing were approximately 14-1/2 inches long by 5-1/8 inches wide by 3/4 inches thick. Reductions due to consolidation on HIPing averaged about 6.5% in length, 8.5% in width and 14% in thickness.

---

\* Although argon increase is suspected in the 304 stainless container as evidenced by abnormally high porosity in the 304 material following HIPing.

Prior to heat treatment or machining of mechanical test specimens, the stainless can now firmly bonded to the X750 sample was machined away. Material for material condition code 60XX (as-HIPed) was used directly after removal of the stainless can material. Material for material condition code 61XX (HIP and STDA) was further cut into specimen blanks and heat treated as follows:

Solution treat - 1800°F for 1 hour in argon, air cool

Double Age - 1350°F for 8 hours in argon, furnace cool  
to 1150°F, hold 8 hours in argon and air cool.

Mechanical properties of this material are reported in Section 6 of this report. Although this was an initial effort at producing HIP X750 material and process conditions are not necessarily optimized, the resulting HIP material in both the as HIP and HIP + STDA conditions nevertheless demonstrated significant improvements in mechanical strength, ductility, notched tensile strength, and fracture toughness over the starting billet material (MP-1).

#### 5.2.3 Cold Working Of Kromarc 58 Stainless Steel

Cold working, i.e. plastic deformation by mechanically rolling unidirectionally well below the normal recrystallization temperature, is one practical method of modifying the microstructure and consequently the strength and toughness of both parent base material and weldments. Kromarc 58 stainless steel, being a fully austenitic stainless steel, is not normally\* hardenable by thermal treatment and is, consequently, an excellent material with which to evaluate the effects of cold working on strength and fracture toughness at cryogenic properties.

A previous in-house study by Hull<sup>(23)</sup> reported the cryogenic tensile and notched tensile properties of cold rolled Kromarc 58

---

\* While not normally considered hardenable by heat treatment, Hull<sup>(23)</sup> has reported a substantial hardness increase (~70 points DPH) obtained in cold worked material followed by aging for 4 hrs at 600° to 1000°F. A similar hardness increase on aging cold worked material for 1 hr at 1000°F-1100°F was observed in this work. Further investigation of this hardness increment is under consideration.

\* Kromarc is a registered trade mark of Westinghouse Electric Corporation.



stainless steel sheet of .050 inch thickness. While not explicitly a part of this present ARPA-NBS program, this earlier data is nevertheless considered significant and relevant and is therefore included as Appendix I. The present work considers Kromarc 58 base material and weldments in plate of thickness an order of magnitude larger than the thin sheet of Hull's work and also employs fracture mechanics testing at cryogenic temperatures to further extend the characterization of this alloy.

The cold working of Kromarc 58 stainless steel plate samples of codes 82XX, 83XX, 84XX, and 85XX (see Table 3-1) was performed in-house in the Metals Processing Section of the Westinghouse Research Laboratories. The starting plate sections measured approximately 14 inches long by 3-1/2 inches wide. All starting material was 1 inch in thickness before cold rolling. Plate sample K-6 was cold rolled to 0.7 inches in thickness for use as code 81XX material. Samples K7 and 8 (Code 82XX) and K-9 (Code 83XX) were reduced to 0.7 inch thickness ( $\sim 30\%$  reduction prior to welding) while samples K-4 (Code 84XX) and K-1 (Code 85XX) were reduced to 5/8 inch thickness ( $\sim 37\%$  reduction) following welding. Reductions were made in approximately .020 inch increments with no intermediate anneals employed. A mechanical pressing of the as-cold-worked plates was necessary to flatten these plate samples sufficiently to allow the subsequent sectioning and machining of the numerous mechanical test specimens. No evidence of cracking of this material was detected during or subsequent to the cold rolling operations.

In selecting the temperature for the post cold-worked recrystallization heat treatment(s) (Code 85XX), it was necessary to subject a brief series of specimens (GTA welded and cold worked) to various "annealing" temperatures to determine the best apparent recrystallization temperature/microstructure combination(s). This was accomplished by taking ten pieces approximately 1/4 inch wide by 5/8 inch thick and 3-1/2 inches long from Kromarc 58 plate section K-1 in the GTA welded and cold worked ( $\sim 37\%$  reduction in thickness) condition. Each sample piece containing a transverse section of the weld was heat treated for

1 hour in an argon atmosphere at one selected temperature within the range from 1000°F to 1900°F. Microhardness measurements were taken on each sample following the 1 hour heat treatment. Figure 5-8 shows a microhardness transverse across one half thickness of several of these sample pieces along both the transverse weld centerline and in the parent base metal. The net averages of these hardness readings for both the base metal and the weld fusion zone locations are shown for each respective "annealing" temperature in Fig. 5-9 along with corresponding base metal and weld fusion zone microstructures. The following points are noted concerning Fig. 5-9:

- The hardness profile vs. "annealing" temperature of the cold worked base metal and the weld fusion zone structures closely parallel each other, although the base metal hardness generally exceeds the weld fusion zone hardness somewhat.
- A distinct "age-hardening" effect is indicated by a hardness increase in both B.M. and F.Z. structures at temperatures of 1000 - 1100°F.
- Recrystallization is readily evident (but not complete) in both microstructures after the 1500°F treatment. The hardness level of the B.M. has dropped ~ 20% and that of the weld fusion zone by ~ 40% over the as cold worked state.
- Recrystallization is essentially completed in both structures (B.M. and F.Z.) after the 1600°F treatment. The residual hardness increment due to the prior cold work and "age-hardening" has been eliminated. The average grain size of the prior weld fusion zone is larger than the corresponding base metal grain size for the same treatment.
- The as-cast structure of the weld fusion zone has been completely modified by the cold working and recrystallization treatment at 1600°F for 1 hour (i.e. the as-cast weld dendritic structure is no longer detectable). The grain size of the recrystallized weld is considerably less than that of the as-welded or cold worked weld fusion zone.



It appears that both the partially recrystallized structures and the fully recrystallized structure are worthy of mechanical property characterization. The partially recrystallized structure would be expected to retain a significant strengthening effect of the prior cold work (since 60 to 80% of the cold work induced hardness increment remains). The fully recrystallized structure would not be expected to retain an appreciably higher strength level than the as-welded structure but is expected to have greater ductility and toughness due to the elimination of the as-cast dendritic weld structure and the reduction in grain size over the as-welded condition.

Plate K-1 material (Code 85XX) therefore, has been cut into two halves with one half heat treated at 1500°F and the second half heat treated at 1600°F. Mechanical property tests have not been completed to date but are in progress and will be reported subsequently.

#### 5.2.4 Kromarc 58 Filler Wire

Kromarc 58 stainless steel filler wire for GTA welding of K-58 plate was produced to the metals processing schedule listed in Table 5-8. The starting Kromarc 58 material (Heat 3736) for filler wire was 0.287 inch diameter redraw stock in the cold worked condition ( $\sim$  Rc 38). Initial attempts at further reducing (swaging) this stock directly led to the incidence of severe internal cracking as shown in Fig. 5-10 (a and b). Examination of the starting material revealed the presence of longitudinal surface cracks (see Fig. 5-10 (d)), of about .005 to 0.20 inch in depth. It is noted that the appreciable cracking of the untreated starting material following swaging to .090" diameter was not associated with the prior existing surface cracks but rather with the occurrence of additional cracking in the center of the already severely cold worked redraw stock. Two corrective measures were taken, namely: (a) complete annealing of the starting stock and, (b) surface grinding away the existing surface cracks before further cold swaging the redraw stock to make the final 3/32" diameter filler wire for welding. Dye penetrant inspection of the starting stock following surface grinding was employed to detect any residual longitudinal surface crack indications.

Any remaining surface cracks (as shown in Fig. 5-10 (c)) were locally hand ground and rechecked by dye penetrant to ensure their complete removal. Such cracks, if not removed, could entrap swaging lubricants and dirt which, if not removed in the final cleaning operation, would contaminate the final weldments. Employing these corrective measures in the processing of the K-58 filler wire resulted in a crack free wire microstructure as shown in Fig. 5-11. This final bare K-58 filler wire proved entirely satisfactory for the GTA weldments of Kromarc 58 evaluated in this program.

### 5.3 Materials Fabrication Considerations

#### 5.3.1 Welding

##### 5.3.1.1 Weldments in Oxygen-Free Copper

Weldments were made in oxygen free high purity copper base metal (CDA Alloy No. 102) by the Gas Metal Arc Welding Process. Some preliminary weldment tests were run to determine best welding parameter conditions along with reviewing available literature<sup>(24-27)</sup> pertaining to GMA welding of copper plate of 1/2 inch thickness. Preheat of the weld plate at 800°F to 900°F was found necessary and was accomplished by heating manually with a reducing oxyacetylene torch and measuring the plate surface temperature with a direct reading contact probe. Filler wire employed was ECu (CDA No. 189) which has tin, silicon and manganese additions for deoxidation of the molten weld pool (since oxygen free copper tends to pick up oxygen during welding). The electrical conductivity of this filler wire is only ~ 30% IACS<sup>(28)</sup> however, and does therefore lower the conductivity of the actual weld joint.\*

Three weld plates measuring approximately 12 inches long by 4-3/4 inches wide by 1/2 inch thick were joined with the welding conditions listed in Table 5-9. These plates were identified as Cu3, Cu4, and Cu5. Photographs of x-rays taken of these weldments are shown in Fig. 5-12. A significant level of porosity is observed in all three of these weld test plates. This porosity is, in part, attributed to the

---

\* Electrical resistivity ratios (RT/4.2°K) are reported in Section 8 of this report as ~ 72 for base metal and ~ 2 for the weldment.

inert gas shielding technique employed which may not be completely effective, even with the deoxidizing filler wire employed. Also, the greater heat input and the lower power density (heat localization) of the GMA process, vs. the GTA process, results in greater porosity<sup>(24)</sup>.

A representative cross section of one of these weld plates is shown in Fig. 5-13 indicating the overall large columnar grain structure of the weld fusion zone with the enlarged equiaxed HAZ and the spherical porosity present in the weld fusion zone. Hardness measurements for the as-received copper plate were measured at  $R_F$  68 (Approx.  $R_B$  19) while the as-welded fusion zone hardness was extremely soft at  $R_R$  17. The mechanical properties of the GMA weldments in the oxygen free copper base metal (see Section 6) nevertheless show both strength and ductility levels comparable to that of the base metal. Fractures of these welded copper samples were all in the base metal.

#### 5.3.1.2 Weldments in AISI 310S Stainless Steel

Weldments were made in AISI 310S Stainless Steel base metal, STQ (Fig. 5-14) by the Shielded Metal Arc (SMA) welding process. This process - material combination was selected for two reasons:

- (a) SMA welding is the most widely used fusion arc welding process and was, in fact, utilized in the fabrication of 310S Stainless components in a Westinghouse 3600 rpm, 5 MVA superconducting generator rotor.
- (b) SMA welding of 310S Stainless Steel has been reported<sup>(29)</sup> to involve microcracks in the weld fusion zone predominantly in weld passes which have been reheated by the deposition of subsequent weld passes. Although the general conclusion of Ref. 29 was that such microcracks in a fully austenitic welded joint "are unlikely to be significant", it was felt desirable to investigate this situation further in the present work.

Two weld test plates were made measuring approximately 18" long by 6" wide by 5/8" thick. These plates were initially solution

treated (2000°F - 1 hr in hydrogen) and water quenched prior to welding in the flat position according to the conditions listed in Table 5-9. Filler wire used was E310-16 of composition shown in Table 5-3. Photograph of x-rays taken of these two weldments are shown in Figs. 5-15 and 5-16. The macro- and microstructure of a representative transverse cross section is shown as Fig. 5-17. The quality of these weldments is considered quite good as no such microcracks as mentioned by Ref. 29 were observed metallographically and only small isolated porosity is evident in the radiographs.

#### 5.3.1.3 Weldments in Inconel X750 Superalloy

Weldments in Inconel X750 nickel-base superalloy were accomplished with two welding processes, namely: High Vacuum Electron Beam Welding (HVEBW) and Gas Tungsten Arc Welding (GTAW). An additional consideration of pre- and post weld heat treatment was also considered with both welding processes as follows:

Pre-weld treatment, ST - Solution treat at 1800°F - 1 hr and air cool;  
STDA - ST + Double Age at 1350°F - 8 hrs furnace cool to 1150°F, hold 8 hrs and air cool. Post weld treatment STDA - same as above.

The HVEB Welding was accomplished at Materials Technology, Inc. in Youngstown, OH on a 6 kW, 150 kV Hamilton Standard EB Welding Machine according to the welding conditions listed in Table 5-9. As the base material was obtained from transverse sections of a 10" diameter billet (MP-1), several relatively small weld test plates were required to provide sufficient welded material for the numerous mechanical test specimens, the results of which are reported in Section 6. Photographs of these weldment x-rays are shown in Figs. 5-18 and 5-19. Some linear weld centerline defect indications are indicated on these radiographs and were avoided in laying out mechanical test specimens from these weld plates wherever possible. Standard optical microstructural examination of transverse sections taken through such linear indications in material with a STDA preweld heat treatment (Condition 33XX) revealed

cracking in the weld fusion zone centerline as shown in Fig. 5-20. Defect 1 was the most extensive crack found and was located in the weld termination crater area approximately 1/4 inch from the end of the weld test plate. Defect 2 was considerably less extensive and was located approximately 1-1/2 inch from the weld finish end of this same test plate. These cracks are indicative of hot (shrinkage) cracking and would be considered unacceptable in an actual component fabrication. Fractographic examination of tested weldment sections did not reveal any evidence of such cracks on the fracture surfaces indicating that specimen layout on these EB welded plates did successfully avoid including them. These centerline defects in the weld fusion zone are visible in the x-rays of many HVEB weldments and are not to be confused with the much smaller intergranular microfissures found in the HAZ of these EB weldments. These later microfissures which were observed in all pre- and post weld heat treatment conditions are discussed in more detail in the previous report<sup>(1)</sup> and are too small to be visible in the radiographs of these weldments. The former defects in the center of the EB weld fusion zone apparently did not influence the tensile and notched tensile mechanical properties measured for these composite weldment specimens as the fractures were all observed in the base metal or weld heat affected zones and not in the weld fusion zone.

The GTA weldments in Inconel X750 were welded in-house at the Westinghouse Research Labs using the conditions listed in Table 5-9. Photographs of x-rays taken of these weldments are shown in Figs. 5-21 through 5-24. No linear defect indications were found in any of these GTA weldment x-rays although some small scattered porosity is observed primarily along the center of the weld fusion zone. No indications of H.A.Z. microfissuring were detected in these weldments contrary to the case of the HVEB weldments in this material. Typical macro- and microstructures of these GTA weldment were shown as Fig. 5-8 in the previous report<sup>(1)</sup>.

#### 5.3.1.4 Weldments in Kromarc 58 Stainless Steel

Previous references (30-33) concerning the welding of Kromarc 58 stainless steel were reviewed. Weldments were made in Kromarc 58 plate material in the following processing/welding conditions:

- Code 82XX (GTAW) - Plates K-7 and K-8 were cold rolled from the original 1 inch plate thickness to 0.7 inch thickness, solution treated 1 hour at 1800°F and water quenched (STQ) and then gas tungsten arc welded as per conditions listed in Table 5-9.
- Code 83XX (CW/GTAW) - Plate K-9 was solution treated (1800°F - 1 hr WQ) cold rolled from the original 1 inch plate thickness to 0.7 inch thickness) and gas tungsten arc welded as per conditions listed in Table 5-9.
- Code 84XX (GTAW/CW) - Plate K-4 was solution treated (1800°F - 1 hr and water quenched prior to gas tungsten arc welding as per conditions listed in Table 5-9 for 1 inch thickness. The 1 inch thick welded plate was then reduced in thickness to 5/8 inch thickness (approx. 37% cold work).
- Code 85XX (GTAW/CW/AN) - Plate K-1 was solution treated (1800°F - 1 hr) and water quenched, gas tungsten arc welded as per conditions listed in Table 5-9, reduced to 5/8 inch thickness (approx. 37% cold work), sectioned into two halves and then given a final anneal at 1500 (1st half) 1600°F (second half) for 1 hr to recrystallize both the weldment and the base metal (see Section 5.2.3 for processing detail).

All base plate material was from the same heat (HT-D8339) of Kromarc 58 stainless steel 1 inch thick starting material. All Kromarc 58 weldments were accomplished with the gas tungsten arc welding (GTAW) process using multipasses of Kromarc 58 stainless filler wire with the weldments made parallel to the rolling direction of the K-58 plate material.

This filler wire was produced in-house in the Metals Processing Section of the Westinghouse Research Labs (see Section 5.2.4 for details).

The GTA welding parameters, process and joint configuration details for all Kromarc 58 weldments in this program are given in Table 5-9. Photographs (contact prints) of radiographs of each of these weldments are shown as Figs. 5-25 to 5-28. A photograph showing the five Kromarc 58 plate weldments from which mechanical property test specimens were obtained is shown in Fig. 5-29 in the as-welded condition. Photographs showing the macro- and microstructure of these multipass GTA K-58 weldments in transverse section are shown in Figs. 5-30 to 5-32.

The philosophy of selecting the various welding and processing combinations in Kromarc 58 employed in this work is as follows:

1. Conditions for Code 82XX material (as-welded, in prior solution treated material) establishes the base line as-welded status for this Kromarc 58 stainless alloy.
2. Conditions for Code 83XX material (cold worked and then welded) allows the evaluation of the strength and toughness degradation associated with a weldment (as-welded) in prior cold worked material. The advantage of cold working an austenitic base material such as Kromarc 58 is in achieving significant strength improvements and yet still retaining relatively high fracture toughness (see Section 6 of this report for comparison of Kromarc 58 STQ base material - Code 80XX - vs cold worked K-58 base metal - Code 81XX - properties). A weldment in such cold worked material, however, is anticipated to have lower ductility and strength in the weld fusion zone and lower strength in the base metal heat-affected-zone (HAZ).
3. Conditions for Code 84XX material (GTA welded and subsequently cold worked) provides a means of avoiding the loss of strength in the HAZ of the prior cold worked base metal since the cold work is here introduced following welding. Additionally, the post weld cold work also plastically deforms and strengthens the weld fusion zone by modifying the as cast weld structure.

4. Conditions for Code 85XX material (GTA welded, cold worked and then subsequently heat treated) are selected to recrystallize and refine the grain size of both the cold worked base metal and the cold worked weld fusion zone. This treatment has the potential of providing both base metal and weld FZ strength levels above that of the STQ and as-welded conditions, yet somewhat less than in the as-cold-worked condition. Toughness, on the other hand, is expected, a priori, to be improved in both the base metal and weld fusion zone over the as-cold-worked condition. In addition, effects of the HAZ and residual stress gradations from welding and cold working are minimized (if not entirely eliminated) by the post cold work recrystallization heat treatment (see Section 5.2.3 for details).

#### 5.3.2 Brazing

As stated earlier in Section 5.3.2 of the preceeding report<sup>(1)</sup>, little information appears available in the open literature concerning the mechanical behavior of brazed joints under cryogenic service (or test) conditions. Several additional references<sup>(34-45)</sup> were reviewed concerning brazing technology and techniques which were felt useful as background to this endeavor. No references have been located concerning the cryogenic behavior of copper brazed Inconel X750. Reed<sup>(44)</sup> has published some data concerning the low temperature mechanical properties of silver brazed (in air) lap joints in 1/4 inch thick phosphorous deoxidized copper. These specimens demonstrated respectable shear strengths whose magnitude decreased as the width of the overlap joint increased at cryogenic temperatures with the inverse strength-temperature relationship of the parent base metal far exceeding that of the brazed joint. No comparable cryogenic data on OFHC copper is known to this author.

In this effort, it is felt that a simple butt type joint configuration instead of a shear lap joint would be far more conducive to meaningful fracture mechanics testing. Consequently, both standard mechanical tensile tests and fracture mechanics tests were planned for specimens of only the butt joint type.

Two brazement test conditions are incorporated into this project, namely, a copper brazed Inconel X750 (ST) condition (Code 38XX)



and a silver alloy brazed OFHC copper condition (Code 13XX). Both brazed joints are of the straight butt joint design in 1/2 inch thick material.

#### 5.3.2.1 Copper Brazement in Inconel X750

The rationale for using a copper brazement with the Inconel X750 may be described as follows:

- Inconel X750 contains elements such as Cr, Al, and Ti which form refractory oxides in normal copper brazing atmospheres. The copper plating technique provides a means to prevent such oxide formation on the joint faces and consequently, should result in a good bond.
- Copper and nickel are mutually soluble and thus no intermetallic compound formation between these elements would form to degrade the brazed joint.
- The high thermal conductivity of copper provides for a high thermal efficiency of the brazed joint which is useful in S.C. machinery applications.
- The high toughness of copper is likewise a desirable attribute of such brazed joints.

The copper brazed joints in Inconel X750 (VIM-VAR) base material consist of a thin (~ 1.0 mil thick) layer of electro-deposited copper on each mating surface. The Inconel X750 surfaces were machined to a 20 microinch rms surface finish initially and then precleaned prior to electroplating as follows:

- Ultrasonic cleaned with acetone
- Ultrasonic cleaned withalconox in deionized water
- Rinsed with deionized water
- Rinsed with methol alcohol

The two X750 plate surfaces were then copper plated at the Westinghouse Research Labs with an approximately 2 mil thickness of high purity copper. The copper plated surfaces were subsequently machined back to a 20 microinch surface finish and to a nominal thickness of 1 mil. The initial test sample plate was then vacuum furnace brazed at 2050°F for 5 minutes and then rapid cooled by backfilling the furnace with argon. Visual examination of the as-brazed sample revealed surface oxidation on the plate surfaces adjacent to the brazed seam and several unbrazed areas along the length of the joint as shown in Fig. 5-33(c). This initial brazed plate was then broken apart and the mating surfaces observed to be likewise oxidized. It is thus apparent that a contamination (oxidizing) problem existed with the vacuum furnace operation or in the argon used for backfill quenching. In addition, the quality of the electrodeposited copper may be suspect. Further investigation into these areas is in progress.

#### 5.3.2.2 Silver Brazement in OFHC Copper

The selection of AWS BAg-8 braze filler metal was based upon its simple binary chemical composition, compatible melting temperature (1435°F) with respect to the melting point of copper (1981°F), and the broad commercial applicability of this combination. No prejudgement is implied by this selection that this braze filler is the optimum choice for cryogenic structures but rather it should provide a baseline status for evaluation upon which further improvements may be desirable.

The initial silver brazements in OFHC Copper were conducted by preplacing flat strip of AWS BAg-8 silver brazing alloy of .003" thickness between two precleaned surfaces of 1/2" thick copper. The nominal chemical composition of this braze filler metal is 72% Ag - 28% Cu, and the combined melting and flow point is 1435°F (780°C). Preparation of the copper mating surfaces consisted of machining to a 20  $\mu$ -in. surface finish and cleaning as listed above for the Inconel X750 brazements. Similar ultrasonic cleaning was performed on the braze strip filler material. The specimens were placed in a special

restraining fixture with the plate vertical and the joint plane horizontal. A vacuum furnace was used to braze the samples. A photograph of an x-ray taken of such a silver brazed test plate specimen is shown in Fig. 5-34(a). Also shown in this figure is a photograph of the brazed copper plate test assembly corresponding to the x-ray above. No apparent lack of bonding is observed in the x-ray or by visual examination. Initial attempts at mechanically separating these brazed plates by restraining one plate half and hammering on the other resulted in no indications of joint separation. These sample brazements may therefore be suitable for subsequent cryogenic mechanical tests. Further metallographic examination is in progress.

### 5.3.3 Soldering

Solder joints might be considered in cryogenic structural applications both in terms of strength and toughness of electrical interconnections and of low stressed metal component (e.g. damper shield interconnections or helium conduits) structural joints required for improved interface thermal/electrical conductivity or for high reliability hermetic seals. Reliable mechanical property and fracture mechanics property design data for such solder joints is extremely limited. Consequently, this effort is an attempt at demonstrating the feasibility of obtaining such data and providing initial baseline data upon which further improvements may be evaluated.

#### 5.3.3.1 Solder Joints in OFHC Copper

As in the case of the above brazed joints (Section 5.3.2), a simple butt joint between two plate sections of 1/2 inch thickness was considered conducive to both mechanical and fracture mechanics type test specimens. The solder filler metal selected for this effort was 90% Pb - 10% Sn which (along with 97.5 Pb - 1.5 Ag - 1.0 Sn solder) was reported by Christian<sup>(46-47)</sup> as being sufficiently "tough" for use at -423°F, although Christian was reporting on parent solder material properties and not on soldered joints. Other authors have discussed mechanical properties of soldered joints<sup>(48, 49)</sup>, reaction of Pb-Sn

solders<sup>(50)</sup>, and effects of process variables<sup>(51)</sup> in copper and copper alloys. However, this data does not relate to either butt type solder joints, cryogenic temperatures or include fracture mechanics tests and evaluation.

Preliminary solder wettability checks were made on OFHC copper sheets using a Kester Solder Flux, Formula A715 at 20% dilution with very good results. Initial solder joints in 1/2 inch thick OFHC copper plates were then attempted. Machined copper plate surfaces were first abraded with steel wool, cleaned with acetone in an ultrasonic cleaner, then with Alconox in an ultrasonic cleaner and finally rinsed in methol alcohol. The plate surfaces were each presoldered to completely wet each surface and the excess solder then wiped clear. The wetted surface was then reabraded and cleaned as above. The solder joint was then made (in air) by using an additional shim of .005 inch thick 90 Pb - 10 Sn solder coated with flux between the two prewetted copper surfaces and clamped. This assembly was placed on a hot plate and heated to 650°F, held at temperature for 5 minutes and allowed to air cool. Radiographs of such initial solder joints (see Fig. 5-34(a)) did not reveal a lack of bonding but such was revealed when the plate surfaces were separated as shown in Fig. 5-35(b). A revised soldering procedure is presently being pursued.

## SECTION 5

### REFERENCES

1. Lessmann, G. G., W. A. Logsdon, R. Kossowsky, M. P. Mathur, and J. M. Wells, "Structural Materials for Cryogenic Applications - First Semiannual Progress Report," Westinghouse Research Report 74-9D4-CRYMT-R1, March 1, 1974.
2. Leverenz, H. W. (Chairman) et al, "Characterization of Materials," Materials Advisory Board Report MAB-229-M, NAS-NAE, NIIS-AD649941, March 1967.
3. Kappelt, G. F. (Chairman) et al, "Testing for Prediction of Material Performance in Components and Structures," National Materials Advisory Board Report NMAB-288, NAS-NAE, NIIS-AD743991, May 1972.
4. Marke, M. L., and E. V. Gillaspay, "Producibility Considerations in Design," NASA SP-5957(03), August 1974, p. 15.
5. Lancaster, J. F., "Research Toward Safer Welded Construction," Welding Journal, Vol. 51, No. 3, March 1972, p. 159.
6. Doran, T. J., "Predictive Testing of Metallic Parts," Metals Engineering Quarterly, Vol. 14, No. 2, May, 1974, p. 32.
7. Harrigan, M. J., "Using Fracture Mechanics Standards to Specify Materials," Metals Engineering Quarterly, Vol. 14, No. 2, May 1974, p. 16.
8. Clark, W. G., Jr., "How Fatigue Crack Initiation and Growth Properties Affect Materials Selection and Design Criteria," Metals Engineering Quarterly, Vol. 14, No. 3, August 1974, p. 16.
9. Schlatter, R., "Melting and Refining Technology of High Temperature Steels and Superalloys - A Review of Recent Process Developments," Superalloys - Processing, MCIC Report 72-10, September 1972, p. A1.

SECTION 5 REFERENCES (CONT'D)

10. Anon., "How New Specialty Metals Technology Benefits Users," Metal Progress, Vol. 106, No. 3, August 1974, p. 39.
11. Bishop, H. L., Jr., "Melting and Refining Specialty Steels at Allegheny Ludlum Industries," Metals Progress, Vol. 106, No. 3, August 1974, p. 53.
12. Kelley, T. N. and Klein, H. J., "Comparing Electroslog and Vacuum Arc-Refined Alloys," Metals Progress, Vol. 102, No. 3, September 1972, p. 97.
13. Bailey, R. E., "Some Effects of Hot Working Practice on Waspaloy's Structure and Tensile Properties," Superalloys - Processing, MCIC Report 72-10, September 1972, p. J1.
14. Cremisio, R. C., "Chapter 13 - Melting," The Superalloys, Ed. by C. T. Sims and W. C. Hagel, J. Wiley and Sons, New York, 1972, p. 373.
15. Anon., "Standard High-Temperature, High-Strength Alloys," Metals Progress, Vol. 106, No. 3, August 1974, p. 61.
16. Anon., "Table I - Limiting Chemical Composition, %," Inconel Alloy X750, Bulletin T38, Huntington Alloy Products Division, Inco, 1970, p. 1.
17. Morris, C. A., and J. W. Smythe, "Comparison of Astroloy Powder Consolidation Processes, Forging and Testing of Astroloy Powder Billet," Superalloys - Processing, MCIC Report 72-10, September 1972, p. Y-1.
18. Moskowitz, L. N., R. M. Pellors, and N. J. Grant, "Properties of In-100 Processed by Powder Metallurgy," Superalloys - Processing, MCIC Report 72-10, September 1972, p. Z-1.
19. Barker, J. F., and E. H. VanDerMolen, "Effect of Processing Variables on Powder Metallurgy Rene 95," Superalloys - Processing, MCIC Report 72-10, September 1972, p. AA-1.

SECTION 5 REFERENCES (CONT'D)

20. Ewing, B., F. Rizzo, and C. ZurLippe, "Powder Metallurgy Products for Advanced Gas Turbine Applications," Superalloys - Processing, MCIC Report 72-10, September 1972, p. BB-1.
21. Fox, H. M., "The Effect of Structure on the Low Temperature (< 1300°F) Properties of P/M Rene 80," Modern Developments in Powder Metallurgy, Ed. by H. H. Hausner and W. E. Smith, Vol. 8, MPIF, Princeton, New Jersey, 1974, p. 491.
22. Larson, J. M., "Powder Metallurgy In-100-Processing, Microstructure and Mechanical Properties," Modern Developments in Powder Metallurgy, Ed. by H. H. Hausner and W. E. Smith, Vol. 8, MPIF, Princeton, New Jersey, 1974, p. 537.
23. Hull, F. C., "Cryogenic Tensile Properties of Cold Rolled Kromarc 58 Stainless Steel Sheet," Westinghouse Research Report 67-JD6-KROMA-R1, May 23, 1967.
24. Anon., "Arc Welding of Copper and Copper Alloys," Welding and Brazing, ASM Metals Handbook, Vol. 6, Eighth Edition, 1971, pp. 349-351.
25. Proger, M., et al, "Copper and Copper Alloys, Welding, Soldering, Brazing, Surfacing," Chapter 68, Vol. 4, Sixth Edition, Welding Handbook, AWS, 1972.
26. Anon., "Welding Copper and Copper Alloys," Section 10, The Procedure Handbook of Arc Welding, 12th Edition, The Lincoln Electric Company, 1973.
27. Hartsell, E. W., Jr., "Joining Copper and Copper Alloys," Welding Journal, Vol. 52. No. 2, February, 1973, p. 88.
28. Anon., "Copper Alloy 189," Standards Handbook, Part 2, Alloy Data, Copper Development Association, Inc., 1973, p. 65.

SECTION 5 REFERENCES (CONT'D)

29. Honeycombe, J., and T. G. Gooch, "Effects of Microcracks on Mechanical Properties of Austenitic Stainless Steel Weld Metals," Welding Research Abroad, Vol. XIX, No. 8, October 1973, p. 46.
30. Hull, F. C., "A High Strength Weldable Stainless Steel for Elevated-Temperature Service," ASTM STP No. 369, 1965, pp. 88-98.
31. Hull, F. C., "Crack Resistant Stainless Steel Alloys," U.S. Patent No. 3,201,233, August 17, 1967.
32. Johnson, E. W., G. R. McGraw, and R. L. Readal, "Fully Austenitic Stainless Steel Welding Electrodes for High Temperature Applications," Welding Journal, Vol. 47, No. 12, December 1968, p. 543-S.
33. Johnson, E. W., "Kromarc 58 Covered Welding Electrodes for Cryogenic Use," U.S. Patent No. 3,645,782, February 29, 1972.
34. Pattee, H. E., "High Temperature Brazing," WRC Bulletin No. 187, September, 1973.
35. Anon., "Cryogenic Brazing and Soldering," NASA Literature Search No. 16832, November 1, 1971.
36. Bredzs, N., and C. C. Tennenhouse, "Metal - Metal Oxide - Hydrogen Atmosphere Chart for Brazing or Bright Metal Processing," Welding Journal, Vol. 49, No. 5, May 1970, p. 189-S.
37. Bredzs, N., and H. Schwartzbart, "Metallurgy of Bonding in Brazed Joints, Part I - Base Metal - Filler Metal Interaction, Excluding Compound Formation," Welding Journal, Vol. 37, No. 11, November, 1958, p. 493-S.
38. Bredzs, N., and H. Schwartzbart, "Metallurgy of Bonding in Brazed Joints, Part II - Migration of the Filler Metal into the Base Metal," Welding Journal, Vol. 38, No. 8, August 1959, p. 305-S.
39. Bredzs, N., and H. Schwartzbart, "Metallurgy of Bonding in Brazed Joints, Part III - The Role of Intermetallic Compounds in Brazed Joints," Welding Journal, Vol. 39, No. 2, February 1960, p. 49-S.



#### SECTION 5 REFERENCES (CONT'D)

40. Suezawa, Y., "Investigation of Roughness Effects on the Tensile Strength of Brazed Joints," Welding Research Abroad, Vol. XX, No. 1, January 1974, p. 25.
41. Anon., "Joining the Huntington Alloys - Copper Brazing," International Nickel Company, Inc., Technical Bulletin T-2 (1972), p. 31.
42. Ricksecker, R. E., et al, "Brazing of Copper and Copper Alloys," Welding and Brazing, ASM Metals Handbook, Eighth Edition, Vol. 6, (1971), p. 685.
43. Prager, M., et al, "Copper and Copper Alloys, Welding, Soldering, Brazing and Surfacing," AWS Welding Handbook, 6th Edition, Vol. 4, Ch. 68, (1972), p. 55.
44. Reed, R. P., "Low-Temperature Mechanical Properties of Welded and Brazed Copper," Adv. in Cry. Engrg., Vol. 14 (1969), p. 83.
45. Munse, W. H. and J. S. Alagia, "Strength of Brazed Joints In Copper Alloys," Welding Journal, Vol. 36, No. 4, April 1957, p. 177-S. (Also Corrections, Ibid., June 1957, p. 312-S).
46. Christian, J. L., "Design Criteria for Solders in Cryogenic Environments," Electro-Technology, 71, June 1963, p. 109.
47. Christian, J. L. and J. F. Watson, "Tensile and Shear Properties of Several Solders at Cryogenic Temperatures," SAE, Oct. 1962, p. 1.
48. Saperstein, Z. P. and M. H. Howes, "Mechanical Properties of Soldered Joints in Copper Alloys," Welding Journal, Vol. 48, No. 8, August 1969, p. 317-S.
49. Howes, M. A. H. and Saperstein, Z. P., "The Reaction of Lead-Tin Solders with Copper Alloys," CDA Report 804/7, September 1967.
50. Howes, M. A. H. and Saperstein, Z. P., "Mechanical Properties of Soldered Joints in Copper Alloys," CDA Report 801/8, June 1968.
51. Beal, R. E., "How Soldering Process Variables Affect Joint Strength," CDA Report 804/9, August 1969.

TABLE 5-1

CANDIDATE MATERIALS FOR STRUCTURAL CRYOGENIC APPLICATIONS

<u>AUSTENITIC STAINLESS STEELS</u>	<u>LOW EXPANSION ALLOYS</u>
* AISI 310S	INCOLOY 903
* KROMARC 58	INCO (UNNAMED)
ARMCO 21-6-9	
ARMCO 21-13-5	<u>TITANIUM ALLOYS</u>
CARPENTER 20Cb-3	Ti-6Al-4V (ELI)
	Ti-5Al--2.5Sn (ELI)
<u>IRON BASE SUPERALLOYS</u>	
A-286	<u>ALUMINUM ALLOYS</u>
W-545	2014
PYROMET 860	2219
DISCALOY	5083
	X2048
<u>NICKEL BASE SUPERALLOYS</u>	<u>COPPER AND COPPER ALLOYS</u>
INCONEL 625	
INCONEL 718 (706)	* OFHC-Cu
* INCONEL X-750 (751)	AMZIRC-Cu (CW/HT)
HASTELLOY C-276	GLIDCOP (Al <sub>2</sub> O <sub>3</sub> - D.S.)
PYROMET 680	PD-135 (Cu-Cr-Cd/PHT)
PYROMET 102	
UNITEMP-HX	
<u>OTHER SUPERALLOYS</u>	
HAYNES 188	
MULTIPHASE MP35N	

\* Materials presently being characterized in Westinghouse FY 1974 Program, NBS Contract CST-8034.

TABLE 5-2  
TEST SPECIMEN IDENTIFICATION SYSTEM

<u>Material</u>	<u>Condition</u>	<u>Code</u>	<u>Specimen ID System</u>
OFHC Cu	As Received, AR	10XX-X	4 digits + Dash No. X X X X - X Material----- Condition----- Test----- Temperature----- Replicate-----
	Stress Relieved, SR	11XX-X	
	GTAW	12XX-X	
	Braze, B	13XX-X	
	Solder, S	14XX-X	
AISI 310S	Sol'n. treated and quenched, STQ	20XX-X	
	Sensitized (STFC)	21XX-X	
	SMAW	22XX-X	
Inconel X-750 (VIM-VAR) MP-1	Sol'n. treated, ST	30XX-X	
	STDA	31XX-X	
	ST/EBW	32XX-X	
	STDA/EBW	33XX-X	
	EBW/STDA	34XX-X	
	ST/GTAW	35XX-X	
	STDA/GTAW	36XX-X	
	GTAW/STDA	37XX-X	
	Brazed	38XX-X	
X-750 (AAM-VAR), MP-2 (VIM), MP-3	STDA	40XX-X	
	STDA	50XX-X	
X-750	HIP	60XX-X	
	HIP/STDA	61XX-X	

TABLE 5-2 (CONTINUED)

TEST SPECIMEN IDENTIFICATION SYSTEM

<u>Material</u>	<u>Condition</u>	<u>Cod<sup>e</sup></u>
Kromarc-58	STQ CW GTAW CW/GTAW GTAW/CW GTAW/CW/AN	80XX-X 81XX-X 82XX-X 83XX-X 84XX-X 85XX-X
<u>Test (3rd Digit)</u>	<u>Code</u>	
Tensile	XX1X-X	XXTX-X
Notched Tensile	XX2X-X	XXNX-X
KIC	XX3X-X	XXKX-X
JIC	XX4X-X	XXJX-X
FCGR	XX5X-X	XXFX-X
<u>Test Temp. (4th Digit)</u>		
+70°F Rm Temp.	XXX1-X	
-320°F Liq. Nit.	XXX2-X	
-452°F Liq. He	XXX3-X	
<u>Sample Replicate</u> <u>(Dash + No.)</u>	XXXX-1 XXXX-2 XXXX-3 etc.	

TABLE 5-3  
CHEMICAL COMPOSITION OF (2) PROGRAM MATERIALS (FY 74)

Material	Cu	Sn	Si	Pb	P	Al	Mn	Zn	Residuals
OFHC Copper Plate- CDA No. 102*	99.95	--	--	--	--	--	--	--	--
Cu Wire-CDA No. 189*	(98.7)	.6/.9	.15/.40	.02 max	.05 max	.01 max	.10/.30	.10 max	<0.1

	C	P	S	Si	Mn	Ni	Cr	Mo	Cu	Others
310S Stainless										
Base Material	.064	.017	.009	.74	1.70	19.66	24.40	.17	.15	--
Weld Plate	.053	.027	.011	.48	1.70	20.80	25.00	.21	.14	--
E310-16 Electrode (1)	.20 max	.03 max	.03 max	.75 max	2.5 max	20.0/22.5	25.0/28.0	--	--	.70 max

	C	P	S	Si	Mn	Ni	Cr	Fe	Al	Ti	Co	O	N	H
X-750 Superalloy														
NP-1 (VIN-VAR)	.04	.003	<.001	.11	.089	73.0	15.2	6.47	.92	2.40	.017	.0016	.004	.00012
NP-2 (AAM-VAR)	.02	.004	.007	.24	.12	74.82	14.19	6.22	.73	2.62	.051	.0006	.004	.00007
NP-3 (VIN)	.04	.004	.003	.27	.13	73.02	15.40	6.87	.68	2.64	.009	.0006	.007	.00010
Filler Wire F69 (HT00F7X5) (2)	.03	--	.007	.14	.08	72.96	15.80	6.72	.71	2.60	--	--	--	--
Filler Wire F69 (HT21C8X) (2)	.05	--	.007	.17	.10	73.63	15.10	6.74	.70	2.54	--	--	--	--

	O	N	H	Ar
Powder (Pre-HIP)	.0105	.0038	.0005	<.0007
(Post-HIP)	.0099	.0056	.000004	<.0001
	.013	.0060	.000022	<.0001

	C	P	S	Si	Mn	Ni	Cr	Mo	Al	Zr	B	V	O	N	H
Kromarc-58 Stainless															
K-58 Base Mat. and Weld Plate	.030	.005	.005	.05	9.3	23.0	15.5	2.2	.02	.008	.016	.16	--	.17	--
K-58 Weld Filler Mat.	.003	.001	.004	.09	11.5	21.4	15.3	2.18	--	<.002	.010	.20	--	.15	--

\* Requirements of Standards Handbook, Part 2 - Alloy Digest, Copper Development Association, Inc., NY, 1973.  
(1) Analysis certified from Supplier to AWS A5.4-69 Class E310-16.  
(2) Certified Analysis from Supplier.

TABLE 5-4

MATERIAL DOCUMENTATION DATA

<u>Material</u>	<u>Source</u>	<u>Heat No.</u>	<u>Form</u>
<u>OFHC Copper (102)</u>	⊕ R&D Stock	Unknown	1/2" and 5/8" thick plate
<u>310S Stainless</u>			
Base Plate	McInnes Steel Co.	500096	Forging Billet - Annealed
Weld Plate	Rolled Alloys, Inc.	20880	5/8" thick Plate, HRAP
E310-16	Arcos Corp.	(a) 3A17B-M9 (b) 2N10B-M16A (c) 2N8B-M16	1/8" dia. SMAW Electrode 5/32" dia. SMAW Electrode 5/32" dia. SMAW Electrode
<u>Inconel X-750</u>			
MP1	Inco-Huntington Div.	HT56CLXY	10" dia. round HFFQ (VIM-VAR)
MP2	Inco-Huntington Div.	HT1250XV	4" dia. round HFFQ (AAM-VAR)
MP3	Inco-Huntington Div.	HT57F8XS	2" dia. round HF (VIM)
Powder for HIP	Federal-Mogul Corp.	HT56CLXY	-60 mesh powder from MP1
Inco Weld Filler 69	Inco-Huntington Div.	HT21C8X HT00F7XS HT21C8X	.093" dia. G1AW Filler Wire .062" dia. G1AW Filler Wire .062" dia. G1AW Filler Wire
<u>Kromarc-58 Stainless</u>			
Base and Weld Plate	⊕ R&D Stock	HT-D8339	1" thick plate
Weld Filler Wire	⊕ R&D Stock	HT-3736	0.287" dia. wire draw stock

TABLE 5-5  
PROCESSING AND HEAT TREATMENT SCHEDULES-WESTINGHOUSE FY 74 PROJECT

Material	Code	Condition
OFHC Cu	10XX	AR
	11XX	SR
	12XX	GMAW
310S	20XX	STQ
	21XX	STFC
	22XX	SMAW
	30XX	ST
IN X750	31XX	STDA
	32XX	ST/EBW
	33XX	STDA/EBW
	34XX	EBW/STDA
	35XX	ST/GTAW
	36XX	STDA/GTAW
	37XX	GTAW/STDA
	60XX	HYP
		HX-1
		HX-2
	61XX	HIP/STDA
K-58	80XX	STQ
	81XX	CW
	82XX	GTAW
	83XX	CW/GTAW
	84XX	GTAW/CW
	85XX	GTAW/CW/AN
	86XX	GTAW/CW/AN

As Received  
AR + 400°F Stress Relief  
AR + Preheat to 800/900°F, GMA Weld with ECu

2000°F - 1 hr - Water Quenched  
2000°F - 1 hr - Furnace Cool to 800°F min; then Air Cool  
STQ, then SMA Weld with E310-16 Electrodes

1800°F - 1 hr - Air Cool  
ST, then age at 1350°F - 8 hrs, F.C. to 1150°F, hold 8 hrs and A.C.

ST, then Vacuum Electron Beam Weld  
STDA, then VEB Weld  
Vacuum EB Weld, then STDA

ST, then Gas Tungsten Arc Weld with Inco 69 Filler  
STDA, then GTA Weld with IN69 Filler  
GTA Weld (F69), then STDA

Hot Isostatic Press  
1st Trial - 1120°C and 10,000 psi - 2 hrs  
2nd Trial - 1200°C and 10,000 psi - 2 hrs\*  
HIP, then Standard STDA Heat Treatment

1800°F - 1 hr - Water Quench  
Cold Work ~ 30% Reduction in Thickness  
Gas Tungsten Arc Welding of STQ Material

STQ, 30% cold work, then GTAW with K-58 Filler  
STQ, GTA Welding, then 30% cold work  
STQ, GTAW, 37% CW, then partial recrystallize at 1500°F - 1 hr - W.Q.  
STQ, GTAW, 37% CW, then fully recrystallize at 1600°F - 1 hr - W.Q.

\* HIP Condition Selected for Project Inclusion

TABLE 5-6

## MATERIAL HARDNESS AND GRAIN SIZE MEASUREMENTS-WESTINGHOUSE FY 74 PROJECT

<u>Material</u>	<u>Code</u>	<u>Condition</u>	<u>Hardness</u>	<u>Grain Size (ASTM No.)</u>
310S (1)	20XX	STQ	73 Rb	4.6
	21XX	STFC	67.3 Rb	5
IN X750	----	MP-1 As Received	29.3 Rc	3.5*
	30XX	ST	29.5 Rc	3.5*
	31XX	STDA	35.7 Rc	3.5*
	----	MP-2/As Received	35.3 Rc	6.5
	40XX	MP-2/STDA	36.0 Rc	6.5
	----	MP-3/As Received	35.3 Rc	9
	50XX	MP-3/STDA	38.5 Rc	9
	----	HIP (HX-1)	36.3 Rc	9
	60XX	(HX-2)	35.0 Rc	8
	----	HIP/STDA (HX-1)	41.7 Rc	9
	61XX	(HX-2)	41.0 Rc	8
Kromarc 58	80XX	STQ	88 R <sub>B</sub>	5.5
	81XX	CW (30%)	33 Rc	9.5
	----	As Received	93 R <sub>B</sub>	9

(1) Weld Plate Material

\* Grain Size Variation in 10" dia. billet,  
See Section 7.3 of First Semi-Annual Report

7525



TABLE 5-7

CHARACTERIZATION DATA FOR INCONEL X-750 POWDER

STARTING MATERIAL: Inconel X-750, MP-1 (VIM-VAR)

POWDER MANUFACTURE METHOD: Vacuum Melted and Atomized in high purity Argon Gas (FM)

<u>Certified Sieve Analysis</u>		<u>Westinghouse Sieve Analysis</u>	
<u>Mesh</u>	<u>%</u>	<u>Mesh</u>	<u>%</u>
+ 60	..	-	-
+ 80	1.8	+ 80	3.65
+ 100	4.5	+ 100	6.45
+ 120	5.2	-	-
+ 140	6.8	+ 140	13.11
+ 170	8.4	-	-
+ 230	16.0	+ 200	17.34
+ 270	7.8		
+ 325	7.9	+ 325	22.66
+ 500	25.6		
- 500	16.0	Pan	36.19
Total	100.0	Total	99.40

FLOW RATE (MPIF Std. No. 3-45) 15.2 Sec. (50 gm sample)

APPARENT DENSITY (MPIF Std. No. 04) 4.23 gm/cc (25 cc sample Std. Cup)

TABLE 5-8 - PROCESSING SCHEDULE FOR KROMARC 58 STAINLESS FILLER WIRE

1. Starting Material: Kromarc 58, Heat No. HT 3736, Redraw rod at 0.287" dia., Rc 38, Cut into 2 foot lengths.
2. Annealed: 1800°F - 2 hrs - Water quenched, R<sub>B</sub>84 (Long) - R<sub>B</sub>89 (Trans).
3. Surface Prep.: Mechanically straighten and centerless grind surface to approx. 0.253" dia.
4. Inspection: Dye penetrant check entire surface to ensure absence of cracking.  
Hand grinding of any remaining small surface cracks.
5. Swagging: Mechanically cold swage from 0.253" to .091" dia. without intermediate heat treatment as per following schedule:
 

1st pass	0.253	→ 0.237, Δ dia = .016"
2nd pass	→ 0.217,	= .020
3rd pass	→ 0.183,	= .034
4th pass	→ 0.161,	= .022
5th pass	→ 0.144,	= .017
6th pass	→ 0.125,	= .019
7th pass	→ 0.106,	= .019
8th pass	→ 0.100,	= .006
9th pass	→ 0.091,	= .009
6. Inspection: Dye penetrant check random lengths to ensure absence of cracking.
7. Cleaning: Thorough degreasing and cleaning by wiping with acetone.

TABLE 5--9 SUMMARY TABLE OF WELDING PROCESSES AND PARAMETERS

Base Metal	Inconel X750	Inconel X750	310S Stainless
Thickness	5/8 Inch	5/8 Inch	5/8 Inch
Weld Joint	Flat Butt	Butt, Double-V, 60° Incl. Angle	Butt, Single-V, 60° Incl. Angle
Process	Vac. E. B.	GTAW-Manual	SMAW-Manual
Filler Metal	None	F-69, 3/32" Dia.	E310-16
Current	42.0 mA	DCSP-180 Amps.	DCRP-150 Amps.
Voltage	150 KV	14-15 Volts	20-23 Volts
Electrode	N/A	EWTh-2, 3/32" Dia.	N/A
Welding Speed	20 ipm	~5 ipm	~5 ipm
No. of Passes	1*	12	15
Shielding Gas	N/A	50% Ar--50% He, 20 cfh	N/A
Backing Gas	N/A	100% Ar; 10 cfh	N/A
Root Gap	None	3/32" Approx.	3/32" Approx.
Dye Check	Yes	Yes	Yes
Radiographs	RD 73643, Plate 1 RD 73642, Plate 2 RD 73641, Plate 3 RD 73645, Pcs. 1 & 2, 3 & 4 RD 73646, Pcs. 5 & 6, 7 & 8 RD 73647, Pcs. 9 & 10, 11 & 12	RD 73841, Plate 4A, 4B RD 73836, Plate 5A, 5B, 5C RD 73842, Plate 6A, 6B, 6C RD 73835, Plates 7A, 7B, 7C	RD 73716, Plate 310-2 RD 73717, Plate 310-2 RD 73789, Plate 310-3 RD 73790, Plate 310-3
	* Initial Tack Weld at 72 ipm		
Base Metal	Kromarc 58 Stainless	Kromarc 58 Stainless	OFHC Copper
Thickness	1 Inch	0.7 Inch	1/2 Inch
Weld Joint	Butt, Double V, 60° Incl. Angle	Butt, Double V, 60° Incl. Angle	Butt, Double V, 90° Incl. Angle
Process	GTAW-Manual	GTAW-Manual	GTAW-Manual
Filler Metal	K-58, 3/32" Dia.,*	K-58, 3/32" Dia.	Deox. Cu-189, 1/16" Dia.
Current	DCSP-180 Amps**	DCSP-180 Amps	DCRP-350-400 Amps
Voltage	15 to 16 Volts	15 to 16 Volts	26.5-27.5 Volts
Electrode	EWTh-2, 3/32" Dia.	EWTh-2, 3/32" Dia.	N/A
Welding Speed	~5 ipm	~5 ipm	13 ipm Travel, 250-270 ipm Wire Feed
No. of Passes	30	16	2
Shielding Gas	100% Ar, 20 cfh	100% Ar, 20 cfh	100% Ar, 40 cfh
Backing Gas	100% Ar, 60 cfh	100% Ar, 60 cfh	N/A
Root Gap	3/32" Approx.	3/32" Approx.	No Gap, 1/8" Root Face
Dye Check	Yes	Yes	No
Radiographs	RD 74338, Plate K-1 RD 74343, Plate K-4	RD 74366, Plate K-7 RD 74367, Plate K-7 RD 74368, Plate K-8 RD 74372, Plate K-8 RD 74370, Plate K-9 RD 74371, Plate K-9	RD 74168, Plate Cu-3 RD 74169, Plate Cu-4 RD 74170, Plate Cu-5
	* Filler Wire Made In House ** Passes 1 & 2, 160 Amps, 14-15 Volts ** Passes 3 & 4, 120 Amps, 12-13 Volts	* Filler Wire Made In House	350 Amps-Pass 1 400 Amps-Pass 2

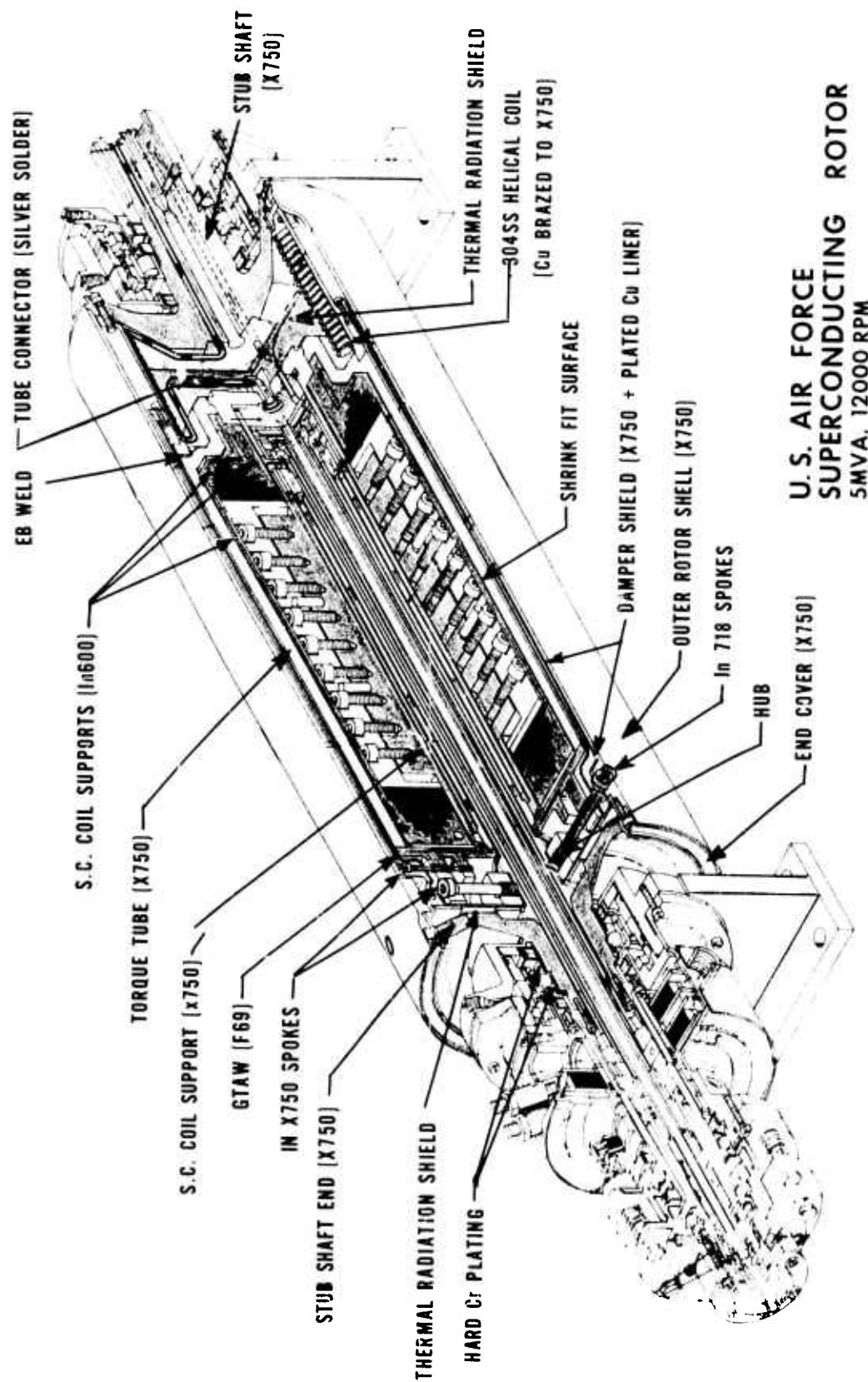


Fig. 5-1 Prototype superconducting generator rotor assembly indicating structural materials utilization and design/fabrication complexity.

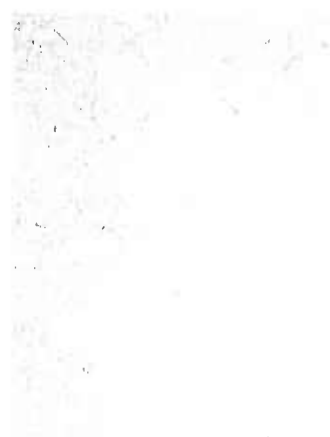


(A) Transverse, View One

MP-1  
(VIM/VAR)



(B) Transverse, View Two

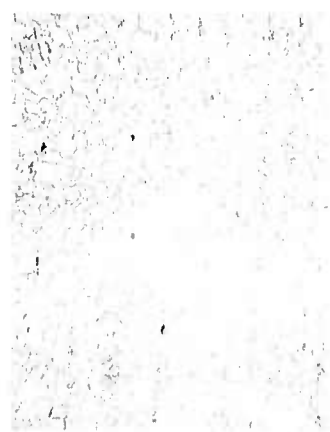


(C) Transverse View

MP-2  
(AAM/VAR)

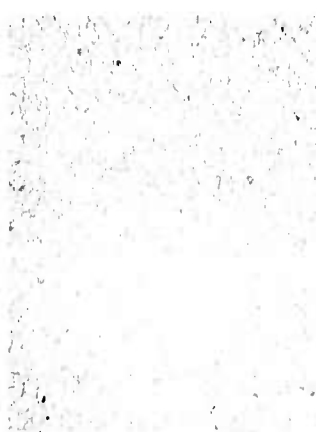


(D) Longitudinal View



(E) Transverse View

MP-3  
(VIM)



(F) Longitudinal View

Figure 5-2 Photomicrographs of Inconel X750 material as-received, (A&B) MP-1 (VIM/VAR), (C&D) MP-2 (AAM/VAR), and (E&F) MP-3 (VIM) (X200)



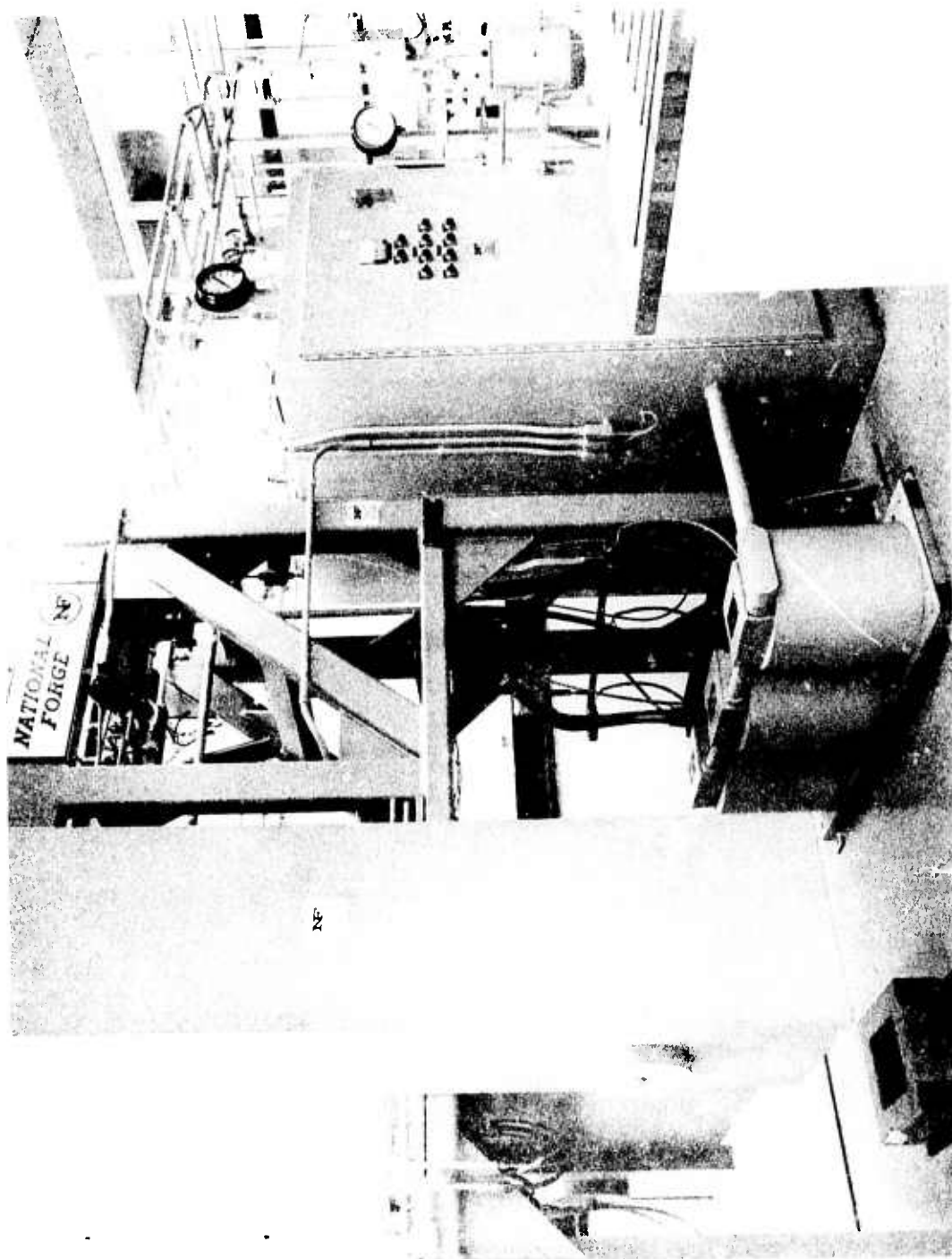


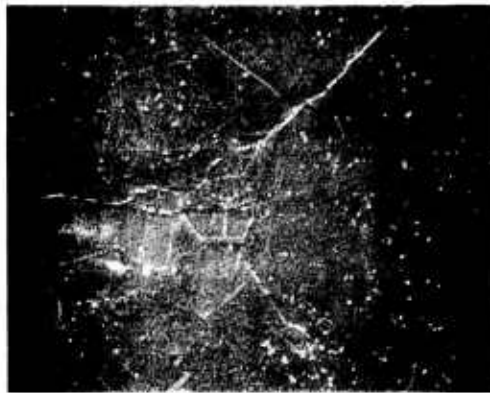
Figure 5-3 Photograph of Hot Isostatic Press (HIP) facility at  
Ⓜ Research Laboratories, Metals Processing section.

I

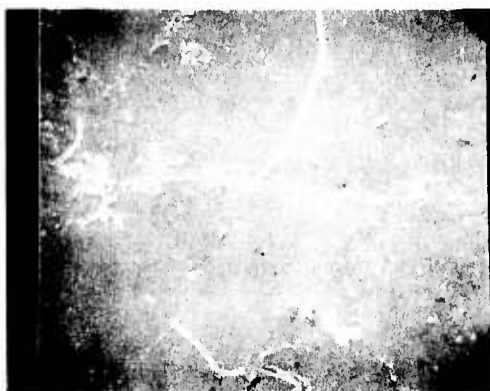


(A) Zero Radius, X2000

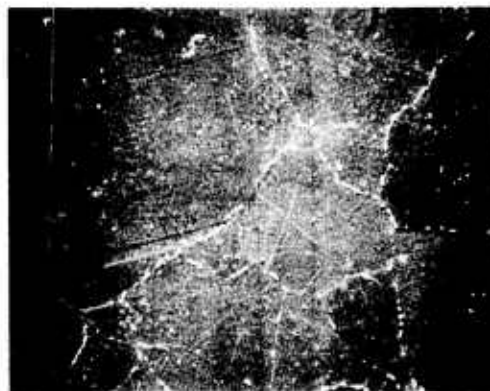
II



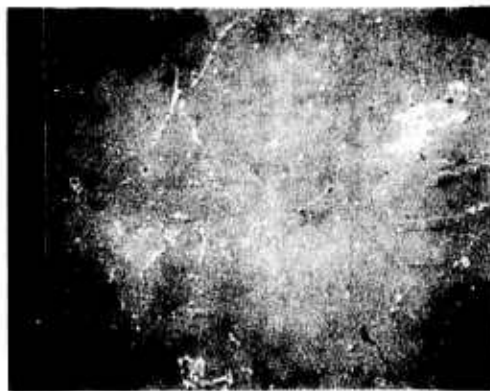
(B) Zero Radius, X2000



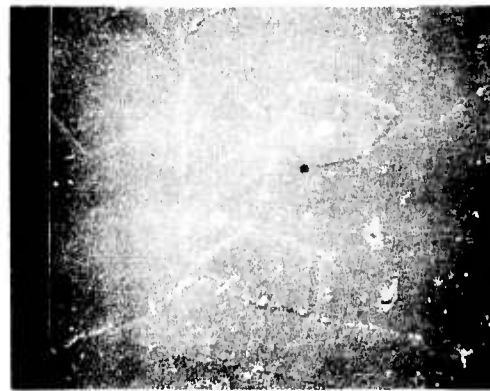
(C)  $\frac{1}{2}$  Radius, X2000



(D)  $\frac{1}{2}$  Radius, X2000



(E)  $\frac{3}{4}$  Radius, X2000



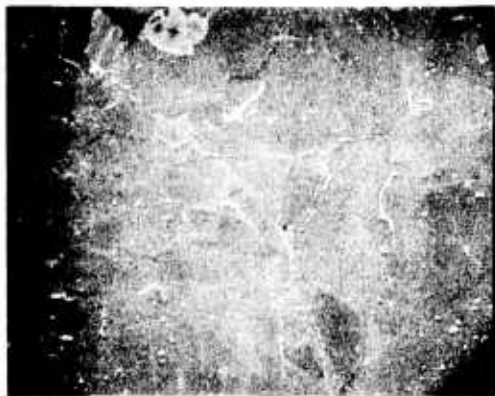
(F)  $\frac{3}{4}$  Radius, X2000

Figure 5-4 Scanning electron micrographs of HIP Inconel X750.

Sample HX-1,  $\frac{1}{2}$ " dia., transverse section.

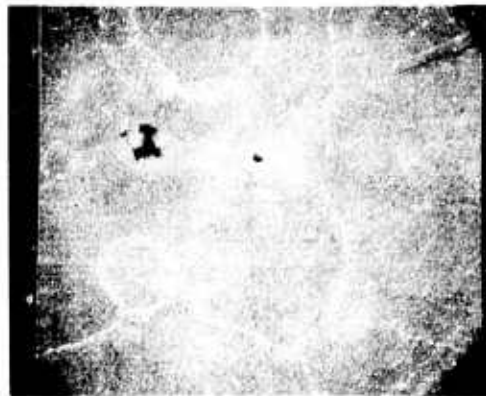
I- as hiped, II- HIP + STDA

I



(A) Zero Radius, X2000

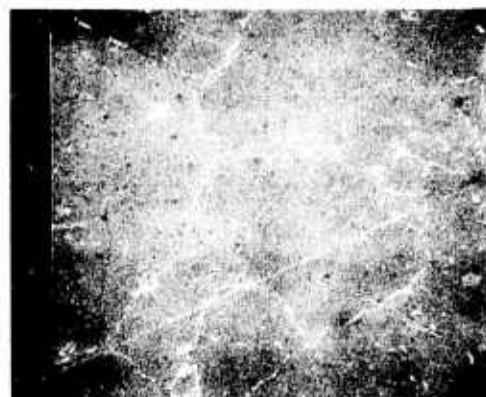
II



(B) Zero Radius, X2000



(C)  $\frac{1}{2}$  Radius, X2000



(D)  $\frac{1}{2}$  Radius, X2000



(E)  $\frac{3}{4}$  Radius, X2000



(F)  $\frac{3}{4}$  Radius, X2000

Figure 5-5 Scanning electron micrographs of  $\mu$ P Inconel X750,  
sample HX-2,  $\frac{1}{2}$ " dia., transverse section  
I—as hiped, II HIP + STDA



(A)



(B)

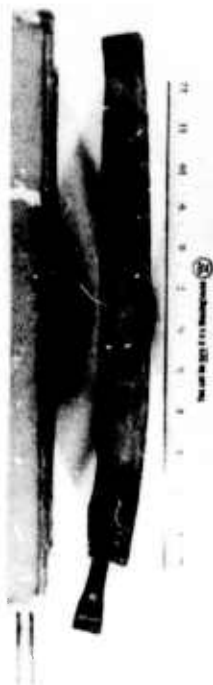


Figure 5-6 Photographs showing Hot Isostatic Press (HIP) samples of Inconel X750.  
(A) Initial test sample, HX-2, as  $\frac{1}{2}$ " dia. as hiped, and (B) Initial flat plate test sample  $\frac{3}{4}$  HX-3 on bottom showing biaxial warpage from hiping in unmodified container (on top)

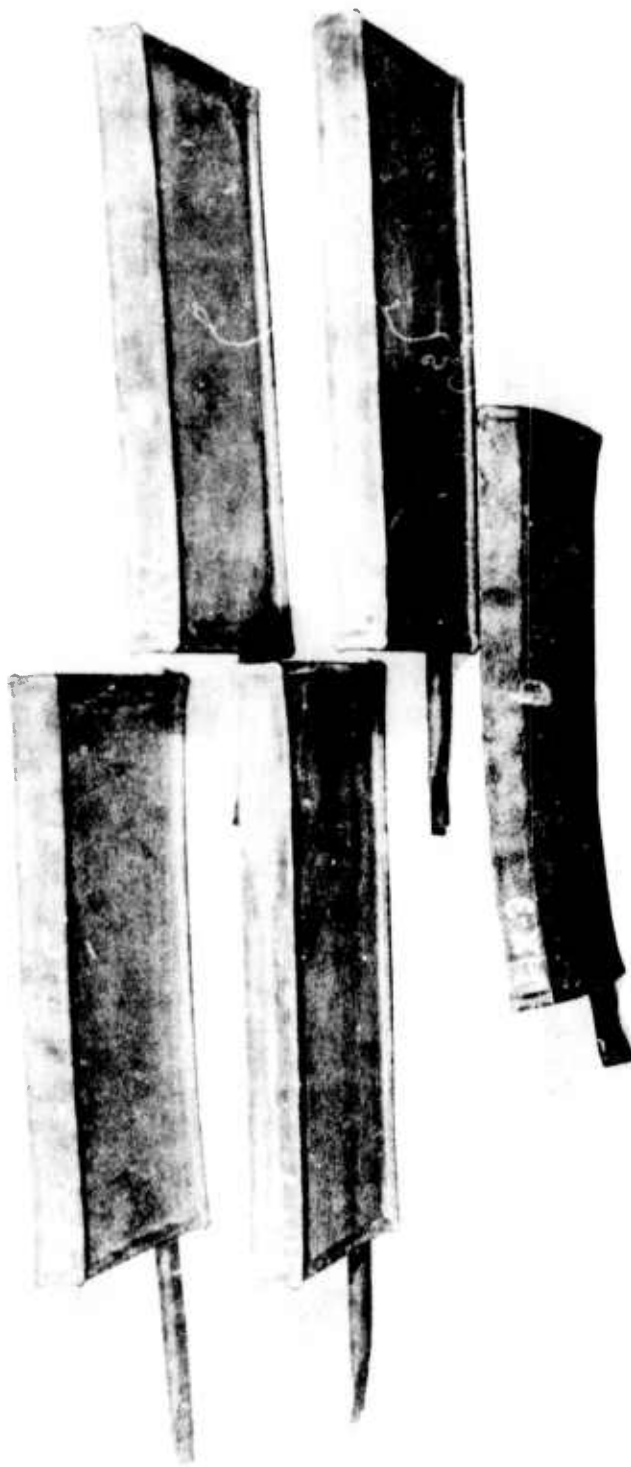


Figure 5--7 Photograph of Hot Isostatic Pressed (HIP) Plate samples of Inconel X750 shown as hiped before removal of AISI 304 stainless containment shells.

Curve 6:7737C-H

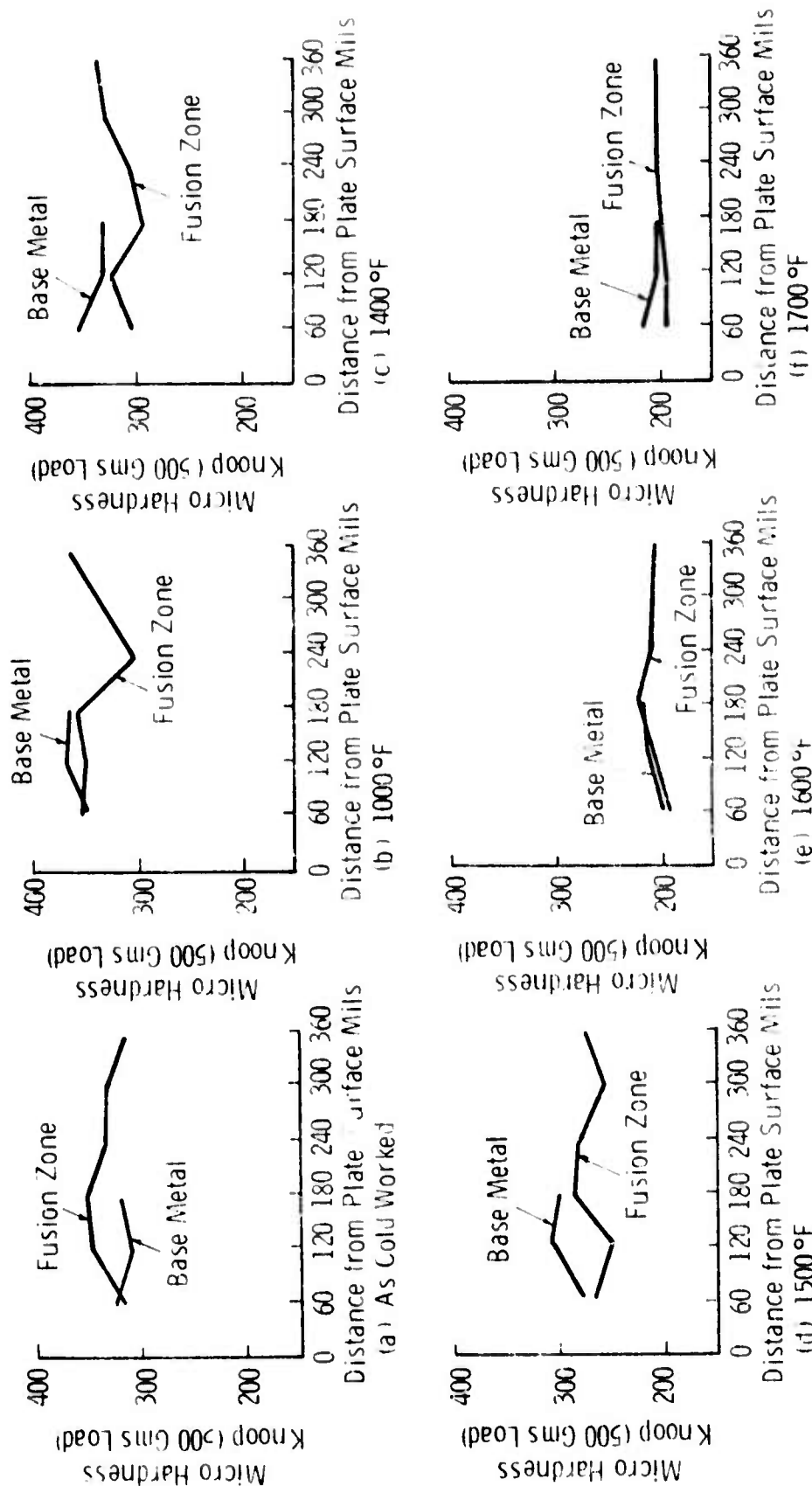


Fig. 8 — Microhardness traverse across transverse section of Kromarc 58 weldment (Plate K-1, GTAW and cold worked ~ 37%) for samples (a) as cold worked, and heated treated for 1 hour in argon at temperatures indicated (b) - (f)

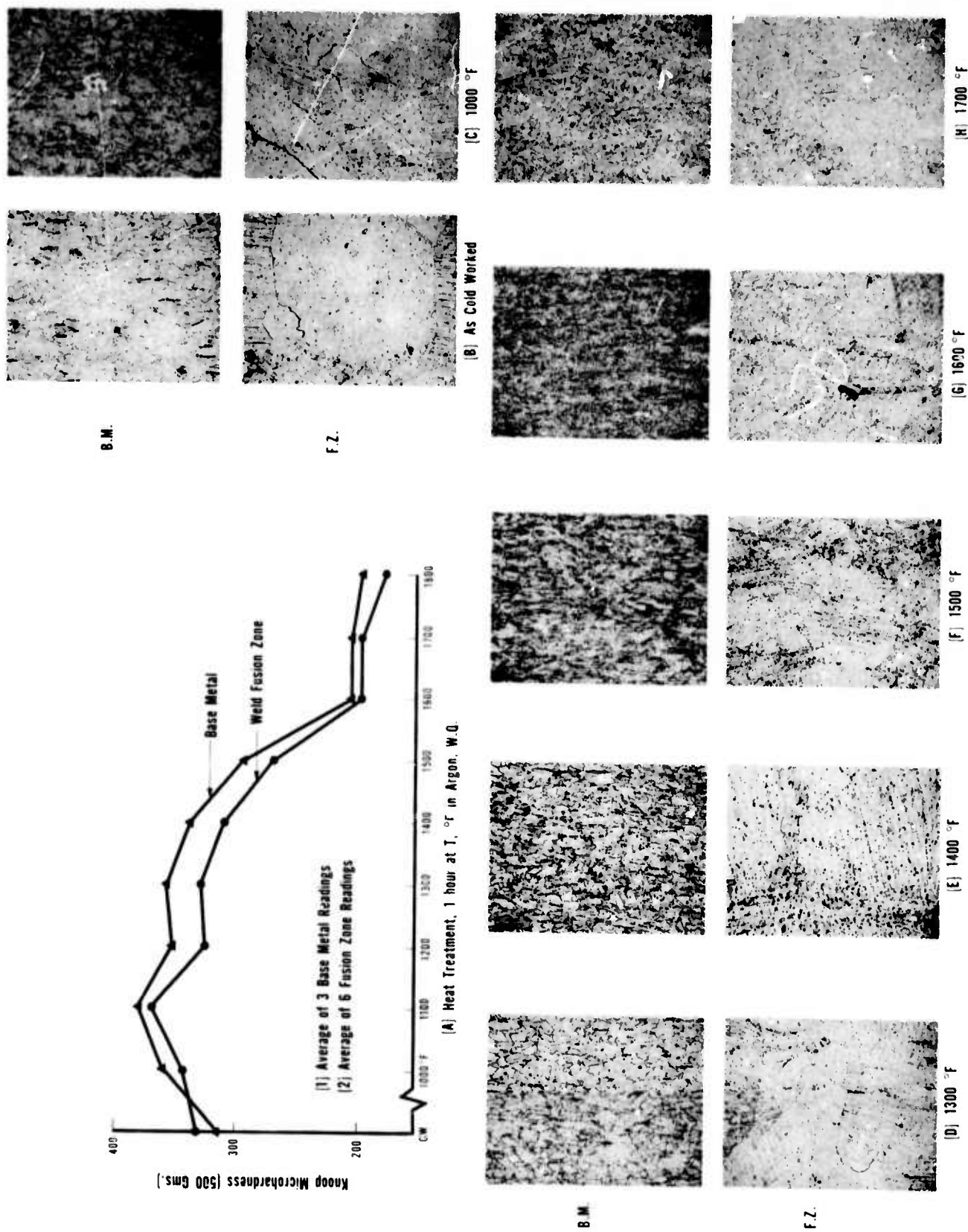
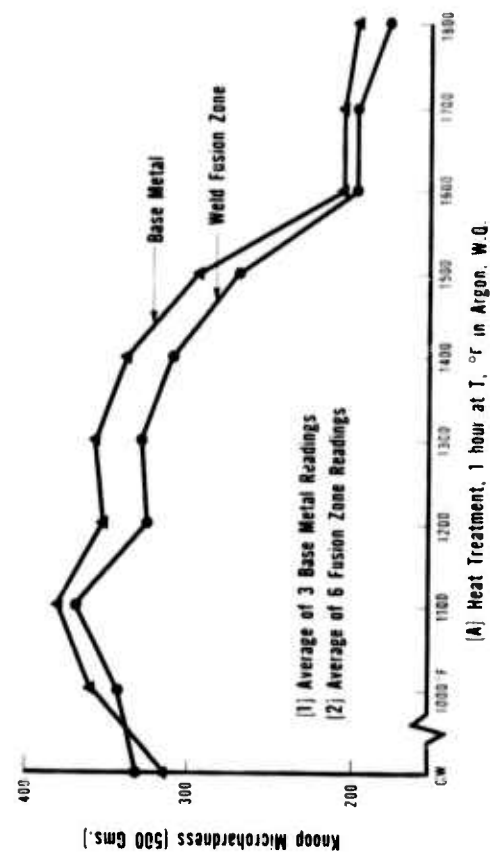
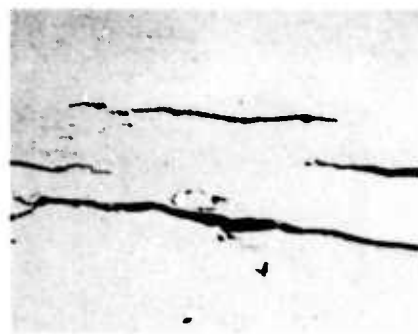


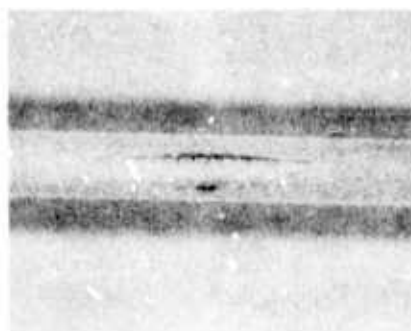
Figure 5-9 Microhardness changes and accompanying Base Metal (B.M.) and Fusion Zone (F.Z.) microstructures in Kromarc 58 stainless steel GTA welded and worked followed by heat treatment at the indicated temperature (X200)



(A)



(B)



(C)



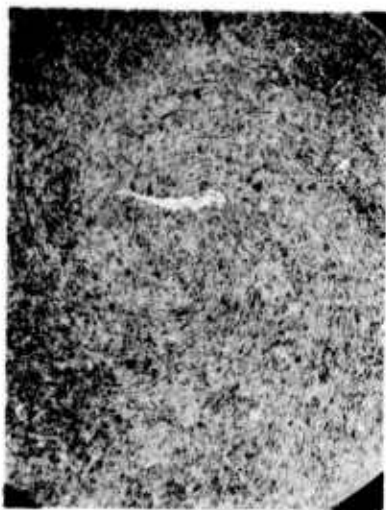
(D)



(E)

**Figure 5-10** Photographs showing defects experienced in initial attempt at fabricating Kromarc 58 stainless filler wire. (A) Transverse section and (B) Longitudinal section of wire swagged to .090" dia. without initial anneal (X50). (C) Residual longitudinal surface cracks in redraw stock after removal of .020" in dia. by surface grinding (X2.5) and (D) Transverse and (E) Longitudinal section of original redraw stock (X200)

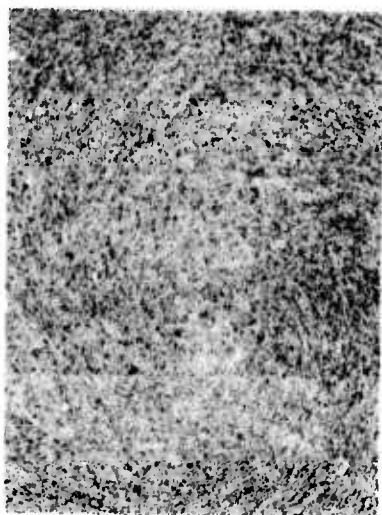
(A)  
X50



(B)  
X50



(A)  
X200



(B)  
X200

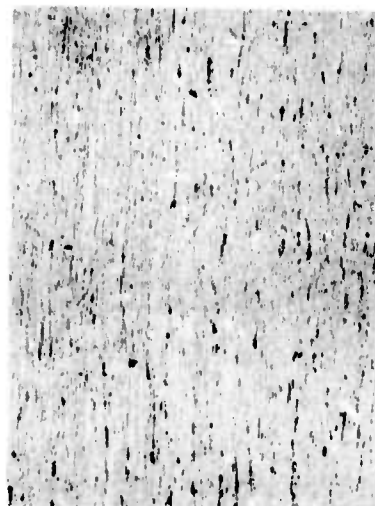
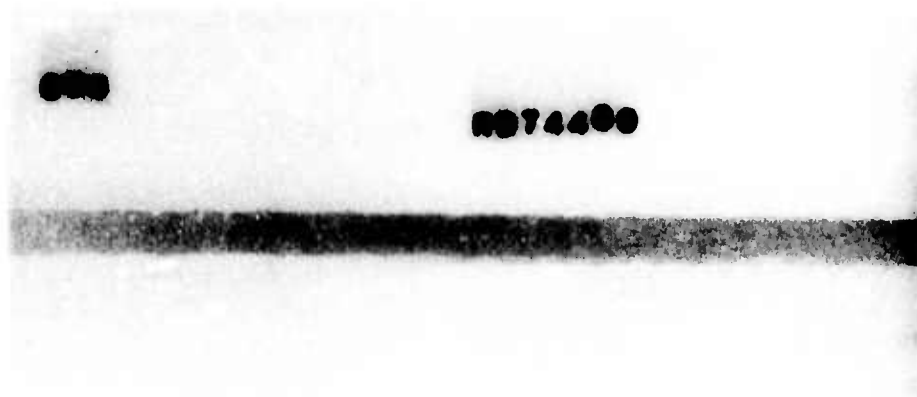


**Figure 5-11** Photographs of final Kromarc 58 filler wire of 0.090" dia.  
produced in-house for GTA welding (A) Transverse section,  
(B) Longitudinal



**C03**

**RD 74400**



**C04**

**RD 74401**

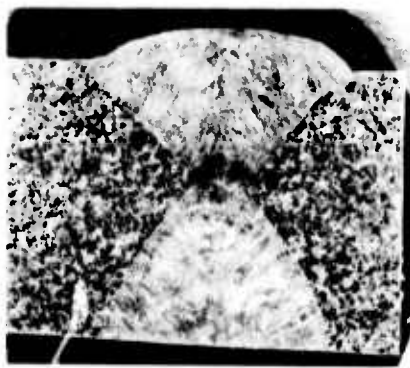


**C05**

**RD 74402**

Fig. 5 - 12 - Photographs of GMA weld radiographs  
 RD 74168, GMA weld plate Cu-3 (Code 12XX)  
 RD 74169, GMA weld plate Cu-4 (Code 12XX)  
 RD 74170, GMA weld plate Cu-5 (Code 12XX)  
 Material OFHC Copper - plate 1/2" thick

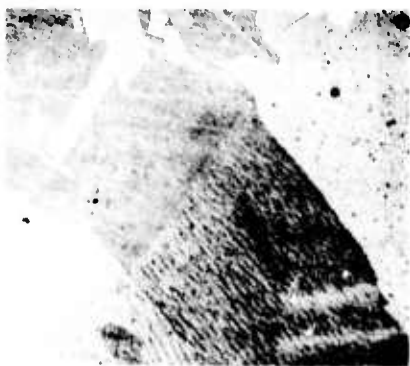




**(A) Transverse Section (X5)**



**(B) Weld Fusion Zone (X100)**



**(C) FZ-HAZ Transition (X100)**



**(D) Base Metal (X100)**

**Figure 5-13 Photomacrograph (A) and photomicrographs of GMA weldment in OFHC copper, (Code 12XX), (B) Weld fusion zone, (C) Weld FZ-HAZ transition and (D) Base metal**





**(A) STQ, Transverse View**



**(B) STQ, Longitudinal View**



**(C) STFC, Transverse View**



**(D) STFC, Longitudinal View**

**Figure 5-14 Photomicrographs of AISI 310S stainless steel.**  
**(A&B) Solution treated at 2000 °F-1hr. and water quenched, (STQ-Code 20XX), (C&D) Solution treated at 2000 °F-1hr. and furnace cooled, (STFC-Code 21XX) (X200)**

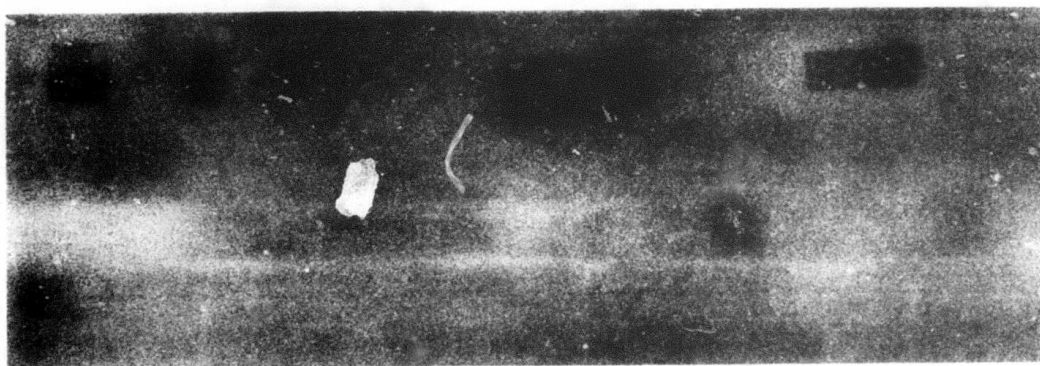


Fig. 5 - 15 - Photographs of SMA weld radiographs  
 RD 73716, SMA weld plate No. 310-2-First Half, (Code 22XX)  
 RD 73717, SMA weld plate No. 310-2-2nd Half, (Code 22XX)  
 Material - AISI 310 S Stainless Steel - Plate 5/8" thick

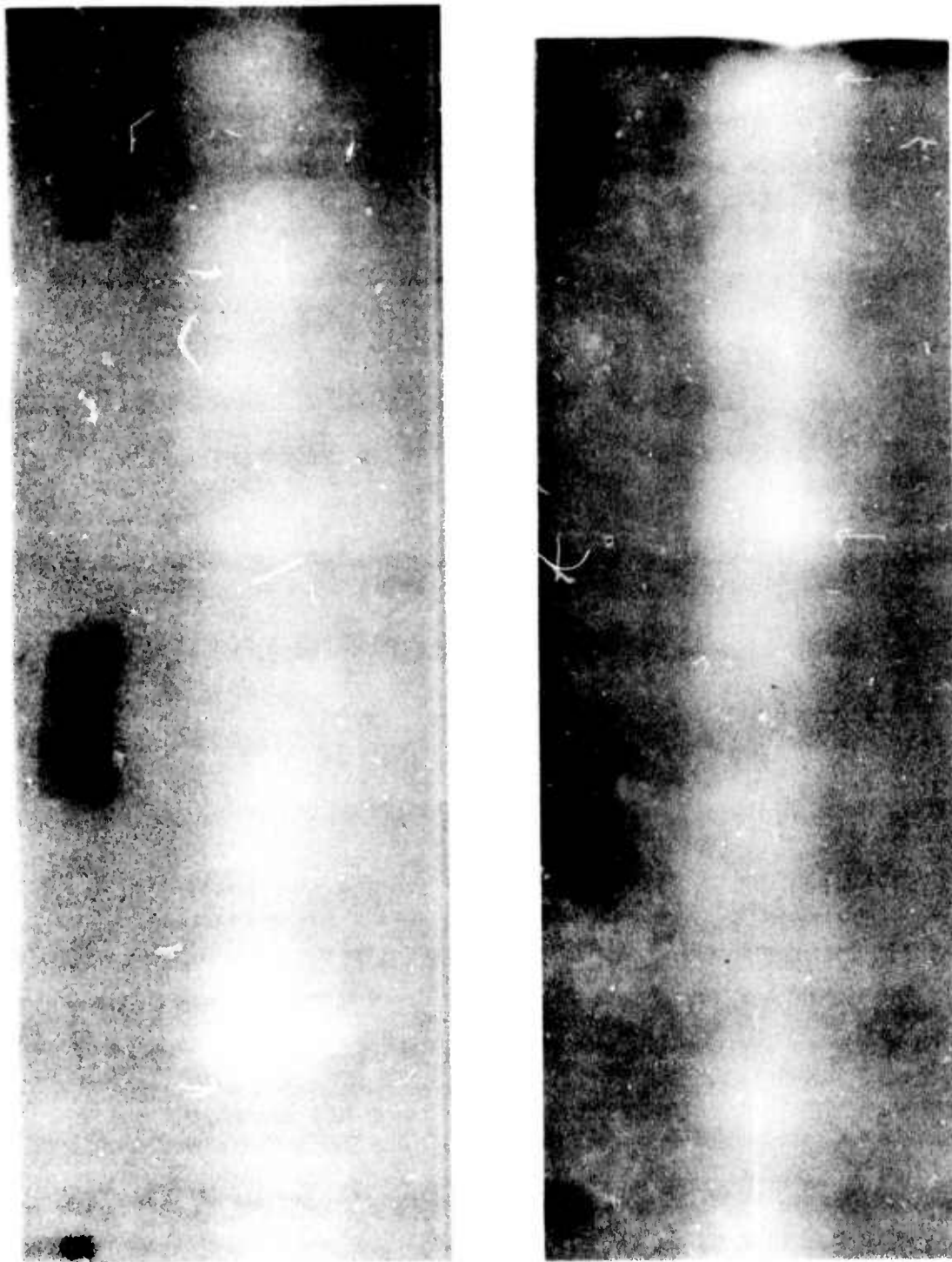
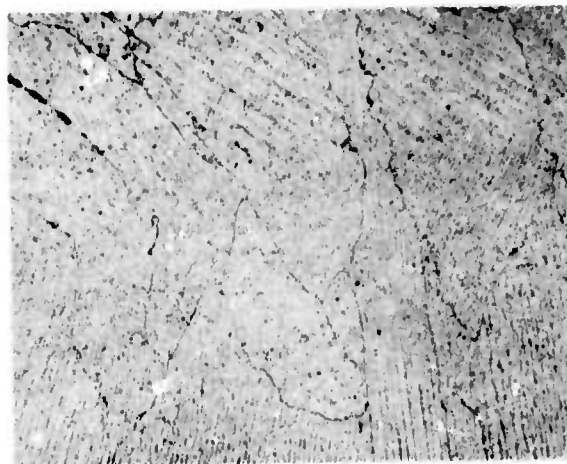


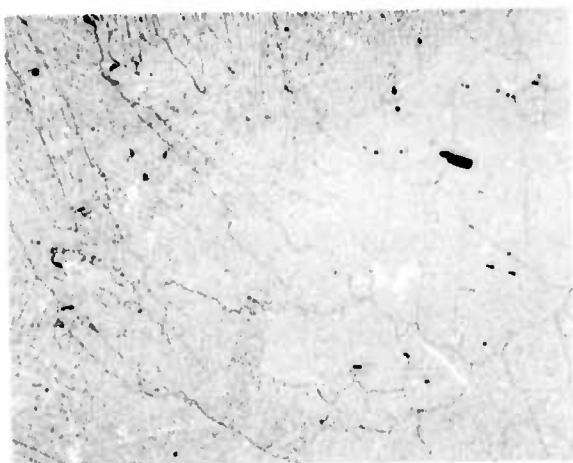
Fig. 5-16 -Photographs of SMA weld radiographs  
RD 73789, SMA weld plate No. 310-3-First Half,(Code 22XX)  
RD 73790, SMA weld plate No. 310-3-2nd Half,(Code 22XX)  
Material - AISI 310S Stainless Steel - Plate 5/8" thick



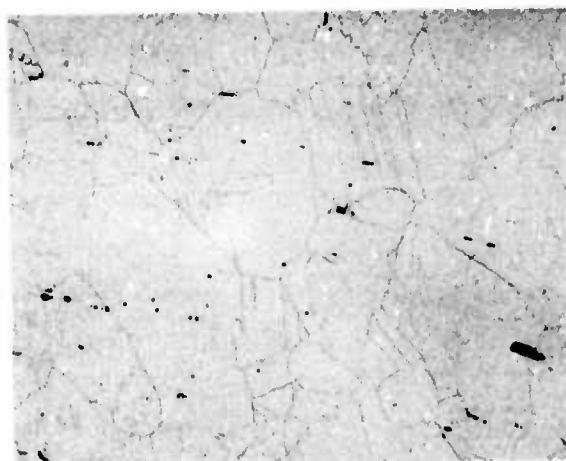
(a) Macro Weld Profile (X5)



(b) Micro Weld Fusion Zone (X200)



(c) Micro Weld FZ-HAZ Transition (X200)



(d) Micro-Base Metal Structure (X200)

Fig. 5-17 Macro (a) and microstructure (b, c, & d) of 310S stainless steel base metal and typical SMA weldment (5/8" thick) using E310-16 covered electrode. (22XX)

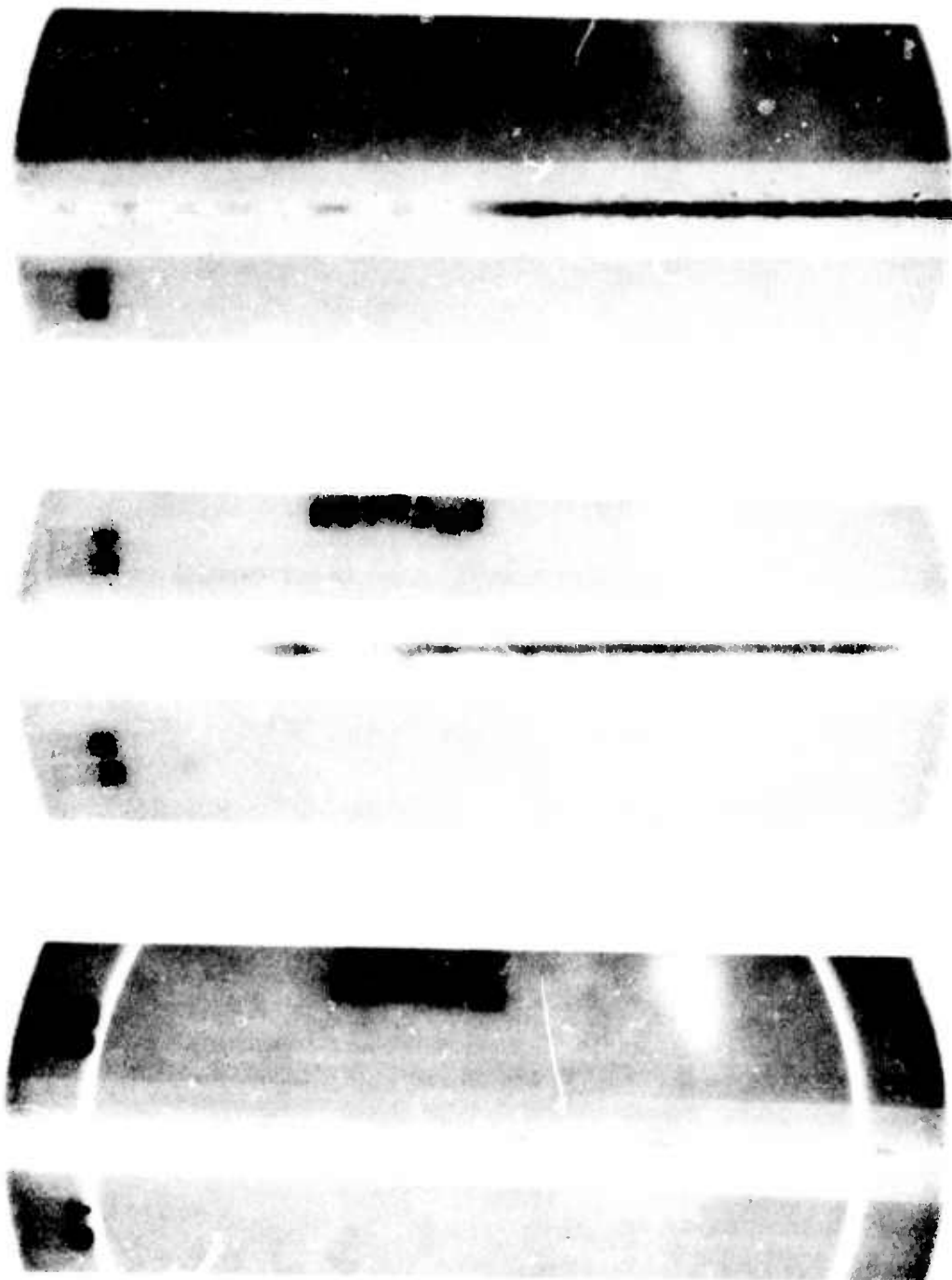


Fig. 5 — 18 —Photographs of vacuum electron beam weld radiographs  
RD 73643-EB Plate No. 1 ST/EBW (Code 32XX)  
RD 73642-EB Plate No. 2 STDA/EBW (Code 33XX)  
RD 73641-EB Plate No. 3 EBW/ STDA (Code 34XX)  
Material Inconel X750 ( VIM-VAR) - Plate 5/8" thick

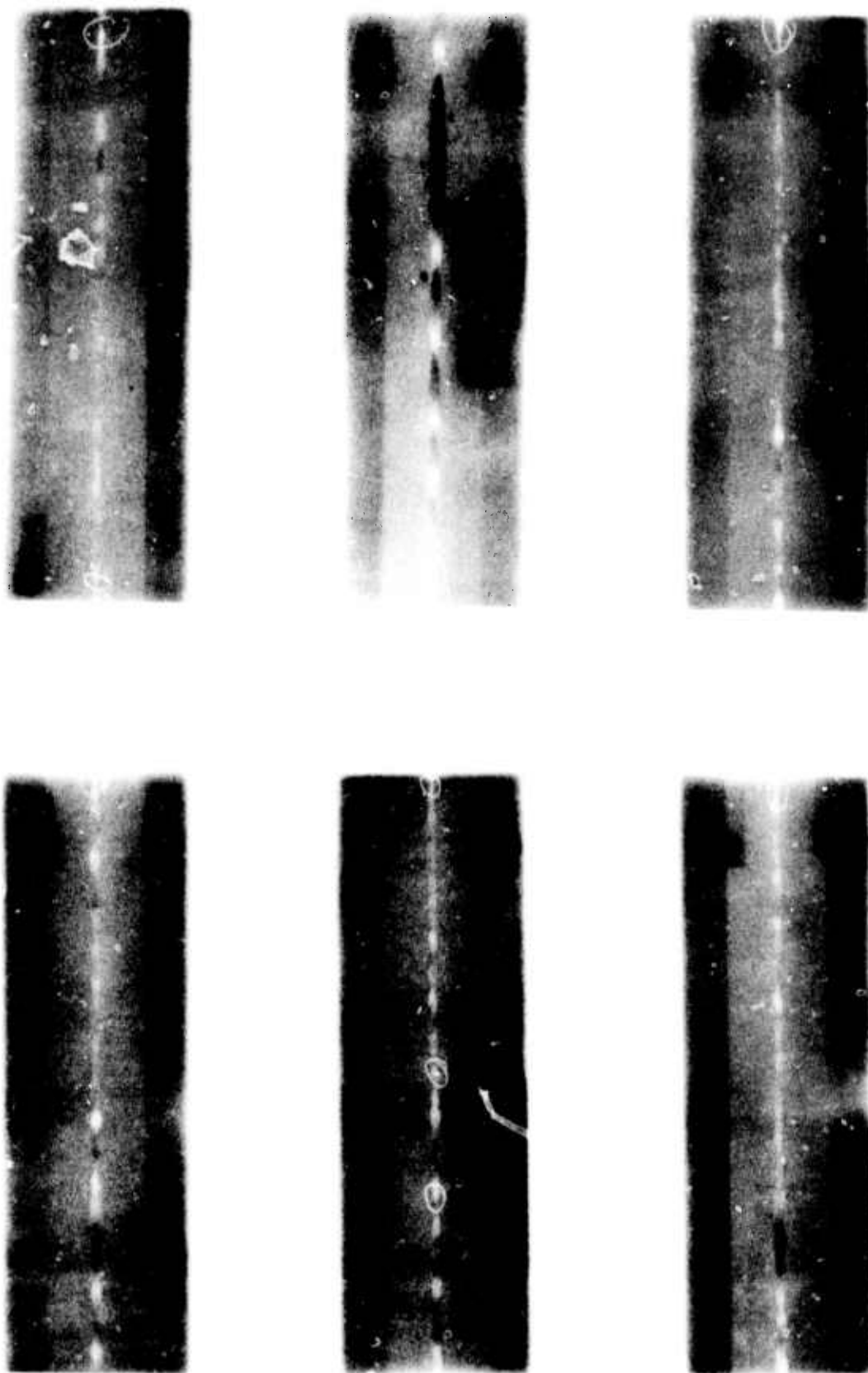
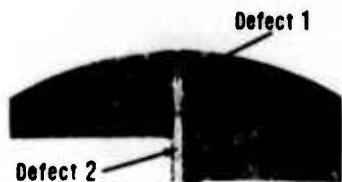


Fig.5 - 19 -Photographs of vacuum electron Beam weld radiographs  
 RD 74645, EB pieces 1&2, 3&4, EBW/ STDA (Code 34XX)  
 RD 74646, EB pieces 5&6, 7&8, ST /EBW (Code 32XX)  
 RD 74647, EB pieces 9&10, 11&12, STDA/EBW (Code 33XX)  
 Material Inconel X750 (VIM-VAR) - plate 5/8" thick

574<





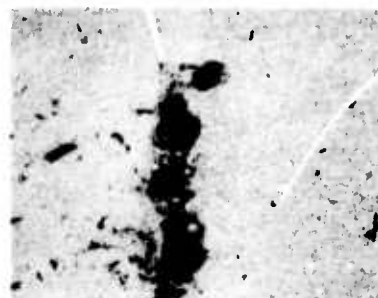
(A) Macro-EB Plate No. 2  
Containing Weld FZ & Defects



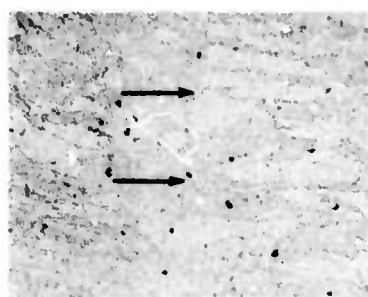
(E) Fusion Zone & Defect 1 (X10)



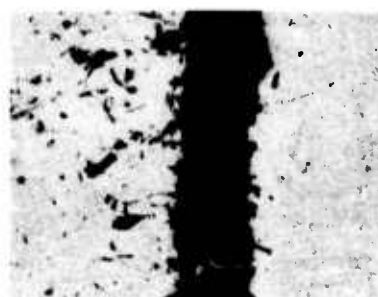
(B) Fusion Zone & Defect 2 (X200)



(F) Defect 1. Top End (X200)



(C) Normal FZ & (X200)



(G) Defect 1. Middle (X200)



(D) Typical FZ HAZ Transition (X200)



(H) Defect 1. Bottom End (X200)

Figure 5—20 Photographs showing macro and microstructure of HVEB weld defects in IN X750, EB plate sample No. 2 (Code 33XX). Both defects are in EB weld fusion zone center line and are visible on RD 73642 radiograph.

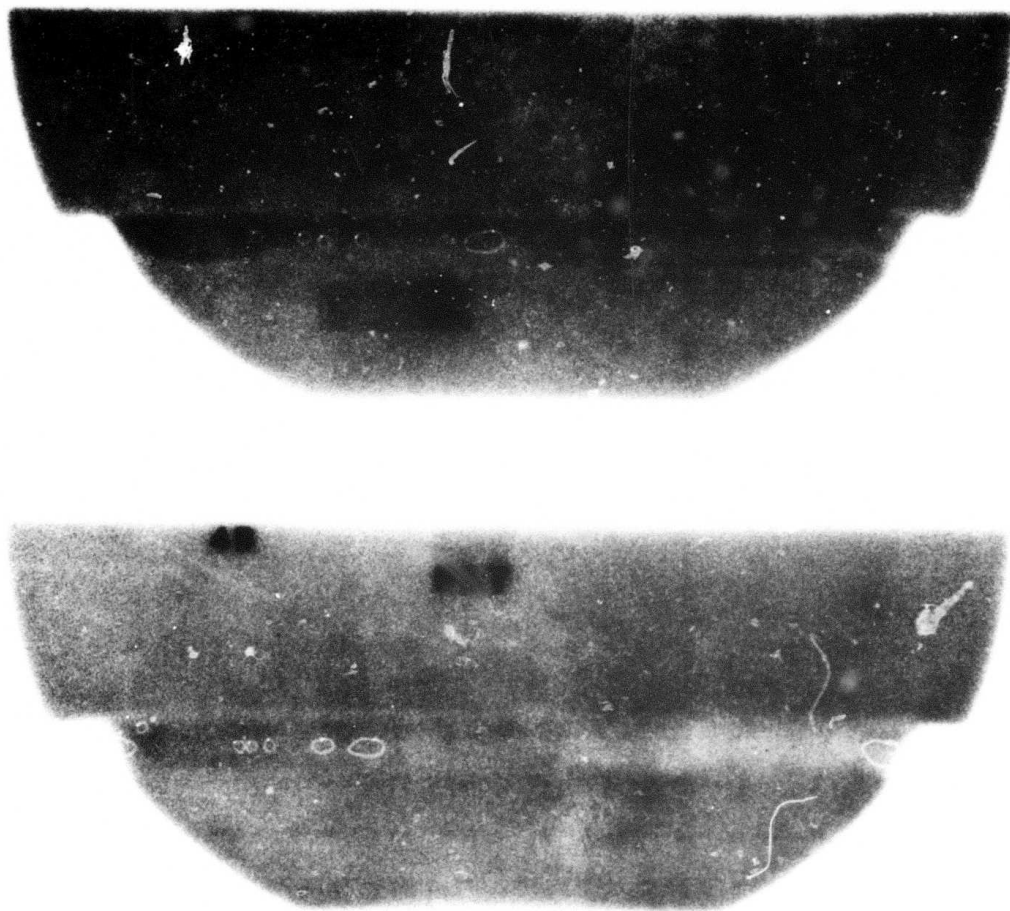


Fig. 5 - 21 - Photographs of GTA weld radiographs  
RD 73841 - GTA weld plate No. 4A ST/ GTAW (Code 35XX)  
RD 73841 - GTA weld plate No. 4B STDA/ GTAW (Code 36XX)  
Material Inconel X750(VIM-VAR) - plate 5/8" thick



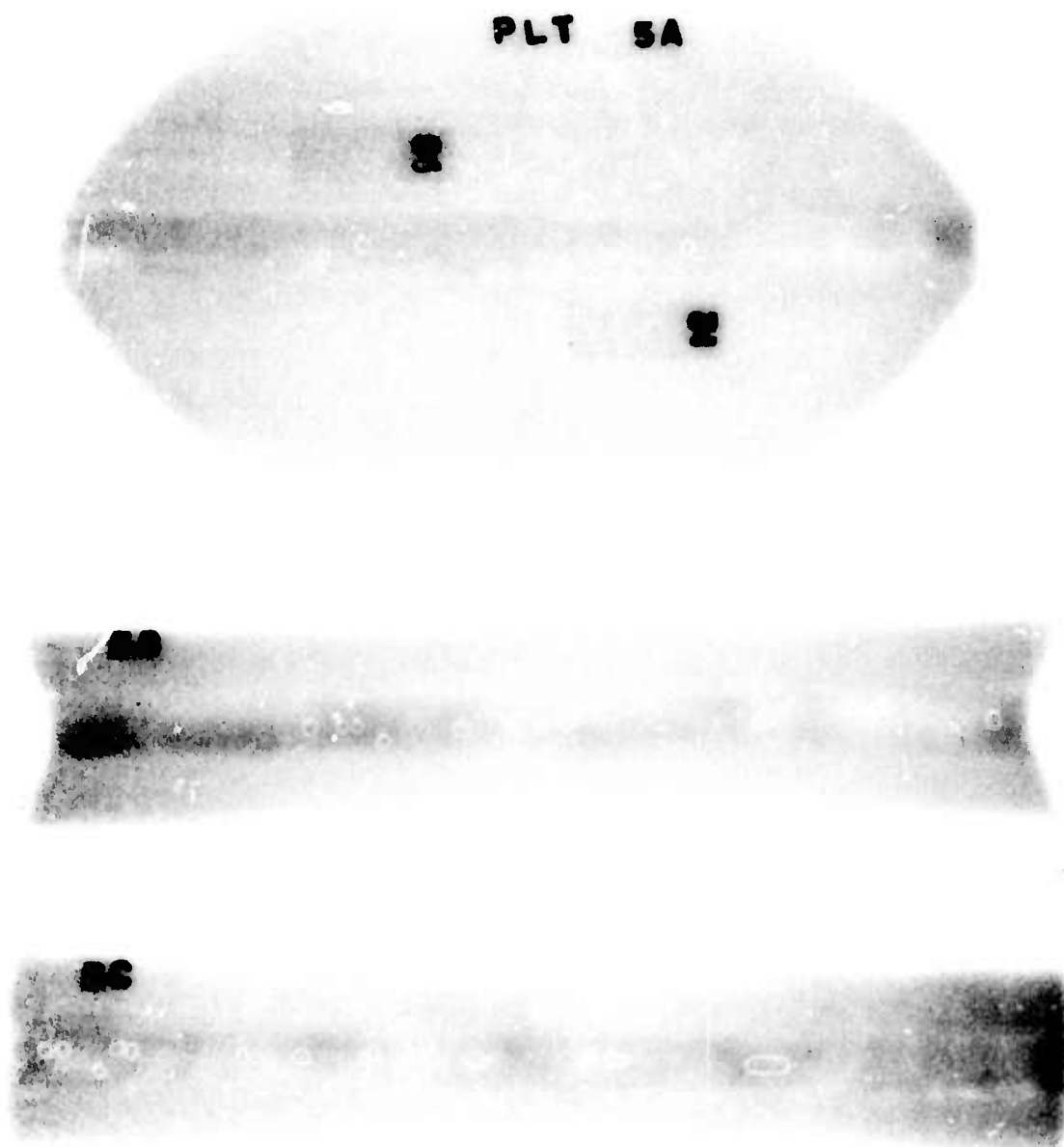


Fig. 5 - 22 - Photographs of GTA weld radiographs  
 RD 73836-GTA weld plate No. 5A, 5B, & 5C ST/GTAW (Code 35XX)  
 Material Inconel X750 (VIM-VAR) - Plate 5/8" thick

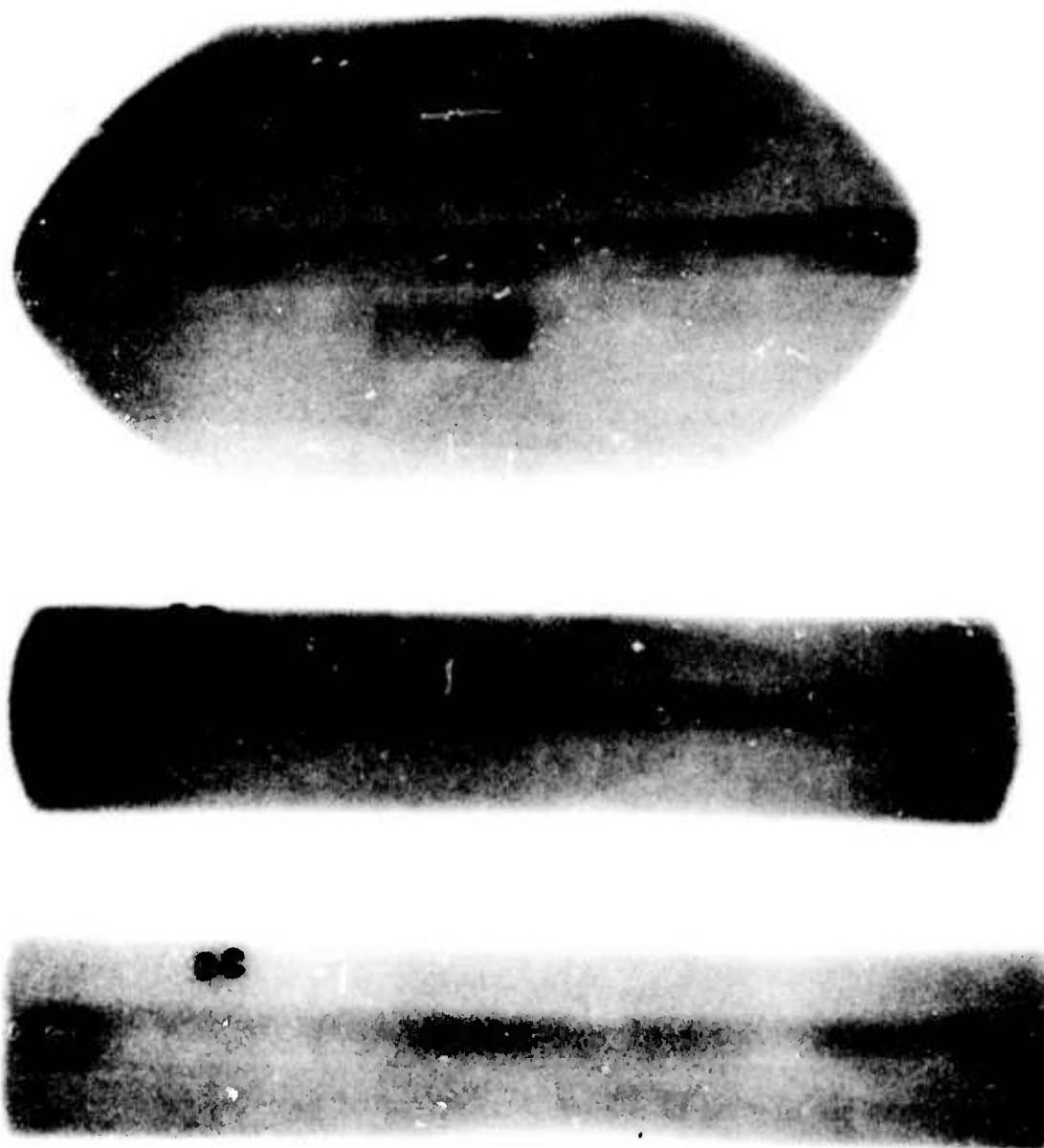


Fig. 5 -23 -Photographs of GTA weld radiographs  
RD 73842-GTA weld plate No. 6A, 6B, & 6C STDA/GTAW (Code 36XX)  
Material Inconel X750 (VIM-VAR) - Plate 5/8" thick

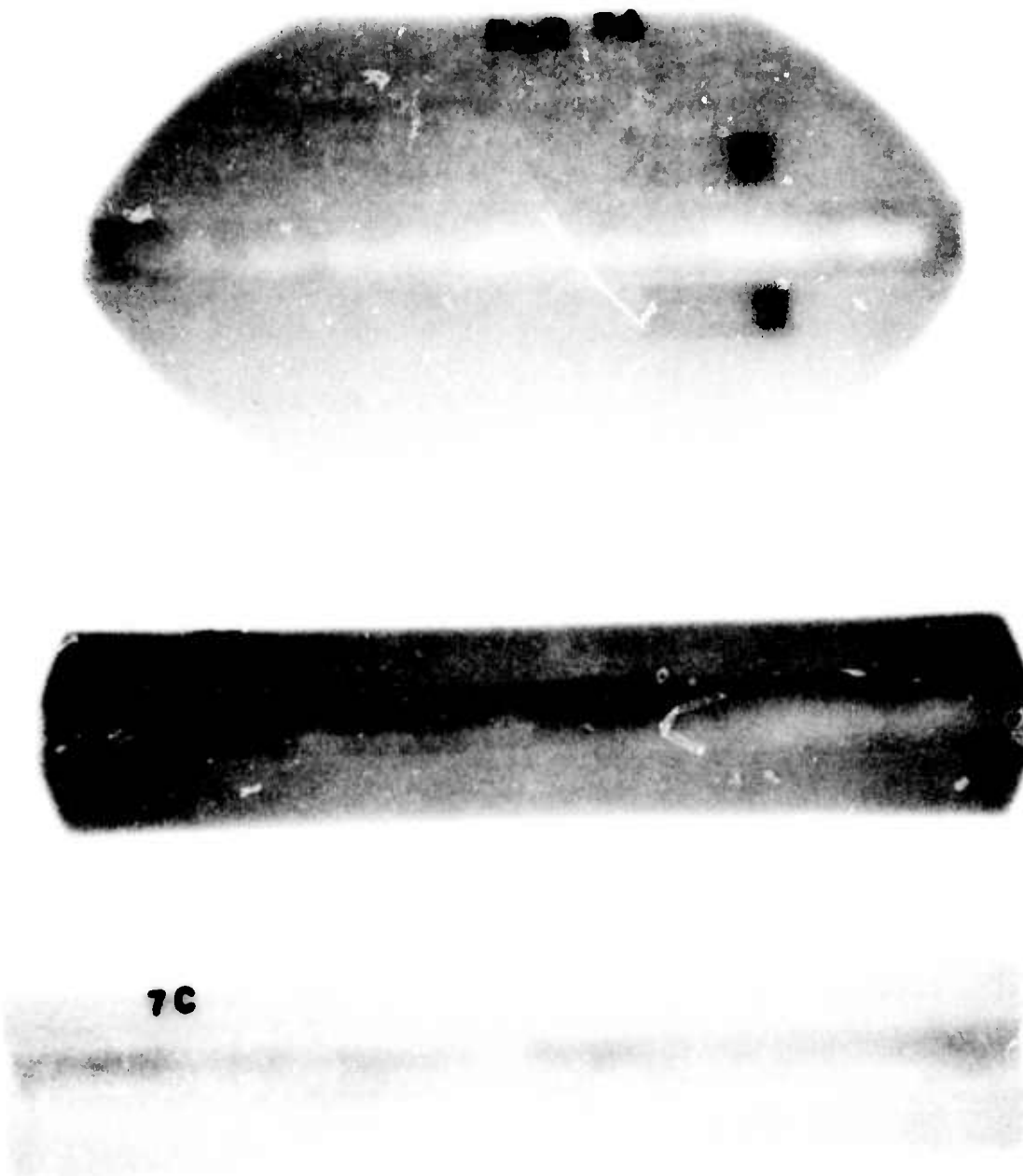


Fig. 5-24 - Photographs of GTA weld radiographs  
RD 73835 - GTA weld plate No. 7A, 7B, & 7C GTAW/STDA (Code 37XX)  
Material Inconel X750 (VIM-VAR) - Plate 5/8" thick



Fig. 5 - 25 -Photographs of GTA weld radiographs  
 RD 74366, GTA weld plate K58-7 First Half, STQ/GTAW (Code 82XX)  
 RD 74367, GTA weld plate K58-7 2nd Half, STQ/GTAW (Code 82XX)  
 Material Kromarc 58 Stainless Steel - Plate thickness 5/8 inch

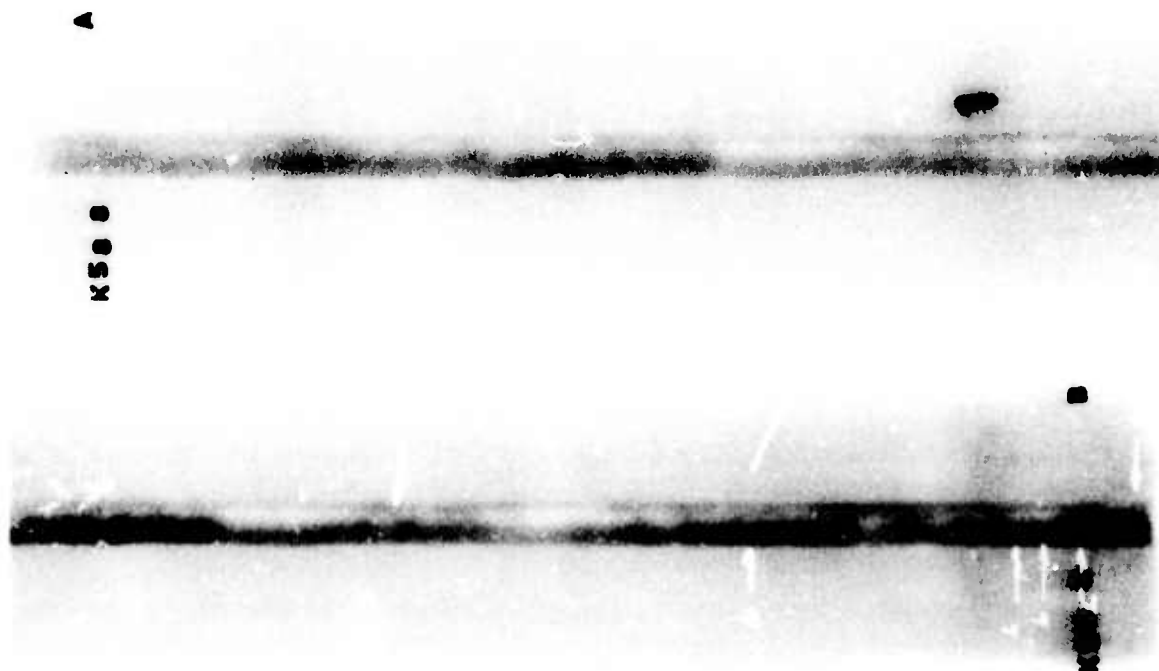


Fig. 5- 26 —Photographs of GTA weld radiographs  
 RD 74368, GTA weld plate K58-8 First Half, STQ/ GTAW (Code 82XX)  
 RD 74372, GTA weld plate K58-8 2nd Half, STQ/ GTAW (Code 82XX)  
 Material Kromarc 58 Stainless Steel - Plate thickness 5/8 inch

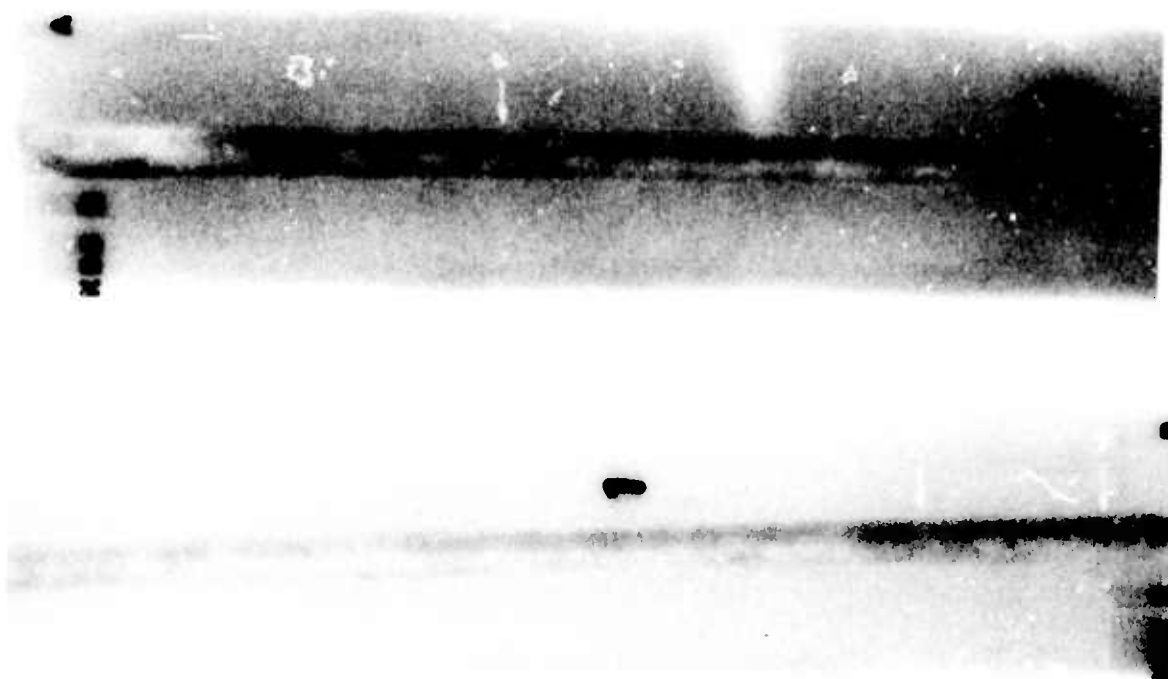


Fig. 5 - 27 -Photographs of GTA weld radiographs  
RD 74370, GTA weld plate K58-9 First Half, cw/ GTAW (Code 83XX)  
RD 74371, GTA weld plate K58-9 2nd Half, cw/ GTAW (Code 83XX)  
Material Kromarc 58 Stainless Steel - Plate thickness 5/8 inch

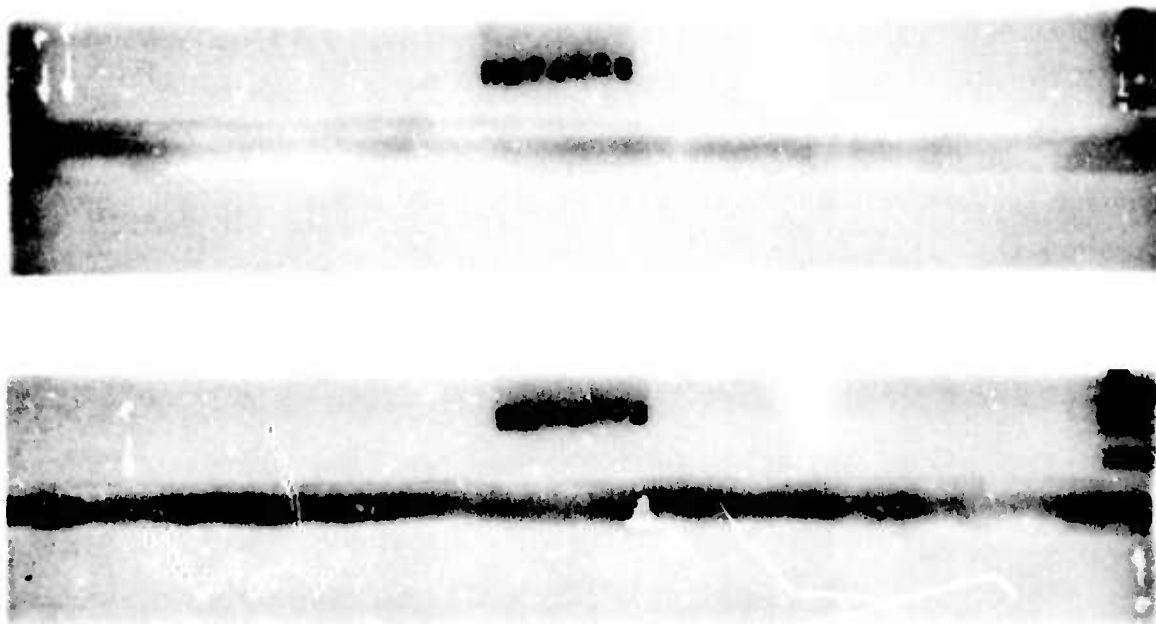


Fig. 5 - 28 - Photographs of GTA weld radiographs  
RD 74338, GTA weld plate No. K58-1 GTAW/ cw/ar. (Code 85XX)  
RD 74343, GTA weld plate No. K58-4 GTAW/ cw (Code 84XX)  
Material Kromare 58 Stainless Steel - Plate thickness 1 in. (as welded)



(A)



(B)



(D)



(C)

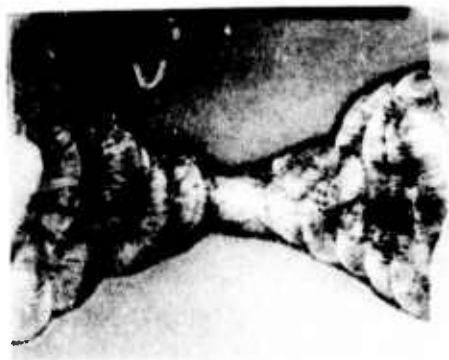


(E)

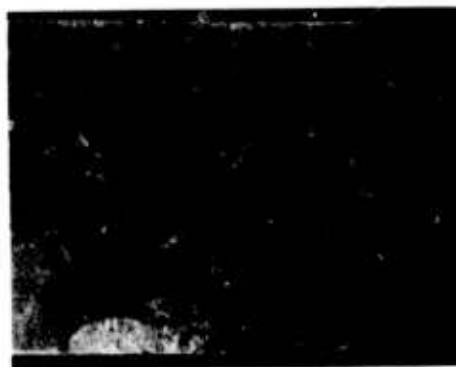
**Figure 5-29 Photograph of Kromarc 58 stainless steel GTA weld plates shown as welded. (A) Plate K-7, (B) Plate K-8, (C) Plate K-9, (D) Plate K-4 and (E) Plate K-1.**

58.4





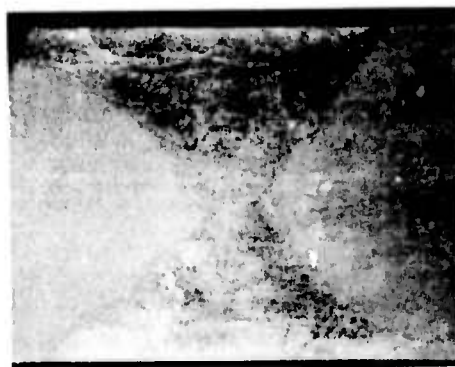
(A) As GTA Welded (X4)



(B) GTAW/Cold worked (37%), (X5)



(C) GTAW/CW/1500 °F (X5)

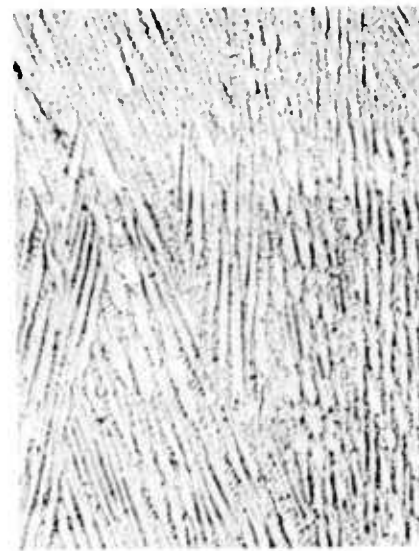


(D) GTAW/CW/1600 °F (X5)

Figure 5-30 Macro-photographs of Kromarc 58 stainless weldments in transverse section (A) as GTA welded (Code 82XX), (B) GTAW/cold worked (37%)—(Code 84XX), (C) Partially recrystallized GTAW/CW/1500 °F—(Code 85XX) and (D) Fully recrystallized GTAW/CW/1600 °F—(Code 86XX)



**(A) Macro Weld Profile (X4)**



**(B) Micro Weld Fusion Zone (X200)**

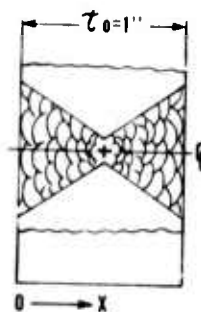
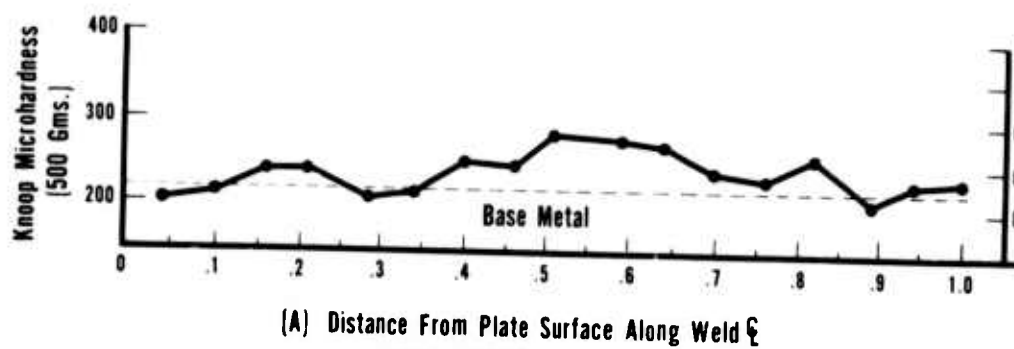


**(C) Micro Weld FZ-HAZ Transition  
(X200)**

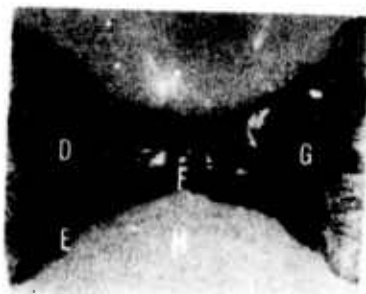


**(D) Micro Base Metal Structure  
(X200)**

**Figure 5—31 Macro (A) and microstructure (B,C, & D) of Kromarc 58 stainless steel base metal and typical GTA weldment (1" thick—as welded) using Kromarc 58 filler wire, (Code 84XX)**



(B) Schematic Cross Section



(C) Macro Section

(D) Weld Fusion Zone

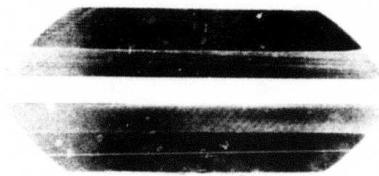
(E) FZ-HAZ Transition

(F) FZ-HAZ Transition

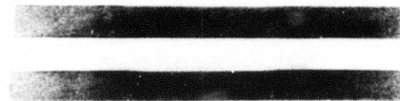
(G) Weld Fusion Zone

(H) Base Metal

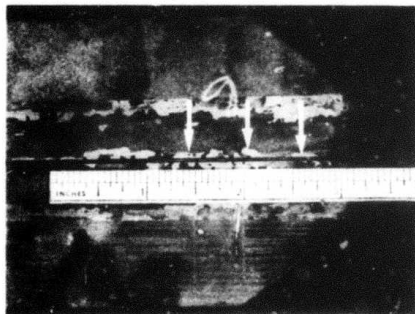
Figure 5-32 Microhardness survey (A) & (B), macrostructure (C) (X4), and microstructure of GTA welded kromarc 58 stainless (plate K-1) as welded, (D) through (H) (X200)



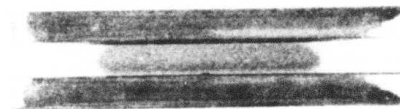
(A) Inconel X750 Braze Plate Sections  
Mating Surfaces Copper Plated



(B) Cu Plated X750 Surfaces  
Before Brazing Attempt

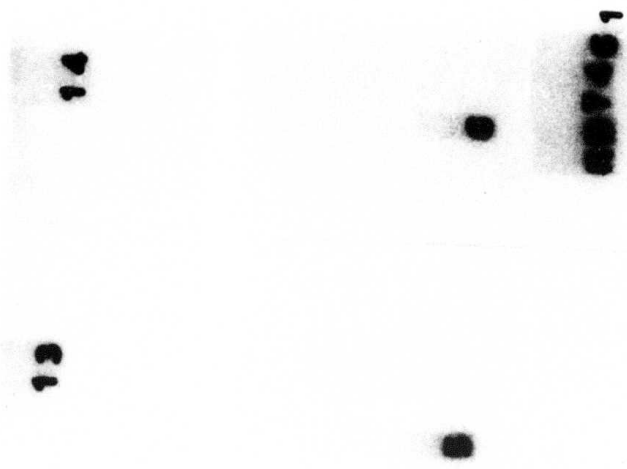


(C) Initial Brazed X750 Assembly  
Note Unbraided Areas (Arrows)



(D) Cu Plated X750 Surfaces after  
1st. Brazing Attempt.

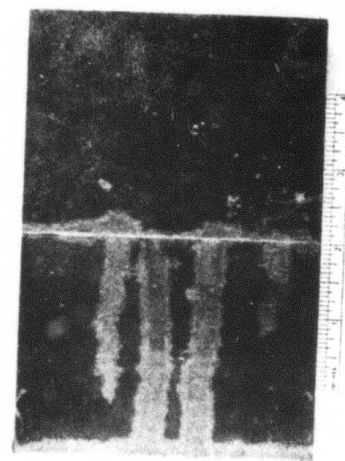
Figure 5-33 Photographs of copper plated Inconel X750 braze specimen before (A & B) and after (C & D) unsuccessful initial brazing test.



**(A) Radiograph Of Copper Solder (13-14) And Braze (5-6) Test Pieces**



**(B) Solder Test Specimen Surface Separated After Soldering (X5)**



**(C) Brazed Test Specimens**

**Figure 5-34 Photographs of initial copper solder and brazed test samples.**

## 6.0 FRACTURE MECHANICS

### Introduction

The advent and necessity of more and more cryogenic or superconducting devices has created a strong demand by designers for the material properties required to insure immunity from structural failure of these systems. Naturally, the cryogenic environment has placed severe restrictions on the development of these required material properties, especially those in the area of fracture mechanics technology. Recent advances in fracture mechanics technology, however, especially in the area of elastic plastic fracture, have now made it possible to determine the required fracture mechanics material properties (specifically fracture toughness and crack growth rate) necessary to permit the application of fracture mechanics technology to structures and components subjected to cryogenic environments, thus insuring their structural performance.

The purpose of this section of the technical report is to present and summarize the material properties data (tensile, notched tensile, fracture toughness and crack growth rate) generated to date on Inconel X750, OFHC copper and 310 S plus Kromarc 58 stainless steels. In addition, the recently developed elastic plastic fracture criterion and the associated resistance curve test technique which was utilized to obtain elastic plastic ( $J_{Ic}$ ) fracture toughness values are briefly reviewed.

### Status

Concerning the overall status of the tensile, notched tensile, fracture toughness and fatigue crack growth rate material properties, some additional work is in progress (see Table 3-1). Naturally, our objective is to complete all of the work indicated in

the test matrix of Table 3-1. The primary reason for our being slightly behind schedule is the added effort (both in additional time and test specimens) required to conduct and develop elastic plastic as opposed to linear elastic fracture toughness values.

As of the writing of this report, the following additional tests have been completed. The results are presently being analyzed.

1. The remaining cryogenic fatigue crack growth rate tests on 310 S stainless steel (conditions STQ and STFC).
2. All cryogenic fatigue crack growth rate tests on 310 S stainless steel shielded metal arc welds.
3. All cryogenic fatigue crack growth rate tests on Kromarc 58 stainless steel (conditions STQ and CW).

#### 6.1 Tensile Results

The base metal tensile properties of Inconel X750 (conditions AAM-VAR, VIM, HIP and HIP/STDA) are illustrated in Figures 6-1 thru 6-4, respectively. In addition, Figure 6-5 presents graphically a comparison of the yield strength levels of every manufacturing process/heat treatment combination of Inconel X750 base metal investigated in this program. Finally, for overall comparison purposes, all the tensile properties generated to date on Inconel X750 at 75°F (297°K), -320°F (77°K) and -452°F (4.2°K) are summarized in Tables 6-1 thru 6-3, respectively.

Returning to Figure 6-5, note the vacuum induction melted (VIM) Inconel X750 produced the maximum 0.2% yield strength level compared with all other manufacturing process/heat treatment combinations of Inconel X750 throughout the majority of the test temperature range. In addition, vacuum induction melted Inconel X750 experienced the largest increase in yield strength with decreasing temperature. Also, both the vacuum induction melted/vacuum are remelted (VIM-VAR) and hot

isostatic pressed (HIP) Inconel X750 sustained a 15 to 25 percent increase in yield strength when solution treated and double aged. Finally, note only the vacuum induction melted/vacuum arc remelted (VIM-VAR) Inconel X750 (both heat treatments) displayed a decrease in yield strength with decreasing temperature (between -320°F and -452°F). This apparent decrease in yield strength at -452°F may be explained by the fact that all specimens tested at -452°F had a grain size about twice as large as those tested at higher temperatures (see Section 7 on Microstructural Analysis, First Semi-annual Progress Report for additional details).<sup>(1)</sup> The lowest yield strength values were also established by this same solution treated vacuum induction melted/vacuum arc remelted (VIM-VAR) Inconel X750.

In general, the ultimate strengths relative to the various manufacturing process/heat treatment combinations of Inconel X750 followed the same trends demonstrated by the corresponding yield strengths. The only significant difference is the larger increase with decreasing temperature experienced by the ultimate strengths as compared with the yield strengths.

Let us now turn our attention to the ductility properties (reduction in area and elongation) of the various manufacturing process/heat treatment combinations of Inconel X750 base metal. First, for all six manufacturing process/heat treatment combinations of Inconel X750 base metal, the reduction in area decreases with decreasing temperature throughout the test temperature range. Concerning the elongation properties, no general trend with temperature is discernible. Overall, the air arc melted/vacuum arc remelted (AAM-VAR) and hot isostatic pressed (HIP) Inconel X750 demonstrated the best reduction in area and elongation properties. The lowest reduction in area and elongation properties were established by solution treated and double aged vacuum induction melted/vacuum arc remelted (VIM-VAR) Inconel X750.

Figure 6-6 illustrates the tensile properties of OFHC copper gas metal arc welds. Note that all the test specimens fractured in the base metal as opposed to the weld or heat affected zone. As a result, these tensile properties and their behavior versus temperature are quite



similar to those previously developed on as received and stress relieved OFHC copper base metal.<sup>(1)</sup> Obviously, the OFHC copper gas metal arc welds will not be a weak link as far as adequate strength or ductility is concerned in an OFHC copper structure or component.

The tensile properties of solution treated and water quenched plus 30 percent cold worked Kromarc 58 stainless steel base metal are illustrated respectively in Figures 6-7 and 6-8 while Figures 6-9 thru 6-11 present the tensile properties of Kromarc 58 stainless steel gas tungsten arc welds. Also, again for overall comparison purposes, all the tensile properties generated to date on OFHC copper, AISI 310 S stainless steel and Kromarc 58 stainless steel at 75°F (297°K), -320°F (77°K) and -452°F (4.2°K) are summarized in Tables 6-4 thru 6-6, respectively.

Regarding the tensile properties of Kromarc 58 stainless steel base metal, note that cold working the Kromarc 58 stainless steel 30 percent causes a substantial increase in yield strength (from a 35 percent increase at -452°F (4.2°K) to a 155 percent increase at 75°F (4.2°K)). Also, the yield strength of cold worked Kromarc 58 stainless steel has a reduced tendency to increase with decreasing temperature when compared with the yield strength behavior of solution treated and water quenched Kromarc 53 stainless steel.

Turning to Figure 6-8, note the excellent ductility (reduction in area and elongation) displayed by solution treated and water quenched Kromarc 58 stainless steel. As expected, cold working the Kromarc 58 stainless steel obviously reduced its ductility. Except for a low room temperature elongation value, however, the 30 percent cold worked Kromarc 58 stainless steel base metal also demonstrates adequate reduction in area and elongation. In fact, the reduction in area experienced by the cold worked Kromarc 58 stainless steel exceeds that of the air arc melted/vacuum arc remelted (AAM-VAR) and hot isostatic pressed (HIP) Inconel X750 regardless of temperature. Overall, the cold worked Kromarc 58 stainless steel certainly warrants solid consideration as a structural material for cryogenic applications based on its high strength in combination with surprisingly good ductility.

The tensile properties of Kromarc 58 stainless steel gas tungsten arc welds (GTA, Code 82xx) are illustrated in Figure 6-9. Note at room temperature the weld specimen fractured in the base metal. Values of yield strength and ultimate strength determined from this specimen, however, are over thirty percent higher than those for solution treated and water quenched Kromarc 58 stainless steel base metal while its reduction in area and elongation properties were ten and twenty percent lower, respectively. This increase in strength and decrease in ductility may have been caused by precipitation of nitride and/or carbides (sensitization) from the gas tungsten arc multipass welding operation. All the remaining Kromarc 58 stainless steel gas tungsten arc weld tensile specimens fractured in the weld or heat affected zone. The yield and ultimate strengths of these gas tungsten arc welds are very similar to the yield and ultimate strengths of solution treated and water quenched Kromarc 58 stainless steel base metal (see Tables 6-5 and 6-6). In addition, the ductility (reduction in area and elongation) of the gas tungsten arc welds is only slightly lower than that of the solution treated and water quenched Kromarc 58 stainless steel base metal. Therefore, although the cryogenic gas tungsten arc weld tensile specimens failed in the weld region, the strength and ductility of these gas tungsten arc welds are nearly equivalent to those of the solution treated and water quenched Kromarc 58 stainless steel base metal, and as such these gas tungsten arc welds should not be considered a weak link in a Kromarc 58 stainless steel structure or component from a strength or ductility standpoint.

The tensile properties of pre-weld and post-weld cold worked Kromarc 58 stainless steel gas tungsten arc welds are illustrated graphically in Figures 6-10 and 6-11, respectively. All these gas tungsten arc weld tensile specimens fractured in the weld or heat affected zone. Observing Tables 6-4 thru 6-6, note the yield and ultimate strengths of Kromarc 58 stainless steel gas tungsten arc welds are increased by either pre-weld or post-weld cold working. As expected, post-weld cold working the gas tungsten arc welds produced the greater increase in yield and ultimate strengths. The reduction in area values of pre-weld cold worked gas tungsten

arc welds are quite similar to those of the standard Kromarc 58 gas tungsten arc welds. The reduction in area values for the post-weld cold worked Kromarc 58 gas tungsten arc welds, however, are 17 to 22 percent lower than those of the non cold worked Kromarc 58 gas tungsten arc welds. Either pre-weld or post-weld cold working the gas tungsten arc welds created a significant decrease in the percent elongation experienced by these welds.

## 6.2 Notched Tensile Results

The purpose of notched tensile tests is to screen the notch toughness in terms of the comparison parameter defined as the ratio of notched tensile fracture strength to the tensile yield strength of a particular material for a specific notch acuity. Increasing values of the ratio above 1.0 are considered to indicate increasing ability of the material for plastic deformation at the notch tip. Stated alternatively, increasing values of the ratio above 1.0 can be utilized as a measure of the material's resistance to catastrophic brittle fracture.

In all cases the root radius at the bottom of a particular test specimen's sharp V-notch was adjusted to yield a stress concentration factor ( $K_t$ ) equivalent to 10. It should be pointed out that the notched tensile fracture strength was calculated by dividing the maximum load experienced by a test specimen, or in a few cases where the load dropped slightly before failure dividing the fracture load, by its original as opposed to final cross sectional area. This was largely due to the great difficulty in accurately measuring the extremely small change in test section diameter (hence cross-sectional area) experienced by the test specimen.

The notched tensile fracture strengths of Inconel X750 (conditions AAM-VAR, VIM, HIP and HIP/STDA) plus Kromarc 58 stainless steel (conditions STQ and CW) are illustrated graphically in Figures 6-12 thru 6-17, respectively. In addition, all the notched tensile fracture strengths and notched tensile fracture strength to tensile yield strength ratios developed in this investigation (including those for OFHC copper gas

metal arc welds plus Kromarc 58 stainless steel gas tungsten arc welds for which no plots are available) are summarized in Tables 6-1 thru 6-6. Keep in mind, in several cases unnotched weld metal specimens fractured in the base metal or heat affected zone. Therefore, the comparison parameter for these particular weld tests is actually the notched tensile fracture strength of the particular weld metal divided by the tensile yield strength of the corresponding base metal or possibly heat affected zone. The ratio of notched tensile fracture strength to tensile yield strength for each base material or weld regardless of manufacturing process, heat treatment or test temperature is always greater than one, the minimum value equalling 1.3.

### 6.3 Fracture Toughness Results

Linear elastic fracture mechanics technology provides a one parameter fracture criterion for a limited class of problems; those of cracked bodies with small scale yielding where the crack tip plastic region is at least an order of magnitude smaller than the physical dimensions of the component. Over the past few years, linear elastic fracture mechanics technology has evolved to the point where, providing we are armed with data for both the rapid propagation ( $K_{Ic}$  fracture toughness) and in addition the slow growth (crack growth rate) phases of fracture, we can evaluate the fracture potential of components in various situations. Specifically, it is possible to: (a) select materials to provide the desired reliability against fracture; (b) develop a quantitative evaluation of the brittle fracture potential of components in specific situations; (c) predict the useful life expectancy of components under sustained and/or cyclic loading conditions; (d) establish realistic acceptance and nondestructive inspection specifications that will assure the desired degree of immunity from brittle failure for the required life of the structure.

Recently, however, an elastic plastic fracture criterion,<sup>(2,3)</sup> based largely on the J integral proposed by Rice,<sup>(4)</sup> and the corresponding resistance curve test technique used to obtain elastic plastic fracture

toughness values,<sup>(5,6)</sup> were developed by Landes and Begley to provide a direct extension of fracture mechanics into the elastic plastic and fully plastic fracture regimes. Therefore, it is now possible to apply fracture mechanics technology to those situations which often occur in dealing with cryogenic structural components where the extent of plasticity rules out the use of linear elastic fracture mechanics (such as defects adjacent to stress concentration sites, etc.).

Although our original Structural Materials for Cryogenic Applications program called for the development of linear elastic  $K_{Ic}$  fracture toughness values at  $-320^{\circ}\text{F}$  ( $77^{\circ}\text{K}$ ) and  $-452^{\circ}\text{F}$  ( $4.2^{\circ}\text{K}$ ), it became obvious at an early stage that to develop valid linear elastic fracture toughness values per the ASTM Test for Plane Strain Fracture Toughness of Metallic Materials (E399-72) was impossible even at  $-452^{\circ}\text{F}$  ( $4.2^{\circ}\text{K}$ ) utilizing one half inch thick compact tension specimens. For example, to obtain a valid linear elastic  $K_{Ic}$  fracture toughness value for solution treated and double aged air arc melted, vacuum arc remelted (AAM-VAR) Inconel X750 at  $-452^{\circ}\text{F}$  ( $4.2^{\circ}\text{K}$ ) would have required a six inch thick compact tension specimen. Similarly, ten inch and four inch thick specimens would be necessary to obtain valid linear elastic  $K_{Ic}$  fracture toughness values at  $-452^{\circ}\text{F}$  ( $4.2^{\circ}\text{K}$ ) on solution treated and water quenched 310 S and Kromarc 58 stainless steels, respectively. Therefore, a tremendous economic advantage (both in test specimen material and machining costs as well as helium conservation) would be realized by conducting elastic plastic  $J_{Ic}$  as opposed to linear elastic  $K_{Ic}$  fracture toughness tests.

In addition, looking at the practical side, based on our experience with superconducting generators, section thicknesses much greater than one inch in highly stressed components (rotors, etc.) are not anticipated. Furthermore, if a failure should occur, proper design of cryogenic structures or components will cause these structures or components to fail plastically (elastic plastic fracture) as opposed to catastrophically

(linear elastic fracture). Therefore, from a practical as well as economic point of view, the decision was made to consolidate the available one half inch thick compact tension specimens thus permitting the development of elastic plastic  $J_{Ic}$  fracture toughness values at  $-452^{\circ}\text{F}$  ( $4.2^{\circ}\text{K}$ ).

The previously mentioned resistance curve test technique created by Landes and Begley was employed to obtain the critical elastic plastic fracture toughness values. A thorough description of this resistance curve test technique is given in Reference 5. The primary steps of this test technique which were applied to obtain the critical  $J_{Ic}$  values for each of the materials tested at  $-452^{\circ}\text{F}$  ( $4.2^{\circ}\text{K}$ ) follow in outline form.

(A) Each specimen was loaded at  $-452^{\circ}\text{F}$  ( $4.2^{\circ}\text{K}$ ) to different displacement values with a universal test machine in displacement control (note Figure 6-18a). Displacement was measured via a linear variable differential transformer (LVDT) attached to the specimen front face. It should be mentioned that each specimen was first precracked at loads considerably less than those anticipated in the subsequent fracture toughness tests.

(B) Each specimen was unloaded and the crack marked utilizing a heat tinting procedure.

(C) Each specimen was pulled apart at low temperature (less than  $-200^{\circ}\text{F}$ ) and its crack extension was measured. The crack extension was measured at its maximum point and taken to include all crack extension from the fatigue precrack to the end of the mark (Figure 6-18b).

(D) J values were calculated from the load versus displacement records using the formula developed by Rice, et. al., for calculating J from single specimen tests<sup>(7)</sup>

$$J = \frac{4a + b}{4(a+c) + b} \frac{2A}{Bb} \left( \begin{array}{l} \text{for displacements measured} \\ \text{at LVDT location} \end{array} \right)$$

where A is the area under the load displacement record in lb. in., c is the distance from the specimen centerline of loading to the LVDT centerline and b is the remaining ligament, or

$$b = W - a$$

where W is the specimen width and "a" is the crack length measured from the specimen centerline of loading.

(E) A plot of J versus crack extension was constructed (Figure 6-18c).

(F) The straight line  $J = 2\sigma_f \Delta a$  was constructed where  $\sigma_f$  is a flow stress equal to half the yield plus ultimate stresses. In addition, a best fit line was constructed through the J versus crack extension points (Figure 6-18d). The critical values of J (termed  $J_{Ic}$ ) is the J value which occurs at the intersection of these two lines. Therefore,  $J_{Ic}$  is based on crack initiation or zero crack growth due to actual material separation. Naturally, corresponding  $K_{Ic}$  values were calculated from the relationship between elastic plastic and linear elastic fracture mechanics parameters<sup>(2,8)</sup>

$$J_{Ic} = G_{Ic} = \frac{1-\nu^2}{E} K_{Ic}^2$$

where  $\nu$  is Poisson's ratio and E is Young's modulus.



J resistance curves relative to Inconel X750, both base metal, electron beam and gas tungsten arc welds, plus various manufacturing processes are illustrated in Figures 6-19 through 6-29. Also, J resistance curves for 310 S stainless steel (both base metal and shielded metal arc welds) plus Kromarc 58 stainless steel are shown in Figures 6-30 through 6-33, respectively. Finally, all the  $J_{Ic}$  and corresponding  $K_{Ic}$  values generated to date are presented in Table 6-7.

For comparison purposes, the ratios  $\frac{K_{Ic}}{\sigma_{ys}}$  and  $\left(\frac{K_{Ic}}{\sigma_{ys}}\right)^2$  have been included in Table 6-7. Typically, the material with the highest  $\frac{K_{Ic}}{\sigma_{ys}}$  ratio can be expected to be the most tough material for a given application.<sup>(9)</sup> Also, when conducting a parametric fracture mechanics analysis (that is, the applied stress is considered to be a fixed percentage of the particular material's yield strength) the critical defect size for failure in one cycle of loading will be proportional to the ratio of  $\left(\frac{K_{Ic}}{\sigma_{ys}}\right)^2$ .<sup>(9)</sup>

Concerning the various Inconel X750 base materials, obviously the air arc melted followed by vacuum arc remelted (AAM-VAR) Inconel X750 is extremely attractive, offering a very high fracture toughness in combination with intermediate yield strength. The non heat treated hot isostatic pressed Inconel X750 also has balanced properties, giving an attractive  $\frac{K_{Ic}}{\sigma_{ys}}$  ratio of slightly less than one. Even for the high strength vacuum induction melted (VIM) Inconel X750, good toughness is realized.

Obviously, both the Inconel X750 gas tungsten arc and electron beam welds provide a higher level of fracture toughness than the corresponding Inconel X750 base metal (VIM-VAR), especially when the particular weld was not given a post-weld heat treatment. Note, for example, the Inconel X750 gas tungsten arc welds (ST/W) yielded a very high ratio of fracture toughness to yield strength. Also, the fracture toughness of the Inconel X750 electron beam welds which were not post-weld heat treated was so high as to exceed the measurement capacity of the 0.5 inch thick compact tension specimens. That is, the proposed size requirement for J testing,<sup>(5)</sup> given by

$$a, B, b \geq 25 \left( \frac{J}{\sigma_{ys}} \right)$$



where B is the specimen thickness, could not be met by the non post-weld heat treated Inconel X750 electron beam weld test specimens. Therefore, from a fracture toughness as well as yield strength standpoint, the high quality Inconel X750 gas tungsten arc and electron beam welds will certainly not prove to be a weak point in a particular Inconel X750 structure or component from a fracture toughness point of view.

Again referring to Table 6-7, note the solution treated and water quenched Kromarc 58 stainless steel is also quite attractive, offering a high level of fracture toughness in combination with a substantial yield strength. In addition, the solution treated and water quenched 310 S stainless steel produced the very high level of fracture toughness expected from 300 series stainless steels in combination with its moderate yield strength. <sup>(10)</sup> Note, unlike the Inconel X750 gas tungsten arc and electron beam welds, the 310 S stainless steel shielded metal arc welds are not nearly as tough as the 310 S stainless steel base metal. This is due in part to the higher yield strength of the shielded metal arc welds. Recall, this actual yield strength level is unknown since all the 310 S stainless steel shielded metal arc weld tensile specimens fractured in the base metal, which is the yield strength value reported in Table 6-7. <sup>(1)</sup>

#### 6.4 Crack Growth Rate Results

Inconel X750 electron beam and gas tungsten arc weld crack growth rate test results are illustrated in Figures 6-34 thru 6-37, respectively. These fatigue crack growth rate tests were conducted in cryogenic environments on side notched half inch thick wedge open loading (WOL) specimens. These WOL specimens were side notched in an attempt to force the fatigue crack to propagate in the plane of the weld. All WOL specimens were precracked in air at alternating loads substantially less than those employed for actual crack growth rate tests.

Fatigue crack growth rate testing was conducted on a universal hydraulic fatigue machine under sinusoidal tension loading. The maximum alternating load ( $\Delta P$ ) was maintained constant throughout each individual test. Test frequency equalled 10 Hertz.

Instantaneous crack length in these cryogenic environments was determined by first measuring test specimen crack opening displacement by utilizing a linear variable differential transformer (LVDT) attached to the specimen front face and finally transforming this crack opening displacement value via specimen compliance into crack length. For illustration of the LVDT in position and the overall crack growth test setup, consult Reference 1. The LVDT had 0.100 in. total travel and was hermetically sealed. Linear output was guaranteed even at  $-452^{\circ}\text{F}$  ( $4.2^{\circ}\text{K}$ ) in a helium environment. Test specimen compliance was determined by utilizing a procedure originally developed by Novak and Rolfe.<sup>(11)</sup>

The raw test data of crack length ( $a$ ) versus number of elapsed cycles ( $N$ ) was subsequently translated into the crack growth rate ( $da/dN$ ) versus stress intensity factor range ( $\Delta K$ ) data required to conduct a fracture mechanics failure prevention analysis. These crack growth rates were established by means of a computerized curve-fitting analysis of the crack length versus number of elapsed cycles data obtained directly from the fatigue crack growth rate experiments.<sup>(12)</sup> The  $\Delta K$  value associated with a specific crack growth rate was determined from the following expression:

$$\Delta K = K_{\max} - K_{\min} = Y \frac{P_{\max} \sqrt{a}}{BW} - Y \frac{P_{\min} \sqrt{a}}{BW}$$

where  $P_{\max}$  and  $P_{\min}$  are the maximum and minimum values of the alternating load, respectively.

The nearly linear relationship between  $\log da/dN$  and  $\log \Delta K$  data shown in Figures 6-34 thru 6-37 is typical of most fatigue crack growth rate data. Since this linear relationship exists, the crack growth rate data can be expressed in terms of the generalized fatigue crack growth rate law developed by Paris.<sup>(13)</sup> This crack growth rate law is expressed as:

$$da/dN = C_0 \Delta K^n$$

where  $da/dN$  is the rate of crack growth,  $C_0$  is an intercept constant determined from the log  $da/dN$  versus log  $\Delta K$  plot,  $n$  is the slope of the log-log plot and  $\Delta K$  is the stress intensity factor range.

Note the upper scatterband which represents the crack growth rate properties of Inconel X750 base metal (VIM-VAR) is included in Figures 6-34 thru 6-37. In all cases, the fatigue crack growth rate data for Inconel X750 electron beam or gas tungsten arc welds falls on or below this base metal upper scatterband. Therefore, this Inconel X750 base metal upper scatterband, described by the crack growth rate expression

$$da/dN = 2.04 \times 10^{-18} \Delta K^{8.0} \quad (\text{inches/cycle, ksi}\sqrt{\text{in.}})$$

gives a conservative estimate of the fatigue crack growth rate properties of Inconel X750 electron beam and gas tungsten arc welds. For the case of the non post-weld heat treated Inconel X750 electron beam welds, the cracks propagated out of the electron beam weld into the base metal despite the fact that the test specimens were side notched. This again indicates that the cracks prefer to propagate in the base metal as opposed to the weld. Therefore, electron beam or gas tungsten arc welds have inherent reasonable toughness and resistance to crack propagation. Recognizing that the Inconel X750 MP-1 base metal (VIM-VAR) was not optimized structurally, one should realize that in high toughness base metal such as Inconel X750 MP-2 (AAM-VAR) crack propagation could proceed in the base metal.

#### 6.5 Design Example, Estimating Cyclic Life of a Superconducting Generator Rotor

In order to demonstrate the use of fracture mechanics concepts as they apply to a structure subjected to a superconducting environment, a hypothetical problem involving a superconducting generator rotor is

presented below. The major concern will be to determine the cyclic life of the superconducting generator rotor under normal operating conditions.

Successful use of fracture mechanics technology as a tool for design against failure requires basic information in three areas of concern: material properties, defect characterization and stress analysis. Regarding material properties, the pertinent material properties (fracture toughness and fatigue crack growth rate data) required for our calculations are presented in Section 6 of this technical report. Observing Table 6-7, note the solution treated and double aged vacuum induction melted/vacuum arc remelted (VIM-VAR) Inconel X750 produced the lowest ratio of fracture toughness to yield strength of any manufacturing process/heat treatment combination of Inconel X750 that was investigated. Therefore, to keep the failure analysis as conservative as possible, the fracture toughness and fatigue crack growth rate material properties developed for this material at  $-452^{\circ}\text{F}$  ( $4.2^{\circ}\text{K}$ ) will be utilized in this analysis.

An adequate fracture mechanics failure prevention analysis requires information concerning the size, shape, location and orientation of the most critical defects which exist or are likely to be developed in the structure of concern. This example assumes that the most critical defect for the application is a long-shallow surface crack intersecting the axial bore or inside diameter of the Inconel X750 superconducting generator rotor with the major plane of the crack normal to the tangential bore stresses. For this example, surface flaws with length to depth ratios of 4:1 and 10:1 were considered. These surface defect geometries span the range of typical surface defects which might be encountered in a generator rotor.

The pertinent nominal stress information required for a fracture mechanics analysis of a structure subjected to cyclic loading includes knowledge of the maximum nominal applied stresses developed in the structure as well as the alternating stresses. For this example problem, the applied nominal stresses and alternating (cyclic) stresses were assigned parametric values equivalent to a specific percentage of the

material's yield strength. The applied nominal and alternating stress to yield stress ratios ( $\frac{\sigma}{\sigma_{ys}}$ ) considered in this analysis equaled 0.25, 0.50 and 0.75.

The first step in the cyclic life calculations is to determine the critical flaw size necessary to cause failure as a result of a single load application. The 0.2 percent yield strength and  $K_{Ic}$  fracture toughness of solution treated and double aged Inconel X750 (VIM-VAR) at  $-452^{\circ}\text{F}$  ( $4.2^{\circ}\text{K}$ ) equals 125.7 ksi and  $70 \text{ ksi}\sqrt{\text{in}}$ , respectively (see Table 6-7).

The pertinent stress intensity expression for this configuration (a surface crack oriented with the major plane of the crack perpendicular to a uniform tension stress field) is

$$K_I^2 = \frac{1.21 a \pi \sigma^2}{Q}$$

where  $K_I$  = nominal stress intensity factor,  $\text{ksi}\sqrt{\text{in}}$ .

$a$  = surface crack depth, in.

$\sigma$  = applied nominal stress, ksi

$Q$  = flaw shape parameter (from Fig. 6-38)

The flaw shape parameter ( $Q$ ) permits us to evaluate the severity of defects with different shapes by accounting for surface or internal defects with various length to depth ratios. The flaw shape parameter  $Q$  is obtained from Fig. 6-38 which also illustrates prototype surface and internal defects and the necessary dimensions required for obtaining length to depth ratios. As mentioned previously, we will consider surface defects with two length to depth ( $\frac{2C}{a}$ ) ratios; 4 to 1 and 10 to 1.

We now have all the information required to calculate the critical flaw sizes necessary to cause failure of the Inconel X750 superconducting generator rotor in one cycle of loading. If we rearrange the terms in the previous equation and set  $K_I$  equal to  $K_{Ic}$  and " $a$ "

equal to the critical flaw size,  $a_{cr}$ , we obtain the following critical flaw size expression

$$a_{cr} = \frac{K_{Ic}^2 Q}{1.21 \pi \sigma^2}$$

Substituting the appropriate values of  $\sigma$ ,  $Q$  and  $K_{Ic}$  (70 ksi $\sqrt{\text{in}}$ ) into the above expression yields the critical flaw sizes presented in Table 6-8 for our three applied stress levels and two surface defect geometries.

Once the critical flaw sizes are known, the cyclic life considerations involve computing the number of loading cycles required for an existing flaw of some subcritical size to grow to the critical size. Recall, this Inconel X750 superconducting generator rotor is subjected to a -452°F (4.2°K) helium environment. Therefore, the fatigue crack growth rate properties previously developed on this Inconel X750 in a helium environment (see Table 6-7) will be utilized in the cyclic life calculations.<sup>(1)</sup> These crack growth rate properties can be represented analytically by the generalized crack growth rate law expressed as

$$\frac{da}{dN} = 2.04 \times 10^{-18} \Delta K^{8.0} \quad (\text{in/cycle, ksi}\sqrt{\text{in}})$$

where  $\frac{da}{dN}$  is the rate of crack growth,  $\Delta K$  is the stress intensity factor range,  $2.04 \times 10^{-18}$  represents the empirical intercept constant ( $C_0$ ) and 8.0 denotes the slope ( $n$ ) of the  $\log \frac{da}{dN}$  versus  $\log \Delta K$  curve.

By combining these crack growth rate properties with our critical defect sizes, it is now possible to compute the number of elapsed cycles required for an existing subcritical flaw to grow to failure. Wilson has developed a generalized cyclic life expression which readily

determines the number of cycles required for an existing defect to grow to the critical flaw size.<sup>(9)</sup> This expression is presented below:

$$N = \frac{2}{(n-2) Co M^{n/2} \Delta \sigma^n} \left[ \frac{1}{a_i^{(n-2)/2}} - \frac{1}{a_{cr}^{(n-2)/2}} \right] \text{ for } n \neq 2$$

$$N = \frac{1}{Co M \Delta \sigma^2} \ln \frac{a_{cr}}{a_i} \text{ for } n = 2$$

where N = number of cycles to failure

n = slope of the  $\log \frac{da}{dN}$  versus  $\log \Delta K$  curve

Co = intercept constant from  $\log \frac{da}{dN}$  versus  $\log \Delta K$  curve

$a_i$  = initial flaw size

$a_{cr}$  = critical flaw size

$\Delta \sigma$  = alternating stress range

M = flaw shape and geometry paramter (for surface defects,

$$M = \frac{1.21 \pi}{Q})$$

The above expression is applicable to those loading situations where the relationship between applied load, flaw size and stress intensity factor has the form of  $K_I = \sigma \sqrt{Ma}$ . In addition, it is assumed that the cyclic stress range ( $\Delta \sigma$ ) remains constant throughout the component life and that the mean stress does not influence the results.

Solving this expression for N at the various cyclic stress ranges of interest and for  $a_i$  values ranging from the minimum detectable flaw size to the appropriate critical flaw size develops cyclic life curves which relate the maximum initial allowable flaw size to the number of cycles required to cause failure at different stress levels.

The resulting cyclic life curves for this problem are presented in Figs. 6-39 and 6-40. These cyclic life curves represent the most convenient form of presenting fatigue life information for a specific application because the total life can readily be determined from a

knowledge of the defect size known or assumed to be present at the start of life. From these results it is possible to establish quantitative material acceptance and inspection requirements as well as realistic safety factors for various practical situations where a given life and safety factor are desired.

As an example, if we assume a desired life of 14,600 cycles (one start-up shut-down cycle per day for forty years), we obtain the following initial allowable flaw sizes.

<u>Surface Flaw Length To Depth Ratio</u>	$\frac{\sigma}{\sigma_{ys}}$	<u>Applied Stress Level (ksi)</u>	<u>Initial Allow. Flaw Size (in.)</u>	
			<u>Depth</u>	<u>Length</u>
4 to 1	0.25	31.425	0.61	2.44
4 to 1	0.50	62.85	0.09	0.36
4 to 1	0.75	94.275	0.03	0.12
10 to 1	0.25	31.425	0.42	4.20
10 to 1	0.50	62.85	0.06	0.60
10 to 1	0.75	94.275	0.02	0.20

These are the initial allowable flaw sizes which will grow to the critical sizes of concern in 14,600 cycles when the Inconel X750 superconducting generator rotor is subjected to either of the three corresponding applied stress levels. Obviously, the inspection techniques employed must accordingly be capable of locating and defining some smaller defect, the exact size of which depends on the safety factors desired. Therefore, it is up to the designer to input whatever safety factors (margins of error) he desires for a specific application.

The example problem described above illustrates how a designer can employ the fracture mechanics technology to quantitatively evaluate the trades-off between material properties, stresses and inspection capabilities. Appropriate safety factors can then be assigned to the specific area where the greatest uncertainties in input information



exist; be it in stress analysis, nondestructive inspection capability or materials properties. In essence this approach enables the designer working in close conjunction with materials, welding, manufacturing and nondestructive inspection engineers to tailor the design, materials choice, welding process, quality control and nondestructive inspection requirements to provide the specific degree of immunity from failure that is desired in the product at a minimum cost (most efficient design, effective use of materials, efficient welding and fabrication methods, and the proper degree of quality control and inspection).

The same basic approach as described above can be applied to any given region in any given cryogenic hardware component. As in any engineering approach, appropriate judgment must be applied in selecting the specific locations or components which will be analyzed; i.e., regions of highest stresses, regions of poorest inspection capability, areas where defects are most likely to exist (welds), components subject to most cyclic loading, etc. With appropriate information in the 3 basic areas of information (stresses, material properties and defects) and with the appropriate selection of a K expression modeling the cracked-body geometry of concern, this approach provides a powerful new tool for quantitatively assuring the desired degree of structural reliability in cryogenic hardware. As obvious, the major effort in this contract is directed at providing the material property information that is required to employ this new systems type engineering approach to designing and building reliable cryogenic machinery.

## REFERENCES - SECTION 6

1. G. G. Lessmann, W. A. Logsdon, R. Kossowsky, M. P. Mathur and J. M. Wells, "Structural Materials for Cryogenic Applications, First Semi-annual Progress Report," Westinghouse Research Report 74-9D4-CRYMT-R1, March 1974.
2. J. A. Begley and J. D. Landes, "The J Integral as a Fracture Criterion," Fracture Toughness, Proceedings of the 1971 National Symposium on Fracture Mechanics, Part II, ASTM STP 514, American Society for Testing and Materials, 1972, pp. 1-20.
3. J. D. Landes and J. A. Begley, "The Effect of Specimen Geometry on  $J_{Ic}$ ," Fracture Toughness, Proceedings of the 1971 National Symposium on Fracture Mechanics, Part II, ASTM STP 514, American Society for Testing and Materials, 1972, pp. 24-39
4. J. R. Rice, "A Path Independent Integral and the Approximate Analysis of Strain Concentration by Notches and Cracks," Journal of Applied Mechanics, Transactions of the American Society of Mechanical Engineers, Vol. 35, Ser. E, June 1968, pp. 379-386.
5. J. D. Landes and J. A. Begley, Test Results from J Integral Studies--An Attempt to Establish a  $J_{Ic}$  Testing Procedure, Presented at the Seventh National Symposium on Fracture Mechanics, College Park, Maryland, August 1973.
6. W. A. Logsdon, "Elastic Plastic ( $J_{Ic}$ ) Fracture Toughness Values: Their Experimental Determination and Comparison with Conventional Linear Elastic ( $K_{Ic}$ ) Fracture Toughness Values for Five Materials," Presented at the Eighth National Symposium on Fracture Mechanics, Brown University, Providence, Rhode Island, August 1974.

7. J. R. Rice, P. C. Paris and J. G. Merkle, "Some Further Results of J-Integral Analysis and Estimates," Progress in Flaw Growth and Fracture Toughness Testing, ASTM STP 536, American Society for Testing and Materials, 1973, pp. 231-245.
8. J. A. Begley, J. D. Landes and E. T. Wessel, Fracture Mechanics, A Practical Tool for Preventing Failures, Presented at the Third International Conference on Fracture, Munich, Germany, April 1973.
9. E. T. Wessel, W. G. Clark and W. K. Wilson, "Engineering Methods for the Design and Selection of Materials Against Fracture," U.S. Army Tank-Automotive Center Report AD No. 801005, June 1966.
10. J. A. Begley, Unpublished research, Westinghouse Research Laboratories, September 1974.
11. S. R. Novak and S. T. Rolfe, "Modified WOL Specimen for  $K_{Isc}$  Environmental Testing," Journal of Materials, JMLSA, Vol. 4, No. 3, September 1969, pp. 701-728.
12. A. J. Federowicz and B. A. Powell, "A Computer Program to Obtain a Min-Max Regression Model by Linear Programming," Unpublished Westinghouse Research data.
13. P. C. Paris, "The Fracture Mechanics Approach to Fatigue," Proc. Tenth Sagamore Army Materials Research Conference, August 1963, Syracuse University Press, 1964.

TABLE 6-1 - TENSILE AND NOTCHED TENSILE PROPERTIES OF INCONEL X750 AT 75°F (297°K)

Material	M.P. No.	Manu. Process	Material Condition	Heat Treatment	Temperature = 75°F (297°K)					Comments
					Yield Strength (ksi)	Ultimate Strength (ksi)	Reduction in Area (%)	Elongation (%)	Notched Tensile Strength (ksi)	
INCONEL X750	1	VIM-VAR	BASE	ST	96.2	143.2	18.2	17.6	174.2	1.7
INCONEL X750	1	VIM-VAR	BASE	STDA	119.5	159.2	12.4	12.2	200.5	1.8
INCONEL X750	1	VIM-VAR	GTAW	ST/W	91.0	121.6	27.0	13.3	159.2	1.8
INCONEL X750	1	VIM-VAR	GTAW	STDA/W	94.1	121.9	27.0	8.2	170.0	1.8
INCONEL X750	1	VIM-VAR	GTAW	ST/W/STDA	124.2	159.0	11.9	9.0	227.8	1.8
INCONEL X750	1	VIM-VAR	EBW	ST/W	80.0	112.0	30.8	8.0	146.3	1.8
INCONEL X750	1	VIM-VAR	EBW	STDA/W	86.2	117.0	30.3	3.2	155.2	1.8
INCONEL X750	1	VIM-VAR	EBW	ST/W/STDA	122.1	157.9	10.3	10.0	217.0	1.8
INCONEL X750	2	AAM-VAR	BASE	STDA	123.0	182.0	38.5	26.7	223.8	1.8
INCONEL X750	3	VIM	BASE	STDA	133.1	191.1	27.7	23.8	244.8	1.8
INCONEL X750	-	HIP	BASE	--	107.8	169.7	38.7	34.9	200.0	1.9
INCONEL X750	-	HIP	BASE	STDA	134.9	193.8	18.0	23.2	232.3	1.7

Each Specimen Fractured in the Base Metal or Heat Affected Zone

TABLE 6-2 - TENSILE AND NOTCHED TENSILE PROPERTIES OF INCONEL X750 AT -320°F (77°K)

Temperature = -320°F (77°K)											
Material	M.P. No.	Manu. Process	Material Condition	Heat Treatment	Yield	Ultimate	Reduction	Elongation	Notched Tensile	NTS oys	Comments
					Strength (ksi)	Strength (ksi)	in Area (%)	(%)	Strength (ksi)		
INCONEL X750	1	VIM-VAR	BASE	ST	111.6	157.5	13.8	15.6	194.7	1.6	Each Specimen Fractured in the Base Metal or Heat Affected Zone
INCONEL X750	1	VIM-VAR	BASE	STDA	129.4	165.4	8.6	9.2	204.2	1.7	
INCONEL X750	1	VIM-VAR	GTAW	ST/W	104.0	143.2	22.0	13.6	202.5	1.9	
INCONEL X750	1	VIM-VAR	GTAW	STDA/W	116.1	140.5	17.0	5.5	208.0	1.8	
INCONEL X750	1	VIM-VAR	GTAW	ST/W/STDA	135.0	160.8	9.2	5.6	248.0	1.8	
INCONEL X750	1	VIM-VAR	EBW	ST/W	98.2	137.5	25.0	11.8	178.0	1.8	
INCONEL X750	1	VIM-VAR	EBW	STDA/W	109.0	133.5	11.4	2.6	191.5	1.6	
INCONEL X750	1	VIM-VAR	EBW	ST/W/STDA	131.0	156.9	8.7	6.4	236.9	1.8	
INCONEL X750	2	AAM-VAR	BASE	STDA	133.3	212.4	29.0	32.4	241.9	1.8	
INCONEL X750	3	VIM	BASE	STDA	164.8	232.5	20.8	26.2	254.2	1.5	
INCONEL X750	-	HIP	BASE	--	124.1	203.9	24.2	29.3	222.4	1.3	
INCONEL X750	-	HIP	BASE	STDA	147.3	212.4	13.9	17.5	246.8	1.7	

TABLE 6-3 - TENSILE AND NOTCHED TENSILE PROPERTIES OF INCONEL X750 AT -452°F (4.2°K)

Temperature = -452°F (4°K)											
Material	M.P. No.	Manu. Process	Material Condition	Heat Treatment	Yield Strength (ksi)	Ultimate Strength (ksi)	Reduction in Area (%)	Elongation (%)	Notched Tensile Strength (ksi)	NTS gys	Comments
INCONEL X750	1	VIM-VAR	BASE	ST	106.8	147.7	12.9	14.1	204.6	1.9	Each Specimen Fractured in the Base Metal or Heat Affected Zone
INCONEL X750	1	VIM-VAR	BASE	STDA	125.7	152.5	6.2	6.1	214.7	1.7	
INCONEL X750	1	VIM-VAR	GTAW	ST/W	108.8	145.5	17.1	12.7	214.0	2.0	
INCONEL X750	1	VIM-VAR	GTAW	STDA/W	125.0	144.0	14.5	4.8	215.4	1.7	
INCONEL X750	1	VIM-VAR	GTAW	ST/W/STDA	139.0	163.0	8.7	5.5	236.2	1.7	
INCONEL X750	1	VIM-VAR	EBW	ST/W	106.0	140.1	19.6	11.6	193.9	1.8	
INCONEL X750	1	VIM-VAR	EBW	STDA/W	111.8	135.8	10.3	3.0	203.5	1.8	
INCONEL X750	1	VIM-VAR	EBW	ST/W/STDA	132.5	154.1	8.7	7.1	244.2	1.8	
INCONEL X750	2	AAM-VAR	BASE	STDA	141.3	228.7	26.8	27.2	256.1	1.8	
INCONEL X750	3	VIM	BASE	STDA	173.2	254.0	19.4	27.1	257.2	1.5	
INCONEL X750	-	HIP	BASE	--	130.1	215.5	22.9	30.5	233.6	1.8	
INCONEL X750	-	HIP	BASE	STDA	150.5	221.3	13.3	18.8	246.2	1.6	

TABLE 6-4 - TENSILE AND NOTCHED TENSILE PROPERTIES OF OFHC COPPER PLUS 310 S AND  
KROMARC 58 STAINLESS STEELS AT 75°F (297°K)

Temperature = 75°F (297°K)											
Material	N.P. No.	Manu. Process	Material Condition	Heat Treatment	Yield Strength (ksi)	Ultimate Strength (ksi)	Reduction in Area (%)	Elongation (%)	Notched Tensile		Comments
									Strength (ksi)	NTS avg	
OFHC COPPER			BASE		8.3	29.6	81.8	66.7	41.3	5.0	
OFHC COPPER			BASE	SR	8.0	29.5	81.8	60.2	41.8	5.2	
OFHC COPPER			GMAW		7.5	30.0	84.8	55.6	43.0	5.7	Specimens Fractured in Base Metal
AISI 310 S			BASE	STQ	37.9	84.8	70.7	53.8	115.8	3.1	
AISI 310 S			BASE	STFC	32.8	83.8	62.2	57.2	110.6	3.4	
AISI 310 S			SMAW	STQ/W	48.5	84.4	76.5	40.3	122.0	2.5	Specimens Fractured in Base Metal
KROMARC 58			BASE	STQ	53.8	101.7	66.8	45.8	134.6	2.5	
KROMARC 58			BASE	CW	137.3	142.2	50.4	13.9	223.5	1.6	
KROMARC 58			GTAW	STQ/W	72.3	132.8	60.8	35.9	167.3	2.3	Specimens Fractured in Base Metal
KROMARC 58			CW/GTAW		120.1	138.8	57.6	12.9	160.7	1.3	Specimens Fractured in the Weld or Heat Affected Zone
KROMARC 58			GTAW/CW		165.0	177.4	43.6	8.0	224.4	1.4	

TABLE 6-5 - TENSILE AND NOTCHED TENSILE PROPERTIES OF OFHC COPPER PLUS 310 S AND  
KROMARC 58 STAINLESS STEELS AT -320°F (77°K)

Temperature = -320°F (77°K)													
Material	M.P. No.	Manu. Process	Material Condition	Heat Treatment	Yield		Ultimate		Reduction		Notched Tensile		Comments
					Strength (ksi)	Strength (ksi)	Strength (ksi)	Strength (ksi)	in Area (%)	in Area (%)	Elongation (%)	Strength (ksi)	
OFHC COPPER			BASE		9.6	47.3	76.4	71.5	59.1	6.2			
OFHC COPPER			BASE	SR	9.4	47.0	82.8	75.5	64.4	6.9			
OFHC COPPER			GMAW		8.6	48.0	83.5	67.0	54.8	6.4			Specimens Fractured in Base Metal
AISI 310 S			BASE	STQ	87.6	159.2	51.6	71.8	196.5	2.2			
AISI 310 S			BASE	STFC	83.2	150.0	31.2	48.6	173.8	2.1			
AISI 310 S			SMAW	STQ/W	96.6	154.6	67.2	46.5	207.1	2.1			Specimens Fractured in Base Metal
KROMARC 58			BASE	STQ	114.3	188.1	58.2	49.8	228.9	2.0			
KROMARC 58			BASE	CW	186.8	220.4	49.7	37.0	308.4	1.6			
KROMARC 58			GTAW	STQ/W	123.6	191.6	41.4	45.6	276.8	2.2			Specimens Fractured in the Weld or Heat Affected Zone
KROMARC 58			CW/GTAW		161.2	189.0	45.7	12.6	278.3	1.7			
KROMARC 58			GTAW/CW		182.8	213.8	37.6	17.5	321.4	1.8			



TABLE 6-6 - TENSILE AND NOTCHED TENSILE PROPERTIES OF OFHC COPPER, 310 S AND  
KROMARC 58 STAINLESS STEELS AT -452°F (4.2°K)

Temperature = -452°F (4.2°K)											
Material	M.P. No.	Manu. Process	Material Condition	Heat Treatment	Yield		Reduction in Area (%)	Elongation (%)	Notched Tensile		Comments
					Strength (ksi)	Strength (ksi)			Strength (ksi)	NTS Oys	
OFHC COPPER			BASE		10.2	56.1	78.3	97.5	71.4	7.0	
OFHC COPPER			BASE	SR	9.2	56.0	79.6	100.5	67.7	7.4	
OFHC COPPER			GMAW		8.8	55.1	83.4	81.8	58.2	6.6	Specimens Fractured in Base Metal
AISI 310 S			BASE	STQ	118.5	189.0	44.6	64.3	231.8	2.0	
AISI 310 S			BASE	STFC	118.5	188.5	43.6	61.0	213.5	1.8	
AISI 310 S			SMAW	STQ/W	120.2	159.8	24.2	26.4	242.5	2.0	Specimens Fractured in Base Metal
KROMARC 58			BASE	STQ	158.7	192.2	55.0	42.0	272.3	1.7	
KROMARC 58			BASE	CW	213.4	220.7	46.0	23.8	356.2	1.7	
KROMARC 58			GTAW	STQ/W	153.8	208.6	40.6	33.4	315.2	2.0	Specimens Fractured in the Weld or Heat Affected Zone.
KROMARC 58			CW/GTAW		184.1	205.3	42.7	11.4	311.7	1.7	
KROMARC 58			GTAW/CW		201.4	227.9	33.9	13.4	343.2	1.7	

TABLE 6-7 - FRACTURE TOUGHNESS AND FATIGUE CRACK GROWTH RATE PROPERTIES OF  
INCONEL X750 AND 310 S PLUS KROMARC 58 STAINLESS STEELS.

Material	M.P. No.	Manu. Process	Matl. Cond.	Heat Treatment	Test Temp. (°F)	Yield Strength (ksi)	$J_{Ic}$ ( $\frac{lb}{in}$ )	$K_{Ic}$ ksi $\sqrt{in}$	$\frac{K_{Ic}}{\sigma_{ys}}$	$\frac{K_{Ic}}{\sigma_{ys}}^2$	n	Co
INCONEL X750	1	VIM-VAR	BASE	ST	-452	106.8	245	92.2	0.86	0.75	8.0	$2.04 \times 10^{-18}$
INCONEL X750	1	VIM-VAR	BASE	ST	75	96.2	320	103.6	1.08	1.16	7.0	$4.83 \times 10^{-16}$
INCONEL X750	1	VIM-VAR	BASE	STDA	-452	125.7	138	69.2	0.55	0.30	8.0	$2.04 \times 10^{-18}$
INCONEL X750	1	VIM-VAR	GTAW	ST/W	-452	108.8	875	174.3	1.60	2.57	8.0	$2.04 \times 10^{-18}$
INCONEL X750	1	VIM-VAR	GTAW	STDA/W	-452	125.0	690	154.8	1.24	1.53	8.0	$2.04 \times 10^{-18}$
INCONEL X750	1	VIM-VAR	GTAW	ST/W/STDA	-452	139.0	425	121.5	0.87	0.76	8.0	$2.04 \times 10^{-18}$
INCONEL X750	1	VIM-VAR	EBW*	ST/W	-452	106.0	>1696	>242.7	>2.29	>5.20	8.0	$2.04 \times 10^{-18}$
INCONEL X750	1	VIM-VAR	EBW*	STDA/W	-452	111.8	>1789	>249.2	>2.23	>4.97	8.0	$2.04 \times 10^{-18}$
INCONEL X750	1	VIM-VAR	EBW	ST/W/STDA	-452	132.5	738	160.1	1.21	1.46	8.0	$2.04 \times 10^{-18}$
INCONEL X750	2	AAM-VAR	BASE	STDA	-452	141.3	1350	216.0	1.53	2.34		
INCONEL X750	3	VIM	BASE	STDA	-452	173.2	500	131.5	0.76	0.58		
INCONEL X750	-	H.I.P.	BASE	----	-452	130.1	465	126.8	0.97	0.95		
INCONEL X750	-	H.I.P.	BASE	STDA	-452	150.5	233	89.7	0.60	0.36		
AISI 310 S			BASE	STQ	-452	118.5	1600	236.3	1.99	3.98	4.85	$1.29 \times 10^{-13}$
AISI 310 S			SMAW	ST/W	-452	120.2	325	106.5	0.89	0.79		
KROMARC 58			BASE	STQ	-452	158.7	1250	195.4	1.23	1.52		
KROMARC 58			BASE	30% CW	-452	213.4	388	108.8	0.51	0.26		

\* Toughness exceeds the measurement capacity of 1/2 TCT specimens. That is, the dimensional parameter of the 1/2 TCT specimens could not meet the size requirement necessary for a valid J test:  $a, B, b \geq 25 \left( \frac{J}{\sigma_{ys}} \right)$ .

TABLE 6-8 - CRITICAL FLAW SIZES FOR INCONEL X750  
SUPERCONDUCTING GENERATOR ROTOR

Surface Flaw Length to Depth Ratio	$\frac{\sigma}{\sigma_{ys}}$	Applied Stress Level (ksi)	Critical Flaw Sizes (in.)	
			Depth	Length
4 to 1	0.25	31.425	1.867	7.468
4 to 1	0.50	62.85	0.454	1.816
4 to 1	0.75	94.275	0.194	0.776
10 to 1	0.25	31.425	1.397	13.97
10 to 1	0.50	62.85	0.339	3.39
10 to 1	0.75	94.275	0.145	1.45

Solution Treated and Double Aged

Yield Strength (-452°F) = 125.7 ksi

Fracture Toughness (-452°F) = 70 ksi $\sqrt{\text{in.}}$

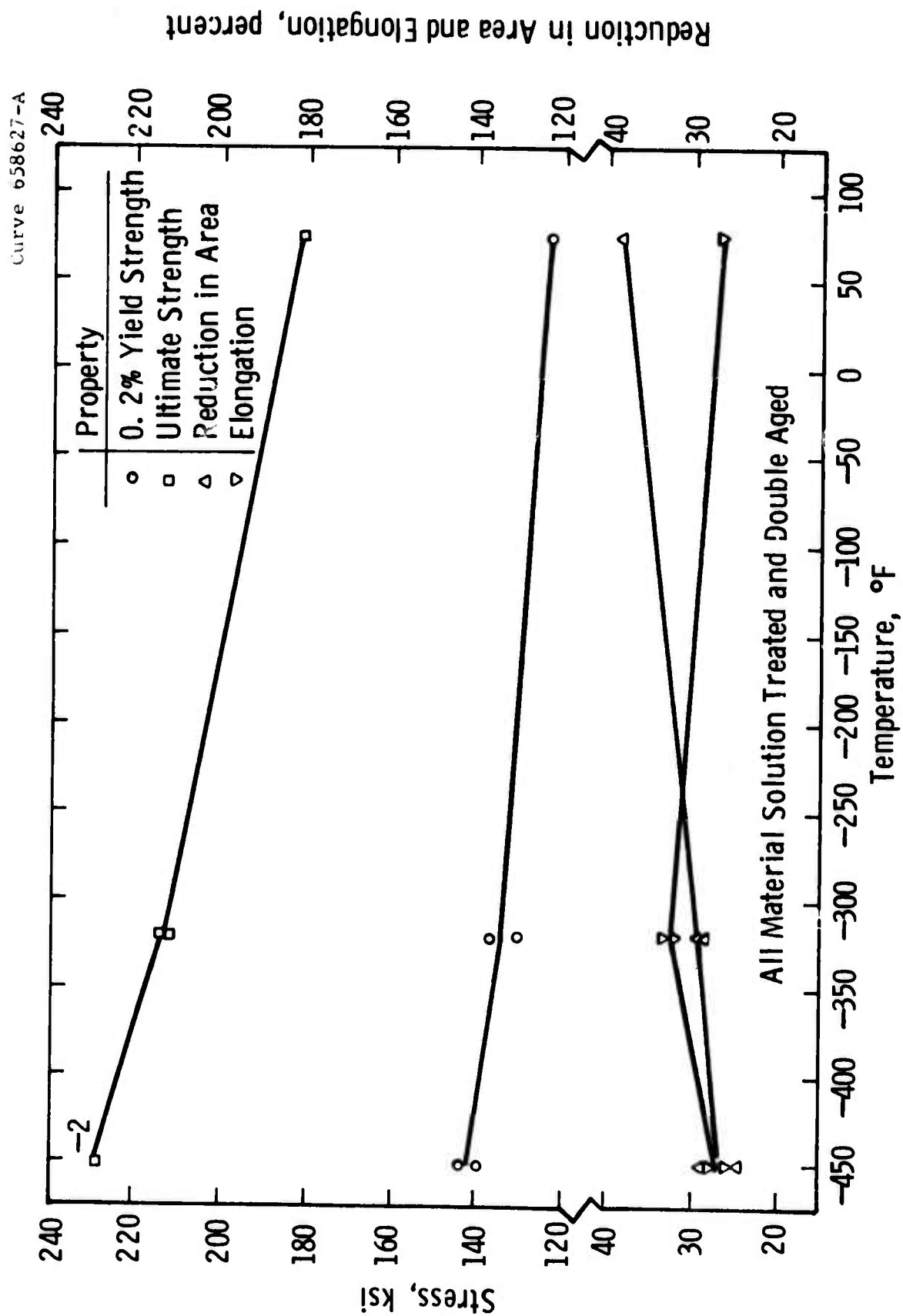


Fig.6-1 -Tensile properties of Inconel X750 ( AAM-VAR)

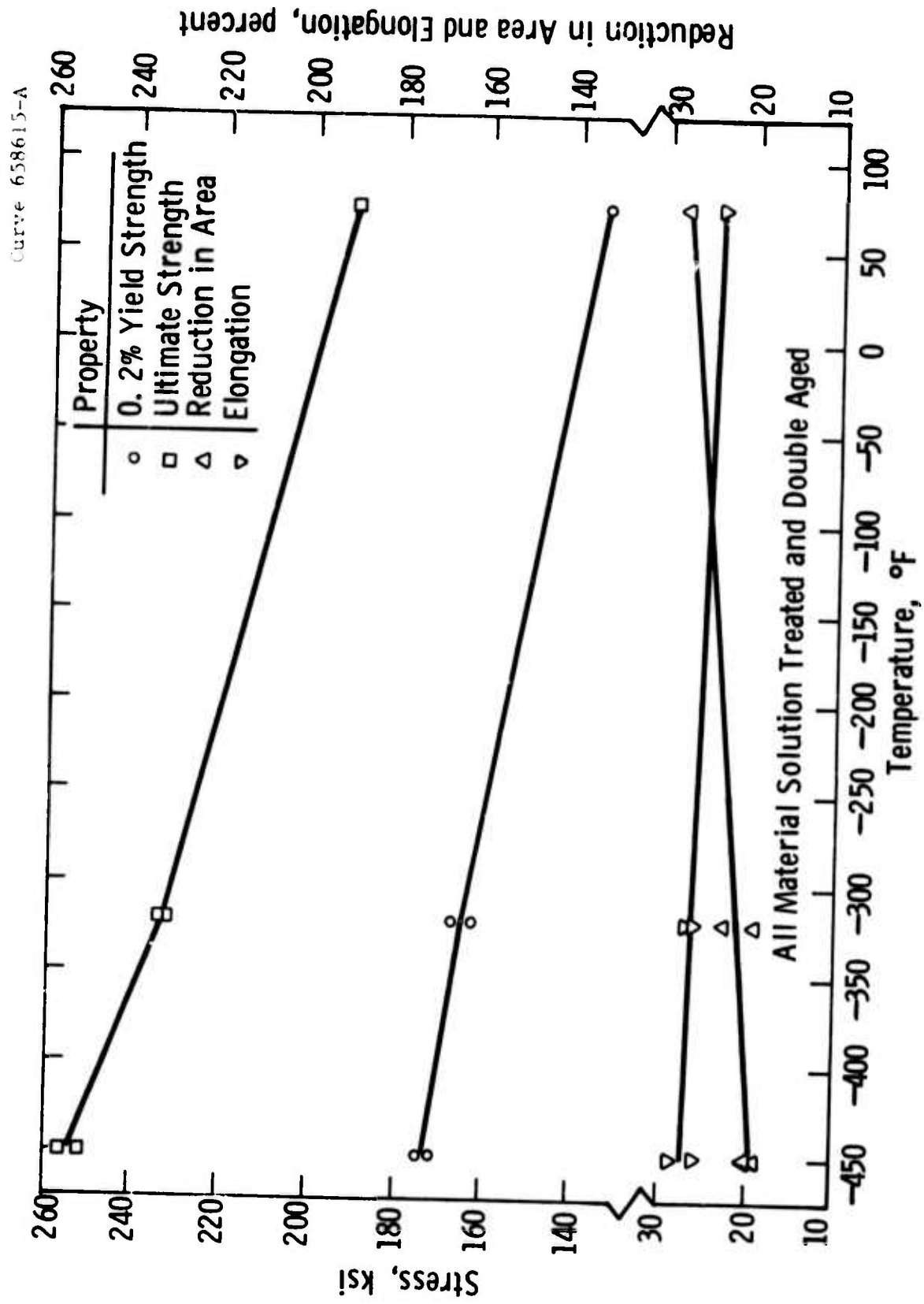


Fig. 6-2 - Tensile properties of Inconel X750 (VIM)

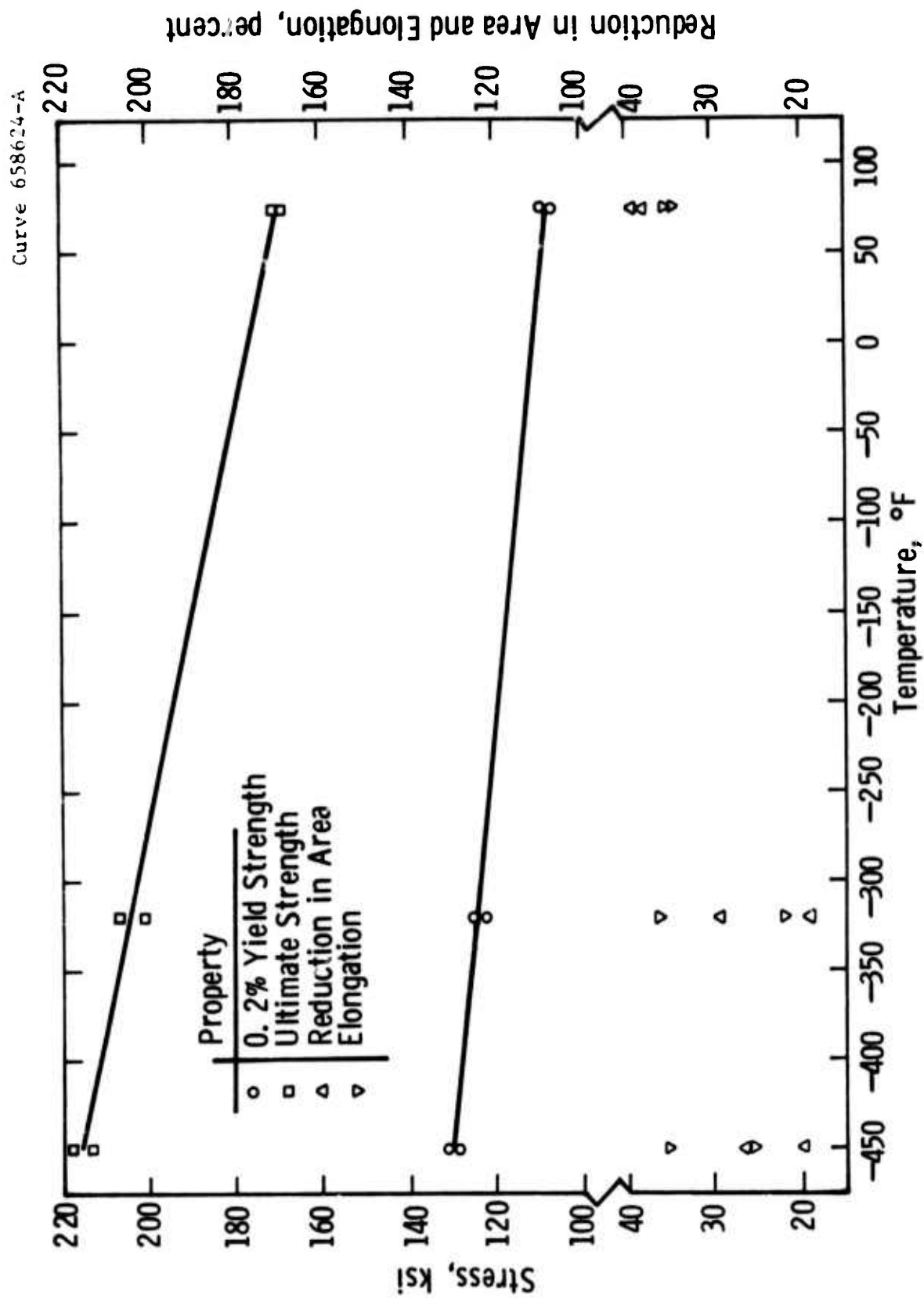


Fig. 6-3—Tensile properties of hot isostatic pressed Inconel X750

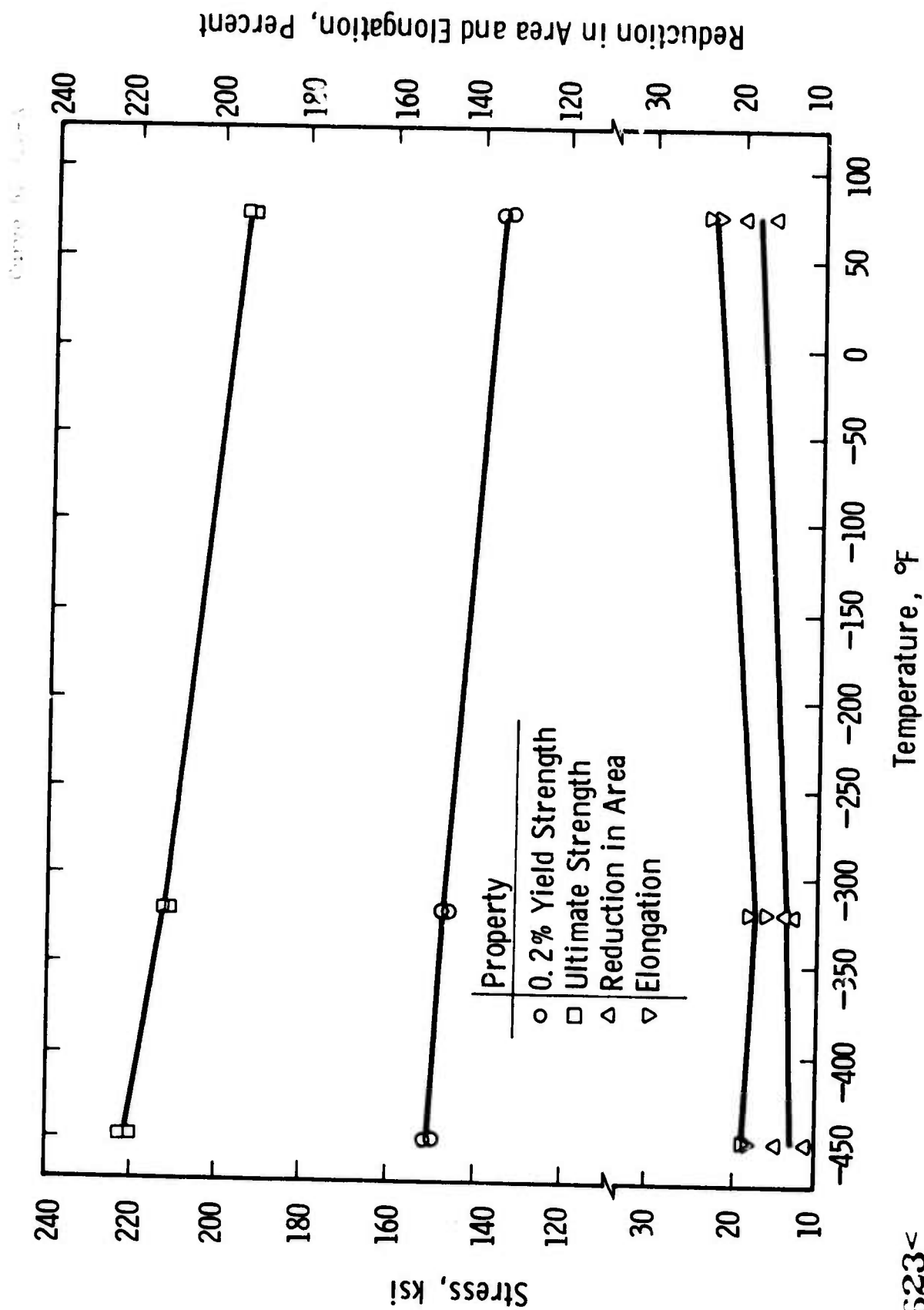


Fig.6-4—Tensile properties of solution treated and double aged hot isostatic pressed Inconel X750

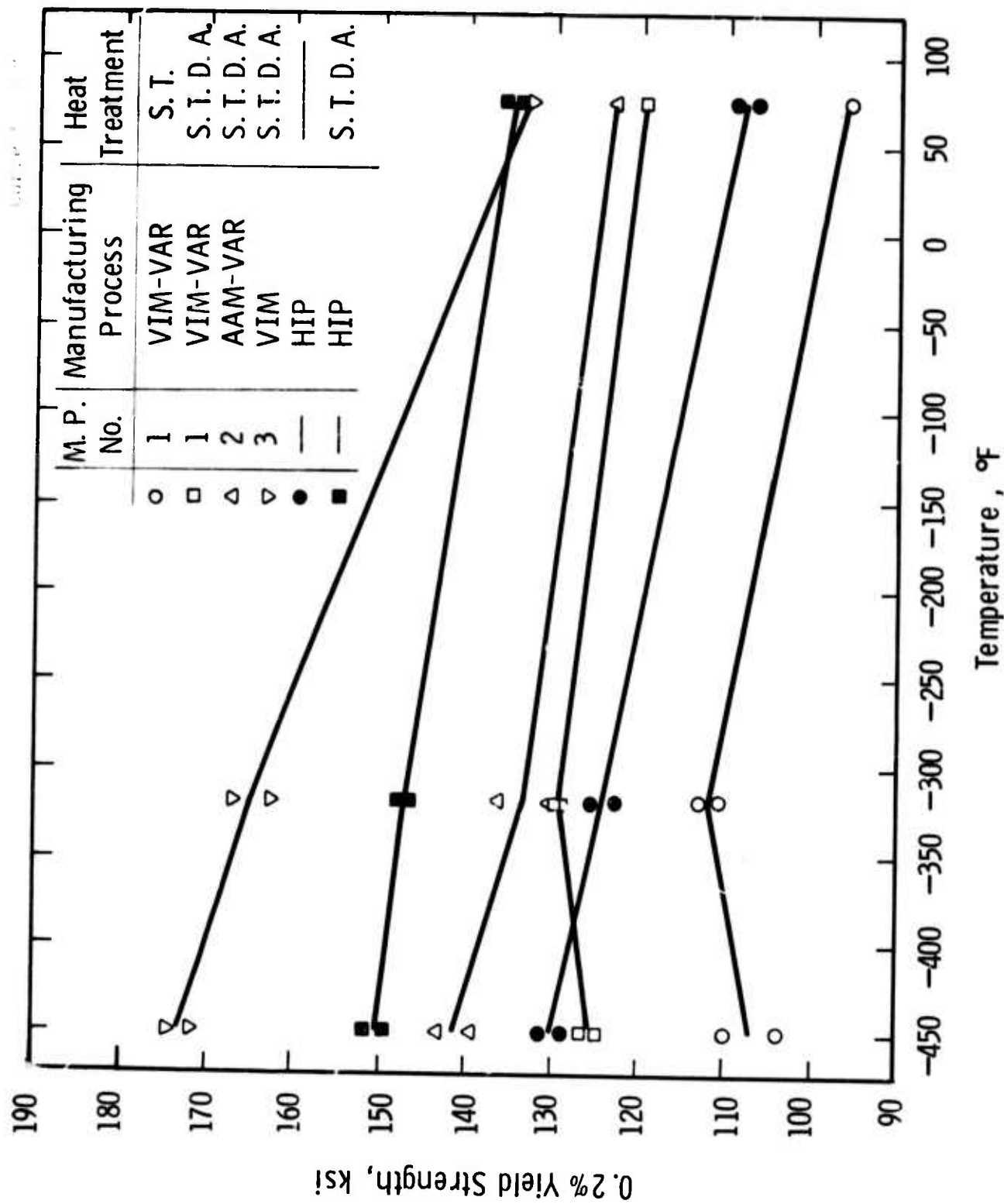


Fig.6-5-0. 2% yield strengths of Inconel X750, various manufacturing processes



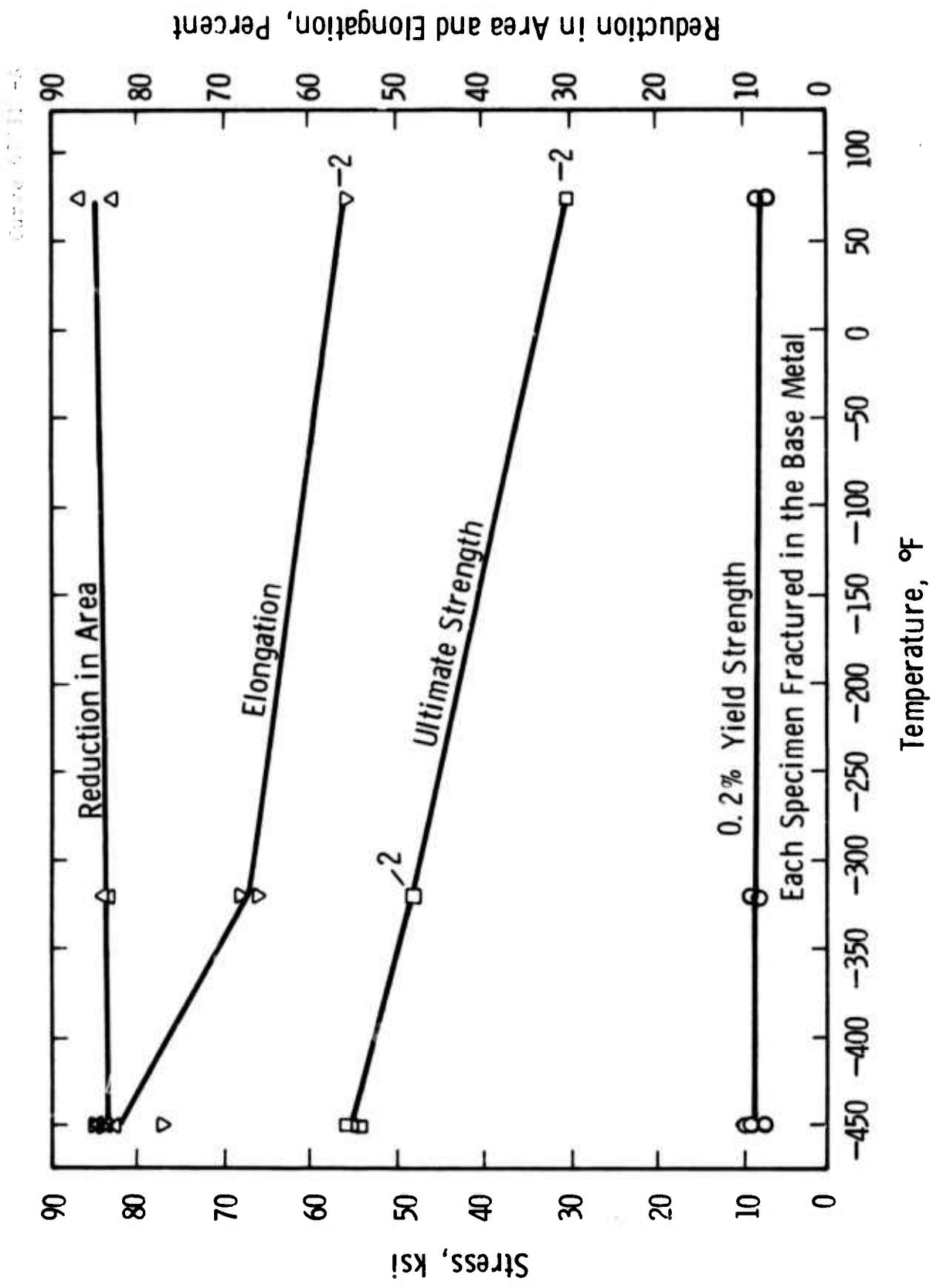


Fig.6-6-Tensile properties of OFHC copper gas metal arc welds

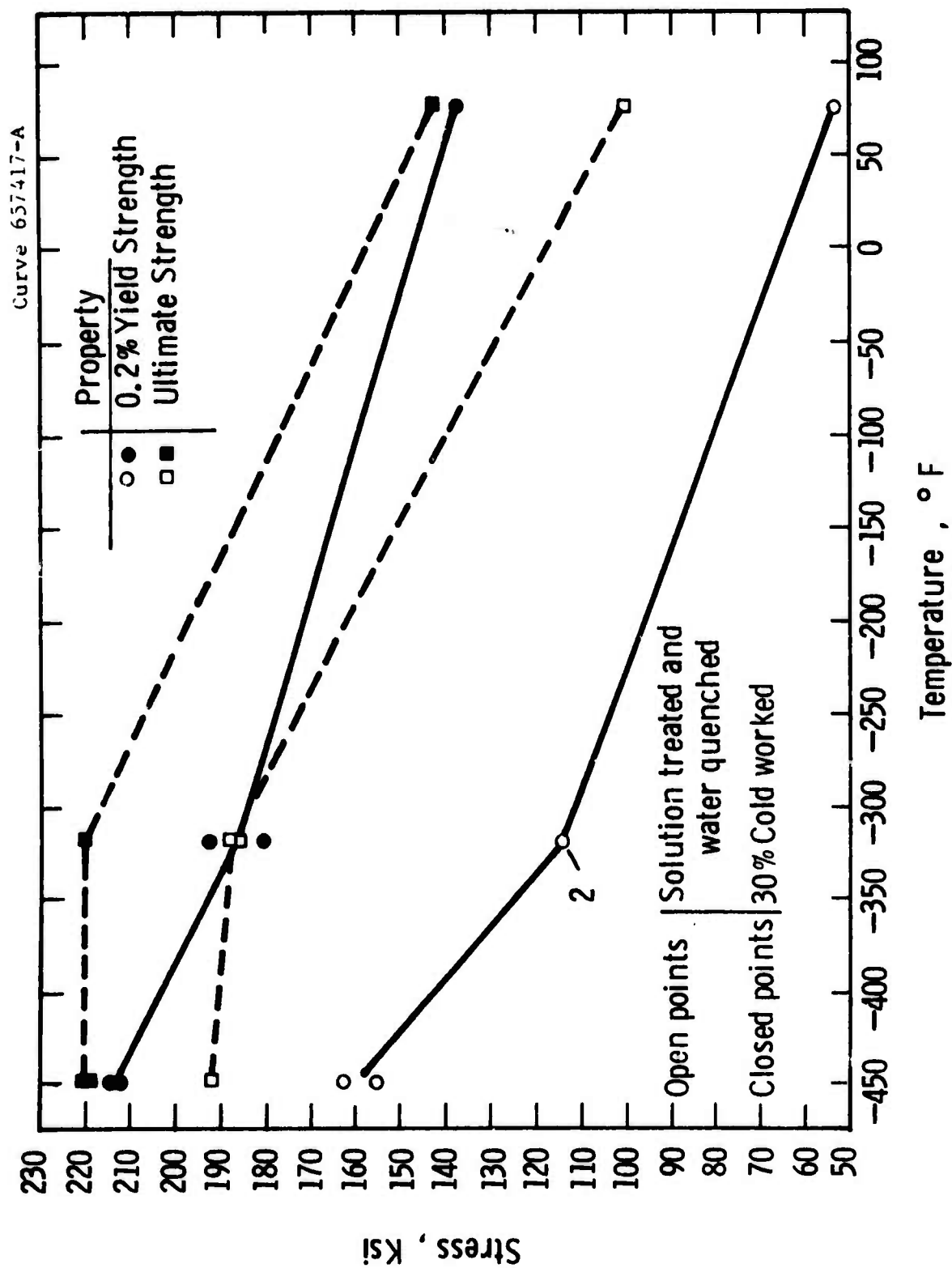


Fig. 6-7 - Tensile properties of Kromarc 58 stainless steel

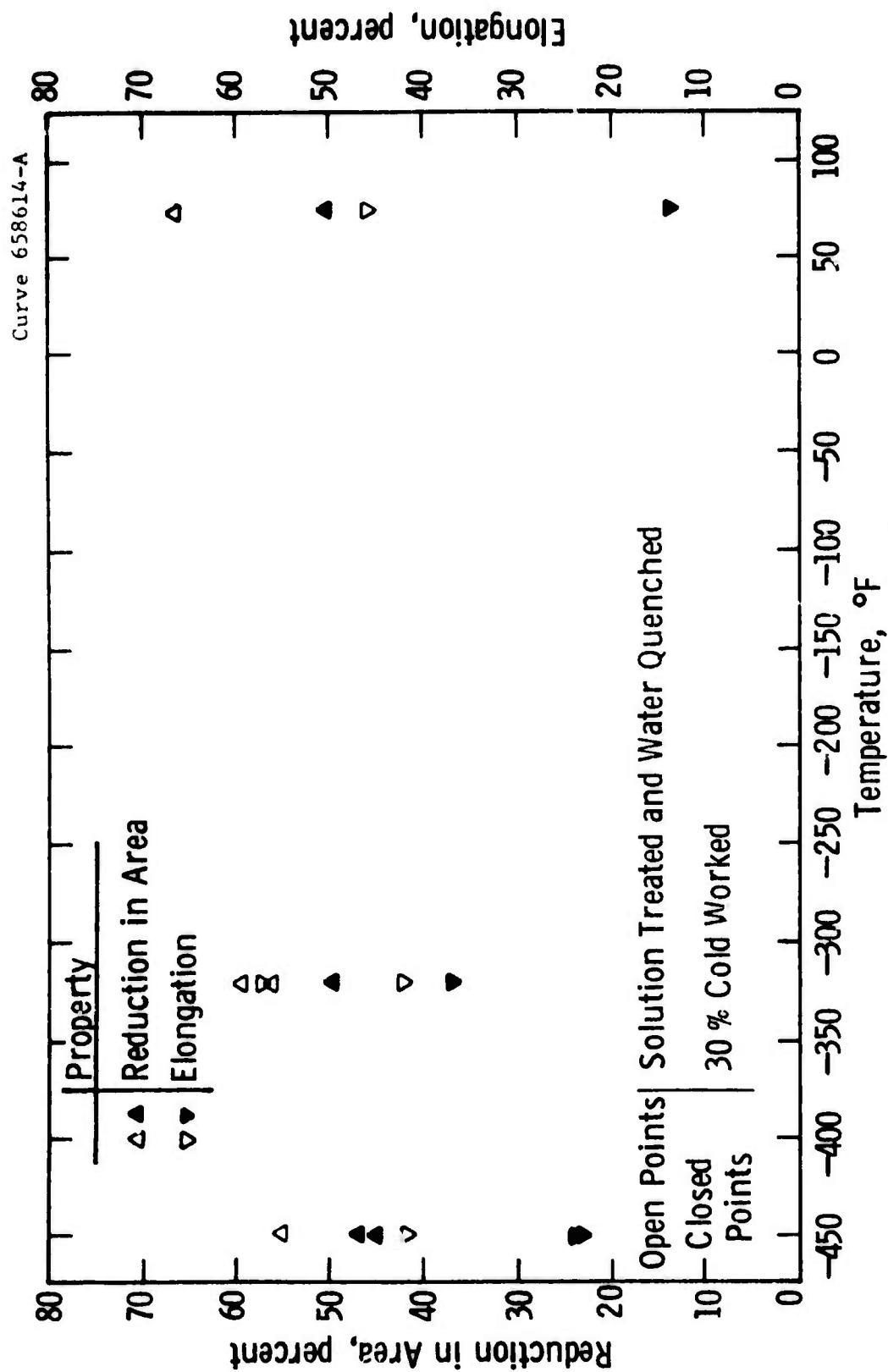


Fig. 6-8-Tensile properties of Kromarc 58 stainless steel

627<

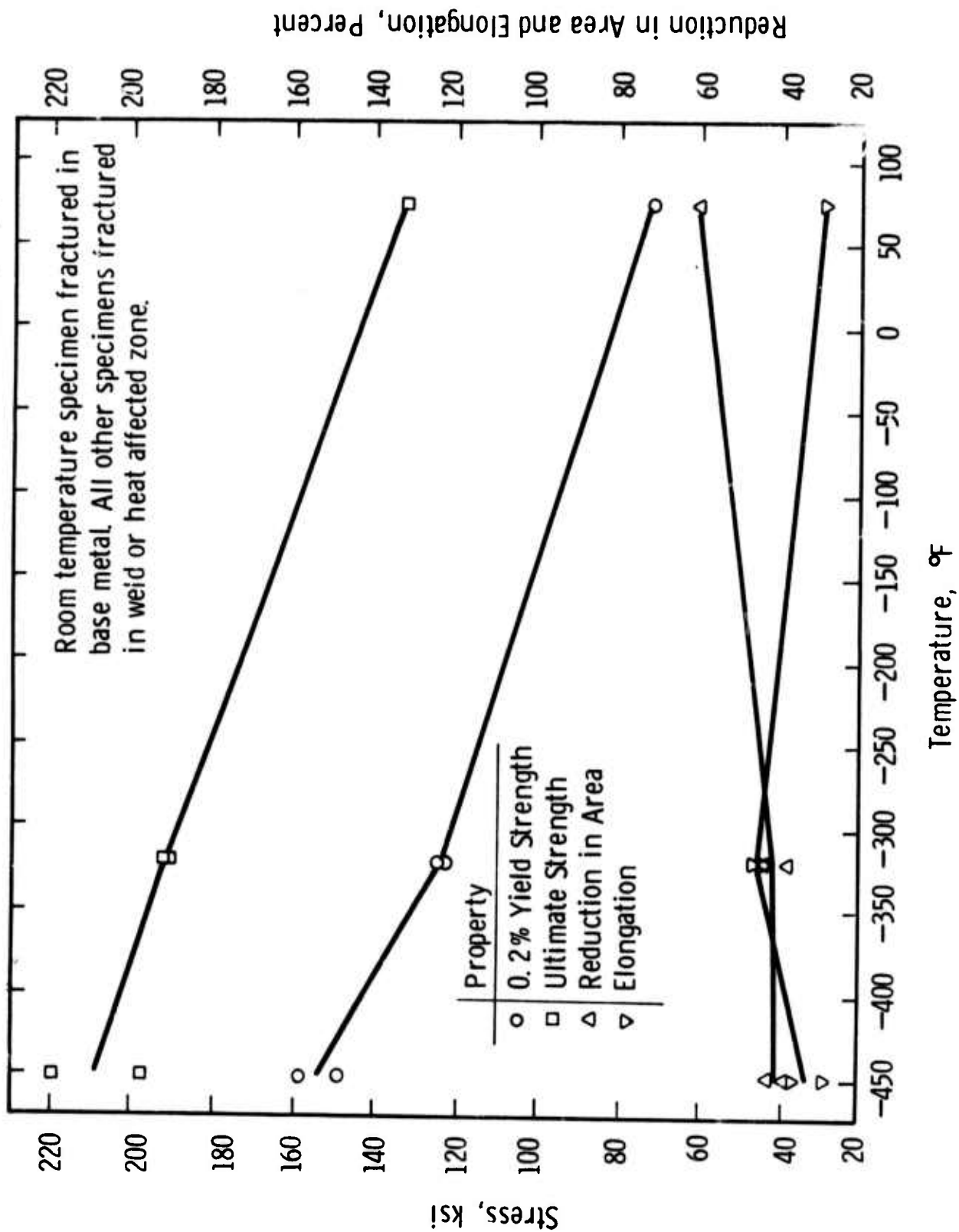


Fig.6-9-Tensile properties of Kromarc 58 stainless steel gas tungsten arc welds

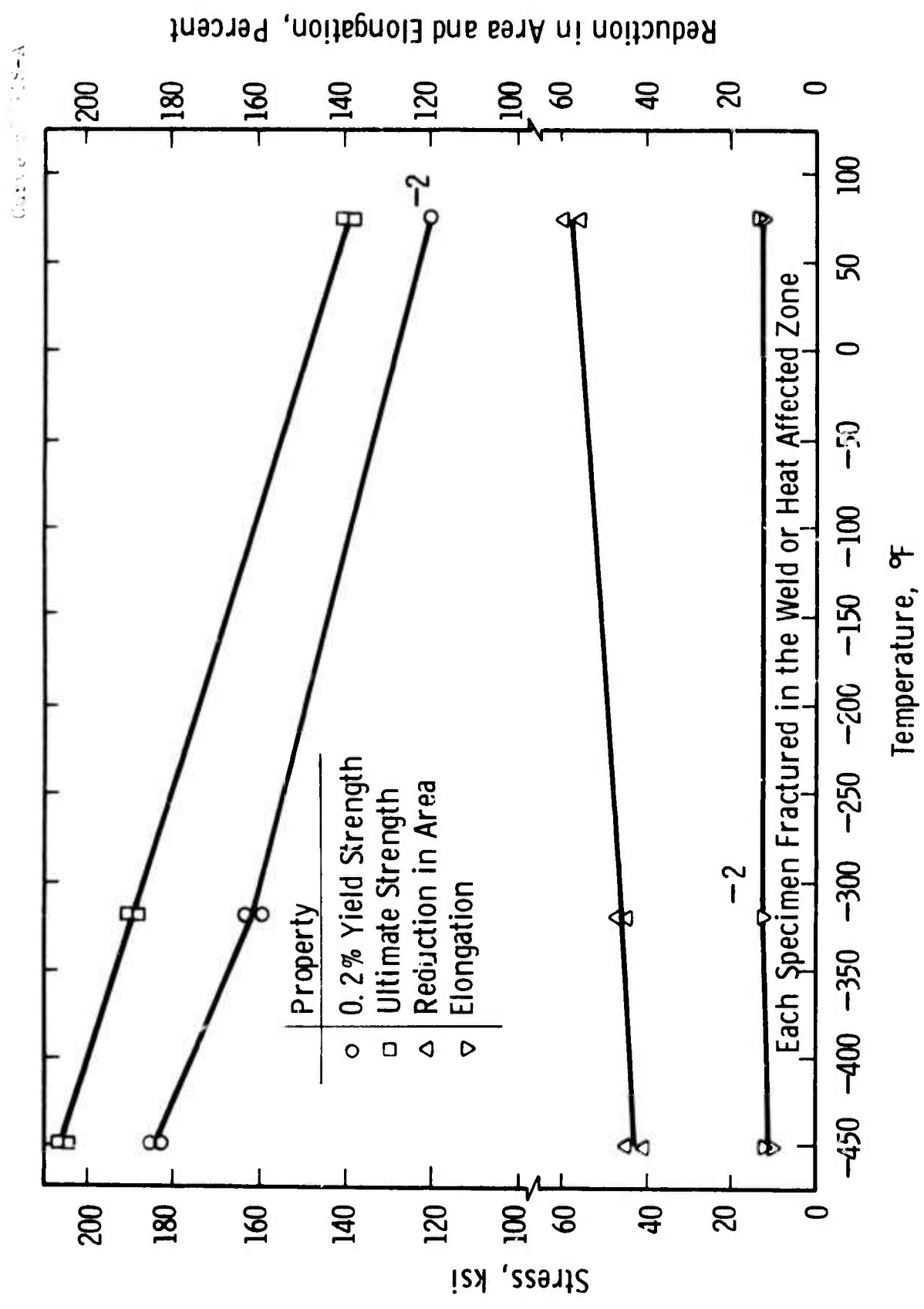


Fig.6-10-Tensile properties of Kromarc 58 stainless steel (cold worked/gas tungsten arc welded)

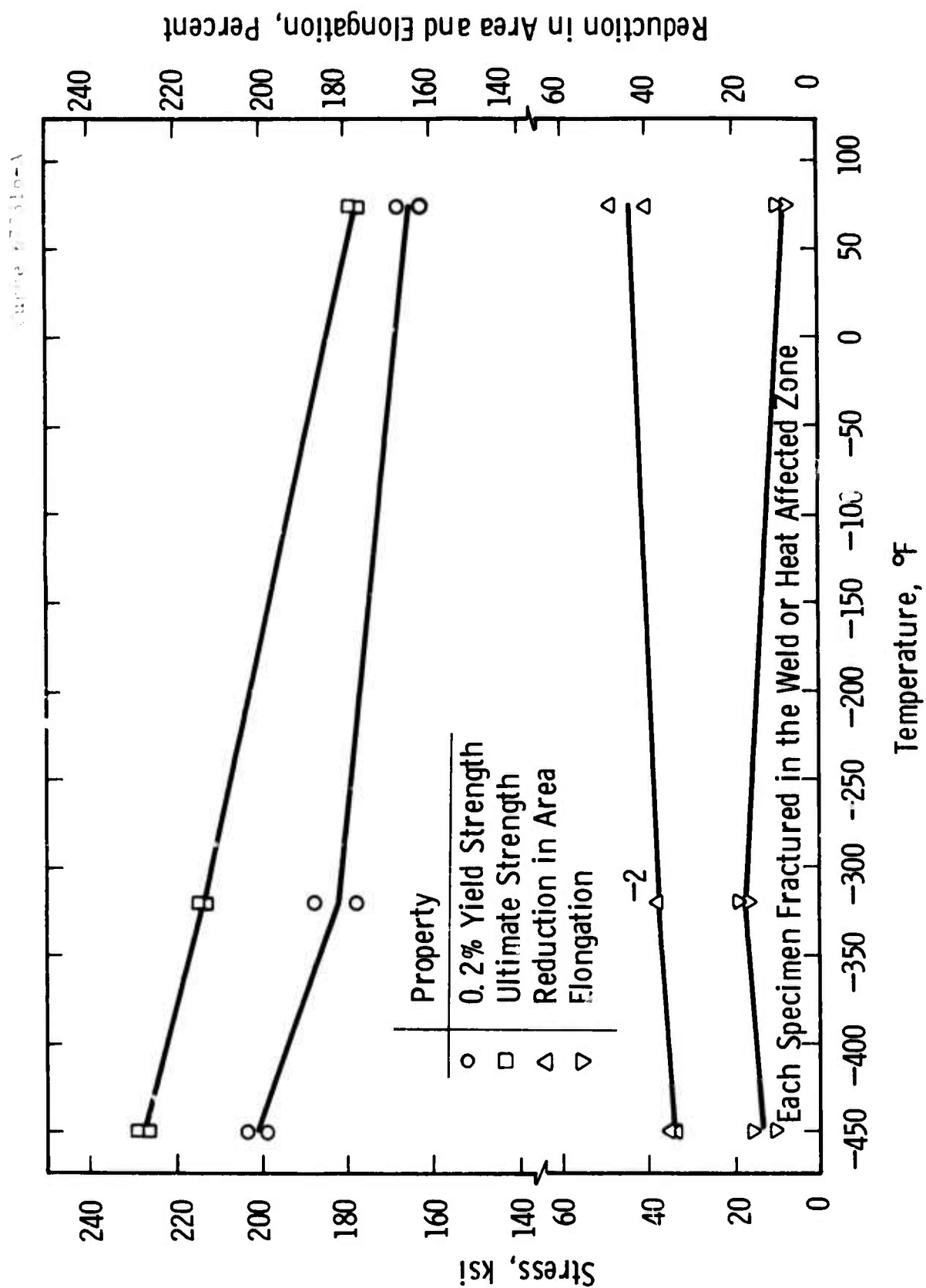


Fig.6-11-Tensile properties of Kromarc 58 stainless steel (gas tungsten arc welded/cold worked)

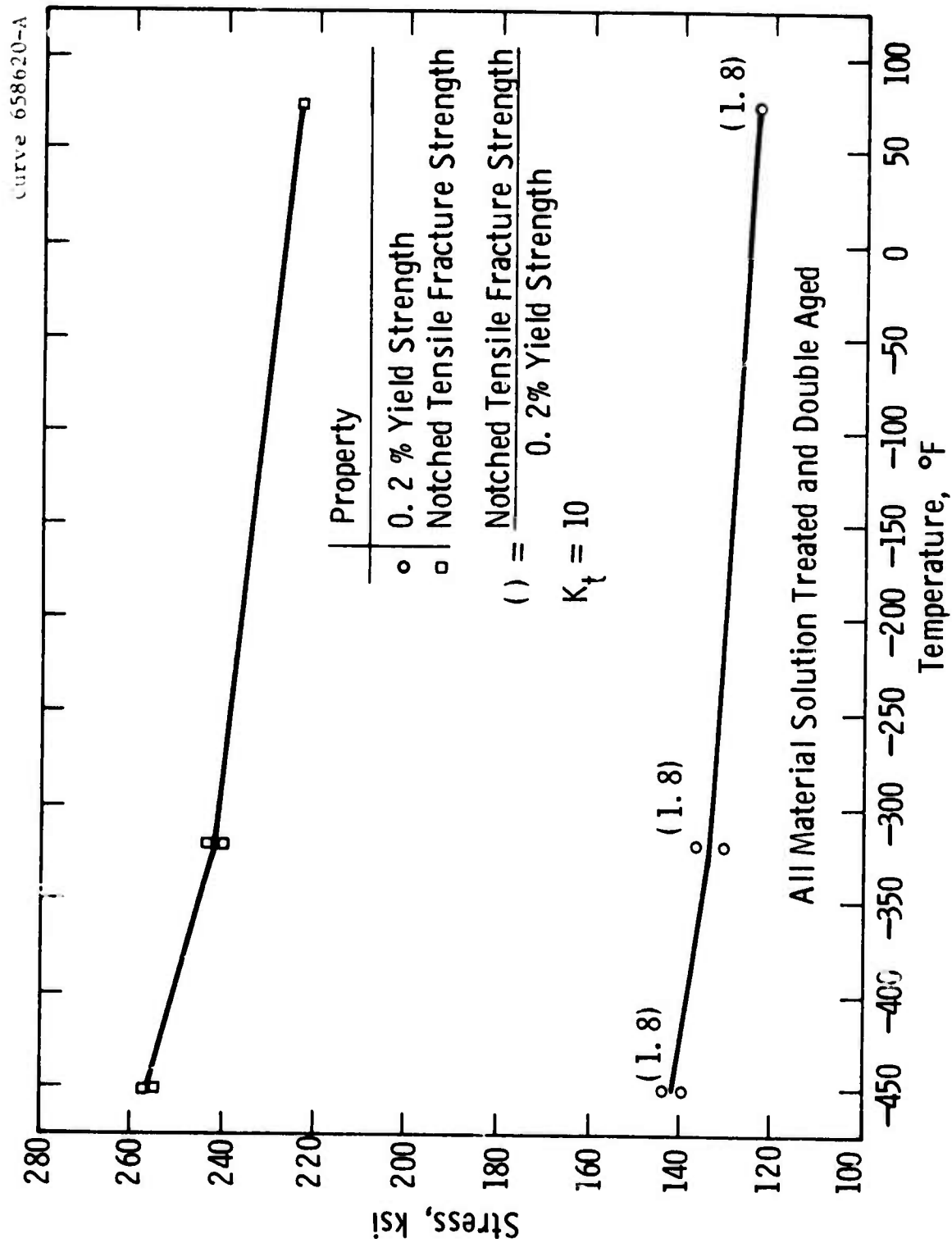


Fig-6-12—Yield strength and notched tensile fracture strength of Inconel X750 (AAM-VAR)

Curve 658619-A

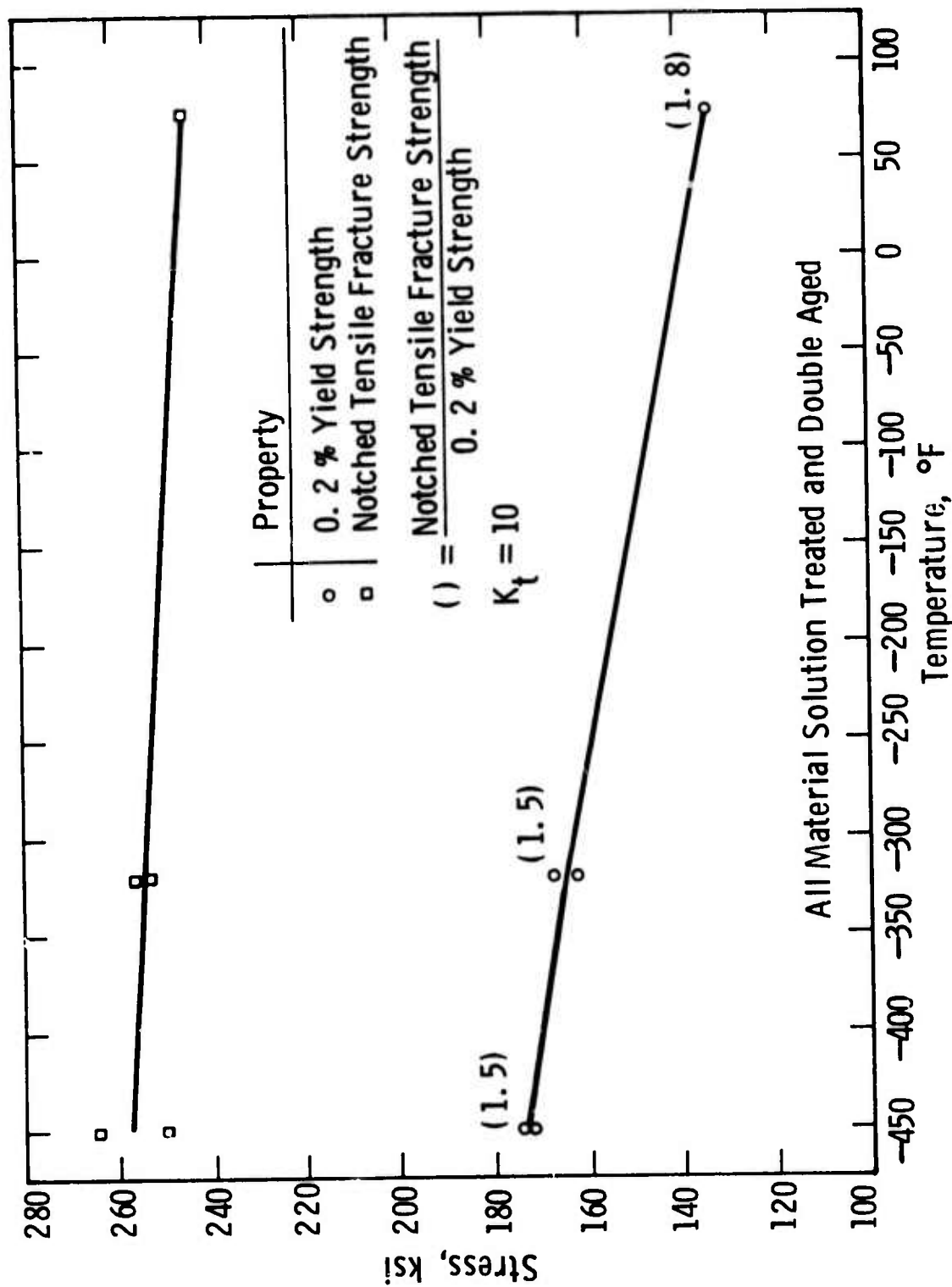


Fig.6-13—Yield strength and notched tensile fracture strength of Inconel X750 (VIM)



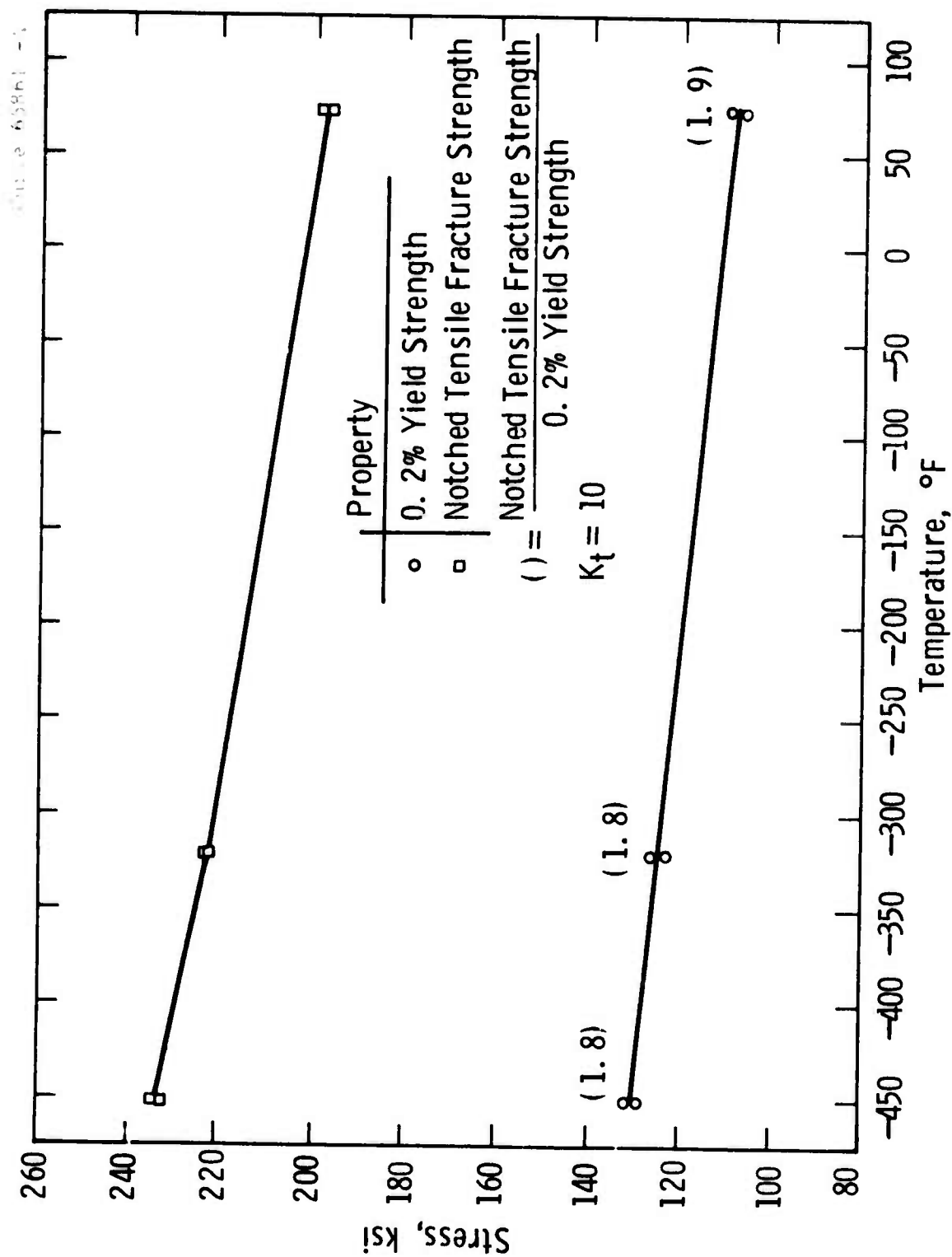


Fig. 6-14—Yield strength and notched tensile fracture strength of hot isostatic pressed Inconel X750

Curve 677330-A

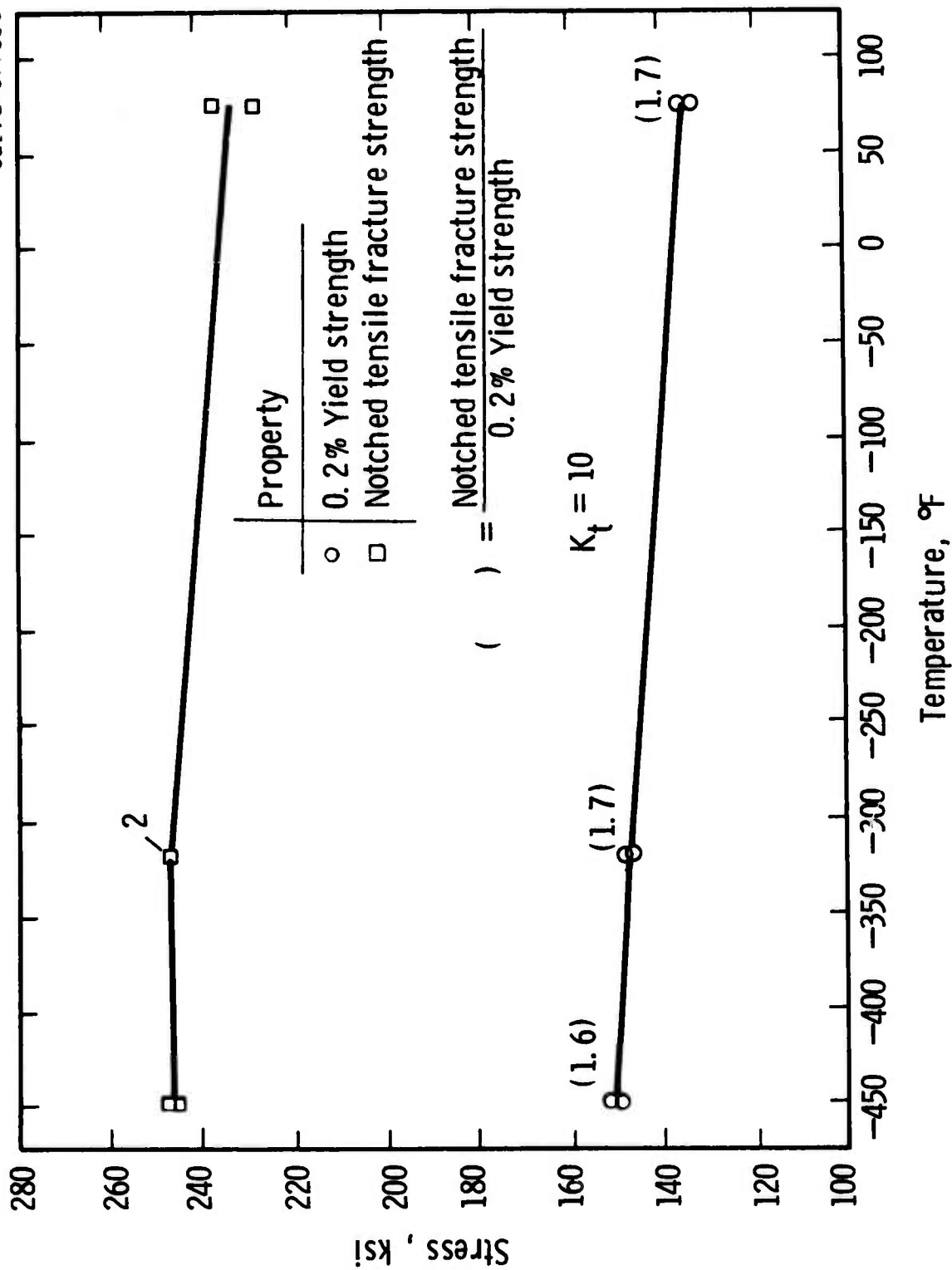


Fig.6-15-Yield strength and notched tensile fracture strength of solution treated and double aged hot isostatic pressed Inconel X750

Curve 658618-A

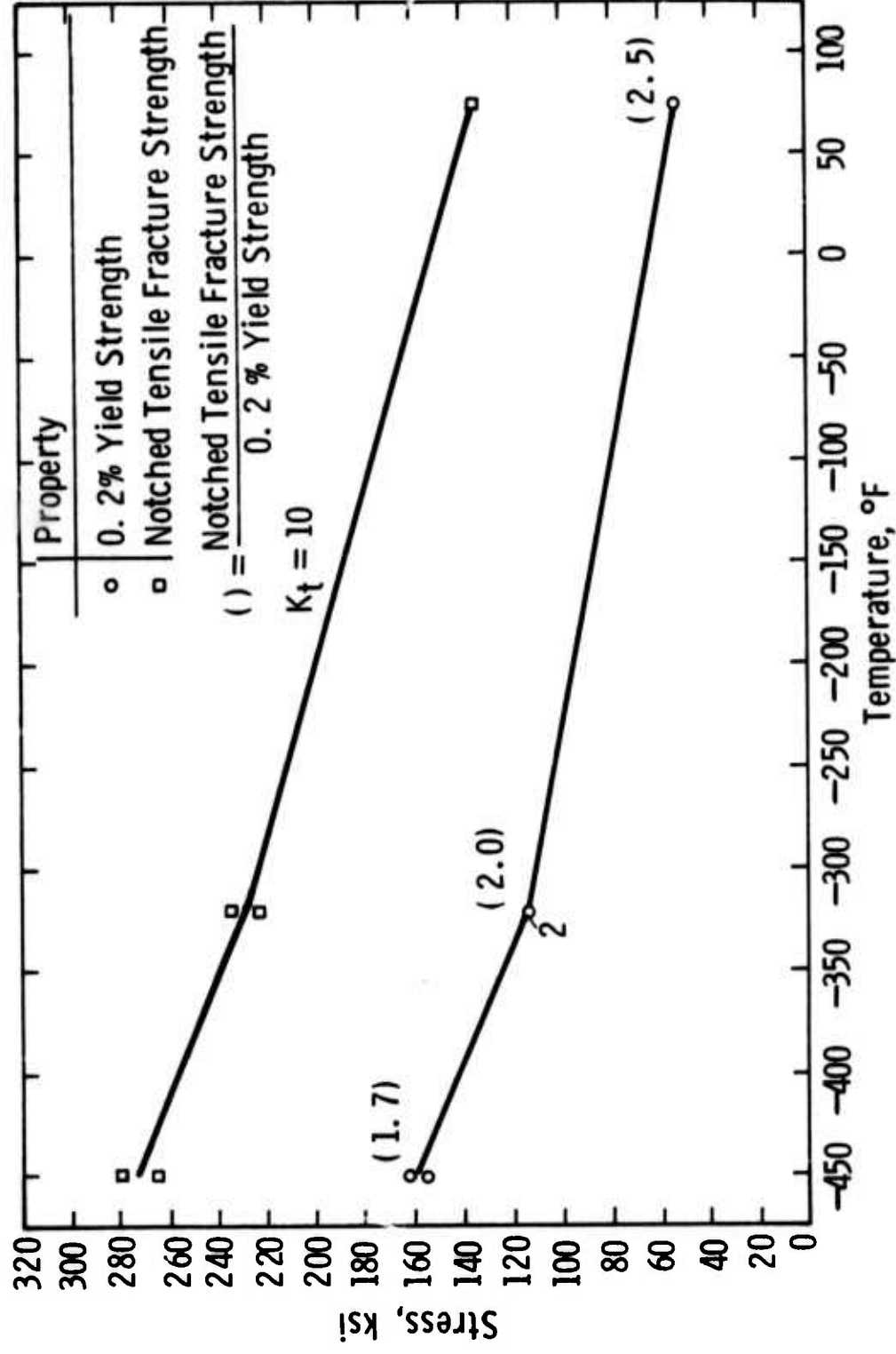


Fig. 6-16-Yield strength and notched tensile fracture strength of solution treated and water quenched Kromarc 58 stainless steel

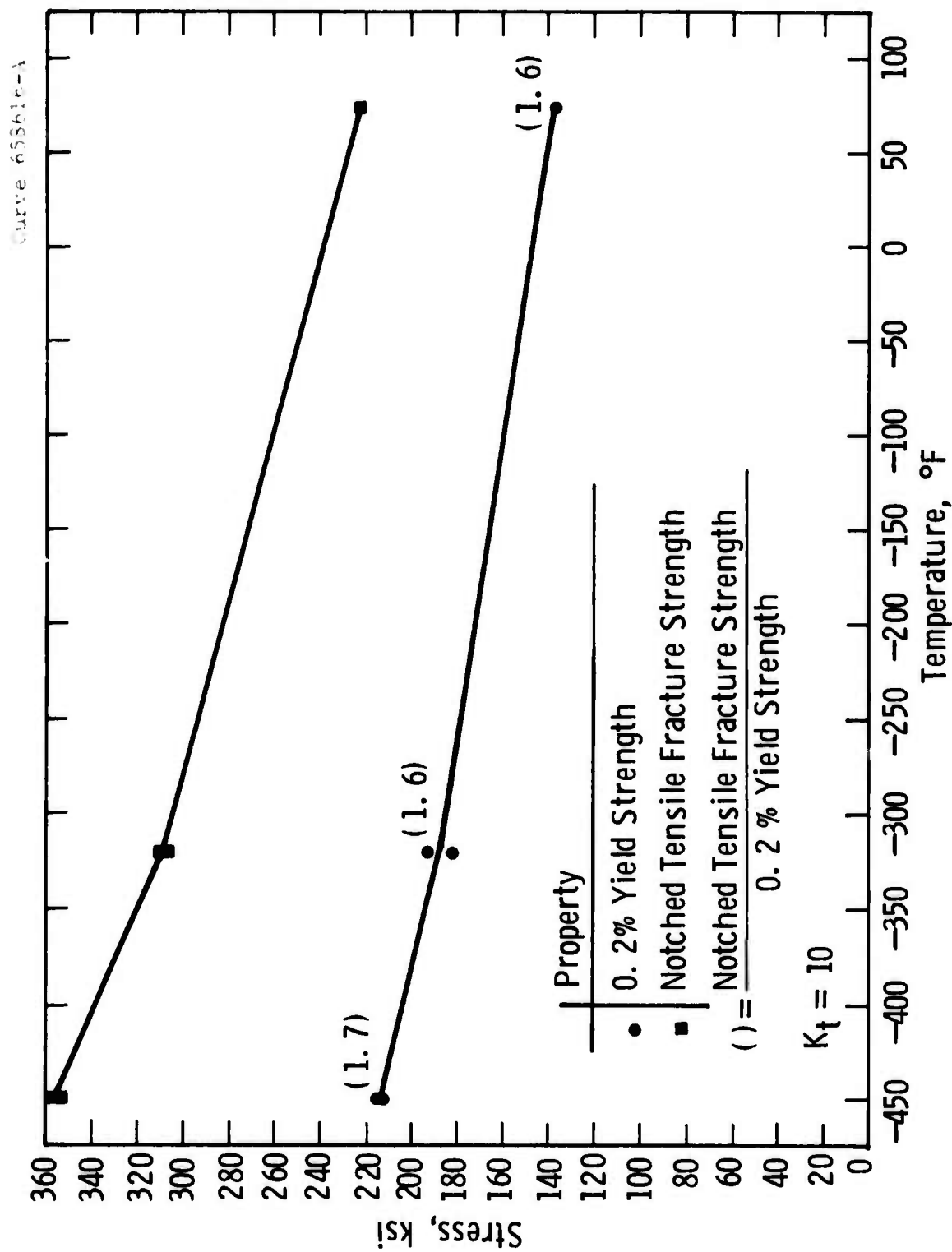
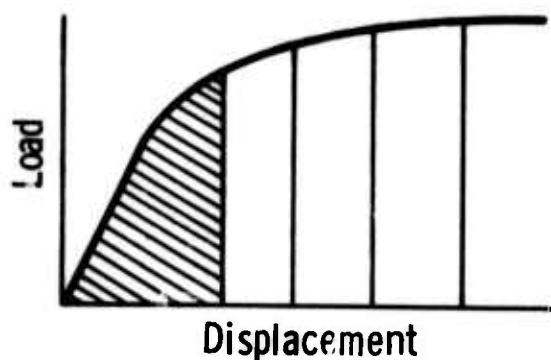
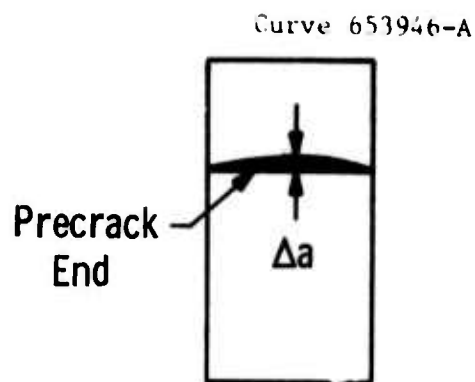


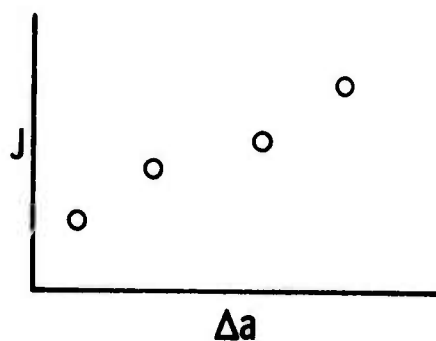
Fig.6-17—Yield strength and notched tensile fracture strength of 30 percent cold worked Kromarc 58 stainless steel



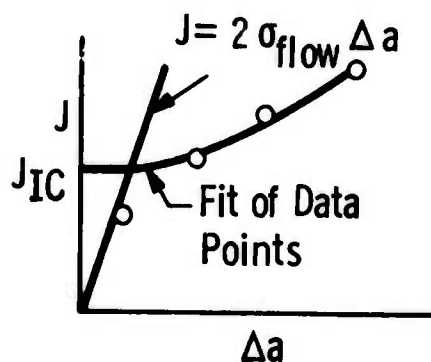
a) Load Specimens to Various Displacements



b) Measure Crack Extension



c) Calculate J for each Specimen and Plot vs.  $\Delta a$



d) Construct Two Curves for  $J_{IC}$  measurement

Fig. 6-18—Procedure for  $J_{IC}$  measurement

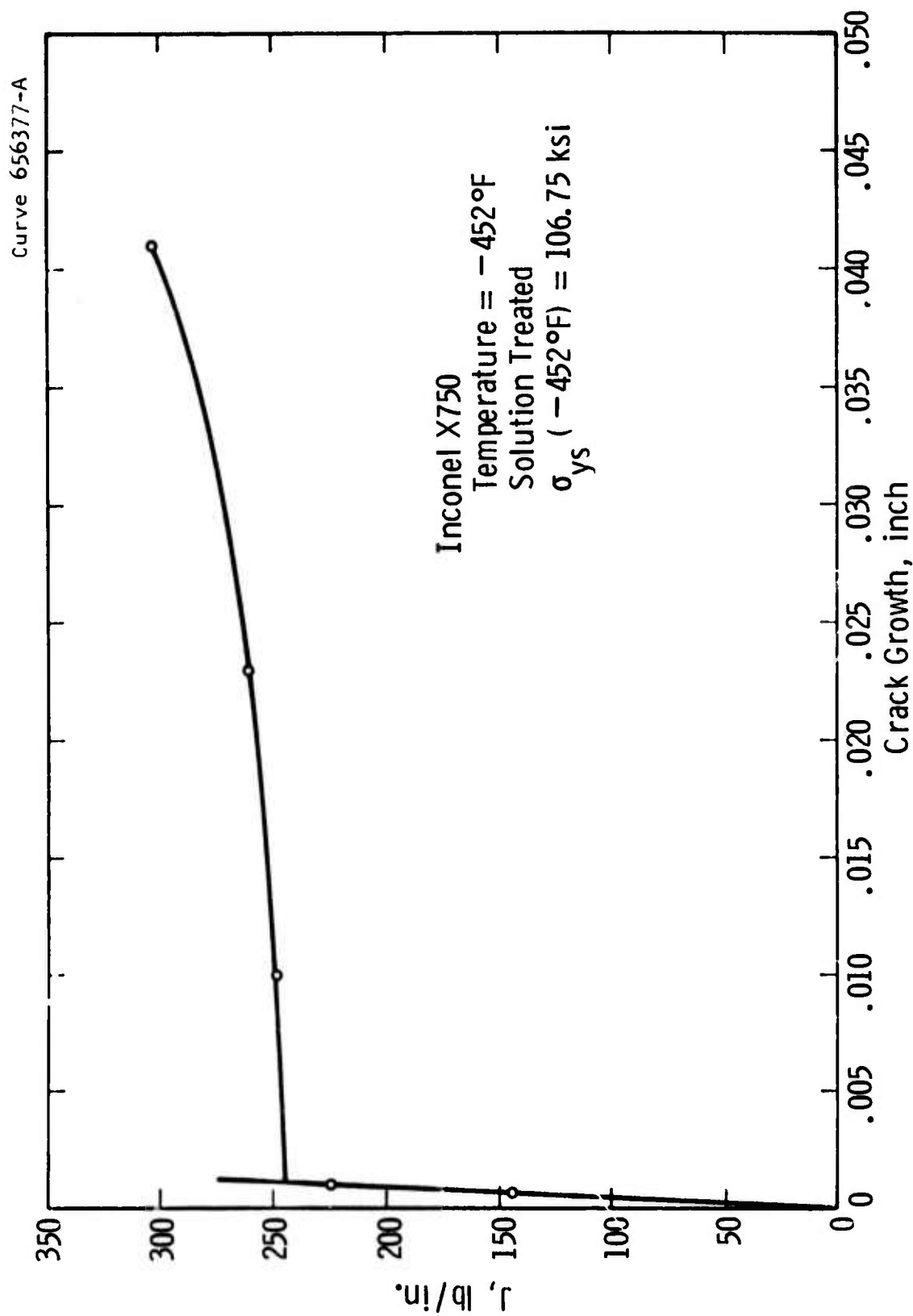


Fig. 6-19 J-resistance curve for solution treated Inconel X750 at a temperature of  $-452^{\circ}\text{F}$

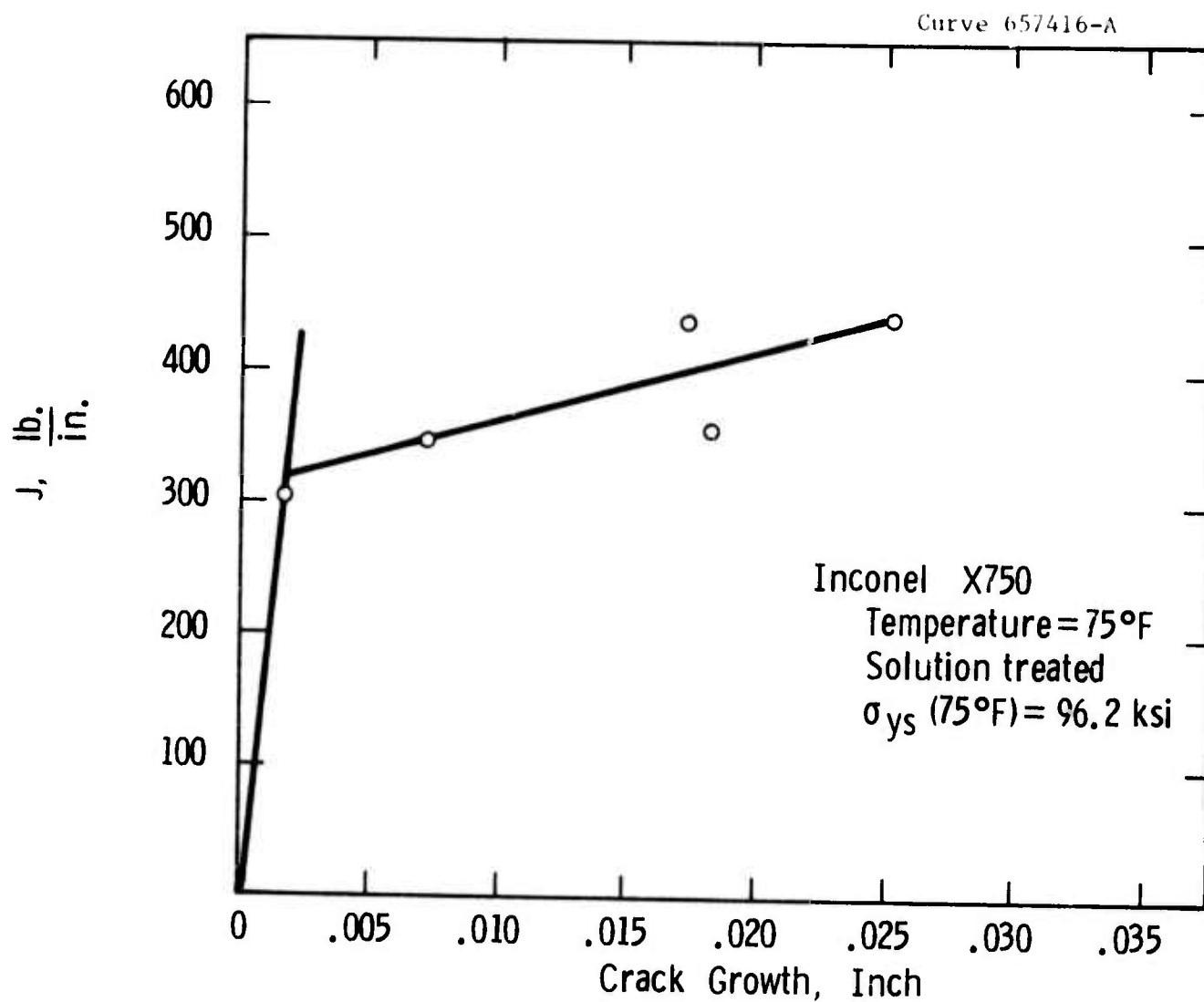


Fig.6-20-J resistance curve for solution treated Inconel X750 at a temperature of 75°F

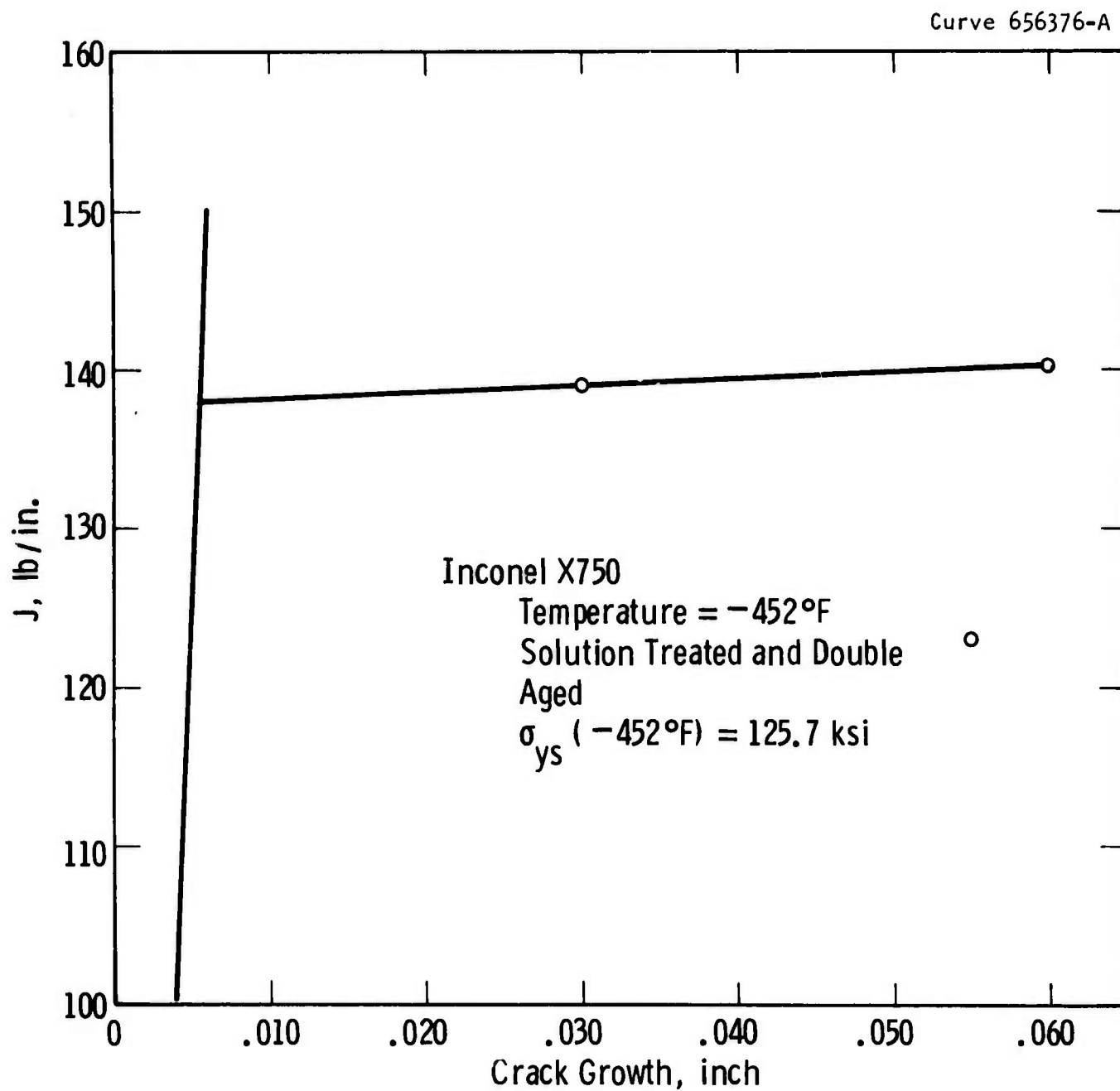


Fig. 6-21 -J resistance curve for solution treated and double aged Inconel X750 at a temperature of  $-452^{\circ}\text{F}$



Curve 677327-A

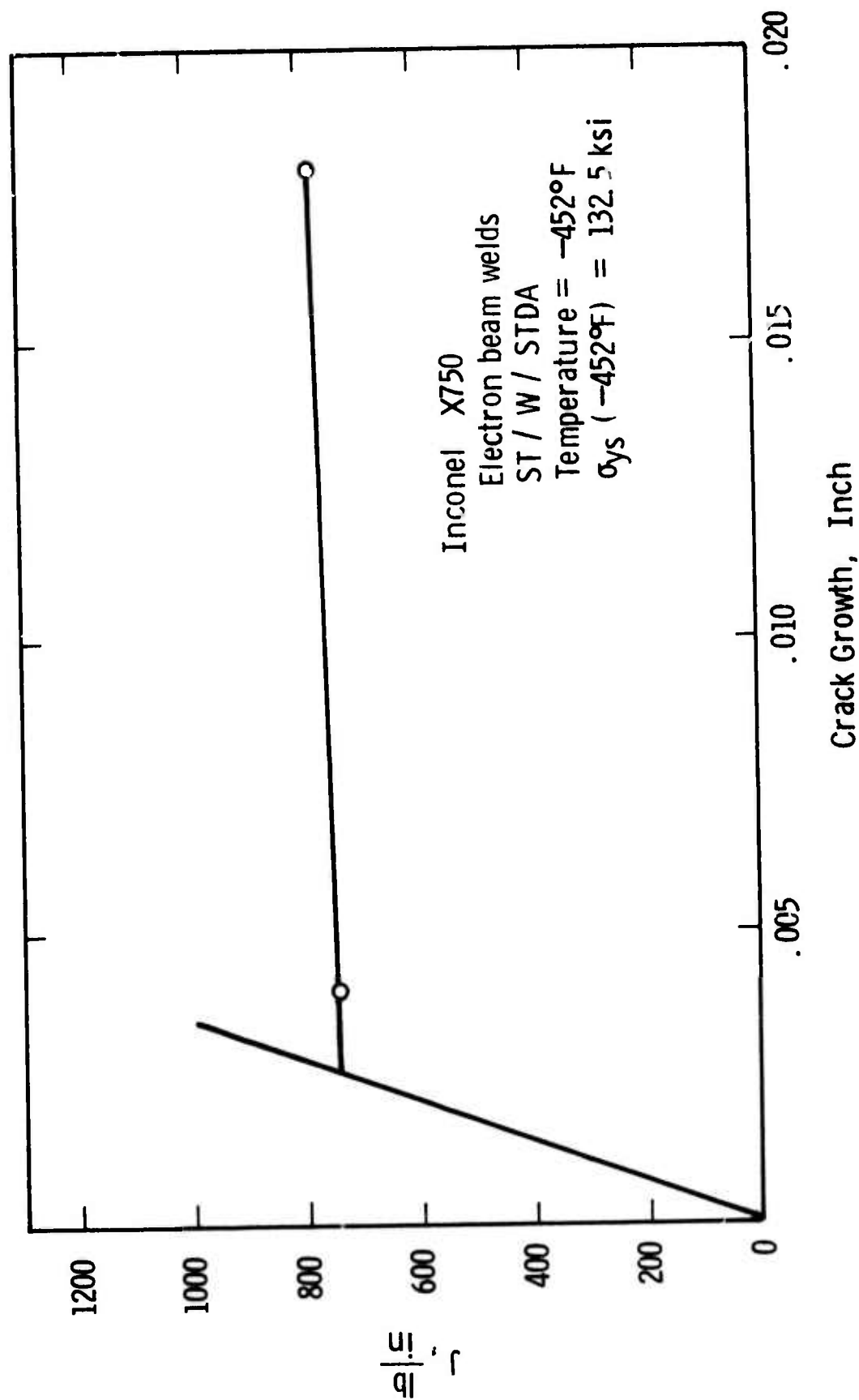


Fig.6-22-J resistance curve for Inconel X750 electron beam welds (ST / W / STDA) at a temperature of -452°F

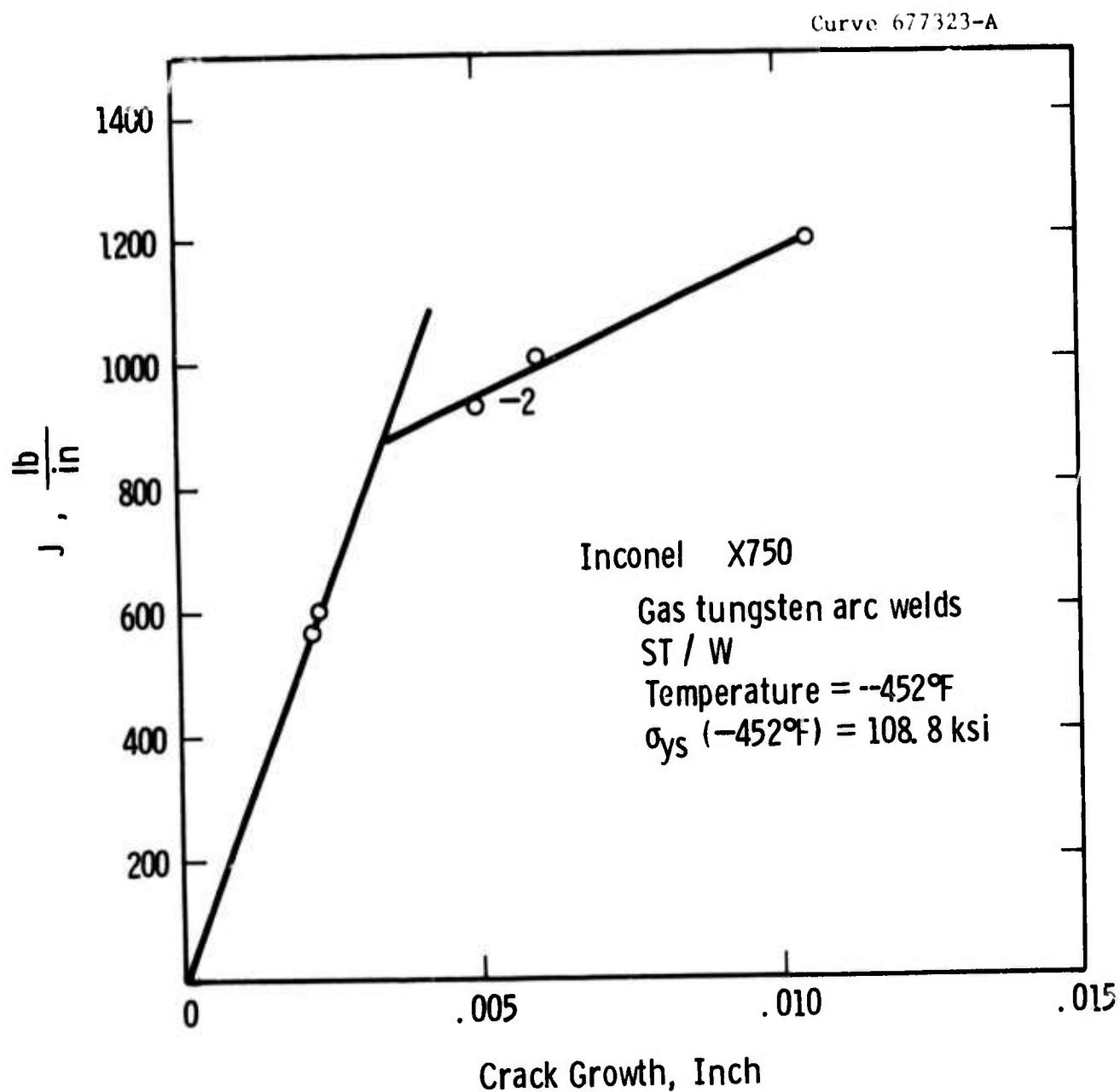


Fig.6-23-J resistance curve for Inconel X750 gas tungsten arc welds (ST / W) at a temperature of  $-452^{\circ}\text{F}$

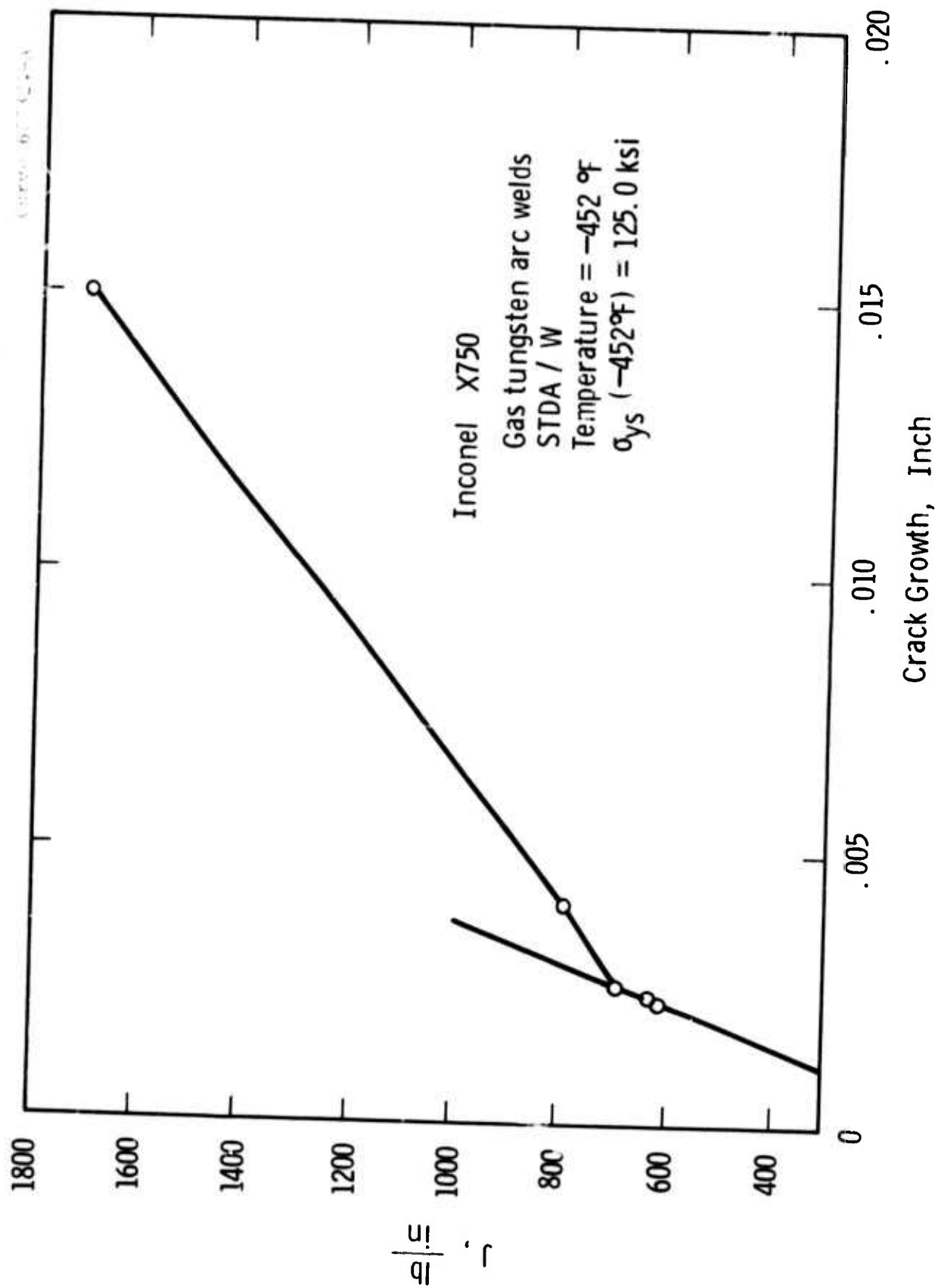


Fig.6-24-J resistance curve for Inconel X750 gas tungsten arc welds ( STDA / W ) at a temperature of  $-452^{\circ}\text{F}$

Curve 677321-A

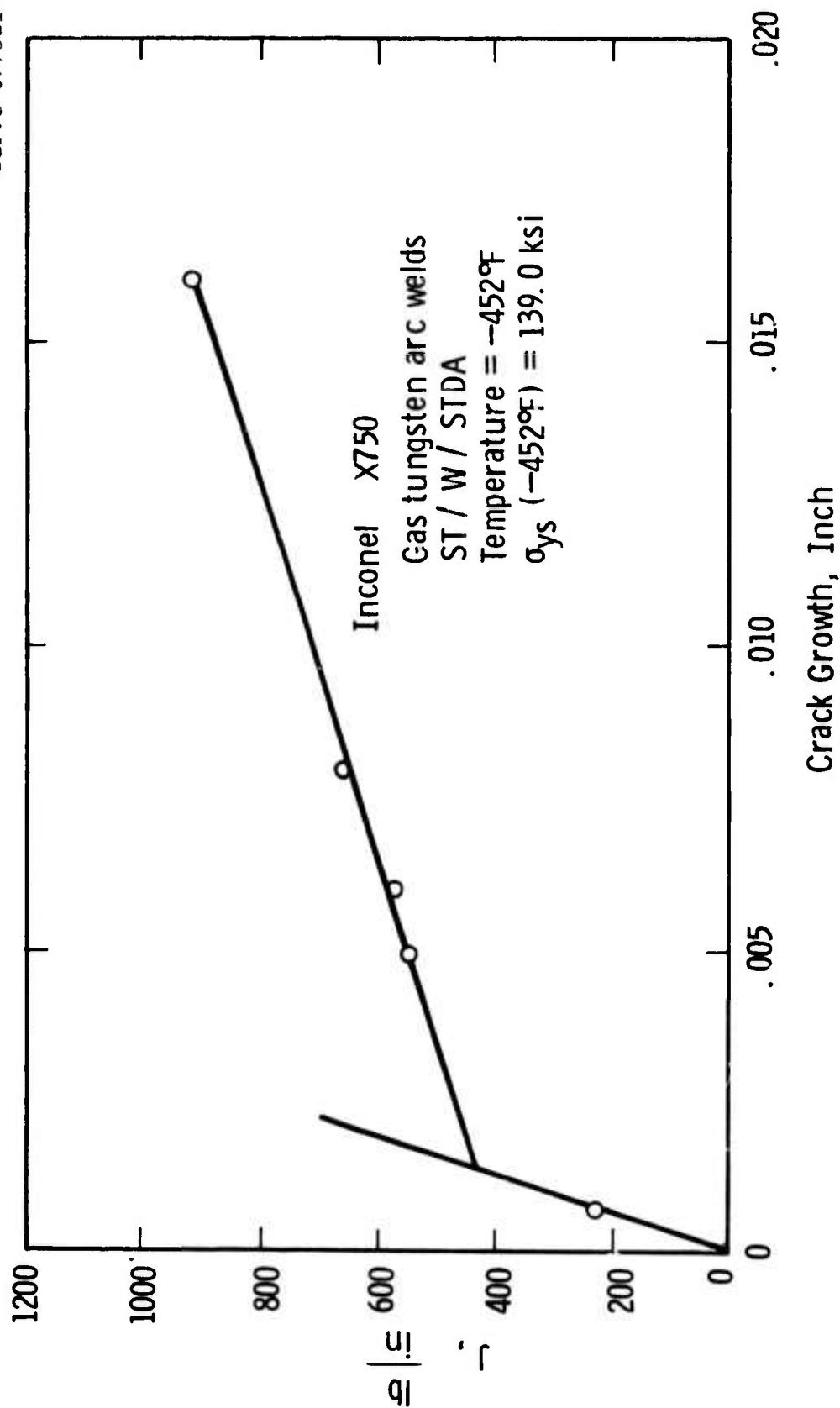


Fig.6-25- J resistance curve for Inconel X750 gas tungsten arc welds (ST/ W / STDA) at a temperature of -452°F

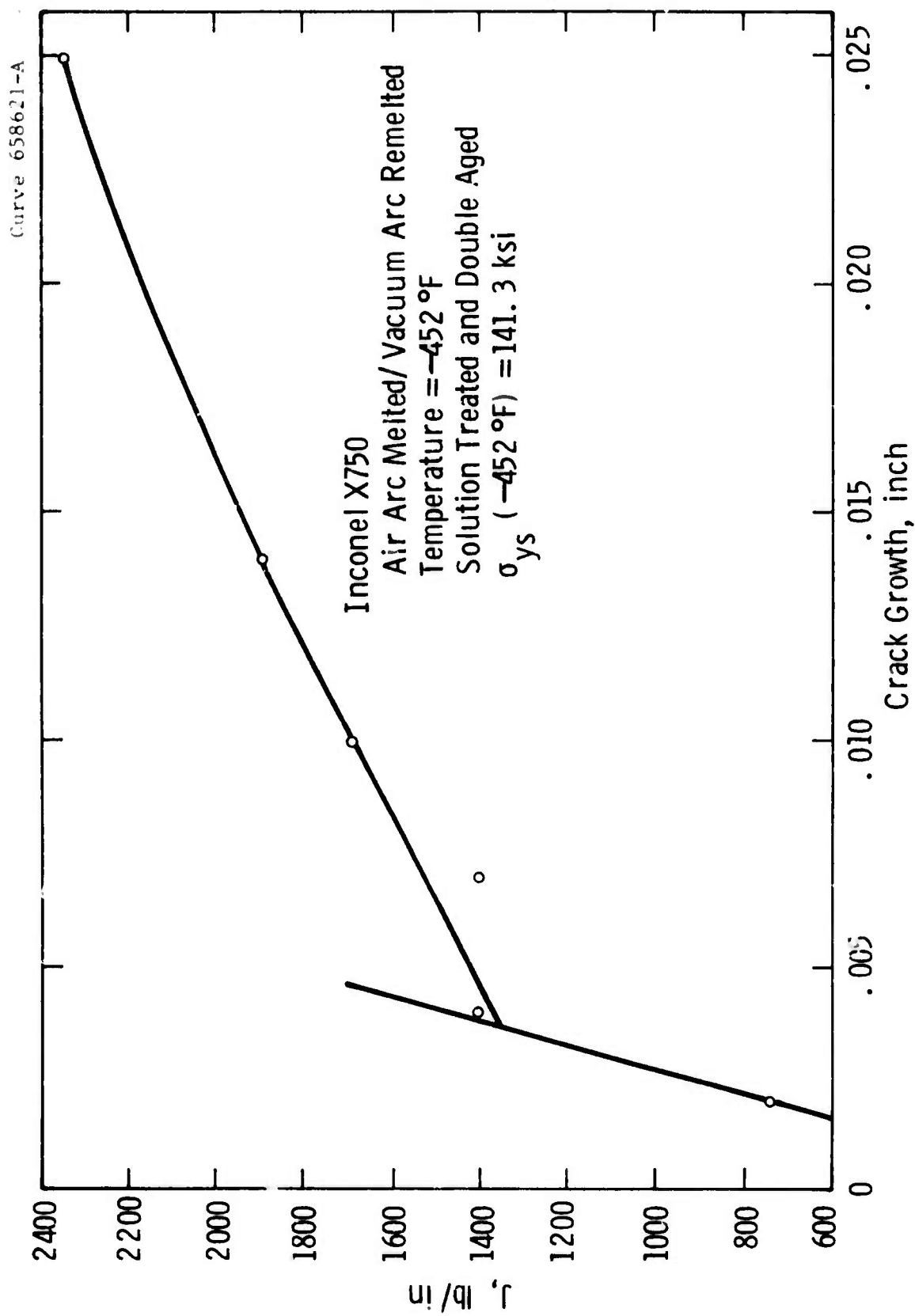


Fig. 6-26-J resistance curve for Inconel X750 ( AAM-VAR) at a temperature of -452 °F

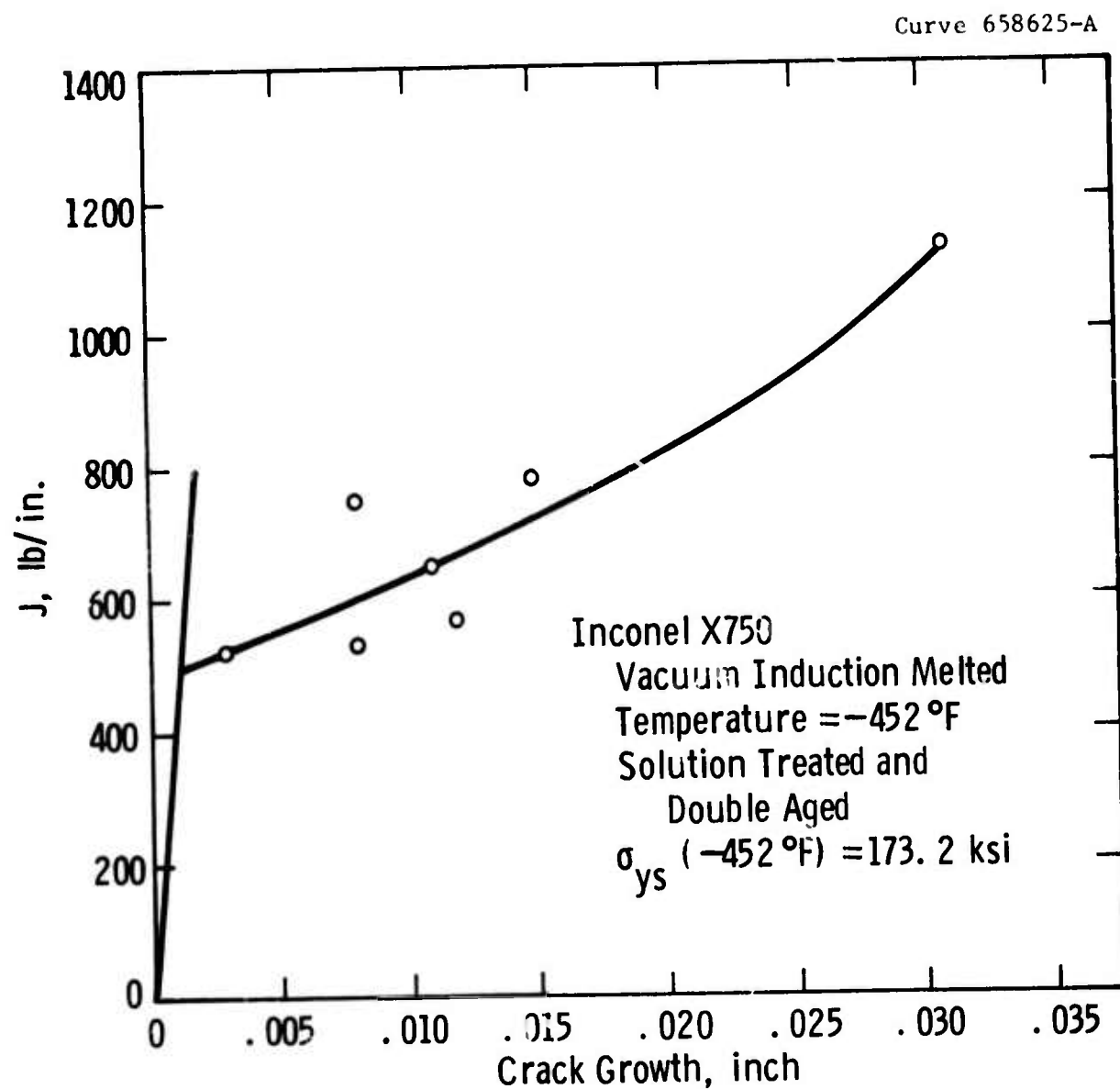


Fig.6-27—J resistance curve for Inconel X750 (VIM) at a temperature of -452 °F

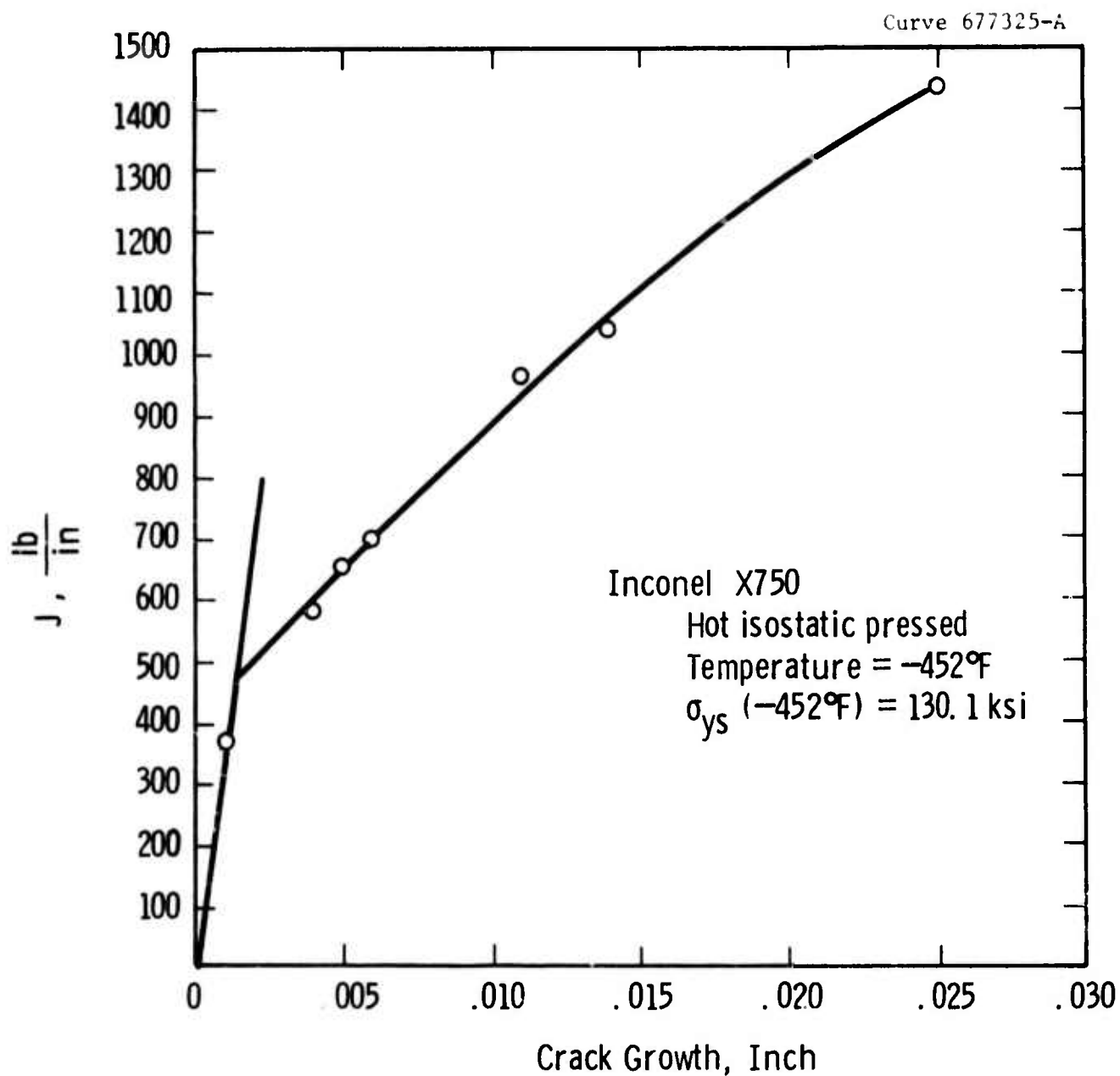


Fig.6-28-J resistance curve for hot isostatic pressed Inconel X750 at a temperature of  $-452^{\circ}\text{F}$

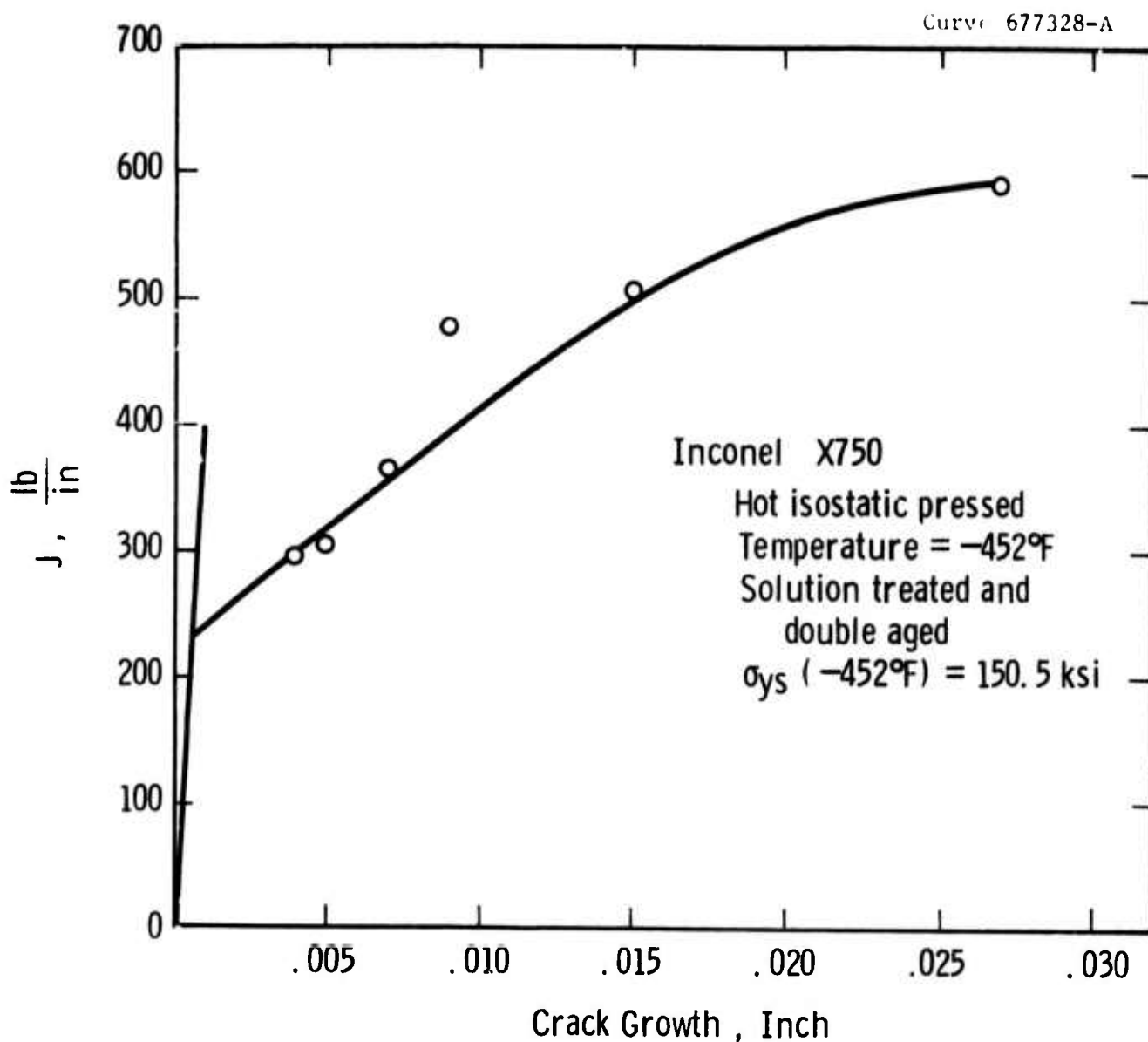


Fig.6-29-J resistance curve for solution treated and double aged hot isostatic pressed Inconel X750 at a temperature of  $-452^{\circ}\text{F}$



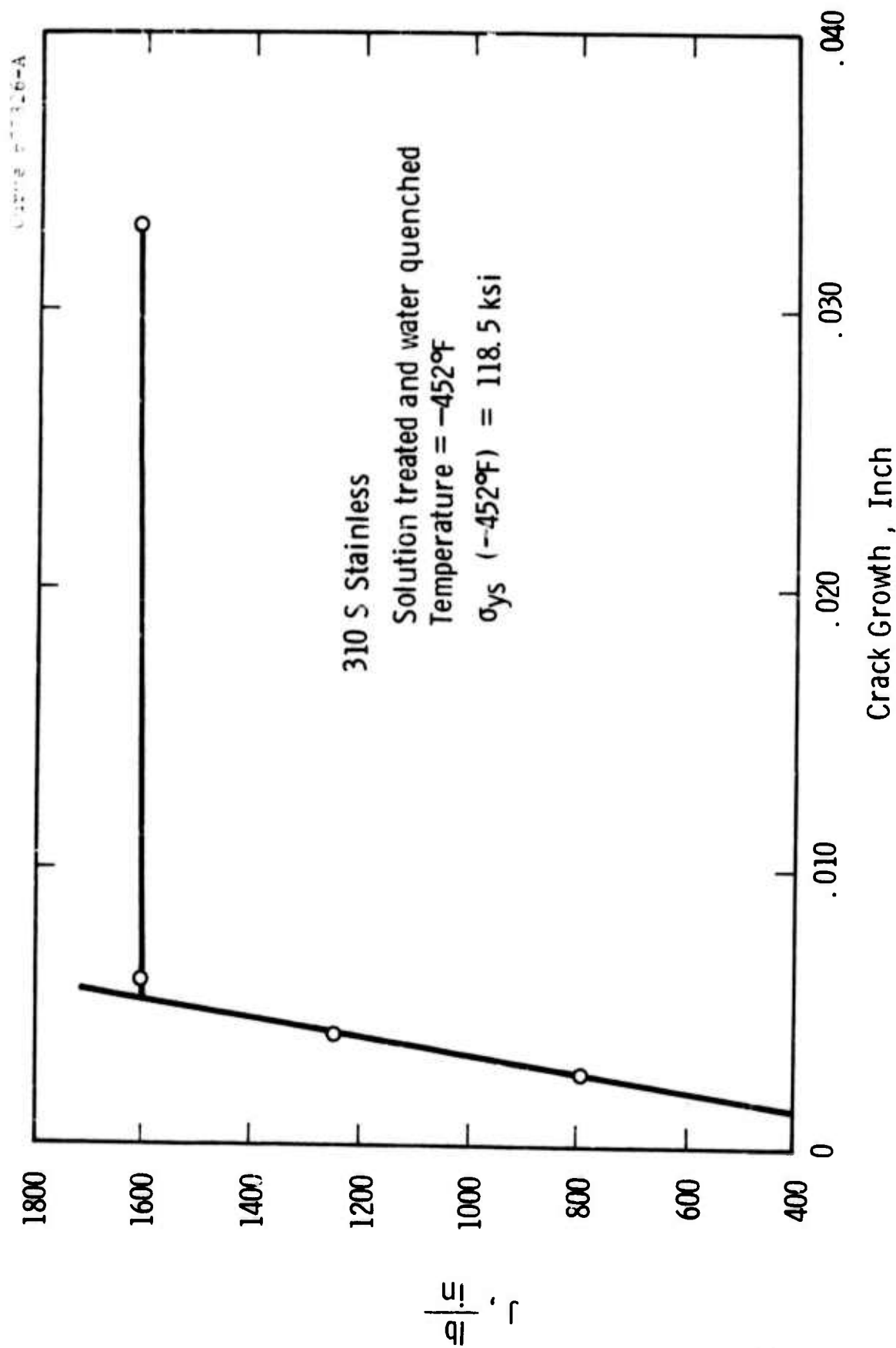


Fig.6-30-J resistance curve for solution treated and water quenched 310 S stainless steel at a temperature of  $-452^{\circ}\text{F}$

Curve 31-J

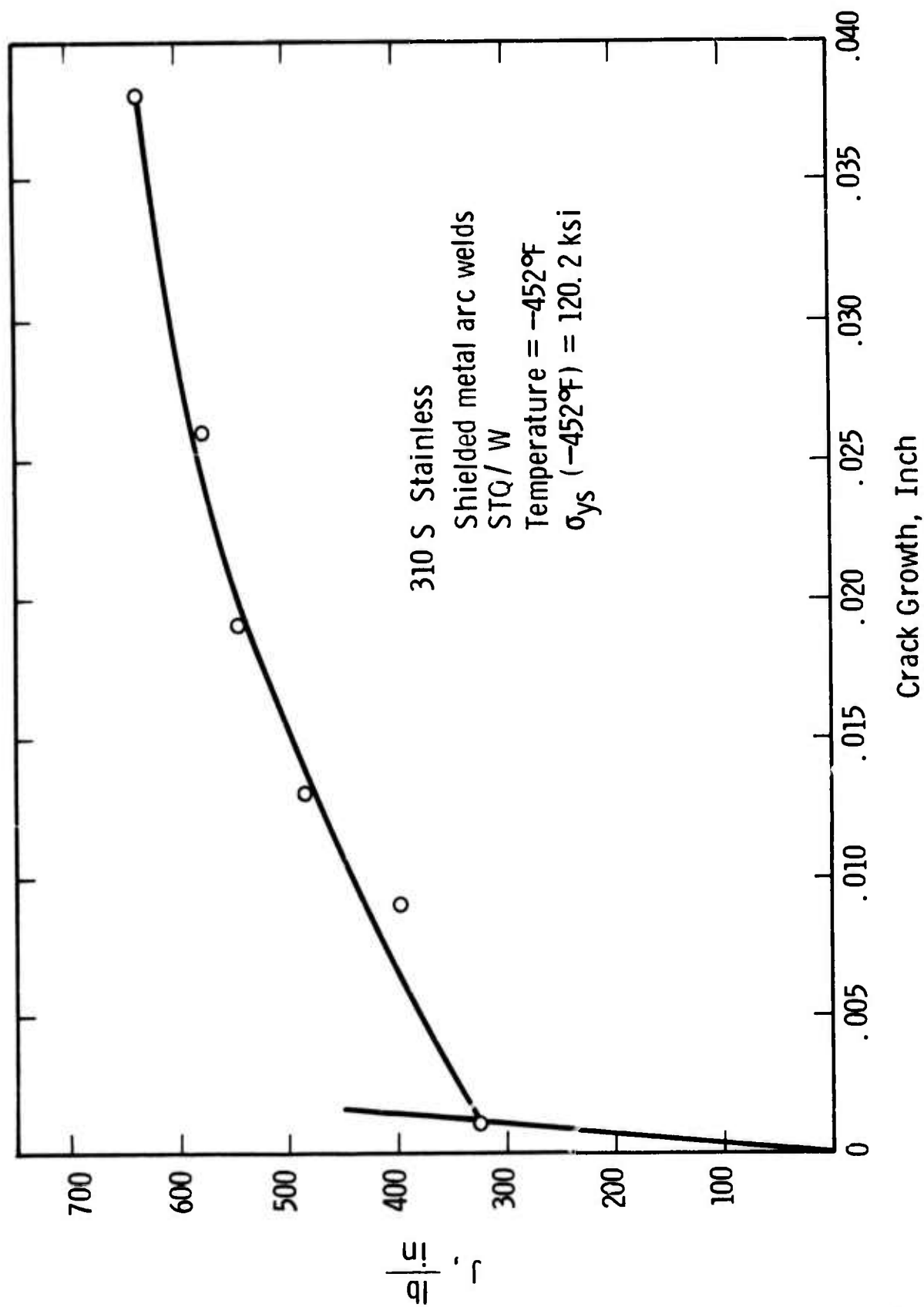


Fig.6-31-J resistance curve for 310 S stainless steel shielded metal arc welds at a temperature of -452°F

650<

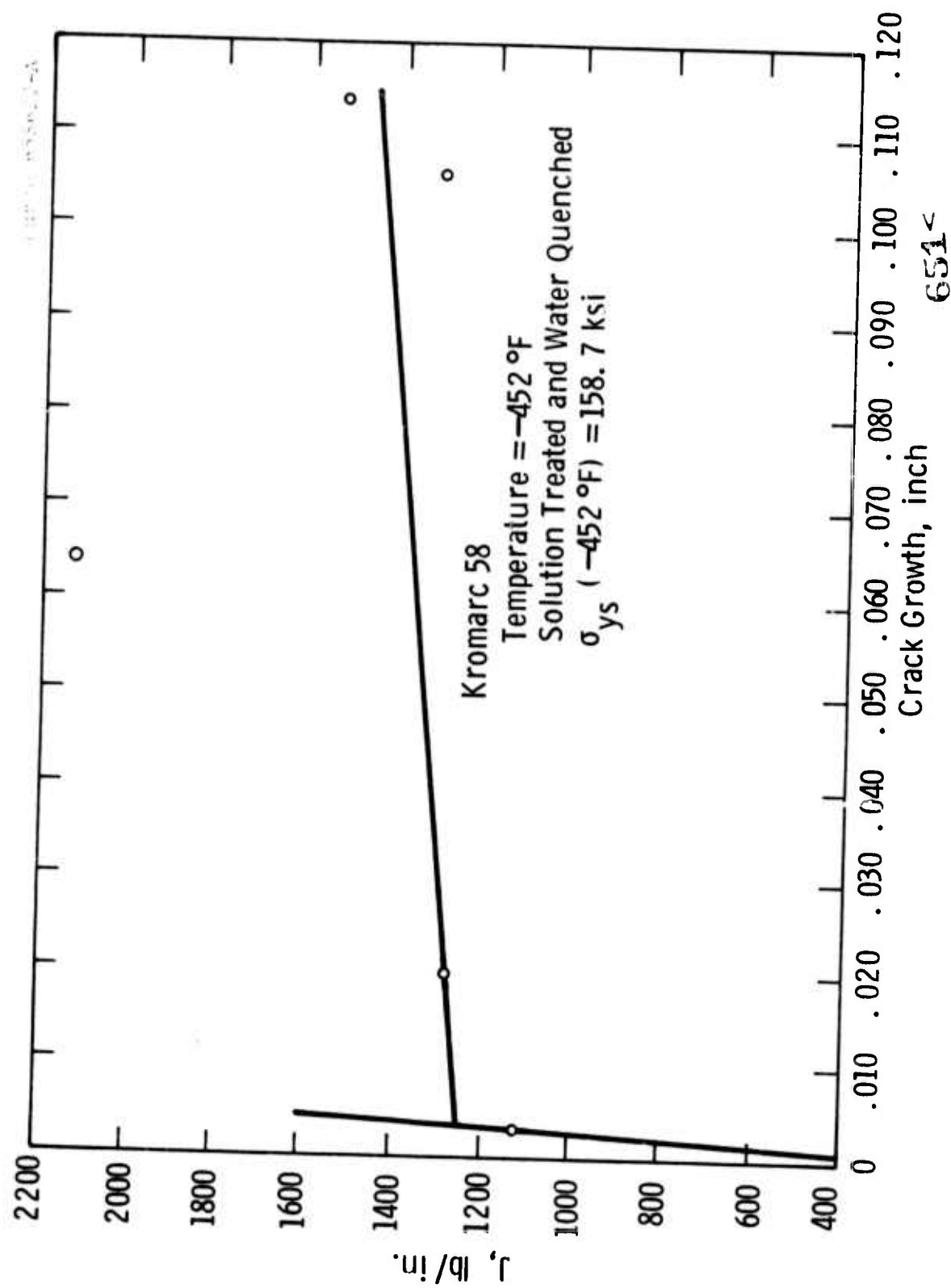


Fig.6-32—J resistance curve for solution treated and water quenched Kromarc 58 stainless steel at a temperature of  $-452^{\circ}\text{F}$

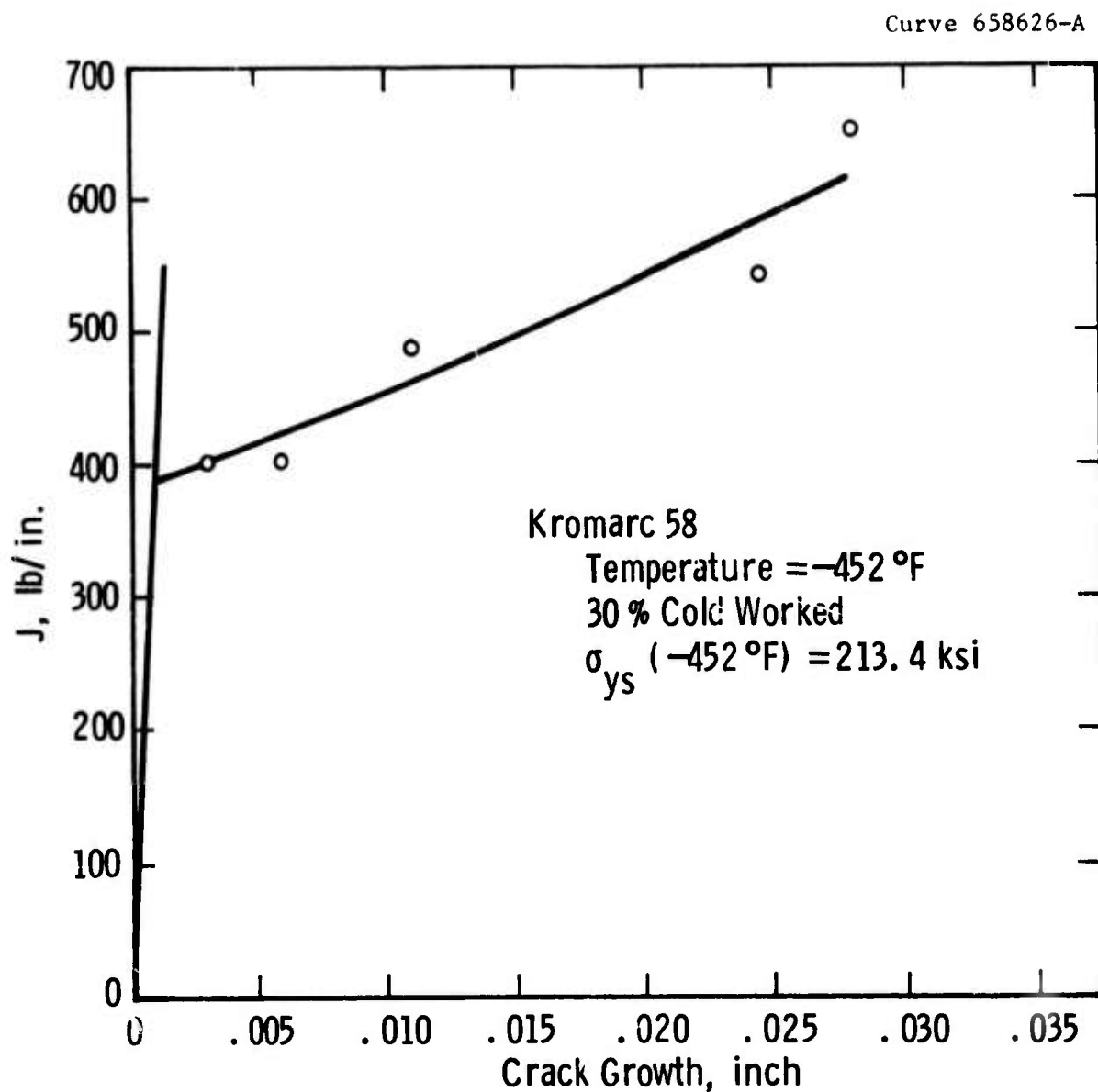


Fig.6-33—J resistance curve for 30 percent cold worked Kromarc 58 stainless steel at a temperature of  $-452^{\circ}\text{F}$

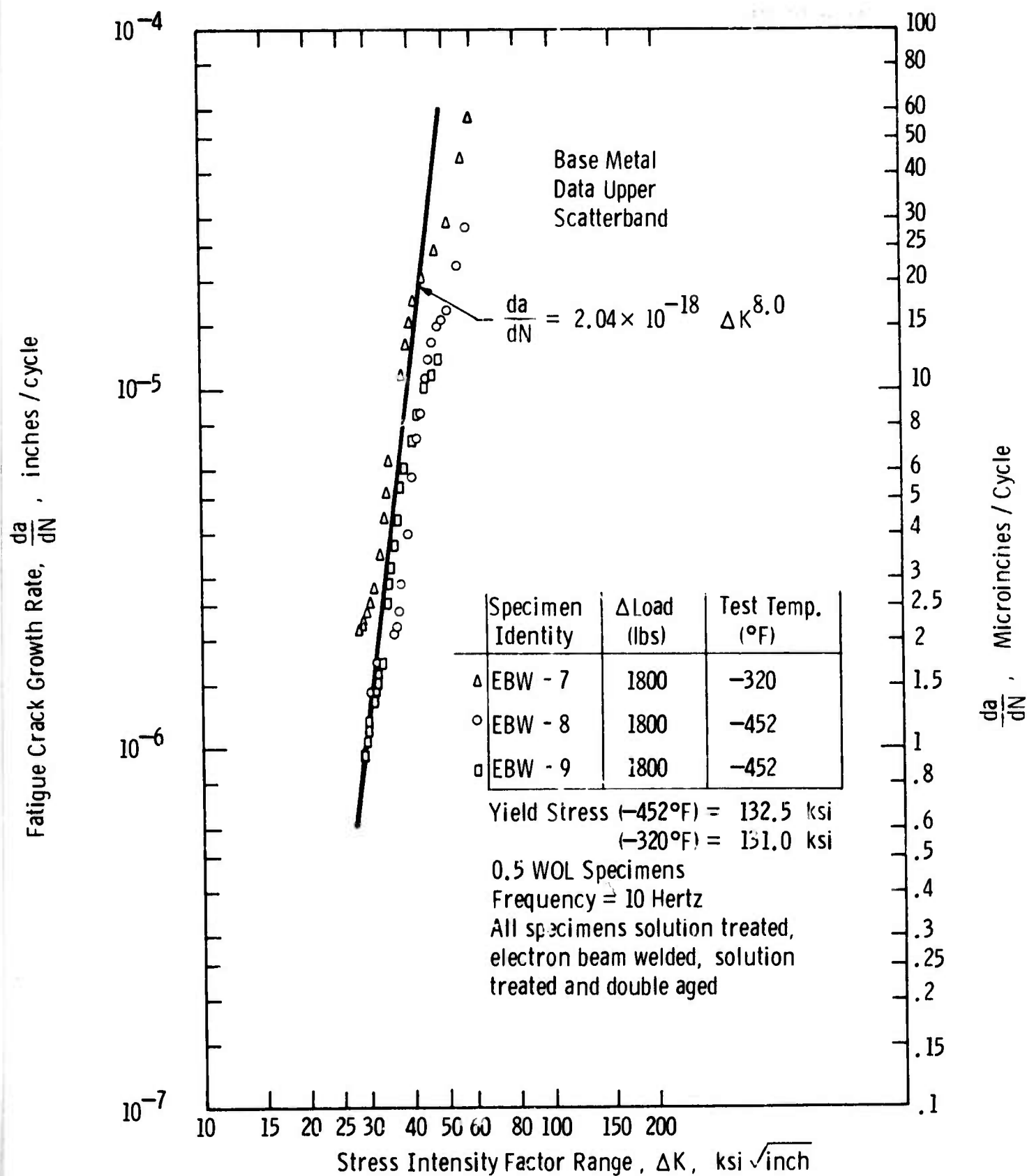


Fig.6-34 Fatigue crack growth rate properties of Inconel X750 electron beam welds in cryogenic environments

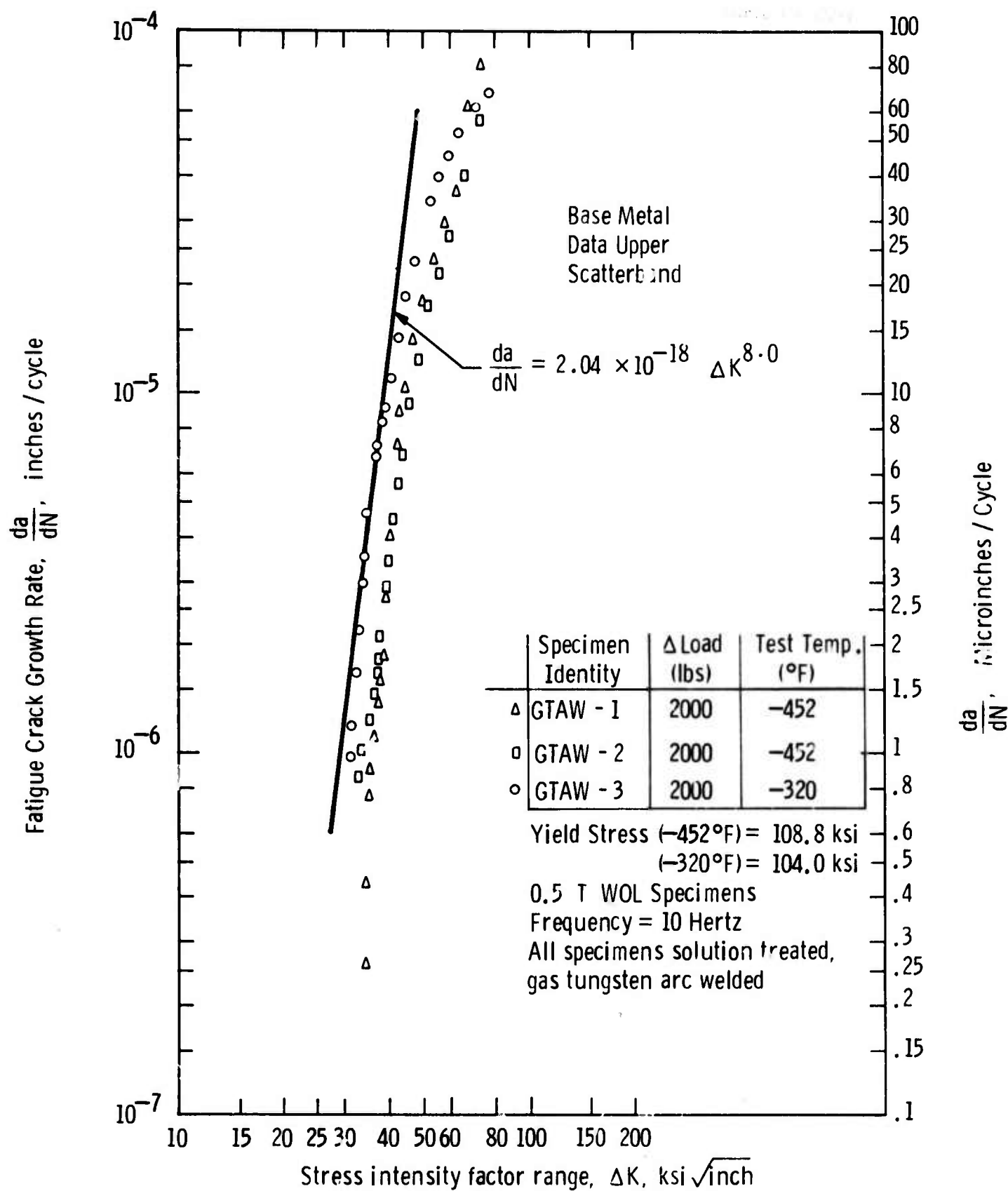


Fig.6-35-Fatigue crack growth rate properties of Inconel X750 gas tungsten arc welds in cryogenic environments

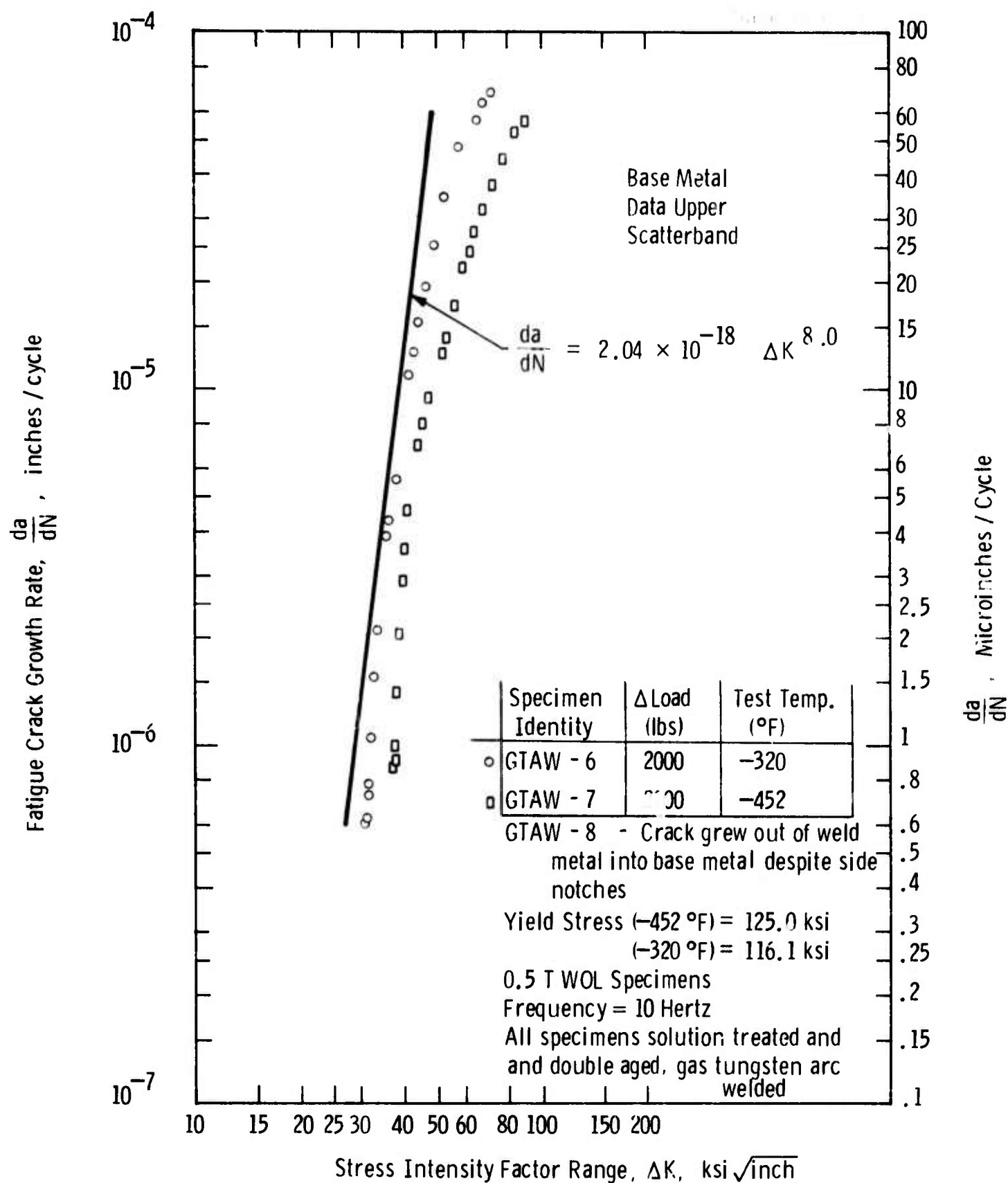


Fig.6-36-Fatigue crack growth rate properties of Inconel X750 gas tungsten arc welds in cryogenic environments

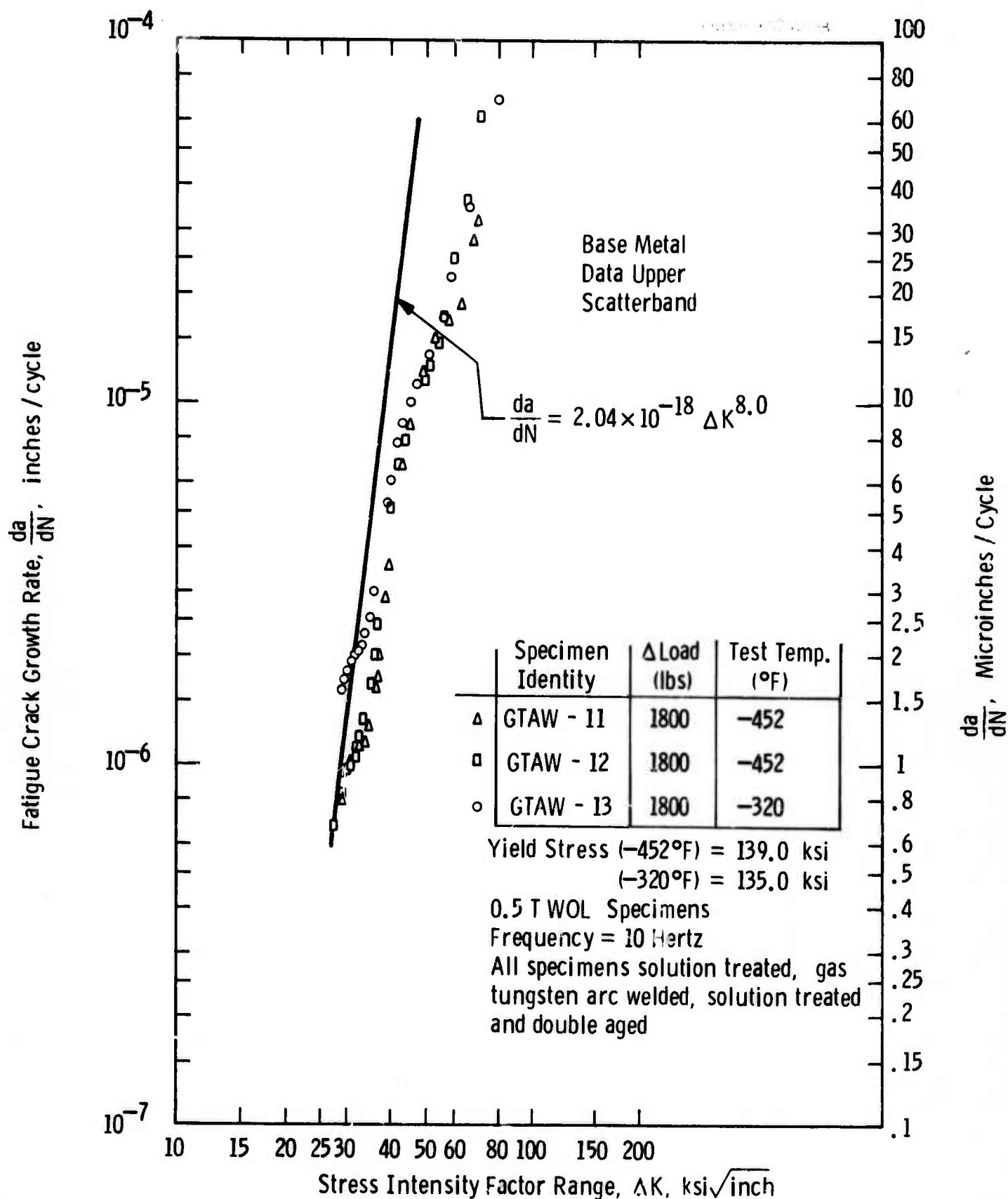


Fig.6-37-Fatigue crack growth rate properties of Inconel X750 gas tungsten arc welds in cryogenic environments



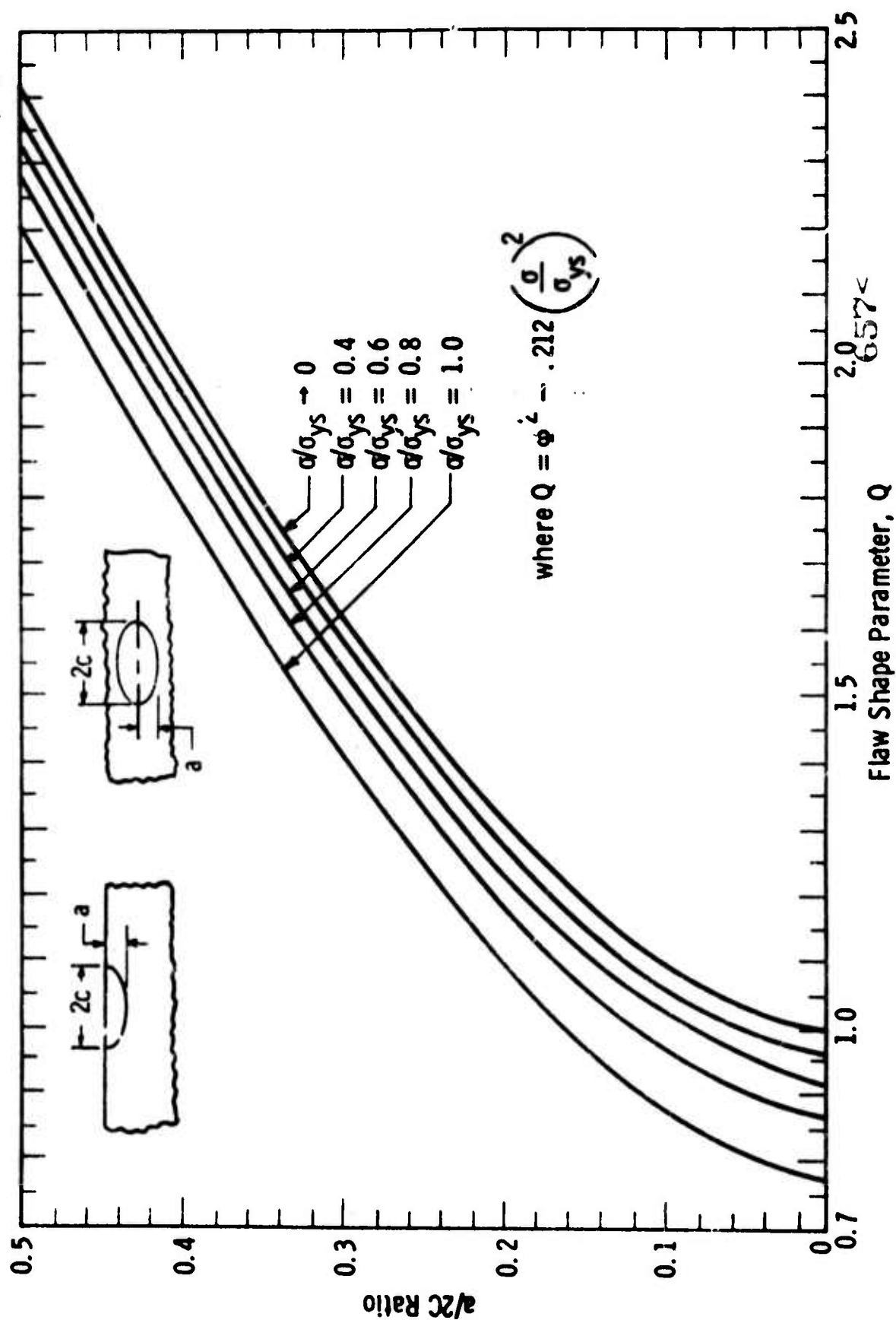


Fig. 6. 38 —Flaw shape parameter curves for surface and internal cracks

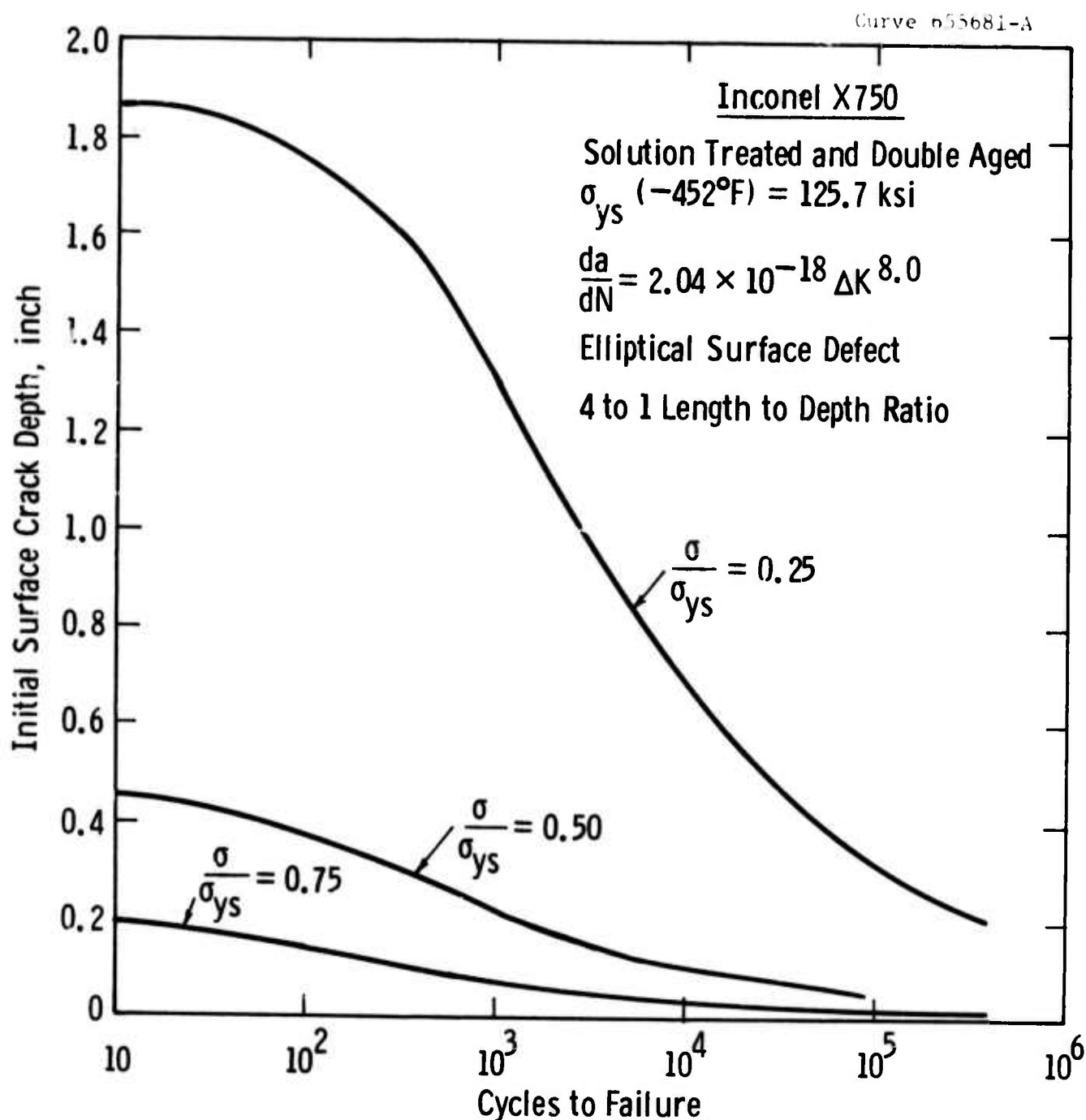


Fig. 6. 39—Cyclic life curves for Inconel X750 superconducting generator rotor

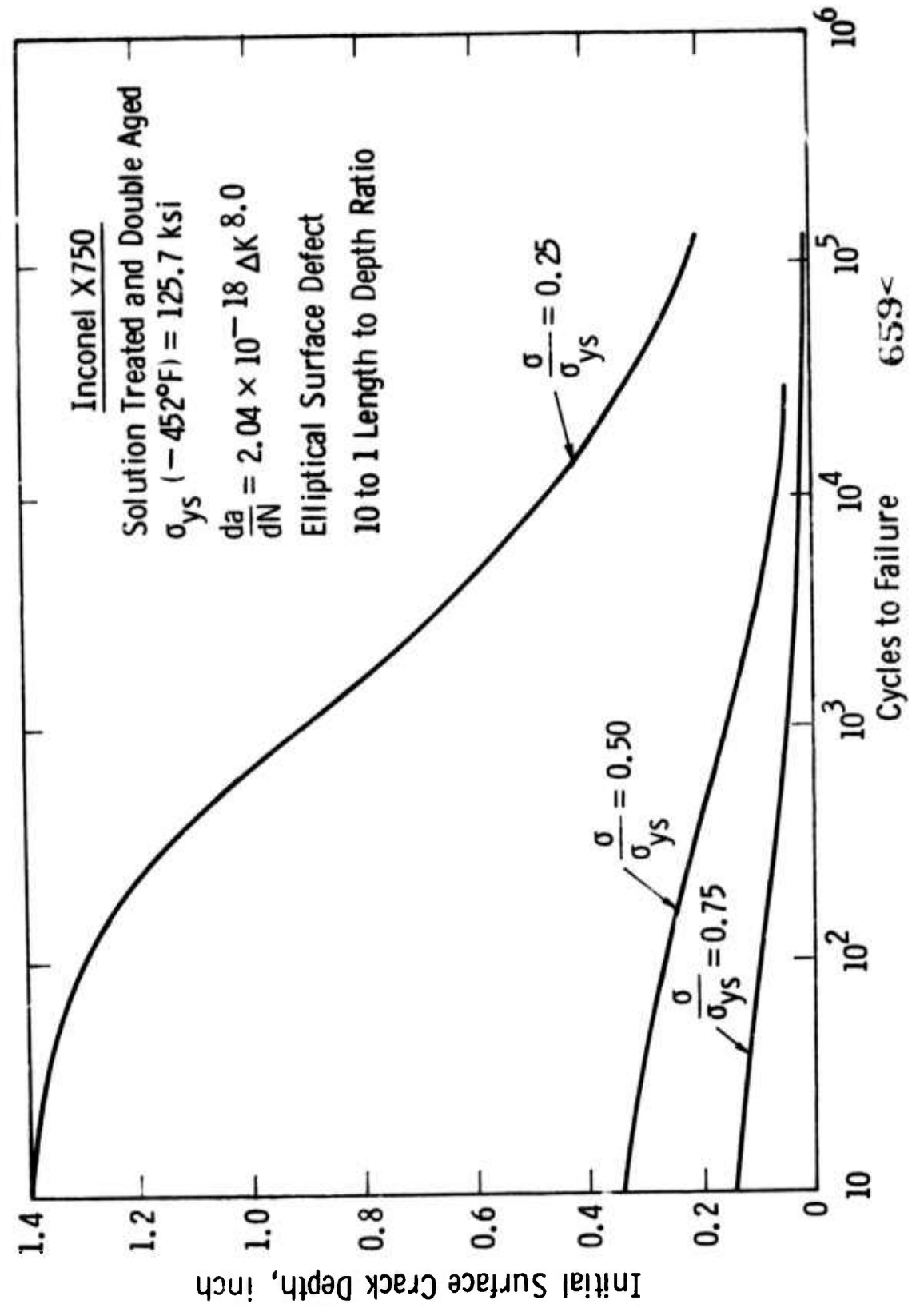


Fig. 6. 40—Cyclic life curves for Inconel X750 superconducting generator rotor

## 7. MICROSTRUCTURAL ANALYSIS

The purpose of this phase of the work is two-fold: (a) examine the microstructure of tested specimens to determine the cause and mode of failure, (b) correlate the microstructural features with mechanical test data to establish failure mechanisms and effects of processing variables. With this knowledge in hand, one is able to identify critical areas in processing or end use and suggest modifications for an optimization of processing, material use, and performance realization. A large portion of the effort during the period of this report was devoted to the Inconel X-750 material. Welded specimens representing tensile, fracture toughness, and crack growth rate tests following various heat treatments were examined (Table 3-1). Also examined were tensile specimens representing two alternative melting practices, and these are compared to the original material reported upon in the previous report. Also examined were test specimens prepared from HIP X-750 (Hot Isostatically Pressed) and K-58 materials.

### 7.1 Inconel X-750 Welds

#### 7.1.1 Tensile Specimens

Two major groups of specimens were examined, i.e., prepared by Gas Tungsten Arc welding and by Electron Beam welding (see section 5.3.1.3 for details). It is of interest to state here that all tensile specimens which were not subjected to post-weld heat treatment failed in the heat affected zone; those specimens which were heat treated following welding broke in the base metal far away from the heat affected zone. The extent of the heat affected zone was determined by microhardness measurements. These measurements indicate that heat affected zones extend to about 9 grain diameters from the weld-base material interface.

Furthermore, the tensile specimens represent a variation in grain size that is consistent with the range of grain sizes reported for the base metal in the First Semi-Annual Report. These results, summarized in Table 7-1, were obtained from the gauge sections of the respective specimens in areas removed from the actual fractured surfaces and the heat affected zones.

TABLE 7-1

Grain Size of Welded  
Inconel X-750 Specimens

<u>Specimen</u>	<u>Material Code (Table 3-1)</u>	<u>Grain Size, <math>\mu\text{m}</math> (Intercept Method)</u>
ST/GTAW	3511	100
ST/GTAW	3512	143
ST/GTAW	3513	105
STDA/GTAW	3611	75
STDA/GTAW	3612	143
STDA/GTAW	3613	128
GTAW/STDA	3711	106
GTAW/STDA	3712	156
GTAW/STDA	3713	140
ST/EBW	3211	94
ST/EBW	3212	154
ST/EBW	3213	99
STDA/EBW	3312	163
EBW/STDA	3411	104
EBW/STDA	3412	133

Figure 7-1 demonstrates the mode of RT fracture typical of welded specimens that were not subjected to post-weld heat treatment. The fracture originates and propagates across the heat affected zone. In no case did the fracture of tensile specimens originate or propagate through

the weld itself. Only in crack growth specimens, discussed below, and in tensile-notched specimens, where the initial fatigue-notch was introduced in the weld, did the fracture originate there and continued to propagate through the weld material. At lower temperature, the response of the material is somewhat different. Figure 7-2 shows light micrographs of cross section near and away from the fracture edge and the heat affected zone. Both micrographs show a high incidence of deformation crack openings that propagate in a laminar fashion and are not confined to either intergranular or cross granular fracture. Both specimens shown in Figs. 7-1 and 7-2 were solution treated and welded without a post-weld treatment.

The origin of fracture in a specimen solution treated and Gas Tungsten Arc welded (Code 3515) is shown in the SEM micrograph of Fig. 7-3. The area is dominated by Al + Si rich impurities, probably in the form of non-conductive aluminum-silicates. Such defects have been previously associated with fractures of base-metal specimens (see Fig. 7-13, First Semi-Annual Report). Other details of the fracture surface are shown in Fig. 7-4. The intergranular nature of fracture is evident in Fig. 7-4(a) where cracking is also marked. A common feature of the fractured surfaces is the dominance of plate-like MC carbides, identified to be of the type (Ti,Nb)C by energy dispersive X-ray analysis.

The degree of incidence of cracking is lower in specimens heat treated after welding, but again, it seems that cracking is more prevalent in specimens tested at low temperatures, Fig. 7-6, as compared to specimens tested at room temperature, Fig. 7-5. As mentioned above, in specimens heat treated after welding, failure was not associated with the heat affected zone. Consequently, the fracture surface will have the general features typical of Inconel X-750 base metal that was subjected to the standard 2-step aging treatment. The SEM micrographs in Fig. 7-7, which can be compared to Fig. 7-14 in the First Semi-Annual Report, show a typical intergranular mode of fracture.

To complete the group of Gas Tungsten-Arc welded specimens we examine now the fracture characteristics of a specimen heat treated prior to welding with no post-weld treatment. The details in Fig. 7-8 are similar to those in Fig. 7-6.

The general characteristics described above for the Gas Tungsten-Arc welds apply also to the electron-beam welds in that specimens that were not post-treated failed in the heat affected zone while specimens treated after welding failed far from the heat affected zone. Failure in the weld itself were observed only in notched tensile specimens and crack growth rate specimens, where the notch was introduced in the center of the weld. Figure 7-9 shows the general fracturing of specimens tested at room temperature with failure in the heat affected zone. The details of this micrograph are similar to the details shown in Fig. 7-1. Another interesting comparison can be made between Figs. 7-10 and 7-2. There is substantially more cracking in the specimen that was welded by Gas Tungsten Arc as compared to the specimen welded by Electron Beam, both were without post-weld treatment and were tested at liquid helium temperature. The same differences were found in specimens heat treated after welding. That is, a specimen welded by Electron Beam (Code 3412) showed less cracking than exhibited by a specimen welded by Gas Tungsten Arc, such as shown in Fig. 7-6.

Typical SEM micrographs of fractured surfaces are shown in Fig. 7-11. In both specimens the intergranular mode of fracture is evident. MC carbides are prevalent on the fracture surface of the specimen not treated after welding. The fracture of the specimen treated after welding is identical to that observed in base metal heat treated Inconel X-750 specimens.

Unusual defects that can be traced to the starting material are shown in Fig. 7-12. The origin of fracture in Fig. 7-12(a) is associated with particles that appear to have been previously molten, (Fig. 7-12(b)) and were identified by energy dispersive X-ray analysis as rich in Al and Si (Fig. 7-12(c)). Defects like these have been found previously in the base material and are, therefore, not associated with the welding process.



### 7.1.2 Fatigue Crack Growth Rate Specimens

Figure 7-13 illustrates the main features of the fatigue crack growth rate specimen. All such specimens discussed in this section were pre-cracked at room temperature in the weld fusion zone centerline, (see Section 5), and the rate of crack propagation was then measured at low temperatures, i.e.,  $-7.7^{\circ}\text{K}$  and  $-4.2^{\circ}\text{K}$ . Figure 7-13(a) shows a ductile fracture typical of the room temperature pre-crack. Figure 7-13(b) shows classical fatigue striations, caused by a planar (at least locally) propagation of the fatigue crack. In Fig. 7-14 we show the now familiar pockets of MC carbides. A typical energy dispersive X-ray trace is shown in Fig. 7-14(a). These carbide pockets are seen also in Fig. 7-13(b) where one may conclude that the carbide pocket (arrow) did not affect the planar propagation of the crack within the confinement of the grain itself. In all micrographs in this section, the large arrow indicates the direction of the motion of the crack front.

The apparent insensitivity of the crack front to carbide particles is further demonstrated in Fig. 7-15 which shows fatigue striations in an area where two isolated acicular  $\text{M}_{23}\text{C}_6$  carbides are embedded. Usually, however, only MC type carbides were found. The fatigue striations show little bending around the carbide; the crack front is assumed to have gone through the carbide-matrix interface. The more pronounced bends in this crack front are due to low angle boundaries. Thus, it seems that the crack front is sensitive to crystallographic orientations, a common feature in "stage I" fatigue crack propagation. Although sections showing a smooth crack front (Fig. 7-15) were frequently observed, the more common appearance of the crack front surface is shown in Fig. 7-16. The direction of propagation of the major crack front, which is normal to the fine striation lines is indicated by the long arrows in both micrographs of Fig. 7-16. It is clear that massive secondary (branching) cracking has occurred along the crack front in both types of specimens, i.e., those that did, and those that did not receive a post-weld heat treatment. Such a process



will absorb high amounts of energy, a fact that may account, at least in part, for the high toughness of the weldment material (see data in Section 6).

Features observed in Gas Tungsten Arc Welds were also observed in Electron-Beam welded crack-growth specimens. It seems, though, that the crack front advancement was smoother, although occasional crack branching were observed also. Figure 7-17 shows smooth crack propagation in (a) and crystallographic orientation of the crack front with secondary cracks at boundary in (b), in a specimen tested at  $-4.2^{\circ}\text{K}$  with no post-weld treatment. Somewhat rougher surfaces, showing crack branching and tearing along the crack front are shown in Fig. 7-18 which depicts typical areas from a specimen subjected to post-weld heat treatment and tested at  $77^{\circ}\text{K}$ .

#### 7.1.3 Comments

The microstructural data presented above and the tensile test results (Section 6) indicate that, regardless of previous history, welded tensile specimens that were not subjected to post-weld treatment failed in the heat affected zone while specimens heat treated after welding exhibited failures and strengths comparable to the base metal subjected to the same heat treatment. From microhardness measurements it was found that the heat affected zones extend to about 9 grain diameters from the weld interface. It was also found that the heat affected zone of GTAW specimens show higher hardness as compared to EBW specimens. This is in agreement with the tensile data which show that at all test temperatures GTAW specimens not subjected to post-weld heat treatment had higher strengths than comparable EBW specimens.

There was no difference in strength for both groups for specimens heat treated after welding. Furthermore, the strengths of these specimens is comparable to the strength of the base metal results for INCO X-750, shown in Figs. 6-9, 6-25 and 6-26, First Semi-Annual Report.

It is therefore clear that the welding process softens the material in the heat affected zone so that the strength of that zone is lower than the rest of the material, further away from the welded area. The temperature generated by EBW is apparently sufficient to cause localized annealing, while the multipasses and slower cooling rates associated with GTAW induces a partial aging effect that results in higher strength of the heat affected zone (compare Figs. 7-4(b) and 7-9(c)). In both cases, as was shown above, the effect is not optimal, thus the strength at the heat affected zone is below that of the fully aged material.

The problem of cracking may be related to a combination of high deformation within the grain and final crack opening at grain boundaries. Cracks shown in Fig. 7-2 were also observed near the fracture surface of the base metal, Fig. 7-12, first Semi-Annual Report. The higher incidence of this cracking effect in the heat affected zones of welded specimen may be attributed to residual stresses following welding.

## 7.2 Processing Practices, Inconel X-750

### 7.2.1 Tensile Specimens

Tensile data was obtained from Inco X-750 material prepared by three different melting practices (see also Table 5-3, First Semi-Annual Report). Material designated MP1 was received in the form of a 10" diameter billet. The billet was press-forged<sup>(1)</sup> to 15" x 17" bar from the original 20" diameter casting (prepared by double melting process, i.e., VIM + VAR), and then hot-rolled at temperatures between 1150 and 1200°C, with intermediate reheats to the final 10" diameter billet. Specimens prepared from this billet exhibited a range of grain sizes, varying from 70 to 150  $\mu\text{m}$ , as indicated in Table 7-1, First Semi-Annual Report and also in Table 7-1 of this report.

Material designated MP-2 was press-forged to 15" x 17" bar from the original 20" diameter billet. This casting was subjected to a

different melting sequence, i.e., AAM + VAR (Air-Arc-Melt + Vacuum-Arc-Remelt). The bar was then hot rolled, to a 4" diameter bar. Specimens prepared from this bar showed little variation in grain size, with a grain diameter much smaller than the MP-1 material, Table 7-2. The material designated MP-3 was received in the form of a 2" diameter billet. The billet was hot-rolled to size from a 20" x 20" square ingot prepared by a single melting process i.e., VIM (Vacuum- Induction-Melt). Specimens prepared from MP-3 material showed also no variation in grain size from specimen to specimen. However, a bimodal distribution of grain sizes was noticed, with most of the grain less than 10  $\mu\text{m}$  in diameter (Table 7-2). The general microstructural features of the three X-750 materials are shown in Fig. 7-19.

TABLE 7-2

Grain Size Distribution in  
MP-2 and MP-3, INCO X-750  
Materials

Grain Size Range, $\mu\text{m}$	Percentage of Grains in the Range	
	MP-2	MP-3
0-5	40	23
5-10	25	45
10-20	25	15
> 20	10	16

TABLE 7-3

Microprobe X-Ray Counts in the Grain;  
Results are Average of 3 Point-Counts  
Per Specimen

	<u>NbKa</u>	<u>TiKa</u>	<u>NiKa</u>	<u>AlKa</u>	<u>CrKa</u>	<u>FeKa</u>
MP-1	150	725	11100	110	8200	1175
MP-2	150	760	10250	70	7800	1100
MP-3	157	710	11600	80	8300	1300
HIP	145	830	10500	95	7800	1130
K-58	83	14	3350	16	7700	7400

The fracture characteristics of specimens prepared from MP-2 and MP-3 materials are also different from those prepared from MP-1. Figures 7-20 and 7-21 should be examined together with Fig. 7-6 where the general deformation characteristics of the three materials can be compared. It is evident from the amount of distortion and slip-band density, that MP-2 and MP-3 specimens were subjected to higher strains before failure as compared to MP-1. This is consistent with the data (Section 6) where the total elongation for MP-1 material at  $-4.2^{\circ}\text{K}$  was less than 10% (see Fig. 6-1, First Semi-Annual Report) while the MP-2 and MP-3 materials sustained more than 25% elongation before failure. Deformation cracking and severe wedge opening at grain boundaries which extended into the grain are characteristic of MP-1 material. On the other hand, Figs. 7-20 and 7-21 indicate only occasional cavitation at grain boundaries without further extension or propagation of these defects. The fracture mode in MP-2 and MP-3 has changed to a mixture of intergranular and cross-granular fracture (Fig. 7-22) as compared to pure intergranular fracture in MP-1 material. It is further interesting to note that intergranular failure is prevalent in the band of larger grains, (Fig. 7-22(c)) while cross-granular failure dominates areas of very small grain sizes (Fig. 7-22(b)) in the same MP-3 material.

Typical microstructural features of HIP material (Code 61) are shown in Fig. 7-23. From the point of view of macroscopic grain boundaries, the HIP material exhibits a wide distribution of grain sizes emanating from hot-pressing a variety of powder particle sizes. It should be noted, however, that the large "grain" probably represent prefused smaller powder particles as is clearly evident from the sub-boundaries which are prevalent in every large particle (Fig. 7-23). The distribution of elements and carbides is, however, dominated by the interparticle boundaries, a point which is discussed later in the text. The fracture characteristics of the HIP condition material is illustrated in Figs. 7-24 and 7-25. Figure 7-24 is a light micrograph showing severe deformation within the grains and indicating a mixture of cross-granular and intergranular failure. The SEM micrographs of fracture surfaces clearly demonstrate the dominance of cross-granular failure in HIP X-750 as compared to intergranular failure in the large grain X-750 material designated MP-1. Both specimens shown in Fig. 7-25 were aged, and then tested at 4.2°K.

#### 7.2.2 Microprobe Analysis

Microprobe analysis was conducted to test for possible differences in elemental and phase distribution among the four X-750 materials, i.e., MP-1, MP-2, MP-3 and HIP. Table 7-3 shows results of point count inside the grain for the various materials. This table indicates that there are no major differences in the basic micro-comparison of the four X-750 materials, in agreement with the chemical analysis shown in Table 5-3 of the First Semi-Annual Report. The data in Table 7-3 indicates a small increase in the level of Ti in the HIP material. Otherwise there are no indications of segregation or depletion in any of the major elements.

The microprobe traces, however, reveal the nature of the major carbide precipitates. Figure 7-26 shows the areas through which the probe traces were taken with the results shown in Figs. 7-26-A1 through 7-26-C1. In all four materials (MP-2 is not shown) the carbides appear

to be of only one kind, namely, the MC, (Nb,Ti)C carbides. None of the traces show a local rise in the level of Cr, which would occur when the beam has passed through a  $M_{23}C_6$  type carbide.

Figure 7-26-A1 shows carbides in the grain boundary (A), and also, occasionally found MC carbides within the grain (B). Note the Al peaks which are associated with areas around the carbides.

Figure 7-26-B1 is typical for the MP-2 and MP-3 materials, STDA conditions. Again, only MC type carbides are resolved. It should be noted that the carbides appear only in high angle grain boundaries but are not associated with twin boundaries. Again Al peaks appear at the edge of the carbide particles. Figure 7-26-C1 represents a longer trace across a few grains in the HIP material (not heat treated). It is evident here that the only precipitates detected are the (Nb,Ti)C carbides which are present in high angle boundaries only (marked A-E). There is no indication of carbide precipitation within the grains or along sub-boundaries within the large grains (grain 1 and 2, for example). The Al trace, not shown in Fig. 7-26-C1 showed a large peak in the boundary marked A.

### 7.2.3 Comments

Although X-750 is a  $\gamma'$  precipitation strengthened superalloy, it is clear that properties of the material are influenced not only by the melting and consolidation practice, but by the thermal-deformation procedure as well.<sup>(2)</sup> Thus, inclusions, elemental distribution, dislocation structures, volume and morphology of  $\gamma'$  and carbides, and grain size, are significant parameters that affect the mechanical behavior of the final product. The microstructural data presented above indicates a substantial difference in the size and size distribution of grains among the various X-750 materials. Chemistry and mode and type of precipitating carbides seem to be the same, i.e., MC type carbides that occur mainly in high angle grain boundaries. Our analysis did not, however, include transmission electron microscopy, which could determine variations in  $\gamma'$  volume and mode of precipitation and variation in

dislocation structures. Since all four X-750 materials were subjected to different amounts and kind of mechanical working, we cannot at this stage of the investigation, relate the observed mechanical behavior to the melting practice alone. It is possible, however, to equate the increase in ductility in the MP-2 and MP-3 materials to the smaller grain size,<sup>(3)</sup> which results in a shift from intergranular to cross-granular fracture.

The smaller grain size in these materials is probably a result of dynamic recrystallization during hot-rolling.<sup>(2,3)</sup> The increase in strength in MP-2 and MP-3 is, at least partially, related to the smaller grain size. The temperature dependence of strength lends support to the above conclusion. The data (Figs. 3-2 and 3-3) show that the difference in strength among the four X-750 materials increases with decreasing temperature. The grain size dependence of strength, usually expressed in terms of the well known Hall-Petch relation, i.e.,  $\sigma = \sigma_0 + Kd^{-1/2}$ , contain the slope term K, which itself is temperature dependent. Thus, as K increases with decreasing temperature, so will the incremental effect of grain size.

The fact that only MC carbides have been identified is in agreement with data obtained for a large variety of high nickel superalloys.<sup>(4)</sup> In these alloys, the dominant precipitates during aging at temperatures below 1400°F are the MC carbides.  $M_{23}C_6$  carbides start to evolve at about 1500°F and above. All X-750 materials were subjected to an aging treatment consisting of 8 hours at 1350°F, then furnace cooled to 1150°F, held for additional 8 hours and air cooled (Table 5-5, First Semi-Annual Report). It has also been observed<sup>(1)</sup> that MC carbides tend to undergo a degeneration process which creates a film of  $\gamma'$  around them. It is possible that the aluminum peaks found at the edge of the carbides are due to the formation of  $\gamma'$  envelopes.

### 7.3 Kromarc-58

Fracture characteristics of a few tensile specimens were examined. Figure 7-27 shows typical microstructural features of solution



treated specimens (Code 8000). There is a considerable amount of cavitation caused by large plastic strains before failure. In the cold worked specimens (Fig. 7-28) deformation is confined more to the fracture area. Elongated fissures which are probably a result of cold work defects are evident in Fig. 7-28(b). Typical ductile fracture is illustrated by the SEM micrograph in Fig. 7-28(a). Note that this specimen was tested at 4.2°K. Melting practice debris is shown in Fig. 7-29(b) where the chemistry of the contaminants could be attributed to slag trapped during the casting process. The fissures shown in Fig. 7-29(b) are shown to contribute to intergranular fracture, Fig. 7-30. It is most likely that the fissures are actual cavities as documented by the microprobe traces, Fig. 7-31. All elements scanned for, showed sharp dips in concentration when the beam passed over the two rows of fissures (Fig. 7-31(a)). It is conceivable that these fissures contribute to the lower fracture toughness of cold-worked K-58 material (see Section 6 ).

#### 7.4 Correlations of Structure and Properties

##### 7.4.1 Inconel X-750

The mechanical test data indicate that the welds in X-750, MP-1 material are both stronger and tougher than the base metal under comparable test conditions. It is to be noted that unless pre-notched, none of the tensile test specimens has failed in the weld. The two fracture-toughness parameters,  $J_{IC}$  and  $K_{IC}$  are higher for welds than the base metal, regardless of method of welding or heat treatment. Furthermore, a comparison of welds and of base metal specimens show that aged materials (STDA) exhibit a lower fracture toughness than solution treated materials.

The major difference between the welds and the base metal (for a given heat treatment) is in the macrostructure. The welds exhibit a dendritic structure with a very fine grain size. We have shown above that in MP-2 and MP-3 materials, which have a smaller grain size compared to MP-1, there is a transition from intergranular failure to cross-granular failure at low temperature. We can thus propose that material with small grain size, of the order of 5  $\mu\text{m}$ , is expected to have superior mechanical properties at low temperatures.



The effect of heat treatment is to be expected. In all cases of X-750, aging increased the mechanical strength which is accompanied by a reduction in fracture toughness. The increase in strength is obviously due to the formation of  $\gamma'$  precipitates (dispersion hardening) while the decrease in toughness is attributed to the formation of carbides in the grain boundaries. From the point of view of low temperature strength, the grain boundary carbides are mostly detrimental.\* It is thus recommended that an improvement in toughness may be obtained by a considerable reduction in the carbon content. It is worth noting here that, although carbon content is not the only microstructural parameter that affects the differences in toughness among the three X-750 materials (MP-1, 2, 3) the MP-2 material shows the highest fracture toughness, with only .02% C, compared to .04% C in MP-1 and MP-3 (see Table 5-3, First Semi-Annual Report). One should also note that MP-2 and MP-3 have received a considerable amount of warm working compared to MP-1. The effect of dislocation structure, interaction of dislocation and precipitates, etc., should be studied, most likely by transmission electron microscopy.

It is significant to note that the crack growth rate parameters  $n$  and  $C_0$  (Table 6-7) are insensitive to heat treatment and are also identical for the welds and the base metal. This is contrasted with a wide variation in  $K_{IC}$  and  $J_{IC}$  with structural parameters.

Fractographic studies of fracture toughness specimens showed that the high velocity critical crack front extends by following a grain boundary path (see First Semi-Annual Report). It stands to reason, therefore, that grain size, and type and morphology of grain boundary carbides would influence the energy involved in propagating this crack, thus affecting the fracture toughness parameters. On the other hand, the slowly moving crack in the fatigue-crack-growth-rate specimens is propagating mainly by following a crystallographic path.

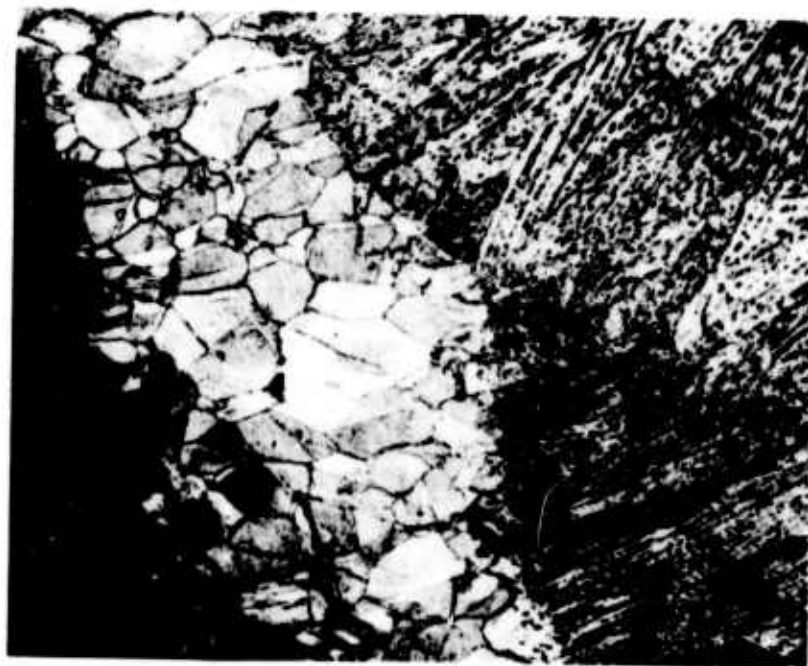
---

\* The superalloys, including X-750, were developed to provide high stress-rupture strength. The discontinuous grain boundary carbides are essential for this purpose.

The energy involved in propagating this type of a crack will be less dependent on grain size and structure of grain boundary. The  $\gamma'$  precipitates within the grain are, apparently, not affecting the motion of the slow crack. It should be possible, however, to affect the motion of the slow crack by carbide precipitation and a dense dislocation structure within the grain. The crack growth rate studies of MP-2 and MP-3 materials should provide the answer.

#### References

- (1) Don Tillick, Huntington Alloys, private communication.
- (2) R. E. Baily, in Superalloys-Processing, Metals and Ceramics Information Center, MCIC Report 72-10, September 1972, p. J-1.
- (3) S. Falop and H. J. McQueen, Ibid, p. H-1.
- (4) The Superalloys, C. T. Sims and W. C. Hagel, eds., John Wiley & Sons, New York, 1972.

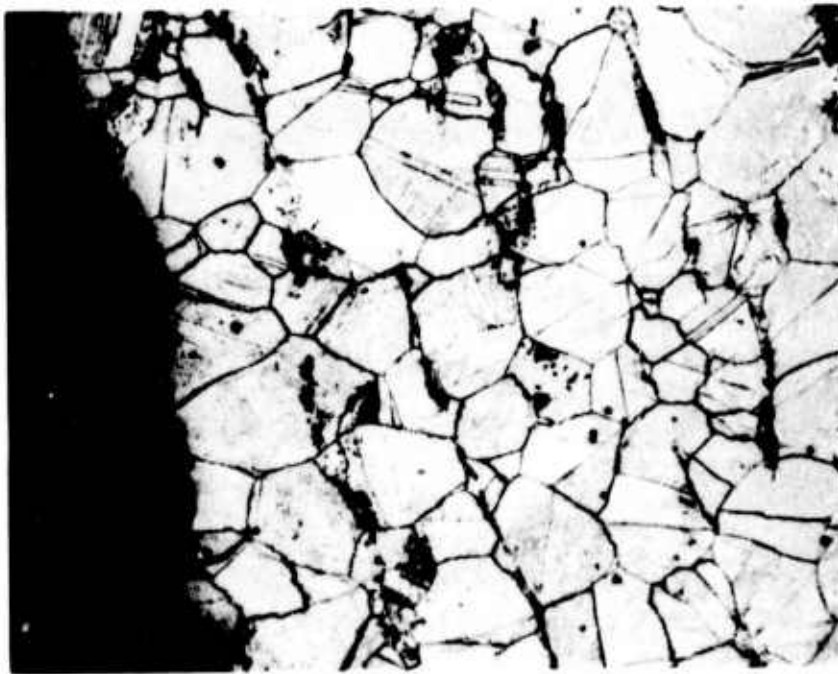


a



b

Fig. 7-1—Light micrographs showing longitudinal sections near fracture. Inco X-750, solution treated and welded specimen (Code-3511) tested at room temperature. (a) 50X (b) detail 200X



a



b

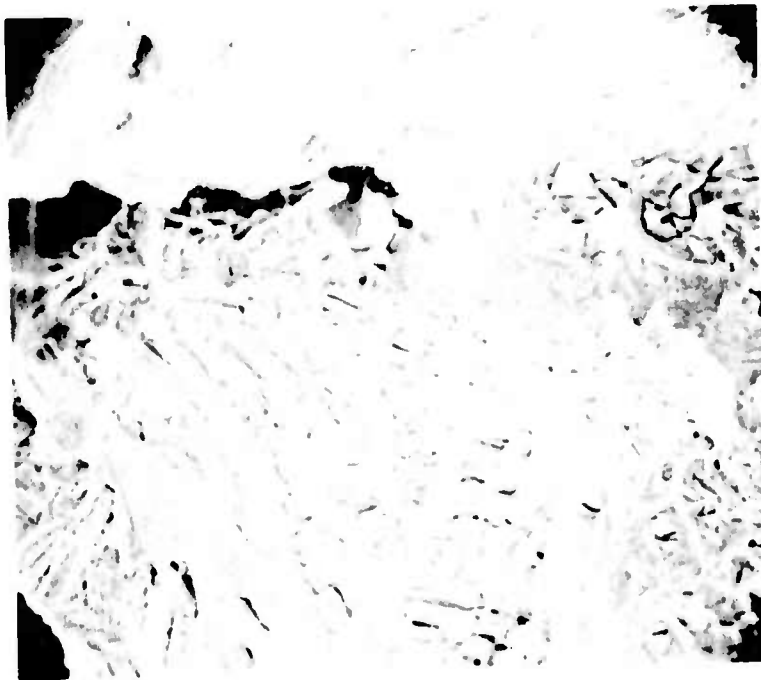
Fig. 7-2—Light micrographs (50X) showing longitudinal sections near fracture (a) and about 2 cm away from the fracture (b). Welded specimen (Code 3513) tested at 4.2°K



Fig. 7-3— SEM micrograph identifying the origin of fracture (arrow) in specimen 3511-T1 (Fig. 7-1) . The bright impurity particles are rich in Al and Si (Energy dispersive x- ray analysis) . The variations in shading are caused by charging effects from the non-conductive particles

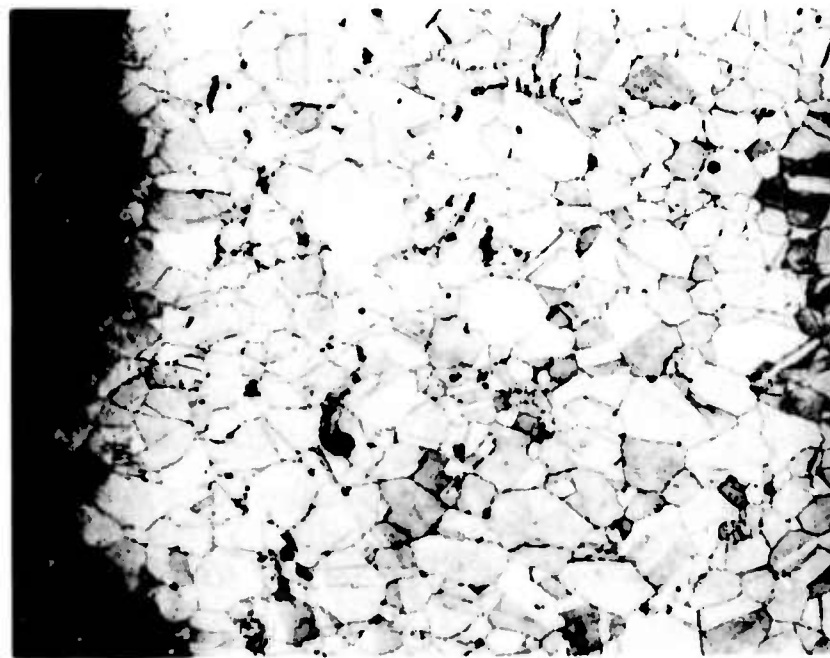


(a) 500 X

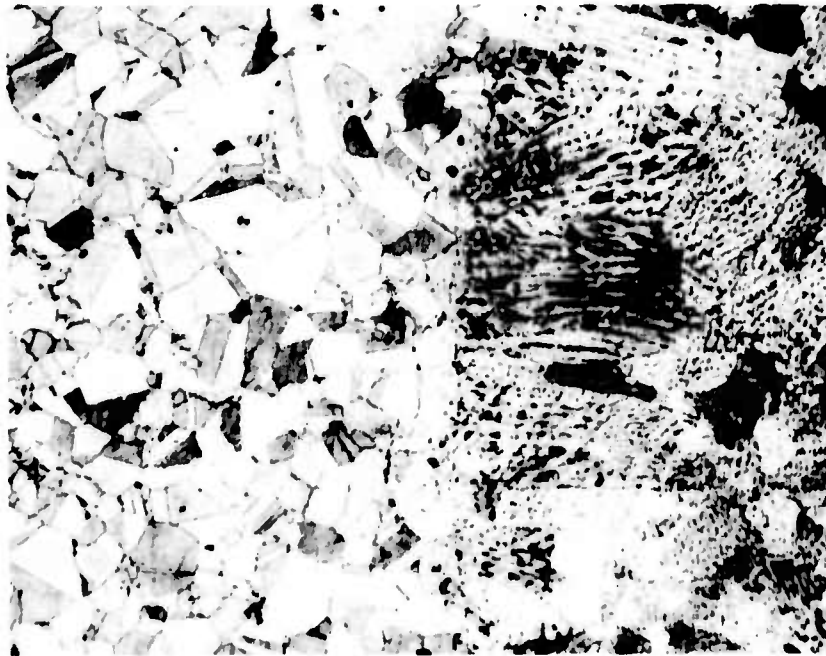


(b) 1000 X

Fig. 7-4- SEM micrographs of fracture surface of specimen 3511 (Fig 7-1) . Intergranular cracking is evident in both photos. Fissioning is marked by long arrows. The particles marked (P) in (a) and covering the surface in (b) are (Ti; Nb) C (MC carbides)



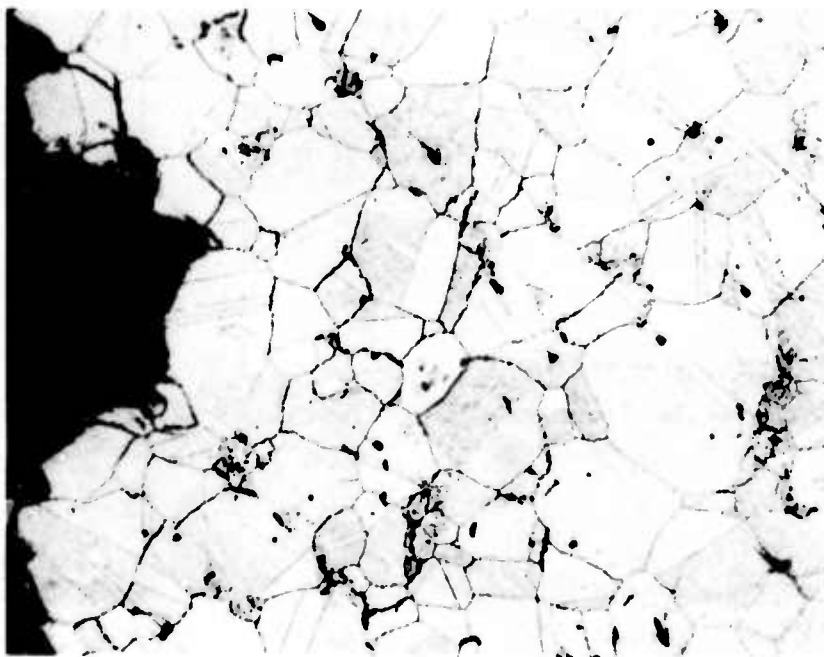
a



b

Fig. 7-5—Light micrographs (50X) of longitudinal sections near the fracture surface (a) and 25 mm away from the fracture at the weld interface (b) welded specimens (Code 3711-T11) heat treated after welding, tested at room temperature





a



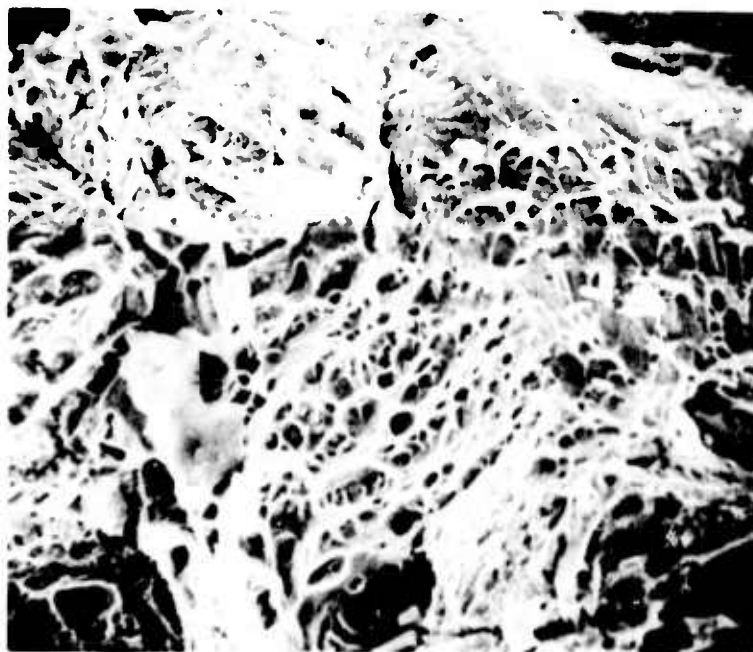
b

Fig. 7-6—Light micrographs (50X) of longitudinal sections near the fracture surface (a) and 22mm away from the fracture at the weld interface (b) Welded specimen, heat treated after welding, tested at 4.2°K (Code 3713 )



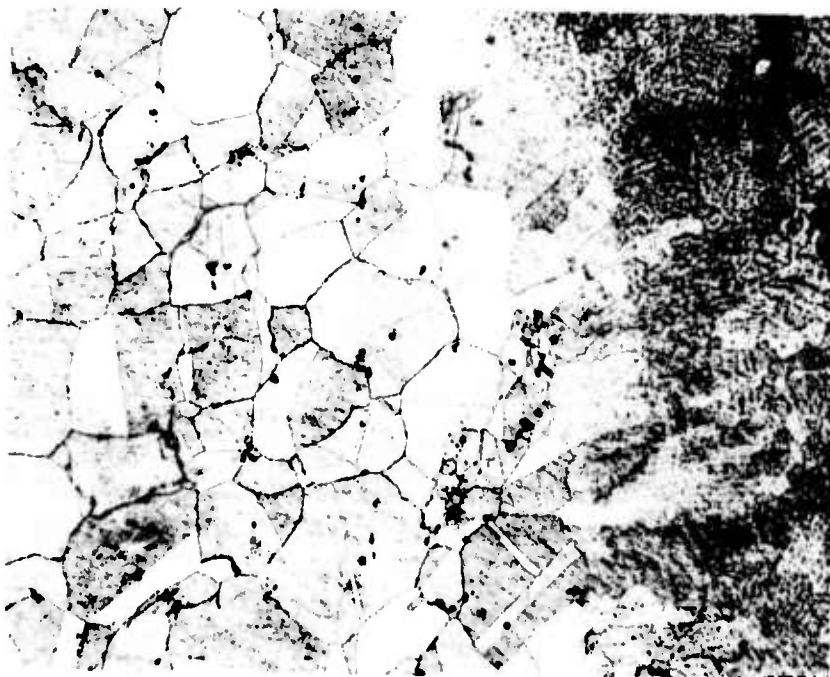


(a) 28 X

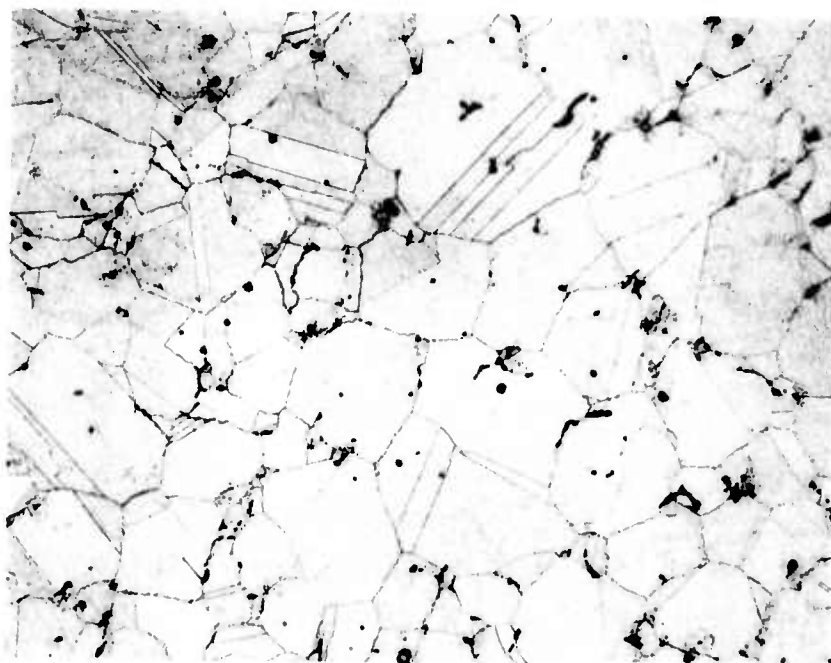


(b) 1450 X

Fig. 7-7— SEM micrographs of the fracture surface in a specimen heat treated after welding (Code 3712-12) tested at 77°K. Ductile deformation within the grain and final failure by intergranular cracking

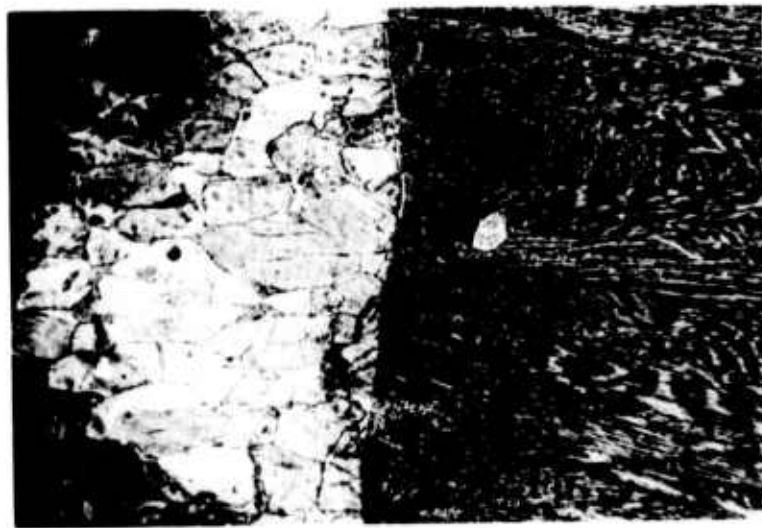


a

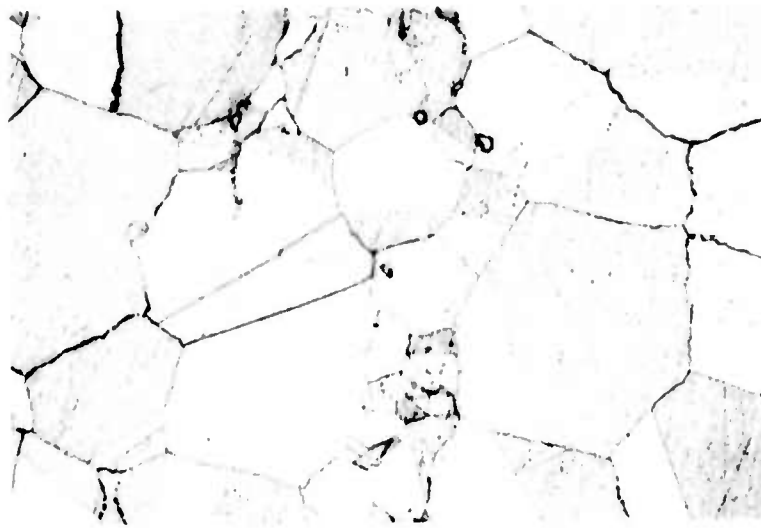


b

Fig. 7-8— Light micrographs (50 X) of longitudinal sections near the fracture surface (a) and 25 mm away from the fracture (b) near the tread of the specimen. Welded specimen (Code 3613-T8) heat treated prior to welding. No post weld treatment, tested at 4.2°K



(a) 50 X

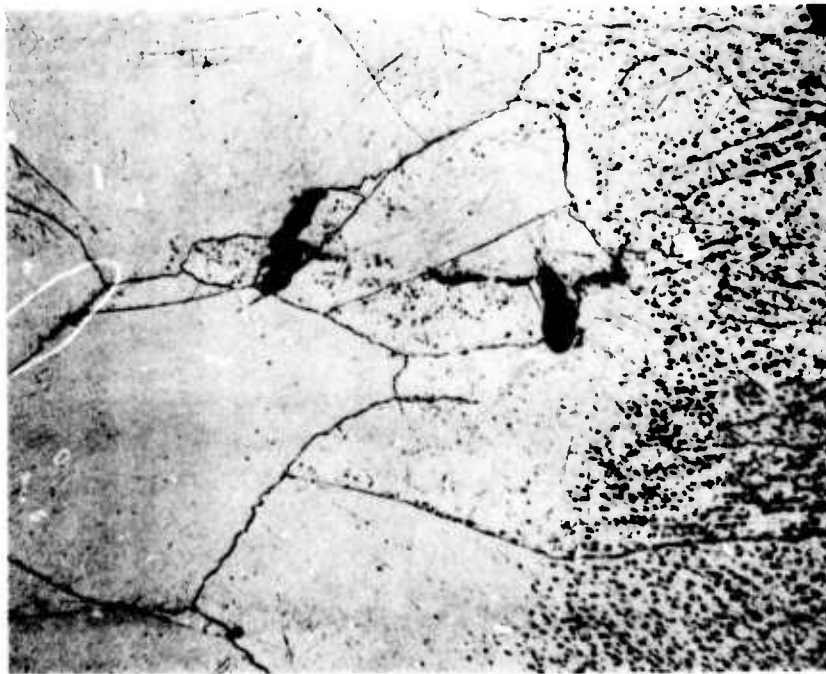


(b) 200 X

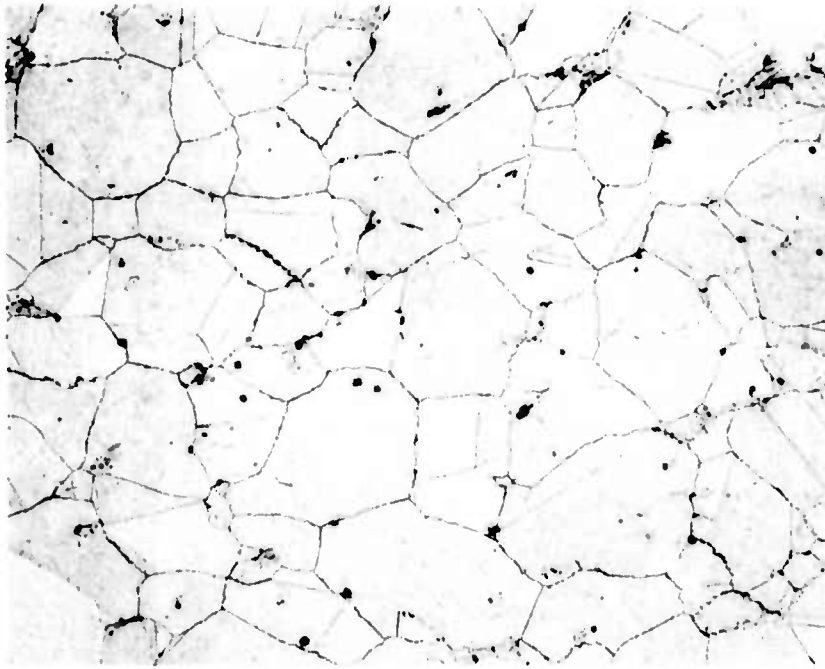


(c) 500 X

Fig. 7-9—Light micrographs of longitudinal section near fracture (a) and 30 mm away from fracture (b). SEM of fracture surface (c) Electron beam weld specimen, not treated after welding (Code 3211), tested at room temperature

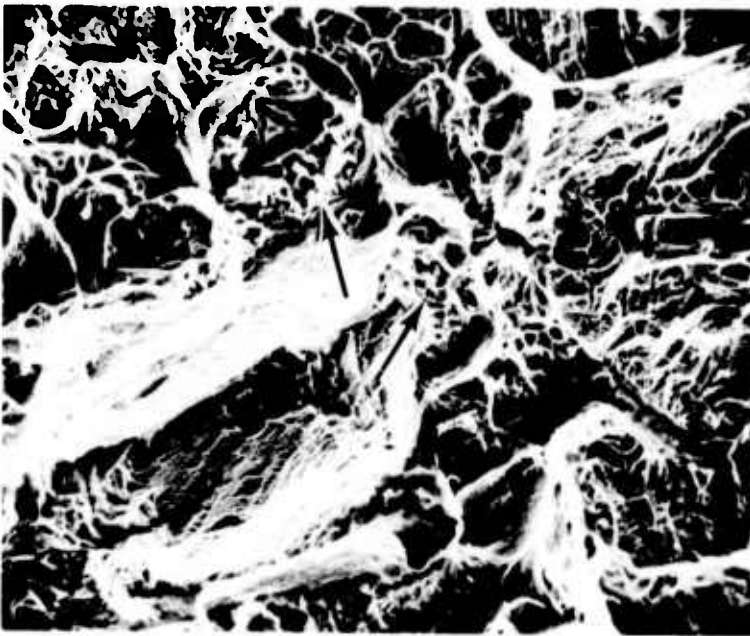


(a) 200 X



(b) 50 X

Fig. 7-10—Light micrographs showing longitudinal sections near the fracture (a) and about 23 mm away from the fracture (b) Welded specimen (Code 3213 ) Tested at 4.2 °K.



(a) 700 X

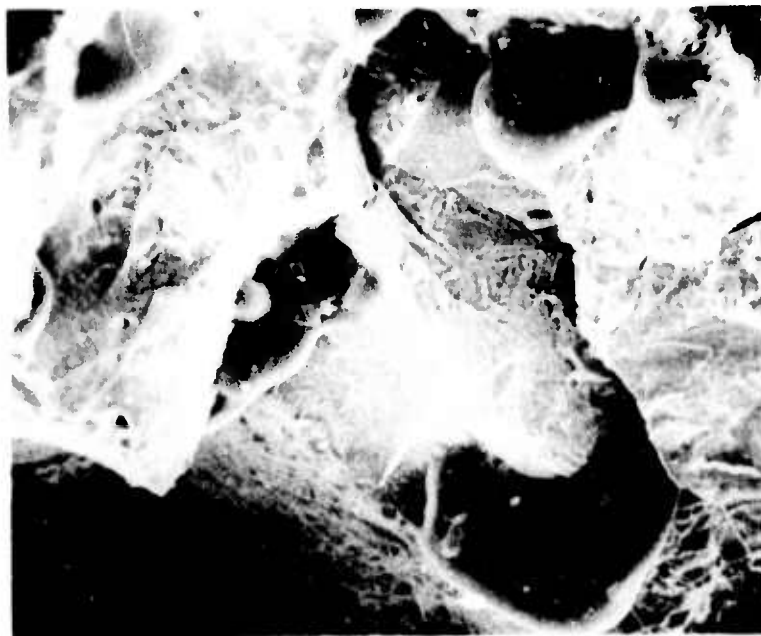


(b) 150 X

Fig. 7-11— SEM micrographs of fracture surfaces of specimen welded by electron beam.  
 (a) specimen tested at room temperature with no post weld treatment (Code 3311 ).  
 Note high incidence of MC carbides on fracture surface (arrows) (b) Specimen tested at  
 77°K heat treated after weld (Code 3412- )



(a) 65X



(b) 650X

Fig. 7-12- SEM micrographs of fracture surface of specimen 3312-T7. Origin of failure is associated with Al-Si rich molten defects



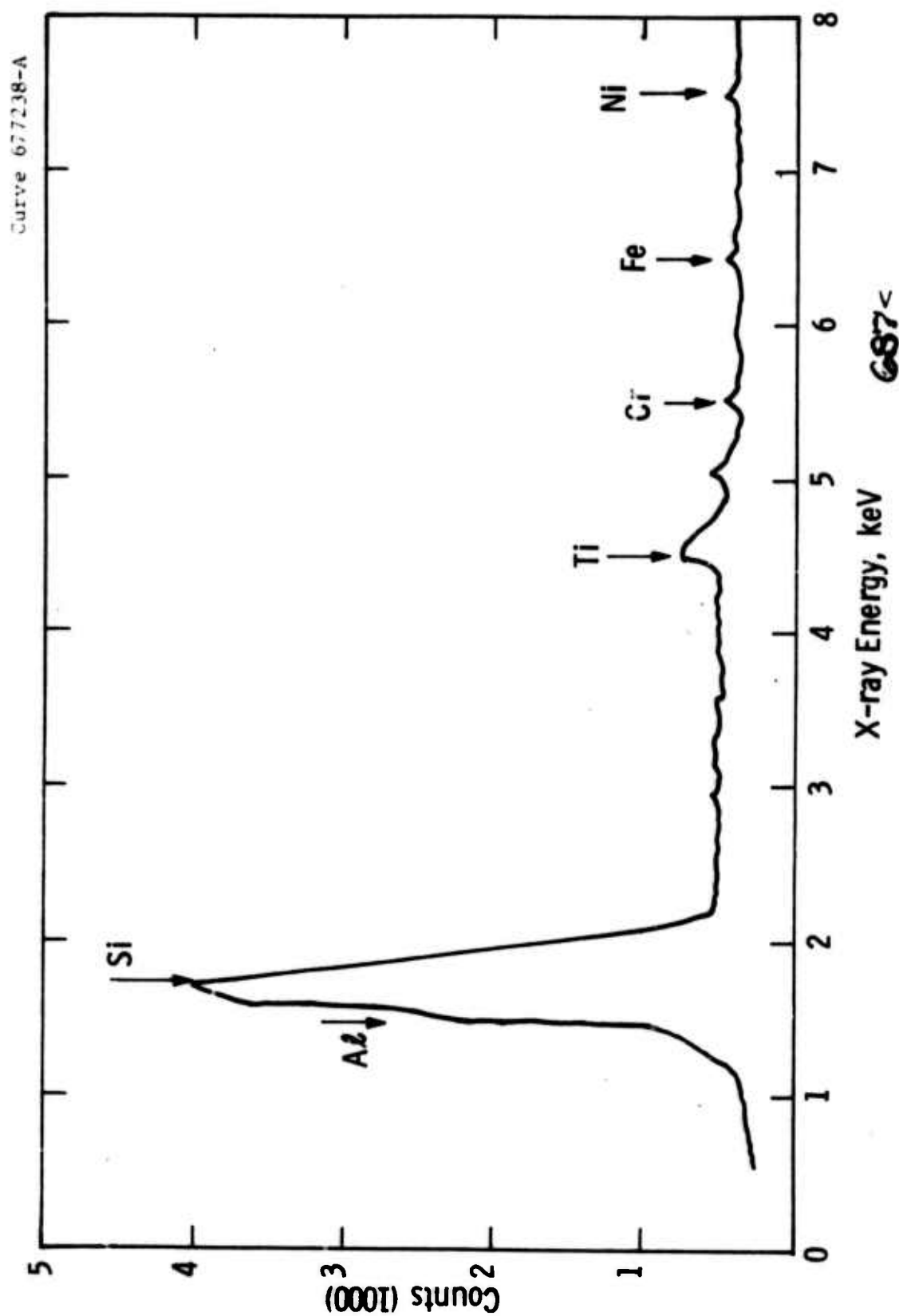
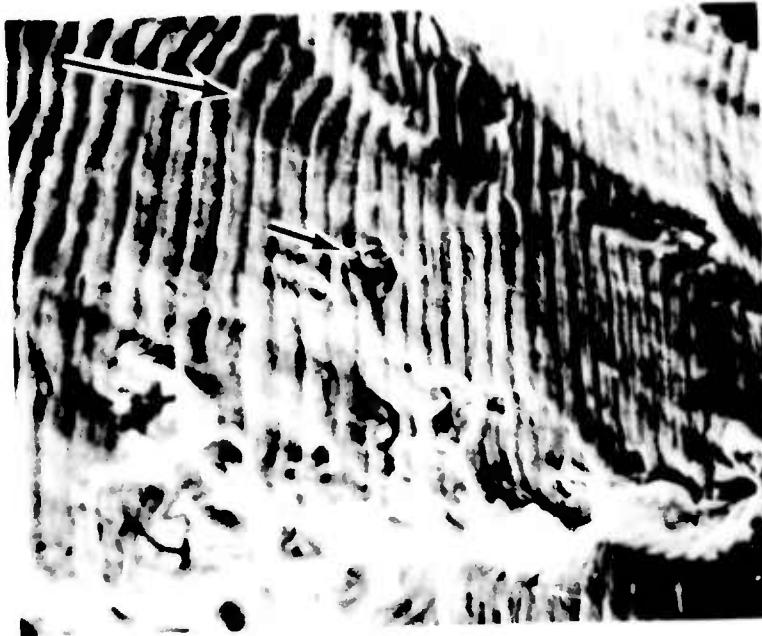


Fig. 7-12c—Energy-dispersive x-ray data from particles shown in Fig. 7-12b.



(a) 1350 X



(b) 2600 X

Fig. 7-13- SEM micrographs of fracture surfaces, crack growth in tungsten arc weld.  
(Code 3552-3) . (a) RT pre-crack. (b) Fatigue striations due to crack propagation at 77°K



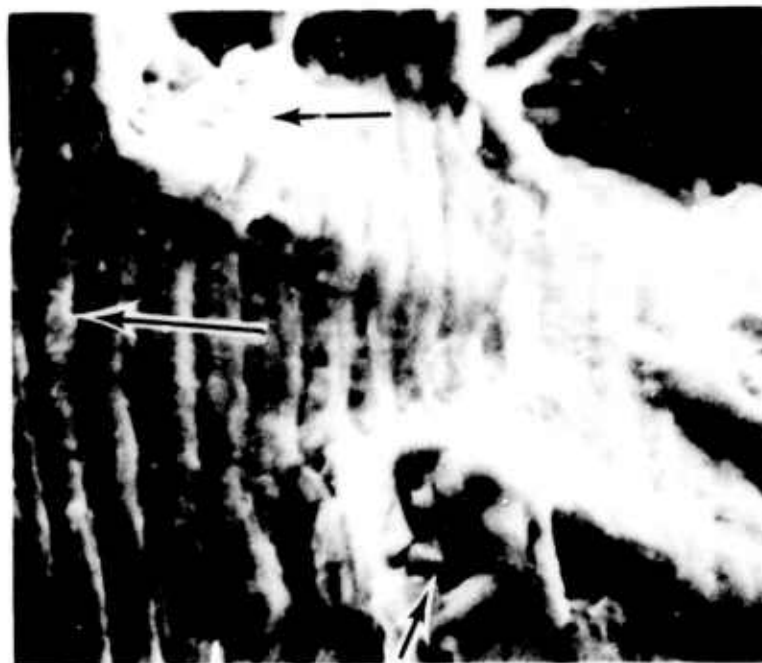


Fig. 7-14- SEM detail of Fig. 7-14-b, 6700X.  
Pockets of MC carbides indicated. Weld was  
not subjected to heat-treatment

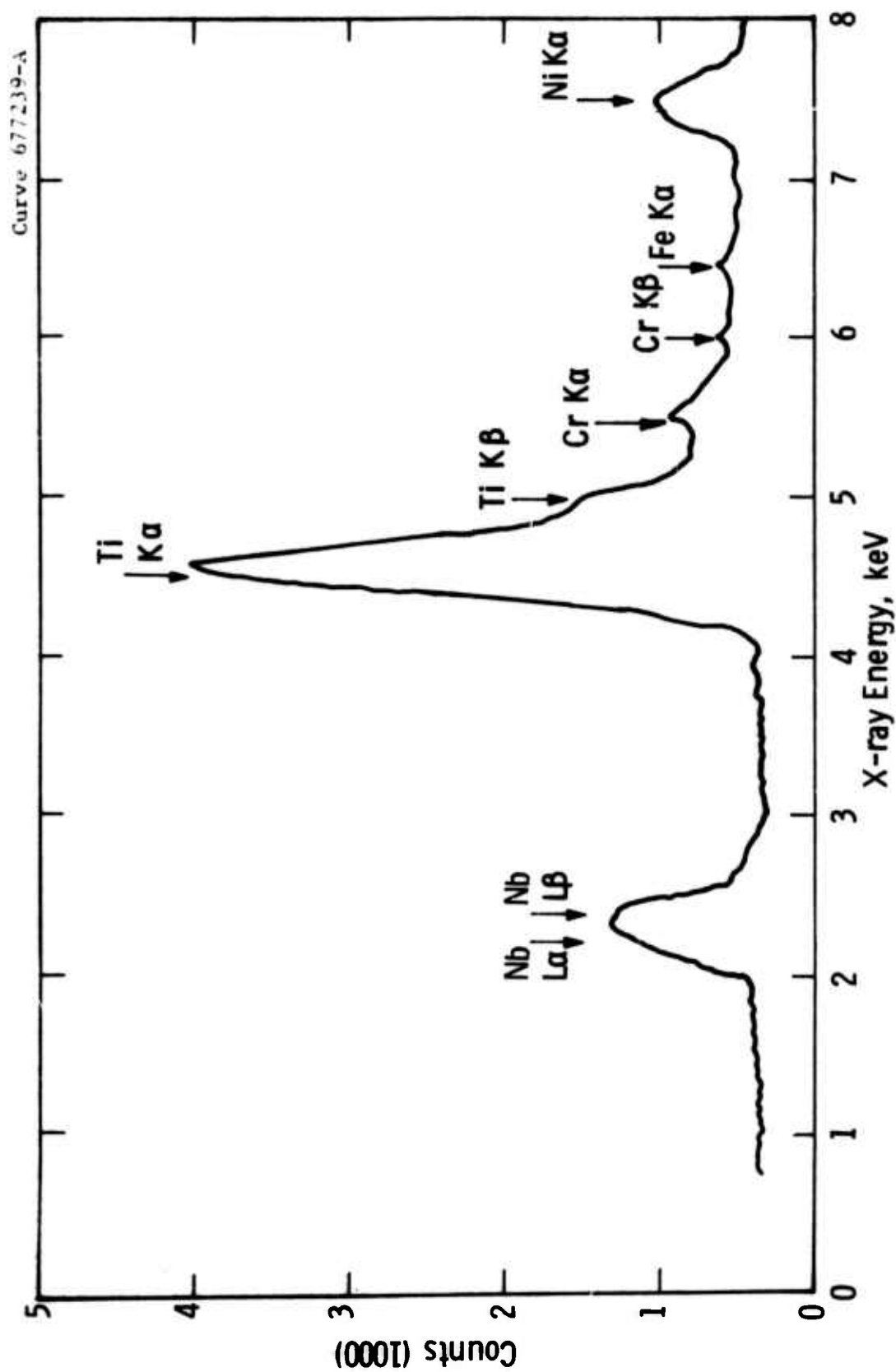


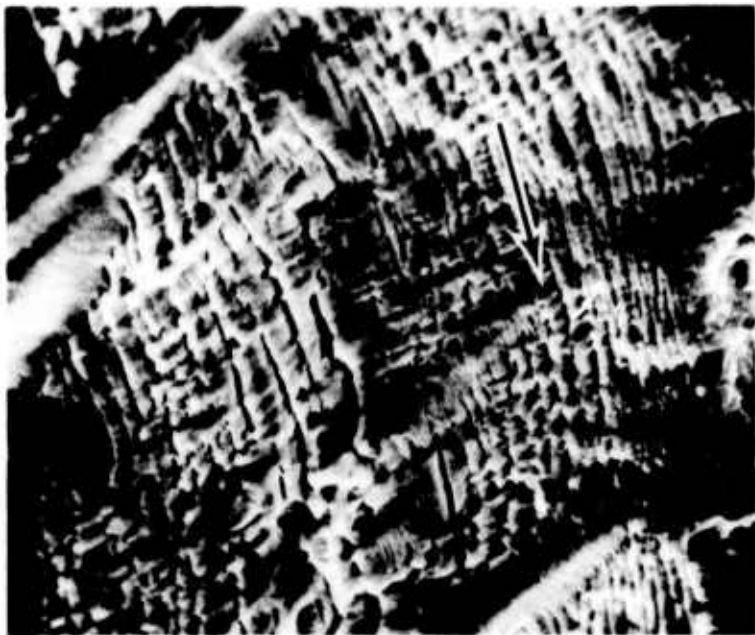
Fig. 7-14a—Energy-dispersive x-ray data from pockets of MC carbides shown in Fig. 7-14.



Fig. 7-15— Fatigue striations and Cr<sub>23</sub>C<sub>6</sub> carbides in weld specimen post weld treated, (Code 3753-3) tested at 4.2°K. (3000 X)

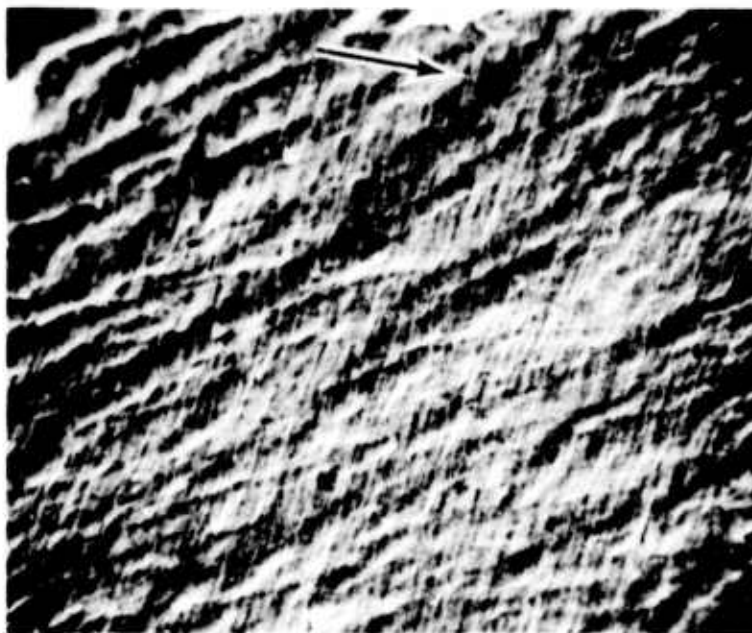


(a) 2800 X



(b) 2900 X

Fig. 7-16—Crack growth fracture surfaces, tungsten-arc welds. Crack front direction shown by large arrows. Note massive secondary cracking normal to crack front specimens tested at 4.2°K. (a) Specimen code 3553-2, no post weld treatment (b) specimen code 3753 post weld heat treated



a



b

Fig. 7-17— Fatigue crack growth in electron-beam weld, no post weld treatment tested at 4.2°K (Code 3253-1). Note crystallographic orientation of crack front and secondary cracking at "grain" boundaries in (b) SEM, 2700 X

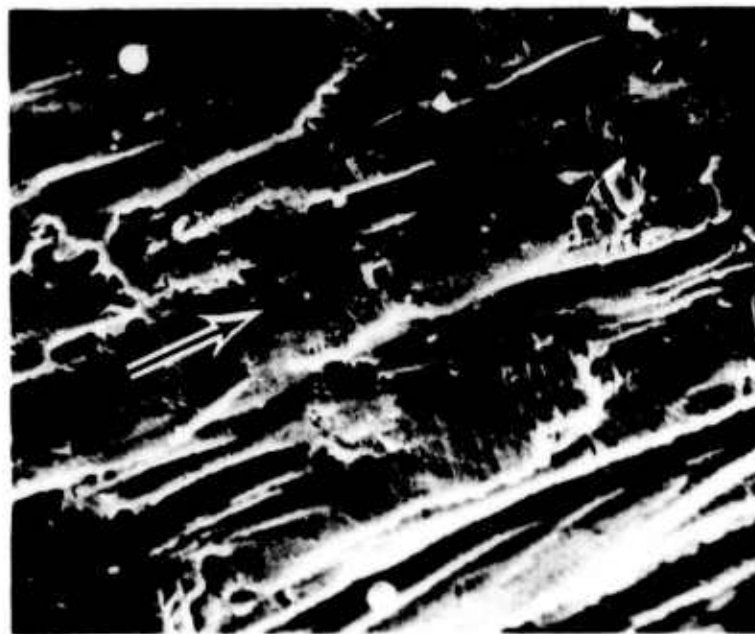
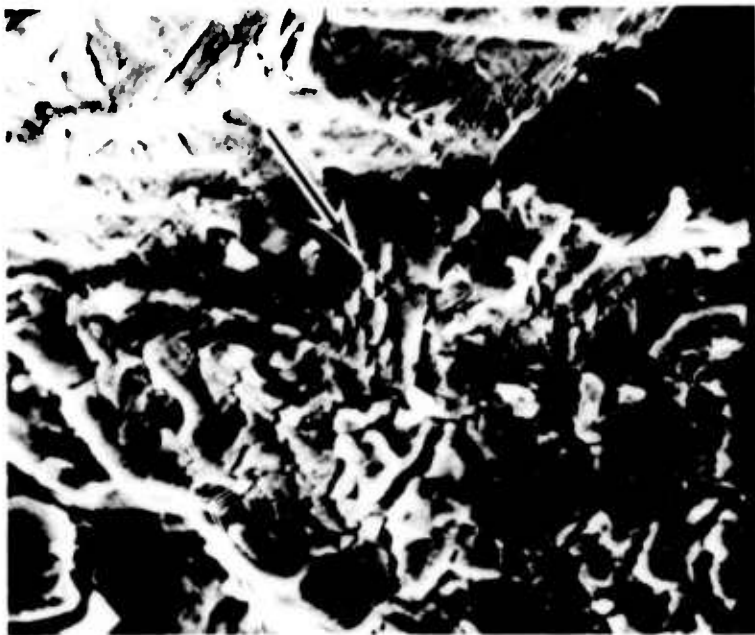
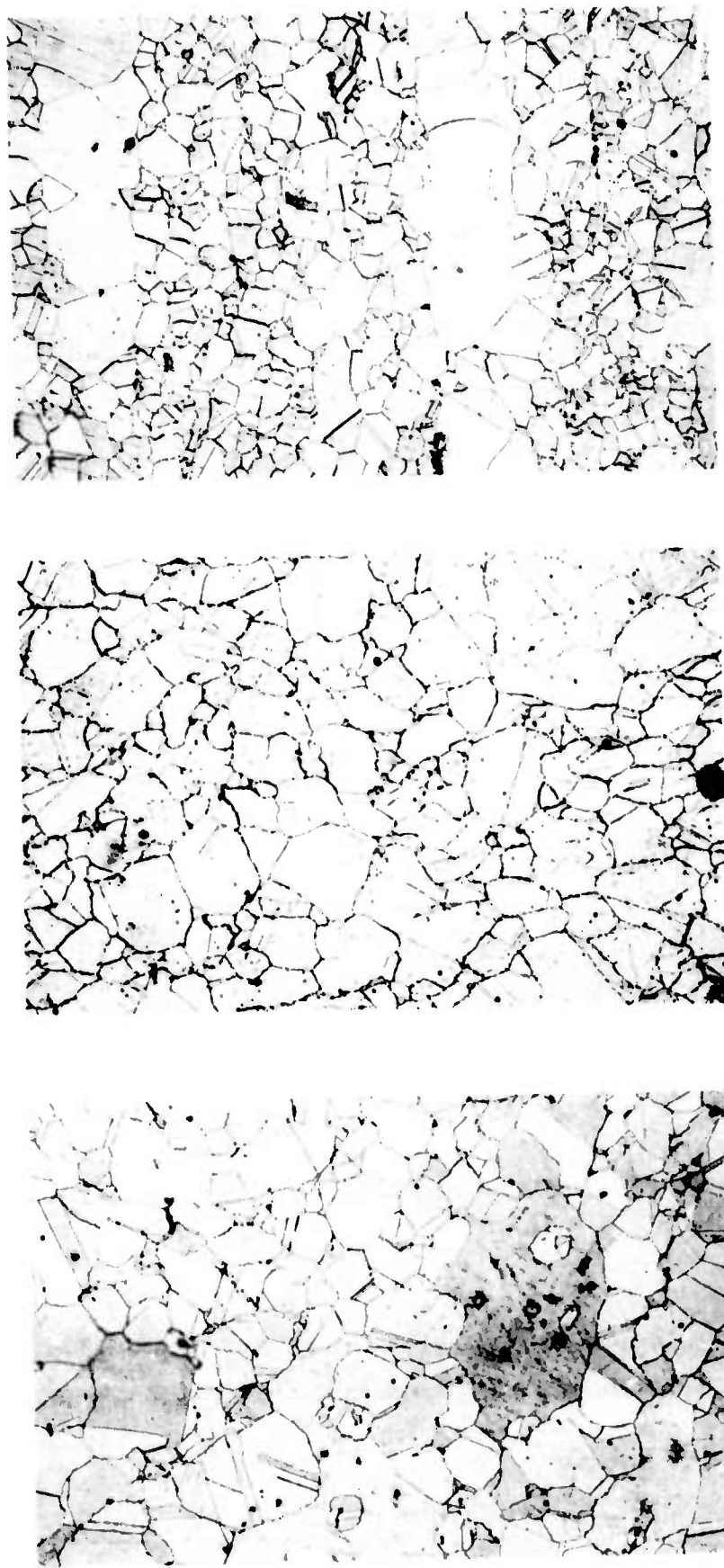


Fig. 7-18— Crack front propagation in electron beam weld subjected to post-weld heat treatment, tested at 77°K. Arrow indicate direction of crack front motion (2800 X)



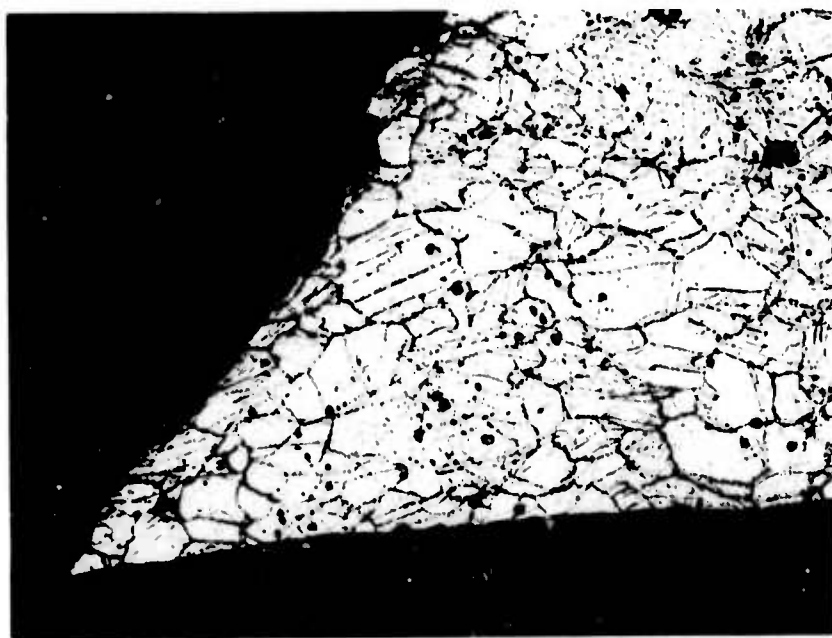
(c) 200 X

(b) 200 X

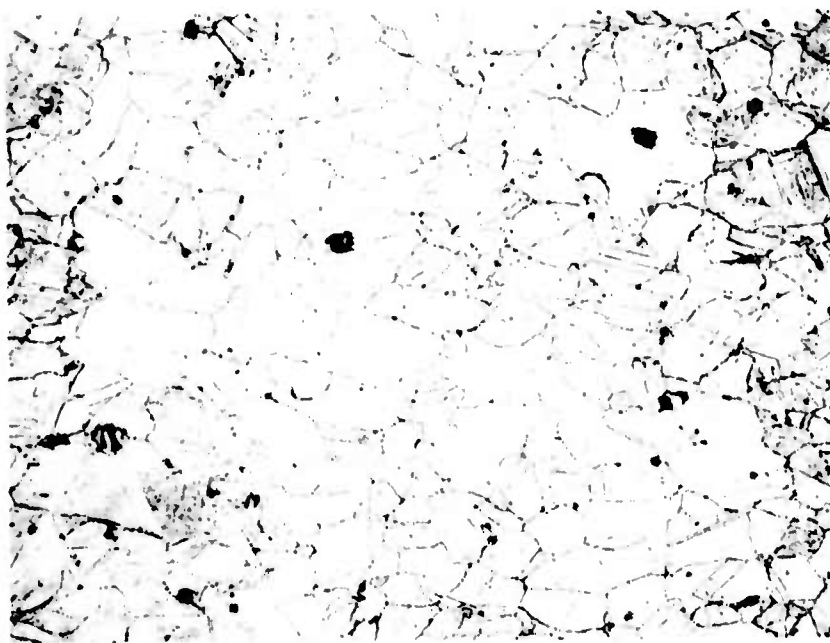
(a) 50 X

Fig. 7-19— Light micrographs showing general grain structure of X-750 material from three melting practices (a) MP1 (Code 3100) (b) MP2 (Code 4000) (c) MP3 (Code 5000). Note smaller grain size in MP2 and binodal distribution in MP3 caused by bands of larger grains





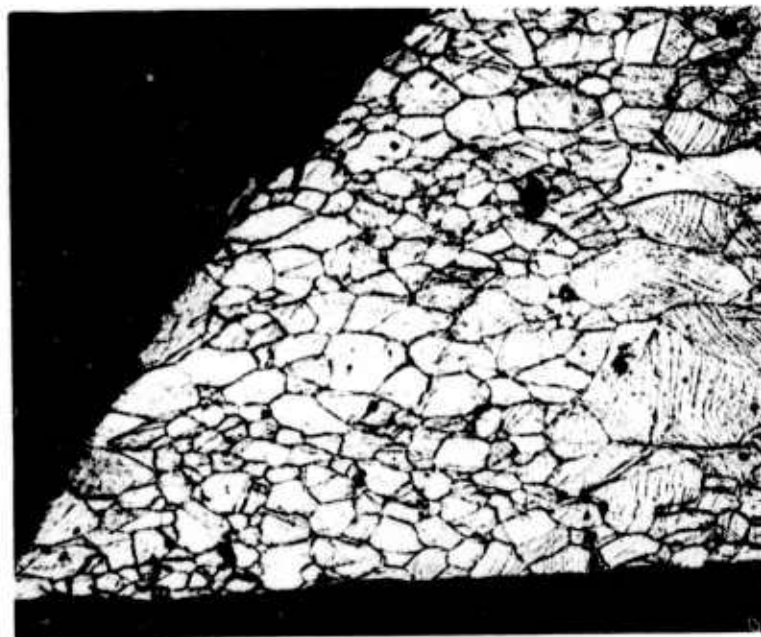
a



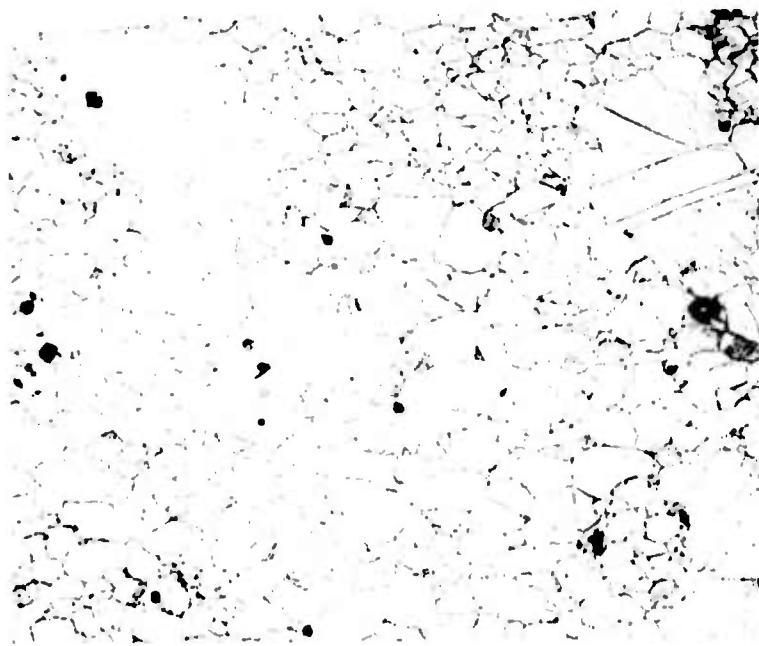
b

Fig. 7-20—Light micrographs showing longitudinal sections at the fracture surface (a) and 30 mm away from the fracture, MP2 tensile specimen (Code 4013-T3) tested at 4.2°K. (200X)





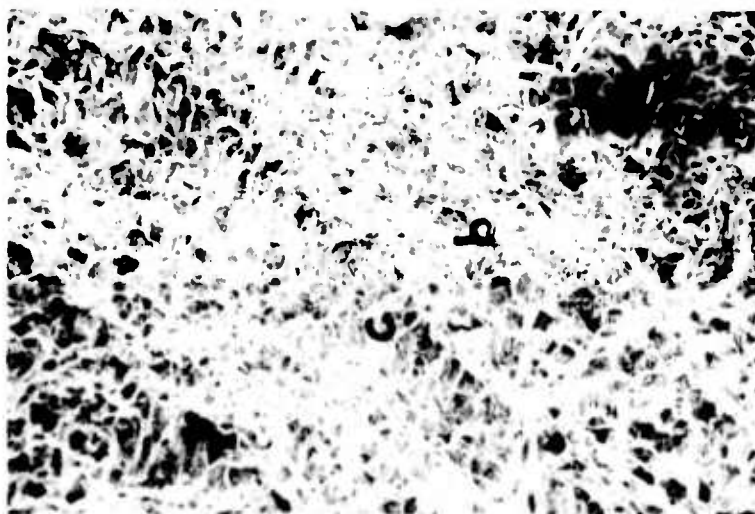
a



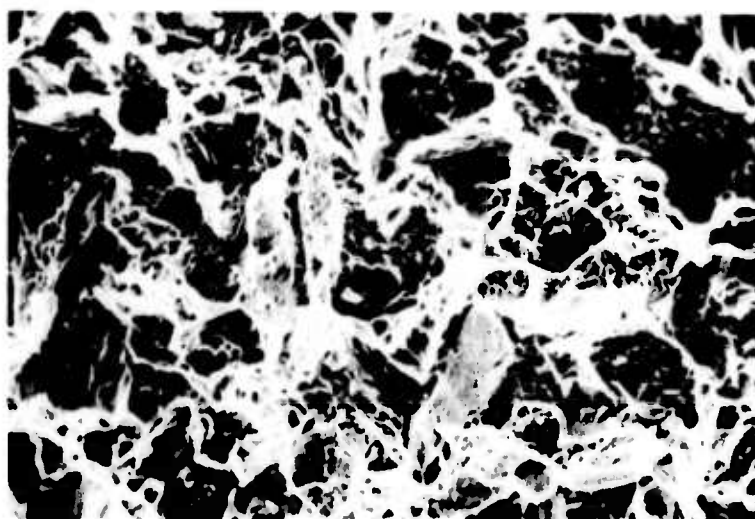
b

Fig. 7-21—Light micrographs showing longitudinal sections at the fracture surface (a) and 28 mm away from the fracture (b), MP3 tensile specimen (Code 5013-T3) tested at  $-4.2^{\circ}\text{K}$  (200 X)

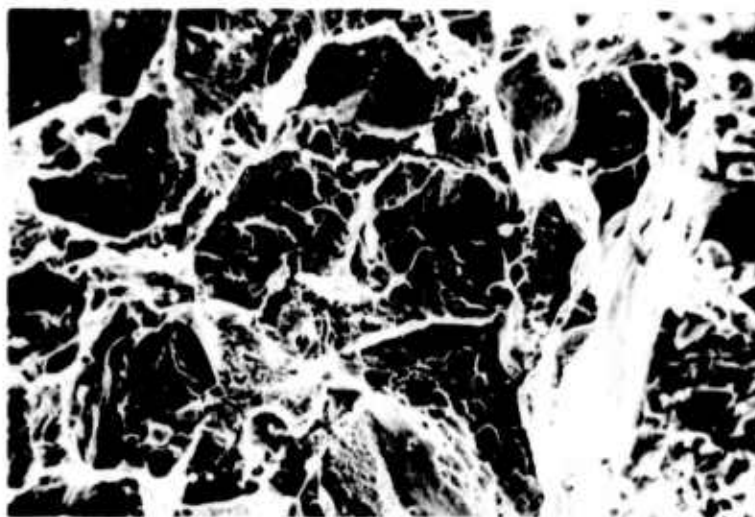
57



(a) 220 X

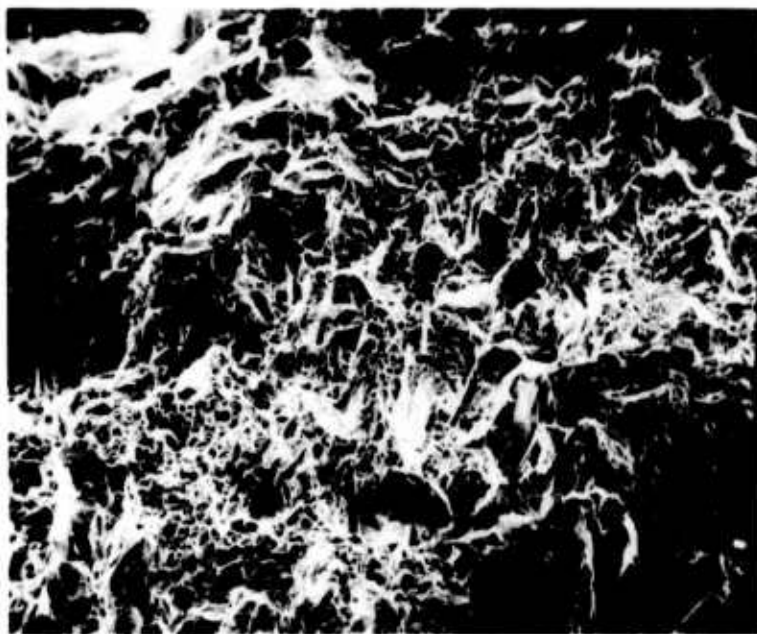


(b) 1200 X

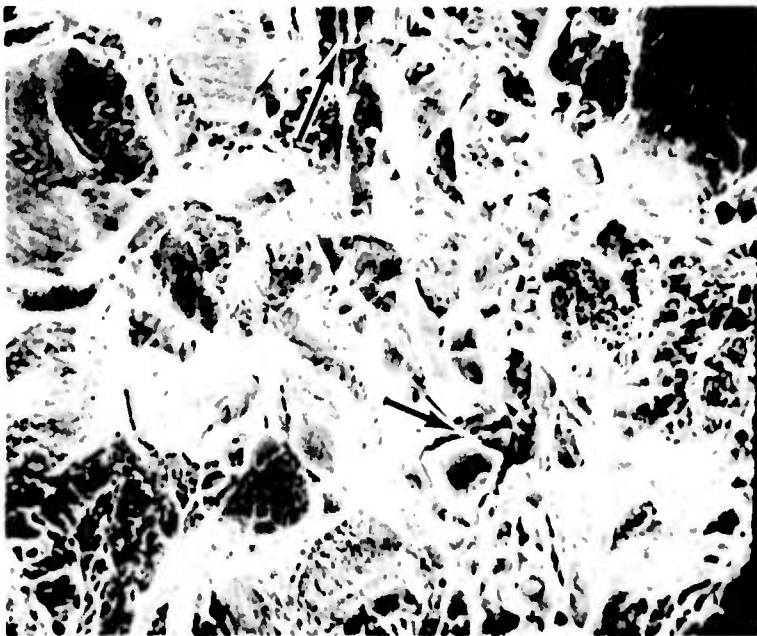


(c) 1200 X

Fig. 22— SEM micrographs of fracture surfaces, MP3 and MP2, X-750 materials. (a) MP3 material (Code 5013-T3) Tested at  $-4.2^{\circ}\text{K}$ . (b) Detail in small grain area. (c) Details in large grain band



(d) 200 X



(e) 1200 X

Fig. 22 (Cont'd) - MP2 material (Code 4013) tested at  $-4.2^{\circ}\text{K}$  (d) 200 X (e) detail at higher magnification. Intergranular (Nb, Ti) C carbides marked by arrows



Fig. 7-23— Light micrograph showing typical microstructural fractures of HIP X-750 material. Note sub-boundaries in large particles. 200X (Code 6113-T4)

700<

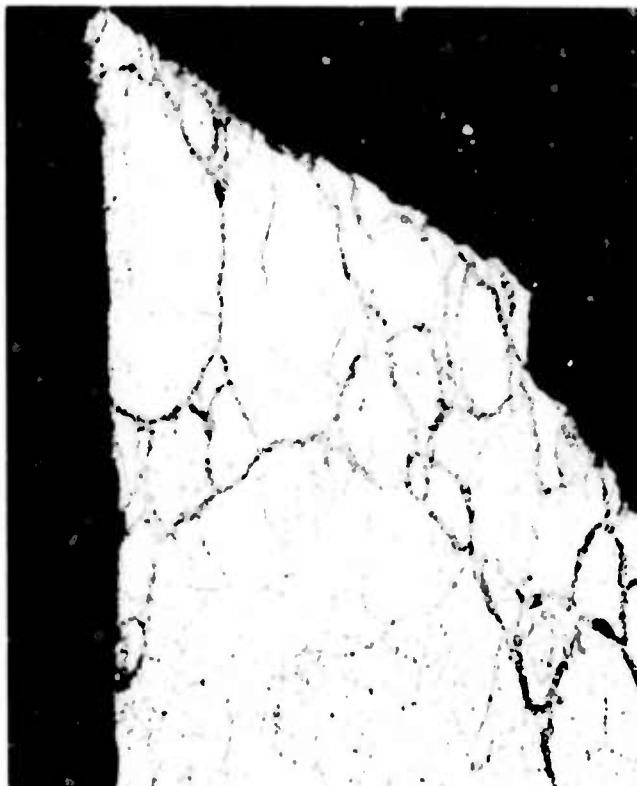
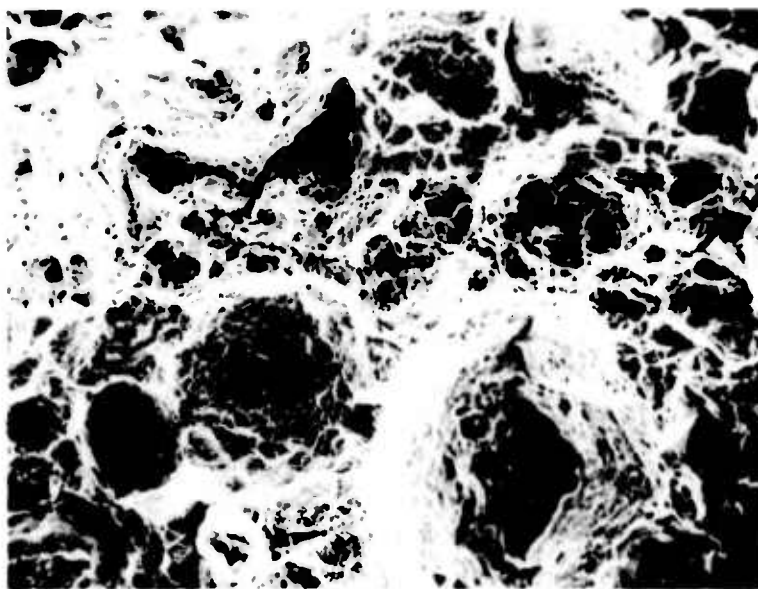
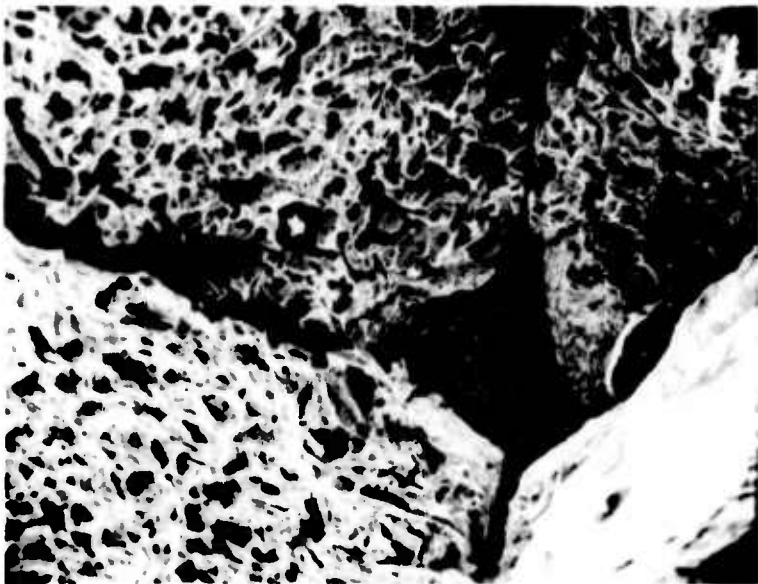


Fig. 7-24— Light micrograph of longitudinal section. HIP specimen tested at 4.2°K (Code 6113-T4) . 500 X



a



b

Fig. 7-25- SEM micrographs of fracture surfaces Inconel X-750 material, 400 X.  
 (a) HIP specimen (Code 6113) (b) MPI specimen (Code 3113). Both specimen  
 solution treated and aged and tested at 4.2°K. Note mostly cross granular failure  
 in (a), intergranular failure in (b)

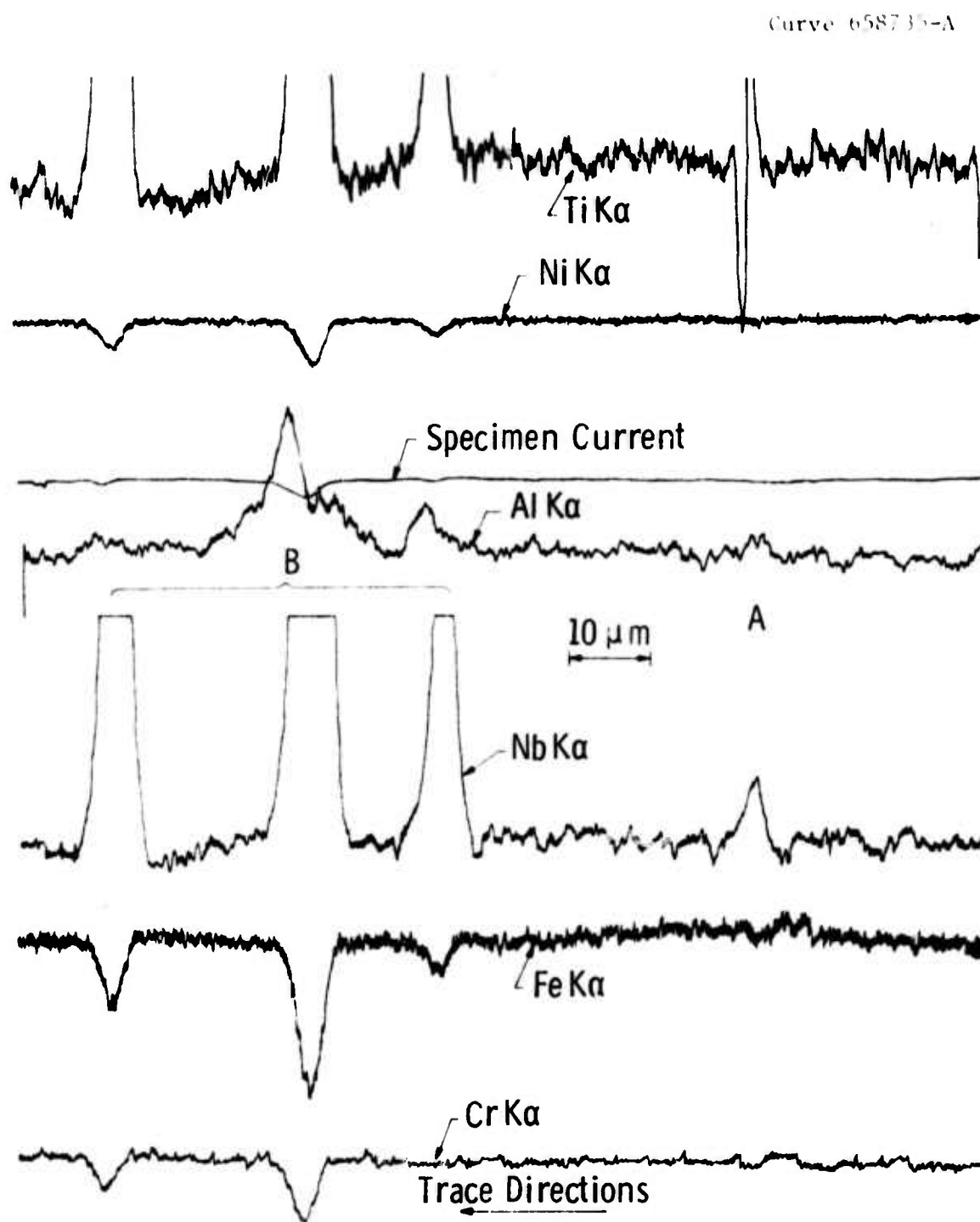


Fig. 7-26-a1—Microprobe traces of Ti, Ni, Al, Nb, Fe and Cr along the line shown in Fig. 7-26-a. MP-1 material. Note (Nb, Ti) C and Al peaks around the carbides



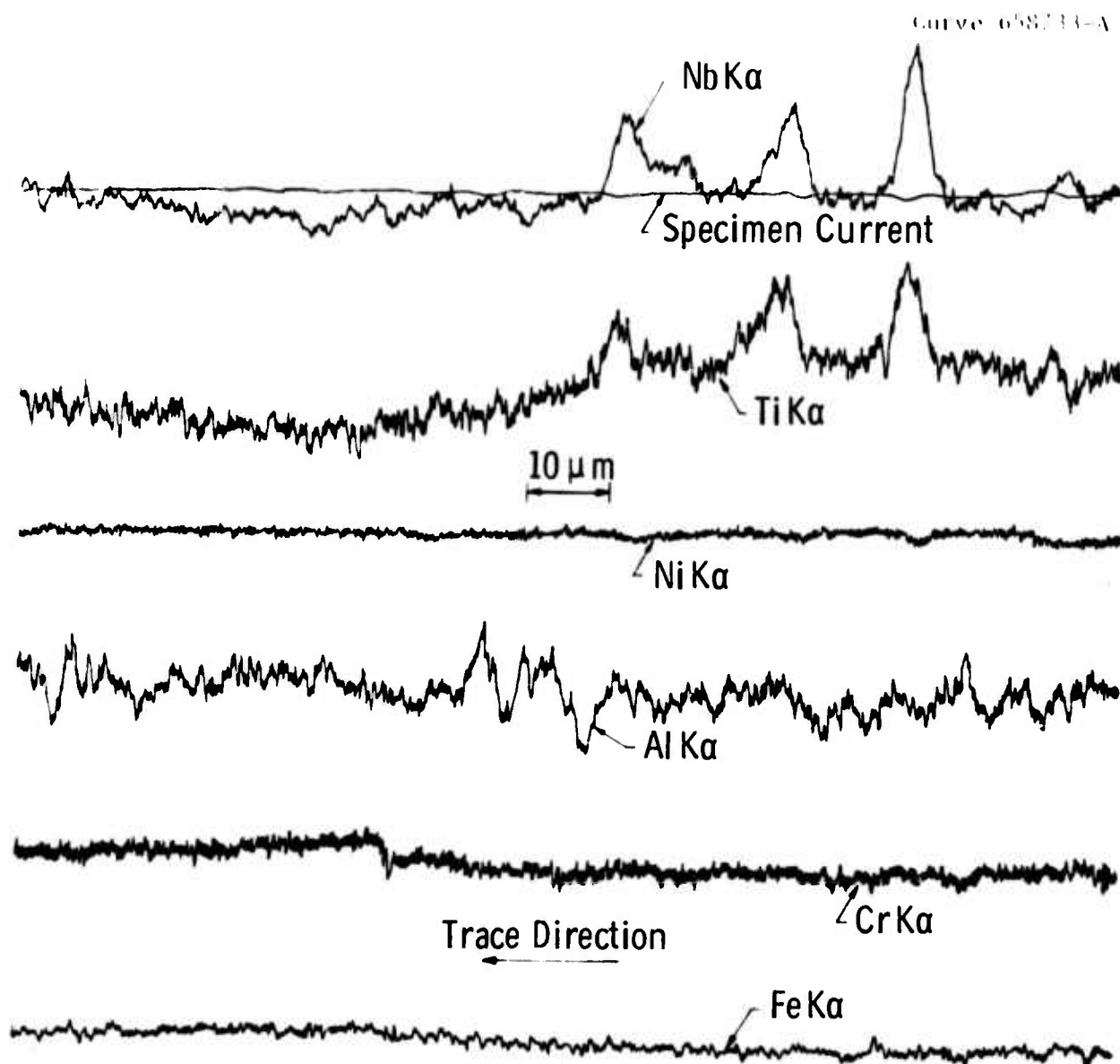


Fig. 7-26-b1—Microprobe traces of Nb, Ti, Ni, Al, Cr and Fe in MP-3 material shown in Fig. 7-26-b. Note uniform distribution of Fe, Cr and Ni and (Nb, Ti) C carbides in high angle boundaries



Curve 658712-A

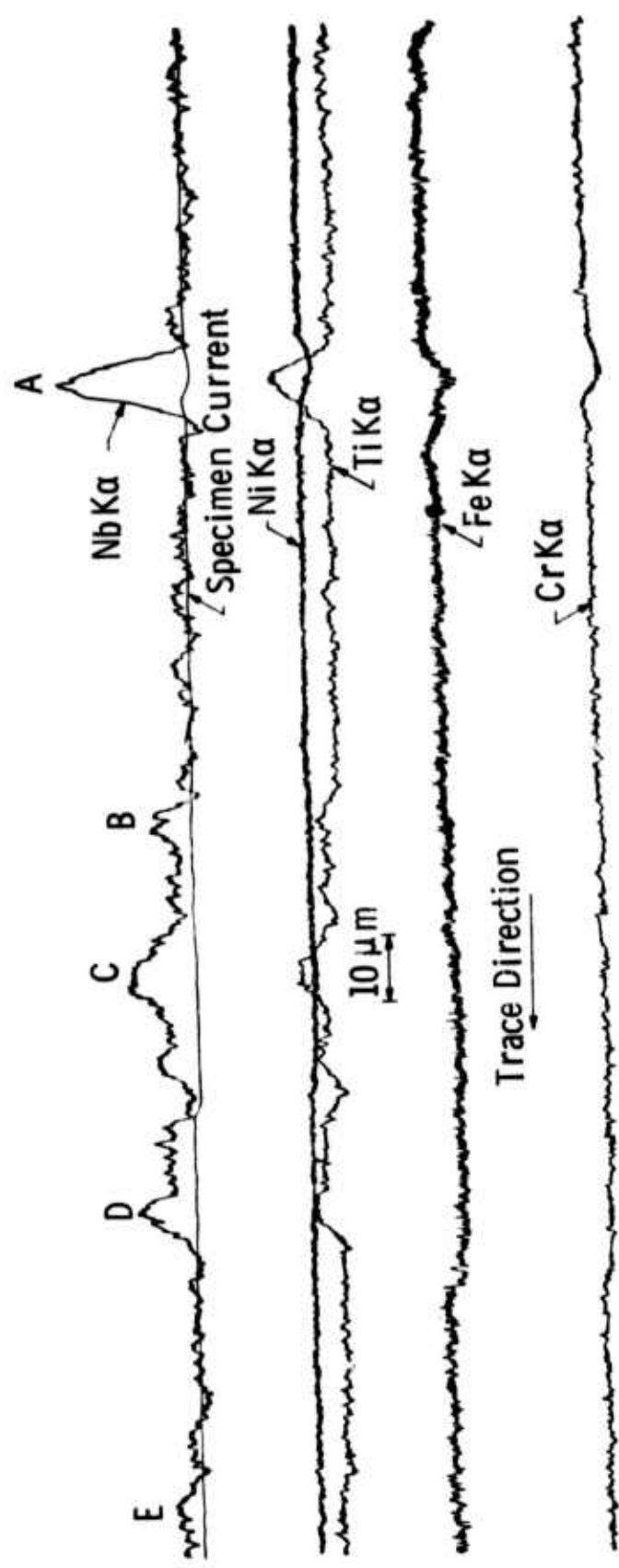


Fig. 7-26-c1— Microprobe traces of Nb, Ti, Fe, Ni and Cr along line shown in Fig. a. HIP material.  
Note (Nb, Ti) C type carbides in high angle boundaries



(a)

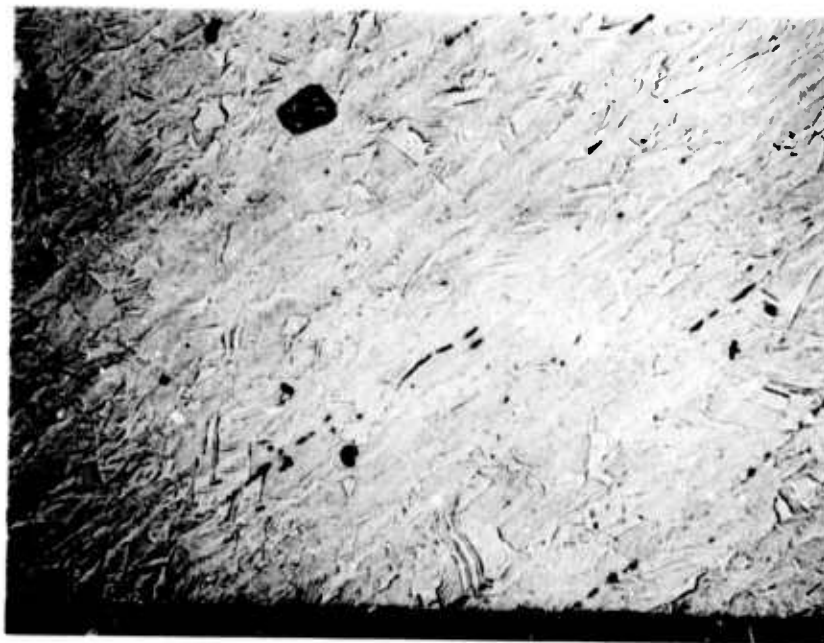


(b)

Fig. 7-27—Tensile specimens, K-58 (Code 8011) solution treated and quenched, tested at R.T. (a) longitudinal section, (b) cross section. 200 X

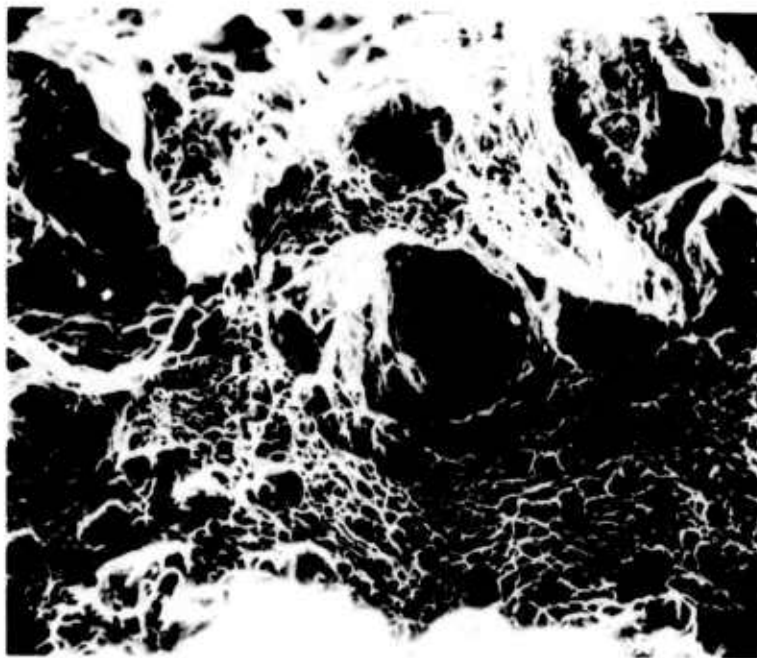


(a)



(b)

Fig. 7-28—Tensile specimens K-58 (Code 8111) CW 30% tested at RT. (a) longitudinal section (b) cross section, 200X



(a)



(b)

Fig. 7-29— SEM micrographs, fracture surface, K-58, (Specimen Code 8022) tested at 4.2°K. (a) Ductile fracture. (b) Low melting particles containing Al, Si, Mo, K, and Ca. (Slag?) 100 X

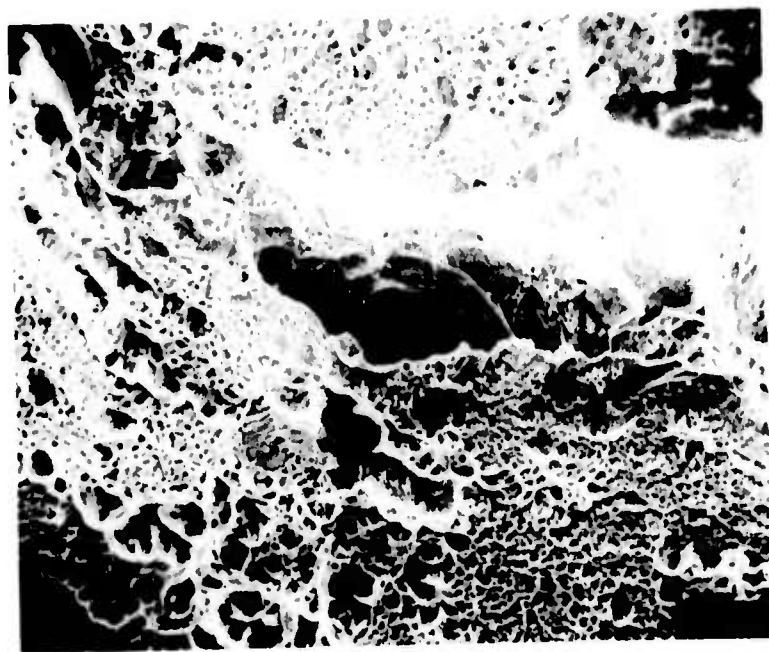


Fig. 30— SEM micrograph, K-58, 30% C.W. (Specimen Code 8113-T10) tested at 4.2°K. Ductile fracture and a deep fissure

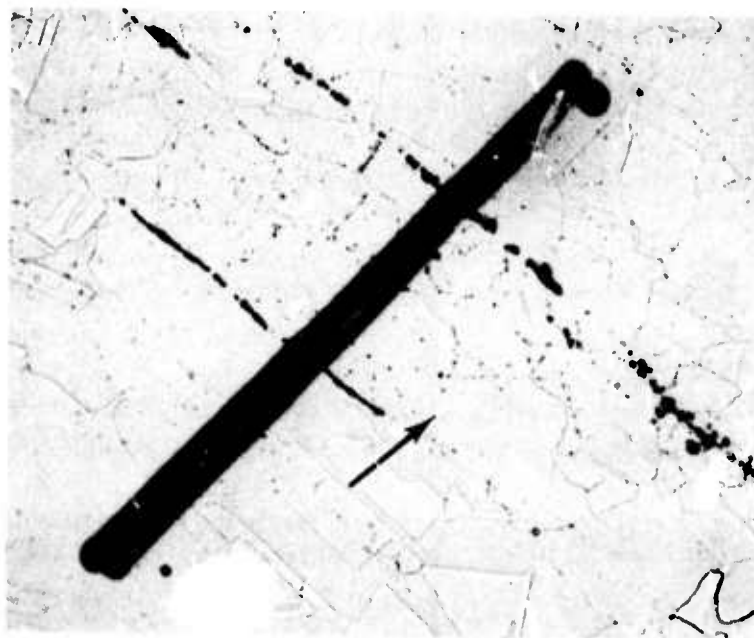


Fig. 7-31— Microprobe trace, K-58 material, specimen 8022-NT2. Fissures appear to be holes. 500 X

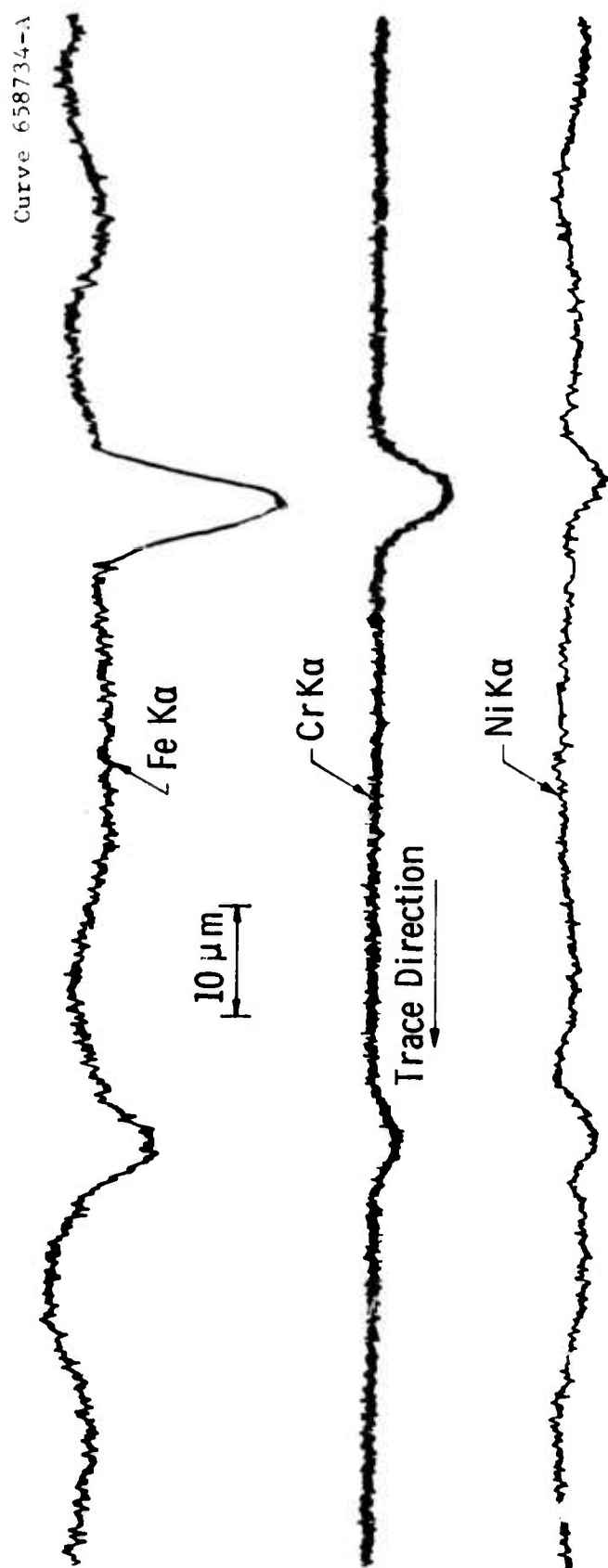


Fig. 7-31-a—Microprobe traces of Fe Cr and Ni along a line shown in Fig. 7-30. The dark fissures seen also in Figs. 7-28-b and 7-30 appear to be holes

## 8.0 PHYSICAL PROPERTIES

### Introduction

This study was conducted to review the suitability of the various materials for use at low and cryogenic temperatures and to discuss the effect of low temperature on their physical properties. Two important aspects of this study were their magnetic and electrical behavior. Samples under different conditions were made and the effect of these conditions on their electrical and magnetic properties was studied.

### 8.1 Magnetic Study

Stable austenitic structural materials have remarkable tensile strengths and ductility which increase substantially as the temperature is lowered.<sup>(1)</sup> However, austenitic materials<sup>(2-5)</sup> can be subject to structural transformation at low temperatures which result in degradation and compromise of their useful engineering properties. Although this transformation, known as martensitic transformation, is usually accompanied by a rapid fall in ductility, no sharp or sudden break from the ductility to brittleness is observed. Other undesirable aspects of this transformation are (i) that the martensitic phase is ferromagnetic, which may create additional problems in an electromagnetic environment; (ii) that the austenite to martensite transformation is sometimes accompanied by an increase in specific volume of the material, which implies a volume expansion on transformation.

It is therefore important to determine the austenitic phase stability of structural materials if they are to be used at low temperatures. Various factors that determine the austenitic phase stability are (i) chemical composition of the material--particularly the carbide content is a very important factor in determining the stability. Mn and



Ni have a strong effect in increasing austenite stability, Mn being very potent. (ii) State of strain or deformation at high temperatures is sometimes responsible for such a transformation. (iii) Cooling to low temperatures, or cycling several times between room temperature and low temperature, can induce the decomposition of the austenite phase. Low temperature deformation is even more potent in promoting the transformation.

Thus, for constructional purposes, it is important either to avoid or arrest the growth of the undesirable martensitic phase. Since the martensitic phase is ferromagnetic, the magnetic study of the materials becomes an important tool in determining the suitability of various structural materials at cryogenic temperatures.

The purpose of the present study was to study the phase stability of several structural materials prepared under different conditions using magnetic technique. This was accomplished by studying the magnetic state of the materials as they are cycled between room temperature, and 4.2K in a magnetic field ranging from 0 to 70 kOe.

The compositions and selected metallurgical conditions being evaluated are given in Table 5.3. The samples for this study were cut from previously tested tensile specimens, away from the deformed region.

Magnetic moment as a function of the applied field and sample temperature was measured using a vibrating sample magnetometer in conjunction with a 70 kiloersted, NbTi superconducting magnet. The magnetometer measures the total magnetic moment of the sample using a sophisticated phase sensitive detection technique that enables changes as small as  $5 \times 10^{-5}$  emu in magnetic moment to be measured over a temperature span from 4.2K to 125°K.

A gallium arsenide diode is used as the sensing element. The sensor is small, stable, and is practically unaffected by strong magnetic fields. The sensor is located very near to the sample in a He-exchange gas enclosure. It has been previously calibrated, and is used in conjunction with P.A.R. Model 156 cryogenic thermometer which gives a

direct readout of the sample temperature from 4.2°K to 125°K. Its resolution is 0.1°K, and has an accuracy of  $\pm 0.2^\circ\text{K}$ . The sample temperature is stabilized by balancing the heat from the sample heater (located near the GaAs diode) and pumping the He-jacket surrounding the sample enclosure.

Direct  $M(H)$  curves at different temperatures are obtained on the X-Y recorder whose inputs are connected to the magnetometer and the magnet power supply.

#### 8.1.1 Review of Different Types of Magnetic Behavior

Four types of magnetic behavior are commonly observed in materials:

##### 1. Diamagnetism

It refers to the phenomenon in which the intensity of magnetization,  $I$ , induced in a body (due to an externally applied field  $H$ ) is less than that produced in a vacuum by the same field. The magnetic susceptibility  $\chi (\equiv I/H)$  of a diamagnetic substance is negative. The origin of this type of magnetism is in the orbital motion of electrons. Hence, this is a universal property. The diamagnetic susceptibility is independent of field as well as temperature.

##### 2. Paramagnetism

If the intensity of magnetization is greater in a substance than the applied field in vacuum, the substance is called "paramagnetic." The magnetic susceptibility is positive. Paramagnetism is usually found among the transition group elements. It is caused by spin and orbital momentum of the unpaired electrons. The paramagnetic system contains permanent magnetic dipoles with no interaction among themselves. All spins are arranged randomly. The paramagnetic susceptibility is independent of the externally applied field, but is inversely

proportional to the temperature as

$$\chi = \frac{C}{T-\theta} \quad 8.1$$

Equation 8.1 is also known as Curie-Weiss law. Here  $C$  and  $\theta$  are material constants and give the net effective magnetic moment,  $\mu_{\text{eff}}$ , and the strength of the interaction respectively.

### 3. Ferromagnetism

The random motion of the spins in a paramagnet is due to thermal energy  $kT$ . As the sample temperature is reduced, the motion of the spins is also reduced. However, if in an external magnetic field the magnetic energy  $\mu H$  of the spin is large compared to  $kT$ , the spins will turn and align themselves along the magnetic field direction. This parallel alignment of spins is called "ferromagnetism." The parallel alignment of spins in a ferromagnet is a result of a strong, positive interaction acting between the neighboring spins. If we increase the temperature, the parallel alignment of the spins is disturbed by thermal agitation, which results in a temperature dependence of spontaneous magnetization. Beyond a critical temperature, called the Curie temperature, the substance starts behaving as a regular paramagnet. The temperature dependence of  $\chi$  is then given by Curie-Weiss law. A plot of  $\chi^{-1}$  versus  $T$  should be a straight line cutting the  $T$ -axis on positive side surface. Ferromagnetism is quite field-dependent, and ferromagnetic substances show typical hysteresis curves and the phenomenon of residual magnetism. It should be pointed out, however, that while paramagnetism is atomic or molecular property, ferromagnetism is a cooperative phenomenon. The induced magnetization in a ferromagnetic material varies directly with the field and attains a very large ( $\sim 10^3$  times) value at lower field strengths; however, with very high fields, a magnetic saturation is produced.

#### 4. Antiferromagnetism

In an antiferromagnetic material, the alignment of the spins is antiparallel. The antiparallel alignment of spins is also a cooperative phenomenon which occurs at a temperature below  $T_N$ , known as Neel temperature. Antiferromagnetism can be described due to two interpenetrating lattices, each lattice having its ions with their spins parallel, but with the spins of one lattice being antiparallel to those on the other. Above  $T_N$ ,  $\chi^{-1}$  versus  $T$  plot should be a straight line with an intercept  $\theta$ . Thus, if  $\theta$  is positive, the material will behave as ferromagnetic below  $T_c$ . However, if  $\theta$  is negative, the material will behave as antiferromagnetic below  $T_N$ . In an antiferromagnetic state, the magnetization  $M$  increases with  $T$  up to  $T_N$ , and then decreases paramagnetically with further increase in  $T$ . The magnetization varies linearly with  $H$  in an antiferromagnetic state, and no saturation occurs as opposed to a ferromagnetic state.

At very low temperatures and in a very high field, it is sometimes possible to turn the antiparallel spin alignment (antiferromagnet) into parallel spin alignment (ferromagnetic).

#### 5. All Other Types

Other special types of magnetic behavior like (i) ferrimagnetism, (ii) metamagnetism, (iii) temperature-independent or Van Vleck paramagnetism, (iv) Pauli or free electron paramagnetism, are also encountered in nature. Out of these, ferrimagnetism and metamagnetism can be considered as special cases of ferromagnetism or antiferromagnetism.

##### 8.1.2 AISI-310S Stainless Steel

AISI 310S samples prepared under two different conditions were tested. The two conditions were: (1) STQ-solution-treated and quenched; (2) STFC-sensitized, where the sample was heated to 2,000°F. for one hour and then allowed to furnace cool.

In Figures 8.1 and 8.2 are shown the plots of total magnetic moment (emu) as a function of the external magnetic field (kOe) at several temperatures ranging from 4.0K to 102K for the STQ sample. Two types of magnetic behavior, depending upon the temperature, are observed. Below 48°K, the magnetization  $M$  increases rapidly with  $H$  initially; and finally, at very high  $H$ , there is a tendency toward its saturation. The  $M(H)$  curve is nonlinear and concave toward the  $H$ -axis. Field dependence of magnetization shows hysteresis; e.g., the magnetic moment does not go to zero when the field is reduced to zero. This behavior of the sample below 48°K is reminiscent of ferromagnetism where 48°K is the ferromagnetic Curie temperature. Temperature and field dependence of magnetization is very complex. For temperature above 48°K, the sample loses its ferromagnetism, and the sample becomes paramagnetic. From Figure 8.3 we note such a transition occurring at about 50°K for AISI-310S sample. We also note two slopes in  $M(H)$  curve for  $T > 50^\circ\text{K}$ . This change in slope can come about from material with two phases each having different magnetic structure.

As we note from Figure 8.2b, complete saturation in magnetization is not obtained up to the highest field of 70 kOe at 4.2°K. By extrapolating these curves backward, we get  $M(0)$ , which we have plotted against the sample temperature in Figure 8.5. The spontaneous magnetization disappears around 60K, which is the Curie temperature. In the Table 8.1, we give an estimate of the peak induction  $B_s$  (gauss) in the material at 4.2°K and at the highest field of 70 kOe. It is about 1,000G for AISI 310S STQ and STFC samples. As a comparison, the saturation induction for iron is 49,000G.

The  $M(H,T)$  data for sample AISI 310S STFC are shown in Figures 8.3 and 8.4. Like the STQ sample, this sample is also feebly ferromagnetic. As before, complete saturation was not obtained up to a field of 70 kOe at 3.8K. In Figure 8.5, we have plotted  $M(0)$  against temperature which shows that the spontaneous magnetization disappears at about 60K. Thus, the Curie temperature is not much different in the two states. Value of  $B_s$  (4.2K) at 70 kOe is about 1,000 gauss, which

is also not too different for the two states. Thus, the two samples are feebly ferromagnetic below 77°K, and sensitization of the sample has little effect on its magnetic structure.

### 8.1.3 Kromarc 58 Stainless Steel

Five samples of Kromarc 58 were tested. The treatment conditions were STQ, CW, GTAW, CW/GTAW and GTAW/CW. In the following, we discuss them separately.

#### 1. Kromarc 58/STQ/Code 80xx)

The magnetic moment,  $M$ , as a function of magnetic field,  $H$ , at various temperatures,  $T$ , are shown in Figures 8.6 through 8.9. We note that at 4.2°K, some hysteresis in  $M(H)$  is present. At low fields below 30 kOe, magnetization varies linearly with field; however, at higher fields, slight bending of the curve is observed. When magnetic moment at constant 13 kOe is plotted against the sample temperature,  $T$ , as in Figure 8.9, we note that the moment increases with increasing temperature up to about 40°K and then decreases as the temperature is further increased. This kind of behavior is expected from an antiferromagnetic phase. Above 40°K, a paramagnetic phase is present, as expected. However, we also note a slight hysteresis in  $M(H)$  curves which persist all the way up to 125°K. It seems that the sample has two magnetic structures: a predominant antiferromagnetic phase which exists up to 40°K, and a comparatively very feeble ferromagnetic phase which persists up to 125°K. These two phases, when combined, can explain an increase in  $M$  with  $T$  (antiferromagnetic), and also a hysteresis in  $M(H)$  curves below 125°K. An antiferromagnetic structure at low fields was also observed earlier<sup>(2)</sup> in a Kromarc 55 sample which has slightly different composition. No measurement was reported at high  $H$  for this sample.

2. Kromarc 58/CW (Code 81xx)

The sample has been cold-rolled 30 percent of its original thickness. In Figures 8.10 through 8.12, magnetization data as a function of field,  $H$ , and temperature,  $T$ , are shown. Here, again, we observe the same behavior as in one STQ sample: For example, (i) magnetic moment increases with increasing  $T$  up to  $40^\circ\text{K}$  at low fields, followed by decreasing  $M$  with decreasing temperature (Figure 8.13). There exists an antiferromagnetic phase of the material at low fields below  $40^\circ\text{K}$ . (ii) Magnetization  $M$  varies nonlinearly with  $H$  at higher fields. Existence of hysteresis in  $M(H)$  curves up to about  $125^\circ\text{K}$ . This implies a second magnetic structure which is feebly ferromagnetic. No saturation in  $M$  was observed in fields up to 70 kOe at  $4.2^\circ\text{K}$ .

3. Kromarc 58/GTAW (Code 82xx)

The magnetic data are shown in Figures 8.14 through 8.16. Two different behaviors are noted, depending upon the magnitude of the external applied field: (i) Below 45 kOe, the magnetic moment increases with temperature up to about  $40^\circ\text{K}$ , and then it decreases with  $T$ . (ii) Above 45 kOe, the moment is decreasing with increasing  $T$ , and the curvature of  $M(H)$  curve is convex to the  $H$ -axis, as against the earlier two cases of Kromarc 58. (iii) A slight hysteresis in  $M(H)$  below  $40^\circ\text{K}$  is also present. These data suggest an antiferromagnetic structure below 45 kOe and a paramagnetic structure above 45 kOe. Few traces of ferromagnetic particles might also be present.

4. Kromarc 58/CW/GTAW (Code 83xx)

In Figures 8.17 through 8.20, all data are shown. The magnetic behavior is very complex, and it is very difficult to separate the different phases because of different ordering temperatures. Few of the things noted are: (i) Hysteresis at low temperatures (below  $30\text{K}$ ); (ii) At low fields, an antiferromagnetic phase with Neel temperature  $T_N$  of about  $40^\circ\text{K}$ ; (iii) At



high fields, another antiferromagnetic with  $T_N$  of about 45°K; (iv) complete paramagnetic behavior above 50K for the whole field range.

5. Kromarc 58/GTAW/CW (Code 84xx)

This is the cold-worked version of Code 83xx. As shown in Figures 8.21 and 8.22, this specimen has also multiple magnetic structure. The following features are observed: (i) Magnetic hysteresis at low temperatures (below 30°K); (ii) below 45 kOe, M varies linearly with H, M at constant field increases with T up to 40°K, and then decreases with further increase in T; (iii) above 45 kOe, M is nonlinear with H, M at constant field decreases with T; (iv) no sign of saturation up to highest H at 4.2°K.

Analysis suggests that an antiferromagnetic phase at low fields and a second paramagnetic phase at high H are present. Hysteresis in M(H) at low temperatures might be due to some dispersion of ferromagnetic particles.

8.1.4 Inconel 718 and X-750

Magnetization data on these samples are presented in Figures 8.3 through 8.20. We shall discuss them individually in the following:

1. Sample IN X-750/ST (Code 30xx)

These samples were heat-treated at 1,800°F. for one hour, and were then allowed to air-cool. From Figures 8.23 and 8.24 we see that the specimen is ferromagnetic at low temperatures. There is spontaneous magnetization at fields of about 3 kOe at 4.2°K. As field is further increased, the domain magnetization orient along the direction of the external field gradually. Even up to the highest field of 65 kOe, all the domains have not turned completely; thus, complete saturation was not attained at any field or temperature. Hysteresis in M(H) curves was also observed at low temperatures. Above 50°K, the nonlinearity in M(H) is



decreasing, which suggests that the thermal motion of the magnetic spins is becoming comparable with the magnetic energy; in other words,  $kT \approx \mu H$ . The extrapolated  $M(0)$  are plotted against temperature in Figure 8.29. This shows that the remnant flux vanishes around 130°K, which is the Curie temperature of the material. Above 130K, the sample is in paramagnetic state and  $kT > \mu H$ , and the susceptibility ( $\chi \equiv M/H$ ) behavior will follow Curie-Weiss law. From the low temperature  $M(H,T)$  curves, one can find out  $B_s$ , which is about 1,433 gauss. This value is quite comparable with AISI 310S discussed earlier, or is about three percent of iron value. Thus, the magnetic behavior is very weak.

## 2. Sample IN X-750/STDA (Code 3lxx) Strained and Unstrained (\*)

Two STDA samples were tested. One was the sample that was used for fracture analysis, and the other one (\*) was unstrained. The magnetic behavior of samples is very similar, and is given below:

(i) Magnetic data as a function of field and temperature are given in Figures 8.25 and 8.26 for STDA, and Figures 8.27 and 8.28 for STDA\* samples.

(ii) Both samples show hysteresis at low temperatures.

(iii) Both samples show nonlinear  $M(H)$  behavior at low temperatures. As temperature increases, the nonlinearity becomes less and less; and at 130°K, it is almost linear. This shows that the Curie temperature is around 130°K.

(iv) Extrapolated  $M(0)$  as a function of  $T$  are shown in Figure 8.29 for both. The Curie temperature is around 130°K, as in ST sample.

(v)  $B_s$  calculated at 4.2°K for this sample is about 1,477G for STDA and 1,552G for MPI-STDA samples. Thus, the heat treatment, double aging, and putting strain in the sample (STDA sample is tensile specimen), and temperature

cycling, do not change the magnetic characteristics of the samples. A very feeble ferromagnetic phase present shows a very mild decomposition of the austenite phase, or the austenite phase is very stable in X-750 under the different conditions mentioned above.

### 3. Sample IN-718

The austenite phase stability of this material was also studied as a comparison with IN X-750. Magnetic data are shown in Figures 8.30 and 8.31. (i) Like IN X-750, this sample is also feebly ferromagnetic. (ii) Hysteresis in M(H) is also observed at low temperatures. (iii) Saturation in M(H) at low T, as in X-750 is partial.  $B_s$  at 4.2°K is 1,335 gauss. (iv) Non-linear behavior in M(H) reduces slowly with temperature. Above 130°K, the behavior is more linear and the sample will be in paramagnetic state. M(0) as a function is shown in Figure 8.29. At about 130K, the remnant flux vanishes, suggesting a Curie temperature at around 130°K.

## 8.2 Electrical Resistivity

### 8.2.1 Experimental

Samples for electrical resistivity measurements were cut in the form of rectangular bars of dimension 1-1/4" x 1/8" x 1/8". For OHFC copper (Code 10xx) and weldment sample (Code 12xx) of copper, the thickness of the samples was reduced to .020". A four-probe technique was used to measure the resistivity. Constant current, I, from a Kepco constant current power supply was allowed to flow through the sample, while the voltage, V, between the two fixed points along the length of the sample was measured by a Keithley digital voltmeter. The resistivity  $\rho$  is given by

$$\rho = \frac{V}{I} \times \frac{A}{l}$$

where  $A$  is the area of cross section of the sample, and  $l$  is the length of the sample across which the voltage  $V$  was measured. The constancy of the sample current was periodically checked by noting the voltage across a resistance shunt, which was placed in series with the sample.

The whole resistivity probe was immersed in different constant temperature baths to determine the temperature dependence of the resistivity. The baths normally used in the range of 77°K to 300°K were: liquid freon F.22 (232°K), dry ice mixed with acetone (195°K), and liquid nitrogen (77°K). The range 13.8°K to 20.4°K was covered using liquid hydrogen. The lowest temperature obtained by pumping on liquid  $H_2$  bath was 13.8°K. The vapor pressure of the  $LH_2$  bath was measured by a Wallace and Tiernan gauge. Using vapor pressure-temperature tables for liquid  $H_2$ , the sample temperature was determined. Since no change in resistivity with temperature was observed for the range  $13.8 < T < 20.4^\circ K$ , only the end point resistivity is given. Similarly, the temperature range 1.5°K to 4.2°K was covered by using liquid He bath in conjunction with a pump. Since no noticeable change in  $\rho$  was observed between 4.2°K and 1.5°K, only  $\rho$  at 4.2°K are given for all samples. The total uncertainty of the data is less than five percent.

#### 8.2.2 Results and Discussion

A comprehensive study of some engineering alloys at low temperatures has been done by other authors.<sup>(6)</sup> Our analysis is similar to theirs.

The resistivity,  $\rho$ , of an alloy is composed of two parts:

$\rho_i$  - The part that is due to electron-phonon interactions, and which goes to zero as the temperature is reduced to zero;

$\rho_o$  - The part that is due to static lattice defects

such as impurity atoms, etc., and which remain independent up to the lowest temperature. In other words,

$$\rho = \rho_0 + \rho_i(T) \quad (2)$$

From the electrical resistivity measurements, one can estimate the thermal conductivities  $\kappa$  of these alloys using Wiedemann Franz's law.<sup>(7)</sup> The law states that  $(\rho\kappa_e)/T$  is a constant quantity called "Lorenz Number L," where  $\kappa_e$  is the electronic part of the thermal conductivity. Using a free electron gas model, Sommerfeld<sup>(7)</sup> calculated L as

$$L \equiv \frac{\rho\kappa_e}{T} = \frac{\pi^2 k^2}{3e^2} = 2.45 \times 10^{-8} \left( \frac{\text{volt}}{\text{degree}} \right)^2$$

where  $\rho$  is expressed in ohm-cm and  $\kappa_e$  in w.u. It will be interesting to check the theoretical value of Lorenz Number against the experimental value. Since thermal conductivity measurements on these samples are being done elsewhere, calculation of L seems to be a worthwhile exercise.

The advantage of such an analysis lies in the fact that a simple measurement of  $\rho$  will give us a good estimate of thermal conductivity  $\kappa$ , which is a very important parameter for heat transfer and other design studies.

The resistivities of all the samples were measured at seven temperatures: 4.2, 13.8, 20.4, 77, 195, 245, and 300 degrees K, and are listed in Table 8.2.

Discussion of individual sets of samples is as follows:

#### 1. Kromarc 58 Stainless Steel

In Figure 8.32, the temperature dependence of resistivity of two Kromarc 58 samples is shown. As expected, the resistivity of the samples decreases with decreasing temperature in more or less the same

fashion, and finally flattens out to a constant value  $\rho_0$  at lower temperatures ( $< 20^\circ\text{K}$ ). A slight minima in  $\rho$  is also indicated around  $30^\circ\text{K}$ . The resistivity of the cold-worked (30% CW) is lower than the STQ sample throughout the whole temperature range. Using these  $\rho(T)$  curves, one can construct  $\rho(T)$  curves for other samples just by measuring  $\rho$  at room temperature.

The minima in resistivity had been observed by other authors<sup>(4)</sup>, but mostly in dilute alloys, and is usually attributed to Kondo's impurity-scattering. In our alloys (nondilute), however, we could not find any satisfactory explanation for the minima.

Since the alloy has a large concentration of Mn in it, it is quite possible that the origin of the minima might be in some form of Rudermann-Kittel-Kasuya-Yosida RKKY<sup>(8)</sup> interaction where an indirect exchange between the two magnetic impurity atoms takes place via the conduction electrons.

Kromarc 58 Codes 82, 83, and 84 were also measured down to 4.2K, as shown in Figure 8.33. Also, these samples follow the same trend as above-mentioned samples. A minima in  $\rho(T)$  is again observed in all samples. Room temperature measurements are good to predict low temperature  $\rho$ .

## 2. Inconel X-750 and Superalloys

In Figure 8.34, resistivity as a function of temperature are shown for Inconel X-750 samples processed in the following conditions: (i) Solution-treated tensile specimen (S.T.); (i) solution-treated double-aged unstrained (STDA\*); (iii) solution-treated double-aged tensile specimen (STDA). Also shown in the same figure is the  $\rho(T)$  curve for

another composition--Inconel 718 in STDA condition. Again, the temperature variation of the resistivity for all samples is very similar (except X-750 ST tensile specimen), and the measurement of  $\rho$  at room temperature should be sufficient to extrapolate the  $\rho$  at low temperatures. We have no explanation for the change in slope of  $\rho(T)$  for sample X-750 ST.

### 3. AISI 310S Stainless Steel

Three AISI 310S stainless steel samples were selected for resistivity measurements: (i) solution-treated (STQ); (ii) solution-treated and then furnace-cooled at 2,000°F. for one hour (STFC); (iii) solution-treated weldment sample (ST/W).

Again, all the three samples show similar  $\rho(T)$  behavior (Figure 8.35), and a simple  $\rho$  measurement at room temperature should be sufficient to characterize the material at low temperatures. No minima in  $\rho(T)$  is observed at low temperatures. As expected because of the second phase in weldment sample SMAW, it has about eight percent overall higher resistivity than the STQ sample.

### 4. Copper: CuOHFC (Code 10xx) CuGMAW (Code 12xx)

The resistivity of the two copper samples was measured using a new setup that is capable of passing very large currents ( $\sim 100$  amps) at 4.2K. This setup is generally used for measuring critical current densities of superconductors. The samples were cut into small rectangles of sides 1-1/2" x 1/8", and thickness was reduced to about .020". The ratio of room temperature and LHe temperature resistivity was 73 for OHFC, and only two for GMAW Cu sample. Thus, the welding changes the resistivity ratio substantially.

SECTION 8  
REFERENCES

1. P.J. Rickards, Cryogenics, 128 (April 1971).
2. D.C. Larbalestier and H.W. King, Cryogenics 10, 410 (1970) and Cryogenics 13, #3, 160 (1973).
3. W. Statius and J.R. Dillinger, J. Appl. Phys. 44, #6, 2887 (1973).
4. H. Nahm, D.J. Michel and J. Moteff, Jour. of Mat. Sci. 8, 104 (1973).
5. J.C. Erdmann, Cryogenics 9, #6, 411 (1969).
6. A.F. Clark, G.E. Childs and G.H. Wallace, Cryogenics 10, #8, 295 (1970).
7. See any text on solid state physics e.g., "Introduction to Solid State Physics" by C. Kittel, third edition, page 222.
8. S. Methfessel and D.C. Mattis, Magnetic Semiconductors Encyclopedia of Physics, Vol. XVIII/1, editor H.P.J. Wijn, Springer-Verlag, Berlin 1968 p. 430-451.

TABLE 8.1  
SUMMARY OF MAGNETIC BEHAVIOR

Samples	Magnetic Structure		T <sub>o</sub> (K)	B <sub>s</sub> (4.2K) Gauss
	Low H	High H		
Kromarc 58/STQ (80xx)	Antiferromagnetic	Nonlinear M(H) Hysteresis Ferromagnetic	40 T <sub>N</sub> 125 T <sub>C</sub>	-
Kromarc 58/CW (81xx)	Antiferromagnetic	Nonlinear M(H) Hysteresis Ferromagnetic	40 T <sub>N</sub> 125 T <sub>C</sub>	-
Kromarc 58/GTAW (82xx)	Antiferromagnetic	Paramagnetic Traces of Ferromagnetic	40 T <sub>N</sub>	-
Kromarc 58/CW/GTAW (83xx)	Antiferromagnetic	Paramagnetic	40 T <sub>N</sub> 50 T <sub>C</sub>	-
Kromarc 58/GTAW/CW (84xx)	Antiferromagnetic	Paramagnetic Traces of Ferromagnetic	40 T <sub>N</sub>	-
AISI 310S/STQ (20xx)	Feebly	Ferromagnetic	50	1003
AISI 310S/STFG (21xx)	Feebly	Ferromagnetic	50	1000
Inconel X-750/ST (30xx)	Feebly	Ferromagnetic	130	1433
Inconel X-750/STDA (31xx)	Feebly	Ferromagnetic	130	1477
*Inconel X-750/STDA (31xx)	Feebly	Ferromagnetic	130	1552
Inconel 718/STDA	Feebly	Ferromagnetic	130	1335

\*Unstrained



TABLE 8.2

SUMMARY OF RESISTIVITY BEHAVIOR,  $\rho$  ( $\mu \Omega$  cm)

Samples	300°K	243°K	194°K	77°K	20.2°K	13.8°K	4.3°K
Inconel 718 STDA	124.7	123.4	121.9	117.9	116.4	116.5	116.8
Inconel X-750 *STDA (31xx)	129.4	128.54	127.29	124.0	122.8	122.8	123.1
Inconel X-750 STDA (31xx)	128.63	127.56	126.44	122.8	120.9	120.9	121.6
Inconel X-750 ST (30xx)	126.98	126.03	125.36	122.9	122.2	122.3	122.4
Kromarc 58 (80xx)	97.44	94.16	91.37	82.7	82.1	82.2	82.5
Kromarc 58 (81xx)	96.75	93.59	90.44	80.9	80.2	80.4	80.6
Kromarc 58 (82xx)	99.19	95.92	92.79	85.40	84.19	-	85.19
Kromarc 58 (83xx)	100.3	96.57	93.31	85.62	83.81	-	85.55
Kromarc 58 (84xx)	99.67	96.33	93.06	85.84	84.15	-	85.26
AISI 310S STRC (20xx)	89.57	85.92	82.70	72.11	71.61	-	68.11
AISI 310S STQ (21xx)	90.38	86.00	82.43	72.18	67.60	-	67.82
AISI 310S GMAW (22xx)	98.58	94.65	90.78	79.91	72.04	-	75.19

Cu OHFC (10xx)  $R_{R.T.}/R_{He} = 73$ Cu GMAW (12xx)  $R_{R.T.}/R_{He} = 2$ 

\*Unstrained

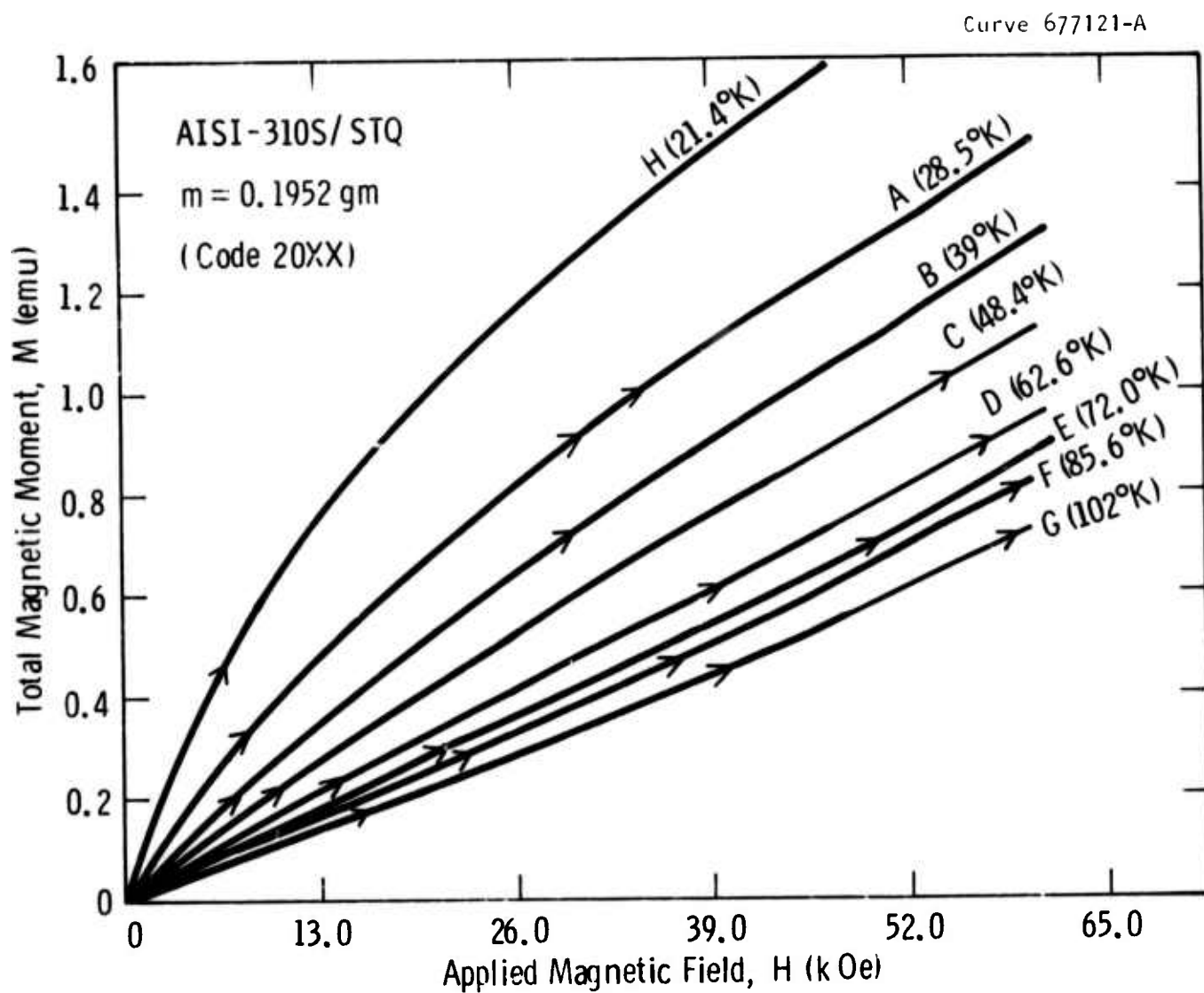


Fig. 8-1 — Total magnetic moment as a function of the external field

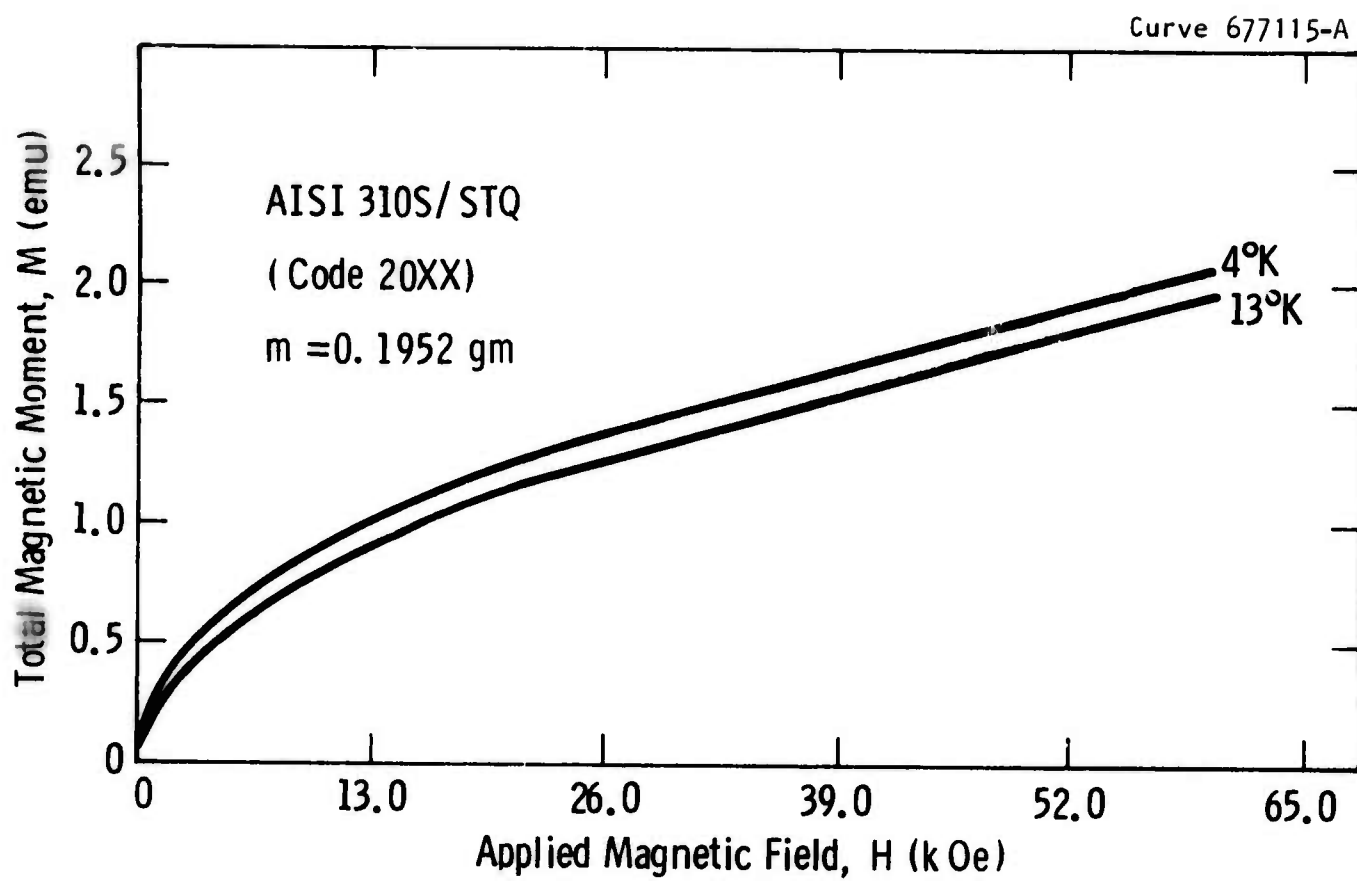


Fig. 8-2 — Magnetization data at low temperatures

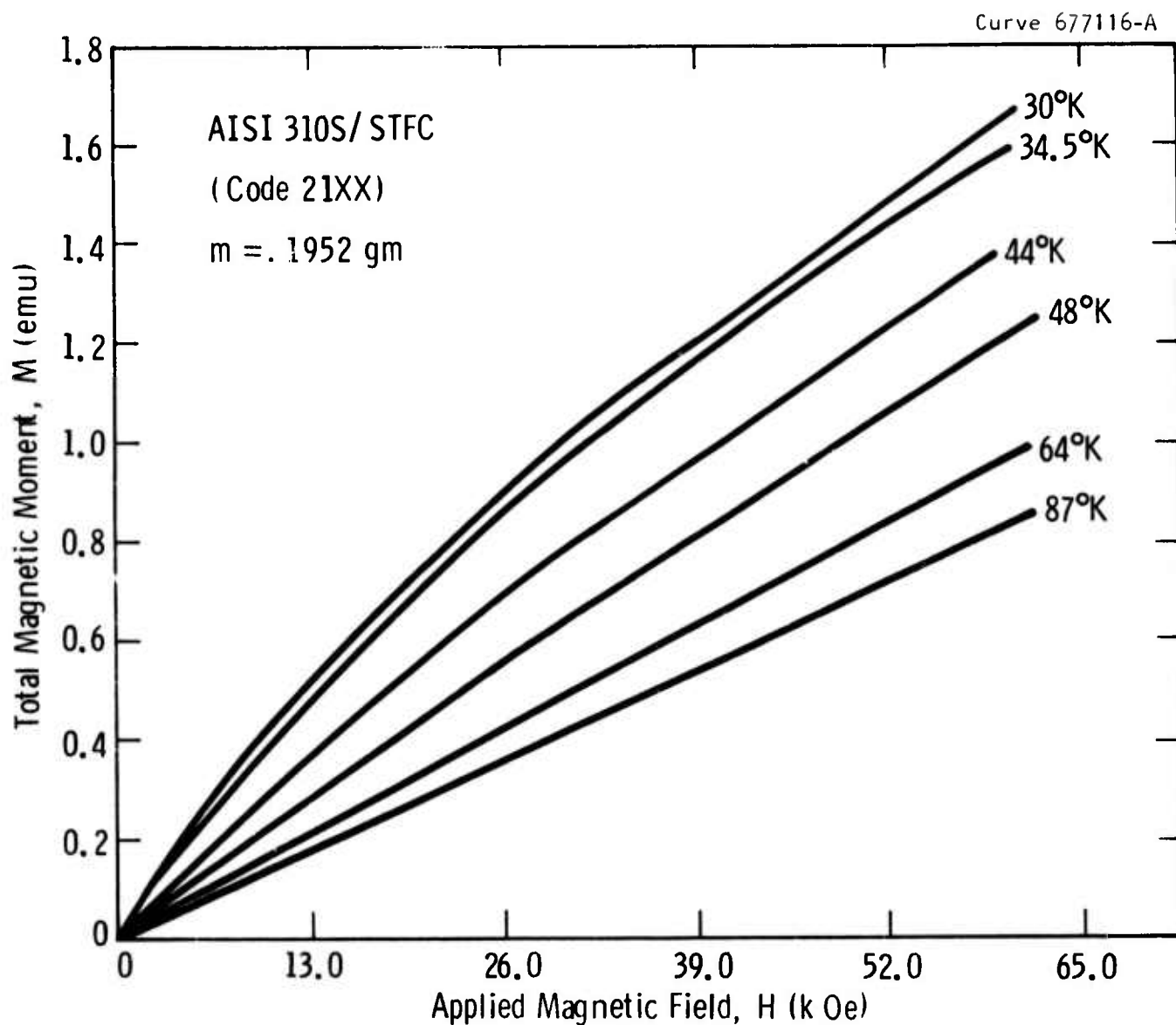


Fig. 8-3—Total magnetic moment as a function of the external field

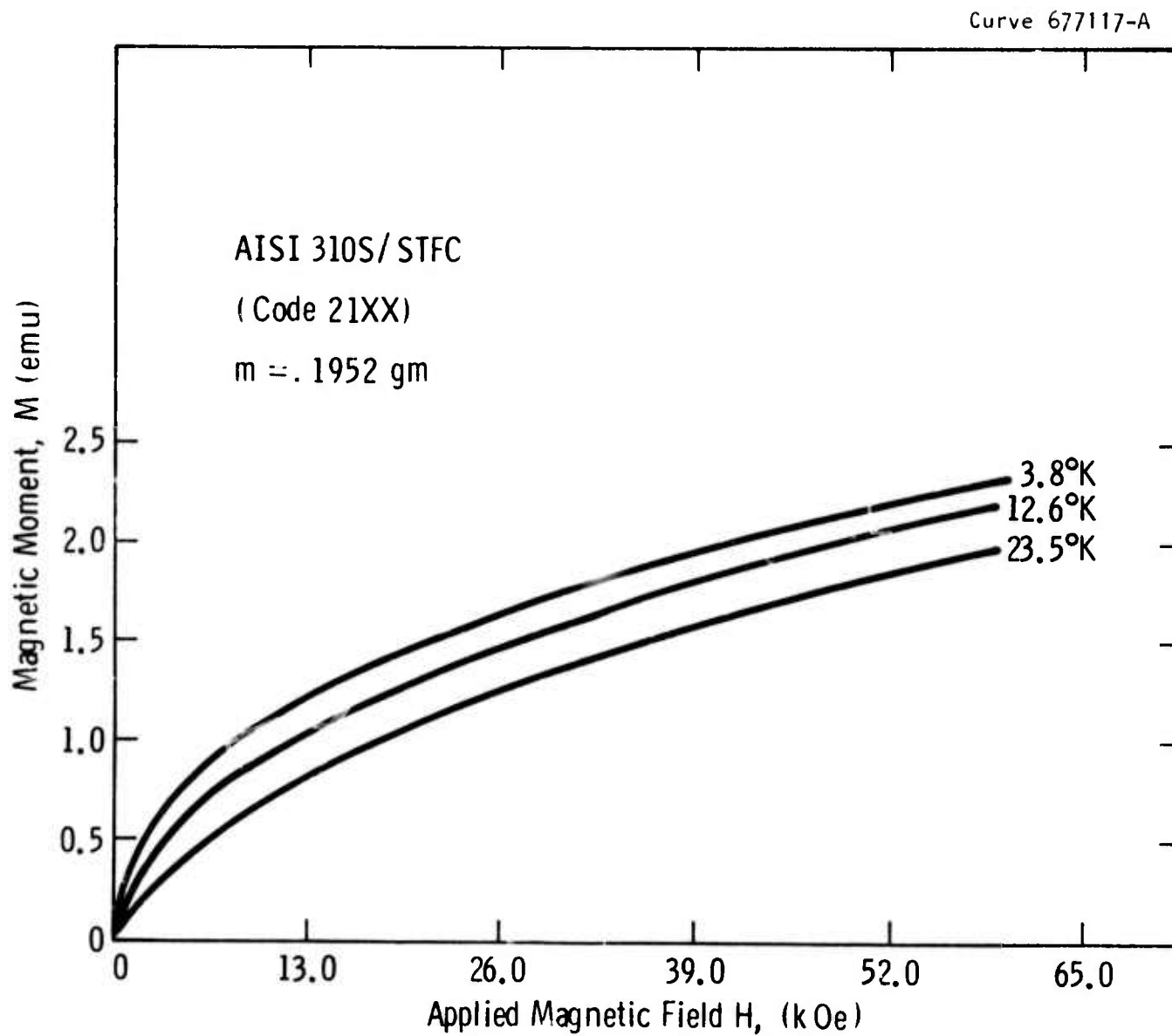


Fig. 8-4 — Magnetization data at low temperatures

Curve 677195-A

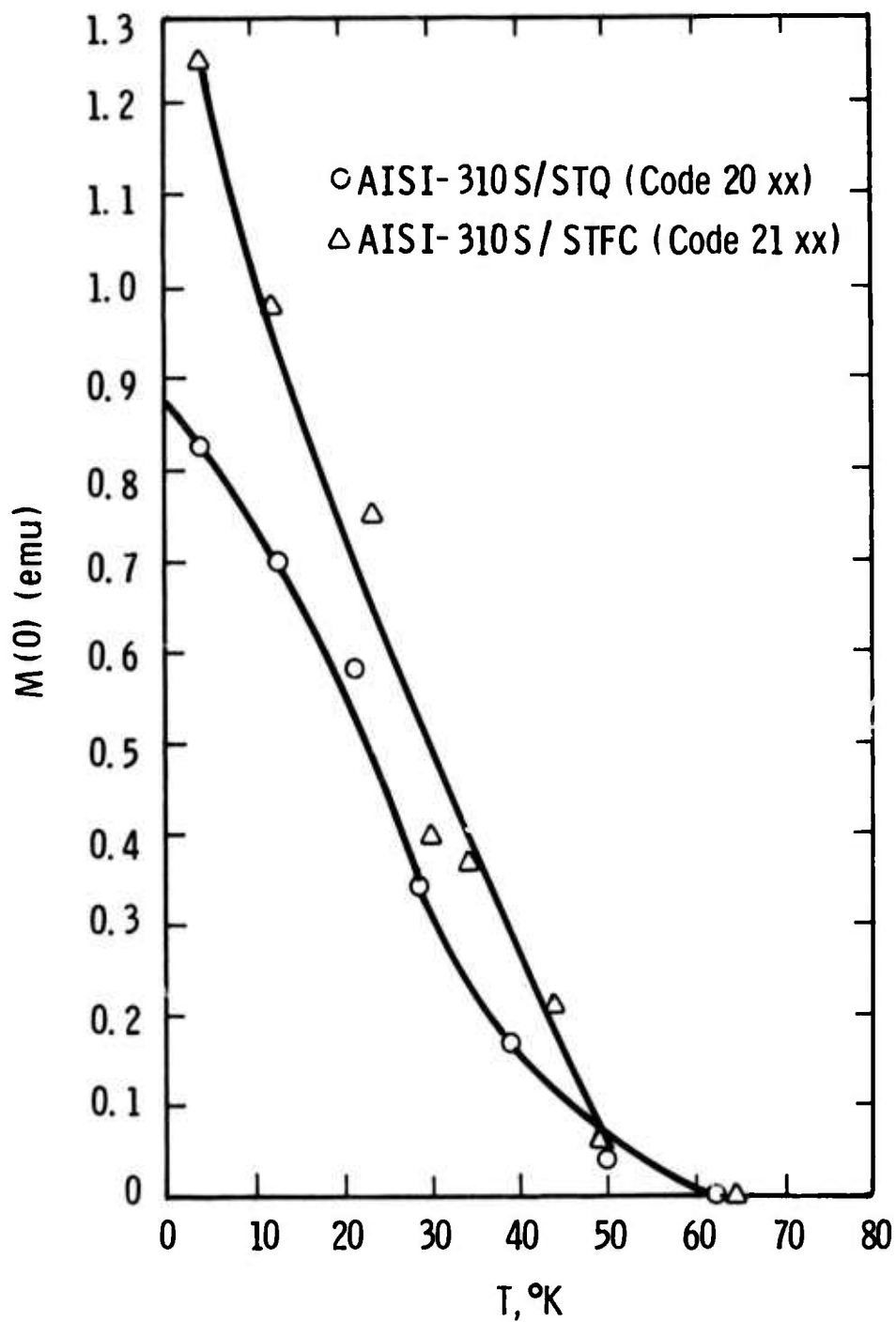


Fig. 8.5—Extrapolated magnetic moment at zero field as a function of temperature

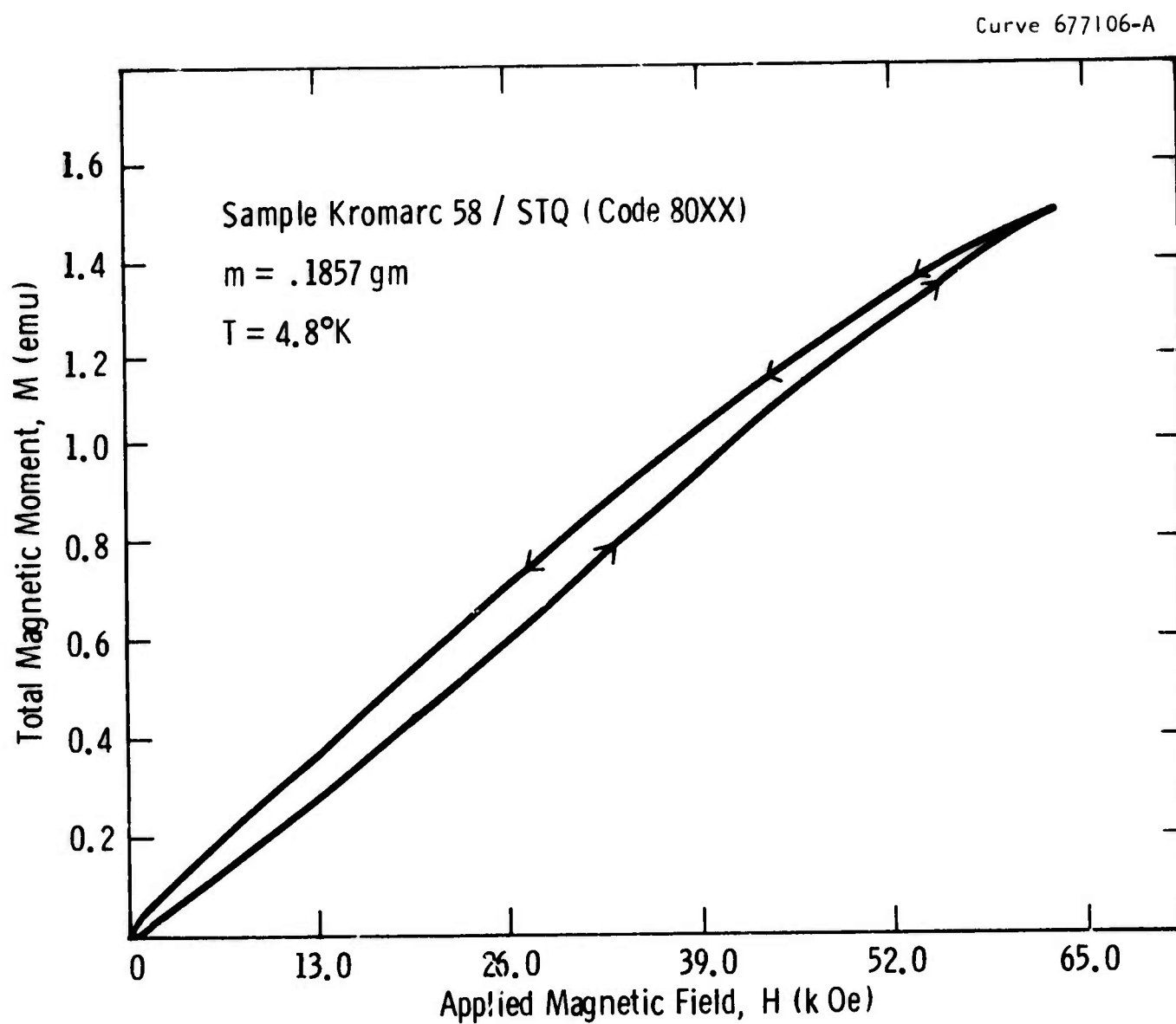


Fig. 8-6—Total magnetic moment as a function of the external field

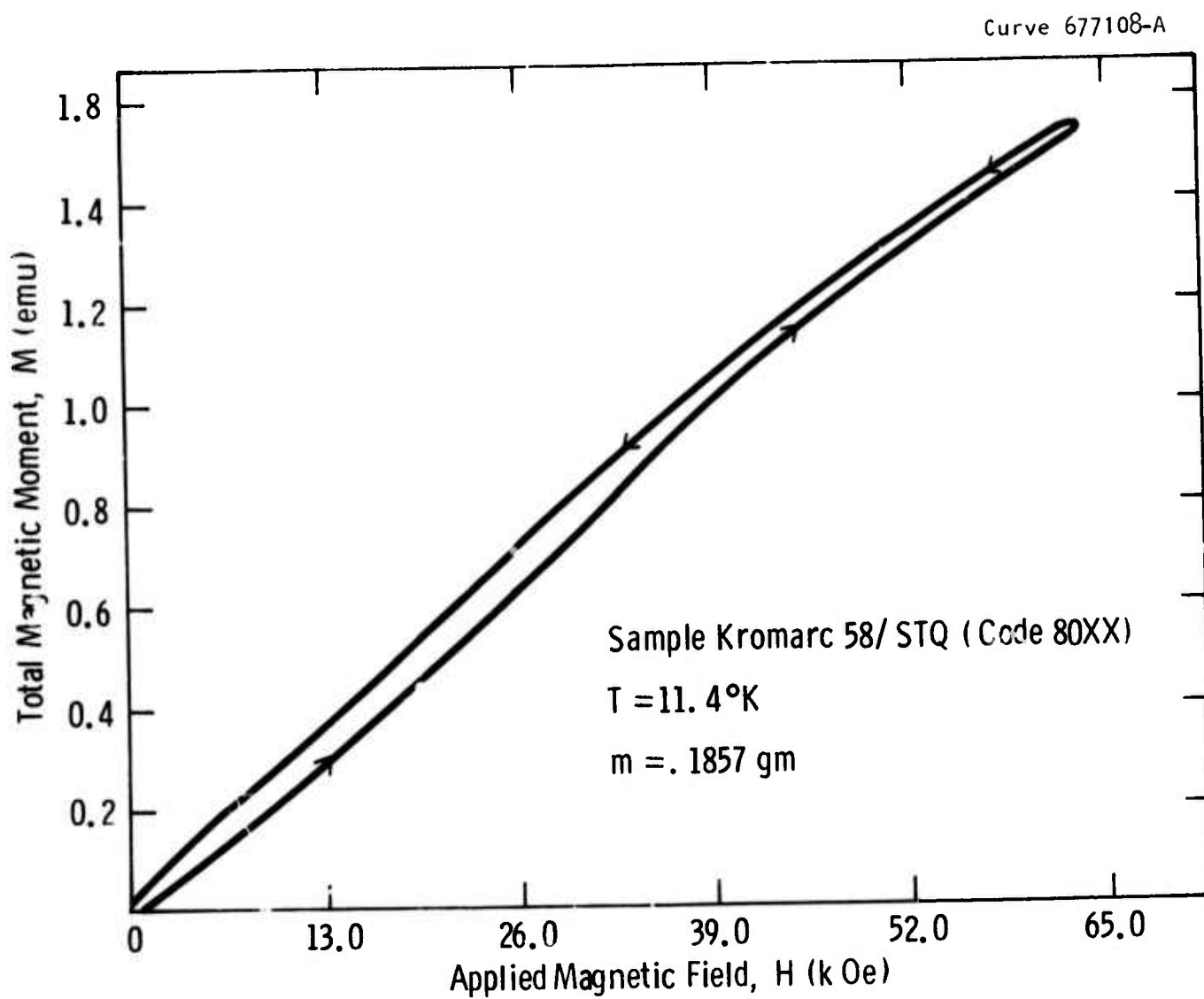


Fig. 8-7—Total magnetic moment as a function of the external field



Curve 677101-A

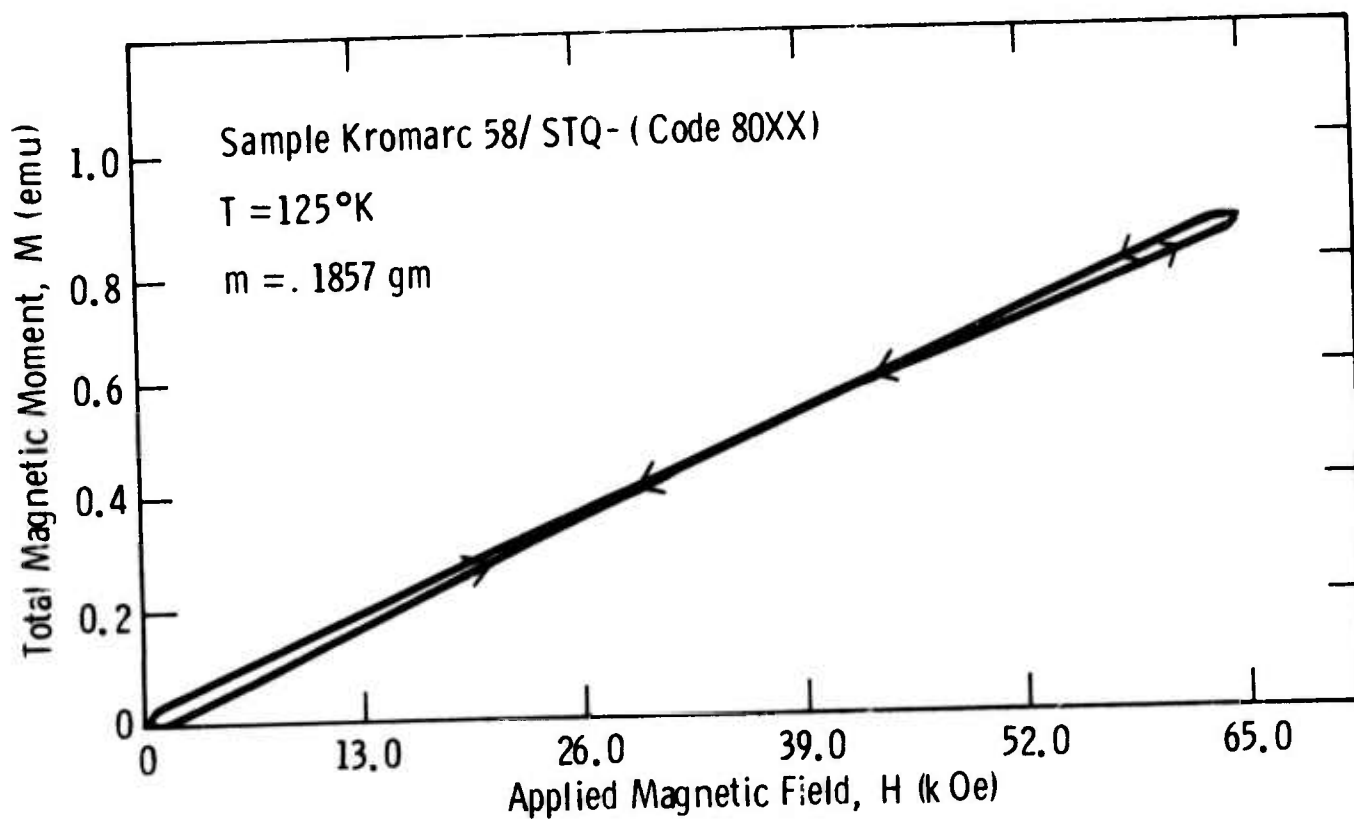


Fig. 8-8—Total magnetic moment as a function of the external field

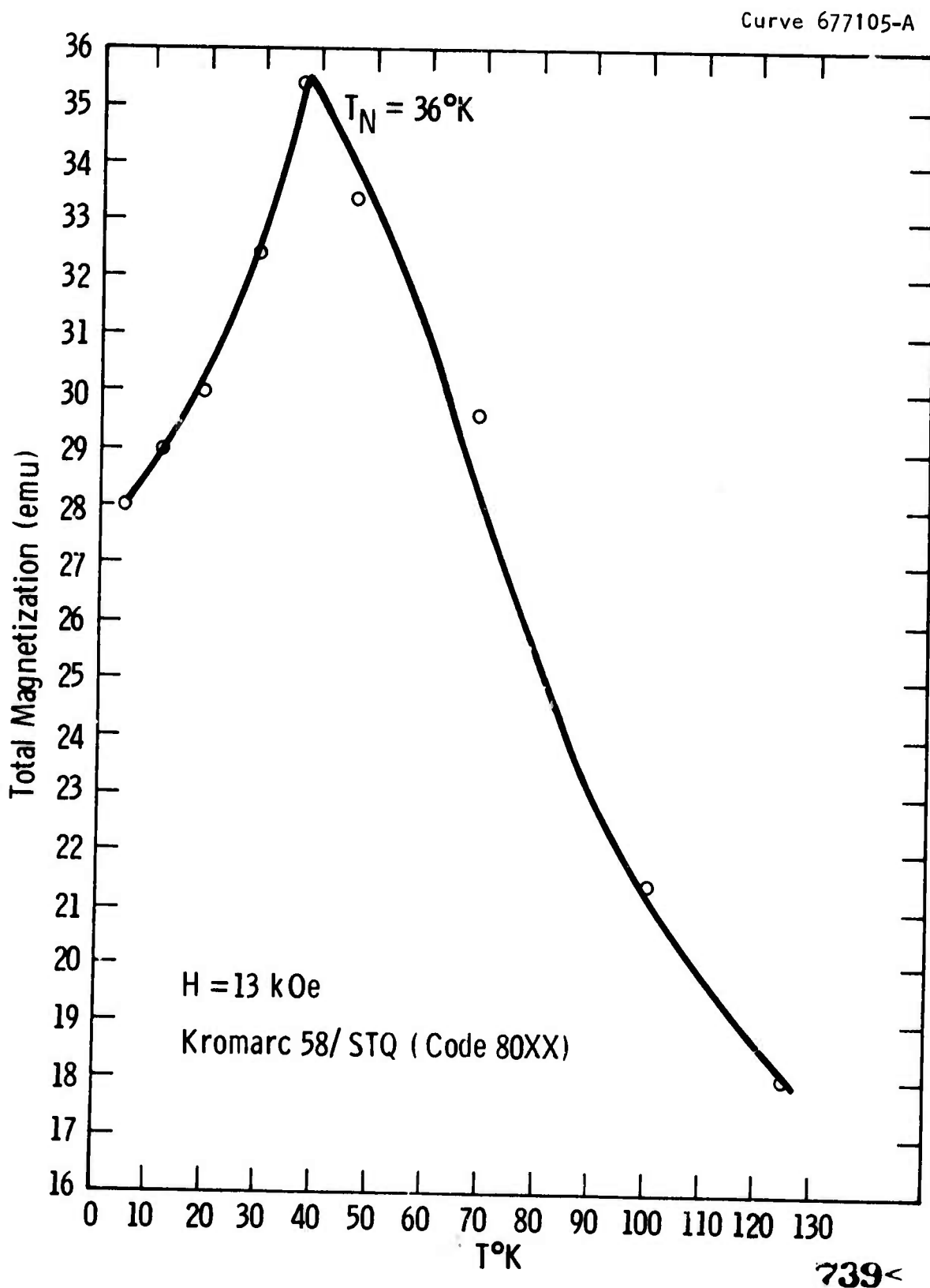


Fig. 8-9 —Magnetic moment at 13 kOe as a function of the temperature

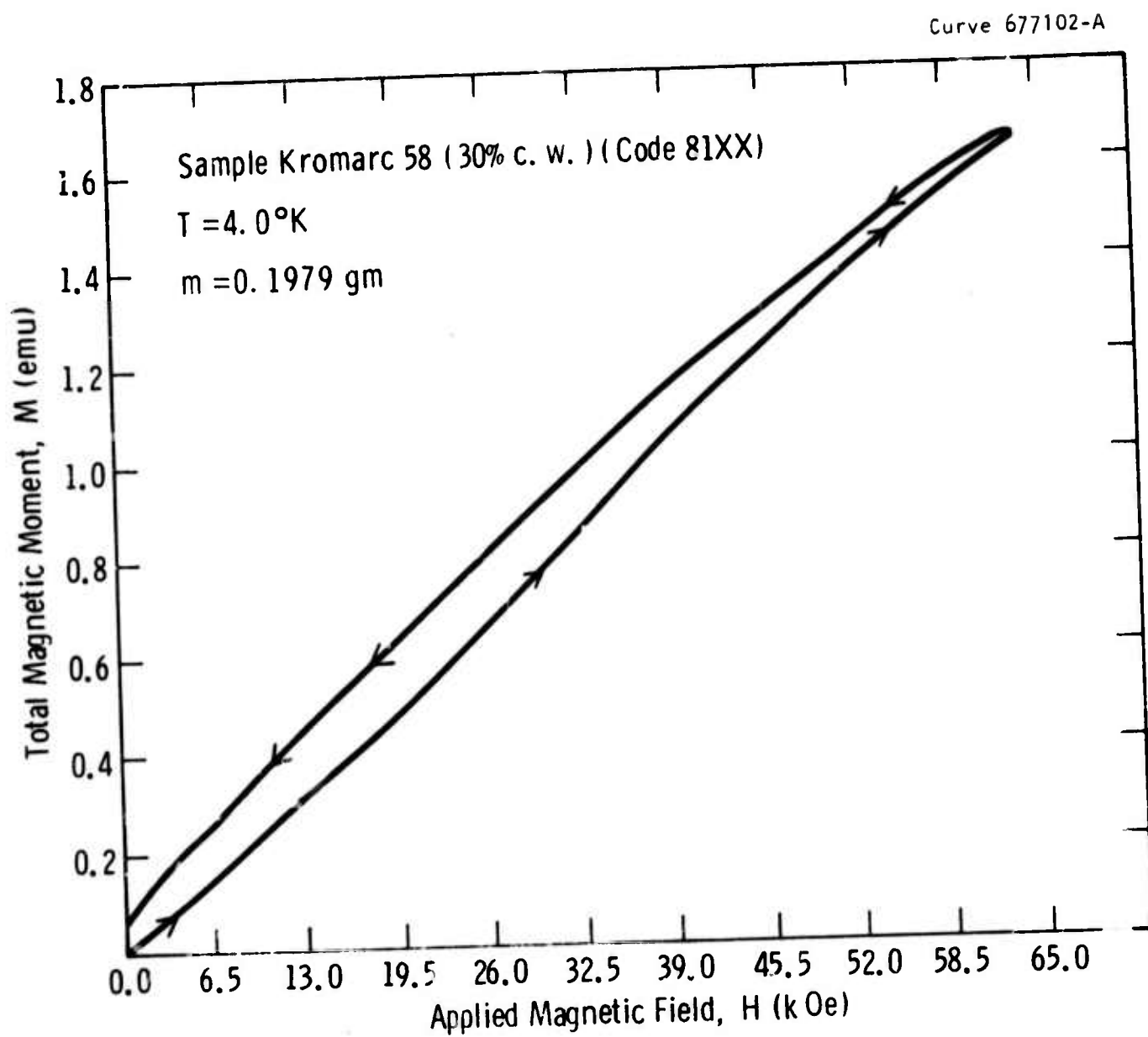


Fig. 8-10 — Magnetic moment as a function of the external field

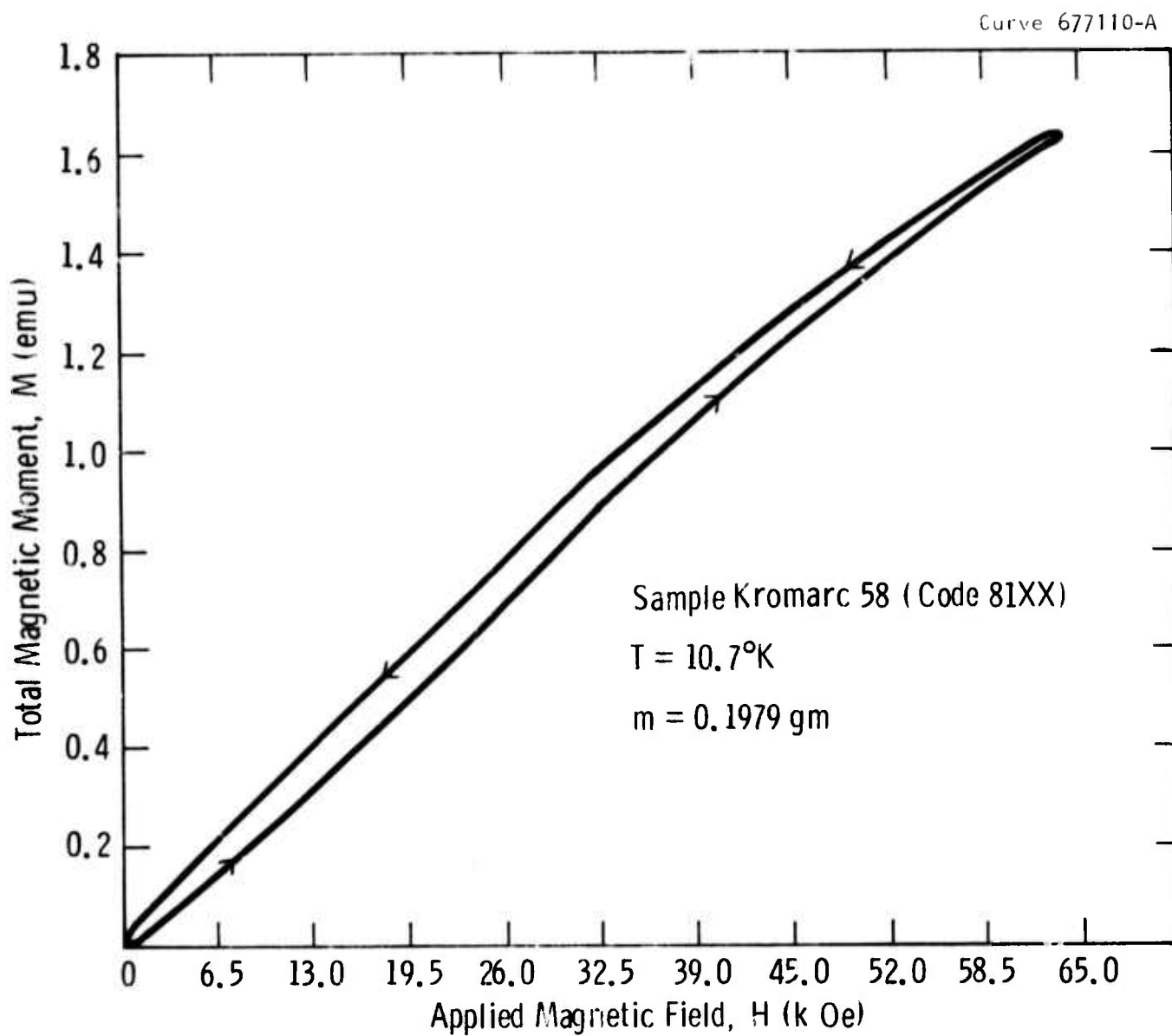


Fig. 8-11 — Magnetic moment as a function of the external field

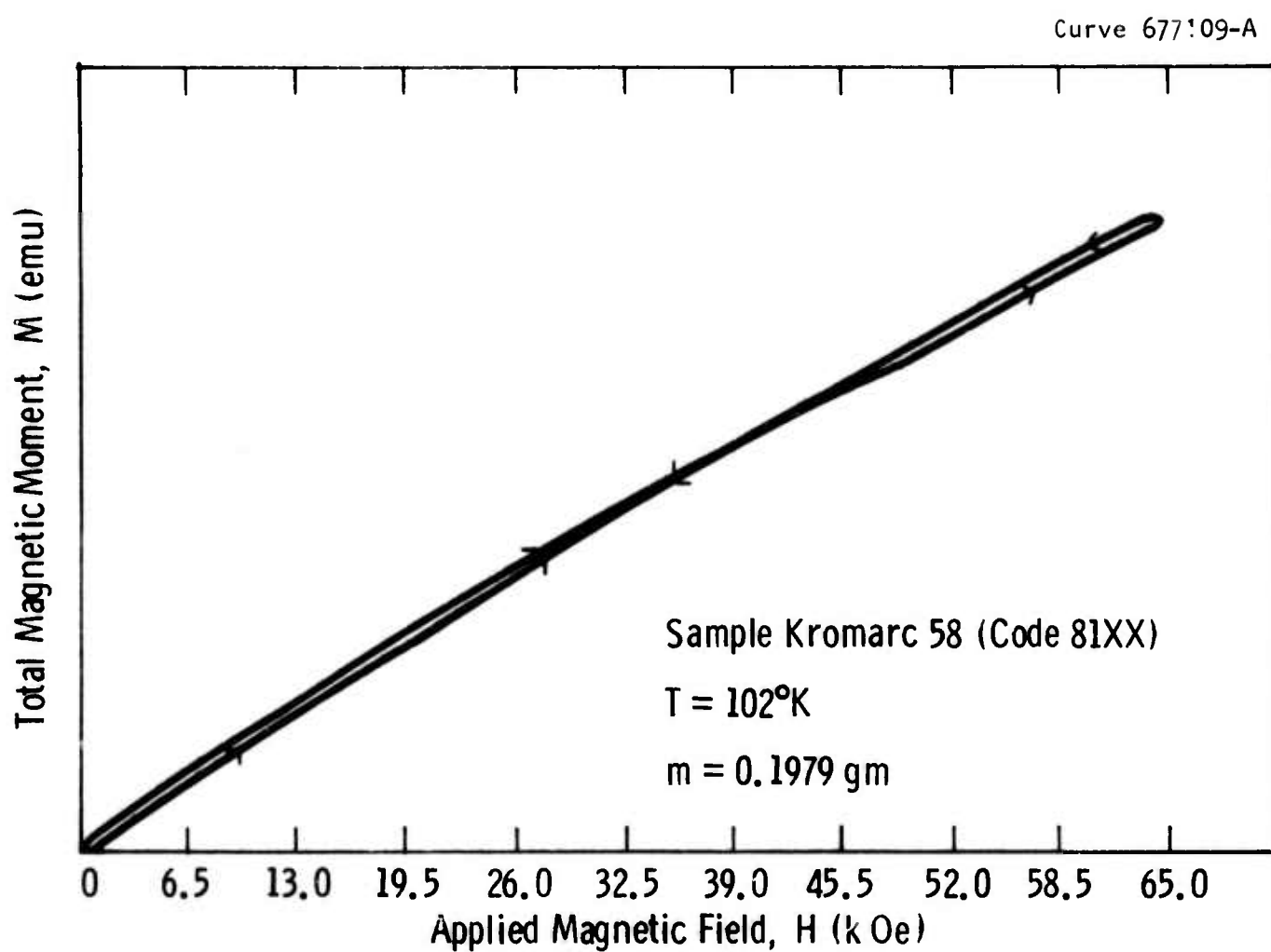


Fig. 8-12 — Magnetic moment as a function of the external field

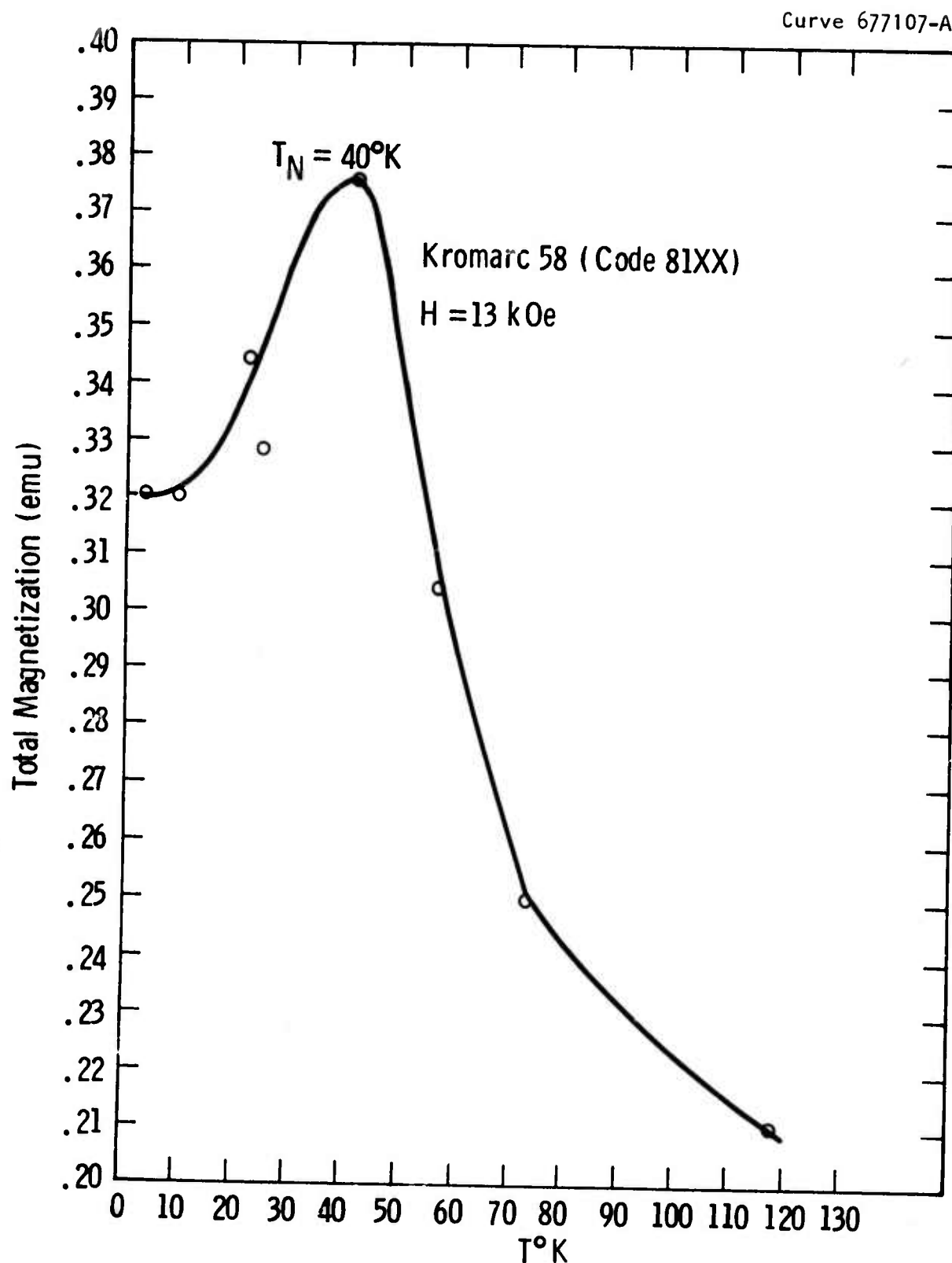


Fig. 8-13 — Magnetic moment at 13 kOe as a function of the temperature

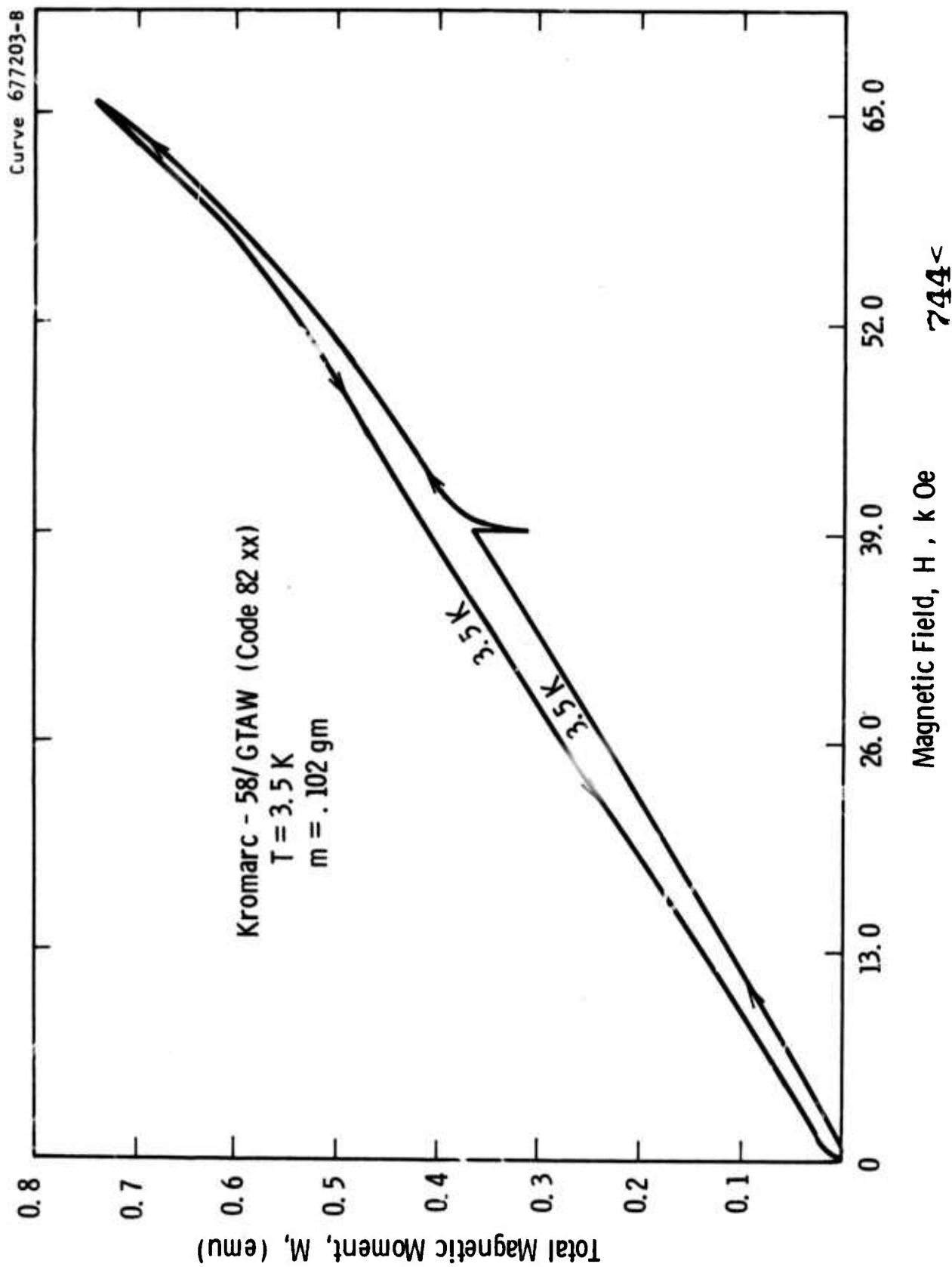


Fig. 8-14—Magnetic moment as a function of the external field

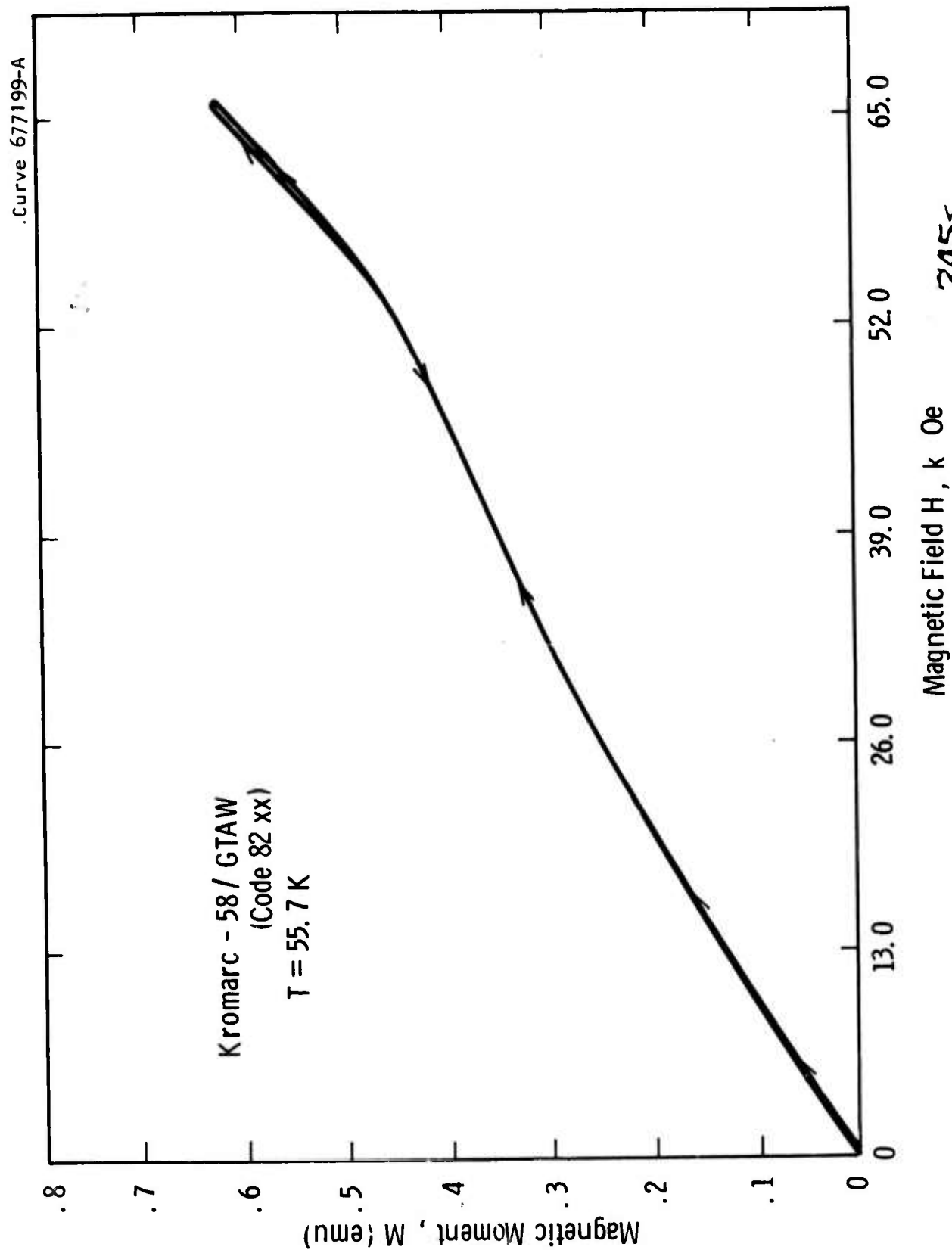


Fig. 8-15—Magnetic moment as a function of the external field



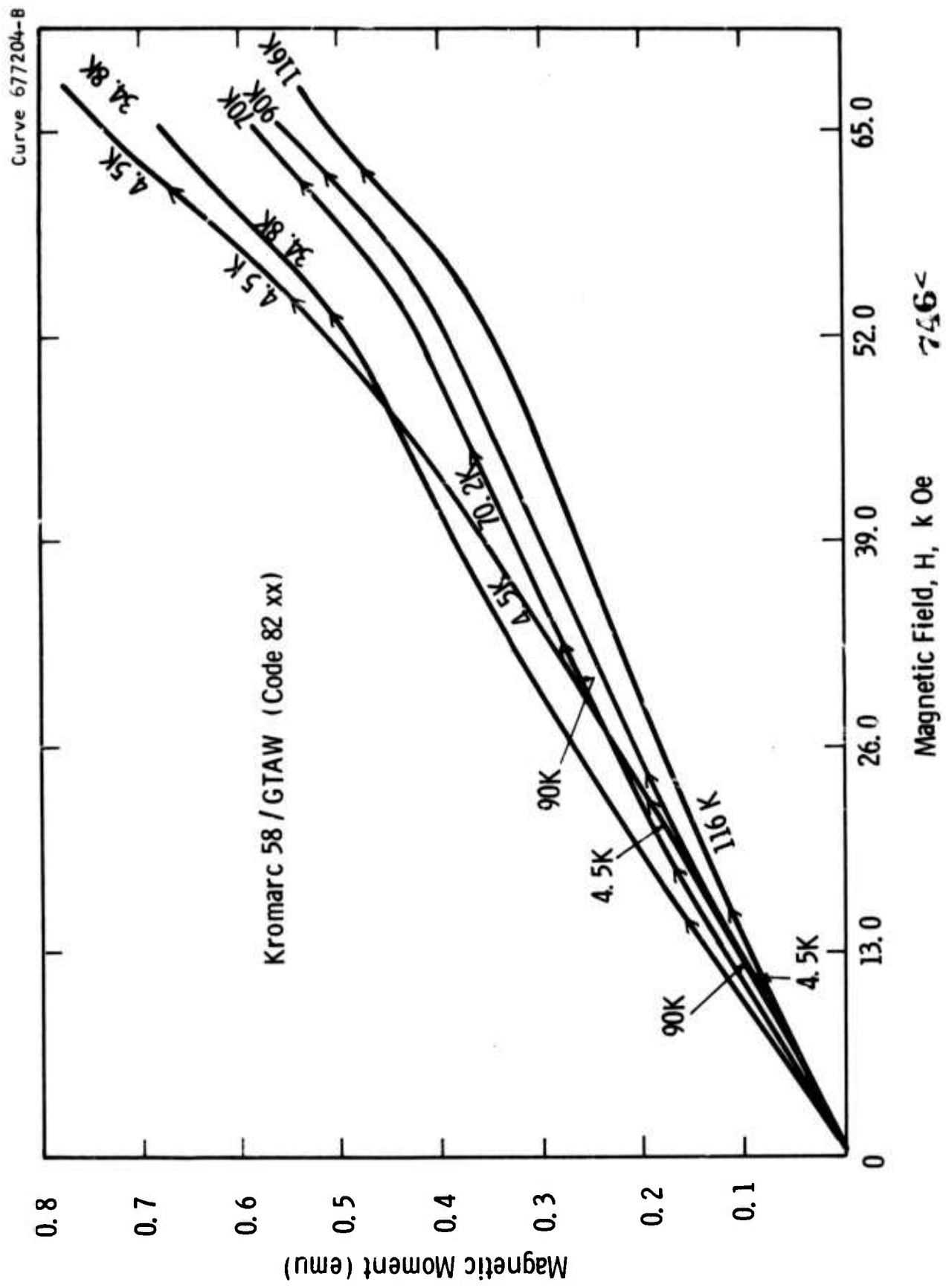


Fig. 8.16—Magnetic moment as a function of the external field

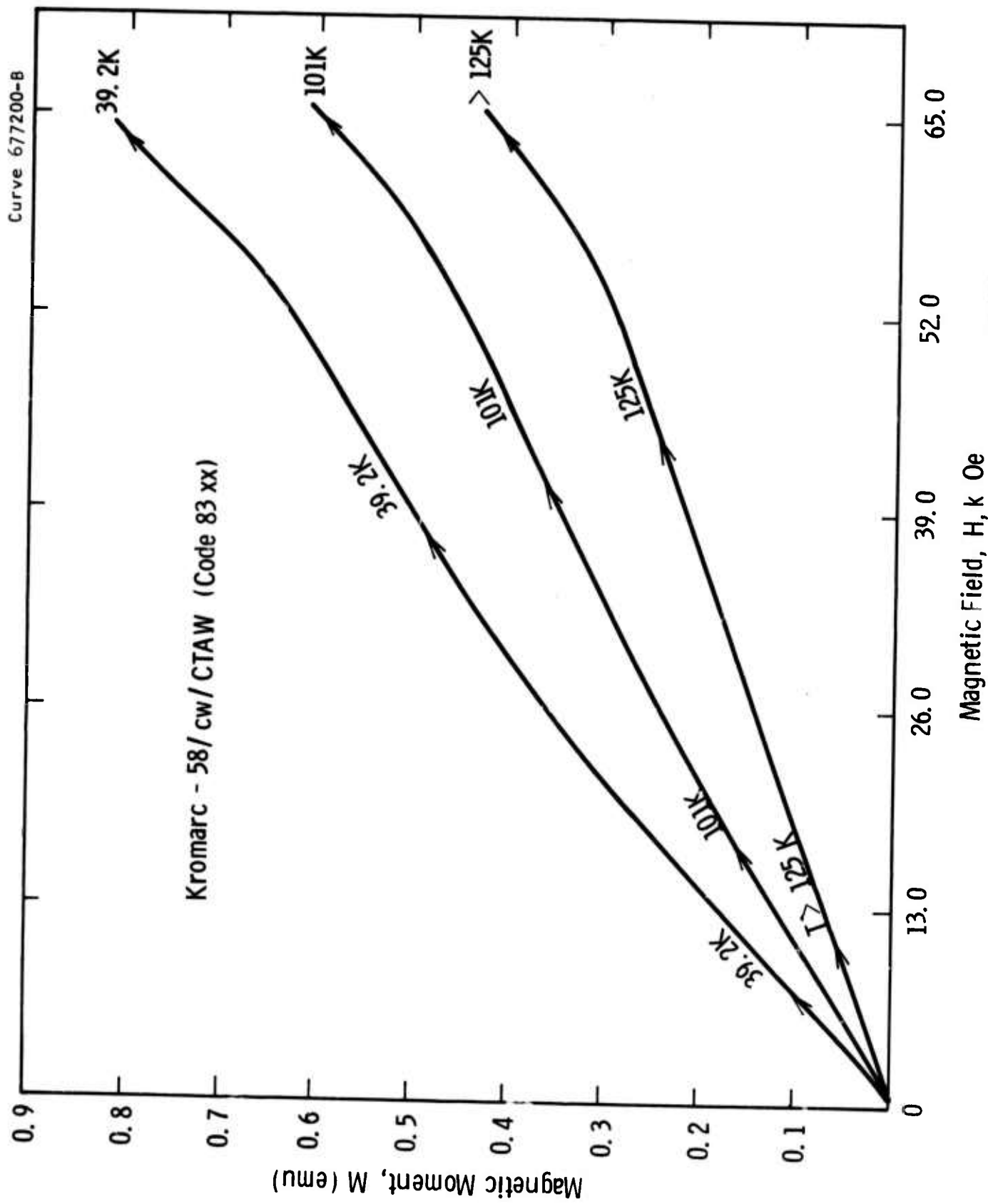


Fig. 8.17—Magnetic moment as a function of the external field

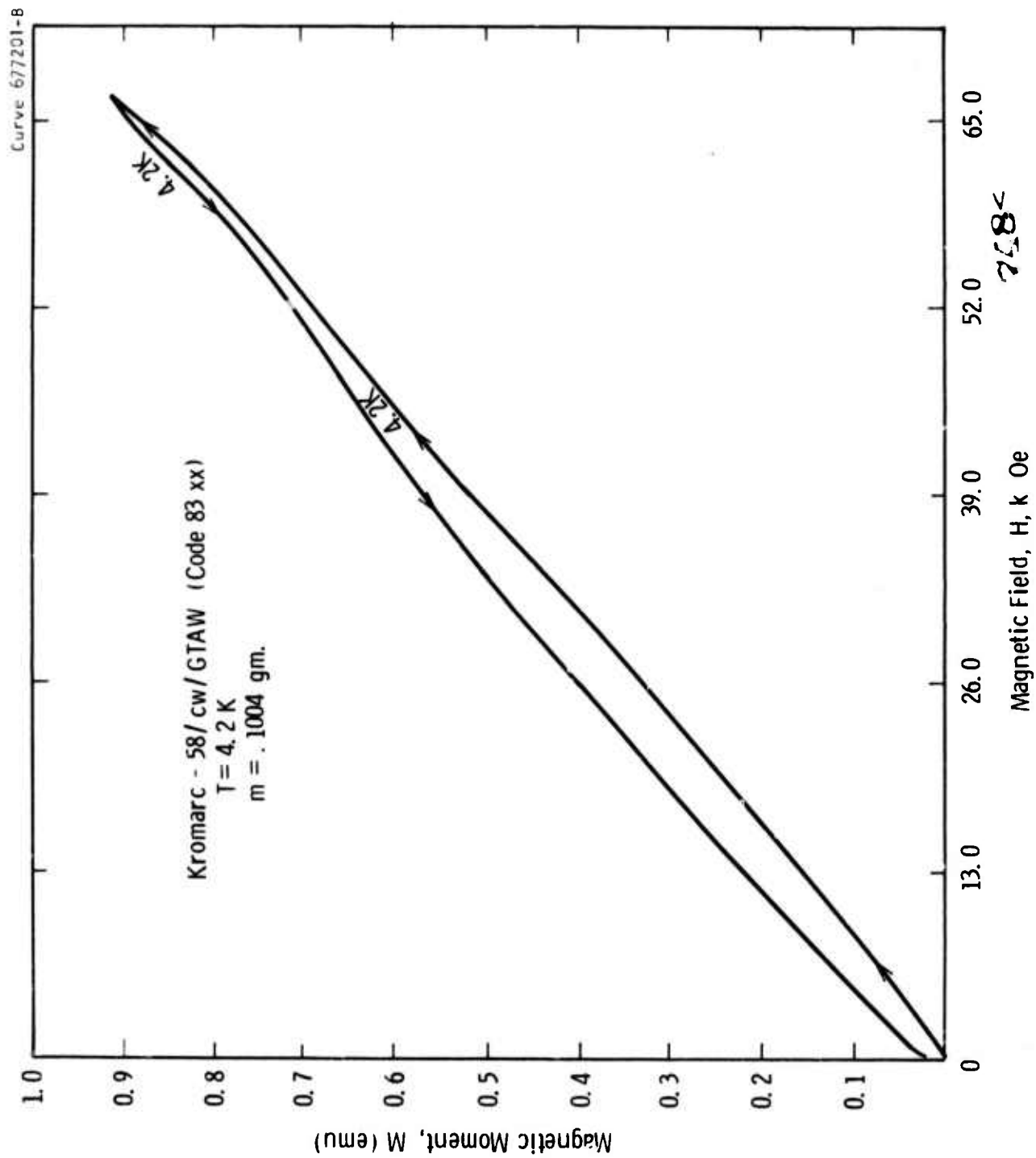


Fig. 8. 18—Magnetic moment as a function of the external field

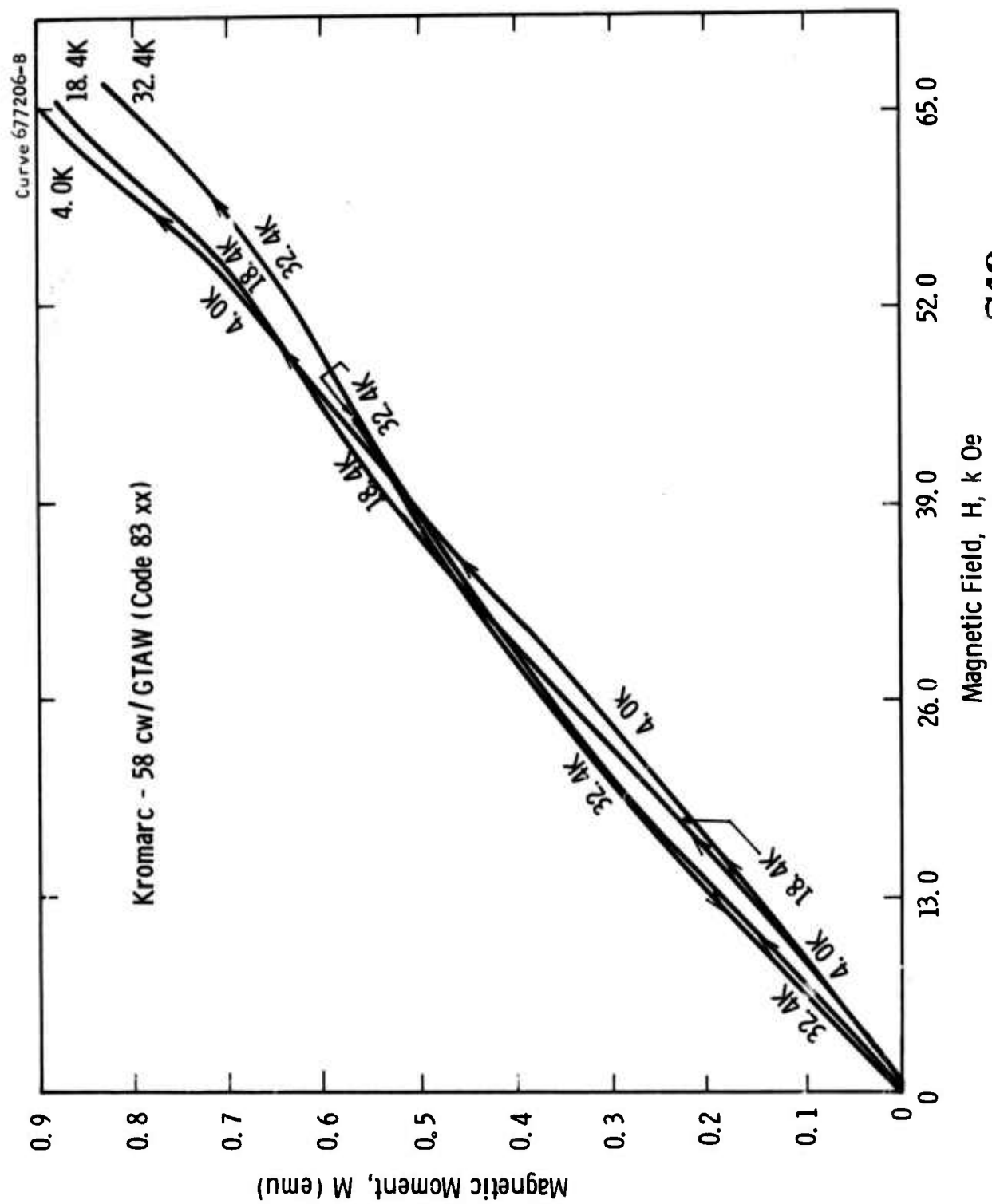


Fig. 8-19-Magnetic moment as a function of the external field

Curve 677207-8

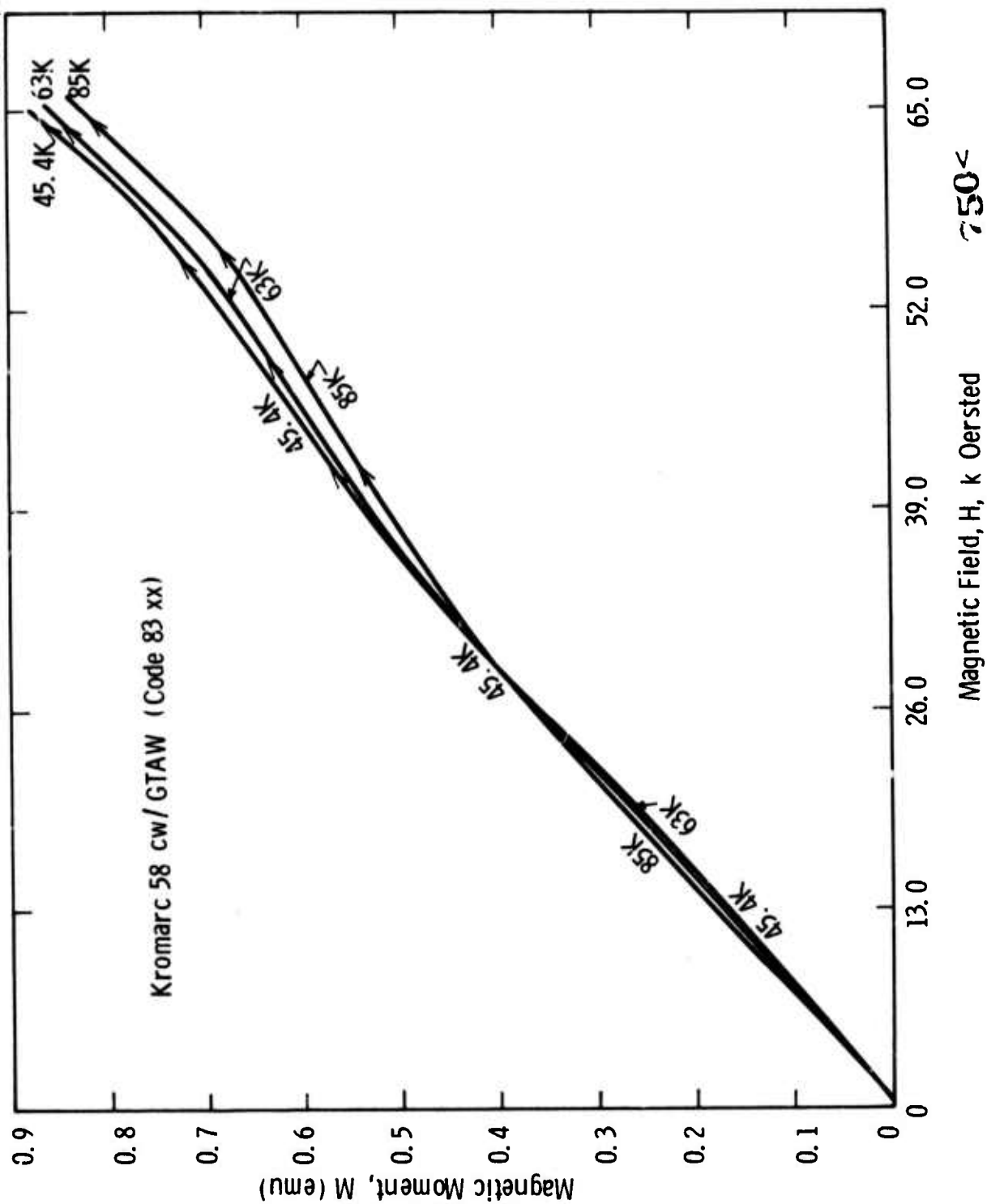


Fig. 8. 20—Magnetic moment as a function the external field

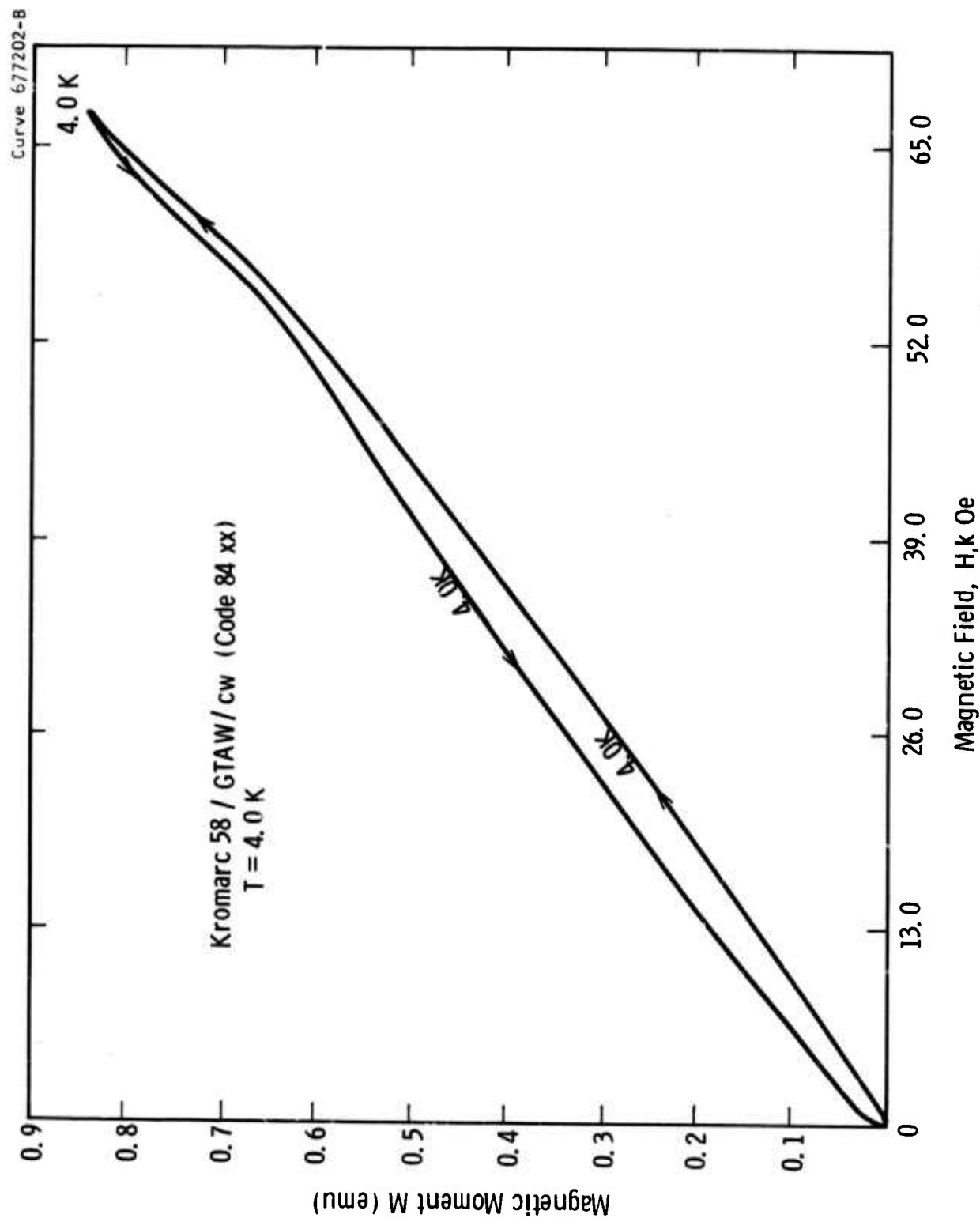


Fig. 8-21—Magnetic moment as a function of the external field

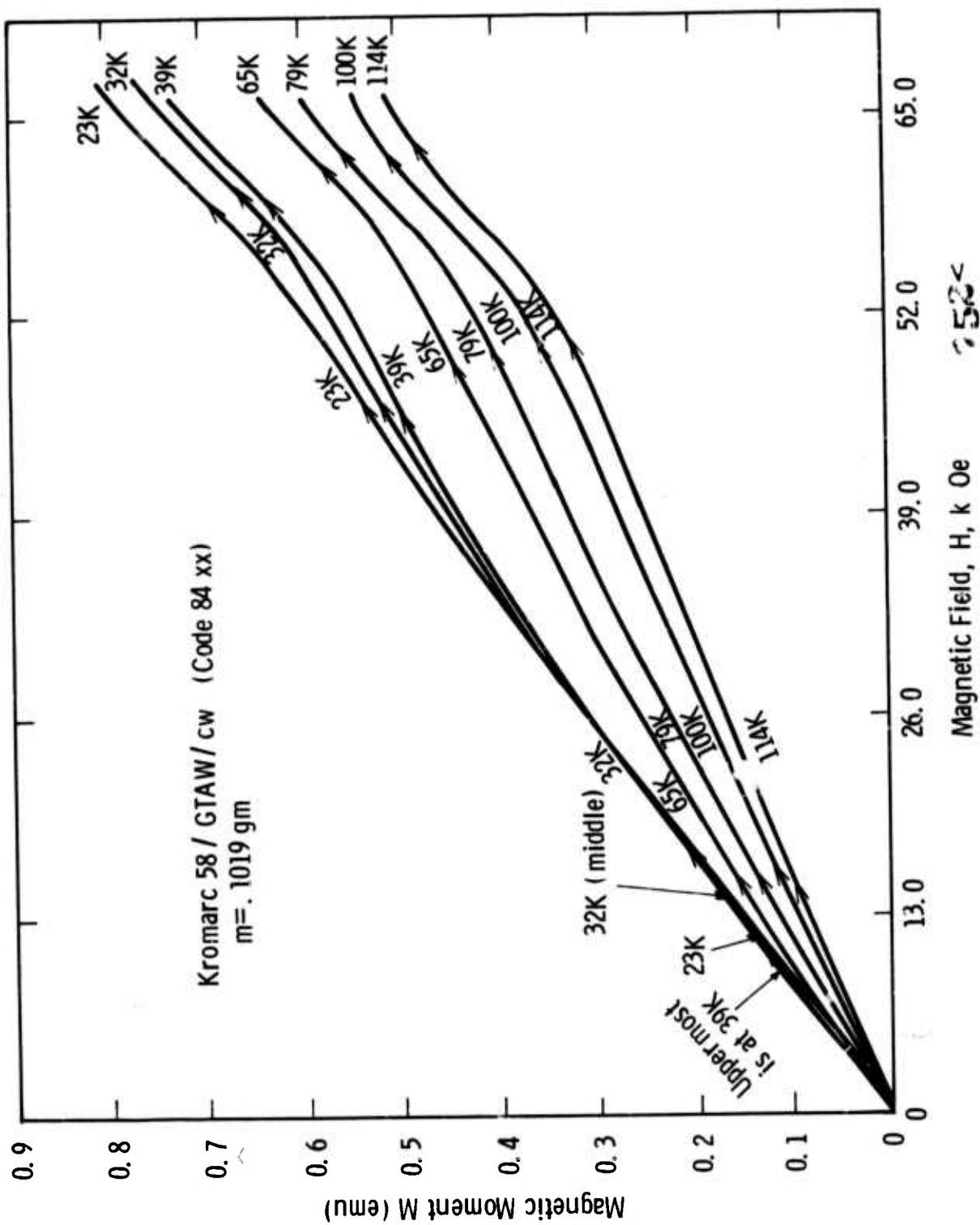


Fig. 8-22—Magnetic moment as a function of the external field

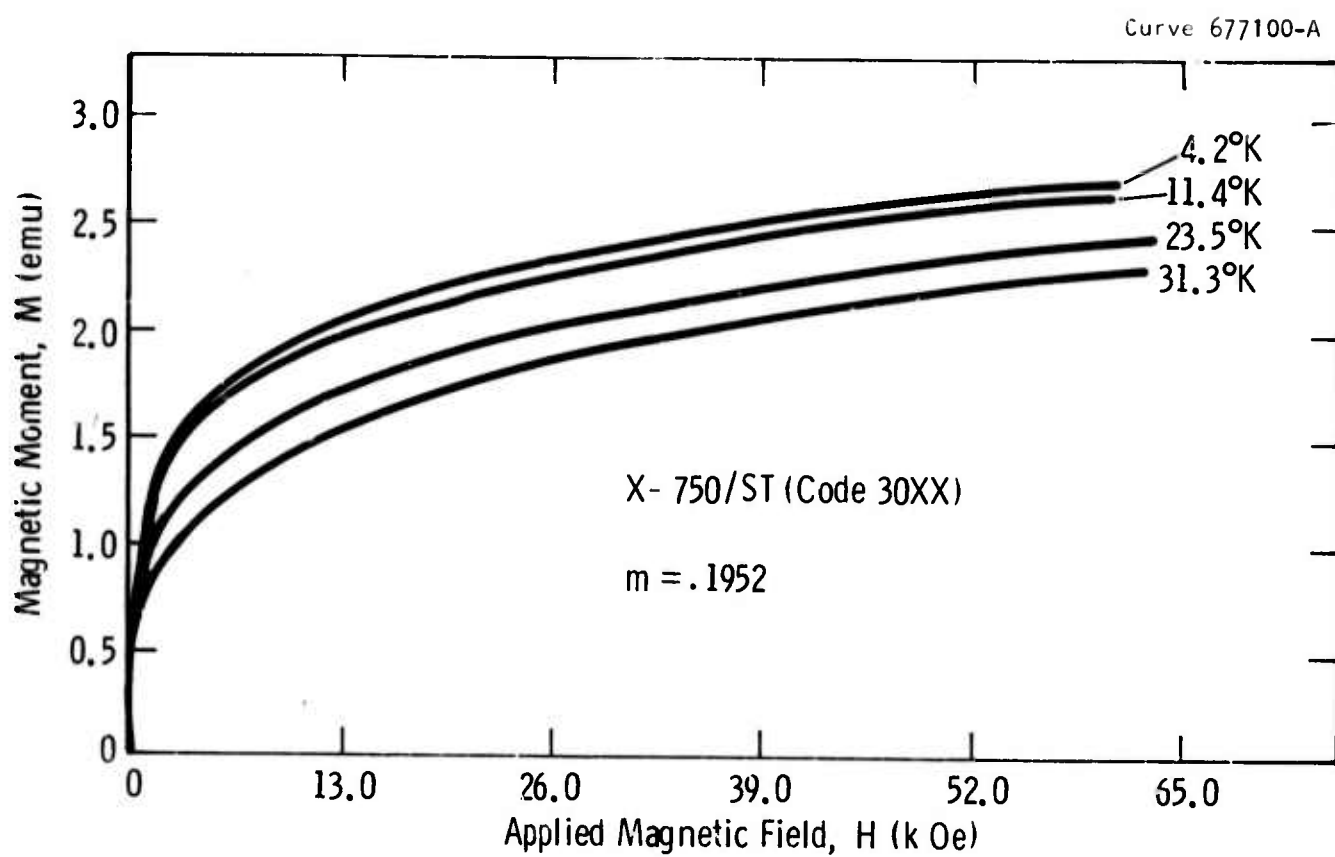


Fig. 8-23—Magnetic moment as a function of the external field at low temperatures



Curve 677114-A

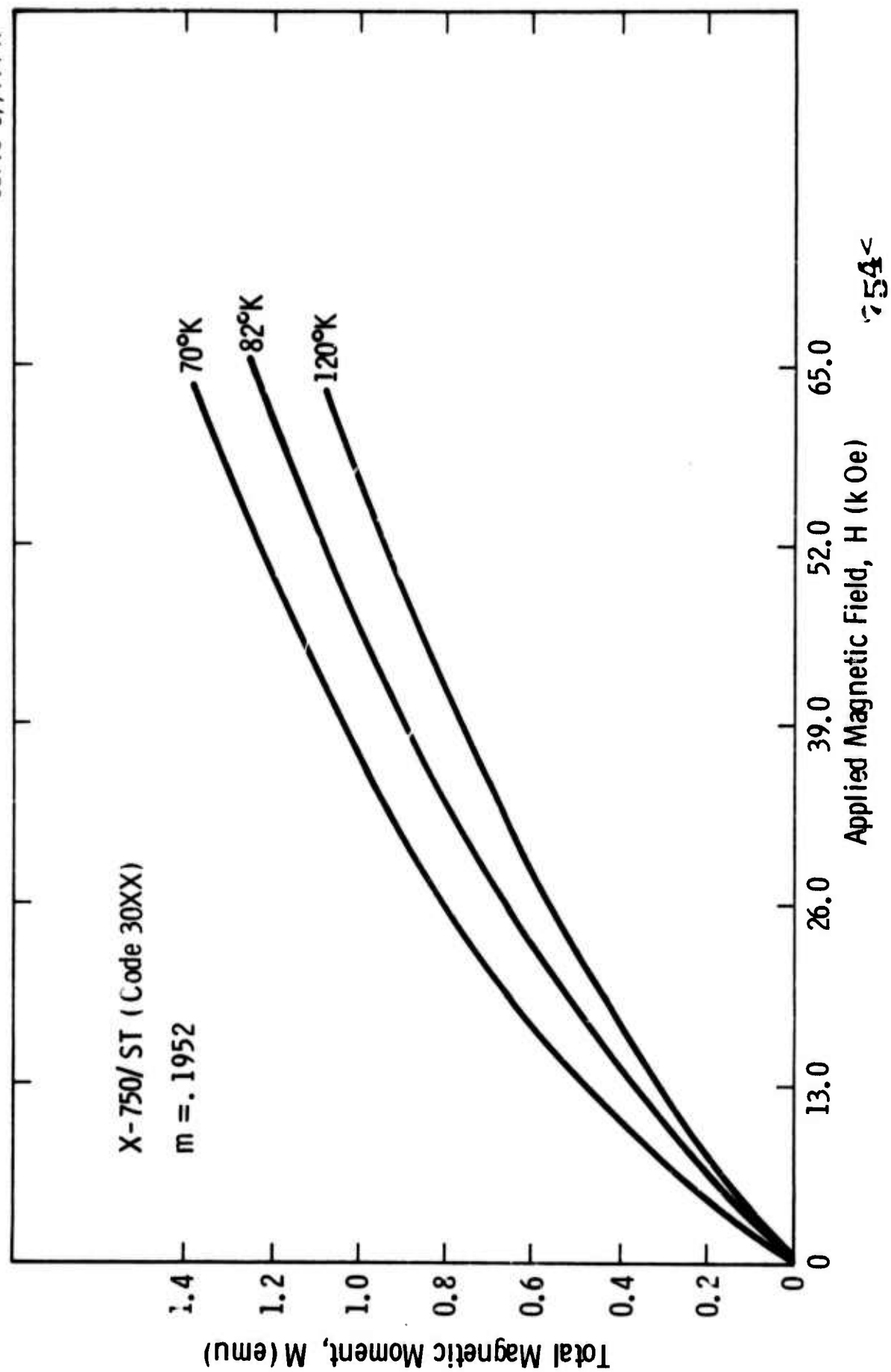


Fig. 8-24 — Magnetic moment as a function of the external field

Curve 677112-A

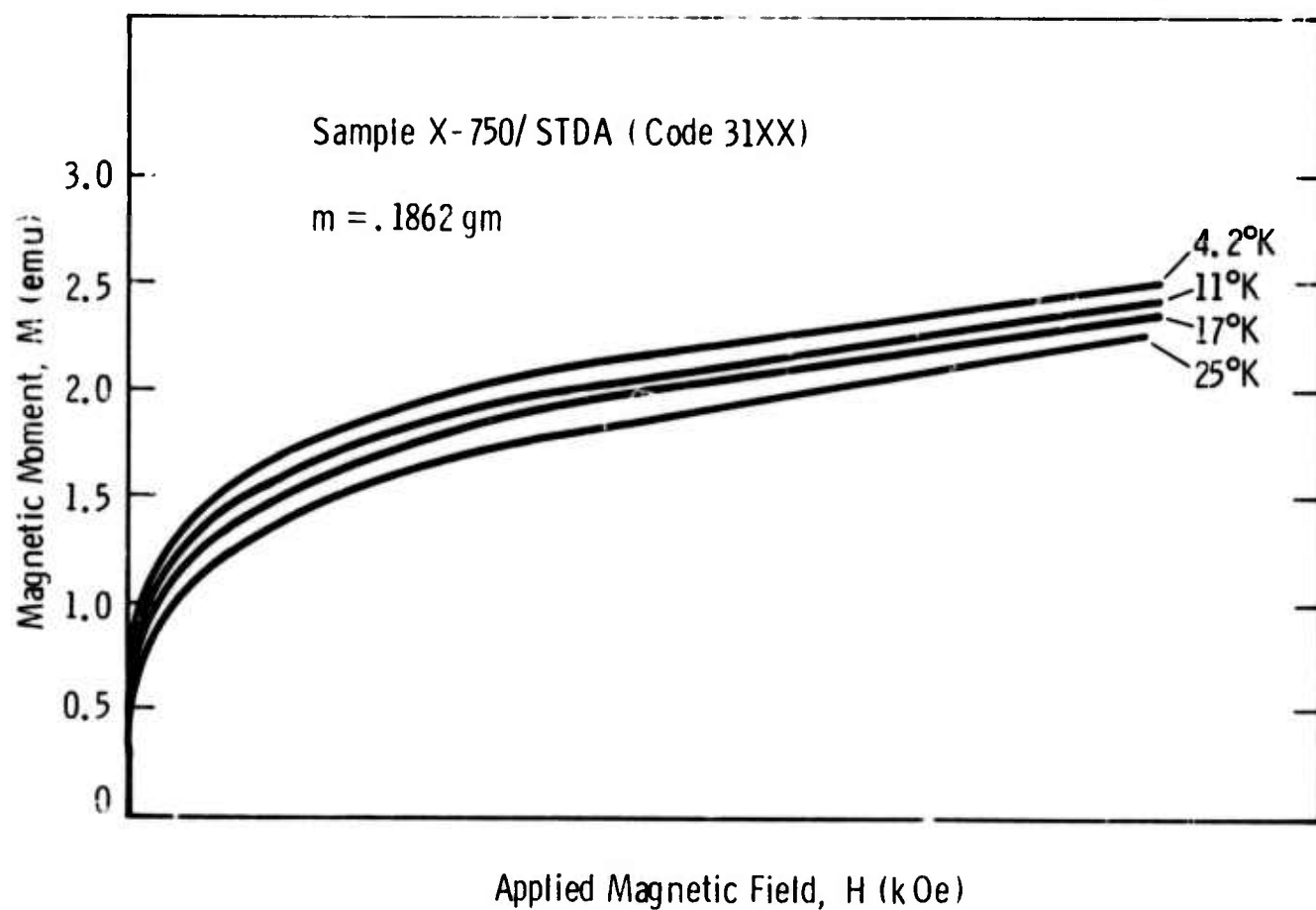


Fig. 8-25—Magnetic moment as a function of the external field

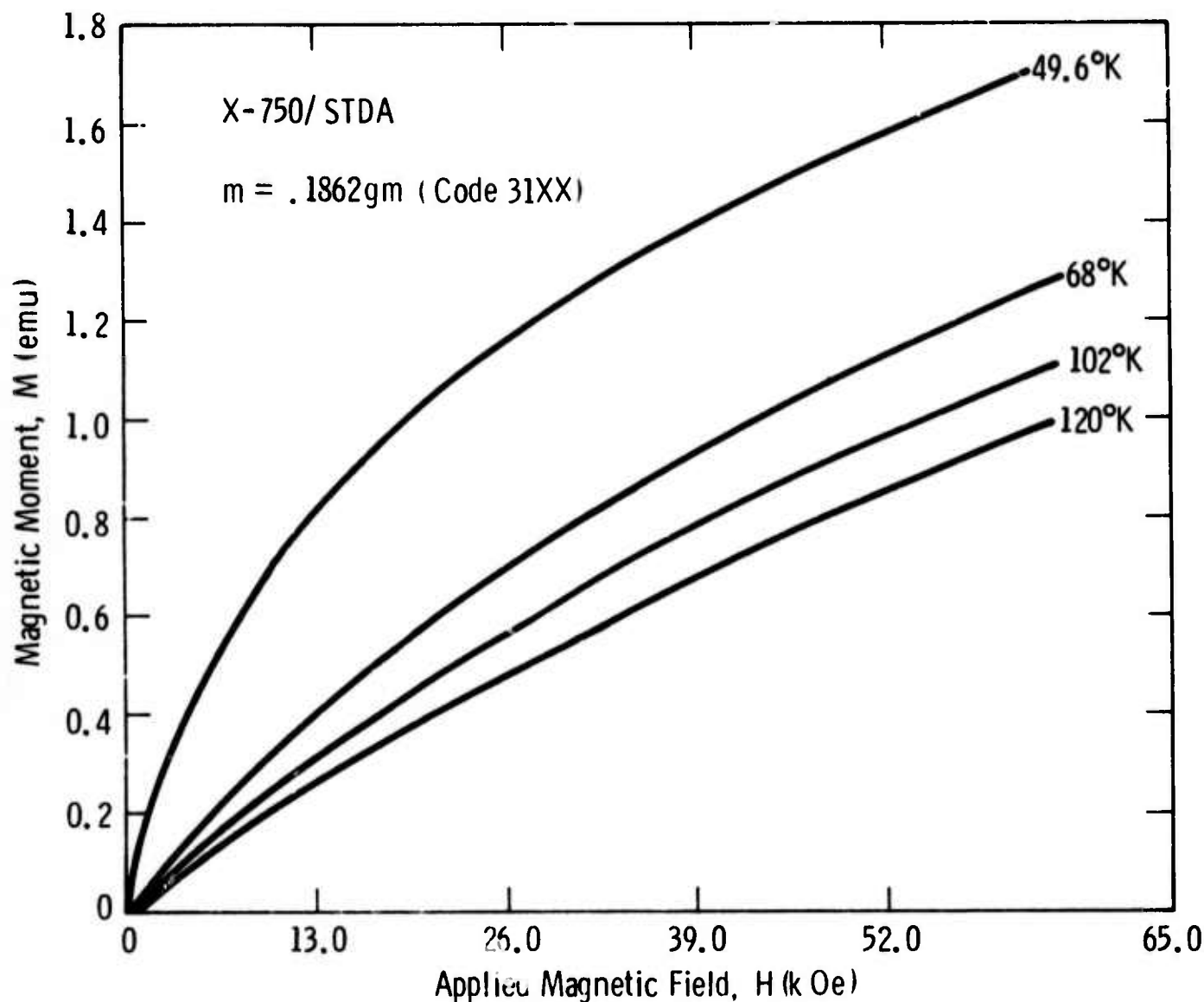


Fig. 8-26—Magnetic moment as a function of the external field

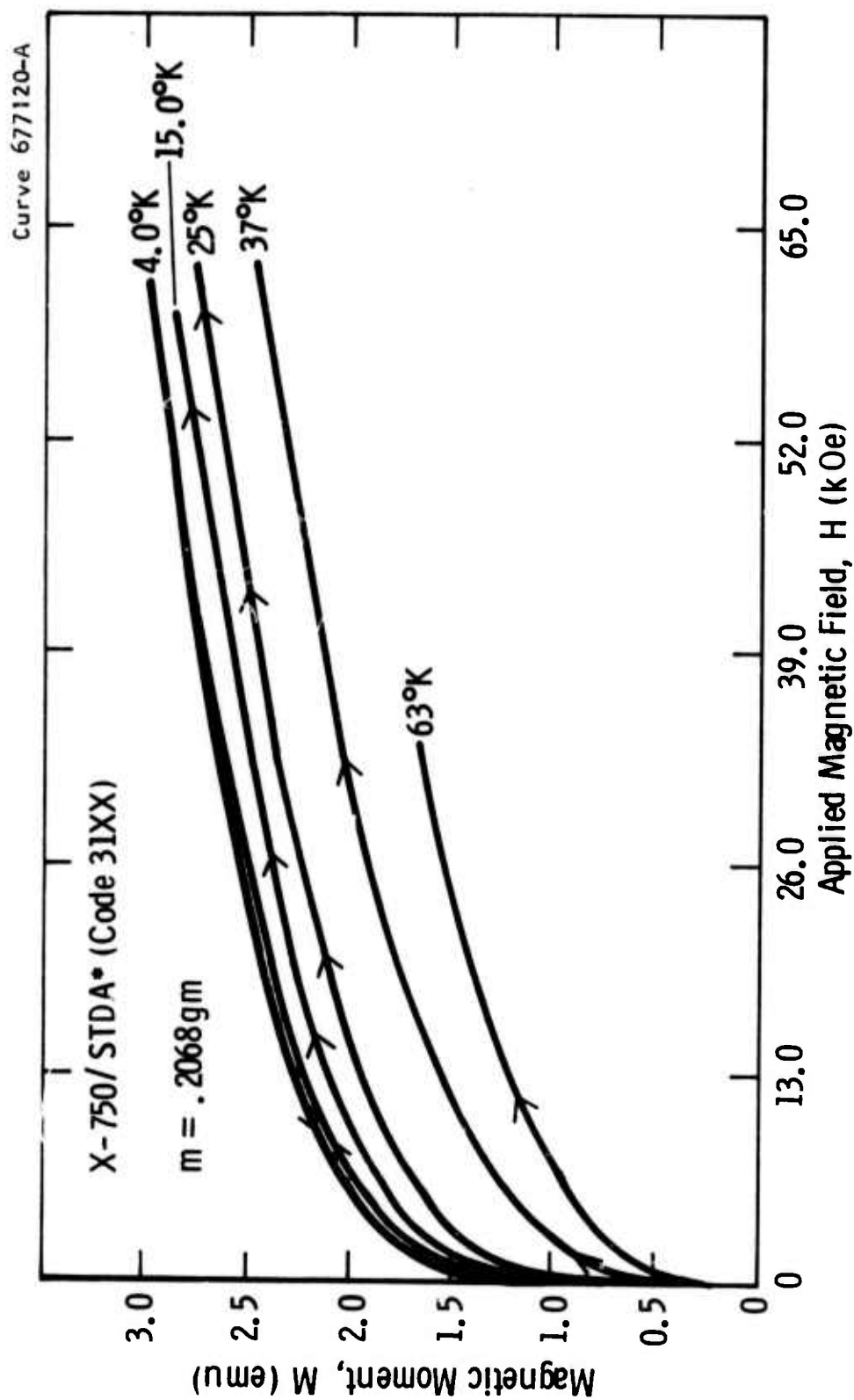


Fig. 8-27 — Magnetic moment as a function of the external field at low temperatures

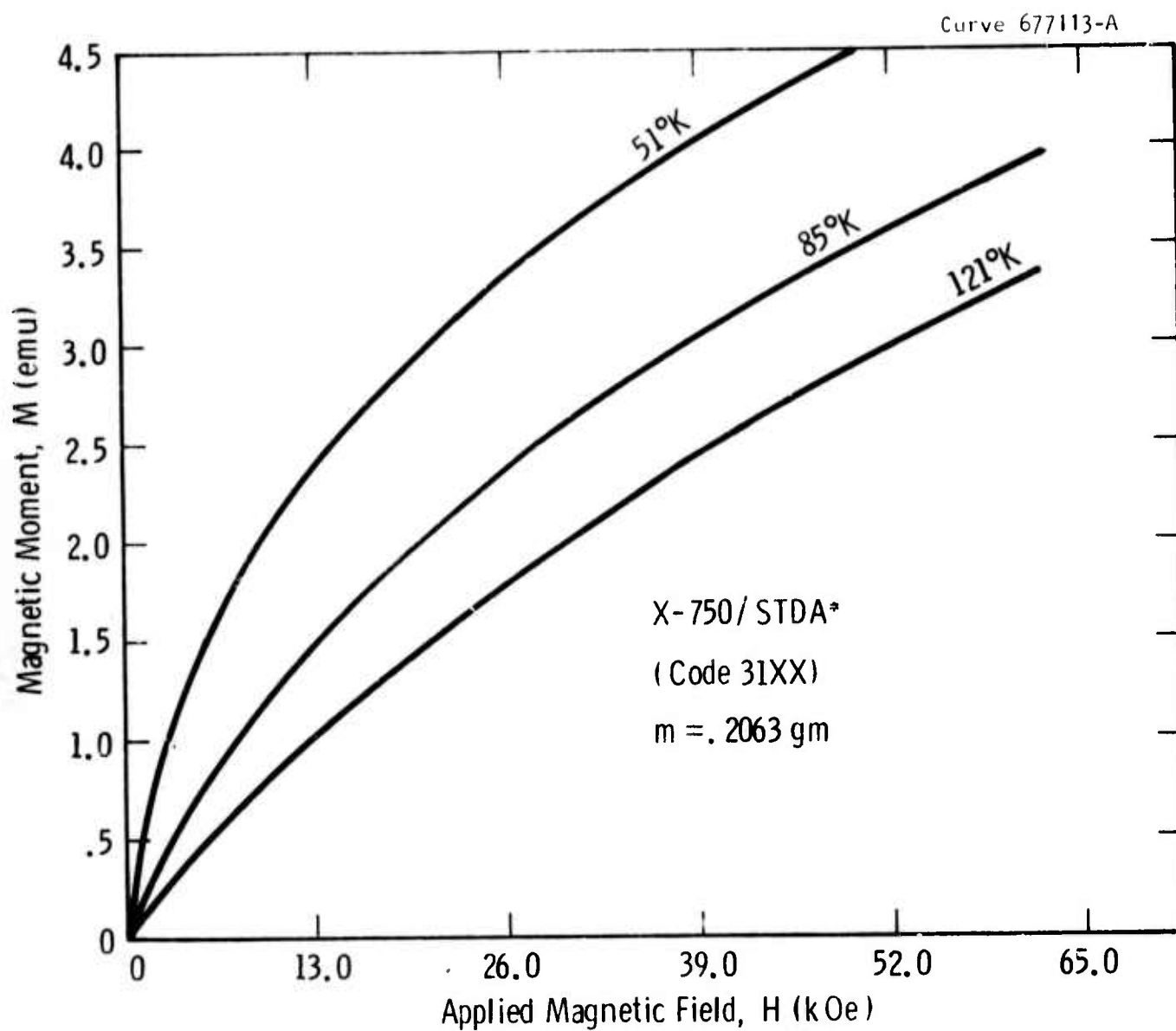


Fig. 8-28 — Magnetic moment as a function of the external field

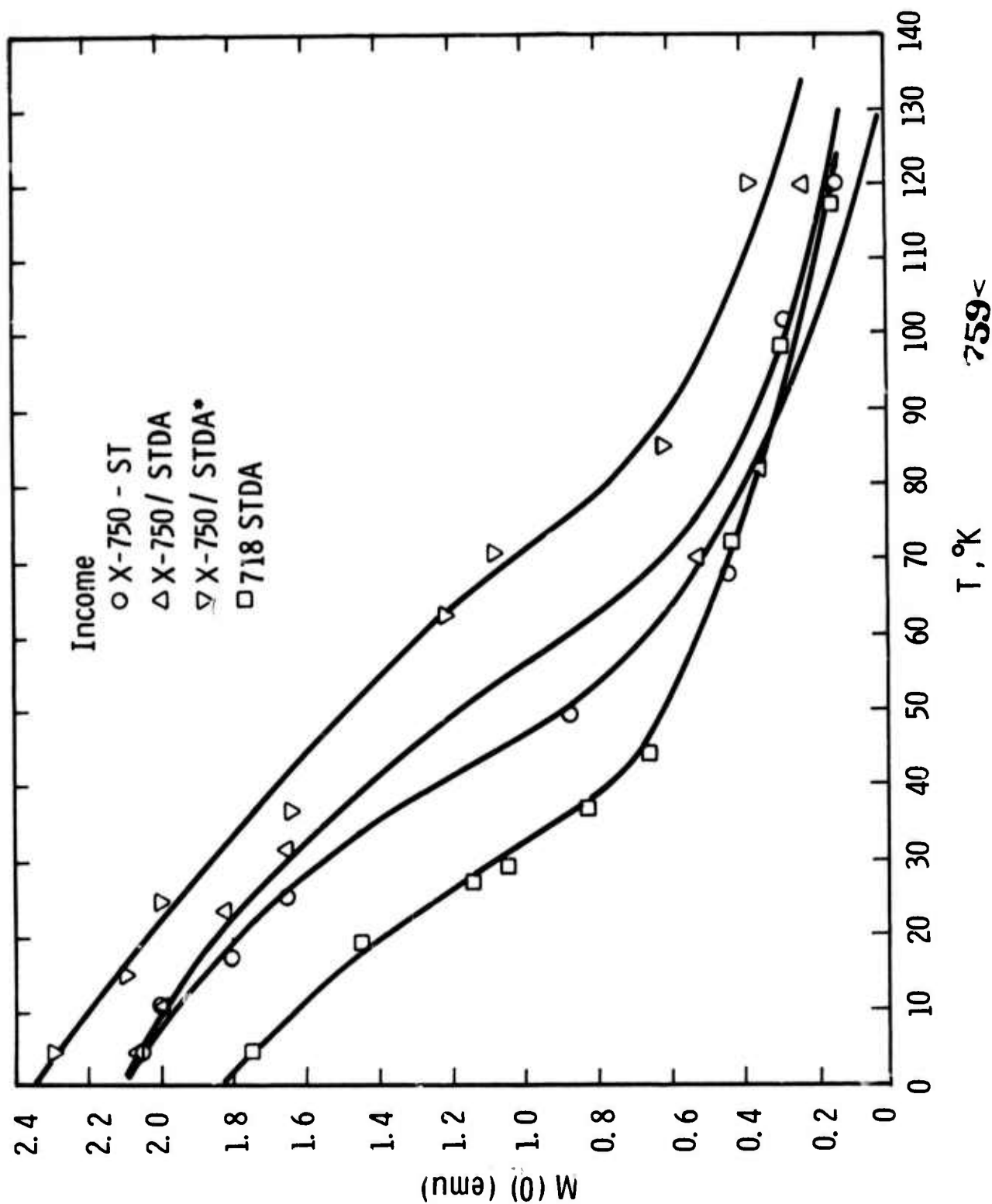


Fig. 8-29—Magnetic moment (extrapolated) as a function of temperature

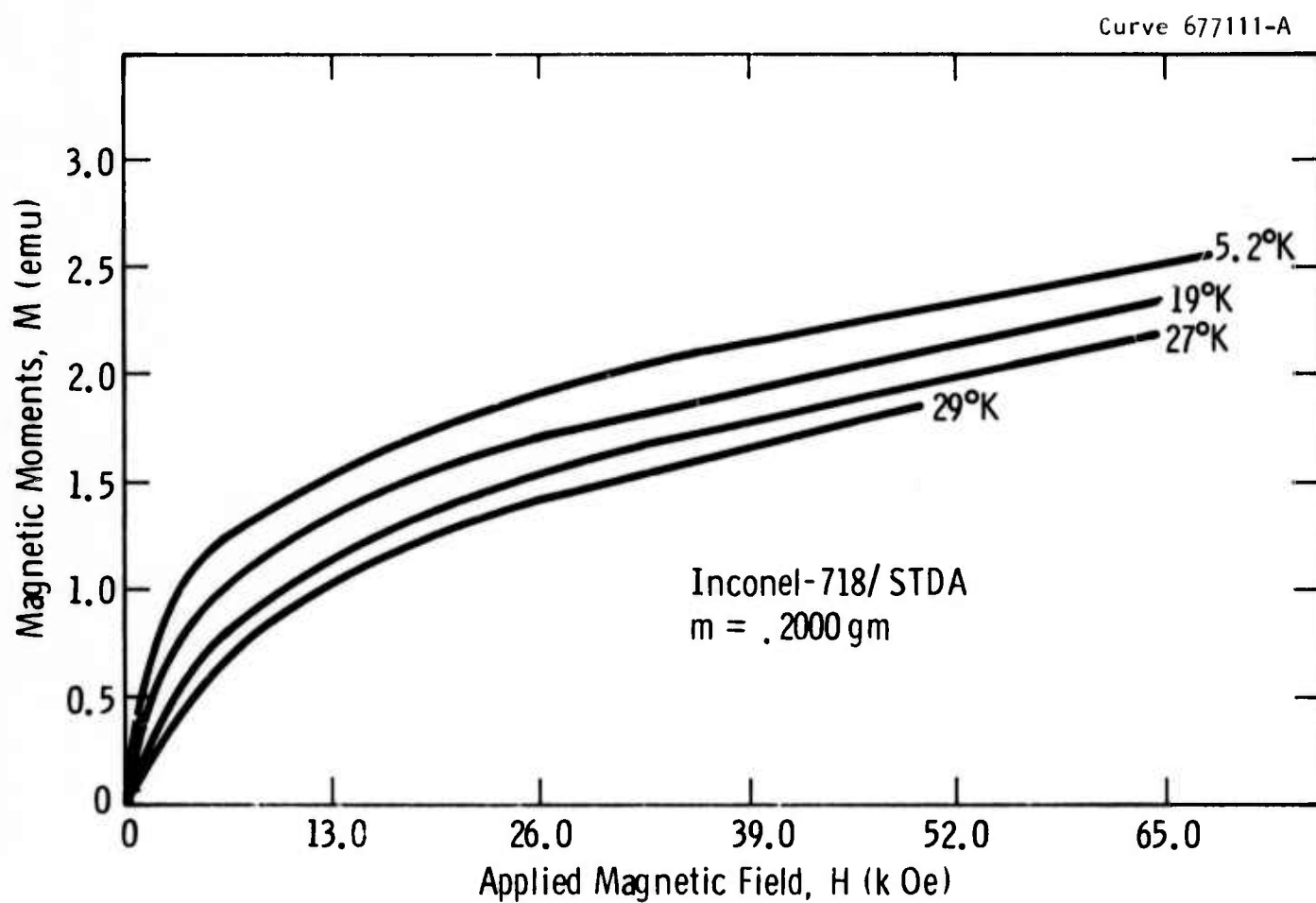


Fig. 8-30 — Magnetic moment as a function of external field at low temperatures

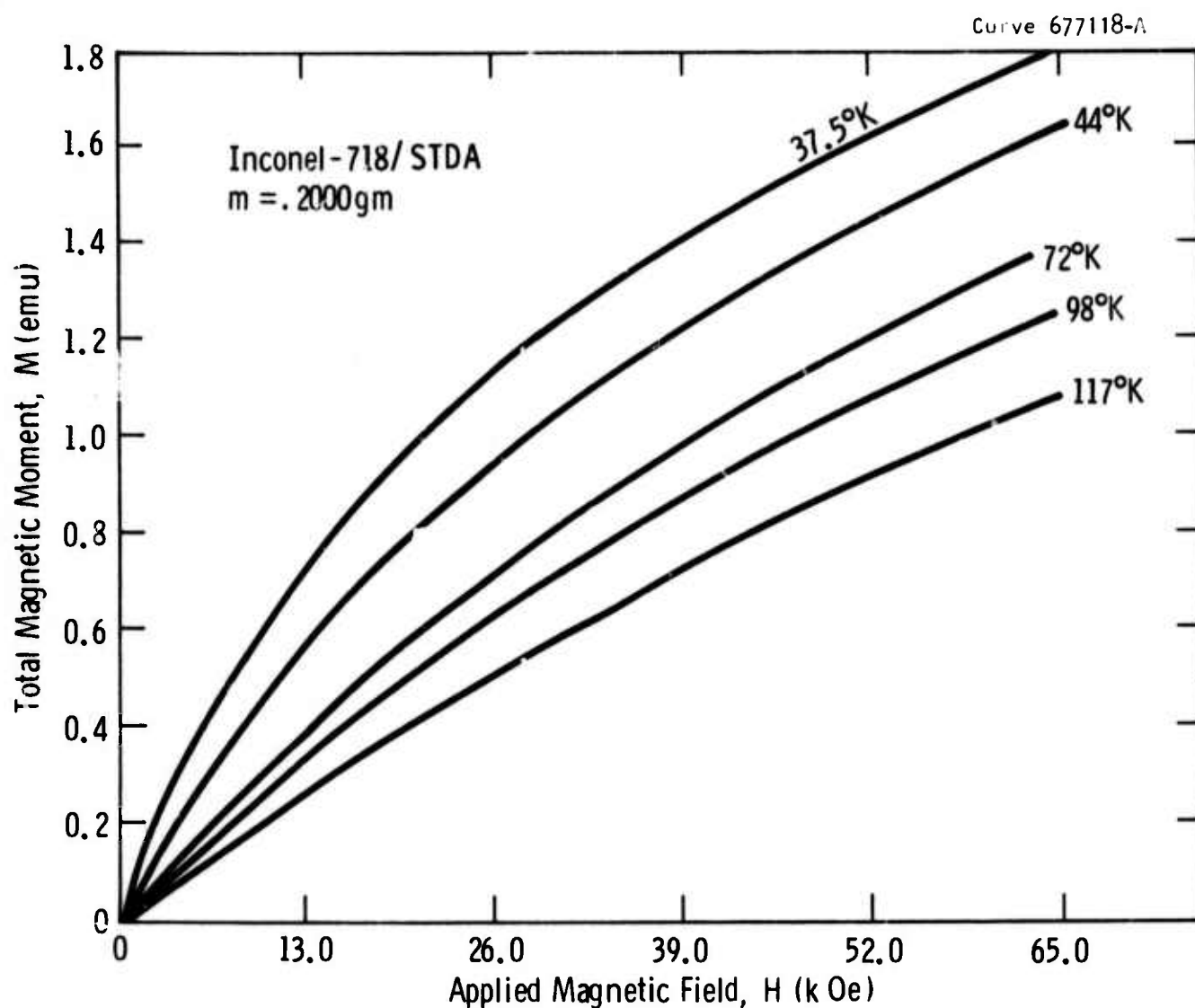


Fig. 8-31 — Magnetic moment as a function of external field



Curve 677103-A

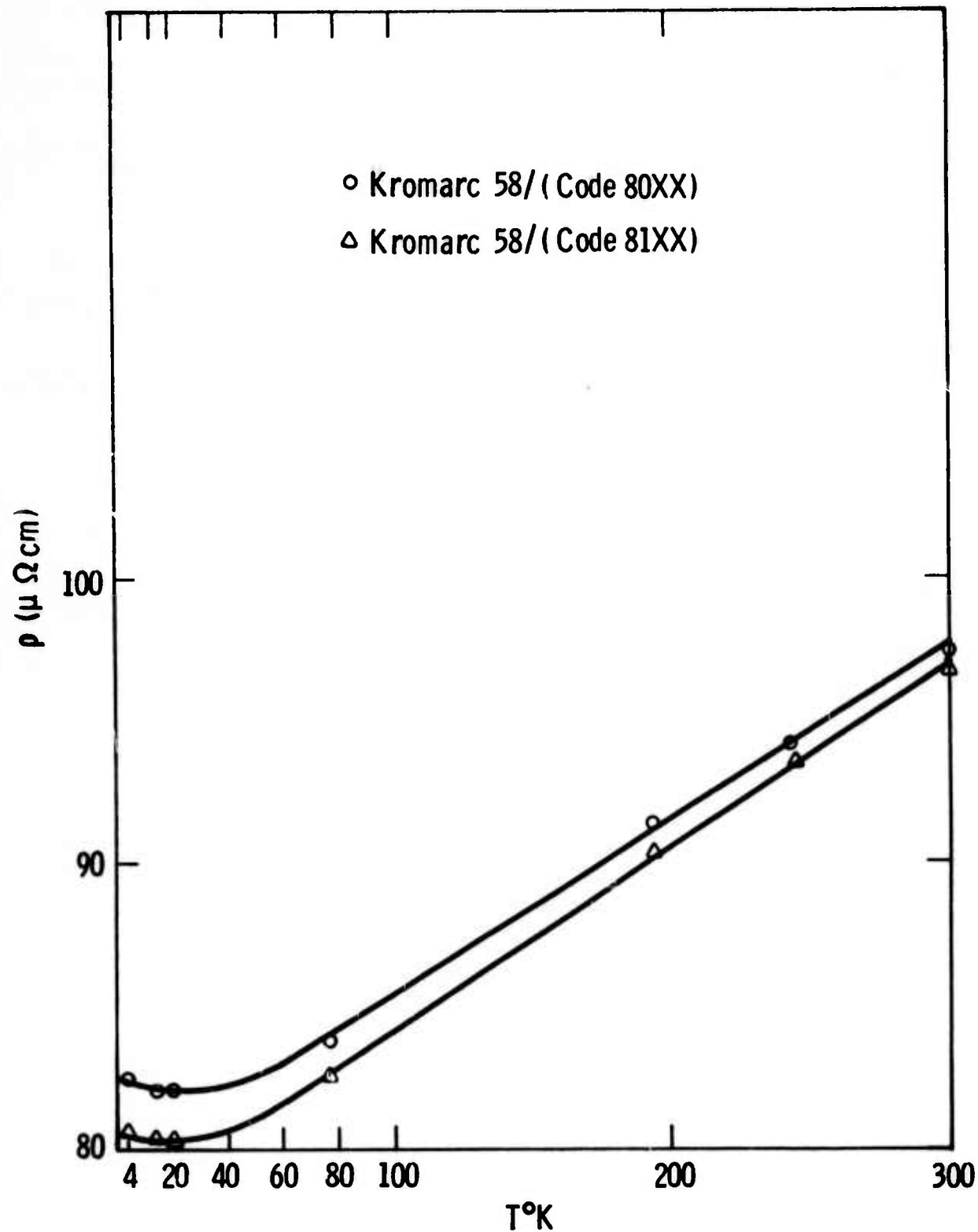


Fig. 8-32 — Resistivity as a function of temperature

762<

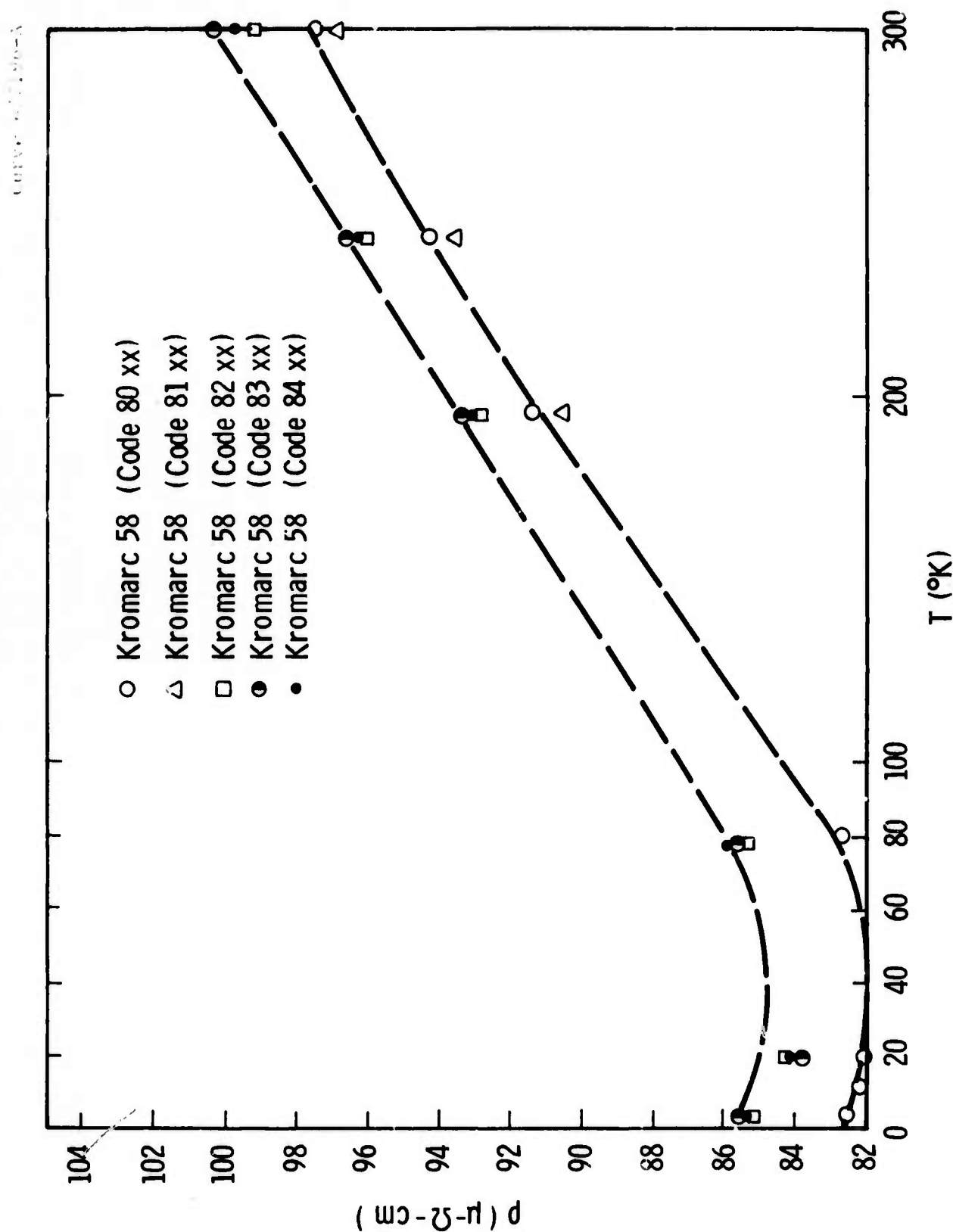


Fig. 8-33—Resistivity as a function of temperature

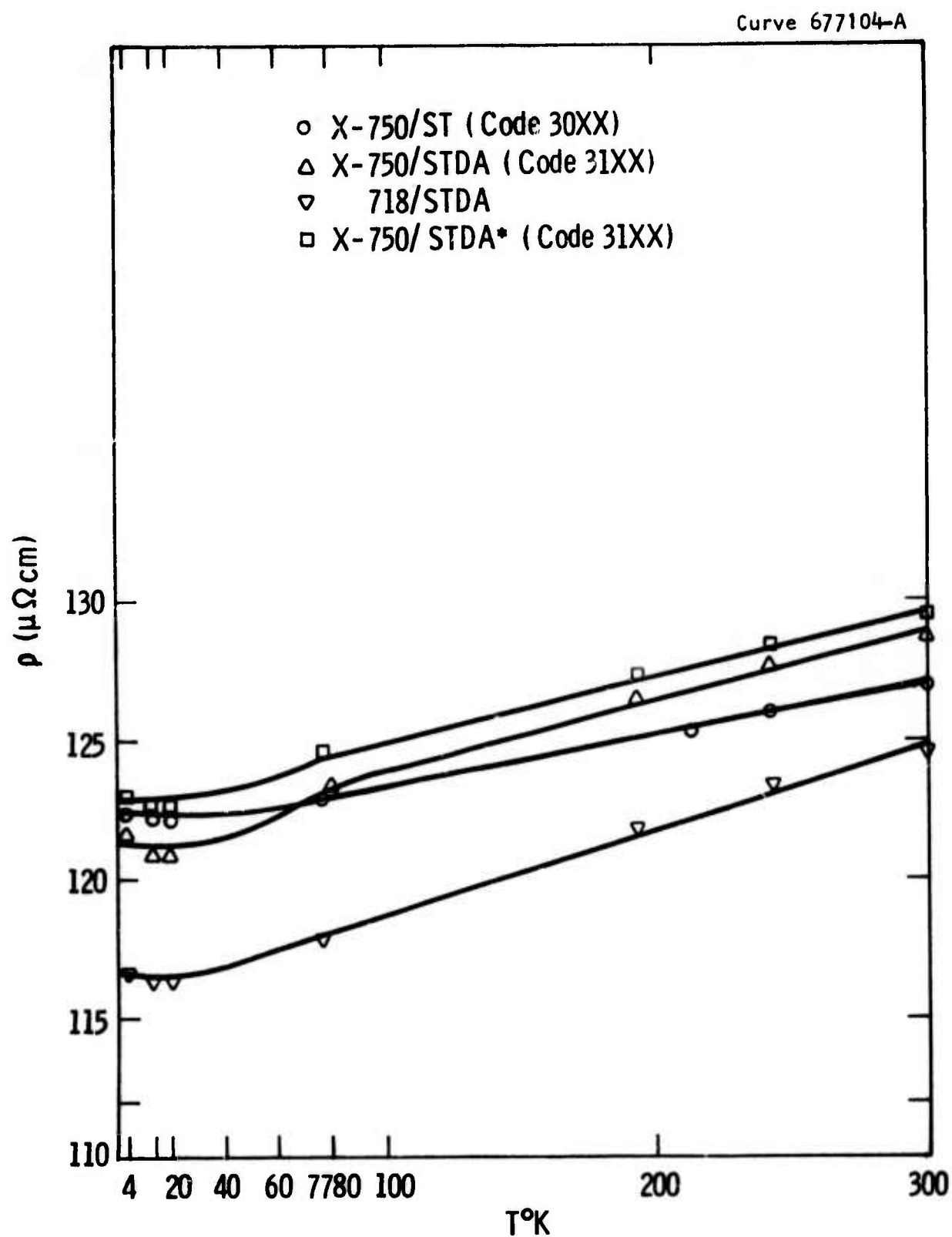


Fig. 8-34—Resistivity as a function of temperature

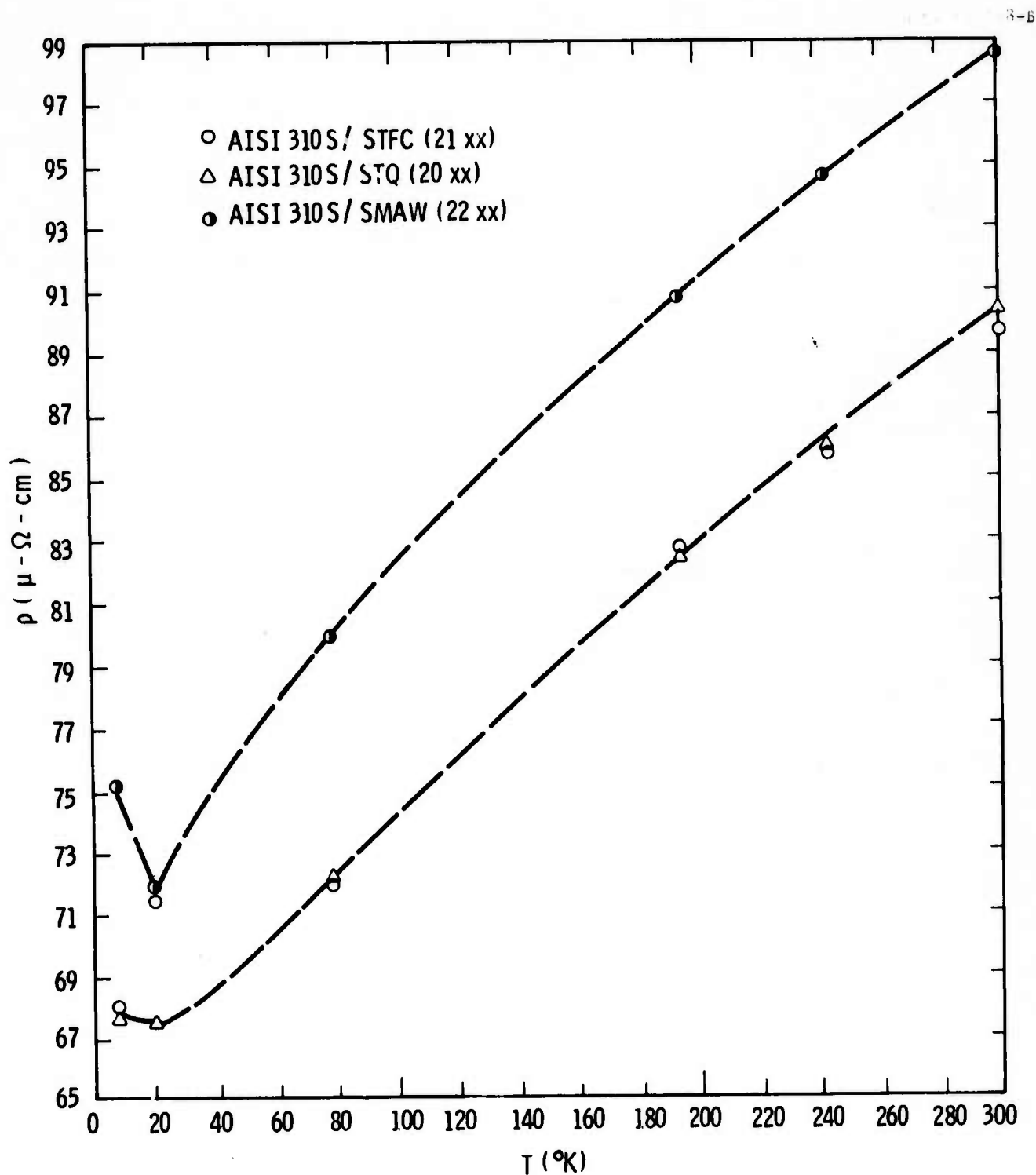


Fig. 8. 35—Resistivity as a function of temperature

#### ACKNOWLEDGMENT

The authors wish to greatly acknowledge the following Westinghouse personnel for their respective advice, contributions and cooperation in the conduct of this work:

Dr. J. H. Parker	E. T. Wessel
Dr. F. C. Hull	W. H. Pryle
J. L. McCabria	D. R. Young
D. C. Litz	R. R. Hovan
C. S. Cook	A. R. Petrush
R. M. Slepian	W. C. Halligan
M. W. Hagadorn	R. C. Brown
W. R. Lovic	H. N. Sopko
W. R. Kuba	P. J. Steve
R. L. Berrier	E. Superior
R. D. Obrokta	M. J. Larkin

Special acknowledgment is extended to the Huntington Alloy Product Division of the International Nickel Company, Inc., for providing the MP-2 and MP-3 Inconel X750 material and for their helpful comments regarding commercial melting and refining practices for this alloy.

## APPENDIX I -- ADDITIONAL KROMARC 58 DATA

The data presented in this appendix is taken from an unclassified Westinghouse Research Report No. 67-1D6-KROMA-R1 dated May 23, 1967. This report is titled "Cryogenic Tensile Properties of Cold Rolled Kromarc 58 Stainless Steel Sheet" and was authored by F. C. Hull. As Hull's data is not generally available in the outside literature and is felt to be of direct interest to this project, this data is included herein Appendix I as the original tables and figures of the above mentioned report.

### ABSTRACT

Tensile tests were run on Kromarc 58 steel 0.050" sheet at room temperature, -110, -320 and -423°F. The effect of the following variables on strength were investigated: cold rolling with 0, 30, 60 and 80% reduction of area; prior heat treatment at 1625 or 1950°F to establish two different grain sizes; comparison of notched and plain sheet properties; and aging. Strengths exceeding 300 ksi were obtained at -423°F with adequate ductility and absence of notch sensitivity. Because the austenite in Kromarc 58 does not transform to martensite even if it is deformed at liquid helium temperatures, the material is non-ferromagnetic and dimensionally stable. Kromarc 58 sheet should be useful for the construction of cryogenic equipment and vessels in which these characteristics as well as strength and weldability are needed.

TABLE 1

## COMPOSITION OF KROMARC 58 STAINLESS STEEL HEATS IN WEIGHT PER CENT

Heat No.	Cr	Ni	Mn	Mo	V	N	C	Si	B	Zr	S	P	Fe
XMM2367	15.9	19.9	10.4	2.28	.16	.17	.025	.67	.009	<.002	.014	.009	Bal.
XMM2390	15.9	19.9	10.8	2.33	.16	.19	.022	.11	.009	.013	.011	.001	Bal.



TABLE 2

EFFECT OF PRIOR ANNEALING TEMPERATURE, PER CENT REDUCTION,  
AND AGING TEMPERATURE ON THE HARDNESS OF KROMARC 58  
STAINLESS STEEL 0.050" SHEET

Prior Annealing Temp. °F (1 hr.)	Heat No.	Cold Work % RA	Diamond Pyramid Hardness - 30 Kg. Load			
			Aged 4 Hrs. 600°F	Aged 4 Hrs. 800°F	Aged 4 Hrs. 1000°F	Aged 4 Hrs. 1200°F
1950	2390	0	149	147	160	155
1950	2390	30	314	341	335	323
1950	2390	60	368	413	427	396
1950	2390	80	393	454	470	409
1950	2367	0	143	140	152	151
1950	2367	30	305	311	305	295
1950	2367	60	364	406	402	379
1950	2367	80	379	449	451	404
1625	2390	0	224	227	240	221
1625	2390	30	341	368	358	353
1625	2390	60	381	434	465	402
1625	2390	80	396	451	457	413
1625	2367	0	217	229	224	217
1625	2367	30	349	379	362	348
1625	2367	60	389	441	436	406
1625	2367	80	402	459	454	418



TABLE 3

**CRYOGENIC TENSILE PROPERTIES OF KROMARC 58 STAINLESS  
STEEL 0.050" SHEET OF HEAT NO. XM2390**

Prior Anneal 1 Hr. °F	Spec. No.	Cold Work % RA	Aging 4 Hrs. 1000°F	Test Temp °F	.01% Yield kpsi	.2% Yield kpsi	Ulti- mate kpsi	True Stress at Fracture kpsi	% Uniform Elong.	% Total Elong.	RA %	Notched: Ult. Str. Ratio	Hard- ness DPH
1625	5A-1	0	-	RT	64.9	70.5	115.0	253.0	35.8	43.2	63.3	-	224
	5A-2	0	-	-320	120.5	131.6	206.0	384.0	47.5	53.6	49.4	-	224
	5B-1	30	-	RT	127.3	152.0	160.4	208.5	1.7	9.8	33.2	-	341
	5B-2	30	-	-320	193.5	223.5	248.0	396.5	19.8	30.2	42.5	-	341
	6C-2	60	-	RT	155.0	178.0	186.6	260.0	1.1	6.6	40.8	-	381
	6C-3	60	-	-320	206.5	251.5	268.0	399.0	5.8	13.6	37.7	-	381
	6C-1	60	Yes	-320	220.0	259.2	277.0	390.5	7.3	15.4	33.8	-	465
	10C-1*	60	Yes	-320	226.5	254.0	270.0	379.5	4.9	12.1	33.6	-	436
	1-1	0	-	RT	37.1	41.5	100.7	199.4	52.9	62.5	59.0	-	149
	1-2	0	-	-110	50.6	57.6	120.0	232.0	52.9	58.8	56.1	-	149
1950	1-3	0	-	-320	91.3	101.0	184.6	380.0	74.5	81.5	54.0	0.87	149
	1-4	0	-	-423	113.2	128.0	210.0	350.5	-	56.0	40.0	-	149
	2-1	30	-	RT	114.8	136.5	144.0	227.5	1.9	13.0	49.9	-	314
	2-2	30	-	-320	175.7	205.0	235.0	384.5	26.9	37.6	43.5	1.12	314
	3-1	60	-	RT	135.5	165.0	174.5	244.5	1.3	6.6	42.5	-	368
	3-2	60	-	-320	218.5	242.0	259.0	380.0	7.8	19.2	37.7	1.14	368
	3-3	60	Yes	-320	214.5	244.0	264.0	374.0	6.7	14.7	34.4	-	427
	8C-1*	60	Yes	-320	205.0	239.5	264.5	392.5	12.7	20.2	37.2	-	402
	4-1	80	-	RT	150.6	174.6	186.3	250.0	1.2	6.3	41.7	1.05	393
	4-2	80	-	-110	166.5	207.0	219.0	293.0	1.3	7.4	38.0	1.08	393
	4-3	80	-	-320	215.5	252.5	272.0	385.0	1.8	8.8	35.1	1.05	393
	4-4	80	-	-423	261.0	288.0	304.0	369.0	-	1.2	17.5	1.04	393
	4-5	80	Yes	-423	256.0	287.0	312.5	429.0	-	2.5	27.1	1.06	470

Heat XM2390

270&lt;

TABLE 4

CRYOGENIC NOTCHED TENSILE PROPERTIES OF KROMARC 58  
STAINLESS STEEL 0.050" SHEET OF HEAT NO. XM2390  
PRIOR ANNEALING 1 HOUR AT 1950°F

Spec. No.	Cold Work % RA	Aging 4 Hrs. 1000°F	Test Temp °F	Nominal Strength, kpsi			True Stress at Fracture, kpsi	% RA
				First Detectable Yielding	Load/Original Area	Ultimate		
1-5	0	-	-320	106.8		159.5	196.7	30.9
2-3	30	-	-320	234.5		262.5	289.0	9.0
3-4	60	-	-320	262.0		296.5	305.5	2.9
4-9	80	-	-320	264.5		289.5	328.0	11.8
4-7	80	-	RT	176.3		198.3	237.0	16.6
4-8	80	-	-110	211.5		237.5	265.0	10.3
4-9	80	-	-320	264.5		289.5	328.0	11.8
4-10	80	-	-423	308.0		315.0	351.5	10.3
4-6	80	Yes	-423	317.5		331.5	372.5	11.1

TABLE 5  
TENSILE PROPERTIES OF TYPE 316 STAINLESS STEEL  
(SECTION B5 REFERENCE 7)

Material Condition	Test Temperature °F	0.2% Yield Strength, kpsi	Ultimate Strength, kpsi	Elongation %	RA %
Annealed	RT	31	85	54	69
	-110	44	100	64	67
	-320	76	158	65	53
	-423	102	180	45	36
60% RA by Cold Rolling	RT	153	175	3	--
	-320	202	230	18	--

172<

TABLE 6

## THERMAL EXPANSION OF KROMARC 58 STEEL

Temperature °F	$\frac{\Delta L}{L_0}$ , in./in. $\times 10^{-6}$	Thermal Expansion Coefficient in./in./°F $\times 10^{-6}$
75	0	8.7
50	- 245	
0	- 690	8.5
- 50	-1120	
-100	-1540	8.4
-150	-1960	
-200	-2310	6.4
-250	-2600	
-300	-2800	4.4

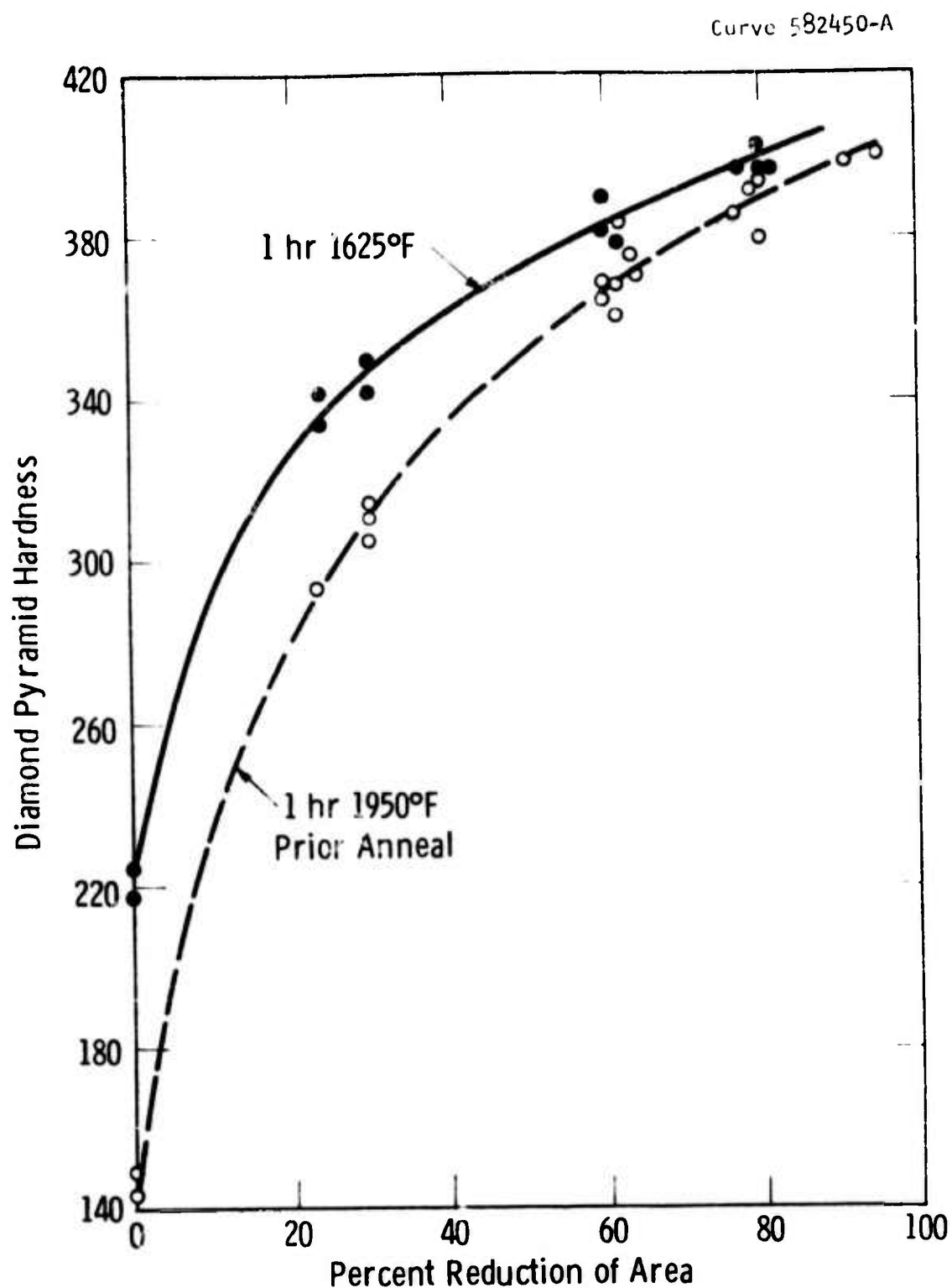


Fig. 1—Work hardening of Kromarc 58 stainless steel sheet during cold rolling

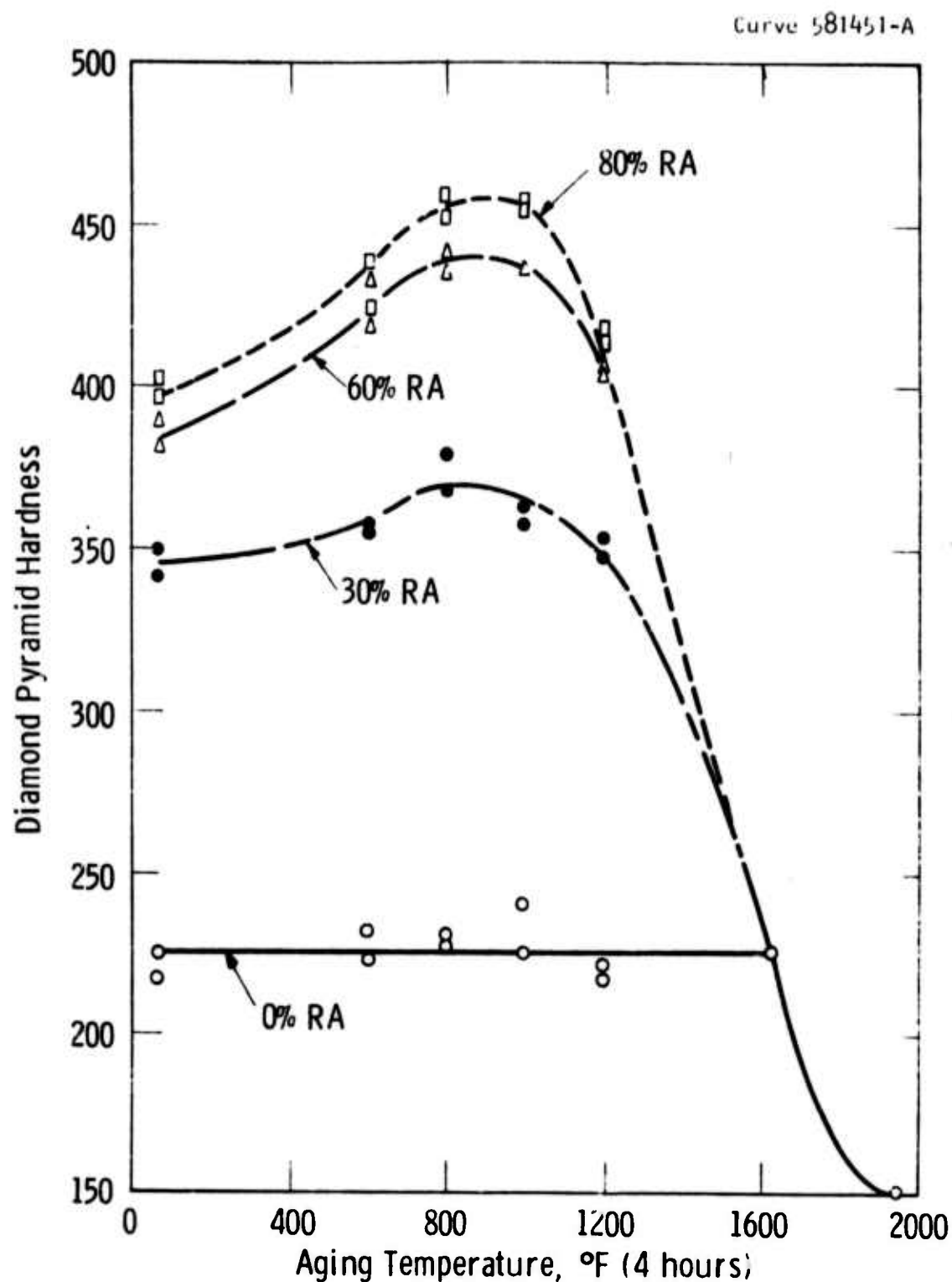
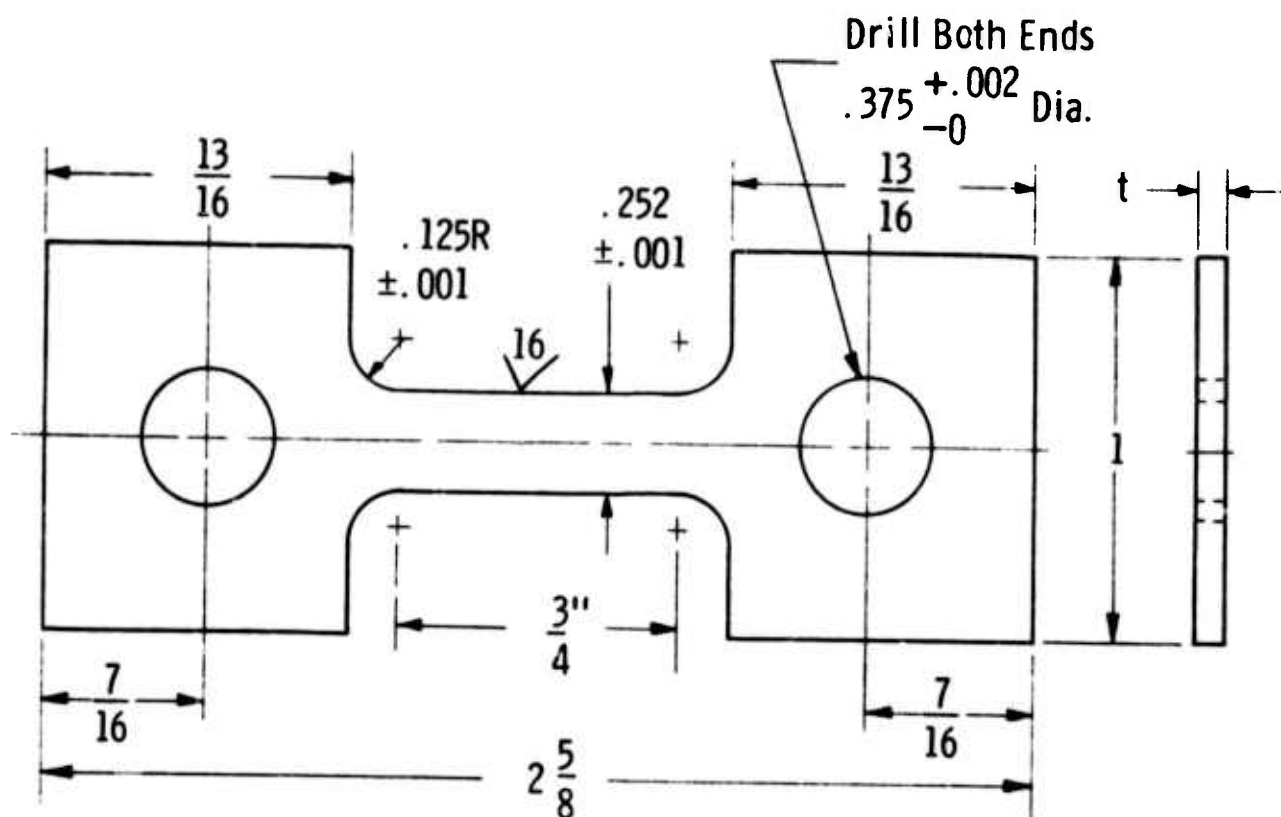


Fig. 2—Effect of cold work and aging temperature on the hardness of Kromarc 58 stainless steel 0.050" sheet.  
1 hour at 1625°F prior anneal

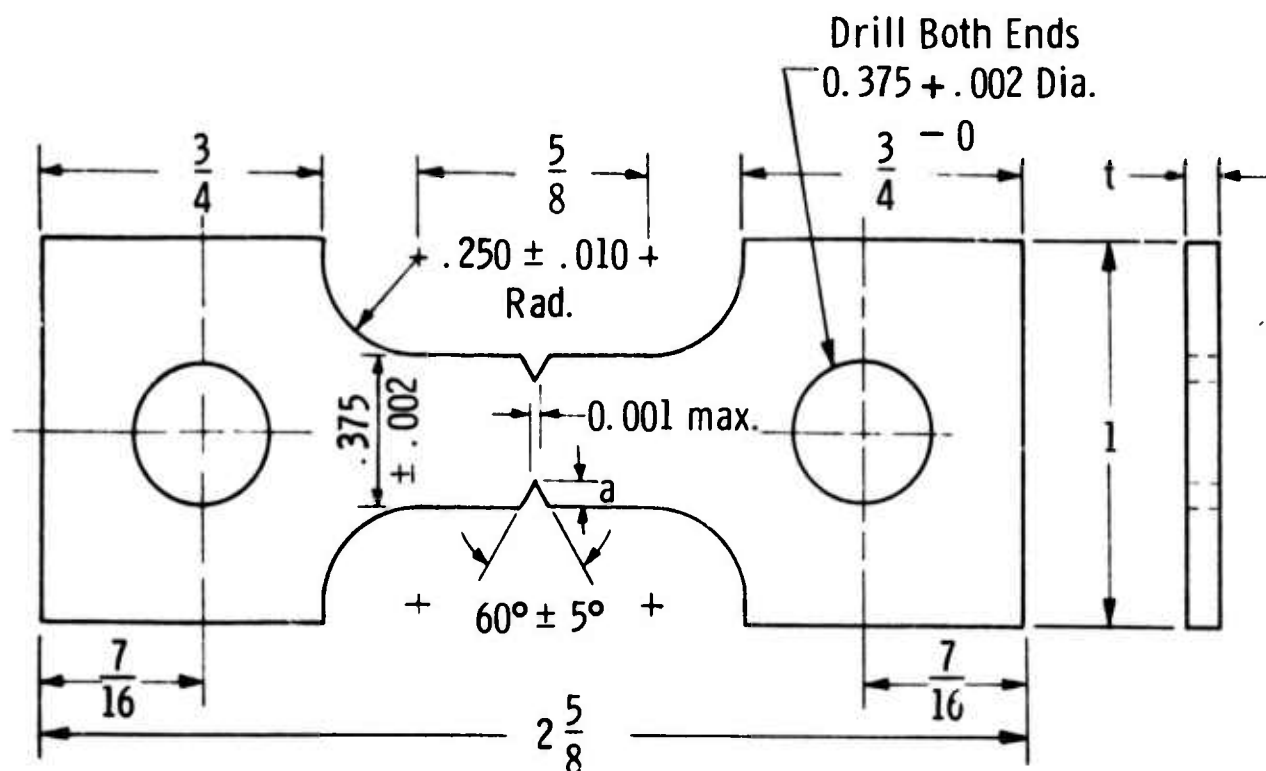
Dwg. 853A728



Notes:

1. Avoid undercutting fillets
2. All dimensions in inches
3. Center line of holes to be within 0.002 of center line of specimen gage length
4. No finishing required on flat faces

Fig. 3—Sheet tensile specimen



## Notes:

1. Notch root radius to be  $0.0035 \pm .0005$
2. Specimen thickness as furnished or specified.  
No finishing required on flat faces.
3. Notch depth,  $a = 0.065 \pm .002$
4. Notch root surface finish  $\sqrt{8}$
5.  $K_t = 6.3$
6. All dimensions in inches
7. Center line of holes to be within 0.002 of center line of specimen.

Fig. 4--Notched sheet tensile specimen



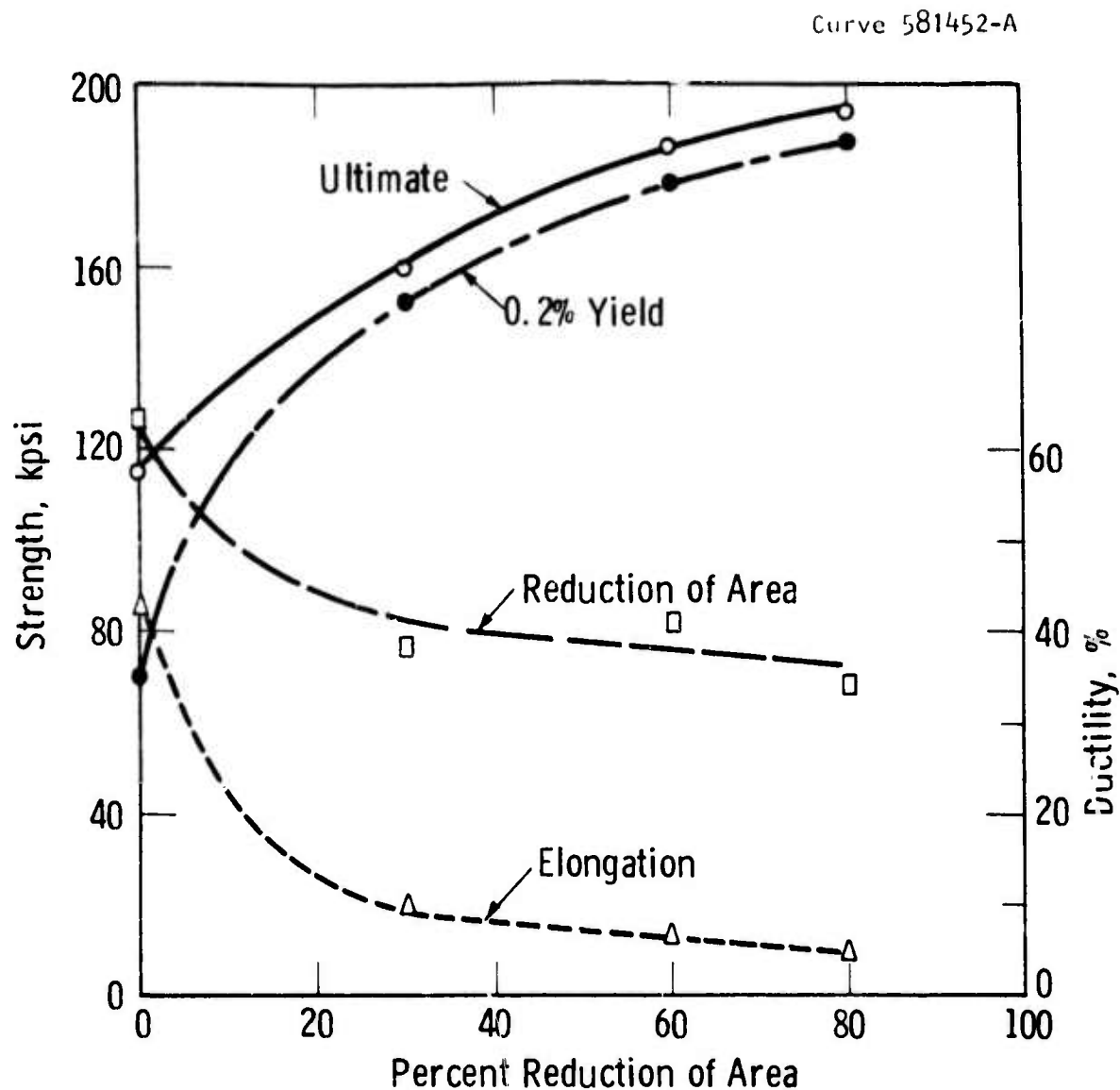


Fig. 5—Effect of cold work on the room temperature tensile properties of Kromarc 58 0.050" sheet. Heat MM2390 annealed 1 hour at 1625°F prior to rolling

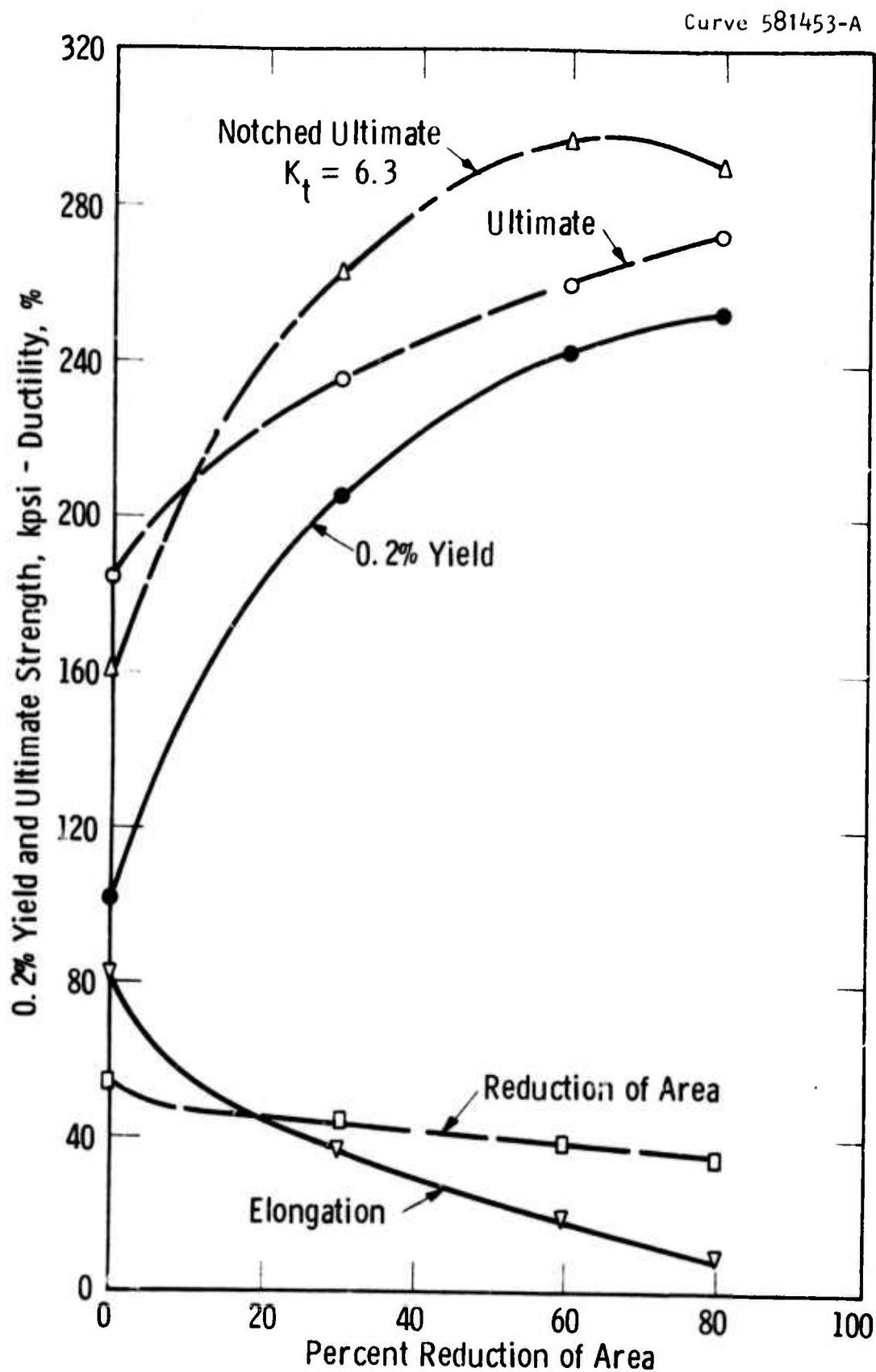


Fig. 6—Longitudinal tensile properties of cold-rolled Kromarc 58 sheet 0.050" thick at  $-320^{\circ}\text{F}$ . Heat MM2390 annealed 1 hour at  $1950^{\circ}\text{F}$

Curve 581454-A

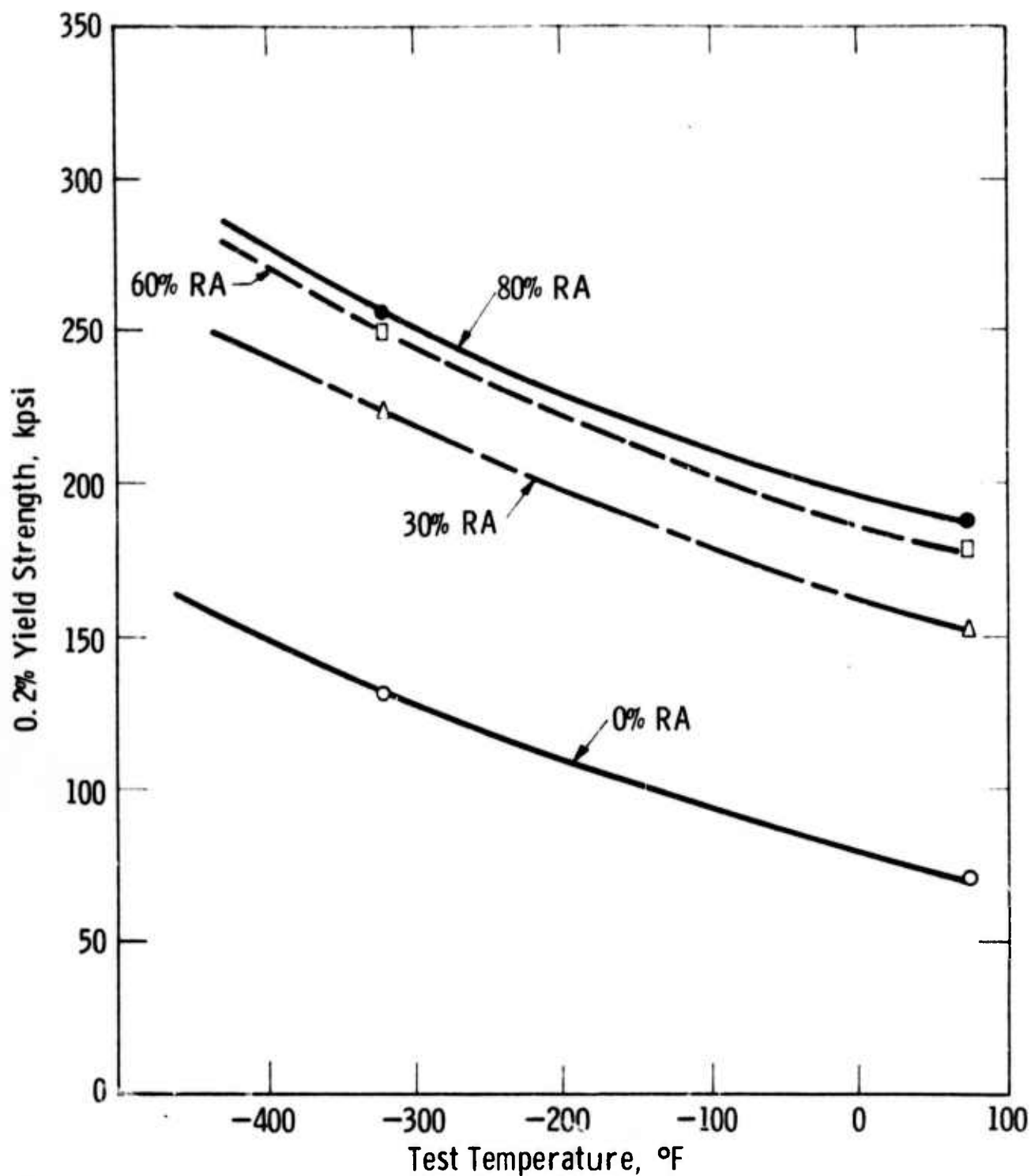


Fig. 7—Effect of cold work and test temperature on the yield strength of Kromarc 58 0.050" sheet of heat MM2390 annealed 1 hour at 1625°F

Curve 581455-A

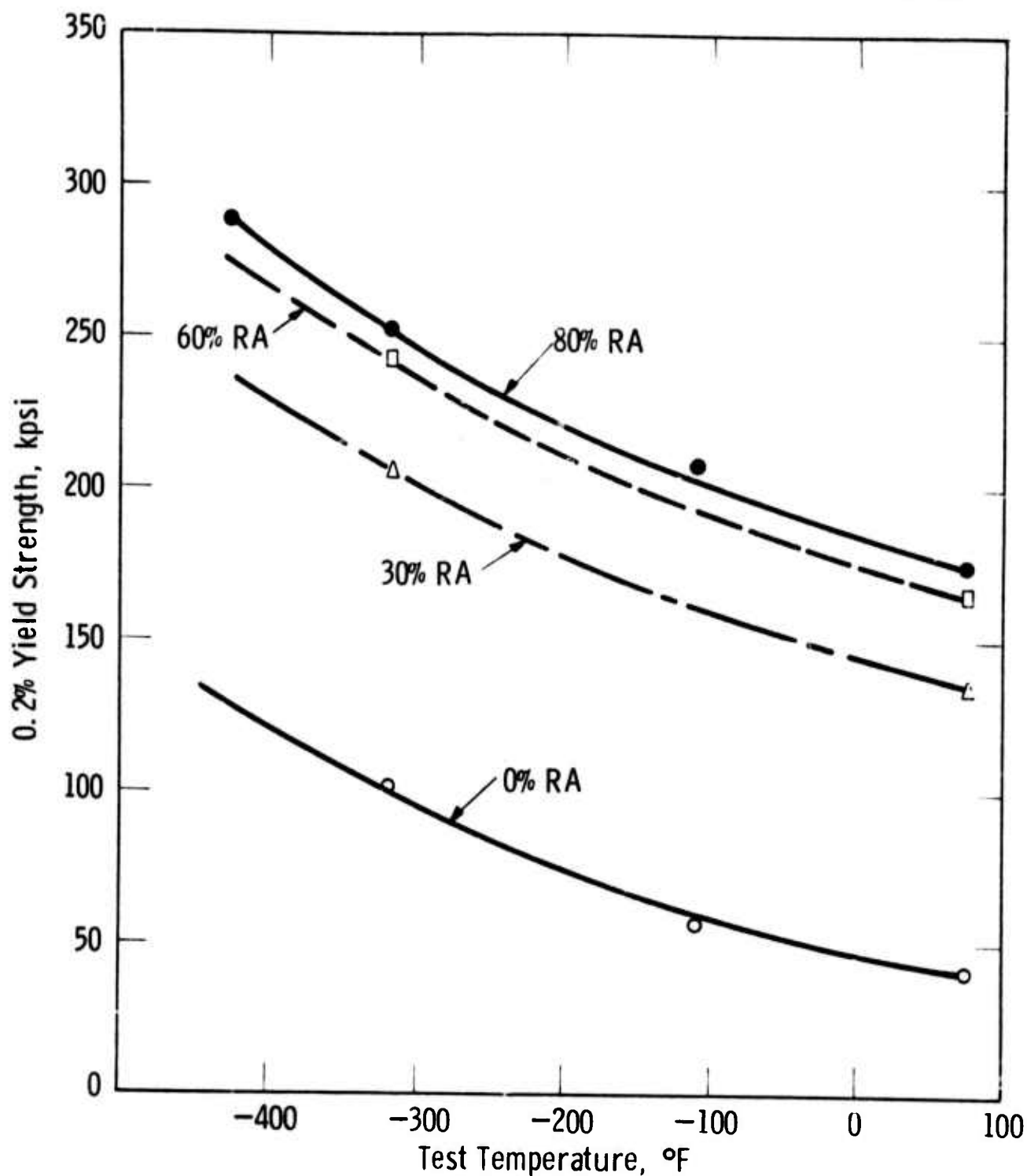


Fig. 8—Effect of cold work and test temperature on the yield strength of Kromarc 58 0.050" sheet of heat MM2390 annealed 1 hour at 1950°F

Curve 581456-A

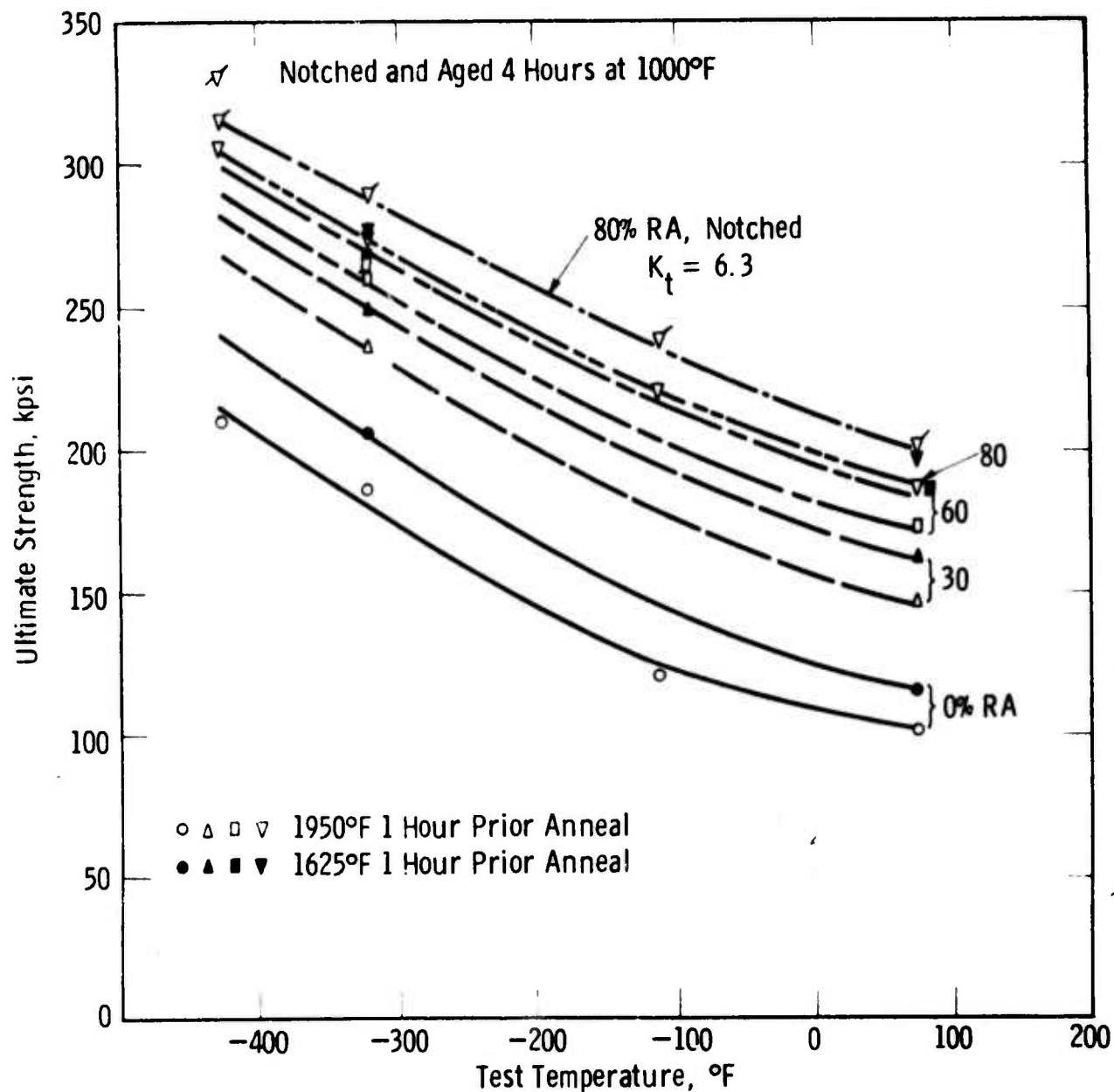


Fig. 9—Effect of prior annealing temperature, % cold work, notches, aging, and test temperature on the ultimate strength of Kromarc 58 0.050" sheet